



Whittier  
College

---

**Jordan C. Hanson**

Jordan C. Hanson  
*Assistant Professor*  
*Department of Physics and Astronomy*  
*13406 East Philadelphia Street*  
*Whittier CA 90602*  
*Email: jhanson2@whittier.edu*

July 1, 2022

Cover Letter: Application for Tenure

Greetings,

My name is Prof. Jordan C. Hanson, and I am currently an Assistant Professor in the Department of Physics and Astronomy at Whittier College. We are contacting you for your consideration as an external reviewer for our tenure and promotion process at Whittier College. This dossier contains my curriculum vitae, tenure and promotion guidelines, and my recent scholarship. Whittier College is a 130-year-old liberal arts college in Whittier, California, near East Los Angeles. We are recognized as a Title-V Hispanic Serving Institution (HSI) with a mission to provide access to higher education for historically marginalized students.

I have focused my scholarship on three broad areas: advancing the field of ultra-high energy neutrino (UHE- $\nu$ ) research as part of IceCube Gen2 (<https://wipac.wisc.edu>), RF engineering research through the Office of Naval Research (ONR: <https://www.nre.navy.mil>), and contributions to diversity, equity, and inclusion (DEI). It is important to note that, at Whittier College, we typically teach six courses per year. I make my research contributions while teaching physics, math, and computer science courses. I have found creative ways to deliver a unique and intellectually enriching environment for my students, often by connecting my research and teaching. I regularly involve undergraduate students in my research, and I have published scholarship with undergraduate authors.

Within this dossier, you will find several types of examples of my scholarship. These are primarily peer-reviewed journal articles in the UHE- $\nu$  and RF engineering areas, but also include *applied* scholarship produced with undergraduates. I provide descriptions of how the applied science or engineering concept connects to our mission at Whittier College, the ONR, and IceCube Gen2. The UHE- $\nu$  and RF engineering research for the ONR is categorized into five areas: computational electromagnetism (CEM), the Askaryan effect, RF antenna design and fabrication, Antarctic ice properties, and drones. The ONR research also adds workforce development in the form of interactive engineering courses.

Finally, I have included three examples of DEI contributions. First, I highlight my participation in the Artemis program, a STEM recruitment and research program for young women from local high schools. The second describes an DEI grant I have earned to develop a mobile application that will help foster inclusion and belonging in introductory STEM courses. The third is an example of my participation in the Whittier Scholars Program (WSP: <https://scholars.domains/>). This program allows students to customize a major within our curriculum, and the interdisciplinary results tend to diversify scholarship within fields by forming new connections.

I am grateful for your consideration, and we at Whittier College want to thank you for taking the time to read and process this dossier.

Sincerely,

Jordan C. Hanson

**Jordan C. Hanson, PhD**

Science and Learning Center, 212 • Dept. of Physics and Astronomy, Whittier College • Whittier, CA, 90602

• Office: 562-907-5130 • Mobile: 562-351-0047 • email: [jhanson2@whittier.edu](mailto:jhanson2@whittier.edu)*Member of the IceCube Gen2 Collaboration**Summer Faculty Research Fellow for the Office of Naval Research**Recipient of the CCAPP Post-doctoral fellowship at The Ohio State University*

---

<b>Position</b>	<b>Assistant Professor of Physics, Department of Physics and Astronomy, Whittier College, 2017-Present</b>
<b>Skills</b>	<i>Extensive experience in high-energy physics research, engineering research, physics education, mentorship, and committee service at Whittier College.</i> <ul style="list-style-type: none"><li>• <b>Physics instruction at high-school, college, and graduate levels: introductory and advanced level</b></li><li>• <b>Computer science teaching: digital signal processing, digital circuit design at college level</b></li><li>• <b>Mathematics teaching: elementary statistics at college level, developed the first summer online statistics program in Whittier College history</b></li><li>• Computational Electromagnetism (CEM) research in RF antenna and phased array design for IceCube Gen2 and the Office of Naval Research (Whittier College)</li><li>• Workforce development and reliability analysis for the Office of Naval Research (Whittier College)</li><li>• Terabyte-scale data analysis and high-performance computing (Ohio State Univ. and UC Irvine)</li><li>• Building simulations and mathematical physics models (Ohio State Univ. and Whittier College)</li><li>• Organizing and leading expeditions to Antarctica to deploy physics hardware (UC Irvine)</li><li>• Performing radio-frequency field measurements and anechoic chamber measurements in support of physics objectives (UC Irvine, Univ. of Kansas)</li><li>• RF circuit design and testing/validation (UC Irvine, Univ. of Kansas)</li><li>• Created the RF design lab at Whittier College; extensive experience in RF test bench equipment, e.g. oscilloscopes, vector network analyzers/spectrum analyzers, power meters, and signal generators (UC Irvine, Univ. of Kansas, OSU, Whittier College)</li><li>• Software skill: C++, Python, MATLAB, Octave, Jupyter, MEEP, WaveDROM, LaTeX</li><li>• Organizing workshops and conferences, public speaking, outreach coordination</li><li>• Organizing and operating STEM recruitment and research programs for young women from local high school students interested in studying STEM at Whittier College</li><li>• Recipient of DEI grant for application development to foster inclusion in introductory STEM courses</li><li>• Studying DEI in introductory STEM through Cottrell Scholars Network</li></ul>
<b>Education</b>	<ul style="list-style-type: none"><li>• Doctor of Philosophy (PhD), Physics, University of California, Irvine (March 2013)</li><li>• Master of Science (M.S), Physics, University of California, Irvine (August 2008)</li><li>• Bachelor of Science (B.S), Intensive Track, in Physics, Yale University (June 2007)</li></ul>
<b>Research Experience</b>	<u>Whittier College</u> Fall 2017 – Present <ul style="list-style-type: none"><li>• <b>Initiated a radio-frequency (RF) testing and design laboratory</b></li><li>• <b>Awarded three Summer Faculty Research Fellowships through the Office of Naval Research</b></li><li>• <b>Mentoring students in firmware and software design, electrical engineering</b></li><li>• <b>Mentoring students in mathematical physics research, publication on Askaryan radiation</b></li><li>• Helped a student create a firmware/software solution in order to upgrade ARIANNA detector boards</li><li>• Helped a student build a from-scratch drone, with designs for solar recharge and polar deployment</li><li>• Published research regarding RF propagation in polar ice and firn, interactions with ice/ocean floor</li><li>• Published mathematical physics model of Askaryan radiation with undergraduate researcher</li><li>• Developed a python-based FDTD model of broadband RF phased arrays for Navy radar testing with two undergraduate researchers</li><li>• Participated in workshop series entitled “Inclusivity in Introductory STEM Courses” through the Cottrell Scholars Network, research focusing on methodology for boosting inclusion and belonging in Introductory STEM courses for marginalized students</li><li>• Received Whittier College DEI grant for application development to boost inclusion in introductory STEM courses</li></ul>

- Created a fully analytic model of the Askaryan effect adopted by the physics community
- Leading the data analysis to discover the world-record highest energy neutrinos
- Organized a workshop at Ohio State pertaining to improved analysis efficiency and machine learning
- Investigating ways to use smartphones as cosmic ray detection arrays

University of Kansas

Spring 2013 – Fall 2015

- Simulated radar-echoes of cosmic ray extensive air showers for the TARA collaboration
- Deployed radar detectors as part of the TARA remote station program
- Performed anechoic chamber measurements to calibrate the ARIANNA and TARA detectors
- Gained teaching and mentoring experience through the QuarkNet program
- Created and taught a summer physics course

University of California, Irvine

Summer 2007 - Spring 2013

- Designed, constructed, tested, and deployed the first ARIANNA neutrino detector in Antarctica
- Led the analysis of the first data collected by ARIANNA stations, constraining the ultra-high energy cosmogenic neutrino flux
- Independently organized and led expeditions to Antarctica to perform glaciological measurements in support of physics objectives
- Ran high-performance computing (HPC) codes, using machine learning, to train software to distinguish low-SNR impulses from RF thermal noise

Yale University

Summer 2006

- Performed Monte Carlo calculations of the interaction length of relativistic electrons in super-fluid helium in support of the XENON dark-matter detector innovation
- Designed a laser-scanning system to reveal helium molecules in superfluid helium

Los Alamos National Laboratory

Summer 2005

- Measured the muon Cherenkov tank event-rates over an altitude range of 0-14,000 ft. from the base to the summit of Mt. Evans, in Colorado, as part of the Milagro collaboration (now High Altitude Water Cherenkov detector)
- Compared results to cosmic-ray theory and presented at Milagro collaboration meeting

**References**

- Amy Connolly, PhD ... Prof. of Physics, The Ohio State University
- Steven Barwick, PhD ... Prof. of Physics, University of California, Irvine
- Dave Besson, PhD ... Prof. of Physics, University of Kansas
- Albrecht Karle, PhD ... Prof. of Physics, University of Wisconsin
- Gary Yeakley ... Retired Engineer at the Naval Surface Warfare Center, Corona, CA
- Jeffery Benson... Engineer at the Naval Surface Warfare Center, Corona, CA
- Allan Halgren, PhD ... Professor of Physics at Uppsala University, Uppsala, Sweden
- Stephanie Wissel, PhD ... Professor of Physics at Pennsylvania State University, State College, PA

**Published  
Papers**

\*Primary or  
Corresponding  
author

- \*J.C. Hanson and R. Hartig “Complex Analysis of Askaryan Radiation: A Fully Analytic Model in the Time-Domain” *Physical Review D*, **105** 123019 (2022).
- The RNO-G Collaboration “In situ, broadband measurement of the radio frequency attenuation length at Summit Station, Greenland” arXiv:2201.07846 (2022). *Accepted for publication in the Journal of Glaciology.*
- \*J.C. Hanson “Broadband RF Phased Array Design with MEEP: Comparisons to Array Theory in Two and Three Dimensions” *Electronics Journal (MDPI)* **10** 4 (2021). *Acknowledged by editor as one of the top 10 papers in Electronics Journal for Dec. 2020 to May. 2021.*
- \*J.C. Hanson “Broadband RF Phased Array Design for UHE neutrino detection.” Proceedings of 37<sup>th</sup> International Cosmic Ray Conference, Berlin, Germany (2021).
- The RNO-G Collaboration “Design and sensitivity of the Radio Neutrino Observatory in Greenland (RNO-G)” *Journal of Instrumentation* **16** P03025 (2021).
- The ARIANNA Collaboration. “Probing the Angular and Polarization Reconstruction of the ARI-

- ANNA Detector at the South Pole.” Journal of Instrumentation (JINST) **15** (2020) p. 09039
- C. Glaser *et al* “NuRadioMC: simulating the radio emission of neutrinos from interaction to detector.” European Physical Journal C (**80**) n. 77 (2020).
- The ARIANNA Collaboration. “White Paper: ARIANNA-200 high energy neutrino telescope.” arXiv:2004.09841
- The ARIANNA Collaboration. “Neutrino Vertex Reconstruction with In-Ice Radio Detectors using Surface Reflections and Implications for the Neutrino Energy Resolution.” Journal of Cosmology and Astroparticle Physics (JCAP) **11** (2019) p. 030
- The ARIANNA Collaboration. “A Search for Cosmogenic Neutrinos with the ARIANNA Test-Bed using 4.5 Years of Data.” Journal of Cosmology and Astroparticle Physics (JCAP) **03** (2020) p. 053
- \*J.C. Hanson et al. “Observation of classically ‘forbidden’ electromagnetic wave propagation and implications for neutrino detection.” Journal of Cosmology and Astroparticle Physics. (**2018**) (2018)
- P. Allison et al. “Measurement of the real dielectric permittivity  $\epsilon_r$  of glacial ice.” Astroparticle Physics Journal **108** (2019) pp. 63-73
- \*J.C. Hanson and A. Connolly. “Complex Analysis of Askaryan Radiation: A Fully Analytic Treatment including the LPM effect and Cascade Form Factor.” Astroparticle Physics. (**91**) pp. 75-89 (2017).
- The ARIANNA Collaboration. “Radio detection of air showers with the ARIANNA experiment on the Ross Ice Shelf”, Astroparticle Physics (**90**) pp. 50-68 (2017).
- The TARA Collaboration. “First Upper Limits on the Radar Cross Section of Cosmic-Ray Induced Extensive Air Showers”, Astroparticle Physics (**87**) pp. 1-17 (2017).
- The ARIANNA Collaboration. “Live-time and sensitivity of the ARIANNA Hexagonal Radio Array.” Proceedings of the International Cosmic-Ray Conference 2015, The Hague, The Netherlands (2015).
- The ARIANNA Collaboration. “Performance of the ARIANNA Hexagonal Radio Array.” Proceedings of the International Cosmic-Ray Conference 2015, The Hague, The Netherlands (2015).
- The ARIANNA Collaboration. “A First Search for Cosmogenic Neutrinos with the ARIANNA Hexagonal Radio Array.” Astroparticle Physics Journal (70) pp. 12-36 (2015)
- \*J.C. Hanson et al. “Time-Domain Response of the ARIANNA Detector.” Astroparticle Physics Journal (62) pp. 139-151 (2015).
- \*J.C. Hanson et al. “Radar absorption, basal reflection, thickness and polarization measurements from the Ross Ice Shelf, Antarctica.” Journal of Glaciology (**61**) 227, pp. 438-446(9) (2015)
- The ARIANNA Collaboration. “Design and Performance of the ARIANNA HRA-3 Neutrino Detector Systems.” IEEE Transactions on Nuclear Science (**62**) 5 pp. 2202-2215 (2015).
- The TARA Collaboration. “Telescope Array Radar (TARA) observatory for Ultra-High Energy Cosmic Rays.” Nuclear Instrumentation and Methods in Physics Research, A (**767**) 322-338 (2014).
- S. Kleinfelder et al. “Design and Performance of the Autonomous Data Acquisition System for the ARIANNA High Energy Neutrino Detector.” IEEE Transactions on Nuclear Science (**60**) 2, 612-618 (2013).
- \*J.C. Hanson, for the ARIANNA Collaboration. “Ross Ice Shelf Thickness, Radio-Frequency Attenuation and Reflectivity: Implications for the ARIANNA UHE Neutrino Detector”. Proceedings of the 32<sup>nd</sup> International Cosmic Ray Conference, Beijing, China (2011).
- L. Gerhardt, S.R. Klein, T. Stezelberger, S.W. Barwick, K. Dookayka, J.C. Hanson, R. Nichol. “A prototype station for ARIANNA: A detector for cosmic neutrinos.” Nuclear Instrumentation and Methods in Physics Research, A (**634**) 85-91, (2010).
- W.G. Rellergert, S.B. Cahn, A. Garvan, J.C. Hanson, W.H. Lippincott, J.A. Nikkel, and D.N. McKinsey. “Detection and Imaging of He<sub>2</sub> Molecules in Superfluid Helium.” Physical Review Letters (**100**) 025301 (2008).

## Invited Lectures

- Invited to teach source entitled “Introduction to GPS Signals for Onboarding of Navy Personnel” (2022). *In service of the Office of Naval Research.*
- Invited to teach source entitled “RF Field Engineering: A practical introduction” (2021). *In service of the Office of Naval Research.*
- “IceCube-Gen2 Radio Array Surface Calibration: Opportunities from Unique Transmitter and Receiver Systems” (2021). *IceCube Generation 2 Calibration Workshop.*
- “Finite Difference Time-Domain Methods for Askaryan Propagation Modeling in IceCube-Gen2” (2021). *IceCube Generation 2 Calibration Workshop.*
- “Classically Forbidden Askaryan Radiation: A decade of exploration in Antarctica in the search for

- cosmic neutrinos” (2018) *Departmental Colloquium for Whittier College*
- “Ultra-high Energy Neutrinos, Antarctica, Greenland, and the Askaryan Effect: A Summary.” (2016) *Invited speaker for the particle physics seminars at Weizmann Institute, Rehovot, Israel, and at Technion University, Haifa, Israel.*
- “Ultra-high Energy Neutrinos, Antarctica, Greenland, and the Askaryan Effect: A Summary.” (2016) *Invited speaker to the TeV Particle Astrophysics (TeVPA) conference at CERN, Geneva, Switzerland.*
- “A Review of UHE neutrino detection using the Askaryan effect.” (2016) *Invited speaker to the Very High Energy particle Astrophysics (VHEPA) conference at the University of Hawaii, Honolulu, Hawaii.*
- “A Review of UHE neutrino detection using the Askaryan effect.” (2016) *Invited speaker to the KICP Workshop, UHEAP 2016, University of Chicago, Chicago, IL.*
- “A Review of UHE neutrino detection using the Askaryan effect.” (2015) *Invited speaker to the KICP Workshop on the Giant Radio Array for Neutrino Detection, University of Chicago, Chicago, IL.*
- “Future Prospects of UHE neutrino detection with Electromagnetic Fields.” (2014) *Invited speaker to the Very High Energy particle Astrophysics (VHEPA) conference at the University of Tokyo (Kashiwa), Kashiwa, Japan.*
- “Searching for Cosmic Rays with the Telescope Array Radar Experiment.” (2014) *Department colloquium at the University of Kansas.*
- “Ultra-high Energy Neutrino Detection in Antarctica with ARIANNA and ARA.” (2013) *Invited seminar in High Energy Physics at the University of Wichita.*
- “Under-water and Under-Ice Neutrino Astronomy.” (2013) *Invited speaker to the 14<sup>th</sup> ICATPP Conference on Astroparticle, Particle, Space Physics and Detectors for Physics Applications, Villa Olmo, Como, Italy.*
- “Developing the Next Generation of UHE Neutrino Detectors in Antarctica.” (2012) *Seminar in High Energy Physics at the University of Kansas.*

## Service

- **Whittier College Committees:**
  - Enrollment and Student Affairs Committee (ESAC), 2018-2020
  - Educational Resources and Digital Liberal Arts Committee (ERC/DLAC), 2020-2021.
  - Educational Policy Committee (EPC), 2021-present
  - Appointed to Whittier Scholars Program Advisory Board, present
  - Artemis Program: STEM recruitment and training for young women in local area high schools
- **Service to the Navy:**
  - Creating online course for engineers in the Navy tasked with maintaining radar and RF infrastructure (2021-present)
- **Whittier College Awards:**
  - Student Life Award for Outstanding Organization Adviser, CRU (Campus Crusade Christian Fellowship), 2018
- Public Panels and Lectures:
  - The Artemis Program: Introducing high-school aged women to physics research at Whittier College 2019-2020 and 2020-2021.
  - “Hunting for Wild Antarctic Astroparticles.” Los Nietos Middle School, Los Nietos, CA (2018)
  - “Our Home.” (2016) *Upper Arlington Library Summer Astronomy Series.*
  - “Experimental Particle Astrophysics in Antarctica.” (2016) *New Vistas in Astronomy Public Lecture Series, Columbus Astronomical Society. Columbus, OH.*
  - “The Martian.” *Participated in a public question/answer panel following screening of The Martian at The Gateway Independent Theater.*
- Current Volunteer Work
  - Volunteer as a Knight of Columbus, Our Lady of the Miraculous Medal Parish, Montebello, CA (2017-present)
    - Repairing parish buildings and fundraising for parish
  - Volunteer at the Knights of Columbus, St. Matthew the Apostle Parish, Gahanna, OH (2016-2017):
    - Serving food for the homeless at YWCA Women and Family Center
    - Volunteer at Columbus Catholic Diocese Soccer Tournament
    - Volunteer Cook/Dishwasher, St. Matthew’s Parish Annual Fish Fry
  - Volunteer, Ohio State Department of Astronomy Observatory (2015-present) (public observing)

- *Providing and operating a 114-mm Newtonian reflector for public observing*
- Instructor for Young Scholars Program (YSP), Ohio State Department of Physics
- Volunteer at the Knights of Columbus, St. John the Evangelist Parish, Lawrence, Kansas (2013-2015)
  - *Volunteer Cook/Dishwasher, St. John's Parish Annual Fish Fry*
  - *Volunteer Groundskeeper, St. John's Parish*

**Tenure and Promotion Guidelines**  
**Physics and Astronomy Department**  
**Whittier College**

## **Teaching**

Physics and Astronomy Department expects, in general, all its faculty members to teach the full load of courses, unless some other arrangement is agreed upon, with the approvals of the Dean of Faculty and the department. Faculty members are expected to contribute not only to the physics major program but also to our college's Liberal Education program by developing, designing, and teaching Lib-Ed courses such as Connections 1, Connections 2, and Communications 1.

Physics and Astronomy faculty must strive to establish excellent teaching practices regardless of their year or rank, as evaluated and judged by their students and colleagues.

## **Advising**

Physics and Astronomy faculty are encouraged to mentor students at least once during their probation period. In general, all Physics and Astronomy faculty are expected to share the advising load of the department as equitably as the circumstances would allow.

## **Service**

All our faculty must participate in our campus-wide faculty-governance system by serving on faculty committees. Tenure-track faculty are encouraged, but not required, to participate in the major committees. Post-tenure promotion seeking faculty are expected to serve on at least one of the major faculty committees, such as the Faculty Executive Council (FEC) or the Faculty Personnel Committee (FPC).

## **Research/Scholarship**

### For Tenure and/or Promotion to Associate Professor

The tenure-track candidate must strive to be a productive researcher/scholar in accord with the relevant Boyer category of scholarship as outlined and explained in the College Faculty Handbook. The Faculty Personnel Committee (FPC) leaves the extent and nature of the research/scholarship demonstration that is expected of every faculty member who is up for tenure to individual departments.

To this end, the following is the expectations, in tangible terms, of the Department of Physics and Astronomy from its tenure-seeking candidate regarding research/scholarship category.

We expect our tenure-track faculty to establish a sustainable research program on campus — although it can be part of a collaboration with external institutions such as research universities and national research labs — that will enable meaningful and high-quality research to take place in our department. To ensure that that is the case, the following requirements exclude any work completed elsewhere by the faculty member prior to his/her appointment by our department. Having said that, the faculty member can engage in research that is a continuation of his/her prior work, and that, if published, will perfectly count toward satisfying the following criteria.

By the end of his/her probationary period, the tenure candidate shall have created at least 3 externally peer-reviewed products. These can be:

- i- Three scientific journal articles in the main research area of the candidate, or
- ii- Two such articles and one external grant for which the candidate is a major and indispensable contributor.

With the approval and discretion of the department, any one of the following would also be an acceptable demonstration of research/scholarship:

- i- One peer-reviewed scientific journal article and one major external grant in the particular research area of the candidate, and two peer-reviewed articles on pedagogy and physics-education topics.
- ii- Two peer-reviewed scientific journal articles, and two peer-reviewed articles on pedagogy and physics-education topics.

The last two scenarios would thus mix the scholarship of discovery with the scholarship of teaching and integration.

In the same context, we also expect the faculty member to engage students in some form of research or projects outside of regular course work.

#### For Promotion to Full Professor

Regarding the research/scholarship criterion for tenured members seeking promotion to full professor echelon, the Physics and Astronomy Department hitherto did not have any tangible requirement, with the understanding that FPC would itself assess and judge the work of the faculty member in light of Boyer's four categories of scholarship, giving the faculty member the latitude

of choosing any single one, or a combination of several, of the four categories of Boyer scholarship. Involving students in research/scholarship activities is also highly encouraged.

## Dossier Research Documents, by Title and Category

*Jordan C. Hanson, PhD*

*Assistant Professor of Physics and Computer Science*

*Department of Physics and Astronomy*

*Whittier College*

Document Title (Research Papers)	Journal or other Resource	Category
Complex Analysis of Askaryan Radiation: A Fully Analytic Model in the Time-Domain	Physical Review D	The Askaryan Effect, neutrino physics and IceCube Gen2
In situ, broadband measurement of the radio frequency attenuation length at Summit Station, Greenland	Accepted for publication in the Journal of Glaciology	Antarctic and Greenlandic ice properties
Broadband RF Phased Array Design with MEEP: Comparisons to Array Theory in Two and Three Dimensions	Electronics Journal	Computational Electromagnetism, RF antenna design and fabrication
Broadband RF Phased Array Design for UHE neutrino detection	Proceedings of 37 <sup>th</sup> ICRC	Computational Electromagnetism, RF antenna design and fabrication
Design and sensitivity of the Radio Neutrino Observatory in Greenland (RNO-G)	Journal of Instrumentation	Neutrino physics, drones
Probing the Angular and Polarization Reconstruction of the ARIANNA Detector at the South Pole	Journal of Instrumentation	Neutrino physics, Antarctic ice properties
NuRadioMC: simulating the radio emission of neutrinos from interaction to detector.	European Physical Journal C	The Askaryan effect, Antarctic ice properties
White Paper: ARIANNA-200 high energy neutrino telescope.”	The arXiv: arXiv:2004.09841	The Askaryan effect, Antarctic ice properties
Neutrino Vertex Reconstruction with In-Ice Radio Detectors using Surface Reflections and Implications for the Neutrino Energy Resolution	Journal of Cosmology and Astroparticle Physics	Antarctic ice properties, the Askaryan effect
A Search for Cosmogenic Neutrinos with the ARIANNA Test-Bed using 4.5 Years of Data	Journal of Cosmology and Astroparticle Physics	Neutrino physics, the Askaryan effect, Antarctic ice properties
Observation of classically ‘forbidden’ electromagnetic wave propagation and implications for neutrino detection	Journal of Cosmology and Astroparticle Physics	Antarctic ice properties
Measurement of the real dielectric permittivity of glacial ice	Astroparticle Physics Journal	Antarctic ice properties
Complex Analysis of Askaryan Radiation: A Fully Analytic Treatment including the LPM effect and Cascade Form Factor	Astroparticle Physics Journal	The Askaryan effect
Radio detection of air showers with the ARIANNA experiment on the Ross Ice Shelf	Astroparticle Physics Journal	Cosmic ray physics, the Askaryan effect
First Upper Limits on the Radar Cross Section of Cosmic-Ray Induced Extensive Air Showers	Astroparticle Physics Journal	Cosmic ray physics
Live-time and sensitivity of the ARIANNA Hexagonal Radio Array	Proceedings of the 36 <sup>th</sup> ICRC	Neutrino physics, Antarctic ice properties, the Askaryan effect

Performance of the ARIANNA Hexagonal Radio Array	Proceedings of the 36 <sup>th</sup> ICRC	Neutrino Physics, Antarctic ice properties, the Askaryan effect
A First Search for Cosmogenic Neutrinos with the ARIANNA Hexagonal Radio Array	Astroparticle Physics Journal	Neutrino Physics, Antarctic ice properties, the Askaryan effect
Time-Domain Response of the ARIANNA Detector	Astroparticle Physics Journal	Computational Electromagnetism, RF antenna design and fabrication
Radar absorption, basal reflection, thickness and polarization measurements from the Ross Ice Shelf, Antarctica	Journal of Glaciology	Antarctic ice properties
Design and Performance of the ARIANNA HRA-3 Neutrino Detector Systems.	IEEE Transactions on Nuclear Science	RF antenna design and fabrication
Telescope Array Radar (TARA) observatory for Ultra-High Energy Cosmic Rays.	Nuclear Instrumentation and Methods in Physics Research A	Computational Electromagnetism, RF antenna design and fabrication
Design and Performance of the Autonomous Data Acquisition System for the ARIANNA High Energy Neutrino Detector	IEEE Transactions on Nuclear Science	Computational Electromagnetism, RF antenna design and fabrication
Ross Ice Shelf Thickness, Radio-Frequency Attenuation and Reflectivity: Implications for the ARIANNA UHE Neutrino Detector	Proceedings of the 32 <sup>nd</sup> ICRC	Antarctic ice properties
A prototype station for ARIANNA: A detector for cosmic neutrinos	Nuclear Instrumentation and Methods in Physics Research A	Computational Electromagnetism, RF antenna design and fabrication
Detection and Imaging of He2 Molecules in Superfluid Helium	Physical Review Letters	Nuclear physics, particle physics

<i>Applied Research Projects Documentation</i>	<i>Project origin</i>	<i>Category</i>
Research Application: Exploration of Antarctic Ice Sheets with Drones	Whittier College internal project	Antarctic exploration with drones
Research Application: Workforce Development for Naval Surface Warfare Systems (NSWC), Corona Division	Office of Naval Research project	Workforce development
RF Field Engineer Course: A Practical Introduction	Office of Naval Research project	Workforce development
Introduction to GPS M-Code Signals for Onboarding of Navy Personnel	Office of Naval Research project	Workforce development

<i>Diversity, Equity, and Inclusion Documentation</i>	<i>Project origin</i>	<i>Category</i>
Schedule of activities for the Artemis Program, a STEM recruitment and research opportunity for young women from local high schools	Whittier College internal project	STEM recruitment and development
Diversity, Equity & Inclusion Innovative Initiatives Grant Proposal	Whittier College internal project	DEI in intro. STEM project
Changing Glaciers: So Much More than Sea Level Rise	Whittier Scholars Program Undergraduate Thesis	Interdisciplinary research

# Complex analysis of Askaryan radiation: A fully analytic model in the time domain

Jordan C. Hanson<sup>\*</sup> and Raymond Hartig

*Department of Physics and Astronomy, Whittier College, 13406 East Philadelphia Street, Whittier, California 90602, USA*



(Received 10 June 2021; accepted 1 June 2022; published 21 June 2022)

The detection of ultra-high-energy (UHE,  $\geq 10$  PeV) neutrinos via detectors designed to utilize the Askaryan effect has been a long-time goal of the astroparticle physics community. The Askaryan effect describes radio-frequency radiation from high-energy cascades. When a UHE neutrino initiates a cascade, cascade properties are imprinted on the radiation. Thus, observed radiation properties must be used to reconstruct the UHE neutrino event. Analytic Askaryan models have three advantages when used for UHE neutrino reconstruction. First, cascade properties may be derived from the match between analytic function and observed data. Second, analytic models minimize computational intensity in simulation packages. Third, analytic models can be embedded in firmware to enhance the real-time sensitivity of detectors. We present a fully analytic Askaryan model in the time domain for UHE neutrino-induced cascades in dense media that builds upon prior models in the genre. We then show that our model matches semianalytic parametrizations used in Monte Carlo simulations for the design of IceCube-Gen2. We find correlation coefficients greater than 0.95 and fractional power differences  $<5\%$  between the fully analytic and semianalytic approaches.

DOI: 10.1103/PhysRevD.105.123019

## I. INTRODUCTION

The extrasolar flux of neutrinos with energies between [0.01–1] PeV has been measured by the IceCube collaboration [1]. Previous analyses have shown that the discovery of ultra-high-energy neutrinos ( $\text{UHE-}\nu$ ) will require an expansion in detector volume because the flux is expected to decrease with energy [2–6]. The  $\text{UHE-}\nu$  flux could potentially explain the origin of UHE cosmic rays (UHECR), and provides the opportunity to study electro-weak interactions at record-breaking energies [7,8]. Utilizing the Askaryan effect expands the effective volume of  $\text{UHE-}\nu$  detector designs, because this effect offers a way to detect  $\text{UHE-}\nu$  with radio pulses that travel more than 1 km in sufficiently RF-transparent media such as Antarctic and Greenlandic ice [9–11].

The Askaryan effect occurs within a dense medium with an index of refraction  $n$ . A relativistic particle with  $v > c/n$  initiates a high-energy cascade with negative total charge. The charge radiates energy in the RF bandwidth, and the radiation may be detected if the medium does not significantly attenuate the signal [12,13]. The IceCube EHE analysis has constrained the  $\text{UHE-}\nu$  flux to be  $E_\nu^2 \phi_\nu \leq 2 \times 10^{-8} \text{ GeV cm}^{-2} \text{ s}^{-1} \text{ sr}^{-1}$  between  $[5 \times 10^{15} - 2 \times 10^{19}] \text{ eV}$  [4]. Arrays of  $\mathcal{O}(100)$  *in situ* detectors encompassing effective areas of  $\approx 10^4 \text{ m}^2 \text{ sr}$  per station, spaced by  $\mathcal{O}(1)$

RF attenuation length could discover a  $\text{UHE-}\nu$  flux beyond the EHE limits. The most suitable ice formations exist in Antarctica and Greenland, and a group of prototype Askaryan-class detectors has been deployed. These detectors seek to probe unexplored  $\text{UHE-}\nu$  flux parameter space from astrophysical and cosmogenic sources [5,6,14,15].

Askaryan radiation was first measured in the laboratory in silica sand, and later ice [16–18]. Cascade properties affect the amplitude and phase of the radiation. At RF wavelengths, cascade particles radiate coherently, and the radiation amplitude scales with the total track length of the excess negative charge. The RF pulse shape is influenced by the *longitudinal length* of the cascade, and the pulse is strongest when the viewing angle is close to the Cherenkov angle,  $\theta_C$ . The *excess charge profile* describes the excess negative charge versus longitudinal position on the cascade axis. Radiation wavelengths shorter than the *lateral width* of the cascade, perpendicular to the cascade axis, are attenuated. At energies far above 10 PeV in ice, however, excess charge profiles generated by *electromagnetic* cascades experience the Landau-Pomeranchuk-Migdal (LPM) effect and can have multiple peaks [19,20]. This theoretical foundation has been constructed from a variety of experimental and simulation results.

The field of Askaryan-class detectors requires this foundation for at least two reasons. First, the theoretical form of the Askaryan RF pulse is used to optimize RF detector designs. Askaryan models are incorporated into

\*jhanson2@whittier.edu

simulations [21–23] in order to calculate expected signals and aid in detector design. For example, reconstruction tools for the radio component of IceCube-Gen2 combine machine learning and insights from Askaryan radiation physics [24–26]. Second, Askaryan models are used as templates to search large data sets for signal candidates [5,27]. The signal-to-noise ratios (SNRs) at RF channels are expected to be small ( $\text{SNR} \approx 3$ ), because the amplitude of the radiated field decreases with the vertex distance ( $1/r$ ), and the signal is attenuated by the ice [9,28,29]. Low SNR signals require correspondingly low RF trigger thresholds, but signals must be sampled for a bandwidth of [0.1–1] GHz. Thus, RF channels are triggered at high rates by thermal noise. UHE- $\nu$  signals will be hidden within millions of thermal triggers. Template-waveform matching between models and data is a powerful technique for isolating RF signals from high-energy particles [27,30].

Askaryan models fall into three categories: full Monte Carlo (MC), semianalytic, and fully analytic. The original work by Zas *et al.* (ZHS) [13] was a full MC model. The properties of cascades with total energy  $\leq 1$  PeV were examined. A parametrization for the Askaryan field below 1 GHz was offered, attenuating modes above 1 GHz via a frequency-dependent form factor tied to the lateral cascade width. The semianalytic approach was introduced by Alvarez-Muñiz *et al.* (ARVZ) [31]. This approach accounts for fluctuations in the charge excess profile, and provides an analytic vector potential observed at the Cherenkov angle. The vector potential at the Cherenkov angle is labeled the form factor, and observed fields are derived from the derivative of the vector potential once convolved with a charge excess profile from MC. Recent work also accounts for differences in fit parameters from electromagnetic and hadronic cascades, and other interaction channels, while matching full MC simulations [32].

Finally, fully analytic models of Askaryan radiation from first principles have been introduced. Ralston and Bunyi (RB) gave a fully analytic model valid for observations of cascades in the near and far field, with the transition encapsulated by a parameter  $\eta$  [33]. The result was a complex frequency-domain model. Recently, a model and software implementation was given by Hanson and Connolly (JCH + AC) that built upon RB by providing an analytic form factor derived from GEANT4 simulations, and accounted for LPM elongation [34]. This work connected the locations of poles in the complex frequency plane to  $\eta$  and the form factor. The poles combine to form a low-pass filter for the Askaryan radiation. The JCH + AC results match the ZHS results while demonstrating the physical origins of model parameters. The RB and JCH + AC results are given in the Fourier domain, but most UHE- $\nu$  searches (like template matching) have taken place in the time domain. The goals of this work are to produce a fully analytic time-domain model accounting for complex poles, valid for all viewing

angles  $\theta$  and  $\eta < 1$ , and to demonstrate that it matches semianalytic models.

In Sec. II, the cascade geometry, units, and vocabulary are defined. In Sec. III, we describe how the JCH + AC form factor fits into the current model [34]. In Sec. IV, the analytic Askaryan field, observed at  $\theta = \theta_C$  (*on-cone*), is presented. In Sec. V, the analytic Askaryan field observed for  $\theta \neq \theta_C$  (*off-cone*) is presented. In Sec. VI, fully analytic fields are matched to semianalytic fields generated with NuRadioMC [23] at 10 PeV (electromagnetic cascades) and 100 PeV (hadronic cascades). Though the LPM effect is activated in NuRadioMC, it has a negligible influence on the waveform comparison at these energies. In Sec. VII, the results are summarized and potential applications of the model are described.

## II. UNITS, DEFINITIONS, AND CONVENTIONS

The coordinate system of the Askaryan radiation from a vector current density  $\vec{J}$  is shown in Figs. 1(a)–1(b). Primed cylindrical coordinates refer to  $\vec{J}$ , and the unprimed spherical coordinates refer to the observer. The zenith or *viewing angle* is measured with respect to the *longitudinal axis* ( $z'$ ). The observer displacement is  $r = |\vec{x} - \vec{x}'|$ , in the  $\hat{r}$  direction. The origin is located where the cascade has the highest instantaneous charge density (ICD). The ICD is treated with cylindrical symmetry, so it has no  $\phi'$  dependence. This assumption is based on the large number of cascade particles and momentum conservation. The lateral extent of the ICD is along the *lateral axis* ( $\rho'$ ). The viewing angle is  $\theta$  in spherical coordinates, and the Cherenkov angle occurs when  $\theta$  satisfies  $\cos(\theta_C) = 1/n_{\text{ice}}$  with  $n_{\text{ice}} = 1.78 \pm 0.003$  [35].

In Fig. 1(c), an example excess charge profile  $n(z')$  is shown with characteristic longitudinal length  $a$ . The individual ICDs represent the excess charge density for small windows of time, and  $n(z')$  refers to the total excess charge as a function of  $z'$ . Approximating the central

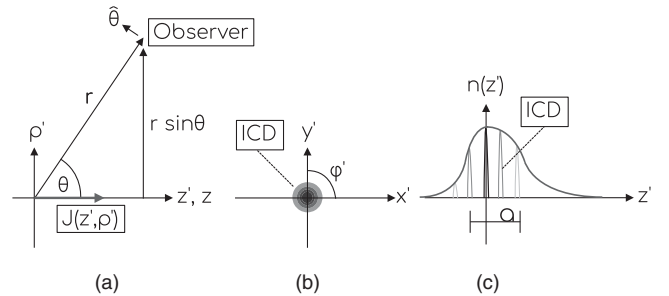


FIG. 1. (a) Side view of the coordinate systems used in the analysis. Spherical unprimed coordinates refer to the observer. Primed cylindrical coordinates refer to  $\vec{J}(\rho', z')$ . (b) Front view of the coordinate system. The ICD is assumed to have no  $\phi'$  dependence. (c) The function  $n(z')$  describes the total cascade excess charge, and it has a characteristic width  $a$ . The ICD has an instantaneous width much smaller than  $a$  [34].

portion of  $n(z')$  as a Gaussian distribution  $N(\mu, \sigma)$  corresponds to setting  $a = 2\sigma$ . Askaryan radiation occurs because  $n(z')$  represents excess negative charge [13,34,36]. Cascades may be characterized as *electromagnetic*, initiated by charged outgoing leptons from UHE- $\nu$  interactions, or *hadronic*, initiated by the interaction between the UHE- $\nu$  and the nucleus. Electromagnetic cascades follow the Greisen distribution and hadronic cascades follow the Gaisser-Hillas distribution. An example of such an implementation via the ARVZ semianalytic parametrization is AraSim [11].

The units of the electromagnetic field in the Fourier domain are V/m/Hz, often converted in the literature to V/m/MHz. To make the distance dependence explicit, both sides of field equations are multiplied by  $r$ , as in  $r\vec{E} = \dots$ , making the units V/Hz. Throughout this work, an overall field normalization constant  $E_0$  is used.  $E_0$  may be linearly scaled with energy, as in other Askaryan models. We show that the on-cone field amplitude is proportional to  $E_0$  times a characteristic frequency squared, so the units of  $E_0$  are V/Hz<sup>2</sup>. For off-cone results, we show that the field amplitude is proportional to  $E_0$  times a characteristic frequency divided by a characteristic pulse width, and the units of  $E_0$  remain V/Hz<sup>2</sup>.

In Sec. III B, we review briefly the energy dependence of the longitudinal length  $a$  in both the electromagnetic and hadronic cases. For the Greisen distribution with critical energy  $E_{\text{crit}}$ , it can be shown that if  $n_{\text{max}} = n(z_{\text{max}})$ , where  $z_{\text{max}} = \ln(E_C/E_{\text{crit}})$ , then  $n_{\text{max}}a \sim E_C/E_{\text{crit}}$ . Thus, the area under the curve  $n(z')$  scales with the total cascade energy  $E_C$ . RB demonstrated that the Askaryan radiation amplitude is proportional to  $n_{\text{max}}a$  and therefore  $E_C$ . The cascade develops over a length  $\approx a$ , but the radiation is coherent over a length  $\Delta z'_{\text{coh}}$  for which the displacement is constant to first order relative to a wavelength. The  $\eta$  parameter is the square of the ratio of  $a$  to  $\Delta z'_{\text{coh}}$ :

$$\eta = \left( \frac{a}{\Delta z'_{\text{coh}}} \right)^2 = \frac{k}{r} (a \sin \theta)^2. \quad (1)$$

In the far field,  $\eta < 1$ . In the first JCH + AC model, a limiting frequency  $\omega_C$  was shown to filter the Askaryan radiation [34]:

$$\eta = \frac{\omega}{\omega_C}. \quad (2)$$

The effect of  $\omega_C$  is described in Sec. IV. The Askaryan radiation is primarily polarized in the  $\hat{\theta}$  direction, with a small amount along  $\hat{r}$  [31,34]. The wave vector is  $k = (2\pi)/(n\lambda)$ , where  $n$  is the index of refraction. A 3D wave vector was defined by RB, equivalent to  $\vec{q} = nk(1, \vec{\rho}/R)$ . The vector current density is treated by RB as a charge density times the velocity of the ICD:  $\vec{J}(t, \vec{x}') = \rho(z' - vt, \rho') \vec{v}$ . Further, the charge density is factored into  $n(z')$  times the ICD:

$\rho(z' - vt, \rho') = n(z')f(z' - vt, \rho')$ . The form factor  $\tilde{F}$  is the three-dimensional spatial Fourier transform of the ICD [33].

The result for  $\tilde{F}$  was derived analytically by JCH + AC [34], and that derivation is briefly described in Sec. III A. JCH + AC define a parameter  $\sigma$ , and  $\tilde{F}$  is a function of  $\sigma$ :  $\tilde{F}(\sigma)$ . The variable  $\sigma$  is related to the ratio of the lateral ICD width to the radiated wavelength. In the derivation of  $\tilde{F}$ , it is convenient to set  $\sigma$  equal to the ratio of the angular frequency to the low-pass cutoff frequency  $\omega_{\text{CF}}$  of  $\tilde{F}$ :

$$\sigma = \frac{\omega}{\omega_{\text{CF}}}. \quad (3)$$

Armed with  $\tilde{F}$ , the longitudinal length  $a$  and the corresponding energy dependence on  $E_0$ , the RB field equations  $\vec{\mathcal{E}}$ , and the displacement  $r$ , the Askaryan electromagnetic field may be assembled according to the following form [33]:

$$r\vec{E}(\omega, \theta) = E_0 \left( \frac{\omega}{2\pi} \right) \psi \vec{\mathcal{E}}(\omega, \theta) \tilde{F}(\omega, \theta). \quad (4)$$

The factor  $E_0$  is proportional to the cascade energy. The factor  $\omega$  is the angular frequency. The variable  $\psi$  is  $\psi = -i \exp(ikr) \sin \theta$ . The function  $\vec{\mathcal{E}}(\omega, \theta)$  contains the vector and complex pole structure of the field (see Refs. [33,34]). The model represented by Eq. (4) is an *all-θ, all-ω* model. That is, Eq. (4) is valid at all frequencies and all viewing angles, provided one accepts the approximation of the central portion of  $n(z')$  as Gaussian. The first goal of this work is to build an *all-θ, all-t* model in the time domain, derived from Eq. (4), and the second goal is to compare it to semianalytic parametrizations.

### III. THE FORM FACTOR AND LONGITUDINAL LENGTH PARAMETER

To arrive at the main electromagnetic field in the time domain, the individual pieces of Eq. (4) must first be assembled. The first piece will be the form factor  $\tilde{F}$  that accounts for the 3D ICD, followed by some remarks about the energy dependence of the longitudinal length parameter  $a$ .

#### A. The form factor

The form factor is the 3D Fourier transform of the ICD  $f(z', \rho')$ , with  $\vec{q} = nk(1, \vec{\rho}/R)$  [33]:

$$F(\vec{q}) = \int d^3x' f(z', \rho') e^{-i\vec{q}\cdot\vec{x}'}. \quad (5)$$

The goal is to evaluate  $\tilde{F}$  in the Fourier domain for an ICD definition informed by cascade simulations. Simulations of the cascade induced by UHE- $\nu$  indicate a

thin wave of charge in  $z'$  spread uniformly in  $\phi'$ , that decreases exponentially in  $\rho'$ . Using these observations JCH + AC completed the derivation in Ref. [34]. The final result was a simple analytic formula:

$$\tilde{F} = \frac{1}{(1 + (\omega/\omega_{\text{CF}})^2)^{3/2}} \quad (6)$$

The form factor acts as a low-pass filter with the cutoff frequency  $\omega_{\text{CF}}$ :

$$\tilde{F} \approx \frac{\omega_0^2}{(\omega + i\omega_0)(\omega - i\omega_0)}. \quad (7)$$

The definition  $\omega_0 = \sqrt{2/3}\omega_{\text{CF}}$  has been used. The effect of the approximation is illustrated in Fig. 2. Equation (7) matches the original ZHS parametrization (see Eq. 20 of Ref. [13]).

### 1. A note about the Molière radius

In Sec. VI B, the decay constant  $l$  of the lateral component of the ICD is inferred from best-fit values of  $\omega_0$ . The connection between the  $l$  parameter and  $\omega_0$  was described by JCH + AC [34]. Put simply, the ICD decays by a factor of  $1/e$  a lateral distance  $l$  from the cascade axis. Note, however, that the  $l$  parameter is not the Molière radius. The Molière radius is the lateral radius which forms a cylinder containing 90% of the energy deposition of the cascade. For ice with a density of  $0.917 \text{ g cm}^{-3}$ , one can estimate  $R_M \approx 9.2 \text{ cm}$  using standard formulas. Although it is tempting to compare  $l$  to  $R_M$ , these parameters have different definitions. Knowing that  $l$  is related to  $\omega_0$ ,  $l$  may be estimated as  $\lambda/2$  in ice at the cutoff frequency. At 3 GHz in ice,  $\lambda/2 \approx 2.8 \text{ cm}$ , and at 1 GHz in ice,  $\lambda/2 \approx 8.4 \text{ cm}$ . Although the results are at the same order of magnitude as  $R_M$ , there are three effects limiting the high-frequency spectrum of the radiation:  $\omega_0$ ,  $\omega_C$ , and the viewing angle. Thus,  $l < R_M$  is possible for a radiation spectrum limited to  $\lesssim 1 \text{ GHz}$ .

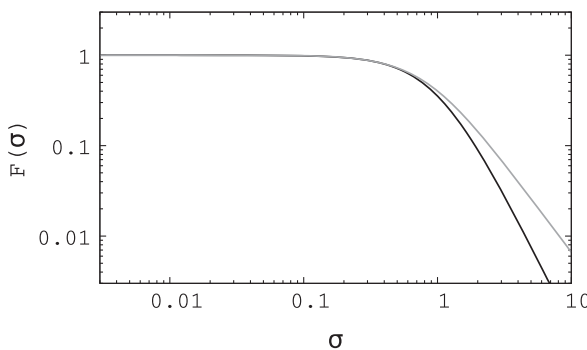


FIG. 2. Black: Eq. (6), graphed versus  $\sigma = \omega/\omega_{\text{CF}}$ . Gray: the two-pole approximation.

## B. The longitudinal length parameter

The next piece required in the assembly of the main electromagnetic field is the energy dependence of the overall amplitude, and the energy dependence of the longitudinal length parameter,  $a$ , which is a part of  $\vec{\mathcal{E}}$  in Eq. (4) [33]. What follows are two separate discussions, one for electromagnetic cascades, and one for hadronic cascades. Though we share these calculations for convenience, note that a variety of theoretical and experimental results on this topic are available [16,37,38].

### 1. Electromagnetic case

The number of charged particles versus distance in radiation lengths  $n(z')$  in an electromagnetic cascade taking place in a dense medium with initial cascade energy  $E_C$ , critical energy  $E_{\text{crit}}$ , normalization parameter  $n_0$ , and age  $s$  is [34]

$$n(z') = \frac{n_0}{\sqrt{\ln(E_C/E_{\text{crit}})}} \exp \left\{ z' \left( 1 - \frac{3}{2} \ln(s) \right) \right\}. \quad (8)$$

To find the energy-dependent width of the Greisen distribution, four steps are necessary: (1) normalization of  $n(z')$  as a fraction of the maximum excess charge, (2) conversion of  $n(z')$  to  $n(s)$ , (3) determination of the width of  $n(s)$  by approximating the central portion as a Gaussian distribution, and (4) conversion of the width from  $s$  units to radiation lengths  $z'$ , and then converting those results to a distance. Define the ratio  $R = n(z_{\text{max}} \pm a/2)/n_{\text{max}}$ , so the FWHM occurs when  $R = 0.5$ . The final result in radiation lengths is

$$a = \sqrt{\ln(E_C/E_{\text{crit}})} \sqrt{-6 \ln(R)} \quad (9)$$

Since  $R < 1$ ,  $\ln(R) < 0$  and  $a$  is real valued, and  $a$  in Eq. (9) is in radiation lengths. In solid ice the density is  $\rho_{\text{ice}} = 0.917 \text{ g cm}^{-3}$ , and the electromagnetic radiation length is  $z_0 = 36.08 \text{ g cm}^{-2}$  [34]. Converting to distance gives

$$a = \frac{z_0}{\rho_{\text{ice}}} \sqrt{\ln(E_C/E_{\text{crit}})} \sqrt{-6 \ln(R)} \quad (10)$$

Note that  $a \propto \sqrt{\ln(E_C)}$ , as shown by RB and others. The product  $n_{\text{max}}a$  is proportional to the energy  $E_C/E_{\text{crit}}$ . For this reason RB took  $n_{\text{max}}a$  as the field normalization rather than  $E_C$  [33]. As an example, letting  $R = 0.4$ , and  $E_{\text{crit}} \approx 10^8 \text{ eV}$ , gives  $a \approx 4 \text{ meters}$  for  $E_C = 10^{16} \text{ eV}$ . We show in Sec. VI that our fitted  $a$  values are close to 4 meters when matched to semianalytic parametrizations.

## 2. Hadronic case

The Gaisser-Hillas distribution describes hadronic cosmic-ray air showers, but has also been applied to hadronic cascades in dense media in codes like AraSim [11,22]. The original function reads

$$n(z') = n_{\max} \left( \frac{z' - z_0}{z_{\max} - z_0} \right)^{(z_{\max} - z_0)/\lambda} e^{\frac{z_{\max} - z'}{\lambda}}. \quad (11)$$

The variables are defined as follows:  $n_{\max}$  is the instantaneous maximum number of particles in the cascade,  $z'$  is the longitudinal distance in radiation lengths,  $z_0$  is the initial starting point,  $\lambda$  is the interaction length, and  $z'_{\max}$  is the location of  $n_{\max}$ . Using the same steps as the electromagnetic case, we find

$$a = \sqrt{z'_{\max}} \sqrt{-8 \ln(R)} \quad (12)$$

The  $a$  parameter again goes as  $\sqrt{z_{\max}} \propto \sqrt{\ln(E_C)}$  which produces similar lengths as the electromagnetic case when scaled by the appropriate interaction length and ice density.

## IV. ON-CONE FIELD EQUATIONS

The  $\hat{\theta}$  component of the electromagnetic field at  $\theta = \theta_C$  will now be built in the time domain from Eq. (4). Setting  $\theta = \theta_C$  in the general RB field equations (Appendix A), with Eq. (6) for  $\tilde{F}$ ,  $\sigma = \omega/\omega_{\text{CF}}$  and  $\eta = \omega/\omega_{\text{CF}}$ , and letting  $E_0$  be proportional to the cascade energy  $E_C$  produces Eq. 45 from JCH + AC [34]:

$$r\tilde{E}(\omega, \theta_C) = \frac{(-i\omega)E_0 \sin(\theta_C)e^{i\omega r/c}}{(1 - i\omega/\omega_C)^{1/2}(1 + (\omega/\omega_{\text{CF}})^2)^{3/2}}. \quad (13)$$

More detail is provided in Appendix A. Let the retarded time be  $t_r = t - r/c$  (with the appropriate value for  $c$  given the index versus depth), and let  $\omega_0 = \sqrt{\frac{2}{3}}\omega_{\text{CF}}$  and  $\hat{E}_0 = E_0 \sin \theta_C$ . Finally, let  $\epsilon = \omega_0/\omega_C$ . The inverse Fourier transform of Eq. (13) is

$$\begin{aligned} rE(t, \theta_C) \\ = \frac{\hat{E}_0 i\omega_C \omega_0^2}{\pi} \frac{d}{dt_r} \int_{-\infty}^{\infty} \frac{e^{-i\omega t_r}}{(2i\omega_C + \omega)(\omega + i\omega_0)(\omega - i\omega_0)} d\omega. \end{aligned} \quad (14)$$

In Eq. (14), the derivative with respect to the retarded time  $d/dt_r$  is introduced to remove a factor of  $(-i\omega)$  from the numerator. Accounting for the complex poles and the sign of  $t_r$ , complex integration and expansion to first order in  $\epsilon$  yields

$$rE(t, \theta_C) = \frac{1}{3} \hat{E}_0 \omega_{\text{CF}}^2 \begin{cases} (1 - \frac{1}{2}\epsilon)e^{\omega_0 t_r} & t_r < 0 \\ (2e^{-2\omega_C t_r} - (1 + \frac{1}{2}\epsilon)e^{-\omega_0 t_r}) & t_r > 0 \end{cases} \quad (15)$$

Equation (15) represents the time-domain solution for the on-cone  $\hat{\theta}$  component of the Askaryan electric field. The expansion to first order in  $\epsilon$  is only performed so the final result resembles semianalytic results for  $\vec{E} = -\partial \vec{A}/\partial t_r$  [31,32]. Table I summarizes the definitions of the parameters in Eq. (15). Fit results for the parameters of Table I are shown in Sec. VI.

Notice that the amplitude is asymmetric, and the parameter  $\epsilon$  influences the asymmetry. The  $\epsilon$  parameter was studied by JCH + AC in detail. For example, Fig. 10 of Ref. [34] shows that  $\epsilon \approx [0.1 - 1]$  for an inverse lateral width  $l^{-1} = \sqrt{2\pi\rho_0} \approx 20 \text{ m}^{-1}$  and  $a \approx 4 \text{ m}$ . The best-fit results for  $\epsilon$  and  $a$  are shown in Sec. VI. JCH + AC showed that the expression for  $\epsilon$  is the product of the ratio of the lateral to longitudinal length, and the ratio of the longitudinal length to the observer displacement, making it a physical parameter connecting the event geometry to the cascade shape [34]. Figure 3 displays normalized examples of Eq. (15) for different values of  $\omega_0$ ,  $\omega_C$ , and  $\epsilon$ .

### A. Verification of the uncertainty principle

As a check on the procedures used to perform the inverse Fourier transform that produces Eq. (15), we verify below that the uncertainty principle holds, for  $\Delta\theta \rightarrow 0$ . JCH + AC provided the Gaussian width of the radiation in the Fourier domain:  $\sigma_\nu$ , where  $\nu$  represents the frequency in Hz. Generally speaking, Fourier transform pairs must obey  $\sigma_\nu \sigma_t \geq 1/(2\pi)$ . The following procedure is used to compute the width  $\sigma_t$  of the on-cone field. First, the  $t_r < 0$  and  $t_r > 0$  cases are each treated as probability distributions and normalized. Next, the average positive and negative retarded times,  $\bar{t}_{r,+}$  and  $\bar{t}_{r,-}$ , are computed. Finally, subtracting the two averages yields  $\sigma_t$ :

TABLE I. Parameters used to build Eq. (15). Fitted values in comparison to semianalytic parametrizations are shown in Sec. VI.

Parameter	Definition
$\hat{E}_0$	$E_0 \sin(\theta_C)$
$E_0$	$\approx n_{\max} a$
$\omega_0$	$\sqrt{\frac{2}{3}}\omega_{\text{CF}}$
$\omega_{\text{CF}}$	$(c\sqrt{2\pi\rho_0})/(n \sin \theta)$ (see Eqs. 22, 23, and 46 of Ref. [34])
$\omega_C$	$(rc)/(na^2 \sin^2 \theta)$ (see Eq. 39 of Ref. [34])
$\epsilon$	$\omega_0/\omega_C$
$t_r$	$t - r/c$

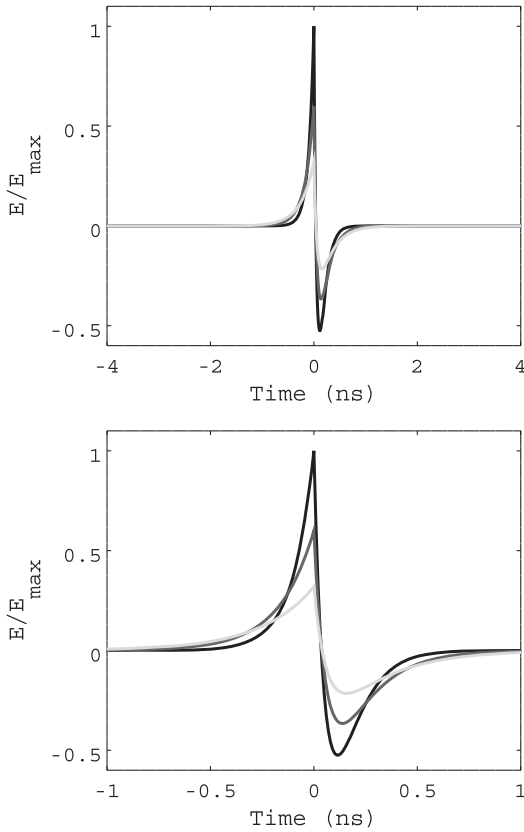


FIG. 3. Top: Eq. (15) from  $[-4, 4]$  ns, with (black)  $\omega_C = 2\pi(1.25)$  GHz,  $\omega_0 = 2\pi(1.56)$  GHz,  $\epsilon = 1.25$ , (gray)  $\omega_C = 2\pi(1.25)$  GHz,  $\omega_0 = 2\pi(0.94)$  GHz,  $\epsilon = 0.75$ , (light gray)  $\omega_C = 2\pi(1.25)$  GHz,  $\omega_0 = 2\pi(0.625)$  GHz, and  $\epsilon = 0.5$ . The amplitudes of all curves are normalized to the peak of the  $\epsilon = 1.25$  (black) data. Bottom: same as top panel, plotted between  $[-1, 1]$  ns.

$$\sigma_t = \bar{t}_{r,+} - \bar{t}_{r,-} = \frac{\epsilon + 2}{\omega_0} = \frac{1}{\omega_C} + \frac{2}{\omega_0}. \quad (16)$$

The result has the correct units and the limiting cases are sensible. If  $\epsilon \rightarrow 0$  ( $\omega_C \gg \omega_0$ ), then  $\sigma_t \rightarrow 2/\omega_0$ , which is expected from observing Eq. (15) if the  $\omega_C$  exponential disappears. If  $\epsilon = 1$  ( $\omega_C = \omega_0$ ), then  $\sigma_t = 3/\omega_0$ . That is, the pulse is wider if there is more than one relevant cutoff frequency.

The expression for  $\sigma_\nu$  is given by Eq. 36 of JCH + AC [34]:

$$\sigma_\nu = \frac{c}{2\pi a \Delta \cos(\theta)} (1 + \eta^2)^{1/2}. \quad (17)$$

Expanding to first order in  $\Delta \cos(\theta) = \cos(\theta) - \cos(\theta_C)$ ,

$$\sigma_\nu \approx \frac{c}{2\pi a \sin(\theta_C) \Delta \theta} (1 + \eta^2)^{1/2}. \quad (18)$$

From Table I:  $\omega_C^{-1} = na^2 \sin^2(\theta_C)/(rc)$ , and  $\omega_0^{-1} = nl \sin(\theta_C)/c$ , with  $l = \sqrt{3/2}/(\sqrt{2}\pi\rho_0)$ . (Recall that  $\rho_0$

is a parameter discussed in Ref. [34]). Multiplying  $\sigma_t$  and  $\sigma_\nu$  with the far-field limit ( $\eta < 1$ ) gives the inequality

$$\sigma_\nu \sigma_t \geq \frac{n}{2\pi} \left( \left( \frac{a}{r} \right) \frac{\sin(\theta_C)}{\Delta \theta} + 2 \left( \frac{l}{a} \right) \frac{1}{\Delta \theta} \right). \quad (19)$$

Therefore, in order to satisfy  $\sigma_\nu \sigma_t > 1/(2\pi)$ ,

$$n \left( \frac{a}{r} \right) \sin(\theta_C) + 2n \left( \frac{l}{a} \right) > \Delta \theta. \quad (20)$$

Although  $a/r \ll 1$  and  $l/a \ll 1$ , as long as these expressions do not approach zero as fast as  $\Delta \theta \rightarrow 0$  in Eq. (20), the uncertainty principle holds. Yet these are exactly the conditions of the problem: a displacement  $r$  in the far field (but not infinitely far away) and a longitudinal length  $a$  much larger (but not infinitely larger) than the lateral ICD width  $l$ . Thus,  $\sigma_\nu \sigma_t > 1/(2\pi)$  holds.

## V. OFF-CONE FIELD EQUATIONS

Turning to the case for which  $\theta \neq \theta_C$ , the  $\hat{\theta}$  component of the electromagnetic field will now be built in the time domain. The RB field equations for the  $\hat{\theta}$  and  $\hat{r}$  components were summarized by both RB and JCH + AC [33,34], and are included here in Appendix A. Recall the general form of the electromagnetic field, given in Eq. (4):

$$r \vec{E}(\omega, \theta) = E_0 \left( \frac{\omega}{2\pi} \right) \psi \vec{\mathcal{E}}(\omega, \theta) \tilde{F}(\omega, \theta). \quad (21)$$

The first task is to simplify  $\vec{\mathcal{E}}(\omega, \theta)$  before taking the inverse Fourier transform. The simplification involves expanding  $\vec{\mathcal{E}}(\omega, \theta)$  in a Taylor series such that  $u = 1 - i\eta \approx 1$ , restricting  $\eta < 1$  (far-field). Once  $\vec{\mathcal{E}}(\omega, \theta)$  is simplified, the inverse Fourier transform of Eq. (21) may be evaluated to produce the result. Table II contains useful variable definitions, Table III contains useful function definitions, and Table IV contains special cases of the functions in Table III.

The original form of  $\vec{\mathcal{E}}(\eta, \theta)$  is shown in Appendix A. Changing variables to  $u$  and  $x$  (Table II) and using the

TABLE II. Useful variables for the derivation of the off-cone Askaryan electromagnetic field.

Variable	Definition
$u$	$1 - i\eta$
$x$	$\cos(\theta)$
$x_C$	$\cos(\theta_C)$
$q$	$(xx_C - x_C^2)/(1 - x^2)$
$y$	$(\frac{1}{2})(ka)^2(\cos \theta - \cos \theta_C)^2$
$p$	$\frac{1}{2}(\frac{a}{c})^2(\cos \theta - \cos \theta_C)^2$

TABLE III. Useful functions for the derivation of the off-cone Askaryan electromagnetic field. The last row contains the vector structure of the  $\hat{\theta}$  component of the field.

Function	Definition
$f(u, x)$	$(u + 3 \frac{(1-u)^2 x^2 - x x_C}{u - 1 - x^2})^{-1/2}$
$g(u, x)$	$\exp(-\frac{1}{2}(ka)^2(x - x_C)^2 u^{-1})$
$h(u, x)$	$(\frac{1-u}{u})q$
$\vec{\mathcal{E}}(u, x) \cdot \hat{\theta}$	$f(u, x)g(u, x)(1 - h(u, x))$

TABLE IV. Special cases of the functions defined in Table III, when  $u = 1$ .

Function ( $u = 1$ )	Result
$f(x, 1)$	1
$\dot{f} _{u=1}$	$-\frac{1}{2}$
$g(x, 1)$	$\exp(-y)$
$\dot{g} _{u=1}$	$y \exp(-y)$
$h(x, 1)$	0
$\dot{h} _{u=1}$	$-q$

function definitions and values in Tables III–IV,  $\vec{\mathcal{E}}(u, x) \cdot \hat{\theta} = \mathcal{E}(u, x)$  becomes

$$\mathcal{E}(u, x) = f(u, x)g(u, x)(1 - h(u, x)). \quad (22)$$

Expanding  $\mathcal{E}(u, x)$  near  $u = 1$  gives

$$\mathcal{E}(u, x) = \mathcal{E}(x, 1) + (u - 1)\dot{\mathcal{E}}(x, 1) + \mathcal{O}(u - 1)^2. \quad (23)$$

The details of the expansion are shown in Appendix B. The result is.

$$\mathcal{E}(x, u) = e^{-y} \left( 1 - \frac{1}{2} j\eta(2y + 2q - 1) \right). \quad (24)$$

The inverse Fourier transform of the  $\hat{\theta}$  component gives the time-domain results, after including the expanded  $\mathcal{E}(u, x)$ :

$$rE(t, \theta) = \mathcal{F}^{-1} \left\{ E_0 \left( \frac{\omega}{2\pi} \right) \tilde{F}\psi\mathcal{E} \right\}. \quad (25)$$

Intriguingly, the result is proportional to the *line-broadening function*,  $H$  (DLMF 7.19, [39]) common to spectroscopy applications. There are three terms in Eq. (24). Two terms ultimately vanish, being integrals over odd integrands (see Appendix B). The integral that remains contains  $H$ , with  $\omega_1 = t_r/(2p)$ :

$$I_0 = 2\pi i \left( \frac{\omega_C}{\omega_0} \right) e^{-\frac{t_r^2}{4p}} H(\sqrt{p}\omega_0, i\omega_1\sqrt{p}). \quad (26)$$

The line-broadening function is similar to a convolution between a Gaussian function and a Lorentzian function, and cannot be expressed analytically, though there are examples of polynomial expansions [40]. Note that, for situations relevant to the current problem,  $\omega > \omega_1$ . Requiring that  $\omega > \omega_1$  amounts to a restriction between  $\Delta\theta$  and  $|t_r|$ :

$$|t_r| < |2p\omega|. \quad (27)$$

It is shown in the next section that  $\sqrt{p}$  is the pulse width  $\sigma_t$ , so  $|2p\omega|$  has units of time. Using the results of Sec. V A below, the restriction on the retarded time may be written as  $|t_r|/\sigma_t < \omega\sigma_t = 2\pi(\sigma_t/T)$ . That is, the accuracy of the waveform should be trusted within a number of pulse widths that is less than  $2\pi$  times the ratio of the pulse width to the period of the lowest frequency. This is not a strong requirement, since the field quickly approaches zero after several pulse widths. Hereafter, this step will be called the *symmetric approximation*, because the result for  $r\vec{E}(t_r, \theta)$  in Eq. (28) has equal positive and negative amplitudes. Evaluating the line-broadening function numerically would account for amplitude asymmetry. The restriction on  $\Delta\theta$  is formalized in Sec. V B. Solving  $I_0$  using the symmetric approximation clears the way for the final result (see Appendix B):

$$rE(t, \theta) = -\frac{E_0 \omega_0 \sin(\theta)}{8\pi p} t_r e^{-\frac{t_r^2}{4p} + p\omega_0^2} \text{erfc}(\sqrt{p}\omega_0) \quad (28)$$

Equation (28) represents the time-domain solution for the off-cone  $\hat{\theta}$  component of the Askaryan electric field. Equation (28) is graphed in Figs. 4 and 5. In Fig. 4 (top),  $E(t, \theta)$  is shown normalized to the maximum value for the angular range displayed,  $[\theta_C + 1.5^\circ, \theta_C + 5.5^\circ]$ , from  $t = [-5, 5]$  ns. Pulses with viewing angles closer to  $\theta_C$  have larger relative amplitudes and shorter pulse widths. Figure 4 (bottom) contains the same results, but for  $t = [-1.5, 1.5]$  ns. The pulses are symmetric and all zero crossings are at  $t_r = 0$  ns as a result of the symmetric approximation. Figure 5 contains contours of the same results as in Fig. 4.

As in the on-cone result, the overall field amplitude scales with energy ( $E_0 \sim n_{\max} a$ ). However, the amplitude also scales with  $\omega_0/p$ . The argument of the complementary error function,  $\sqrt{p}\omega_0$ , is unitless. This factor is strictly positive, so the range of the complementary error function is (0,1). The factor  $\sqrt{p}\omega_0$  cannot be zero without setting  $\theta = \theta_C$ , or setting  $\omega_{CF} = 0$ . Both cases are not allowed. Equation (28) represents the *off-cone* ( $\theta \neq \theta_C$ ) solution, so  $p \neq 0$ . Setting  $\omega_{CF} = 0$  is not physical, for

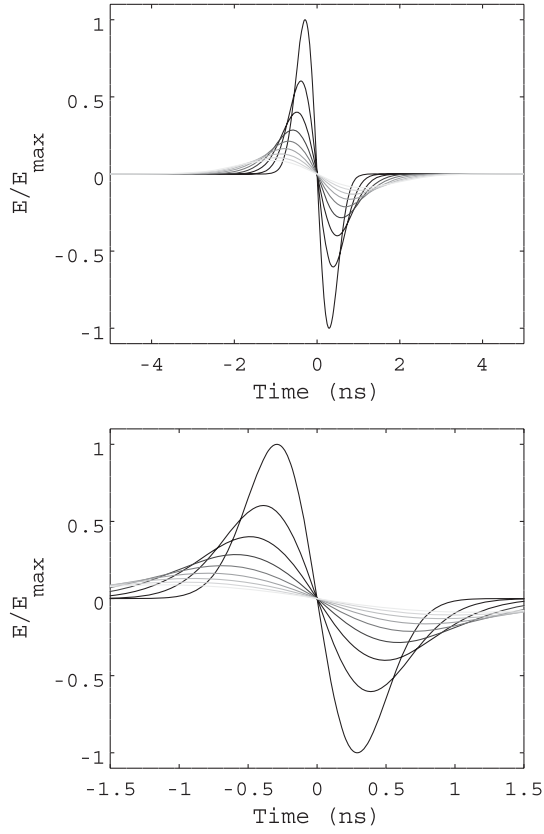


FIG. 4.  $E(t, \theta)$  versus  $t_r$  [Eq. (28)], normalized. The viewing angle  $\theta$  is varied from  $\theta_C + 1.5^\circ$  to  $\theta_C + 5.5^\circ$  in steps of  $0.5^\circ$ . Top:  $\omega_0/(2\pi) = 1.0$  GHz. Bottom: same as top, but zoomed in on the central region.

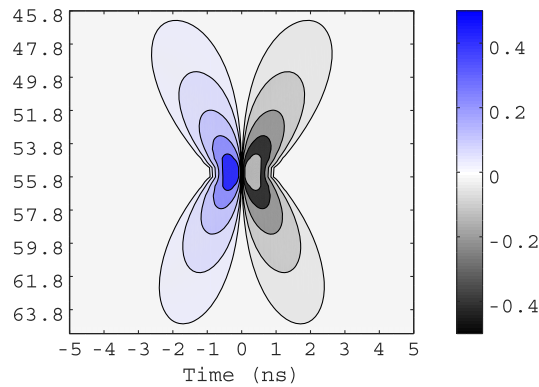


FIG. 5. Contours of  $E(t, \theta)$  versus  $\theta$  versus  $t_r$  [Eq. (28)], normalized. The normalization is the same as in Fig. 4. Although the contour lines extend into the region near  $\theta_C$ , Eq. (5) is only being evaluated at  $\Delta\theta > 1.5^\circ$  (see text for details).

this implies infinite lateral width ( $l$ ) and cascade particles have finite transverse momentum. Another possibility is that  $p = 0$  if  $a = 0$ , but this implies  $E_0 = 0$ . Therefore,  $0 < \text{erfc}(\sqrt{p}\omega_0) < 1$ .

### A. Verification of the uncertainty principle

As in Sec. IV A, the uncertainty principle should be checked. Equation (28) is an antisymmetric Gaussian function with pulse width  $\sigma_t = \sqrt{2p}$ . Let  $\Delta \cos \theta = (\cos \theta - \cos \theta_C)$ . Using Table II, the expression  $\sqrt{2p}$  evaluates to

$$\sigma_t = \sqrt{2p} = \left(\frac{a}{c}\right)(\Delta \cos \theta). \quad (29)$$

Recall that  $\sigma_\nu$  is given by

$$\sigma_\nu = \frac{c}{2\pi a \Delta \cos \theta} (1 + \eta^2)^{1/2}. \quad (30)$$

The uncertainty product is

$$\sigma_t \sigma_\nu = \frac{1}{2\pi} (1 + \eta^2)^{1/2}. \quad (31)$$

In the far field,  $\eta < 1$ , so  $\sigma_t \sigma_\nu \geq 1/(2\pi)$  holds.

### B. Usage of the on-cone versus off-cone fields

The form of Eq. (28), and the restriction between  $\Delta\theta$  and  $|t_r|$  from the symmetric approximation suggests the limit  $\Delta\theta \rightarrow 0$  must be examined carefully. Since  $p \propto (\cos \theta - \cos \theta_C)^2$ , probing the model near  $\theta = \theta_C$  is equivalent to taking the limit that  $p \rightarrow 0$ . Intriguingly, the  $p^{-1}$  dependence in the field does not lead to a divergence. As the field grows in amplitude from  $p^{-1}$  as  $p \rightarrow 0$ , the field width,  $\sqrt{2p}$ , approaches zero.

Equations (16) and (29) contain the pulse widths of the on-cone and off-cone fields, respectively. Power in the off-cone case is limited by the pulse width  $\sqrt{2p}$ , and the observed power increases as  $\Delta\theta$  and  $\sqrt{2p}$  both decrease. Thus, a reasonable constraint on when  $\Delta\theta_{\min}$  is large enough to use Eq. (28) is given by setting the off-cone pulse width to the on-cone pulse width:

$$\frac{1}{\omega_C} + \frac{2}{\omega_0} = \sqrt{2p}. \quad (32)$$

Expanding the expression for  $p$  near  $\theta = \theta_C$ , and evaluating the square root leads to

$$\frac{1}{\omega_C} + \frac{2}{\omega_0} = \frac{a}{c} \sin \theta_C \Delta\theta_{\min}. \quad (33)$$

Using  $\epsilon = \omega_0/\omega_C$ , and letting  $k_0 = \omega_0/c$ , the formula may be rearranged:

$$\epsilon + 2 = ak_0 \sin \theta_C \Delta\theta_{\min}. \quad (34)$$

Squaring both sides, and then dividing both sides by  $r$  yields

$$\frac{(\epsilon + 2)^2}{r} = k_0 \left( \frac{k_0(a \sin \theta_C)^2}{r} \right) \Delta\theta_{\min}^2. \quad (35)$$

The quantity in parentheses on the right-hand side is  $\eta$ , with  $\omega = \omega_0$ . Setting  $\omega = \omega_0$  means  $\eta = \epsilon$ . Solving for  $\Delta\theta_{\min}$  gives

$$\Delta\theta_{\min} = \frac{\epsilon + 2}{\sqrt{\epsilon k_0 r}}. \quad (36)$$

Assuming  $\epsilon \approx 1$ ,  $f_0 \approx 1$  GHz,  $n = 1.78$  for solid ice, and  $c = 0.3$  m ns<sup>-1</sup> (see Sec. VI A),  $k_0 \approx 35$  m<sup>-1</sup>. Taking  $r = 1000$  m,  $\Delta\theta_{\min} \approx 1^\circ$ . Simple rules of thumb for the application of Eq. (28) field are

$$\Delta\theta_{\min} \geq 1^\circ, \quad (37)$$

$$\Delta\theta_{\min} \propto \frac{1}{\sqrt{kr}}. \quad (38)$$

## VI. COMPARISON TO SEMIANALYTIC PARAMETRIZATIONS

The fully analytic model will now be compared to the ARVZ semianalytic parametrization used in NuRadioMC to predict signals in IceCube-Gen2 Radio [23]. Specifically, the comparison is between Eqs. (15) and (28) and the NuRadioMC implementation of the semianalytic parametrization given in Ref. [32]. To provide concrete comparisons, a small set of waveforms was generated with NuRadioMC, for both electromagnetic and hadronic cascades, on- and off-cone. The electromagnetic cascades have  $E_C = 10^{16}$  eV, while the hadronic cascades have  $E_C = 10^{17}$  eV. These choices minimize the impact of the LPM effect, though the LPM effect was activated in the NuRadioMC code.

The comparison involves three stages. First, waveforms and  $a$  values are generated for each cascade type, energy, and angle:  $\theta = \theta_C + 3.0^\circ$ , and  $\theta = \theta_C$ . Second, Eqs. (15) and (28) are tuned to match the waveforms. In each fit, the Pearson correlation coefficient ( $\rho$ ) is maximized, and the sum squared of amplitude differences [ $(\Delta E)^2$ ] is minimized. Finally, best-fit parameters are tabulated.

Two remarks are important regarding the fit criteria. First, the Pearson correlation coefficient is not sensitive to changes in amplitude because it is normalized:

$$\rho = \frac{\text{cov}(f_{\text{data}}, f_{\text{model}})}{\sigma_{\text{data}} \sigma_{\text{model}}}. \quad (39)$$

If  $E_i$  represent the samples of the models, then

$$(\Delta E)^2 = \sum_{i=1}^N (E_{i,\text{data}} - E_{i,\text{model}})^2. \quad (40)$$

### A. Waveform comparison: $\theta = \theta_C$

#### 1. Electromagnetic case

Six different electromagnetic cascades and the corresponding Askaryan fields were generated using the ARZ2019 model from NuRadioMC [23,32] for comparison to Eq. (15). The cascades have  $E_C = 10$  PeV, and  $r = 1000$  meters. The LPM effect is activated in NuRadioMC for all comparisons in this work. The units of  $\vec{E}(t_r, \theta_C)$  are mV/m versus nanoseconds, so the units of  $r\vec{E}$  are volts. The sampling rate of the digitized semianalytic parametrizations was 100 GHz, with  $N = 2048$  samples. Let  $f_C = \omega_C/(2\pi)$  and  $f_0 = \omega_0/(2\pi)$ . The frequencies  $f_C$  and  $f_0$  were varied from [0.6–6.0] GHz. The parameter  $E_0$  was varied from [0.05 – 5.0] V GHz<sup>-2</sup>. In a simple two-level for loop, the Pearson correlation coefficient  $\rho$  was maximized by varying  $f_0$  and  $f_C$ . Next, the sum of the squared amplitude differences  $(\Delta E)^2$  was minimized by varying  $E_0$ , while holding  $f_0$  and  $f_C$  fixed. Several other schemes were studied, including a three-level for loop, but the two-stage process produced the best results. The results are shown in Fig. 6.

Maximizing  $\rho$  corresponds to minimizing  $(\Delta E)^2$ . In Fig. 7,  $(\Delta E)^2$  is graphed versus  $\rho$  for one event. Best-fit  $\rho$  values are  $\approx 0.97$  for this set, corresponding to best-fit  $(\Delta E)^2$  values of  $\approx 7\%$ . Contours of  $\rho > 0.95$  for  $f_0$  versus  $f_C$  are shown in Fig. 6 (left column). The crosses represent the best-fit locations. The dashed gray line at  $y = x$  corresponds to  $f_0/f_C = \epsilon = 1$ . Though Eq. (15) contains an expansion to first order in  $\epsilon$ , making it resemble the derivative of the vector potential from the ARVZ semianalytic parametrization [32], the expansion is optional. There is a restriction that  $\epsilon \neq 2$  [see Eq. (A14) of Appendix A]. Thus, the best-fit  $\epsilon$  values avoid the solid black lines ( $\epsilon = 2$ ) in Fig. 6, but are large enough to account for pulse asymmetry. The best-fit waveforms are shown in Fig. 6 (right column). The gray curves correspond to the semianalytic parametrization, and the black curves represent Eq. (15).

Table V contains the best-fit results for the Eq. (15) parameters, along with best-fit  $\rho$  values and  $(\Delta E)^2$  values. The horizontal and vertical distances from the crosses to the  $\rho > 0.95$  contour are used as error estimates for  $f_0$  and  $f_C$  in Table V. The  $a$  errors typically encompass the  $a$  values from NuRadioMC. The full region in  $[f_0, f_C]$  space for which UHE- $\nu$  signals are expected the radio component of the IceCube Gen2 detector will be the topic of future studies, along with the apparent difference in  $\epsilon$  values depending on the electromagnetic or hadronic classification of the cascade (see Fig. 8).

#### 2. Hadronic case

Using the same procedure as in the electromagnetic case, NuRadioMC was used to generate six hadronic cascades at 100 PeV for comparison to Eq. (15). The energy was

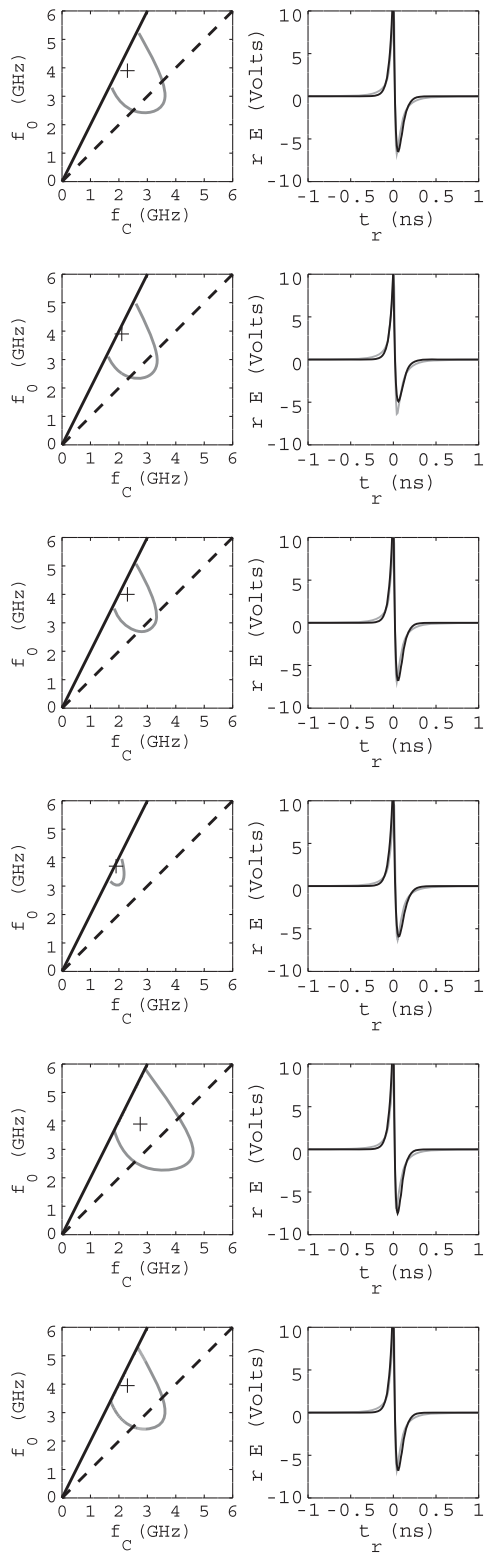


FIG. 6. Fit results: electromagnetic case,  $\theta = \theta_C$ ,  $E_C = 10$  PeV. The rows correspond to NuRadioMC waveforms 1–6, with 10 PeV electromagnetic cascades. Left column: best fits for  $f_0$  and  $f_C$ . Dashed line:  $\epsilon = 1$ . Solid line:  $\epsilon = 2$ . Gray contour:  $\rho > 0.95$ . Black cross: best fit. Right column: best-fit waveforms. Gray: semianalytic parametrizations from Ref. [23]. Black: Eq. (15).

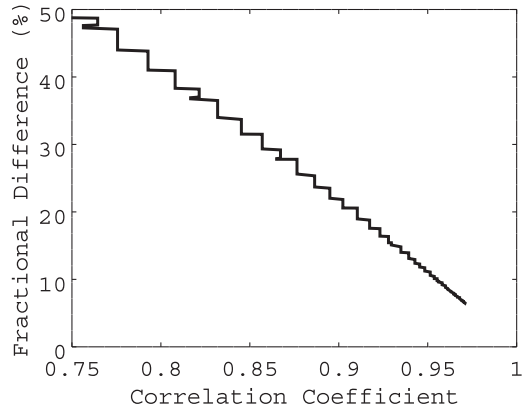


FIG. 7. Fractional difference in the sum of amplitude differences squared  $[(\Delta E)^2]$  versus correlation coefficient ( $\rho$ ) for waveform 1 at  $E_C = 10$  PeV, for the electromagnetic case.

increased to show that the model describes a range of energies, so the waveform amplitudes are larger by a factor of 10 relative to the 10 PeV case. The LPM effect is activated in NuRadioMC for all comparisons in this work. The main results are shown in Fig. 8, and the correlation contours represent  $\rho = 0.985$ .

The results shown in Fig. 8 demonstrate that modeling hadronic cascades at  $\theta = \theta_C$  is similar to the electromagnetic case, with one interesting difference. The contours enclose best-fit  $\epsilon$  values below the dashed line, whereas the fits to the electromagnetic cases were above the dashed line. This could indicate a potential discriminator for cascade classification. Another difference between the electromagnetic and hadronic cases is that the gray contours in Fig. 8 correspond to  $\rho = 0.985$ , as opposed to  $\rho = 0.95$  in the electromagnetic case.

TABLE V. Fit results: electromagnetic case,  $\theta = \theta_C$ ,  $E_C = 10$  PeV. The six rows (from top to bottom) correspond to NuRadioMC waveforms 1–6, WITH 10 PeV electromagnetic cascades. From left to right: the form-factor cutoff frequency, coherence cutoff frequency, energy-scaling normalization, longitudinal length parameter, the best-fit correlation coefficient, and the relative power difference between the NuRadioMC semianalytic parametrization and the fully analytic model. The parameter means and errors in the mean are quoted in the bottom two rows.

No.	$f_0$ (GHz)	$f_C$ (GHz)	$E_0$ (V GHz $^{-2}$ )	$a_{\text{wave}}$ (m), $a_{\text{MC}}$ (m)	$\rho$	$(\Delta E)^2$ (%)
1	$3.9^{+0.2}_{-1.9}$	$2.3^{+1.3}_{-0.3}$	0.3	$4.1^{+1.2}_{-0.3}$ , 4.85	0.97	6.5
2	$3.9^{+0.3}_{-1.5}$	$2.1^{+0.9}_{-0.1}$	0.5	$4.3^{+1.8}_{-0.2}$ , 6.35	0.97	10.9
3	$4.0^{+1.2}_{-1.0}$	$2.3^{+0.8}_{-0.4}$	0.35	$4.1^{+0.7}_{-0.4}$ , 4.48	0.96	7.5
4	$3.7^{+0.1}_{-0.5}$	$1.9^{+0.5}_{-0.1}$	1.85	$4.5^{+1.1}_{-0.3}$ , 5.6	0.955	8.9
5	$3.9^{+1.4}_{-0.9}$	$2.7^{+1.4}_{-0.8}$	0.18	$4.0^{+2.0}_{-1.2}$ , 4.48	0.97	5.7
6	$3.9^{+1.3}_{-1.9}$	$2.3^{+1.3}_{-0.3}$	0.31	$4.1^{+2.0}_{-0.5}$ , 4.85	0.97	6.4
Average	3.88	2.3	0.6	4.18	0.966	7.7
Error	3.08	0.1	0.3	0.07	0.003	0.8

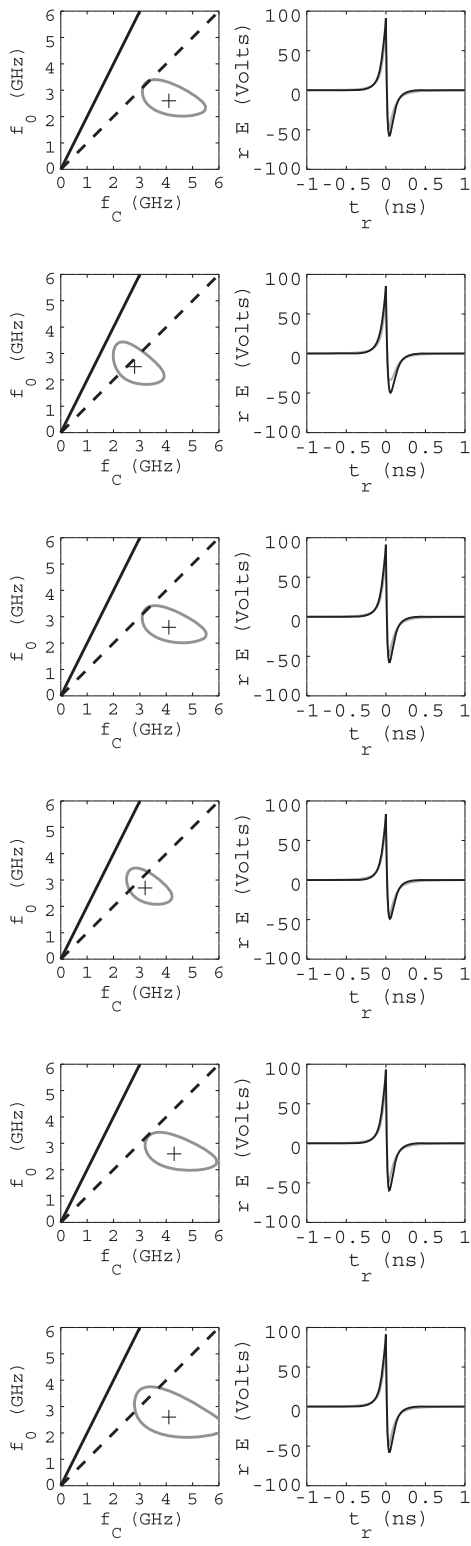


FIG. 8. Fit results: hadronic case,  $\theta = \theta_C$ ,  $E_C = 100$  PeV. The six rows (from top to bottom) correspond to NuRadioMC waveforms 1–6, with 100 PeV hadronic cascades. Left column: best fits for  $f_0$  and  $f_C$ . Dashed line:  $\epsilon = 1$ . Solid line:  $\epsilon = 2$ . Gray contour:  $\rho > 0.985$ . Black cross: best fit. Right column: best-fit waveforms. Gray: semianalytic parametrizations from Ref. [23]. Black: Eq. (15).

Table VI contains the best-fit parameters corresponding to Fig. 8. The typical power difference  $(\Delta E)^2$  has decreased with respect to the electromagnetic case. The  $\rho$  values all exceed 0.985, and the  $(\Delta E)^2$  results are typically below 2 percent. Intriguingly,  $\epsilon < 1$  means higher  $f_C$  values, which in turn yields systematically low  $a$  values relative to those generated in NuRadioMC, despite the increased energy. Reconstructed  $a$  values are still within a factor of 2 of the MC-true values. Despite the systematic offset, the best-fit  $a$  and the NuRadioMC  $a$  values are tightly correlated (see Fig. 11 below).

## B. Waveform comparison: $\theta \neq \theta_C$

### 1. Electromagnetic case

The general comparison procedure of Sec. VIA was repeated with the same semianalytic parametrization from NuRadioMC, but with 12 new events each viewed at  $\theta = \theta_C + 3.0^\circ$  (six electromagnetic cascades, six hadronic). One difference is that  $\omega_0$  only changes the waveform amplitude, along with  $E_0$ . The pulse width  $\sigma_t = \sqrt{2}p$  connects the longitudinal length  $a$  and the viewing angle with respect to the Cherenkov angle.

The fit procedure was performed in two stages. First,  $\theta$  values and  $a$  values were scanned from  $[\theta_C + 1.5^\circ, \theta_C + 10.0^\circ]$  and  $[0.1, 10]$  meters, respectively, to maximize  $\rho$ . Once the best-fit values for  $a$  and  $\theta$  were determined,  $(\Delta E)^2$  was minimized by varying  $f_0 = \omega_0/(2\pi)$  and  $E_0$  from  $[0.3, 3.0]$  GHz and  $[0.1, 2.0]$  V GHz $^{-2}$ , respectively. The  $(\theta, a)$  scan and the  $(f_0, E_0)$  scan were each separate two-level for loops. The results are shown in Fig. 9.

TABLE VI. Fit results: hadronic case,  $\theta = \theta_C$ ,  $E_C = 100$  PeV. The six rows (from top to bottom) correspond to NuRadioMC waveforms 1–6, with 100 PeV hadronic cascades. From left to right: the form-factor cutoff frequency, coherence cutoff frequency, energy-scaling normalization, longitudinal length parameter, the best-fit correlation coefficient, and the relative power difference between the NuRadioMC semianalytic parametrization and the fully analytic model. The parameter means and errors in the mean are quoted in the bottom two rows.

No.	$f_0$ (GHz)	$f_C$ (GHz)	$E_0$ (V GHz $^{-2}$ )	$a_{\text{wave}}$ (m), $a_{\text{MC}}$ (m)	$\rho$ (%)	$(\Delta E)^2$
1	$2.6^{+0.6}_{-0.6}$	$4.1^{+1.1}_{-1.0}$	1.0	$3.1^{+0.8}_{-0.8}$ , 5.23	0.99	1.86
2	$2.5^{+0.7}_{-0.6}$	$2.8^{+0.9}_{-0.8}$	1.25	$3.75^{+1.2}_{-1.1}$ , 6.35	0.99	1.83
3	$2.6^{+0.7}_{-0.6}$	$4.1^{+1.2}_{-0.9}$	1.0	$3.1^{+0.7}_{-0.7}$ , 5.23	0.99	1.83
4	$2.7^{+0.6}_{-0.5}$	$3.2^{+0.8}_{-0.6}$	1.0	$3.5^{+0.9}_{-0.7}$ , 6.35	0.99	2.5
5	$2.6^{+0.7}_{-0.6}$	$4.3^{+1.4}_{-1.1}$	1.0	$3.0^{+1.0}_{-0.75}$ , 4.85	0.99	1.755
6	$2.6^{+1.4}_{-0.7}$	$4.1^{+1.9}_{-1.2}$	1.0	$3.1^{+1.4}_{-0.9}$ , 5.23	0.99	1.86
Average	2.60	3.75	1.04	3.3	0.99	1.9
Error	0.03	0.25	0.04	0.1	0.0	0.1

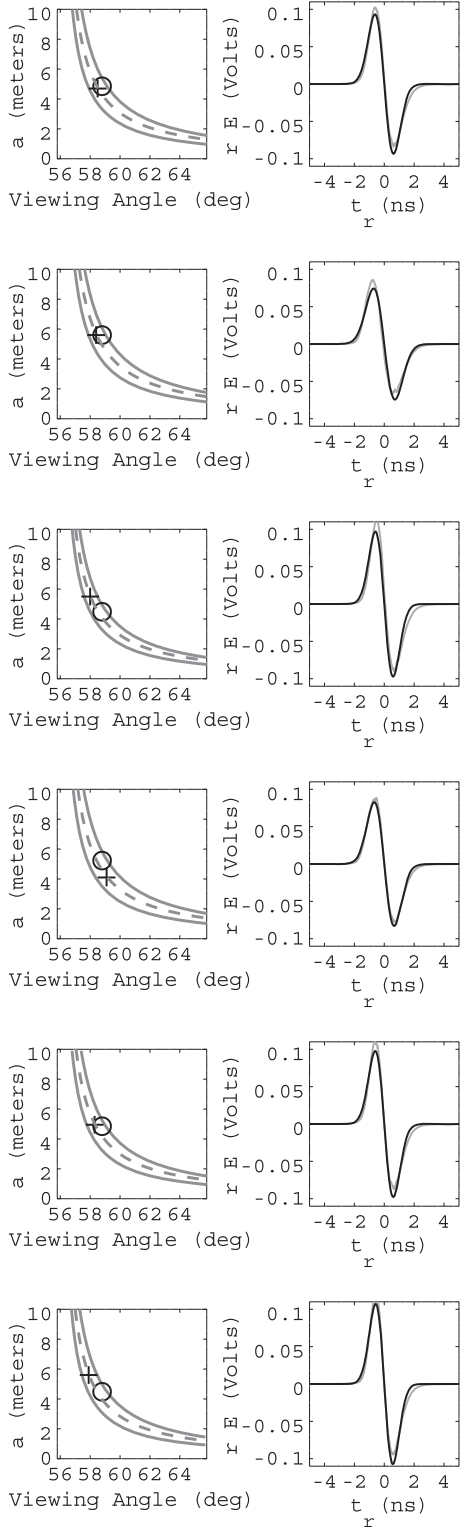


FIG. 9. Fit results: electromagnetic case,  $\theta \neq \theta_C$ ,  $E_C = 10$  PeV. The six rows (from top to bottom) correspond to NuRadioMC waveforms 1–6, with 10 PeV electromagnetic cascades. Left column: best-fit  $\theta$  and  $a$  values. Crosses: best fits. Circles: MC true values. Gray contour:  $\rho > 0.95$ . Dashed line:  $a$  versus  $\theta$  from Eq. (29). Right column: best-fit waveforms. Gray: semianalytic parametrizations from Ref. [23]. Black: Eq. (28).

In Fig. 9 (left column), the best-fit  $a$  values and  $\theta$  values are marked with a cross. The circles represent the MC-true values. Circles and crosses lie on the dashed lines, because an uncertainty principle connects  $a$  values to  $\theta$  values (see Sec. V A). Specifically, Eq. (29) may be used to show, to first order in  $\Delta\theta = \theta - \theta_C$ ,

$$a\Delta\theta = \frac{c\sqrt{2p}}{\sin\theta_C} = \text{const.} \quad (41)$$

The pulse width  $\sigma_t = \sqrt{2p}$  is a constant derived from the waveform, implying that the product of  $a$  and  $\Delta\theta$  is constant. The parameters  $a$  and  $\Delta\theta$  are therefore inversely proportional:  $a \propto \Delta\theta^{-1}$ . The shape of the  $\rho > 0.95$  contour follows this inverse proportionality. The dashed lines represent Eq. (41). These results suggest that a measurement of the Askaryan pulse width would constrain the cascade shape and geometry. The best-fit waveforms are shown in Fig. 9 (right column). Typical correlation coefficients exceed  $\rho = 0.98$ . Table VII contains the fit results. The fit results include estimates of the lateral width parameter,  $l$ , derived from  $f_0$  (see Sec. III A). Despite making the symmetric approximation to arrive at Eq. (28), the fits include fractional power differences of  $\approx 3\%$ .

TABLE VII. Fit results: electromagnetic case,  $\theta \neq \theta_C$ ,  $E_C = 10$  PeV. The six rows (from top to bottom) correspond to NuRadioMC waveforms 1–6, with 10 PeV electromagnetic cascades. From left to right: the viewing angle, longitudinal length parameter, form-factor cutoff frequency, the energy-scaling normalization, the lateral width of the cascade, the best-fit correlation coefficient, and the relative power difference between the NuRadioMC semianalytic parametrization and the fully analytic model. The parameter means and errors in the mean are quoted in the bottom two rows.

No.	$\theta_{\text{wave}}$ (deg), $\theta_{\text{MC}}$ (deg)	$a_{\text{wave}}$ (m), $a_{\text{MC}}$ (m)	$f_0$ (GHz)	$E_0$ (V GHz $^{-2}$ )	$l$ (cm)	$\rho$	$(\Delta E)^2$
1	$58.5^{+0.7}_{-0.6}$ , 58.8	$4.7^{+1.3}_{-1.0}$ , 4.85	0.75	1.2	$3.4^{+0.9}_{-0.7}$	0.99	1.93
2	$58.4^{+0.6}_{-0.5}$ , 58.8	$5.6^{+1.4}_{-1.1}$ , 5.60	1.0	1.2	$2.6^{+0.4}_{-0.3}$	0.99	2.61
3	$58.0^{+0.5}_{-0.4}$ , 58.8	$5.5^{+1.3}_{-1.0}$ , 4.48	1.0	1.1	$2.6^{+0.3}_{-0.2}$	0.98	4.47
4	$59.1^{+0.9}_{-0.7}$ , 58.8	$4.1^{+1.2}_{-0.9}$ , 5.23	0.75	1.2	$3.4^{+0.5}_{-0.5}$	0.995	0.80
5	$58.3^{+0.7}_{-0.5}$ , 58.8	$4.95^{+1.4}_{-1.1}$ , 4.85	0.75	1.2	$3.4^{+0.4}_{-0.3}$	0.99	1.8
6	$57.9^{+0.6}_{-0.4}$ , 58.8	$5.6^{+1.5}_{-1.2}$ , 4.48	0.75	1.2	$3.5^{+0.5}_{-0.4}$	0.99	1.83
Average	58.4	5.1	0.83	1.18	3.2	0.989	2.2
Error	0.2	0.2	0.05	0.02	0.2	0.002	0.5

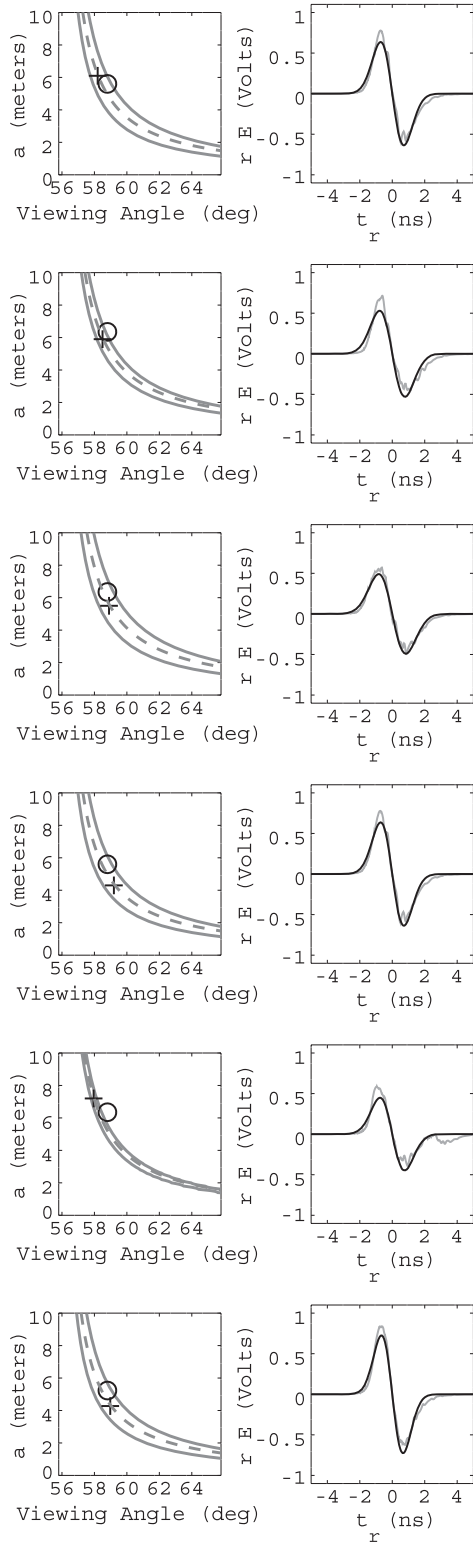


FIG. 10. Fit results: hadronic case,  $\theta \neq \theta_C$ ,  $E_C = 100$  PeV. The six rows (from top to bottom) correspond to NuRadioMC waveforms 1–6, with 100 PeV hadronic cascades. Left column: best-fit  $\theta$  and  $a$  values. Crosses: best fits. Circles: MC true values. Gray contour:  $\rho > 0.95$ . Dashed line:  $a$  versus  $\theta$  from Eq. (29) (uncertainty principle). Right column: best-fit waveforms. Gray: semianalytic parametrizations from Ref. [23]. Black: Eq. (28).

## 2. Hadronic case

The fit procedure for the hadronic cascades was the same as the electromagnetic case, except that the range for  $E_0$  was expanded to  $[1.0, 20.0]$  V GHz $^{-2}$ . As in the on-cone procedure, the hadronic cascade energy was  $E_C = 100$  PeV. The results are shown in Fig. 10.

As with the electromagnetic case,  $\rho$  is maximized and  $(\Delta E)^2$  is minimized. Table VIII contains the best-fit parameters, along with  $\rho$  and  $(\Delta E)^2$ . Solutions with  $\rho \approx 0.98$  and  $(\Delta E)^2 \approx 5\%$  were found. Similar to the results shown in Table VII, the results in Table VIII are in agreement with the MC values from NuRadioMC. The  $E_0$  values match expectations for 100 PeV cascades, because they are a factor of 10 higher than those of the 10 PeV electromagnetic case. The results for  $a$ ,  $l$ , and  $f_0$ , however, are not statistically different between Tables VII and VIII. Future studies will require computing the probability distributions of these parameters from large numbers of UHE- $\nu$  cascades.

As a first exercise for statistical energy reconstruction from waveform parameters, assume that  $\theta = \theta_C + 3.0^\circ$  is already measured. For example,  $\theta$  could be determined by measuring the cutoff frequency in the Fourier domain below 1 GHz (see Fig. 5 of Ref. [34], for example). Scanning Eq. (28) over all NuRadioMC waveforms at fixed  $\theta = \theta_C + 3.0^\circ$  yields Fig. 11, in which the fitted  $a$  value from each waveform

TABLE VIII. Fit results: hadronic case,  $\theta \neq \theta_C$ ,  $E_C = 100$  PeV. The six rows (from top to bottom) correspond to NuRadioMC waveforms 1–6, with 100 PeV hadronic cascades. From left to right: the viewing angle, longitudinal length parameter, form-factor cutoff frequency, the energy-scaling normalization, the lateral width of the cascade, the best-fit correlation coefficient, and the relative power difference between the NuRadioMC semianalytic parametrization and the fully analytic model. The parameter means and errors in the mean are quoted in the bottom two rows.

No.	$\theta_{\text{wave}}$ (deg), $\theta_{\text{MC}}$ (deg)	$a_{\text{wave}}$ (m), $a_{\text{MC}}$ (m)	$f_0$ (GHz) 5.5 6.35	$E_0$ (V GHz $^{-2}$ ) 10.6 5.6	$l$ (cm) 3.2 5.6	$\rho$ (%) 0.98 7.1	$(\Delta E)^2$ 3.55 7.1
1	$58.2^{+0.6}_{-0.4}$ , 58.8	$6.1^{+1.5}_{-1.2}$ , 5.6	0.8	10.6	$3.2^{+0.5}_{-0.5}$	0.98	3.55
2	$58.5^{+0.4}_{-0.3}$ , 58.8	$5.9^{+0.9}_{-0.8}$ , 6.35	0.85	10.3	$3.0^{+0.3}_{-0.2}$	0.96	7.1
3	$58.9^{+0.8}_{-0.6}$ , 58.8	$5.5^{+1.4}_{-1.1}$ , 6.35	0.9	10.8	$2.8^{+0.5}_{-0.5}$	0.98	2.64
4	$59.2^{+0.8}_{-0.7}$ , 58.8	$4.3^{+1.1}_{-0.8}$ , 5.6	0.85	10.5	$3.0^{+0.5}_{-0.5}$	0.98	3.10
5	$58.0^{+0.2}_{-0.2}$ , 58.8	$7.2^{+0.6}_{-0.6}$ , 6.35	0.9	8.2	$2.9^{+0.3}_{-0.3}$	0.955	8.76
6	$59.0^{+0.8}_{-0.6}$ , 58.8	$4.3^{+1.1}_{-0.9}$ , 5.23	0.85	10.4	$3.0^{+0.5}_{-0.5}$	0.985	3.00
Average	58.6	5.5	0.86	10.1	3.2	0.973	5
Error	0.2	0.5	0.015	0.4	0.2	0.005	1

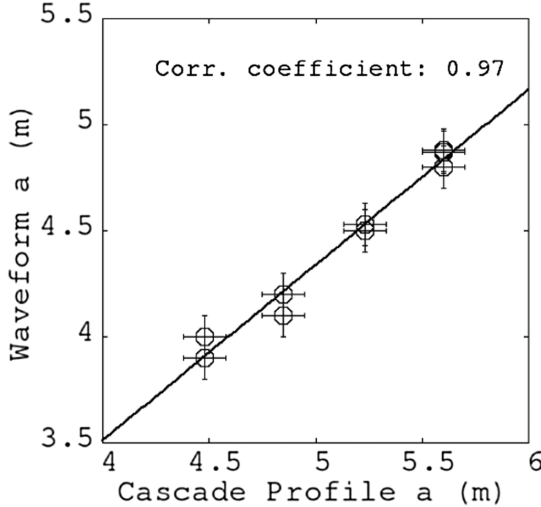


FIG. 11. The longitudinal length parameter  $a$  derived from the Eq. (28) best fit versus the  $a$  value derived from the cascade profile in NuRadioMC. A linear fit and correlation coefficient are shown (slope:  $0.83 \pm 0.05$ ; intercept:  $0.2 \pm 0.2$  (m); correlation coefficient = 0.97).

is graphed versus the MC-true  $a$  value. The  $a$  errors in all cases are taken to be  $\pm 10$  cm ( $\pm$  two  $\Delta a$  step sizes). A least-squares linear fit was applied to the data. The linear function fits the data, and the correlation coefficient is 0.97. The results in Fig. 11 imply an energy reconstruction technique using the formulas found in Sec. III B. Consider the relationship between  $a$  and  $\ln(E_C/E_{\text{crit}})$ :  $a = c_1 \sqrt{\ln(E_C/E_{\text{crit}})}$ . The fractional error in  $\ln(E_C/E_{\text{crit}})$  is proportional to the fractional error in  $a$ :

$$\frac{\sigma_{\ln(E_C/E_{\text{crit}})}}{\ln(E_C/E_{\text{crit}})} = 2c_1 \left( \frac{\sigma_a}{a} \right). \quad (42)$$

If a reliable fit for the  $a$  parameter is obtained from observed Askaryan waveforms, Eq. (42) shows that the logarithm of the energy can be constrained.

## VII. CONCLUSION

We have presented a fully analytic Askaryan model in the time domain, and we have shown that it matches results generated with semianalytic parametrizations used in NuRadioMC. Pearson correlation coefficients between the fully analytic and semianalytic parametrizations were found to be greater than 0.95, and typical fractional differences in total power were found to be  $\approx 5\%$ . New results and potential applications are summarized in the following sections.

### A. Summary of new results

The main results are summarized in Table IX. This work represents the first time the two distinct pole frequencies  $f_0$  and  $f_C$  have been used to characterize the time-domain

TABLE IX. Summary of results in this work.

Result	Location
$r\vec{E}(t_r, \theta_C)$ , on-cone field ( $\hat{\theta}$ )	Eq. (15), Sec. IV
$\sigma_t \sigma_\nu \geq 1/(2\pi)$ , on-cone	Eq. (20), Sec. IVA
$r\vec{E}(t_r, \theta)$ , off-cone field ( $\hat{\theta}$ )	Eq. (28), Sec. V
$\sigma_t \sigma_\nu \geq 1/(2\pi)$ , off-cone	Eq. (31), Sec. VA
On-cone EM comparison to [32]	Fig. 6, Table V
On-cone HAD comparison to [32]	Fig. 8, Table VI
Off-cone EM comparison to [32]	Fig. 9, Table VII
Off-cone HAD comparison to [32]	Fig. 10, Table VIII

field equations of the Askaryan effect for both  $\theta = \theta_C$  and  $\theta \neq \theta_C$ . The uncertainty principle was verified on-cone ( $\theta = \theta_C$ ), serving as a check on the model. By fitting on-cone cascade parameters, we have shown that an analytic model matches semianalytic predictions. The  $\epsilon$  parameter reveals a potential cascade classification scheme. Next, the off-cone ( $\theta \neq \theta_C$ ) field equations were derived, and again the uncertainty principle was verified. Off-cone cascade parameters were fit, and the results are in excellent agreement with semianalytic results. Fitting  $a$  values has revealed a potential energy reconstruction.

To obtain the fields on- and off-cone,  $\eta < 1$  was assumed. The restriction  $\eta < 1$  means that Eqs. (15) and (28) must be applied to the far field. Given that  $a$  and  $\theta_C$  are fixed by cascade physics and ice density, and that the relevant Askaryan bandwidth for ice is [0.1–1] GHz, the parameter most easily varied within  $\eta$  is the observer distance  $r$ . Taking  $\nu = 0.5$  GHz,  $n = 1.78$ ,  $c = 0.3$  m GHz,  $\theta = \theta_C$ , and  $a = 5$  m, requiring that  $\eta = 1$  gives  $r \geq 0.4$  km. Scaling to  $\nu = 0.25$  GHz gives  $r \geq 0.2$  km. According to NuRadioMC [23] (Fig. 13), the  $r$  corresponding to UHE- $\nu$  at  $10^{18}$  eV ranges from 0.7–3.2 km, and 0.2 km is rare.

The “acceleration argument” invoked by RB in Ref. [33] states that if  $r(t)$  points to the ICD,  $r(t)$  must be constant enough to ensure that  $\Delta r < \lambda$ . Using the law of cosines, with two sides being  $r$  and  $r + \Delta r$ , and a third being  $a$ , the criteria that  $(a/r)^2 \ll 1$  leads to  $|\Delta r| \approx a/n$  which is  $\mathcal{O}(2)$  m. When in doubt about usage and event geometry, determining if  $(a/r)^2 \ll 1$  is a good check. If the UHE- $\nu$  event is a charged-current interaction with an electromagnetic cascade far above the LPM energy for ice,  $a$  grows faster than  $\sqrt{\ln(E_C/E_{\text{crit}})}$  [20].

### B. Utility of the analytic model

There are at least four advantages of fully analytic Askaryan models. First, when analytic models are matched to observed data, cascade properties may be derived directly from the waveforms. Second, in large-scale simulations, evaluating a fully analytic model technically provides a speed advantage over other approaches. Third, fully analytic models, combined with RF channel

response, can be embedded in firmware to form a *matched filter* that enhances UHE- $\nu$  detection probability. Fourth, parameters in analytic models may be *scaled* to produce results that apply to media of different density than ice. This application is useful for understanding potential signals in the Antarctic firn, or the upper layer of snow and ice that is of lower density than the solid ice beneath it.

The ability to fit cascade properties from waveforms will be a useful tool for the radio component of IceCube-Gen2. Examples of current reconstruction techniques include the forward-folding method [25] and information field theory [26]. In particular, the longitudinal length parameter  $a$  leads to a reconstruction of  $\ln(E_C)$ , given knowledge of  $\Delta\theta$  [Fig. 11 and Eq. (42)]. Further, all designs for detector stations in IceCube-Gen2 radio include many distinct RF channels and one phased array of channels. Matching our analytic model to each channel waveform will provide a separate measurement of parameters like  $a$  and  $\theta$  (see gray contours of Figs. 4 and 5). The ensuing global fit should constrain the event energy and geometry.

The most intriguing usage for a fully analytic Askaryan model would be to embed the model as a *matched filter* in detector firmware. Because cascade properties are unknown *a priori*, an array of matched filters could be implemented to form a *matched filter bank*. One example of this approach was the TARA experiment [41], which was designed to detect low-SNR cosmic ray radar echoes. This is similar to the challenge faced by the radio component of the IceCube Gen2 detector: pushing the limit of low-SNR RF pulse detection in a remote setting. For example, a matched filter bank could be formed with an array of off-cone field formulas with fixed  $a$  value and varying  $\theta$  values, which would then be convolved with the RF channel impulse response (see Sec. 6 of Ref. [27]).

Finally, a fully analytic model enhances the ability of IceCube-Gen2 radio to identify signals that originate in the firn. At the South Pole, the RF index of refraction begins around 1.35 and does not reach the solid ice value of 1.78 until 150–200 meters [28]. There are at least two signals that could originate in the firn: UHE- $\nu$  events that create Askaryan radiation, and UHE cosmic-ray cascades partially inside or fully inside the firn. The altitude of the South Pole makes the latter possible. The Askaryan radiation of the firn UHE- $\nu$  events could be modeled via appropriate density scaling of the cascade parameters.

## ACKNOWLEDGMENTS

We would like to thank our colleagues for helpful discussions regarding analysis techniques. In particular, we want to thank Profs. Steve Barwick, Dave Besson, and Christian Glaser for useful discussions. Finally, we would like to thank the Whittier College Fellowships Committee, and specifically the Fletcher-Jones Fellowship Program for providing financial support for this work. This work was

partially funded by the Fletcher-Jones Summer Fellowship of 2020, Whittier College Fellowships program.

## APPENDIX A: DETAILS OF THE ON-CONE FIELD EQUATION DERIVATION

The original equations for the  $\hat{\theta}$  component of  $\vec{\mathcal{E}}$  are

$$\mathcal{W}(\eta, \theta) = \frac{\exp(-\frac{1}{2}(ka)^2 \frac{(\cos \theta - \cos \theta_C)^2}{1-i\eta})}{(1 - i\eta(1 - 3i\eta \frac{\cos \theta \cos \theta - \cos \theta_C}{\sin^2 \theta}))^{1/2}}, \quad (\text{A1})$$

$$\vec{\mathcal{E}}(\eta, \theta) \cdot \hat{\theta} = \mathcal{W}(\eta, \theta) \left( 1 - i\eta \frac{\cos \theta_C \cos \theta - \cos \theta_C}{\sin^2 \theta} \right). \quad (\text{A2})$$

Letting  $\theta = \theta_C$  yields

$$\vec{\mathcal{E}}(\eta, \theta) \cdot \hat{\theta} = \frac{1}{\sqrt{1 - i\eta}}. \quad (\text{A3})$$

The complete field from the original RB model [33], including the form factor  $\tilde{F}$ ,  $\psi = -i \exp(ikr) \sin \theta$ , and  $\vec{\mathcal{E}}$  is

$$r\vec{E}(\omega, \theta) = E_0 \left( \frac{\omega}{2\pi} \right) \psi \vec{\mathcal{E}}(\eta, \theta) \tilde{F}. \quad (\text{A4})$$

Take Eq. 6 for the form factor  $\tilde{F}$ . Let  $E_0$  be proportional to cascade energy  $E_c$  and let  $\theta = \theta_C$ :

$$r\tilde{E}(\omega, \theta_C) = \frac{(-i\omega)E_0 \sin(\theta_C) e^{i\omega r/c}}{(1 - i\omega/\omega_C)^{1/2} (1 + (\omega/\omega_{CF})^2)^{3/2}}. \quad (\text{A5})$$

Suppose  $\omega < \omega_C$ , and  $\omega < \omega_{CF}$ , such that the following approximations of the factors in the denominator are valid:

$$(1 - i\omega/\omega_C)^{1/2} \approx 1 - \frac{i}{2} \frac{\omega}{\omega_C}, \quad (\text{A6})$$

$$(1 + (\omega/\omega_{CF})^2)^{3/2} \approx 1 + \frac{3}{2} \left( \frac{\omega}{\omega_{CF}} \right)^2. \quad (\text{A7})$$

Using the approximations introduces simple poles into the complex formula for the frequency-dependent electric field. Inserting the approximations in the denominator of Eq. (A5), we have

$$r\tilde{E}(\omega, \theta_C) = \frac{(-i\omega)E_0 \sin(\theta_C) e^{i\omega r/c}}{(1 - \frac{i}{2}\omega/\omega_C)(1 + \frac{3}{2}(\omega/\omega_{CF})^2)}. \quad (\text{A8})$$

The denominator can be rearranged by factoring the  $\omega$  coefficients, and defining  $\omega_0 = \sqrt{\frac{2}{3}}\omega_{CF}$ :

$$r\tilde{E}(\omega, \theta_C) = \frac{2i\omega_C\omega_0^2(-i\omega)E_0 \sin(\theta_C)e^{i\omega r/c}}{(2i\omega_C + \omega)(\omega + i\omega_0)(\omega - i\omega_0)}. \quad (\text{A9})$$

Let  $\hat{E}_0 = E_0 \sin(\theta_C)$ , and let the retarded time be  $t_r = t - r/c$ . Taking the *inverse* Fourier transform, using the same sign convention as RB [33] [ $f(t) = (2\pi)^{-1} \int_{-\infty}^{\infty} \tilde{F}(\omega) e^{-i\omega t} d\omega$ ], converts the field to the time domain:

$$\begin{aligned} rE(t, \theta_C) &= \frac{\hat{E}_0 i\omega_C \omega_0^2}{\pi} \frac{d}{dt_r} \int_{-\infty}^{\infty} \frac{e^{-i\omega t_r}}{(2i\omega_C + \omega)(\omega + i\omega_0)(\omega - i\omega_0)} d\omega. \\ &\quad (\text{A10}) \end{aligned}$$

- (1) If  $t_r > 0$ : Consider the contour comprised of the real axis and the clockwise-oriented negative infinite semicircle. On the contour, the exponential phase factor in Eq. (A10) goes as

$$\exp(-i\omega t_r) = \exp(-i(R \cos \phi + iR \sin \phi)t_r). \quad (\text{A11})$$

For the semicircle,  $\phi \in [\pi, 2\pi]$ , so  $\sin \phi < 0$  and  $t_r > 0$ . Exponential decay occurs and the integrand vanishes on the semicircle for  $|\omega| = R \rightarrow \infty$ .

- (2) If  $t_r < 0$ : Consider the contour comprised of the real axis and the counterclockwise-oriented positive infinite semicircle. On the contour, the exponential phase factor in Eq. (A10) goes again as

$$\exp(-i\omega t_r) = \exp(-i(R \cos \phi + iR \sin \phi)t_r). \quad (\text{A12})$$

For the semicircle,  $\phi \in [0, \pi]$ , so  $\sin \phi > 0$  and  $t_r < 0$ . Exponential decay occurs and the integrand vanishes on the semicircle for  $|\omega| = R \rightarrow \infty$ .

Using cases 1 and 2, Eq. (A10) can be solved using the Cauchy integral formula. Beginning with  $t_r > 0$ , two poles are enclosed in the semicircle: one that originated from the coherence cutoff frequency, and the other that originated from the form factor. The Cauchy integral formula yields

$$\begin{aligned} rE(t, \theta_C) &= 2\hat{E}_0 \omega_C \omega_0^2 \frac{d}{dt_r} \left( \frac{e^{-2\omega_C t_r}}{i^2(-2\omega_C + \omega_0)(-2\omega_C - \omega_0)} \right. \\ &\quad \left. + \frac{e^{-\omega_0 t_r}}{i^2(-\omega_0 + 2\omega_C)(-2\omega_0)} \right). \quad (\text{A13}) \end{aligned}$$

Define the ratio of the cutoff frequencies:  $\epsilon = \omega_0/\omega_C$ . After evaluating the time derivatives, Eq. (A13) becomes

$$rE(t, \theta_C) = \hat{E}_0 \omega_0^2 \left( \frac{e^{-2\omega_C t_r}}{(1 - \frac{\epsilon}{2})(1 + \frac{\epsilon}{2})} - \frac{e^{-\omega_0 t_r}}{(2)(1 - \frac{\epsilon}{2})} \right). \quad (\text{A14})$$

Expanding to linear order in  $\epsilon$ , assuming  $\epsilon < 1$ , and recalling that  $\omega_0^2 = \frac{2}{3}\omega_{\text{CF}}^2$ ,

$$rE(t, \theta_C) \approx \frac{1}{3} \hat{E}_0 \omega_{\text{CF}}^2 \left( 2e^{-2\omega_C t_r} - \left( 1 + \frac{\epsilon}{2} \right) e^{-\omega_0 t_r} \right). \quad (\text{A15})$$

Turning to the case of  $t_r < 0$ , consider integrating Eq. (A10) along the contour comprised of the real axis and the counterclockwise-oriented positive infinite semicircle. The contour encloses one pole, and the exponent ensures convergence:

$$rE(t, \theta_C) = (2\pi i) \hat{E}_0 (\pi)^{-1} i\omega_C \omega_0^2 \frac{d}{dt_r} \left( \frac{e^{\omega_0 t_r}}{(2i\omega_C + i\omega_0)(2i\omega_0)} \right). \quad (\text{A16})$$

After evaluating the derivative, the expression simplifies with  $\epsilon = \omega_0/\omega_C$ :

$$rE(t, \theta_C) = \frac{1}{2} \hat{E}_0 \omega_0^2 \left( \frac{e^{\omega_0 t_r}}{1 + \frac{1}{2}\epsilon} \right). \quad (\text{A17})$$

Finally, using the same first-order approximation in  $\epsilon$  as the  $t_r > 0$  case,

$$rE(t, \theta_C) \approx \frac{1}{3} \hat{E}_0 \omega_{\text{CF}}^2 \left( 1 - \frac{1}{2}\epsilon \right) e^{\omega_0 t_r}. \quad (\text{A18})$$

Collecting the  $t_r > 0$  and  $t_r < 0$  results together,

$$rE(t, \theta_C) = \frac{1}{3} \hat{E}_0 \omega_{\text{CF}}^2 \begin{cases} (1 - \frac{1}{2}\epsilon) e^{\omega_0 t_r}, & t_r < 0, \\ (2e^{-2\omega_C t_r} - (1 + \frac{1}{2}\epsilon) e^{-\omega_0 t_r}), & t_r > 0. \end{cases} \quad (\text{A19})$$

## APPENDIX B: DETAILS OF THE OFF-CONE FIELD EQUATION DERIVATION

Using Tables II–IV, Eq. (A2) reduces to

$$\mathcal{E}(u, x) = f(u, x)g(u, x)(1 - h(u, x)). \quad (\text{B1})$$

Expanding to first order with respect to  $u$  near ( $u = 1$ ) gives

$$\mathcal{E}(u, x) = \mathcal{E}(x, 1) + (u - 1)\dot{\mathcal{E}}(x, 1) + \mathcal{O}(u - 1)^2. \quad (\text{B2})$$

The first term is  $fg(1 - h)$  evaluated at  $u = 1$ :  $\exp(-y)$  (Table IV). The second term requires the first derivative of  $\mathcal{E}(u, x)$  with respect to  $u$ , evaluated at  $u = 1$ :

$$\dot{\mathcal{E}}(u, x) = f\dot{g} + \dot{f}g - (fgh + f\dot{g}h + \dot{f}gh) \quad (\text{B3})$$

$$\dot{\mathcal{E}}(1, x) = (f\dot{g} + \dot{f}g - (fgh + f\dot{g}h + \dot{f}gh))|_{u=1} \quad (\text{B4})$$

The first derivatives of  $f$ ,  $g$ , and  $h$ , evaluated at  $u = 1$ , are given in Table IV. Because  $h(x, 1) = 0$ , terms proportional to  $h$  will vanish. The result is

$$\dot{\mathcal{E}}(1, x) = \frac{1}{2} e^{-y} (2y + 2q - 1). \quad (\text{B5})$$

Inserting Eq. (B5) into Eq. (B2),

$$\mathcal{E}(u, x) = e^{-y} \left( 1 + \frac{1}{2} (u - 1)(2y + 2q - 1) \right). \quad (\text{B6})$$

Using the definition of  $u$  (Table II), the result may be written as

$$\mathcal{E}(u, x) = e^{-y} \left( 1 - \frac{1}{2} j\eta (2y + 2q - 1) \right). \quad (\text{B7})$$

Proceeding with the inverse Fourier transform of the  $\hat{\theta}$  component,

$$rE(t, \theta) = \mathcal{F}^{-1} \left\{ E_0 \left( \frac{\omega}{2\pi} \right) \tilde{F} \psi \mathcal{E} \right\}. \quad (\text{B8})$$

Let  $\eta = \omega/\omega_C$ ,  $y = p\omega^2$  (Table II). Inserting the Taylor series for  $\mathcal{E}$ , the form factor  $\tilde{F}$ , and  $\psi = -i \exp(ikr) \sin \theta$  (Sec. II), and following the same steps as the on-cone case produces

$$\begin{aligned} 2\pi rE(t, \theta) &= \frac{E_0 \omega_0^2 \sin(\theta)}{4\pi i \omega_C} \\ &\times \frac{d}{dt_r} \int_{-\infty}^{\infty} \frac{e^{-i\omega t_r - p\omega^2} (2i\omega_C + 2p\omega^3 + (2q - 1)\omega)}{\omega^2 + \omega_0^2} d\omega. \end{aligned} \quad (\text{B9})$$

Unlike the on-cone case, Eq. (B9) cannot be integrated with infinite semicircle contours, because the exponential term diverges along the imaginary axis far from the origin.

Let  $I_0$  represent the constant term with respect to  $\omega$  in the numerator:

$$I_0 = \int_{-\infty}^{\infty} \frac{e^{-i\omega t_r - p\omega^2} (2i\omega_C)}{\omega^2 + \omega_0^2} d\omega. \quad (\text{B10})$$

Further, let  $I_1$  and  $I_3$  represent the linear and cubic terms, respectively. Completing the square in the exponent of  $I_0$ , with  $\omega_1 = t_r/(2p)$ , yields

$$I_0 = 2i\omega_C e^{-\frac{t_r^2}{4p}} \int_{-\infty}^{\infty} \frac{e^{-p(\omega+i\omega_1)^2}}{\omega^2 + \omega_0^2} d\omega. \quad (\text{B11})$$

Equation (B11) may be recast as the *line-broadening function*,  $H$  (DLMF 7.19, [39]) common to spectroscopy applications:

$$I_0 = 2\pi i \left( \frac{\omega_C}{\omega_0} \right) e^{-\frac{t_r^2}{4p}} H(\sqrt{p}\omega_0, i\sqrt{p}\omega_1). \quad (\text{B12})$$

Assume that  $\omega > \omega_1$ . This approximating step will be called the *symmetric approximation*:

$$I_0 \approx 2i\omega_C e^{-\frac{t_r^2}{2p}} \int_{-\infty}^{\infty} \frac{e^{-p\omega^2}}{\omega^2 + \omega_0^2} d\omega. \quad (\text{B13})$$

The result for  $I_0$  involves the complementary error function (DLMF 7.7.1, [39]):

$$I_0 = 2i\omega_C e^{-\frac{t_r^2}{2p}} \pi \omega_0^{-1} e^{p\omega_0^2} \operatorname{erfc}(\sqrt{p}\omega_0). \quad (\text{B14})$$

The integrals  $I_1$  and  $I_3$  are zero by symmetry, with odd integrands over  $(-\infty, \infty)$ . Inserting the result for  $I_0$  into Eq. (B9) and evaluating the derivative finishes the problem (see Sec. V).

- 
- [1] The IceCube Collaboration, Evidence for high-energy extraterrestrial neutrinos at the IceCube detector, *Science* **342**, 1242856 (2013).
  - [2] M. Ahlers, L. Anchordoqui, M. Gonzalez-Garcia, F. Halzen, and S. Sarkar, GZK neutrinos after the Fermi-LAT diffuse photon flux measurement, *Astropart. Phys.* **34**, 106 (2010).
  - [3] K. Kotera, D. Allard, and A. Olinto, Cosmogenic neutrinos: Parameter space and detectability from PeV to ZeV, *J. Cosmol. Astropart. Phys.* **10** (2010) 013.
  - [4] The IceCube Collaboration, Differential limit on the extremely-high-energy cosmic neutrino flux in the presence of astrophysical background from nine years of IceCube data, *Phys. Rev. D* **98**, 062003 (2018).
  - [5] The ARIANNA Collaboration, A search for cosmogenic neutrinos with the ARIANNA test bed using 4.5 years of data, *J. Cosmol. Astropart. Phys.* **03** (2020) 053.
  - [6] The ARA Collaboration, Constraints on the diffuse flux of ultrahigh energy neutrinos from four years of Askaryan Radio Array data in two stations, *Phys. Rev. D* **102**, 043021 (2020).
  - [7] M. Ackermann *et al.*, Astrophysics uniquely enabled by observations of high-energy cosmic neutrinos, *Bull. Am. Astron. Soc.* **51**, 185 (2019).
  - [8] M. Ackermann *et al.*, Fundamental physics with high-energy cosmic neutrinos, *Bull. Am. Astron. Soc.* **51**, 215 (2019).

- [9] J. C. Hanson *et al.*, Radar absorption, basal reflection, thickness and polarization measurements from the Ross Ice Shelf, Antarctica, *J. Glaciol.* **61**, 438 (2015).
- [10] J. Avva, J. Kovac, C. Miki, D. Saltzberg, and A. Vieregg, An in situ measurement of the radio-frequency attenuation in ice at Summit Station, Greenland, *J. Glaciol.* **61**, 1005 (2015).
- [11] The ARA Collaboration, Design and initial performance of the Askaryan Radio Array prototype EeV neutrino detector at the south pole, *Astropart. Phys.* **35**, 457 (2012).
- [12] G. Askaryan, On the coherent emission of radio frequency radiation from high energy particle showers, Sov. Phys. JETP **15** (1962).
- [13] E. Zas, F. Halzen, and T. Stanev, Electromagnetic pulses from high-energy showers: Implications for neutrino detection, *Phys. Rev. D* **45**, 362 (1992).
- [14] I. Kravchenko, S. Hussain, D. Seckel, D. Besson, E. Fensholt, J. Ralston, J. Taylor, K. Ratzlaff, and R. Young, Updated results from the RICE experiment and future prospects for ultra-high energy neutrino detection at the south pole, *Phys. Rev. D* **85**, 062004 (2012).
- [15] The ANITA Collaboration, Constraints on the ultrahigh-energy cosmic neutrino flux from the fourth flight of ANITA, *Phys. Rev. D* **99**, 122001 (2019).
- [16] D. Saltzberg, P. Gorham, D. Walz, C. Field, R. Iverson, A. Odian, G. Resch, P. Schoessow, and D. Williams, Observation of the Askaryan Effect: Coherent Microwave Cherenkov Emission from Charge Asymmetry in High-Energy Particle Cascades, *Phys. Rev. Lett.* **86**, 2802 (2001).
- [17] P. Miocinovic, R. Field, P. Gorham, E. Guillian, R. Milincic, D. Saltzberg, D. Walz, and D. Williams, Time-domain measurement of broadband coherent Cherenkov radiation, *Phys. Rev. D* **74**, 043002 (2006).
- [18] P. W. Gorham, S. W. Barwick, J. J. Beatty, D. Z. Besson, W. R. Binns, C. Chen, P. Chen, J. M. Clem, A. Connolly, P. F. Dowkontt *et al.* (ANITA Collaboration), Observations of the Askaryan Effect in Ice, *Phys. Rev. Lett.* **99**, 171101 (2007).
- [19] J. Alvarez-Muñiz, C. James, R. Protheroe, and E. Zas, Thinned simulations of extremely energetic showers in dense media for radio applications, *Astropart. Phys.* **32**, 100 (2009).
- [20] L. Gerhardt and S. R. Klein, Electron and photon interactions in the regime of strong Landau-Pomeranchuk-Migdal suppression, *Phys. Rev. D* **82** (2010).
- [21] K. Dookayka, Characterizing the search for ultra-high energy neutrinos with the ARIANNA detector, Ph.D. thesis, University of California, Irvine, 2011.
- [22] The ARA Collaboration, First constraints on the ultra-high energy neutrino flux from a prototype station of the Askaryan Radio Array, *Astropart. Phys.* **70**, 62 (2015).
- [23] C. Glaser *et al.*, NuRadioMC: Simulating the radio emission of neutrinos from interaction to detector, *Eur. Phys. J. C* **80**, 77 (2020).
- [24] C. Glaser, A. Nelles, I. Plaisier, C. Welling, S. W. Barwick, D. García-Fernández, G. Gaswint, R. Lahmann, and C. Persichilli, NuRadioReco: A reconstruction framework for radio neutrino detectors, *Eur. Phys. J. C* **79**, 464 (2019).
- [25] The ARIANNA Collaboration, Probing the angular and polarization reconstruction of the ARIANNA detector at the south pole, *J. Instrum.* **15**, P09039 (2020).
- [26] C. Welling, P. Frank, T. A. Enßlin, and A. Nelles, Reconstructing non-repeating radio pulses with information field theory, *J. Cosmol. Astropart. Phys.* **04** (2021) 071.
- [27] J. C. Hanson *et al.*, Time-domain response of the ARIANNA detector, *Astropart. Phys.* **62**, 139 (2015).
- [28] The ARIANNA Collaboration, Observation of classically ‘forbidden’ electromagnetic wave propagation and implications for neutrino detection, *J. Cosmol. Astropart. Phys.* **07** (2018) 055.
- [29] The ARA Collaboration, Measurement of the real dielectric permittivity  $\epsilon_r$  of glacial ice, *Astropart. Phys.* **108**, 63 (2019).
- [30] S. Barwick, E. Berg, D. Besson, G. Binder, W. Binns, D. Boersma, R. Bose, D. Braun, J. Buckley, V. Bugaev *et al.*, A first search for cosmogenic neutrinos with the ARIANNA Hexagonal Radio Array, *Astropart. Phys.* **70**, 12 (2015).
- [31] J. Alvarez-Muniz, A. Romero-Wolf, and E. Zas, Practical and accurate calculations of Askaryan radiation, *Phys. Rev. D* **84**, 103003 (2011).
- [32] J. Alvarez-Muniz, P. M. Hansen, A. Romero-Wolf, and E. Zas, Askaryan radiation from neutrino-induced showers in ice, *Phys. Rev. D* **101**, 083005 (2020).
- [33] R. V. Buniy and J. P. Ralston, Radio detection of high energy particles: Coherence versus multiple scales, *Phys. Rev. D* **65** (2001).
- [34] J. C. Hanson and A. L. Connolly, Complex analysis of Askaryan radiation: A fully analytic treatment including the LPM effect and cascade form factor, *Astropart. Phys.* **91**, 75 (2017).
- [35] V. Bogorodsky, C. Bentley, and P. Gudmandsen, *Radio-glaciology* (Springer, Netherlands, 1985).
- [36] S. Razzaque, S. Seunarine, D. Z. Besson, D. W. McKay, J. P. Ralston, and D. Seckel, Coherent radio pulses from GEANT generated electromagnetic showers in ice, *Phys. Rev. D* **65**, 103002 (2002).
- [37] S. Andringa, R. Conceição, and M. Pimenta, Mass composition and cross-section from the shape of cosmic ray shower longitudinal profiles, *Astropart. Phys.* **34**, 360 (2011).
- [38] K. F. Fadhel, A. Al-Rubaiee, H. A. Jassim, and I. T. Al-Alawy, Estimating the lateral distribution of high energy cosmic ray particles by depending on Nishimura-Kamata-Greisen function, *J. Phys.* **1879**, 032089 (2021).
- [39] DLMF, *NIST Digital Library of Mathematical Functions*, <http://dlmf.nist.gov/>, Release 1.1.1 of 2021-03-15, edited by f. W. J. Olver, A. B. Olde Daalhuis, D. W. Lozier, B. I. Schneider, R. F. Boisvert, C. W. Clark, B. R. Miller, B. V. Saunders, H. S. Cohl, and M. A. McClain, <http://dlmf.nist.gov/>.
- [40] T. T. García, Voigt profile fitting to quasar absorption lines: An analytic approximation to the Voigt–Hjerting function, *Mon. Not. R. Astron. Soc.* **369**, 2025 (2006).
- [41] The Telescope Array Collaboration, First upper limits on the radar cross section of cosmic-ray induced extensive air showers, *Astropart. Phys.* **87**, 1 (2017).

# In situ, broadband measurement of the radio frequency attenuation length at Summit Station, Greenland

J. A. Aguilar<sup>1</sup>, P. Allison<sup>2</sup>, J. J. Beatty<sup>2</sup>, D. Besson<sup>3,4</sup>, A. Bishop<sup>5</sup>, O. Botner<sup>6</sup>, S. Bouma<sup>7</sup>, S. Buitink<sup>8</sup>, M. Cataldo<sup>7</sup>, B. A. Clark<sup>9</sup>, Z. Curtis-Ginsberg<sup>10</sup>, A. Connolly<sup>2</sup>, P. Dasgupta<sup>1</sup>, S. de Kockere<sup>11</sup>, K. D. de Vries<sup>11</sup>, C. Deaconu<sup>10</sup>, M. A. DuVernois<sup>5</sup>, C. Glaser<sup>6</sup>, A. Hallgren<sup>6</sup>, S. Hallmann<sup>12</sup>, J. C. Hanson<sup>13</sup>, B. Hendricks<sup>14</sup>, C. Hornhuber<sup>3</sup>, K. Hughes<sup>10</sup>, A. Karle<sup>5</sup>, J. L. Kelley<sup>5</sup>, I. Kravchenko<sup>15</sup>, R. Krebs<sup>14</sup>, R. Lahmann<sup>7</sup>, U. Latif<sup>11</sup>, J. Mammo<sup>15</sup>, Z. S. Meyers<sup>12,7</sup>, K. Michaels<sup>10</sup>, K. Mulrey<sup>16</sup>, A. Nelles<sup>12,7</sup>, A. Novikov<sup>3</sup>, A. Nozdrina<sup>3</sup>, E. Oberla<sup>10</sup>, B. Oeyen<sup>17</sup>, Y. Pan<sup>18</sup>, H. Pandya<sup>8</sup>, I. Plaisier<sup>7,12</sup>, N. Punzelsay<sup>18</sup>, L. Pyras<sup>12,7</sup>, D. Ryckbosch<sup>17</sup>, O. Scholten<sup>11,19</sup>, D. Seckel<sup>18</sup>, M. F. H. Seikh<sup>3</sup>, D. Smith<sup>\*10</sup>, D. Southall<sup>10</sup>, J. Torres<sup>2</sup>, S. Toscano<sup>1</sup>, D. Tosi<sup>5</sup>, D. J. Van Den Broeck<sup>11,8</sup>, N. van Eijndhoven<sup>11</sup>, A. G. Vieregg<sup>10</sup>, C. Welling<sup>7,12</sup>, D. R. Williams<sup>20</sup>, S. Wissel<sup>14,21</sup>, R. Young<sup>3</sup>, A. Zink<sup>7</sup>

<sup>1</sup>Université Libre de Bruxelles, Science Faculty CP230, B-1050 Brussels, Belgium

<sup>2</sup>Dept. of Physics, Center for Cosmology and AstroParticle Physics, Ohio State University, Columbus, OH 43210, USA

<sup>3</sup>University of Kansas, Dept. of Physics and Astronomy, Lawrence, KS 66045, USA

<sup>4</sup>National Nuclear Research University MEPhI, Kashirskoe Shosse 31, 115409, Moscow, Russia

<sup>5</sup>Wisconsin IceCube Particle Astrophysics Center (WIPAC) and Dept. of Physics,  
University of Wisconsin-Madison, Madison, WI 53703, USA

<sup>6</sup>Uppsala University, Dept. of Physics and Astronomy, Uppsala, SE-752 37, Sweden

<sup>7</sup>Erlangen Center for Astroparticle Physics (ECAP),

Friedrich-Alexander-University Erlangen-Nuremberg, 91058 Erlangen, Germany

<sup>8</sup>Vrije Universiteit Brussel, Astrophysical Institute, Pleinlaan 2, 1050 Brussels, Belgium

<sup>9</sup>Dept. of Physics and Astronomy, Michigan State University, East Lansing MI 48824, USA

<sup>10</sup>Dept. of Physics, Enrico Fermi Inst., Kavli Inst. for Cosmological Physics, University of Chicago, Chicago, IL 60637, USA

<sup>11</sup>Vrije Universiteit Brussel, Dienst ELEM, B-1050 Brussels, Belgium

<sup>12</sup>DESY, Platanenallee 6, 15738 Zeuthen, Germany

<sup>13</sup>Whittier College, Whittier, CA 90602, USA

<sup>14</sup>Dept. of Physics, Dept. of Astronomy & Astrophysics, Penn State University, University Park, PA 16801, USA

<sup>15</sup>Dept. of Physics and Astronomy, Univ. of Nebraska-Lincoln, NE, 68588, USA

<sup>16</sup>Department of Astrophysics/IMAPP, Radboud University, PO Box 9010, 6500 GL, The Netherlands

<sup>17</sup>Ghent University, Dept. of Physics and Astronomy, B-9000 Gent, Belgium

<sup>18</sup>Dept. of Physics and Astronomy, University of Delaware, Newark, DE 19716, USA

<sup>19</sup>Kapteijn Institute, University of Groningen, Groningen, The Netherlands

<sup>20</sup>Dept. of Physics and Astronomy, University of Alabama, Tuscaloosa, AL 35487, USA

<sup>21</sup>Physics Dept. California Polytechnic State University, San Luis Obispo CA 93407, USA

**ABSTRACT.** Over the last 25 years, radiowave detection of neutrino-generated signals, using cold polar ice as the neutrino target, has emerged as perhaps the most promising technique for detection of extragalactic ultra-high energy neutrinos (corresponding to neutrino energies in excess of 0.01 Joules, or  $10^{17}$  electron volts). During the summer of 2021 and in tandem with the initial deployment of the Radio Neutrino Observatory in Greenland (RNO-G), we conducted radioglaciological measurements at Summit Station, Greenland to refine our understanding of the ice target. We report the result of one such measurement, the radio-frequency electric field attenuation length  $L_\alpha$ . We find an approximately linear dependence of  $L_\alpha$  on frequency with the best fit of the average field attenuation for the upper 1500 m of ice:  $\langle L_\alpha \rangle = ((1024 \pm 50) - (0.65 \pm 0.06)(\nu/\text{MHz})) \text{ m}$  for frequencies  $\nu \in [145 - 350] \text{ MHz}$ .

## INTRODUCTION

We report a measurement of the radio frequency electric field attenuation length of deep glacial ice at the National Science Foundation's Summit Station in Greenland. This measurement is of interest to the ultra-high energy neutrino (UHEN) community due to the development of the Radio Neutrino Observatory in Greenland (RNO-G), a particle astrophysics experiment that uses the ice as a target material in the search for astrophysical and cosmogenic neutrinos (Aguilar and others, 2021a).

The IceCube experiment has placed a flux upper limit for astrophysical neutrinos of  $E^2\phi \lesssim 2 \times 10^{-8}$  GeV/(cm<sup>2</sup> s sr) at  $E_\nu = 1$  EeV (Aartsen and others, 2018). At such fluxes, a particle detector requires an active volume of  $O(10 \text{ km}^3)$  or larger for a discovery-level detection within a detector's lifetime. A sparsely instrumented array of radio antennas, deployed in and on an extensive dielectric medium can satisfy this volume requirement. An UHEN interaction creates an extensive electromagnetic shower that produces impulsive radio emission via the Askaryan effect (Askaryan, 1961). If the interaction occurs in an environment of low radio attenuation, a relatively small number of radio antennas can probe target volumes at the scale needed for UHEN observations.

Glacial ice has been measured to have long radio attenuation lengths due to low temperature and high purity at depths below the firn (Barwick and others, 2005; Besson and others, 2008; Allison and others, 2012; Avva and others, 2015; Barrella and others, 2011; Hanson and others, 2015). This, combined with the volume of glacial ice available in Greenland and Antarctica, makes polar ice sheets attractive sites for the construction of a radio neutrino detector.

RNO-G is one such experiment based on radio detection of UHEN in glacial ice (Aguilar and others, 2021a), among others (Allison and others, 2012, 2020; Anker and others, 2019; Kravchenko and others, 2003; Gorham and others, 2009, 2019). RNO-G is being constructed near NSF's Summit Station at the highest point of the Greenlandic Ice Sheet. The detector will ultimately be composed of 35 autonomous stations separated by 1.25 km in a grid pattern. Each station is instrumented with radio antennas, with good response over the range 100–600 MHz, deployed both just below the surface and at depths down to 100 m in boreholes. Construction of the detector began during the summer of 2021 with the installation of the first three stations.

Previous measurements of radio attenuation lengths in Antarctica (Barwick and others, 2005; Besson and others, 2008; Allison and others, 2012; Barrella and others, 2011; Hanson and others, 2015) and Greenland (Avva and others, 2015;

MacGregor and others, 2015; Paden and others, 2005) have demonstrated that radio attenuation lengths vary at different ice locations, due primarily to differences in ice temperature and impurity levels. Since electric field attenuation length is a primary determinant of the expected number of observed UHENs at energies greater than 1 EeV, a precise, *in situ* measurement is required at Summit Station to assess RNO-G's science potential.

Our work builds upon one previous *in situ* measurement of the bulk ice electric field attenuation length performed at Summit Station by Avva and others (2015); that effort reported a depth-averaged attenuation length  $\langle L_\alpha \rangle = 947^{+92}_{-85}$  m at 75 MHz. We herein quantify the attenuation length at higher frequencies to better match RNO-G's frequency range of 100–600 MHz. In addition to that prior analysis, there have been several previous measurements of the radio ice properties at Summit Station, including radar attenuation length measurements from air-borne radio sounding in the Greenland Ice Sheet Project (MacGregor and others, 2015) and *in situ* radio sounding to investigate layering in the ice (Paden and others, 2005). We include a comparison of our reported attenuation with previous measurements at Summit Station and Antarctica in the **Discussion and Summary** section.

## EXPERIMENTAL APPROACH

Our approach is similar to previous work in the astro-particle physics field (Avva and others, 2015; Barrella and others, 2011; Besson and others, 2008; Hanson and others, 2015; Barwick and others, 2005).

We transmit an impulsive, broadband radio signal downwards into the ice via a wideband, directional antenna, and measure the return signal as a voltage versus time trace on a second, identical antenna. The transmitted signal propagates through the ice sheet, reflects off of the bedrock, and returns to the receiving antenna on the surface. After correcting for geometric path loss, bedrock coefficient of reflection, and electric field amplification from the focusing effect of the firn, the remaining power loss is attributed to absorption and scattering in the ice. Note that, experimentally, we do not distinguish between the two – our quoted attenuation length implicitly includes both effects. Contributions from dispersion effects at the bedrock are quantified in the **Bedrock Echo** section. To reduce systematic uncertainties, we remove the system response of the electronics (initial impulse, antenna response, cables, amplifiers, filters) by normalizing against a second measurement run in air. We recreate the through-ice setup (same initial impulse, antenna polarization, cables, amplifiers, and filters but additional attenuators) for two antennas transmitting over a

\*e-mail: danielsmith@uchicago.edu, authors@rno-g.org

short distance in air and thereby cancel dependence on the system response from the in-ice data run.

Assuming specular, mirror-like reflection off the bedrock, the radar range equation reduces to the Friis equation (Friis, 1946), and the direct through-air transmission formalism is applicable to our observed bedrock echoes. In that case, following the notation used by Avva and others (2015), the ratio of recorded voltages for each configuration (through-air vs. through-ice) as a function of frequency  $\nu$  is,

$$\frac{V_{\nu,ice}}{V_{\nu,air}} = \sqrt{F_f R} T_{ratio} \frac{d_{air}}{d_{ice}} \exp\left(-\frac{d_{ice}}{\langle L_\alpha \rangle}\right), \quad (1)$$

where  $d_{air}$  and  $d_{ice}$  are the distances the ice and air signals travel between antennas,  $R$  is the power reflection coefficient of the bedrock,  $F_f$  is a focusing factor from the changing index of refraction in the firn (Stockham and others, 2016; Stockham, 2018),  $T_{ratio}$  corrects for the change of transmission coefficient at the antenna feed between the antenna operating in air and in ice, and  $\langle L_\alpha \rangle$  is the depth-averaged electric field attenuation length over the entire depth of the ice. Solving for the attenuation gives,

$$\langle L_\alpha \rangle = d_{ice} / \ln\left(\sqrt{F_f R} T_{ratio} \frac{V_{\nu,air}}{V_{\nu,ice}} \frac{d_{air}}{d_{ice}}\right). \quad (2)$$

This equation differs from that in Avva and others (2015) by the inclusion of the focusing factor, which arises from the amplification of field strength from propagation in the firn (Sodha and others, 1969). With the addition of the focusing factor, the bulk attenuation result from Avva and others (2015) goes from  $947^{+92}_{-85}$  m to  $913^{+85}_{-79}$  m. We assume that the firn has an index of refraction varying linearly with the ice density profile  $\rho(z)$  at Summit Station (Kovacs and others, 1995). The density profile has been experimentally measured (Arthern and others, 2013; Hawley and others, 2008; Alley and Koci, 1988; Alley and others, 1997) and fit to a double exponential (Deaconu and others, 2018), leading to a refractive index varying between  $n \sim 1.4$  at the surface and  $n \sim 1.78$  in deep ( $< 100$  m) ice. The changing index of refraction focuses power from the transmitter down towards the bedrock but, due to a different return path, does not completely defocus the power on the return trip to the surface; we have used the finite-difference time domain electrodynamics simulation software MEEP (Oskooi and others, 2010) to confirm this effect.

## EXPERIMENTAL SETUP

A system diagram of the experiment is presented in Fig. 1. This measurement was performed in August 2021 at Summit Station, Greenland, using a separation distance of 244

meters between the transmitter (coordinates N  $72^\circ 34' 48.2''$  W  $38^\circ 27' 24.8''$ ) and receiver (coordinates N  $72^\circ 34' 43.1''$  W  $38^\circ 27' 9.55''$ ) sites. The large separation distance assured that direct propagation from the transmitting antenna to the receiving antenna did not saturate the receiving amplifier. All antennas used were commercially available Create CLP-5130-2N (Creative Design Corp., 1994) log-periodic dipole antennas (LPDA) with  $\sim 8$  dBi in-air forward gain over the band 105 - 1300 MHz.

Due to the large distance between stations, two parallel electronics signal chains are used, for triggering and the bedrock echo measurement, respectively. The bedrock echo electronics signal chain starts with the self-triggered high voltage FID Technology<sup>1</sup> model FPG6-1PNK pulse generator, which delivers a +5 kV signal to a  $50\Omega$  coaxial feed. After the FID output, we apply a 100 MHz high pass filter using a Minicircuits<sup>2</sup> NHP-100 filter to prevent potentially damaging reflections from the poor match at the antenna feed for out-of-band frequencies. Following the filter, the signal is conveyed over 12 m of LMR-400  $50\Omega$  coaxial cable to an LPDA buried in the ice and pointed vertically downwards towards the bedrock; the bedrock-reflected return signal is then measured by a similarly-buried, downwards-pointing, receiver LPDA. The receiving antenna, located 244 m away along the surface of the ice, is aligned so that each antenna is in the gain null of the other to minimize contamination from horizontal ray paths. After measurement in the receiving antenna, the signal travels over a 10 m LMR-400 cable, bandpass filtered from 145-575 MHz using Minicircuits VHF-145+ and VLF-575+ filters, and then amplified by a custom RNO-G design low-noise amplifier with +59 dB of gain over the band 80 - 750 MHz. After the amplifier, the signal is bandpass filtered again using Minicircuits NHP-200 and VLF-575+ filters, and then recorded on a 2 GHz-bandwidth Tektronix MSO5204B oscilloscope.

The oscilloscope is triggered by the second electronic signal chain, ensuring a stable trigger over the distance between transmitter and receiver. The second chain begins with an AVTECH AVIR-1-C pulse generator triggered by the FID pulse generator TRG OUT, producing an impulsive,  $O(1\text{ ns})$  pulse. The pulse generator is connected over a 12 m LMR-400 cable to an elevated, in-air LPDA pointed at a similarly elevated receiver LPDA located 244 m away and viewing the transmitter on boresight. The received in-air signal is then attenuated by 20 dB to prevent saturation, bandpass filtered using Minicircuits VHF-145+ and VLF-575+ filters, amplified by +59 dB using the RNO-G low-noise amplifier, bandpass filtered again using Minicircuits VHF-145+ and VLF-575+ fil-

<sup>1</sup><http://www.fidtechnology.com>

<sup>2</sup><https://www.minicircuits.com/products/RF-Filters.html>

ters and finally captured by the oscilloscope. This in-air signal was used to trigger the oscilloscope, and therefore provides the reference  $t_0$  for our measurements.

The oscilloscope was set to collect data over a  $50 \mu\text{s}$  window; 10,000 individual triggers are averaged to suppress incoherent noise contributions and that average is written to scope memory. Twenty 10,000-event runs were collected, and then again averaged in post-processing, bringing the total number of triggers to 200,000.

To perform the air  $\rightarrow$  air normalization run, we swapped the cables for the in-ice antennas with those from the in-air antennas. On the receiving side, two modifications were made: we added a 46 dB attenuator to prevent amplifier saturation and, for this configuration, we self-triggered on the arriving signal.

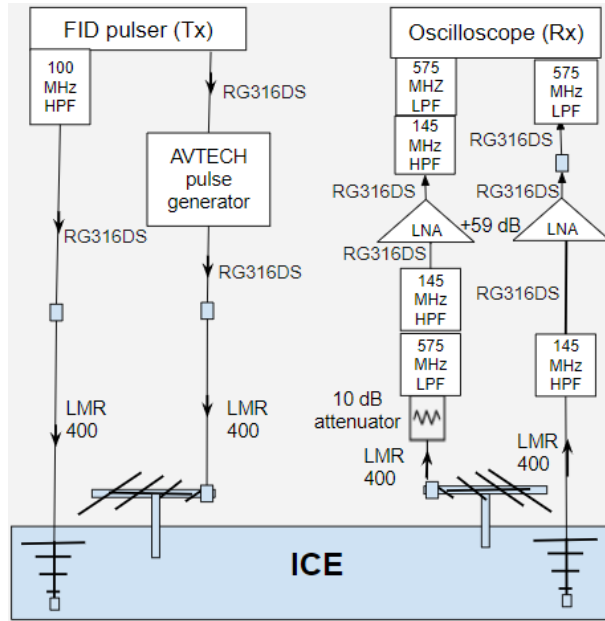


**Fig. 1.** Diagram of experimental setup for bedrock reflection. On the transmitting side, we use a self-triggering FID Technologies +5 kV high voltage pulse generator connected to a buried log-periodic dipole antenna (LPDA); an AVTECH fast pulse generator triggered by the FID pulser is connected to an in-air LPDA. On the receiving side, both the buried downward-pointing, and the in-air LPDAs are connected to a +59 dB low noise amplifier; those outputs are then recorded on a Tektronix digital oscilloscope, triggered by the in-air signal.

## EXPERIMENTAL RESULTS

### Bedrock Power Reflection Coefficient

The power reflection coefficient at the ice-rock interface is not well-known and constitutes the largest uncertainty in our measurement of attenuation length. Taking an approach similar to Avva and others (2015), we take the power reflection coefficient to have a mean value of 0.3, a typical value for ice-bedrock interfaces as derived from radio sounding experiments (Barwick and others, 2005; Paden and others, 2005). For uncertainty analysis, we assume the reflection coefficient can be drawn from a probability density function, uniformly distributed in the log of the reflection coefficient over the range from 0.1 to 1.0, which represent plausible extrema for the ice-bedrock interface.

The observed return echo, in principle, could include both coherent and also incoherent contributions. Whereas the former sum linearly with the number of average triggers, the latter will scale as the square root of the number of events averaged  $N_{avg}$  (Paden, 2006). We have explicitly verified that our final results are insensitive to  $N_{avg}$ , consistent with the assumption that the observed specular return echo is dominated by coherent scattering.

### Bedrock Echo

The reflection from the bedrock is visible above thermal noise in the time domain voltage trace of the receiving antenna, at a signal onset time of  $35.55 \mu\text{s}$  after the oscilloscope trigger (Fig. 2). The bedrock echo is observed to include two components: a predominantly-specular, sharp, faster impulse (of duration  $\sim 500 \text{ ns}$ ), and a long ( $> 2 \mu\text{s}$ ) extended signal which we associate with more diffuse, multi-path reflections off irregular features, both on the surface of, and within, the underlying bed reflector. For the purposes of the bulk radio attenuation measurement, and since an extended tail is not present for the in-air normalization run, we restrict consideration to the fast, specular component.

The uncertainty in the time window of the specular reflection is of  $O(10 \text{ ns})$ , dominated by noise fluctuations at the edges of the window. This uncertainty is neglected since it is sub-dominant relative to the other systematic uncertainties in our final measurement. The final window start and end times are defined to be  $35.55$  and  $36.05 \mu\text{s}$ , respectively.

To determine the impact of neglecting the diffuse component of the bedrock echo on our final measured value of bulk attenuation, we investigate the dependence of our numerical result on the window length used in our analysis. We expect the measured attenuation to increase with increased

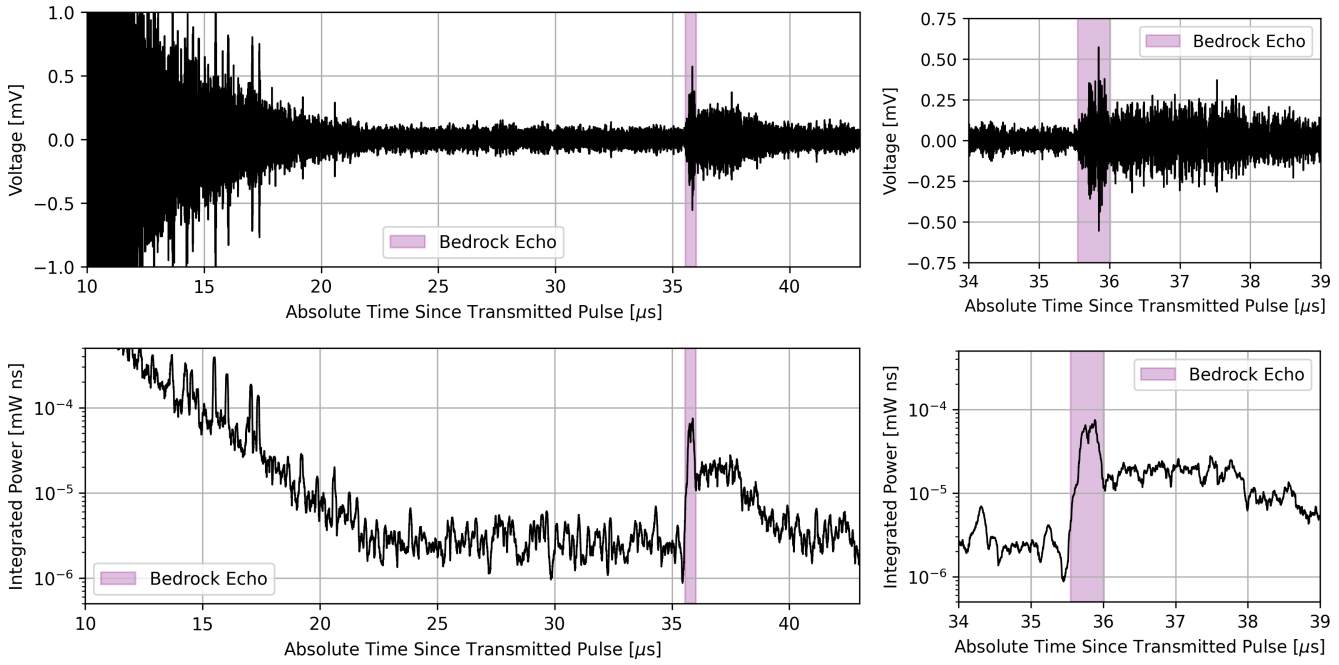


**Fig. 2.** Top: Recorded voltage as a function of time for the receiving in-ice antenna. Bottom: Recorded power, integrated in a sliding window of 100 ns to account for the group delay of the LPDA antennas. The specular component of the bedrock echo ‘signal’ is highlighted in magenta. Sub-surface internal layer reflections are visible at times earlier than 22  $\mu\text{s}$ , after which noise dominates up to the point at which the bedrock echo is evident.

window length due to the extended integration of power returning from the bedrock; at frequencies below 250 MHz, we obtain a  $\sim 10\%$  larger attenuation length, but with increased uncertainty, as seen in Fig. 3. At frequencies above 250 MHz, there is a negligible increase in attenuation length with increased window length. We note that the additional attenuation length is within the systematic uncertainties of our stated result due to the large bedrock reflection coefficient uncertainty.

The relationship between bulk ice attenuation and received power is different for the specular vs. diffuse components. We define attenuation from the Friis transmission equation (implicit in Eq. 1) (Friis, 1946). The Friis transmission equation is applicable for a specular reflection as it assumes direct line-of-sight propagation without interference within the first Fresnel zone, leading to a geometric path loss  $\propto d_{\text{ice}}^2$ . The radar range equation is more applicable to the diffuse component since it includes power contributions from a rough surface via the definition of a radar cross section and a geometric path loss  $\propto (d_{\text{ice}}/2)^4$  (Balanis, 2016). We find that use of the radar range equation instead of the Friis equation over the combined specular and diffuse components also increases the measured attenuation length at

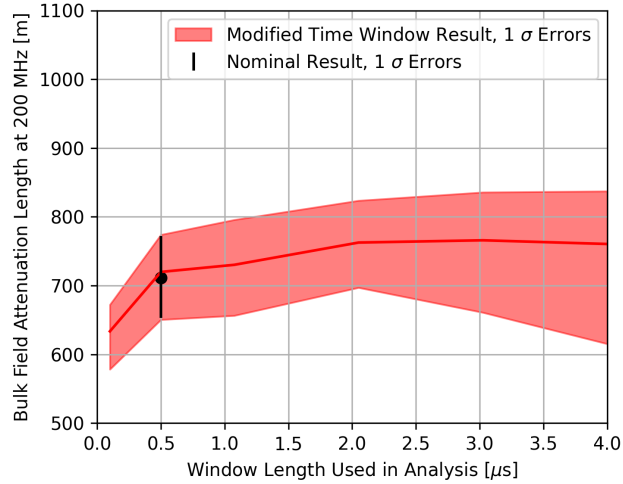


**Fig. 3.** Measurement of the depth-averaged electric field attenuation at 200 MHz as a function of the window length used to select the bedrock echo. We note that including the entire diffuse component of the reflection into the final attenuation calculation increases the final result by no more than 10%.

lower frequencies by a maximum of 10%, albeit introducing more model dependence from the unknown value of bedrock radar cross section.

Based on the relatively small increase in obtained attenuation length from including the diffuse component, we quote our final result based on the Friis equation; this choice is consistent with previous similar measurements (Barwick and others, 2005; Besson and others, 2008; Barrella and others, 2011; Hanson and others, 2015; Avva and others, 2015; Paden and others, 2005).

## Bedrock Depth

The bedrock depth can be derived from the absolute time of flight of the transmitted pulse and a model for the index of refraction of the ice as a function of depth. We measure the bedrock depth instead of using previous measurements to reduce systematic biases (from location extrapolation and bedrock radio properties) and as a cross check of our absolute timing calibration. The relationship between time of flight ( $\Delta t$ ) and bedrock depth (half of the total distance propagated by the transmitted signal,  $d_{ice}$ ) can be found by solving for  $d_{ice}$  in the integral:

$$\Delta t = \frac{2}{c} \int_0^{d_{ice}/2} n(z) dz, \quad (3)$$

where  $n(z)$  is the model for the index of refraction as a function of depth [m]. Index of refraction is related to dielectric constant ( $\epsilon'$ ) via  $n(z) = \sqrt{\epsilon'(z)}$ . The value of  $\epsilon'(z)$  is derived from its relationship with measured ice density ( $\rho$ , [kg / m<sup>3</sup>]) (Kovacs and others, 1995; Barwick and others, 2018):

$$\epsilon'(z) = (1 + 0.854\rho(z))^2. \quad (4)$$

The parameterization of the dependence of ice density on depth follows Deaconu and others (2018), which performed a double exponential fit with a critical density at a depth of 14.9 m (Herron and Langway, 1980):

$$\rho(z) = \begin{cases} 0.917 - 0.594e^{-z/30.8} & z \leq 14.9 \text{ m} \\ 0.917 - 0.367e^{-(z-13.9)/40.5} & z > 14.9 \text{ m} \end{cases} \quad (5)$$

The uncertainty on the depth determination arises primarily from the uncertainty in the asymptotic index of refraction of deep glacial ice, which we take to be  $n = 1.78 \pm 0.03$  (Bogorodsky and others, 1985) for ice below the firn (deeper than 100 m at Summit Station). Using this refractive index profile, we calculate the bedrock to be at a depth of  $3004^{+50}_{-52}$  m, corresponding to  $d_{ice} = 6008^{+100}_{-104}$  m for the through-ice bedrock echo total travel distance.

We note that, while our transmitting and receiving antennas were separated by 244 m, the through-ice signal approximately propagates vertically and Eq. 3 holds true. Over the measured 6 km propagation distance, horizontal propagation results in 4 m extra path length.

This bedrock depth is consistent with previous measurements of the bedrock depth from Greenland Ice Core Project (1994), at 3053.5 m in 1993, and from Avva and others (2015), at  $3014^{+48}_{-50}$  m in 2015.

## Antenna Coupling

The antenna transmission coefficient is defined as the quantity of power transmitted by the antenna from an incident radio frequency signal on a  $50 \Omega$  transmission line at the antenna feed point ( $S_{21}$  in the scattering matrix). The transmission coefficient depends upon the dielectric properties of the antenna's embedded environment (Glaser and others, 2019; Barwick and others, 2015). To increase the power transmitted into the ice, we buried our antennas so that all active conductors were at least  $\sim 20$  cm below the surface, thereby embedding them in an environment of  $n \approx 1.4$ . The antennas used for the normalization are in air, for which  $n \sim 1.0$ . To correct for the change in match, we calculate a  $T_{ratio}$  from the measured reflection coefficient ( $S_{11}$  as shown in Fig. 4) of the four antennas, two in air and two in ice, taken in the field. Assuming that all power not reflected at the feed is transmitted, the ratio becomes, in terms of the reflection coefficient  $S_{11}$  in dB,

$$T_{ratio} = \frac{1 - 10^{S_{11,ice}/10}}{1 - 10^{S_{11,air}/10}}. \quad (6)$$

The antennas were found to transmit nearly all incident power in the frequency range of interest (150 - 550 MHz) in both the in-air and in-ice cases, resulting in a small  $T_{ratio}$  correction. Averaged over frequency in the range of interest,  $T_{ratio} = 1.00 \pm 0.05$ , with the uncertainty assessed empirically from the variance of the measured match over the band. Our result is consistent with  $T_{ratio}$  measured by other groups using the same or similar antennas (Barrella and others, 2011; Avva and others, 2015).

*In situ* measurements, as well as simulations (Barwick and others, 2015; Glaser and others, 2019), have shown that the frequency-dependent antenna gain also changes when the antenna is embedded in a dielectric medium. This change can be modeled as a down-shift in frequency, by the index of refraction of the medium ( $G'(v) = G_0(v/n)$ ). For the LPDA used in this work, the gain over the frequency band of interest is uniform to  $< 0.5dB$  (Creative Design Corp., 1994), rendering the shift between in-air and in-ice measurements a subdominant systematic bias. The down-shift in frequency

will cause a corresponding shift in low-frequency cutoff both in the gain and in the  $S_{11}$  (as shown in Fig. 4). The cutoff in both environments is below the high-pass filter of our analysis.

We note that there will be different contributions from the ice surface in both the in-air and in-ice antenna responses. We neglect these effects because they are likely to be small so long as the directional antennas (front-to-back (F/B) ratio of the LPDA is -15 dB) are pointed away from the surface Barwick and others (2015).

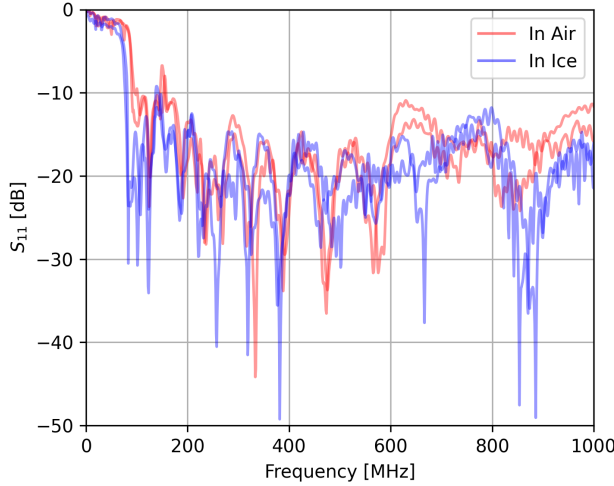


**Fig. 4.** Measured  $S_{11}$  of each antenna used in the experiment. The difference in the low-frequency cutoff of the antenna when it is embedded in the ice compared to in air is due to the different index of refraction of the two environments.

## Firn Focusing

There is a geometric amplification of the bedrock echo electric field at the surface of the ice due to the changing index of refraction of the firn. To calculate the power focusing factor, for a negligibly thin firn layer, Snell's law prescribes (Stockham and others, 2016):

$$F_f = \left( \frac{n(z=0)}{n(z=d_{ice}/2)} \right)^2. \quad (7)$$

We have verified that this equation agrees with a ray tracing simulation and 3D FDTD simulation. The uncertainty on the focusing factor arises from the uncertainty in the index of refraction model. Using  $n = 1.78 \pm 0.03$  (Bogorodsky and others, 1985) (as described previously in the **Bedrock Depth** section), and  $n = 1.4 \pm 0.1$  for the surface ice (Bo-

gorodsky and others, 1985), we obtain a final focusing factor of  $F_f = 1.61 \pm 0.24$ .

## In-Air Normalization Amplitude

The amplitude of the signal from the in-air normalization run can be systematically biased from reflections off of the ice surface, increasing or decreasing the recorded power observed from the direct line-of-sight signal. Given the antenna heights above the ice (1.5 m) and distance between antennas (244 m), the first Fresnel zone is comprised by a nearly uniform, planar surface ice reflector, at all frequencies of interest. This leads to potential interference from reflections, depending on geometry: direct rays will interfere destructively/constructively with rays at the center/periphery of the Fresnel zone. To quantify any possible systematic bias, we compare the data against the absolute amplitude expectation of the signal from simulation. The absolute amplitude is derived from a measurement of the FID pulse shape, amplifier response, filter response, free space path loss, and two independent simulations of the LPDA antenna response. Our simulations use either the Method of Moments software WIPL-D<sup>3</sup> or Finite Difference Time Domain software xFDTD<sup>4</sup>, and have been found to agree with anechoic chamber measurements to 10% uncertainty (Barwick and others, 2017, 2015). The comparison of the simulated result with our data, seen in Fig. 5, demonstrates that any possible systematic bias is not greater than 10% in voltage, consistent with previous agreement (Barwick and others, 2017, 2015).

## Result and Error Analysis

The measured depth-averaged field attenuation length is presented in Fig. 6. The previous *in situ* measurement reported by Avva and others (2015) is included for comparison, adjusted to remove the systematic bias from firn focusing not previously included in that analysis, resulting in a correction of their published result (from  $947^{+92}_{-85}$ m to  $913^{+85}_{-79}$ m). We report the measurement only within the bandpass limits of our system, over which we have the highest sensitivity and lowest systematic biases from antenna modeling and filter response. Beyond the system bandpass limits, we have checked that our procedure yields an attenuation length numerically consistent with zero.

Contributions of different sources of uncertainty are calculated using a Monte Carlo method. We numerically calculate the estimated probability density distribution (PDF) of the bulk electric field attenuation within each frequency

<sup>3</sup><https://wipl-d.com>

<sup>4</sup><https://www.remcom.com/xfDTD-3D-EM-Simulation-Software>

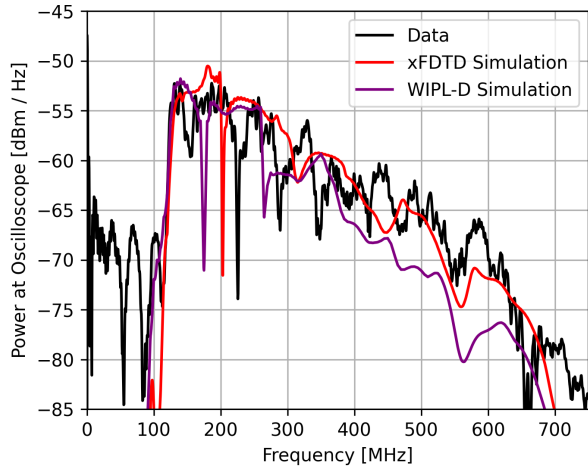


**Fig. 5.** Comparison of data from the in-air normalization run compared against an absolute amplitude expectation as derived from two separate LPDA simulations. No systematic bias is evident within the frequency band of this analysis and within the  $\pm 10\%$  voltage uncertainty in the antenna model (Barwick and others, 2017, 2015). The sharp dip between 180–220 MHz seen in data and simulations is most likely due to fine details in tine length and separation, which are difficult to simulate accurately (Barwick and others, 2017).

bin by repeatedly drawing random values of each component of the final measurement from their respective PDFs. For systematic uncertainties, we assume that each measured quantity used in the calculation of bulk field attenuation is uncorrelated and has a PDF either of a normal distribution (as is the case for  $F_f$ ,  $T_{ratio}$  and  $d_{ice}$ ) or the distribution already described in the text (as is the case for  $R$ ). The main component of statistical uncertainty is due to fluctuations in the power contributions from thermal noise in the recorded oscilloscope trace. In the 150–300 MHz band, the uncertainty from noise statistical fluctuation is sub-dominant to systematic uncertainties, contributing less than 10% to the quoted uncertainty of each frequency bin. The final measurement is reported as a central value with one standard deviation (statistical plus systematic) error bars for those frequency bins that yield statistically significant results. For all other frequency bins, we report a 95% confidence level upper limit.

It is important to note that the majority of uncertainties are correlated in each frequency bin of the final measurement, with the primary contributions to the uncertainty arising from limited noise statistics and small systematic biases from the difference in LPDA response in ice vs. air. For the linear fit presented below, the visibly high goodness of fit is due to this correlation of uncertainties between frequency

bins.

The reported bulk attenuation length includes losses from layer scattering. While expected to be a subdominant effect for vertical propagation due to the low reflection coefficient of the observed layers (Paden and others, 2005), quantifying effects due to layer scattering for the more horizontal neutrino geometries must account for the larger Fresnel reflection coefficients at more glancing layer incidence angles (Aguilar and others, 2021b).

Birefringence of the ice can result in rotation of the signal that is dependant on polarization, leading to apparent loss of power at the co-polarized receiver. Measurements of the crystal orientation at Summit Station indicate uniaxial fabric at all depths (Thorsteinsson, 1996), unlike South Pole (Matsuoka and others, 2003; Barwick and others, 2005), indicating that birefringence will matter less for the Greenland site, though this remains to be quantified.

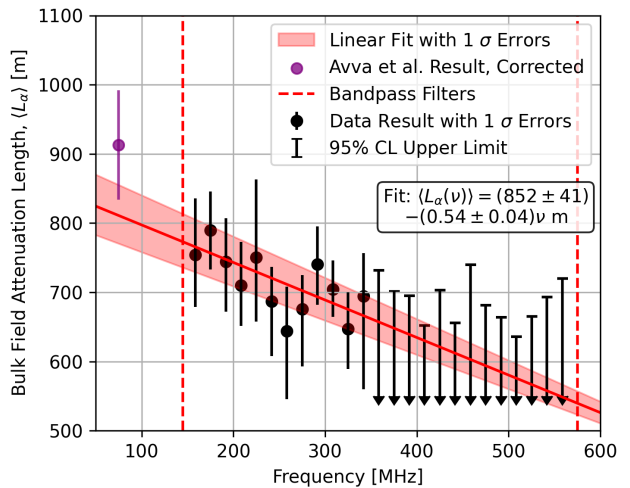


**Fig. 6.** Measurement of the depth-averaged electric field attenuation as a function of frequency at Summit Station, within the system bandpass (shown as red dashed lines). Definitions of the error bars (and displayed upper limits) are provided in the text. The corrected result from Avva and others (2015) is shown for comparison. The frequency  $v$  in the fit has units of MHz.

## Discussion and Summary

Using the same approach as Avva and others (2015), we derive the electric field attenuation length as a function of depth using a model of the field attenuation dependence on temperature. We then unfold, requiring that the depth-integrated attenuation matches our measured depth-averaged attenuation, using the temperature profile of ice at Summit Station

measured at the GRIP borehole (Greenland Ice Core Project, 1994). We assume a linear relationship between the log of the attenuation versus the temperature of the ice:

$$L_\alpha(T(z)) = A 10^{m T(z)}. \quad (8)$$

The parameter  $m$  is taken to be the average of the two sites measured by Bogorodsky and others (1985) and set equal to  $-0.017$  ( $^{\circ}\text{C}$ ) $^{-1}$ . The parameter  $A$  is derived from our measured value of bulk field attenuation at each frequency and set equal to 200 - 280 m. The result reported for two different frequencies is plotted in Fig. 8.

The average electric field attenuation length of the top 1500 m of ice is of particular interest to RNO-G as the majority of neutrino interactions detectable by the experiment occur in this region (Aguilar and others, 2021b). It can be extracted from the bulk result using the field attenuation versus depth relation defined above. The average field attenuation length for the top 1500 m of ice result is shown in Fig. 7. For reference, the bulk attenuation measurement at 300 MHz is  $705^{+42}_{-39}$  m ( $-12.29^{+0.68}_{-0.74}$  dB / km) while the average attenuation measurement of the top 1500 m of ice is  $845^{+51}_{-47}$  m ( $-10.27^{+0.60}_{-0.62}$  dB / km).

Our measurement can be used in simulations that calculate RNO-G's sensitivity to astrophysical neutrinos. For those simulations, we include, for convenience, a linear fit to the average electric field attenuation length for the top 1500 m of ice, shown in Fig. 7. We find a significant correlation between the two parameters of the linear fit, which yields a slope of  $-0.65 \pm 0.06$  m / MHz ( $-0.15 \pm 0.01$  dB / km / MHz), intercept of  $1024 \pm 50$  m ( $-8.48 \pm 0.41$  dB / km), and a correlation coefficient  $\rho = -0.95$ .

We compare our obtained result of the average electric field attenuation length for the top 1500 m at 300 MHz of  $\langle L_\alpha \rangle = 845^{+51}_{-47}$  m to other similar measurements. Avva and others (2015) extrapolated their results at 75 MHz to 300 MHz and estimated  $\langle L_\alpha \rangle = 1022^{+230}_{-253}$  m, consistent (within uncertainty) with the result presented herein. The electric field attenuation length at the South Pole has been measured, with the focusing factor included, to be  $\langle L_\alpha \rangle = 1660^{+255}_{-120}$  m at 300 MHz for the top 1500 m of ice (Allison and others, 2012). This longer attenuation can be attributed to the colder ice at the South Pole,  $\sim -50^{\circ}\text{C}$  compared to  $\sim -30^{\circ}\text{C}$  at Summit Station. Given the linear fit on the log of attenuation length versus temperature from Bogorodsky and others (1985), 20°C colder ice results in an attenuation length  $\sim 2.2$  times longer, making our results at Summit Station consistent with measurements at South Pole.

Measurements of the bulk radio field attenuation length at Summit Station have also been performed using air-borne radio sounding data. MacGregor and others (2015) inferred

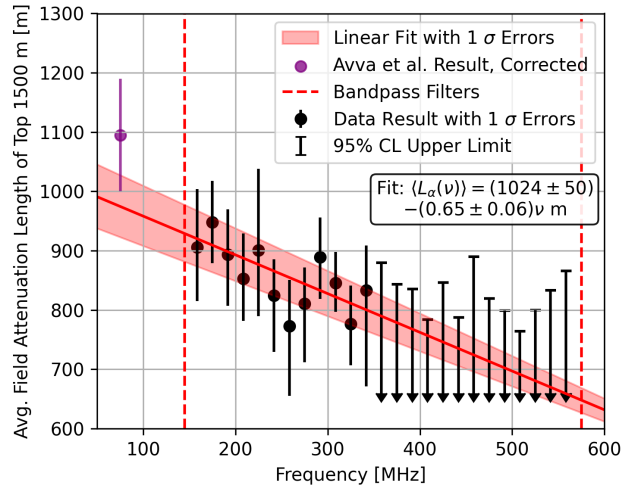


**Fig. 7.** Measurement of the average electric field attenuation for the top 1500 m of the ice sheet, as a function of frequency at Summit Station, derived from the measured bulk field attenuation in Fig. 6 and the relationship between attenuation and temperature. Overlaid is the  $\pm 1\sigma$  confidence interval of a linear fit of the data. Parameters of the fit are described in the text. Frequency  $v$  in the fit is in units of MHz.

the bulk radio field attenuation by comparing the relative strengths of internal reflectors, obtaining attenuation lengths of 750 - 850 m at 150-200 MHz around Summit Station, consistent (within uncertainty) with the result presented herein. Stockham and others (2016) measured the bulk radio field attenuation using the relative strength of the radio echo from the snow surface and the bedrock, obtaining at an attenuation length of  $546 \pm 23$  m at 150-200 MHz around Summit Station. This measurement is notably lower than our result and the measurement done by MacGregor and others (2015) potentially due to radiometric calibration issues (MacGregor and others, 2015; Stockham and others, 2016).

The RNO-G experiment, currently under construction at Summit Station in Greenland, is set to be one of the world's largest particle detectors. Our measurement of the bulk electric field attenuation length at Summit Station is consistent with previous measurements, with reduced systematic uncertainties. Our measurement will ultimately increase the precision of RNO-G's UHEN sensitivity estimates, which will either better motivate upper limits in the case of a null result or decrease uncertainties on the measured flux of ultra-high energy neutrinos in the universe in the case of observation.

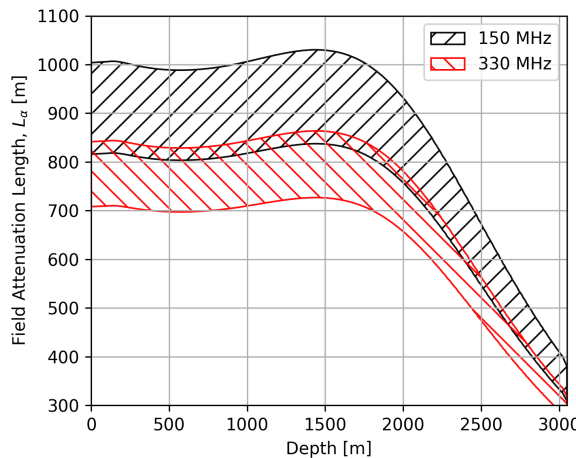


**Fig. 8.** Electric field attenuation length as a function of depth as derived from a model of ice attenuation versus temperature and the ice temperature profile measured by the GRIP borehole (Greenland Ice Core Project (1994)). Hatched region denotes  $\pm 1\sigma$ .

## Acknowledgements

We would like to thank the staff at Summit Station and Polar Field Services for logistical support in every way possible and to our colleagues at the British Antarctic Survey for unending enthusiasm while building and operating the BigRAID borehole drill for RNO-G.

We would like to acknowledge our home institutions and funding agencies for supporting the RNO-G work; in particular the Belgian Funds for Scientific Research (FRS-FNRS and FWO) and the FWO programme for International Research Infrastructure (IRI), the National Science Foundation through the NSF Awards 2118315 and 2112352 and the IceCube EPSCoR Initiative (Award ID 2019597), the German research foundation (DFG, Grant NE 2031/2-1), the Helmholtz Association (Initiative and Networking Fund, W2/W3 Program), the University of Chicago Research Computing Center, and the European Research Council under the European Unions Horizon 2020 research and innovation programme (grant agreement No 805486).

## REFERENCES

- Aartsen MG and others (2018) Differential limit on the extremely-high-energy cosmic neutrino flux in the presence of astrophysical background from nine years of IceCube data. *Phys. Rev. D*, **98**(6), 062003 (doi:10.1103/PhysRevD.98.062003)
- Aguilar JA and others (2021a) Design and Sensitivity of the Ra-

dio Neutrino Observatory in Greenland (RNO-G). *JINST*, **16**(03), P03025 (doi:10.1088/1748-0221/16/03/P03025)

Aguilar JA and others (2021b) Reconstructing the neutrino energy for in-ice radio detectors: A study for the Radio Neutrino Observatory Greenland (RNO-G)

Alley R and Koci B (1988) Ice-Core Analysis at Site A, Greenland: Preliminary Results. *Annals of Glaciology*, **10**, 1–4 (doi:10.3189/S0260305500004067)

Alley R, Shuman C, Meese D, Gow A, Taylor K, Cuffey K, Fitzpatrick J, Grootes P, Zielinski G, Ram M, Spinelli G and Elder B (1997) Visual-stratigraphic dating of the GISP2 ice core: Basis, reproducibility, and application. *Journal of Geophysical Research: Oceans*, **102**(C12), 26367–26381, ISSN 2169-9275 (doi:10.1029/96JC03837), publisher Copyright: Copyright 1997 by the American Geophysical Union.

Allison P and others (2012) Design and Initial Performance of the Askaryan Radio Array Prototype EeV Neutrino Detector at the South Pole. *Astropart. Phys.*, **35**, 457–477 (doi:10.1016/j.astropartphys.2011.11.010)

Allison P and others (2020) Constraints on the diffuse flux of ultrahigh energy neutrinos from four years of Askaryan Radio Array data in two stations. *Phys. Rev. D*, **102**(4), 043021 (doi:10.1103/PhysRevD.102.043021)

Anker A and others (2019) Targeting ultra-high energy neutrinos with the ARIANNA experiment. *Adv. Space Res.*, **64**, 2595–2609 (doi:10.1016/j.asr.2019.06.016)

Arthern RJ, Corr HFJ, Gillet-Chaulet F, Hawley RL and Morris EM (2013) Inversion for the density-depth profile of polar firn using a stepped-frequency radar. *Journal of Geophysical Research (Earth Surface)*, **118**(3), 1257–1263 (doi:10.1002/jgrf.20089)

Askaryan GA (1961) Excess negative charge of an electron-photon shower and the coherent radio emission from it. *Soviet Physics JETP*, **41**

Avva J, Kovac JM, Miki C, Saltzberg D and Vieregg AG (2015) An in situ measurement of the radio-frequency attenuation in ice at Summit Station, Greenland. *J. Glaciol.*, **61**, 1005–1011 (doi:10.1080/2015JoG15J057)

Balanis CA (2016) *Antenna Theory: Analysis and Design*. Wiley Interscience, 4th edition, ISBN 978-1-118-64206

Barrella T, Barwick S and Saltzberg D (2011) Ross Ice Shelf (Antarctica) in situ radio-frequency attenuation. *Journal of Glaciology*, **57**(201), 61–66 (doi:10.3189/002214311795306691)

Barwick SW, Besson DZ, Gorham PW and Saltzberg DP (2005) South Polar in situ radio-frequency ice attenuation. *Journal of Glaciology*, **51**(173), 231–238 (doi:10.3189/172756505781829467)

- Barwick SW and others (2015) Time Domain Response of the ARIANNA Detector. *Astropart. Phys.*, **62**, 139–151 (doi:10.1016/j.astropartphys.2014.09.002)
- Barwick SW and others (2017) Radio detection of air showers with the ARIANNA experiment on the Ross Ice Shelf. *Astropart. Phys.*, **90**, 50–68 (doi:10.1016/j.astropartphys.2017.02.003)
- Barwick SW and others (2018) Observation of classically ‘forbidden’ electromagnetic wave propagation and implications for neutrino detection. *JCAP*, **07**, 055 (doi:10.1088/1475-7516/2018/07/055)
- Besson DZ and others (2008) In situ radioglaciological measurements near Taylor Dome, Antarctica and implications for ultra-high energy (UHE) neutrino astronomy. *Astroparticle Physics*, **29**(2), 130–157, ISSN 0927-6505 (doi:<https://doi.org/10.1016/j.astropartphys.2007.12.004>)
- Bogorodsky VV, Bentley CR and Gudmandsen PE (1985) *Radio-glaciology*. Reidel Publishing Co. (doi:10.1007/978-94-009-5275-1)
- Creative Design Corp (1994) *Instruction Manual CLP5130-2 Create Radio Antenna*
- Deaconu C, Vieregg AG, Wissel SA, Bowen J, Chipman S, Gupta A, Miki C, Nichol RJ and Saltzberg D (2018) Measurements and Modeling of Near-Surface Radio Propagation in Glacial Ice and Implications for Neutrino Experiments. *Phys. Rev. D*, **98**(4), 043010 (doi:10.1103/PhysRevD.98.043010)
- Friis H (1946) A note on a simple transmission formula. *Proceedings of the IRE*, **34**(5), 254–256 (doi:10.1109/JRPROC.1946.234568)
- Glaser C, Nelles A, Plaisier I, Welling C, Barwick SW, García-Fernández D, Gaswint G, Lahmann R and Persichilli C (2019) Nu-RadioReco: a reconstruction framework for radio neutrino detectors. *The European Physical Journal C*, **79**(6), ISSN 1434-6052 (doi:10.1140/epjc/s10052-019-6971-5)
- Gorham PW and others (2009) The Antarctic Impulsive Transient Antenna Ultra-high Energy Neutrino Detector Design, Performance, and Sensitivity for 2006–2007 Balloon Flight. *Astropart. Phys.*, **32**, 10–41 (doi:10.1016/j.astropartphys.2009.05.003)
- Gorham PW and others (2019) Constraints on the ultrahigh-energy cosmic neutrino flux from the fourth flight of ANITA. *Phys. Rev. D*, **99**(12), 122001 (doi:10.1103/PhysRevD.99.122001)
- Greenland Ice Core Project (1994) <ftp://ftp.ncdc.noaa.gov/pub/data/paleo/icecore/greenland/summit/grip/physical/griptemp.txt>
- Hanson JC and others (2015) Radar absorption, basal reflection, thickness and polarization measurements from the Ross Ice Shelf, Antarctica. *Journal of Glaciology*, **61**(227), 438–446 (doi:10.3189/2015JoG14J214)
- Hawley RL, Morris EM and McConnell JR (2008) Rapid techniques for determining annual accumulation applied at Summit, Greenland. *Journal of Glaciology*, **54**(188), 839–845 (doi:10.3189/002214308787779951)
- Herron MM and Langway CC (1980) Firn densification: An empirical model. *Journal of Glaciology*, **25**(93), 373–385 (doi:10.3189/S002214300015239)
- Kovacs A, Gow AJ and Morey RM (1995) The in-situ dielectric constant of polar firn revisited. *Cold Regions Science and Technology*, **23**(3), 245–256, ISSN 0165-232X (doi:[https://doi.org/10.1016/0165-232X\(94\)00016-Q](https://doi.org/10.1016/0165-232X(94)00016-Q))
- Kravchenko I and others (2003) Performance and simulation of the RICE detector. *Astropart. Phys.*, **19**, 15–36 (doi:10.1016/S0927-6505(02)00194-9)
- MacGregor JA, Li J, Paden JD, Catania G, Clow GD, Fahnestock MA, Gogineni S, Grimm RE, Morlighem M, Nandi S, Seroussi H and Stillman DE (2015) Radar attenuation and temperature within the Greenland Ice Sheet. *Journal of Geophysical Research*, **120**, 983–1008 (doi:10.1002/2014JF003418)
- Matsuoka K, Furukawa T, Fujita S, Maeno H, Uratsuka S, Naruse R and Watanabe O (2003) Crystal orientation fabrics within the antarctic ice sheet revealed by a multipolarization plane and dual-frequency radar survey. *Journal of Geophysical Research*, **108**, 2499
- Oskooi AF, Roundy D, Ibanescu M, Bermel P, Joannopoulos J and Johnson SG (2010) Meep: A flexible free-software package for electromagnetic simulations by the FDTD method. *Computer Physics Communications*, **181**(3), 687–702, ISSN 0010-4655 (doi:<https://doi.org/10.1016/j.cpc.2009.11.008>)
- Paden J (2006) *Synthetic aperture radar for imaging the basal conditions of the polar ice sheets*. Ph.D. thesis, Department of Electrical Engineering and Computer Science, University of Kansas, Lawrence, Kansas
- Paden J, Allen C, Gogineni S, Jezek K, Dahl-Jensen D and Larsen L (2005) Wideband measurements of ice sheet attenuation and basal scattering. *IEEE Geoscience and Remote Sensing Letters*, **2**(2), 164–168 (doi:10.1109/LGRS.2004.842474)
- Sodha MS, Sirohi RS and Chakravarti AK (1969) Focusing factor in a stratified medium. *BRIT. J. APPL. PHYS.*, **2**(2) (doi:10.1088/0022-3727/2/4/317)
- Stockham M (2018) *Bulk and Surface Radio-Frequency Response of Ice*. Ph.D. thesis, University of Kansas, Lawrence, Kansas
- Stockham M, Macy J and Besson DZ (2016) Radio Frequency Ice Dielectric Permittivity Measurements Using CReSIS Data. *Radio Science*, **51**, 194–212 (doi:10.1002/2015RS005849)

Thorsteinsson T (1996) Textures and fabrics in the GRIP ice core, in relation to climate history and ice deformation. *Berichte zur Polarforschung (Reports on Polar Research)*, **205** (doi:<https://doi.org/10.1029/97JC00161>)

Article

# Broadband RF Phased Array Design with MEEP: Comparisons to Array Theory in Two and Three Dimensions

Jordan C. Hanson

Science &amp; Learning Center, Whittier College, Whittier, CA 90602, USA; jhanson2@whittier.edu

**Abstract:** Phased array radar systems have a wide variety of applications in engineering and physics research. Phased array design usually requires numerical modeling with expensive commercial computational packages. Using the open-source MIT Electromagnetic Equation Propagation (MEEP) package, a set of phased array designs is presented. Specifically, one and two-dimensional arrays of Yagi-Uda and horn antennas were modeled in the bandwidth [0.1–5] GHz, and compared to theoretical expectations in the far-field. Precise matches between MEEP simulation and radiation pattern predictions at different frequencies and beam angles are demonstrated. Given that the computations match the theory, the effect of embedding a phased array within a medium of varying index of refraction is then computed. Understanding the effect of varying index on phased arrays is critical for proposed ultra-high energy neutrino observatories which rely on phased array detectors embedded in natural ice. Future work will develop the phased array concepts with parallel MEEP, in order to increase the detail, complexity, and speed of the computations.

**Keywords:** FDTD methods; MEEP; phased array antennas; antenna theory; Askaryan effect; UHE neutrinos



**Citation:** Hanson, J.C. Broadband RF Phased Array Design with MEEP: Comparisons to Array Theory in Two and Three Dimensions. *Electronics* **2021**, *10*, 415. <https://doi.org/10.3390/electronics10040415>

Academic Editor: Hirokazu Kobayashi

Received: 28 December 2020

Accepted: 27 January 2021

Published: 8 February 2021

**Publisher's Note:** MDPI stays neutral with regard to jurisdictional claims in published maps and institutional affiliations.



**Copyright:** © 2021 by the authors. Licensee MDPI, Basel, Switzerland. This article is an open access article distributed under the terms and conditions of the Creative Commons Attribution (CC BY) license (<https://creativecommons.org/licenses/by/4.0/>).

## 1. Introduction

Radio-frequency phased array antenna systems with design frequencies of order 0.1–10 GHz have applications in 5G mobile telecommunications, ground penetrating radar (GPR) systems, and scientific instrumentation [1–4]. In the one-dimensional case, a series of three-dimensional antenna elements are arranged in a line with fixed spacing [5]. Common antenna designs like loops and dipoles can be used to limit the *elements* to two dimensions. In this special case, phased array radiation may be modeled in two spatial dimensions plus time. In the two-dimensional case, a series of three-dimensional antenna elements are arranged in a two-dimensional pattern, often a grid with fixed element spacing in both dimensions. The elements may be strictly two-dimensional, but there is still an increase in computational complexity and the radiation is calculated in three dimensions plus time.

Proprietary RF modeling packages like XFDTD and HFSS are often used to model the response of elements within phased arrays and the behavior of arrays [6–9]. The XFDTD package, for example, relies on the finite difference time domain (FDTD) method. The FDTD approach is a computational electromagnetics (CEM) technique in which spacetime and Maxwell's equations are broken into discrete form. One variant of the FDTD method is the conformal FDTD method (CFDTD), recently used to study phased array concepts on a large scale [9]. The NEC2 and NEC4 family of codes relies on the method-of-moments (MoM) approach [10]. Aside from the cost, a drawback of proprietary modeling software can be a lack of fine control over each individual object in the simulation. Because Maxwell's equations are scale-invariant, in principle open-source FDTD codes designed for optical regimes could be re-purposed for RF design workflows. One such open-source package is the MIT Electromagnetic Equation Propagation (MEEP) package [11].

A recent review [12] covered how open radio design software like openEMS [13], gprMax [14], and the NEC2 family of codes [10] facilitate design workflows. In this work, the radiation patterns of one-dimensional and two-dimensional phased array designs

are simulated with the MEEP package. MEEP takes advantage of the scale-invariance of Maxwell's equations. Common MEEP applications are found in optical wavelength  $\mu\text{m}$ -scale designs, but scale-invariance allows the user to treat designs as cm-scale RF elements (see Appendix A for details). Although MEEP has been used to optimize antenna designs [15], this work appears to be the first to model entire phased arrays in MEEP with a variable index of refraction. Two classes of phased array element are considered: Yagi-Uda and horn antennas. The former is applied to single-frequency designs, while the latter is applied to broadband design. Each element class is treated in both the one-dimensional and two-dimensional cases. The phase-steering properties and radiation patterns of all designs are shown to match theoretical predictions. The appropriate array theory is shown in Section 2, based on Chapter 1 of Reference [16]. Section 3 contains comparisons between theory and simulation for one-dimensional cases, and Section 4 contains the corresponding two-dimensional comparisons. In Section 5, the varying index of refraction is introduced. Results and future work are summarized in Section 6.

A workflow using MEEP for phased array design is outlined in Figure 1 based on Figure 1 from Reference [12]. Examples of decisions within the *specifications* category are: single-frequency or broadband, desired directivity and beamwidth, side-lobe tolerance, and number of antenna elements. These decisions lead to the choice of element type which must be implemented in MEEP. Simple shapes like dipoles can be modeled with built-in MEEP objects. Complex shapes like horns and dishes can be assembled from groups of objects. Radiation sources and current functions must be defined. For these studies, pure sinusoidal currents are passed to radiators which in turn radiate sinusoidal fields. The dielectric constant and boundary conditions of the simulation volume and objects within the volume are defined in the next step. The information is loaded into a simulation object and run for a number of time-steps. Once complete, near-to-far field routines are called to produce the power at a set of angles. The power versus angle is converted to normalized E and H-plane array radiation patterns and compared to theoretical models. Given a match, the frequency is updated and the process is repeated. If there is not a match, element separation and other array parameters are adjusted.

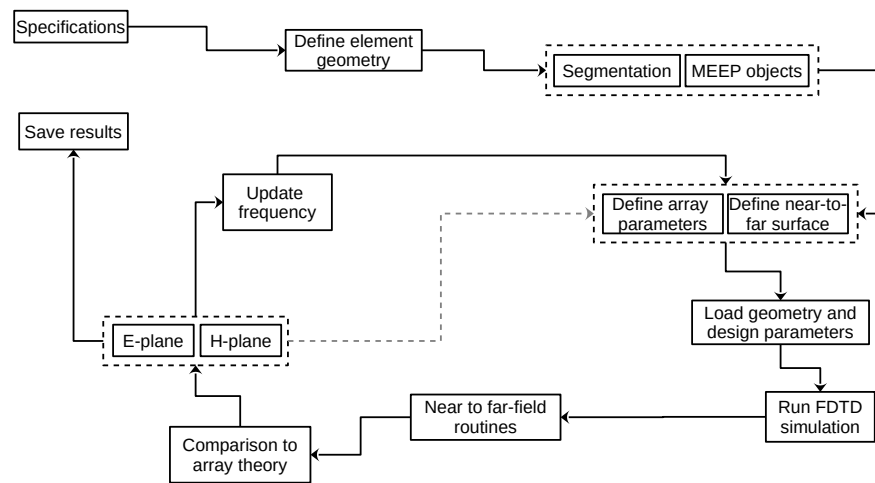


**Figure 1.** A detailed workflow for phased array design with MEEP. See text for details.

The workflow in Figure 1 represents a non-parallelized approach. Much development has gone into enhancing the speed, accuracy, and utility of the FDTD method. First, MEEP itself may be run in parallel mode, providing a speed enhancement. In a high-performance computing (HPC) environment, where each node has allocated memory (implying local RAM is not the limiting factor) running MEEP in parallel would speed up results. There has also been CEM research devoted to enhancing the FDTD approach itself. Decreasing

memory usage and avoiding repetitive computations in favor of a more subtle approach is presented in [7]. A three-dimensional implementation of FDTD algorithms on GPUs via CUDA has also been explored [17]. The results of this work were obtained using the simplest version of MEEP: non-parallel with the python3 interface run in Jupyter notebooks on a laptop. Therefore the results shown in Sections 3 and 4 could benefit from speed and memory enhancements in future studies.

## 2. Phased Array Antenna Theory

The basic structure of a one-dimensional phased array of RF radiating elements is shown in Figure 2. Two important numerical constants that determine the beam angle  $\Delta\phi$  of the array are the inter-element spacing  $d_y$  and the phase shift per antenna  $\Delta\Phi$ . Letting the subscript  $i$  label each of the  $N$  elements, the one-dimensional inter-element spacing in Figure 2 is  $d_y \hat{f} = \vec{r}_{i+1} - \vec{r}_i$ , where  $\vec{r}_i$  records the position of element  $i$ . The phase shift per antenna is  $\Delta\Phi = \Phi_{i+1} - \Phi_i$ . The relationship between  $d_y$ ,  $\Delta\Phi$ , and  $\Delta\phi$  is derived in Section 2.1. The radiation pattern for a given  $\Delta\phi$  is derived in Section 2.2. For all coordinate systems, the azimuthal angle in the xy-plane is  $\phi$ , and the polar angle from the z-axis is  $\theta$ .

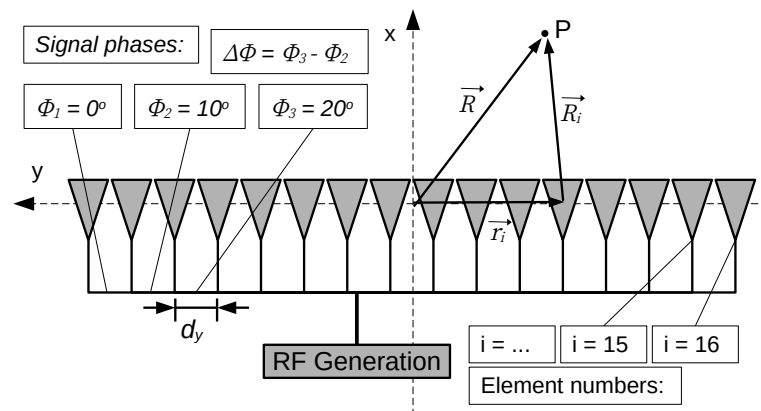


**Figure 2.** Definitions for the coordinate system, element label  $i$ , position vectors, and phase shift per antenna for a one-dimensional phased array of RF radiating elements. An example phase shift per antenna of  $\Delta\Phi = \Phi_2 - \Phi_1 = \Phi_3 - \Phi_2 = \Phi_{i+1} - \Phi_i = 10^\circ$  value is shown. Example position vectors for the 12th element are shown:  $\vec{R} = \vec{r}_{12} + \vec{R}_{12}$ .

### 2.1. Phase Steering and Beam Angle

The beam angle  $\Delta\phi$  of the array given  $\Delta\Phi$  and  $d_y$  will now be derived for the coordinate system in Figure 2. First, the relevant far-field approximation will be described. Second, it will be assumed that the elements all radiate at the same frequency  $\omega$  and have the same vector radiation pattern  $\vec{f}(\theta, \phi)$  that accounts for co-polarized and cross-polarized radiated power. Third, the  $\vec{E}$ -field at point P will be treated as a sum of the  $\vec{E}_i$  radiated from each element. Fourth, the calculations will be restricted to the xy-plane and the relationship between the beam angle  $\Delta\phi$  and array parameters will be obtained for a one-dimensional array.

According to Figure 2, the position of P can be written

$$\vec{R} = \vec{r}_i + \vec{R}_i \quad (1)$$

Rearranging, the displacement between the  $i$ -th element and P is

$$\vec{R}_i = \vec{R} - \vec{r}_i \quad (2)$$

The magnitude of the displacement is

$$R_i = \sqrt{(\vec{R} - \vec{r}_i) \cdot (\vec{R} - \vec{r}_i)} = (R^2 - 2\vec{R} \cdot \vec{r}_i + r_i^2)^{1/2} \quad (3)$$

Factoring an  $R^2$ , and neglecting the third term because it is small compared to the others,

$$R_i \approx R \left( 1 - \frac{2\vec{R} \cdot \vec{r}_i}{R^2} \right)^{1/2} \quad (4)$$

Expanding in a Taylor series to first order in  $2\vec{R} \cdot \vec{r}_i/R^2$ , with  $\hat{r} = \vec{R}/R$ , yields

$$R_i \approx R \left( 1 - \frac{\hat{r} \cdot \vec{r}_i}{R} \right) \quad (5)$$

Distributing the  $R$  gives the approximation:

$$R_i \approx R - \hat{r} \cdot \vec{r}_i \quad (6)$$

The electric field at  $P$  due to the  $i$ -th element with individual radiation pattern  $\vec{f}_i(\theta, \phi)$  is

$$\vec{E}_i(R, \theta, \phi) = \frac{\vec{f}_i(\theta, \phi) \exp(-jkR_i)}{R_i} \quad (7)$$

Substituting Equations (6) into (7):

$$\vec{E}_i(R, \theta, \phi) = \vec{f}_i(\theta, \phi) \frac{\exp(-jkR)}{R} \exp(jk\vec{r}_i \cdot \hat{r}) \quad (8)$$

The element positions are written in Cartesian coordinates, while  $P$  is written in spherical coordinates using  $u = \sin \theta \cos \phi$  and  $v = \sin \theta \sin \phi$ :

$$\vec{r}_i = \hat{x}x_i + \hat{y}y_i + \hat{z}z_i \quad (9)$$

$$\hat{r} = \hat{x}u + \hat{y}v + \hat{z}\cos \theta \quad (10)$$

The total field  $\vec{E}$  at  $P$  requires summing over elements. The current delivered to the  $i$ -th element could have a potentially complex amplitude  $a_i$ . The details of how the currents  $a_i$  are converted to radiated  $\vec{E}$ -field are taken to be part of  $\vec{f}(\theta, \phi)$ . The summation for  $\vec{E}$  over elements is

$$\vec{E}(R, \theta, \phi) = \frac{\exp(-jkR)}{R} \sum_i a_i \vec{f}_i(\theta, \phi) \exp(jk\vec{r}_i \cdot \hat{r}) \quad (11)$$

For identical radiating elements:  $\vec{f}_i = \vec{f}$ :

$$\vec{E}(R, \theta, \phi) = \vec{f}(\theta, \phi) \frac{\exp(-jkR)}{R} \sum_i a_i \exp(jk\vec{r}_i \cdot \hat{r}) \quad (12)$$

Define the *array-factor*  $F(\theta, \phi) = \sum_i a_i \exp(jk\vec{r}_i \cdot \hat{r})$ :

$$\vec{E}(R, \theta, \phi) = \vec{f}(\theta, \phi) \frac{\exp(-jkR)}{R} F(\theta, \phi) \quad (13)$$

Thus, if  $F = 1$ , then the  $\vec{E}$ -field is a plane wave, modified only by the elemental radiation pattern. Complex amplitudes  $a_i$  that cause a plane wave with wavevector pointed to  $(\theta_0, \phi_0)$  are

$$a_i = |a_i| \exp(-jk\vec{r}_i \cdot \hat{r}_0) \quad (14)$$

The notation for beam angle  $\Delta\phi = \phi - \phi_0$  will be introduced shortly. For  $\hat{r}_0$ ,  $u_0$  and  $v_0$  take the corresponding  $\theta_0$  and  $\phi_0$  for the angles:  $\hat{r}_0 = \hat{x}u_0 + \hat{y}v_0 + \hat{z}\cos \theta_0$ . The angles  $(\theta_0, \phi_0)$  correspond to the plane wave because the phases in the array factor in Equation (13)

are cancelled by those in Equation (14), and the summation is over just the magnitudes  $|a_i|$ . For a *linear array* in one-dimension, oriented along the y-axis as shown in Figure 2,  $\theta_0 = \pi/2$  and  $\vec{r}_i = id_y\hat{y}$ :

$$\vec{E}(R, \theta, \phi) = \vec{f}(\theta, \phi) \frac{\exp(-jkR)}{R} \sum_i a_i \exp(jk(id_y v)) \quad (15)$$

The summation is  $F(\pi/2, \phi_0)$ ,  $v = \sin(\phi)$  and  $v_0 = \sin(\phi_0)$ . The weights  $a_i$  may be arranged to produce a plane wave at  $\phi_0$ :

$$a_i = |a_i| \exp(-jki d_y v_0) \quad (16)$$

The  $i$ -th phase of  $\vec{E}$  in the array factor is

$$\Phi_i = k i d_y (\sin \phi - \sin \phi_0) \quad (17)$$

The difference  $\Delta\Phi = \Phi_{i+1} - \Phi_i$  for angles not far from the x-axis,  $|\phi| < 1$  and  $|\phi_0| < 1$ , is

$$\Delta\Phi \approx d_y k (\phi - \phi_0) = 2\pi(d_y/\lambda)(\phi - \phi_0) = 2\pi(d_y/\lambda)\Delta\phi \quad (18)$$

The *beam angle* is  $\Delta\phi = \phi - \phi_0$ , the angular distance between a reference angle and the angle at which all contributions to  $\vec{E}$  are in phase. Equation (18) reveals that the relationship between  $\Delta\phi$  and  $\Delta\Phi$  is linear, with slope  $\lambda/(2\pi d_y)$ . In Section 3, the relationship between  $\Delta\Phi$  and  $\Delta\phi$  obtained from FDTD calculations via MEEP are shown to match precisely the theoretical prediction. For two-dimensional grid arrays, the relationship “factors,” in that phase shift per element row and phase shift per element column govern  $\Delta\phi$  and  $\Delta\theta$  independently. This theoretical prediction is matched precisely by the FDTD calculations shown in Section 4 as well.

## 2.2. Radiation Patterns and Beam Width

The radiation pattern, or relative power  $P$  emitted versus beam angle, is obtained from the array factor  $F(\pi/2, \phi)$  summation. Summation over the phased array with identical elements causes the vector element pattern  $\vec{f}(\theta, \phi)$  and the common phase and amplitude factors  $\exp(jkR)/R$  to cancel upon normalization. The parameters that characterize the radiation patterns of arrays are  $N$ , the number of elements, and  $d_y/\lambda$ . The magnitude of the complex current to each element is assumed to be the same,  $|a_i| = a$ . Recall the array factor from Equation (13), with  $\theta = \pi/2$  and  $a_i = a$ :

$$F(\phi, \phi_0) = a \sum_i \exp(jk i d_y (v - v_0)) \quad (19)$$

Let  $\chi = k d_y (v - v_0)$  so that  $z = \exp(j\chi)$ . The sum is a geometric series from  $i = 1$  to  $i = N$ , the number of elements:

$$F(z) = a \sum_{i=1}^N z^i = a \left( \frac{1 - z^N}{1 - z} \right) \quad (20)$$

Using the Euler formula for  $\sin(\chi)$ , the array factor simplifies to

$$F(\chi) = -a \exp(j(N-1)\chi/2) \left( \frac{\sin(N\chi/2)}{\sin(\chi/2)} \right) \quad (21)$$

The radiation pattern is proportional to power, so it is prudent to take the magnitude of  $F(\phi)$ :

$$|F(\chi)| = a \left( \frac{\sin(N\chi/2)}{\sin(\chi/2)} \right) \quad (22)$$

The normalized radiation pattern will be  $(F/F_{max})^2$ , so it is necessary to find  $F_{max}$ :

$$\lim_{\chi \rightarrow 0} |F(\chi)| = a \lim_{\chi \rightarrow 0} \left( \frac{\sin(N\chi/2)}{\sin(\chi/2)} \right) = aN \quad (23)$$

So  $|F(\chi)|/F_{max}$  is

$$\frac{F(\chi)}{F_{max}} = \frac{\sin(N\chi/2)}{N \sin(\chi/2)} \quad (24)$$

Finally, with  $\chi = kd_y(v - v_0)$ ,  $v = \sin(\phi)$ , and  $v_0 = \sin(\phi_0)$ , the radiation pattern  $P$  is  $|F(\chi)/F_{max}|^2$ :

$$P(\phi) = \left( \frac{\sin(\pi N(d_y/\lambda)(\sin(\phi) - \sin(\phi_0)))}{N \sin(\pi(d_y/\lambda)(\sin(\phi) - \sin(\phi_0)))} \right)^2 \quad (25)$$

The  $-3$  dB beamwidth is  $0.886\lambda/L$ , where  $L = (N - 1)d_y$ . In fact, Equation (19) is a function of  $v - v_0$ , so altering the  $\Delta\Phi$  in the  $a_i$  only rotates  $P(\phi)$  in  $\phi$ -space, corresponding to a translation in  $v$ -space. The radiation pattern in Equation (25) is shown to match precisely the main beam of FDTD calculations via MEEP for one-dimensional arrays in Section 3. For two-dimensional grid arrays, the E and H plane radiation patterns “factor,” in that  $P(\theta, \phi) = P(\theta)P(\phi)$ . In Section 4, precision matches for two-dimensional grid arrays are shown.

### 2.3. Regarding Array Radiation Patterns

Because one-dimensional and two-dimensional arrays are considered, some notes about radiation patterns are necessary. First, all one-dimensional array radiation patterns correspond to the E-plane (the xy-plane). The arrays are specified using elements situated in the xy-plane, and the array extends along the y-axis. Radiators are linearly polarized such that the E-plane at some radius  $r$  is  $(r \cos(\phi), r \sin(\phi), 0)$ . The H-plane at  $r$  would be  $(r \sin(\theta), 0, r \cos(\theta))$ , but this data is not relevant for a one-dimensional array. Second, the MEEP python routine `get_farfield` is evaluated at a radius  $r \gg L$ , the length of the array, to obtain the far-fields  $\vec{E}$  and  $\vec{H}$ . Notice that not all open-source FDTD codes offer near-field to far-field transition modeling [12].

All two-dimensional phased array elements presented in Section 4 are arrayed in the yz-plane, and the E and H-planes have the same definitions as the one-dimensional case. However, the H-plane results have been shifted so that the main beam occurs at  $\theta = 0$  degrees, rather than the expected 90 degrees. This is purely for visual comparison to Equation (25) cast as  $P(\theta)$  with  $\theta_0 = 0$ , and does not mean the phased array is radiating orthogonally to broadside. Equation (25) is matched to E and H-plane two-dimensional patterns, and both are normalized to 0 dB at peak power.

## 3. Phased Array Designs in One Dimension: Two-Dimensional Fields

Two antenna designs were considered in modeling one-dimensional phased arrays: Yagi-Uda and horn, corresponding to narrowband and wideband applications, respectively. The two designs are depicted in Figure 3 with associated parameters described in Section 3.1 below. The Yagi-Uda antennas have 6 elements with the same radius, oriented in the xy-plane: one reflector, one radiator, three directors and a connecting boom. The current  $a_i$  is connected only to the radiator. The horn antennas have three structures: the box containing the linearly polarized radiator, the radiator which is connected to  $a_i$ , and the curves of the horn. An exponential function  $y = f(x) = k_1 \exp(k_2(x - a))$  describes the curves (see Figure 3), and the origin is taken to be at the center of the back edge of the box. The constants are  $k_1 = a/2$  and  $k_2 = (1/c) \ln(2d/a)$ . The curves are built from  $n$  slices where  $n = c/dx$ . All objects comprising the antenna elements have the same metallic conductivity, and the surrounding volume has an index of refraction  $n = 1$ . At the edge of

the space is a layer  $1 \Delta x$  unit thick called the perfectly matched layer (PML) which cancels reflections.

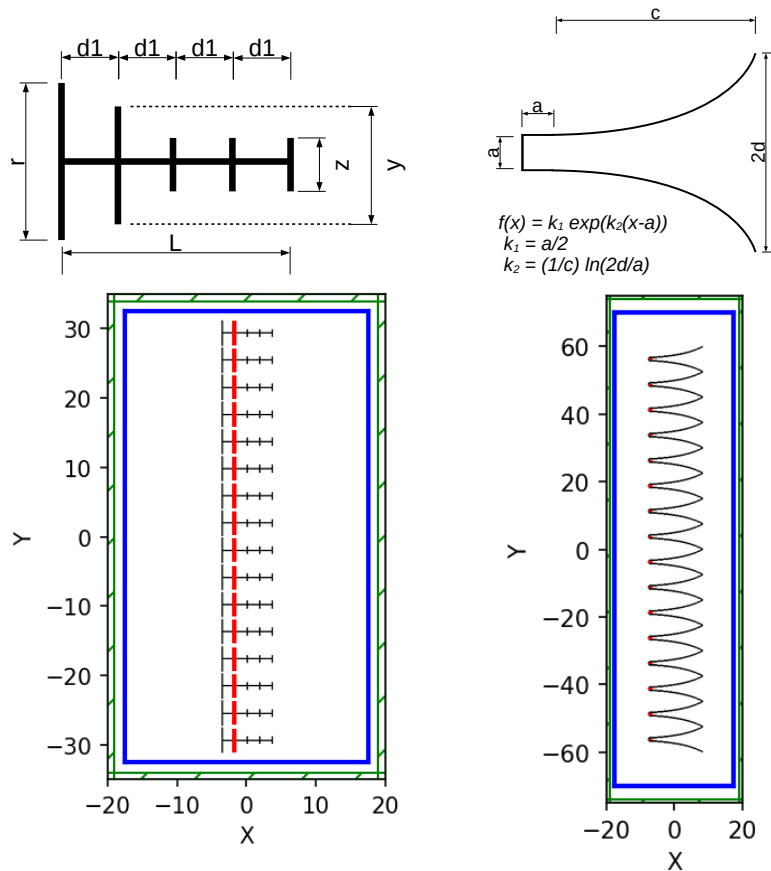


**Figure 3.** The two-dimensional antenna designs used in the one-dimensional phased array simulations. (See Section 3.1 for details). (Left) The Yagi-Uda antenna, and the  $N = 16$  array. (Right) The horn antenna, and the  $N = 16$  array. The white regions have  $\epsilon = \epsilon_0$ , the green borders are perfectly matched layers (PML), and the blue surfaces are MEEP *Near2FarRegion* objects where flux is recorded for near-to-far projection. The black lines represent metal structures, and the red lines represent the radiating elements. All dimensions are in centimeters.

### 3.1. Phase Steering, Beam Angle, and Beamwidth

As described in Section 2, the beam angle is controlled by the phase shift per antenna. Simulation results were run with the parameters in Table 1 for the one-dimensional arrays. The main results are shown in Figure 4. A discussion about scan loss below references data from Table 1.

The phase-steering results are shown in Figure 4. The y-axes of Figure 4 (top left) and (top right) are the beam angles of the Yagi-Uda arrays, divided by the beam widths. The x-axes for these graphs are the phase shifts per element. The top left plot and top right plots correspond to  $N = 8$  and  $N = 16$ , respectively. For the  $N = 16$  horn case (bottom left and right), the value of  $d_y/\lambda = fd_y/c$  varies because the elements can radiate from  $\approx 0.3\text{--}5.0$  GHz. The black solid lines in the top left and top right graphs of Figure 4 are linear fits to the Yagi-Uda data. The gray lines represent the function  $f(x) = bx$ , with  $b = \lambda/(2\pi d_y)$ . For these models,  $d_y = 3.92$  cm and  $\lambda = 6$  cm (Table 1). The slopes match almost exactly, with slight errors arising from radiation pattern distortion at high beam angle  $\Delta\phi$ . At such large  $\Delta\Phi$  values, side lobes can shift the location of the main beam by  $\mathcal{O}(1)$  degree by merging with the main beam. In the  $N = 8$  case the fitted slope is slightly higher, and in the  $N = 16$  case the fitted slope is slightly lower. In each model, the observed beamwidths are within 1% of the value predicted by Equation (18).

**Table 1.** Yagi-Uda: The first and second columns contain the geometric parameters describing the antenna elements for the Yagi-Uda array. Horn: The third and fourth columns contain those for the horn array. Scan-loss: The fifth through eighth columns contain scan loss ( $SL_{dB}$ ) data, reported for different frequencies and different  $d_y/\lambda$  values for the  $N = 16$  horn array.

Yagi-Uda		Horn		$SL_{dB}$			
Parameter	Value	Parameter	Value	f (GHz)	$\Delta\Phi$ (degrees)	$d_y/\lambda$	$SL_{dB}$
$N$	8.16	$N$	8.16	0.5	80	0.125	-11.6
$L$	7.20	$a$	0.95	1.0	80	0.25	-1.2
$d_1$	1.80	$c$	15.0	2.0	80	0.5	-1.0
$r$	3.75	$d$	3.8	4.0	80	1.0	-0.9
$y$	2.81	$dx$	0.1				
$z$	1.24	$n = c/dx$	150				
$d_y$	3.92	$d_y$	2d				
resolution	6	resolution	6				

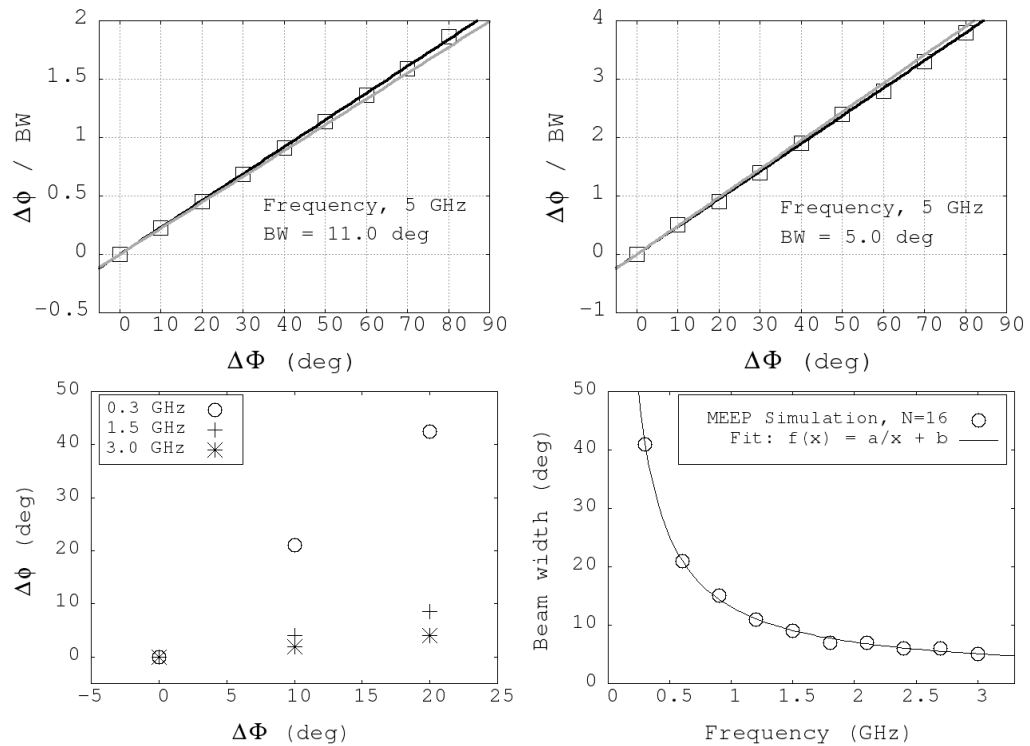


**Figure 4.** (Top left) The beam angle  $\Delta\phi$  divided by the beam width  $BW$  for the  $N = 8$  one-dimensional Yagi array versus  $\Delta\Phi$ , the phase shift per element. (Top right) The same results for the  $N = 16$  array. (Bottom left)  $\Delta\phi$  versus  $\Delta\Phi$  for the  $N = 16$  version of the one-dimensional horn array, for several frequencies. (Bottom right) The dependence of the beam width on frequency for the one-dimensional  $N = 16$  horn array.

For the broadband horn case in the bottom left of Figure 4, three frequency cases are shown: 0.3, 1.5, and 3.0 GHz. The intercepts are all consistent with zero and the slopes scale correctly: dividing the frequency by a factor of 2 increases the slope by a factor of 2, and dividing by a factor of 10 increases it by a factor of 10. Graphs like the top left and top right of Figure 4 would be misleading for horn antennas since the beamwidth depends on frequency (bottom right). The fit parameters for beam width were  $a = 12.0 \pm 0.1$  degree GHz, and  $b = 1.1 \pm 0.2$  degrees. For these two-dimensional antennas, the  $1/f$ -dependence

is a good description of the beamwidth across the [0.3–5 GHz] bandwidth. The constant term  $b$  is only necessary since the array has finite length  $L$ . The beamwidth ( $BW$ ) scales inversely with array length  $L$ :  $BW \approx 0.886\lambda/L$ , from Equation (25).

A discussion of scan loss is merited when analyzing normalized radiation patterns, which are shown below in Section 3.2. Scan loss may be quantified as the peak power at the given beam angle divided by the peak power at a beam angle of zero degrees. In the form of an equation in decibels, scan loss becomes a subtraction:

$$SL_{dB} = P_\phi - P_{\phi=0} \quad (26)$$

The scan loss  $SL_{dB}$  is shown for the  $N = 16$  one-dimensional horn array in Table 1 (right), as it varies with frequency and  $d_y/\lambda$ . The conservative value  $\Delta\Phi = 80$  degrees was chosen because it is associated with the largest beam angles that do not generate side lobes larger than  $-15$  dB. Given the beam width of the  $N = 16$  design (5.04 degrees), this corresponds to a scan range of  $\pm 20.16$  degrees. The largest beam angles tend to have the largest scan losses, so the numbers in Table 1 should be the most conservative. Scan losses of less than 1 dB are observed at high frequencies, but at  $d_y/\lambda$  values that begin to admit large side lobes (Section 3.2).

### 3.2. Radiation Patterns

Radiation patterns in the E-plane from  $N = 16$  one-dimensional Yagi and horn arrays are shown in Figures 5 and 6, respectively. As described above, the x-direction ( $\Delta\phi = 0$ ) corresponds to no phase shift per element ( $\Delta\Phi = 0$ ). The radiation patterns are normalized to the power at the beam angle, and are shown in blue. The red curves represent Equation (25) with the correct  $N$ -value and  $d_y/\lambda$ -value. Equation (25) is symmetric, with identical forward and backward lobes. The front-to-back or FB ratio would be 1.0 or 0 dB for a row of ideal point sources. Although there is no backplane in either simulated one-dimensional array, the FB ratios of  $\leq -15$  dB are observed.

The Yagi-Uda results are shown for 2.5 and 5.0 GHz frequencies in Figure 5, with  $\Delta\Phi = 0, 20, 40$ , and 60 degrees. Though the radiating elements are 6 cm long, good agreement between simulation and Equation (25) is observed at both 2.5 GHz and 5.0 GHz, including side-lobes. The beamwidth is proportionally larger at 2.5 GHz relative to 5.0 GHz, and at 5.0 GHz, the theoretical  $-3$  dB beam width of 5.0 degrees is achieved. The amplitudes of all side-lobes are limited to  $\approx -15$  dB, except at the highest beam angles where scan losses are experienced. Finally, the effect of frequency on beam steering is evident. The same  $\Delta\Phi$  does not generate as large a  $\Delta\phi$  at higher frequencies because the slope implied by Equation (18) is proportional to  $\lambda$ .

The horn results are shown in Figure 6 for 0.5 GHz and 5.0 GHz frequencies, corresponding to the lower and upper end of the bandwidth. The phase shifts per element are  $\Delta\Phi = 0, 10, 20$ , and 30 degrees. The angular range of  $\Delta\Phi$  is restricted relative to the Yagi-Uda case. Wideband systems experience a natural trade-off in angular range versus bandwidth. A  $d_y/\lambda$  value that is acceptably smaller than one at low frequencies can grow larger with increasing frequency, leading to interference patterns. At 5.0 GHz, the horns radiate at  $\pm 45$  degrees from  $\Delta\phi = 0$ . The prediction from Equation (25) is that these side-lobes, or *grating lobes*, are equal in relative power to the main beam. The actual array limits them to  $-15$  dB, but only if  $|\Delta\Phi| < 35$  degrees. For larger phase shifts per element, the opposite side-lobe grows above  $-15$  dB. If the beam is steered too far in the  $-\hat{\phi}$ -direction, the side-lobe on the  $\hat{\phi}$  side grows, and vice versa.

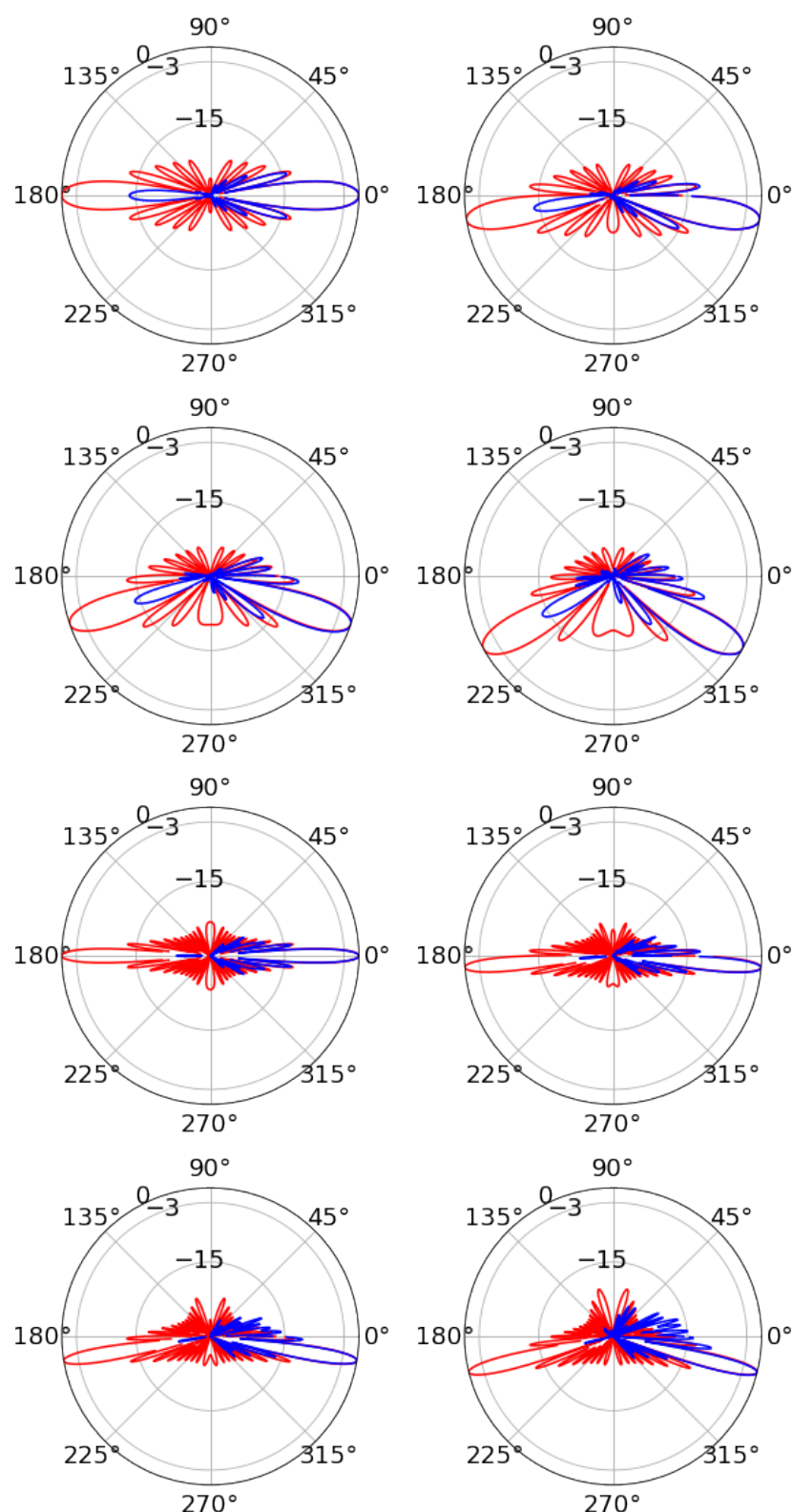


**Figure 5.** Yagi-Uda results, two-dimensional elements, one-dimensional array. **(Top row)**  $f = 2.5 \text{ GHz}$ , and  $\Delta\Phi = 0, 20$  degrees from left to right. **(Second row)**  $f = 2.5 \text{ GHz}$ , and  $\Delta\Phi = 40, 60$  degrees from left to right. **(Third row)**  $f = 5.0 \text{ GHz}$ , and  $\Delta\Phi = 0, 20$  degrees from left to right. **(Bottom row)**  $f = 5.0 \text{ GHz}$ , and  $\Delta\Phi = 40, 60$  degrees from left to right. The radial units are dB, and the angular units are degrees.

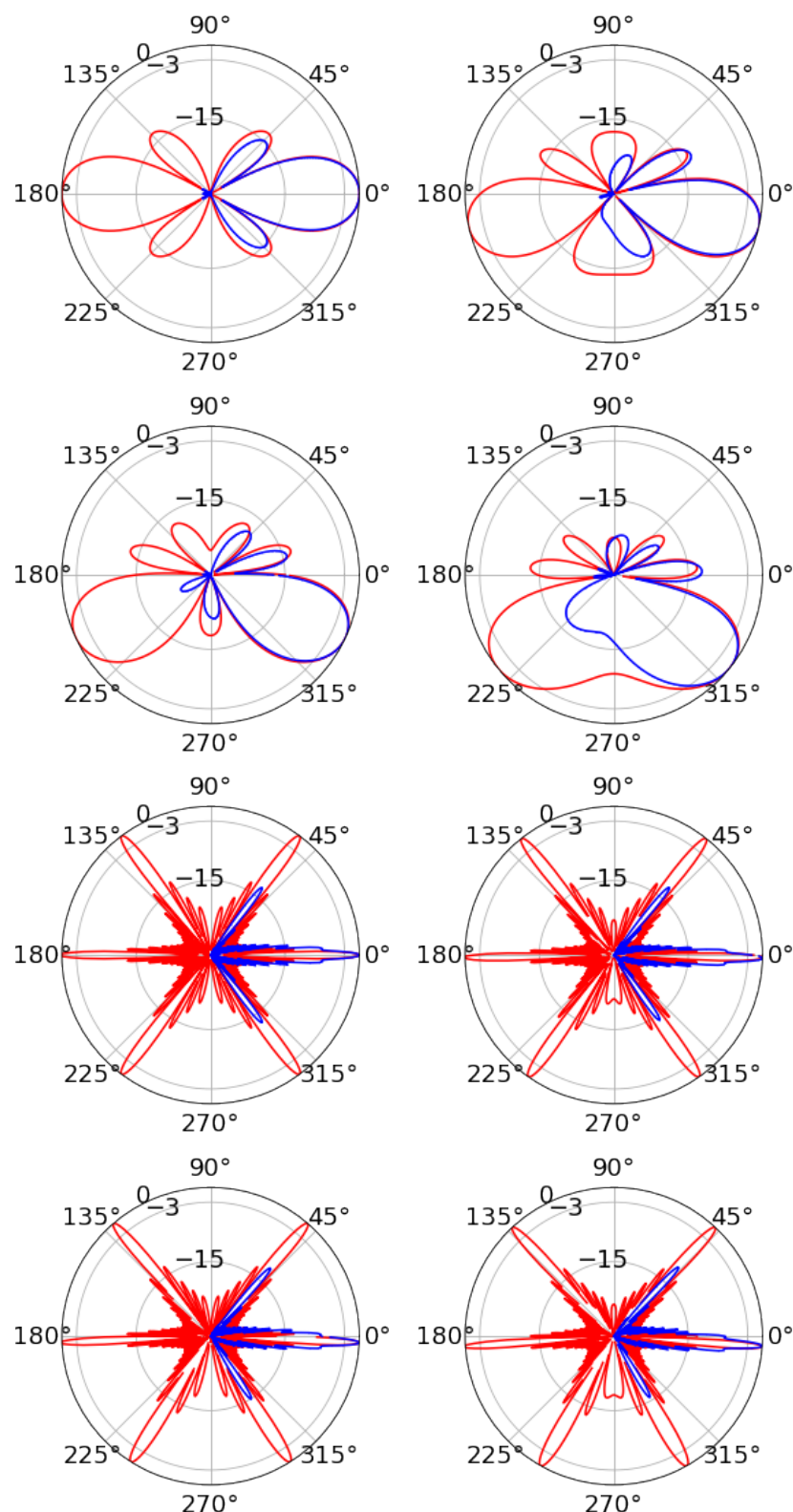


**Figure 6.** Horn results, two-dimensional elements, one-dimensional array. (**Top row**)  $f = 0.5$  GHz, and  $\Delta\Phi = 0, 10$  degrees from left to right. (**Second row**)  $f = 0.5$  GHz, and  $\Delta\Phi = 20, 30$  degrees from left to right. (**Third row**)  $f = 5.0$  GHz, and  $\Delta\Phi = 0, 10$  degrees from left to right. (**Bottom row**)  $f = 5.0$  GHz, and  $\Delta\Phi = 20, 30$  degrees from left to right.

The general features of the radiation pattern compare well to the theoretical prediction. The  $1/f$ -dependence of the main beamwidth is evident in Figure 6. Like the Yagi-Uda

array, the minimum theoretical beamwidth is reached at the highest frequencies (Figure 4 bottom right). The mini-lobes that are partially merged with the main beam widen the beam, however, the beamwidth is calculated at angles corresponding to  $-3$  dB relative power. Since the mini-lobes are below  $-3$  dB, the beamwidth calculation is unaffected. The simulation also matches the location and width of side-lobes to the theoretical prediction across the bandwidth. The six grating lobes at 5 GHz are a result of the pattern multiplication theorem, which states that the normalized radiation pattern is a product of the horn pattern and the pattern of an array of point sources. At 5 GHz, this multiplication suppresses the horn element pattern in the multiplication.

The field magnitude  $|\vec{E}(x, y, t)|$  for the  $N = 16$  horn array is shown in Figure 7 for  $t = 0.5, 1.0, 1.5, 2.0$  ns at a frequency of 2.5 GHz, along with the radiation pattern (far right). The original amplitude of the radiation source within the horns is  $\pm 1$  units, and the color scale for radiated  $|\vec{E}(x, y, t)|$  is  $\pm 0.002$ . The  $\Delta\phi$  is 9 degrees, with  $\Delta\Phi = -35$  degrees, and the beamwidth is  $5.5 \pm 0.5$  degrees. The area is  $480 \times 900$  pixels describing  $80 \times 150 \text{ cm}^2$  with a resolution of 6 pixels per  $\Delta x$ . The dimensions of the box (Table 1:  $a = 0.95 \text{ cm}$ ) are smaller than  $\lambda = 12 \text{ cm}$ . As the radiation escapes to free space, the wavefront forms several  $\lambda$  in front of the horns. Higher-frequency modes with  $f \gg 2.5 \text{ GHz}$  are observed at the wavefront that correspond to start-up effects at  $t = 0$  ns. With 72 pixels per wavelength, minute features of  $|\vec{E}(x, y, t)|$  can be interpreted as physical rather than numerical. These features can be eliminated with amplitude smoothing near  $t = 0$  ns, a feature available in the MEEP CustomSource class. Amplitude smoothing, however, makes the location of the wavefront less precise.

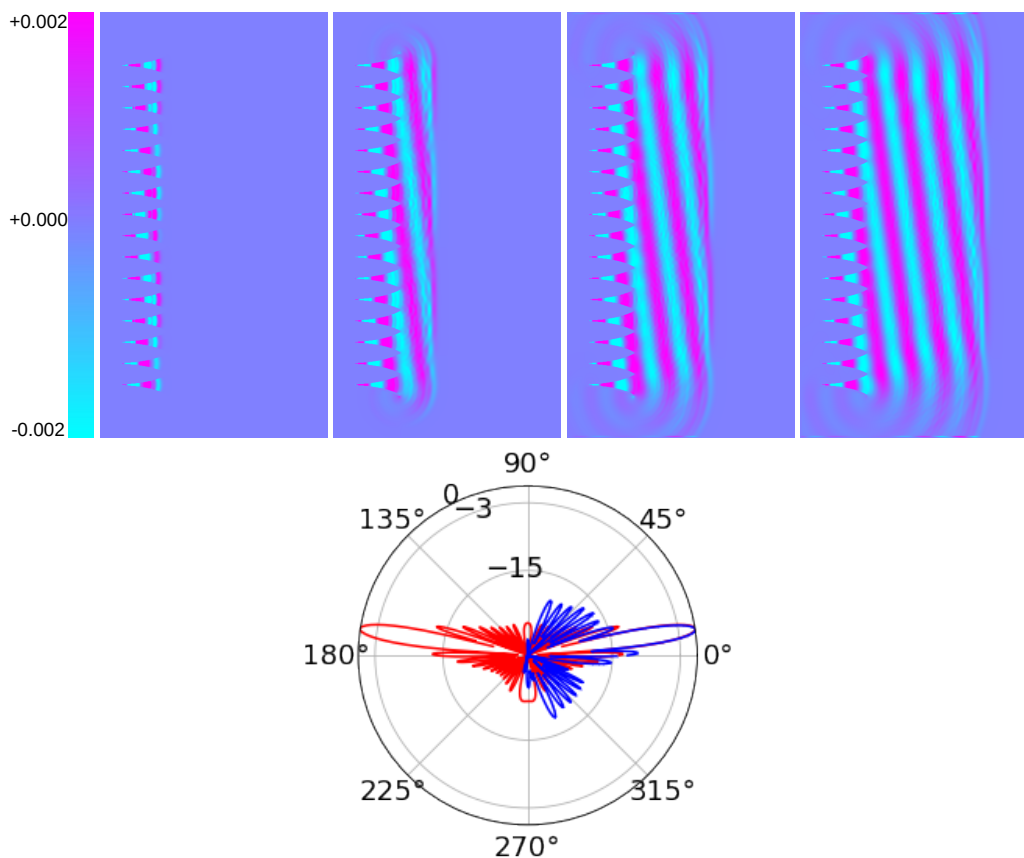


**Figure 7.** (From top left to top right) The  $N = 16$  horn one-dimensional linearly polarized electric field  $|\vec{E}(x, y, t)|$  at  $t = 0.5$  ns,  $t = 1.0$  ns,  $t = 1.5$  ns, and  $t = 2.0$  ns. The 2D area is  $80 \times 150 \text{ cm}^2$ , with resolution of 6 pixels per distance unit ( $480 \times 900$  pixels). The frequency is 2.5 GHz, and the beam angle is 9 degrees from broadside. (Bottom) The corresponding radiation pattern.

The radiation pattern in Figure 7 matches the theoretical prediction for the main lobe and first few side lobes. The origin of the side lobes is apparent from the  $|\vec{E}(x, y, t)|$  images, where diffraction patterns at the edges of the array are visible. At 0.5 ns, radiation in an element is confined to the horn. By 1.0 ns, that radiation joins the waves from horns on either side. However, horns at the end of the array have no partner on one side, and some radiation leaks outside the main lobe. The side lobes can change if the total run time is not sufficient. The `get_farfield` routine in MEEP requires `Near2FarRegion` surfaces that form the near-field box that collects flux information at the radiation frequency. The parameters of the near-field box are set by the `add_near2far` routine. The `get_farfield` routine performs a near-to-far field projection to the given radius ( $r = 1000$  cm) where the field is computed for the radiation pattern. The propagation code must be run for sufficient units of  $\Delta t$  so that enough radiation can cross the near-field box. The code is run for 6.67 ns to generate the radiation pattern in Figure 7. Thus, the side lobes are averaged over many radiation periods.

#### 4. Phased Array Designs in Two Dimensions: Three-Dimensional Fields

For two-dimensional grids of radiating elements, the array-factor  $F(u, v)$  factors:

$$F(\theta, \phi) = F(u - u_0)F(v - v_0) \quad (27)$$

The radiation pattern in Equation (25) applies to the E and H plane separately. The two-dimensional arrays modeled below are square  $N \times N$  arrays, so beamwidths implied by Equation (25) are equal for the E and H planes. The complex phasing of Equation (27) also indicates that  $\Delta\phi_E \propto \Delta\Phi_E$ , and  $\Delta\phi_H \propto \Delta\Phi_H$ , as shown in Equation (18) for the one-dimensional case. For the designs presented, the H-plane corresponds to the xz-plane, and to varying the phase in the z-direction (by array row). The E-plane corresponds to the xy-plane, and to varying the phase in the y-direction (by array column). In Figure 8, the basic shape of the two-dimensional array is shown in the yz-plane with  $\Delta\Phi_E = 15$  degrees, and  $\Delta\Phi_H = 15$  degrees. Section 4.1 contains results along the lines of Section 3.1 but for two-dimensional Yagi and horn arrays, and Section 4.2 contains results along the lines of Section 3.2 but for two-dimensional Yagi and horn arrays. As before, Table 1 contains the typical run parameters, with a few important exceptions.

The first exception is that for the two-dimensional case  $N$  becomes  $N \times N$ . However, squaring the number of antennas raises the memory requirements. In order to stay within a 16 GB memory limit, the two-dimensional *horn array* results had to be restricted to  $N \times N = 8 \times 8$ . The 2D horn array still has over  $\mathcal{O}(10^4)$  metal objects, compared to the  $\mathcal{O}(10^3)$  objects for the  $N \times N = 16 \times 16$  2D Yagi-Uda. The typical memory consumption is listed in Table 2, along with modified run parameters. Further, the resolution parameter was restricted to 4.0 for the horns. Restricting to 4 pixels per  $\Delta x$  unit limits memory consumption, but then the box containing the radiator has too few pixels. Enlarging the box allows the proper sized radiator to be fully contained. A final object was added to reduce the FB ratio: a back-plane with parameters listed in Table 2. One interesting modification is the doubling of the ratio of the box size ( $a$ ) and the final horn width ( $d$ ). This had the effect of limiting the maximum frequency to  $\approx 1$  GHz. At 1 GHz,  $d/\lambda \approx 0.5$ . A full optimization study on the horn parameters is warranted, though outside the present scope.

The horn elements radiate linearly polarized radiation in the y-direction, so the width in the z-direction does not follow the exponential functions but remains fixed at  $a$ . Initial runs were performed with horn elements that simultaneously widened according to the exponential function defined in Section 3. That design allowed reflections internal to the horns to distort the initial wavefront. Holding the horn-width constant in the z-direction produces radiation patterns that match Equation (25) because it follows the one-dimensional example of Section 3. To obtain z-polarized wavefronts, all that is necessary is to rotate the array. Practically, there are already examples of dually polarized RF band horns used in particle astrophysics [18,19], meaning that if this design were created with such elements, no rotation would be necessary.

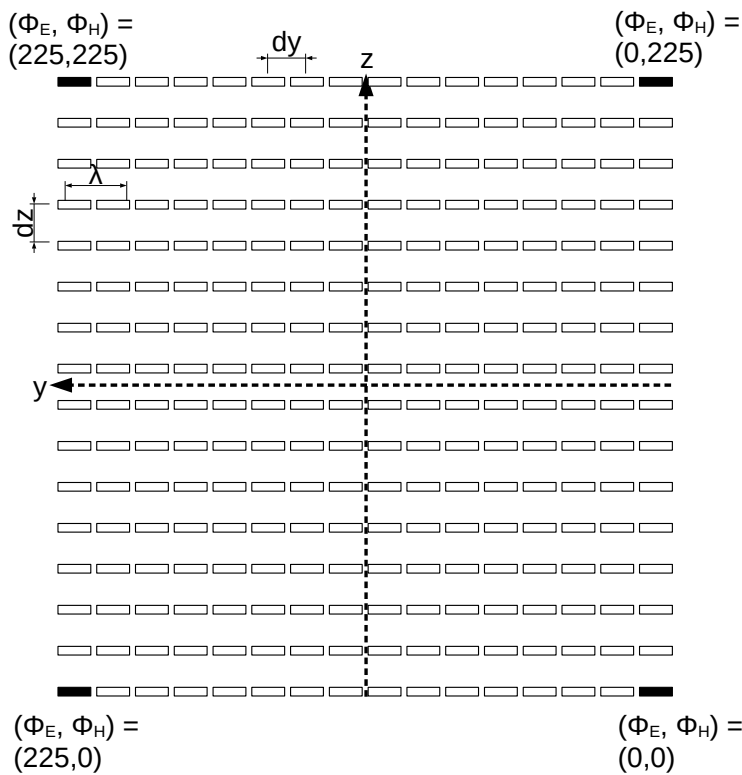


**Figure 8.** The two-dimensional  $N \times N = 16 \times 16$  Yagi-Uda/horn y-polarized array layout. The alignment with 3D Cartesian coordinates is depicted, along with the array spacing variables  $d_y$  and  $d_z$ , the wavelength  $\lambda$  (to scale), and the phases for each row and column if  $\Delta\Phi_E = \Delta\Phi_H = 15$  degrees.

**Table 2.** The parameters for the  $N \times N = 8 \times 8$  horn array, modified from Table 1. The Yagi-Uda  $N \times N = 16 \times 16$  array did not require modification. The number of CPU cores was 4 in hardware, but was effectively 8 with hyperthreading. The most memory-intensive simulation was the  $8 \times 8$  horn array, which consumed 11.7 GB of memory out of 15.5 GB free. The code was written with the Python3 interface to MEEP, installed with the conda package manager, and run in Jupyter notebooks.

Horn		System Information	
Parameter	Value		
$N \times N$	$8 \times 8$	Memory Consumption	
$a$	2.0	11.7 GB out of 15.5 GB	
$c$	15.0	CPU cores	
$d$	8.0	Intel i7 1.80 GHz (8)	
$dx$	0.5	MEEP installation	
$n = c/dx$	30	Python3 interface (conda)	
$d_y$	16		
resolution	4		
backplane location	$-2a$		
backplane thickness	0.5		
backplane dim.	$142 \times 142$		

#### 4.1. Phase Steering, Beam Angle, and Beamwidth

The  $\Delta\phi$  vs.  $\Delta\Phi$  results for the two-dimensional  $N \times N = 16 \times 16$  Yagi-Uda array are shown in Figure 9. Figure 9 (top left) contains  $\Delta\phi_E$  versus  $\Delta\Phi_E$  data at 5 GHz. The data match the theoretical linear slope  $\lambda/(2\pi d_y)$  and  $\lambda/(2\pi d_z)$ , with  $d_y = d_z$ . The phase shift per antenna is varied over  $[0, 75]$  degrees in 15 degree increments independently by row and column. The circles and squares correspond to  $\Delta\Phi_H = 0$  and 45 degrees, respectively. Both the circles and squares follow the same line, implying the correct phase independence: when  $\Delta\Phi_H$  is held at either constant,  $\Delta\phi_E$  still varies with  $\Delta\Phi_E$  correctly. Figure 9 (bottom

left) contains  $\Delta\phi_H$  versus  $\Delta\Phi_H$  data at 5 GHz. The circles and squares correspond to  $\Delta\Phi_E = 0$  and 45 degrees, respectively. Beyond  $\Delta\Phi_E = 75$  degrees or  $\Delta\Phi_H = 75$  degrees, side lobes appear ( $>-15$  dB). Figure 9 (right) contains the beam angle results after steering the beam to 36 of the possible  $11 \times 11$  positions in the E and H plane using increments of  $\Delta\Phi_{E/H} = 15$  degrees. The xy-errorbars correspond to the beamwidths.

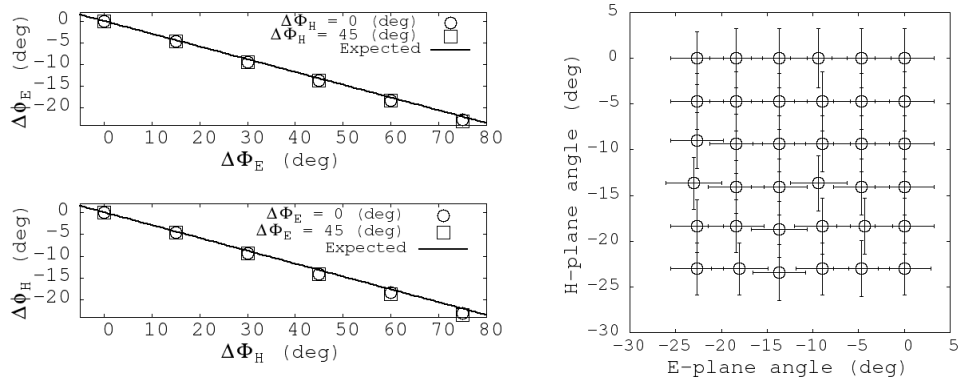


**Figure 9.** (Left) The beam angles  $\Delta\phi_E$  and  $\Delta\phi_H$  versus the phase shifts for the  $N \times N = 16 \times 16$  Yagi-Uda array at 5 GHz. The black lines represent the theoretical prediction of a linear dependence with slope  $\lambda/(2\pi d_y)$  or  $\lambda/(2\pi d_y)$ , ( $d_y = d_z$ ). In each graph, the circles and squares correspond to two different  $\Delta\Phi$  constant values for the other array plane. In these examples, location of zero phase on the array is chosen to cause a negative beam angle. (Right) The data points correspond to beam angles in the E and H-planes, with the associated beamwidths as errorbars. These data represent one-quarter of the possible scan positions with  $\Delta\Phi_{E/H} = 15$  degrees.

The  $\Delta\phi$  vs.  $\Delta\Phi$  results for the two-dimensional  $N \times N = 8 \times 8$  horn array are shown in Figure 10 (left). Figure 10 (top left) contains  $\Delta\phi_E$  versus  $\Delta\Phi_E$  data at 1 GHz. The larger horn size relative to those in Section 3 means the upper frequency is  $\approx 1.2$  GHz. The data match the theoretical slopes just as in Figure 9. The phase shift per antenna is varied in the same pattern as in Figure 9. The circles and squares correspond to  $\Delta\Phi_H = 0$  and 45 degrees, respectively, and both data sets follow the theory. Figure 10 (bottom left) contains  $\Delta\phi_H$  versus  $\Delta\Phi_H$  data at 1 GHz. The circles and squares correspond to  $\Delta\Phi_E = 0$  and 45 degrees, respectively, and both data sets follow the theory. The beamwidth as a function of frequency across the bandwidth for the design is shown in Figure 10 (right). The fit parameter mean values and standard errors are:  $a = 10.6 \pm 0.2$  degree GHz,  $b = 2.8 \pm 0.3$  degrees,  $c = 8.7 \pm 0.4$  degree GHz, and  $d = 5.0 \pm 0.9$  degrees. The width of the mouth of the horns is 16 cm in the E-plane direction and 2 cm in the H-plane direction, so some small difference in beamwidth is not surprising.

#### 4.2. Radiation Patterns

The radiation patterns in the E and H plane for the two-dimensional Yagi-Uda array are shown in Figure 11. The phase combinations  $(\Delta\Phi_E, \Delta\Phi_H) = (0, 0), (30, 60), (60, 30)$  degrees are shown for E and H planes at 3 and 4 GHz. As in Section 3.2, Equation (25) is shown in red, and the simulation results are shown in blue. The main beam and first several side lobes are modeled correctly in each case, and the FB ratio is  $\leq -15$  dB. The side lobes are also at the  $\approx -15$  dB level. Following Figure 10 (right), the main beam is narrower at 4 GHz than at 3 GHz. Though not generally designed to be broadband elements, the Yagi-Uda elements do display some flexibility in frequency. The log-periodic dipole array (LPDA) is a broadband example constructed from dipoles as the Yagi is [20].

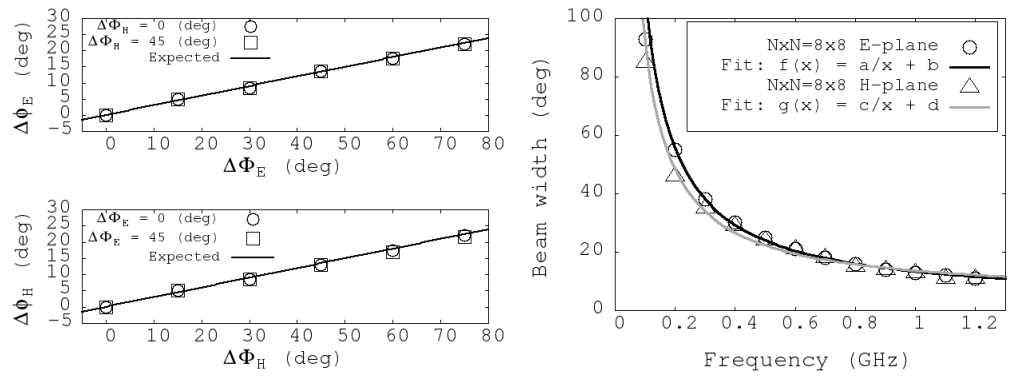


**Figure 10.** (Left) The beam angles  $\Delta\phi_E$  and  $\Delta\phi_H$  versus the phase shifts per column (for the E-plane) and per row (for the H-plane) for the  $N \times N = 8 \times 8$  horn array at 1 GHz. The black lines represent the theoretical prediction. In each graph, the circles and squares correspond to two different  $\Delta\Phi$  constant values for the other array plane. (Right) The beamwidth in the E and H-planes versus frequency.

Producing the radiation patterns in Figure 11 requires only  $\mathcal{O}(10)$  seconds to run near-field calculations, and only another  $\approx 5$  min each to run the `get_farfield` routine over the E and H-planes. Modeling arrays constructed from dipole elements is orders of magnitude faster than for the array of horns, due to the two-dimensional nature of the dipole elements. Producing the radiation patterns of Figure 12 for the two-dimensional horn array requires  $\approx 60$  min combined for the E and H-plane patterns, *per frequency*. Unlike the Yagi case, the vast majority of time is not dedicated to the `get_farfield` routine, but to the near-field calculations. The near-field calculations require “sub-pixel smoothing” for the many edges of the blocks that comprise the horn structure.

The radiation patterns in the E and H plane for the two-dimensional horn array are shown in Figure 12. The phase combinations  $(\Delta\Phi_E, \Phi_H) = (0, 0), (30, 60), (60, 30)$  degrees are shown for E and H planes at 0.5 and 1.0 GHz. As in Section 3.2, Equation (25) is shown in red, and the simulation results are shown in blue. The main beam and first several side lobes are modeled correctly in each case, and the FB ratio is  $\leq -15$  dB. The side lobes are also at the  $\approx -15$  dB level. Due to the higher bandwidth, a wider range of beamwidths is available (see Figure 10). The main beam is narrower at 1 GHz than at 0.5 GHz. The horns produce the correct pattern for  $(\Delta\Phi_E, \Delta\Phi_H) = (0, 0)$  degrees from 0.1 to 1.2 GHz. However, grating lobes above  $-15$  dB are a known problem that occur when attempting to steer phased arrays built from broadband horns to wide angles (see Chapter 9 of Reference [16]). The addition of the backplane limits diffraction of the radiation around the edges of the array and therefore limits the FB ratio, but grating lobes appear at  $\pm 45$  degrees from the main beam. There is occasionally a back lobe, which can be attributed to the diffraction of fields around the edge of the backplane. This effect is more pronounced when the main beam is steered to a wide angle and occurs in the hemisphere opposite to the main beam.

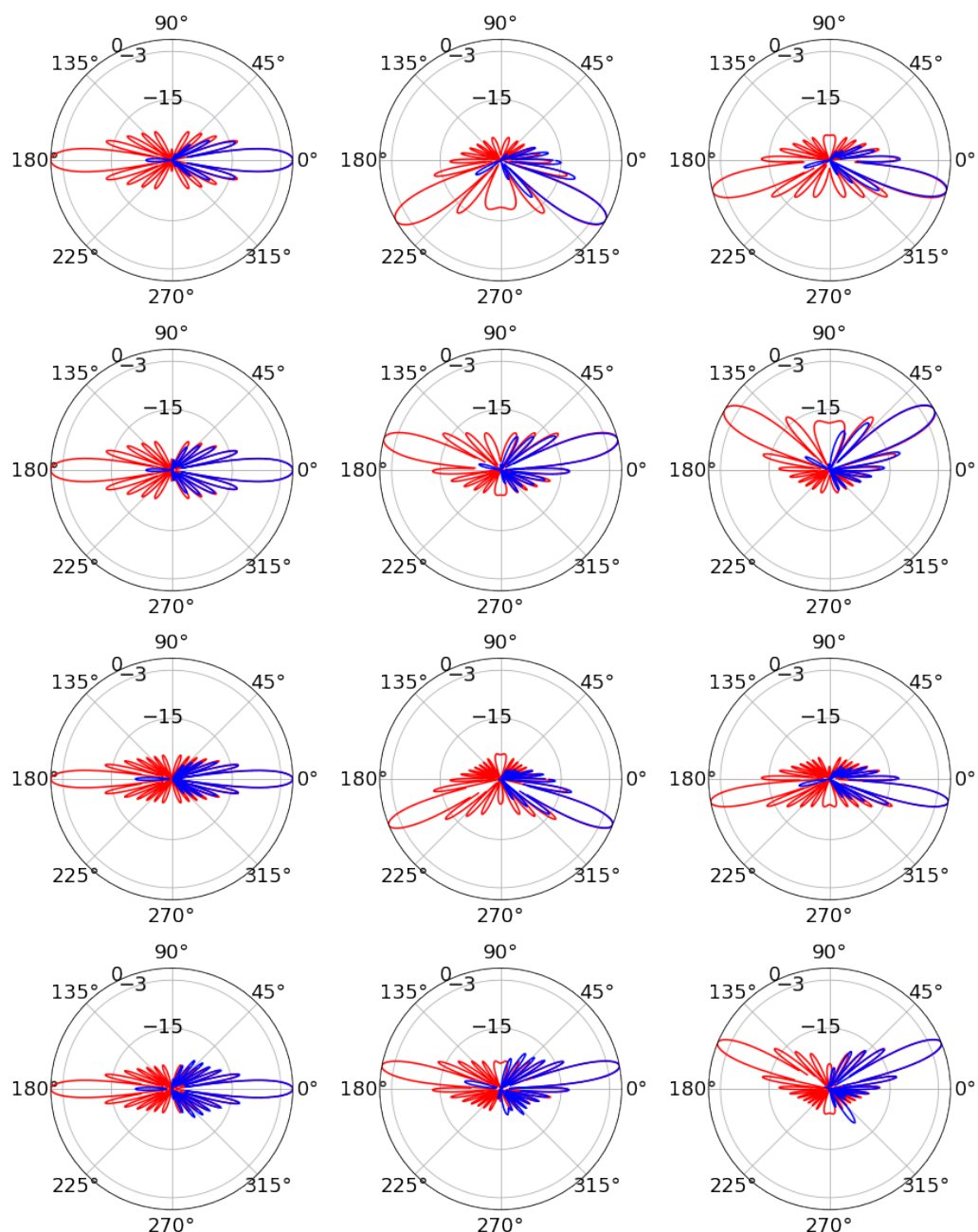


**Figure 11.** Yagi-Uda results, two-dimensional array (**First row**)  $f = 3$  GHz, with (from left to right) E-plane  $(\Delta\Phi_E, \Delta\Phi_H) = (0, 0)$  degrees, E-plane  $(\Delta\Phi_E, \Delta\Phi_H) = (60, 30)$  degrees, E-plane  $(\Delta\Phi_E, \Delta\Phi_H) = (30, 60)$  degrees. (**Second row**)  $f = 3$  GHz, with (from left to right) H-plane  $(\Delta\Phi_E, \Delta\Phi_H) = (0, 0)$  degrees, H-plane  $(\Delta\Phi_E, \Delta\Phi_H) = (60, 30)$  degrees, H-plane  $(\Delta\Phi_E, \Delta\Phi_H) = (30, 60)$  degrees. (**Third row**)  $f = 4$  GHz, with (from left to right) E-plane  $(\Delta\Phi_E, \Delta\Phi_H) = (0, 0)$  degrees, E-plane  $(\Delta\Phi_E, \Delta\Phi_H) = (60, 30)$  degrees, E-plane  $(\Delta\Phi_E, \Delta\Phi_H) = (30, 60)$  degrees. (**Fourth row**)  $f = 4$  GHz, with (from left to right) H-plane  $(\Delta\Phi_E, \Delta\Phi_H) = (0, 0)$  degrees, H-plane  $(\Delta\Phi_E, \Delta\Phi_H) = (60, 30)$  degrees, H-plane  $(\Delta\Phi_E, \Delta\Phi_H) = (30, 60)$  degrees.

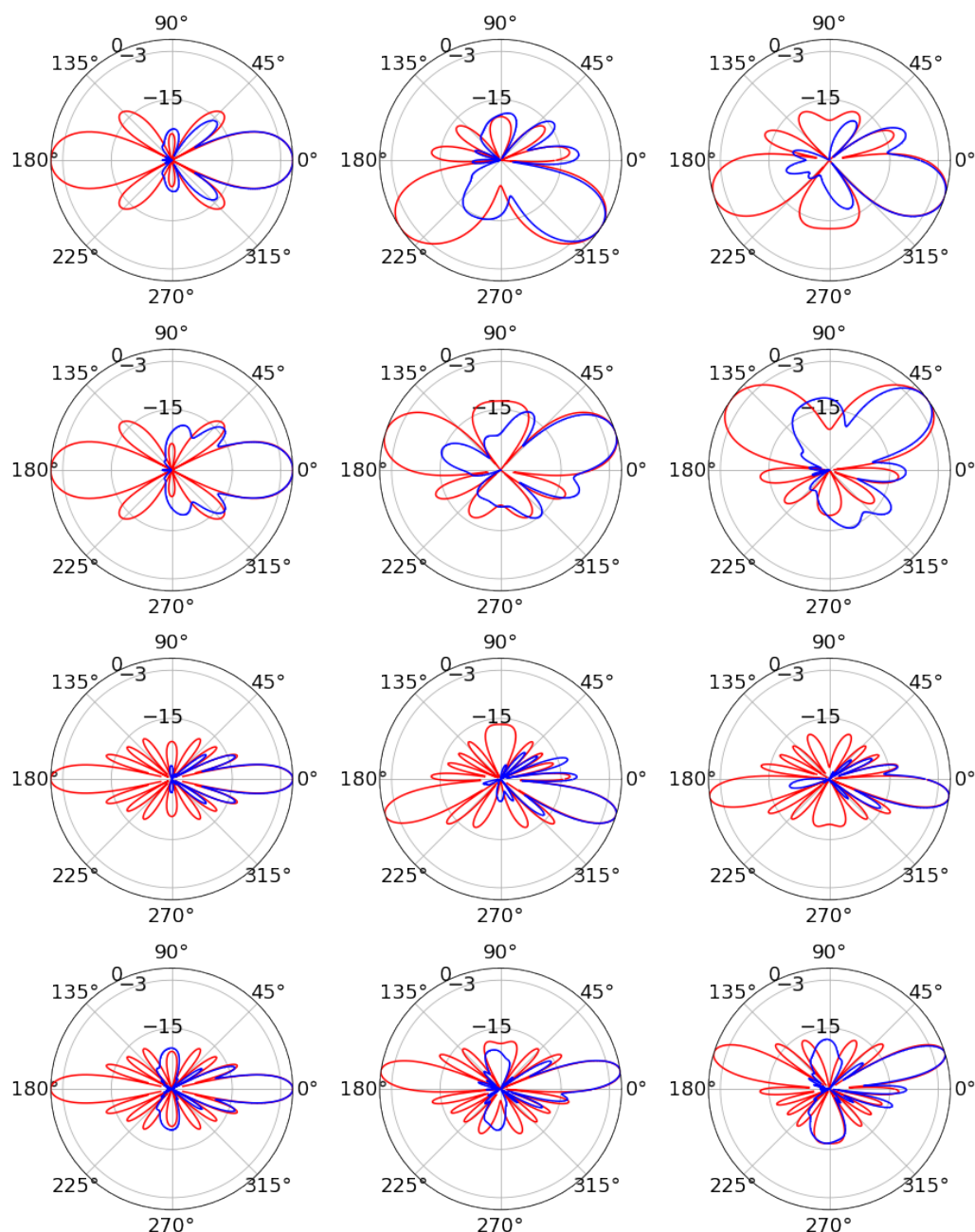


**Figure 12.** Horn results, two-dimensional array (**First row**)  $f = 0.5$  GHz, with (from left to right) E-plane  $(\Delta\Phi_E, \Delta\Phi_H) = (0, 0)$  degrees, E-plane  $(\Delta\Phi_E, \Delta\Phi_H) = (60, 30)$  degrees, E-plane  $(\Delta\Phi_E, \Delta\Phi_H) = (30, 60)$  degrees. (**Second row**)  $f = 0.5$  GHz, with (from left to right) H-plane  $(\Delta\Phi_E, \Delta\Phi_H) = (0, 0)$  degrees, H-plane  $(\Delta\Phi_E, \Delta\Phi_H) = (60, 30)$  degrees, H-plane  $(\Delta\Phi_E, \Delta\Phi_H) = (30, 60)$  degrees. (**Third row**)  $f = 1.0$  GHz, with (from left to right) E-plane  $(\Delta\Phi_E, \Delta\Phi_H) = (0, 0)$  degrees, E-plane  $(\Delta\Phi_E, \Delta\Phi_H) = (60, 30)$  degrees, E-plane  $(\Delta\Phi_E, \Delta\Phi_H) = (30, 60)$  degrees. (**Fourth row**)  $f = 1.0$  GHz, with (from left to right) H-plane  $(\Delta\Phi_E, \Delta\Phi_H) = (0, 0)$  degrees, H-plane  $(\Delta\Phi_E, \Delta\Phi_H) = (60, 30)$  degrees, H-plane  $(\Delta\Phi_E, \Delta\Phi_H) = (30, 60)$  degrees.

### 5. Variation of the Index of Refraction

The behavior of a one-dimensional phased array embedded within a dielectric medium with spatially-dependent index of refraction  $n(z)$  is interesting to the ultra-high energy (UHE) neutrino community [3,5]. Phased arrays represent an opportunity to lower the RF detection threshold for RF pulses generated by UHE neutrinos via the Askaryan effect. Antarctic ice is the most convenient and natural medium for Askaryan pulse detection, due to the RF transparency and large pristine volumes located in Antarctic and Greenlandic

ice sheets and shelves [21–23]. The index of refraction varies within the ice because of the transition between surface snow ( $\rho \approx 0.4 \text{ g/cm}^3$ ) and the solid ice below ( $\rho = 0.917 \text{ g/cm}^3$ ). Most recent and intricate studies of phased array beam behavior still assume a uniform medium [24–26]. Embedded phased arrays with varying  $n(z)$  emit signals that curve in the direction of increasing  $n(z)$ .

The *shadow zone* is the volume of ice from which RF signals do not reach a receiver due to the excess curvature of the ray trace [27]. While there is evidence that RF signals can propagate horizontally through Antarctic ice [28], data from Greenland suggests the relative strength of the effect is small compared to the curved radiation [29]. Using the tools developed in this work, it is possible to map out the shadow zone for an embedded phased array radiating sinusoidal signals at fixed frequency. Intriguingly, when the phased array *radiates*, the grating lobe power reflect downward from the snow-air interface, and radiates into the shadow zone. Grating lobe power also refracts into the air above the interface. Grating lobe power leaves the array at a different angle than the main beam, so their presence in the shadow zone does not represent forbidden RF propagation.

A two-parameter fit to the  $n(z)$  data versus depth  $z$  below the surface is given by [28]

$$n(z) = \begin{cases} 1 & z > 0 \\ n_{\text{ice}} - \Delta n \exp(z/z_0) & z \leq 0 \end{cases} \quad (28)$$

The fit parameters in Equation (28) come from Reference [28]:  $\Delta n = 0.423 \pm 0.004$  and  $z_0 = 77 \pm 2 \text{ m}$ , with  $n_{\text{ice}} = 1.78$  for RF frequencies. These values are derived from the SPICE core data taken in 2015 near the South Pole, and are in statistical agreement with fits from data obtained by the RICE experiment (see also Reference [28]). Equation (28) was implemented in the one-dimensional horn array case, but the horn structure surrounding each radiating element was removed. The array is therefore a one-dimensional dipole array. Further, the length scale was reinterpreted to be meters rather than centimeters, which is an ability conferred by the scale invariant FDTD algorithms. In this medium, there is no fixed *in-situ* value of  $\lambda$  so the  $\lambda/4$  dipoles were spaced by  $\lambda/2$  according to their free space  $\lambda$  value. At the selected frequency of 200 MHz, the dipole length is 0.375 m, and the spacing is 0.75 m.

Figures 13 and 14 contain the results of a  $N = 8$  one-dimensional dipole array embedded in a medium with the index profile in Equation (28). Figure 13 shows the schematic of the calculation, and Figure 14 shows the magnitude of the  $z$ -component of the  $z$ -polarized array. Figure 14 represents the same physical dimensions as Figure 13. Equation (28) was sampled 100 times vertically, and with a resolution parameter of 10, the effective  $\Delta z$  is 0.1 m. The units in Figure 13 are meters, and the unit-less frequency in MEEP was scaled accordingly, to correspond to 200 MHz. The distances between the air-snow interface and the first phased array element is 15 m (top) and 35 m (bottom).

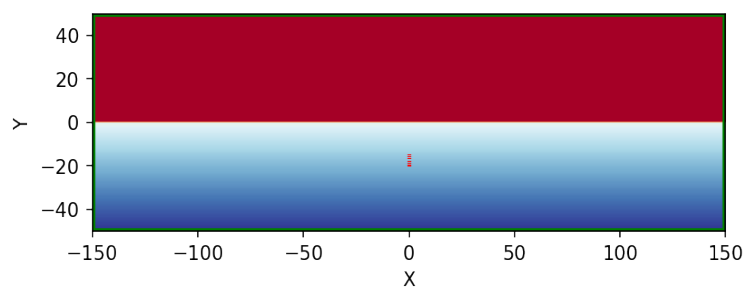


**Figure 13.** The simplified  $N = 8$  one-dimensional vertical phased array with dimensions in meters. For this array,  $d_z = \lambda/2.0$ , and the length of the dipole radiators is  $\lambda/4.0$ . The colorscale represents  $n(z)$  in Equation (28).

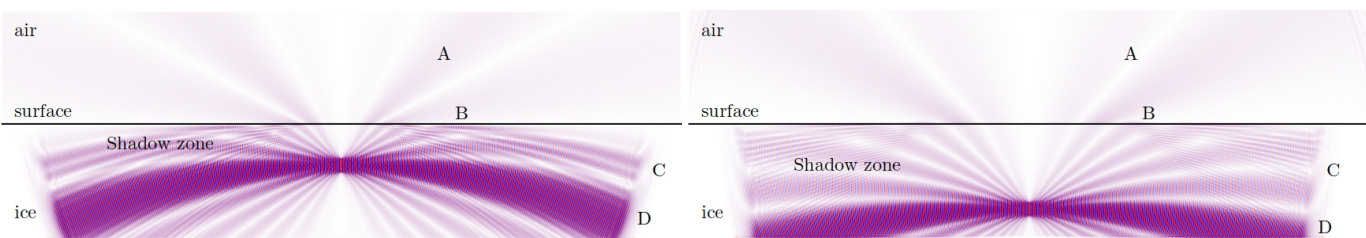


**Figure 14.** The magnitude of the  $z$ -component of the  $z$ -polarized dipoles as they radiate as a phased array with  $\Delta\Phi = 0$  degrees. The air, surface, and ice regions are the same as Figure 13, with the same dimensions. (**Top**) The array depth is  $-15$  m. (**Bottom**) The array depth is  $-35$  m. (**A**) Radiation refracting through the surface into the air. (**B**) Grating lobes reflect from the surface into the shadow zone. (**C**) Grating lobes propagating through the shadow zone. (**D**) The main beam bent downward due to the gradient in  $n(z)$ .

The color scale in Figure 14 is  $\pm 0.05$  with the signal amplitude of the elements  $\pm 1.0$  at 200 MHz. The amplitude scale is less important than observing *where* the radiation has penetrated the ice after 200 time steps. In Figure 14 (top), the main beam has curved downwards in the direction of increasing  $n(z)$ , while grating lobes have both diffracted to the air and reflected into the shadow zone. The rate of curvature of the main beam is controlled by the fit parameter  $z_0$  in Equation (28). In Figure 14 (bottom), the physics is the same as Figure 14 (top), but the effect of  $n(z)$  curvature is weakened. The beam travels farther horizontally because the gradient of  $n(z)$  is smaller at the larger depth. The geometry of the larger depth is such that the reflected grating lobe power is interfering with grating lobe power that was curved downwards without reflection. This can be seen just above the C marker in Figure 14 (bottom).

## 6. Summary and Future Analysis

Four phased array designs have been modeled with the MIT Electromagnetics Equation Propagation (MEEP) package in non-parallel mode. Two types of individual radiating element were explored: the narrow-band Yagi-Uda and broadband horn antennas. Two phased array geometries were explored: *one-dimensional* and *two-dimensional*. The one and two-dimensional Yagi-Uda phased arrays were designed for  $\leq 5$  GHz, however, scale-invariance makes this design scalable to a variety of frequencies. The one-dimensional horn array performs in the range [0.3–5] GHz, using two-dimensional versions of the horn elements. The two-dimensional horn array had to be modified due to memory constraints. The result was an array that performed in the range [0.1–1.2] GHz. In all cases, comparisons to array theory were shown.

The one-dimensional array of Yagi-Uda antennas was analyzed in Section 3. The array demonstrated the correct linear relationship between  $\Delta\phi$  and  $\Delta\Phi$  (Figure 4) (top left and right). Although any row of point sources would obey the relationship in Equation (18), a row of point sources has two main beam solutions by symmetry. Thus Figure 4 could not be interpreted correctly were it not for the proper functioning of the Yagi elements. The radiation patterns produced with the one-dimensional Yagi array were compared to Equation (25) in Figure 5. The radiation pattern in the E-plane is shown to agree with Equation (25) in both the main beam and the first several grating lobes. The calculation takes place in two-dimensions, so an H-plane comparison is not relevant.

The one-dimensional array of horn antennas was analyzed in Section 3. The array demonstrated the correct linear relationship between  $\Delta\phi$  and  $\Delta\Phi$  (Figure 4). In that case, the slope of  $\Delta\phi$  vs.  $\Delta\Phi$  was *increased* by a factor of 2 and then 10 by *decreasing* the frequency by a factor of 2 and then 10. The bandwidth of the two-dimensional versions of the horns allows the variation of scan range. The scan range is smaller at high frequencies, as indicated in Figure 4 (bottom left). However, the beamwidth is also smaller at high frequencies, as indicated in Figure 4 (bottom right). The design trade-off is between small beamwidth and large scan range. In Figure 6 the one-dimensional horn array radiation pattern is shown to match Equation (25) at both 0.5 and 5.0 GHz. There are 2–4 side lobes

at 0.5 GHz to match per pattern, and the simulation results match them as well as the wide main beam. At 5.0 GHz, the main beam is accompanied by two prominent grating lobes at  $\pm 45$  degrees that should be as powerful as the main beam. The simulation finds them at the  $-15$  dB level. The grating lobes are being suppressed by the the pattern null from the horn element pattern [16]. At lower frequencies, however, scan loss takes a toll on radiated power (Table 1).

The two-dimensional,  $N \times N = 16 \times 16$  Yagi-Uda array was analyzed in Section 4. The array demonstrated the correct linear relationships between  $\Delta\phi_E$  and  $\Delta\Phi_E$ , and  $\Delta\phi_H$  and  $\Delta\Phi_H$  (Figure 9) (left). Given the narrow beamwidth, the array design can be scanned  $\pm 5$  beamwidths in the E-plane and  $\pm 5$  beamwidths in the H-plane before side lobes become too large. One fourth of these scan positions are shown in Figure 9 (right). The radiation pattern of the full two-dimensional array was displayed in Figure 11 at 3 and 4 GHz, for several scan angles. In each case, the pattern matched Equation (25) in the E and H-planes in the main beam and dominant side lobes. The addition of a metal back plane helps to suppress back lobes. Peculiarly, the two-dimensional array did not match the theoretical prediction at 5 GHz as well as the one-dimensional case when scanned.

The two-dimensional,  $N \times N = 8 \times 8$  horn array was analyzed in Section 4. The array demonstrated the correct linear relationships between  $\Delta\phi_E$  and  $\Delta\Phi_E$ , and  $\Delta\phi_H$  and  $\Delta\Phi_H$  (Figure 10) (left). The beamwidth is again inversely proportional to frequency (Figure 10) (right). It is not surprising that the fits differ slightly in the E and H-planes, since the horn width changes in the E-plane but does not in the H-plane. The quality of the fits to  $1/f + const$  are excellent. The additive constants in these fits are only necessary because the array cannot be infinitely long. Technically, Equation (25) implies that the beamwidth would go to zero as  $N \rightarrow \infty$ . The radiation patterns of the two-dimensional horn array are displayed in Figure 12 at 0.5 and 1.0 GHz, for the same sampling of scan angles as in Figure 11. The high-frequency beam is narrower and accompanied by grating lobes at  $\pm 45$  degrees. The patterns agree with theoretical expectations, with the exception of the H-plane lobes at  $\pm 90$  degrees. At low frequency, the beam is wider and is accompanied by grating lobes at  $\pm 45$  degrees from the main beam. The results match in the main lobe, but the simulation does not match the theoretical grating lobes. This is pronounced when the beam is moved far from broadside in the H-plane.

Finally, a simplified version of the  $N = 8$  one-dimensional case of dipoles was embedded in a medium with varying index of refraction,  $n(z)$ . The model for  $n(z)$  was a simple fit to the profile of the ice at the South Pole, which is a location of interest for planned phased array detectors designed to record Askaryan signals from UHE neutrinos passing through ice. Though the studies in this work are restricted to phased-arrays as transmitters, and not receivers, the shadow zone of the array was mapped at 200 MHz under realistic conditions. An interesting side effect of the phased array being the radiating system was that the grating lobes managed to propagate into the shadow zone.

Future work would include several enhancements to the simulations. Calculations of S-parameters for individual elements should be added, and optimization studies on horn and Yagi geometric parameters are warranted. However, other RF element types should also be studied. Due to the relevance of one-dimensional phased array receivers for UHE neutrino physics, one interesting choice is the wide-radius dipole used by the Radio Neutrino Observatory Greenland (RNO-G) collaboration [30]. Such elements already have low VSWR measurements in the relevant bandwidth. Finally, upgrading the simulation code to utilize parallel MEEP capabilities will increase the potential speed and complexity. Additional complexity will come in the form of more accurate antenna structure modeling, thereby improving the precision across a wide bandwidth.

**Funding:** This research was funded by the Office of Naval Research (ONR) under the Summer Faculty Research Program (SFRP).

**Institutional Review Board Statement:** Not applicable.

**Informed Consent Statement:** Not applicable.

**Data Availability Statement:** The data presented in this study are available on request from the corresponding author. Due to large file sizes and restricted bandwidth, please contact corresponding author to set up collaborative sharing.

**Acknowledgments:** We would like to thank the Office of Naval Research (ONR) for helping to support this research. In particular, we would like to thank the Naval Surface Warfare Center Corona Division and their continued support of the ONR Summer Faculty Research Program (SFRP). Conversations with Christopher Clark and Gary Yeakley were especially helpful. We are also grateful to Van Nguyen, Jeffery Benson, and Golda McWhorter. Karon Myles deserves our special thanks for helping to coordinate the SFRP program.

**Conflicts of Interest:** The authors declare no conflict of interest.

## Appendix A

MEEP FDTD is more often applied to 1  $\mu\text{m}$  scale lengths than the 1 cm-scale RF elements, so scale-invariance must be highlighted. Scale invariant units with  $c = 1$  are used in MEEP when solving Maxwell's equations with the FDTD technique. The typical length scale in MEEP analysis is usually called the "a-value." Systems with dimensions of order 1  $\mu\text{m}$  are said to have an "a-value of 1  $\mu\text{m}$ ." A value of  $a = 1 \text{ cm}$  is chosen for models presented in Sections 3 and 4. For example, if the frequency  $f = 7.5 \text{ GHz}$ , the wavelength is  $4.0 \text{ cm} = 4.0a$ , or simply 4.0 with  $f = 1/\lambda = 0.25$ . Since  $c = 1$ ,  $\lambda = f^{-1} = T$ . The period is 4.0, so a simulation run of  $50T = 200$  time units corresponds to 6.67 ns. Assuming 1 pixel/a-value, simulated radiation would therefore propagate 200 units of  $\Delta x$  in a straight line before time was up. A *resolution* parameter sets the number of pixels per distance unit and is usually larger than 1.0. Selecting the right resolution is often a subtle balance between capturing the most relevant effects while limiting the memory usage of the simulation results.

## References

1. Syrytsin, I.; Zhang, S.; Pedersen, G.F. Circularly Polarized Planar Helix Phased Antenna Array for 5G Mobile Terminals. In Proceedings of the 2017 International Conference on Electromagnetics in Advanced Applications (ICEAA), Verona, Italy, 11–15 September 2017; pp. 1105–1108. [[CrossRef](#)]
2. Kikuchi, K.; Mikada, H.; Takekawa, J. Improved Imaging Capability of Phased Array Antenna in Ground Penetrating Radar Survey. In Proceedings of the Conference Proceedings, 79th EAGE Conference and Exhibition, Paris, France, 12–15 June 2017. [[CrossRef](#)]
3. Vieregg, A.; Bechtol, K.; Romero-Wolf, A. A technique for detection of PeV neutrinos using a phased radio array. *J. Cosmol. Astropart. Phys.* **2016**, *2016*, 005. [[CrossRef](#)]
4. Munekata, T.; Yamamoto, M.; Nojima, T. A Wideband 16-Element Antenna Array Using Leaf-Shaped Bowtie Antenna and Series-Parallel Feed Networks. In Proceedings of the 2014 IEEE International Workshop on Electromagnetics (iWEM), Sapporo Hokkaido, Japan, 4–6 August 2014; pp. 80–81. [[CrossRef](#)]
5. Avva, J.; Bechtol, K.; Chesebro, T.; Cremonisi, L.; Deaconu, C.; Gupta, A.; Ludwig, A.; Messino, W.; Miki, C.; Nichol, R.; et al. Development Toward a Ground-Based Interferometric Phased Array for Radio Detection of High Energy Neutrinos. In *Nuclear Instruments and Methods in Physics Research Section A: Accelerators, Spectrometers, Detectors and Associated Equipment*; Elsevier: Amsterdam, The Netherlands, 2016.
6. Ansys, Inc. *3D Electromagnetic Field Simulator for RF and Wireless Design*; Ansys, Inc.: Canonsburg, PA, USA, 2020.
7. Feng, N.; Zhang, Y.; Tian, X.; Zhu, J.; Joines, W.T.; Wang, G.P. System-Combined ADI-FDTD Method and Its Electromagnetic Applications in Microwave Circuits and Antennas. *IEEE Trans. Microw. Theory Tech.* **2019**, *67*, 3260–3270. [[CrossRef](#)]
8. Zhu, L.; Hwang, H.S.; Ren, E.; Yang, G. High Performance MIMO Antenna for 5G Wearable Devices. In Proceedings of the 2017 IEEE International Symposium on Antennas and Propagation & USNC/URSI National Radio Science Meeting, San Diego, CA, USA, 9–15 July 2017; pp. 1869–1870. [[CrossRef](#)]
9. Ho, T.Q.; Hunt, L.N.; Hewett, C.A.; Ready, T.G.; Mittra, R.; Yu, W.; Zolnick, D.A.; Kragalott, M. Analysis of Electrically Large Patch Phased Arrays via CFDTD. In Proceedings of the 2006 IEEE Antennas and Propagation Society International Symposium, Albuquerque, New Mexico, 9–14 July 2006; pp. 1571–1574. [[CrossRef](#)]
10. Burke, G.J.; Miller, E.K.; Poggio, A.J. The Numerical Electromagnetics Code (NEC)—A Brief History. *IEEE Antennas Propag. Soc. Symp.* **2004**, *3*, 2871–2874. [[CrossRef](#)]
11. Oskooi, A.F.; Roundy, D.; Ibanescu, M.; Bermel, P.; Joannopoulos, J.; Johnson, S.G. Meep: A flexible free-software package for electromagnetic simulations by the FDTD method. *Comput. Phys. Commun.* **2010**, *181*, 687–702. [[CrossRef](#)]
12. Fedeli, A.; Montecucco, C.; Gragnani, G.L. Open-Source Software for Electromagnetic Scattering Simulation: The Case of Antenna Design. *Electronics* **2019**, *8*, 1506. [[CrossRef](#)]

13. Liebig, T.; Rennings, A.; Held, S.; Erni, D. openEMS—A free and open source equivalent-circuit (EC) FDTD simulation platform supporting cylindrical coordinates suitable for the analysis of traveling wave MRI applications. *Int. J. Numer. Model. Electron. Networks Dev. Fields* **2013**, *26*, 680–696. [[CrossRef](#)]
14. Warren, C.; Giannopoulos, A.; Giannakis, I. gprMax: Open source software to simulate electromagnetic wave propagation for Ground Penetrating Radar. *Comput. Phys. Commun.* **2016**, *209*, 163–170. [[CrossRef](#)]
15. Richie, J.E.; Ababei, C. Optimization of patch antennas via multithreaded simulated annealing based design exploration. *J. Comput. Des. Eng.* **2017**, *4*, 249–255. [[CrossRef](#)]
16. Mailloux, R. *The Phased Array Antenna Handbook*; Artech House: Norwood, MA, USA, 2018.
17. Wahl, P.; Gagnon, D.S.L.; Debaes, C.; Erps, J.V.; Vermeulen, N.; Miller, D.A.B.; Thienpont, H. B-CALM: An Open-Source Multi-GPU-based 3D-FDTD with Multi-pole dispersion for Plasmonics. *Prog. Electromagn. Res.* **2013**, *138*, 467–478. [[CrossRef](#)]
18. Gorham, P.; Allison, P.; Barwick, S.; Beatty, J.; Besson, D.; Binns, W.; Chen, C.; Chen, P.; Clem, J.; Connolly, A.; et al. The Antarctic Impulsive Transient Antenna ultra-high energy neutrino detector: Design, performance, and sensitivity for the 2006–2007 balloon flight. *Astropart. Phys.* **2009**, *32*, 10–41. [[CrossRef](#)]
19. Gorham, P.; Barwick, S.; Beatty, J.; Besson, D.; Binns, W.; Chen, C.; Chen, P.; Clem, J.; Connolly, A.; Dowkontt, P. Observations of the Askaryan effect in ice. *Phys. Rev. Lett.* **2007**, *99*, 171101. [[CrossRef](#)] [[PubMed](#)]
20. Barwick, S.; Berg, E.; Besson, D.; Duffin, T.; Hanson, J.; Klein, S.; Kleinfelder, S.; Piasecki, M.; Ratzlaff, K.; Reed, C.; et al. Time-domain response of the ARIANNA detector. *Astropart. Phys.* **2015**, *62*, 139–151. [[CrossRef](#)]
21. Hanson, J.C. Ross Ice Shelf Thickness, Radio-frequency Attenuation and Reflectivity: Implications for the Arianna Uhe Neutrino Detector. In Proceedings of the 32nd International Cosmic Ray Conference, Beijing, China, 11–18 August 2011. [[CrossRef](#)]
22. Hanson, J.C.; Barwick, S.W.; Berg, E.C.; Besson, D.Z.; Duffin, T.J.; Klein, S.R.; Kleinfelder, S.A.; Reed, C.; Roumi, M.; Stezelberger, T.; et al. Radar absorption, basal reflection, thickness and polarization measurements from the Ross Ice Shelf, Antarctica. *J. Glaciol.* **2015**, *61*, 438–446. [[CrossRef](#)]
23. Avva, J.; Kovac, J.; Miki, C.; Saltzberg, D.; Vieregg, A. An in situ measurement of the radio-frequency attenuation in ice at Summit Station, Greenland. *J. Glaciol.* **2014**. [[CrossRef](#)]
24. Adamidis, G.A.; Vardiambasis, I.O.; Ioannidou, M.P.; Kapetanakis, T.N. Design and implementation of an adaptive beamformer for phased array antenna applications. *Microw. Opt. Technol. Lett.* **2020**, *62*, 1780–1784. [[CrossRef](#)]
25. Ahn, B.; Hwang, I.J.; Kim, K.S.; Chae, S.C.; Yu, J.W.; Lee, H.L. Wide-Angle Scanning Phased Array Antenna using High Gain Pattern Reconfigurable Antenna Elements. *Sci. Rep.* **2019**, *9*, 18391. [[CrossRef](#)] [[PubMed](#)]
26. Gampala, G.; Reddy, C.J. Advanced Computational Tools for Phased Array Antenna Applications. In Proceedings of the 2016 IEEE International Symposium on Phased Array Systems and Technology (PAST), Waltham, MA, USA, 18–21 October 2016; pp. 1–5. [[CrossRef](#)]
27. Dookayka, K. Characterizing the Search for Ultra-High Energy Neutrinos with the ARIANNA Detector. Ph.D. Thesis, University of California at Irvine, Irvine, CA, USA, 2011.
28. Barwick, S.W.; Berg, E.C.; Besson, D.Z.; Gaswint, G.; Glaser, C.; Hallgren, A.; Hanson, J.C.; Klein, S.R.; Kleinfelder, S.; Köpke, L.; et al. Observation of classically ‘forbidden’ electromagnetic wave propagation and implications for neutrino detection. *J. Cosmol. Astropart. Phys.* **2018**, *2018*, 055. [[CrossRef](#)]
29. Deaconu, C.; Vieregg, A.G.; Wissel, S.A.; Bowen, J.; Chipman, S.; Gupta, A.; Miki, C.; Nichol, R.J.; Saltzberg, D. Measurements and Modeling of Near-Surface Radio Propagation in Glacial Ice and Implications for Neutrino Experiments. *Physic. Rev. D* **2018**, *98*, 043010. [[CrossRef](#)]
30. Aguilar, J.A.; Allison, P.; Beatty, J.J.; Bernhoff, H.; Besson, D.; Bingefors, N.; Botner, O.; Buitink, S.; Carter, K.; Clark, B.A.; et al. Design and Sensitivity of the Radio Neutrino Observatory in Greenland (RNO-G). *arXiv* **2020**, arXiv:2010.12279.

# Subject: [Electronics] Most Notable Articles (December 2020–February 2021)



*electronics*

IMPACT  
FACTOR  
**2.412**

## Most Notable Articles (December 2020–February 2021)

New CMOS Devices and Their Applications  
**One-Transistor Dynamic Random-Access Memory Based on Gate-All-Around Junction-Less Field-Effect Transistor with a Si/SiGe Heterostructure**  
Young Jun Yoon et al.

Reliability Assessment and Modeling of Optical and Semiconductor Devices  
**LTPS TFTs with an Amorphous Silicon Buffer Layer and Source/Drain Extension**  
Hye In Kim et al.

Applications of Thin Films in Microelectronics  
**Electrical Performance and Stability Improvements of High-Mobility Indium-Gallium-Tin Oxide Thin-Film Transistors Using an Oxidized Aluminum Capping Layer of Optimal Thickness**  
Hyun-Seok Cha et al.

Microwave and Wireless Communications  
**Broadband RF Phased Array Design with MEEP: Comparisons to Array Theory in Two and Three Dimensions**  
Jordan C. Hanson

10th Anniversary of Electronics: Recent Advances in Computer Science & Engineering  
**Muon–Electron Pulse Shape Discrimination for Water Cherenkov Detectors Based on FPGA/SoC**  
Luis Guillermo Garcia et al.

AI-Based Transportation Planning and Operation  
**Estimating Micro-Level On-Road Vehicle Emissions Using the K-Means Clustering Method with GPS Big Data**  
Hyejung Hu et al.

Microelectronics and Optoelectronics  
**A Compact and Robust Technique for the Modeling and Parameter Extraction of Carbon Nanotube Field Effect Transistors**  
Laura Falaschetti et al.

Evolutionary Machine Learning for Nature-Inspired Problem Solving  
**Data Analytics and Mathematical Modeling for Simulating the Dynamics of COVID-19 Epidemic—A Case Study of India**  
Himanshu Gupta et al.

Ubiquitous Sensor Networks  
**Low-Cost Distributed Acoustic Sensor Network for Real-Time Urban Sound Monitoring**  
Ester Vidaña-Vila et al.

10th Anniversary of Electronics: Advances in Circuit and Signal Processing  
**Circuit Model and Analysis of Molded Case Circuit Breaker Interruption Phenomenon**  
Kun-A Lee et al.

Data according to Altmetric, a service collecting metrics and qualitative data that are complementary to traditional, citation-based metrics.

## Call for Papers



### Emerging Internet of Things Solutions and Technologies

edited by Franco Cicirelli, Antonio Guerrieri, Carlo Mastroianni and Andrea Vinci  
submission deadline **31 March 2021**



### Smart Processing for Systems under Uncertainty or Perturbation

edited by Sanghyuk Lee, Mihail Popescu and Eneko Osaba  
submission deadline **9 April 2021**

**Electronics 2021 Best Paper Awards for Women**  
Winner announcement date: 31 March 2022

**Journal Awards**

## Why Submit to *Electronics*?

- **Open Access** Unlimited and free access for readers.
- **No Copyright Constraints** Retain copyright of your work and free use of your article.
- **Impact Factor 2.412** (2019 Journal Citation Reports®).
- **Thorough Peer-Review**
- **Coverage by Leading Indexing Services** Chemical Abstracts (American Chemical Society), Current Contents - Engineering, Computing & Technology/Web of Science (Clarivate), DOAJ, Inspec (IET), SCIE/Web of Science (Clarivate), Scopus (Elsevier).
- **Rapid Publication** Manuscripts are peer-reviewed and a first decision provided to authors approximately 15.1 days after submission; acceptance to publication is undertaken in 3.4 days (median values for papers published in this journal in the second half of 2020).
- **No Space Constraints, No Extra Space or Color Charges** No restriction on the length of the papers, number of figures or colors.
- **Discounts on Article Processing Charges (APC)** If you belong to an institute that participates with the MDPI Institutional Open Access Program (IOAP).

**Open Access Journals for Academic Conferences**

<p><b>PROCEEDINGS</b> <b>CHEMISTRY PROCEEDINGS</b> <b>ENGINEERING PROCEEDINGS</b></p> <p> <b>proceedings</b></p> <p> <b>chemistry proceedings</b></p> <p> <b>engineering proceedings</b></p>	<p><b>MATERIALS PROCEEDINGS</b> <b>ENVIRONMENTAL SCIENCES PROCEEDINGS</b></p> <p> <b>materials proceedings</b></p> <p> <b>environmental sciences proceedings</b></p> <p> <b>engineering proceedings</b></p>	<p><b>MDPI</b></p>
---	---	--------------------

## Journal Information

*Electronics* (ISSN 2079-9292) is an international, peer-reviewed, open access journal on the science of electronics and its applications.

To submit to the journal click [here](#).

[Unsubscribe](#)

[Manage your subscriptions](#)



Academic Open Access Publishing  
since 1996

MDPI

[www.mdpi.com](http://www.mdpi.com)

St. Alban-Anlage 66, 4052 Basel, Switzerland

Tel. +41 61 683 77 34

Fax +41 61 302 89 18

---

Disclaimer: MDPI recognizes the importance of data privacy and protection. We treat personal data in line with the General Data Protection Regulation (GDPR) and with what the community expects of us. The information contained in this message is confidential and intended solely for the use of the individual or entity to whom they are addressed. If you have received this message in error, please notify me and delete this message from your system. You may not copy this message in its entirety or in part, or disclose its contents to anyone.



## Subject: [Electronics] Most Notable Articles (February–May 2021)



IMPACT  
FACTOR  
**2.412**

### Most Notable Articles (February–May 2021)

#### Bioelectronics

**Evaluation of Large-Area Silicon Photomultiplier Arrays for Positron Emission Tomography Systems**  
Minjee Seo et al.

#### Circuit and Signal Processing

**Area-Time Efficient Two-Dimensional Reconfigurable Integer DCT Architecture for HEVC**  
Pramod Kumar Meher et al.

#### Bioelectronics

**Evaluation Method of Immediate Effect of Local Vibratory Stimulation on Proprioceptive Control Strategy: A Pilot Study**  
Yohei Ito et al.

#### Artificial Intelligence

**Evaluating the Quality of Machine Learning Explanations: A Survey on Methods and Metrics**  
Jianlong Zhou et al.

**Microwave and Wireless Communications Broadband RF Phased Array Design with MEEP: Comparisons to Array Theory in Two and Three Dimensions**  
Jordan C. Hanson

#### Networks

**Identity and Access Management Resilience against Intentional Risk for Blockchain-Based IOT Platforms**  
Alberto Partida et al.

#### Circuit and Signal Processing

**Investigating the Effects of Training Set Synthesis for Audio Segmentation of Radio Broadcast**  
Satvik Venkatesh et al.

#### Computer Science & Engineering

**An Assessment of Deep Learning Models and Word Embeddings for Toxicity Detection within Online Textual Comments**  
Danilo Dessì et al.

#### Networks

**UAV Forensic Analysis and Software Tools Assessment: DJI Phantom 4 and Matrice 210 as Case Studies**  
Fahad E. Salamh et al.

#### Computer Science & Engineering

**When Data Fly: An Open Data Trading System in Vehicular Ad Hoc Networks**  
Markus Lücking et al.

Data according to Altmetric, a service collecting metrics and qualitative data that are complementary to traditional, citation-based metrics.

#### 10th Anniversary of Electronics: Advances in Networks

**Guest Editors:** Prof. Dr. Dongkyun Kim, Prof. Dr. Qinghe Du, Dr. Mehdi Sookhak, Prof. Dr. Lei Shu, Assoc. Prof. Dr. Nurul I. Sarkar, Prof. Dr. Jemal H. Abawajy, Prof. Dr. Francisco Falcone  
**Deadline :** 31 October 2021

[mdpi.com/si/66341](http://mdpi.com/si/66341)

**Special Issue**  
Invitation to submit

## Call for Papers

---



### Application of Neural Networks in Biosignal Process

edited by Andrzej Czyżewski and Piotr Szczykko  
submission deadline **30 June 2021**



### Recent Advances in Antenna Design for 5G Heterogeneous Networks

edited by Issa Tamer Elfergani, Raed A. Abd-Alhameed and Abubakar Sadiq Hussaini  
submission deadline **30 June 2021**

## Why Submit to *Electronics*?

---

- **Open Access** Unlimited and free access for readers.
- **No Copyright Constraints** Retain copyright of your work and free use of your article.
- **Impact Factor 2.412** (2019 Journal Citation Reports®).
- **Thorough Peer-Review**
- **Coverage by Leading Indexing Services** Chemical Abstracts (American Chemical Society), Current Contents - Engineering, Computing & Technology/Web of Science (Clarivate), DOAJ, Inspec (IET), SCIE/Web of Science (Clarivate), Scopus (Elsevier).
- **Rapid Publication** Manuscripts are peer-reviewed and a first decision provided to authors approximately 15.1 days after submission; acceptance to publication is undertaken in 3.4 days (median values for papers published in this journal in the second half of 2020).
- **No Space Constraints, No Extra Space or Color Charges** No restriction on the length of the papers, number of figures or colors.
- **Discounts on Article Processing Charges (APC)** If you belong to an institute that participates with the MDPI Institutional Open Access Program (IOAP).

## Journal Information

---

*Electronics* (ISSN 2079-9292) is an international, peer-reviewed, open access journal on the science of electronics and its applications.

To submit to the journal click [here](#).

[Unsubscribe](#)

[Manage your subscriptions](#)



Academic Open Access Publishing  
since 1996

MDPI  
[www.mdpi.com](http://www.mdpi.com)  
St. Alban-Anlage 66, 4052 Basel, Switzerland  
Tel. +41 61 683 77 34  
Fax +41 61 302 89 18

---

Disclaimer: MDPI recognizes the importance of data privacy and protection. We treat personal data in line with the General Data Protection Regulation (GDPR) and with what the community expects of us. The information contained in this message is confidential and intended solely for the use of the individual or entity to whom they are addressed. If you have received this message in error, please notify me and delete this message from your system. You may not copy this message in its entirety or in part, or disclose its contents to anyone.



## Broadband RF Phased Array Design for UHE neutrino detection

---

Jordan C. Hanson<sup>a,\*</sup>

<sup>a</sup>Whittier College,  
13406 East Philadelphia Street, Los Angeles, California, 90602  
E-mail: [jhanson2@whittier.edu](mailto:jhanson2@whittier.edu)

Radio-frequency (RF) phased array systems have a wide variety of applications in engineering and physics research. Among these applications is ultra-high energy neutrino (UHE- $\nu$ ) detection above 100 PeV via the Askaryan effect. Phased array design usually requires numerical modeling with expensive commercial computational packages. Using the open-source MIT Electromagnetic Equation Propagation (MEEP) package, a set of phased array designs relevant for UHE- $\nu$  detection is presented. Specifically, one-dimensional arrays of Yagi-Uda and horn antennas were modeled in the bandwidth of the Askaryan effect [0.1 - 5] GHz, and compared to theoretical expectations. Precise matches between MEEP simulation and radiation pattern predictions at different frequencies and beam angles are demonstrated. Finally, the effect of embedding a phased array within Antarctic ice is studied. Askaryan-class UHE- $\nu$  detectors are being constructed in Antarctic ice because it is an ideal detection medium for UHE- $\nu$ . Future work will develop the phased array concepts with parallel MEEP, in order to increase the detail, complexity, and speed of the computations.

37<sup>th</sup> International Cosmic Ray Conference (ICRC 2021)  
July 12th – 23rd, 2021  
Online – Berlin, Germany

---

\*Presenter

## 1. Introduction

Phased arrays have applications in 5G, ground penetrating radar (GPR), and scientific instrumentation [13, 14, 16]. A series of three-dimensional antenna elements are arranged in a line with fixed spacing [2]. Proprietary RF modeling packages like XFDTD and HFSS are often used to model phased arrays [1, 8, 12]. The XFDTD package, for example, relies on the finite difference time domain (FDTD) method. The FDTD approach is a computational electromagnetics (CEM) technique in which Maxwell's equations are solved in discrete spacetime. Two advantages of the open-source approach to RF design are zero-cost and fine control over simulation objects. Maxwell's equations are scale-invariant, so FDTD codes designed for  $\mu\text{m}$ -wavelengths can be re-purposed for RF designs. One such package is the MIT Electromagnetic Equation Propagation (MEEP) package [15].

A recent review [7] covered open-source software facilitates RF antenna design. In this work, the radiation patterns of one-dimensional phased array designs are simulated with the MEEP package. Common MEEP applications have  $\mu\text{m}$ -scale wavelengths, but scale-invariance allows the user to treat designs as cm-scale RF elements. Two classes of phased array element are considered: Yagi-Uda and horn antennas. The former is applied to single-frequency designs, while the latter is applied to broadband design. The phase-steering properties and radiation patterns of all designs are shown to match theoretical predictions. The appropriate array theory is shown in Section 2. Section 3 contains comparisons between theory and simulation. In Section 4, the effect of a varying index of refraction is introduced.

## 2. Phased Array Antenna Theory

The structure of a one-dimensional phased array is shown in Figure 1. Two constants that determine the beam angle  $\Delta\phi$  of the array are the spacing  $d_y$  and the phase shift per antenna  $\Delta\Phi$ . Letting the subscript  $i$  label each of the  $N$  elements, the one-dimensional spacing in Figure 1 is  $d_y \hat{j} = \vec{r}_{i+1} - \vec{r}_i$ . The phase shift per antenna is  $\Delta\Phi = \Phi_{i+1} - \Phi_i$ . The relationship between  $d_y$ ,  $\Delta\Phi$ , and  $\Delta\phi$  is quoted in Section 2.1. The radiation pattern for a given  $\Delta\phi$  is quoted in Section 2.2. For all coordinate systems, the azimuthal angle in the xy-plane is  $\phi$ , and the polar angle from the z-axis is  $\theta$ .

### 2.1 Phase Steering and Beam Angle

According to [10], the beam angle  $\Delta\phi$  of the array given  $\Delta\Phi$  and  $d_y$  is

$$\Delta\Phi \approx 2\pi(d_y/\lambda)\Delta\phi \quad (1)$$

Equation 1 relates  $\Delta\phi$ , the beam angle, and  $\Delta\Phi$ , the phase shift per element, via a linear relationship with slope  $\lambda/(2\pi d_y)$ .

### 2.2 Radiation Patterns and Beam Width

Let  $N$  be the number of radiating elements in the phased array. Further, let the beam angle be  $\Delta\phi = \phi - \phi_0$ , where  $\phi_0$  is some reference angle (usually in the direction orthogonal to the phased array). According to [10], the radiation pattern is

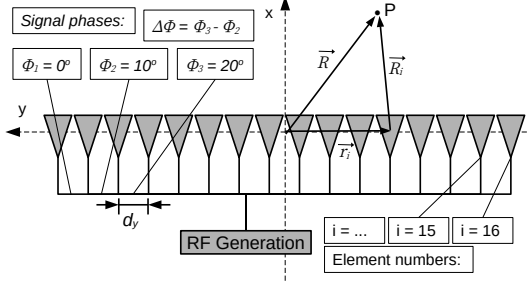


**Figure 1:** Definitions for the coordinate system, element label  $i$ , position vectors, and phase shift per antenna for a one-dimensional phased array of RF radiating elements. An example phase shift per antenna of  $\Delta\Phi = \Phi_2 - \Phi_1 = \Phi_3 - \Phi_2 = \Phi_{i+1} - \Phi_i = 10^\circ$  value is shown. Example position vectors for the 12th element are shown:  $\vec{R} = \vec{r}_{12} + \vec{R}_{12}$ .

$$P(\phi) = \left( \frac{\sin(\pi N(d_y/\lambda)(\sin(\phi) - \sin(\phi_0)))}{N \sin(\pi(d_y/\lambda)(\sin(\phi) - \sin(\phi_0)))} \right)^2 \quad (2)$$

The radiation pattern in Equation 2 is shown to match precisely the main beam of FDTD calculations via MEEP for one-dimensional arrays in Section 3. All one-dimensional array radiation patterns correspond to the E-plane (the xy-plane). The MEEP python routine `get_farfield` is evaluated at a radius  $r \gg L$ , the length of the array, to obtain the far-fields  $\vec{E}$  and  $\vec{H}$ . Notice that not all open-source FDTD codes offer near-field to far-field projection [7].

### 3. Results: Phase Steering, Beam Angle, Beamwidth, and Radiation Pattern

The two element designs are depicted in Figure 2. The Yagi-Uda antennas have 6 elements with the same radius, oriented in the xy-plane: one reflector, one radiator, three directors and a connecting boom. The horn antennas have three structures: the box containing the linearly polarized radiator, the radiator, and the curves of the horn. An exponential function describes the curves. All antenna elements have metallic conductivity, and the edge of space consists of a perfectly matched layer (PML) to cancel reflections.

#### 3.1 Phase Steering, Beam Angle, and Beamwidth

Phase steering, beam angle, and beamwidth results are shown in Figure 3. The y-axes of Figure 3 (top left) and (top right) are the beam angles of the Yagi-Uda arrays, divided by the beam widths. The x-axes are the phase shifts per element. The top left and top right plots correspond to  $N = 8$  and  $N = 16$ , respectively. For the  $N = 16$  horn case (bottom left and right), the value of  $d_y/\lambda = f d_y/c$  varies because the elements can radiate from  $\approx 0.3 - 5.0$  GHz. The black solid lines in the top left and top right graphs of Figure 3 are linear fits to the Yagi-Uda data. The gray lines represent the function  $f(x) = bx$ , with  $b = \lambda/(2\pi d_y)$ . The slopes match, with 1% errors arising from pattern distortion for large  $\Delta\phi$ . At large  $\Delta\Phi$ , side lobes can merge with the main beam to shift the location of the main beam by  $O(1)$  degree.

For the broadband horn case in the bottom left of Figure 3, data from three frequencies are shown: 0.3, 1.5, and 3.0 GHz. The intercepts are all zero and the slopes scale correctly. The fit

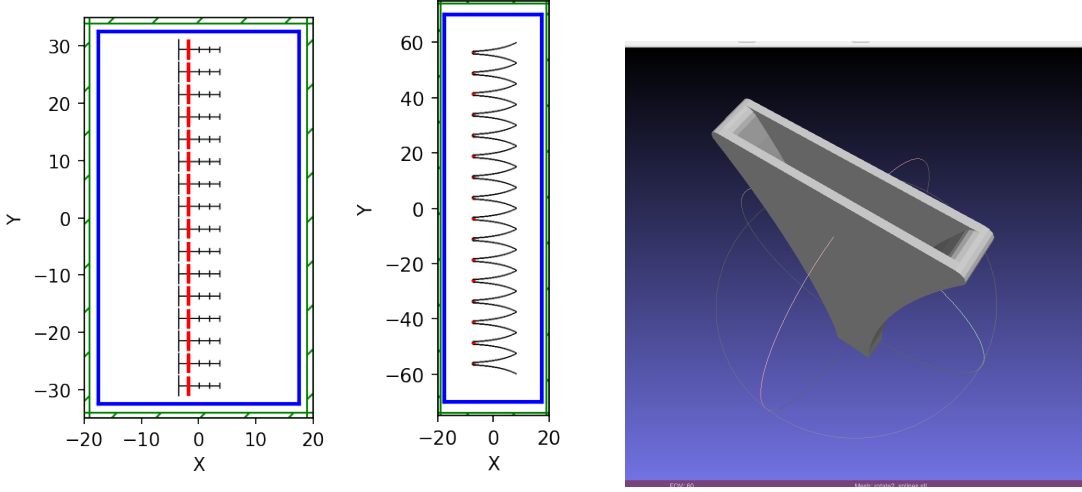


**Figure 2:** The 2D antenna designs used in the 1D phased array simulations. (Left) The  $N = 16$  Yagi-Uda array. (Middle) The  $N = 16$  horn array. The blue surfaces are MEEP *Near2FarRegion* objects for near-to-far projection. All dimensions are in centimeters. (Right) Example STL file for 3D version of horn.

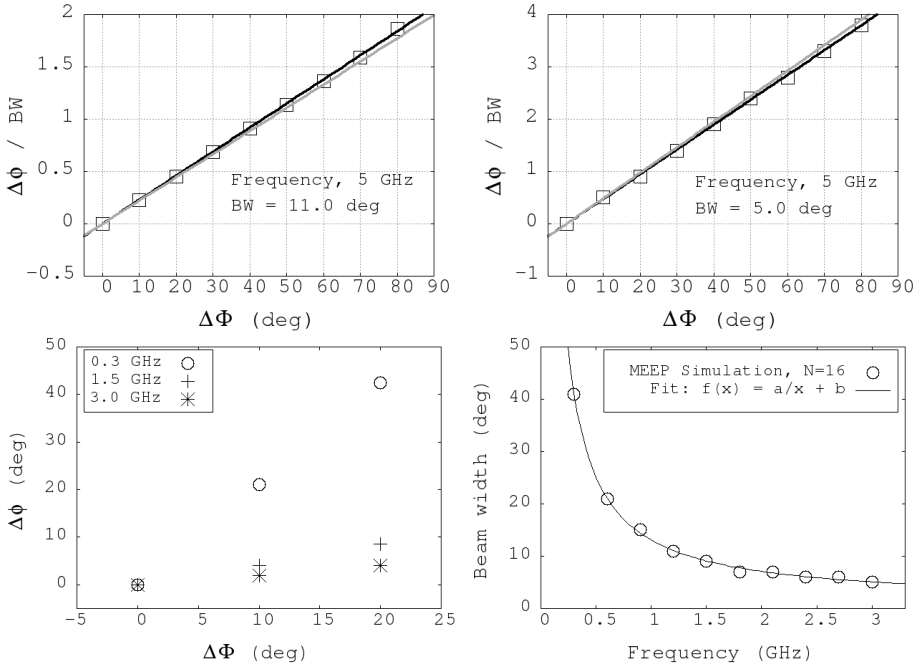


**Figure 3:** (Top left) The beam angle  $\Delta\phi$  divided by the beam width  $BW$  for the  $N = 8$  one-dimensional Yagi array versus  $\Delta\Phi$ , the phase shift per element. (Top right) The same results for the  $N = 16$  array. (Bottom left)  $\Delta\phi$  versus  $\Delta\Phi$  for the  $N = 16$  version of the one-dimensional horn array, for several frequencies. (Bottom right) The dependence of the beam width on frequency for the one-dimensional  $N = 16$  horn array.

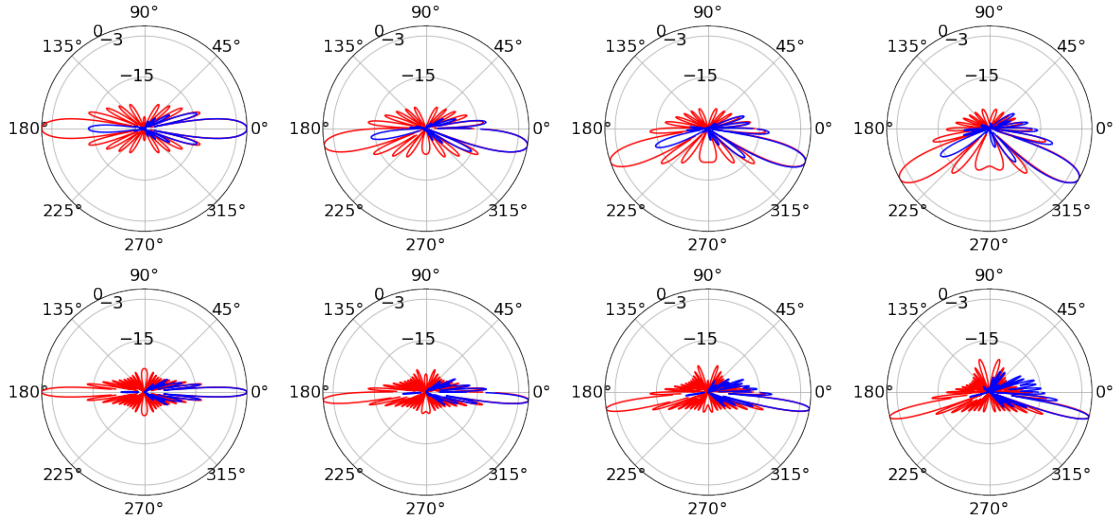


**Figure 4: Yagi-Uda results.** (Top row)  $f = 2.5$  GHz, and  $\Delta\Phi = 0, 20, 40, 60$  degrees from left to right. (Second row)  $f = 5.0$  GHz, and  $\Delta\Phi = 0, 20, 40, 60$  degrees from left to right. The radial units are dB, and the angular units are degrees.

parameters for beam width  $f(x) = a/x + b$  were  $a = 12.0 \pm 0.1$  degree GHz, and  $b = 1.1 \pm 0.2$  degrees. The  $1/f$ -dependence is a good description of the beamwidth across the [0.3 - 5 GHz] bandwidth. The constant term  $b$  is only necessary since the array has finite length  $L$ .

### 3.2 Radiation Patterns

Radiation patterns for  $N = 16$  one-dimensional arrays are shown in Figures 4 and 5, respectively. As described above, the x-direction ( $\Delta\phi = 0$ ) corresponds to no phase shift per element ( $\Delta\Phi = 0$ ). The radiation patterns are shown in blue, and the red curves represent Equation 2. Equation 2 is symmetric, with identical forward and backward lobes.

The Yagi-Uda results are shown for 2.5 and 5.0 GHz frequencies in Figure 4, with  $\Delta\Phi = 0, 20, 40$ , and 60 degrees. The amplitudes of all side-lobes are limited to  $\approx -15$  dB, except at the highest beam angles where scan losses are experienced. The effect of frequency on beam steering is evident. The same  $\Delta\Phi$  does not generate as large a  $\Delta\phi$  at higher frequencies because the slope implied by Equation 1 is proportional to  $\lambda$ .

The horn results are shown in Figure 5 for 0.5 GHz and 5.0 GHz frequencies. The phase shifts per element are  $\Delta\Phi = 0, 10, 20$ , and 30 degrees. Wideband systems experience a natural trade-off in angular range versus bandwidth. A  $d_y/\lambda$  value that is acceptably smaller than one at low frequencies can grow larger with increasing frequency, leading to interference patterns. At 5.0 GHz, the horns radiate at  $\pm 45$  degrees from  $\Delta\phi = 0$ . The prediction from Equation 2 is that these *grating lobes* are equal in relative power to the main beam. The horns limit them to -15 dB if  $|\Delta\Phi| < 35$  degrees.

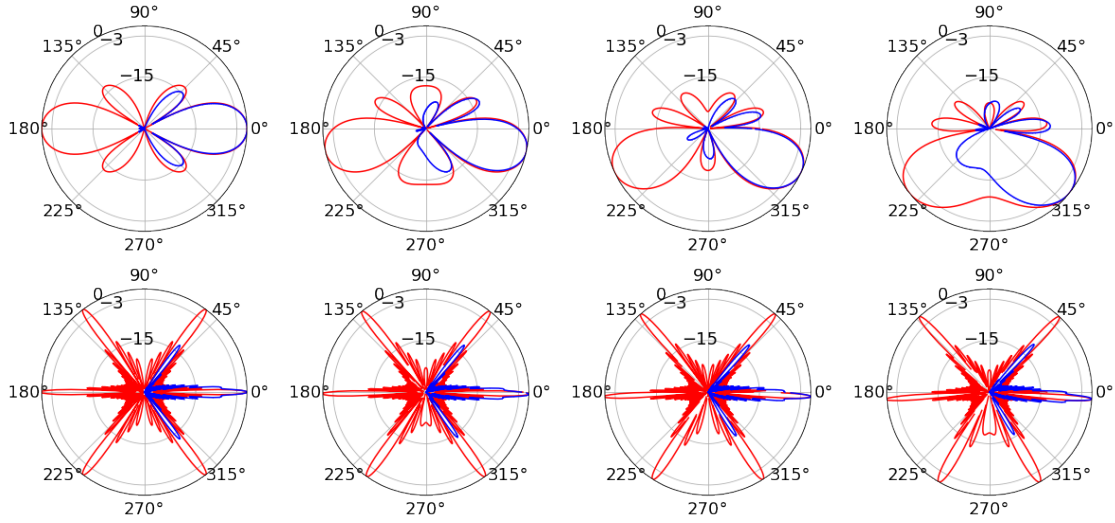


**Figure 5: Horn results.** (Top row)  $f = 0.5$  GHz, and  $\Delta\Phi = 0, 10, 20, 30$  degrees from left to right. (Second row)  $f = 5.0$  GHz, and  $\Delta\Phi = 0, 10, 20, 30$  degrees from left to right. The radial units are dB, and the angular units are degrees.

#### 4. Variation of the Index of Refraction

The behavior of a phased array embedded within a spatially-dependent index of refraction  $n(z)$  is interesting to the UHE- $\nu$  community [2, 16]. Phased arrays represent an opportunity to lower the RF detection threshold for RF pulses generated by UHE- $\nu$  via the Askaryan effect. Ice is the most convenient medium for Askaryan pulse detection due to the RF transparency and large pristine volumes located in Antarctic and Greenlandic ice sheets and shelves [3, 9, 11]. The index of refraction varies within the ice because of the transition between surface snow ( $\rho \approx 0.4$  g/cm $^3$ ) and the solid ice below ( $\rho = 0.917$  g/cm $^3$ ). Embedded phased arrays with varying  $n(z)$  emit signals that curve in the direction of increasing  $n(z)$ .

The *shadow zone* is the volume of ice from which RF signals do not reach a receiver due to the excess curvature of the ray trace [6]. While there is evidence that RF signals can propagate horizontally through Antarctic ice [4], data from Greenland suggests the relative strength of the effect is small compared to the curved radiation [5]. It is possible to map out the shadow zone for an embedded phased array radiating at fixed frequency. Grating lobe power reflects downward from the snow-air interface, and radiates into the shadow zone. Grating lobe power also refracts into the air above the interface.

A two-parameter fit to the  $n(z)$  data versus depth  $z$  below the surface is given by [4]

$$n(z) = \begin{cases} 1 & z > 0 \\ n_{\text{ice}} - \Delta n \exp(z/z_0) & z \leq 0 \end{cases} \quad (3)$$

The fit parameters in Equation 3 come from Reference [4]:  $\Delta n = 0.423 \pm 0.004$  and  $z_0 = 77 \pm 2$  meters, with  $n_{\text{ice}} = 1.78$ . These values are derived from the SPICE core near the South Pole. Equation 3 was implemented in a volume surrounding a horn array with all but the radiators removed. Further, the length scale was reinterpreted to be meters rather than centimeters. The  $\lambda/4$

dipoles were spaced by  $\lambda/2$  according to their free space  $\lambda$  value. At 200 MHz, the dipole length is 0.375 meters, and the spacing is 0.75 meters.

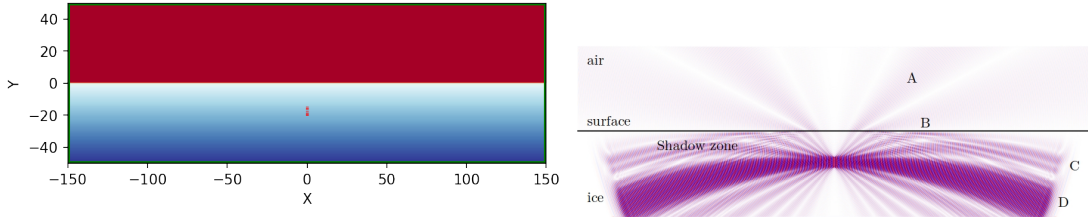


**Figure 6:** (Left) The simplified  $N = 8$  phased array with dimensions in meters. The colorscale represents  $n(z)$  in Equation 3. (Right) The magnitude of the z-component of the E-field from the vertical dipoles. The air, surface, and ice regions are the same as (left). The array depth is -15 meters. (A) Radiation refracting through the surface into the air. (B) Grating lobes reflect from the surface into the shadow zone. (C) Grating lobes propagating through the shadow zone. (D) The main beam bent downward due to the gradient in  $n(z)$ .

Figure 6 contains the results of a  $N = 8$  dipole array embedded in a medium with the index profile in Equation 3. Figure 6 (left) shows the schematic of the calculation, and Figure 6 (right) shows the magnitude of the z-component of the radiated E-field. The units in Figure 6 are meters, and the radiation frequency is 200 MHz. The distance between the air-snow interface and the first phased array element is 15 meters. The color scale in Figure 6 (right) is  $\pm 0.05$  with the signal amplitude of the elements  $\pm 1.0$  at 200 MHz. The amplitude scale is less important than observing *where* the radiation has penetrated the ice after 200 radiation periods. In Figure 6 (right), the main beam has curved downwards in the direction of increasing  $n(z)$ , while grating lobes have both diffracted to the air and reflected into the shadow zone. The rate of curvature of the main beam is controlled by the fit parameter  $z_0$  in Equation 3.

## References

- [1] Ansys, Inc., Canonsburg, Pennsylvania. *3D Electromagnetic Field Simulator for RF and Wireless Design*, 2020.
- [2] J. Avva, K. Bechtol, T. Chesebro, L. Cremonesi, C. Deaconu, A. Gupta, A. Ludwig, W. Messino, C. Miki, R. Nichol, E. Oberla, M. Ransom, A. Romero-Wolf, D. Saltzberg, C. Schlupf, N. Shipp, G. Varner, A. Vieregg, and S. Wissel. Development toward a ground-based interferometric phased array for radio detection of high energy neutrinos. *Nuclear Instruments and Methods in Physics Research Section A: Accelerators, Spectrometers, Detectors and Associated Equipment*, 869:46 – 55, 2017.
- [3] J. Avva, J. Kovac, C. Miki, D. Saltzberg, and A. Vieregg. An in situ measurement of the radio-frequency attenuation in ice at Summit Station, Greenland. *Journal of Glaciology*, 2014.
- [4] S. W. Barwick, E. C. Berg, D. Z. Besson, G. Gaswint, C. Glaser, A. Hallgren, J. C. Hanson, S. R. Klein, S. Kleinfelder, L. Köpke, I. Kravchenko, R. Lahmann, U. Latif, J. Nam, A. Nelles, C. Persichilli, P. Sandstrom, J. Tatar, and E. Unger. Observation of classically ‘forbidden’ electromagnetic wave propagation and implications for neutrino detection. *Journal of Cosmology and Astroparticle Physics*, 2018(07):055–055, 2018.

- [5] C. Deaconu, A. G. Vieregg, S. A. Wissel, J. Bowen, S. Chipman, A. Gupta, C. Miki, R. J. Nichol, and D. Saltzberg. Measurements and modeling of near-surface radio propagation in glacial ice and implications for neutrino experiments. *Phys. Rev. D*, 98:043010, Aug 2018.
- [6] K. Dookayka. *Characterizing the Search for Ultra-High Energy Neutrinos with the ARIANNA Detector*. PhD thesis, Univeristy of California at Irvine, 2011.
- [7] A. Fedeli, C. Montecucco, and G. L. Gragnani. Open-Source Software for Electromagnetic Scattering Simulation: The Case of Antenna Design. *Electronics*, 8(12):1506, 2019.
- [8] N. Feng, Y. Zhang, X. Tian, J. Zhu, W. T. Joines, and G. P. Wang. System-Combined ADI-FDTD Method and Its Electromagnetic Applications in Microwave Circuits and Antennas. *IEEE Transactions on Microwave Theory and Techniques*, 67(8):3260–3270, 2019.
- [9] J. C. Hanson. Ross Ice Shelf Thickness, Radio-frequency Attenuation and Reflectivity: Implications for the ARIANNA UHE Neutrino Detector. In *Proceedings of the 32nd International Cosmic Ray Conference, Beijing, China, August 2011*, 2011.
- [10] J. C. Hanson. Broadband rf phased array design with meep: Comparisons to array theory in two and three dimensions. *Electronics*, 10(4), 2021.
- [11] J. C. Hanson, S. W. Barwick, E. C. Berg, D. Z. Besson, T. J. Duffin, S. R. Klein, S. A. Kleinfelder, C. Reed, M. Roumi, T. Stezelberger, J. Tatar, J. A. Walker, and L. Zou. Radar absorption, basal reflection, thickness and polarization measurements from the Ross Ice Shelf, Antarctica. *Journal of Glaciology*, 61(227):438–446, 2015.
- [12] T. Q. Ho, L. N. Hunt, C. A. Hewett, T. G. Ready, R. Mittra, W. Yu, D. A. Zolnick, and M. Kragalott. Analysis of Electrically Large Patch Phased Arrays via CFDTD. *2006 IEEE Antennas and Propagation Society International Symposium, Albuquerque, New Mexico, July 2006*.
- [13] K. Kikuchi, H. Mikada, and J. Takekawa. Improved Imaging Capability of Phased Array Antenna in Ground Penetrating Radar Survey. *Conference Proceedings, 79th EAGE Conference and Exhibition 2017, Paris, France, June 2017*, 2017.
- [14] T. Munekata, M. Yamamoto, and T. Nojima. A Wideband 16-Element Antenna Array Using Leaf-Shaped Bowtie Antenna and Series-Parallel Feed Networks. *2014 IEEE International Workshop on Electromagnetics (iWEM), Sapporo Hokkaido, Japan, August 2014*, pages 80–81, 2014.
- [15] A. F. Oskooi, D. Roundy, M. Ibanescu, P. Bermel, J. Joannopoulos, and S. G. Johnson. Meep: A flexible free-software package for electromagnetic simulations by the FDTD method. *Computer Physics Communications*, 181(3):687–702, 2010.
- [16] A. Vieregg, K. Bechtol, and A. Romero-Wolf. A technique for detection of PeV neutrinos using a phased radio array. *Journal of Cosmology and Astroparticle Physics*, 2016(02):005, feb 2016.

# Design and Sensitivity of the Radio Neutrino Observatory in Greenland (RNO-G)

---

J. A. Aguilar<sup>1</sup> P. Allison<sup>2</sup> J. J. Beatty<sup>2</sup> H. Bernhoff<sup>3</sup> D. Besson<sup>4,5</sup> N. Bingefors<sup>6</sup> O. Botner<sup>6</sup>  
 S. Buitink<sup>7</sup> K. Carter<sup>8</sup> B. A. Clark<sup>9</sup> A. Connolly<sup>2</sup> P. Dasgupta<sup>1</sup> S. de Kockere<sup>10</sup> K. D. de  
 Vries<sup>10</sup> C. Deaconu<sup>11</sup> M. A. DuVernois<sup>12</sup> N. Feigl<sup>13</sup> D. García-Fernández<sup>13,14</sup> C. Glaser<sup>6</sup>  
 A. Hallgren<sup>6</sup> S. Hallmann<sup>14</sup> J. C. Hanson<sup>15</sup> B. Hendricks<sup>17</sup> B. Hokanson-Fasig<sup>12</sup>  
 C. Hornhuber<sup>4</sup> K. Hughes<sup>11</sup> A. Karle<sup>12</sup> J. L. Kelley<sup>12</sup> S. R. Klein<sup>16</sup> R. Krebs<sup>17</sup> R. Lahmann<sup>13</sup>  
 M. Magnuson<sup>4</sup> T. Meures<sup>12</sup> Z. S. Meyers<sup>13,14</sup> A. Nelles<sup>14,13</sup> A. Novikov<sup>4</sup> E. Oberla<sup>11</sup>  
 B. Oeyen<sup>18</sup> H. Pandya<sup>7</sup> I. Plaisier<sup>13,14</sup> L. Pyras<sup>19,14</sup> D. Ryckbosch<sup>18</sup> O. Scholten<sup>10</sup> D. Seckel<sup>20</sup>  
 D. Smith<sup>11</sup> D. Southall<sup>11</sup> J. Torres<sup>2</sup> S. Toscano<sup>1</sup> D. J. Van Den Broeck<sup>10,7</sup> N. van  
 Eijndhoven<sup>10</sup> A. G. Vieregg<sup>11</sup> C. Welling<sup>13,14</sup> S. Wissel<sup>17,8</sup> R. Young<sup>4</sup> A. Zink<sup>13</sup>

<sup>1</sup>Université Libre de Bruxelles, Science Faculty CP230, B-1050 Brussels, Belgium<sup>2</sup>Dept. of Physics, Center for Cosmology and AstroParticle Physics, Ohio State University, Columbus, OH 43210, USA<sup>3</sup>Uppsala University, Dept. of Engineering Sciences, Division of Electricity, Uppsala, SE-752 37, Sweden<sup>4</sup>University of Kansas, Dept. of Physics and Astronomy, Lawrence, KS 66045, USA<sup>5</sup>National Nuclear Research University MEPhI, Kashirskoe Shosse 31, 115409, Moscow, Russia<sup>6</sup>Uppsala University, Dept. of Physics and Astronomy, Uppsala, SE-752 37, Sweden<sup>7</sup>Vrije Universiteit Brussel, Astrophysical Institute, Pleinlaan 2, 1050 Brussels, Belgium<sup>8</sup>Physics Dept. California Polytechnic State University, San Luis Obispo CA 93407, USA<sup>9</sup>Dept. of Physics and Astronomy, Michigan State University, East Lansing MI 48824, USA<sup>10</sup>Vrije Universiteit Brussel, Dienst ELEM, B-1050 Brussels, Belgium<sup>11</sup>Dept. of Physics, Enrico Fermi Inst., Kavli Inst. for Cosmological Physics, University of Chicago, Chicago, IL 60637, USA<sup>12</sup>Wisconsin IceCube Particle Astrophysics Center (WIPAC) and Dept. of Physics, University of Wisconsin-Madison, Madison, WI 53703, USA<sup>13</sup>Erlangen Center for Astroparticle Physics (ECAP), Friedrich-Alexander-University Erlangen-Nuremberg, 91058 Erlangen, Germany<sup>14</sup>DESY, Platanenallee 6, 15738 Zeuthen, Germany<sup>15</sup>Whittier College, Whittier, CA 90602, USA<sup>16</sup>Lawrence Berkeley National Laboratory, Berkeley, CA 94720, USA<sup>17</sup>Dept. of Physics, Dept. of Astronomy & Astrophysics, Penn State University, University Park, PA 16801, USA<sup>18</sup>Ghent University, Dept. of Physics and Astronomy, B-9000 Gent, Belgium<sup>19</sup>Humboldt-Universität zu Berlin, Unter den Linden 6, 10117 Berlin, Germany<sup>20</sup>Dept. of Physics and Astronomy, University of Delaware, Newark, DE 19716, USA

*E-mail:* [anna.nelles@desy.de](mailto:anna.nelles@desy.de), [authors@rno-g.org](mailto:authors@rno-g.org)

**ABSTRACT:** This article presents the design of the Radio Neutrino Observatory Greenland (RNO-G) and discusses its scientific prospects. Using an array of radio sensors, RNO-G seeks to measure neutrinos above 10 PeV by exploiting the Askaryan effect in neutrino-induced cascades in ice. We discuss the experimental considerations that drive the design of RNO-G, present first measurements of the hardware that is to be deployed and discuss the projected sensitivity of the instrument. RNO-G will be the first production-scale radio detector for in-ice neutrino signals.

---

## Contents

<b>1</b>	<b>Introduction</b>	<b>2</b>
1.1	Scope of RNO-G	2
1.2	Relation to previous and current radio experiments	2
<b>2</b>	<b>Science case and design requirements</b>	<b>4</b>
2.1	Diffuse neutrino flux	5
2.2	Sky coverage	6
2.3	Transient sources	7
2.4	Fundamental physics	8
2.5	Radio emission from neutrino interactions in ice and consequences for site selection	9
2.6	Air showers as both a potential background and calibration signal	10
<b>3</b>	<b>Experimental design considerations</b>	<b>12</b>
3.1	Summit Station, Greenland	14
3.2	A low-power, low-threshold trigger and data acquisition system	15
3.3	Detector geometry: An integrated approach with deep and surface components	16
3.4	High analysis efficiency and low background to enhance discovery potential	17
<b>4</b>	<b>The RNO-G instrument design</b>	<b>20</b>
4.1	Antennas	21
4.2	Radio-Frequency front-end design	22
4.3	Triggering, digitization, and data acquisition	23
4.4	Autonomous power and wireless communications	26
<b>5</b>	<b>Installation, calibration, and operations</b>	<b>28</b>
5.1	Drilling and installation plan	29
5.2	Calibration requirements and strategies	29
5.3	Operations and data systems	30
<b>6</b>	<b>Projected sensitivity of RNO-G</b>	<b>31</b>
6.1	Sensitivity to diffuse flux	32
6.2	Energy measurement	33
6.3	Angular sensitivity	35
6.4	Sensitivity to transient events	37
6.5	Sensitivity to air shower signals	38
<b>7</b>	<b>Conclusions</b>	<b>39</b>
<b>8</b>	<b>Acknowledgements</b>	<b>39</b>

---

## 1 Introduction

This paper describes the Radio Neutrino Observatory Greenland (RNO-G) as it will be constructed at Summit Station in Greenland starting in 2021. RNO-G science targets astrophysical neutrinos of several PeV in energy up to the EeV range.

In this paper, we first motivate the science case for RNO-G, elaborate on experimental design considerations and then outline the instrument design. Awaiting in-field performance data, this article does not serve as a technical document, but describes the concept, the current hardware developments and boundary conditions behind the RNO-G approach. We conclude with a description of initial estimates of the design sensitivity of the instrument, as well as the expected resolution for such quantities as neutrino arrival direction and energy.

### 1.1 Scope of RNO-G

RNO-G will be constructed over three installation seasons. RNO-G will reach unprecedented yearly sensitivity to neutrino signals above 10 PeV, and will demonstrate a large-scale implementation (35 stations) of the in-ice radio neutrino detection technique. Even further scaling up of the in-ice radio technique, beyond the scale of RNO-G, is being developed as part of IceCube-Gen2 [1].

Considering both logistical constraints and also science opportunities (detailed below), RNO-G will be constructed at Summit Station in Greenland. The RNO-G collaboration consists of members of all previous radio in-ice neutrino experiments from both Europe and the United States.

### 1.2 Relation to previous and current radio experiments

Due to the extremely low neutrino flux at energies above 10 PeV, no neutrino has yet been detected using the radio technique. However, several experiments have shown the feasibility of this detection method and its potential. RNO-G builds heavily on the experience of previous radio neutrinos detectors, like the pioneering RICE [2, 3], the ARA [4–6] and ARIANNA [7, 8] experiments, as well as the balloon-borne ANITA [9, 10] experiment. These efforts tested different aspects of the radio technique and helped illuminate technologically important aspects of operating in remote locations in harsh polar conditions.

The first experience with in-ice radio detectors was gained with the Radio Ice Cherenkov Experiment (RICE) [2] at the South Pole. After a number of prototypes and initial measurements of the ice characteristics, the main experiment operated from 1999 until 2010. RICE provided the first neutrino limits [3] from radio detectors and valuable experience in operating radio detectors at depths of down to 200 m.

The Askaryan Radio Array (ARA) [5] has operated at South Pole since 2010 [11] and is a direct successor to RICE. While the RICE antennas were co-located with the AMANDA and IceCube experiments at South Pole, all five ARA stations operate in dedicated dry holes of depths 50 m–200 m. While different hardware has been deployed in different ARA stations, the station layout is mostly uniform. Every station consists of four receiver strings down to 200 m. Each string is equipped with two vertically-polarized birdcage dipole antennas (VPol) and two ferrite-loaded slot antennas (Hpol) to reconstruct the radio signals. In addition, one or two calibration strings as well as surface antennas (on the earlier stations) are deployed. As the narrow cylindrical borehole

geometry limits the intrinsic antenna gain, ARA pioneered the phased-array technique for radio detection of neutrinos at the most recently completed station [12].

To date, the ARA collaboration has published constraints on the diffuse ultra-high energy (UHE) neutrino flux [6], neutrinos from gamma-ray bursts (GRBs) [13], and radio emission from solar flares [14]. The performance of the instrument has been verified using transmitters lowered into the SPICE borehole [15], which also allowed for the measurement of glaciological properties of the ice – some of which can be used for improved neutrino event reconstruction [16, 17].

The Antarctic Ross Ice-Shelf ANtenna Neutrino Array (ARIANNA) began construction at the Ross Ice-Shelf in 2010, with a first hexagonal radio array being completed in 2015 [7, 8]. The ARIANNA concept is based around surface stations, i.e. the antennas are deployed just underneath the snow-surface. High-gain log-periodic dipole antennas (LPDAs) are deployed in shallow slots in the snow, where they are not restricted by the borehole geometry and exhibit broadband characteristics and dedicated polarization sensitivity, particularly to horizontally polarized signals. By placing the antennas at Moore’s Bay on the Ross Ice-Shelf, the neutrino-detection strategy utilizes the reflective surface at the bottom of the ice at the water interface, which reflects downward going neutrino signals back to the stations. Without external infrastructure, ARIANNA pioneered autonomous low-power stations, based on renewable energy sources, operated via wireless communications. Most recently wind turbines were added to the solar power-provision system [18].

ARIANNA has successfully detected the radio signal of air showers as calibration and verification signals [19] and published limits on the UHE neutrino flux [20]. The collaboration also published the effectiveness of recording signals reflected from the surface by monitoring snow accumulation [21]. Two ARIANNA stations have also been deployed at South Pole to test the robustness of the hardware under environmental circumstances differing from the Ross Ice Shelf. The same calibration source as used for ARA from the SPICE borehole was then also used to verify the reconstruction capabilities of the ARIANNA experiment with respect to arrival direction and polarization [22].

The Antarctic Impulsive Transient Antenna (ANITA) experiment has flown four separate missions over Antarctica. ANITA is a balloon-borne radio receiver array that scans the surface from afar for upcoming neutrino signals generated below the ice surface. Several components of the ANITA hardware have been incorporated into the ARA and ARIANNA designs [9, 10, 23]. While equipped with much different power and lifetime requirements, the technological challenges remain similar. A data acquisition system with high timing accuracy and thorough calibration is needed to reliably reconstruct neutrino or cosmic-ray signals. ANITA was the first radio-neutrino experiment to report the detection of air shower signals [24], which helped to verify the simulation chain and the understanding of the energy calibration [25]. The ANITA collaboration observed several events which, if neutrinos, would seem to be in tension with Standard-Model cross-sections [26–28]. Those events may also stem from unexplained systematics or ice effects [29, 30].

Operation of existing ARA stations continue in close cooperation with IceCube. In addition, proposals for an ANITA-successor ballooning effort are being discussed, as well as an extension of the ARIANNA array at Moore’s Bay.

In addition to building on experiences with dedicated radio neutrino experiments, RNO-G also profits from knowledge gained at accelerator experiments about the nature of the in-medium emission from particle showers [31–34], as well as those from mid-scale air shower arrays measuring the

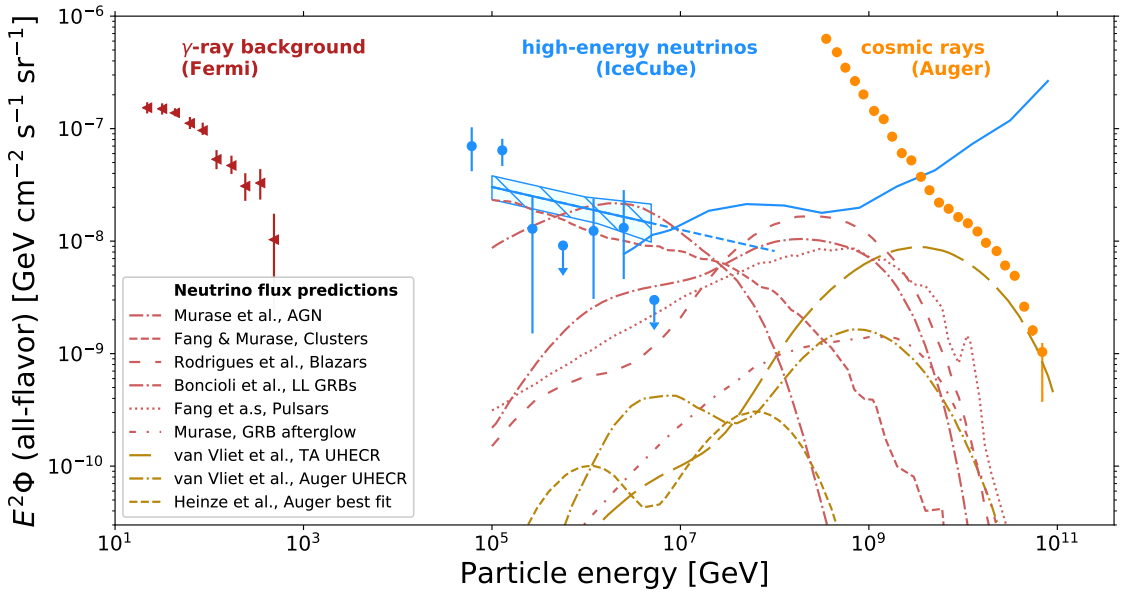


**Figure 1.** A multi-messenger view of the high-energy universe, inspired by [43], showing the science reach for radio detection of neutrinos. Shown are models predicting neutrinos from sources (in red lines) [44–49] and those from the interaction of the ultra-high energy cosmic rays with various photon backgrounds (in dark yellow lines). Overlaid are [50, 51] the  $\gamma$ -ray measurements from Fermi [52], the IceCube neutrino measurements and the fit to the muon neutrino spectrum [53–55], as well as the spectrum of ultra-high energy cosmic rays as reported by the Pierre Auger Observatory [56].

radio emission of cosmic ray induced showers e.g. [35–39]. First efforts at exploring the feasibility of a detector in Greenland have been conducted previously by members of the collaboration [40–42] and have encouraged the development of RNO-G.

## 2 Science case and design requirements

Neutrinos are ideal messengers to identify the UHE sources in the universe. Unlike cosmic rays, which are deflected by magnetic fields and interact with intervening matter and radiation, neutrinos point back to their sources and can reach Earth from the most distant corners of the universe. Furthermore, due to their low interaction cross section, neutrinos are unique messengers to convey information about the inner engine of cosmic accelerator sites. Unlike  $\gamma$ -rays, which can also be created by inverse Compton scattering, the observation of high-energy neutrinos from astronomical objects provides incontrovertible evidence for hadronic cosmic-ray acceleration. Identifying the sources of cosmic rays and the acceleration mechanisms requires a comprehensive multi-messenger observation program comprising cosmic rays,  $\gamma$ -rays, and neutrinos across many decades of energy.

In the last years, neutrinos have delivered on their promise to provide a key piece of this astronomical puzzle with the discovery of a diffuse flux of astrophysical neutrinos [57–60]. IceCube has measured the neutrino energy spectrum to above 1 PeV – the highest-energy neutrinos ever observed. Beyond the PeV scale, the limited size of IceCube prohibits observation of the steeply falling neutrino flux. Fig. 1 compares the neutrino flux measured by IceCube with the diffuse flux

of  $\gamma$ -rays measured by Fermi [52] and the cosmic-ray spectrum measured by Auger [56]. The three spectra display tantalizingly similar energy densities, suggesting a common origin. In such a scenario, cosmic-ray collisions produce pions, where gamma-rays then stem from decays of neutral pions and neutrinos from those of charged pions. The figure also shows the gap in observations of UHE neutrinos beyond the energies reachable by IceCube.

Multi-messenger observations are even more intriguing in light of the announcement in July 2018 of the first coincident observation of a neutrino from the direction of a source (the blazar TXS 0506+056) that was flaring simultaneously in  $\gamma$ -rays [61, 62]. This was also the first multi-messenger observation triggered by a high-energy neutrino, demonstrating the capability to send real time alerts and establishing the field as a vital pillar of multi-messenger astronomy. To fully understand the neutrino sky, however, a larger detector must be built and observations extended to the PeV–EeV energy range.

The radio detection technique naturally targets neutrino energies beyond the reach of IceCube. Due to the kilometer scale attenuation length of radio waves in ice, very sparse radio detectors cover large volumes of material, providing huge effective volumes at 10 PeV to 100 EeV. In this energy range, several transient and diffuse sources of neutrinos are expected and an experimental measurement would strongly impact identification of the sources of ultra-high energy cosmic rays.

The general science case of neutrino astronomy has been reviewed in the context of the 2020 US decadal survey [63, 64]. This section will thus focus specifically on the science program that can be conducted by radio detectors for high-energy neutrinos.

## 2.1 Diffuse neutrino flux

The radio detection of neutrinos targets the energy range from 10 PeV to beyond 100 EeV. In this range, diffuse neutrino fluxes both directly from sources (*astrophysical neutrinos*), as well as from the interaction of ultra-high energy cosmic rays (UHECRs) with photon backgrounds (*cosmogenic neutrinos*) are predicted. Detecting either will enable studies of high-energy neutrino production mechanisms locally, at the still unknown sources.

Fig. 1 shows different models for astrophysical (red) and cosmogenic (yellow) neutrinos that fall in the energy range of radio detectors. Cosmogenic neutrinos result from interactions of UHECRs with photon fields like the extra-galactic background light, the infra-red background, or the cosmic microwave background [65]. The flux and spectrum of these neutrinos are grounded in the UHECR mass composition, but are subject to model assumptions about the cosmological luminosity and chemical evolution of the sources, which can differ outside of the local universe probed by UHECRs [66]. For the cosmogenic neutrino predictions shown in Fig. 1, we compare predictions based on compositions measured by the Telescope Array (TA) [67, 68] and the Pierre Auger Observatory (Auger) [50, 69]. These are in fact only examples of the full range of possible models admitted by current constraints [51].

While the cosmogenic fluxes predicted assuming the Auger and TA compositions vary significantly, composition measurements from the two experiments are compatible within systematic uncertainties [70]. With a measurement of UHE neutrinos, radio detectors can resolve the question of a pure-proton composition, which is disfavored by Auger, but still allowed by TA data. More generally, measuring UHE neutrinos will constrain a combination of proton fraction, source evolution and highest-energy cutoffs of UHECRs well beyond local sources.

We consider ‘astrophysical’ neutrinos as those created directly in (or very close to) the sources of UHECRs. These neutrinos tend to have lower energies than cosmogenic neutrinos, but also reach the energy range of radio detectors. They will definitely trace their sources, allowing for stacking analyses to reveal them. These neutrinos are not necessarily time-coincident with explosive events (see Sect. 2.3), but contribute to a constant diffuse flux. Potential candidates range from Active Galactic Nuclei (AGN) [47] to various types of gamma-ray bursts (GRBs) [46, 49], pulsars [45], galaxy clusters [44], Flat Spectrum Radio Quasars (FSRQs) [71], and blazars [48].

The diversity of models of astrophysical neutrinos is already large and promising, but we expect more models to become available as detectors with the necessary sensitivities are commissioned.

It remains to be explored whether astrophysical neutrinos are the source of the diffuse flux as measured by IceCube or whether the observed flux is the low energy tail of the cosmogenic neutrinos. So far, despite the multi-messenger successes, studies demonstrate that neutrinos from blazars cannot comprise the bulk of the diffuse neutrino spectrum at energies accessible by IceCube [72–77]. A radio detector will be able to measure the continuation of the IceCube flux to higher energies and thereby provide additional information on the spectral shape of the flux, which may be useful to disentangle the source contributions.

A successful search for the diffuse neutrino flux at energies beyond 10 PeV requires, above all, an adequate flux sensitivity to ensure a first observation. To subsequently discriminate putative production mechanisms, a detector must provide an adequate energy estimate for every neutrino and an angular reconstruction that allows for the correlation of arrival directions with known sources.

## 2.2 Sky coverage

Fig. 2 demonstrates the field of view of a radio neutrino telescope sited in Greenland. When targeting point-like sources, either steady or transient (see Sec. 2.3), the field of view of the detector becomes relevant. The Earth is opaque to neutrinos at PeV to EeV energies, such that UHE neutrino observatories are most sensitive to down-going or Earth-skimming neutrinos. As will be discussed in more detail Sec. 2.5, a radio neutrino detector in glacial ice on bedrock will be most sensitive to an annulus above the horizon.

Combining the opacity of the Earth to neutrinos above PeV energies with the inherent radio detector sensitivity means that, for example, a follow-up of TeV-scale IceCube events at higher energies requires a Northern detector such as RNO-G. A *single event* observed by a radio detector in the Northern hemisphere will define the flux in a new energy regime, and even a non-detection will constrain the allowed flux through *multi-wavelength* neutrino observations.

The continuous sky coverage and large field-of-view will enable studies of point sources of high-energy neutrinos. The hotspot of UHECRs observed by TA [79] (red ellipse in Fig. 2) lies in the Northern Hemisphere. While the cosmogenic neutrino flux is expected to be diffuse, studies attributing the TA hotspot to a single source of cosmic rays like M82 predict point sources of EeV neutrinos [80]. There are additionally four intriguing point sources nearing the threshold for a high-confidence long-term detection in IceCube (shown as navy blue diamonds in Fig. 2), all of which lie in the Northern Hemisphere due to the sensitivity of IceCube. These include not only TXS 0506+056, but also NGC 1068, an AGN which lies near the strongest hotspot in IceCube’s all-sky scan [78].

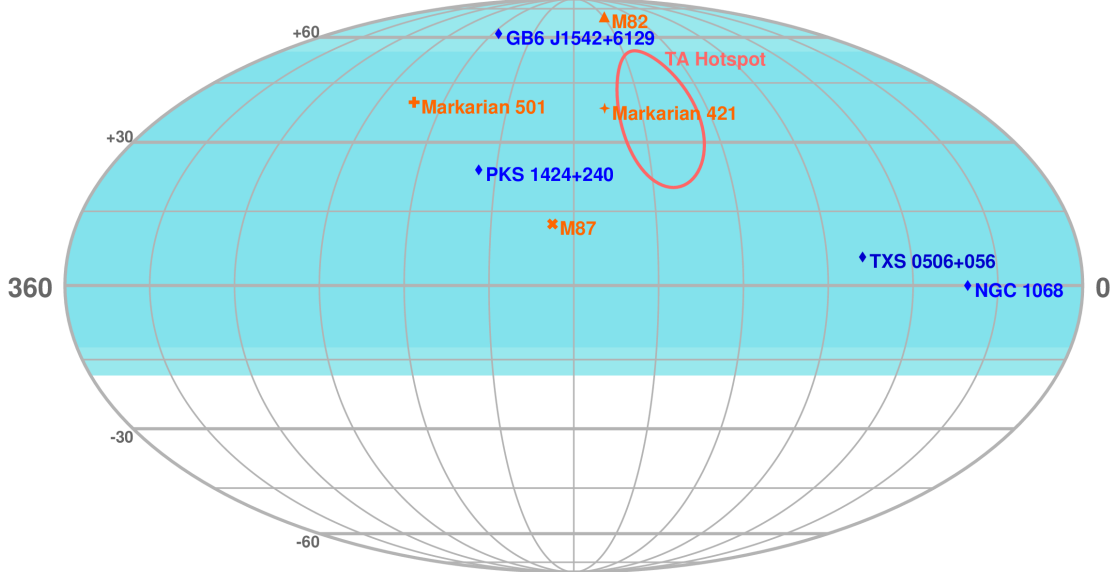


**Figure 2.** The field of view, in equatorial coordinates, of an in-ice radio detector for neutrinos in Greenland. The colored background represents the diurnally-averaged total field of view of the detector. Also shown are targets with interesting multi-messenger implications. The blue sources are those seen by IceCube as the most significant sources in a point-source search [78]. In orange, we show other interesting candidates, with strong  $\gamma$ -ray emission and/or radio emission. Furthermore, we indicate what is known as the *TA hotspot* as indicated by the anisotropy measurement in cosmic ray measured with the Telescope Array [79].

### 2.3 Transient sources

Detecting neutrino emission in temporal and spatial coincidence with an explosive event has shaped and will continue to shape multi-messenger astronomy [61, 62]. By uniquely identifying sources, neutrinos will help to characterize and discover the most energetic non-thermal sources on the sky. Many models of astrophysical transient phenomena predict neutrinos in the detectable energy range of radio neutrino detectors.

The overlap in sky coverage with IceCube, where IceCube has its best efficiency for directional reconstruction of astrophysical neutrinos, will enable studies of several interesting flaring, transient sources over a broad energy band. Should the first tentative extra-galactic neutrino source, the blazar TXS 0506+056, flare [61, 62] again, observations made by IceCube and RNO-G may be able to define the neutrino spectrum. Similarly, the first blazars known to flare with TeV  $\gamma$ -rays emission, Markarian 501 [81] and Markarian 421 [82], also lie in the Northern sky. Models of transient bursts of neutrinos due to tidally disrupted stars [83–89] and binary neutron star mergers [90, 91] also predict neutrinos in the PeV to EeV energy scale. The latter are targets for multi-messenger observations of gravitational waves and neutrinos. Fig. 3 shows a fraction of the parameter space over which neutrinos are expected as transient phenomena from various source classes. In the figure, model-dependent fluence is compared to duration for varying neutrino energies around EeV. Furthermore, different populations of blazars, including low-luminosity BL Lacs, high-luminosity BL Lacs and FSRQs [48], the most powerful blazars in the  $\gamma$ -ray band [71], could provide intriguing candidates for multi-wavelength follow up. The energy threshold of RNO-G will allow sensitive

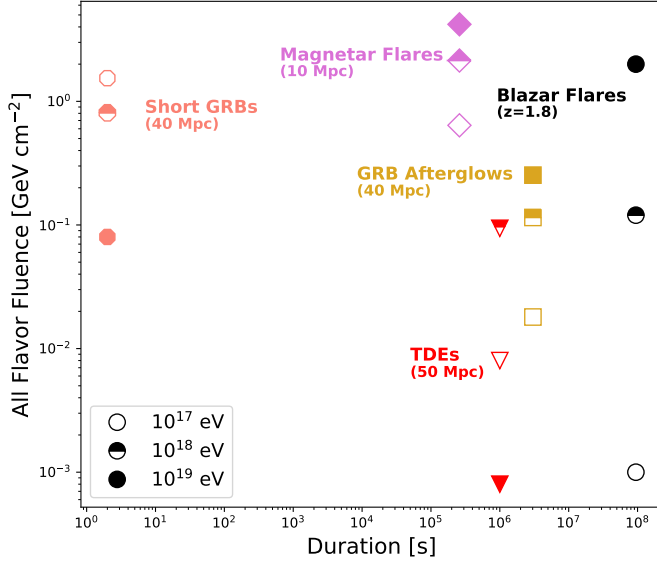


**Figure 3.** Expected neutrino flux at Earth integrated over transient duration from different classes of astrophysical objects placed at probable and previously studied distances. These include short GRBs (possibly associated with a Neutron Star-Neutron Star merger) [130] and GRB afterglows [49] at a distance of 40 Mpc, the high state SED of Tidal Disruption Events (TDEs) at 50 Mpc [89], and stable fast-spinning young magnetars [131] at 10 Mpc roughly 4 days post merger. Blazar flares [132] are shown based on a proton synchotron model applied to multi-wavelength observations of PKS 1502+106, which has a redshift of  $z=1.8$ . The expected transient fluence for each object is plotted against duration, or flare time, for three neutrino energies:  $10^{17}$  eV (hollow shapes),  $10^{18}$  eV (half shapes), and  $10^{19}$  eV (filled shapes).

searches for GRBs [46, 49, 92–113, 113–128] with lower neutrino luminosity than previously conducted with radio neutrino experiments [13, 129].

A successful radio detector for transient signals needs reliable absolute timing and good angular reconstruction. Ideally, the angular reconstruction is both sufficiently rapid and accurate to allow meaningful alerts to be quickly sent to the multi-messenger community. Absolute timing is critical to the multi-messenger mission.

## 2.4 Fundamental physics

High-energy cosmic neutrinos uniquely probe fundamental particles and interactions in an uncharted and otherwise unreachable energy and redshift regime, as summarized in [64].

The energy regime of neutrino radio detectors encompasses a relatively unmapped parameter space, helping to answer questions about the fundamental neutrino properties such as the behavior of neutrino cross-sections [133–140] and flavor mixing at high energies [141–147], or even whether neutrinos are stable in general [144, 148–154]. There is the chance to contribute to broader phenomenology such as the nature of dark matter [155–171], the quest for the fundamental symmetries of nature, [172–184] and/or potential hidden interactions with cosmic backgrounds [144, 185–190].

Overall, for a radio detector to provide experimental data for fundamental physics experiments, the highest priority is to detect neutrinos with adequate statistics. After this is given, the accuracy of statements regarding fundamental physics will strongly depend on the accuracy of the reconstruction.

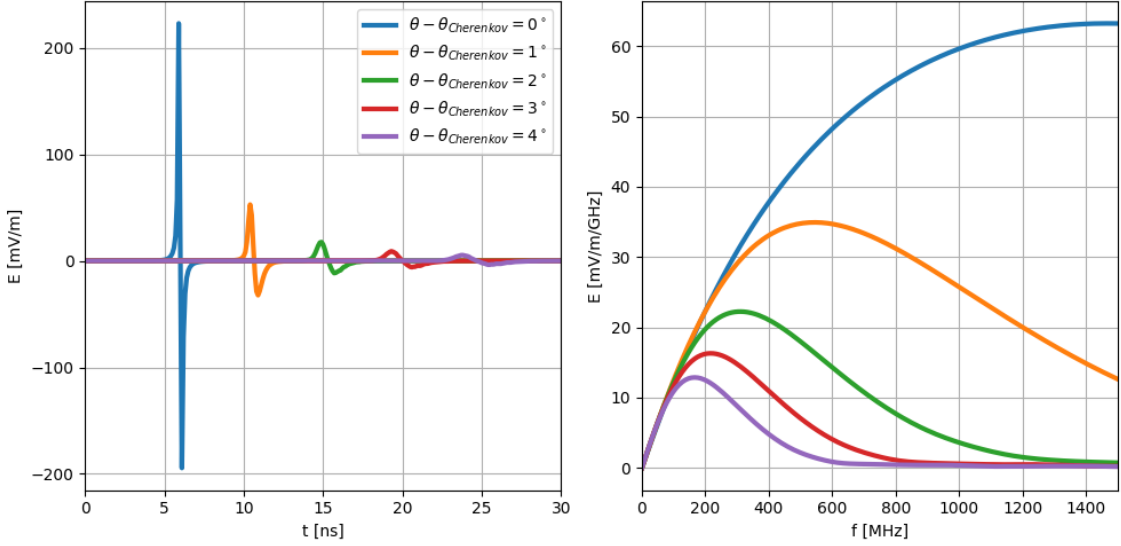


**Figure 4.** Electric-field waveforms (left) and spectra (right) of the radio signal emitted at different viewing angles relative to the Cherenkov angle, for a hadronic shower with energy deposition of 1 EeV. For enhanced readability, the waveforms have been offset in time. No propagation or detector effects have been included.

The obtainable energy resolution directly impacts spectral measurements and the accuracy of energy dependent quantities in fundamental physics. For studies relying on for example the amount of matter traversed, angular resolution has a direct impact. Potential flavor sensitivity of radio experiments would be interesting to answer yet another set of fundamental physics questions.

## 2.5 Radio emission from neutrino interactions in ice and consequences for site selection

The radio emission following a neutrino interaction stems from the Askaryan effect [191]. Postulated more than 50 years ago, the effect has been demonstrated in accelerator experiments in several dielectrics including ice [31–34], as well as identified as secondary emission mechanisms in air showers [192, 193].

Askaryan emission is caused by showers developing in a (dense) medium. Thus, a radio signal follows the interaction of neutrino of all flavors, as long as a particle shower is generated, both for hadronic and electromagnetic showers [194]. It is also possible to detect showers induced by catastrophic energy-losses of secondaries such as muons or taus [195]. The emission is a coherent effect, originating in the charge imbalance resulting from medium electrons either Compton scattering into the advancing shower or annihilating with shower positrons. With respect to the surrounding medium a net-negative charge is present in the shower front.

The radio signal itself is a broad-band bipolar pulse with  $\sim$ ns-duration. Coherence is given over all frequencies (typically tens of MHz to tens of GHz) close to the Cherenkov angle, where the signal is strongest as the emission at all frequencies arrives in phase. Coherence is lost off the Cherenkov angle first at high frequencies, so that the Cherenkov ring is rather narrow at high frequencies and broader at low frequencies. A discussion of a variety of models for the radio emission of neutrinos can be found in [196], they range from simplified parameterized models in

the frequency domain to more advanced semi-analytical time-domain models. In Fig. 4 we show typical pulses and their frequency spectra derived from [197], for an illustration of the variety and the behavior.

The energy threshold for a neutrino detection is significantly higher in radio than for optical instruments [2]. Depending on the exact instrumental parameters, the pulse amplitude at a distance of 100 m reaches the level of the typical thermal noise in low-noise radio receivers at approximately 1 PeV. Although the energy per radio photon is significantly smaller than for optical photons, signal coherence compensates as the charge imbalance grows. As a coherent effect, the amplitude scales linearly with the number of excess electrons, which itself is linear in shower energy [31, 198]. However, it should be noted that the detected signal amplitude scales with  $\frac{1}{r}$ , with  $r$  being the distance to the neutrino interaction vertex.

At the same observer distance  $r$ , the detected signal amplitudes linearly as function of energy. This has been confirmed in air showers since the attenuation in air is negligible [37]. The situation is different for instrumentation deployed in-ice. The kilometer-scale attenuation length in ice [5, 41, 199–201], determines the range to an observable neutrino interaction, and, therefore, the detector effective volume. The attenuation length decreases with increasing temperature, which favors cold and thick ice for deployment.

Naturally occurring ice follows a depth-dependent density profile with a gradient, from fresh snow to solid ice, resulting in a varying light velocity with depth, and therefore non-rectilinear ray trajectories. In a medium with a refractive index gradient, radio signals are bent towards the denser medium, producing bent trajectories and a limited field of view for detectors in or close to the near-surface firn layer. These bent trajectories complicate the reconstruction, particularly when there are uncertainties in the ice properties. The simplest ansatz assumes a smooth ice density gradient. Calculations demonstrate that anisotropies in the firn (or below) may support unexpected horizontal propagation, as borne out by experimental data [42, 202]. A radio detector should therefore preferably be built at a site with a small firn layer and otherwise smooth and homogeneous ice.

Starting from PeV energies, the Earth is opaque to neutrinos, such that radio detectors will be sensitive to an annulus of neutrino directions above and slightly below the horizon. The deeper the detector, the more vertically incoming neutrino directions can be detected. For a detector at a few hundred meters depth, the sensitivity does not reach far beyond 30° elevation, unless the reflective property of the bottom of a shelf-ice is used, as for the ARIANNA experiment [203].

In summary, an in-ice radio neutrino detector in glacial ice on bedrock will have the largest acceptance if installed in thick, smooth and cold ice. It will never be able to provide full sky coverage, but only be sensitive to a ring of elevations above and slightly below the local horizon.

Figure 5 provides an overview of the geometry for the detection radio signals with a detector buried in the ice. Every station monitors a large volume of ice, which means that by sheer geometry a detection is most likely to show small signals as this corresponds to an interaction in the largest visible volume.

## 2.6 Air showers as both a potential background and calibration signal

The radio emission of air showers from the electron charge excess is similar to that for neutrino induced showers in ice. However, in air the geomagnetic emission [204, 205] dominates over

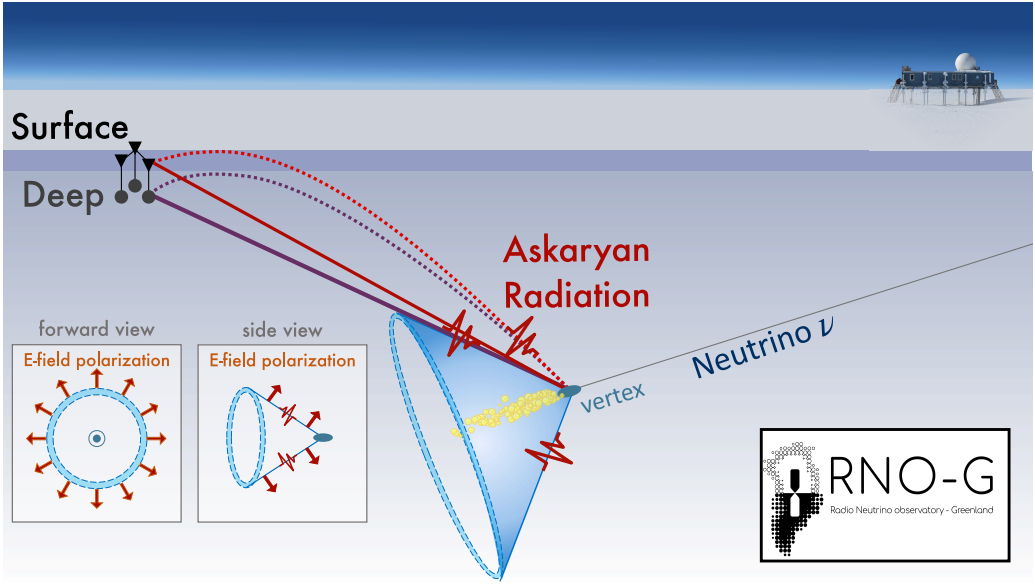


**Figure 5.** Schematic of the detection of the radio emission following a neutrino interaction (not to scale). The emission is strongest at the Cherenkov angle (blue cone) and can follow straight and bent trajectories to the receiving station depending on the profile of the index of refraction of the ice. The signal is usually detected at large distances and is strongly polarized as illustrated in the insets.

the Askaryan effect. The geomagnetic emission stems from the charge separation induced by the Lorentz force in the Earth's magnetic field. The different signatures of the two contributions can be disentangled by their polarization. While still mostly linearly polarized, the main axis of the polarization from geomagnetic emission is aligned with the cross-product of shower axis and magnetic field [192, 193].

Due to their larger extent and the resulting consequences for coherence, air shower signals typically contain more low frequencies than those from showers in dense media [206]. Nevertheless, signals from air showers and denser in-ice showers are remarkably similar, which makes the much more abundant air shower signals a suitable calibration signal. Since the cosmic ray energy spectrum is well-known (e. g. [70]) and the radio energy scale understood [37, 207], measuring air showers will allow any detector to be calibrated *in-situ*, which includes checking the sensitivity simulations on an absolute scale. This will lend confidence to the signal identification and reconstruction [19].

The remarkable similarity can of course also be a reason for concern. The in-air signal will be (partly) refracted into the ice, where it may be picked-up by antennas and incorrectly identified as neutrino induced signal. While the signal will clearly be down-going, so may be signals from neutrino interactions, due to the ray bending properties of the ice [196]. It has also been argued that an incompletely developed air shower may cause transition radiation and other phenomena observable in deep detector stations [208]. In addition, stochastic energy losses by high energy muons in an air shower penetrating the ice may mimic the interaction of a neutrino [195]. Without additional detectors, the muons themselves are invisible to radio detectors, while the energy losses are detectable. Depending on the exact detector configuration and trigger, these background events may limit the analysis efficiency, albeit dropping sharply in number with energy.

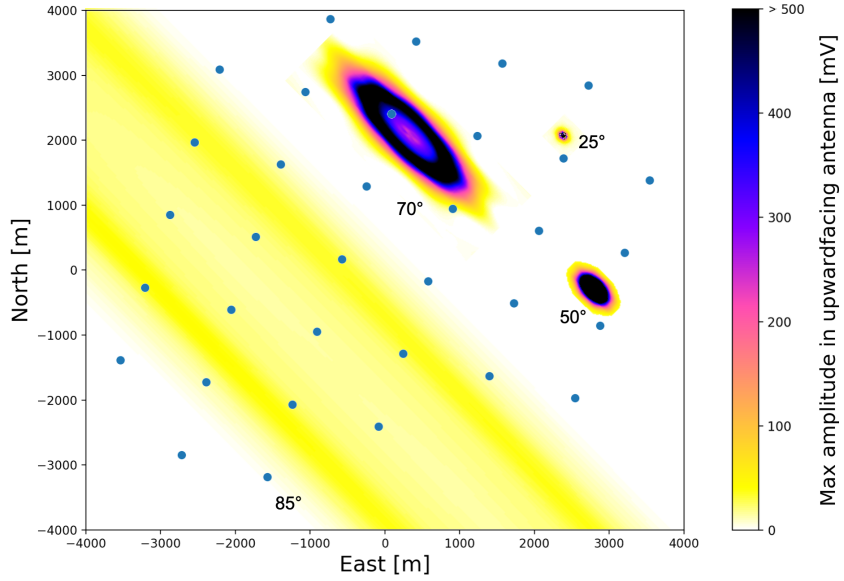


**Figure 6.** Simulated radio air shower footprints at 4 different incoming zenith angles. Simulations were performed using CORSIKA and the RNO-G site (magnetic field and height above sea level) in Greenland, and include the response of upward facing logarithmic periodic dipole antennas, as planned for RNO-G (see Fig. 7. The global maximum of the amplitudes in three antennas is shown. The air shower energy is  $3.2 \times 10^{18}$  eV for all showers, and the zenith angles are indicated in the figure.

Overall, this argues to equip all radio neutrino detectors with their own dedicated air shower array, for both calibration and veto purposes. Conveniently, due to the signal similarity, no additional technology is needed for such a detector, but does require additional surface antennas connected to the same data-acquisition system (DAQ). A dedicated air shower trigger, optimized to the lower frequency content of the air shower signals, would significantly enhance efficiency and detection rate. Due to the height of the interaction in the atmosphere and the fact that  $n_{air} \approx 1.0$  co-aligns the emission with the shower axis, the detectable footprint of the radio signal from air showers is centered on the shower axis, with lateral extent distributed ellipsoidally on the ground, as shown in Fig. 6. The exact size is governed by the distance to shower maximum and the projection effect of the zenith angle [209]. The figure qualitatively illustrates that vetoing horizontal air showers will be relatively straightforward, while retaining high efficiency for vertical showers presents more of a challenge. The typical threshold for air shower detection is around 10 PeV, which is again similar to the threshold of in-ice detection.

### 3 Experimental design considerations

RNO-G is designed to demonstrate the scalability of the radio detection technology, while enabling the world's-best UHE neutrino sensitivity through low thresholds and also high efficiency. The system is designed to provide high fidelity identification of neutrino signals and reconstruction of

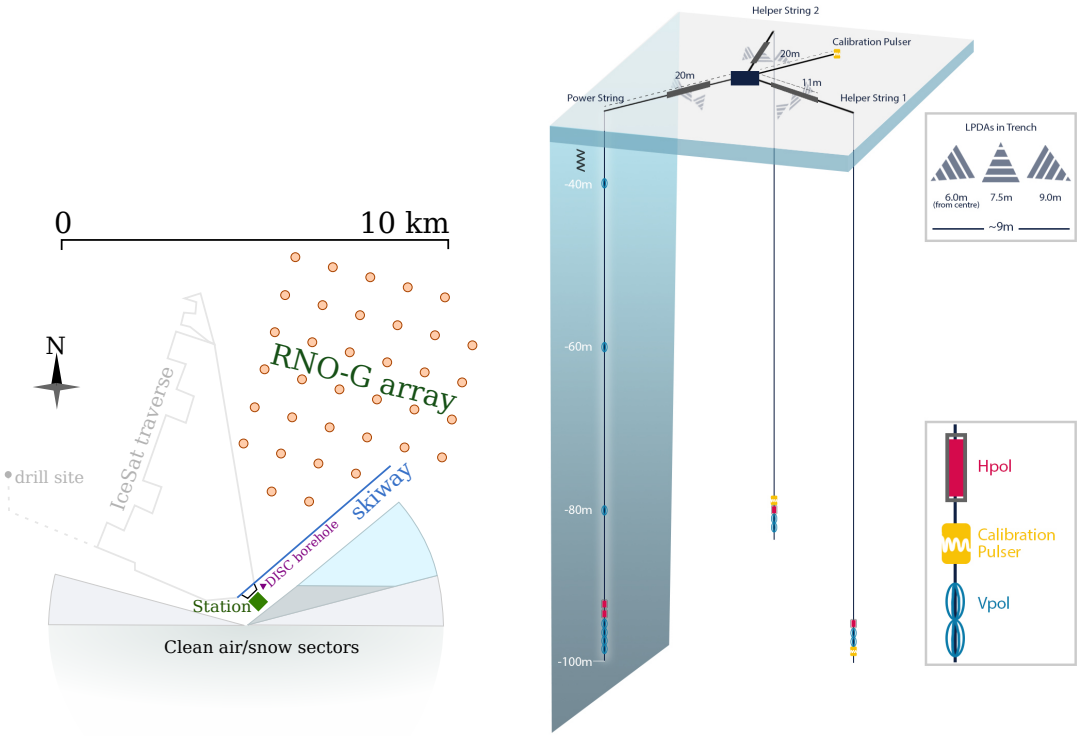


**Figure 7.** Left: Map of the planned RNO-G array at Summit Station; grid spacing is approximately 1 km. Right: A single RNO-G station consists of three strings of antennas (Hpol and Vpol) plus surface antennas (LPDAs), as well as three calibration pulsers located both deep in the ice and also at the surface. The string containing the phased array trigger is designated as the *power string*, while the two additional strings are designated as *support strings*.

neutrino properties. Building on these requirements, a station and array design as schematically depicted in Fig. 7 was developed.

The design of RNO-G combines the experience gained with all prior in-ice radio neutrino experiments, especially ARA [5] and ARIANNA [210], and also builds on lessons learned with radio air shower arrays that have first demonstrated the experimental power of the radio detection technique, e.g. [37, 38].

As outlined above, a location is needed with thick, homogeneous and cold ice to yield the best experimental results. An additional requirement is the availability of a sufficiently developed infrastructure to allow for installation, running and maintenance of the detector. While the instrumented stations can be fully autonomous, the amount of cargo and personnel needed for installation requires accessibility by plane or large vehicle. The number of accessible research stations fitting these requirements in either Antarctica or Greenland is limited. The host institutions of the RNO-G collaboration members and their access to national infrastructure additionally excludes some obvious candidate sites (Dome A, Dome C and Vostok in Antarctica, e.g.), leaving essentially South Pole Station and Summit Station in Greenland. South Pole station already houses a premier CMB instrument (the South Pole Telescope [211]), as well as the world's largest neutrino telescope (IceCube), which is in the process of installing the IceCube-Upgrade [212]. The logistical burden

is, thus, already high at South Pole.

If RNO-G is also to be used to develop and test hardware for the radio component of IceCube-Gen2 [1], a site similar to South Pole has advantages, if South Pole station is unavailable. Interesting coastal sites, like the Ross-Ice-Shelf close to McMurdo Station, which hosts the ARIANNA experiment [213], can assist in developing other technologies, but would be unable to replicate some of the particular challenges of South Pole.

To achieve a high trigger efficiency, a cosmic-ray veto, and the ability to reconstruct events with high accuracy, the RNO-G design combines a surface with a deep array capable of operating at low threshold (see Fig. 7). The collaboration will develop the necessary expertise for rapid installation with a minimum of logistical impact, enabled by newer, fast drilling technology and lightweight, low-power, autonomous stations that still achieve excellent single-station effective volume.

### 3.1 Summit Station, Greenland

Going to Greenland also has some fundamental consequences for the design decisions. The Antarctic has been host to several pioneering arrays that aim to detect in-ice radio emission from UHE neutrinos. Through previous efforts, the Arctic has been established as a parallel site for a future radio neutrino observatory [41, 42, 214]. Summit Station offers several advantages as a testbed site. It is located at  $72^{\circ}35'46''$  N,  $38^{\circ}25'19''$  W at the peak of the Greenland ice cap, atop more than 3 km of glacial ice that we have measured to be remarkably radio transparent [41] at  $\sim 100$  MHz, and with a  $\sim 100$  m deep firn layer that we have preliminarily characterized [42]. It is a year-round scientific research station sponsored by the National Science Foundation. It has a snow runway that accommodates LC-130 Hercules flights to deliver cargo and personnel, and facilities on site to support science. Compared to sites in Antarctica, Summit Station ( $72^{\circ}$  N Latitude) is easier to access from the Northern hemisphere, in particular through commercial flights from Europe, and has a larger fraction of the year with daily periods of light, providing a higher livetime for autonomous solar-powered stations. This final aspect is particularly important, given the reduced electrical generator infrastructure at Summit compared to South Pole. The restriction to renewable energies, combined with battery buffering limitations and the desire for high livetime, cap the amount of power the detector can draw and ultimately drive the station design.

Logistical considerations at Summit also favor a compact geometry with fewer, more sensitive stations rather than more, less sensitive stations. Similarly, the drilling technique must be lightweight and mobile and, therefore, mechanical.

The ASIG drill, which is able to drill  $5.75''$  diameter boreholes to 100 m at a rate of 1 hole per day, was initially considered as the main option [215]; subsequent antenna design was adapted to that form factor. Alternatively, the British Antarctic Survey (BAS) has been developing a mechanical drill that provides larger boreholes of  $11.2''$ , which will allow for greater flexibility in antenna design. Both drills satisfy the drilling rate, hole diameter and logistical impact specifications. See Sec. 5.1 for an in-depth discussion of drilling and installation.

To compensate for the warmer, more attenuating ice in Greenland compared to South Pole, triggering is performed with the deeper antennas, below the firn. Since no detector has detected the radio emission following a neutrino interaction yet, the exact experimental signature is predicted by simulations only, arguing for a detector design that detects the neutrino signal in a multitude of

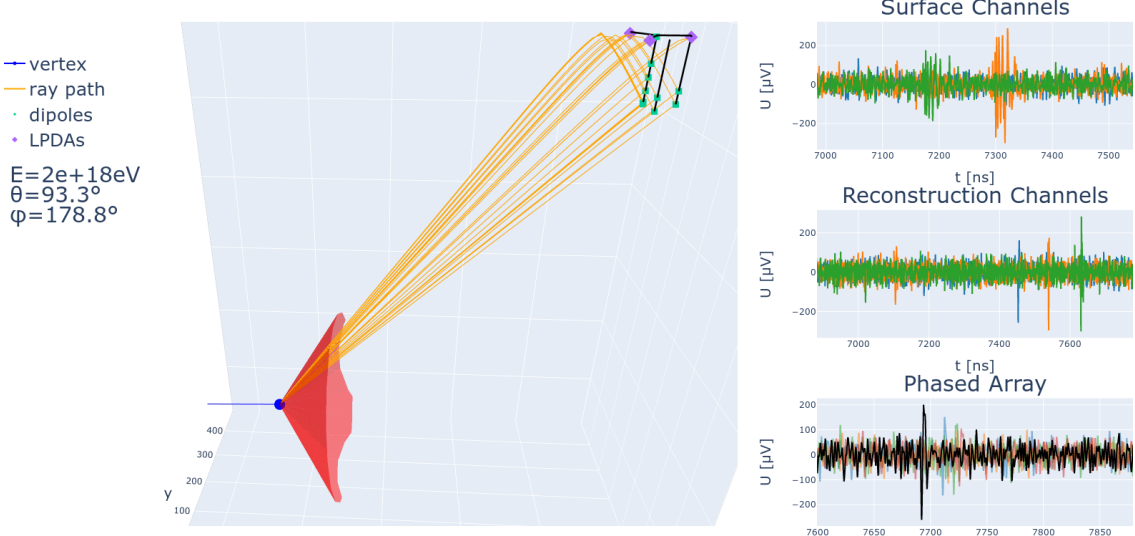


**Figure 8.** A simulated RNO-G neutrino event. The left side shows the event geometry illustrating both the direct and reflected ray-paths to the antennas, as well as the incoming neutrino and interaction vertex (blue) and its Cherenkov cone (red), where the strongest signals are expected. The right side shows the waveforms in selected antennas, and the improvement in signal-to-noise-ratio obtained by phasing the signals as done in the phased array trigger (shown in black, bottom row). This simulation and online event display utilize tools developed by the greater radio community [196, 216]. For better visibility, only selected channels are shown.

channels to increase confidence. It can be considered to adapt and simplify the detection strategy once the first neutrino has been conclusively identified.

### 3.2 A low-power, low-threshold trigger and data acquisition system

The RNO-G stations are built around an interferometric phased array, similar to what has been demonstrated *in situ* at the South Pole on the ARA experiment [12, 214], achieving the lowest sustainable signal trigger threshold demonstrated in the field. Since the astrophysical neutrino flux shows a falling spectrum, improved sensitivity to lower-energy events dramatically increases the detected neutrino event rate. The phased-array technology has been adapted for RNO-G to provide similar sensitivity, albeit with a reduced power consumption.

The phased array trigger coherently sums single channel waveforms with time delays corresponding to a range of angles of incident plane waves, improving the trigger-level signal-to-noise ratio roughly linearly with the number of antennas in the array [12], as illustrated in Fig. 8. Projecting the performance of the existing ARA system, we expect to achieve an elevation-averaged 50% trigger efficiency point at a  $2\sigma_{\text{noise}}$  threshold in voltage. This low threshold is needed to observe the largest volume of ice possible as discussed in Sec. 2.5.

It should be noted that for the simulations, the following definition for signal-to-noise ratio (SNR) and noise is handled. SNR is defined as the amplitude of the noiseless signal over the standard deviation  $\sigma_{\text{noise}}$  of a pure noise waveform. A threshold of  $2\sigma_{\text{noise}}$  thus means a threshold of twice the standard deviation of a trace without signal.

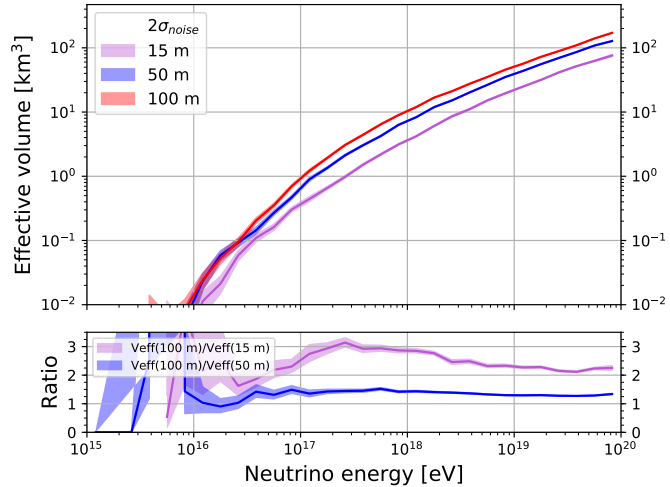


**Figure 9.** Scaling of the effective volume as a function of the depth of antennas used for the phased-array trigger for a single station deployed at Summit Station. 100 m was used during the design process as the technological limit due to drilling restrictions. As the trigger antennas are placed deeper into the ice, the effective volume increases, due to the number of allowed ray trajectories in the ice. The curves have been obtained using a  $2\sigma_{\text{noise}}$  dipole proxy for the phased array. Shown are statistical uncertainties only. Below 10 PeV the uncertainties on the effective volume become too large to draw firm conclusions.

### 3.3 Detector geometry: An integrated approach with deep and surface components

After extensive trade studies, we have coalesced on a station design that integrates a deep component with a surface component, as shown in Fig. 7. This integrated design achieves the highest effective volume per station given the phased-array trigger and mechanical drilling technology to 100 m. As shown in Fig. 9, the effective volume per station increases with increasing depth, so our design places the deep component of the station as deep as is logically feasible, given the current constraints of drilling.

In addition to maximizing effective volume, the station design has been optimized for neutrino reconstruction efficiency. The string containing the phased array trigger will feature additional Vpol antennas almost equally spaced vertically along the string allowing us to pin-point the neutrino vertex and zenith angle of the signal arrival direction, and achieving high accuracy by exploiting azimuthal symmetry. Since the down-hole Vpol antennas are typically more sensitive than the Hpol antennas and the trigger selects signals having a measurable component in the vertical polarization, the Vpol antennas dominate vertex and signal arrival direction reconstruction. Adding two Hpol antennas above the phased array will allow us to improve the reconstruction of the full electric field. Combining the four Vpol antennas of the phased array with the two Hpol in proximity, should provide sufficient information to reconstruct the polarization of the signal, as well as its frequency slope, and thereby the off-Cherenkov signal angle and neutrino arrival direction.

The radio signal from a neutrino interaction often travels along direct, refracted or reflected paths (designated  $DnR$ ) to the deep array, as shown in Fig. 8. The characteristic double pulse would be a smoking-gun signature of an in-ice source. The difference in direct and refracted arrival times significantly improves the reconstruction of the neutrino vertex position, and thereby the shower

energy, as well as arrival direction [21]. The probability to observe both a direct and a reflected signal is depth dependent. The spacing of the Vpol antennas on the main string is the result of an optimization between double pulse detection and long lever arm for good angular reconstruction.

The two additional deep boreholes are needed for a full direction reconstruction. Three independent measurements are needed for azimuthal information, which is provided by the Vpol antennas. By placing the Hpol antennas at different depths on every string, both zenith and azimuth information will be provided for those signals with a strong horizontal polarization component, as well as increasing the probability to reconstruct a signal for those events with little signal strength in the horizontal component.

The additional strings also host the calibration pulsers, which will ensure regular monitoring of the performance of the station and provide information useful for precise calibration of the antenna geometry. In addition, a surface pulser is foreseen, which will be deployed in a hand-drilled hole below the surface.

The surface component will deliver precision polarization measurements and timing information for all events detected at the surface. Also, the broad-band sensitivity of the log-periodic dipole antennas (LPDAs) will broaden the frequency coverage of the detector, which helps determine the radio detection angle with respect to the Cherenkov cone, improving energy reconstruction and pointing resolution. Events detected only in the surface components, however, only add minimally to the total neutrino effective volume.

With the planned layout, any events observed in coincidence between the surface component and the deep component are particularly valuable for event reconstruction; the fraction of these events is discussed in Sect. 3.4. In addition, the surface channels serve as an efficient air shower veto, reducing the background for neutrino searches as will be discussed in the following section.

The stations will be deployed on a square grid with 1 km baseline. This means that at energies beyond  $1 \times 10^{18}$  eV the effective volumes of the stations start to overlap and coincident measurements of the same neutrino become likely. This can be seen from Fig. 10, where the fraction of events triggered in coincidence is shown for different neutrino energies and grid spacings. While limiting the total effective volume of the system, 1 km was chosen to restrict the logistical impact in installation and preserve the opportunity of coincident events, which will simplify event identification and provide excellent reconstructed properties. As the project advanced, one may consider spacing stations further apart.

### 3.4 High analysis efficiency and low background to enhance discovery potential

In addition to triggering on and extracting event parameters from neutrino events, we must be able to separate any neutrino events in our recorded data set with high efficiency from all backgrounds. The three major sources of background are incoherent thermal noise, impulsive anthropogenic noise, and radio impulses resulting from cosmic-ray air showers. A discovery experiment of this scale requires low backgrounds at the level of 0.01 per station per year (or less). RNO-G is designed to achieve this ambitious background level by building on two key measures that have been developed to ensure event purity.

- (1) Triggering from deep in the ice (at a depth of 100 m), where the backgrounds are smaller than at the surface: ARA has shown that the anthropogenic and thermal backgrounds decrease

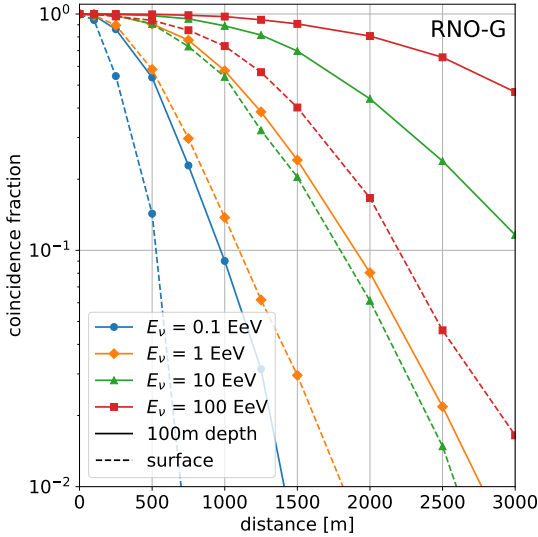


**Figure 10.** Fraction of coincident triggers on nearby stations as a function of the grid distance between stations for different neutrino energies. In addition to the 100 m deep power string, the coincidence fraction expected for a trigger near the surface is given for comparison.

for receivers deployed deeper in the ice [217] and further from human activity at research stations, achieving a background on the most recent analysis of 0.01 events in two stations over 1100 days of livetime [4]. This shows that successful background rejection can be achieved also during the summer at South Pole when anthropogenic backgrounds are more significant.

- (2) Vetoing backgrounds using a surface detector component: Non-thermal backgrounds are introduced from the surface or from close to the surface by man-made sources or air shower remnants. Surface antennas will help to separate neutrino induced signals originating within the ice from those of air showers [208] and those from showers caused by catastrophic energy losses from atmospheric muons [195].

Neutrino events triggered near threshold in the phased array system carry the risk to have low SNR in antennas needed for reconstruction. The information content in different numbers of antennas is illustrated in Fig. 11. Three channels detecting a signal  $>3\sigma_{\text{noise}}$  is taken as a simple proxy for events that can be identified and reconstructed with currently available analysis techniques such as interferometry [218], template matching [7] and signal de-dispersion [23]. With a signal in the antennas of the phased array as well as in an antenna on the support string, it is possible to reconstruct the neutrino arrival direction (see Sect. 6.3). To reconstruct the shower energy, at least 3 of the reconstruction antennas on the *power string* need to detect a pulse so that the distance to the interaction vertex can be reconstructed (see Sect. 6.2). In some cases, the radio signal is reflected off the ice-air interface or diffracted downwards, so that two signals from the same shower can be detected. These so-called *DnR pulses* become more likely with higher neutrino energies and can be used to greatly improve the reconstruction accuracy. More details on reconstruction and resolution

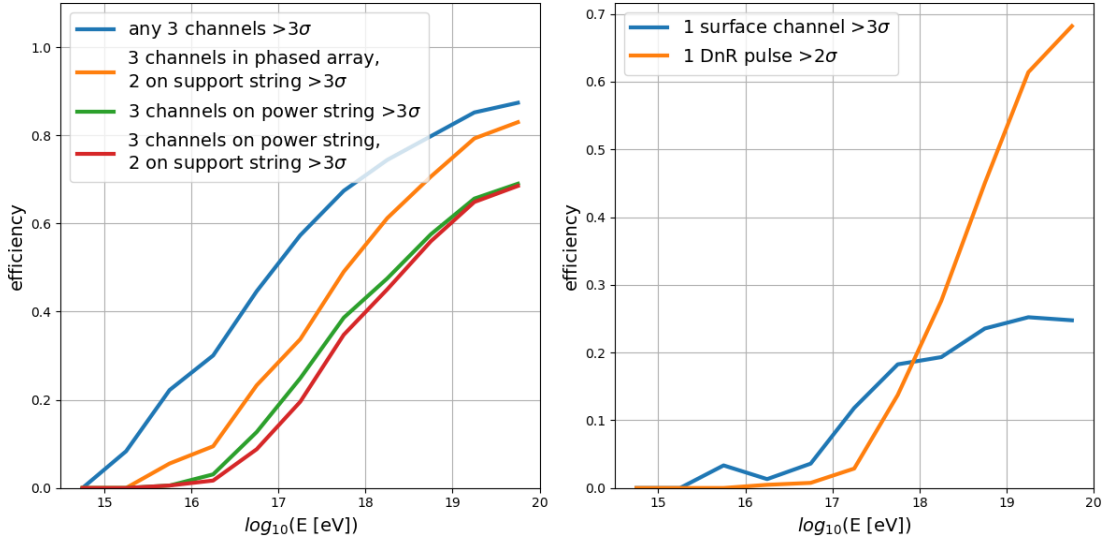


**Figure 11.** Estimate of anticipated analysis efficiency, defined here as the fraction of events recorded in a pre-defined number of antennas (channels) above a given threshold. The left figure illustrates detections in the deep part of the array only. A detection in the support string (see Fig. 7) will allow for a reconstruction of the arrival direction of the signal and three antennas on the power string are needed for a vertex reconstruction. The right figure shows the fraction of DnR signals, which are particularly valuable for the vertex reconstruction and the fraction of very valuable events measured in both the deep array and the surface antennas. For these simulations we assume a trigger at  $2.0\sigma_{\text{noise}}$  trigger in the phased array.

is given in Sect. 6.2 and 6.3. Foreseeable advances in analysis techniques will further improve the efficiency near threshold, both in firmware and also in off-line analysis.

An accurate knowledge of the existing background is needed in order to project what fraction of triggers are due to non-neutrino backgrounds, and also to assess whether a veto mechanism is advisable (or mandatory). An important type of background which is difficult to distinguish from actual neutrino events is the background created by the energy losses from atmospheric muons from cosmic ray showers. These muons are produced in the atmosphere, continue their propagation into the ice; their subsequent interactions (mainly bremsstrahlung, photonuclear interaction, and pair production) create hadronic and electromagnetic showers that emit radiation and are therefore detectable by an in-ice radio array [219]. These muons share shower characteristics, arrival directions and vertex positions with the sought-after neutrinos (see [195]). We have calculated the number of expected muon-initiated showers for a 35-station array at Summit Station, using a 100 m-deep dipole with an amplitude threshold between  $1.5\sigma_{\text{noise}}$  and  $2.5\sigma_{\text{noise}}$  as a proxy for the phased array. The effective areas have been calculated using NuRadioMC [196] and its interface to PROPOSAL [220]. Then, these effective areas are convolved with the expected muon flux at the detector, calculated by MCEq [221]. The chosen cosmic ray flux model is the Global Spline Fit from [222]. This procedure is explained more in detail in [195]. The results are presented in Fig. 12, where each band represents the results for a hadronic interaction model. Shown are the expected number of detected muons for the phased array proxies (from 1.5 to  $2.5\sigma_{\text{noise}}$ ) and also the 68% CL interval for the uncertainty due to cosmic ray flux, hadronic modeling and effective area. Fig. 12, left, contains the expected detected number of muons per year for 35 stations as a function

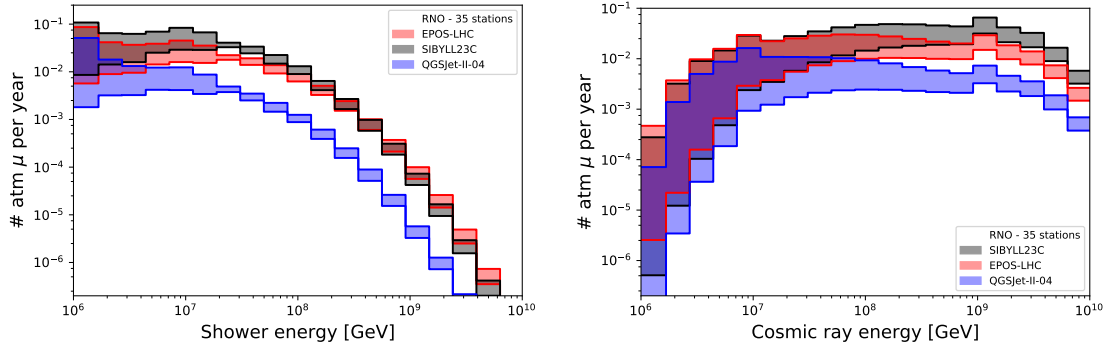


**Figure 12.** Number of atmospheric muons detected by a 35-station array at Summit Station. The phased array is modeled with dipoles having amplitude thresholds varying from  $1.5$  to  $2.5\sigma_{\text{noise}}$ , at  $100$  m of depth. Each color represents a different hadronic model, as specified in the legend. The bands include the range of expected events for the different simulated thresholds as well as the  $68\%$  CL contour corresponding to the effective area uncertainty. Left: number of detected atmospheric muons per year as a function of shower energy. Right: same results, presented as a function of cosmic ray energy. The drop off at low energies is an artifact of only simulating muons down to  $1 \times 10^6$  GeV.

	$2.5\sigma_{\text{noise}}$ 68% CL LB	$2.0\sigma_{\text{noise}}$ average	$1.5\sigma_{\text{noise}}$ 68% CL UB
SIBYLL 2.3C	0.212	0.296	0.684
EPOS-LHC	0.129	0.173	0.444
QGSJet-II-04	0.031	0.044	0.180

**Table 1.** Number of detected atmospheric muons per year for a 35-station layout. Three hadronic models are shown. The numbers shown are the lower  $68\%$  CL lower bound for a  $2.5\sigma_{\text{noise}}$  trigger (first column), the average values for a  $2.0\sigma_{\text{noise}}$  trigger, and the  $68\%$  upper bound for a  $1.5\sigma_{\text{noise}}$  trigger. See text for details.

of shower energy, while Fig. 12, right, presents the same results as a function of cosmic ray energy.

The lower and upper bounds on the number of detected atmospheric muons per year for a 35-station layout, as well as the average number for a  $2.0\sigma_{\text{noise}}$  trigger, can be found in Table 1. While these values are relatively benign, we remind that the neutrino event rate may be equally low, at least at the threshold energy of the detector. Hence, the air shower self-vetoing on the detector deserves special attention, as well as the development of algorithms using event parameters such as arrival direction and vertex location to disentangle neutrino signals from those potential background events. Also, since the flux and composition of cosmic rays at the relevant energies is subject to large uncertainties, those same uncertainties propagate into the background prediction for radio arrays.

#### 4 The RNO-G instrument design

RNO-G will provide high-quality science data and a robust, low trigger threshold with minimal power consumption using a station design schematically depicted in Fig. 13. In nominal operating

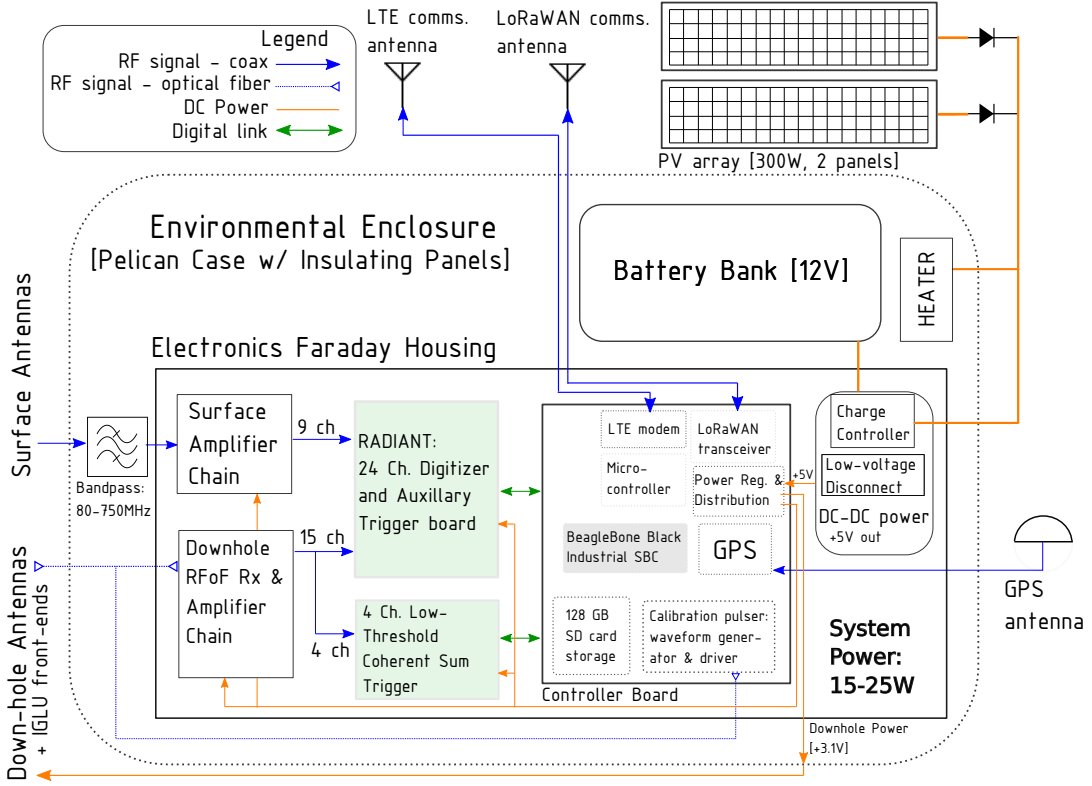


**Figure 13.** System diagram for an RNO-G station. See text for details.

mode, a station will use 25 W, including DC-DC converter losses. All equipment is rated to operate at  $-40^{\circ}$  C and 3200 m altitude.

#### 4.1 Antennas

The initial downhole antenna designs are driven by the 5.75" diameter of the boreholes (ASIG drill [215]), with some modifications possible, if bigger boreholes are available (see Sect. 3.1). The vertically-polarized (Vpol) antennas will be a *fat dipole* design (see Fig. 14) previously used in neutrino detection experiments, which have an azimuthally symmetric beam pattern and usable bandwidth ranging from 150-600 MHz [2, 214]. For horizontal polarization (Hpol), cylindrical *tri-slot antennas* are considered. They are nearly azimuthally-symmetric in gain, with differences of less than 1 dB up to 800 MHz, which corresponds to differences of less than 12% in effective length. Only Vpol antennas are used for the trigger because the Hpol antennas inherently have narrower usable bandwidth than the fat dipoles, as shown in Fig. 15. With the current Hpol designs, there is enough overlap with the Vpol band to combine the signals for polarization reconstruction in analysis. Larger boreholes (RAID drill) will especially help improve the broadband characteristics of the Hpol antennas. It is under consideration to exchange the tri-slot design for 8" quad-slot antennas, which will have a lower frequency turn-on and improved gain characteristics taking advantage of the larger allowed diameter.

The surface component employs commercially available log-periodic dipole antennas (LPDAs,

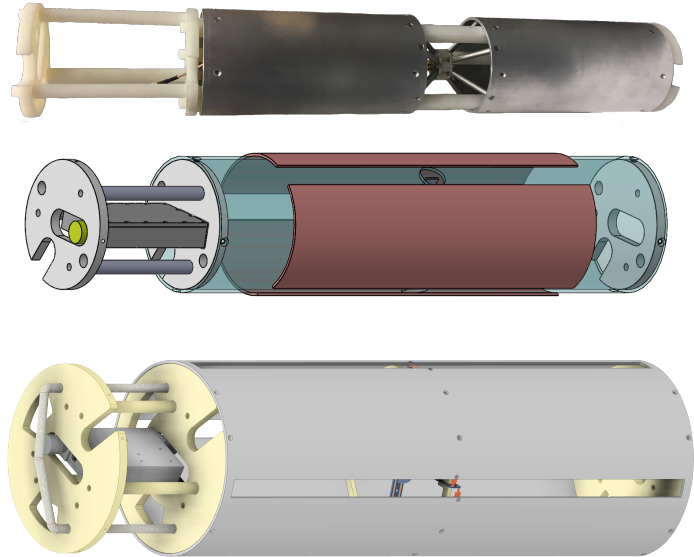


**Figure 14.** Photo of a Vpol prototype (top) and technical drawings of options for the Hpol antennas (trislot, middle, quadslot, bottom). The Vpol and trislot are the first iterations of the deep antennas for RNO-G, while the quadslot is being considered for use in conjunction with larger diameter boreholes.

Create CLP-5130-2N), successfully used by the ARIANNA experiment. ARIANNA’s extensive in-field experience with these antennas will significantly simplify calibration. Owing to the high gain allowed without the borehole constraints, the nine LPDAs arranged in various orientations (see Fig. 7, right) will measure all polarization components with high-precision, and provide a clear separation of upgoing versus downgoing signals. Due to their size the LPDAs have the largest gain of all employed antennas and will provide the greatest frequency coverage for the detected signals.

Particular care will be taken to placement and alignment of the LPDAs in the trenches at the surface, as well as surveying the position of boreholes and antenna locations to ensure good starting values for the system calibration using the *in situ* pulsers.

## 4.2 Radio-Frequency front-end design

To minimize system noise temperature, the feed of each antenna deployed in the borehole is connected with a short coaxial cable to a downhole front-end (Fig. 13, where a Low-Noise Amplifier (LNA, type IGLU, see Fig. 16) boosts the signal strength. To prevent a significant gain slope from long lengths of copper coaxial cable, each front-end contains a Radio Frequency over Fiber (RFoF) transmitter. The RFoF link and LNA are both powered by a DC connection from the surface, which is the only through-going coaxial cable in the boreholes. The LNA and RFoF are custom designs optimized for minimal noise temperature ( $\leq 150$  K) and low power. Each downhole channel consumes 140 mW, compared to 2.5 W in the previous installation of the phased-array in ARA. A total of 15 downhole antennas are distributed across three boreholes.

After being transmitted over fiber, the signals are received by another set of amplifiers in the DAQ box (type DRAB, see Fig. 16) and converted back to analog signals. At the DAQ box, the signals from the surface channels are also received and amplified. Given the relatively short run

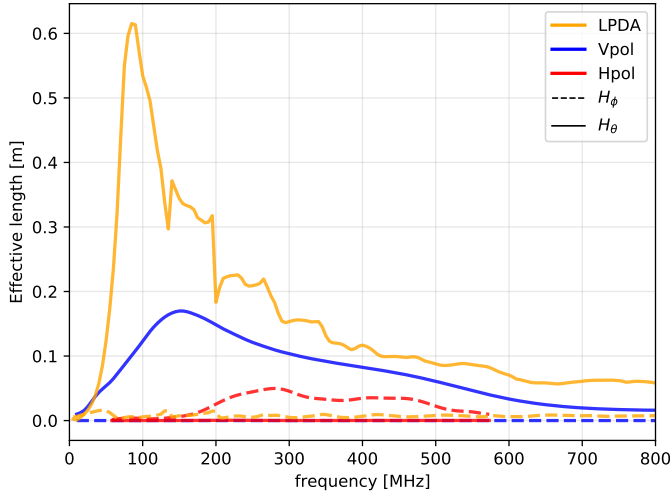


**Figure 15.** Antenna effective length magnitude for the LPDA, Vpol and Hpol (tri-slot) in the direction of maximum gain  $H_\theta$  (V-pol and LPDA) or  $H_\phi$  (H-pol). Results of detailed antenna simulations of the v1 iterations as shown in Fig. 14

of coaxial cable from the LPDAs to the DAQ box of less than 20 m, the signals require only one amplification stage after being fed into the DAQ box (type SURFACE, see Fig. 16).

All amplifiers are placed in custom-designed RF-tight housings using iridited aluminium (chromate conversion coating). This significantly reduces the influence of noise on the amplifiers and protects the IGLU amplifiers in the boreholes from the environment. The amplifiers exhibit excellent uniformity in laboratory tests (see Fig. 17). Nevertheless, all amplifiers will be calibrated individually to reduce systematic uncertainties on the reconstructed signals.

#### 4.3 Triggering, digitization, and data acquisition

The main trigger of RNO-G will come from a phased-array at depth of 100 m. The design of the field-proven phased-array installed at ARA [12] had to be changed to accommodate the lower power requirements of autonomous stations and was optimized with respect to the neutrino signals typically expected in Greenland and with respect to per-item cost for the scalability of the array.

The primary trigger will thus be a coherent-sum and beam-forming trigger from a compact array of four vertically-polarized antennas installed at the bottom of the main borehole string at a depth of 100 m. A commercially available 8-bit 500 MSa/s ADC is used to digitize and continuously stream data to an FPGA. This reduces the effective band to operate at the low-end of the signal bandwidth, 80 MHz–250 MHz. The lower cut-off is determined by the amplifier design that takes advantage of the full-range of low-frequency power that the antenna delivers.

Eight beams will be formed that cover the full range of expected signal arrival directions. Compared to the previous phased-array implementation in ARA there will be fewer beams, but each of them wider, thus no angular coverage loss is incurred. Overall, the power-savings total to about a factor of 10 for the trigger board, using 4 W in full operation mode.

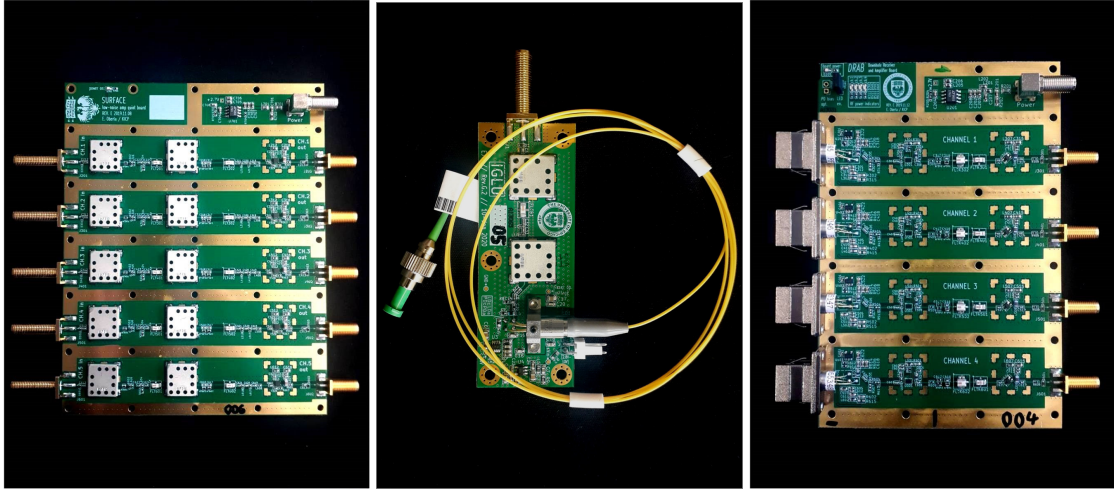


**Figure 16.** Amplifiers as designed for RNO-G. Left: SURFACE amplifiers for the signals coming from the LPDAs via coaxial cable. Middle: an IGLU board (In-ice Gain with Low-power Unit) used to convert signals from antennas deep in the ice to analog RF signals and then feed them into the indicated fiber. Right: DRAB board (Down-hole Receiver and Amplifier Board) located within the station housing. All amplifiers are shown without their environmental enclosures.

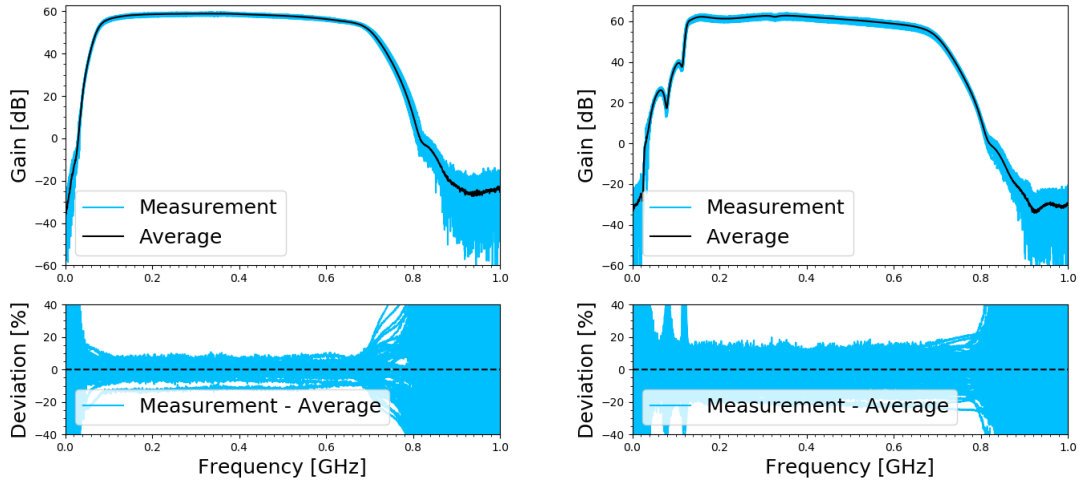


**Figure 17.** Gain of the RNO-G amplifiers. Left: 12 SURFACE amplifiers. Right: Combination of 23 IGLU and DRAB amplifiers, including a 50 m optical fiber cable. All amplifiers are revision v1 hardware.

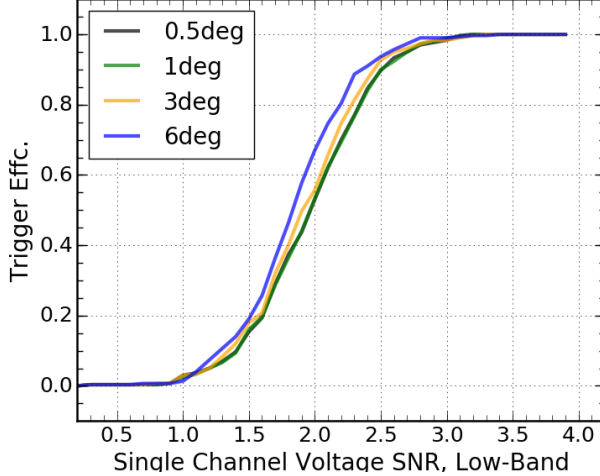


**Figure 18.** End-to-end simulation of the 4-antenna phased array trigger design for RNO-G. The simulated trigger efficiency for a number of neutrino signals at different off-cone viewing angles in the trigger bandwidth of 80 MHz–250 MHz.

A single-antenna voltage threshold of  $2\sigma_{\text{noise}}$  can be achieved with this trigger, based on simulation studies as shown in Fig. 18. The smaller bandwidth reduces the SNR of on-cone signals (i.e. 0.5 deg in Fig. 18) by 10%, however, increases the SNR for off-cone events by up to 80%, thereby incurring very little loss on the absolute neutrino effective volume. This is due to the limited high-frequency content of off-cone neutrino signals (see also Fig. 4).

The full-band waveforms for all 24 antennas within a station will be digitized using the RAdio DIgitizer and Auxiliary Neutrino Trigger (RADIANT) board (Fig. 19). The single-channel LAB4D switched-capacitor array sampling ASIC is used for waveform recording at a rate up to 3.0 GSa/s with an adjustable record length up to  $\sim$ 700 ns and the capability for multi-event buffering on-chip [223]. For RNO-G it is planned to operate the LAB4D in 2x 2048-sample buffers for essentially deadtime-less performance.

A trigger decision can be made using input from the primary neutrino trigger board (phased-array) or an auxiliary on-board trigger using similar Schottky diode detector circuits. The auxiliary on-board trigger is formed using a comparison between a DC voltage level and the enveloped waveform, which is fed to the on-board FPGA to build a combinatoric trigger decision. As the auxiliary trigger will have a higher overall threshold than is possible with the primary neutrino trigger board, it will predominately be used as additional trigger for the surface antennas as an air shower trigger. In periods in which the power available to the stations is low (see Sec. 4.4) it can serve as main trigger, however, with a much weaker sensitivity to neutrino signals.

Once an event is digitized, the waveforms and metadata are transferred to a BeagleBoneBlack Industrial, an ARMv7l Linux system, over a Serial Peripheral Interface (SPI) link, which allows data transfer at up to 20 Mbps. The operating system and acquisition software are stored on robust eMMC storage, while a 128 GB industrial SD card stage data before it is transmitted wirelessly to Summit Station. The acquisition software is an evolution of field-proven ARA phased array acquisition software.

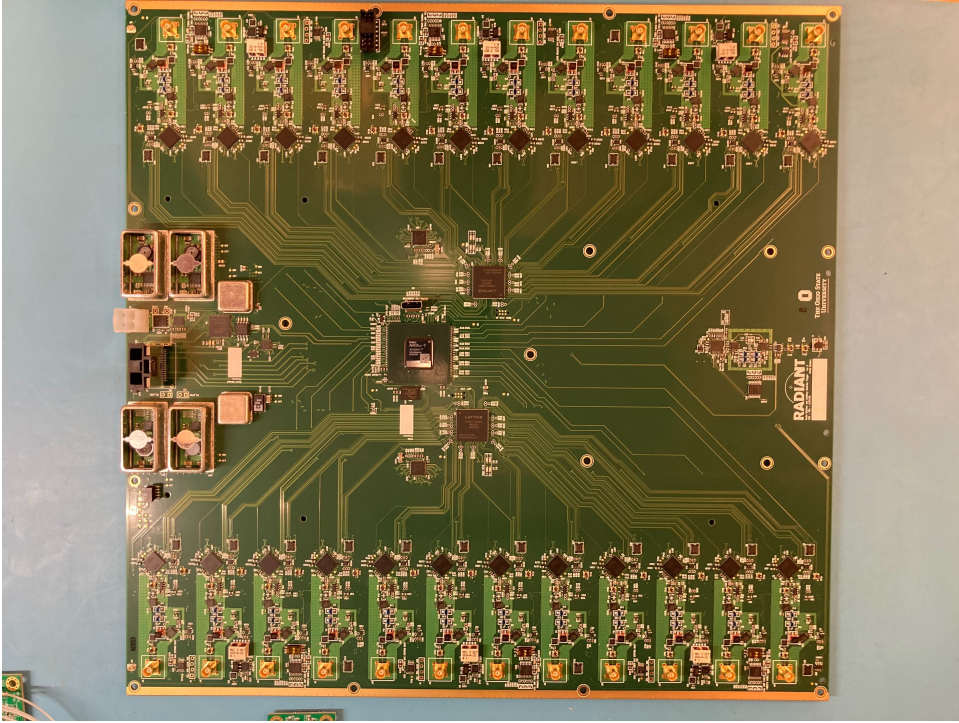


**Figure 19.** First iteration of the Radian Board that will be the main DAQ of RNO-G. All 24 channels are accommodated on one board and read out by LAB-4D chips.

#### 4.4 Autonomous power and wireless communications

Autonomous power and wireless communications simplify logistics for an experiment of this scale and become even more efficient for even larger arrays, such as IceCube-Gen2. Each station will be powered by two solar panels, with a total maximum power output of 300 W, and a 5 kWh sealed lead-acid battery bank that provides three days of full-system (24 W) running capacity during cloudy or inclement conditions, with a 60% de-rating margin. Lead-acid batteries, when lightly discharged relative to total capacity, have a proven track record in Arctic environments as demonstrated by the UNAVCO remote stations [224]. The daily solar energy delivered to a RNO-G station using a 300 W solar panel array is shown in Fig. 20, using realistic estimates of 70% total sun fraction (including diffuse and snow-reflected contributions) and a 90% charge-controller efficiency. A low-power microcontroller ( $\mu$ C) will manage the power system and turn parts of the detector on and off as necessary. The  $\mu$ C communicates with the Beaglebone SBC via a serial connection so that the SBC may be shut down cleanly if necessary. Enough power granularity is available to run the detector in a low-power, lower-sensitivity mode if needed.

The RNO-G station can be operated in several different modes depending on the available solar power capacity, in order to maintain constant science data during long stretches of inclement weather and during the shoulder seasons, when the sun only rises above the horizon for short periods per day. These operating modes include:

1. **Full-station mode:** Power, trigger, and data acquisition on the full 24-channel station including the low-threshold trigger and full LTE data telemetry. Power:~24 W.

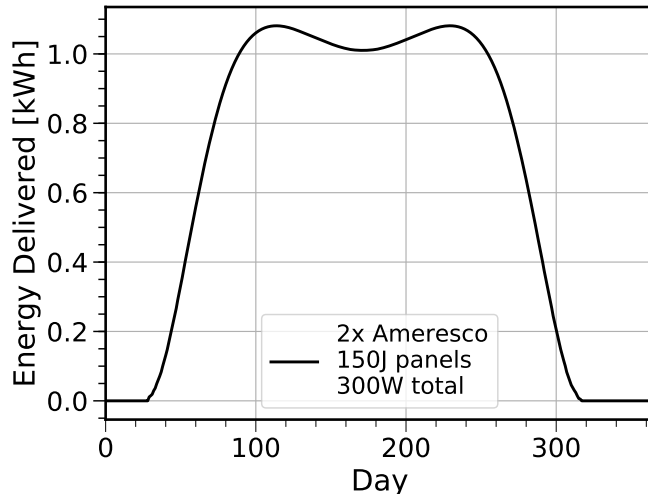


**Figure 20.** Predicted daily energy delivered by a 300 W photo-voltaic (PV) array to an RNO-G station at Summit Station. The PV array comprises two Ameresco 150J rugged panels mounted vertically and facing south. The total PV area is  $2\text{ m}^2$ .

2. **High-threshold mode:** Power, trigger, and data acquisition on the full 24-channel station without the low-threshold trigger and minimal LTE data telemetry. Power:  $\sim 17\text{ W}$ .
3. **Surface-only mode:** Power, trigger, and data acquisition only on the 9 surface LPDAs and minimal LTE data telemetry. Power:  $\sim 6\text{ W}$ .
4. **Winter-over mode:** Operating mode during the polar night. All power is turned off except to the charge-controller, LoRaWAN network, and station-control microcontroller. Only minimal housekeeping data is telemetered over LoRa. The estimated power draw is  $\sim 70\text{ mW}$ .

The expected uptime for an RNO-G station at Summit Camp with the 300 W PV panel array is 216 days in operating mode 1 (59%), 25 days in mode 2 (7%), and another 20 days in mode 3 (5%) for a total science livetime of  $\sim 70\%$  averaged over the year. For the remaining 30% of the year, the station will be put in winter-over mode. These different operating modes can be engaged by the RNO-G station controller autonomously or commanded remotely over one of the wireless networks.

Options to operate further into the winter are being explored. This R&D is particularly relevant for a potential larger array at the South Pole such as IceCube-Gen2, where the polar night is longer. Although not part of the baseline RNO-G design, wind-turbines may allow to extend the full-station mode operations of RNO-G throughout the winter. Development of radio-quiet wind turbines that can survive in the polar environment is ongoing [18]. Modeling using historical wind data [225, 226] suggests that a feasible 25%-efficient turbine at a height of 10 m would produce a daily average of 1200 Wh per square meter of collection area. Due to extended periods of low wind speeds a larger battery buffer will be needed for operation on wind power.

The main data transfer link from each detector to Summit Station will use modern cellular technology. A private LTE network provides high bandwidth (up to 75 Mbps total uplink) and long



**Figure 21.** The station solar charge controller and high-efficiency DC-DC board for RNO-G.

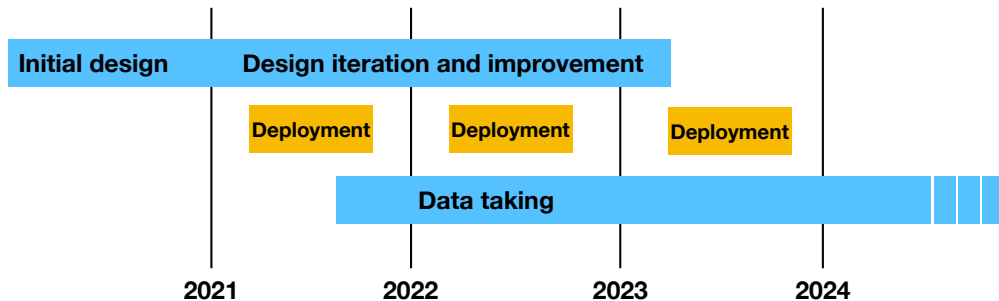


**Figure 22.** The anticipated timeline of RNO-G. The initial design work is ongoing. Installation will take place in the summer of 2021, 2022, and 2023, tentatively scheduling the installation of 10, 10 and 15 stations, respectively. Data taking will commence with the first deployed station.

range while consuming minimal power (<1 W average) at each station. A commercially-sourced LTE base station will be deployed with an antenna on the roof of the Science and Operations Building at Summit Station. As a compromise between range and minimizing interference with our detectors, LTE Band 8 (880-915 MHz uplink, 925-960 MHz downlink) was chosen and a permit has been acquired from the Greenlandic Radio Administration. Link modeling, including terrain shielding and a 10 dB fading margin, predicts a usable range up to 10 km.

A 34-dBi roof-top sectorial antenna at Summit can cover the azimuthal extent of the array and each station will be equipped with a 9 dBi antenna on a 3 m mast. A secondary LoRaWAN [227] network will also be deployed, providing a backup low-power but low-bandwidth connection for control and monitoring.

## 5 Installation, calibration, and operations

The anticipated timeline of the construction of RNO-G is shown in Fig. 22. The initial design work is already on-going and a first installation of stations is anticipated for 2021, provided that there are no continued restrictions due to the COVID-19 virus.

## 5.1 Drilling and installation plan

The main tasks for installation of each RNO-G station are:

1. drill boreholes for deep instrumentation,
2. deploy the solar panels and communications,
3. deploy detector instrumentation in boreholes and trenches,
4. confirm station operation and take calibration data.

The baseline RNO-G scenario assumed use of the ASIG mechanical drilling technology. The ASIG drill, owned and operated by the US Ice Drilling Program (IDP) is an auger with add-in drill sections. One 100 m deep hole requires a single working shift of 10 hours for three people. Therefore, the three holes required for each RNO-G station can be drilled in three days assuming one work shift per day, or one and a half days assuming two work shifts per day.

The preferred drill under consideration is the Rapid Access Isotope Drill (RAID) from the British Antarctic Survey (BAS). Holes of the diameter of 3" were successfully drilled to 461 m at Little Dome C. For RNO-G larger diameter holes are needed, which is why an existing proto-type development BigRAID is being considered [228]. It will provide 285 mm or 11.2" holes, taking about 0.85 days to reach 200 m or 0.38 days to reach 100 m, making it both faster and more versatile than the ASIG drill.

Using a mechanical drilling approach is much more scalable than previous drilling efforts for the ARA experiment at the South Pole, which used a hot water drill to reach 200 m depths. Mechanical drills are significantly lighter weight and less complex. Future development in drilling technology may enable exploring a wider range of more aggressive designs with RNO-G, which may lead to further improved sensitivity or event reconstruction capability. Drilling below the firn layer may provide significant increases in field-of-view due to fewer limitations in ray bending. However, care needs to be taken that any drill remains fast enough so as not to be the rate limiting step in installation and that personnel to operate the drill remains limited. Partly autonomous drilling operation is also under consideration.

Although subject to considerations such as firn thickness (which impacts drill depth) and ice temperature, local snow accumulation rate, average daily temperatures and the availability of solar and wind power, the station design is purposely general. This allows easy adaptation of the design for future larger in-ice arrays at other sites, such as IceCube-Gen2 at the South Pole.

The installation of both infrastructure (solar panels and communication antennas) and instrumentation is anticipated to be faster than hole-drilling. A drilling and installation team of seven people is foreseen for the first installation season, with installation beginning a week after commencing drilling. We project that an installation of up to 20 stations a year at Summit Station seems feasible. After installation, additional time will be required in the field to commission and validate station operation.

## 5.2 Calibration requirements and strategies

In order to optimally reconstruct events, the relative antenna positions must be known to a small fraction of the wavelength. Calibration using a local radio transmitter is necessary to achieve the

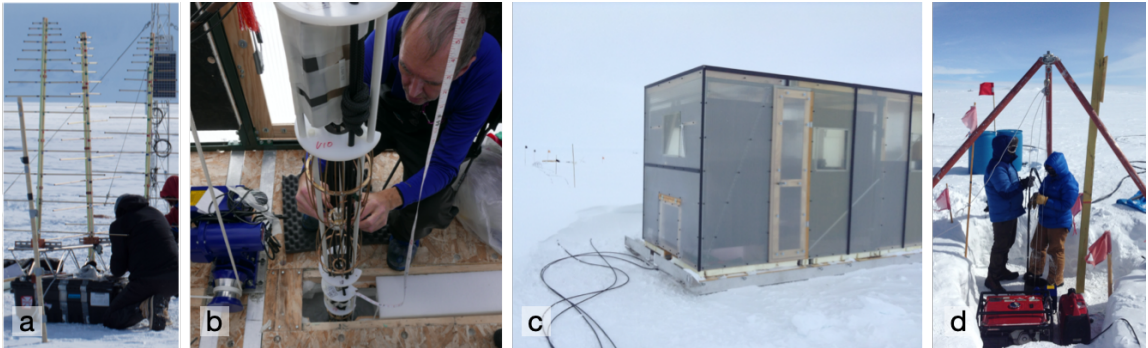


**Figure 23.** RNO-G installation plans are based on prior deployments of (a) surface stations at ARIANNA and (b) strings of antennas deployed in boreholes for ARA, both in compact phased arrays and reconstruction strings. A deployment shed for the drill and installation will be built on skis based on prior work done for ARA (c). Site studies conducted at Summit Station in Greenland also informed the installation plans (d).

required few-cm precision. Two deep transmitting antennas will be included with each station, as well as one at the surface. The calibration signal is generated in the surface controller board and sent downhole over RFoF. By measuring the relative time delays of the signal at each receiving antenna, the positions may be determined. After initial calibration, occasional runs of the pulser serve as a check of system stability.

An existing 740 m deep nearby borehole (DISC) [229], will also be used to send pulses to the array from various depths. This serves as a check of the antenna position and, by varying the depth of transmission, allows inversion of the radio properties of the ice. Understanding the refractive index profile of the firn is key to reconstruction and sensitivity modeling. Additional pulsing from the surface will be performed to further understand the ice.

Every station is equipped with a GPS, which will be used to synchronize event timing between stations at the 10 ns level. This is especially important for analyzing extensive air shower events, multi-station neutrino events and for absolute time difference measurements useful for ice studies. The GPS will also track the movement of station locations with the ice flow, which will provide valuable input for ice-modeling. A higher timing precision between stations can be obtained if suitable transmitters are identified at site [230] or through the usage of airplane signals [231]. This may also allow the combined reconstruction of neutrino signals detected in multiple stations [195], which would then yield improved precision.

All S-parameters of amplifiers, cables, and components will be calibrated before installation. Experience from radio air shower arrays has shown that a measurement of all individual components, including a temperature-dependent gain correction will be crucial to reduce systematic uncertainties. A continually-updated MongoDB database fully integrated with the simulation and reconstruction software [196, 216] will be used to track the parameters of all components.

### 5.3 Operations and data systems

The acquisition software on the Single-board computer (SBC) adjusts the trigger thresholds to maintain as fast a trigger rate as possible ( $\mathcal{O}(10\text{ Hz})$ ) without incurring significant deadtime. This high sustained rate drives system performance downstream, so second-stage filtering is applied

on the SBC to reduce the rate of saved triggers to a time-averaged 1 Hz. Additionally, 0.1 Hz of forced-trigger data will be recorded at regular intervals to help characterize the noise environment.

The on-disk compressed size of each event is an estimated 30 kB, implying an average data rate of around 260 kbps per station at 1.1 Hz. The LTE network can easily accommodate this rate with a relatively low duty-cycle at each modem, thereby saving power. This rate allows storage for six weeks on the local SD cards in the event of an unexpected network outage. If more time is needed, the station can be instructed via LoraWAN to reduce the rate. In the unlikely case of simultaneous LTE and LoraWAN failure, the software on the station will automatically throttle the rate. Once data is transmitted to Summit Station, it will be stored on a redundant disk array for collection each summer. At the estimated 1 TB/station/per year of data, full build-out requires a redundant storage capacity (with margin) of 35 TB, which can easily be achieved with a single commodity rack server (e.g. Dell PowerEdge R7515).

All instrument status data and event metadata as well as a subset of the waveform data (5 GB/day total) will be transmitted with low latency via Summit Station’s satellite link to the University of Wisconsin for monitoring and quality assurance. A small portion of available bandwidth will be reserved for remote login for any configuration changes or remote maintenance required. The JADE software [232] successfully developed and deployed for IceCube data management will be used for RNO-G. For data acquisition performance, all data is initially stored in a compressed packed-binary format resembling the in-memory format used by the data acquisition system. Converters will be maintained from the raw data format to more convenient archival formats (e.g. HDF5).

All low-latency data will be readily available to the collaboration via an interactive monitoring web site<sup>1</sup>. A comprehensive set of checks on the metadata and system health will be performed by the computer systems at Summit Station. Any anomalies will result in an email alert.

Monitoring duty will be apportioned to institutes on a rotating basis. While monitoring, an institution is responsible for timely investigation of all alerts and daily checks of the low-latency data for potential issues. Weekly monitoring reports will be issued to provide historical context for any issues that may arise.

Several mock stations, taking pure thermal noise data from terminated amplifiers, will be operated at collaborating institutions. These provide a testing ground for any configuration changes, assist with training, and help debug any issues that may arise. The pure thermal noise data also serves as a useful tool in developing analyses.

## 6 Projected sensitivity of RNO-G

In order to calculate the sensitivity of RNO-G, we have simulated the full 35-station array with a detailed modelling of the baseline hardware. Simulations for radio detectors are constantly evolving, incorporating experience from air shower simulations [38, 233–235] and previous codes for neutrino radio detectors [217, 236–238].

All simulation results presented herein have been performed with the NuRadioMC code [196]. For the same emission model, ice model and detector quantities, the results of this code have been shown to agree to the percent level with previous and independent codes, both for single event

---

<sup>1</sup>Based on <https://github.com/vPhase/monutor>

signatures as well as for the calculations of effective volumes. It has been found that the trigger-level sensitivities are in particular affected by the precise implementation of the trigger, the exact frequency band of the detector, the noise temperature of the system, the chosen emission model describing the Askaryan effect, whether a complete array is simulated or the array is scaled up from one station (impacting the number of events detected by multiple stations), and whether the interactions of secondary particles (taus and muons) are included in the sensitivity calculation. The latter three factors are most significant, with variations up to 50% in effective area depending on the energy. Since, in the design process, many of the instrument parameters are not completely fixed, we carefully quote in the following the assumptions made for the array and the hardware, bearing in mind that these design sensitivities are subject to change as the instrument design matures.

For the simulations, we use as a simplified proxy for the trigger in Sect. 4.3, a single vertical dipole per station with an amplitude threshold. A range of thresholds was used from  $1.5\sigma_{\text{noise}}$  to  $2.5\sigma_{\text{noise}}$  to account for possible variations in the exact design of the phased-array. Currently,  $2.0\sigma_{\text{noise}}$  is the expected to be the best proxy for the phased-array trigger using 4 dipole antennas that is in production (see Fig. 18). Dipoles are simulated at 100 m of depth, roughly at the same depth as the planned phased array.

We have simulated the response of a dipole of 50 cm length similar to the one in Fig. 14 and used it for the sensitivity calculation. The simulations performed with XFDTD [239] provide full gain and phase information as a function of incoming signal direction.

We have used NuRadioMC [196] with the ARZ2020 parameterization given in [197, 240] as our model for signal emission. We have included triggers induced by secondary particles produced by the outgoing lepton after a charged current (CC) interaction, following the procedure outlined in [195]. The simulated station layout is that shown in Fig. 7, with 35 stations having 1 km spacing between them on a rectangular grid.

We first discuss the sensitivity of RNO-G to a diffuse neutrino flux and how the neutrino energy will be determined, then its angular sensitivity and lastly the sensitivity to a transient event. We will also briefly report on the expected sensitivity to air shower signals.

## 6.1 Sensitivity to diffuse flux

Fig. 24 shows the expected 90% CL upper limit to an all-flavor flux for 5 years of operation of the full 35 station array, assuming a 67% duty cycle, as expected under only solar power. This is using effective volumes for an isotropic all-sky flux and full-decade energy bins. See [196] for more details on the  $V_{\text{eff}}$  calculation, and the inclusion of the interaction length to convert from  $A_{\text{eff}}$  to  $V_{\text{eff}}$ .

We have applied the Feldman-Cousins method [243] for no detected events and zero background. The zero background assumption is justified as a first approximation, as according to Table 1, we expect  $\sim 0.58$  detected muons over the full energy range for five years of operation time (using SIBYLL 2.3C for signal generation and a  $2\sigma_{\text{noise}}$  proxy).

The expected upper limit is shown in Fig. 24 along with other experimental bounds and model predictions. The red band shows the expected range of 90% CL upper limits for noise levels varying from  $1.5\sigma_{\text{noise}}$ -equivalent trigger (lower part of the band) to  $2.5\sigma_{\text{noise}}$ -equivalent trigger (higher part), and includes 95% CL contours due to the effective volume uncertainty. The black band shows the obtained 90% CL sensitivity for a  $2.0\sigma_{\text{noise}}$ -equivalent trigger, which is the most realistic

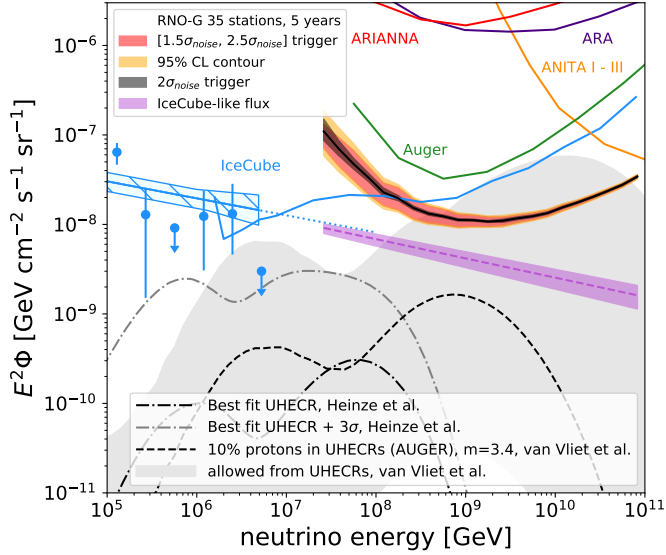


**Figure 24.** The five-year sensitivity (90% CL upper limits) of RNO-G to the all-flavor diffuse flux for 35 stations (assuming the stations are active two thirds of the total time), compared with existing experiments and several predicted fluxes [4, 23, 241, 242]. The red band represents the differential sensitivity band for a range of phased array proxies, spanning the interval from  $1.5\sigma_{\text{noise}}$  to  $2.5\sigma_{\text{noise}}$  using decade energy bins. 95% CL contours are represented by the orange band. The black band is the sensitivity expected for a  $2.0\sigma_{\text{noise}}$  trigger, including 95% CL contours. The purple band depicts the expected integrated sensitivity (90% CL upper limits) for an IceCube-like flux, over the  $[1.5\sigma_{\text{noise}}, 2.5\sigma_{\text{noise}}]$  trigger range.

assumption for the RNO-G experiment. We also show in Fig. 24 the sensitivity for a single power law spectrum with exponents in the range indicated by the flux observed in IceCube. The purple band represents the upper limit for the IceCube flux spanned by the  $[1.5\sigma_{\text{noise}}, 2.5\sigma_{\text{noise}}]$  range. The dashed line in the middle of the band is the result for the  $2.0\sigma_{\text{noise}}$  trigger. These upper limits have been calculated using the expected number of events above 20 PeV for a range IceCube flux spectral indices and finding that value that yields the number of events equal to the Feldman-Cousins 90% CL upper limit under the assumption of no background. The median upper limit exponents for the plausible trigger range cover the interval  $[-2.24, -2.19]$ , with  $-2.21$  being the median upper limit spectral index for a  $2.0\sigma_{\text{noise}}$  trigger. If no neutrino events are detected, RNO-G will be able to exclude IceCube-like fluxes above these levels.

## 6.2 Energy measurement

The ability of RNO-G to measure the neutrino spectrum will depend on the accuracy at which the energy of each event can be determined. The relation between the neutrino energy  $E_\nu$  and the amplitude  $|\vec{E}|$  of the electric field of the radio signal at the station is given by:

$$|\vec{E}| \sim E_\nu \cdot y \cdot f(\varphi) \cdot \frac{\exp(-d/l_{\text{atten}})}{d} \quad (6.1)$$

where  $y$  is the fraction of the neutrino energy deposited into the shower, and  $f(\varphi)$  a dependence on the angle under which the particle shower is observed. The last term accounts for the attenuation of

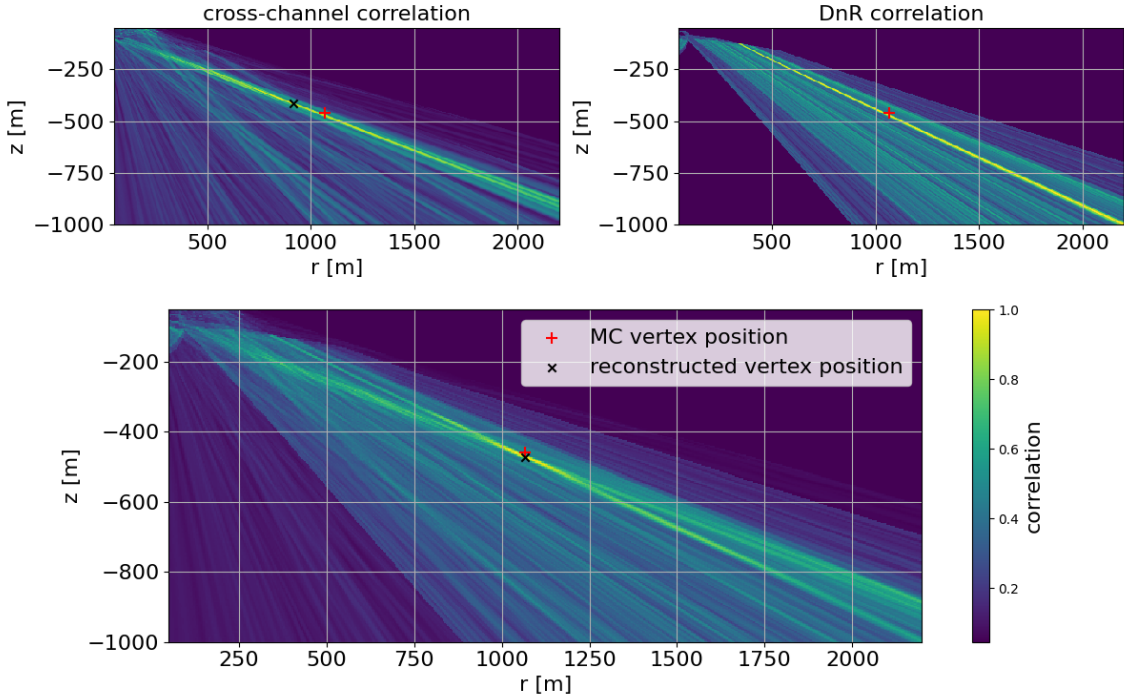


**Figure 25.** Neutrino interaction vertex reconstruction for one event using correlations between different channels (top left), correlations between different rays reaching the same antenna (top right) and a combination of both (bottom). Colors specify the normalized sum of correlations between channels, shifted by the difference in signal travel time expected for a given vertex position.

the radio signal as it travels to the antenna, with  $d$  being the distance of the interaction vertex from the station and  $l_{\text{atten}}$  the attenuation length of the ice.

In general, the (*inelasticity*) fraction  $y$  of the neutrino energy that contributes to a particle shower undergoes event-by-event fluctuations and cannot be reconstructed on a single-event basis. It therefore must be estimated from theory, resulting in a statistical uncertainty of, on average, a factor of  $\sim 2$  [21]. This restriction imposes a hard bound on the energy resolution obtainable with any neutrino detector that only observes the cascade. The goal is therefore to reconstruct the other parameters in Eq. 6.1 precisely enough for the uncertainty in  $y$  to be dominant. It should be noted that in case of an electron neutrino interaction, the full amount of energy is transferred to two particle showers very close to each other, which argues against having the unknown fraction  $y$  as bound. However, these two cascades can interfere constructively or destructively and pure-electromagnetic cascades are subject to the LPM-effect [244, 245] at high energies, which changes their radio emission [246]. This makes it reasonable to treat the inelasticity for all cases as bound in a first general consideration.

The resolution on the RNO-G measurement of the full electric field  $|\vec{E}|$  depends on a number of factors. Ideally, the amplitude should be obtained for all polarization components, with separate levels of noise. In general, the larger the detected amplitude of the signals (larger measured signal-to-noise ratio ( $\text{SNR}_m$ ), see below), the smaller the influence of noise on the uncertainty. Similarly,

noise effects are mitigated as antenna hit-multiplicities increase. As the Hpol antennas have lower gain than the Vpol antennas, the Hpol signals will typically have smaller  $\text{SNR}_m$ . Several methods such as *forward folding* [196], template matching [19], or information field theory [247] can be used to mitigate noise effects; nevertheless, the obtainable resolution of the amplitude will vary significantly from event to event.

It should be pointed out that using  $\text{SNR}_m$  differs from the situation of simulations (as defined in Sec. 3.2), as the true amplitude of the signal  $S$  without noise is unknown, so the measured  $\text{SNR}_m = (\text{signal} + \text{noise}) / \text{noise}$ . Using a definition of  $\text{SNR}_m = 0.5(\max(S) - \min(S))/\sigma_{\text{noise}}$ , a typical waveform of the length of RNO-G has a roughly 50% chance of reaching  $\text{SNR}_m = 3$  simply by fluctuations of noise. At  $\text{SNR}_m = 3.5$  this probability is reduced to about 1%.

Due to constructive interference, the radio signal emitted by the particle shower is strongest if viewed directly at the Cherenkov angle, and diminishes (in a frequency-dependent manner) the further the observer viewing angle departs from the Cherenkov angle. As shown in Fig. 4, the higher frequencies lose signal coherence earliest. Therefore, the shape of the frequency spectrum of the signal can be used to reconstruct the viewing angle relative to the Cherenkov angle and, ultimately, make a correction. This method has been demonstrated for particle showers in air [206], and our first simulations indicate the same to be true for neutrino showers. Quantitatively, we anticipate that  $f(\varphi)$  will be obtainable for RNO-G for signals detected with at least a measured  $\text{SNR}_m = 3.5$ .

The signal pathlength  $d$  (Eq. 6.1) will depend on the reconstruction of the interaction vertex, so the resolution of the vertex position is another important ingredient for energy reconstruction.

Fig. 25 shows one example of vertex reconstruction for a simulated neutrino interaction detected with RNO-G. This method to obtain the vertex position is based on cross-correlating the signals detected in all antennas with each other and deriving a probability map of the vertex location. Especially for those events in which RNO-G records both the direct emission, as well as the one reflected at-/refracted-below the surface, the resolution on the vertex position will be excellent, making the unknown factor  $y$  (Eq. 6.1) the dominating uncertainty. Further work will be carried out to determine the fraction of events for which a good vertex resolution will be obtainable and the  $\text{SNR}_m$  for which this will be possible. Preliminary results indicate that, conservatively, an analysis efficiency at least corresponding to the green curve in Fig. 11 is reachable for the vertex and thereby energy reconstruction.

The profile of the attenuation length of the ice in Greenland, which defines  $l_{\text{atten}}$  in Eq. 6.1 has been measured [41] and is used for the simulations. The remaining systematic uncertainty and variations across the array will be addressed by additional calibration campaigns as discussed in Sec. 5.2.

### 6.3 Angular sensitivity

The sky coverage of RNO-G is mostly determined by the geometry of its location in Greenland. In Fig. 26 we show the effective areas for different zenith angle bands for RNO-G, as well as their projection onto equatorial coordinates. Outside of these bands, the effective area decreases rapidly (see also [195]), making RNO-G mostly sensitive to an annulus of roughly 45° just above the horizon.

The ability of RNO-G to provide an accurate arrival direction for detected neutrinos depends on its ability to detect the signal arrival direction and the angle with respect to the Cherenkov cone,

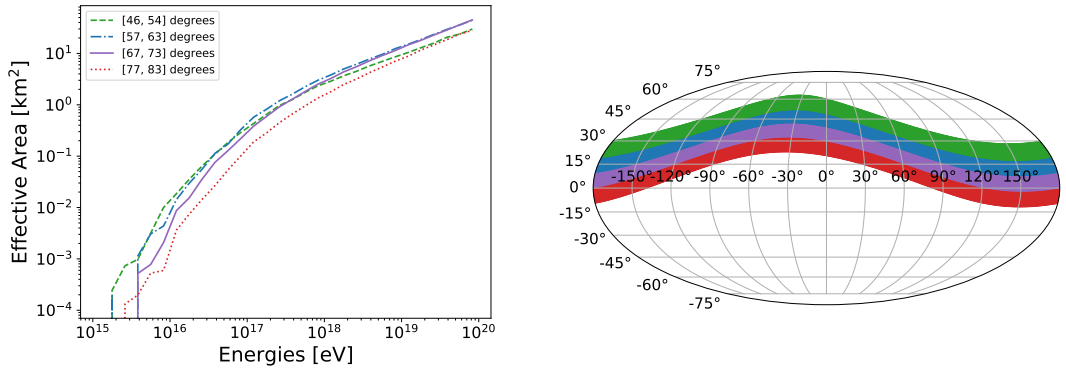


**Figure 26.** RNO-G instantaneous sky coverage. Left: Simulated effective area as a function of neutrino energy is shown for the four most sensitive zenith bands, centered at  $50^\circ$ ,  $60^\circ$ ,  $70^\circ$ , and  $80^\circ$ . Simulations were performed for the full RNO-G array of 35 stations with a distance of 1 km. Right: These bands are projected in Right Ascension (RA) and Declination (Dec) for one particular time of day to illustrate the instantaneous sky coverage. Bands outside this range still show some, albeit a strongly reduced ( $< 0.1$  fraction of maximum effective area), sensitivity for neutrino interactions.

as well as the signal polarization, and is again a strong function of the number of antennas with detected signal and their  $\text{SNR}_m$ .

The signal arrival direction can be directly determined from the time difference in the captured channel-by-channel waveforms, using (for example) cross-correlation. The obtained resolution is a function of the number of antennas with signal; sub-degree values have typically been obtained by previous experiments [4, 16, 21, 22]. Knowing only the arrival direction for the signal at a specific station, the neutrino arrival direction can be determined to lie on a cone, projecting to a ring on-sky as shown in Fig. 27. Only a fraction of the ring corresponds to a probable physical solution, as many arrival directions can be excluded by the known Earth absorption.

The radio signal is the strongest on the Cherenkov cone and then weakens once the angle to the shower axis deviates from the Cherenkov angle. Depending on the type of event, viewing angles of more than 10 degrees with respect to the Cherenkov angle may still be observable. As discussed in Sec. 6.2, the electric-field is a function of the viewing angle, as the higher frequencies fall off further away from the Cherenkov cone, so the viewing angle is reconstructable via the frequency slope. Combining signal arrival direction and viewing angle narrows the ring of possible arrival directions.

As the radio signal is due to the Askaryan effect, the polarization of the induced electric-field points radially inwards towards the shower axis. Therefore, a measure of the polarization is needed for a unique neutrino arrival direction. As shown in Fig. 27, adding polarization allows reducing the entire ring to a small patch on the sky. The absolute angular resolution as function of energy, elevation and  $\text{SNR}_m$  per antenna is still under study. Thus, Fig. 27 has been constructed to highlight the influence of different signal parameters on the angular resolution, while using a simulated event, as detectable in RNO-G, including noise but no detector uncertainties. The event shown has an  $\text{SNR}_m \approx 6$  in both Vpol and Hpol antennas, meaning that all pulses can be clearly identified.

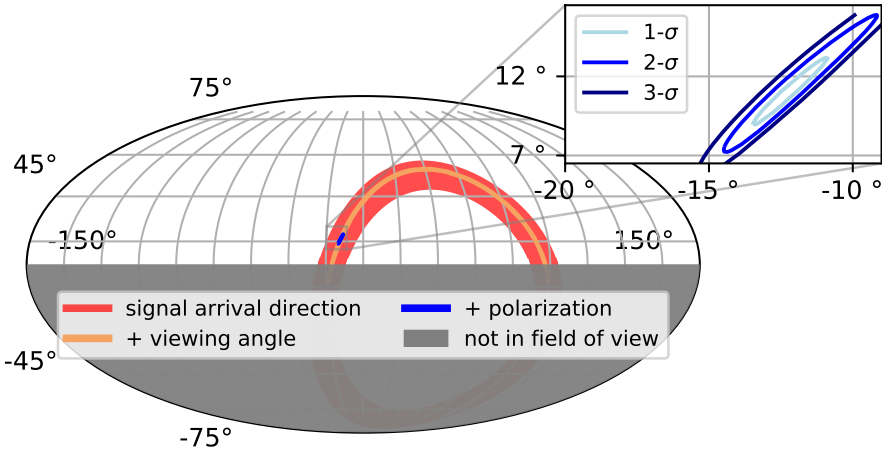


**Figure 27.** Radio neutrino detector arrival direction reconstruction. Given the limited field of view, the reconstructed signal arrival direction restricts the neutrino arrival direction to the red circular band shown. Adding information from the frequency content constrains the viewing angle, and reduces the width of the band. Finally, including data from both Hpol and Vpol antennas, polarization reconstruction reduces the allowed arrival direction to a small area on sky. The reconstruction and uncertainties are shown for one event simulated for RNO-G with NuRadioMC. The coordinates are local azimuth and zenith angle.

#### 6.4 Sensitivity to transient events

Using the same simulations as performed for Sec. 6.1, the sensitivity of RNO-G to transient events has been obtained, as shown in Fig. 28. Most models predict small neutrino fluxes in the energy range of RNO-G, as compiled in Fig. 3. However, given, e.g., large uncertainties in the modelling of mergers of neutron stars and that this area of multi-messenger astronomy is still in its infancy, RNO-G may make serendipitous discoveries. Its location in the Northern hemisphere makes it uniquely sensitive, and complementary to other planned radio neutrino observatories in the Southern Hemisphere.

GRBs and other cataclysmic events are promising candidates for transient flares of UHE neutrinos. GRB afterglows are expected to produce the highest energy neutrinos over months-long time scales [49]. Short GRBs resulting from binary neutron star mergers may be detectable with RNO-G if they are nearby or connected with the production of giant flares from magnetars [248]. Similarly, magnetars resulting from binary neutron star mergers can drive UHE neutrino production [131]. As shown in Fig. 28, RNO-G can constrain the neutrino fluence from GRB afterglows, short GRBs, and long-lived magnetars within tens of Megaparsecs. Furthermore, Tidal Disruption Events (TDEs) are another cataclysmic source class still in the infancy of their discovery, with frequent new observations and population increases thanks to transient observatories such as the Zwicky Transient Facility (ZTF) [249]. As more is uncovered about their nature, they may also become a viable multi-messenger target for RNO-G.

Flaring blazars are particularly interesting targets for RNO-G. As an example, a model of the neutrino fluence expected from the flare of the bright gamma-ray blazar PKS 1502+106 [132] is

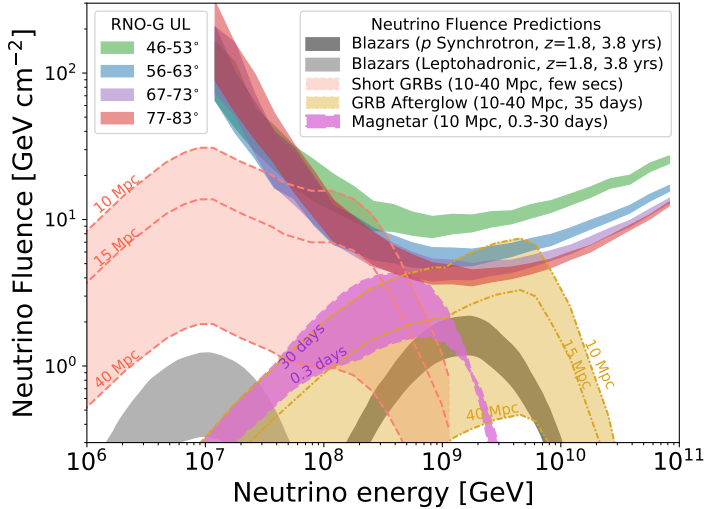


**Figure 28.** 95% CL fluence sensitivities between triggers at  $1.5\sigma_{\text{noise}}$  and  $2.5\sigma_{\text{noise}}$  are shown for four zenith bands centered at (top to bottom)  $50^\circ$  (green),  $60^\circ$  (blue),  $70^\circ$  (purple), and  $80^\circ$  (red). Sensitivities are calculated for a full decade in energy. Model-predicted fluences from several transient classes (bright gamma-ray blazars [132], short GRBs [130], magnetars [131], and GRB afterglows [49]) are also shown for direct comparison. We scale the short GRB and GRB afterglows by several luminosity distances to demonstrate the distance over which RNO-G will be sensitive to transients; a similar scaling can be applied to other source classes. For the calculation of sensitivities here we have used an integrated background expectation of no events. Note that for longer duration transients, integrated background may become non-negligible.

compared to the RNO-G sensitivities in Fig. 28. This particular blazar is an FSRQ, which are notable for their expected high UHE neutrino fluxes [71], and spatially coincident with a “golden” event (IC190730A) seen in IceCube [250, 251]. In the model, neutrinos are produced in the two different scenarios that are consistent with multi-wavelength photon observations, but the neutrino spectrum is strongly impacted by the radiation mechanism. Stacking searches in RNO-G for flares of blazars or multi-messenger driven searches may reveal UHE neutrinos or constrain the neutrino spectrum at the highest energies. Note that while PKS 1506+106 is at a distant redshift, closer blazars will have a stronger neutrino fluence.

RNO-G has unique capabilities to process alerts in nearly real time. Summit Station’s continuous satellite link and the LTE communications strategy can permit alerts from other multi-messenger observatories to be sent to and from the RNO-G stations.

## 6.5 Sensitivity to air shower signals

RNO-G will be equipped with upward-facing LPDAs, sensitive to air shower signals. These will be triggered through the auxiliary trigger as described in Sec. 4.3. First simulations indicate a turn-on of the trigger efficiency to air showers between  $1 \times 10^{16}$  eV and  $1 \times 10^{17}$  eV, with details depending on the exact system noise temperature and environmental noise conditions that will need to be confirmed during the first deployment season in-situ. The DAQ is designed to store 0.1 Hz of triggers from the surface antennas, dedicated to the detection of air showers. The passband of the

envelope trigger has been optimized for the highest surface antenna trigger efficiency and will be between 80 MHz and 180 MHz. We expect the detection in the order of one air shower per day per station.

The air shower trigger at RNO-G will serve two purposes. As discussed in Sect. 3.4, the muonic component of air showers may constitute a background for neutrino detection with RNO-G. While the flux of these background events depends strongly on the composition of the cosmic ray flux, as well as hadronic interaction models, the safest way to contain the impact of this background is to unambiguously tag air showers. RNO-G will therefore continue to be optimized to provide its own air shower veto. In addition, air shower reconstruction will help calibrate the system and ensure an independent cross-check of up-time and efficiency.

## 7 Conclusions

We have presented the concept of the Radio Neutrino Observatory in Greenland (RNO-G), currently scheduled to commence installation at Summit Station in 2021. The location in Greenland both drives design considerations, such as autonomous low-power stations, and, given the unique field of view from the Northern Hemisphere, also defines the strong science case.

The RNO-G hardware builds on previous radio array experience and strives for a very low-noise system that can sustain a low trigger-threshold, but high duty-cycle operation of autonomous stations. Each of the 35 RNO-G stations will consist of log-periodic dipole antennas deployed at the surface and custom-made dipole and tri- or quad-slot antennas deployed in three mechanically drilled holes to a depth of 100 m. The stations will mainly be triggered by a phased array of four deep dipoles at the 100 m maximum depth, which will ensure the best neutrino aperture. Auxiliary envelope triggers are available for low-power operations in the seasons with less abundant solar-power and for reading out the surface antennas to detect and veto air showers.

RNO-G will be the first uniform deployment of a neutrino radio array that will demonstrate the feasibility of scaling to arbitrarily large arrays. The delivered per-year sensitivity will be the largest achieved to-date with a radio array. RNO-G with its unique view of the Northern hemisphere may provide insights into transient sources of UHE neutrinos and will bring the detection of a continuation of the astrophysical neutrinos flux to high energies as detected by IceCube within reach. Additionally, models for cosmogenic neutrinos assuming a significant proton fraction in UHE cosmic-rays will be either be conclusively ruled out or will lead, if confirmed, to a detection of neutrinos with RNO-G.

## 8 Acknowledgements

We would like to acknowledge our home institutions and funding agencies for supporting the RNO-G work; in particular the Belgian Funds for Scientific Research (FRS-FNRS and FWO) and the FWO programme for International Research Infrastructure (IRI), the German research foundation (DFG, Grant NE 2031/2-1), and the Helmholtz Association (Initiative and Networking Fund, W2/W3 Program).

## References

- [1] ICECUBE GEN2 collaboration, *IceCube-Gen2: The Window to the Extreme Universe*, *Journal of Physics G*, in press (2020) [[2008.04323](#)].
- [2] RICE collaboration, *Performance and simulation of the RICE detector*, *Astropart. Phys.* **19** (2003) 15 [[astro-ph/0112372](#)].
- [3] I. Kravchenko et al., *RICE limits on the diffuse ultrahigh energy neutrino flux*, *Phys. Rev. D* **73** (2006) 082002 [[astro-ph/0601148](#)].
- [4] ARA collaboration, *Performance of two Askaryan Radio Array stations and first results in the search for ultrahigh energy neutrinos*, *Phys. Rev. D* **93** (2016) 082003 [[1507.08991](#)].
- [5] ARA collaboration, *Design and Initial Performance of the Askaryan Radio Array Prototype EeV Neutrino Detector at the South Pole*, *Astropart. Phys.* **35** (2012) 457 [[1105.2854](#)].
- [6] ARA collaboration, *Constraints on the Diffuse Flux of Ultra-High Energy Neutrinos from Four Years of Askaryan Radio Array Data in Two Stations*, *Phys. Rev. D* **102** (2020) 043021 [[1912.00987](#)].
- [7] ARIANNA collaboration, *A First Search for Cosmogenic Neutrinos with the ARIANNA Hexagonal Radio Array*, *Astropart. Phys.* **70** (2015) 12 [[1410.7352](#)].
- [8] ARIANNA collaboration, *Design and Performance of the ARIANNA HRA-3 Neutrino Detector Systems*, *IEEE Trans. Nucl. Sci.* **62** (2015) 2202 [[1410.7369](#)].
- [9] ANITA collaboration, *The Antarctic Impulsive Transient Antenna Ultra-high Energy Neutrino Detector Design, Performance, and Sensitivity for 2006-2007 Balloon Flight*, *Astropart. Phys.* **32** (2009) 10 [[0812.1920](#)].
- [10] ANITA collaboration, *Observational Constraints on the Ultra-high Energy Cosmic Neutrino Flux from the Second Flight of the ANITA Experiment*, *Phys. Rev. D* **82** (2010) 022004 [[1003.2961](#)].
- [11] P. Allison et al., *IceRay: An IceCube-centered radio-Cherenkov GZK neutrino detector*, *Nuclear Instruments and Methods in Physics Research A* **604** (2009) S64 [[0904.1309](#)].
- [12] ARA collaboration, *Design and Performance of an Interferometric Trigger Array for Radio Detection of High-Energy Neutrinos*, *Nucl. Instrum. Meth. A* **930** (2019) 112 [[1809.04573](#)].
- [13] ARA collaboration, *Constraints on the Ultra-High Energy Neutrino Flux from Gamma-Ray Bursts from a Prototype Station of the Askaryan Radio Array*, *Astropart. Phys.* **88** (2017) 7 [[1507.00100](#)].
- [14] ARA collaboration, *Observation of Reconstructable Radio Emission Coincident with an X-Class Solar Flare in the Askaryan Radio Array Prototype Station*, arXiv:1807.03335 (Submitted to *Astropart. Phys.*) (2018) [[1807.03335](#)].
- [15] K. Casey, T. Fudge, T. Neumann, E. Steig, M. Cavitte and D. Blankenship, *The 1500 m South Pole ice core: recovering a 40 ka environmental record*, *Annals of Glaciology* **55** (2014) 137–146.
- [16] ARA collaboration, *Measurement of the real dielectric permittivity  $\epsilon_r$  of glacial ice*, *Astropart. Phys.* **108** (2019) 63 [[1712.03301](#)].
- [17] ARA collaboration, *Long-baseline horizontal radio-frequency transmission through polar ice*, [\[1908.10689\]\(#\)](#).
- [18] A. Nelles for the ARIANNA Collaboration, *A wind-turbine for autonomous stations for radio detection of neutrinos*, *PoS ICRC2019* (2019) 968.
- [19] ARIANNA collaboration, *Radio detection of air showers with the ARIANNA experiment on the Ross Ice Shelf*, *Astropart. Phys.* **90** (2017) 50 [[1612.04473](#)].

- [20] ARIANNA collaboration, *A search for cosmogenic neutrinos with the ARIANNA test bed using 4.5 years of data*, *JCAP* **03** (2020) 053 [[1909.00840](#)].
- [21] ARIANNA collaboration, *Neutrino vertex reconstruction with in-ice radio detectors using surface reflections and implications for the neutrino energy resolution*, *JCAP* **1911** (2019) 030 [[1909.02677](#)].
- [22] ARIANNA collaboration, *Probing the angular and polarization reconstruction of the ARIANNA detector at the South Pole*, *JINST* **15** (2020) P09039 [[2006.03027](#)].
- [23] ANITA collaboration, *Constraints on the diffuse high-energy neutrino flux from the third flight of ANITA*, *Phys. Rev.* **D98** (2018) 022001 [[1803.02719](#)].
- [24] ANITA collaboration, *Observation of Ultra-high-energy Cosmic Rays with the ANITA Balloon-borne Radio Interferometer*, *Phys. Rev. Lett.* **105** (2010) 151101 [[1005.0035](#)].
- [25] ANITA collaboration, *Energy and Flux Measurements of Ultra-High Energy Cosmic Rays Observed During the First ANITA Flight*, *Astropart. Phys.* **77** (2016) 32 [[1506.05396](#)].
- [26] ANITA collaboration, *Characteristics of Four Upward-pointing Cosmic-ray-like Events Observed with ANITA*, *Phys. Rev. Lett.* **117** (2016) 071101 [[1603.05218](#)].
- [27] ANITA collaboration, *Observation of an Unusual Upward-going Cosmic-ray-like Event in the Third Flight of ANITA*, *Phys. Rev. Lett.* **121** (2018) 161102 [[1803.05088](#)].
- [28] A. Romero-Wolf et al., *Comprehensive analysis of anomalous ANITA events disfavors a diffuse tau-neutrino flux origin*, *Phys. Rev. D* **99** (2019) 063011 [[1811.07261](#)].
- [29] K. D. de Vries and S. Prohira, *Coherent transition radiation from the geomagnetically-induced current in cosmic-ray air showers: Implications for the anomalous events observed by ANITA*, *Phys. Rev. Lett.* **123** (2019) 091102 [[1903.08750](#)].
- [30] I. M. Shoemaker, A. Kusenko, P. Kuipers Munneke, A. Romero-Wolf, D. M. Schroeder and M. J. Siegert, *Reflections on the anomalous ANITA events: the Antarctic subsurface as a possible explanation*, *Annals of Glaciology* (2020) 1–7.
- [31] D. Saltzberg et al., *Observation of the Askaryan effect: Coherent microwave Cherenkov emission from charge asymmetry in high-energy particle cascades*, *Phys. Rev. Lett.* **86** (2001) 2802 [[hep-ex/0011001](#)].
- [32] P. W. Gorham et al., *Accelerator measurements of the Askaryan effect in rock salt: A Roadmap toward teraton underground neutrino detectors*, *Phys. Rev. D* **72** (2005) 023002 [[astro-ph/0412128](#)].
- [33] ANITA collaboration, *Observations of the Askaryan effect in ice*, *Phys. Rev. Lett.* **99** (2007) 171101 [[hep-ex/0611008](#)].
- [34] T-510 collaboration, *Accelerator measurements of magnetically-induced radio emission from particle cascades with applications to cosmic-ray air showers*, *Phys. Rev. Lett.* **116** (2016) 141103 [[1507.07296](#)].
- [35] LOPES collaboration, *Detection and imaging of atmospheric radio flashes from cosmic ray air showers*, *Nature* **435** (2005) 313 [[astro-ph/0505383](#)].
- [36] D. Ardouin et al., *Geomagnetic origin of the radio emission from cosmic ray induced air showers observed by CODALEMA*, *Astropart. Phys.* **31** (2009) 192 [[0901.4502](#)].
- [37] PIERRE AUGER collaboration, *Measurement of the Radiation Energy in the Radio Signal of Extensive*

*Air Showers as a Universal Estimator of Cosmic-Ray Energy*, *Phys. Rev. Lett.* **116** (2016) 241101 [[1605.02564](#)].

- [38] LOFAR collaboration, *Detecting cosmic rays with the LOFAR radio telescope*, *Astron. Astrophys.* **560** (2013) A98 [[1311.1399](#)].
- [39] TUNKA-REX collaboration, *Radio measurements of the energy and the depth of the shower maximum of cosmic-ray air showers by Tunka-Rex*, *JCAP* **01** (2016) 052 [[1509.05652](#)].
- [40] S. A. Wissel et al., *Site Characterization and Detector Development for the Greenland Neutrino Observatory*, *PoS ICRC2015* (2016) 1150.
- [41] J. Avva et al., *An in situ measurement of the radio-frequency attenuation in ice at Summit Station, Greenland*, *J. Glaciol.* **61** (2015) 1005 [[1409.5413](#)].
- [42] C. Deaconu et al., *Measurements and Modeling of Near-Surface Radio Propagation in Glacial Ice and Implications for Neutrino Experiments*, *Phys. Rev. D* **98** (2018) 043010 [[1805.12576](#)].
- [43] M. Ahlers, *Neutrino Sources from a Multi-Messenger Perspective*, in *Proceedings, 7th Roma International Conference on Astroparticle Physics (RICAP18) Rome, Italy, September 4-7, 2018*, 2018.
- [44] K. Fang and K. Murase, *Linking High-Energy Cosmic Particles by Black Hole Jets Embedded in Large-Scale Structures*, *Phys. Lett. B* **14** (2018) 396 [[1704.00015](#)].
- [45] K. Fang et al., *Testing the Newborn Pulsar Origin of Ultrahigh Energy Cosmic Rays with EeV Neutrinos*, *Phys. Rev. D* **90** (2014) 103005 [[1311.2044](#)].
- [46] D. Boncioli, D. Biehl and W. Winter, *On the common origin of cosmic rays across the ankle and diffuse neutrinos at the highest energies from low-luminosity Gamma-Ray Bursts*, *Astrophys. J.* **872** (2019) 110 [[1808.07481](#)].
- [47] K. Murase, Y. Inoue and C. D. Dermer, *Diffuse Neutrino Intensity from the Inner Jets of Active Galactic Nuclei: Impacts of External Photon Fields and the Blazar Sequence*, *Phys. Rev. D* **90** (2014) 023007 [[1403.4089](#)].
- [48] X. Rodrigues, J. Heinze, A. Palladino, A. van Vliet and W. Winter, *Blazar origin of the UHECRs and perspectives for the detection of astrophysical source neutrinos at EeV energies*, [2003.08392](#).
- [49] K. Murase, *High energy neutrino early afterglows gamma-ray bursts revisited*, *Phys. Rev. D* **76** (2007) 123001 [[0707.1140](#)].
- [50] J. Heinze et al., *A new view on Auger data and cosmogenic neutrinos in light of different nuclear disintegration and air-shower models*, *Astrophys. J.* **873** (2019) 88 [[1901.03338](#)].
- [51] A. van Vliet, R. Alves Batista and J. R. Hörandel, *Determining the fraction of cosmic-ray protons at ultrahigh energies with cosmogenic neutrinos*, *Phys. Rev. D* **100** (2019) 021302 [[1901.01899](#)].
- [52] FERMI-LAT collaboration, *The spectrum of isotropic diffuse gamma-ray emission between 100 MeV and 820 GeV*, *Astrophys. J.* **799** (2015) 86 [[1410.3696](#)].
- [53] ICECUBE collaboration, *A measurement of the diffuse astrophysical muon neutrino flux using eight years of IceCube data.*, *PoS ICRC2017* (2018) 1005 [[1710.01191](#)].
- [54] ICECUBE collaboration, *Observation of Astrophysical Neutrinos in Six Years of IceCube Data*, *PoS ICRC2017* (2018) 981 [[1710.01191](#)].
- [55] ICECUBE collaboration, *Differential limit on the extremely-high-energy cosmic neutrino flux in the presence of astrophysical background from nine years of IceCube data*, *Phys. Rev. D* **98** (2018) 062003 [[1807.01820](#)].

- [56] PIERRE AUGER collaboration, *The Pierre Auger Observatory: Contributions to the 34th International Cosmic Ray Conference (ICRC 2015)*, in *Proceedings, 34th International Cosmic Ray Conference (ICRC 2015): The Hague, The Netherlands, July 30-August 6, 2015*, 2015, <http://lss.fnal.gov/archive/2015/conf/fermilab-conf-15-396-ad-ae-cd-td.pdf> [[1509.03732](#)].
- [57] ICECUBE collaboration, *Evidence for High-Energy Extraterrestrial Neutrinos at the IceCube Detector*, *Science* **342** (2013) 1242856 [[1311.5238](#)].
- [58] ICECUBE collaboration, *Observation of High-Energy Astrophysical Neutrinos in Three Years of IceCube Data*, *Phys. Rev. Lett.* **113** (2014) 101101 [[1405.5303](#)].
- [59] ICECUBE collaboration, *Evidence for Astrophysical Muon Neutrinos from the Northern Sky with IceCube*, *Phys. Rev. Lett.* **115** (2015) 081102 [[1507.04005](#)].
- [60] ICECUBE collaboration, *Observation and Characterization of a Cosmic Muon Neutrino Flux from the Northern Hemisphere using six years of IceCube data*, *Astrophys. J.* **833** (2016) 3 [[1607.08006](#)].
- [61] LIVERPOOL TELESCOPE, MAGIC, H.E.S.S., AGILE, Kiso, VLA/17B-403, INTEGRAL, KAPTEYN, SUBARU, HAWC, FERMI-LAT, ASAS-SN, VERITAS, KANATA, ICECUBE, SWIFT NuSTAR collaboration, *Multimessenger observations of a flaring blazar coincident with high-energy neutrino IceCube-170922A*, *Science* **361** (2018) eaat1378 [[1807.08816](#)].
- [62] ICECUBE collaboration, *Neutrino emission from the direction of the blazar TXS 0506+056 prior to the IceCube-170922A alert*, *Science* **361** (2018) 147 [[1807.08794](#)].
- [63] M. Ackermann et al., *Astrophysics uniquely enabled by observations of high-energy cosmic neutrinos*, *Bull. Am. Astron. Soc.* **51** (3) (2019) 185 [[1903.04334](#)].
- [64] M. Ackermann et al., *Fundamental physics with high-energy cosmic neutrinos*, *Bull. Am. Astron. Soc.* **51** (3) (2019) 215 [[1903.04333](#)].
- [65] V. Beresinsky and G. Zatsepin, *Cosmic rays at ultra high energies (neutrino?)*, *Phys. Lett.* **B28** (1969) 423 .
- [66] M. Ahlers and F. Halzen, *Minimal cosmogenic neutrinos*, *Phys. Rev.* **D86** (2012) 083010 [[1208.4181](#)].
- [67] A. van Vliet, *CRPropa simulations, similar to PoS(ICRC2019)190, private communication* (2019) .
- [68] D. Bergmann for the Telescope Array Collaboration, *Combined Fit of the Spectrum and Composition from Telescope Array, PoS(ICRC2019)* (2019) 190.
- [69] A. Aab et al., *Combined fit of spectrum and composition data as measured by the Pierre Auger Observatory*, *JCAP* **2017** (2017) 038.
- [70] PIERRE AUGER, TELESCOPE ARRAY collaboration, *The energy spectrum of ultra-high energy cosmic rays measured at the Pierre Auger Observatory and at the Telescope Array*, *PoS ICRC2019* (2020) 234 [[2001.08811](#)].
- [71] C. Righi, A. Palladino, F. Tavecchio and F. Vissani, *EeV astrophysical neutrinos from flat spectrum radio quasars*, *Astron. Astrophys.* **642** (2020) A92 [[2003.08701](#)].
- [72] K. Murase and E. Waxman, *Constraining High-Energy Cosmic Neutrino Sources: Implications and Prospects*, *Phys. Rev.* **D94** (2016) 103006 [[1607.01601](#)].
- [73] S. Ando, M. R. Feyereisen and M. Fornasa, *How bright can the brightest neutrino source be?*, *Phys. Rev. D* **95** (2017) 103003 [[1701.02165](#)].
- [74] ICECUBE collaboration, *The contribution of Fermi-2LAC blazars to the diffuse TeV-PeV neutrino flux*, *Astrophys. J.* **835** (2017) 45 [[1611.03874](#)].

- [75] A. Neronov, D. V. Semikoz and K. Ptitsyna, *Strong constraints on hadronic models of blazar activity from Fermi and IceCube stacking analysis*, *Astron. Astrophys.* **603** (2017) A135 [[1611.06338](#)].
- [76] ICECUBE collaboration, *Results of IceCube searches for neutrinos from blazars using seven years of through-going muon data*, *PoS ICRC2017* (2018) 994 [[1710.01179](#)].
- [77] D. Hooper, T. Linden and A. Vieregg, *Active Galactic Nuclei and the Origin of IceCube’s Diffuse Neutrino Flux*, *JCAP* **1902** (2019) 012 [[1810.02823](#)].
- [78] ICECUBE collaboration, *Time-Integrated Neutrino Source Searches with 10 Years of IceCube Data*, *Phys. Rev. Lett.* **124** (2020) 051103 [[1910.08488](#)].
- [79] TELESCOPE ARRAY collaboration, *Indications of Intermediate-Scale Anisotropy of Cosmic Rays with Energy Greater Than 57 EeV in the Northern Sky Measured with the Surface Detector of the Telescope Array Experiment*, *Astrophys. J.* **790** (2014) L21 [[1404.5890](#)].
- [80] H.-N. He, A. Kusenko, S. Nagataki, B.-B. Zhang, R.-Z. Yang and Y.-Z. Fan, *Monte Carlo Bayesian search for the plausible source of the Telescope Array hotspot*, *Phys. Rev. D* **93** (2016) 043011 [[1411.5273](#)].
- [81] J. Quinn et al., *Detection of Gamma Rays with  $E > 300$  GeV from Markarian 501*, *Astrophys. Journ. Lett.* **456** (1996) L83.
- [82] M. Punch et al., *Detection of TeV photons from the active galaxy Markarian 421*, *Nature* **358** (1992) 477.
- [83] X.-Y. Wang and R.-Y. Liu, *Tidal disruption jets of supermassive black holes as hidden sources of cosmic rays: explaining the IceCube TeV-PeV neutrinos*, *Phys. Rev. D* **93** (2016) 083005 [[1512.08596](#)].
- [84] L. Dai and K. Fang, *Can tidal disruption events produce the IceCube neutrinos?*, *Mon. Not. Roy. Astron. Soc.* **469** (2017) 1354 [[1612.00011](#)].
- [85] N. Senno, K. Murase and P. Mészáros, *High-energy Neutrino Flares from X-Ray Bright and Dark Tidal Disruption Events*, *Astrophys. J.* **838** (2017) 3 [[1612.00918](#)].
- [86] C. Lunardini and W. Winter, *High Energy Neutrinos from the Tidal Disruption of Stars*, *Phys. Rev. D* **95** (2017) 123001 [[1612.03160](#)].
- [87] B. T. Zhang et al., *High-energy cosmic ray nuclei from tidal disruption events: Origin, survival, and implications*, *Phys. Rev. D* **96** (2017) 063007 [[1706.00391](#)].
- [88] D. Biehl et al., *Tidally disrupted stars as a possible origin of both cosmic rays and neutrinos at the highest energies*, *Sci. Rep.* **8** (2018) 10828 [[1711.03555](#)].
- [89] C. Guépin et al., *Ultra-High Energy Cosmic Rays and Neutrinos from Tidal Disruptions by Massive Black Holes*, *Astron. Astrophys.* **616** (2018) A179 [[1711.11274](#)].
- [90] K. Fang and B. D. Metzger, *High-Energy Neutrinos from Millisecond Magnetars formed from the Merger of Binary Neutron Stars*, *Astrophys. J.* **849** (2017) 153 [[1707.04263](#)].
- [91] S. S. Kimura, K. Murase, I. Bartos, K. Ioka, I. S. Heng and P. Mészáros, *Transejecta high-energy neutrino emission from binary neutron star mergers*, *Phys. Rev. D* **98** (2018) 043020.
- [92] E. Waxman and J. N. Bahcall, *High-energy neutrinos from cosmological gamma-ray burst fireballs*, *Phys. Rev. Lett.* **78** (1997) 2292 [[astro-ph/9701231](#)].
- [93] J. P. Rachen and P. Mészáros, *Photohadronic neutrinos from transients in astrophysical sources*, *Phys. Rev. D* **58** (1998) 123005 [[astro-ph/9802280](#)].

- [94] C. D. Dermer and A. Atoyan, *High energy neutrinos from gamma-ray bursts*, *Phys. Rev. Lett.* **91** (2003) 071102 [[astro-ph/0301030](#)].
- [95] D. Guetta et al., *Neutrinos from individual gamma-ray bursts in the BATSE catalog*, *Astropart. Phys.* **20** (2004) 429 [[astro-ph/0302524](#)].
- [96] S. Razzaque, P. Mészáros and E. Waxman, *Neutrino signatures of the supernova-gamma-ray burst relationship*, *Phys. Rev.* **D69** (2004) 023001 [[astro-ph/0308239](#)].
- [97] K. Murase and S. Nagataki, *High energy neutrino emission and neutrino background from gamma-ray bursts in the internal shock model*, *Phys. Rev.* **D73** (2006) 063002 [[astro-ph/0512275](#)].
- [98] K. Murase, *Prompt High-Energy Neutrinos from Gamma-Ray Bursts in the Photospheric and Synchrotron Self-Compton Scenarios*, *Phys. Rev.* **D78** (2008) 101302 [[0807.0919](#)].
- [99] X.-Y. Wang and Z.-G. Dai, *Prompt TeV neutrinos from dissipative photospheres of gamma-ray bursts*, *Astrophys. J.* **691** (2009) L67 [[0807.0290](#)].
- [100] P. Baerwald, S. Hummer and W. Winter, *Magnetic Field and Flavor Effects on the Gamma-Ray Burst Neutrino Flux*, *Phys. Rev.* **D83** (2011) 067303 [[1009.4010](#)].
- [101] M. Ahlers, M. C. Gonzalez-Garcia and F. Halzen, *GRBs on probation: testing the UHE CR paradigm with IceCube*, *Astropart. Phys.* **35** (2011) 87 [[1103.3421](#)].
- [102] K. Murase et al., *The Role of Stochastic Acceleration in the Prompt Emission of Gamma-Ray Bursts: Application to Hadronic Injection*, *Astrophys. J.* **746** (2012) 164 [[1107.5575](#)].
- [103] Z. Li, *Note on the Normalization of Predicted GRB Neutrino Flux*, *Phys. Rev.* **D85** (2012) 027301 [[1112.2240](#)].
- [104] S. Hummer, P. Baerwald and W. Winter, *Neutrino Emission from Gamma-Ray Burst Fireballs, Revised*, *Phys. Rev. Lett.* **108** (2012) 231101 [[1112.1076](#)].
- [105] H.-N. He et al., *IceCube non-detection of GRBs: Constraints on the fireball properties*, *Astrophys. J.* **752** (2012) 29 [[1204.0857](#)].
- [106] B. Zhang and P. Kumar, *Model-dependent high-energy neutrino flux from Gamma-Ray Bursts*, *Phys. Rev. Lett.* **110** (2013) 121101 [[1210.0647](#)].
- [107] R.-Y. Liu and X.-Y. Wang, *Diffuse PeV neutrinos from gamma-ray bursts*, *Astrophys. J.* **766** (2013) 73 [[1212.1260](#)].
- [108] S. Gao, K. Kashiyama and P. Mészáros, *On the neutrino non-detection of GRB 130427A*, *Astrophys. J.* **772** (2013) L4 [[1305.6055](#)].
- [109] M. Petropoulou, *The role of hadronic cascades in GRB models of efficient neutrino production*, *Mon. Not. Roy. Astron. Soc.* **442** (2014) 3026 [[1405.7669](#)].
- [110] M. Petropoulou, D. Giannios and S. Dimitrakoudis, *Implications of a PeV neutrino spectral cutoff in GRB models*, *Mon. Not. Roy. Astron. Soc.* **445** (2014) 570 [[1405.2091](#)].
- [111] M. Bustamante et al., *Neutrino and cosmic-ray emission from multiple internal shocks in gamma-ray bursts*, *Nature Commun.* **6** (2015) 6783 [[1409.2874](#)].
- [112] X.-Y. Wang, S. Razzaque and P. Mészáros, *On the Origin and Survival of UHE Cosmic-Ray Nuclei in GRBs and Hypernovae*, *Astrophys. J.* **677** (2008) 432 [[0711.2065](#)].
- [113] K. Murase et al., *High-energy cosmic-ray nuclei from high- and low-luminosity gamma-ray bursts and implications for multi-messenger astronomy*, *Phys. Rev.* **D78** (2008) 023005 [[0801.2861](#)].

- [114] A. Calvez, A. Kusenko and S. Nagataki, *The role of Galactic sources and magnetic fields in forming the observed energy-dependent composition of ultrahigh-energy cosmic rays*, *Phys. Rev. Lett.* **105** (2010) 091101 [[1004.2535](#)].
- [115] N. Globus et al., *UHECR acceleration at GRB internal shocks*, *Mon. Not. Roy. Astron. Soc.* **451** (2015) 751 [[1409.1271](#)].
- [116] D. Biehl et al., *Cosmic-Ray and Neutrino Emission from Gamma-Ray Bursts with a Nuclear Cascade*, *Astron. Astrophys.* **611** (2018) A101 [[1705.08909](#)].
- [117] B. Paczynski and G. H. Xu, *Neutrino bursts from gamma-ray bursts*, *Astrophys. J.* **427** (1994) 708.
- [118] I. Bartos et al., *Detection Prospects for GeV Neutrinos from Collisionally Heated Gamma-ray Bursts with IceCube/DeepCore*, *Phys. Rev. Lett.* **110** (2013) 241101 [[1301.4232](#)].
- [119] K. Murase, K. Kashiyama and P. Mészáros, *Subphotospheric Neutrinos from Gamma-Ray Bursts: The Role of Neutrons*, *Phys. Rev. Lett.* **111** (2013) 131102 [[1301.4236](#)].
- [120] K. Murase and S. Nagataki, *High Energy Neutrino Flash from Far-UV/X-ray Flares of Gamma-Ray Bursts*, *Phys. Rev. Lett.* **97** (2006) 051101 [[astro-ph/0604437](#)].
- [121] E. Waxman and J. N. Bahcall, *Neutrino afterglow from gamma-ray bursts: Similar to  $10^{18}$  eV*, *Astrophys. J.* **541** (2000) 707 [[hep-ph/9909286](#)].
- [122] C. D. Dermer, *Neutrino, neutron, and cosmic ray production in the external shock model of gamma-ray bursts*, *Astrophys. J.* **574** (2002) 65 [[astro-ph/0005440](#)].
- [123] S. Razzaque, *Long-lived PeV–EeV neutrinos from gamma-ray burst blastwave*, *Phys. Rev.* **D88** (2013) 103003 [[1307.7596](#)].
- [124] K. Murase et al., *High Energy Neutrinos and Cosmic-Rays from Low-Luminosity Gamma-Ray Bursts?*, *Astrophys. J.* **651** (2006) L5 [[astro-ph/0607104](#)].
- [125] N. Gupta and B. Zhang, *Neutrino Spectra from Low and High Luminosity Populations of Gamma Ray Bursts*, *Astropart. Phys.* **27** (2007) 386 [[astro-ph/0606744](#)].
- [126] N. Senno, K. Murase and P. Mészáros, *Choked Jets and Low-Luminosity Gamma-Ray Bursts as Hidden Neutrino Sources*, *Phys. Rev.* **D93** (2016) 083003 [[1512.08513](#)].
- [127] B. T. Zhang et al., *Low-luminosity gamma-ray bursts as the sources of ultrahigh-energy cosmic ray nuclei*, *Phys. Rev. D* **97** (2018) 083010 [[1712.09984](#)].
- [128] B. T. Zhang and K. Murase, *Ultrahigh-energy cosmic-ray nuclei and neutrinos from engine-driven supernovae*, 2018.
- [129] ANITA collaboration, *The First Limits on the Ultra-high Energy Neutrino Fluence from Gamma-ray Bursts*, *Astrophys. J.* **736** (2011) 50 [[1102.3206](#)].
- [130] S. S. Kimura, . Murase, P. Mészáros and K. Kiuchi, *High-Energy Neutrino Emission from Short Gamma-Ray Bursts: Prospects for Coincident Detection with Gravitational Waves*, *Astrophys. J.* **848** (2017) L4 [[1708.07075](#)].
- [131] K. Fang and B. D. Metzger, *High-Energy Neutrinos from Millisecond Magnetars formed from the Merger of Binary Neutron Stars*, *Astrophys. J.* **849** (2017) 153 [[1707.04263](#)].
- [132] X. Rodrigues et al., *Multi-wavelength and neutrino emission from blazar pks 1502+ 106*, *arXiv preprint* (2020) [[2009.04026](#)].

- [133] A. Connolly, R. S. Thorne and D. Waters, *Calculation of High Energy Neutrino-Nucleon Cross Sections and Uncertainties Using the MSTW Parton Distribution Functions and Implications for Future Experiments*, *Phys. Rev.* **D83** (2011) 113009 [[1102.0691](#)].
- [134] A. Cooper-Sarkar, P. Mertsch and S. Sarkar, *The high energy neutrino cross-section in the Standard Model and its uncertainty*, *JHEP* **08** (2011) 042 [[1106.3723](#)].
- [135] V. Bertone, R. Gauld and J. Rojo, *Neutrino Telescopes as QCD Microscopes*, *JHEP* **01** (2019) 217 [[1808.02034](#)].
- [136] I. Romero and O. A. Sampayo, *Leptoquarks signals in KM\*\*3 neutrino telescopes*, *JHEP* **05** (2009) 111 [[0906.5245](#)].
- [137] D. Hooper, *Measuring high-energy neutrino nucleon cross-sections with future neutrino telescopes*, *Phys. Rev.* **D65** (2002) 097303 [[hep-ph/0203239](#)].
- [138] S. R. Klein and A. Connolly, *Neutrino Absorption in the Earth, Neutrino Cross-Sections, and New Physics*, in *Proceedings, Community Summer Study 2013: Snowmass on the Mississippi (CSS2013): Minneapolis, MN, USA, July 29-August 6, 2013*, **1304.4891**.
- [139] J. Ellis, K. Sakurai and M. Spannowsky, *Search for Sphalerons: IceCube vs. LHC*, *JHEP* **05** (2016) 085 [[1603.06573](#)].
- [140] S. R. Klein, *Probing high-energy interactions of atmospheric and astrophysical neutrinos*, in *Particle Physics with Neutrino Telescopes*, pp. 75–107, World Scientific. ISBN: 978-981-3275-01-0, (2020), [1906.02221](#), DOI.
- [141] M. Bustamante, J. F. Beacom and W. Winter, *Theoretically palatable flavor combinations of astrophysical neutrinos*, *Phys. Rev. Lett.* **115** (2015) 161302 [[1506.02645](#)].
- [142] J. G. Learned and S. Pakvasa, *Detecting tau-neutrino oscillations at PeV energies*, *Astropart. Phys.* **3** (1995) 267 [[hep-ph/9405296](#)].
- [143] C. A. Argüelles, T. Katori and J. Salvado, *New Physics in Astrophysical Neutrino Flavor*, *Phys. Rev. Lett.* **115** (2015) 161303 [[1506.02043](#)].
- [144] I. M. Shoemaker and K. Murase, *Probing BSM Neutrino Physics with Flavor and Spectral Distortions: Prospects for Future High-Energy Neutrino Telescopes*, *Phys. Rev. D* **93** (2016) 085004 [[1512.07228](#)].
- [145] M. C. Gonzalez-Garcia, M. Maltoni, I. Martinez-Soler and N. Song, *Non-standard neutrino interactions in the Earth and the flavor of astrophysical neutrinos*, *Astropart. Phys.* **84** (2016) 15 [[1605.08055](#)].
- [146] R. W. Rasmussen, L. Lechner, M. Ackermann, M. Kowalski and W. Winter, *Astrophysical neutrinos flavored with Beyond the Standard Model physics*, *Phys. Rev. D* **96** (2017) 083018 [[1707.07684](#)].
- [147] M. Ahlers, M. Bustamante and S. Mu, *Unitarity Bounds of Astrophysical Neutrinos*, *Phys. Rev. D* **98** (2018) 123023 [[1810.00893](#)].
- [148] Y. Chikashige, R. N. Mohapatra and R. D. Peccei, *Spontaneously Broken Lepton Number and Cosmological Constraints on the Neutrino Mass Spectrum*, *Phys. Rev. Lett.* **45** (1980) 1926.
- [149] G. B. Gelmini, S. Nussinov and M. Roncadelli, *Bounds and Prospects for the Majoron Model of Left-handed Neutrino Masses*, *Nucl. Phys. B* **209** (1982) 157.
- [150] R. Tomas, H. Pas and J. W. F. Valle, *Generalized bounds on Majoron - neutrino couplings*, *Phys. Rev. D* **64** (2001) 095005 [[hep-ph/0103017](#)].

- [151] J. F. Beacom, N. F. Bell, D. Hooper, S. Pakvasa and T. J. Weiler, *Decay of High-Energy Astrophysical Neutrinos*, *Phys. Rev. Lett.* **90** (2003) 181301 [[hep-ph/0211305](#)].
- [152] P. Baerwald, M. Bustamante and W. Winter, *Neutrino Decays over Cosmological Distances and the Implications for Neutrino Telescopes*, *JCAP* **1210** (2012) 020 [[1208.4600](#)].
- [153] M. Bustamante, J. F. Beacom and K. Murase, *Testing decay of astrophysical neutrinos with incomplete information*, *Phys. Rev. D* **95** (2017) 063013 [[1610.02096](#)].
- [154] P. B. Denton and I. Tamborra, *Invisible Neutrino Decay Could Resolve IceCube’s Track and Cascade Tension*, *Phys. Rev. Lett.* **121** (2018) 121802 [[1805.05950](#)].
- [155] J. L. Feng, *Dark Matter Candidates from Particle Physics and Methods of Detection*, *Ann. Rev. Astron. Astrophys.* **48** (2010) 495 [[1003.0904](#)].
- [156] J. F. Beacom, N. F. Bell and G. D. Mack, *General Upper Bound on the Dark Matter Total Annihilation Cross Section*, *Phys. Rev. Lett.* **99** (2007) 231301 [[astro-ph/0608090](#)].
- [157] H. Yuksel, S. Horiuchi, J. F. Beacom and S. Ando, *Neutrino Constraints on the Dark Matter Total Annihilation Cross Section*, *Phys. Rev. D* **76** (2007) 123506 [[0707.0196](#)].
- [158] K. Murase and J. F. Beacom, *Constraining Very Heavy Dark Matter Using Diffuse Backgrounds of Neutrinos and Cascaded Gamma Rays*, *JCAP* **1210** (2012) 043 [[1206.2595](#)].
- [159] B. Feldstein, A. Kusenko, S. Matsumoto and T. T. Yanagida, *Neutrinos at IceCube from Heavy Decaying Dark Matter*, *Phys. Rev. D* **88** (2013) 015004 [[1303.7320](#)].
- [160] A. Esmaili and P. D. Serpico, *Are IceCube neutrinos unveiling PeV-scale decaying dark matter?*, *JCAP* **1311** (2013) 054 [[1308.1105](#)].
- [161] T. Higaki, R. Kitano and R. Sato, *Neutrinoful Universe*, *JHEP* **07** (2014) 044 [[1405.0013](#)].
- [162] C. Rott, K. Kohri and S. C. Park, *Superheavy dark matter and IceCube neutrino signals: Bounds on decaying dark matter*, *Phys. Rev. D* **92** (2015) 023529 [[1408.4575](#)].
- [163] E. Dudas, Y. Mambrini and K. A. Olive, *Monochromatic neutrinos generated by dark matter and the seesaw mechanism*, *Phys. Rev. D* **91** (2015) 075001 [[1412.3459](#)].
- [164] Y. Ema, R. Jinno and T. Moroi, *Cosmic-Ray Neutrinos from the Decay of Long-Lived Particle and the Recent IceCube Result*, *Phys. Lett. B* **733** (2014) 120 [[1312.3501](#)].
- [165] J. Zavala, *Galactic PeV neutrinos from dark matter annihilation*, *Phys. Rev. D* **89** (2014) 123516 [[1404.2932](#)].
- [166] K. Murase, R. Laha, S. Ando and M. Ahlers, *Testing the Dark Matter Scenario for PeV Neutrinos Observed in IceCube*, *Phys. Rev. Lett.* **115** (2015) 071301 [[1503.04663](#)].
- [167] L. A. Anchordoqui, V. Barger, H. Goldberg, X. Huang, D. Marfatia, L. H. M. da Silva et al., *IceCube neutrinos, decaying dark matter, and the Hubble constant*, *Phys. Rev. D* **92** (2015) 061301 [[1506.08788](#)].
- [168] S. M. Boucenna, M. Chianese, G. Mangano, G. Miele, S. Morisi, O. Pisanti et al., *Decaying Leptophilic Dark Matter at IceCube*, *JCAP* **1512** (2015) 055 [[1507.01000](#)].
- [169] P. S. B. Dev, D. Kazanas, R. N. Mohapatra, V. L. Teplitz and Y. Zhang, *Heavy right-handed neutrino dark matter and PeV neutrinos at IceCube*, *JCAP* **1608** (2016) 034 [[1606.04517](#)].
- [170] N. Hiroshima, R. Kitano, K. Kohri and K. Murase, *High-energy neutrinos from multibody decaying dark matter*, *Phys. Rev. D* **97** (2018) 023006 [[1705.04419](#)].

- [171] M. Chianese, G. Miele and S. Morisi, *Interpreting IceCube 6-year HESE data as an evidence for hundred TeV decaying Dark Matter*, *Phys. Lett. B* **773** (2017) 591 [[1707.05241](#)].
- [172] G. Amelino-Camelia, J. R. Ellis, N. E. Mavromatos, D. V. Nanopoulos and S. Sarkar, *Tests of quantum gravity from observations of gamma-ray bursts*, *Nature* **393** (1998) 763 [[astro-ph/9712103](#)].
- [173] D. Hooper, D. Morgan and E. Winstanley, *Lorentz and CPT invariance violation in high-energy neutrinos*, *Phys. Rev. D* **72** (2005) 065009 [[hep-ph/0506091](#)].
- [174] M. C. Gonzalez-Garcia, F. Halzen and M. Maltoni, *Physics Reach of High-Energy and High-Statistics IceCube Atmospheric Neutrino Data*, *Phys. Rev. D* **71** (2005) 093010 [[hep-ph/0502223](#)].
- [175] L. A. Anchordoqui et al., *Probing Planck scale physics with IceCube*, *Phys. Rev. D* **72** (2005) 065019 [[hep-ph/0506168](#)].
- [176] J. L. Bazo, M. Bustamante, A. M. Gago and O. G. Miranda, *High energy astrophysical neutrino flux and modified dispersion relations*, *Int. J. Mod. Phys. A* **24** (2009) 5819 [[0907.1979](#)].
- [177] M. Bustamante, A. M. Gago and C. Pena-Garay, *Energy-independent new physics in the flavour ratios of high-energy astrophysical neutrinos*, *JHEP* **04** (2010) 066 [[1001.4878](#)].
- [178] A. Kostelecky and M. Mewes, *Neutrinos with Lorentz-violating operators of arbitrary dimension*, *Phys. Rev. D* **85** (2012) 096005 [[1112.6395](#)].
- [179] J. S. Diaz, A. Kostelecky and M. Mewes, *Testing Relativity with High-Energy Astrophysical Neutrinos*, *Phys. Rev. D* **89** (2014) 043005 [[1308.6344](#)].
- [180] F. W. Stecker, S. T. Scully, S. Liberati and D. Mattingly, *Searching for Traces of Planck-Scale Physics with High Energy Neutrinos*, *Phys. Rev. D* **91** (2015) 045009 [[1411.5889](#)].
- [181] F. W. Stecker and S. T. Scully, *Propagation of Superluminal PeV IceCube Neutrinos: A High Energy Spectral Cutoff or New Constraints on Lorentz Invariance Violation*, *Phys. Rev. D* **90** (2014) 043012 [[1404.7025](#)].
- [182] G. Tomar, S. Mohanty and S. Pakvasa, *Lorentz Invariance Violation and IceCube Neutrino Events*, *JHEP* **11** (2015) 022 [[1507.03193](#)].
- [183] J. Ellis, N. E. Mavromatos, A. S. Sakharov and E. K. Sarkisyan-Grinbaum, *Limits on Neutrino Lorentz Violation from Multimessenger Observations of TXS 0506+056*, *Phys. Lett. B* **789** (2019) 352 [[1807.05155](#)].
- [184] R. Laha, *Constraints on neutrino speed, weak equivalence principle violation, Lorentz invariance violation, and dual lensing from the first high-energy astrophysical neutrino source TXS 0506+056*, [1807.05621](#).
- [185] J. Lykken, O. Mena and S. Razzaque, *Ultrahigh-energy neutrino flux as a probe of large extra-dimensions*, *JCAP* **0712** (2007) 015 [[0705.2029](#)].
- [186] K. Ioka and K. Murase, *IceCube PeV–EeV neutrinos and secret interactions of neutrinos*, *PTEP* **2014** (2014) 061E01 [[1404.2279](#)].
- [187] K. C. Y. Ng and J. F. Beacom, *Cosmic neutrino cascades from secret neutrino interactions*, *Phys. Rev. D* **90** (2014) 065035 [[1404.2288](#)].
- [188] K. Blum, A. Hook and K. Murase, *High energy neutrino telescopes as a probe of the neutrino mass mechanism*, [1408.3799](#).

- [189] W. Altmannshofer, C.-Y. Chen, P. S. Bhupal Dev and A. Soni, *Lepton flavor violating Z' explanation of the muon anomalous magnetic moment*, *Phys. Lett. B* **762** (2016) 389 [[1607.06832](#)].
- [190] G. Barenboim, P. B. Denton and I. M. Oldengott, *Constraints on inflation with an extended neutrino sector*, *Phys. Rev. D* **99** (2019) 083515 [[1903.02036](#)].
- [191] G. Askar’yan, *Excess negative charge of an electron-photon shower and its coherent radio emission*, *Sov. Phys. JETP* **14** (1962) 441.
- [192] PIERRE AUGER collaboration, *Probing the radio emission from air showers with polarization measurements*, *Phys. Rev. D* **89** (2014) 052002 [[1402.3677](#)].
- [193] P. Schellart et al., *Polarized radio emission from extensive air showers measured with LOFAR*, *JCAP* **10** (2014) 014 [[1406.1355](#)].
- [194] A. Connolly and A. G. Vieregg, *Radio Detection of High Energy Neutrinos*, *Neutrino Astronomy - Current status, future prospects*, Eds. T. Gaisser & A. Karle (World Scientific) (2017) 217 [[1607.08232](#)].
- [195] D. García-Fernández, A. Nelles and C. Glaser, *Signatures of secondary leptons in radio-neutrino detectors in ice*, *Phys. Rev. D* **102** (2020) 083011.
- [196] C. Glaser et al., *NuRadioMC: Simulating the radio emission of neutrinos from interaction to detector*, *Eur. Phys. J. C* **80** (2020) 77 [[1906.01670](#)].
- [197] J. Alvarez-Muñiz, A. Romero-Wolf and E. Zas, *Practical and accurate calculations of Askaryan radiation*, *Phys. Rev. D* **84** (2011) 103003 [[1106.6283](#)].
- [198] E. Zas, F. Halzen and T. Stanev, *Electromagnetic pulses from high-energy showers: Implications for neutrino detection*, *Phys. Rev. D* **45** (1992) 362.
- [199] T. Barrella, S. W. Barwick and D. Saltzberg, *Ross Ice Shelf in situ radio-frequency ice attenuation*, *J. Glaciol.* **57** (2011) 61 [[1011.0477](#)].
- [200] ANITA collaboration, *In situ radioglaciological measurements near Taylor Dome, Antarctica and implications for UHE neutrino astronomy*, *Astropart. Phys.* **29** (2008) 130 [[astro-ph/0703413](#)].
- [201] S. W. Barwick et al., *South Polar in situ radio-frequency ice attenuation*, *J. Glaciol.* **51** (2005) 231.
- [202] S. W. Barwick et al., *Observation of classically ‘forbidden’ electromagnetic wave propagation and implications for neutrino detection*, *JCAP* **1807** (2018) 055 [[1804.10430](#)].
- [203] ARIANNA collaboration, *Targeting ultra-high energy neutrinos with the ARIANNA experiment*, *Adv. Space Res.* **64** (2019) 2595 [[1903.01609](#)].
- [204] F. D. Kahn and I. Lerche, *Radiation from cosmic ray air showers*, *Proceedings of the Royal Society A* **289** (1966) .
- [205] H. Allan, *Low frequency radio emission from extensive air showers*, *Nature* **237** (1972) 384.
- [206] C. Welling, C. Glaser and A. Nelles, *Reconstructing the cosmic-ray energy from the radio signal measured in one single station*, *JCAP* **10** (2019) 075 [[1905.11185](#)].
- [207] K. Mulrey et al., *On the cosmic-ray energy scale of the LOFAR radio telescope*, *JCAP* **11** (2020) 017 [[2005.13441](#)].
- [208] K. D. de Vries et al., *The cosmic-ray air-shower signal in Askaryan radio detectors*, *Astropart. Phys.* **74** (2016) 96 [[1503.02808](#)].

- [209] A. Nelles, S. Buitink, H. Falcke, J. Hörandel, T. Huege and P. Schellart, *A parameterization for the radio emission of air showers as predicted by CoREAS simulations and applied to LOFAR measurements*, *Astropart. Phys.* **60** (2015) 13 [[1402.2872](#)].
- [210] ARIANNA collaboration, *Performance of the ARIANNA Hexagonal Radio Array*, *PoS ICRC2015* (2016) 1149 [[1509.00109](#)].
- [211] J. E. Carlstrom et al., *The 10 Meter South Pole Telescope*, *PASP* **123** (2011) 568 [[0907.4445](#)].
- [212] ICECUBE collaboration, *The IceCube Upgrade – Design and Science Goals*, *PoS ICRC2019* (2020) 1031 [[1908.09441](#)].
- [213] L. Gerhardt et al., *A prototype station for ARIANNA: a detector for cosmic neutrinos*, *Nucl. Instrum. Meth.* **A624** (2010) 85 [[1005.5193](#)].
- [214] J. Avva et al., *Development Toward a Ground-Based Interferometric Phased Array for Radio Detection of High Energy Neutrinos*, *Nucl. Instrum. Meth.* **A869** (2017) 46 [[1605.03525](#)].
- [215] U.S. Ice Drilling Program, *Agile Sub-Ice Geological Drill Operations and Maintenance Manual*, <https://icedrill.org/library/agile-sub-ice-geological-drill-operations-and-maintenance-manual> (2019) .
- [216] C. Glaser et al., *NuRadioReco: A reconstruction framework for radio neutrino detectors*, *Eur. Phys. J.* **C79** (2019) 464 [[1903.07023](#)].
- [217] ARA collaboration, *First Constraints on the Ultra-High Energy Neutrino Flux from a Prototype Station of the Askaryan Radio Array*, *Astropart. Phys.* **70** (2015) 62 [[1404.5285](#)].
- [218] A. Romero-Wolf et al., *An interferometric analysis method for radio impulses from ultra-high energy particle showers*, *Astropart. Phys.* **60** (2015) 72.
- [219] S. I. Dutta, M. H. Reno, I. Sarcevic and D. Seckel, *Propagation of muons and taus at high-energies*, *Phys. Rev.* **D63** (2001) 094020 [[hep-ph/0012350](#)].
- [220] J.-H. Koehne et al., *PROPOSAL: A tool for propagation of charged leptons*, *Computer Physics Communications* **184** (2013) 2070 .
- [221] T. Gaisser, D. Soldin, A. Fedynitch and A. Crossman, *Precision of analytical approximations in calculations of atmospheric leptons*, in *PoS 36th ICRC*, 2019, [1910.08676](#).
- [222] H. P. Dembinski, R. Engel, A. Fedynitch, T. Gaisser, F. Riehn and T. Stanev, *Data-driven model of the cosmic-ray flux and mass composition from 10 GeV to  $10^{11}$  GeV*, *PoS ICRC2017* (2018) 533 [[1711.11432](#)].
- [223] J. Roberts et al., *LAB4D: A low power, multi-GSa/s, transient digitizer with sampling timebase trimming capabilities*, *Nucl. Instrum. Meth.* **A925** (2019) 92 [[1803.04600](#)].
- [224] UNAVCO, *Remote station engineering - power systems*, <https://www.unavco.org/projects/project-support/polar/remote/power/power.html> (2014) (accessed July 2019).
- [225] K. Steffen, J. Box and W. Abdalati, *Greenland climate network: GC-Net*, US Army Cold Regions Research and Engineering (CRREL), CRREL Special Report (1996) 98.
- [226] NOAA, *Global Monitoring Laboratory*, <https://www.esrl.noaa.gov/gmd/dv/data.html> (2020) .
- [227] LoRA Alliance, *LoRaWAN Specification v. 1.03*, 2018.
- [228] private communication, British Antarctic Survey (BAS).

- [229] J. A. Johnson et al., *A new 122 mm electromechanical drill for deep ice-sheet coring (DISC): 5. Experience during Greenland field testing*, *Annals of Glaciology* **47** (2007) 54–60.
- [230] A. Corstanje et al., *Timing calibration and spectral cleaning of LOFAR time series data*, *Astron. Astrophys.* **590** (2016) A41 [[1603.08354](#)].
- [231] PIERRE AUGER collaboration, *Nanosecond-level time synchronization of autonomous radio detector stations for extensive air showers*, *JINST* **11** (2016) P01018 [[1512.02216](#)].
- [232] P. Meade, *jade: An End-To-End Data Transfer and Catalog Tool*, *Journal of Physics: Conference Series* **898** (2017) 062050.
- [233] T. Huege, M. Ludwig and C. James, *Simulating radio emission from air showers with CoREAS*, *AIP Conf. Proc.* **1535** (2013) 128 [[1301.2132](#)].
- [234] J. Alvarez-Muniz, J. Carvalho, Washington R. and E. Zas, *Monte Carlo simulations of radio pulses in atmospheric showers using ZHAireS*, *Astropart. Phys.* **35** (2012) 325 [[1107.1189](#)].
- [235] PIERRE AUGER collaboration, *Advanced Functionality for Radio Analysis in the Offline Software Framework of the Pierre Auger Observatory*, *Nucl. Instrum. Meth. A* **635** (2011) 92 [[1101.4473](#)].
- [236] K. Dookayka, *Characterizing the Search for Ultra-High Energy Neutrinos with the ARIANNA Detector*, Ph.D. thesis, University of California, Irvine, 2011.
- [237] ANITA collaboration, *The Simulation of the Sensitivity of the Antarctic Impulsive Transient Antenna (ANITA) to Askaryan Radiation from Cosmogenic Neutrinos Interacting in the Antarctic Ice*, *JINST* **14** (2019) P08011 [[1903.11043](#)].
- [238] B. Hokanson-Fasig, *Design Studies for the Radio Neutrino Observatory (RNO)*, *PoS (ICRC2019)* **913** (2019) .
- [239] REMCOM, *XFdtd 3D Electromagnetic Simulation Software*, <https://www.remcom.com/xfdtd-3d-em-simulation-software> (2020) .
- [240] J. Alvarez-Muñiz, P. M. Hansen, A. Romero-Wolf and E. Zas, *Askaryan radiation from neutrino-induced showers in ice*, *Phys. Rev. D* **101** (2020) 083005.
- [241] PIERRE AUGER collaboration, *Improved limit to the diffuse flux of ultrahigh energy neutrinos from the Pierre Auger Observatory*, *Phys. Rev. D* **91** (2015) 092008 [[1504.05397](#)].
- [242] ICECUBE collaboration, *A Measurement of the Diffuse Astrophysical Muon Neutrino Flux Using Eight Years of IceCube Data*, *PoS ICRC2017* (2017) 1005 [[1710.01191](#)].
- [243] G. J. Feldman and R. D. Cousins, *A Unified approach to the classical statistical analysis of small signals*, *Phys. Rev. D* **57** (1998) 3873 [[physics/9711021](#)].
- [244] L. D. Landau and I. Pomeranchuk, *Limits of applicability of the theory of bremsstrahlung electrons and pair production at high-energies*, *Dokl. Akad. Nauk Ser. Fiz.* **92** (1953) 535.
- [245] A. B. Migdal, *Bremsstrahlung and pair production in condensed media at high-energies*, *Phys. Rev.* **103** (1956) 1811.
- [246] L. Gerhardt and S. R. Klein, *Electron and photon interactions in the regime of strong Landau-Pomeranchuk-Migdal suppression*, *Phys. Rev. D* **82** (2010) 074017.
- [247] M. Selig, M. R. Bell, H. Junklewitz, N. Oppermann, M. Reinecke, M. Greiner et al., *NIFTY - Numerical Information Field Theory. A versatile PYTHON library for signal inference*, *Astronomy & Astrophysics* **554** (2013) A26 [[1301.4499](#)].

- [248] J. Yang et al., *GRB 200415A: A Short Gamma-Ray Burst from a Magnetar Giant Flare?*, *Astrophys. J.* **899** (2020) 106 [[2010.05128](#)].
- [249] S. van Velzen et al., *Seventeen Tidal Disruption Events from the First Half of ZTF Survey Observations: Entering a New Era of Population Studies*, *arXiv preprint* (2020) [[2001.01409](#)].
- [250] IceCube Collaboration, *IceCube-190730A - IceCube observation of a high-energy neutrino candidate event*, *GRB Coordinates Network* **25225** (2019) 1.
- [251] A. Franckowiak et al., *Patterns in the Multiwavelength Behavior of Candidate Neutrino Blazars*, *Astrophys. J.* **893** (2020) 162 [[2001.10232](#)].

# Probing the angular and polarization reconstruction of the ARIANNA detector at the South Pole

---

## ARIANNA collaboration

**A. Anker<sup>a</sup> S. W. Barwick<sup>a</sup> H. Bernhoff<sup>b</sup> D. Z. Besson<sup>c,d</sup> N. Bingefors<sup>e</sup> D. García-Fernández<sup>f,g</sup> G. Gaswint<sup>a,1</sup> C. Glaser<sup>a,e</sup> A. Hallgren<sup>e</sup> J. C. Hanson<sup>h</sup> S. R. Klein<sup>i</sup> S. A. Kleinfelder<sup>j</sup> R. Lahmann<sup>a,g</sup> U. Latif<sup>c</sup> Z. S. Meyers<sup>f,g</sup> J. Nam<sup>k</sup> A. Novikov<sup>c</sup> A. Nelles<sup>f,g</sup> M. P. Paul<sup>a</sup> C. Persichilli<sup>a</sup> I. Plaisier<sup>f,g</sup> J. Tatar<sup>a,l</sup> S.-H. Wang<sup>k</sup> C. Welling<sup>f,g</sup>**

<sup>a</sup>*Department of Physics and Astronomy, University of California, Irvine, CA 92697, USA*

<sup>b</sup>*Uppsala University Department of Engineering Sciences, Division of Electricity, Uppsala, SE-752 37 Sweden*

<sup>c</sup>*Department of Physics and Astronomy, University of Kansas, Lawrence, KS 66045, USA*

<sup>d</sup>*National Research Nuclear University MEPhI (Moscow Engineering Physics Institute), Moscow 115409, Russia*

<sup>e</sup>*Uppsala University Department of Physics and Astronomy, Uppsala, SE-752 37, Sweden*

<sup>f</sup>*DESY, 15738 Zeuthen, Germany*

<sup>g</sup>*ECAP, Friedrich-Alexander-Universität Erlangen-Nürnberg, 91058 Erlangen, Germany*

<sup>h</sup>*Whittier College Department of Physics, Whittier, CA 90602, USA*

<sup>i</sup>*Lawrence Berkeley National Laboratory, Berkeley, CA 94720, USA*

<sup>j</sup>*Department of Electrical Engineering and Computer Science, University of California, Irvine, CA 92697, USA*

<sup>k</sup>*Department of Physics and Leung Center for Cosmology and Particle Astrophysics, National Taiwan University, Taipei 10617, Taiwan*

<sup>l</sup>*Research Cyberinfrastructure Center, University of California, Irvine, CA 92697 USA*

*E-mail:* [ggaswint@uci.edu](mailto:ggaswint@uci.edu), [sbarwick@uci.edu](mailto:sbarwick@uci.edu), [christian.glaser@physics.uu.se](mailto:christian.glaser@physics.uu.se)

---

<sup>1</sup>Corresponding author

**ABSTRACT:** The sources of ultra-high energy (UHE) cosmic rays, which can have energies up to  $10^{20}$  eV, remain a mystery. UHE neutrinos may provide important clues to understanding the nature of cosmic-ray sources. ARIANNA aims to detect UHE neutrinos via radio (Askaryan) emission from particle showers when a neutrino interacts with ice, which is an efficient method for neutrinos with energies between  $10^{16}$  eV and  $10^{20}$  eV. The ARIANNA radio detectors are located in Antarctic ice just beneath the surface. Neutrino observation requires that radio pulses propagate to the antennas at the surface with minimum distortion by the ice and firn medium. Using the residual hole from the South Pole Ice Core Project, radio pulses were emitted from a transmitter located up to 1.7 km below the snow surface. By measuring these signals with an ARIANNA surface station, the angular and polarization reconstruction abilities are quantified, which are required to measure the direction of the neutrino. After deconvolving the raw signals for the detector response and attenuation from propagation through the ice, the signal pulses show no significant distortion and agree with a reference measurement of the emitter made in an anechoic chamber. Furthermore, the signal pulses reveal no significant birefringence for our tested geometry of mostly vertical ice propagation. The origin of the transmitted radio pulse was measured with an angular resolution of  $0.37^\circ$  indicating that the neutrino direction can be determined with good precision if the polarization of the radio-pulse can be well determined. In the present study we obtained a resolution of the polarization vector of  $2.7^\circ$ . Neither measurement show a significant offset relative to expectation.

---

## Contents

<b>1</b>	<b>Introduction</b>	<b>1</b>
<b>2</b>	<b>Measurement Setup</b>	<b>3</b>
2.1	Geometry and ARIANNA station at South Pole	3
2.2	Characteristics of the signal transmitter and ice propagation	4
2.2.1	Anechoic chamber measurement of signal emitter	4
2.2.2	Calculation of incoming signal direction	6
<b>3</b>	<b>Processing of data taken in the field</b>	<b>7</b>
3.1	Main processing steps	7
3.2	In-situ calibration of cable delays	8
<b>4</b>	<b>Direction reconstruction and angular resolution</b>	<b>8</b>
<b>5</b>	<b>Measurement and interpretation of the signal polarization</b>	<b>12</b>
5.1	Polarization reconstruction and resolution	13
5.2	Polarization-dependent birefringence	17
<b>6</b>	<b>Discussion and Conclusion</b>	<b>19</b>
<b>7</b>	<b>Acknowledgements</b>	<b>20</b>

---

## 1 Introduction

Ultra-high-energy (UHE) neutrino detection probes the universe at energy scales beyond the reach of photons, giving astrophysics unique insights in the observation and location of extreme astrophysical sources. These extreme sources can shed light on outstanding questions in astrophysics, in particular what the sources of UHE cosmic rays are [1, 2]. This is because UHE cosmic rays at or near the source can interact hadronically with the surrounding media, or with photons of the cosmic microwave background, ultimately producing astrophysical or cosmogenic neutrinos, respectively, from charged pion decay [3, 4]. Using charged cosmic rays such as protons and heavier nuclei to find sources instead of neutrinos is problematic as they are deflected by galactic, and extra-galactic magnetic fields, scrambling their source direction. Neutrinos, however, are electrically neutral and therefore travel in straight paths. This makes neutrino detection an excellent candidate for identifying the sources of UHE cosmic rays. In order to find these sources, it is crucial for a neutrino detector to be able to reconstruct the neutrino direction with excellent precision [5, 6].

The aim of the ARIANNA detector [7] is to search for these sources of UHE neutrinos. ARIANNA complements IceCube [2] in extending the reach of neutrino detection to energies greater than  $10^{17}$  eV. In this energy range, the most effective means of measurement is through

radio Askaryan radiation [8, 9] created when UHE neutrinos interact within a dielectric medium. Ice is a dense and relatively transparent dielectric medium for radio waves due to an attenuation length on the order of a kilometer [10]. Naturally, the large sheets of ice found in (Ant)arctic regions serve as an excellent location for the ARIANNA detector. ARIANNA deploys autonomous detector stations with radio antennas placed just beneath the surface. The 1 km scale of the station spacing means that each station is an independent neutrino detector, thus maximizing the overall sensitivity. Currently, ARIANNA has nine detector stations in Moore’s Bay, Antarctica, and two additional detector stations located at the South Pole.

To reconstruct the direction of a neutrino, ARIANNA needs to be able to measure the incoming signal direction and polarization as well as the viewing angle, i.e., the angle at which the particle shower is observed with respect to the Cherenkov angle [11]. Since the density of Antarctic ice varies near the surface ‘firn’, radio signals bend as they propagate up towards the ARIANNA surface detector. Thus, one needs to be able to model accurately how the ice affects the radio signal during propagation. This paper will focus on ARIANNA’s ability to reconstruct the angular direction and polarization from a source deep in the ice. These reconstruction capabilities are also an important ingredient in the energy reconstruction [11].

The angular and polarization reconstruction accuracy of the ARIANNA station has been studied previously for the stations on the Ross Ice Shelf [12]. Calibration transmitter antennas buried slightly below the ice surface emitted radio pulses toward the bottom water-ice interface at Moore’s Bay. The absolute measurement of the arrival direction of the reflected signal agreed with expectation to within 1 degree or better [13]. Reflected signals also demonstrated that polarization of the electric field was preserved during propagation and reflection [12]. Though these studies were encouraging, they were mostly confined to nearly vertical propagation. The new data presented in this paper extends those prior studies to include a range of more representative propagation directions for neutrino-induced radio signals.

Another test of the angular and polarization reconstruction was performed with ARIANNA by observing cosmic rays [14]. Cosmic ray interactions in the atmosphere generate radio pulses, which are well-understood (e.g. [15, 16]). Hence, such cosmic rays act as an in-situ calibration source. These signals are more representative of neutrinos than the previous study in that the signal-to-noise ratio and frequency-content are neutrino-like. The pulse forms are very similar; air showers and in-ice particle showers both produce short bipolar pulses with frequencies of order  $O(100\text{ MHz})$ . Those ARIANNA stations configured with upward-facing LPDAs reconstruct the polarization and direction of incoming radio pulses over a much broader range of incoming angles and physical conditions than the previous study (see also [11, 14]). A newly developed forward folding technique was used to reconstruct the 3 dimensional electric-field pulse from the measured voltages [17]. The reconstructed polarization shows a resolution of  $7.06^\circ$  around the theoretical expectation [11, 14]. That study uses signals from the air, which excludes any effects from the ice. ARIANNA searches for neutrinos coming from the ice, however, and thus a test of the effects of the ice is crucial.

For such a test, a radio pulser was lowered in a fluid-filled hole provided by the South Pole Ice Coring Experiment (SPICE) to a depth of 1.7 km [18]. The main focus of this paper will be to test systematic uncertainties of the direction and polarization reconstruction from ice propagation and detector calibration using this SPICE data set, and with this, determine the capabilities of the

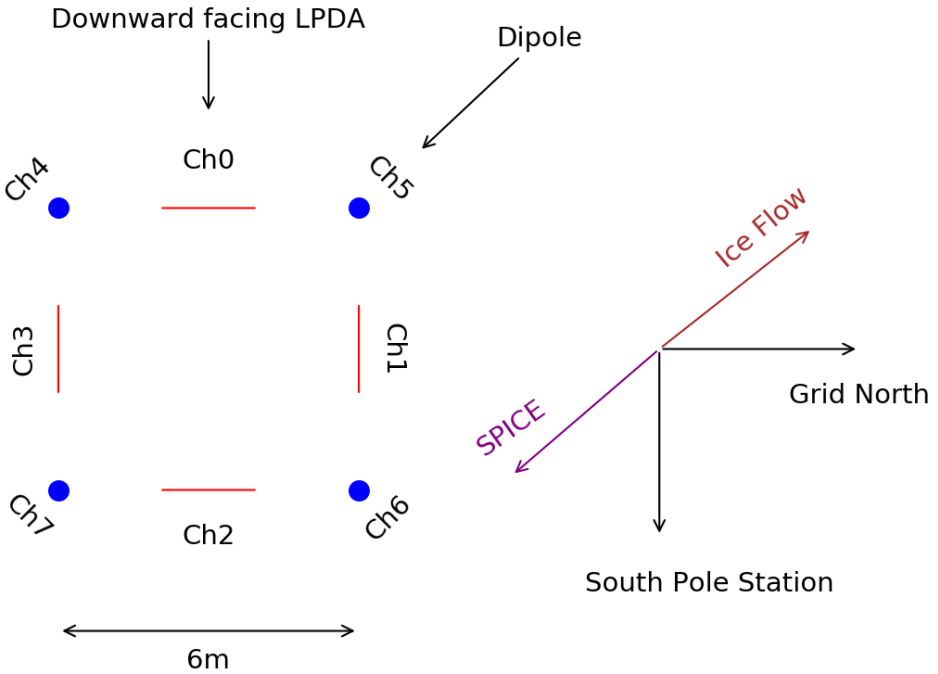


**Figure 1.** Overhead view of station 51 layout with direction to SPICE hole. Channels 0-3 are the 4 downward facing LPDAs buried beneath the surface, and channels 4-7 are the 4 vertically-oriented dipole antennas also buried beneath the surface. The angle between the ice flow direction (see 5.2) and signals coming from the SPICE borehole is  $1.4^\circ$ .

ARIANNA detector to resolve the direction of an incoming neutrino.

## 2 Measurement Setup

Data used for this measurement were collected by an ARIANNA South Pole station, which will be referred to as station 51 throughout this paper, during the last week of December, 2018. The signal transmitter (IDL-1 pulser [19]) was connected to a bicone antenna which was lowered to a depth of 1.7 km inside the SPICE hole and was vertically-oriented (to match the form-factor of the SPICE hole) [18]. The IDL-1 pulser broadcasts short duration radio frequency pulses through the bicone antenna with a repetition rate of 1 Hz, which is then detected by the ARIANNA station. Several thousand pulser events were directly transferred over the Iridium satellite network for offline analysis of the angular and polarization reconstruction capabilities of ARIANNA.

### 2.1 Geometry and ARIANNA station at South Pole

Station 51 is located roughly 1 km from South Pole Station and 0.65 km from the SPICE hole. Although there are no direct measurements, it is nevertheless plausible that the SPICE hole may be tilted by  $1^\circ$  which translates to a systematic uncertainty in the relative position of the emitter

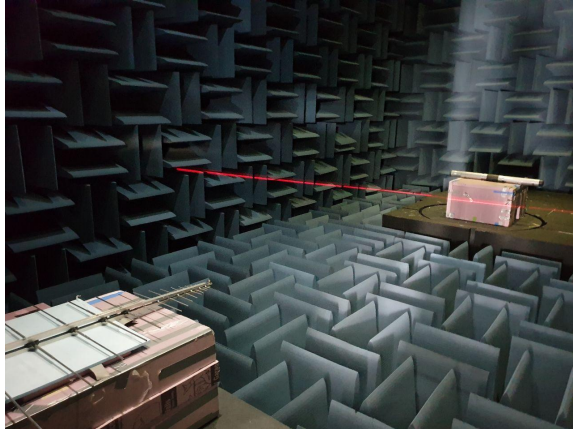


**Figure 2.** Photo of the anechoic chamber experimental setup. The transmitting bicone antenna was rotated horizontally. The receiving LPDA antenna was orientated in two ways for every measurement. The first orientation being what is shown in the photo (tines laid horizontally), and the second orientation had the tines vertically oriented which was stabilized with foam bricks.

with respect to the detector station, which in turn results in a systematic uncertainty in the predicted signal arrival direction.

Station 51 is equipped with 8 antennas [20]. Four of these are down-facing (nose pointing at  $180^\circ$  from zenith) Create CLP5130-2N log-periodic dipole arrays (LPDAs) oriented in a square pattern with 6 m sides. The longest ( $\frac{\lambda}{2}$ ) dipole is 1.45 m, and the length ratio of adjacent dipoles is 0.83. The boom holding the dipoles in place has a length of 1.385 m, and the cable feed point is at the shortest dipole [21]. The top of the LPDAs were located during deployment at a depth of 0.5 m into the firn and is subject to snow accumulation. Additionally, there are four vertically-oriented Kansas University bicone antennas located at the corners of the square. The bicone antennas are 0.52 m in length, with the cable feed point at the top. The top of the bicone antennas were also located at a depth of 0.5 m. The LPDAs provide two orthogonal Hpol (polarization parallel to the surface) measurements, whereas the bicones measure the Vpol component (vertical polarization). We provide a layout of station 51 in Fig. 1.

## 2.2 Characteristics of the signal transmitter and ice propagation

The characteristics of the signal transmitter were tested in an anechoic chamber and combined with simulations of the known ice effects on signal propagation from transmitter to receiver in the SPICE run [22, 23].

### 2.2.1 Anechoic chamber measurement of signal emitter

The IDL-1 pulser with the same bicone antenna used in the SPICE measurements, and an ARIANNA LPDA receiver were set up in an anechoic chamber to make a prediction for the polarization expected in the SPICE data. The separation distance between receiver and transmitter in the anechoic chamber was 3 m and the data recorded with a 5 GSa/s sampling oscilloscope. The anechoic chamber has dimensions 11.58 m x 7.29 m x 7.36 m [24]. Fig. 2 shows an image of the measurement setup.

To test the polarization calibration as a function of launch angle, the transmitting antenna was rotated between  $0^\circ$  and  $90^\circ$  in the horizontal plane while the receiving LPDA was pointing towards the dipole antenna and orientated either at  $0^\circ$  (tines parallel to ground) or  $90^\circ$  (tines perpendicular to ground). This allowed us to capture the two polarization components of the emitted electric field for a range of launch angles. For each setup, 10 individual measurements were recorded.

The anechoic chamber data are processed in the same way as the SPICE data, as described in the next section. To account for the difference in dielectric environments, after reconstructing the anechoic chamber electric-field, the frequency content is shifted from an in-air medium to an in-ice medium by dividing by the index of refraction of deep ice ( $n = 1.78$ ). Shifting the frequencies by  $\frac{1}{n}$  serves as a first-order approximation since the antenna is wavelength-resonant; to convert from a wavelength to a frequency in a different medium, a factor of  $n$  must be applied [17]. After performing this frequency correction, a rectangular band pass filter between 80 MHz to 300 MHz is applied in order to remove unwanted noise. Lastly, the signals are up-sampled to 50 GHz for better time resolution.

An example of a transmitted pulse taken from the anechoic chamber, following these corrections, is shown in Fig. 3. This example pulse was emitted at an angle of  $60^\circ$  off the direction of maximal gain (a typical geometry in the SPICE data). The electric field is mainly theta-polarized (polarized along the main symmetry axis of the dipole). This serves as a baseline signal for the ARIANNA polarization reconstruction. Defining the polarization as the angle between the energy fluence of the theta and phi polarization (see Sec. 5 for more details), the signal polarization measurement derived from the average of the calculated electric-field magnitudes from the 10 measured voltages for each polarization captured for a given geometry is shown in Fig. 4, which shows that the polarization reconstruction relevant for the launch angles in the SPICE experiment are between  $8^\circ$  to  $10^\circ$  (highlighted by the green band).

We note that this calibration signal is more difficult to reconstruct than a neutrino-induced signal for two reasons:

1. **Polarization:** The anechoic signal is almost entirely polarized in the theta direction. Therefore, the noise in the weaker phi component will have a large influence on the polarization reconstruction. For neutrinos, the signals are expected to have comparable theta and phi content.
2. **Pulse shape:** The phi component of the anechoic chamber signals have an extended pulse form, and with different frequency content compared to the theta component. A minimum integration window of 70 ns is necessary to sufficiently capture both components. Neutrinos will have signals with polarization projections equal in both length and frequency and differing only in amplitude between the two components. Therefore the polarization reconstruction will not strongly depend on the integration window and frequency cut.

With this in mind, this analysis can be considered a lower bound on the polarization reconstruction capabilities of neutrino signals, which should give cleaner signals.

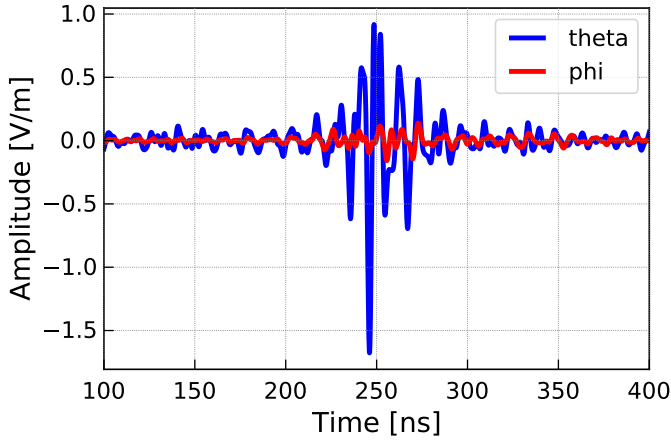


**Figure 3.** Observed electric-field from the IDL-1 pulser at an angle of  $30^\circ$  off boresight and captured inside an anechoic chamber. The LPDA antenna acts as receiver and a bicone antenna was used as the emitter. The LPDA antenna response was factored out of the voltage traces to obtain the electric-field. The theta polarization corresponds to the polarization along the axis of the dipole, while phi polarization is the cross polarized component.

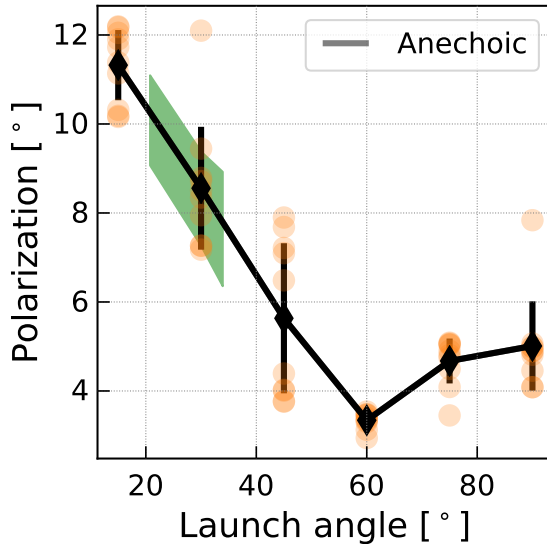


**Figure 4.** Expected polarization angle of the received electric field as a function of transmitted angle with respect to the main symmetry axis of the dipole. The orange data points are the polarization angle's found from using a single pair of voltage measurements. The black data points are the averages of the orange data, with the error bars being the standard deviation of the orange data points. Green shows the relevant transmitted angles for the SPICE data with a  $1\sigma$  spread based off of the 16% and 84% quantile.

### 2.2.2 Calculation of incoming signal direction

Testing the ARIANNA angular reconstruction capabilities requires an accurate model of how ice affects propagation. The density, and therefore the index-of-refraction, changes in the upper 200 m of the South Pole ice sheet from  $n = 1.78$  for deep ice to about  $n = 1.35$  at the surface. As a

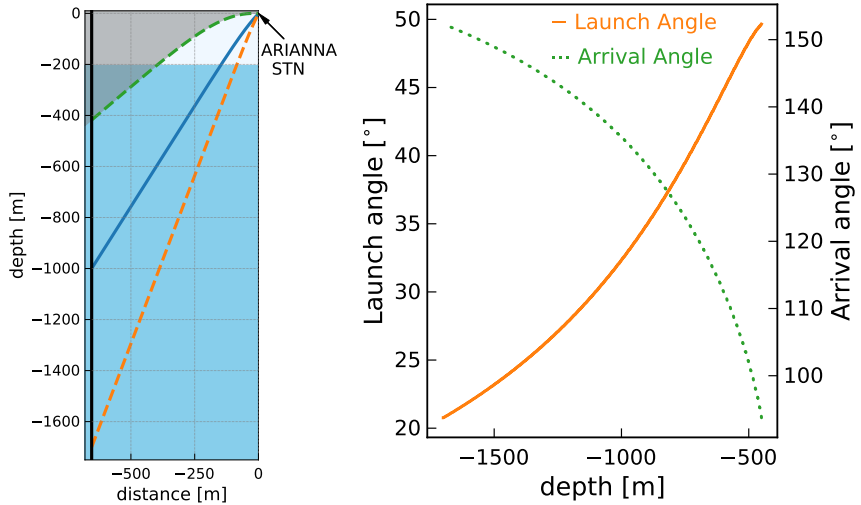


**Figure 5.** (Left) Ray tracing solution from a transmitter at depths 418 m, 1 km and 1.7 km to the South Pole ARIANNA station 51 calculated with the NuRadioMC code [23]. Light blue shaded region above 200 m is the firn layer, over which the ice approaches (within 2%) its nominal density. The grayed area is the shadow zone, from which classical propagation to the station is forbidden. The vertical black line on the y-axis represents the SPICE borehole. (Right) Expected arrival zenith angle and expected launch zenith angle as a function of transmitter depth. 180° corresponds to the nadir.

consequence, radio signals do not propagate rectilinearly but are refracted as illustrated in Fig. 5 [23]. We use an exponential index-of-refraction ( $n$ ) vs depth ( $z$ ) profile which provides a good description of  $n(z)$  data that was derived from density measurements [22, 25]. The gray shading indicates the range of positions of the transmitter that permit no classical propagation solutions, which is termed the 'shadow zone'. Signals in the shadow zone, bend back into the ice before reaching the ARIANNA detector. However, signals can be seen in the shadow zone through horizontal propagation, likely due to deviations from a purely exponential density profile [22, 26]. These effects are not discussed in this paper.

Three representative allowed solutions are displayed in Fig. 5 corresponding to pulser depths of 418 m, 1 km and 1.7 km. The right panel gives the expected arrival and launch zenith angle (measured with respect to 0 degrees zenith) at the ARIANNA station as a function of transmitter depth.

### 3 Processing of data taken in the field

This section describes how data from radio pulses emitted by the antenna in the SPICE hole are processed and which additional calibration steps had to be performed to reduce systematic uncertainties.

#### 3.1 Main processing steps

Four main processing steps are applied to all events from the measurement campaign from the SPICE borehole:

1. **Initial quality cut:** The readout electronics of the ARIANNA station become non-linear when the signal amplitude exceeds 600 mV. During the 2018 SPICE core run, events in the linear regime occur at depths greater than 800 m and only these events are retained for analysis.
2. **Band pass filter:** To reduce out-of-band noise, the frequency content of the events is restricted with a rectangular band pass filter to between 80 MHz (set by the frequency threshold of the receivers) and 300 MHz. This cut also reduces the influence of noise on the time correlations of the signal pulses, improving the accuracy of the direction reconstruction.
3. **Deconvolution of signal chain:** To properly compare measured data from different channels, the amplifier response is deconvolved along with time delays from cables and electronics (as measured in the lab).
4. **Upsampling:** The traces are up-sampled from 1 GHz to 50 GHz, using the Fourier method provided by resample from the scipy package in python [27], to improve the timing resolution. This allows us to correlate the signals to 0.02 ns accuracy.

### 3.2 In-situ calibration of cable delays

The cables in ARIANNA station 51 were measured with a precision of 0.5 ns. We can use the data itself to improve this calibration to about 0.1 ns by the following procedure. For each data point we calculate the expected propagation time from the emitter to each receiving antenna using the signal propagation (ray tracing) module of NuRadioMC [23]. Also for each data point, we calculate the time differences between the signal pulses received in the antennas (separately for the LPDAs and the dipoles) by cross-correlating the signal pulses against the signal pulse of one reference channel, chosen arbitrarily as channel 3 for the LPDAs and channel 6 for the dipoles. Knowing the source location and the ray trajectories, we then subtract the expected time delays from signal propagation from the measured time delays. We find largely constant time offsets that are compatible within the experimental uncertainties of the station calibration. The distributions are approximately Gaussian with offsets of up to 1 ns between channels and standard deviation up to  $\sim 0.1$  ns. The variation is much smaller than the mean offset, though there is a slight depth dependence that was not consistent between channels. The mean of the distribution is assumed to be associated with cable delays or other delays along the signal chain. These time offsets ( $\Delta T$ ) are presented in Tab. 1 and are added to the cable delays when deconvolving the signal chain (step three above). We note that this procedure does not necessarily center the mean of the expected arrival direction (using all antennas) to the predicted arrival direction since we have used a single reference channel for our calculation of  $\Delta T$ .

## 4 Direction reconstruction and angular resolution

The direction reconstruction capabilities of ARIANNA were previously reported at the 2019 ICRC [28]. Here, we report on the same study but with a larger data set. The analysis has been improved by accepting a larger bandwidth for the angular reconstruction, and improving the precision of the time delays between channels. The overall conclusion, however, is unchanged.

Channel	Reference Channel	Mean [ns]	STD [ns]
0	3	-1.34	0.12
1	3	-0.70	0.09
2	3	-0.16	0.07
3	3	0.0	0.0
4	6	0.11	0.12
5	6	-0.07	0.10
6	6	0.0	0.0
7	6	-0.99	0.09

**Table 1.** Time differences between channels after deconvolution of the hardware response and subtracting the expected time delays for each individual channel. First 4 rows use channel 3 (LPDA) as the reference channel, whereas the last four rows use channel 6 (dipole) as a reference channel. The mean of the time delay offsets from zero can be associated with uncertainties in cable delays.

The incoming direction of a triggered event can be reconstructed through the timing delays between antennas. The NuRadioReco framework [17] is used to reconstruct the incoming direction of a triggered event in the ARIANNA detector. The particular algorithm used is called the *cross correlation method* as it uses the time differences between two parallel pairs of antennas (found through correlating the two signals together) to determine the signal arrival direction. (See [17] for details of the reconstruction algorithm.) Correlating two signals together is typically improved with a filter in the time domain, and thus for the angular reconstruction, a Hanning window with a rise time of 20 ns and a width of 50 ns, and for which the filter is centered around the pulse maximum is applied. This aids the reconstruction by reducing the influence of noise and by removing after-pulses and other artifacts that could lead to spurious correlations of the trace not associated with the main signal.

We measure the arrival direction using the four LPDA waveforms; an independent measurement from the four dipole antennas provides a cross-check. In Fig. 6, we present the reconstructed signal arrival directions, relative to prediction, as a function of the emitter depth (cf. Fig. 5). The full range of SPICE data is included in Fig. 6 along with an average of 10 m depths of the reconstructed angular directions. Each point in the averaged data has roughly 30 events. For the LPDAs we apply an additional cut on the data where the reflection coefficient of the firn-air boundary is 50% or less which corresponds to a depth of 938 m. This extra cut is applied to minimize the influence of interference between reflected and direct signals arriving at the receiving LPDAs. We find a resolution in azimuth and zenith to better than  $0.3^\circ$  centered around  $-0.1^\circ$  and  $0.1^\circ$  respectively. The dipoles are equally sensitive to signals arriving from above and below and were buried just 0.5 m below the surface and therefore the interference between reflected signals and direct signals is more pronounced. Thus, we apply a more stringent cut to the dipoles, requiring the reflection coefficient is 10% or less which corresponds to a transmitter depth of 1180 m. The dipoles give a resolution of  $0.2^\circ$  in zenith with a  $-0.3^\circ$  offset and resolution of  $0.3^\circ$  in azimuth centered around  $0.1^\circ$ .

Another Askaryan based neutrino detector, ARA, has looked at reconstructing deep pulser

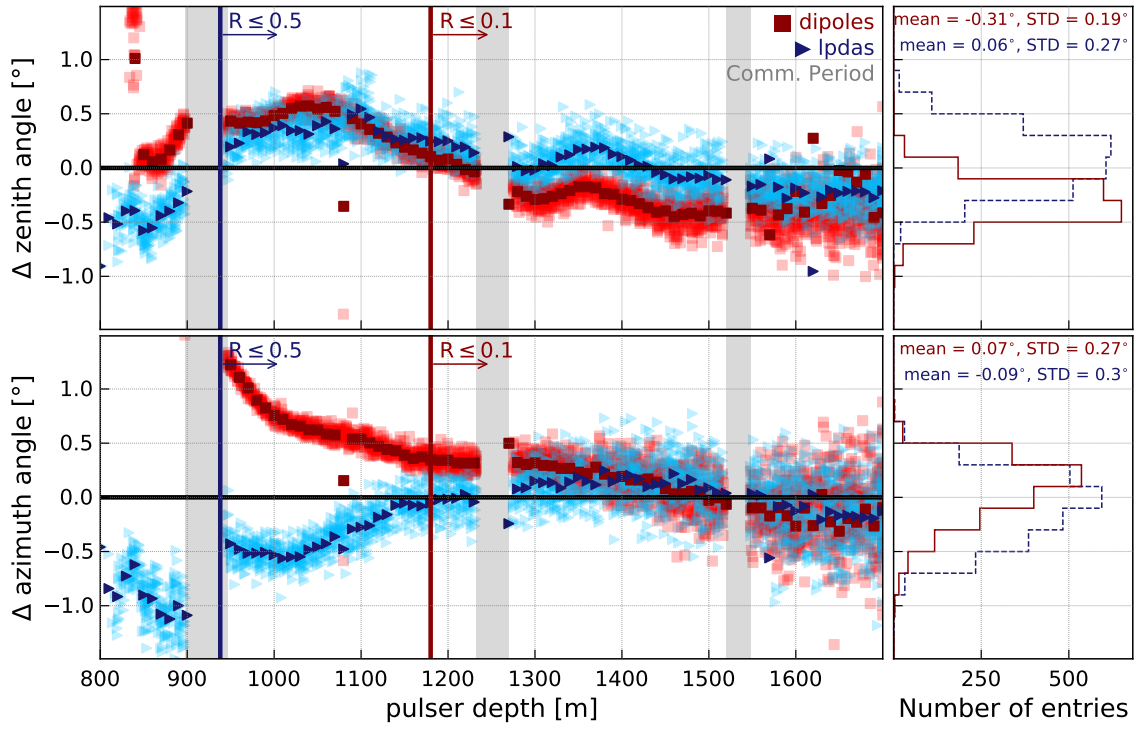


**Figure 6.** Reconstructed arrival direction minus expected arrival direction. Left plots show the depth dependence; histogram projections are shown on the right. This data is corrected for the time differences between channels shown in Table 1. The expected arrival direction is found using the NuRadioMC ray tracer while the reconstructed arrival direction is found through the cross correlation method. Light blue triangles show the residuals using the four LPDAs along with a 10 m average shown in a darker blue color. Red squares show the residuals using the four dipoles along with a 10 m average shown in a darker red color. Each average has roughly 30 events. The red vertical line corresponds to a reflection coefficient of 0.1, while the blue vertical line corresponds to a reflection coefficient of 0.5. The gray shaded area indicates the periods where station 51 was in communication mode and thus not taking data. The data in the projected histograms present the residuals on an event-by-event basis (i.e. without the averaging). Blue dashed is used for LPDAs, and red is used for dipoles. For the LPDAs all data-points with  $R \leq 0.5$  are included and for the dipoles all data-points with  $R \leq 0.1$  are included (see text for details). The mean and standard deviation is reported in the upper right corner of the histograms.

events [29]. The ARA experiment uses birdcage dipoles for the vertical polarization and ferrite loaded quad-slot antennas for the horizontal polarization buried at depths between 170 m and 190 m which greatly reduces firn effects on the signal propagation. ARA reports an azimuthal resolution of  $1.3^\circ$  or better, with an offset of up to  $2.0^\circ$ . Without taking any firn effects into account, ARA reports sub-degree precision of at most  $0.4^\circ$  in zenith, albeit with a systematic offset of up to  $4.8^\circ$  [29].

To estimate the resolution on the ARIANNA directional reconstruction, the 3D angular difference between the reconstructed and predicted arrival direction is calculated. For the LPDAs, ARIANNA achieves a directional resolution of  $0.37^\circ$  whereas for the dipoles ARIANNA achieves a resolution of  $0.43^\circ$ . If we do not apply a depth cut to remove reflections, but instead take all data

from when the transmitter was at depths greater than 800 m into consideration, then ARIANNA is able to achieve an angular resolution of  $0.41^\circ$  using the LPDAs and  $0.55^\circ$  using the dipoles. The measurement of the radio incoming direction is important for an accurate reconstruction of the vertex direction and the neutrino direction reconstruction (see [11]).

The slight offset seen in the zenith reconstruction using the dipoles is due to the four dipoles recording slightly different pulse shapes. It was assumed that the 4 dipoles had the exact same antenna response. The offset suggests significant antenna to antenna variations which we speculate are due to the  $\sim 50$  cm proximity of the dipoles to the surface, with additional uncertainties associated with possible slight variations in orientations. Further investigations of the antenna-to-antenna response will hopefully mitigate any variations in the dipole zenith reconstruction.<sup>1</sup>

There are some slight depth dependencies seen in Fig 6, which may result from:

- **Ice profile:** An uncertainty in the index-of-refraction profile used to predict the signal arrival direction from the depth of the emitter will affect the prediction of the zenith angle. However, the azimuthal angle would remain unaffected as ice cannot affect the angle orthogonal to signal propagation (under the assumption of a vertical index of refraction profile, without horizontal components). The residuals from LPDAs and dipoles are affected in the same way.
- **Tilt of SPICE hole:** To predict the signal arrival direction we assume that the SPICE borehole is straight down, i.e., only the z-position of the emitter changes. However, the hole could have a tilt up to  $1^\circ$  which would lead to a change in the zenith and/or azimuth prediction as a function of depth depending on the direction of the tilt. The residuals from LPDAs and dipoles are affected in the same way.
- **Antenna position:** Uncertainties in the antenna position can lead to uncertainties in the directional reconstruction that are dependent on the signal arrival direction and therefore depth-dependent. In this case, the residuals from LPDAs and dipoles would be affected differently.
- **Antenna response:** Differences in the antenna response within the separate sets of dipoles and LPDAs can lead to antenna-dependent and signal arrival direction-dependent time delays and pulse distortions. Although mechanical differences are unlikely to cause any significant difference, since the antennas are so shallow, the close vicinity to a boundary is likely to influence the antennas differently. This effect should be mostly visible at signal arrival directions for which the surface becomes reflective. Furthermore, the effect should be mostly visible in the dipoles because they are equally sensitive to upward and downward coming signals, whereas the LPDAs have a reduced gain for signals entering the (downward-facing) LPDAs from above.

We observe the strongest deviations from the prediction for dipoles at signal arrival directions for which the surface become reflective. We attribute this to uncertainties in the antenna response. The scatter of the LPDA reconstruction is also larger when the surface becomes reflective, although the

---

<sup>1</sup>We note that the proposed ARIANNA-200 detector [30] aims to install the same mark dipoles at a depth of at least 5 m, and that the antenna depth will naturally increase with time due to snow accumulation. Thus, we expect that antenna-to-antenna variations will be much smaller than observed here.

effect is less pronounced than for the dipoles, consistent with this hypothesis. There is no consistent depth dependence between the LPDA and dipole reconstruction which disfavors a dominant influence of the ice profile or tilt of the SPICE hole. In particular, we can conclude that the ice is understood well enough to correct signal arrival directions for the ray bending to better than  $1^\circ$ , an important result for reconstruction of the neutrino direction.<sup>2</sup>

## 5 Measurement and interpretation of the signal polarization

In this section, the reconstruction of the polarization of the SPICE pulser signals is presented. To measure the polarization, ARIANNA needs to be able to measure the electric field using at least two perpendicular antennas. Using the two orthogonally oriented LPDAs, the framework NuRadioReco [17] is used to reconstruct the electric field from the recorded voltage traces. The electric field is reconstructed by solving the following system of equations.

The electric field  $\mathcal{E}^{\phi,\theta}$  relates to the voltage output  $\mathcal{V}_i$  of an antenna  $i$  in Fourier space as

$$\begin{pmatrix} \mathcal{V}_1(f) \\ \mathcal{V}_2(f) \\ \dots \\ \mathcal{V}_n(f) \end{pmatrix} = \begin{pmatrix} \mathcal{H}_1^\theta(f) & \mathcal{H}_1^\phi(f) \\ \mathcal{H}_2^\theta(f) & \mathcal{H}_2^\phi(f) \\ \dots \\ \mathcal{H}_n^\theta(f) & \mathcal{H}_n^\phi(f) \end{pmatrix} \begin{pmatrix} \mathcal{E}^\theta(f) \\ \mathcal{E}^\phi(f) \end{pmatrix}, \quad (5.1)$$

where  $\mathcal{H}_i^{\theta,\phi}$  represents the response of antenna  $i$  to the  $\phi$  and  $\theta$  polarization of the electric field  $\mathcal{E}^{\theta,\phi}$  arriving from a particular direction. The polarization states  $\theta$  and  $\phi$  are the two orthogonal vectors in spherical coordinates that are perpendicular to the signal propagation direction. For a horizontally propagating signal,  $\vec{e}_\phi$  lies in the horizontal plane whereas  $\vec{e}_\theta$  is oriented vertically.

The SPICE data was measured with 2 pairs of LPDA antennas with orthogonal polarization sensitivity. We apply a linear least square minimization to extract the electric field vector from the overdetermined system of equations. The anechoic chamber measurement was performed with just two orthogonal LPDAs which leads to an exact solution of Eq. (5.1). The polarization is then calculated from the electric fields via:

$$P = \arctan \frac{f_\phi}{f_\theta} \quad (5.2)$$

with,

$$f_\phi = \sqrt{\sum_{t=t_m-35\text{ ns}}^{t_m+35\text{ ns}} |E_\phi(t)|^2} - f_{\phi,\text{noise}} \quad (5.3)$$

where  $f_\phi$  is the energy fluence for the  $\phi$  component,  $E_\phi$  is the electric field for the  $\phi$  component, and  $P$  is the polarization. The time  $t_m$  is the position of the maximum of the Hilbert envelope of the (dominant)  $\theta$  component of the electric field. The  $\theta$  component of the energy fluence is defined analogously. The quantity  $f_{\phi,\text{noise}}$  is an estimate of the noise contribution which is calculated from a part of the recorded trace that does not contain signal. This definition is general and robust against different experimental configurations such as the anechoic chamber data vs. the SPICE data, and

---

<sup>2</sup>We also note that the antenna-related uncertainties will improve in a future ARIANNA-200 detector [30] by installing the antennas deeper into the ice to reduce interference between reflected and direct signals.

can also be directly applied to a neutrino event. Because noise is subtracted, this definition is also largely independent of the exact choice of the integration window; this was confirmed by analyzing the data with different choices of integration windows.

### 5.1 Polarization reconstruction and resolution

The transmitting angles for the range of depths that was analyzed by ARIANNA in the SPICE data are between  $21^\circ$  and  $32^\circ$  (with respect to the vertical) and which is also highlighted in green in Fig. 4. These angles are determined through the ray-tracing solutions found using NuRadioMC as outlined in Sec. 2.2.2. The expected polarization angles for this depth-range are between  $8^\circ$  and  $10^\circ$ , see Sec. 2.2.1. Ice effects, including the bending of the signal, and the frequency-dependent ice attenuation are accounted for in this calculation. The ice attenuation used is the *South Pole simple* model in NuRadioMC [23] and is derived from RICE data gathered in 2004 [22].

A typical electric field from the SPICE data is shown in Fig. 7, overlaid with the corresponding electric field reconstructed from the anechoic chamber data. We observe that the IDL-1 pulser used in the 2019 anechoic chamber tests produced a lower amplitude than the 2018 SPICE data. This was confirmed in 2019, one month after the anechoic chamber measurement, when the same IDL-1 pulser was lowered into the SPICE hole. The resulting events recorded with station 51 were all consistently lower in amplitude than in the 2018 test. Therefore, we overlay a 2019 SPICE reconstructed electric field (which includes ice effects) with the reconstructed electric field obtained in the anechoic chamber. The SPICE electric fields appear identical between the 2018 and 2019 setup, modulo an overall scaling in amplitude. As seen in Fig. 7, the main pulse of the electric fields between the SPICE hole data and the anechoic chamber data is similar in frequency and amplitude, which demonstrates that the applied ice corrections (frequency-dependent ice attenuation and bending of the signal) are well-understood. There is evidence of interference in both measurements, but the two setups have different geometries. Also, the frequency scaling of the anechoic data from in-air to in-ice is only a first order approximation, and the dipole emitter might behave differently when placed in ice which can cause some of the residual differences.

In Fig. 8, we compare the reconstructed polarization from the SPICE data to the prediction from the anechoic chamber measurement (cf. Fig. 4), where the launch angle has been converted to depth according to Fig. 5. The resulting polarization measurements are then averaged over 10 m depths which results in roughly 30 polarization measurements being averaged together. This is shown as dark blue circles in Fig. 8, where the error bars represent the  $1\sigma$  spread of the distribution averaged. The light blue shading in Fig. 8 represents systematic uncertainties of the measurement resulting from uncertainties in the orientation of the LPDA antennas. When comparing the SPICE measurements to the anechoic measurements, we exclude data where the reflection coefficient is greater than 0.5 as indicated by the vertical blue line in Fig. 8 just as we had done for the angular reconstruction of the LPDAs. The SPICE data reconstructs a polarization that scatters around  $9^\circ$ , whereas the anechoic data reconstructs the polarization at  $8^\circ$  -  $10^\circ$ . The histogram of Fig. 9 shows the difference between SPICE measurement (on an event-by-event basis, i.e. without averaging) and the anechoic chamber prediction. We find a small mean offset of  $0.35^\circ$  and a scatter of  $2.7^\circ$ . We infer that we can make a precise polarization measurement for neutrino-induced Askaryan signals from the ability to determine the polarization of the radio pulser events.

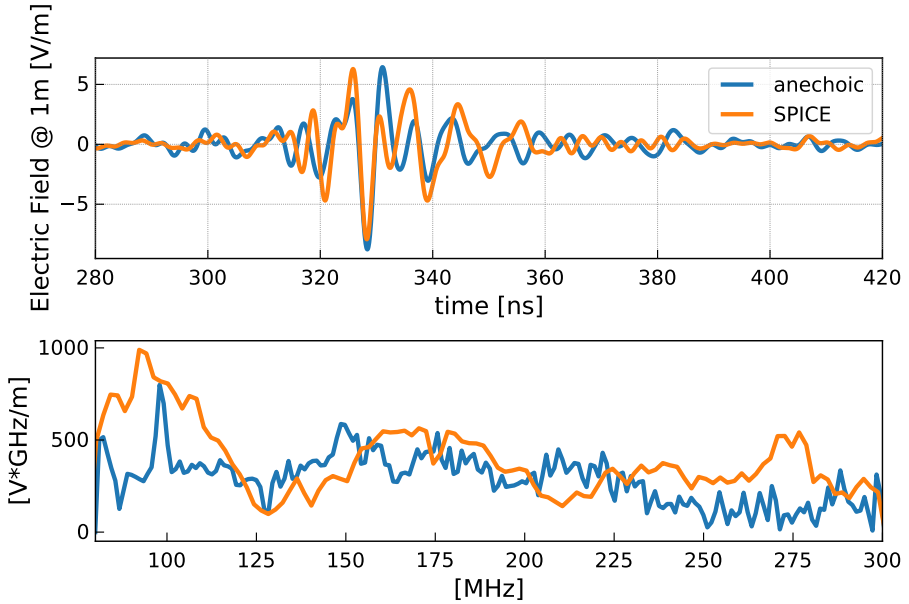


**Figure 7.** Overlays the reconstructed electric field from 2019 SPICE hole experiment (including ice effects) with the reconstructed electric field from tests in the anechoic chamber.

There is some depth dependence seen in Fig 8. In particular, the reconstructed polarization from the SPICE data oscillates around the prediction from the anechoic chamber measurement. We observe that the amplitude of the  $\theta$  component decreases monotonically with depth, as expected from ice attenuation and  $1/r$  field diminution. The  $\phi$  component, which has a lower signal-to-noise ratio<sup>3</sup> ( $\sim 4\text{-}8$ ) than the  $\theta$  component's signal-to-noise ratio ( $\sim 20\text{-}40$ ), also shows this trend but with an additional oscillation of its amplitude. This results in the observed oscillation in the polarization, which is itself defined as the ratio of the amplitudes of the two components (cf. Eq. (5.2) and (5.3)). Although the exact reason for this effect is not known, we have considered the following potential sources:

- **Arrival Direction:** An uncertainty in the signal arrival direction will affect the antenna response pattern which is used in the polarization reconstruction. However, small angular changes of a few degrees have little impact on the antenna response. We find that changing the incident direction by  $\pm 2^\circ$  does not change the oscillatory behavior seen in Fig. 8 and only leads to a depth-independent shift in the reconstructed polarization of  $\pm 1^\circ$ .
- **Antenna response:** Boundary effects are hard to accurately model for antennas very close to a boundary. Since the receiver antennas are so shallow, the close proximity to the ice/air interface is likely to influence the antenna response. We have repeated the polarization reconstruction with antenna response patterns simulated for the LPDA immersed in finite firn (our nominal results), 1 m and 1 cm below the snow surface and did not observe any significant differences for transmitter depths below 1 km where surface reflections are small. However,

<sup>3</sup>using the standard definition of maximum signal amplitude divided by the RMS noise

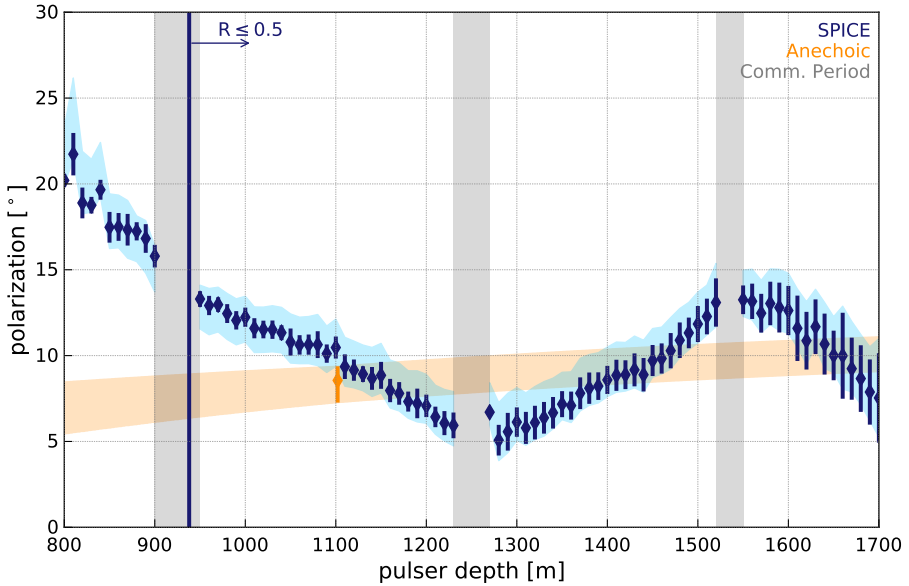


**Figure 8.** Measured polarization angle (blue data points) from 2018 SPICE hole experiment compared to measured polarization angle from tests in the anechoic chamber (orange band). The vertical blue line at 938 m indicates the boundary for which the reflection coefficient is 0.5. The gray bands shows the periods where the station was in communication mode and thus not taking data. The SPICE data was averaged over 10 m depths, and the  $1\sigma$  spread of the distribution averaged is shown with the blue error bars. The light blue shading indicates the systematic uncertainty on the reconstruction stemming from systematic uncertainties in the ARIANNA LPDA orientations. There is only one anechoic data point that fits in the depth ranges of the SPICE data and is indicated as an orange diamond; the error bar represents the spread of the 10 event average. The orange band shows the linear interpolation to the next data points, outside of the depth range plotted. For the anechoic data the representative depth was calculated from the launch angle as in Fig. 5.

the different LPDAs might be impacted differently by the boundary due to small differences in the geometry or snow surface which could impact the reconstructed polarization.<sup>4</sup>

- **Ice profile:** If propagation through the ice affected the polarization, a monotonic increase or decrease of the polarization with emitter depth would be expected. Thus, attributing the oscillatory behaviour to ice properties is challenging and would require different inhomogeneities for different paths. A prior analysis [22] demonstrated that local ice density fluctuations, particularly in the firn, can result in classically unexpected signal propagation modes. Without additional *in situ* studies, we cannot rule out the possibility that such effects contribute to our observations.
- **Change in emitter response with time:** If the emitted signal changed with time, then the polarization would also change with time and therefore depth. However, this is unlikely since ARIANNA observes the same polarization trend when analyzing SPICE data taken while the pulser was being lowered versus being raised.

---

<sup>4</sup>We note that the antenna-related uncertainties will improve in a future ARIANNA-200 detector [30] by installing the antennas deeper into the ice.

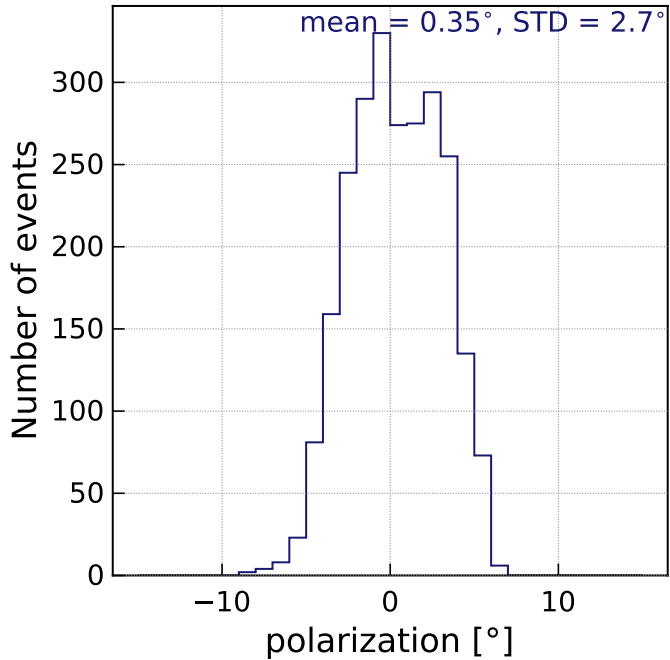


**Figure 9.** Difference between measured polarization from 2018 SPICE hole experiment (without averaging) and measured polarization from tests in the anechoic chamber.

- **Emitter characteristics:** If the emitted signal had some depth dependence, then the polarization would also change with depth. This might originate from depth dependent properties of the SPICE borehole, such as slight changes in the SPICE hole radius. Also, the emitter was lowered by a metal cable that will impact the response pattern of the emitting antenna, especially for launch angles close to the vertical. This may also result in the observed oscillatory behavior.
- **Reference measurement:** The anechoic chamber measurement was performed at discrete launch angles (cf. Fig. 4); only one laboratory launch angle lies within the corresponding range of emitter depths analyzed here. This reference point is shown as the orange diamond in Fig. 8. The predicted polarization is obtained via linear interpolation to reference measurements corresponding to depths outside our depth range. Interestingly, the reconstructed polarization from the SPICE data matches the anechoic measurement at the 1100 m reference point. A possible origin of the oscillatory behaviour is thus a change in the emitter characteristics with launch angle that was not captured by the discrete measurements performed in the anechoic chamber.

From the discussion above and because the change in polarization originates from amplitude variations of the small  $\phi$  polarization component, we speculate that a change of the emitter characteristics is the most likely origin of this effect. The  $\phi$  polarization corresponds to the cross-polarization component, for which an ideal dipole should have zero transmission. Thus, a change of the cross-polarization amplitude with depth and launch angle seems plausible (cf section 5.2). This would also mean that the polarization can be measured much better because the scatter of  $2.7^\circ$  is

largely determined by the oscillations. The scatter of the reconstructed polarization within a narrow depth range is often smaller than  $1^\circ$ . We also note the expected radio pulses from neutrinos will be cleaner: The signal will be the same in both polarization components in that the frequency spectrum and time domain behavior will be identical and only differ in amplitude which will facilitate the polarization reconstruction. This is in contrast to the SPICE transmitter which does not have the same frequency spectrum and time domain behavior in both polarization components.

## 5.2 Polarization-dependent birefringence

In birefringent media, signal propagation wave speeds are anisotropic [31]. For polar ice, which is known to be birefringent over a frequency range stretching from ultra-violet through radio, vertical gravitational pressure and lateral ice flow, at a given depth, break spatial symmetry. Although a perfectly hexagonal ice crystal has no preferred planar symmetry axis, the vertical strain profile of the ice sheet, physically originating in the hydrostatic pressure gradient towards lower surface elevations combined with ‘grounding’ of the ice sheet on the bedrock below, results in a bulk distortion of the crystal fabric along the strain direction. At South Pole, for example, the surface ice flow velocity is approximately 9 m/yr, decreasing to near zero at the bedrock (save for episodic ‘slip’ events). Correspondingly, it is reasonable to expect that the birefringent axes align along i) the vertical, ii) the ice flow direction in the horizontal plane, and iii) a perpendicular to ice flow in the horizontal plane, with refractive indices  $n_3$ ,  $n_1$  and  $n_2$ , respectively (cf. [32]). Numerically, below the firn layer, at depths (greater than 150 m) for which the ice has reached its asymptotic density,  $n_2 \approx n_3$ , whereas  $(n_2 - n_1)/(n_2 + n_1) \sim 0.1\%$ . Signals emitted from the SPICE core transmitter project into the three orthogonal planes (aka ‘rotation planes’, since a polarized continuous wave signal would appear to rotate as it advances owing to birefringent asymmetries) defined by these three axes at the source point. Each projected electric-field polarization vector within a given plane then has two components which independently propagate with wave velocities corresponding to the respective refractive indices for the axes defining that plane. The laboratory-measured values for these three refractive indices, coupled with the measured alignment of typical ice crystals (stacked vertically and elongated in the direction of ice flow) derived from SPICE core data [33] can then be used to make absolute predictions for the relative time delays for the three components at the ARIANNA antenna measurement point. Accounting for the known directivity of the ARIANNA LPDAs or dipoles yields the expected amplitude for a given component, arriving with that time delay.

A vector from the SPICE core to the ARIANNA station is nearly coincident (cf. Fig. 1) with the local ice-flow direction, simplifying the problem considerably. Anechoic chamber data indicates that the source transmitter dipole has a measured cross-polarization (corresponding to the  $\vec{e}_\phi$  direction in spherical coordinates) amplitude, in the plane perpendicular to the propagation direction and the long axis of the antenna, of order 10%. The dominant transmitter component is polarized perpendicular to the signal propagation direction and in the plane containing the dipole long axis (corresponding to the  $\vec{e}_\theta$  direction in spherical coordinates). This component therefore projects into the  $n_1 - n_3$  and  $n_2 - n_3$  planes, but not  $n_1 - n_2$ . At the receiver, the cross-polarization  $\phi$  component parallel to  $n_2$  is nearly simultaneous with the arrival of the vertically polarized signal (i.e. the  $\theta$  component projected onto the vertical axis) since  $n_2 \approx n_3$ . The horizontal component

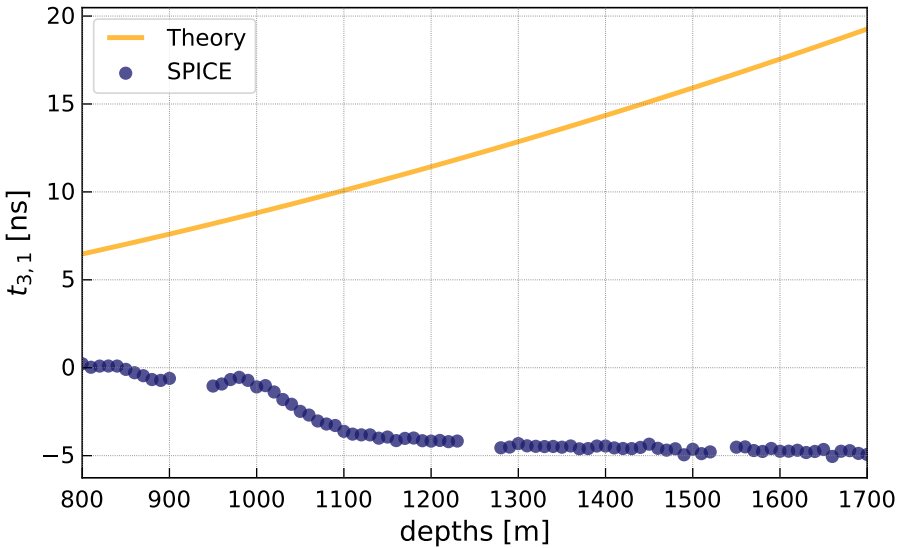


**Figure 10.** Distribution for  $t_{3,1}$ , defined as the signal arrival time of the dipoles minus the signal arrival time of the  $\theta$  component of the LPDAs. Blue circles show the SPICE measured values as a function of depth. The theoretical prediction (orange line) is based on the model developed in [32] (see text for details).

parallel to  $n_1$  (i.e. the  $\theta$  component projected onto the  $n_1$  axis) leads by  $O(10\text{--}20\text{ ns})$  relative to the vertically-polarized signal, with an amplitude increasing with transmitter depth (cf. [32]).

In the following, we compare the pulse arrival time of the vertical and horizontal component parallel to the ice flow. These two components have both similar amplitude and a significant time delay is expected which can be compared to the measured signals.

The dipole antennas are only sensitive to vertically polarized signals. Thus, we use the electric field reconstructed from the dipole measurement to estimate the signal arrival time of the vertical component. The LPDAs are only sensitive to horizontally polarized signals and for our geometry, the  $\theta$  polarization component projected onto the horizontal plane is approximately parallel to the ice flow. Thus, we use the  $\theta$  component of the electric field derived from the LPDAs to estimate the signal arrival time of the horizontal component parallel to the ice flow. For both components we define the maximum of the Hilbert envelope as the signal arrival time. We denote  $t_{3,1}$  as the signal arrival time of the dipoles minus the signal arrival time of the  $\theta$  component of the LPDAs. The measured  $t_{3,1}$  distribution is presented in Fig. 10, together with the theoretical prediction described above (cf. [32]).

Birefringence would appear as a depth-dependent time delay between the signal arrival for the two antenna types. However, we observe an approximately constant time delay of less than 5 ns. From 1000 m to 1150 m the time delay changes from  $\approx 0$  ns to 4 ns which corresponds to the depth region where the reflection coefficient transitions from total internal reflection to negligible reflection. Hence, this small change in time delay might be attributed to a change in the interference with the reflected signal. In any case, the measurement does not show the nearly linear dependence with depth as predicted from our model and the absolute time delays are much smaller than the predicted values, which is consistent with previous measurements made with RICE data [34]. We therefore conclude that we do not observe evidence of birefringence for this geometry.

The ARA experiment measured birefringent asymmetries derived from the same pulser data set described herein [35]; in contrast to ARIANNA, the signal propagation geometry for ARA is predominantly horizontal rather than vertical. ARA measures 20-30 ns signal arrival time differences for horizontally vs. vertically polarized signals consistent, to within 30%, of expectation based on the same  $n_1$ ,  $n_2$  and  $n_3$  data used as input for the model/data comparison shown in Fig. 10. Given that the SPICE ice fabric measurements do not explicitly measure the orientation of the ice crystals in the horizontal plane, one may consider whether relaxing the assumption that  $n_1$  aligns with ice flow can alleviate this tension. Within the context of our model, however, a simple azimuthal rotation of the underlying birefringent principal axes cannot reconcile the discrepancy between the ARA and ARIANNA measurements, which is further constrained by the nearly perfect alignment of the ARIANNA receiver station with the ice flow direction; a more refined ice model is therefore likely required.

## 6 Discussion and Conclusion

We presented the measurement of calibration pulser signals, which were emitted deep in the ice at South Pole, with LPDA and dipole antennas placed slightly below the surface. The variable depth of the emitter and the large propagation distances of up to 2 km validated the modeling of the signal propagation with high precision.

We measured the signal arrival directions and compared it with the expectation which was computed from the emitter depth and a detailed calculation of the bending of the signal trajectories while propagating through the firn. We observe a negligible offset between measurement and prediction with an event-by-event scatter to better than  $0.4^\circ$ . This result is of direct importance for the measurement of neutrinos: The effect of the ice on the propagation direction can be corrected with high precision which is important for reconstructing the neutrino direction. The corresponding uncertainty from ice modelling is likely much smaller than  $0.4^\circ$  as this scatter is mostly due to statistical event-by-event uncertainties. No evidence for a systematic shift in reconstructed direction with depth was found.

We reconstructed the three-dimensional incident electric field using two pairs of orthogonal oriented LPDA antennas and compared it with a reference measurement of the emitter in an anechoic chamber. After correcting for detector response and ice attenuation, we find agreement in amplitude, pulse shape and frequency content. This shows that the attenuation of radio signals is well understood and that the propagation through the ice does not lead to any significant distortion of the radio pulse.

We also calculated the polarization from the reconstructed electric fields. We find a good agreement with the reference measurement of the anechoic chamber with an offset of  $0.35^\circ$  averaged over all depths, and a scatter of  $2.7^\circ$ . We observe an oscillation of the reconstructed polarization with depth which is likely due to changes in the emitter characteristics which would suggest that the polarization can be measured with even higher precision. Further studies are needed to find the origin of this effect and are planned for the future.

We do not observe birefringence effects in this particular station and transmitter geometry. This is different to what is observed at nearly horizontal propagation at greater depth. These results

encourage the development of an improved model for the description of the birefringence of the South Polar ice.

These results are of direct importance for the reconstruction of the direction and energy of neutrinos. The neutrino direction is a function of a) the signal arrival direction corrected for bending in the firn, b) the polarization, and c) an additional weak dependence on the viewing angle. The resolution of the neutrino direction is approximately the square root of the quadratic sum of the individual uncertainties of the three parameters. This analysis showed that uncertainties in the ice modelling will affect the neutrino direction resolution by not more than 3° and likely less depending on the origin of the scatter in the polarization reconstruction.

## 7 Acknowledgements

We thank Tom Jordan for valuable discussions of birefringence.

We are grateful to the U.S. National Science Foundation-Office of Polar Programs, the U.S. National Science Foundation-Physics Division (grant NSF-1607719) for granting the ARIANNA array at Moore's Bay. Without the invaluable support of the people at McMurdo, the ARIANNA stations would have never been built.

We acknowledge funding from the German research foundation (DFG) under grants GL 914/1-1 (CG) and NE 2031/2-1 (DGF, ANe, IP, CW), and the Taiwan Ministry of Science and Technology (JN, SHW). HB acknowledges support from the Swedish Government strategic program Stand Up for Energy. DB and ANo acknowledge support from the MEPhI Academic Excellence Project (Contract No. 02.a03.21.0005) and the Megagrant 2013 program of Russia, via agreement 14.12.31.0006 from 24.06.2013.

## References

- [1] A. M. Hillas, *The origin of ultra-high-energy cosmic rays*, *Annual Review of Astronomy and Astrophysics* **22** (1984) 425.
- [2] ICECUBE collaboration, *Constraints on ultrahigh-energy cosmic-ray sources from a search for neutrinos above 10 PeV with IceCube*, *Physical Review Letters* **117** (2016) 241101 Erratum 119 (2017) 259902.
- [3] E. Waxman and J. Bahcall, *High energy neutrinos from astrophysical sources: An upper bound*, *Physical Review D* **59** (1998) 023002.
- [4] K. Kotera and A. V. Olinto, *The astrophysics of ultrahigh-energy cosmic rays*, *Annual Review of Astronomy and Astrophysics* **49** (2011) 119.
- [5] M. Ackermann et al., *Astrophysics Uniquely Enabled by Observations of High-Energy Cosmic Neutrinos*, *Bulletin of the American Astronomical Society* **51** (2019) 185 [[1903.04334](#)].
- [6] M. Ackermann et al., *Fundamental Physics with High-Energy Cosmic Neutrinos*, *Bulletin of the American Astronomical Society* **51** (2019) 215 [[1903.04333](#)].
- [7] ARIANNA collaboration, *Time-domain response of the ARIANNA detector*, *Astroparticle Physics* **62** (2015) 139–151.
- [8] G. A. Askar'yan, *Coherent Radio Emission from Cosmic Showers in Air and in Dense Media*, *Soviet Journal of Experimental and Theoretical Physics* **21** (1965) 658.

- [9] ANITA collaboration, *Observations of the Askaryan Effect in Ice*, *Physical Review Letters* **99** (2007) 171101.
- [10] S. Barwick, D. Besson, P. Gorham and D. Saltzberg, *South polar in situ radio-frequency ice attenuation*, *Journal of Glaciology* **51** (2005) 231–238.
- [11] C. Glaser for the ARIANNA collaboration, *Neutrino direction and energy resolution of Askaryan detectors*, in *36th International Cosmic Ray Conference (ICRC2019)*, vol. 36 of *International Cosmic Ray Conference*, p. 899, July, 2019, [1911.02093](#).
- [12] J. C. Hanson et al., *Radar Absorption, Basal Reflection, Thickness, and Polarization Measurements from the Ross Ice Shelf*, *Journal of Glaciology* (2014) [[1410.7134](#)].
- [13] C. Reed for the ARIANNA collaboration, *Performance of the ARIANNA Hexagonal Radio Array*, in *34th International Cosmic Ray Conference (ICRC2019)*, vol. 34 of *International Cosmic Ray Conference*, July, 2015, [1509.00109](#).
- [14] A. Nelles for the ARIANNA collaboration, *Cosmic-ray detection with and novel reconstruction algorithms for the ARIANNA experiment*, in *36th International Cosmic Ray Conference (ICRC2019)*, vol. 36 of *International Cosmic Ray Conference*, p. 366, July, 2019.
- [15] T. Huege, *Radio detection of cosmic ray air showers in the digital era*, *Physics Reports* **620** (2016) 1.
- [16] C. Glaser, M. Erdmann, J. R. Hörandel, T. Huege and J. Schulz, *Simulation of Radiation Energy Release in Air Showers*, *Journal of Cosmology and Astroparticle Physics* **2016** (2016) 24.
- [17] C. Glaser et al., *NuRadioReco: A reconstruction framework for radio neutrino detectors*, *European Physical Journal* **C79** (2019) 464 [[1903.07023](#)].
- [18] J. M. Souney et al., *The South Pole ice core (SPICEcore) project*, American Geophysical Union, Fall Meeting 2018, abstract C41C-1771 (2018).
- [19] A. Shultz, U. Latif and A. S. Novikov, “SPICE Pulser: The Guide.” <https://usermanual.wiki/Document/SpicePulserTheGuide.1535821065/html>, 2018.
- [20] ARIANNA collaboration, *Targeting ultra-high energy neutrinos with the ARIANNA experiment*, *Advances in Space Research (in press)* (2019) [[1903.01609](#)].
- [21] W. D. Reeve, “Modeling and measuring the creative design clp5130-2n log periodic antenna.” [http://www.reeve.com/Documents/ArticlesPapers/Reeve\\_LogPeriodicAntennaModel.pdf](http://www.reeve.com/Documents/ArticlesPapers/Reeve_LogPeriodicAntennaModel.pdf), 2013.
- [22] S. Barwick et al., *Observation of classically ‘forbidden’ electromagnetic wave propagation and implications for neutrino detection.*, *Journal of Cosmology and Astroparticle Physics* **2018** (2018) 055 [[1804.10430](#)].
- [23] C. Glaser et al., *NuRadioMC: Simulating the radio emission of neutrinos from interaction to detector*, *European Physical Journal* **C80** (2020) 77 [[1906.01670](#)].
- [24] “The University of Kansas, Anechoic Chamber.” <https://chamber.ku.edu/specifications>.
- [25] I. Kravchenko, D. Besson and J. Meyers, *In situ index-of-refraction measurements of the South Polar firn with the RICE detector*, *Journal of Glaciology* **50** (2004) 522.
- [26] R. Lahmann for the ARIANNA collaboration, *Investigations of ice and emitter properties from radio signals recorded with ARIANNA*, in *36th International Cosmic Ray Conference (ICRC2019)*, vol. 36 of *International Cosmic Ray Conference*, p. 939, July, 2019.
- [27] P. Virtanen et al., *SciPy 1.0: Fundamental Algorithms for Scientific Computing in Python*, *Nature Methods* **17** (2020) 261.

- [28] G. Gaswint for the ARIANNA collaboration, *New results on angular reconstruction of deep pulser radio signals*, in *36th International Cosmic Ray Conference (ICRC2019)*, vol. 36 of *International Cosmic Ray Conference*, p. 897, July, 2019.
- [29] ARA collaboration, *Performance of two Askaryan Radio Array stations and first results in the search for ultrahigh energy neutrinos*, *Phys. Rev. D* **93** (2016) 082003 [[1507.08991](#)].
- [30] A. Anker et al., *White Paper: ARIANNA-200 high energy neutrino telescope*, [2004.09841](#).
- [31] N. D. Hargreaves, *The radio-frequency birefringence of polar ice*, *Journal of Glaciology* **21** (1978) 301–313.
- [32] T. M. Jordan et al., *Modelling ice birefringence and oblique radio wave propagation for neutrino detection at the South Pole*, *Annals of Glaciology*, 1-8 (2019) [[1910.01471](#)].
- [33] D. Voigt, *c-Axis Fabric of the South Pole Ice Core*, SPC14 U.S. Antarctic Program (USAP) Data Center., ([doi: 10.15784/601057](#)) (2017) .
- [34] D. Besson, I. Kravchenko, A. Ramos and J. Remmers, *Radio Frequency Birefringence in South Polar Ice and Implications for Neutrino Reconstruction*, *Astroparticle Physics* **34** (2011) 755 [[1005.4589](#)].
- [35] ARA collaboration, *Long-baseline horizontal radio-frequency transmission through polar ice*, subm. to *Journal of Cosmology and Astroparticle Physics* [[1908.10689](#)].



# NuRadioMC: simulating the radio emission of neutrinos from interaction to detector

C. Glaser<sup>1,a</sup>, D. García-Fernández<sup>2,3,b</sup>, A. Nelles<sup>2,3,c</sup>, J. Alvarez-Muñiz<sup>4</sup>, S. W. Barwick<sup>1</sup>, D. Z. Besson<sup>5</sup>, B. A. Clark<sup>6</sup>, A. Connolly<sup>6</sup>, C. Deaconu<sup>7</sup>, K. D. de Vries<sup>8</sup>, J. C. Hanson<sup>9</sup>, B. Hokanson-Fasig<sup>10</sup>, R. Lahmann<sup>1,3</sup>, U. Latif<sup>5</sup>, S. A. Kleinfelder<sup>11</sup>, C. Persichilli<sup>1</sup>, Y. Pan<sup>12</sup>, C. Pfendner<sup>13</sup>, I. Plaisier<sup>2,3</sup>, D. Seckel<sup>12</sup>, J. Torres<sup>6</sup>, S. Toscano<sup>14</sup>, N. van Eijndhoven<sup>8</sup>, A. Vieregg<sup>7</sup>, C. Welling<sup>2,3</sup>, T. Winchen<sup>8,15</sup>, S. A. Wissel<sup>16</sup>

<sup>1</sup> Department of Physics and Astronomy, University of California, Irvine, CA 92697, USA

<sup>2</sup> DESY, Platanenallee 6, 15738 Zeuthen, Germany

<sup>3</sup> Erlangen Centre for Astroparticle Physics, Friedrich-Alexander-Universität Erlangen-Nürnberg, 91058 Erlangen, Germany

<sup>4</sup> IGFAE, Depto. de Física de Partículas, Universidade de Santiago de Compostela, Santiago de Compostela, Spain

<sup>5</sup> Department of Physics and Astronomy, University of Kansas, Lawrence, USA

<sup>6</sup> Department of Physics and Center for Cosmology and Astroparticle Physics, The Ohio State University, Columbus, USA

<sup>7</sup> Kavli Institute for Cosmological Physics, University of Chicago, Chicago, USA

<sup>8</sup> Vrije Universiteit Brussels, Brussels, Belgium

<sup>9</sup> Department of Physics, Whittier College, Whittier, CA, USA

<sup>10</sup> Department of Physics and Wisconsin IceCube Particle Astrophysics Center, University of Wisconsin, Madison, USA

<sup>11</sup> Department of Electrical Engineering and Computer Science, University of California, Irvine, CA 92697, USA

<sup>12</sup> Department of Physics and Astronomy, Bartol Research Institute, University of Delaware, Newark, USA

<sup>13</sup> Otterbein University, Westerville, OH, USA

<sup>14</sup> Université Libre, Brussels, Belgium

<sup>15</sup> Max-Planck Institute for Radio Astronomy, Bonn, Germany

<sup>16</sup> Physics Department, California Polytechnic State University, San Luis Obispo, CA 93407, USA

Received: 3 June 2019 / Accepted: 5 January 2020 / Published online: 31 January 2020  
© The Author(s) 2020

**Abstract** NuRadioMC is a Monte Carlo framework designed to simulate ultra-high energy neutrino detectors that rely on the radio detection method. This method exploits the radio emission generated in the electromagnetic component of a particle shower following a neutrino interaction. NuRadioMC simulates everything from the neutrino interaction in a medium, the subsequent Askaryan radio emission, the propagation of the radio signal to the detector and finally the detector response. NuRadioMC is designed as a modern, modular Python-based framework, combining flexibility in detector design with user-friendliness. It includes a state-of-the-art event generator, an improved modelling of the radio emission, a revisited approach to signal propagation and increased flexibility and precision in the detector simulation. This paper focuses on the implemented physics processes and their implications for detector design. A variety of models and parameterizations for the radio emission of neutrino-induced showers are compared and reviewed. Comprehensive examples are used to discuss the capabilities of

the code and different aspects of instrumental design decisions.

## 1 Introduction

High-energy neutrino astronomy is a most promising approach to address the still unanswered question of the origin of high-energy cosmic rays [1]. Neutrinos are the perfect messenger. Because they have negligible mass, are electrically neutral and have an extremely low interaction probability, they traverse the universe essentially unimpeded and point directly back to their sources. However, measuring neutrinos requires the instrumentation of large volumes to observe sufficient target material in which a rare interaction of these particles may occur. Currently the largest detector having observed neutrinos is IceCube, which uses the Antarctic ice as a target medium and instruments it with optical sensors [2].

Neutrino astronomy recently took a significant leap forward when the IceCube detector at the South Pole was used to measure a yet unexplained excess of events that provides

<sup>a</sup> e-mail: christian.glaser@uci.edu

<sup>b</sup> e-mail: daniel.garcia@desy.de

<sup>c</sup> e-mail: anna.nelles@desy.de

the first strong evidence for astrophysical neutrino sources [3]. The sources have not yet been identified, though compelling evidence for a first source was delivered with the observation of a spatial and temporal coincidence between a flaring blazar, observed with gamma-ray telescopes, and a high-energy neutrino [4]. However, detection of astrophysical neutrinos above a few tens of PeV has not been achieved yet, possibly due to the neutrino flux expected to steeply fall with energy, which calls for instrumented volumes larger than those currently existing. A two orders of magnitude increase in the volume instrumented by IceCube is considered cost-prohibitive due to the attenuation and scattering of optical light in ice [5]. Such a detector may measure the continuation of the neutrino flux, as well as the expected fluxes in the ultra-high energy regime [1].

### 1.1 Experimental and physical context of radio detection

High-energy neutrinos ( $E_\nu > 10^{16}$ eV) can be most efficiently observed with the radio technique. Radio signals are produced via the Askaryan effect [6] from particle cascades generated in the ice following interactions of the neutrinos. The Askaryan effect arises from the development of a charge excess in the shower front as it accumulates electrons from the surrounding medium. The resulting changing current leads to measurable radio emission in the MHz–GHz frequency range. The Antarctic ice is transparent to these radio signals which allows for a cost-effective instrumentation of large volumes with sparse arrays. The attenuation length is about 1 km, depending on the frequency and ice temperature [7]. This results in an effective volume in the order of  $1\text{km}^3$  per single detector station, similar to the size of the entire IceCube detector.

The radio technique has already been successfully piloted with detectors at the South Pole and at Moore’s Bay on the Ross ice-shelf. The ARIANNA project [8,9] uses an array of autonomous detector stations with antennas located close to the ice surface, whereas the ARA project [10] uses antennas at a depth of up to 200 m below the firn layer. The experimental techniques matured substantially over the last years [11,12] and the community is well prepared for the construction of a large scale Askaryan detector with enough exposure to measure the continuation of the astrophysical neutrino flux to higher energies [1], to potentially discover cosmogenic neutrinos [13–15], and measure particle physics properties at yet unachieved energies [16].

With the developments on the experimental side, improved Monte Carlo simulations became imperative, leading to the development of NuRadioMC, which is presented in this article. A versatile and validated simulation of the radio signal in an Askaryan detector is crucial in many areas: for the determination of the sensitivity of a specific detector, for the optimization of the detector layout, to establish the require-

ments of the hardware to record the relevant parts of the signal, for the computation of a realistic signal expectation that is used to search for neutrino induced signals out of a large background of thermal and anthropogenic triggers, and finally, for the development of reconstruction techniques to determine the neutrino properties from the short radio flashes. In particular, the usage of modern deep-learning techniques requires a large and precise training data set.

The diversity of possible station layouts (e.g. compare the ARA and ARIANNA approach) requires a flexible software which is one of the main limitations of existing codes that were each targeted at a very specific experimental layout [17–19]. NuRadioMC is not tailored to a specific experimental design, and a detector station can have any number of antennas at arbitrary positions. In addition, the Askaryan radio technique is not limited to in-ice detectors. For example the lunar regolith has similar radio properties as ice and provides a immense neutrino target that can be observed from Earth with radio telescopes [20,21], providing the opportunity for synergies in simulations. Hence, from the beginning NuRadioMC was designed for maximum flexibility while maintaining user-friendliness.

### 1.2 Structure of NuRadioMC

The Monte-Carlo simulation of Askaryan signals from neutrino induced in-ice<sup>1</sup> particle showers is logically split up into four independent steps, the four pillars of NuRadioMC:

- 1. Event generation** The simulation of a neutrino flux. This includes the simulation of different neutrino properties (energy, direction, flavor, etc.), lepton propagation, the position of the interaction vertices, and the properties of the induced particle shower, i.e., how much neutrino energy is transferred into the shower, whether it is an electromagnetic or hadronic shower, etc.
- 2. Signal generation** The calculation of the Askaryan radio pulse generated from the particle shower.
- 3. Signal propagation** The propagation of the radio signal through the medium, from its origin to each antenna. Naturally occurring media typically have a density gradient resulting in bent rather than straight trajectories of the radio signal. Also, multiple distinct paths from the interaction vertex to the antenna may exist for typical geometries and ice typically shows a frequency-dependent attenuation length.
- 4. Detector simulation** The simulation of all components of the detector hardware. This step includes the conver-

<sup>1</sup> We will continue to refer to the standard case of a neutrino interaction in ice, when describing NuRadioMC. However, the code is designed in such a way that it can also support media other than ice, and exotic particles such as for instance dark photons [22].

sion from the electric-field pulses at the antenna positions to the measured voltages of each antenna channel, as well as the simulation of the trigger. It accounts for frequency dependent gain and group-delay, sampling-speed, record-length, etc.

The separation of the four steps follows the temporal structure of the physical processes. In a MC simulation this sequence will be different and not linear, e.g., we determine the signal path before generating it, so that we only need to calculate the Askaryan signal at the particular emission angle leading to that path. Moreover, after having calculated the signal, we need to use the propagation module again to determine the signal attenuation along the path.

We note that the separation of signal generation and propagation is a valid approximation when the difference in travel time from different points of the emission region to an observer in a homogeneous medium and one in a medium with a density gradient (bent trajectories) is small with respect to the observation frequency. We find that this assumption holds for all but rare and extreme geometries of an in-ice detector at frequencies up to 1 GHz.

The four pillars are complemented by a set of utility classes that are accessible at all times throughout the simulation such as a model of the medium, or a model of the signal attenuation. To ensure maximum flexibility and ease of use of different codes and programming languages the four pillars are separated as much as possible. The modules can be written in any language but Python wrappers of the relevant functions are required (this can be achieved e.g. with Cython [23]), so that the simulation can be steered from Python. This design was chosen to maximize user-friendliness and allow for the interfacing with other existing frameworks.

### 1.3 Improvements on the simulated physics in NuRadioMC

NuRadioMC does not only improve in flexibility and ease of use over existing codes, but also includes more physics processes in the simulation than previous codes and improves on precision. In the event generation, the subsequent decay of taus following a tau-neutrino interaction is modelled and the interface to simulate any *multi-bang* model is provided. Hence, models predicting several spatially-separated interactions can be implemented and simulated.

In the signal generation pillar, various Askaryan signal generation models are implemented. Previous MC codes relied on parameterizations of the frequency spectrum of radio emission [24] or on time-domain calculations mostly restricted to electromagnetic shower profiles [25]. NuRadioMC improves this approach by providing a time-domain calculation from an extensive library of electromagnetic, hadronic and tau-initiated showers. In particular, this

allows for a realistic treatment of the Landau–Pomeranchuk–Migdal effect (LPM effect) [26,27].

In the signal propagation pillar, new ray-tracing techniques based on an analytic solution of possible signal paths are implemented. This implementation results in unprecedented combination of speed and accuracy. Furthermore, we provide the interface to a more detailed numerical calculation that can simulate the signal paths in arbitrary 3D density profiles.

In the detector simulation pillar, we use the *NuRadioReco* code [28] that allows for the simulation of any detector geometry. In particular, it includes a detailed antenna response for a variety of antenna types and arbitrary orientations, treating the full set of complex gains as well as complex triggers such as phased-arrays.

In this article, we first describe each of the four pillars in detail and discuss different approaches. Then, we present three examples of how to use NuRadioMC and discuss the implications for the design of a high-energy neutrino radio detector.

## 2 Event generation

The event generation is logically separated from the simulation and provides general event parameters as input to the simulation. The results of the event generation are stored in an HDF5 file [29], which ensures that the event generator is easy to change in order to cover a variety of physics cases, as well as practical cases such as the simulation of calibration pulser data. This section describes the standard case implemented in NuRadioMC and provides an outlook for future implementation and special cases.

Having the event generation separated from the other simulation steps is beneficial because it allows the user to test the influence of different parameters on the same events. For example, the influence of different signal generation models, ice properties that influence the signal propagation or attenuation, and trigger schemes and thresholds, while using the same set of events.

### 2.1 Considerations concerning the coordinate system

All coordinates are specified in a local Cartesian coordinate system with its origin centered at the surface of the ice (see Fig. 1). The implementation of a global coordinate system that takes into account the curvature of the Earth is not required at this stage of precision: Due to attenuation of radio signals in the ice, the maximum propagation distance of radio signals is  $\mathcal{O}(1 - 5)$  km where the impact of Earth attenuation is less than 2 m. Thus, effects of Earth curvature can be ignored from the signal propagation step onwards. The maximum propagation distance also defines the neces-

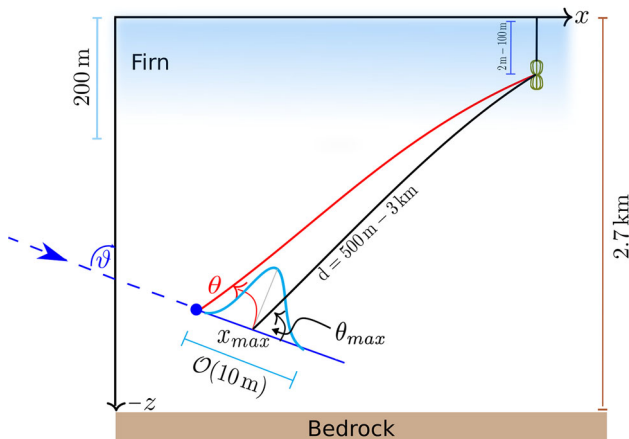


**Fig. 1** Sketch of the coordinate system used by NuRadioMC and typical dimensions in the radio detection of neutrino interactions. The coordinate origin is at the ice surface. A quantity of particular interest is the viewing angle  $\theta$ , i.e., the angle at which the in-ice shower is observed. Due to the longitudinal extent of the shower, the viewing angle is not uniquely defined. By default, we measure the angle with respect to the neutrino interaction vertex, but sometimes it is appropriate to measure the angle with respect to the maximum of the charge-excess profile, which we denote with  $\theta_{X\max}$ . It should be noted that this is just one typical set-up, other choices of geometry are supported

sary volume where neutrino interactions are simulated in. Thus, also for the standard event generation, a flat Cartesian coordinate system is sufficient.

Earth curvature starts to matter in the tracking of tau leptons and simulation of their subsequent decay as the tau decay length can reach values above 10 km. At 10 km distance, the difference between a flat and curved surface is 8 m which is still small compared to the thickness of the ice sheet at the South Pole of 2.7 km. Hence, the difference in target volume is also small. Another effect is that the probability of a neutrino reaching the simulation volume (referred to as *neutrino event weight*, see Sect. 6.2) is calculated based on the angle between the incident neutrino direction and the (flat) surface. Consequently, the neutrinos originating close to the horizon will have a systematic uncertainty in their assigned weights. However, at 10 km distance, this effect is again small with a displacement of only 0.1°. In the future, effects of Earth curvature can be considered by correcting this angle in the neutrino event weight calculation. The additional complexity of implementing a global coordinate system does not seem required at this point.

## 2.2 Default event generator and file format details

The default event generator creates a list of neutrino interaction vertices, specifies all relevant neutrino properties, and stores everything in an HDF5 file (see structure in Appendix A).

The event generator specifies the following parameters:

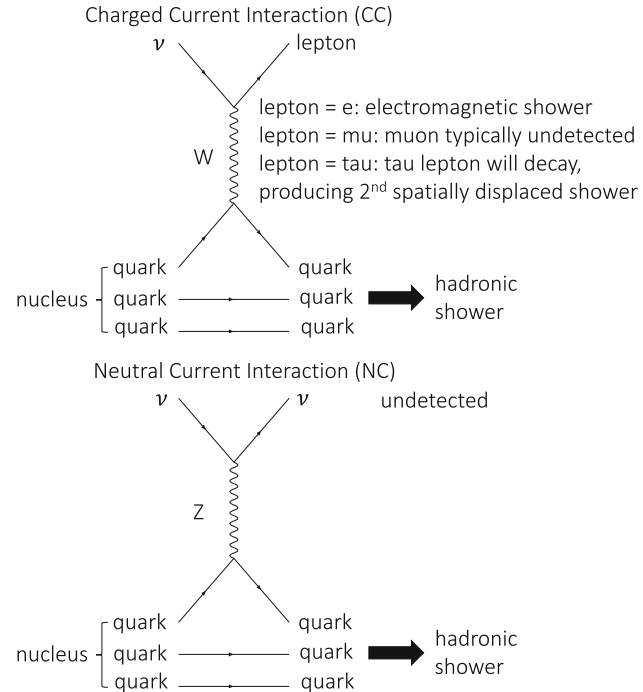


**Fig. 2** Feynman diagrams of a charged current and neutral current neutrino interaction

- the position of the neutrino interaction, randomly placed in a cylindrical volume surrounding the detector. The user can control the minimum and maximum radius and the vertical extent.
- the neutrino energy, drawn from a user definable energy spectrum between a minimal and maximal energy. We also allow to specify the *deposited* energy instead, i.e., the amount of neutrino energy that ends up in a particle shower producing an Askaryan signal.
- the neutrino flavor. By default all flavors and particle/anti-particle nature have equal probability. Internally, this is specified using the Particle Data Group ID (PDGID) [30], which allows for cross-referencing with other Monte-Carlo codes.
- the neutrino direction. By default the full sky is uniformly covered but the user can restrict neutrino directions to specific ranges in zenith and azimuth angles.
- whether the neutrino undergoes a neutral current (NC) or charged current (CC) interaction (see Fig. 2 for an illustration of the two interaction types). We use a constant ratio CC:NC 0.7064:0.2936 according to the CTEQ4-DIS cross sections for the neutrino energy between  $10^{16}$  eV and  $10^{21}$  eV [31].
- the inelasticity, i.e., the fraction of the neutrino energy going into the hadronic part of the interaction. The inelasticity distributions from [32–34] have been implemented.

We note that we place neutrino vertices with equal probability per volume. The probability of a neutrino reaching the detection volume is taken into account later by assigning a *weight* to each event (see Sect. 6.2 for how the neutrino absorption is calculated). Similarly, it is currently ignored, if the density of the simulation volume is not uniform which changes the neutrino interaction cross section and thereby the interaction probability. As the density of the typical use-case of ice, only changes in the upper  $\sim 100$  m this effect is ignored at this stage of precision. It can be taken into account in the future by an additional weighting factor or by an event-by-event calculation of the neutrino cross section.

All these parameters are saved in a HDF5 table. This has several advantages. The data is saved efficiently, the format is platform and programming-language independent, stand-alone viewers exist to quickly inspect the files, and apart from storing the actual data tables, it allows saving meta attributes such as the parameters the event set was generated for.

Typical data sets consist of millions of events which would take too long to simulate in a single process. Therefore, the event generator allows to automatically split up the data set into smaller chunks, i.e., into separate HDF5 files with typically 10,000 to 100,000 events per file. Then, the NuRadio-MC simulation can be performed for each file separately, and we provide the tools to merge the individual output files back together.

### 2.3 Multiple showers

Previous radio simulations only considered particle showers created by the initial neutrino interaction. However, in case of charged current interactions of muon and tau neutrinos, the produced muons and taus might interact or decay producing a second spatially displaced particle shower that generates Askaryan radiation.

The typical decay length of a tau lepton range from 50 m at tau energies of 1 PeV to 50 km at tau energies of 1 EeV. This increases the sensitivity of an Askaryan detector because tau neutrinos can interact far away from the detector but still produce a visible signal if the tau happens to decay close enough to the detector.

Muons in turn are unlikely to decay but they can undergo a catastrophic  $dE/dX$  energy loss, depositing a substantial fraction of their energy into the ice and initializing a hadronic shower [35, 36]. In general, more exotic models can also be considered that predict multiple spatially displaced showers per neutrino. Hence, NuRadioMC offers the flexibility to specify an arbitrary number of interaction vertices per event. This is incorporated into the file format by inserting additional events into the event list with the same event ID.

We consider several levels of detail. While a simple treatment of tau decays exists in NuRadioMC itself, we also foresee the inclusion of more complete particle decay codes,

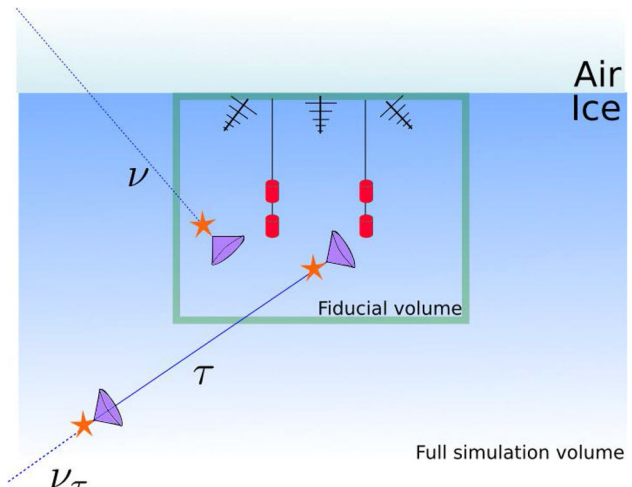


**Fig. 3** Sketch of the geometry and the concept of a fiducial volume of the event generator. Neutrino tracks are generated in a full simulation volume, but only the radio emission of primary or secondary interactions are considered, when they take place in a fiducial volume encompassing the detector

such as PROPOSAL [35, 36] that tracks secondary losses of all types of lepton.

### 2.4 Tau neutrinos

In NuRadioMC, for the first time in an in-ice simulation, we provide the inclusion of secondary sub-showers from tau-decays that add additional detection channels, flavor sensitivity and contribute to the effective volume.

Due to the large decay length of tau leptons, a large volume needs to be simulated to catch the few cases in which there is a secondary interaction close enough to the detector. This increases the computation time enormously as it scales proportionally to the simulated volume, and makes this brute-force approach unfeasible. Therefore, we developed the following technique: we generate neutrino interactions in an arbitrarily large volume including all secondary interaction vertices (e.g. from tau decays) but save only those primary and secondary interactions that take place in a much smaller fiducial volume surrounding the detector while keeping track of the total number of simulated events (see Fig. 3 for an illustration). The user needs to make sure that the fiducial volume is chosen large enough such that the probability to trigger the detector is negligible for interaction vertices outside of this volume. This allows for a computationally efficient simulation of complex physics models.

Once a tau is created after the interaction of a tau neutrino in the volume, we calculate its decay time  $t_{decay}$  and energy at decay. We first randomly sample a decay time  $\tau_{decay}$  in the tau particle rest frame from an exponential distribution using a mean tau decay lifetime  $2.903 \times 10^{-13}$  s [37]. If the tau energy is less than  $E_\tau = 1$  PeV, we do not account for tau

energy losses along the path, and the decay time is simply given by the product of the Lorentz factor  $\gamma$  and the sampled decay time  $\tau_{\text{decay}}$  in the tau rest frame

$$t_{\text{decay}} = \gamma(E_\tau)\tau_{\text{decay}}. \quad (1)$$

The decay length  $l_\tau$  is calculated multiplying  $t_{\text{decay}}$  by the particle speed, while the energy of the  $\tau$  at decay is equal to the initial tau energy.

In the case the tau has an energy greater than 1 PeV, we include photonuclear tau energy losses in our calculation. These are not very well constrained and we use a simple model inspired by the results in [38]. We take the mean energy loss per amount of traversed matter in ice to be,

$$\left\langle \frac{dE_\tau}{dX} \right\rangle \approx f(E_\tau) = b_1 E_\tau + b_2 E_\tau \log_{10}(E_\tau/E_0), \quad (2)$$

with  $b_1 = 1 \times 10^{-7} \text{ cm}^2/\text{g}$ ,  $b_2 = 1.8 \times 10^{-7} \text{ cm}^2/\text{g}$ , and  $E_0 = 1 \text{ PeV}$ . Above  $E_\tau = E_0$ , it is a good approximation to assume that the tau speed is equal to the speed of light in vacuum  $c$ . This allows us to write the time  $t$  that it takes a tau with initial energy  $E_{\tau,i}$  to reach a lower energy  $E_\tau$  as,

$$t(E_\tau) = \frac{1}{c\rho_{\text{ice}}} \int_{E_{\tau,i}}^{E_\tau} \frac{dE'}{f(E')}. \quad (3)$$

Once  $t(E_\tau)$  is known, we numerically obtain the inverse function  $E_\tau(t)$  for equally-spaced times by interpolation. The decay time is obtained by solving the following integral equation for  $t_{\text{decay}}$ :

$$\int_0^{t_{\text{decay}}} \frac{m_\tau}{E_\tau(t)} dt = \tau_{\text{decay}}, \quad (4)$$

from which the tau decay length above 1 PeV is obtained as:

$$l_\tau \approx ct_{\text{decay}}. \quad (5)$$

In Fig. 4, left, we show the decay length  $l_\tau$  as a function of tau energy. The straight dashed line represents the mean decay length without tau energy losses, which increases linearly with energy. The solid line indicates the decay length assuming that the decay time in the rest frame is equal to the mean decay time  $\tau_{\text{decay}}$  and accounting for deterministic tau-energy losses during propagation given in Eq. (2). The shaded band represents an 80% confidence interval for the decay length, where the decay time has been drawn from an exponential distribution. Stochastic energy losses have not been accounted for. In Fig. 4, right, we show the tau energy at decay obtained with the same assumptions used for obtaining the tau decay length shown in the left panel. Tau energy losses become important around 100 PeV.

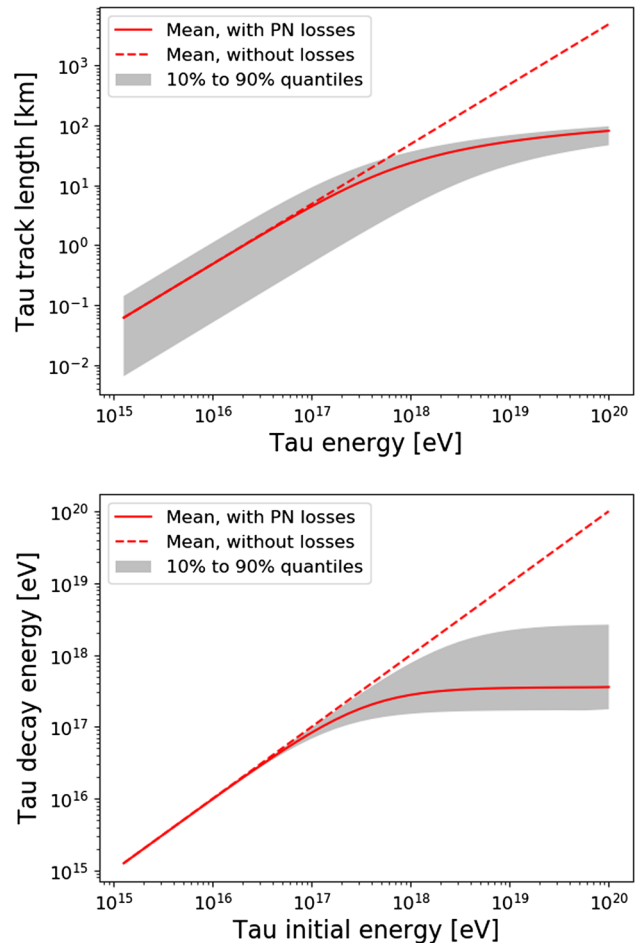


**Fig. 4** Top: Tau decay length as a function of the tau energy. Bottom: Tau decay energy as a function of the initial tau energy. Due to the one-tailed nature of the exponential decay function, we show the decay length for the mean proper decay time with photonuclear losses (solid line) and without any losses (dashed line). The shaded band represents the area spanning from the 10% proper decay time quantile to the 90% quantile (80% of total probability). This implementation matches what has been shown previously in [39]

## 2.5 Options for additional physics processes or calibration purposes

The event generation described above is the default event generator in NuRadioMC. However, emission from a standard-model neutrino-induced shower is only one possible scenario that can be covered. The users have the freedom to implement their own event generators according to other physics assumptions, e.g., new physics or for simulating calibration signal generators. We provide an example to simulate a calibration measurement online [40]. As long as the events are saved according to the well-defined file structure, NuRadioMC can process any input files. A skeleton event generator is provided as an example [41].

### 3 Signal generation

NuRadioMC provides several modules for the generation of the radio signal from showers. The user may choose from a selection ranging from well-known frequency-domain parameterizations of the Askaryan signal to a state-of-the art semi-analytic calculation.

A uniform interface in the form of a simple function is provided for all models (see [42] and List. 3 in Appendix D.3). In this way the NuRadioMC code also serves as a reference implementation for all models. Furthermore, the well-defined interface allows for an easy extension of NuRadioMC with additional models. Even calibration emitters can be (and are) implemented to simulate a calibration measurement with NuRadioMC.

In the following, we first present the different signal generation models available in NuRadioMC before discussing their differences and giving recommendations for use in different cases. We discuss a variety of models, some for more pedagogical reasons, others because they are fast, and others because they are accurate. We hope that this section also serves as reference discussion of several widely used emission models, however, it is not an attempt at completeness.

#### 3.1 Frequency-domain parametrizations

NuRadioMC currently provides two frequency-domain parameterizations of the Askaryan signal. One, referred to as *Alvarez2000*, is also used in the simulation code for the ANITA detector (IceMC) [19] and for the ARIANNA array (ShelfMC) [17,43], and is an implementation of the parameterization of [24], which was validated against a full simulation of Askaryan radiation performed with the ZHS Monte Carlo [44]. This is a microscopic simulation of the shower and its radio emission, that does not contain signal propagation and detector simulation.

The other parameterization (*Alvarez2009*) is an updated version of the first one. It is based on the so-called “box model” of shower development [45] and separate parameterizations for electromagnetic [46] and hadronic [47] showers are provided. Both parameterizations are the product of three functions. The first is a scaling function  $A$  that grows linearly with the primary energy  $E_0$ , frequency  $f$ , and the sine of the observing angle  $\theta$ . The second and third functions are two continuous cutoff frequency factors  $d_L$  and  $d_R$  that account for deviations from linearity due to incoherence effects associated to the longitudinal and lateral extensions of the shower. For electromagnetic showers, the LPM effect is modelled including random fluctuations of the size of the effect.

Although we encourage the use of the *Alvarez2009* parameterization, we have also included the older parameterization *Alvarez2000* for comparison with previous work and other

codes. The latter can be understood as a simplified version of the former, with constant factors, a simple continuous cut-off factor instead of two, and a Gaussian function for the dependence of emission on viewing angle. Because of its simplicity, it provides qualitative and easily understandable, however, not necessarily precise insights into the main dependencies of the Askaryan signal. For pedagogical reasons, we explicitly provide the parameterization of this model here and give an example of the resulting Askaryan signals.

If the shower is observed on the Cherenkov angle, the electric field (scaled to a distance of 1 m) according to *Alvarez2000* is given by

$$\frac{\varepsilon_c^{lm}}{V/m/MHz}(E_{sh}, f) = 2.53 \times 10^{-7} \cdot \frac{E_{sh}}{\text{TeV}} \cdot \frac{f}{f_0} \cdot \frac{1}{1 + (\frac{f}{f_0})^{1.44}}, \quad (6)$$

with the shower energy  $E_{sh}$ , frequency  $f$  and  $f_0 = 1.15$  GHz. Signal amplitudes off the Cherenkov cone,  $\varepsilon^{lm}$ , are modeled as a Gaussian profile according to

$$\varepsilon^{lm}(E_{sh}, f, \theta_v) = \varepsilon_c^{lm}(E_{sh}, f) \cdot \frac{\sin \theta_v}{\sin \theta_c} \cdot \exp \left[ -\ln 2 \cdot \left( \frac{\theta_v - \theta_c}{\sigma_\theta} \right)^2 \right] \quad (7)$$

with  $\varepsilon_c^{lm}$  given in Eq. (6), and where  $\theta_v$  is the viewing angle relative to the shower axis. The angular width of the cone around the Cherenkov angle  $\sigma_\theta$  is a function of both frequency and energy. For hadronic showers  $\sigma_\theta$  is given in Eq. (6) of [48], for which a factor to account for the so-called missing energy, energy going mainly into muons and neutrinos that does not contribute to the Askaryan signal, is included in Eq. (6).

For electromagnetic showers above 2 PeV, the shower profile becomes elongated due to the Landau–Pomeranchuk–Migdal (LPM) effect. In the simple model of *Alvarez2000* such an elongation corresponds to a reduced  $\sigma_\theta$  which is modeled according to the prescription in [49]. This in turn manifests itself as a rapid decrease in the high frequency content of the Askaryan signal off the Cherenkov cone for EM showers, as seen in Fig. 5.

For NuRadioMC, the time-domain signal based on *Alvarez2000* and *Alvarez2009* is generated by taking the simple approximation of a phase that is constant with frequency and equal to 90°, yielding a bipolar pulse in the time domain.

#### 3.2 Fully analytic treatment including the LPM effect and Cascade Form Factor

NuRadioMC provides an implementation of the analytic model of Askaryan radiation (*HCRB2017*) [50] that builds on previous work by [51]. This fully analytic model accounts

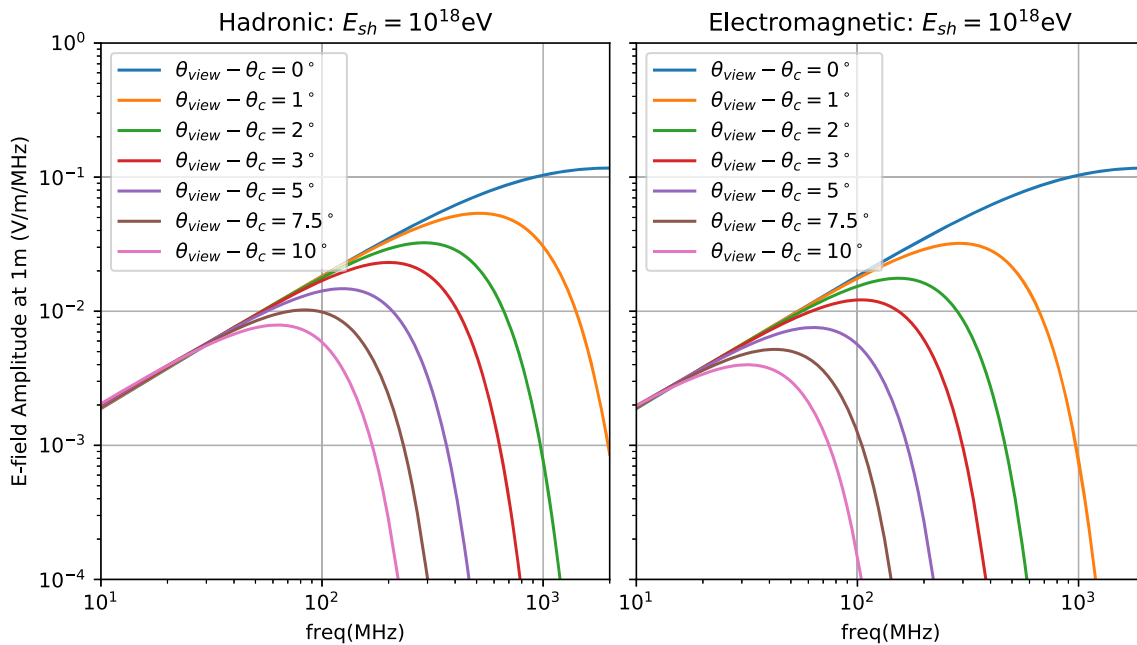


**Fig. 5** Electric field amplitude  $\varepsilon^{1m}$ , 1 m from the neutrino interaction vertex (Eq. (7)) for hadronic (left) and electromagnetic (right) showers with  $E_{sh} = 10^{18}$  eV using the parameterization Alvarez2000. Note that

as the viewing angle shifts away from the Cherenkov cone angle, high frequency components fall off. For the EM showers, the cone width  $\sigma_\theta$  is reduced due to the LPM effect

simultaneously for the three-dimensional *form factor* of the cascade, and the cascade elongation. The form factor is the spatial Fourier transform of the instantaneous charge distribution of the cascade. The form factor affects the Askaryan signal properties in the same way a multi-pole filter affects any time-domain signal. Although some authors have provided partial solutions for the three-dimensional form-factor in the past [52], in [50] a complete solution is presented that includes dependence on the viewing angle  $\theta$ . This allows for the analytic exploration of the relevant parameter space affecting  $\sigma_\theta$  and  $\sigma_v$ , the width of the Cherenkov cone and the Fourier spectrum, respectively.

This module builds upon the work of [51] where the authors provide analytic functions for Askaryan radiation correct in both the near and far-field regimes. When a cascade is elongated due to the LPM effect, both regimes become important given the three-dimensional nature of the form-factor. *HCRB2017* treats the LPM effect as a smooth stretching of the shower profile using the results of [53].

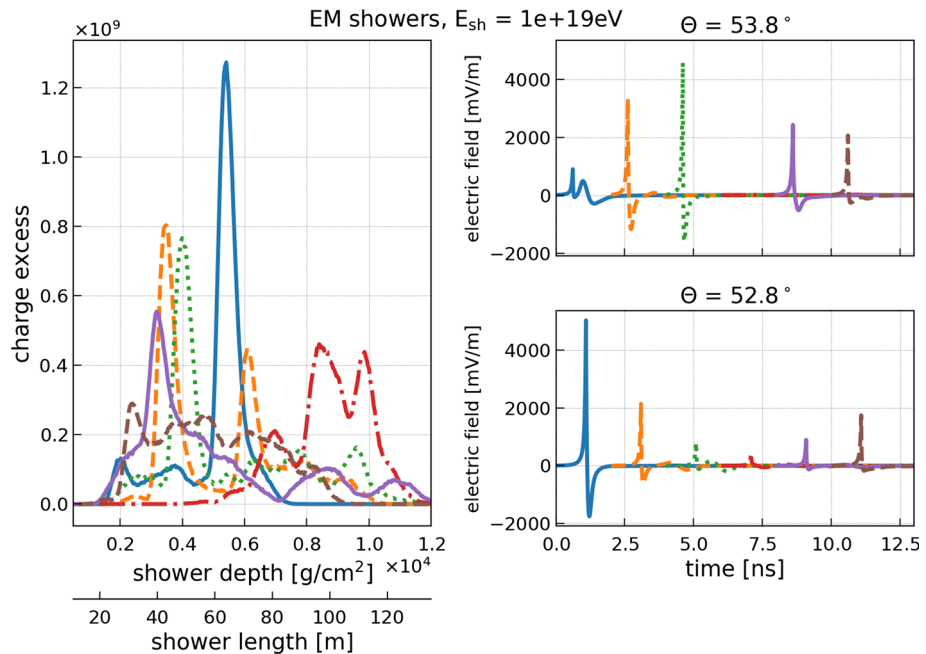
The fully analytic nature of this model has the advantage that it gives direct insights into the physical dependencies of the Askaryan signal. However, as shown in the radio emission of air showers [54] a purely analytic model comes at the cost of a poorer accuracy.

### 3.3 Semi-analytic model in the time domain

A third option for the signal generation is to calculate the Askaryan radiation individually from detailed charge-excess profiles in the time domain, following the approach in [55]. The implementation in NuRadioMC referred to as *ARZ*, is based on a realistic shower library. This allows to precisely model the effects of LPM elongation [26,27] and the resulting large shower-to-shower fluctuations on the Askaryan signal on a single event basis, rather than describing an average behaviour. The model also captures subtle features of the cascades like sub-showers and accounts for stochastic fluctuations in the shower development which can alter the Askaryan signal amplitudes significantly (see e.g. discussion in [47] or Fig. 6). This model is the most accurate treatment of Askaryan radiation implemented in NuRadioMC, but it comes at the expense of larger computation times as it involves computationally expensive convolutions of the Askaryan vector-potential with Monte-Carlo generated cascade profiles.

The main idea behind the *ARZ* method is that the electromagnetic vector potential  $\mathbf{A}$  in Coulomb gauge can be expressed as an integral in shower depth containing the shower profile, a factor that accounts for polarization, another factor that accounts for distance to the emitting point of the shower, and a form factor  $F_p$ :

**Fig. 6** Charge-excess profiles and resulting Askaryan signal (unfiltered). (left) Charge-excess, i.e., number of electrons minus number of positrons, as a function of shower depth and length of six electromagnetic shower with an initial energy of  $10^{19}$  eV. The variation in the charge-excess profile is due to the stochastic nature of the shower development effected by the LPM elongation. (right) The resulting Askaryan signal for the charge-excess profiles according to the ARZ model for two different viewing angles at 1 km distance. The pulse start time is shifted for a better visibility of all pulses



$$\mathbf{A}(r, z, t) = \frac{\mu}{4\pi} \int_{-\infty}^{\infty} dz' \frac{Q(z')}{\sqrt{r^2 + (z - z')^2}} \mathbf{p}(z') F_p \left( t - \frac{z'}{v} - \frac{n\sqrt{r^2 + (z - z')^2}}{c} \right), \quad (8)$$

where  $r$  is the radial distance of the observer to the shower,  $z$  is the vertical coordinate of the observer,  $z'$  is the shower depth,  $Q(z')$  the excess charge profile,  $\mathbf{p}$  is the polarization vector and  $F_p$  is the form factor (see [55] for more details). This form factor  $F_p$  has approximately the same shape for every particle shower in ice, which allows us to treat it as a constant function. It only depends on the type of the shower, i.e., hadronic or electromagnetic, and a parameterization of the form factor for both shower types is provided.

The charge profile  $Q(z')$  depends on the nature of the shower (hadronic or electromagnetic), the shower energy, and is also subject to random fluctuations. The LPM effect, for instance, modifies the charge profile, which in turns modifies  $\mathbf{A}$  through Eq. (8). All the physical processes that are relevant for the electric-field calculation contribute to  $Q(z')$ , so as long as a correct description of the charge profile is available in the shower library, an accurate electromagnetic potential  $\mathbf{A}$  can be calculated with Eq. (8).

Once  $\mathbf{A}$  is known, the radiation electric field can be calculated with a derivative, since in Coulomb gauge  $\mathbf{E}_{\text{rad}} = -\frac{\partial \mathbf{A}}{\partial t}$ . The agreement between the electric field predicted by the ZHS Monte Carlo and the one obtained with the ARZ model is quite satisfactory, yielding a few percent of error up to 2 GHz (see Fig. 3 in [25]). The ARZ model considers that the shower has a volume and therefore is adequate for computing the fields of observers near the shower as long as the con-

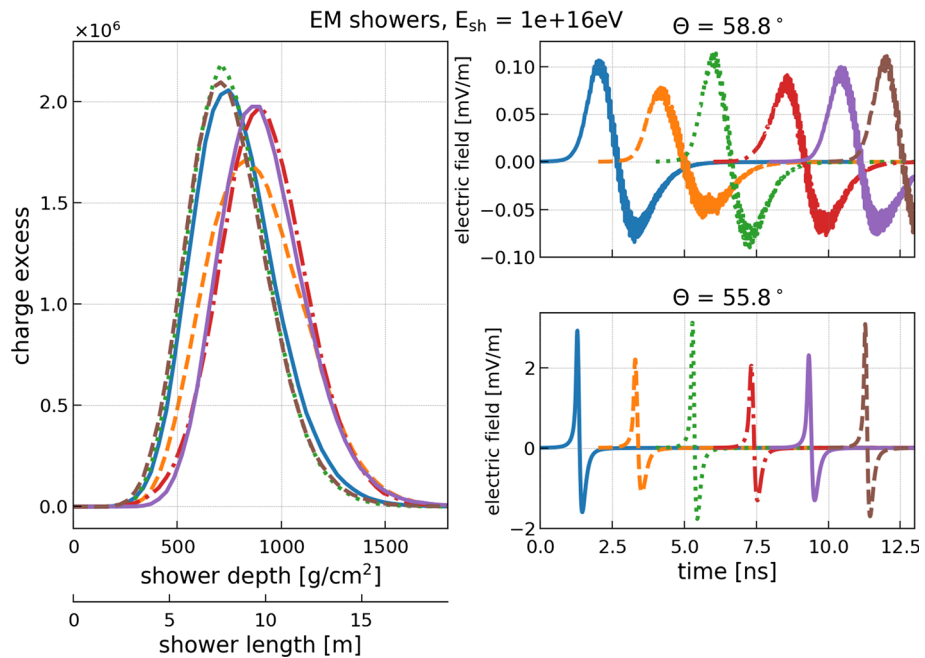
sidered wavelengths are small with respect to the distance to the shower.

NuRadioMC provides a modern Python-based implementation of the code used in [55] and optimized routines for numerical integration. The code includes a shower library of charge-excess profiles for different shower types:

1. electromagnetic: purely electromagnetic showers from  $\nu_e$  charge current interactions.
2. hadronic (neutrino): showers started by the fragmentation of the nucleon struck by the neutrino, i.e., the result of neutrino neutral current interactions and the hadronic part of an electron neutrino charged current interaction.
3. hadronic (tau): showers initiated by a hadronic decay of a tau lepton. A tau decay into muons will not produce any significant shower, and tau decays into electrons correspond to purely electromagnetic showers.

The last category is not simulated explicitly. Instead, the branching ratios of a tau decay and the fraction of energy ending up in the particle cascades is parameterized using the results of [35, 36]. Then, the shower library of electromagnetic (category 1) or hadronic (category 2) showers is used with the appropriate shower energy. We note that the initial hadronic particles that start the hadronic shower are different between a fragmenting nucleon and a hadronic tau decay. This might lead to small differences in the hadronic shower developments. However, for now we ignore this subtle difference and use category 2 also for hadronic tau decays. In the future, we will provide a separate shower library for category 3. Currently, NuRadioMC comes with version 1.2

**Fig. 7** Charge-excess profiles and resulting Askaryan signal (unfiltered). Same as Fig. 6 but for electromagnetic showers with an initial energy of  $10^{16}$  eV. At this energy the LPM effect only has a small influence on the shower development and stochastic shower-to-shower fluctuations are small



of the shower library that will be described in the following.

The showers were simulated using HERWIG [56] for the simulation of the first neutrino nucleon interaction, and ZHAireS [57] for the subsequent simulation of the particle shower in ice. The charge-excess profiles are binned in bins of  $37 \text{ g/cm}^2$  for electromagnetic showers and  $18 \text{ g/cm}^2$  for hadronic showers. To optimize the computation speed, we integrate Eq. (8) numerically using the trapezoid rule given the binning of the charge-excess profile. The form factor is a strongly peaked function which requires a more precise integration around the peak. This is achieved by dynamically interpolating the charge-excess profile at the positions corresponding to the peak of the form factor.

The shower library (version 1.2) contains 10 showers for every shower energy ranging from  $10^{15}$  eV to  $10^{20.5}$  eV in steps of  $\Delta \log_{10}(E) = 0.1$  for both electromagnetic and hadronic showers. To obtain charge-excess profiles for shower energies that were not explicitly simulated we do the following: At first order, the charge-excess amplitude scales with shower energy. Hence, in a simulation, we pick one shower realization randomly from the nearest energy bin and re-scale the charge-excess amplitude by  $E_{\text{event}}/E_{\text{library}}$ .

To discuss and illustrate the improvement in accuracy when using the ARZ approach as opposed to a parameterization, we consider the influence of the LPM effect on the radio signal. The main consequence of the LPM effect is that the interaction probability of high-energy electrons, positrons and photons is suppressed leading to an elongation of the shower profile. The strength of the effect is proportional to the energy of the particle. Therefore, it mostly affects highly-

energetic electromagnetic showers above a few PeV in ice, in which a large amount of energy is carried by individual particles. Previously in the literature (e.g. [50, 57]), the effect was often modelled via stretching of a smooth shower profile. However, this does not take into account the stochastic nature of the process and the fact that the first few particles of an electromagnetic shower are impacted differently by the LPM effect as the energy is not equally distributed. As a consequence, one gets multiple spatially displaced EM showers as shown in Fig. 6. In this figure, also the resulting Askaryan signals are shown for two different viewing angles  $\theta$  which are significantly different for different realizations of the shower (see Fig. 1 for a sketch of the coordinate system). Low energy EM showers are less influenced by the LPM effect and the resulting Askaryan signals are similar for all shower realizations (cf. Fig. 7). Hadronic showers exhibit little shower-to-shower fluctuations except for the rare cases where a high-energy electromagnetic shower is initiated in one of the first interactions that then gets LPM elongated (see Fig. 8).

### 3.4 Comparison of models

Each signal generation module in NuRadioMC has its own strengths and shortcomings. We first compare the signal models with respect to their resulting signal properties and then discuss practical considerations. We provide a quick overview of the discussion in Table 1. In Fig. 9, a comparison of the predicted peak-to-peak amplitudes in a typical detector bandwidth of 100 MHz–500 MHz is presented that will be discussed below.

**Fig. 8** Charge-excess profiles and resulting Askaryan signal (unfiltered). Same as Fig. 6 but for hadronic showers with an initial energy of  $10^{17}$  eV. Most hadronic showers are not influenced by the LPM effect and show only very little shower-to-shower fluctuations. Different energies mostly scale the charge-excess and electric-field amplitudes approximately linear with energy but have a small effect on the shower length. However, sometimes a high-energy  $\pi^0$  that is created in one of the first interactions decays instead of interacting leading to an electromagnetic sub-shower that experiences significant LPM elongation (green dotted curve in this figure)

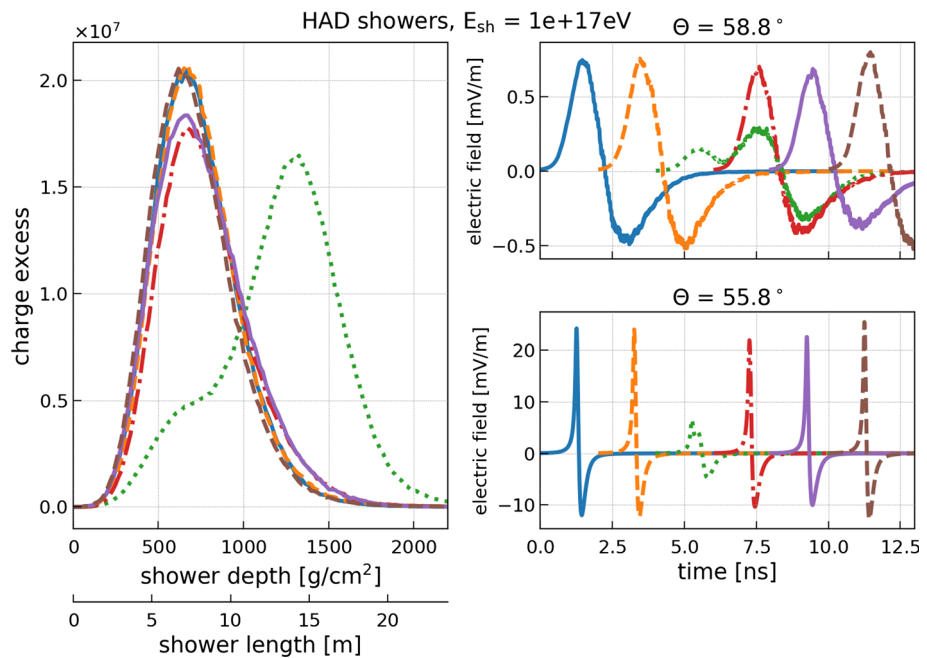


**Table 1** Overview of alternative methods implemented in NuRadioMC to calculate the signal following a neutrino interaction

Model	Advantages	Shortcomings
Parameterization ( <i>Alvarez2009</i> )	Fast, accurate representation of the signal amplitudes, includes statistical fluctuations from LPM	No phase information, only valid in far-field
Fully analytic ( <i>HCRB2017</i> )	Fast, phase information provided, valid in near and far-field, LPM is treated as elongated shower	No statistical fluctuations from LPM, generalization, absolute amplitudes less accurate
Semi analytic ( <i>ARZ</i> )	Phase information provided, near and far-field, realistic LPM treatment based on simulated shower library	Computationally expensive
Full MC	Precise modelling of all details of shower development	Slow, no implementation in NuRadioMC yet

The frequency-domain parameterizations are based on a detailed full Monte Carlo simulation of the particle shower and a calculation of the resulting radio signal using the ZHAireS code [46]. Thus, their predictions of the signal amplitudes are accurate, the narrowing of the Cherenkov cone due to the LPM effect is modelled and even statistical fluctuations in the shower development are parameterized (only *Alvarez2009*). The models are fast to evaluate and the computing time is negligible compared to the other parts of the simulation. We also provide an older version, *Alvarez2000*, that was most commonly used in previous simulation frameworks and is therefore important for comparison. However, we strongly recommend the usage of the newer model *Alvarez2009* as the older model typically overestimates the Askaryan amplitudes by roughly 20–30%. The

*Alvarez2009* model is in good agreement with the more precise *ARZ* time-domain calculation (cf. Fig. 9).

The main shortcomings of such parametrizations are that no phase information is provided which leads to inaccuracies in the time domain. Typically, the phases are approximated as constant  $90^\circ$  as function of frequency, which results in a perfectly symmetric bipolar pulse. While this may be a reasonable approximation for many cases, it does not capture the details of the shape of the pulses and does not account for physical time delays. Thus, these models are suitable for general sensitivity calculations given the correct prediction of amplitudes. However, more detailed models are recommended to study trigger efficiencies and event reconstruction that are based on pulse shape and timing.

Another option is the fully analytic model *HCRB2017* that also calculates the phases and is thus suitable for the time-

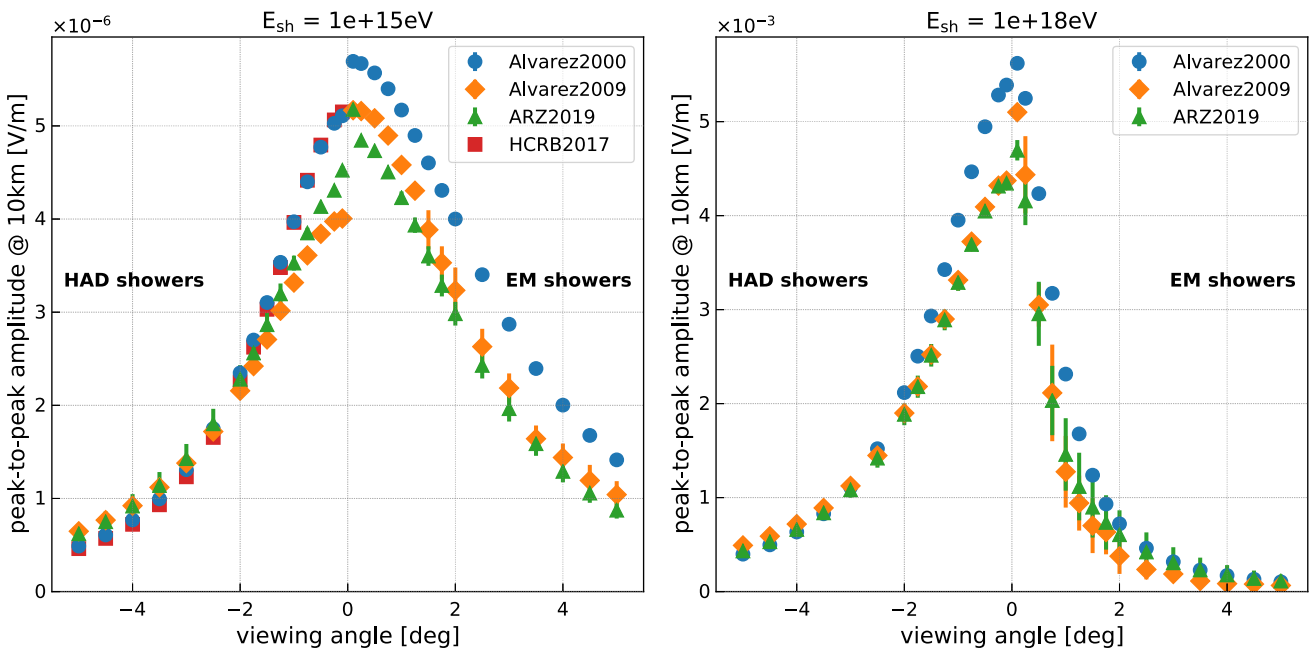


**Fig. 9** Comparison of Askaryan models. Shown the peak-to-peak amplitude (the difference between the maximum and the minimum of the Askaryan pulse) as a function of viewing angle. The pulses are filtered in a typical experimental bandwidth of 100 MHz to 500 MHz. The

left part of the plot (negative angles) shows the prediction for hadronic showers and the right part of the plot (positive angles) the prediction for electromagnetic showers of the same shower energy. (left)  $10^{15}\text{ eV}$  shower energy. (right)  $10^{18}\text{ eV}$  shower energy

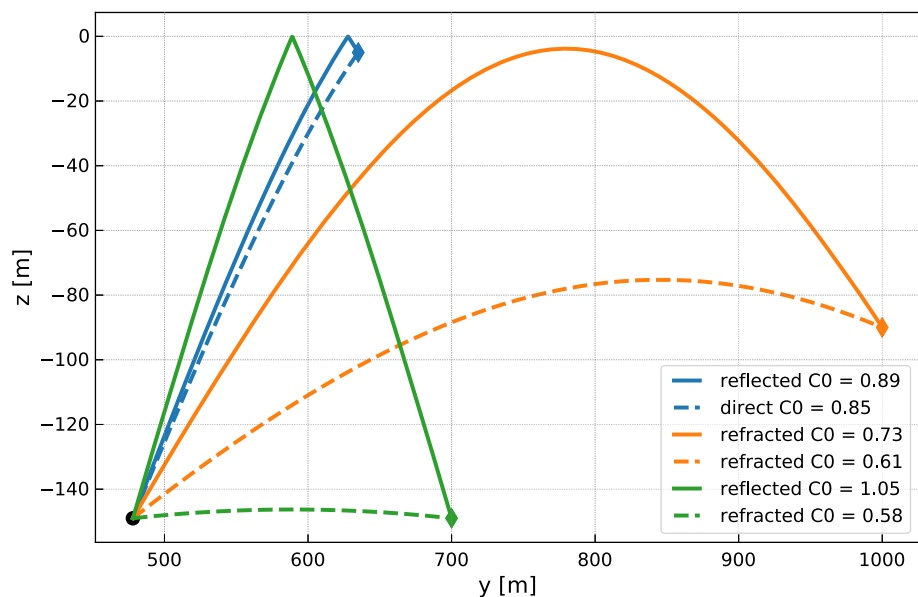
domain. It provides helpful insights into the dependencies of the Askaryan signals on shower elongation and shower width. As being analytically it does not model the statistical fluctuations occurring in showers that can be substantial as shown in Fig. 6. The signal strength prediction depends strongly on the longitudinal cascade width  $a$ , which has to be approximated with a Gaussian function for different cases (electromagnetic, hadronic and LPM showers). The approximations lead to a mis-match between the predictions of this model and the ones of the other models that are based on a microscopic Monte Carlo simulation where the calculation of the radio signal is based on first principles resulting in a few percent accuracy as shown in the radio emission of air showers [58]. In particular, the HCRB2017 model overpredicts the amplitudes at higher shower energies and the reduction of the cone width due to the LPM effect. Therefore, we only show the HCRB2017 model for low-energy hadronic showers in Fig. 9. Furthermore, the treatment of pulse arrival times is complex in an analytic model, complicating the integration with the different signal propagation modules (see Sect. 4). Naturally, the model is computationally very fast given its analytic approach.

The semi-analytic model ARZ builds on a shower library of charge-excess profiles and thus models all details like sub-showers including statistical fluctuations in the shower development. The calculation is performed in the time domain. It therefore includes all phase information and gives an accurate

prediction of the pulse shape and timing. The model provides valid results even when the distance from observer to shower is comparable to or smaller than the shower dimensions, as long as the distance is large compared the considered wavelengths. Above 100 MHz, and at distances greater than 10 m, the use of the ZHS formula, on which the ARZ model is based, is justified [59]. It is the most precise model available and recommended for the development of neutrino identification and reconstruction algorithms. Its disadvantage is that it is computationally more expensive. In a full end-to-end simulation it takes up roughly 90% of the computing time. When using this model, the computing time increases roughly by a factor of 10.

The next level of precision can be achieved with full Monte Carlo simulations where each shower particle is tracked and the radio emission is calculated from the acceleration and creation of each charged particle. This is done for air showers in codes like CoREAS [60] and ZHAireS [57], which are required to achieve the necessary accuracy for modern air shower experiments that are pushing the reconstruction uncertainties (e.g. [58, 61–63]). Currently, there is no urgency to require this level of accuracy for neutrino predictions, given the experimental uncertainties and the computational costs of a full Monte Carlo. However, future developments like a next generation of CORSIKA [64] are followed closely to allow for synergies and compatibility with NuRadioMC.

**Fig. 10** Example of typical ray-tracing solutions for receiver locations differing in depth and horizontal distance to a given emitter. The emitter is indicated by the black circle at the bottom left. Lines of the same color belong to the same receiver location. Shown are the combinations of direct and reflected ray (blue), refracted and reflected ray (green), and two refracted rays (orange). The numbers in the legend show the  $C_0$  parameter of Eq. (10) that defines the shape of the curve



One could also consider another future improvement in the combination of signal generation and propagation. As discussed earlier, the decoupling of signal generation and propagation leads to noticeable inaccuracies in an inhomogeneous medium (where the signal trajectories are bent, cf. next section) if the extent of the emission region becomes large with respect to the distance to the receiver and if the trajectory is substantially refracted in the firn. Then, the time delay of the propagation time from different emission points to the receiver vary between a homogeneous and inhomogeneous medium, so that signal generation and propagation cannot be separated without loss of accuracy. This effect can be taken into account naturally in a microscopic Monte Carlo simulation by calculating the (curved) path from each emission point to the observer. In an intermediate step, one could use the ARZ2019 model, where the Askaryan signal is calculated from the charge-excess profile to address the issue: Instead of calculating the emission from the full charge-excess profile at once, a shower can be subdivided into small chunks. The Askaryan radiation can then be calculated per chunk and propagated individually to the receiver.

#### 4 Signal propagation

The signal propagation pillar of NuRadioMC handles the propagation of the Askaryan signal through the medium to the observer positions. Like the other pillars, this part of the code is clearly separated so that different signal propagation modules can be implemented and exchanged by the user. This is achieved by defining an interface in form of a Python class (see general example in [65]).

The signal propagation problem is typically approximated via ray tracing but more general techniques such as a finite difference time-domain (FDTD) method that evolves Maxwell's equation can be foreseen in the future [66, 67]. In the ray-tracing approximation, the different ray paths connecting an emitter and receiver can be classified as *direct*, if the depth is monotonously decreasing or increasing along the path between emitter and receiver, as *refracted*, if the path shows a turning point, and as *reflected*, if the ray is reflected off the ice-air interface at the surface which acts as a perfect mirror for most geometries. A few typical ray-tracing solutions are presented in Fig. 10.

#### 4.1 Analytic ray tracing

The default signal propagation module in NuRadioMC is an analytic ray-tracing technique that provides an unprecedented combination of speed and precision relative to traditional ray-tracing techniques. Traditional ray-tracing techniques locate the path connecting an emitter and receiver by time intensive trial-and-error methods, where numerous rays are “thrown” until a ray which connects the emitter and receiver is found. This is necessary because the index-of-refraction ( $n$ ) of glacial ice is known to vary with depth, and so a light ray is bent and follows a curved path as it travels from an emitter to a receiver. Because the index-of-refraction does not need to be a well-behaved function it is impossible to predict the path traversed by the ray with full generality.

However, ice density measurements and the resulting index-of-refraction profiles from the South Pole and Moore’s Bay site exhibit a simple, depth-dependent index-of-refraction  $n(z)$ . The data can be described to within a few percent

[68] by an exponential function of the following form:

$$n(z) = n_{\text{ice}} - \Delta_n e^{z/z_0}, \quad (9)$$

where  $z$  is the depth and  $n_{\text{ice}}$ ,  $\Delta_n$ ,  $z_0$  are the parameters of the model. For this specific exponential  $n(z)$  profile, an *analytic* solution of the ray path as a function of depth ( $y(z)$ ) exists and is given by

$$y(z) = \pm z_0 \sqrt{n_{\text{ice}}^2 C_0^2 - 1} \cdot \ln \left( \gamma / \left[ 2\sqrt{c(\gamma^2 - b\gamma + c)} - b\gamma + 2c \right] \right) + C_1, \quad (10)$$

with  $\gamma = \Delta_n e^{z/z_0}$ ,  $b = 2n_{\text{ice}}$ , and  $c = n_{\text{ice}}^2 - C_0^{-2}$ . We provide a derivation of this equation in Appendix C.1. The parameters  $C_0$  and  $C_1$  uniquely describe the ray path and need to be determined from two initial conditions which are given by the two points the ray goes through, e.g., the neutrino interaction vertex (the point of emission) and the observer position.

The parameter  $C_1$  corresponds to a vertical translation in the coordinate system and can be calculated analytically from the initial conditions. The parameter  $C_0$  must be determined numerically, and is found through a least-squares minimization. For each receiver-emitter coordinate pair, we can either have no, one or two solutions, corresponding to no connecting ray, one connecting ray, or two connecting rays. To quickly and stably find all possible solutions, we leverage numerical algorithms as documented in Appendix C.2.

#### 4.1.1 Derived quantities

Once a ray path is found, several derived quantities are needed in the simulation. The *launch vector* of the ray is needed to calculate the *viewing angle* (the angle between shower axis and launch vector) which is required to calculate the Askaryan emission. The *receive vector* is needed to evaluate the antenna response for the arrival direction of the incident radiation. As discussed in Appendix C.2, the ray-tracing problem can be reduced to the y-z plane with a simple coordinate rotation. Hence, only the launch and receive angles are required, which can be calculated analytically from the derivative  $dy(z)/dz$  which we specify in appendix Appendix C.4.

The path length can be calculated numerically via the following line integral

$$d = \int_{z_1}^{z'_2} \left| \frac{d\mathbf{x}}{dz} \right| dz = \int_{z_1}^{z'_2} \sqrt{1 + \left( \frac{dy(z)}{dz} \right)^2} dz, \quad (11)$$

where  $\mathbf{x} = (y(z), z)^T$ , and  $z_1/2$  refer to the z position of the emitter/receiver. In case of a direct ray we have  $z'_2 = z_2$ . In case of a refracted or reflected ray, we first need to integrate from  $z_1$  to the turning point and then the same path backwards to  $z_2$ .

Similarly, the travel time  $t$  and the signal attenuation  $\exp(-A)$  can be calculated as

$$t = \int_{z_1}^{z'_2} n(z)/c \left| \frac{d\mathbf{x}}{dz} \right| dz = \int_{z_1}^{z'_2} n(z)/c \sqrt{1 + \left( \frac{dy(z)}{dz} \right)^2} dz, \quad (12)$$

and

$$A = \int_{z_1}^{z'_2} \left| \frac{d\mathbf{x}}{dz} \right| / L(z, f) dz \quad (13)$$

$$= \int_{z_1}^{z'_2} \sqrt{1 + \left( \frac{dy(z)}{dz} \right)^2} / L(z, f) dz \quad (14)$$

where  $L(z, f)$  is the attenuation length as a function of depth and frequency which is discussed in Sect. 6.5.

If the index of refraction profile is described with an exponential function as in Eq. 9, an analytic expression for the path length and travel time can be derived. This analytic function is used by default due to its improved computing time. The derivation can be found in Appendix C.5. For the attenuation factor no analytic solution has been found and a numerical integration is required.

#### 4.1.2 Computational speed

We provide a Python implementation of the analytic ray-tracing technique described above which leverages the NumPy [69] and SciPy [70] computational packages. In addition, we implemented the time critical operations of finding the ray-tracing solution and determining the signal attenuation in a standalone C++ module. This C++ module leads to a substantial speed improvement of a factor of 20, so that the calculation of the ray-tracing solutions and the calculation of travel time and distance as well as the signal attenuation takes less than 4 ms in ice. The C++ module utilizes the highly optimized and broadly supported GNU Scientific Library (GSL) [71] for numerical integration and root-finding.

We provide a Cython wrapper to the C++ implementation so that it can be called as a sub-routine. Selection of routine (C++ or Python) is done in a transparent fashion. If the user compiled the C++ extension, NuRadioMC will automatically pick the faster C++ implementation, and otherwise utilize the Python implementation. In this way, the

NuRadioMC code works out-of-the-box without additional dependencies. The Python implementation is still sufficiently fast to be used for many problems.

#### 4.2 Focusing effect due to ray bending

Applying the ray approximation to signals from neutrinos in case of ray bending, requires an additional correction factor on the signal amplitude. In general, when considering many rays which are bent there can either be a convergence or divergence of rays. If there is a convergence the ray density and thereby the amplitude of the signal will increase, and conversely so for a divergence. For the ice geometry, refraction contains the signal within the ice, and an amplification is expected if the receiver is above the point of emission and the ray is not reflected from the surface.

We calculate a correction factor from an energy conservation argument: The intensity along the ray is given by

$$I = \sqrt{\frac{\epsilon \varepsilon^2}{\mu c}} = \frac{n \varepsilon^2}{c}, \quad (15)$$

for  $\mu = \mu_0$  where  $\varepsilon$  is the electric-field amplitude,  $c$  the speed of light and  $n$  the index of refraction. The total power contained in a ray bundle is  $P = I A$  with  $A$  being an area perpendicular to the propagation direction, so the electric field strength propagates as

$$\varepsilon' = \varepsilon \sqrt{\frac{n A}{n' A'}}. \quad (16)$$

The power radiated into a given solid angle is fixed by the source. For a spherical geometry we have

$$dA = R^2 d\Omega = R d\theta \times R \sin \theta d\phi. \quad (17)$$

For refracted rays the relation  $\frac{dA}{d\Omega}$  changes during propagation. Assuming a planar index of refraction model, i.e., it only depends on the depth  $z$ , only the  $R d\theta$  part changes and is given by

$$dA' = \frac{dz}{d\theta} \sin \theta' d\theta \times R \sin \theta' d\phi. \quad (18)$$

See Appendix C.6 for a derivation of this relation. Then, the ratio of electric field amplitudes is given by

$$\frac{\varepsilon'^2}{\varepsilon^2} = \frac{n}{n'} \frac{dA}{dA'} = \frac{n}{n'} \frac{R}{\sin \theta' \frac{dz}{d\theta}} \quad (19)$$

in the limit of  $\theta \approx \theta'$ , which is applied as a correction factor to the calculated electric field amplitude from the signal generation module. The factor  $\frac{dz}{d\theta}$  is calculated numerically using the ray tracing code by calculating a new ray to the

receiver position which is vertically displaced by a small amount  $\Delta z \approx 1 \text{ cm}$ .

Emitter positions very close to the shadow zone boundary require special attention as the correction diverges because  $\frac{dz}{d\theta}$  approaches zero. This is not physical but an artifact from treating both emitter and receiver as a point. However, in reality the emission region is extended over several meters due to the extent of the particle shower (cf. Fig. 7) and also the antenna is an extended object. Thus, we studied the stability of the correction factor under small changes of the emitter position by  $\pm 5 \text{ m}$  corresponding to typical dimensions of the emission region. We find that correction factors below about a factor of  $2 \times$  in amplitude vary by less than 10% when the emitter position is varied. Larger amplification factors in-turn are not stable. Hence, limiting the amplification to a maximum of  $2 \times$  removes unphysical correction factors. Furthermore, we studied the effect of the limit value. Limiting the focusing correction to a factor of  $1.5 \times$ ,  $2 \times$  and  $3 \times$  results in essentially the same effective volume (i.e. sensitivity of the detector) over a broad range of neutrino energies. Thus, the exact choice limit value is not that important as long as very large amplification factors are removed. As default we limit the focusing correction to a factor of  $2 \times$  but allow the user to configure this value via the config file.

The effect of focusing is strongest when the rays pass near the surface and experience significant refraction. For a receiver close to the surface we find an increase in the effective volume of the order of 10% due to this correction.

#### 4.3 Numerical ray tracing for arbitrary density fields

In the future, it may become necessary to describe the ice in more detail than an exponential profile that only depends on the depth. This will require a more detailed ray tracing that takes into account an arbitrary 3D index of refraction profile  $n(x, y, z)$ . We have already foreseen this case and ensured that necessary hooks are available in the code.

Interestingly, the computational problem of the propagation of ultra-high energy cosmic rays through the universe is similar to propagating a ray through the ice. Instead of magnetic fields bending the trajectories of charged cosmic-ray particles, the ray is bend according to the spatial distribution of the index of refraction. Where the cosmic ray can spallate into secondaries, a ray can be partly transmitted and reflected. Consequently, we considered the cosmic-ray propagation code CRPropa [72] as one option and have started to modify it for our needs.

The resulting code RadioPropa [73] solves the Eikonal equation in a local paraxial approximation thus enabling casting of rays through materials with arbitrary varying refractive index as may be required here. In addition, RadioPropa handles effects from boundary traversals such as reflection or partial reflection and allows for the implementation of prop-

agating components of the electric field differently, such as needed for birefringence. It automatically tracks several parts of the original ray, making it also suitable for other less well understood phenomena in the ice. In the same way as NuRadioMC, RadioPropa is modular and flexible, leaving room for future developments. It is currently under heavy development and therefore not yet fully included in NuRadioMC.

#### 4.4 Signal propagation beyond ray tracing

Ray tracing describes the path taken by light in the limit where the wavelength is much smaller than any relevant feature sizes. While this is appropriate in most practical cases, i.e., when the ice is uniform or has a slowly-varying index of refraction, ray tracing does not offer a full description of light propagation near dielectric interfaces, where additional solutions to Maxwell's equations exist, (see e.g. [74] for a pedagogical tutorial on some of the solutions, or [75] for a complete solution for the field of a particle track). In addition to the ice-air interface at the surface, variations in ice density are present below the surface, producing a set of dielectric interfaces. These may result in signals being observed at locations, where simple models assuming a smooth gradient predict no radio signals [68]. While adaptations to the analytic ray-tracing requiring a smooth gradient of the index of refraction, deliver solutions for special cases, the finite-difference time-domain (FDTD) method may be used to model propagation in ice even in the presence of inhomogeneities in all its aspects [66, 67].

Interesting phenomena that arise include the existence of potentially detectable (though generally small) signals coming from regions where there is no ray-tracing solution, diffraction and interference of the radio waves, and the presence of caustics, where the small electric field may be significantly amplified in some geometries [67].

While these effects will slightly modify the effective volume of a detector and provide additional opportunities for event reconstruction, direct integration of an FDTD solver into NuRadioMC is challenging for the purpose of providing a simulation framework. FDTD methods are very computationally and memory intensive, requiring discretization on the scale of a tenth of the smallest relevant wavelength in all spatial dimensions as well as time. Directly simulating the entire volume seen by a typical in-ice station is extremely computationally challenging in three dimensions with our present capabilities – we estimate a single simulation of a cubic kilometer volume valid up to 500 MHz would take  $\mathcal{O}(10^7)$  CPU-hours. One can envision the usage for a single event (in case of re-simulation of a detected shower for example), the integration for all events is, however, impractical.

By considering only azimuthally-symmetric antennas and density variations dependent only on depth, it is possible to simulate a transmitting in-ice antenna in just two dimensions,

greatly reducing the computational burden. We are investigating techniques exploiting reciprocity in order to tabulate the propagation properties of the equivalent time-reversed geometry, corresponding to a receiving antenna. Such tabulated properties could then be incorporated into NuRadioMC in an efficient manner.

## 5 Detector simulation

The fourth pillar of NuRadioMC is the detector simulation, i.e., the calculation of the detector response to an electric field at the antenna and subsequent trigger simulation. We use the software *NuRadioReco* for this task [28]. NuRadioReco is a software for the detector simulation and event reconstruction of radio neutrino and cosmic-ray detectors. It is written in Python and also follows a modern modular design so that it nicely integrates into NuRadioMC.

### 5.1 Antenna simulation

The most important part in the simulation of the detector response is the impact of the antenna. NuRadioReco provides antenna response pattern of typically used antennas such as LPDAs, dipoles or bicone antennas that were simulated with dedicated codes such as WIPL-D [76] and XFDTD [77]. NuRadioReco also provides an interface to the output of these codes such that new antenna models can be added if necessary.

In earlier software, the response of the antennas was typically treated in a simplified way, only assuming real gain factors and a simple polarization response, i.e. ignoring contributions polarized orthogonal to the main antenna sensitivity. According to methods already standard in the treatment of radio signal from cosmic rays (e.g. [63, 78]), the antenna response is modelled fully frequency-dependent in NuRadioReco, also taking into account the group delay induced by the antenna and its sensitivity to two orthogonal polarization components.

### 5.2 Trigger simulation

Especially when looking for small signals, as expected from neutrinos, the simulation of the trigger mechanism is essential. The trigger simulation is set up as such that any instrumental trigger can be rebuilt in software. NuRadioReco offers modules to simulate different trigger conditions, e.g., a simple threshold trigger, a high and low trigger as implemented on the SST electronic [79] used by ARIANNA [8] that also allows to specify temporal coincidences between different channels, or more complex triggers such as the phased array concept used by ARA [12] have been included to model the instrument response as implemented in the fields.

### 5.3 Usage in complex detectors

NuRadioReco was built to reconstruct data from an existing detector. In order to facilitate complex detectors without creating too much overhead, the detector description is stored in a database allowing for a description of every single detector component. While this functionality will be helpful to simulate specific events for an existing detector, it is much too complex for design studies. Therefore, NuRadioReco also allows the user to define the detector description in a human readable JSON format, with reduced complexity. This means both that the detector description only needs to be as complex as minimally required and it significantly speeds up simulations. The information ranges from basic parameters such as the positions of the antennas, their type and orientation to more detailed properties such as the sampling rate of the digitizing electronics, the cable lengths or details about the amplifier and ADC. The detector simulation modules have access to these properties and will simulate the detector response accordingly. An example of a typical detector simulation is provided in Appendix E.

## 6 Utilities

The four pillars of NuRadioMC are complemented by a set of utility classes that are available to all modules, such as units and medium properties.

### 6.1 Cross-sections and inelasticities

The cross-section of neutrinos at energies relevant for radio detection are still subject to study, given that these energies have never been probed. Different current extrapolations [31, 33, 34] have been implemented in NuRadioMC in the central utilities, so that the cross-sections can easily be exchanged throughout the code, if so desired.

### 6.2 Earth models for neutrino absorption

To simulate the sensitivity of a neutrino detector, we need to calculate the probability of a neutrino reaching the detection volume. The Earth atmosphere has negligible absorption for high energy neutrinos but the Earth becomes opaque at high neutrino energies. Hence, NuRadioMC comes with multiple models to calculate the Earth absorption so that we can assign each simulated neutrino a weight, i.e., a probability of reaching the detection volume.

Right now, NuRadioMC provides two Earth models: a simple Earth model with a constant density and a core-mantle-crust Earth model with three layers of different densities. Due to the modularity, it is straight forward to add more detailed models if deemed necessary.

Currently, we do not model *tau regeneration*: A tau lepton that is created following a tau neutrino interaction can propagate significantly through the Earth and potentially decay with a relatively large energy and producing another tau neutrino that can interact close to the detector. We plan to include this effect in a future version of NuRadioMC using e.g. the code of [80, 81].

#### 6.2.1 Simple Earth model

This model uses a constant density of  $2900 \text{ kg/m}^3$  and by default uses the cross section ( $\sigma$ ) based on [31]. It then calculates the distance the neutrino goes through the Earth as

$$d = 2R_e \cos(\pi - \vartheta), \quad (20)$$

where  $R_e$  is the radius of the Earth and  $\vartheta$  is the zenith angle of the neutrino direction. The weight of an event is then

$$\text{weight} = e^{-d\sigma\rho/\text{AMU}}, \quad (21)$$

where  $\rho$  is the constant density of the Earth and AMU is the atomic mass unit in kg.

#### 6.2.2 Core-mantle-crust Earth model

NuRadioMC provides a more realistic Earth model with three layers of different densities which is the default model. In this model, the cross section is per default calculated based on [33] and the propagation distance is calculated through three different layers. The weight is calculated as

$$\text{weight} = e^{-(d_1\rho_1 + d_2\rho_2 + d_3\rho_3)\sigma/\text{AMU}}, \quad (22)$$

where  $d_1, d_2, d_3$  are the distances through three layers and  $\rho_1, \rho_2, \rho_3$  are the three densities.

### 6.3 Handling of Fourier transforms

NuRadioMC provides a consistent internal handling of Fourier transforms. A common source of errors when using time- and frequency-domain calculations simultaneously is the normalization of the Fourier transforms. There are several reasons for different normalizations depending on the purpose and context. All NuRadioMC Fourier transforms adhere to Parseval's theorem and previously existing Askaryan signal parameterizations have been adjusted to match the FFT definition used in NuRadioMC. Details are discussed in Appendix D.

### 6.4 Handling of units

In simulations, typical errors occur during the handling of units. To prevent that, NuRadioMC (just like NuRadioReco)

employs a default system of units, a concept borrowed from the Pierre Auger Observatory offline analysis framework [82]: every time a physical variable is defined, it is multiplied by its unit, and every time a variable is plotted or printed out in a certain unit, it is divided by the unit of choice. All other calculations within the code can then be done without considering units.

```
from NuRadioMC.utilities import units
time = 132. * units.ms # define 132 milliseconds
distance = 5. * units.mm # define 5 mm
speed = distance/time
print("the speed is {:.2f} km/h"
      .format(speed/units.km*units.hour))
# the speed is 0.14 km/h
```

The units utilities are available to modules written in both Python and C. In order to facilitate this, no standard Python package was used.

## 6.5 Attenuation length and other medium characteristics

As discussed in Sect. 4 the signal propagation is a significant part of the neutrino simulation and an area where lots of development is still to be expected. Consequently characteristics of the interaction medium are stored centrally in the utilities to avoid contradicting definitions in modules. We describe the index-of-refraction profile and signal attenuation properties separately to allow for simulation with different combinations of the two. Which model is being used in a NuRadioMC simulation is controlled via the central config file (see Sect. 7.2).

Currently, a signal attenuation model for South Pole ice is provided that is based on a custom model used by the ARA experiment [83]. For the index-of-refraction profile we provide exponential parameterizations to data from for the South Pole and Moore's Bay [68], as well as from Greenland [84, 85].

## 6.6 Flux calculations and sensitivity limits

In order to compare the performance of different experimental designs, typically quantities like the effective area, volume or expected limits are compared. Since also here, many definitions are common (e.g. 90% confidence upper limits vs.  $5\sigma$  discovery fluxes), utility functions are provided centrally.

## 7 Example 1: calculation of the sensitivity of an Askaryan neutrino detector

In this section we present a full example of the capabilities of NuRadioMC to simulate the sensitivity of an Askaryan

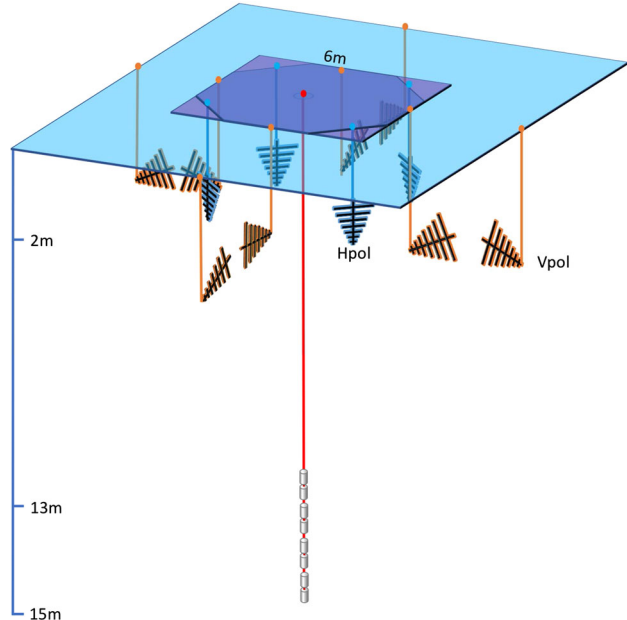


**Fig. 11** Sketch of the station layout simulated in Example 1

detector. We choose a station layout that combines log-periodic dipole antennas (LPDA) near the surface with slim dipoles deployed in a borehole deeper in the ice. The specific layout is depicted in Fig. 11. This station layout does not necessarily reflect the authors' opinion on the optimal detector layout but was chosen because it highlights NuRadioMC's capabilities: Antennas of different type, orientation and depth are simulated, the location close to the surface makes a detailed propagation of the signal through the firn necessary, and multiple trigger conditions need to be calculated for different sets of antennas. In the following, only the relevant code snippets are shown. A comprehensive tutorial can be found online [86].

### 7.1 Event generation

The first step in the simulation is the event generation. The event generation is done stand-alone and produces a list of neutrino interactions in the ice with all necessary properties saved in a simple HDF5 format (see Sect. 2 for details and advantages of separating this step). We choose to generate several input lists, each for a fixed neutrino energy to study the energy dependence. We only consider the initial neutrino interaction. A discussion of the impact of additional Askaryan signals from decaying taus or interacting muons goes beyond the scope of this publication.

A list of one million neutrino interactions with an energy of  $E_\nu = 10^{18}$  eV in a cylindrical volume saved in chunks of 10,000 events can be generated with

```
generate_eventlist_cylinder('1e18_n1e6.hdf5',
    n_events=1e6, n_events_per_file=1e4,
    Emin=1e18 * units.eV, Emax=1e18 * units.eV,
    fiducial_rmin=0, fiducial_rmax=5 * units.km,
    fiducial_zmin=-2.7 * units.km, fiducial_zmax=0)
```

The radius needs to be set large enough to include all events that can trigger the detector and is set to 4 km here. For larger neutrino energies, the radius needs to be extended and for lower energies the simulation volume can be decreased to save computing time. The vertical extent of the volume ranges from the surface to the bottom of the ice layer at a depth of 2.7 km at the South Pole.

## 7.2 Configuration of simulation parameters

The settings of the simulation are controlled with a config file in the human-readable yaml format. The user only needs to specify a parameter if it should be different from its default value. An example configuration with typical settings is shown in listing 1. Typical parameters are the choice of signal generation model (*Alvarez2009* in this example), the ice model, or if noise should be generated and added to the signal in the simulation.

```
noise: False # specify if simulation should be
    run with or without noise
sampling_rate: 5. # sampling rate in GHz used
    #internally in the simulation.
speedup:
    minimum_weight_cut: 1.e-5
    delta_C_cut: 0.698 # 40 degree
propagation:
    ice_model: southpole_2015
signal:
    model: Alvarez2009
trigger:
    noise_temperature: 300 # in Kelvin
weights:
    weight_mode: core_mantle_crust # core_mantle_crust:
        #use the three layer earth model,
        #which considers the different densities of the
        #core, mantle and crust.
        #Simple: use the simple earth model,
        #which applies a constant earth density
```

Listing 1: Example of NuRadioMC’s config file. All parameters are specified in a default system of units. See text for details.

## 7.3 Detector description

The detector description consists of two parts. First, we need to define the layout of the detector (position, type, and orientation of the antennas), and the sampling rate. Additional parameters such as cable delays and amplifiers can be specified if needed (cf. Sect. 5.3 and NuRadioReco [28]). However, in this example we will perform a simplified detec-

tor simulation sufficient to estimate the sensitivity of an Askaryan detector. The detector description is specified in a JSON file presented in List. 2.

```
{
    "channels": {
        "1": {
            "station_id": 101,
            "channel_id": 0,
            "ant_type": "createLPDA_100MHz",
            "ant_position_x": 3,
            "ant_position_y": 0,
            "ant_position_z": -2.0,
            "ant_rotation_phi": 180,
            "ant_rotation_theta": 90,
            "ant_orientation_phi": 0,
            "ant_orientation_theta": 180,
        },
        ...
    },
    "stations": {
        "1": {
            "pos_altitude": 0,
            "pos_easting": 0,
            "pos_northing": 0,
            "pos_site": "southpole",
            "station_id": 101
        }
    }
}
```

Listing 2: Example of detector description. Only the first channel is shown which defines a downward facing LPDA at a depth of 2 m with its tines oriented along the Northing direction.

Second, we need to specify basic details of the signal chain, i.e., what filter is being used and which triggers are calculated. These tasks are done by dedicated NuRadioReco modules [28] (see Sect. 5.3) that interface directly with NuRadioMC. Instead of simulating just a single trigger condition as shown in the example, a separate trigger can be simulated for each parallel pair of LPDA antennas and for the dipole antennas. This is achieved by calling the same trigger module several times with different arguments. The full example can be found in the online tutorial [86].

## 7.4 Running the simulation, results, and visualization tools

The NuRadioMC simulation is run by executing the steering script from the command line. The flexibility to split up the input data set into smaller chunks is part of the event generator, so multi-processing computing resources can be used right away. A detailed example on how to run NuRadioMC on a cluster is available in the online tutorial [87].

The sensitivity of the detector is quantified in terms of effective volume to an isotropic neutrino flux. It is given by the weighted sum of all triggered events divided by the total

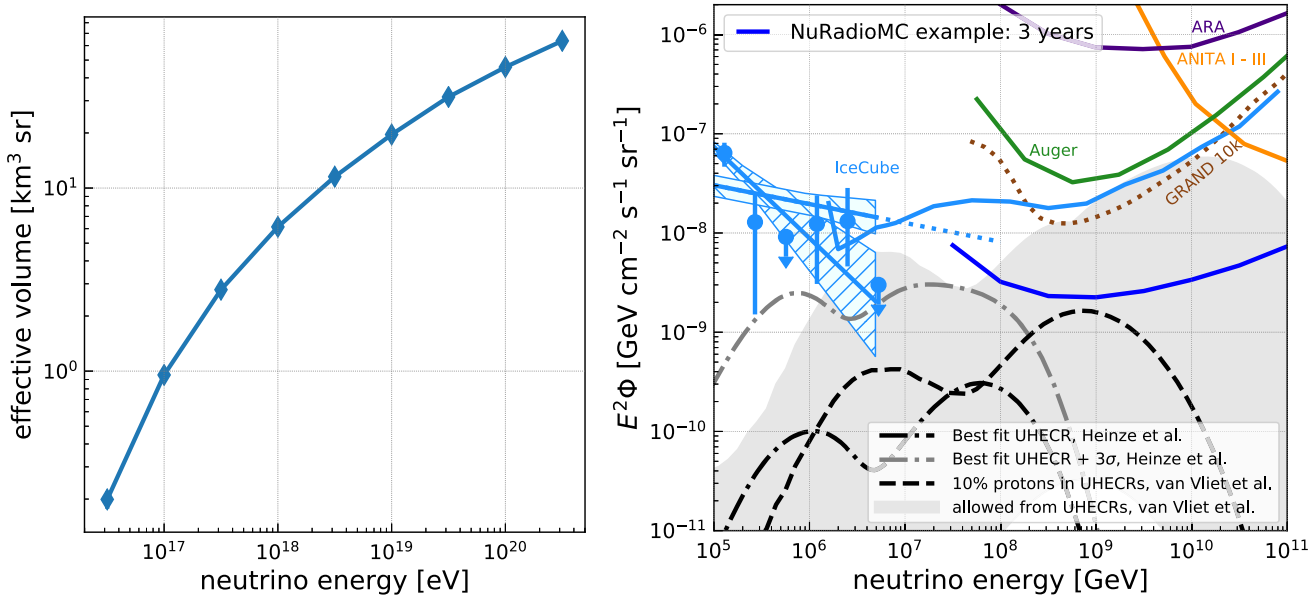


**Fig. 12** (left) Effective volume of one example detector station (right) corresponding expected limit for a diffuse neutrino flux for a detector comprising 100 stations and an uptime of 3 years. Shown are for comparison neutrino flux measurements from IceCube [88–90], the Pierre

Auger Observatory [91], ANITA [92], and ARA [10], as well as neutrino flux prediction models from [93,94] calculated using the restrictions from ultra-high energy cosmic rays. We also compare to other proposed arrays [95]

number of events multiplied by the simulation volume and the simulated solid angle (typically  $4\pi$ ). The weighting factor is the probability of a neutrino reaching the simulation volume (and not being absorbed by the Earth). The effective volume of our example detector station is presented in Fig. 12 (left). This effective volume can be converted into an expected limit on the diffuse neutrino flux which is shown in the right panel of Fig. 12. The required tools to make these standard post-processing plots are also part of NuRadioMC.

Furthermore, a standard set of debug plots can be automatically generated from the output files. The distribution of the neutrino interaction vertices of events that triggered the detector is shown in Fig. 13 (left). The upper right (triangular) part of the volume correspond to positions in the *shadow zone* where signals cannot reach the detector according to the ray tracing. The lower left region has little events because the Askaryan signal is only emitted towards the antennas if the neutrino is up-going, i.e., it travelled through the Earth and its probability of reaching the detector is small. The right panel shows the ratio of neutrino flavors and interaction types that triggered the detector. In this case, most triggered events were electron neutrino charged-current (CC) interactions where the full neutrino energy is deposited in particle showers producing an Askaryan signal.

## 8 Example 2: calculation of the efficiency to detect a signal from both the direct and reflected path

In this example, we calculate the efficiency of an in-ice antenna to observe both the direct Askaryan signal and the signal reflected at the ice surface. For most shower geometries there is total internal reflection of the Askaryan signal at the ice surface, i.e., the ice-air interface acts as a mirror. Consequently, an antenna installed within the ice has the chance to see two pulses: one pulse that propagated straight to the antenna and a second pulse that was reflected off the surface. Detecting this *D'n'R* (direct and reflected) signature is advantageous and an Askaryan neutrino detector will benefit strongly from detecting both pulses: First, it provides a unique method to identify a neutrino interaction in the ice as origin of the detected radio signal, and second, the time difference between the two pulses allows for an improvement in the reconstruction of the distance to the neutrino interaction vertex which is a crucial ingredient for the reconstruction of the neutrino energy. See [9] and [96] for first experimental results concerning this effect using pulsars deployed in the Antarctic ice at South Pole.

There are several effects that influence the efficiency of detecting both pulses that are all taken into account in the NuRadioMC simulation:

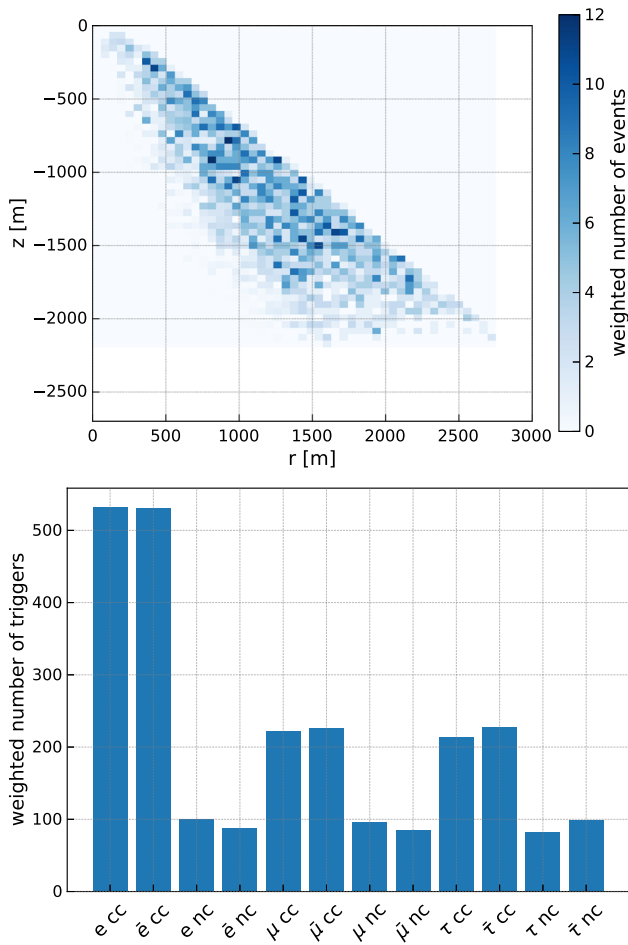


**Fig. 13** Visualization for the energy bin of  $10^{18}$  eV neutrino energy. (top) Distribution of neutrino interaction vertices of all triggered events. (bottom) Flavor and interaction type (charged or neutral current) distribution of triggered events

- The reflection coefficient depends on the incident angle of the radio pulse at the ice surface and can range from 1 (total internal reflection) to 0 (no reflection) at the Brewster angle.
- The reflection results in a phase shift of the Askaryan pulse which can alter the amplitude of the pulse. This is modelled using the complex Fresnel coefficients.
- Due to the changing index of refraction in the upper ice layers the signal propagates on curved paths. We find all possible paths to each antenna via ray-tracing. We note that not only a ‘direct’ and ‘reflected’ path will provide a useful signature but any two distinct paths through the ice to the antenna. In case only one solution exists, the efficiency to detect two pulses is of course zero.
- The different ray paths correspond to different launch angles of the signal. This results in a potentially large difference of the amplitude of the Askaryan signal as the launch angles correspond to different viewing angles.

- Antennas have a different sensitivity to different incoming signal directions.
- The two ray paths have different propagation distances and potentially propagate through ice with different attenuation lengths.

In the following we describe an example of how to simulate the D’n’R detection efficiency with NuRadioMC and explain the relevant parts of the code. The full code of this example can be found online at [97].

The D’n’R efficiency depends on the depth of an antenna, hence, we want to define a detector with several antennas of the same kind at different depths. As antenna type we choose a bicone antenna as used by the ARA experiment as such an antenna is sensitive to the dominant vertical polarization, fits into narrow boreholes, and has very little signal dispersion which helps to measure the time difference between the two pulses. Hence, we set up a detector with vertically oriented bicone antennas every 10 m down to a depth of 100 m.

It does make sense to study the D’n’R efficiency as a function of neutrino energy. Therefore, we can use the same script to generate the input event list as in the previous example.

### 8.1 Set-up of detector simulation

In the previous example we have discussed how to simulate the detector response and the trigger. In the detector simulation so far, all signals that reach the antenna from the different ray path solutions, are combined into a single voltage trace on which the trigger condition is determined. However, for the D’n’R study, we not only need to determine if the detector could observe/trigger a certain event, but also if both pulses are visible. Hence, a dedicated *NuRadioReco* module called *calculateAmplitudePerRaySolution* was written, which simulates the antenna response to each pulse separately and calculates and saves the resulting maximum amplitude. Following this we can calculate if a triggered event has two visible pulses.

As trigger condition we choose a simple threshold trigger of  $2 V_{rms}$  that runs on all channels (i.e. antennas) independently. The NuRadioMC simulation is then executed as described in Example 1.

### 8.2 Results

We now assume a more stringent cut in which all events that produce at least a  $3\sigma$  ( $3 V_{rms}$ ) signal can be recorded. For the second pulse the requirement for identification is assumed smaller at  $2\sigma$ . Furthermore, we require that the time difference between the two pulses is smaller than 430 ns

which is assumed as typical record length. We then calculate if an event has triggered via

$$B_i = A_1^i \geq 3 V_{\text{rms}} \quad \text{or} \quad A_2^i \geq 3 V_{\text{rms}} \quad (23)$$

and if both pulses are visible via

$$C_i = ((A_1^i \geq 3 V_{\text{rms}}) \text{ or } (A_2^i \geq 3 V_{\text{rms}})) \quad (24)$$

$$\text{and } ((A_1^i \geq 2 V_{\text{rms}}) \text{ and } (A_2^i \geq 2 V_{\text{rms}})) \quad (25)$$

$$\text{and } (\Delta T < 430 \text{ ns}), \quad (26)$$

where  $A_1^i$  and  $A_2^i$  are the amplitudes of the two pulses of event  $i$ .

Then the D'n'R efficiency is then given by

$$\epsilon = \sum_i C_i / \sum_i B_i \quad (27)$$

where the summation runs over all simulated events  $i$ . This calculation is performed for each simulated antenna depths, and for each set of simulated neutrino energy separately.

We simulated 10 million events per neutrino energy and obtain the result presented in Fig. 14. The D'n'R efficiency depends strongly on depth and energy and is best at shallow depth and high energies.

It should be noted that D'n'R efficiency is not the only parameter that one should optimize an array for. For example, a shallower station generally has a smaller effective volume than a deep station, and the fraction of sky coverage also depends of depth. Together with a diverse choice of antennas influencing reconstruction capabilities, data volume restrictions, and instrument costing, optimizing a detector layout is a complex problem, for which NuRadioMC provides guidance.

## 9 Example 3: Optimization of station spacing for an Askaryan neutrino detector

In this example we calculate the probability to detect a signal from the same neutrino in multiple stations of an array. For a discovery detector, one objective is a large sensitivity which means that it is beneficial to separate stations far enough to minimize station coincidences. However, one may want to optimize differently in the future to have a large fraction of coincidences to improve reconstruction quality. Here, we show how the coincidence fraction can be studied as a function of station separation distance, neutrino energy, and antenna depth. The full code of this example can be found online at [98].

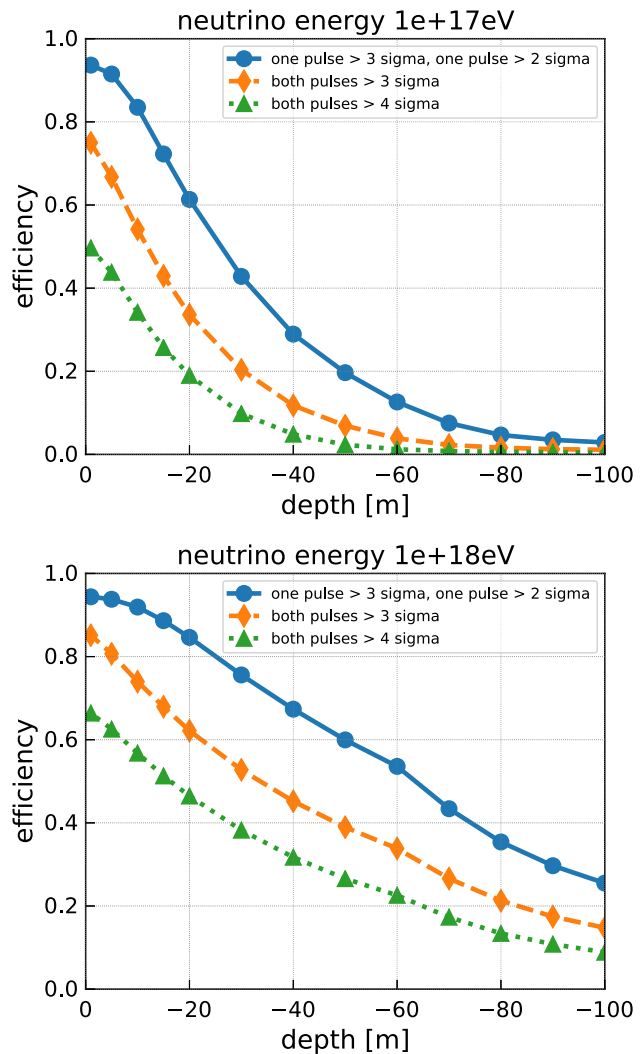


**Fig. 14** Efficiency to detect both the direct and reflected Askaryan pulse as a function of depth of the receiver. (top) For a neutrino energy of  $10^{17}$  eV. (bottom) For a neutrino energy of  $10^{18}$  eV. Different markers and colors correspond to different trigger thresholds. All events with a signal of at least a  $3\sigma$  in any of the pulses were considered which explains the smaller efficiency at the surface for the 'both pulses  $> 4\sigma$ ' criterion

### 9.1 Simulation strategy

We consider a simplified detector with two components. The first one is a surface oriented component consisting of LPDAs and dipoles. To save computing time, we only simulate two orthogonally-oriented horizontal LPDAs at 2 m depth and one dipole at 5 m depth to be sensitive to all signal polarizations. The second component is a deep one, approximated with a single dipole antenna at 50 m depth. We combine the four antennas into a single station so that only one simulation needs to be run, but we can still evaluate the coincidence fraction independently.

In principle, one would need to simulate a full 2D grid for every station separation distance that one wanted to test, because there might be cases where not the nearest station triggered but the next-to nearest neighboring station or stations even further out. However, as this will drastically increase computing time (which scales linearly with the number of stations) this small second order effect is ignored in this example. Our analysis will show that the coincidence rate is dominated by the nearest neighbors, i.e., the coincidence rate quickly drops if the separation between stations is doubled, justifying this approximation.

For every station separation distance we consider the eight nearest stations around the central station as illustrated in Fig. 15 on the left. We consider distances ranging from 100 m to 3 km.

We run the NuRadioMC simulation for event lists of different neutrino energies. The Askaryan signal is filtered from 80 MHz - 500 MHz and all events are saved that exceed a signal threshold of  $1V_{\text{RMS}}$  for a noise temperature of 300 K.

## 9.2 Accessing the results and coincidence fraction

Part of the HDF5 output file is the maximum amplitude of each channel of each event stored in a two dimensional array. This allows for a quick calculation of the coincidence requirements. We first check if the central station fulfilled the trigger condition which we assume to be a signal above  $3V_{\text{RMS}}$  in any channel. Then, for each simulated distance, we select the channels corresponding to this distance and check if any channel fulfills the trigger condition. The coincidence rate is then given by the ratio of events where both the central station and any of its nearest neighbors triggered, divided by the number of triggers of the central station alone. The result is presented in Fig. 15 (right). It shows that the coincidence fraction increases with energy. At a station distance of 1 km more than 20% of the events at  $10^{18}$  eV for a surface station (and more than 40% for a 50 m deep station) are detected in at least two stations. This suggests that for a design optimizing on effective volume, stations should be separated further than 1 km from each other, or even further when optimizing for the highest energies. An array of surface stations shows in general a smaller coincidence fraction.

## 10 Summary and outlook

We have presented NuRadioMC as a versatile framework to simulate different aspects of radio neutrino detectors. NuRadioMC provides a state-of-the-art implementation of the four pillars of a radio neutrino simulation: *event generation*, *signal generation*, *signal propagation*, and *detector simulation*. All properties of the simulation chain can be adapted and compared to each other. Following the design goals of flex-

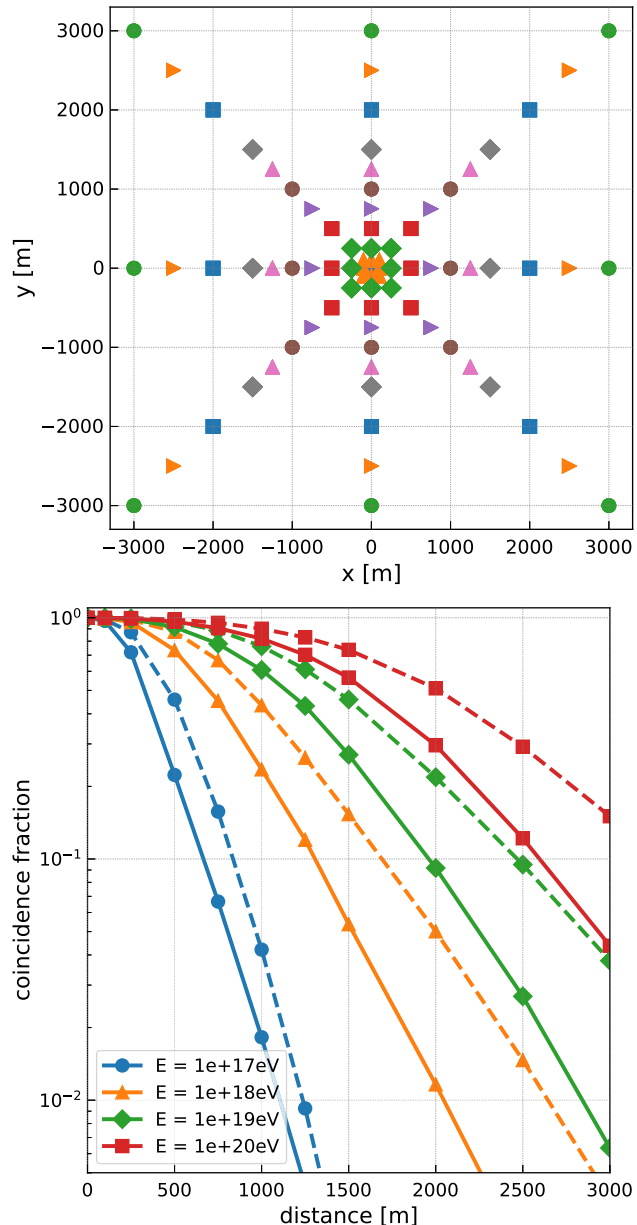


**Fig. 15** (top) Station layout of example 3 to determine the station coincidence rate. Each color and symbol combination corresponds to the nearest neighbors of one station separation distance. (bottom) The probability to detect the same neutrino in multiple stations as a function of separation between the stations. The different colors/symbols correspond to different neutrino energies. The solid line is the result for a surface detector, the dashed line is the result for a 50 m deep detector

ibility and usability, NuRadioMC combines the knowledge and experience from all previous radio detectors for neutrino and cosmic-rays. We have presented a detailed discussion of many radio emission models and documented an improved time-domain approach using a shower library which provides a realistic treatment of the LPM effect and its random fluctuations. In three comprehensive examples, we have shown how to calculate effective volumes and sensitivities,

the efficiency to detect multiple pulses from the same shower (multi-path events), and the coincidence fraction between stations in a large array, depending on the distance between stations. This provides valuable tools for design decisions, depending on the goals one wants to optimize for. Proposed radio neutrino experiments such as RNO, ARIANNA, GRAND, ANITA/PUEO or BEACON [9, 95, 99, 100] may soon or already have profited from the capabilities of NuRadioMC.

NuRadioMC provides a solid foundation for reliable simulations, but also leaves room for future developments from the radio neutrino community. NuRadioMC is publicly available on github [101] and is open to low-threshold further code development from interested parties. As experiments progress and as soon as neutrinos are detected through their radio emission, the areas of prioritized need for development will be indicated by the data.

**Acknowledgements** This article and NuRadioMC itself would not exist without the constructive spirit of the InIceMC working group of the ARA and ARIANNA collaborations. We acknowledge funding from the German research foundation (DFG) under grant GL 914/1-1 (CG) and grant NE 2031/2-1 (DGF, AN, IP, and CW). JAM is supported by Ministerio de Economía, Industria y Competitividad (FPA 2017-85114-P), Xunta de Galicia (ED431C 2017/07), Feder Funds, RENATA Red Nacional Temática de Astropartículas (FPA2015-68783-REDT) and María de Maeztu Unit of Excellence (MDM-2016-0692). We are grateful to the U.S. National Science Foundation-Office of Polar Programs, the U.S. National Science Foundation-Physics Division (grant NSF-1607719) and the U.S. Department of Energy (SWB and CP). BAC thanks the National Science Foundation for support through the Graduate Research Fellowship Program Award DGE-1343012. AC acknowledges funding from the NSF CAREER award 28820 and NSF award 49285. We acknowledge Belgian Funds for Scientific Research (FRS-FNRS and FWO) (ST and NvE), the FWO programme for International Research Infrastructure, and funds from the ERC-StG (No. 805486) of the European Research Council (KDdV).

**Data Availability Statement** This manuscript has associated data in a data repository. [Authors' comment: The source code and example data files are available open source on github: <https://github.com/nuradio/NuRadioMC>.]

**Open Access** This article is licensed under a Creative Commons Attribution 4.0 International License, which permits use, sharing, adaptation, distribution and reproduction in any medium or format, as long as you give appropriate credit to the original author(s) and the source, provide a link to the Creative Commons licence, and indicate if changes were made. The images or other third party material in this article are included in the article's Creative Commons licence, unless indicated otherwise in a credit line to the material. If material is not included in the article's Creative Commons licence and your intended use is not permitted by statutory regulation or exceeds the permitted use, you will need to obtain permission directly from the copyright holder. To view a copy of this licence, visit <http://creativecommons.org/licenses/by/4.0/>.

Funded by SCOAP<sup>3</sup>.

## Appendix A: HDF5 event files structure

The HDF5 files created by the event generator consist of a collection of arrays containing the properties of the neutrinos and other secondary particles (taus, for instance). The array keys and contents are the following:

- *azimuths*, the arrival azimuth angles in radians.
- *zeniths*, the arrival zenith angles in radians.
- *xx*, *yy*, and *zz*, the *x*, *y* and *z* coordinates in meters for the point where the particles interact or decay.
- *event\_ids*, the event identification numbers
- *n\_interaction*, the interaction number. 1 indicates a neutrino interaction, 2 and greater indicates decay or interaction of a lepton created after the neutrino interaction.
- *flavors*, neutrino flavors. 12 for electron neutrino, 14 for muon neutrino, and 16 for tau neutrino. Antineutrinos are represented by –12, –14, and –16. A value of 15 indicates a tau lepton. The numbers are following the standard of [30].
- *energies*, the particle energies in electronvolts
- *interaction\_type*, the interaction type. 'cc' for charged current, and 'nc' for neutral current. 'tau\_had', 'tau\_em', 'tau\_mu' indicate the tau decays into the hadronic, electromagnetic and muonic channels respectively.
- *inelasticities*, the inelasticities for the neutrino interactions and the tau decays, that is, the energy fractions taken by the product cascades.

In these HDF5 files we also save as attributes the number of events and the characteristics of the fiducial and total simulated volumes, along with maximum and minimum energies and angles for the neutrinos.

## Appendix B: NuRadioMC HDF5 output files structure

NuRadioMC creates as output an HDF5 file with information on the events and on the simulation outcome. The user can choose between saving all the information for all events or only for those that have triggered. The NuRadioMC HDF5 output files contain all the values that can be found in the event files (Appendix A), along with the following additional arrays:

- *triggered*, with ones indicating a triggering event and zeroes a non-triggering event.
- *weights*, the weights given to each event as a consequence of propagation through the Earth.
- *multiple\_triggers*, indicates if the triggering condition has been met individually for each simulated trigger. The first axis of this array gives the event number, and the second the type of trigger.

The rest of the output arrays are stored in several HDF5 groups, each group corresponding to a simulated station. The following arrays (except for the SNRs array) contained within the station group are multidimensional. Their first axis is the event number, and the second one the antenna. Each group for a given station contains:

- *SNRs*, the signal to noise ratios for each event defined as the maximum signal amplitude divided by the RMS noise.
- *triggered*, with ones indicating a triggering station and zeroes a non-triggering station.
- *multiple\_triggers*, indicates if the triggering condition has been met individually for each simulated trigger. The first axis of this array gives the event number, and the second the type of trigger.
- *maximum\_amplitudes*, the maximum amplitudes for the voltages of each antenna.
- *maximum\_amplitudes\_envelope*, the maximum amplitudes of the voltage envelope of each antenna.
- *travel\_distances*, the distances traveled by the rays. There can be up to two, one for each ray-tracing solution. The third axis of the array indicates the ray-tracing solution. The same principle applies to all arrays containing ray-tracing information.
- *travel\_times*, the times taken by the rays from emitter to observer.
- *ray\_tracing\_C0*,  $C_0$  parameters for the ray tracing solutions.
- *ray\_tracing\_C1*,  $C_1$  parameters for the ray tracing solutions.
- *ray\_tracing\_solution\_type*, strings containing the type of ray tracing solutions: direct, reflected, or refracted.

The following arrays of the HDF5 group contain three-dimensional vectors, and therefore they have a fourth axis that allows us to find the  $x$ ,  $y$ , and  $z$  components of said vectors.

- *launch\_vectors*, the launch vectors for the ray tracing solutions.
- *receive\_vectors*, the receive vectors for the ray tracing solutions.
- *polarization*, the polarization of the electric field.

In the attributes of the output files the names of the simulated triggers (using the string *trigger\_names*) can be found.

## Appendix C: Analytic ray tracing

The analytic ray tracing in NuRadioMC provides a novel and fast solution of the ray-tracing problem. For completeness we

provide the full derivation of the analytic solution, the path, the path length and the travel time.

### Appendix C.1: Derivation of analytic solution

In this section, we will derive the analytic solution to the ray tracing problem. Fermat's principle states that the optical path of a ray of light travelling between two points is stationary. Suppose the index of refraction depends on one coordinate in a three-dimensional Cartesian coordinate system:

$$n(x, y, z) = n(z) \quad (C.1)$$

Further, let  $dx/dz = \dot{x}$  and  $dy/dz = \dot{y}$ , so that the metric may be expressed as:

$$ds = \sqrt{dx^2 + dy^2 + dz^2} = dz\sqrt{\dot{x}^2 + \dot{y}^2 + 1} \quad (C.2)$$

The symmetry of  $n(z)$  implies that the coordinate system may be rotated such that  $\dot{x} = 0$ . Thus the metric becomes

$$ds = dz\sqrt{\dot{y}^2 + 1} \quad (C.3)$$

Inserting this metric into Fermat's Principle gives

$$S = \int_A^B n ds \quad (C.4)$$

$$\delta S = 0 \quad (C.5)$$

$$\delta \int_A^B n(z)\sqrt{1 + \dot{y}^2} dz = 0 \quad (C.6)$$

Defining  $u = \dot{y}$  and applying the Euler-Lagrange equations yields

$$\dot{u} = -\frac{\dot{n}}{n}(u^3 + u) \quad (C.7)$$

Letting  $v = -\ln n$ , Eq. C.7 simplifies to

$$\dot{u} = \dot{v}(u^3 + u) \quad (C.8)$$

Noting that  $\dot{v} = dv/dz$ , and applying the chain rule gives

$$\frac{du}{dz} \frac{dz}{dv} = \frac{du}{dv} = u^3 + u \quad (C.9)$$

Rearranging and then integrating gives

$$\int \frac{du}{u^3 + u} = \int dv \quad (C.10)$$

$$\ln u - \frac{1}{2} \ln(u^2 + 1) = v + C_0 \quad (C.11)$$

Equation C.11 may be solved for  $dz/dy$  after re-scaling  $C_0$ :

$$\frac{dz}{dy} = \pm \sqrt{C_0^2 n^2 - 1} \quad (\text{C.12})$$

In the case of South Pole and Moore's Bay glacial ice, it is found that  $n(z)$  is described to within a few percent by an exponential function [68] which allows us to proceed further in solving for the ray-path.

$$n(z) = n_{ice} - \Delta_n \exp(z/z_0) \quad (\text{C.13})$$

Let  $\gamma = \Delta_n \exp(z/z_0)$ , which implies

$$n(z) = n_{ice} - \gamma \quad (\text{C.14})$$

$$dz = \gamma^{-1} z_0 d\gamma \quad (\text{C.15})$$

Inserting Eq. C.13 into Eq. C.12 and integrating, with  $b = 2n_{ice}$  and  $c = n_{ice}^2 - C_0^{-2}$ :

$$\int \frac{d\gamma}{\gamma(\gamma^2 - b\gamma + c)^{1/2}} = \pm C_0 \left( \frac{\gamma}{z_0} + C_1 \right) \quad (\text{C.16})$$

The second integration constant is  $C_1$ . Intriguingly, for depths much greater than the scale height ( $|z_i| \gg z_0, z_i < 0$ ), the integral in Eq. C.16 has a singularity in the denominator when the ray is initially horizontal. This is discussed further below. The solution to Eq. C.16 is available in standard tables. The solution with  $y$  as a function of  $z$  via  $\gamma$  is:

$$y(z) = \pm C_0^{-1} c^{-1/2} z_0 \ln \left( \frac{\gamma}{2c^{1/2}(\gamma^2 - b\gamma + c)^{1/2} - b\gamma + 2c} \right) \mp z_0 C_1 \quad (\text{C.17})$$

Let the function within the logarithm in Eq. C.17 be  $F(\gamma)$ :

$$F(\gamma) = \frac{\gamma}{2c^{1/2}(\gamma^2 - b\gamma + c)^{1/2} - b\gamma + 2c} \quad (\text{C.18})$$

Inserting Eq. C.18 into Eq. C.17, we recover a function which returns the ray path as a function of depth:

$$y(z) = \pm C_0^{-1} c^{-1/2} z_0 \ln(F(\gamma)) \mp z_0 C_1 \quad (\text{C.19})$$

Because the ice model is horizontally symmetric, the constant  $C_1$  is set by the choice of origin. All that remains is to understand the physical meaning of  $C_0$ . Let the initial angle

with respect to the horizontal be  $\theta_i$ , which should obey

$$\frac{dy}{dz} = \cot(\theta_i) \quad (\text{C.20})$$

$$\frac{dy}{d\gamma} = z_0 \gamma^{-1} \cot(\theta_i) \quad (\text{C.21})$$

Given Eq. C.19, Eq. C.21 may be solved in terms of  $F(\gamma)$ . The result is

$$\tan \theta_i = \pm C_0 c^{1/2} \frac{F(\gamma)}{\gamma F'(\gamma)} \quad (\text{C.22})$$

Inserting the definition of  $c$  and solving for  $C_0$ :

$$C_0(\gamma, \theta_i) = \pm n_{ice}^{-1} \left( \frac{\gamma^2 F'^2(\gamma)}{F^2(\gamma)} \tan^2 \theta_i + 1 \right)^{1/2} \quad (\text{C.23})$$

The right-hand side of Eq. C.23 resembles a secant function. Restricting to initial depths much greater than the scale depth ( $|z_i| \gg z_0, z_i < 0$ ) causes

$$\frac{\gamma^2 F'^2(\gamma)}{F^2(\gamma)} \rightarrow 1 \quad (\text{C.24})$$

If this limit is taken, then Eq. C.23 simplifies:

$$C_0(\gamma, \theta_i) = \pm n_{ice}^{-1} \left( \tan^2 \theta_i + 1 \right)^{1/2} = \pm n_{ice}^{-1} \sec \theta_i \quad (\text{C.25})$$

$C_0$  is a constant that depends on the boundary conditions, so Eq. C.25 may be inverted:

$$n_{ice} \cos \theta_i = \pm C_0^{-1} \quad (\text{C.26})$$

Equation C.26 is Snell's Law, because  $C_0$  is constant and  $\theta_i$  is defined with respect to the horizontal. Thus, in the limit ( $|z_i| \gg z_0, z_i < 0$ ) the singularity in Eq. C.16 is for  $\cos \theta_i = \pm 1$ , i.e. horizontal propagation. Further, in the limit ( $|z_i| \gg z_0, z_i < 0$ ) the factor in front of Eq. C.19,  $C_0^{-1} c^{-1/2}$ , simplifies:

$$c = n_{ice}^2 - C_0^{-2} \quad (\text{C.27})$$

$$c^{-1/2} = \left( n_{ice}^2 - C_0^{-2} \right)^{-1/2} \quad (\text{C.28})$$

$$C_0^{-1} c^{-1/2} = \left( C_0^2 n_{ice}^2 - 1 \right)^{-1/2} \quad (\text{C.29})$$

$$C_0^{-1} c^{-1/2} = \cot(\theta_i) \quad (\text{C.30})$$

In the last step, Eq. C.12 has been used. Thus, the closed form of  $y(z)$  is

$$y(z) = \pm z_0 \cot \theta_i \ln(F(\gamma)) \quad (\text{C.31})$$

If the depth  $z$  does not satisfy the limit ( $|z_i| \gg z_0, z_i < 0$ ),  $C_0$  must first be obtained from Eq. C.23, and then inserted into Eq. C.19 to obtain the ray-tracing path.

### Appendix C.2: Putting the analytic solution into practical usability

In this section, we demonstrate how to efficiently solve the analytic equations for the ray path derived in Appendix C.1. Without loss of generality, we can use only the positive solution which corresponds to rays propagating into the positive  $y$  direction. Equally, we can only consider rays in the  $y - z$  plane. This is because such a start configuration can always be achieved with a simple coordinate transformation.

In addition, it is sufficient to only compute solution from a deeper to a shallower position without loss of generality by flipping the initial condition. Hence we can always reduce the problem to finding all possible path's between two points

$$\mathbf{x}_1 = (y_1, z_1)^T \quad \text{and} \quad \mathbf{x}_2 = (y_2, z_2)^T \\ \text{with } y_1 < y_2 \quad \text{and} \quad z_1 < z_2. \quad (\text{C.32})$$

The analytic solution only describes the “first part” of the solution until the *turning point*. This is the position where the ray either hits the surface and is reflected down, or it reaches the point where the propagation direction of the ray becomes horizontal (i.e. into the  $y$  direction) due to continuous refraction. This is of course a consequence of the solution being  $y(z)$  and not  $z(y)$  which is needed to describe the ray path in a single analytic function (because  $z(y)$  is not bijective).

The turning point is the position where the second root of Eq. (10) becomes undefined, i.e., for

$$\gamma^2 - b\gamma + c = 0 \Rightarrow \gamma_{\text{turn}} = \frac{1}{2}b - \sqrt{\frac{b^2}{4} - c}. \quad (\text{C.33})$$

The  $z_{\text{turn}}$  position can be calculated from  $\gamma_{\text{turn}}$ . If  $z_{\text{turn}}$  is positive, the turning points is above the surface. Hence, the ray is reflected off the surface and  $z_{\text{turn}}$  is set to zero. Then,  $y_{\text{turn}}$  can be calculated by inserting  $z_{\text{turn}}$  into Eq. (10).

Hence, from an implementation perspective, we have two distinct cases: either we have a direct ray ( $y_2 < y_{\text{turn}}$ ) or we have a reflected or refracted ray ( $y_2 > y_{\text{turn}}$ ).

### Appendix C.3: Determination of free parameters

Now, we present how to determine the two free parameters  $C_0$  and  $C_1$  in a fast and robust way from the initial condition that the ray path goes through the points  $\mathbf{x}_1$  and  $\mathbf{x}_2$ . The parameter  $C_1$  is given by

$$C_1 = y_1 - y(z_1, C_0 = C'_0, C_1 = 0) \quad (\text{C.34})$$

with  $y()$  being Eq. (10) evaluated for  $C_0 = C'_0$  and  $C_1 = 0$ .

The parameter  $C_0$  needs to be determined numerically by minimizing the following objective function:

$$\chi^2 = (y_2 - y'(z_2, C_0, C_1))^2. \quad (\text{C.35})$$

As Eq. (10) describes only half of the solution, we first check if  $\mathbf{x}_2$  is before or after the turning point. It is after the turning point if  $y_{\text{turn}} < y_2$ . Then the following coordinate transformation is performed.

$$y'(z_2, C_0, C_1) = 2y_{\text{turn}} - y(z_2, C_0, C_1). \quad (\text{C.36})$$

To increase the numerical stability of the minimizer it is useful to perform the following coordinate transformation

$$D = \ln(C_0 - 1/n_{\text{ice}}). \quad (\text{C.37})$$

Then Eq. (10) is defined for all values of  $D$ .

For typical geometries not just one but two solutions are present. Once one solution is found, the second solution can be determined fast and efficiently using the Brent root finding algorithm [102], and using the displacement in  $y$  at position  $\mathbf{x}_2$  as objective function (cf. Fig. 16 right). Utilization of Brent’s algorithm is possible because for a second solution to exists,  $\Delta y$  needs to change sign in one of the open intervals  $(-\infty, C_0^1)$  and  $(C_0^1, \infty)$ , where  $C_0^1$  is the first solution.

### Appendix C.4: Derivative of analytic ray tracing path

The derivative of the analytic ray tracing solution is given by

$$\begin{aligned} & \frac{dy(z)}{dz} \\ &= \left( -\sqrt{c} e^{\frac{z}{z_0}} b \Delta_n + 2 \sqrt{-b \Delta_n e^{\frac{z}{z_0}} + \Delta_n^2 e^{2 \frac{z}{z_0}} + c} c + 2 c^{3/2} \right) \\ & \times \left( 2 \sqrt{c} \sqrt{-b \Delta_n e^{\frac{z}{z_0}} + \Delta_n^2 e^{2 \frac{z}{z_0}} + c} - b \Delta_n e^{\frac{z}{z_0}} + 2 c \right)^{-1} \\ & \times \frac{1}{\sqrt{-b \Delta_n e^{\frac{z}{z_0}} + \Delta_n^2 e^{2 \frac{z}{z_0}} + c}} \frac{1}{\sqrt{C_0^2 n_{\text{ice}}^2 - 1}}. \end{aligned} \quad (\text{C.38})$$

### Appendix C.5: Analytic solution of path length and travel time

In this section, the analytic solution of the path length and travel time for an exponential index-of-refraction profile is derived.

To find the path(s) between two given points in the ice,  $(r_0, z_0)$  and  $(r_1, z_1)$ , we need to find the launch angle(s)  $\theta_0$  of the ray(s). The radial coordinate  $r$  is equivalent to the  $y$  coordinate used in the previous sections, since we are restricted to the vertical plane where the wave propagates. Given the

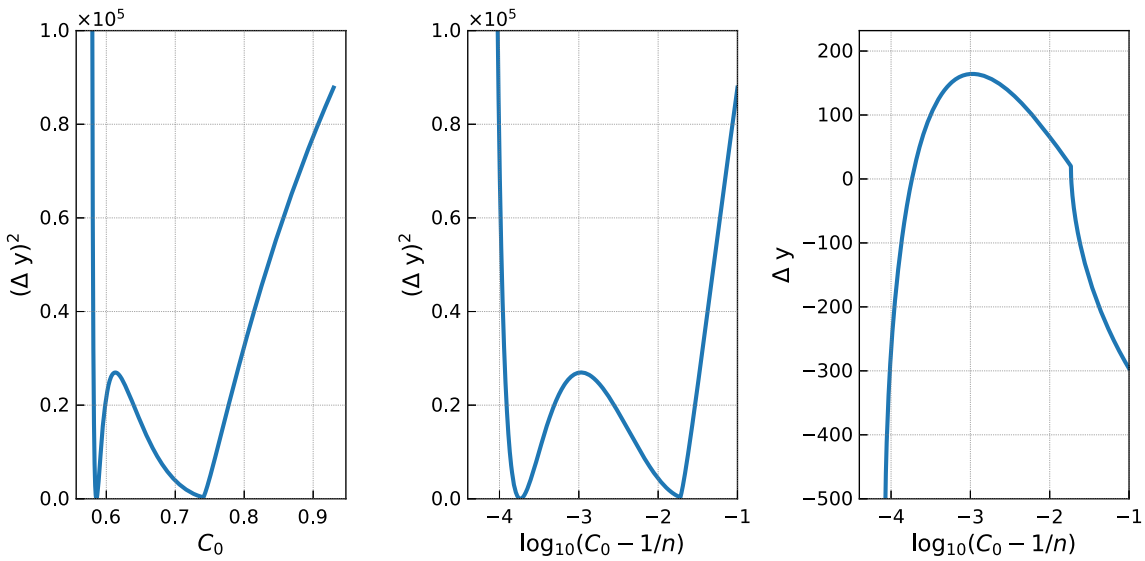


**Fig. 16** Example of a typical objective function as a function of  $C_0$  (left) and  $\log_{10}(C_0 - 1/n)$  (center). Displacement in  $y$  as used for the determination of the second solution via the root finding algorithm (right)

launch angle  $\theta_0$  then we can find  $\theta$  as a function of  $z$  using Snell's Law:

$$n(z) \sin(\theta(z)) = n(z_0) \sin(\theta_0) \quad (\text{C.39})$$

$$\theta(z) = \arcsin\left(\frac{n(z_0) \sin(\theta_0)}{n(z)}\right) \quad (\text{C.40})$$

Since we know the radial distance between our starting and ending points, we can calculate the launch angle by first working out the radial distance integral as a function of launch angle, and then inverting it.

$$\begin{aligned} \frac{dr}{dz} &= \frac{dr}{ds} \frac{ds}{dz} = \tan(\theta) \\ \int_{r_0}^{r_1} dr &= \int_{z_0}^{z_1} \tan(\theta) dz \end{aligned}$$

And then using Eq. C.40, this becomes

$$r_1 - r_0 = \int_{z_0}^{z_1} \tan\left(\arcsin\left(\frac{n(z_0) \sin(\theta_0)}{n(z)}\right)\right) dz \quad (\text{C.41})$$

To calculate the launch angle(s) for ray(s) between our two points, solve this equation for  $\theta_0$ . While we will continue solving this problem in generality for any  $n(z)$  now, in a following section we will simplify the answer for a specific ice model.

Once we know the launch angle of our path we have all we need to calculate its properties. The total path length can be calculated by integrating  $\frac{dz}{ds}$ :

$$s = \int_{z_0}^{z_1} \frac{1}{\cos(\theta)} dz \quad (\text{C.42})$$

$$= \int_{z_0}^{z_1} \sec\left(\arcsin\left(\frac{n(z_0) \sin(\theta_0)}{n(z)}\right)\right) dz \quad (\text{C.43})$$

The time of flight  $t$  along the path can be calculated by combining  $\frac{dz}{ds}$  with the following differential equation for the time of flight (where  $c$  is the speed of light):

$$\frac{dt}{ds} = \frac{n(z)}{c} \quad (\text{C.44})$$

Which then gives

$$\begin{aligned} \frac{dt}{dz} &= \frac{dt}{ds} \frac{ds}{dz} = \frac{n(z)}{c} \frac{1}{\cos(\theta)} \\ t &= \int_{z_0}^{z_1} \frac{n(z)}{c} \frac{1}{\cos(\theta)} dz \end{aligned} \quad (\text{C.45})$$

$$= \frac{1}{c} \int_{z_0}^{z_1} n(z) \sec\left(\arcsin\left(\frac{n(z_0) \sin(\theta_0)}{n(z)}\right)\right) dz \quad (\text{C.46})$$

For an exponential index-of-refraction profile of the form

$$n(z) = n_{\text{ice}} - \Delta_n e^{z/z_0} \quad (\text{C.47})$$

we can finish the calculations. We will use a few substitutions to make our equations clearer. The substitutions are as follows, where  $n(z)$  is as above,  $z_0$  is the starting depth, and  $\theta_0$  is the launch angle:

$$\begin{aligned}\beta &= n(z_0) \sin(\theta_0) \\ \alpha &= n_{\text{ice}}^2 - \beta^2 \\ \gamma &= n(z)^2 - \beta^2 \\ \ell_1 &= n_{\text{ice}} n(z) - \beta^2 - \sqrt{\alpha \gamma} \\ \ell_2 &= n(z) + \sqrt{\gamma}\end{aligned}\quad (\text{C.48})$$

Plugging in our ice model, the radial distance integral in equation C.41 becomes

$$r_1 - r_0 = \frac{\beta}{\sqrt{\alpha}} (-z + z_0 \log(\ell_1)) \Big|_{z_0}^{z_1} \quad (\text{C.49})$$

after equation C.48's substitutions. Solving this equation for the launch angle is an alternative approach to find the ray tracing path. Unfortunately, since the launch angle appears in so many places ( $\alpha$ ,  $\beta$ , and  $\ell_1$ ), this equation is not invertible and so cannot be directly solved for  $\theta_0$ . As a result, root-finding algorithms will need to be used to calculate the launch angle(s) for the ray(s) between  $(r_0, z_0)$  and  $(r_1, z_1)$ . In the NuRadioMC code, we calculate the ray paths using the approach of Sect. Appendix C.2 and just calculate the launch angle from the parameter  $C_0$  of the analytic ray-tracing path.

Plugging in our ice model and substituting according to equation C.48, the path length (equation C.42) becomes

$$s = \frac{n_{\text{ice}}}{\sqrt{\alpha}} (-z + z_0 \log(\ell_1)) + z_0 \log(\ell_2) \Big|_{z_0}^{z_1} \quad (\text{C.50})$$

By the same process, the time of flight (equation C.45) becomes

$$t = \frac{1}{c} \left( z_0 \left( \sqrt{\gamma} + n_{\text{ice}} \log(\ell_2) + \log(\ell_1) \frac{n_{\text{ice}}^2}{\sqrt{\alpha}} \right) - z \frac{n_{\text{ice}}^2}{\sqrt{\alpha}} \right) \Big|_{z_0}^{z_1} \quad (\text{C.51})$$

Note that these integrals are specifically for a direct path. For an indirect path, the bounds must be changed to reflect the fact that the path goes up to  $z_{\text{turn}}$  before coming back down to  $z_1$ .

#### Appendix C.6: Derivation of focusing correction

Here, we derive how ray density per unit area changes. The geometry in case of straight line propagation is depicted in Fig. 17. We read off that  $a = R \sin \Delta\theta$ . In the limit of  $\Delta\theta \ll 1$  we get  $a = R \Delta\theta$ . The relation between the length  $a$  and vertical displacement  $\Delta z$  is given by  $a = \sin \theta \Delta z$ . Thus, we get

$$R = \frac{\Delta z}{\Delta\theta} \sin \theta \quad (\text{C.52})$$

and in the limit  $\Delta z \Rightarrow 0$

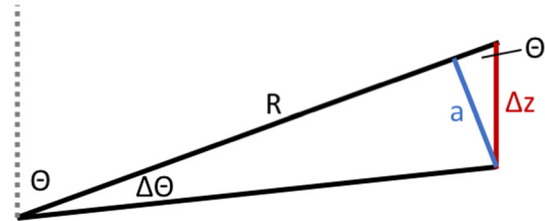


**Fig. 17** Sketch of geometry for focusing correction

$$R = \frac{dz}{d\theta} \sin \theta . \quad (\text{C.53})$$

The area  $dA$  perpendicular to a ray is given by

$$dA = R d\theta \times R \sin \theta d\phi , \quad (\text{C.54})$$

and will change due to ray bending to

$$dA = \frac{dz}{d\theta} \sin \theta d\theta \times R \sin \theta d\phi . \quad (\text{C.55})$$

#### Appendix D: FFT normalization in NuRadioMC

In NuRadioMC we use a real fast Fourier transform (rFFT) as it only deals with real valued signals in the time-domain. Furthermore, we assume that the number of samples in the time domain is even. Then,  $n_t$  bins (with real values) in the time domain correspond to  $n_f = n_t/2 + 1$  bins (with complex values) in the frequency domain where the first bin is the zero frequency component. This is because we exploit the symmetry between negative and positive frequencies for real valued input and only compute the positive frequency components.

The rFFT is normalized such that Parseval's theorem holds without any additional normalization factor, i.e.,

$$\sum_{m=0}^{n_t-1} x_m^2 = \sum_{k=0}^{n_t/2} \tilde{X}_k^2 . \quad (\text{D.56})$$

where  $x_m$  are the time domain samples of the signal, and  $\tilde{X}_k$  are the frequency domain samples. In the case of electric fields, the dimensions of both  $x_m$  and  $\tilde{X}_k$  are voltage/length.

This means that the energy fluence, i.e., the time integral over the pulse amplitudes, calculated in the frequency domain and in the time domain give the same results which is a useful physical property. Then, the rFFT and inverse rFFT is defined as

$$\tilde{X}_k = \frac{\sqrt{2}}{\sqrt{N}} \times \sum_{m=0}^{n_t-1} x_m \exp \left( -2\pi i \frac{mk}{n_t} \right) , k = 0, \dots, n_t/2 \quad (\text{D.57})$$

and

$$x_m = \frac{1}{\sqrt{2}\sqrt{N}} \times 2 \sum_{k=0}^{n_t/2} \tilde{X}_k \exp\left(2\pi i \frac{mk}{n_t}\right), m = 0, \dots, n_t - 1 \quad (\text{D.58})$$

We added an additional factor of  $\sqrt{2}$  with respect to the standard orthogonal normalization to compensate for the negative frequencies that we did not compute so that the Eq. (D.56) holds.

### Appendix D.1: Relation to a continuous Fourier transform

In literature, one also finds the continuous Fourier transform with different conventions for the normalization. One typical choice is to define the Fourier transform as

$$\tilde{E}(v) = \int_{-\infty}^{\infty} dt \exp(i2\pi vt) E(t) \quad (\text{D.59})$$

and

$$E(t) = \int_{-\infty}^{\infty} dv \exp(-i2\pi vt) \tilde{E}(v). \quad (\text{D.60})$$

If the signal in the time domain has units V/m the units in the frequency domain become V/m/Hz. A common task is to transform a frequency-domain parameterization of the Askaryan signal into the time domain via a discrete Fourier transform. For the definition of Eq. (D.59), the corresponding discrete inverse transform is

$$x_m = \frac{1}{n_t} \times 2 \sum_{k=0}^{n_t/2} \tilde{X}_k / \Delta t \exp\left(2\pi i \frac{mk}{n_t}\right) \quad (\text{D.61})$$

$$= 2 \sum_{k=0}^{n_t/2} \tilde{X}_k \Delta f \exp\left(2\pi i \frac{mk}{n_t}\right) \quad (\text{D.62})$$

where we exploit the relation  $\Delta t = 1/(n_t \Delta f)$  of a discrete Fourier transform. The additional factor of 2 was added because we only sum over the positive frequencies here. This factor of 2 is already part of real FFT packages such as `numpy.fft` and does not need to be taken into account by the user (see Sect. Appendix D.3 for details).

### Appendix D.2: Adjustments to different normalizations

All publications of a frequency-domain parameterization of the Askaryan signal that is based on the *ZHS* model use an unusual normalization of the continuous Fourier transform

where an additional factor of 2 is added to the forward transform (Eq. D.59), and correspondingly a factor of 1/2 in the backward transform (Eq. D.60) (see e.g. [47]). Therefore, Eq. (D.62) needs an additional factor of 1/2 if a ZHS parameterization is used.

### Appendix D.3: Implementation details

Most parts of the code use the `numpy` real fft routines. The default normalization has the direct transforms unscaled and the inverse transforms are scaled by  $1/n_t$ . Hence, a analytic parametrization of the amplitudes in the frequency domain  $A(v)$  with units V/m/Hz can be transformed into the time domain via

```
import numpy as np
n = 2**12 # number of bins in time domain
dt = 0.5 * units.ns # bin width in time domain
ff = np.fft.rfftfreq(n, dt)
# get array of frequencies
trace = np.fft.irfft(A(ff) / dt)
```

If  $A(v)$  is a parametrization from a ZHS paper, we get the correct time domain representation via

```
trace = 0.5 * np.fft.irfft(A(ff) / dt)
# additional factor of 2 due to
# ZHS Fourier transform normalization
```

All other Fourier transforms are normalized such that Eq. (D.56) is satisfied which is achieved with `numpy` via:

```
def time2freq(trace):
    """
    performs forward FFT with correct
    normalization that conserves the power
    """
    return np.fft.rfft(trace,
axis=-1, norm="ortho") * 2 ** 0.5
# an additional sqrt(2) is added because
# negative frequencies are omitted.
```

```
def freq2time(spectrum):
    """
    performs backward FFT with correct
    normalization that conserves the power
    """
    return np.fft.irfft(spectrum, axis=-1,
norm="ortho") / 2 ** 0.5
```

## Appendix E: Detector simulation

The code snippet in List. 4 shows a typical detector simulation. With just a few lines of code, we can calculate the antenna response, downsample the time trace to the detec-

tor sampling rate, bandpass filter the signal and simulate a high/low trigger with a 2 out of 4 antennas coincidence logic.

```
def get_time_trace(energy, theta, N, dt, shower_type, n_index, R, model,
                   interp_factor=None, interp_factor2=None,
                   same_shower=False, **kwargs):
    """
    returns the Askaryan pulse in the time domain of the eTheta component

    We implement only the time-domain solution and obtain the frequency spectrum
    via FFT (with the standard normalization of NuRadioMC). This approach assures
    that the units are interpreted correctly. In the time domain, the amplitudes
    are well defined and not details about fourier transform normalizations needs
    to be known by the user.

    Parameters
    -----
    energy : float
        energy of the shower
    theta: float
        viewangle: angle between shower axis (neutrino direction) and the line
        of sight between interaction and detector
    N : int
        number of samples in the time domain
    dt: float
        time bin width, i.e. the inverse of the sampling rate
    shower_type: string (default "HAD")
        type of shower, either "HAD" (hadronic), "EM" (electromagnetic) or
        "TAU" (tau lepton induced), note that TAU showers
        are currently only implemented in the ARZ2019 model
    n_index: float
        index of refraction
    R: float
        distance from vertex to observer
    model: string
        specifies the signal model
        * ZHS1992: the original ZHS parametrization from E. Zas, ...
        * Alvarez2000: parameterization based on ZHS mainly based on J. Alvarez-...
        * Alvarez2009: parameterization based on ZHS from J. Alvarez-...
        * HCRB2017: analytic model from J. Hanson, A. Connolly ...
        * ARZ2019 semi MC time domain model
    interp_factor: float or None
        controls the interpolation of the charge-excess profiles in the ARZ model
    interp_Factor2: float or None
        controls the second interpolation of the charge-excess profiles in the ARZ model
    same_shower: bool (default False)
        controls the random behaviour of picking a shower from the library in the ARZ model,
        see description there for more details

    Returns
    -----
    time trace: array
        the amplitudes for each time bin
    """


```

Listing 3: Signature of the signal generation interface. NuRadioMC provides a uniform interface in form of simple function to all implemented Askaryan modules. This allows to use the Askaryan modules outside of a NuRadioMC simulation and is a well tested resource/reference implementation for the radio community.

```

class mySimulation(simulation.simulation):
    def _detector_simulation(self):
        # 1st convolve efield with antenna pattern
        efieldToVoltageConverterPerChannel.run(self._evt, self._station, self._det)
        # downsample trace back to detector sampling rate
        channelResampler.run(self._evt, self._station, self._det, sampling_rate=1. / self._dt)
        # bandpass filter the signal
        channelBandPassFilter.run(self._evt, self._station, self._det,
                                  passband=[80 * units.MHz, 500 * units.GHz],
                                  filter_type='butter', order=2)
        # run a high/low trigger on the 4 downward pointing LPDAs
        triggerSimulatorHighLow.run(self._evt, self._station, self._det,
                                     threshold_high=4 * self._Vrms,
                                     threshold_low=-4 * self._Vrms,
                                     coinc_window=40 * units.ns,
                                     triggered_channels=[0, 1, 2, 3], # select the LPDA channels
                                     number_cedicences=2, # 2/4 majority logic
                                     trigger_name='LPDA_2of4_4sigma')

```

Listing 4: Example of performing a detector simulation using NuRadioReco.

## References

1. M. Ackermann et al., Astrophysics uniquely enabled by observations of high-energy cosmic neutrinos, astro 2020 decadal whitepaper (2019). [arXiv:1903.04334](https://arxiv.org/abs/1903.04334)
2. IceCube collaboration, The IceCube Neutrino Observatory: instrumentation and online systems. *J. Instrum.* **12**, P03012 (2017). [arXiv:1612.05093](https://arxiv.org/abs/1612.05093). <https://doi.org/10.1088/1748-0221/12/03/P03012>
3. IceCube collaboration, A combined maximum-likelihood analysis of the high-energy astrophysical neutrino flux measured with IceCube. *Astrophys. J.* **809**, 98 (2015). [arXiv:1507.03991](https://arxiv.org/abs/1507.03991). <https://doi.org/10.1088/0004-637X/809/1/98>
4. IceCube collaboration, Neutrino emission from the direction of blazar TXS 0506+056 prior to the IceCube-170922A alert. *Science* **361**, 147 (2018)
5. IceCube collaboration, Measurement of South Pole ice transparency with the IceCube LED calibration system. *Nucl. Instrum. Methods* **A711**, 73 (2013). [arXiv:1301.5361](https://arxiv.org/abs/1301.5361). <https://doi.org/10.1016/j.nima.2013.01.054>
6. G.A. Askar'yan, Coherent radio emission from cosmic showers in air and in dense media. *Sov. J. Exp. Theor. Phys.* **21**, 658 (1965)
7. S. Barwick, D. Besson, P. Gorham, D. Saltzberg, South polar in situ radio-frequency ice attenuation. *J. Glaciol.* **51**, 231–238 (2005). <https://doi.org/10.3189/172756505781829467>
8. ARIANNA collaboration, Design and performance of the ARIANNA HRA-3 neutrino detector systems. *IEEE Trans. Nucl. Sci.* **62**, 2202 (2015). [arXiv:1410.7369](https://arxiv.org/abs/1410.7369). <https://doi.org/10.1109/TNS.2015.2468182>
9. ARIANNA collaboration, Targeting ultra-high energy neutrinos with the ARIANNA experiment. *Adv. Space Res.* **64**(12), 2595–2609 (2019). [arXiv:1903.01609](https://arxiv.org/abs/1903.01609) <https://doi.org/10.1016/j.asr.2019.06.016>
10. ARA collaboration, Performance of two Askaryan Radio Array stations and first results in the search for ultrahigh energy neutrinos. *Phys. Rev. D* **93**, 082003 (2016). [arXiv:1507.08991](https://arxiv.org/abs/1507.08991). <https://doi.org/10.1103/PhysRevD.93.082003>
11. ARIANNA collaboration, A first search for cosmogenic neutrinos with the ARIANNA Hexagonal Radio Array. *Astropart. Phys.* **70**, 12 (2015). [arXiv:1410.7352](https://arxiv.org/abs/1410.7352). <https://doi.org/10.1016/j.astropartphys.2015.04.002>
12. P. Allison et al., Design and performance of an interferometric trigger array for radio detection of high-energy neutrinos. *Nucl. Instrum. Methods Phys. Res. A* **930**, 112 (2019). <https://doi.org/10.1016/j.nima.2019.01.067>. [arXiv:1809.04573](https://arxiv.org/abs/1809.04573)
13. K. Greisen, End to the cosmic-ray spectrum? *Phys. Rev. Lett.* **16**, 748 (1966). <https://doi.org/10.1103/PhysRevLett.16.748>
14. G.T. Zatsepin, V.A. Kuz'min, Upper limit of the spectrum of cosmic rays. *Sov. J. Exp. Theor. Phys. Lett.* **4**, 78 (1966)
15. V.S. Beresinsky, G.T. Zatsepin, Cosmic rays at ultra high energies (neutrino?). *Phys. Lett. B* **28**, 423 (1969). [https://doi.org/10.1016/0370-2693\(69\)90341-4](https://doi.org/10.1016/0370-2693(69)90341-4)
16. M. Ackermann et al., Fundamental physics with high-energy cosmic neutrinos, Astro 2020 Decadal Whitepaper (2019). [arXiv:1903.04333](https://arxiv.org/abs/1903.04333)
17. K. Dookayka, *Characterizing the Search for Ultra-High Energy Neutrinos with the ARIANNA Detector*; Ph.D. thesis (University of California, Irvine, 2011)
18. ARA collaboration, First constraints on the ultra-high energy neutrino flux from a prototype station of the Askaryan Radio Array. *Astropart. Phys.* **70**, 62 (2015). [arXiv:1404.5285](https://arxiv.org/abs/1404.5285). <https://doi.org/10.1016/j.astropartphys.2015.04.006>
19. ANITA collaboration, ICEMC: a Monte Carlo Simulation for Cosmogenic Neutrinos interacting in the Antarctic ice as viewed by the Antarctic Impulsive Transient Antenna (ANITA). [arXiv:1903.11043](https://arxiv.org/abs/1903.11043)
20. T. Winchen et al., Realtime processing of LOFAR data for the detection of nano-second pulses from the Moon, in *Journal of Physics Conference Series*, vol. 898, p. 032004 (2017). [arXiv:1612.06592](https://arxiv.org/abs/1612.06592). <https://doi.org/10.1088/1742-6596/898/3/032004>
21. C.W. James et al., Overview of lunar detection of ultra-high energy particles and new plans for the SKA, in *European Physical Journal Web of Conferences*, vol. 135, p. 04001 (2017). [arXiv:1704.05336](https://arxiv.org/abs/1704.05336). <https://doi.org/10.1051/epjconf/201713504001>
22. R. Essig et al., Dark sectors and new, light, weakly-coupled particles, FERMILAB-CONF-13-653 (2013). [arXiv:1311.0029](https://arxiv.org/abs/1311.0029)
23. “Cython.” <http://cython.org>
24. J. Alvarez-Muñiz, R.A. Vázquez, E. Zas, Calculation methods for radio pulses from high energy showers. *Phys. Rev. D* **62** (2000). <https://doi.org/10.1103/physrevd.62.063001>

25. J. Alvarez-Muñiz, A. Romero-Wolf, E. Zas, Practical and accurate calculations of Askaryan radiation. *Phys. Rev. D* **84**, 103003 (2011). [arXiv:1106.6283](https://arxiv.org/abs/1106.6283). <https://doi.org/10.1103/PhysRevD.84.103003>
26. L.D. Landau, I. Pomeranchuk, Limits of applicability of the theory of bremsstrahlung electrons and pair production at high-energies. *Dokl. Akad. Nauk Ser. Fiz.* **92**, 535 (1953)
27. A.B. Migdal, Bremsstrahlung and pair production in condensed media at high-energies. *Phys. Rev.* **103**, 1811 (1956). <https://doi.org/10.1103/PhysRev.103.1811>
28. C. Glaser, A. Nelles, I. Plaisier, C. Welling, S.W. Barwick, D. Garca-Fernndez, et al., NuRadioReco: A reconstruction framework for radio neutrino detectors. *Eur. Phys. J. C* **79** (2019). [arXiv:1903.07023](https://arxiv.org/abs/1903.07023). <https://doi.org/10.1140/epjc/s10052-019-6971-5>
29. The HDF Group, Hierarchical Data Format, version 5, 1997-NNNN
30. C. Amsler et al., (Particle Data Group), Monte Carlo particle numbering scheme. *Phys. Lett. B* **667** (2018)
31. R. Gandhi, C. Quigg, M.H. Reno, I. Sarcevic, Neutrino interactions at ultrahigh energies. *Phys. Rev. D* **58**, 58 (1998). <https://doi.org/10.1103/PhysRevD.58.093009>
32. R. Gandhi, C. Quigg, M.H. Reno, I. Sarcevic, Ultrahigh-energy neutrino interactions. *Astropart. Phys.* **5**, 81–110 (1996). [https://doi.org/10.1016/0927-6505\(96\)00008-4](https://doi.org/10.1016/0927-6505(96)00008-4)
33. A. Connolly, R.S. Thorne, D. Waters, Calculation of high energy neutrino-nucleon cross sections and uncertainties using the MSTW parton distribution functions and implications for future experiments. *Phys. Rev. D* **83**, 113009 (2011). [arXiv:1102.0691](https://arxiv.org/abs/1102.0691). <https://doi.org/10.1103/PhysRevD.83.113009>
34. A. Cooper-Sarkar, P. Mertsch, S. Sarkar, The high energy neutrino cross-section in the Standard Model and its uncertainty. *JHEP* **08**, 042 (2011). [arXiv:1106.3723](https://arxiv.org/abs/1106.3723). [https://doi.org/10.1007/JHEP08\(2011\)042](https://doi.org/10.1007/JHEP08(2011)042)
35. J.H. Koehne, K. Frantzen, M. Schmitz, T. Fuchs, W. Rhode, D. Chirkov et al., PROPOSAL: a tool for propagation of charged leptons. *Comput. Phys. Commun.* **184**, 2070 (2013). <https://doi.org/10.1016/j.cpc.2013.04.001>
36. M. Dunsch, J. Soedingrekso, A. Sandrock, M. Meier, T. Menne, W. Rhode, Recent improvements for the lepton propagator PROPOSAL. [arXiv:1809.07740](https://arxiv.org/abs/1809.07740)
37. Particle Data Group collaboration, Review of particle physics. *Phys. Rev. D* **98**, 030001 (2018). <https://doi.org/10.1103/PhysRevD.98.030001>
38. T. De Young, S. Razzaque, D.F. Cowen, Astrophysical tau neutrino detection in kilometer-scale Cherenkov detectors via muonic tau decay. *Astropart. Phys.* **27**, 238 (2007). [arXiv:astro-ph/0608486](https://arxiv.org/abs/astro-ph/0608486). <https://doi.org/10.1016/j.astropartphys.2006.11.003>
39. S. Iyer Dutta, M.H. Reno, I. Sarcevic, D. Seckel, Propagation of muons and taus at high energies. *Phys. Rev. D* **63**, 094020 (2001). <https://doi.org/10.1103/PhysRevD.63.094020>
40. NuRadioMC, “Example: Pulser calibration measurement.” <https://github.com/nu-radio/NuRadioMC/wiki/Example:-Pulser-calibration-measurement>
41. NuRadioMC, “Event generation skeleton.” [https://github.com/nu-radio/NuRadioMC/blob/master/NuRadioMC/EvtGen/generator\\_skeleton.py](https://github.com/nu-radio/NuRadioMC/blob/master/NuRadioMC/EvtGen/generator_skeleton.py)
42. NuRadioMC, “Online documentation.” <https://github.com/nu-radio/NuRadioMC/wiki/Interface-to-Askaryan-modules>
43. C.R. Persichilli, *Performance and Simulation of the ARIANNA Pilot Array, with Implications for Future Ultra-high Energy Neutrino Astronomy*, Ph.D. thesis (University of California, Irvine, 2018)
44. E. Zas, F. Halzen, T. Stanev, Electromagnetic pulses from high-energy showers: implications for neutrino detection. *Phys. Rev. D* **45**, 362 (1992). <https://doi.org/10.1103/PhysRevD.45.362>
45. J. Alvarez-Muñiz, E. Marqués, R.A. Vázquez, E. Zas, Coherent radio pulses from showers in different media: a unified parameterization. *Phys. Rev. D* **74**, 023007 (2006). [arXiv:astro-ph/0512337](https://arxiv.org/abs/astro-ph/0512337). <https://doi.org/10.1103/PhysRevD.74.023007>
46. J. Alvarez-Muñiz, W.R. Carvalho, M. Tueros, E. Zas, Coherent Cherenkov radio pulses from hadronic showers up to EeV energies. *Astropart. Phys.* **35**, 287 (2012). [arXiv:1005.0552](https://arxiv.org/abs/1005.0552). <https://doi.org/10.1016/j.astropartphys.2011.10.002>
47. J. Alvarez-Muñiz, C. James, R. Protheroe, E. Zas, Thinned simulations of extremely energetic showers in dense media for radio applications. *Astropart. Phys.* **32**, 100 (2009). <https://doi.org/10.1016/j.astropartphys.2009.06.005>
48. J. Alvarez-Muñiz, E. Zas, The LPM effect for EeV hadronic showers in ice: implications for radio detection of neutrinos. *Phys. Lett. B* **434**, 396 (1998). [https://doi.org/10.1016/s0370-2693\(98\)00905-8](https://doi.org/10.1016/s0370-2693(98)00905-8)
49. J. Alvarez-Muñiz, E. Zas, Cherenkov radio pulses from EeV neutrino interactions: the LPM effect. *Phys. Lett. B* **411**, 218 (1997). [https://doi.org/10.1016/s0370-2693\(97\)01009-5](https://doi.org/10.1016/s0370-2693(97)01009-5)
50. J.C. Hanson, A.L. Connolly, Complex analysis of askaryan radiation: a fully analytic treatment including the LPM effect and cascade form factor. *Astropart. Phys.* **91**, 75 (2017). [arXiv:1605.04975](https://arxiv.org/abs/1605.04975). <https://doi.org/10.1016/j.astropartphys.2017.03.008>
51. R.V. Buniy, J.P. Ralston, Radio detection of high energy particles: coherence versus multiple scales. *Phys. Rev. D* **65**, 016003 (2001). <https://doi.org/10.1103/PhysRevD.65.016003>
52. C.-Y. Hu, C.-C. Chen, P. Chen, Near-field effects of Cherenkov radiation induced by ultra high energy cosmic neutrinos. *Astropart. Phys.* **35**, 421 (2012). [arXiv:1012.5155](https://arxiv.org/abs/1012.5155). <https://doi.org/10.1016/j.astropartphys.2011.11.008>
53. L. Gerhardt, S.R. Klein, Electron and photon interactions in the regime of strong LPM suppression. *Phys. Rev. D* **82**, 074017 (2010). [arXiv:1007.0039](https://arxiv.org/abs/1007.0039). <https://doi.org/10.1103/PhysRevD.82.074017>
54. K. Werner, K.D. de Vries, O. Scholten, A realistic treatment of geomagnetic Cherenkov radiation from cosmic ray air showers. *Astropart. Phys.* **37**, 5 (2012). [arXiv:1201.4471](https://arxiv.org/abs/1201.4471). <https://doi.org/10.1016/j.astropartphys.2012.07.007>
55. J. Alvarez-Muñiz, A. Romero-Wolf, E. Zas, Čerenkov radio pulses from electromagnetic showers in the time domain. *Phys. Rev. D* **81**, 123009 (2010). [arXiv:1002.3873](https://arxiv.org/abs/1002.3873). <https://doi.org/10.1103/PhysRevD.81.123009>
56. J. Bellm et al., Herwig 7.1 Release Note. [arXiv:1705.06919](https://arxiv.org/abs/1705.06919)
57. J. Alvarez-Muñiz, W.R. Carvalho, Jr., E. Zas, Monte Carlo simulations of radio pulses in atmospheric showers using ZHAireS. *Astropart. Phys.* **35**, 325 (2012). [arXiv:1107.1189](https://arxiv.org/abs/1107.1189). <https://doi.org/10.1016/j.astropartphys.2011.10.005>
58. M. Gottowik, C. Glaser, T. Huege, J. Rautenberg, Determination of the absolute energy scale of extensive air showers via radio emission: systematic uncertainty of underlying first-principle calculations. *Astropart. Phys.* **103**, 87 (2018). [arXiv:1712.07442](https://arxiv.org/abs/1712.07442). <https://doi.org/10.1016/j.astropartphys.2018.07.004>
59. D. García-Fernández, J. Alvarez-Muñiz, W.R. Carvalho, A. Romero-Wolf, E. Zas, Calculations of electric fields for radio detection of ultrahigh energy particles. *Phys. Rev. D* **87**, 023003 (2013). <https://doi.org/10.1103/PhysRevD.87.023003>
60. T. Huege, M. Ludwig, C.W. James, Simulating radio emission from air showers with CoREAS, in American Institute of Physics Conference Series, R. Lahmann, T. Eberl, K. Graf, C. James, T. Huege, T. Karg et al. (eds.) American Institute of Physics Conference Series, vol. 1535, pp. 128–132 (2013). [arXiv:1301.2132](https://arxiv.org/abs/1301.2132). <https://doi.org/10.1063/1.4807534>
61. Pierre Auger collaboration, Measurement of the radiation energy in the radio signal of extensive air showers as a universal estimator of cosmic-ray energy. *Phys. Rev. Lett.* **116**, 241101

- (2016). arXiv:1605.02564. <https://doi.org/10.1103/PhysRevLett.116.241101>
62. C. Glaser, M. Erdmann, J.R. Hörandel, T. Huege, J. Schulz, Simulation of radiation energy release in air showers. *JCAP* **1609**, 024 (2016). arXiv:1606.01641. <https://doi.org/10.1088/1475-7516/2016/09/024>
  63. LOFAR collaboration, Detecting cosmic rays with the LOFAR radio telescope. *Astron. Astrophys.* **560**, A98 (2013). arXiv:1311.1399. <https://doi.org/10.1051/0004-6361/201322683>
  64. R. Engel, D. Heck, T. Huege, T. Pierog, M. Reininghaus, F. Riehn et al., Towards a next generation of CORSIKA: a framework for the simulation of particle cascades in astroparticle physics. *Comput. Softw. Big Sci.* **3**, 2 (2019). arXiv:1808.08226. <https://doi.org/10.1007/s41781-018-0013-0>
  65. NuRadioMC, “Signal propagation base class.” [https://github.com/nu-radio/NuRadioMC/blob/master/NuRadioMC/SignalProp/propagation\\_base\\_class.py](https://github.com/nu-radio/NuRadioMC/blob/master/NuRadioMC/SignalProp/propagation_base_class.py)
  66. S. Buitink, Using FDTD simulations to study radio propagation effects, Proceedings of the ARENA 2018, Catania Sicily (2018)
  67. C. Deaconu, A.G. Vieregg, S.A. Wissel, J. Bowen, S. Chipman, A. Gupta et al., Measurements and modeling of near-surface radio propagation in glacial ice and implications for neutrino experiments. *Phys. Rev. D* **98**, 043010 (2018). arXiv:1805.12576. <https://doi.org/10.1103/PhysRevD.98.043010>
  68. S. Barwick et al., Observation of classically ‘forbidden’ electromagnetic wave propagation and implications for neutrino detection. *J. Cosmol. Astropart. Phys.* **07**, 055 (2018). arXiv:1804.10430. <https://doi.org/10.1088/1475-7516/2018/07/055>
  69. S. van der Walt, S.C. Colbert, G. Varoquaux, The numpy array: a structure for efficient numerical computation. *Comput. Sci. Eng.* **13**, 22 (2011). <https://doi.org/10.1109/MCSE.2011.37>
  70. E. Jones, T. Oliphant, P. Peterson et al., “SciPy: Open source scientific tools for Python.” <http://www.scipy.org/> (2001)
  71. M. Galassi et al., “GNU Scientific Library Reference Manual.” <http://www.gnu.org/software/gsl/%22>
  72. R.A. Batista, A. Dundovic, M. Erdmann, K.-H. Kampert, D. Kuempel, G. Müller et al., CRPropa 3—a public astrophysical simulation framework for propagating extraterrestrial ultrahigh energy particles. *JCAP* **1605**, 038 (2016). arXiv:1603.07142. <https://doi.org/10.1088/1475-7516/2016/05/038>
  73. T. Winchen, RadioPropa—a modular raytracer for in-matter radio propagation, in *Proceedings of the ARENA 2018*, Catania Sicily (2018). arXiv:1810.01780
  74. F. Frezza, N. Tedeschi, Electromagnetic inhomogeneous waves at planar boundaries: tutorial. *J. Opt. Soc. Am. A* **32**, 1485 (2015). <https://doi.org/10.1364/JOSAA.32.001485>
  75. D. García-Fernández, B. Revenu, A. Escudie, L. Martin, Influence of a planar boundary on the electric field emitted by a particle shower. *Phys. Rev. D* **99**, 063009 (2019). arXiv:1811.11003. <https://doi.org/10.1103/PhysRevD.99.063009>
  76. B. Kolundzija, WIPL-D: from university software to company product, in *Proceedings of the 5th European Conference on Antennas and Propagation (EUCAP)*, pp. 2844–2846 (2011)
  77. K.S. Kunz, R.J. Luebers, *The Finite Difference Time Domain Method for Electromagnetics* (CRC Press, Boca Raton, 1993)
  78. Pierre Auger collaboration, Advanced functionality for radio analysis in the Offline software framework of the Pierre Auger Observatory. *Nucl. Instrum. Methods Phys. Res. A* **635**, 92 (2011). arXiv:1101.4473. <https://doi.org/10.1016/j.nima.2011.01.049>
  79. S.A. Kleinfelder, E. Chiem, T. Prakash, The SST Multi-G-Sample/s Switched Capacitor Array Waveform Recorder with Flexible Trigger and Picosecond-Level Timing Accuracy. arXiv:1508.02460
  80. J. Alvarez-Muñiz, W. R. Carvalho, K. Payet, A. Romero-Wolf, H. Schoorlemmer, E. Zas, Comprehensive approach to tau-lepton production by high-energy tau neutrinos propagating through the earth. *Phys. Rev. D* **97** (2018). <https://doi.org/10.1103/physrevd.97.023021>
  81. J. Alvarez-Muñiz, W.R. Carvalho, A.L. Cummings, K. Payet, A. Romero-Wolf, H. Schoorlemmer et al., Erratum: Comprehensive approach to tau-lepton production by high-energy tau neutrinos propagating through the earth [Phys. Rev. D 97, 023021 (2018)]. *Phys. Rev. D* **99** (2019). <https://doi.org/10.1103/physrevd.99.069902>
  82. S. Argirò et al., The offline software framework of the Pierre Auger Observatory. *Nucl. Instrum. Methods Phys. Res. A* **580**, 1485 (2007). <https://doi.org/10.1016/j.nima.2007.07.010>. arXiv:0707.1652
  83. ARA Project, “Attenuation model.” <https://icecube.wisc.edu/araproject/radio/#icetabsorption>
  84. R.L. Hawley, E.M. Morris, J.R. McConnell, Rapid techniques for determining annual accumulation applied at Summit. Greenland. *J. Glaciol.* **54**, 839 (2008). <https://doi.org/10.3189/00221430878779951>
  85. R. Alley, B. Koci, Ice-Core analysis at site A, Greenland: preliminary results. *Ann. Glaciol.* **10**, 1–4 (1988). <https://doi.org/10.3189/S026030550004067>
  86. NuRadioMC, “Tutorial.” <https://github.com/nu-radio/NuRadioMC/wiki/Tutorial>
  87. NuRadioMC, “Cluster documentation.” <https://github.com/nu-radio/NuRadioMC/wiki/Running-on-a-cluster>
  88. IceCube collaboration, A measurement of the diffuse astrophysical muon neutrino flux using eight years of IceCube data. *PoS ICRC2017*, 1005 (2018). arXiv:1710.01191. <https://doi.org/10.22323/1.301.1005>
  89. IceCube collaboration, Observation of astrophysical neutrinos in six years of IceCube data, *PoS ICRC2017*, 981 (2018). arXiv:1710.01191. <https://doi.org/10.22323/1.301.0981>
  90. IceCube collaboration, Differential limit on the extremely-high-energy cosmic neutrino flux in the presence of astrophysical background from nine years of IceCube data. *Phys. Rev. D* **98**, 062003 (2018). arXiv:1807.01820. <https://doi.org/10.1103/PhysRevD.98.062003>
  91. Pierre Auger collaboration, Improved limit to the diffuse flux of ultrahigh energy neutrinos from the Pierre Auger Observatory. *Phys. Rev. D* **91**, 092008 (2015). arXiv:1504.05397. <https://doi.org/10.1103/PhysRevD.91.092008>
  92. ANITA collaboration, Constraints on the diffuse high-energy neutrino flux from the third flight of ANITA. *Phys. Rev. D* **98**, 022001 (2018). arXiv:1803.02719. <https://doi.org/10.1103/PhysRevD.98.022001>
  93. J. Heinze, A. Fedynitch, D. Boncioli, W. Winter, A new view on Auger data and cosmogenic neutrinos in light of different nuclear disintegration and air-shower models. arXiv:1901.03338
  94. A. van Vliet, R. Alves Batista, J.R. Hörandel, Determining the fraction of cosmic-ray protons at ultra-high energies with cosmogenic neutrinos. arXiv:1901.01899
  95. GRAND collaboration, The Giant Radio Array for Neutrino Detection (GRAND): science and design. arXiv:1810.09994
  96. ARA collaboration, Measurement of the real dielectric permittivity  $\epsilon_r$  of glacial ice. *Astropart. Phys.* **108**, 63 (2019). <https://doi.org/10.1016/j.astropartphys.2019.01.004>
  97. NuRadioMC, “Example: D’n’r analysis.” <https://github.com/nu-radio/NuRadioMC/wiki/Example:-D'n'R-analysis>
  98. NuRadioMC, “Example: Multi station coincidences.” <https://github.com/nu-radio/NuRadioMC/wiki/Example:-Multi-station-coincidences>

99. A. Karle, A. Nelles, The Radio Neutrino Observatory, in *Proceedings of the XVIII International Workshop on Neutrino Telescopes*, Venice (2019)
100. S. Wissel, *A new concept for high-elevation radio detection of tau neutrinos*, in *Proceedings of the ARENA 2018* (Catania, Sicily, 2018)
101. “NuRadioMC.” <https://github.com/nu-radio/NuRadioMC>
102. R.P. Brent, *An algorithm with guaranteed convergence for finding a zero of a function*, in *Algorithms for Minimization without Derivatives* (Prentice-Hall, Englewood Cliffs, 1973)

# White Paper: ARIANNA-200 high energy neutrino telescope

A. Anker<sup>a</sup>, P. Baldi<sup>b</sup>, S. W. Barwick<sup>\*a</sup>, D. Bergman<sup>c</sup>, H. Bernhoff<sup>d</sup>, D. Z. Besson<sup>e,f</sup>, N. Bingefors<sup>g</sup>, O. Botner<sup>g</sup>, P. Chen<sup>h</sup>, Y. Chen<sup>h</sup>, D. García-Fernández<sup>i,j</sup>, G. Gaswint<sup>a</sup>, C. Glaser<sup>a,g</sup>, A. Hallgren<sup>g</sup>, J. C. Hanson<sup>k</sup>, J. J. Huang<sup>h</sup>, S. R. Klein<sup>l</sup>, S. A. Kleinfelder<sup>m</sup>, C.-Y. Kuo<sup>h</sup>, R. Lahmann<sup>a,j</sup>, U. Latif<sup>e</sup>, T. Liu<sup>h</sup>, Y. Lyu<sup>l</sup>, S. McAleer<sup>b</sup>, J. Nam<sup>h</sup>, A. Novikov<sup>e,f</sup>, A. Nelles<sup>i,j</sup>, M. P. Paul<sup>a</sup>, C. Persichilli<sup>a</sup>, I. Plaisier<sup>i,j</sup>, J. Y. Shiao<sup>h</sup>, J. Tatar<sup>n</sup>, A. van Vliet<sup>i</sup>, S.-H. Wang<sup>h</sup>, Y.-H. Wang<sup>h</sup> and C. Welling<sup>i,j</sup>

<sup>a</sup>*Department of Physics and Astronomy, University of California, Irvine, CA 92697, USA*

<sup>b</sup>*School of Information and Computer Sciences, University of California, Irvine, CA 92697, USA*

<sup>c</sup>*Department of Physics and Astronomy, University of Utah, USA*

<sup>d</sup>*Uppsala University Department of Engineering Sciences, Division of Electricity, Uppsala, SE-75237 Sweden*

<sup>e</sup>*Department of Physics and Astronomy, University of Kansas, Lawrence, KS 66045, USA*

<sup>f</sup>*National Research Nuclear University MEPhI (Moscow Engineering Physics Institute), Moscow 115409, Russia*

<sup>g</sup>*Uppsala University Department of Physics and Astronomy, Uppsala, SE-75237, Sweden*

<sup>h</sup>*Department of Physics and Leung Center for Cosmology and Particle Astrophysics, National Taiwan University, Taipei 10617, Taiwan*

<sup>i</sup>*DESY, 15738 Zeuthen, Germany*

<sup>j</sup>*ECAP, Friedrich-Alexander-Universität Erlangen-Nürnberg, 91058 Erlangen, Germany*

<sup>k</sup>*Whittier College Department of Physics, Whittier, CA 90602, USA*

<sup>l</sup>*Lawrence Berkeley National Laboratory, Berkeley, CA 94720, USA*

<sup>m</sup>*Department of Electrical Engineering and Computer Science, University of California, Irvine, CA 92697, USA*

<sup>n</sup>*Research Cyberinfrastructure Center, University of California, Irvine, CA 92697 USA*

April 2020

---

\*sbarwick@uci.edu

## Abstract

The proposed ARIANNA-200 neutrino detector, located at sea-level on the Ross Ice Shelf, Antarctica, consists of 200 autonomous and independent detector stations separated by 1 kilometer in a uniform triangular mesh, and serves as a pathfinder mission for the future IceCube-Gen2 project. The primary science mission of ARIANNA-200 is to search for sources of neutrinos with energies greater than  $10^{17}$  eV, complementing the reach of IceCube. An ARIANNA observation of a neutrino source would provide strong insight into the enigmatic sources of cosmic rays. ARIANNA observes the radio emission from high energy neutrino interactions in the Antarctic ice. Among radio based concepts under current investigation, ARIANNA-200 would uniquely survey the vast majority of the southern sky at any instant in time, and an important region of the northern sky, by virtue of its location on the surface of the Ross Ice Shelf in Antarctica. The broad sky coverage is specific to the Moore’s Bay site, and makes ARIANNA-200 ideally suited to contribute to the multi-messenger thrust by the US National Science Foundation, Windows on the Universe – Multi-Messenger Astrophysics, providing capabilities to observe explosive sources from unknown directions. The ARIANNA architecture is designed to measure the angular direction to within  $3^\circ$  for every neutrino candidate, which too plays an important role in the pursuit of multi-messenger observations of astrophysical sources.

## 1 Science enabled by ARIANNA-200

The ARIANNA-200 neutrino detector, located at sea-level on the Ross Ice Shelf, Antarctica, consists of 200 autonomous and independent detector stations separated by 1 kilometer in a uniform triangular mesh. As a consequence of the reflection properties at the ice-water interface at the bottom of the Ross Ice Shelf, ARIANNA-200 views almost the entire southern sky, including the galactic center, with nearly uniform exposure. ARIANNA-200 (Figure 1) exceeds the instantaneous sky coverage of all other radio-based neutrino detectors being studied. Its broad sky coverage is ideally suited to contribute to multi-messenger campaigns initiated by gravitational-wave detectors, gamma-ray telescopes, cosmic ray observatories, and neutrino telescopes targeting lower energies such as IceCube [1] in the Southern hemisphere, and KM3NeT [2] and Baikal-GVD [3] in the Northern hemisphere.

The sky coverage of ARIANNA-200 augments the point source capabilities of IceCube. At high neutrino energies ( $E_\nu > \sim 10^{14}$  eV), the Earth becomes opaque. Thus, at higher energies, both IceCube and ARIANNA-200 observe mostly the Southern sky, leading to a substantial overlap in sky coverage. Figure 2 examines the relative sensitivity as a function of energy for an explosive or flaring source at an arbitrary declination of  $-23^\circ$  in the Southern sky. The strong second minimum at  $10^{18}$  eV indicates that ARIANNA-200 will observe about one event for every three sources of the highest energy cosmic rays observed by IceCube, assuming neutrino production above  $10^{15}$  eV with an unbroken power law up to  $10^{20}$  eV proportional to  $E_\nu^{-2}$ . A spatially and temporally coincident detection of the same source would establish a hard spectrum up to an energy of  $10^{18}$  eV or greater, and provide a direct link to an accelerator of the very highest energy cosmic rays. A more speculative spectrum proportional to  $E_\nu^{-1.8}$  would produce one event in ARIANNA-200 for every neutrino in IceCube with  $E_\nu > 10^{15}$  eV. The model parameter-space for neutrino fluxes of sources is large. Some models suggest that the flux from some neutrino sources may be enhanced at energies close to maximum sensitivity of ARIANNA-200, for example [4, 5, 6], while others predict no observable emission. It is quite possible that new experimental results will be able to guide theory in this respect.

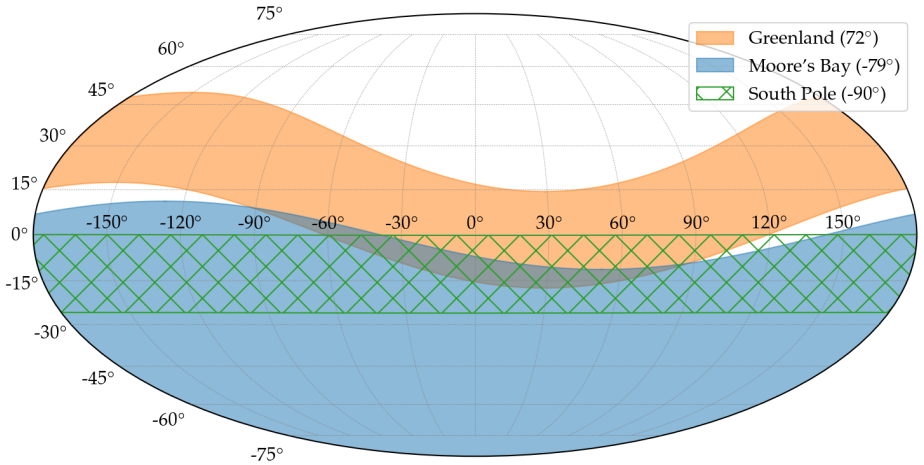


Figure 1: Instantaneous sky coverage of ARIANNA-200 at Moore’s Bay, Antarctica (Blue), plotted in Right Ascension (RA) and Declination (Dec) at one particular time of the day. For comparison, the sky coverage is shown for radio-based neutrino detectors located at Summit Station in Greenland (gold) and South Pole, Antarctica (green hatch).

The simultaneous observation of a point source by IceCube and ARIANNA-200 in different energy ranges would create transformational progress in understanding the half-century old mystery of cosmic rays. Cosmic rays possess extraordinary high energy, but we do not know the sources of their power, nor the physics responsible for their acceleration. The ARIANNA architecture is designed to measure the angular direction to within  $3^\circ$  or better for every neutrino candidate, which too plays an important role in the pursuit of multi-messenger observations of astrophysical sources. Perhaps as few as one neutrino detected by ARIANNA-200, correlated in time and direction with an explosive event observed by IceCube or in some other messenger channel, would provide conclusive steps forward in field of cosmic ray astrophysics.

Apart from the astrophysical neutrinos produced directly at the sources of cosmic rays, cosmogenic neutrinos are produced by the interaction of UHECR protons and cosmic microwave photons [7, 8, 9, 10]. These interactions typically still happen close to the source, and the neutrino preserves the cosmic-ray direction. Thus, also cosmogenic neutrinos can reveal the sources of cosmic rays. They have not been detected so far. In 10 years of operation, ARIANNA-200 will be sensitive to cosmogenic fluxes at a level of  $E_\nu^2 \Phi \leq 4 \times 10^{-9}$  GeVcm $^{-2}$ s $^{-1}$ sr $^{-1}$ , corresponding to  $\sim 10\%$  of the current limits for neutrino energies above  $10^{18}$  eV, and meets the suggested sensitivity for a IceCube-Gen2 pathfinder mission. The observation or upper limit from ARIANNA-200 will constrain model parameters, such as source evolution, energy cutoff and cosmic ray composition.

With a combined fit to the energy spectrum and  $X_{\max}$  distribution (an estimator of the cosmic-ray mass) of UHECR data, the parameters of cosmic-ray sources are estimated from which the cosmogenic neutrino flux can be predicted. However, the analysis is based on a number of simplified assumptions (e.g. a continuous distribution of identical sources and rigidity dependent maximum energies) and the results possess large uncertainties. For example, analysis of the data of the Pierre Auger Observatory located in Argentina [11, 12] results in substantial differences to an analysis of the data of the Telescope Array (TA) located in Utah

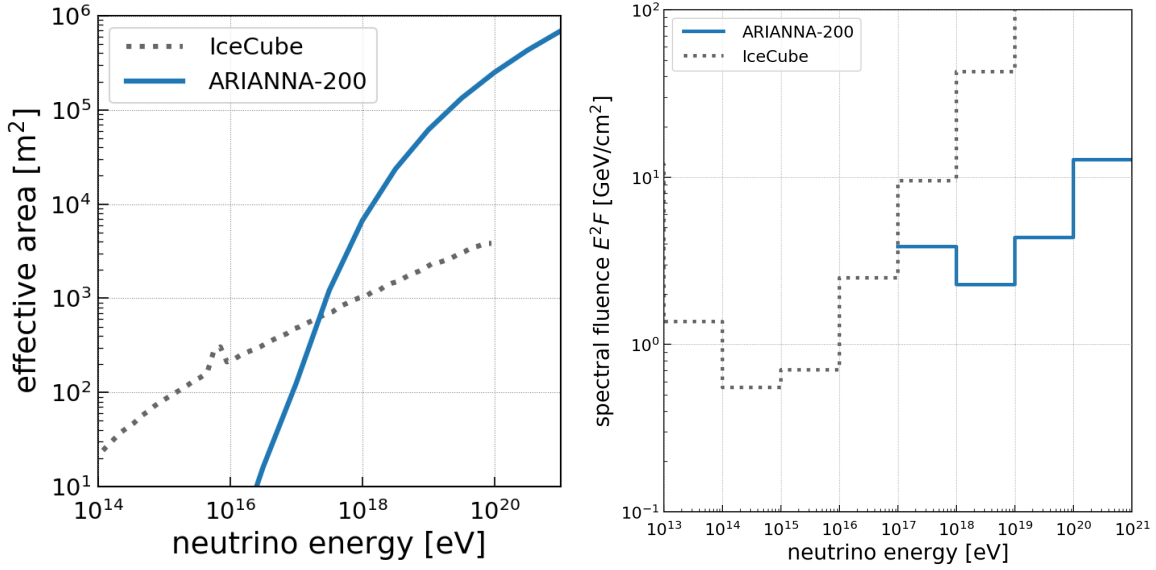


Figure 2: (left) Comparison of effective area for ARIANNA-200 and IceCube as a function of neutrino energy, averaged over neutrino flavor and averaged over the sky. (right) Comparison of point fluence sensitivity at 90% C.L. for ARIANNA-200 and IceCube as function of energy, both observing a source at declination of  $-23^\circ$ .

[13]. The former favors a heavy composition with a low rigidity cutoff at the source resulting in a small cosmogenic neutrino flux, whereas the former favors a high rigidity cutoff and a slightly lighter source composition resulting in a much higher neutrino flux. Furthermore, data of the Pierre Auger Observatory is compatible with an additional proton contribution resulting in substantial increase in the expected neutrino flux [14].

We summarize the different predictions of cosmogenic neutrinos as well as the predicted ARIANNA-200 sensitivity, and results from existing experiments in Fig. 3. The prediction from TA data is well within the reach of ARIANNA-200. For the more pessimistic source parameters derived from Auger data, ARIANNA-200 may observe cosmogenic neutrinos if the proton fraction is larger than 20% of the total particle number. Thus, ARIANNA-200 will provide new insights into the properties of cosmic-ray sources.

ARIANNA-200 serves as a pathfinder mission for IceCube-Gen2 [23]. The ARIANNA-200 approach provides a wide  $2\pi$  field of view of mostly the Southern Sky, and the largest overlap with IceCube-Gen2 of any location discussed by the community. The autonomous architecture employed by ARIANNA-200 has successfully operated at the South Pole, and is a viable technological option for devices located at high elevations, such as the South Pole and Greenland. The surface design of the ARIANNA-200 station provides strong performance in terms of energy and angular resolution, and it provides this level of performance for a large fraction of neutrino candidates [24].

## 2 Detection principle

Radio emission is generated in ice by particle showers through the Askaryan effect [25]. If the shower occurs in a dielectric medium, such as ice, the shower develops a time-varying negative

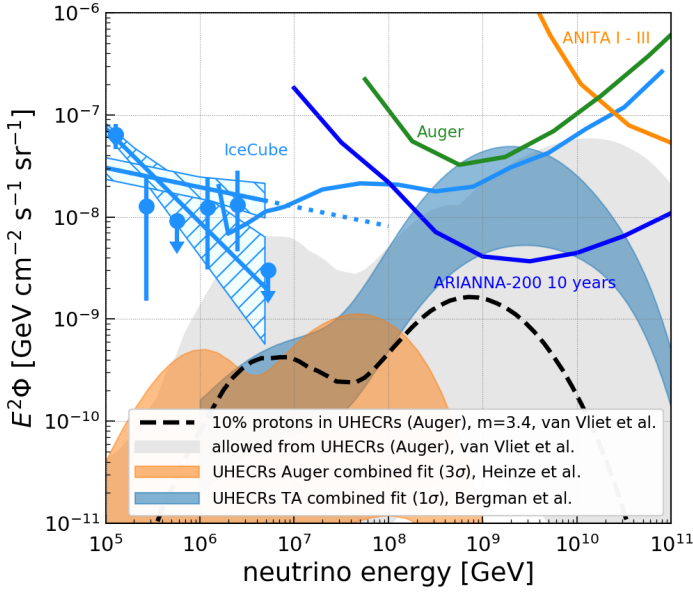


Figure 3: Expected sensitivity of the ARIANNA-200 detector in one-decade energy bins calculated using NuRadioMC [15] for 10 years of operation assuming a uptime of 100%. Also shown is the measured astrophysical neutrino flux from IceCube using the high-energy starting event (HESE) selection [16] and using a muon neutrino sample [17], limits from existing experiments (IceCube [18], Auger [19] and Anita [20]). The color shaded bands show predictions using a simple astrophysical model with commonly discussed source evolution parameters based on cosmic ray data of the Telescope Array (blue) [13, 21] and the Pierre Auger Observatory (orange) [22]. The dashed line shows a slightly more complex model with an additional small proton component [14]. The gray band indicates the range of theoretical uncertainties on model parameters [14].

charge-excess in the shower front which is primarily due to a collection of electrons from the surrounding medium. The resulting radio emission can be calculated precisely using classical electrodynamics by tracking the movement of the individual particles (see e.g. [26, 27, 28, 29, 30]) using the well-tested Monte Carlo code ZHS/ZHAireS [31, 28]. The code incorporates important phenomena such as the LPM effect [32, 33] that strongly affects the emission for  $\nu_e$  charged current interactions. In ice, the electric field increases linearly from MHz frequencies up to a characteristic cutoff of a few GHz. Due to coherence effects, the emission is only strong at angles close to the Cherenkov angle, and linearly polarized in the plane defined by the shower direction and propagation direction of the radio signal. Because of this, both the signal arrival direction as well as the polarization need to be measured experimentally to determine the neutrino direction. The observed frequency range is strongest between 100 MHz and 1 GHz due to properties of the emission and ice attenuation.

The theoretical calculation of the Askaryan emission has been confirmed in accelerator experiments [34, 35, 36, 37, 38], in particular for showers developing in ice [36]. All measurements are consistent with the theoretical prediction within experimental uncertainties. Furthermore, the Askaryan effect has been observed in cosmic ray induced air showers where the Askaryan radiation is subdominant to radio signals emitted by the geomagnetic effect because of the

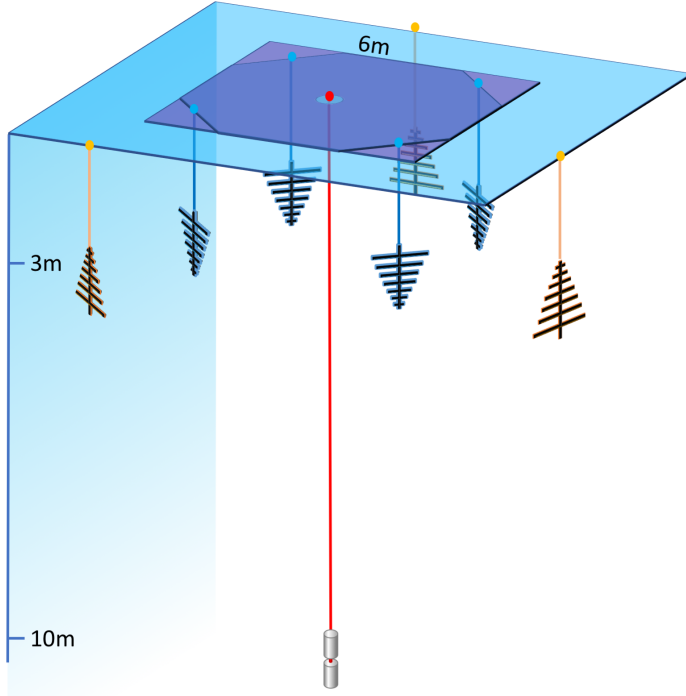


Figure 4: Schematic illustration of one of 200 autonomous, independent stations in the ARIANNA-200 array. All detector components are within 10 m of the surface. One dipole transmitter for calibration purposes is not shown.

much lower density of air compared to ice [39, 40]. As it was the case for accelerator measurements, the measurement of the Askaryan radiation from air showers is in agreement with theoretical calculations (e.g. [41]).

Radio signals can propagate with little attenuation through ice, allowing an observation of large volumes with a sparse array of detector stations. Field studies at Moore’s Bay measured round trip field attenuation between 300 m–500 m in vertical directions [42], and confirmed expectation of excellent reflection from the water-ice interface [43]. In-situ radio pulsers at Moore’s Bay [44] and South Pole [45] demonstrated that the direction of the radio emission can be measured to an accuracy of  $0.4^\circ$  from typical propagation paths originating from neutrino interactions which probes that the bending of signal trajectories in the firn is well understood. Also the measured polarization is consistent with its expectation, which was obtained from an anechoic chamber measurement of the in-ice pulser, and was reconstructed with a precision of better than  $3^\circ$ . Also the received signal amplitudes are consistent with expectation after correcting for attenuation from the propagation through the ice [46].

In addition, ARIANNA verified its polarization capabilities by measuring cosmic rays which generate radio pulses in the atmosphere with well-characterized polarization. The ARIANNA test bed measured the polarization of these signals to a precision of  $7^\circ$  [47], providing an independent check on the predicted angular resolution of ARIANNA-200 [24]. There is no expectation of significant birefringence, which would complicate a polarization measurement, in the ice at Moore’s Bay, and site studies are consistent with that expectation.

### 3 Description of ARIANNA-200 and performance

Similar in basic design to several stations in the 10 station test-bed array, each ARIANNA-200 station includes 8 antenna channels: 4 log periodic dipole antennas (LPDA) pointing down, 3 LPDAs pointing up, and a dipole (Fig. 4 left). The LPDAs, which are high-gain broadband receivers, are installed to a depth of only 2 m, while the dipole is located 10 m below the surface. Each station will operate autonomously using solar and wind power and will communicate in almost real time through the Iridium satellite network. Based on the ARIANNA test bed experience [48], there are several options to deploy two hundred ARIANNA stations. In one method, for example, the deployment team installs all LPDA antennas in rectangular slots created by electrically heated melting devices, which incorporates the key design elements of the cylindrical hole-melter that successfully drilled several holes to the required depth without the need for continuous supervision. Based on the ARIANNA test bed experience, we estimate that two ARIANNA-200 stations can be deployed per day with an 8 person team. The complete ARIANNA-200 array can be deployed in three years.

The performance and reliability of the ARIANNA architecture was also demonstrated by the ARIANNA test bed array, consisting of 10 ARIANNA stations. It ran successfully from December 2014 to completion of the program in November 2019, achieving operational live-time of 86% during the sunlit summer months, and a neutrino analysis efficiency of 80% relative to trigger level at a trigger threshold of 4 times the RMS noise [48]. An experimental prototype of a portable wind generator survived for 2 years and achieved 39% runtime during periods when sunlight was not available. Incremental changes in the geometry of the wind generator and battery capacity are expected to increase the operational live-time to 70% during the completely dark winter months [49]. To summarize: ARIANNA-200 is expected to operate for more than 80% of the year using non-centralized fuel-free sources of power.

ARIANNA-200 achieves state-of-the-art sensitivity by optimizing the trigger bandwidth for the high gain LPDA antennas, reaching an equivalent threshold in signal to noise of 2 times the RMS noise. The effective area of ARIANNA-200 (Fig. 2 left) grows rapidly at neutrino energies above  $10^{17}$  eV, complementing the capabilities of IceCube at lower energies.

The angular direction of the neutrino is computed from the polarization angle, the arrival direction at the detector and the viewing angle relative the Cherenkov cone. The viewing angle measurement benefits from the large bandwidth of the LPDAs and data acquisition electronics. ARIANNA-200 will measure the angular direction of nearly every event with an accuracy of  $3^\circ$  or better and the energy to within a factor 2 [24]. Neutrino energy requires a measurement of the distance to the interaction vertex, which is measured by the powerful DnR technique, to identify the location of the vertex of nearly every event with high precision [50]. In the DnR method, the distance to the vertex is related to time difference between two signal paths of the radio emission, one that propagates directly to the dipole receiver and the second ray that reflects from the surface to the dipole. Many systematic uncertainties are reduced by observing the time delay in a single dipole. Consequently, ARIANNA test bed studies have shown that the relative precision of the time delay is  $<0.1$  ns [50].

Though the baseline reconstruction capabilities have been established by the ARIANNA test bed, we plan additional in-situ calibration campaigns to improve the precision of ice modeling and reduce systematic errors currently limiting the response of the detector. These goals will be facilitated by continuous monitoring of the snow accumulation.

## 4 Practical advantages of architecture and site location

The Moore’s Bay site is only 110 km from McMurdo Station, the largest science base in Antarctica. The relatively close location provides important logistical flexibility, including the possibility to support construction operations by using overland tracked vehicles to transport cargo. The sea-level location is generally warmer than higher elevation sites in Antarctica, and the site has better conditions for wind-generated power [49].

ARIANNA technologies consume only 5 watts of power per station, which is supplied by solar panels during summer months and wind generators during the continuously dark winter months. The ARIANNA concept avoids the need to deploy (and eventually retrieve) hundreds of kilometers of power and/or communication cables from a central location. The utility of this forward-looking feature will be more evident as the area footprint of the neutrino telescopes increase in future designs.

Due to advances by the ARIANNA collaboration in event recognition by deep-learning and other proven analysis techniques [48], high priority neutrino candidates will be transmitted over the reliable Iridium satellite network, which was used routinely in the ARIANNA test bed. Deep learning will be employed to identify neutrino candidates in a matter of seconds, providing a real time alert for the multi-messenger communities.

The near surface location of the components of the ARIANNA station allows routine maintenance and possibility of technology upgrades, providing the opportunity for ARIANNA to follow the science. The existing infrastructure provides advanced capabilities to implement system upgrades. For example, new trigger software can be uploaded remotely over wireless connections during summer operations.

## 5 Backgrounds

The protected geography of Moore’s Bay shields ARIANNA-200 from anthropogenic radio-frequency noise created by McMurdo Station, about 100 km distant. Backgrounds associated with radio production by cosmic ray collisions in the atmosphere are intrinsically directional and they can be identified by upward facing LPDA antennas [51]. In addition, cosmic ray signals will not produce the characteristic double pulse waveform in the dipole antenna employed by the DnR method for neutrino vertex reconstruction [50]. Perhaps the most serious background arises from high-energy muons in cosmic ray air showers that penetrate the ice surface and occasionally radiate high energy photons within the ice [52]. The photons initiate an electromagnetic shower in the vicinity of the ARIANNA station that appears identical to a neutrino signal. We thoroughly studied this potential background and found that the expected rate of background events for the full ARIANNA-200 array is less than 0.01 events per year. Thus, for the sensitivity of this pathfinder project, muon background events are negligible even after 10 years of operation. We note that a large part of the background events can be rejected by tagging cosmic-ray air showers and by measuring the muon energy so that this background can be further mitigated if required by a future detector with significantly larger sensitivity.

## 6 Summary

ARIANNA architecture is fully vetted and ready to contribute to the multi-messenger science program by searching for high-energy neutrino emission from more than half the sky. We propose to expand ARIANNA to 200 stations, with the potential to produce transformative science, by measuring the energy and direction of every neutrino candidate, which is vital to unraveling the mystery of cosmic ray acceleration.

## 7 Acknowledgements

We are grateful to the U.S. National Science Foundation-Office of Polar Programs, the U.S. National Science Foundation-Physics Division (grant NSF-1607719) for granting the ARIANNA test bed array at Moore’s Bay. Without the invaluable support of the people at McMurdo, the ARIANNA stations would have never been built.

We acknowledge funding from the German research foundation (DFG) under grants GL 914/1-1 (CG) and NE 2031/2-1 (DGF, ANe, IP, CW) and the Taiwan Ministry of Science and Technology (JN, SHW). HB acknowledges support from the Swedish Government strategic program Stand Up for Energy. DB and ANo acknowledge support from the MEPhI Academic Excellence Project (Contract No. 02.a03.21.0005) and the Megagrant 2013 program of Russia, via agreement 14.12.31.0006 from 24.06.2013. AvV acknowledges financial support from the European Research Council (ERC) under the European Union’s Horizon 2020 research and innovation programme (Grant No. 646623).

## References

- [1] ICECUBE collaboration, *Evidence for high-energy extraterrestrial neutrinos at the IceCube detector*, *Science* **342** (2013) 6161 1242856.
- [2] KM3NET collaboration, *Sensitivity of the KM3net/ARCA neutrino telescope to point-like neutrino sources*, *Astroparticle Physics* **111** (2019) 100.
- [3] A. D. Avrorin et al., *The Baikal-GVD neutrino telescope: first results of multi-messenger studies*, *Proc. 36th ICRC 2019, Madison, Wisconsin, USA, PoS(ICRC2019)1013* (2019) .
- [4] K. Fang, B. D. Metzger, K. Murase, I. Bartos and K. Kotera, *Multimessenger implications of AT2018cow: High-energy cosmic-ray and neutrino emissions from magnetar-powered superluminous transients*, *Astrophys. J.* **878** (2019) 34.
- [5] E. Waxman and J. N. Bahcall, *Neutrino Afterglow from Gamma-Ray Bursts:  $10^{18}$  eV*, *Astrophys. J.* **541** (2000) 707.
- [6] K. Fang and B. D. Metzger, *High-energy neutrinos from millisecond magnetars formed from the merger of binary neutron stars*, *Astrophys. J.* **849** (2017) 153 [1707.04263].
- [7] K. Greisen, *End to the cosmic ray spectrum?*, *Phys. Rev. Lett.* **16** (1966) 748.
- [8] G. Zatsepin and V. Kuzmin, *Upper Limit of the Spectrum of Cosmic Rays*, *JETP Lett.* **4** (1966) 78.

- [9] V. Beresinsky and G. Zatsepin, *Cosmic rays at ultra high energies (neutrino?)*, *Physics Letters B* **28** (1969) 423.
- [10] F. W. Stecker, *Diffuse fluxes of cosmic high-energy neutrinos*, *Astrophys. J.* **228** (1979) 919.
- [11] PIERRE AUGER collaboration, *The Pierre Auger Cosmic Ray Observatory*, *Nucl. Instrum. Meth. A* **798** (2015) 172.
- [12] PIERRE AUGER collaboration, *Combined fit of spectrum and composition data as measured by the Pierre Auger Observatory*, *Journal of Cosmology and Astroparticle Physics* **2017** (2017) 038.
- [13] D. Bergman for the Telescope Array Collaboration, *Combined fit of the spectrum and composition from Telescope Array*, *Proc. 36th ICRC 2019, Madison, Wisconsin, USA, PoS(ICRC2019)190* (2019) .
- [14] A. van Vliet, R. A. Batista and J. R. Hörandel, *Determining the fraction of cosmic-ray protons at ultrahigh energies with cosmogenic neutrinos*, *Phys. Rev. D* **100** (2019) 021302.
- [15] C. Glaser et al., *NuRadioMC: simulating the radio emission of neutrinos from interaction to detector*, *European Physical Journal C* **80** (2020) 77 [[1906.01670](#)].
- [16] ICECUBE collaboration, *Observation of Astrophysical Neutrinos in Six Years of IceCube Data*, in *Proc. of 35th International Cosmic Ray Conference, Busan, South Korea — PoS(ICRC2017)981*, aug, 2017, DOI.
- [17] ICECUBE collaboration, *A measurement of the diffuse astrophysical muon neutrino flux using eight years of IceCube data.*, in *Proceedings of 35th International Cosmic Ray Conference — PoS(ICRC2017)*, Busan, South Korea, Sissa Medialab, aug, 2017, DOI.
- [18] ICECUBE collaboration, *Differential limit on the extremely-high-energy cosmic neutrino flux in the presence of astrophysical background from nine years of IceCube data*, *Phys. Rev. D* **98** (2018) 062003 [[1807.01820](#)].
- [19] PIERRE AUGER collaboration, *An improved limit to the diffuse flux of ultra-high energy neutrinos from the Pierre Auger Observatory*, *Phys. Rev. D* **91** (2015) 092008 [[1504.05397](#)].
- [20] P. W. Gorham et al., *Constraints on the diffuse high-energy neutrino flux from the third flight of ANITA*, *Phys. Rev. D* **98** (2018) 022001 [[1803.02719](#)].
- [21] D. Bergman. personal communication.
- [22] J. Heinze, A. Fedynitch, D. Boncioli and W. Winter, *A New View on Auger Data and Cosmogenic Neutrinos in Light of Different Nuclear Disintegration and Air-shower Models*, *The Astrophysical Journal* **873** (2019) 88.
- [23] IceCube Collaboration, *IceCube-Gen2: The Window to the Extreme Universe*, *in prep.* (2020) .

- [24] C. Glaser for the ARIANNA Collaboration, *Neutrino direction and energy resolution of Askaryan detectors*, Proc. 36th ICRC 2019, Madison, Wisconsin, USA, PoS(ICRC2019)899 (2019) [1911.02093].
- [25] G. A. Askaryan, *Excess negative charge of an electron-photon shower*, Sov. Phys. JETP **14** (1962) 441.
- [26] J. Alvarez-Muñiz, A. Romero-Wolf and E. Zas, *Cerenkov radio pulses from electromagnetic showers in the time domain*, Phys. Rev. D **81** (2010) 123009 [1002.3873].
- [27] J. Alvarez-Muñiz, A. Romero-Wolf and E. Zas, *Practical and accurate calculations of Askaryan radiation*, Phys. Rev. D **84** (2011) 103003 [1106.6283].
- [28] J. Alvarez-Muñiz, W. R. Carvalho, M. Tueros and E. Zas, *Coherent cherenkov radio pulses from hadronic showers up to EeV energies*, Astropart. Phys. **35** (2012) 287.
- [29] C. W. James, H. Falcke, T. Huege and M. Ludwig, *General description of electromagnetic radiation processes based on instantaneous charge acceleration in endpoints*, Phys. Rev. E **84** (2011) 56602.
- [30] J. Alvarez-Muñiz, P. M. Hansen, A. Romero-Wolf and E. Zas, *Askaryan radiation from neutrino-induced showers in ice*, 2003.09705v1.
- [31] E. Zas, F. Halzen and T. Stanev, *Electromagnetic pulses from high-energy showers: Implications for neutrino detection*, Phys. Rev. D **45** (1992) 362.
- [32] L. D. Landau and I. Pomeranchuk, *Limits of applicability of the theory of bremsstrahlung electrons and pair production at high-energies*, Dokl. Akad. Nauk Ser. Fiz. **92** (1953) 535.
- [33] A. B. Migdal, *Bremsstrahlung and pair production in condensed media at high-energies*, Phys. Rev. **103** (1956) 1811.
- [34] D. Saltzberg et al., *Observation of the Askaryan effect: Coherent microwave Cherenkov emission from charge asymmetry in high-energy particle cascades*, Physical Review Letters **86** (2001) 2802.
- [35] P. W. Gorham et al., *Accelerator measurements of the Askaryan effect in rock salt: A roadmap toward teraton underground neutrino detectors*, Physical Review D **72** (2005) .
- [36] P. W. Gorham et al., *Observations of the Askaryan Effect in Ice*, Physical Review Letters **99** (2007) .
- [37] P. Miočinović et al., *Time-domain measurement of broadband coherent cherenkov radiation*, Physical Review D **74** (2006) .
- [38] K. Belov et al., *Accelerator Measurements of Magnetically Induced Radio Emission from Particle Cascades with Applications to Cosmic-Ray Air Showers*, Phys. Rev. Lett. **116** (2016) 141103.
- [39] PIERRE AUGER collaboration, *Probing the radio emission from air showers with polarization measurements*, Phys. Rev. D **89** (2014) 52002.

- [40] P. Schellart et al., *Polarized radio emission from extensive air showers measured with LOFAR*, *J. Cosmol. Astropart. Phys.* **2014** (2014) 14 [[1406.1355](#)].
- [41] O. Scholten et al., *Measurement of the circular polarization in radio emission from extensive air showers confirms emission mechanisms*, *Physical Review D* **94** (2016).
- [42] T. Barrella, S. Barwick and D. Saltzberg, *Ross Ice Shelf in situ radio-frequency ice attenuation*, *J. Glaciol.* **57** (2011) 61.
- [43] S. W. Barwick et al., *Radar Absorption, Basal Reflection, Thickness, and Polarization Measurements from the Ross Ice Shelf*, *J. Glaciol.* **61** (2015) 438.
- [44] C. Reed for the ARIANNA Collaboration, *Livetime and sensitivity of the ARIANNA Hexagonal Radio Array*, *Proc. 34th ICRC 2015, The Hague, Netherlands* (2025) [[1509.00115](#)].
- [45] G. Gaswint for the ARIANNA Collaboration, *New results on angular reconstruction of deep pulser radio signals*, *Proc. 36th ICRC 2019, Madison, Wisconsin, USA, PoS(ICRC2019)897* (2019) .
- [46] ARIANNA collaboration, *New results on polarization and angular reconstruction of deep pulser radio signals by ARIANNA detector*, *in preparation* (2020) .
- [47] A. Nelles for the ARIANNA Collaboration, *Cosmic-ray detection with and novel reconstruction algorithms for the ARIANNA experiment*, *Proc. 36th ICRC 2019, Madison, Wisconsin, USA, PoS(ICRC2019)366* (2019) .
- [48] ARIANNA collaboration, *A search for cosmogenic neutrinos with the ARIANNA test bed using 4.5 years of data*, *Journal of Cosm. and Astropartphys.* **2020(03)035** [[1909.00840](#)].
- [49] A. Nelles for the ARIANNA Collaboration, *A wind-turbine for autonomous stations for radio detection of neutrinos*, *Proc. 36th ICRC 2019, Madison, Wisconsin, USA, PoS(ICRC2019)968* (2019) .
- [50] ARIANNA collaboration, *Neutrino vertex reconstruction with in-ice radio detectors using surface reflections and implications for the neutrino energy resolution*, *Journal of Cosmology and Astroparticle Physics* **11** (2019) 030 [[1909.02677](#)].
- [51] S. W. Barwick et al., *Radio detection of air showers with the ARIANNA experiment on the Ross Ice Shelf*, *Astropart. Phys.* **90** (2017) 50.
- [52] D. García-Fernández, C. Glaser and A. Nelles, *The signatures of secondary leptons in radio-neutrino detectors in ice*, [2003.13442](#).

## Neutrino vertex reconstruction with in-ice radio detectors using surface reflections and implications for the neutrino energy resolution

To cite this article: A. Anker *et al* JCAP11(2019)030

View the [article online](#) for updates and enhancements.

### You may also like

- [Neutrino–nucleus cross sections for oscillation experiments](#)  
Teppei Katori and Marco Martini
- [The neutrino–neutrino interaction effects in supernovae: the point of view from the ‘matter’ basis](#)  
Sébastien Galais, James Kneller and Cristina Volpe
- [Neutrino physics with JUNO](#)  
Fengpeng An, Guangpeng An, Qi An et al.



**IOP | ebooks™**

Bringing together innovative digital publishing with leading authors from the global scientific community.

Start exploring the collection—download the first chapter of every title for free.

# Neutrino vertex reconstruction with in-ice radio detectors using surface reflections and implications for the neutrino energy resolution

A. Anker,<sup>a</sup> S.W. Barwick,<sup>a</sup> H. Bernhoff,<sup>b</sup> D.Z. Besson,<sup>c,d</sup>  
N. Bingefors,<sup>e</sup> D. García-Fernández,<sup>f,g</sup> G. Gaswint,<sup>a</sup> C. Glaser,<sup>a,1</sup>  
A. Hallgren,<sup>e</sup> J.C. Hanson,<sup>h</sup> S.R. Klein,<sup>i</sup> S.A. Kleinfelder,<sup>j</sup>  
R. Lahmann,<sup>a,g</sup> U. Latif,<sup>c</sup> J. Nam,<sup>k</sup> A. Novikov,<sup>c,d</sup> A. Nelles,<sup>f,g</sup>  
M.P. Paul,<sup>a</sup> C. Persichilli,<sup>a</sup> I. Plaisier,<sup>f,g</sup> T. Prakash,<sup>i</sup> S.R. Shively,<sup>a</sup>  
J. Tatar,<sup>a,l</sup> E. Unger,<sup>e</sup> S.-H. Wang,<sup>k</sup> C. Welling<sup>f,g</sup> and S. Zierke<sup>m</sup>

<sup>a</sup>Department of Physics and Astronomy, University of California,  
Irvine, CA 92697, U.S.A.

<sup>b</sup>Uppsala University Department of Engineering Sciences, Division of Electricity,  
Uppsala, SE-752 37 Sweden

<sup>c</sup>Department of Physics and Astronomy, University of Kansas,  
Lawrence, KS 66045, U.S.A.

<sup>d</sup>National Research Nuclear University MEPhI (Moscow Engineering Physics Institute),  
Moscow 115409, Russia

<sup>e</sup>Uppsala University Department of Physics and Astronomy,  
Uppsala, SE-752 37, Sweden

<sup>f</sup>DESY, 15738 Zeuthen, Germany

<sup>g</sup>ECAP, Friedrich-Alexander-Universität Erlangen-Nürnberg,  
91058 Erlangen, Germany

<sup>h</sup>Whittier College Department of Physics,  
Whittier, CA 90602, U.S.A.

<sup>i</sup>Lawrence Berkeley National Laboratory,  
Berkeley, CA 94720, U.S.A.

<sup>j</sup>Department of Electrical Engineering and Computer Science, University of California,  
Irvine, CA 92697, U.S.A.

<sup>k</sup>Department of Physics and Leung Center for Cosmology and Particle Astrophysics,  
National Taiwan University,  
Taipei 10617, Taiwan

---

<sup>1</sup>Corresponding author.

<sup>l</sup>Research Cyberinfrastructure Center, University of California,  
Irvine, CA 92697 U.S.A.

<sup>m</sup>III. Physikalisches Institut, RWTH Aachen University,  
Aachen, Germany

E-mail: [christian.glaeser@uci.edu](mailto:christian.glaeser@uci.edu)

Received September 9, 2019

Revised November 5, 2019

Accepted November 6, 2019

Published November 25, 2019

**Abstract.** Ultra high energy neutrinos ( $E_\nu > 10^{16.5}$  eV) are efficiently measured via radio signals following a neutrino interaction in ice. An antenna placed  $\mathcal{O}(15)$  m below the ice surface will measure two signals for the vast majority of events (90% at  $E_\nu = 10^{18}$  eV): a direct pulse and a second delayed pulse from a reflection off the ice surface. This allows for a unique identification of neutrinos against backgrounds arriving from above. Furthermore, the time delay between the direct and reflected signal (D'n'R) correlates with the distance to the neutrino interaction vertex, a crucial quantity to determine the neutrino energy. In a simulation study, we derive the relation between time delay and distance and study the corresponding experimental uncertainties in estimating neutrino energies. We find that the resulting contribution to the energy resolution is well below the natural limit set by the unknown inelasticity in the initial neutrino interaction. We present an in-situ measurement that proves the experimental feasibility of this technique. Continuous monitoring of the local snow accumulation in the vicinity of the transmit and receive antennas using this technique provide a precision of  $\mathcal{O}(1)$  mm in surface elevation, which is much better than that needed to apply the D'n'R technique to neutrinos.

**Keywords:** neutrino astronomy, neutrino detectors, neutrino experiments, ultra high energy photons and neutrinos

**ArXiv ePrint:** [1909.02677](https://arxiv.org/abs/1909.02677)

---

## Contents

<b>1</b>	<b>Introduction</b>	<b>1</b>
<b>2</b>	<b>Energy reconstruction</b>	<b>2</b>
<b>3</b>	<b>Determination of neutrino vertex position</b>	<b>4</b>
3.1	Vertex distance resolution	6
3.2	Energy resolution	7
3.3	Systematic uncertainties	9
<b>4</b>	<b>Experimental test of D'n'R technique</b>	<b>10</b>
4.1	Systematic uncertainties	12
4.2	Measurement of density profile	12
4.3	Time resolution at low signal-to-noise ratios	13
<b>5</b>	<b>Monitoring of snow accumulation</b>	<b>14</b>
5.1	Snow accumulation at the ARIANNA site	14
5.1.1	Interpretation	15
5.2	Synergies with geophysics	16
<b>6</b>	<b>Discussion and conclusions</b>	<b>16</b>

---

## 1 Introduction

High-energy neutrino astronomy opens a new window to the universe and its most violent processes [1]. Neutrinos are undeflected in their journey through the universe and point back to their sources. In particular, a multi-messenger observation, including neutrinos together with electromagnetic measurements ranging from radio to optical to gamma rays allows to pinpoint and better understand the sources. The multi-messenger era was initiated when the IceCube detector at the South Pole observed a  $3 \times 10^{14}$  eV neutrino in coincidence with a flaring blazar observed with gamma-ray telescopes [2]. Additional neutrino detectors with a similar sensitivity are currently being constructed in the Mediterranean sea [3] and Lake Baikal [4] to observe the Northern hemisphere.

To extend the detectable neutrino energy range beyond  $10^{16}$  eV, which will potentially link neutrinos with gravitational wave observations [5, 6], one needs a different detection technology. The radio technique allows to cost-efficiently instrument large volumes [7] to cover neutrino energies above  $10^{16.5}$  eV due to the large attenuation length of radio signals in ice of  $\mathcal{O}(1\text{ km})$ . A neutrino interacting in the ice produces a particle cascade that generates a short radio pulse over the frequency range 50 MHz to 1 GHz via the Askaryan effect [8].

This promising technique was successfully explored in two pilot arrays ARA [9] at the South Pole and ARIANNA [10] on the Ross ice shelf and at the South Pole. The requisite hardware and technology has matured in these pilot arrays and the construction of a large-scale detector with enough sensitivity to detect statistically significant numbers of ultra-high energy neutrinos is foreseen in the near future.

With the transition from a pilot to production phase, the focus shifts from building a working detector with large sensitivity to determining the relevant neutrino properties,

specifically direction and energy, from the observed few-nanosecond duration radio flashes. As the detectors are optimized for maximum sensitivity, most neutrinos will be observed in only a few antennas of a single detector station, which makes reconstruction of neutrino properties challenging. In this article, we explore in depth how the distance to the neutrino interaction vertex can be determined and then translated into a neutrino energy estimate.

The distance to the neutrino vertex can be measured precisely via the D'n'R (direct and reflected) technique [11, 12]. An antenna placed  $\mathcal{O}(15\text{ m})$  below the ice surface will measure two pulses for the vast majority of detected neutrinos [13], one direct signal and a slightly delayed signal that is reflected off the ice surface. The time delay between the two pulses is a proxy for the vertex distance. The geometries are such that most reflections are totally internally reflected (TIR) meaning that both pulses are comparable in amplitude. For simplicity we use the term ‘vertex position’ to refer to the point of emission although they are not exactly the same because of the extent of the particle shower (see also discussion in section 3).

We first perform a Monte-Carlo study using NuRadioMC [13] in which we determine the relation between time delay and distance, and simulate the resolution on the vertex distance and the corresponding contribution to the neutrino energy uncertainty. Then, we present an in-situ measurement performed with the ARIANNA detector on the Ross ice shelf to demonstrate the experimental feasibility of this technique. In the last section, we demonstrate how this technique can be used to continuously monitor snow accumulation; we also present a several-month snow accumulation measurement.

## 2 Energy reconstruction

In this section, the steps necessary to reconstruct the neutrino energy from a radio detector are briefly summarized and the performance required of the D'n'R technique to determine the vertex distance are established.

The relation between the neutrino energy ( $E_\nu$ ) and the radio signal amplitude observed at the detector ( $\varepsilon$ ), for a neutrino interaction at a range  $R$  from the detector is summarized in the following equation

$$\varepsilon(f) = \varepsilon_0(f, E_\nu, y, \dots) \times \frac{e^{-R/L(f)}}{R} \times \exp\left[\frac{-(\theta - \theta_C)^2}{2\sigma_\theta(f)^2}\right], \quad (2.1)$$

where  $\varepsilon$  describes the observed frequency spectrum of the Askaryan signal,  $\varepsilon_0$  is the Askaryan signal as a function of neutrino energy  $E_\nu$ , inelasticity  $y$  and other properties of the neutrino interaction. The parameter  $L(f)$  is the frequency dependent attenuation length and  $R$  the distance. The angles  $\theta$  and  $\theta_C$  are the viewing angle and the Cherenkov angle respectively, and  $\sigma_\theta$  is the width of the Cherenkov cone. Please refer to [14] for a more detailed discussion of each of the terms.

The second and third terms on the right-hand side of this equation depend on the measurable quantities *vertex distance*  $R$  and *viewing angle*  $\theta$ . The first term represents the fraction of the primary neutrino energy manifest as radio emission. It depends on stochastic processes in the neutrino interaction and imposes an irreducible energy uncertainty. Thus, it sets the scale for the experimental precision required for the second and third terms in eq. (2.1).

The radio signal amplitude at the source scales linearly with the energy of the particle shower ( $E_{\text{sh}}$ ) generated following a neutrino interaction. Energy is transferred into the shower stochastically and depends on the specific type of interaction. For charged-current electron

neutrino interactions, an electromagnetic shower is induced by an electron generated in the neutrino interaction, and a hadronic shower results from the interaction of the neutrino with the nucleus. For all other types of interactions, only a hadronic shower is created (we neglect decays of tau leptons and catastrophic  $dE/dx$  from muons for simplicity). We note that a hadronic shower will eventually transfer most of its energy into electromagnetic sub-showers which are responsible for the radio emission. Thus, with the term ‘hadronic showers’ we refer to a particle shower with initial hadronic interaction that will transfer most of its energy into electromagnetic sub-showers.

The shower energy can be related to the neutrino energy via

$$E_{\text{sh}} = \begin{cases} y E_\nu & \text{for hadronic showers} \\ (1 - y) E_\nu & \text{for electromagnetic showers} \end{cases} \quad (2.2)$$

We note that only the shower energy that ends up in electromagnetic sub-showers is relevant to the radio emission. For hadronic showers only 90% to 95% of the energy ends up in electromagnetic cascades [15] which is precisely modelled in the Askaryan emission codes.

The distribution of inelasticity  $y$  (see e.g. [16] or [17]) cannot be used directly as a proxy for the scatter in reconstructed neutrino energy because of the detector acceptance. An interaction with an inelasticity value that leads to a small shower energy is less likely to be detected than those showers for which a significant part of the neutrino energy is transferred to the shower.

To study this effect under realistic conditions, we performed a full Monte Carlo simulation using NuRadioMC [13], i.e., we simulate the initial neutrino interaction, followed by radio signal generation and propagation to a detailed detector simulation. We simulate an initial neutrino energy spectrum following a  $E^{-2.2}$  power law, corresponding to an extrapolation of the astrophysical neutrino flux measured by IceCube [18], superimposed upon a cosmogenic neutrino spectrum, i.e., neutrinos generated via cosmic-ray interactions with the cosmic microwave background, for a 10% proton fraction and for a standard choice of source evolution [19] (see also [10] for a discussion of the models).

In figure 1 left, we present the ratio of shower energy to initial neutrino energy for all triggered events, and also separately for hadronic and electromagnetic showers. The distribution is strongly biased towards high transferred energy such that the shower energy can be close to the neutrino energy with the bias most pronounced for electromagnetic showers. The distribution is also energy dependent (see figure 1 right), broadening with increasing neutrino energy because already a small energy transfer results in sufficiently energetic showers to trigger the detector. The distribution in figure 1 is clearly non-Gaussian; we choose to describe it via the median value and the 68% quantiles which we calculate for the astrophysical + cosmogenic spectrum and discrete neutrino energies:

$$\log_{10}(E_{\text{sh}}/E_\nu) = \begin{cases} -0.12^{+0.11}_{-0.33} & \text{for astrophysical + cosmogenic spectrum} \\ -0.06^{+0.06}_{-0.22} & \text{at } 10^{17} \text{ eV neutrino energy} \\ -0.25^{+0.18}_{-0.34} & \text{at } 10^{18} \text{ eV neutrino energy} \\ -0.33^{+0.26}_{-0.49} & \text{at } 10^{19} \text{ eV neutrino energy} \end{cases} \quad (2.3)$$

We estimate the resulting uncertainty on the neutrino energy to be about 0.3 in the logarithm of  $\log_{10}(E_{\text{sh}}/E_\nu)$ , corresponding to a factor of 2 on a linear scale. This imposes a natural limit on the maximum experimentally achievable energy resolution for high-energy neutrino

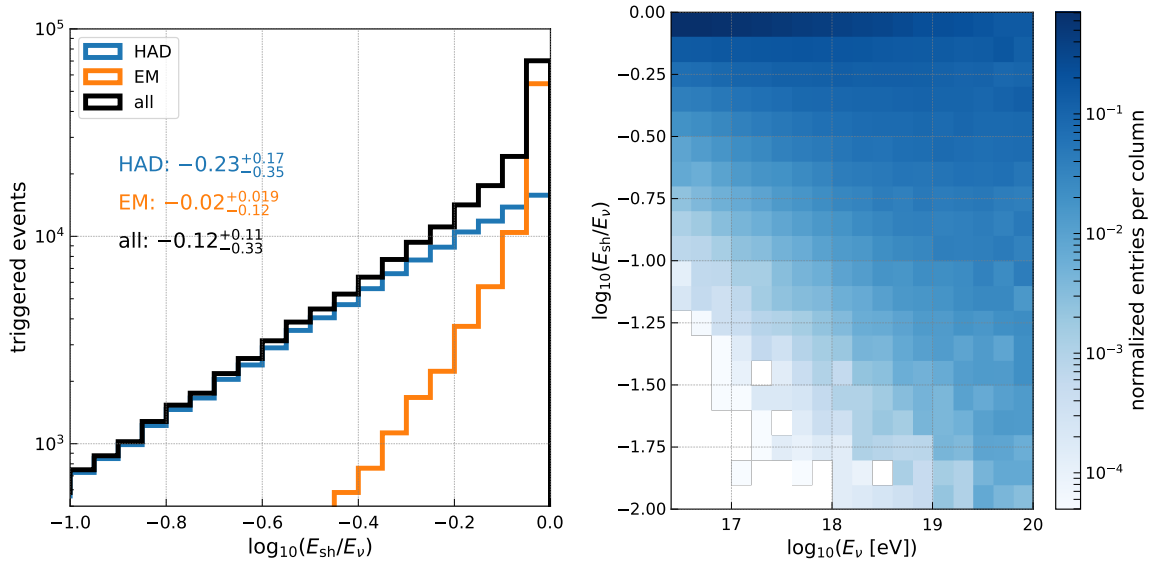


**Figure 1.** (left) Distribution of the ratio between shower energy and neutrino energy for triggered events. The solid curve is for an initial neutrino energy spectrum obtained by summing astrophysical plus cosmogenic signal components (see text for details). (right) Ratio between shower energy and neutrino energy as a function of neutrino energy for all triggered events.

detection, and sets the scale for the optimal experimental precision: The uncertainty of the vertex distance and viewing angle should be small enough so as not to significantly increase the energy uncertainty beyond this inelasticity limit.

We note that for a subset of detected events the neutrino energy might be determined more precisely. At high neutrino energies ( $E_{\nu} > 10^{18}$  eV) electromagnetic and hadronic showers might be differentiated: Electromagnetic showers are elongated by the LPM effect [20], resulting in a reduced Cherenkov cone width that can be measured with an array of antennas with enough spatial separation. Furthermore, for  $\nu_e$  charge-current interactions, both the electromagnetic and hadronic showers might be detected either if both showers are sufficiently spatially displaced [21] or by measuring the distinct frequency spectrum with broadband antennas. In this case the inelasticity uncertainty can be removed completely as the sum of hadronic and electromagnetic shower energy gives the neutrino energy. As these signatures will be measurable only for a small fraction of neutrino events, we ignore them in the following discussion and use the irreducible limit on the neutrino energy resolution of 0.3 in  $\log_{10}(E_{\text{sh}}/E_{\nu})$  as a lower bound on the achievable precision.

### 3 Determination of neutrino vertex position

In this section, we study how to determine the distance to the neutrino vertex by measuring the time delay between the direct and reflected signal path. At the end of this section, we estimate the expected vertex resolution and how this propagates into the neutrino energy resolution.

We illustrate a few typical signal paths in figure 2. The time delay  $\Delta t$  between the direct and reflected ray depends on the distance between receiver and emitter, their depths, and the incoming signal direction. In all calculations, we take into account the change in the speed-of-light at different depth resulting from the changing index-of-refraction profile.

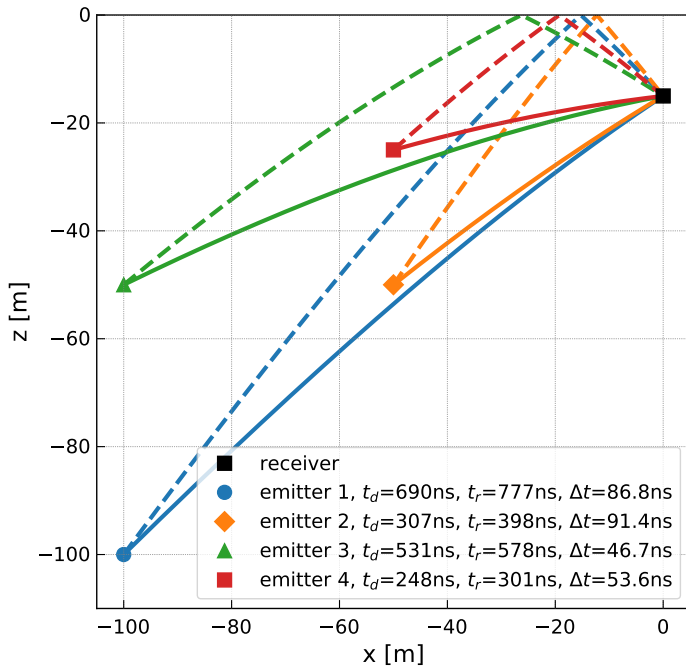


**Figure 2.** Illustration of typical signal paths. The solid curves show direct rays; the dashed curves show rays that are reflected off the snow-air surface. The legend specifies the propagation time of direct rays  $t_d$  and reflected rays  $t_r$  as well as their time difference  $\Delta t$ . Here, we show relatively close emitter positions for better readability. Typically, neutrino vertices will be further away (cf. figure 4).

Similarly, all quoted distances are determined along the curved signal paths dictated by Fermat’s least-time principle.

With the additional information of the radio-frequency signal arrival direction, which is well-known experimentally (e.g. [10, 11]), the neutrino vertex position can be determined by following the signal path, defined by the arrival direction, backwards. Hence, once the signal path is prescribed, the vertex distance prescribes vertex position (and vice versa). We note that the neutrino interaction vertex is not exactly the position where the Askaryan signal originates from because of the extent of the initiated particle shower. Most radio signal is emitted at the maximum of the particle shower which is  $\mathcal{O}(10\text{ m})$  closer to the receiver than the interaction vertex. The exact displacement depends on energy and the degree of LPM elongation [13]. For simplicity, however, we ignore this subtle difference and refer to the point of emission as the ‘vertex position’.

In the following, we will first focus on a 15 m deep receiver which is a good compromise between high efficiency to detect both D’n’R pulses and good time resolution on their separation in a waveform. Later, we extend this study to include a range of possible receiver depths.

We simulated 70 million vertex positions randomly placed within a cylinder of 5 km radius and 2.7 km depth (the thickness of the ice sheet at South Pole), and calculated the signal trajectories to a 15 m deep receiver. We used the fast analytic ray tracer of NuRadioMC [13] to calculate the signal trajectories and the propagation times using the *SPICE 2015* parameterization of the index of refraction profile of South Pole from [22]. For a shallow receiver, most vertex positions have either no possible signal path to reach the receiver, or a direct and reflected signal path to the receiver. Geometries with a refracted and reflected

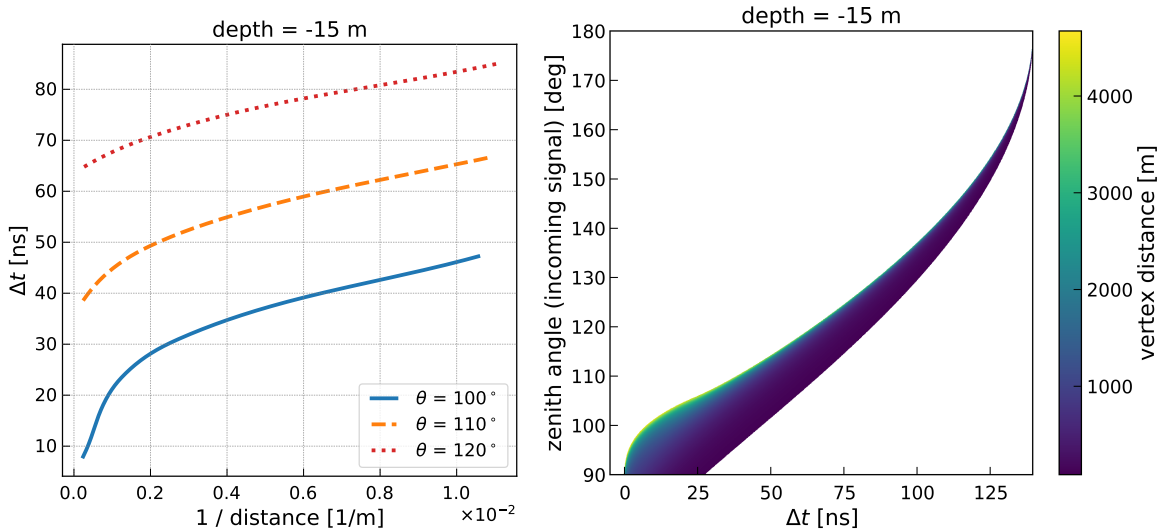


**Figure 3.** (left) Time delay between direct and reflected signal as a function of the inverse distance to the neutrino vertex, for three incoming signal directions. (right) Distance to the neutrino vertex (color coded) as a function of the incoming signal direction and time delay.

path or two refracted signal paths will be ignored in the following. For a realistic simulation of expected neutrino signals, the fraction of such events is only 4%.

The time delay as a function of distance for three incoming directions is presented in the left panel of figure 3. The incoming direction is defined in terms of the zenith angle  $\theta$ . Because of radial symmetry, the azimuth direction is irrelevant here. The time delay inversely correlates with the distance to vertex, as well as the signal elevation angle. We bin all simulations in  $0.1^\circ$  zenith angle and  $0.1\text{ ns}$   $\Delta t$  steps and illustrate the dependence on the vertex distance in the right panel of figure 3. The bin widths are chosen to be smaller than the typical experimental uncertainties such that the binning does not limit the vertex resolution. This 2D profile serves as a lookup table to quickly translate a measured time delay and signal direction into vertex distance.

### 3.1 Vertex distance resolution

The resolution on vertex distance depends not only on the  $\Delta t$  and zenith angle  $\theta$  resolution but also on the vertex distance and incoming signal direction itself. This is because the slope of  $\Delta t$  vs. distance  $R$  is smaller for distant vertices and vertically arriving signals. Thus, nearby vertices will have better resolution than distant vertices. Similarly, incoming directions from close to the horizon have better distance resolution than signals arriving from straight down. Therefore, we fold in the expected vertex distribution of neutrinos and corresponding incoming signal directions. The distribution depends on the neutrino energy, with larger neutrino energies having more distant vertices on average. Hence, we study the resolution for a fixed neutrino energies of  $10^{17}\text{ eV}$  and  $10^{18}\text{ eV}$ , corresponding to the peak sensitivity of an Askaryan detector.

Figure 4 presents the expected distribution of vertex positions and incoming signal directions for high-energy neutrinos to illustrate the relevant parameter space. We obtained these distributions from NuRadioMC, employing a detailed calculation of the Askaryan signal using the *Alvarez2009* model [23, 24], signal propagation including ice attenuation effects,

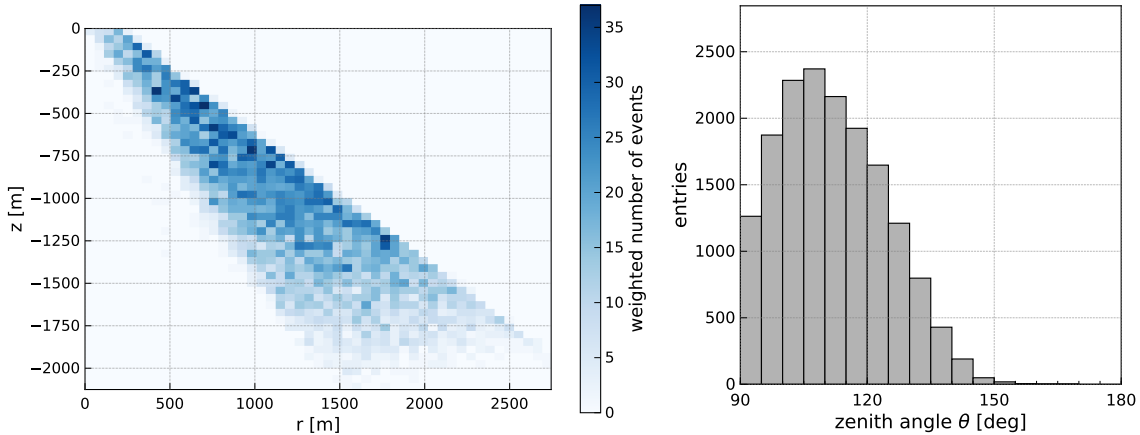


**Figure 4.** Vertex distribution (left) and zenith angle distribution of the incoming signal direction (of the direct signal path) (right) from a full MC simulation using NuRadioMC for a fixed neutrino energy of  $10^{18}$  eV and a receiver depth of 15 m. A zenith angle of  $90^\circ$  points to the horizon and  $180^\circ$  points straight down.

and a full detector simulation. (This simulation corresponds to Example 2 of ref. [13].) The distribution of incoming signal directions (for the direct signal path) is favorable for obtaining good distance resolution, as most signals arrive from close to the horizon, where the  $\Delta t$  vs. distance dependence is large. The shape of the distribution a result of the Earth being opaque at these neutrino energies and because the emission is mostly concentrated around the Cherenkov cone with an opening angle of  $54^\circ$ . Thus, for the corner case of a neutrino coming from the horizon, the signal can be emitted upwards with a maximum zenith angle of  $90^\circ + 54^\circ = 144^\circ$ . Furthermore, the signal trajectories are bent downwards due to the change in the index-of-refraction profile resulting in more horizontal incoming directions.

We determine the vertex distance resolution as follows: For each event of the NuRadioMC simulation that triggered the detector, the true zenith angle and  $\Delta t$  is smeared 200 times according to a Gaussian-distributed uncertainty in  $\sigma_\theta$  and  $\sigma_{\Delta t}$ . The histogram of figure 3 (right) is used to look up the corresponding vertex distance, which is then compared to the true vertex distance.

In figure 5 (left), we present the vertex-distance resolution assuming a  $\Delta t$  resolution of 0.2 ns and a zenith angle resolution of  $0.2^\circ$ , corresponding to our estimate for the achievable experimental resolution of a future Askaryan detector [10]. As expected, the resolution is better for lower neutrino energies. For  $10^{17}$  eV, we find a 68% quantile of 0.04 in  $\log 10(R_{\text{rec}}/R_{\text{true}})$ , corresponding to a linear resolution of 10%. For  $10^{18}$  eV, we find a 68% quantile of 0.05 in  $\log 10(R_{\text{rec}}/R_{\text{true}})$ , corresponding to a linear resolution of 12%.

### 3.2 Energy resolution

For multi-messenger science, the relevant quantity of interest is not the vertex resolution but the neutrino energy resolution. Thus, for each vertex distance we calculate the ‘shower energy’ as

$$E_{\text{sh}} \propto \frac{R}{\exp(-R/L_a)}, \quad (3.1)$$

where  $R$  is the distance from the vertex to the antenna along the direct ray path and  $L_a$  is the attenuation length. This formula is essentially correcting a unit measured signal for

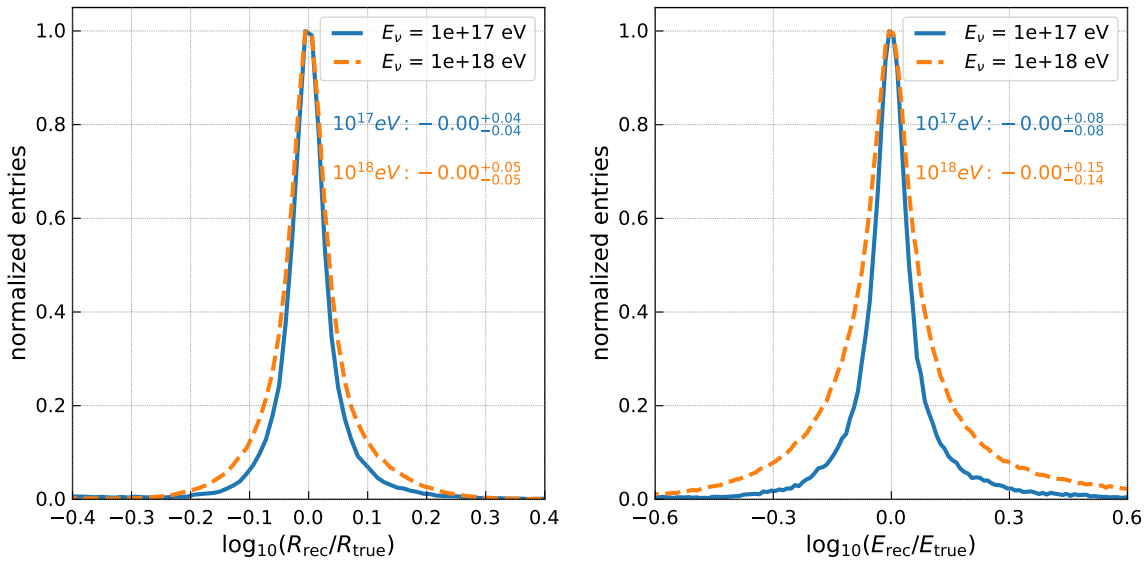


**Figure 5.** (left) Vertex distance resolution for a  $-15 \text{ m}$  deep receiver and uncertainties of  $0.2 \text{ ns}$  in the D'n'R time delay and  $0.2^\circ$  in the zenith direction. (right) Corresponding contribution to the energy resolution from uncertainties in the vertex distance.

attenuation. We use an attenuation length of  $1 \text{ km}$  matching measurements from the South Pole [13, 25]. The resulting energy resolution (from uncertainties of the vertex distance only) is presented in the right panel of figure 5. For neutrino energies of  $10^{17} \text{ eV}$ , we find a resolution of  $\log_{10}(E_{\text{rec}}/E_{\text{true}})$  of  $\sim 0.08$ , corresponding to  $20\%$  on a linear scale. For  $10^{18} \text{ eV}$ , we find a resolution of  $+0.15$  and  $-0.14$  in  $\log_{10}(E_{\text{rec}}/E_{\text{true}})$ , corresponding to  $38\%-41\%$  on a linear scale. Thus, the energy uncertainty from the vertex distance is significantly smaller than the natural limit imposed by the inelasticity of the initial neutrino interaction of  $0.3$  in  $\log_{10}(E_{\text{rec}}/E_{\text{true}})$  (cf. section 2).

In figure 6 (left), we present the dependence of the energy resolution on the uncertainty in  $\Delta t$  and  $\sigma_\theta$ . Even for larger uncertainties of  $0.5^\circ$  and  $0.5 \text{ ns}$ , the resulting energy resolution is still well below the inelasticity limit for  $10^{17} \text{ eV}$  neutrino energies.

In figure 6 (right), we show the energy resolution as a function of receiver depth. Over the first  $\sim 10 \text{ m}$  the resolution improves dramatically. At greater depths, the resolution is continuously improving, but the relative improvement diminishes. Already at  $10 \text{ m}$  depth, the contribution to the energy resolution from the vertex distance uncertainty is well below the natural limit of the energy resolution from the unknown inelasticity.

To draw conclusions for an optimal detector layout from the depth dependence, the efficiency to detect both D'n'R pulses must also be considered. This was already studied in [13] and is also shown in figure 6 (right) for the case of a  $3 V_{\text{RMS}}$  trigger threshold and the requirement that the second pulse has at least a  $2 \times V_{\text{RMS}}$  signal. This simulation includes all relevant effects such as a realistic neutrino vertex distribution, viewing angle differences of the two signal trajectories, incoming signal directions, reflection at the surface, etc. (see [13] for details).

Especially for neutrino energies of  $10^{17} \text{ eV}$ , the detection efficiency decreases quickly with depth. Thus, the optimal depth for exploiting the D'n'R technique represents a compromise between energy resolution which increases with depth, and the fraction of neutrino events that

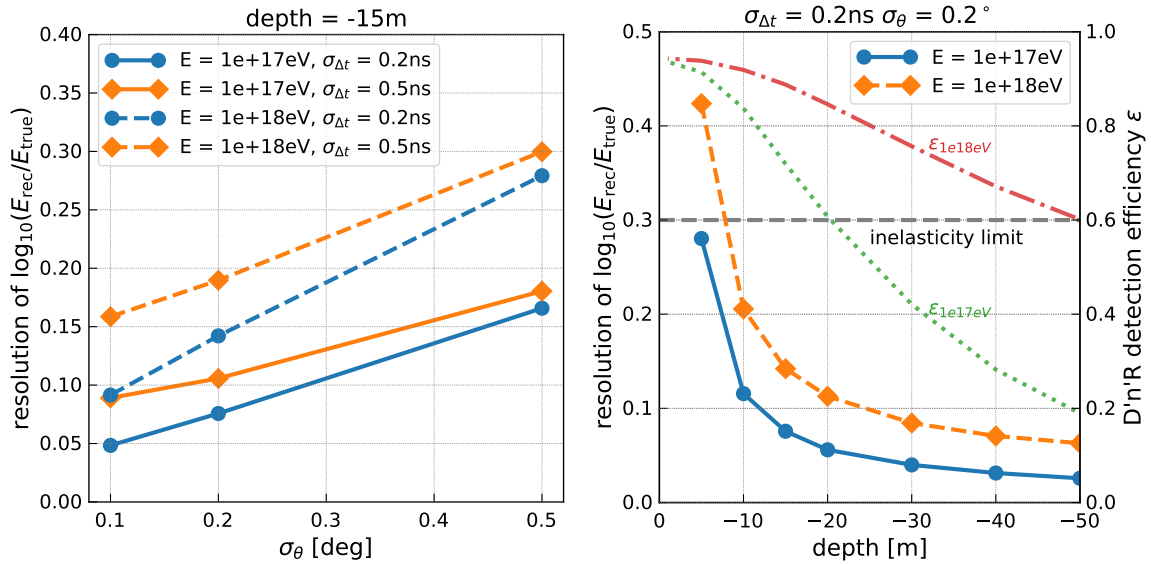


**Figure 6.** Dependence of energy resolution on  $\Delta t$  and  $\theta$  resolution (left) and dependence on depth (right). To interpret this figure, note that the efficiency to detect both D'n'R pulses decreases with depth. This is shown with the dotted ( $E = 10^{17}$  eV) and dash-dotted ( $E = 10^{18}$  eV) curves (see the right y-axis). Also shown is the limit on the energy resolution due to the unknown inelasticity, as a dashed horizontal line.

have a D'n'R signature, which decreases with depth. As the energy resolution is ultimately limited by the unknown inelasticity, it is not required to be much better than this limit. Therefore, shallower depths are favored, for which the energy resolution is already well below the inelasticity limit, but the detection efficiency is still high. We estimate  $-15$  m to be the optimal receiver depth.

### 3.3 Systematic uncertainties

This section briefly discusses the relevant sources of systematic uncertainties. The level of systematic uncertainty will depend on the exact experimental setup and the quality of calibration procedures. Hence, we will not be able to quantify systematic uncertainties but we will list the relevant parameters to guide the design of the station layout and calibration procedures of a future experiment.

The depth of the receiver directly affects the translation from  $\Delta t$  to vertex distance. The depth uncertainty should be small compared to the experimental uncertainty of  $\Delta t$ , i.e.,  $\sigma_d \ll 0.2\text{ ns} \times c \approx 46\text{ mm}$ , where we used the speed-of-light for an index-of-refraction of  $n = 1.3$ . A change in the depth of the receiver due to snow accumulation can be monitored precisely using the setup described in section 5.

Uncertainties in the index-of-refraction  $n(z)$  profile propagate to a systematic uncertainty in the conversion from  $\Delta t$  and zenith angle to distance. A good understanding of the ice properties and especially the change of the  $n(z)$  profile in the upper part of the ice is mandatory. Fortunately, the D'n'R measurement itself in combination with calibration transmitters can be used to measure the  $n(z)$  profile with adequate precision (cf. section 4.2).

The incoming signal direction is typically determined by the signal arrival times in multiple spatially separated antennas. Thus, the position of the antennas as well as the time delays from cables etc. are the relevant source of systematic uncertainty (cf. [26]).

The direct and reflected signal path are, in general, launched at different angles with respect to the Cherenkov cone and thus the two signals might have a different frequency content which can complicate the experimental determination of the time delay between the two signals. Propagation effects (like frequency dependent attenuation) due to the additional path length of the reflected ray are negligible for typical vertex distances of beyond several hundreds of meters. The effect of a different frequency content is reduced by the relatively narrowband response of a dipole receiver. In general, the different launch angles and the correspondingly different frequency content of the two pulses might even be beneficial for the reconstruction as it adds sensitivity to the viewing angle (cf. eq. (2.1) and [14]).

## 4 Experimental test of D'n'R technique

We tested the feasibility to measure the direct and reflected pulse with the following in-situ measurement. We use one ARIANNA detector station installed at Moore’s Bay on the Ross Ice shelf that is equipped with a dipole at a depth of  $-8.6\text{ m}$ . We drilled a  $20\text{ m}$  deep hole  $\sim 40\text{ m}$  away from the station using a newly developed portable cylindrical electrothermal drill [27, 28] — this technique allowed a fast setup and to drill the borehole for the dipole within a few hours and required very little monitoring. We installed a dipole antenna at  $-18.2\text{ m}$  connected through a coax cable to an Avtech pulse generator. The emitting antenna is a copper fat-dipole of  $35\text{ cm}$  length and diameter of  $5\text{ cm}$ , providing ample clearance in the  $9\text{ cm}$  wide borehole. The receiving antenna of the ARIANNA station is a  $52\text{ cm}$  long dipole with a diameter of  $8\text{ cm}$  [29]. Deployment of the larger antenna here takes advantage of the larger-diameter hole that can be drilled at these relatively shallow depths.

The geometry of the measurement setup and the two signal paths from emitter to receiver are shown in figure 7. The signal paths are calculated with NuRadioMC [13] using the *Moore’s Bay #2* index-of-refraction profile from [22]. The emitted signal is  $\vec{e}_\theta$  polarized, as the emitting dipole is vertically oriented. We calculate the Fresnel reflection coefficient for the  $\vec{e}_\theta$  polarization and find that the signal undergoes total internal reflection with a phase shift of  $57^\circ$ . The expected time delay between the reflected and direct signal is  $\Delta t = 22.4\text{ ns}$ . We also calculated the expected ratio of signal amplitudes taking into account the signal attenuation (which is proportional to the path length), and the directional sensitivity of the emitting and receiving dipole antennas. We predict an amplitude ratio between direct and reflected signal of  $A_d/A_r = 1.66$ . We note that we expect equal D/R amplitudes for Askaryan signals from neutrinos as the emission point is much farther away than the depth of the receiver.

We performed two measurement runs with different amplitudes. The first run was with a pulse amplitude of  $5\text{ V}$  and a repetition rate of  $0.5\text{ Hz}$ . The second run was with a pulse amplitude of  $2.5\text{ V}$  and a repetition rate of  $5\text{ Hz}$ . In both cases, the width of the pulse was set to  $0.5\text{ ns FWHM}$ . Data were taken for approximately  $10\text{ min}$  each, resulting in about  $300$  events for run 1, and  $3500$  events for run 2. The readout of the ARIANNA station was triggered externally by generating a trigger signal along with the pulse. Each recorded voltage trace has a physical length of  $256\text{ ns}$  sampled with  $1\text{ Gsample/s}$ . One of the recorded waveforms of run 2 is presented in figure 8. The direct and reflected pulses are clearly visible.

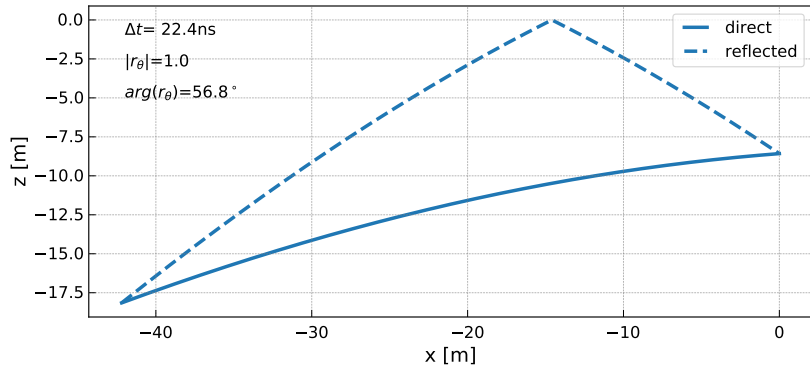


**Figure 7.** Signal paths from emitter to receiver. The legend shows the time difference between the reflected and direct signal path, as well as the magnitude and phase of the reflection coefficient for the  $\theta$  polarization (p-wave).

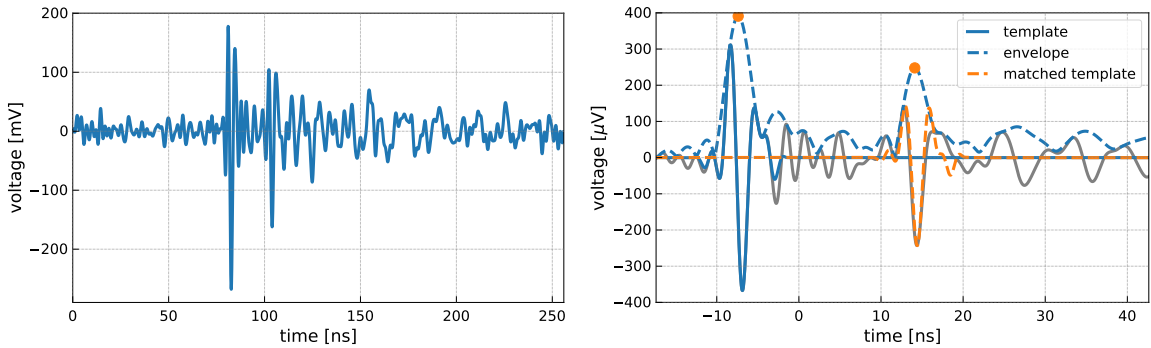


**Figure 8.** (left) Measured voltage trace of run 2 of the Avtech pulser run (see text for details). Shown is the voltage as a function of time. (right) Average over all run 2 events after correcting for the hardware response. The dashed blue line shows the Hilbert envelope of the voltage trace. The signal template is shown as the solid blue curve. The phase shifted template of the reflected pulse, for the best fit, is shown as the orange dashed curve.

We process the data using the NuRadioReco software [30], as follows. The voltage traces are upsampled at 100 Gsamples/s and the amplifier and cable responses are unfolded. A 5th order Butterworth filter with a passband of 100 MHz to 450 MHz is applied to filter out noise outside of the signal bandwidth. The timing between the measurements is synchronized by shifting all traces in time to match the first recorded trace. Then, the average over all measured traces of each run is calculated. The result for run 2 is presented in the right panel of figure 8.

The time delay  $\Delta t$  is determined as follows: A template of the signal pulse is obtained by filtering out the first pulse using a modified Hanning window in the time domain. The Hanning window is adjusted to transition from 0 to 1 (and 1 to 0) within 3 ns and set to 1 for 6 ns. The window is centered around the maximum of the Hilbert envelope (dotted blue curve and orange circle of figure 8 (right)). The resulting signal pulse template is shown as the blue curve. Then, the signal template is adjusted for the phase shift of  $57^\circ$  resulting from the Fresnel reflection off the ice surface. The optimal time shift is found by determining the time shift value that maximizes the cross correlation between the matched template and

the measured trace. The precision is further improved by fitting a Gaussian function to the cross correlation around the maximum. The matched template is shown as the orange dotted curve. We measure  $\Delta t = 21.743$  ns. The same procedure was repeated for run 1, yielding  $\Delta t = 21.762$  ns. Thus, the measurement is reproducible to within 19 ps which is remarkable given that the data is sampled with only 1 Gsample/s, corresponding to 1 ns wide time bins. A comparison with theoretical expectation and a discussion of systematic uncertainties is presented later in section 4.1.

The amplitude ratio can be estimated either from the ratio of the maxima of the Hilbert envelope (cf. figure 8 right), yielding  $A_d/A_r = 1.43$  for run 1 and  $A_d/A_r = 1.58$  for run 2, or by scaling the amplitude of the reflected template to the minimum of the reflected pulse, yielding  $A_d/A_r = 1.47$  for run 1 and  $A_d/A_r = 1.61$  for run 2. The determination of the amplitude ratio is more challenging because the reflected pulse interferes with after-pulses from the first direct pulse, altering the signal amplitude. The after-pulse hypothesis is supported by the observation of oscillations above the noise level after the first direct signal pulse, and the observation that the last part of the reflected template does not exactly follow the measurement. The measurements of the two runs agree within  $\sim 10\%$ . Given this level of experimental uncertainty, the measurement is in agreement with the theoretical expectation of  $A_d/A_r = 1.66$ . We conclude that the ice surface acts as a flat reflector and specularly reflects the radio pulse without significant attenuation.

#### 4.1 Systematic uncertainties

As illustrated above, one of the advantages of the D'n'R technique is that the time difference can be measured experimentally with high accuracy. The time difference is determined from a single voltage trace. Time synchronization between different channels, cable delays, amplifier characteristics, etc are irrelevant. Thus, systematic uncertainties of the experimental determination of  $\Delta t$  are negligible.

However, several uncertainties influence the theoretical calculation of the expected  $\Delta t$ : Uncertainties in the geometry (the position of the emitter and receiver) influence the calculation; the modelling of the index-of-refraction profile also impacts the calculated signal paths and propagation times.

The experimental uncertainties in the positioning of the emitting dipole antenna are 20 cm in depth and 10 cm in  $x$  and  $y$ . The position of the receiving antenna was measured more precisely to 10 cm accuracy in depth, and 5 cm in  $x$  and  $y$ . A variation in the depth of 10 cm leads to a change in the predicted  $\Delta t$  of 0.14 ns, and a change of 10 cm in the horizontal distance leads to a change in  $\Delta t$  of 0.08 ns. Changes in  $\Delta t$  scale roughly linearly with the displacement. Thus, changing the position of receiver and emitter by one standard deviation can lead up to variations of  $\pm 0.56$  ns.

#### 4.2 Measurement of density profile

The index-of-refraction profile, which is directly linked to the density of the snow/ice via the Schytt equation, is described by an exponential function with two free parameters. These parameters were optimized to match in-situ index-of-refraction measurements of different depths. The exponential profile describes the data well but the parameters carry an uncertainty [22]. Varying the parameters within one standard deviation of their uncertainty leads to a maximum variation in the predicted  $\Delta t$  of  $\pm 0.38$  ns.

Hence, the difference between the predicted and measured  $\Delta t$  of 0.66 ns is compatible within the systematic uncertainties. In the future, with a more precise measurement of the

geometry, this measurement can be used to precisely determine the index-of-refraction profile  $n(z)$  near the surface. The  $n(z)$  profile can be described with an exponential function

$$n(z) = 1.78 - \Delta n e^{-z/z_0} \quad (4.1)$$

with the two free parameters  $\Delta n$  and  $z_0$ . The parameters for the Moore's Bay site that were determined via an optimization to in-situ measurements are  $\Delta n = 0.481 \pm 0.007$  and  $z_0 = (37 \pm 1) \text{ m}$  [22]. Thus, two independent  $\Delta t$  measurements are required to determine both parameters. This can be achieved, e.g., with two receivers at 10 m and 20 m depth and an emitter 40 m away and at a depth of 15 m, similar to our measurement setup but with two receivers at different depths.

We studied the achievable uncertainty in a toy MC assuming a  $\Delta t$  resolution of 10 ps. From the two  $\Delta t$  measurements we can determine the parameter  $\Delta n$  to a precision of 0.0006 and  $z_0$  to a precision of 0.2 m which constitutes an order of magnitude improvement over the parameters derived from snow density measurements of [22].

The resolution can be further improved by an improved geometry: The more distinct the ray paths to the two receivers, the better the sensitivity to the  $n(z)$  parameters. Possible geometries are constrained by the demand of having two ray paths to the receiver and having total-internal-reflection at the surface. Increasing the distance between emitter and the shallower receiver (-10 m) to 80 m improves the precision by another factor of 2. In general, adding more receivers at different depths and distances would allow to determine the parameters of more elaborate  $n(z)$  models, having more free parameters. Another prospect of multi receiver measurements is a long term measurement of the snow accumulation in conjunction with the  $n(z)$  profile to track possible snow compaction at the surface.

### 4.3 Time resolution at low signal-to-noise ratios

So far we have considered only measurements at relatively high signal-to-noise ratios and even an average over several events to improve the  $\Delta t$  resolution. In the case of a neutrino signal, only one measurement is possible, at often small signal-to-noise ratios (SNRs) just above the trigger threshold. We now consider the evolution of the  $\Delta t$  resolution with SNR.

The typical distance to the neutrino interaction vertex is typically far away from the detector (see figure 4 left and [13]) such that both the direct and reflected pulse have a similar amplitude when received with a dipole antenna with equal sensitivity to upward and downward coming signals equally displaced from the horizon. We calculate the predicted Askaryan signal using the precise *ARZ2019* time-domain model [13, 31], fold this pulse with the antenna response, place two copies of the pulse 10 ns apart, add thermal noise and calculate the time delay between the two pulses using the same cross-correlation method as discussed above. We repeat this a thousand times for each signal-to-noise ratio to estimate the  $\Delta t$  resolution from the standard deviation of the time-delay distribution. The result is presented in figure 9 for two different sampling frequencies of 1 and 2 Gsamples/s.

In addition, we calculate the  $\Delta t$  resolution from the in-situ measurement. For each of the 3500 events of run 2 we calculate the time delay individually and estimate the uncertainty via the standard deviation of the  $\Delta t$  distribution. The signal-to-noise ratio of the smaller second pulse is SNR=15; this measurement is also shown in figure 9. It is close to the simulated resolution but slightly higher indicating that noise is not the only source of uncertainty at these high SNRs.

At typical trigger thresholds above  $4 \times V_{\text{RMS}}$  [32] and a sampling rate of 2 Gsamples/s, the maximum  $\Delta t$  uncertainty is 0.1 ns and therefore well below the  $\Delta t$  uncertainty of 0.2 ns

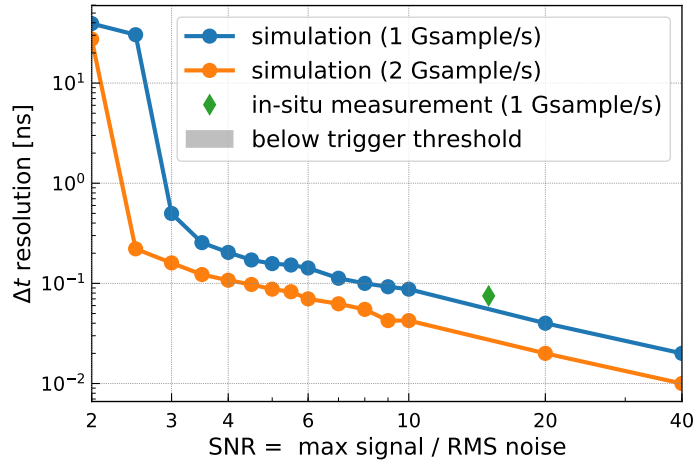


**Figure 9.** Resolution of time delay between direct and reflected pulse as a function of signal-to-noise ratio. Two simulations of different sampling frequencies are compared to an in-situ measurement.

assumed in the simulation study of section 3. There are efforts to lower the trigger thresholds substantially to about  $2 \times V_{\text{RMS}}$  using a phased array [33]: Four to eight antennas are phased up to increase the signal-to-noise ratio by a factor of  $\sqrt{\text{number of antennas}}$ . Although this lowers the trigger threshold, the available signal-to-noise ratio for reconstruction is still above 4 as multiple antennas can be combined. Actually, a phased-array component at around 15 m depth will be ideally suited to precisely measure the D'n'R time delay, and thus, provide an excellent vertex distance resolution.

## 5 Monitoring of snow accumulation

The time difference between the direct and reflected signal path is sensitive to the depth of the receiving antenna. Due to variations in snow accumulation, this depth changes over time. Thus, a precise monitoring of snow accumulation is crucial for the success of the D'n'R technique. Fortunately, the calibration measurement outlined in the previous section can be easily turned into a precise snow accumulation monitoring device.

### 5.1 Snow accumulation at the ARIANNA site

The ARIANNA electronics are capable of creating a pulse similar to the capabilities of the Avtech pulse generator, with an FWHM pulse width of 2 ns. This so-called heartbeat pulser was connected through two 25 m LMR-600 and one 20 m LMR-240 cable to the transmitting antenna. An additional 100 MHz high pass filter was installed to prevent leakage of low-frequency noise from the electronics box. Both the transmitting and receiving antenna are held in place by a rope with a small expansion coefficient that was attached to a bamboo pole which was stuck into the snow.

The heartbeat pulser can be activated remotely. The data acquisition system was set up to start a heartbeat run every 12 hours. For 5 min, the heartbeat pulser was activated with a repetition rate of 0.5 Hz, yielding 150 events per run. This periodic calibration run reduces the time in neutrino observation mode by less than 1% and allows continuous monitoring of the snow accumulation.

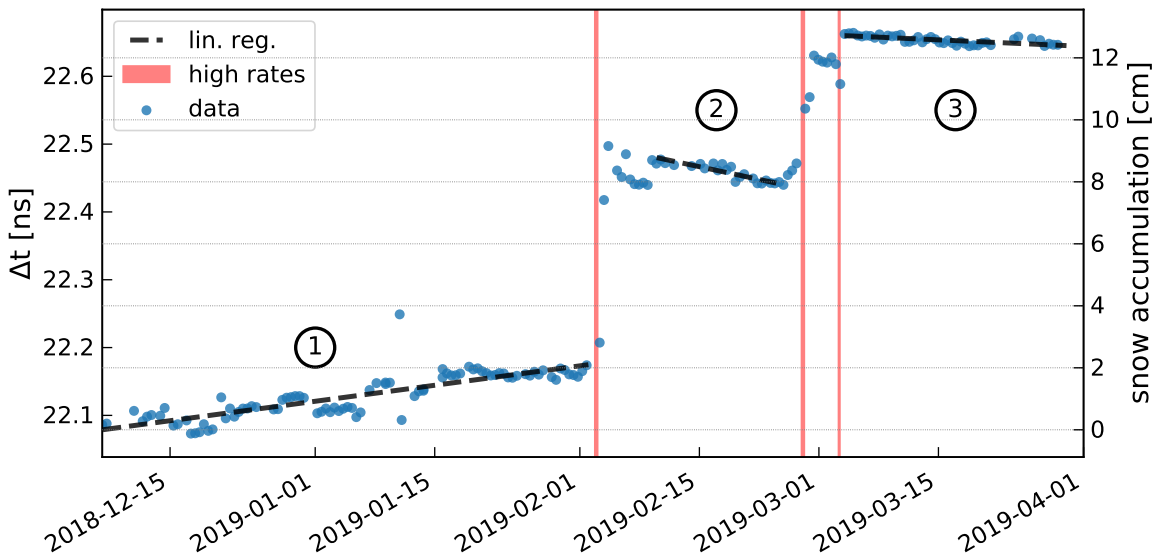


**Figure 10.** Monitoring of snow accumulation. Measured  $\Delta t$  (left axis) is overlaid with the corresponding snow accumulation (blue circles, corresponding to the right axis) as a function of time. The red shaded areas show periods of extended high rates, an indicator of storms. The dashed black lines show a linear regression to the data points.

This calibration system ran from the beginning of December 2018 (after the deployment team left the site) until April 2019 when the station turned off as the solar panel output fell below threshold. We process the data in the same way as described in the previous section, but without the bandpass filter. Because of the larger pulse width, additional signal dispersion from the high pass filter and larger attenuation of high frequencies in the long coax cables, the heartbeat pulse has more low frequency content. However, this does not impact the capability to measure the  $\Delta t$ , as demonstrated below. We average over each set of 150 events and calculate  $\Delta t$  from the average trace. The measured time delays as a function of time are presented in figure 10.

### 5.1.1 Interpretation

The change in the measured  $\Delta t$ 's is converted to a change in the snow accumulation and shown on the right y-axis of figure 10. We observe three clear jumps in snow accumulation — one at the beginning of February and two at the beginning of March. These times are correlated with an extended period of atypically high trigger rates in all ARIANNA stations. This feature is known to correlate with high winds associated with storms. These observations support the interpretation that the change in  $\Delta t$  is due to an increase in the snow level.

The Fresnel reflection zone has a radius of several meters. Thus, our measurement probes the average snow accumulation over an extended area around the point of reflection determined by the ray-tracing model (cf. figure 7). The present measurement does not distinguish between precipitation or snowdrift.

The snow surface at Moore's Bay is not perfectly flat but exhibits variations in height of a few centimeters over meter scales. These features are present near the ARIANNA station, but larger amplitude features, such as tilts or Sastrugi, are absent. Possible timing errors introduced by the averaging of small scale surface features within the Fresnel reflection zone are anticipated to be insignificant.

For neutrino studies, the position of the snow surface must be known for any relevant reflection point. Though we expect that the observed patch of snow surface is representative of any nearby surface position, this hypothesis must be confirmed by additional study. For example, azimuthal symmetry can be tested by installing several emitters at opposite sides of the station.

We subdivide the data into three time ranges where no large snow accumulation occurred and describe the average trend with a straight line obtained via a linear regression. In the first period, the snow accumulation slowly and constantly rose by 2.6 mm/week. A plausible explanation for this effect is that piles of snow left by the deployment teams are redistributed due to wind giving rise to a slight increase of the snow overburden. In the second and third time periods, we observe a reduction in snow accumulation by  $-4.1$  mm/week and  $-0.9$  mm/week. This is likely because fresh snow compacts over time due to solar illumination. This also explains why the slope in the third period is smaller: At this time of year the number of sunlight hours per day is decreasing and the sun is at a lower declination. We note that a change in the density of the new snow layer corresponds to a change in the index-of-refraction which will effect the signal trajectories and thereby the relation between  $\Delta t$  and snow accumulation. However, this effect should be small compared to the reduction in snow accumulation itself. A setup with multiple receivers at different positions would allow to disentangle these effects (cf. discussion in section 4.2) and is foreseen for the future.

We estimate the resolution in this method by calculating the scatter around the linear trend in the three time periods. We measure a scatter of 18 ps in the first period and scatters of 5.6 ps and 4.1 ps in the second and third period, respectively. This translates into a resolution in the snow accumulation of 4 mm and  $\sim$ 1 mm. This resolution is an order of magnitude lower than the assumed  $\Delta t$  resolution of section 3 of 0.2 ns. Thus, changes in snow accumulation do not present any limitation on the D'n'R technique, can be corrected for, and do not deteriorate the energy resolution.

## 5.2 Synergies with geophysics

A construction of a large scale radio neutrino detector with  $\mathcal{O}(100)$  stations separated by 1.5 km is foreseen for the future (see e.g. [10]). If each station is equipped with the functionality to measure the snow accumulation, a continuous large scale monitoring of the surface mass balance is possible which is crucial goal in geophysics and important for predicting future behavior of ice sheets and their effect on sea level [34]. With a precision of 1 mm and measurement timescales measured in hours, our measurement is competitive with, or possibly even more precise than, traditional methods. A high-energy neutrino detector can thus also contribute to geophysics and the monitoring of ice sheets in Arctic regions.

## 6 Discussion and conclusions

The D'n'R technique provides unique opportunities for the detection of high-energy neutrinos. An antenna placed  $\mathcal{O}(15\text{ m})$  below the ice surface will measure a direct pulse and a pulse reflected off the ice surface for most detected neutrino interactions in the ice. This signature does not only provide a unique characteristic of a neutrino origin of the signal but also allows to measure the distance to the neutrino interaction vertex precisely, a crucial property to determine the neutrino energy.

With reasonable assumptions on the uncertainties of the zenith angle of  $0.2^\circ$  and time delay between the two pulses of 0.2 ns, we find a vertex distance resolution of better than

12%. The good timing resolution is possible because the time delay of two pulses within the same channel is calculated. Thus, most experimental uncertainties normally affecting the timing (such as cables delays, antenna differences, position of receivers, time synchronization of channels etc.) cancel out. In addition, the time delay and the zenith angle can be reconstructed independently and are thus uncorrelated. These two properties are the main advantage compared to a reconstruction of the shower front from the pulse arrival times of spatially displaced antennas where the distance, zenith and azimuth angles need to be determined simultaneously and are correlated with each other.

The neutrino energy depends on the measured quantities energy fluence, distance, viewing angle and inelasticity. The stochastic process of the latter imposes a irreducible energy uncertainty of a factor of two. The vertex distance uncertainty of the D'n'R technique translates into a contribution to the energy uncertainty of 20% (at  $E_\nu = 10^{17}$  eV) and  $\sim 40\%$  (at  $E_\nu = 10^{18}$  eV). Thus, it is much smaller than the inelasticity limit and does not increase the energy uncertainty significantly. Also the uncertainties of the remaining contributions to the neutrino energy are smaller than the inelasticity limit as estimated in [14]. Hence, a shallow high-energy neutrino detector will have an excellent energy resolution limited by the irreducible inelasticity fluctuations.

The D'n'R technique was tested experimentally at Moore's Bay on the Ross ice shelf. An ARIANNA detector station equipped with a 8.6 m deep dipole antenna received signals from a 20 m deep transmitter. The observed time delay, the amplitude ratio as well as the phase shift of the reflected pulse matches the expectation within systematic uncertainties providing an important proof-of-concept of the method. We found a time resolution of 80 ps for the signal-to-noise ratio of 15 of the measurement. The uncertainty decreases slightly with smaller signal-to-noise ratios but remains below 0.2 ns which was determined in a simulation study.

This test setup was also used as a snow accumulation monitoring device: the ARIANNA hardware is equipped with a remotely configurable pulse generator that was connected to the transmitting antenna. The D'n'R time delay was measured every 12 h over several months which was translated into snow accumulation, as the time delay increases proportional to the snow accumulation. From this long-term measurement, we derived a statistical uncertainty of 5 ps corresponding to a 1 mm resolution on the snow accumulation. A large scale neutrino detector equipped with such a calibration device might contribute important data on the surface mass balance of ice sheets, a crucial property for global climate models.

## Acknowledgments

We are grateful to the U.S. National Science Foundation-Office of Polar Programs, the U.S. National Science Foundation-Physics Division (grant NSF-1607719) for granting the ARIANNA array at Moore's Bay. Without the invaluable support of the people at McMurdo, the ARIANNA stations would have never been built.

We acknowledge funding from the German research foundation (DFG) under grants GL 914/1-1 (CG), NE 2031/1-1, and NE 2031/2-1 (DGF, ANe, IP, CW) and the Taiwan Ministry of Science and Technology (JN, SHW). HB acknowledges support from the Swedish Government strategic program Stand Up for Energy. EU acknowledges support from the Uppsala university Vice-Chancellor's travel grant (sponsored by the Knut and Alice Wallenberg Foundation) and the C.F. Liljewalch travel scholarships. DB and ANo acknowledge support from the MEPhI Academic Excellence Project (Contract No. 02.a03.21.0005) and the Megagrant 2013 program of Russia, via agreement 14.12.31.0006 from 24.06.2013.

The used melting probes (cf. section 4) were developed within the EnEx-RANGE project, which was funded by the German Federal Ministry of Economics and Energy (BMWi) by resolution of the German Federal Parliament under the funding code 50NA1501.

## References

- [1] M. Ackermann et al., *Astrophysics Uniquely Enabled by Observations of High-Energy Cosmic Neutrinos*, *Bull. Am. Astron. Soc.* **51** (2019) 185 [[arXiv:1903.04334](#)] [[inSPIRE](#)].
- [2] ICECUBE, FERMI-LAT, MAGIC, AGILE, ASAS-SN, HAWC, H.E.S.S., INTEGRAL, KANATA, KISO, KAPTEYN, LIVERPOOL TELESCOPE, SUBARU, SWIFT NuSTAR, VERITAS and VLA/17B-403 collaborations, *Multimessenger observations of a flaring blazar coincident with high-energy neutrino IceCube-170922A*, *Science* **361** (2018) eaat1378 [[arXiv:1807.08816](#)] [[inSPIRE](#)].
- [3] KM3NET collaboration, *Letter of intent for KM3NeT 2.0*, *J. Phys. G* **43** (2016) 084001 [[arXiv:1601.07459](#)] [[inSPIRE](#)].
- [4] BAIKAL-GVD collaboration, *Neutrino Telescope in Lake Baikal: Present and Future*, in proceedings of the *36th International Cosmic Ray Conference (ICRC 2019)* Madison, Wisconsin, U.S.A., July 24 – August 1, 2019, *PoS(ICRC2019)1011* [[arXiv:1908.05427](#)] [[inSPIRE](#)].
- [5] S.S. Kimura, K. Murase, P. Mészáros and K. Kiuchi, *High-Energy Neutrino Emission from Short Gamma-Ray Bursts: Prospects for Coincident Detection with Gravitational Waves*, *Astrophys. J.* **848** (2017) L4 [[arXiv:1708.07075](#)] [[inSPIRE](#)].
- [6] K. Fang and B.D. Metzger, *High-Energy Neutrinos from Millisecond Magnetars formed from the Merger of Binary Neutron Stars*, *Astrophys. J.* **849** (2017) 153 [[arXiv:1707.04263](#)] [[inSPIRE](#)].
- [7] ICECUBE collaboration, *Constraints on Ultrahigh-Energy Cosmic-Ray Sources from a Search for Neutrinos above 10 PeV with IceCube*, *Phys. Rev. Lett.* **117** (2016) 241101 [Erratum *ibid.* **119** (2017) 259902] [[arXiv:1607.05886](#)] [[inSPIRE](#)].
- [8] G.A. Askar'yan, *Excess negative charge of an electron-photon shower and its coherent radio emission*, *Sov. Phys. JETP* **14** (1962) 441 [[inSPIRE](#)].
- [9] ARA collaboration, *Performance of two Askaryan Radio Array stations and first results in the search for ultrahigh energy neutrinos*, *Phys. Rev. D* **93** (2016) 082003 [[arXiv:1507.08991](#)] [[inSPIRE](#)].
- [10] ARIANNA collaboration, *Targeting ultra-high energy neutrinos with the ARIANNA experiment*, *Adv. Space Res.* **64** (2019) 2595 [[arXiv:1903.01609](#)] [[inSPIRE](#)].
- [11] P. Allison et al., *Measurement of the real dielectric permittivity  $\epsilon_r$  of glacial ice*, *Astropart. Phys.* **108** (2019) 63 [[arXiv:1712.03301](#)] [[inSPIRE](#)].
- [12] J.L. Kelley for the ARA collaboration, *Interferometric Reconstruction and Analysis Methods for the Askaryan Radio Array*, in proceedings of the *8th international workshop on Acoustic and Radio EeV Neutrino Detection Activities (ARENA 2018)*, Catania, Italy, 12–15 June 2018.
- [13] C. Glaser et al., *NuRadioMC: Simulating the radio emission of neutrinos from interaction to detector*, [arXiv:1906.01670](#) [[inSPIRE](#)].
- [14] C. Glaser for the ARIANNA collaboration, *Neutrino direction and energy resolution of Askaryan detectors*, in proceedings of the *36th International Cosmic Ray Conference*, Madison, WI, U.S.A., July 24 – August 1, 2019, *PoS(ICRC2019)899*.
- [15] J. Alvarez-Muñiz and E. Zas, *The LPM effect for EeV hadronic showers in ice: Implications for radio detection of neutrinos*, *Phys. Lett. B* **434** (1998) 396 [[astro-ph/9806098](#)] [[inSPIRE](#)].

- [16] R. Gandhi, C. Quigg, M.H. Reno and I. Sarcevic, *Ultrahigh-energy neutrino interactions*, *Astropart. Phys.* **5** (1996) 81 [[hep-ph/9512364](#)] [[INSPIRE](#)].
- [17] A. Connolly, R.S. Thorne and D. Waters, *Calculation of High Energy Neutrino-Nucleon Cross Sections and Uncertainties Using the MSTW Parton Distribution Functions and Implications for Future Experiments*, *Phys. Rev. D* **83** (2011) 113009 [[arXiv:1102.0691](#)] [[INSPIRE](#)].
- [18] C. Haack for the IceCube collaboration, *A measurement of the diffuse astrophysical muon neutrino flux using eight years of IceCube data*, in proceedings of the 35th International Cosmic Ray Conference (ICRC2017), Bexco, Busan, Korea, 10–20 July, 2017, [PoS\(ICRC2017\)1005](#).
- [19] A. van Vliet, R. Alves Batista and J.R. Hörandel, *Determining the fraction of cosmic-ray protons at ultrahigh energies with cosmogenic neutrinos*, *Phys. Rev. D* **100** (2019) 021302 [[arXiv:1901.01899](#)] [[INSPIRE](#)].
- [20] L. Gerhardt and S.R. Klein, *Electron and Photon Interactions in the Regime of Strong LPM Suppression*, *Phys. Rev. D* **82** (2010) 074017 [[arXiv:1007.0039](#)] [[INSPIRE](#)].
- [21] ICECUBE collaboration, *Measurements using the inelasticity distribution of multi-TeV neutrino interactions in IceCube*, *Phys. Rev. D* **99** (2019) 032004 [[arXiv:1808.07629](#)] [[INSPIRE](#)].
- [22] S.W. Barwick et al., *Observation of classically ‘forbidden’ electromagnetic wave propagation and implications for neutrino detection*, *JCAP* **07** (2018) 055 [[arXiv:1804.10430](#)] [[INSPIRE](#)].
- [23] J. Alvarez-Muñiz, C.W. James, R.J. Protheroe and E. Zas, *Thinned simulations of extremely energetic showers in dense media for radio applications*, *Astropart. Phys.* **32** (2009) 100 [[INSPIRE](#)].
- [24] J. Alvarez-Muñiz, W.R. Carvalho Jr., M. Tueros and E. Zas, *Coherent Cherenkov radio pulses from hadronic showers up to EeV energies*, *Astropart. Phys.* **35** (2012) 287 [[arXiv:1005.0552](#)] [[INSPIRE](#)].
- [25] S. Barwick, D. Besson, P. Gorham and D. Saltzberg, *South polar in situ radio-frequency ice attenuation*, *J. Glaciol.* **51** (2005) 231.
- [26] G. Gaswint for the ARIANNA collaboration, *New results on angular reconstruction of deep pulser radio signals*, in proceedings of the 36th International Cosmic Ray Conference, Madison, WI, U.S.A., July 24 – August 1, 2019, [PoS\(ICRC2019\)897](#).
- [27] D. Heinen et al., *EnEx-RANGE — Robust autonomous Acoustic Navigation in Glacial ice*, in proceedings of the 7th International Conference on Acoustic and Radio EeV Neutrino Detection Activities (ARENA 2016), *EPJ Web Conf.* **135** (2017) 06007.
- [28] RWTH Innovation, *Patent: High efficiency head for fast melting probes*, (2018).
- [29] I. Kravchenko et al., *Event Reconstruction and Data Acquisition for the RICE Experiment at the South Pole*, [arXiv:0705.4491](#) [[INSPIRE](#)].
- [30] C. Glaser et al., *NuRadioReco: A reconstruction framework for radio neutrino detectors*, *Eur. Phys. J. C* **79** (2019) 464 [[arXiv:1903.07023](#)] [[INSPIRE](#)].
- [31] J. Alvarez-Muñiz, A. Romero-Wolf and E. Zas, *Practical and accurate calculations of Askaryan radiation*, *Phys. Rev. D* **84** (2011) 103003 [[arXiv:1106.6283](#)] [[INSPIRE](#)].
- [32] A. Anker et al., *A search for cosmogenic neutrinos with the ARIANNA test bed using 4.5 years of data*, [arXiv:1909.00840](#) [[INSPIRE](#)].
- [33] P. Allison et al., *Design and performance of an interferometric trigger array for radio detection of high-energy neutrinos*, *Nucl. Instrum. Meth. A* **930** (2019) 112 [[arXiv:1809.04573](#)] [[INSPIRE](#)].
- [34] J.T.M. Lenaerts, B. Medley, M.R. Broeke and B. Wouters, *Observing and modeling ice sheet surface mass balance*, *Rev. Geophys.* **57** (2019) 376.

# A search for cosmogenic neutrinos with the ARIANNA test bed using 4.5 years of data

**A. Anker<sup>a</sup> S. W. Barwick<sup>a</sup> H. Bernhoff<sup>b</sup> D. Z. Besson<sup>c,d</sup> N. Bingefors<sup>e</sup> D. García-Fernández<sup>f,g</sup> G. Gaswint<sup>a</sup> C. Glaser<sup>a</sup> A. Hallgren<sup>e</sup> J. C. Hanson<sup>h</sup> S. R. Klein<sup>i</sup> S. A. Kleinfelder<sup>j</sup> R. Lahmann<sup>a,g</sup> U. Latif<sup>c</sup> J. Nam<sup>k</sup> A. Novikov<sup>c,d</sup> A. Nelles<sup>f,g</sup> M. P. Paul<sup>a</sup> C. Persichilli<sup>a,1</sup> I. Plaisier<sup>f,g</sup> T. Prakash<sup>i</sup> S. R. Shively<sup>a</sup> J. Tatar<sup>a,l</sup> E. Unger<sup>e</sup> S.-H. Wang<sup>k</sup> C. Welling<sup>f,g</sup>**

<sup>a</sup>Department of Physics and Astronomy, University of California, Irvine, CA 92697, USA

<sup>b</sup>Uppsala University Department of Engineering Sciences, Division of Electricity, Uppsala, SE-752 37 Sweden

<sup>c</sup>Department of Physics and Astronomy, University of Kansas, Lawrence, KS 66045, USA

<sup>d</sup>National Research Nuclear University MEPhI (Moscow Engineering Physics Institute), Moscow 115409, Russia

<sup>e</sup>Uppsala University Department of Physics and Astronomy, Uppsala, SE-752 37, Sweden

<sup>f</sup>DESY, 15738 Zeuthen, Germany

<sup>g</sup>ECAP, Friedrich-Alexander-Universität Erlangen-Nürnberg, 91058 Erlangen, Germany

<sup>h</sup>Whittier College Department of Physics, Whittier, CA 90602, USA

<sup>i</sup>Lawrence Berkeley National Laboratory, Berkeley, CA 94720, USA

<sup>j</sup>Department of Electrical Engineering and Computer Science, University of California, Irvine, CA 92697, USA

<sup>k</sup>Department of Physics and Leung Center for Cosmology and Particle Astrophysics, National Taiwan University, Taipei 10617, Taiwan

<sup>l</sup>Research Cyberinfrastructure Center, University of California, Irvine, CA 92697 USA

---

<sup>1</sup>Corresponding author

E-mail: [cpersich@uci.edu](mailto:cpersich@uci.edu), [sbarwick@uci.edu](mailto:sbarwick@uci.edu), [christian.glaeser@uci.edu](mailto:christian.glaeser@uci.edu)

**Abstract.** The primary mission of the ARIANNA ultra-high energy neutrino telescope is to uncover astrophysical sources of neutrinos with energies greater than  $10^{16}$  eV. A pilot array, consisting of seven ARIANNA stations located on the surface of the Ross Ice Shelf in Antarctica, was commissioned in November 2014. We report on the search for astrophysical neutrinos using data collected between November 2014 and February 2019. A straight-forward template matching analysis yielded no neutrino candidates, with a signal efficiency of 79%. We find a 90% confidence upper limit on the diffuse neutrino flux of  $E^2\Phi = 1.7 \times 10^{-6} \text{ GeV cm}^{-2} \text{s}^{-1} \text{sr}^{-1}$  for a decade wide logarithmic bin centered at a neutrino energy of  $10^{18}$  eV, which is an order of magnitude improvement compared to the previous limit reported by the ARIANNA collaboration. The ARIANNA stations, including purpose built cosmic-ray stations at the Moore's Bay site and demonstrator stations at the South Pole, have operated reliably. Sustained operation at two distinct sites confirms that the flexible and adaptable architecture can be deployed in any deep ice, radio quiet environment. We show that the scientific capabilities, technical innovations, and logistical requirements of ARIANNA are sufficiently well understood to serve as the basis for large area radio-based neutrino telescope with a wide field-of-view.

---

## Contents

<b>1</b>	<b>Introduction</b>	<b>1</b>
<b>2</b>	<b>The ARIANNA Detector</b>	<b>3</b>
2.1	The 7 Station Test Bed	3
2.2	The ARIANNA Site	4
2.3	Communication and Data Transfer	5
2.4	Antennas	6
2.5	Data Acquisition	6
2.6	Amplifiers	7
2.7	Power Systems	7
2.8	Cosmic Ray Stations	8
2.9	South Pole Demonstrator Stations	8
<b>3</b>	<b>Data-set and Simulation</b>	<b>8</b>
3.1	Definition of the Data Set	8
3.2	Operational Livetime	9
3.3	Monte Carlo Simulations	10
3.4	Neutrino Signal Simulation	11
<b>4</b>	<b>Analysis</b>	<b>13</b>
4.1	Definition of Analysis Variables	13
4.2	Defining the Signal Region	14
4.3	Limits on the Diffuse UHE Neutrino Flux	15
4.4	Transient Event Sensitivity	16
4.5	Impact of Site Location on Analysis	17
<b>5</b>	<b>Conclusion</b>	<b>18</b>
<b>6</b>	<b>Acknowledgements</b>	<b>19</b>

---

## 1 Introduction

Since the discovery of extremely energetic cosmic rays more than a half century ago, the elusive quest to uncover the sources of these enigmatic particles has provided many challenges. Despite progress in experimental capabilities and theoretical insight, we do not yet know the acceleration mechanism for those particles with energies that have been measured in excess of  $10^{20}$  eV [1]. Being electrically charged, cosmic rays are deflected by galactic and intergalactic magnetic fields such that the arrival direction at the Earth no longer points back to their origin, making source identification difficult. In addition, interactions with cosmic microwave photons limit the direct observation of ultra-high energy cosmic rays sources to our local supercluster (the GZK horizon) [2, 3].

Neutrino astronomy offers a new and powerful tool to provide insight into the physics associated with the acceleration process, and complements and extends measurements not

accessible through the observation of other messengers. Charged cosmic rays which interact with gas, dust, or radiation near an accelerating object produce  $\gamma$ -rays and high-energy neutrinos; referred to here as astrophysical neutrinos. Whereas  $\gamma$ -rays can be absorbed in dense environments, these astrophysical neutrinos can escape and travel unimpeded to a detector ([4] and references therein). Neutrinos effectively propagate at the speed of light and, unlike charged cosmic rays, neutrinos are not deflected by magnetic fields; which allows for identification of sources, as well as directional and temporal coincidence with photons and gravitational waves from the source object.

The most energetic cosmic rays which do escape their source can interact with the cosmic microwave background en route to the Earth, generating cosmogenic neutrinos with a characteristic energy distribution peaking at  $10^{18}$  eV [5, 6]. Since the interaction lengths for these neutrinos through the cosmic microwave background would be larger than the observable universe, the detection of neutrinos originating well outside the GZK horizon of 100 Mpc becomes possible.

Since neutrinos interact very weakly with matter, and the expected fluxes at the relevant energies are low, large volumes of detection medium are necessary to make a significant measurement. The glaciers of Antarctica and Greenland provide a natural target, and have been leveraged in several detectors including IceCube, ANITA, and RICE [7–9]. The best limit on the ultra-high energy (UHE,  $E_\nu > 10^{16}$  eV) neutrino flux up to approximately  $10^{20}$  eV is currently set by the IceCube collaboration [7]. However, this limit is still orders of magnitude away from contesting the most conservative models of the cosmogenic flux.

The evidence for astrophysical neutrinos in the energy interval between 10 TeV and 10 PeV has grown strong over the last decade [7, 10, 11]. The arrival directions do not cluster around galactic matter but rather follow a uniform distribution indicating an extragalactic origin. Furthermore, the intriguing spatial coincidence of high energy neutrinos with the blazar TXS 0506+056 [12, 13] reported by the IceCube Collaboration prompted renewed interest in the role of point sources in multi-messenger astronomy. Theories of UHE cosmic-ray production predict a deep relationship between gamma-rays, astrophysical neutrinos, and UHE charged cosmic rays [14]. The ability of future radio-based neutrino detectors to measure luminous transient or variable events will be a key requirement for multi-messenger astronomy, and the large effective volumes made possible by radio neutrino detectors provide a low cost opportunity to discover rare or unexpected explosive sources.

While the current paucity of neutrino point sources for neutrino energies between TeV to PeV suggests a population of weak extragalactic sources, it remains an open question if this conclusion is valid at much greater neutrino energies. Perhaps rarer, more luminous, sources will be the keys to understanding the generation of the highest energy cosmic rays. There is growing recognition that "the spatial distribution and clustering of high-energy neutrinos across the sky are key observables for revealing their origins" [4]. This requirement prioritizes sky coverage and pointing resolution for every neutrino event. The ARIANNA [15–17] concept achieves large sensitivity by minimizing logistical and component costs, simplifying system complexity, and reducing data management costs. Equally important, the ARIANNA design broadens the science capabilities through accurate direction and energy reconstruction, which are discussed in detail in [18] and [19].

Though experiments such as IceCube will continue to improve the limits on diffuse flux by continuing to accrue livetime, sensitivity to transient point sources only depends on effective volume and backgrounds, which create interesting opportunities for radio-based neutrino observatories. The virtues of the ARIANNA concept have been discussed previously

[16], and a summary of the detector design can be found in Sec. 2. By taking advantage of  $\mathcal{O}(1\text{ km})$  attenuation lengths of radio signals in the relevant frequency range in glacial ice, a sparse grid of radio detectors can feasibly instrument hundreds of  $\text{km}^3$ , which is difficult for an optical (IceCube style) detector [20].

There are several pilot-stage projects which are exploring contrasting designs for the radio-based detection of ultra-high energy (UHE) neutrinos. ARA [21], for example, is an in-situ radio array located near the South Pole. The ARA design employs antennas which are placed in boreholes  $\sim 200\text{ m}$  below the snow surface. Locating the antennas below the firn allows for a slightly greater field of view than a surface detector at the same location (site location impacts field of view, as discussed in Sec. 2.2).

Other proposed designs would aspire to measure a single flavor flux of tau neutrinos. A  $\nu_\tau$  which undergoes a charged current interaction within the crust, or a mountain, produces a  $\tau$  lepton which may decay within the atmosphere. The decaying high-energy  $\tau$  would then produce a measurable radio signal through the same mechanisms as a typical cosmic-ray air shower. Projects which aim to leverage this effect include GRAND [22], TAROGE [23] and BEACON [24]. The ARIANNA site at Moore’s Bay is also suited for this detection channel, as it is adjacent to a large mountain range. A prototype tau neutrino station has been running successfully since 2017 [25].

It may be non-obvious that a neutral particle should produce a strong radio signal, but the interaction of UHE neutrinos in ice produce particle showers containing millions of charged particles. Such showers produce coherent radio emission through the Askaryan effect [26], which has been experimentally verified in ice [27]. Interactions between the shower and the dense medium produce a time-varying charge excess along the shower front and near the shower axis. This macroscopic charge excess leads to coherent radio emission concentrated within a few degrees of the Cherenkov cone angle, which is  $55.8^\circ$  in deep ice with an index-of-refraction of  $n = 1.78$ . This signal takes the form of an  $\approx 1\text{ ns}$  bipolar pulse with broad-band frequency content exceeding 1 GHz.

## 2 The ARIANNA Detector

The ARIANNA test bed of radio-based neutrino stations is primarily located in Moore’s Bay on the Ross Ice Shelf, with two additional demonstrator stations located at the South Pole. Each ARIANNA station is designed to operate autonomously, with self-contained power, data acquisition (DAq), and communication systems. A single station is capable of identifying and reconstructing a neutrino signal without the need for multi-station coincidence. This allows stations to be deployed in any configuration at multiple sites, providing a straightforward path towards large area and full sky coverage. In this section, we will discuss the hardware, design philosophy, and capabilities of the detector. For a more thorough description, see [28].

### 2.1 The 7 Station Test Bed

The main goals of the now complete ARIANNA pilot program were to:

1. Assess the durability and efficacy of the ARIANNA architecture.
2. Evaluate the radio noise environment.
3. Study the propagation of waves at radio frequencies through the polar ice medium.
4. Gain experience with deployment and other logistical issues.

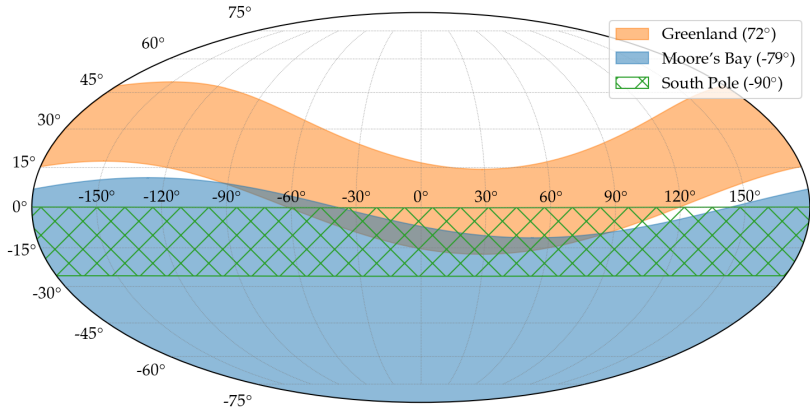


**Figure 1.** Instantaneous sky coverage for different radio detector locations in declination and right ascension. The field of view is defined to cover the solid angle which contain 90% of triggering events for an isotropic flux. The sky coverage was calculated for a 60 m deep detector at the South Pole (green hash), for a 50 m deep detector at Greenland (orange solid), and for an ARIANNA station at Moore’s Bay (solid blue), including the reflections at the ice-water interface. Over 24 h, the sky-coverage bands for Moore’s Bay (at  $-79^\circ$  latitude) and Greenland (at  $72^\circ$  latitude) rotate horizontally due to the rotation of the Earth, increasing the field-of-view. In contrast, a detector at the South Pole always sees the same part of the sky.

To address these goals, a total of seven ARIANNA stations were deployed on the surface of Moore’s Bay on the Ross Ice Shelf in Antarctica and successfully operated for more than four years. The first four of the seven stations [29] that make up the current test bed were deployed in the 2014-2015 Antarctic summer season, with the remaining three deployed the following season, replacing the previous generations of stations that was analyzed in [16].

## 2.2 The ARIANNA Site

The ARIANNA site at Moore’s Bay provides several unique advantages for the test bed. At a thickness of  $(576 \pm 8)$  m [30], the ice shelf at Moore’s Bay provides sufficient volume for the interaction of UHE neutrinos. The low flow rate at Moore’s Bay yields ice which is remarkably free of crevasses, and is expected to limit the effects of birefringence. The depth averaged attenuation length, as a function of frequency, was measured to be  $\langle L(f) \rangle = (460 \pm 20)$  m  $- (180 \pm 40)$  m/GHz  $\times f$  between the relevant frequency range of 100 MHz to 800 MHz assuming a reflection coefficient at the bottom of the ice shelf of 1, making the measurement conservative (i.e., attributing all losses to ice attenuation) [30].

In addition, the ARIANNA stations are designed to take advantage of the boundary between the ice shelf and the Ross Sea beneath. This boundary acts as a highly efficient mirror with an electric field reflection coefficient of  $\sqrt{R} = 0.82 \pm 0.07$  [30], reflecting radio signals from neutrino interactions back up towards the surface mounted receivers. Correcting the attenuation length measurement for this reflection coefficient results in a depth-averaged attenuation length of approximately 500 m at low frequencies.

Because of this unique feature, ARIANNA stations at Moore’s Bay can view half the sky at any given instant in time with approximately uniform angular sky coverage (cf. Sec. 3.3). Due to the latitude of the ARIANNA site, different parts of the sky are exposed as the Earth rotates, increasing the field-of-view for sources which are sustained more than a few hours. The reflective layer is a unique feature in contrast to other locations, such as the South Pole

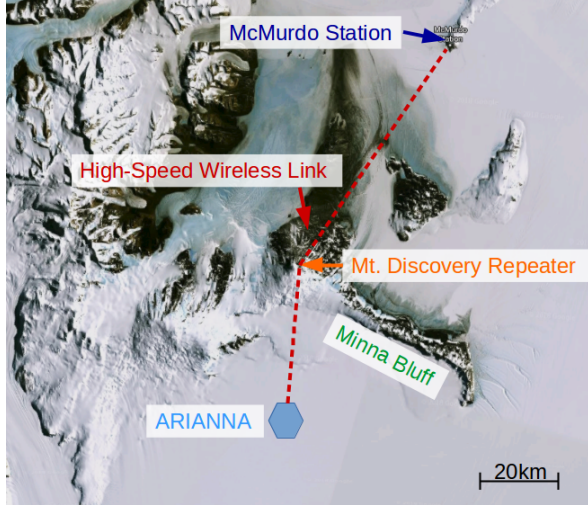


**Figure 2.** Location of the ARIANNA site in Moore’s Bay (array size is not to scale). Imagery courtesy of the U.S. Geological Survey, via Google Maps [33].

and Greenland, where the field-of-view is limited to a  $\sim 30^\circ$  band in declination (see Fig. 1) at any given moment.

A future detector at Moore’s Bay would complement IceCube in the search for point sources in the southern sky, and provide comparable or better angular resolution where events are dominated by shower topologies. Since ARIANNA’s field-of-view extends approximately  $11^\circ$  into positive declination, it overlaps a region of the sky which contains the highest energy tracks observed by IceCube. For example, the declination band of ARIANNA includes the neutrino event observed by IceCube from the blazar TXS 0506+056 [12], a region of the sky unavailable to a radio detector at the South Pole. A detector at Moore’s Bay would also scan over parts of the sky covered by optical neutrino telescopes under construction in the northern hemisphere [31, 32].

At the same time, the site is shielded from anthropogenic radio frequency (RF) noise originating from McMurdo operations by the nearby mountain ranges, especially Minna Bluff (see Fig. 2). This feature, along with its distance from McMurdo Station, makes the site remarkably radio quiet.

At a distance of 110 km, the ARIANNA site is relatively close proximity to the largest U.S. research base in Antarctica (McMurdo Station) allows for a variety of logistical support options, ranging from short-haul helicopter flights (used to transport personnel, cargo, tents, and fuel) to overland traverse (an option for a large scale future array).

### 2.3 Communication and Data Transfer

The geographical proximity to McMurdo Station enabled the installation of a bidirectional high-speed wireless link to McMurdo (Fig. 2), which maintains internet access 24/7. Each station contains a long range AFAR pulsAR 2.4 GHz wireless ethernet bridge [34] for near real-time data transfer. When ARIANNA stations connect over this ethernet link, they will transfer all data from the previous data taking window, which is typically set to a 30 minute period. This system is capable of transmission speeds of up to 200 kB/s, with each event taking approximately 2 kB.

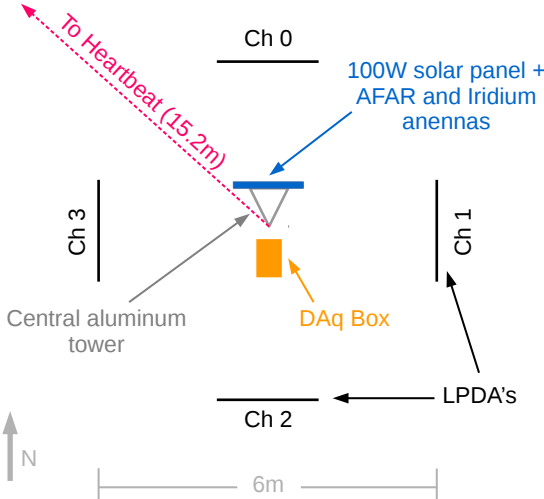


**Figure 3.** Top-down view of the ARIANNA station layout. The southern vertex of the triangular tower acts as a reference for station center. Next to the 7 neutrino stations of this configuration, ARIANNA has five additional stations in various configurations, which are illustrated in [17].

ARIANNA stations also contain an Iridium satellite modem for communication via the short burst data (SBD) protocol. This provides a redundant command and (limited) data transfer channel for the ARIANNA test bed. While the ethernet repeater on Mt. Discovery (Fig. 2) operates on solar power and is only available during the summer, the Iridium network is available year-round.

ARIANNA stations operate asynchronously, periodically communicating with the control server at University of California-Irvine to transmit data and/or receive new configuration instructions. All data is saved on an SD card on the main DAq board, so data which is not transferred immediately can be later retrieved in a bulk data transfer, or physically recovered.

## 2.4 Antennas

The main detection element of each station consists of four Create Design Corp. CLP5130-2 log-periodic dipole antennas (LPDA) [35]. These are arranged, buried face-down just below the snow level, in two pairs with perpendicular orientation, at a 3 m radius from the station center (see Fig. 3). These antennas have an effective bandwidth of 80 - 1000 MHz when buried at the top of the firn [15]. Each test bed station also contains a "heartbeat" LPDA placed 15.2 m from the station center, which can direct a calibration pulse towards the detector.

## 2.5 Data Acquisition

The ARIANNA DAq mainboard is designed around the Synchronous Sampling plus Triggering (SST) chip [29, 36, 37]. Incoming signals are sampled at 2 GSa/s and held in a 256 sample circular buffer, which is read out when a triggering condition is met. The SST has a remarkably accurate time synchronization of less than 5 ps between samples and between channels. This timing precision is invaluable for a precise event reconstruction, given the stations' modest 6 m antenna separation (see [17] and [38] for an example event reconstruction using the ARIANNA DAq).

The SST employs a multi-stage coincidence trigger in order to dramatically reduce trigger rates from thermal noise. The first stage requires a 5 ns coincidence between high and low threshold crossing on a single input channel. Both the high and low threshold are adjustable separately per channel. The second stage requires that two or more channels trigger within a 30 ns window, taking advantage of the expectation that parallel pairs of LPDA's should see largely the same signal. A level one (L1) trigger can also be applied on triggered events after readout, to filter out narrow-band anthropogenic background. The L1 trigger has a negligible effect on sensitivity, with a rejection rate of  $1.8 \times 10^{-5}$  on simulated neutrino events [39].

The ARIANNA electronics can save data to SD card at a maximum event rate of 75 Hz for the 4 channel configurations (and half that rate for the 8 channel configurations), though more typically the trigger rate ranges between  $10^{-3}$  to  $10^{-2}$  Hz corresponding to a trigger threshold of four times the RMS noise ( $4 \times V_{\text{RMS}}$ ). These rates were selected to reduce the time required to transmit data over the communication links. Since the ARIANNA station cannot search for neutrino events during data transmission, this strategy reduced the deadtime of the detector.

During most of the data taking time, the triggers are dominated by thermal noise fluctuations. Thus, the typical trigger rate is a function of trigger threshold, where the global trigger rate increases by roughly an order of magnitude when the trigger threshold is lowered by  $0.13 \times V_{\text{RMS}}$ . Hence, the detector sensitivity depends only weakly on the trigger rate. Low trigger rates come with the advantage of real-time data transfer off-continent and allows modest technical requirements for data management and archiving.

In addition to the threshold trigger, ARIANNA stations generates a collection of minimum bias events by periodically forcing an event readout (typically once every 67 seconds). For the study of background conditions as much as possible of this minimum bias data is transmitted in real-time.

## 2.6 Amplifiers

Each input channel contains a custom designed amplifier with a gain of roughly 60 db over a bandwidth of 100 - 1000 MHz. Each amplifier consists of four AC-coupled stages, each composed of a Avago MGA-68563 chip [29]. There are two amplifier revisions deployed with the ARIANNA test bed, referred to as "100 series" and "200 series". The 200 series was developed in order to reduce cost and weight, and was also adjusted for a flatter gain in the bandwidth of interest. As these two amplifier types have slightly different impulse response, they are treated separately in the analysis. All versions of the ARIANNA amplifiers begin to clip at approximately 800 mV, which limits the dynamic range of the system.

## 2.7 Power Systems

All ARIANNA stations in Moore's Bay are solar powered, with a cold weather optimized *LiFePO<sub>4</sub>* battery system. The battery system can power a station for approximately 3 days without sun, and significantly increases the stations uptime during the shoulder seasons when the sun sets each day. The current battery system, along with a custom configured charge controller, was deployed on all stations during the 2015-2016 field season, and lead to a significant improvement in reliability and livetime [39].

There has also been an effort to develop and operate wind power systems which can survive Antarctic conditions. This would potentially allow remote ARIANNA stations to operate through winter without access to a power grid, greatly increasing the livetime of the array. Prototype wind generators have been installed on one of the test bed stations, and have

shown promising results. The most recent prototype, deployed in November 2018, reached an operational livetime of 40% for a station without solar panels. We estimate that it is feasible to achieve at least 95% livetime for a radio array running solely on renewable energies by scaling the turbine and battery size. See [40] for more details.

## 2.8 Cosmic Ray Stations

In addition to the 7 station test bed, several specialized stations were deployed at the Moore’s Bay site to answer specific questions associated with the detection and identification (or tagging) of cosmic-ray-induced extended air showers [41], which generate radio pulses of similar strength, frequency content, and duration as expected for signals from neutrinos. These stations comprise four (additional) upward facing LPDA’s. The more abundant radio signals from air showers are not only an important background to tag, but also offer a unique way for an in-situ calibration and test of the detector. Using cosmic-ray data we already demonstrate a resolution in the polarization reconstruction of  $7^\circ$  [42], as well as measurement of the viewing angle, i.e., the angle between the shower axis and the line-of-sight to the emission point [42, 43]. These are crucial properties to determine the neutrino direction and energy, respectively [19].

Another station was deployed to measure cosmic rays arriving from directions close to the horizon [25, 44]. The goal of this configuration was to measure the flux at large zenith angles and evaluate the design as a first step toward a tau neutrino detector.

## 2.9 South Pole Demonstrator Stations

The autonomous design of the ARIANNA system allows for a station to be deployed essentially anywhere there is ice of sufficient quality. To demonstrate this capability, two ARIANNA detector stations were deployed near the South Pole Station.

The first South Pole demonstrator, SP-1, was deployed in December of 2017. The station is located at a distance of approximately 2.5 km from the main Amundsen-Scott Station. The SP-1 station receives DC power from the ARA [45] electrical grid, allowing it to operate throughout the year. The power is routed approximately 20 m from a junction box at the base of ARA Wind Turbine 3.

In December 2018 a second station was deployed at a more remote location, approximately 5 km from the main station. This detector, SP-2, is fully independent, operating on a solar power system like the stations at Moore’s Bay. This station was designed to test the feasibility of operating a solar/battery power system in the colder temperatures at the South Pole, and performed reliably while sunlight was available.

## 3 Data-set and Simulation

This section will define the data set to be used in this analysis (Sec. 4), as well as provide detail on the determination of the livetime used in the calculation of the limit of the diffuse neutrino flux (Sec. 4.3). We also discuss the Monte Carlo simulations that are used to calculate the detector effective volume, and construction of the simulated neutrino signal.

### 3.1 Definition of the Data Set

The analysis will concern the seven station ARIANNA test bed deployed at the Moore’s Bay site. Only those stations based on the SST data acquisition hardware will be considered here,

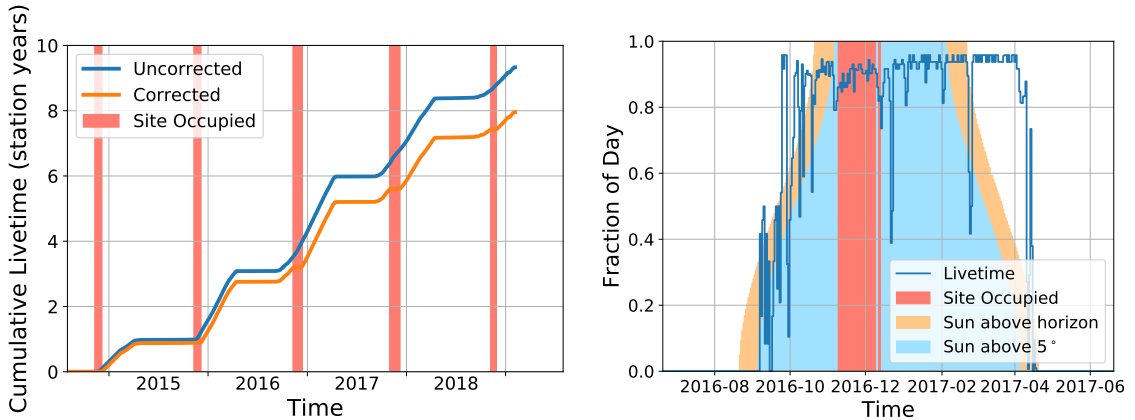


**Figure 4.** (left) Cumulative livetime for all SST based neutrino stations since deployment. The corrected curve represents the livetime used for analysis (details in Sec. 3.2). Since the stations rely on solar power, they shut down during the winter and do not accrue livetime. (right) The livetime fraction per day for a solar-powered station in Moore’s Bay. Configurations are tuned to maximize livetime after the end of the field season, after which stations typically show livetimes  $> 90\%$ . Shaded regions show the fraction of each day in which the sun is above the horizon, and greater than  $5^\circ$  above the horizon.

with the previous generation of detectors being independently analyzed in [16]. Data collected between December 8<sup>th</sup>, 2014 and February 5<sup>th</sup>, 2019 will be analyzed.

### 3.2 Operational Livetime

Current ARIANNA hardware does not take data during communication with the server in the US. This introduces downtime which is dependent on the station configuration. Since ARIANNA is a test array, station configurations are often not set to optimize for livetime. During the 2016-2017 season, however, there was a concerted effort to run the array in an efficient manner. Stations were shown to reliably operate with 90% livetime efficiency for extended periods (see Fig. 4), collecting an average of 151 days of livetime per station through the season.

The livetime calculated for analysis excludes times when the field camp at the ARIANNA site was occupied as a precaution against contaminating the data due to camp activities. In principle, only small periods of time involving pulsed radio studies or operating equipment near stations should be unsuitable for analysis, so this is a conservative measure of the usable livetime. Several hours were also removed on Dec 11-13<sup>th</sup>, 2016 during the operation of ANITA’s HiCal pulser [46], which was observed by the stations in Moore’s Bay.

The livetime is also corrected for DAq deadtime due to event readout, which only becomes significant during infrequent periods where event rates increase above 1 Hz. After these corrections, the stations collected a total of 2906.9 days (7.96 station years, with a 365 day year) of livetime for analysis in the period between December 2014 and February 2019 (see Fig. 4), which is the time frame for this analysis. This figure is based on the data which has been successfully transferred from the ARIANNA stations. We estimate that the uncollected data, which can be physically recovered from the stations’ SD cards, would increase the livetime for analysis by approximately 5%.

### 3.3 Monte Carlo Simulations

The *ShelfMC* Monte Carlo code [28] was used to calculate the sensitivity of the detector, as well as to generate parameter distributions for the neutrino signal space. *ShelfMC* is based on a fork of the *icemc* simulation originally developed by the ANITA collaboration [47]. This section provides a brief overview of the simulation method.

Neutrino interaction vertices are generated uniformly within a fiducial volume, with isotropically distributed arrival directions. Neutrino flavor is also uniformly and randomly assigned, with no special treatment given between  $\nu$  or  $\bar{\nu}$ . The frequency domain Askaryan signal near the vertex is calculated according to the parametrization in [48], which is validated against results from the ZHS Monte Carlo [49]. The signal is then propagated through the ice, via a direct and reflected path. The signal strength after accounting for antenna response is calculated for each channel of the detector, and is counted as a triggered event if it satisfies a 2-of-4 majority logic trigger above a specified threshold.

Each trigger is assigned a weight value, which is the probability that the neutrino reached the simulation volume (and was not absorbed by the Earth) to interact at the vertex location. The event weight also contains a factor of  $\rho(z)/\rho_{ice}$  where  $\rho(z)$  is the ice density at the interaction vertex, and  $\rho_{ice} = 0.9167 \text{ gcm}^{-3}$  is the density of solid ice. This factor accounts for the variation in the density of nuclear targets within the ice shelf. Weight values are further modified to account for effects of  $\nu_\tau$  regeneration, wherein  $\tau$  produced by the charged current interaction of  $\nu_\tau$  quickly decay to produce a  $\nu_\tau$  at lower energy (and longer interaction length) en route to the detector, as described in [50].

The Askaryan signal amplitude falls rapidly off the Cherenkov cone, especially at high frequencies. This limits the arrival direction for triggering neutrinos such that the signal path to the detector must lie close to the Cherenkov cone. This constrains the arrival direction to be near horizontal for direct signals, but the reflection at the ice/sea boundary allows for neutrinos from the entire sky to potentially trigger. This effect is illustrated in Fig. 5.

Electromagnetic showers resulting from  $\nu_e$  charged current interactions are elongated due to the LPM effect, which is treated in the simulation as a narrowing of the Cherenkov cone width, according to [51]. It is expected that this picture is complicated at shower energies above  $10^{18} \text{ eV}$  because the electromagnetic component breaks into multiple sub-showers (see [52] and references therein). In this work, simulated elongation of the EM shower effectively eliminates their contribution to the effective volume above  $10^{19} \text{ eV}$  (see Fig. 6). This treatment avoids the complication of event-by-event variations in the highest energy EM showers, leading to an underestimation of the effective volume for charge current  $\nu_e$  interactions at the highest energies.

The ice shelf is modeled as having an exponential density profile [30, 53], which leads to the following dependence of index of refraction with depth:

$$n(d) = n_{ice} + (n_0 - n_{ice})e^{-d/C} \quad \text{where } d > 0, n_0 = 1.3, n_{ice} = 1.78, \text{ and } C = 34.48 \text{ m.} \quad (3.1)$$

As the index of refraction changes with depth, it causes the signal ray path to bend, and creates a region in which signal can not propagate to the detector, which is referred to here as the "shadow zone." Recent measurements show that it is, in fact, possible to measure signals generated within this zone [53]. However, only a small fraction of the Askaryan signal couples into such a propagation mode such that the influence of *shadow zone signals* on the effective volume is small. An exception might be very high energy events where sufficient energy fluence is channeled into this propagation mode [54]. For this analysis, no interaction

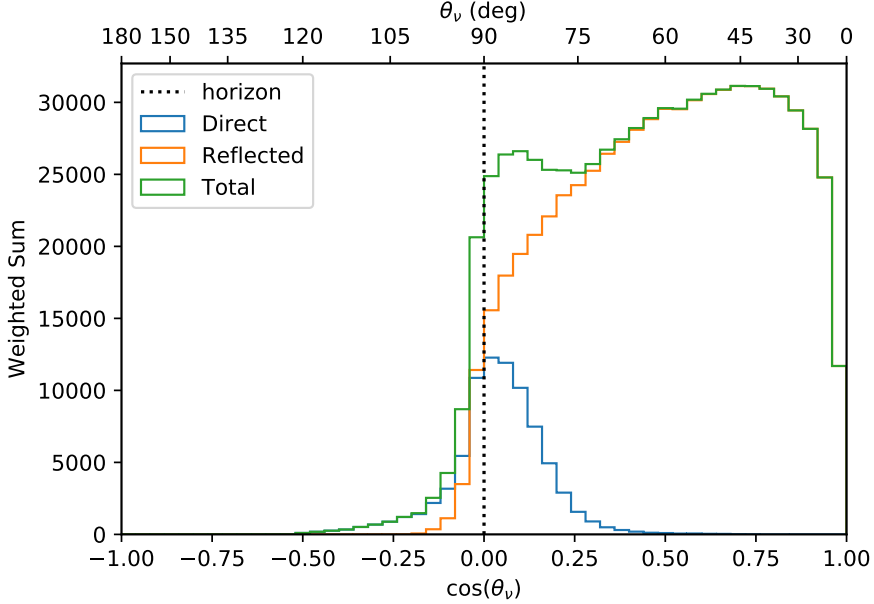


**Figure 5.** Arrival zenith angle for neutrinos which lead to a trigger in simulation.  $0^\circ$  represents a downward going neutrino. The addition of the reflected signal greatly amplifies the effective volume, while also generating more uniform sky coverage. See Table 1 for simulation parameters. Neutrino energies are distributed according to a GZK spectrum, identically to the neutrino signal space in Sec. 3.4.

vertices are generated in the shadow zone. In the shelf-mc code, the shadow zone boundary is calculated via a numerical ray tracing technique using the density profile from Eq. (3.1). For emitter positions outside the shadow zone, the signal ray path is approximated with two straight line segments where the ray is refracted once at a depth corresponding with the bottom of the firn (for more details see [28]).

For effective volume simulations, neutrinos at several energies are simulated, and the weighted number of triggers is used to calculate the water-equivalent effective volume according to

$$V_{eff} = V_{fid} \cdot \frac{\rho_{ice}}{\rho_{water}} \cdot 4\pi \cdot \frac{1}{n} \cdot \sum_{i=1}^{n_{trig}} w_i, \quad (3.2)$$

where  $V_{fid}$  is the fiducial volume,  $n$  is the total number of simulated events, and  $w_i$  are the weights of the triggered neutrinos. The normalization factor of  $4\pi$  corresponds to an integration over the solid angle of the simulation. This is a typical choice for expressing the sensitivity to a diffuse/isotropic flux, which is the primary interest of this analysis. The effective volume for a single ARIANNA test bed station is shown in Fig. 6.

### 3.4 Neutrino Signal Simulation

In order to model the sensitivity of the ARIANNA detector, it is first necessary to generate a population of simulated neutrino signals from Monte Carlo. For this purpose, one billion neutrino interactions were simulated in *ShelfMC* with a GZK energy spectrum from [55], using a detector configuration matching the currently deployed ARIANNA test bed stations

Parameter	Setting
Spectrum	GZK
Energy Range	$10^{15.5} - 10^{21.5}$ eV
Ice Thickness	575 m
C (see Eqn. 3.1)	34.48 m
Firn Depth	68.96 m
Depth Averaged Attenuation Length	500 m
Noise Temperature	350 K
Bandwidth	50 - 1000 MHz
Noise Before Trigger	Disabled
Reflection Coefficient	0.9
Trigger Threshold	$4\sigma$
Majority Logic	2 of 4
Tau Regeneration	Enabled
Shadowing	Enabled

**Table 1.** *ShelfMC* simulation parameters for the currently deployed ARIANNA stations. While there is no discrete transition between the firn and the bulk ice, we take the firn depth to correspond to 2 e-foldings of density (*depth* =  $2C$ ). A detailed description of each parameter can be found in [28].

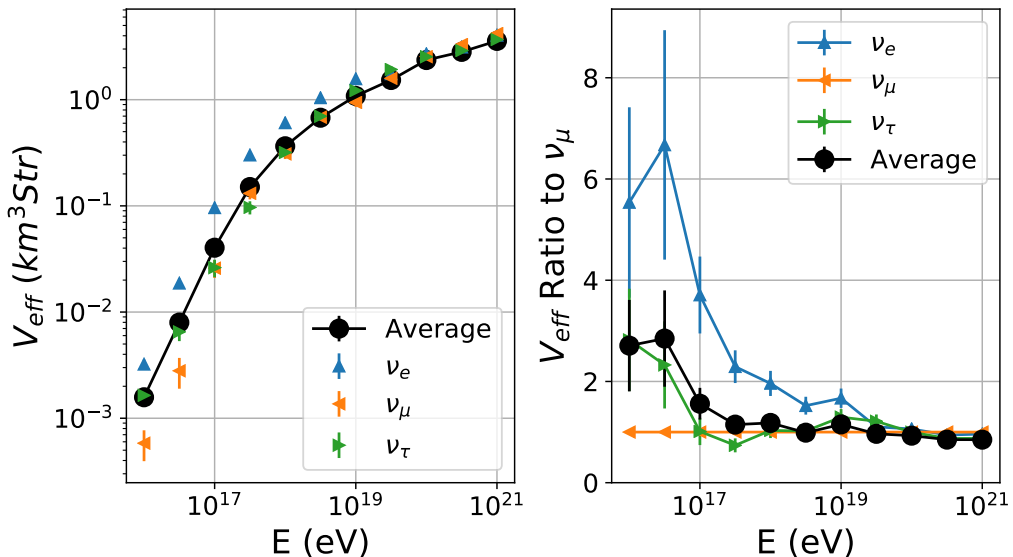


**Figure 6.** (left) Effective Volume for a single 4-channel station, simulated according to the simulation parameters in 1. (right) Ratio of single-flavor  $V_{eff}$  to the  $\nu_\mu$  effective volume.  $\nu_e$  effective volume is enhanced due to the presence of an electron (or positron) induced electromagnetic shower for charged current interactions, though this advantage diminishes at higher energy due to the LPM effect. Low energy  $\nu_\tau$  see an enhancement due to tau regeneration effects, with a GZK spectrum assumed [55].

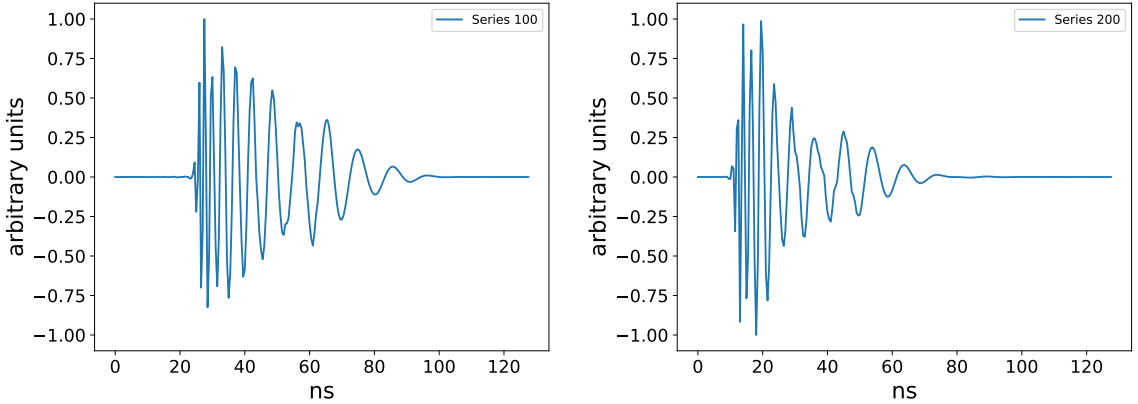


**Figure 7.** Reference neutrino templates for 100 series (left) and 200 series (right) amps. Both templates correspond to on-cone neutrino signals with E-plane and H-plane angles of  $30^\circ$  for the LPDA response. The chirped response, with the higher frequency components arriving earlier in the pulse is due to both the antenna dispersion and amplifier group delay, and is characteristic of the system response to an impulse.

in Moore’s Bay (see Table 1 for details). This produced a sample of approximately 1.3 million events which triggered the simulated station at a  $4\sigma$  level above the thermal noise  $V_{rms}$ .

To produce the time domain signal for neutrino events, a template procedure is used. Neutrino templates are generated which incorporate the direction dependent response of the LPDA’s as well as the amplifier response, according to the procedure in [56]. Templates are spaced in  $10^\circ$  increments in E-plane and H-plane angle of the antenna (see Fig. 1 of [56] for a definition of the E and H plane of the LPDA), and  $0.5^\circ$  increments in viewing angle. Two versions of the ARIANNA amplifiers are in use in the pilot array (see Sec. 2.6), which have slight differences in their impulse response. To account for these differences, separate templates are constructed for each type of amplifier (see Fig. 7 for example templates), and the stations are analyzed separately. For each triggered *ShelfMC* event, the arrival direction and polarization relative to the antenna orientation, and the viewing angle relative to the Cherenkov cone are used to choose the most appropriate template. The template is then scaled according to the appropriate amplitude, and finite bandwidth random noise is added. This data is converted to the same format as typical ARIANNA data, and run through exactly the same analysis as the triggered events.

## 4 Analysis

A search for neutrino signal was carried out using all available data as described in Sec. 3. The methods and results from this analysis are discussed in detail in this section.

### 4.1 Definition of Analysis Variables

The main technique for the separation of signal and background in this analysis is a template matching procedure, similar to that which was carried out in [16]. The signal on each channel is compared to a specific reference template, shown in Fig. 7. The signal is shifted in time relative to the template until the absolute value of the Pearson correlation coefficient is maximized. This maximum value,  $\chi$ , is a measure of similarity between the signal and

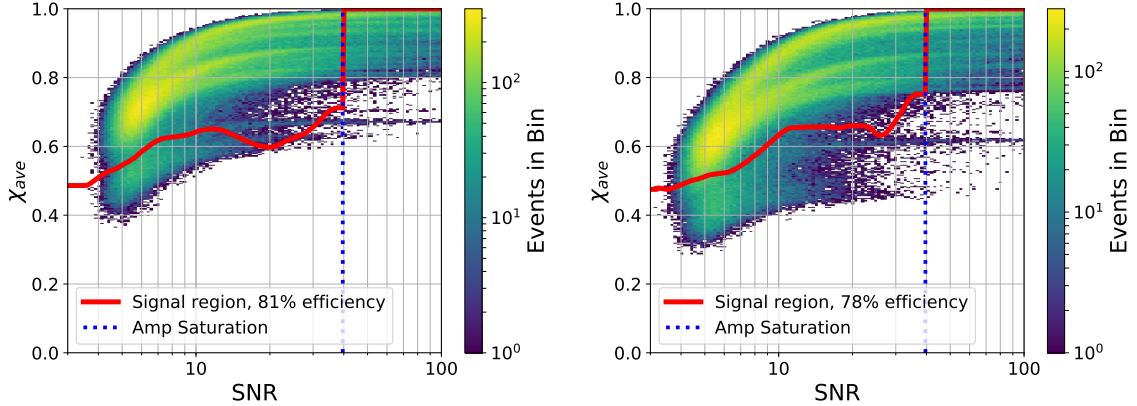


**Figure 8.** Distribution of simulated neutrino signal in  $\chi_{ave}$  vs SNR. Different neutrino templates are used for stations with Series 100 amps (left) and Series 200 amps (right). Larger values of SNR correspond to larger values in  $\chi_{ave}$ , since lower SNR leads to worse cross-correlation to the reference template. The dashed blue line represents a 800 mV cutoff where the amplifiers would be strongly non-linear. The red line represents the lower bound of the signal region, which is discussed in Sec. 4.2.

reference template, with values ranging from 0 (no correlation) to 1 (identically similar). After calculating  $\chi$  for each channel, we combine the results into a single parameter per event,  $\chi_{ave}$ , which is the greater of the two averages between co-polarized pairs of LPDA's. High values of  $\chi_{ave}$  essentially imposes a condition that pairs of antennas see similar signals, which is expected, as the neutrino signal does not significantly change over the 6 m separation of the antennas.

By also considering the signal amplitude, it is possible to leverage the general behavior that a high signal-to-noise ratio (SNR) neutrino signal event is likely to have a larger value of  $\chi_{ave}$ . This greater discriminating power for large amplitude events raises the analysis efficiency. In this text the SNR of an event will be defined as  $V_{PTP}/2\sigma$ , where  $V_{PTP}$  is the peak-to-peak amplitude and  $\sigma$  is the root-mean-squared voltage of minimum bias noise events.

We create a 2D parameter space using  $\chi_{ave}$  and SNR in which we will define a signal region for this analysis. Analysis in a space of template correlation vs amplitude has previously been successfully used to identify cosmic-ray air showers in ARIANNA stations [41]. The distribution of the simulated neutrino signal in this space is shown in Fig. 8.

## 4.2 Defining the Signal Region

We present the ARIANNA test bed data (cf. Sec. 3) in the  $\chi_{ave}$  and SNR space in Fig. 9. The data itself is used to define a signal region that maximizes the analysis power, i.e., achieves a high neutrino signal efficiency while rejecting background events efficiently.

We can safely assume that the vast majority of all triggered events are background, and therefore use the data to estimate the background distribution in our 2D parameters space  $\chi_{ave}$  and SNR. We bin the data in SNR bins of  $\log_{10} \text{SNR} = 0.2$ . For each bin we calculate the cumulative histogram in  $\chi_{ave}$ , i.e., calculate how many events are present with  $\chi_{ave}$  greater than or equal to a certain value. For illustration purposes we show one of these distributions in Fig. 10. The tail of the cumulative distribution, except for the single highest value, is fit to a power law, and extrapolated to calculate the expected number of background events at higher  $\chi_{ave}$  thresholds, extending a technique employed in [16].

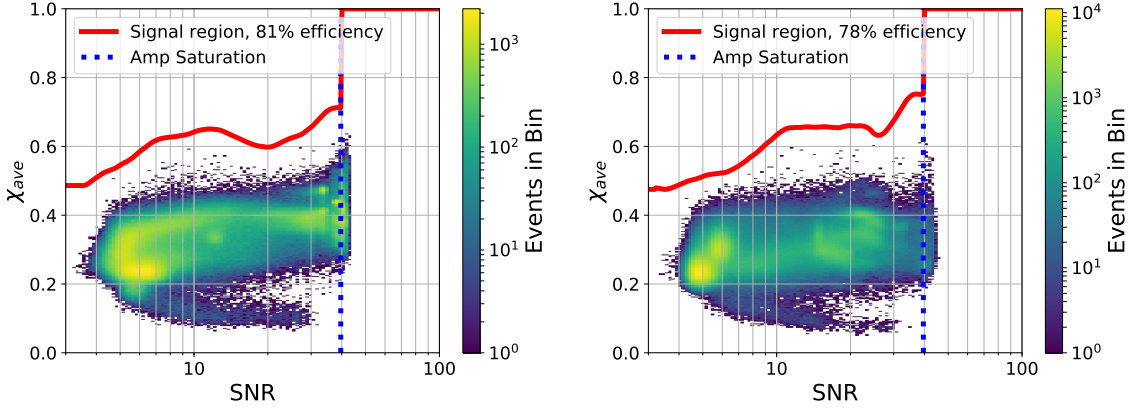


**Figure 9.** Distribution of triggered events in  $\chi_{ave}$  vs SNR for series 100 amplifiers (left), and series 200 amplifiers (right). Larger values of SNR correspond to larger values in  $\chi_{ave}$  up to  $SNR \approx 10$ , since lower SNR leads to worse cross-correlation to the reference template. The blue horizontal line represents a 800 mV where a noticeable pile-up effect is observed due to amp clipping. The red line represents the lower bound of the signal region, which is discussed in Sec. 4.2. No triggered events remain in the signal region.

We calculate the  $\chi_{ave}$  thresholds for each SNR bin that result in an expectation of a total of 0.5 background events that pass the signal cut over the total livetime. We treated both amplifier types separately with the expected number of background events for each set weighted by the fraction of the total livetime contribution by that station type. We weighted each SNR bin by the fraction of expected neutrino events in the bin (from Fig. 8). The resulting curve is then smoothed by a second order Savitzky-Golay filter [57] and shown as red curve in Fig. 8 and 9. This procedure effectively produces a curve of constant signal to background ratio.

The signal region defined through this procedure contains no triggered events on any ARIANNA station during the complete run, so we conclude that no neutrinos were observed (Fig. 9). The analysis efficiency of the signal region, which is the fraction of weighted simulated neutrinos which fall above the cutoff is 81% for the 100 series stations and 78% for the 200 series.

### 4.3 Limits on the Diffuse UHE Neutrino Flux

In the absence of observed events in the signal region, a model independent 90% confidence upper limit on the diffuse neutrino flux is given by,

$$E^2 \Phi(E) \leq \frac{FC_{90} E L(E)}{\ln 10 d \log E V_{eff} \sum_i (\epsilon_i t_i)} \quad (4.1)$$

where  $E$  is the energy of the neutrino,  $d \log E = 1$  is the bin width (set to 1 decade),  $V_{eff}$  is the effective volume of a single ARIANNA station averaged over all flavors,  $L$  is the water equivalent neutrino interaction length calculated using the cross section in [61], and  $t_i$  and  $\epsilon_i$  are, respectively, the total livetime and the analysis efficiency for each ARIANNA station  $i$ .  $\epsilon_i$  for each station is given by the analysis efficiency for stations with that amplifier type, as calculated in Sec. 4.2.  $t_i$  for each station is the useful livetime collected, according to the conditions outlined in Sec. 3.2.  $FC_{90} = 2.44$  is the Feldman Cousins 90% confidence

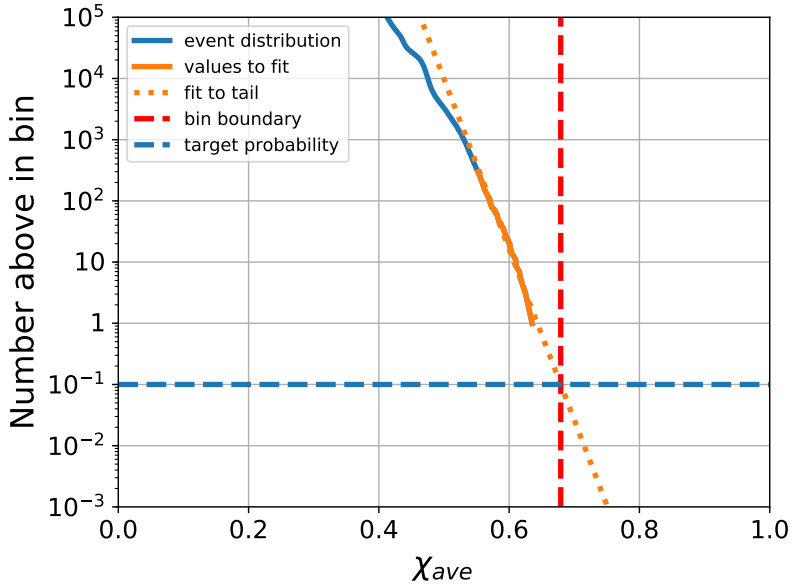


**Figure 10.** An illustration of the procedure for calculating the signal region boundary for a particular sliding amplitude bin. A power law is fit to the 300 highest  $\chi_{ave}$  events in the bin (the single highest value event is excluded from the fit in order to limit the effect of outliers), and extrapolated to intersect the desired background event probability, yielding the signal region lower bound value of  $\chi_{ave}$ .

upper limit for 0 measured events and an expected background of 0 events in each decade-wide energy bin [62]. Though the expected background is estimated to be 0.5 events over the entire energy interval, or approximately 0.08 events per decade energy bin, we chose to set the expected number of background events per energy bin to 0. This procedure produces a slightly larger upper limit than a more accurate calculation that computes the expected background in each energy bin.

The results of this calculation for the seven stations of the ARIANNA test bed are shown in Fig. 11. For a decade wide logarithmic bin centered at a neutrino energy of  $10^{18}$  eV, the 90% confidence upper limit is  $E^2\Phi = 1.7 \times 10^{-6} \text{ GeVcm}^{-2}\text{s}^{-1}\text{sr}^{-1}$ . While the diffuse flux limit from the test bed is not competitive with the current state of the art, it represents an order of magnitude improvement over the previous published limit from the ARIANNA collaboration [16] and demonstrates the long-term reliability of the ARIANNA hardware in-situ.

Also shown in Fig. 11 is a projected limit from an optimized array based on ARIANNA technologies (the ARIA proposal [17]). This optimized design achieves greater effective volume per station by lowering thresholds to  $3\sigma$  (by a more advanced L1 trigger on the FPGA) and taking advantage of the colder ice at the South Pole. Assuming that such an array could operate at 100% uptime on a wired power grid or through a combination of solar and wind power, a 5 year run would be sensitive enough to limit the proton fraction of the highest energies to 10% or less [17].

#### 4.4 Transient Event Sensitivity

As equation 4.1 shows, the flux sensitivity for diffuse sources depends on effective volume and time, which benefits from the steady accumulation of livetime over years of operation.

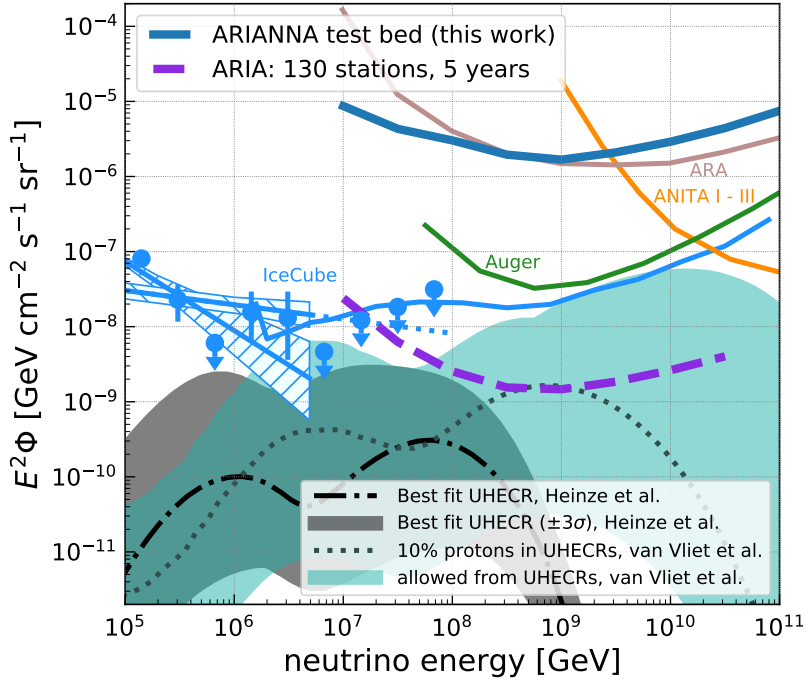


**Figure 11.** Model independent diffuse flux limit for the ARIANNA test bed for a sliding decade wide energy bin. IceCube measured fluxes of astrophysical neutrino spectra were taken from [10, 11] and the limit from [7]. Also shown are published limits from the Pierre Auger [58] and ANITA collaborations [8]. The published ARA limit from [21] is shown in comparison. To illustrate the neutrino parameter space, diffuse flux models from [59] and [60] are shown. For details of the calculation see Sec. 4.3. The sensitivity for ARIA [17] represents a proposal for an optimized future surface detector based on the ARIANNA technology.

However, the sensitivity to a specific transient point source depends solely on effective volume and whether the object is in the field-of-view.

The transient source sensitivity of the seven station ARIANNA test bed is fairly uniform over the entire upward sky (Figs. 5 and 1). It is comparable to the shown limit from the Auger collaboration in the direction of the neutron star merger GW170817 (Fig. 12). Already now, benefiting from the large sky coverage and realtime data transfer, ARIANNA provides useful information on transient events (see e.g. [65]). A future detector based on ARIANNA technologies [17] can deliver unparalleled sensitivity to transient sources within its field of view.

#### 4.5 Impact of Site Location on Analysis

The deployment of the ARIANNA demonstrator station SP-1 approximately 2.5 km from the Amundsen-Scott Station at the South Pole (see Sec. 2.9 for more detail) creates the opportunity to assess the effect of the different RF backgrounds on analysis efficiency. For this purpose, data from runs where SP-1 (South Pole) and the cosmic-ray station at Site X (Moore’s Bay) were triggering on their downward facing antennas (i.e., searching for upward propagating radio signals from neutrinos) was selected. The data of both stations were analyzed by the same methods discussed above. These two stations were chosen for direct

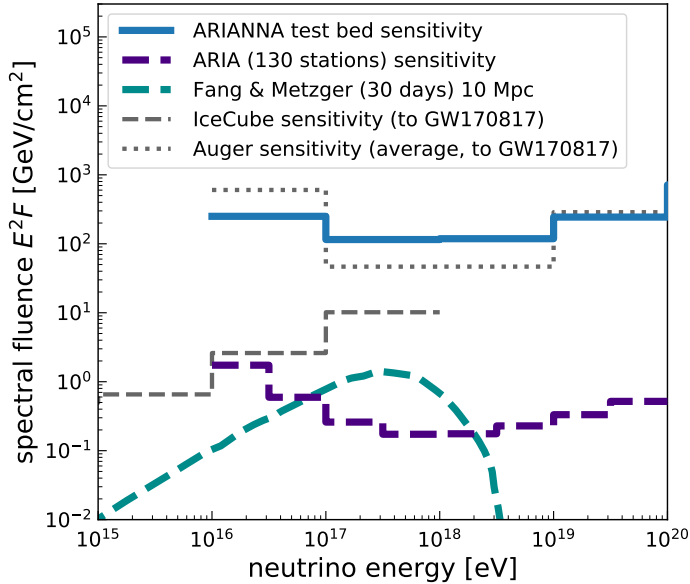


**Figure 12.** Sensitivity of the ARIANNA test bed to transient events. Sensitivities of other experiments in the direction of the neutron star merger GW170817 (black lines) are taken from [63]. A theoretical flux of ultra-high energy neutrinos from a neutron star merger [64] is also shown (dashed cyan line). The ARIA sensitivity [17] (dashed purple line) represents the capability of a future detector based on the ARIANNA technology to detect transient sources in its field of view.

comparison because they are both constructed using an updated 8 channel version of the ARIANNA DAq board.

We present all triggered events in the 2D signal space ( $\chi_{ave}$  vs. SNR) in Fig. 13. The signal region is calculated using the same procedure as described in Sec. 4.2, which we show as red curve in Fig. 13. We apply this signal cut to a dedicated simulation data set of SP-1 and find that SP-1 achieves a signal efficiency of 73% despite its close proximity to the Amundsen-Scott Station. A decommissioned ARA wind turbine also contributes to the background radio noise during wind gusts. These events were identified due to their consistent waveform properties and their arrival direction.

The same type of station at Site X in Moore’s Bay was operated for less than 40 days in neutrino trigger mode, so there are a limited number of triggered events to examine and compare. However, the distribution lacks any significant number of events with a value of  $\chi_{ave} > 0.4$  and  $SNR < 10$ , so the expected analysis efficiency for a neutrino search would be significantly higher.

## 5 Conclusion

The operation of the ARIANNA test bed at Moore’s Bay, since its completion in November 2014, has provided a robust proof of concept for an in-situ, radio-based UHE neutrino detector. Iterative improvements in data acquisition and power systems since the first ARIANNA prototypes [15] and initial test bed stations [29] have improved reliability and livetime. We have presented the analysis of 4.5 years of data, leading to a 90% confidence upper limit on the diffuse neutrino flux of  $E^2\Phi = 1.7 \times 10^{-6} \text{ GeVcm}^{-2}\text{s}^{-1}\text{sr}^{-1}$  for a decade wide logarithmic bin centered at a neutrino energy of  $10^{18}$  eV.

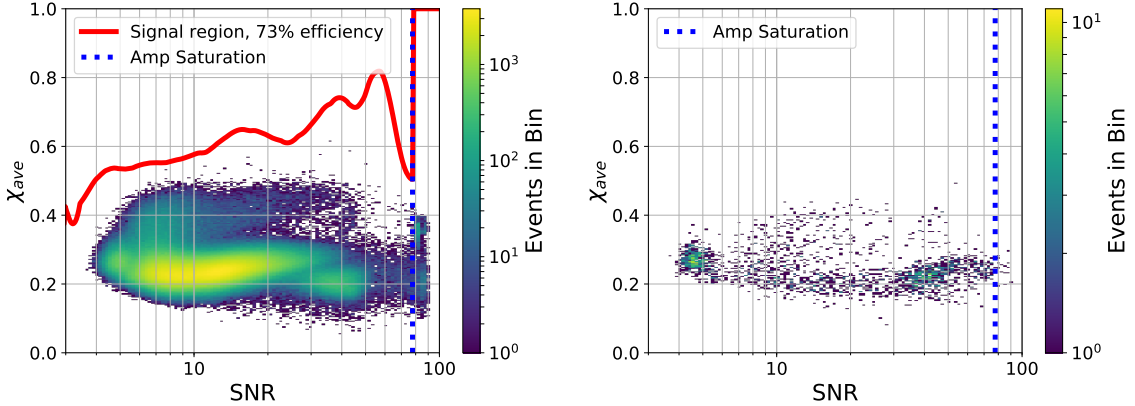


**Figure 13.** Distribution of triggered events for two 8 channel ARIANNA stations. SP-1 (left) is located near the South Pole, while the station at Site X (right) is located at the Moore’s bay site. The signal region is drawn using the same procedure as shown in Sec. 4.2. The relative lack of low SNR, high  $\chi_{ave}$  events at Site X is evidence that the radio-quiet environment in Moore’s Bay is advantageous in this analysis.

Since each ARIANNA station serves as an autonomous and self-contained detector, this platform can be deployed at sites in both the northern and southern hemisphere to attain full sky coverage. Near-surface detectors allow for the easy installation of high-gain antennas in any polarization, providing increased information for precise event reconstruction.

We have demonstrated that a simple template matching procedure is capable of rejecting all observed backgrounds over the operation of the test bed, while maintaining a combined signal efficiency of 79% at a  $4\sigma$  trigger threshold in amplitude. Future detectors will make use of more advanced triggering and analysis techniques to push the sensitivity threshold lower, and increase the effective volume per station.

The near-surface design of ARIANNA station provides the essential tools to contribute to the multi-messenger revolution in high energy astrophysics: reliable operation, pointing, wide-field of view, energy and real-time identification of neutrino candidates. ARIANNA can fully participate in campaigns involving multi-wavelength (radio to gamma-ray), gravitational wave, and cosmic ray observations, with the goal of establishing both the sources of the most energetic particles known, and the mechanisms that are responsible for producing particles of extreme energy.

## 6 Acknowledgements

We are grateful to the U.S. National Science Foundation-Office of Polar Programs, the U.S. National Science Foundation-Physics Division (grant NSF-1607719) for granting the ARIANNA array at Moore’s Bay. Without the invaluable support of the people at McMurdo, the ARIANNA stations would have never been built.

We acknowledge funding from the German research foundation (DFG) under grants GL 914/1-1 (CG), NE 2031/1-1, and NE 2031/2-1 (DGF, ANe, IP, CW) and the Taiwan Ministry of Science and Technology (JN, SHW). HB acknowledges support from the Swedish Government strategic program Stand Up for Energy. EU acknowledges support from the Uppsala university Vice-Chancellor’s travel grant (sponsored by the Knut and Alice Wallenberg Foundation) and the C.F. Liljewalch travel scholarships. DB and ANo acknowledge support from

the MEPhI Academic Excellence Project (Contract No. 02.a03.21.0005) and the Megagrant 2013 program of Russia, via agreement 14.12.31.0006 from 24.06.2013.

## References

- [1] Francesco Fenu for the Pierre Auger collaboration, *The cosmic ray energy spectrum measured using the Pierre Auger Observatory*, in *Proceedings of 35th International Cosmic Ray Conference — PoS(ICRC2017)486*, 2017, [DOI](#).
- [2] K. Greisen, *End to the cosmic-ray spectrum?*, *Physical Review Letters* **16** (1966) 748.
- [3] G. Zatsepin and V. Kuz'min, *Upper limit of the spectrum of cosmic rays*, *JETP Letters* **4** (1966) 78.
- [4] M. Ackermann et al., *Astrophysics Uniquely Enabled by Observations of High-Energy Cosmic Neutrinos*, *Bull. Am. Astron. Soc.* **51** (2019) 185.
- [5] F. W. Stecker, *Ultrahigh Energy Photons, Electrons, and Neutrinos, the Microwave Background, and the Universal Cosmic-Ray Hypothesis*, *Astrophysics and Space Science* **20** (1973) 47.
- [6] V. Beresinsky and G. Zatsepin, *Cosmic rays at ultra high energies (neutrino?)*, *Physics Letters B* **28** (1969) 423.
- [7] ICECUBE collaboration, *Differential limit on the extremely-high-energy cosmic neutrino flux in the presence of astrophysical background from nine years of IceCube data*, *Physical Review D* **98** (2018) 062003.
- [8] ANITA collaboration, *Constraints on the diffuse high-energy neutrino flux from the third flight of ANITA*, *Physical Review D* **98** (2018) 022001.
- [9] RICE collaboration, *Updated results from the RICE experiment and future prospects for ultra-high energy neutrino detection at the south pole*, *Physical Review D* **85** (2012) .
- [10] C. Koppen for the IceCube collaboration, *Observation of astrophysical neutrinos in six years of IceCube data*, in *Proceedings of 35th International Cosmic Ray Conference — PoS(ICRC2017)981*, 2017, [DOI](#).
- [11] C. Haack and C. Wiebusch for the IceCube collaboration, *A measurement of the diffuse astrophysical muon neutrino flux using eight years of IceCube data.*, in *Proceedings of 35th International Cosmic Ray Conference — PoS(ICRC2017)1005*, 2017, [DOI](#).
- [12] ICECUBE collaboration, *Multimessenger observations of a flaring blazar coincident with high-energy neutrino IceCube-170922a*, *Science* (2018) eaat1378.
- [13] ICECUBE collaboration, *Neutrino emission from the direction of the blazar TXS 0506+056 prior to the IceCube-170922a alert*, *Science* (2018) eaat2890.
- [14] M. Ahlers and F. Halzen, *Opening a new window onto the universe with IceCube*, *Progress in Particle and Nuclear Physics* **102** (2018) 73.
- [15] L. Gerhardt et al., *A prototype station for ARIANNA: A detector for cosmic neutrinos*, *Nuclear Instruments and Methods in Physics Research Section A* **624** (2010) 85 .
- [16] ARIANNA collaboration, *A first search for cosmogenic neutrinos with the ARIANNA Hexagonal Radio Array*, *Astroparticle Physics* **70** (2015) 12.
- [17] ARIANNA collaboration, *Targeting ultra-high energy neutrinos with the ARIANNA experiment*, *Adv. Space Res.* **64** (2019) 2595 [[1903.01609](#)].
- [18] ARIANNA collaboration, *Neutrino vertex reconstruction with in-ice radio detectors using surface reflections and implications for the neutrino energy resolution*, *Journal of Cosmology and Astroparticle Physics* **11** (2019) 030 [[1909.02677](#)].

- [19] C. Glaser for the ARIANNA collaboration, *Neutrino direction and energy resolution of Askaryan detectors*, in *Proceedings of 36th International Cosmic Ray Conference — PoS(ICRC2019)899*, 2019.
- [20] ICECUBE collaboration, *Constraints on Ultrahigh-Energy Cosmic-Ray Sources from a Search for Neutrinos above 10 PeV with IceCube*, *Physical Review Letters* **117** (2016) 241101.
- [21] ARA collaboration, *Performance of two Askaryan Radio Array stations and first results in the search for ultrahigh energy neutrinos*, *Physical Review D* **93** (2016) 082003.
- [22] GRAND collaboration, *The giant radio array for neutrino detection (GRAND): Science and design*, [1810.09994](https://arxiv.org/abs/1810.09994).
- [23] J. Nam for the ARIANNA and TAROGE collaborations, *High-elevation synoptic radio array for detection of upward moving air-showers, deployed in the antarctic mountains*, in *Proceedings of 36th International Cosmic Ray Conference — PoS(ICRC2019)967*, 2019.
- [24] S. Wissel et al., *Concept Study for the Beamforming Elevated Array for Cosmic Neutrinos (BEACON)*, in *Proceedings of the 36th International Cosmic Ray Conference (ICRC2019)*, 2019.
- [25] S.-H. Wang for the ARIANNA and TAROGE collaborations, *Status, Calibration, and Cosmic Ray Detection of ARIANNA-HCR Station*, in *Proceedings of 36th International Cosmic Ray Conference — PoS(ICRC2019)462*, 2019.
- [26] G. A. Askar'yan, *Coherent Radio Emission from Cosmic Showers in Air and in Dense Media*, *Soviet Journal of Experimental and Theoretical Physics* **21** (1965) 658.
- [27] ANITA collaboration, *Observations of the Askaryan Effect in Ice*, *Physical Review Letters* **99** (2007) 171101.
- [28] C. Persichilli, *Performance and Simulation of the ARIANNA Pilot Array, with Implications for Future Ultra-high Energy Neutrino Astronomy*, Ph.D. thesis, University of California, Irvine, 2018.
- [29] ARIANNA collaboration, *Design and Performance of the ARIANNA HRA-3 Neutrino Detector Systems*, *IEEE Transactions on Nuclear Science* **62** (2015) 2202.
- [30] J. C. Hanson et al., *Radar absorption, basal reflection, thickness and polarization measurements from the Ross Ice Shelf, Antarctica*, *Journal of Glaciology* **61** (2015) 438.
- [31] U. Katz, *KM3NeT: Towards a km<sup>3</sup> Mediterranean neutrino telescope*, *Nuclear Instruments and Methods in Physics Research Section A* **567** (2006) 457 .
- [32] A. Avrorin et al., *The prototyping/early construction phase of the BAIKAL-GVD project*, *Nuclear Instruments and Methods in Physics Research Section A* **742** (2014) 82 .
- [33] “Google Maps.” [Online <https://www.google.com/maps/@-78.3853509,163.1242104,196008m/data=!3m1!1e3>; accessed 27-August-2018], 2018.
- [34] “Afar communications inc..” [Online <http://afar.net/>; accessed 25-July-2019].
- [35] “Create design corp..” [Online <http://www.cd-corp.com/english/>; accessed 25-July-2019].
- [36] T. Prakash, *A Fully-Synchronous Multi-GHz Analog Waveform Recording And Triggering Circuit*, Ph.D. thesis, University of California, Irvine, 2017.
- [37] E. Chiem, *Multi-Gigahertz Synchronous Sampling and Triggering (SST) Circuit with Picosecond Timing Resolution*, Ph.D. thesis, University of California, Irvine, 2017.
- [38] G. Gaswint for the ARIANNA collaboration, *New results on angular reconstruction of deep pulser radio signals*, in *Proceedings of the 36th International Cosmic Ray Conference (ICRC2019)*, 2019.

- [39] C. Persichilli for the ARIANNA collaboration, *Radio search for EHE neutrinos with the ARIANNA pilot array, and ARIANNA performance projections*, in *Proceedings of The 35th International Cosmic Ray Conference — PoS(ICRC2017)977*, 2017.
- [40] A. Nelles for the ARIANNA collaboration, *A wind-turbine for autonomous stations for radio detection of neutrinos*, in *Proceedings of 36th International Cosmic Ray Conference — PoS(ICRC2019)968*, 2019.
- [41] ARIANNA collaboration, *Radio detection of air showers with the ARIANNA experiment on the Ross Ice Shelf*, *Astroparticle Physics* **90** (2017) 50.
- [42] A. Nelles for the ARIANNA collaboration, *Cosmic-ray detection with and novel reconstruction algorithms for the ARIANNA experiment*, in *Proceedings of 36th International Cosmic Ray Conference — PoS(ICRC2019)366*, 2019.
- [43] C. Welling, C. Glaser and A. Nelles, *Reconstructing the cosmic-ray energy from the radio signal measured in one single station*, *JCAP* **1910** (2019) 075 [[1905.11185](#)].
- [44] S. H. Wang for the ARIANNA collaboration, *Calibration, Performance, and Cosmic Ray Detection of ARIANNA-HCR Prototype Station*, in *Proceedings of The 35th International Cosmic Ray Conference — PoS(ICRC2017)358*, 2017.
- [45] ARA collaboration, *Design and initial performance of the Askaryan Radio Array prototype EeV neutrino detector at the South Pole*, *Astroparticle Physics* **35** (2012) 457.
- [46] ANITA collaboration, *HiCal 2: An instrument designed for calibration of the ANITA experiment and for antarctic surface reflectivity measurements*, *Nuclear Instruments and Methods in Physics Research Section A* **918** (2019) 60 .
- [47] ANITA collaboration, *The Simulation of the Sensitivity of the Antarctic Impulsive Transient Antenna (ANITA) to Askaryan Radiation from Cosmogenic Neutrinos Interacting in the Antarctic Ice*, *JINST* **14** (2019) P08011 [[1903.11043](#)].
- [48] J. Alvarez-Muñiz, R. A. Vázquez and E. Zas, *Calculation methods for radio pulses from high energy showers*, *Physical Review D* **62** (2000) .
- [49] E. Zas, F. Halzen and T. Stanev, *Electromagnetic pulses from high-energy showers: Implications for neutrino detection*, *Physical Review D* **45** (1992) 362.
- [50] F. Halzen and D. Saltzberg, *Tau neutrino appearance with a 1000 megaparsec baseline*, *Physical Review Letters* **81** (1998) 4305.
- [51] J. Alvarez-Muñiz and E. Zas, *The LPM effect for EeV hadronic showers in ice: implications for radio detection of neutrinos*, *Physics Letters B* **434** (1998) 396.
- [52] L. Gerhardt and S. R. Klein, *Electron and photon interactions in the regime of strong Landau-Pomeranchuk-Migdal suppression*, *Physical Review D* **82** (2010) 074017.
- [53] S. Barwick et al., *Observation of classically “forbidden” electromagnetic wave propagation and implications for neutrino detection.*, *Journal of Cosmology and Astroparticle Physics* **2018** (2018) 055.
- [54] R. Lahmann for the ARIANNA collaboration, *Investigations of ice and emitter properties from radio signals recorded with arianna*, in *Proceedings of the 36th International Cosmic Ray Conference (ICRC2019)*, 2019.
- [55] R. Engel, D. Seckel and T. Stanev, *Neutrinos from propagation of ultrahigh energy protons*, *Physical Review D* **64** (2001) .
- [56] ARIANNA collaboration, *Time-domain response of the ARIANNA detector*, *Astroparticle Physics* **62** (2015) 139.
- [57] A. Savitzky and M. J. E. Golay, *Smoothing and differentiation of data by simplified least squares procedures.*, *Analytical Chemistry* **36** (1964) 1627.

- [58] PIERRE AUGER collaboration, *Improved limit to the diffuse flux of ultrahigh energy neutrinos from the Pierre Auger Observatory*, *Physical Review D* **91** (2015) 092008.
- [59] A. van Vliet, R. Alves Batista and J. R. Hörandel, *Determining the fraction of cosmic-ray protons at ultrahigh energies with cosmogenic neutrinos*, *Phys. Rev. D* **100** (2019) 021302.
- [60] J. Heinze, A. Fedynitch, D. Boncioli and W. Winter, *A New View on Auger Data and Cosmogenic Neutrinos in Light of Different Nuclear Disintegration and Air-shower Models*, *The Astrophysical Journal* **873** (2019) 88.
- [61] A. Connolly et al., *Calculation of high energy neutrino-nucleon cross sections and uncertainties using the Martin-Stirling-Thorne-Watt parton distribution functions and implications for future experiments*, *Physical Review D* **83** (2011) 113009.
- [62] G. J. Feldman and R. D. Cousins, *Unified approach to the classical statistical analysis of small signals*, *Physical Review D* **57** (1998) 3873.
- [63] A. Albert et al., *Search for High-energy Neutrinos from Binary Neutron Star Merger GW170817 with ANTARES, IceCube, and the Pierre Auger Observatory*, *The Astrophysical Journal* **850** (2017) L35.
- [64] K. Fang and B. D. Metzger, *High-energy Neutrinos from Millisecond Magnetars Formed from the Merger of Binary Neutron Stars*, *The Astrophysical Journal* **849** (2017) 153.
- [65] C. Glaser, S. Barwick, G. Gaswint and C. Persichilli, *GRB 190114C: Search for ultra-high-energy neutrinos with ARIANNA*, *The Astronomer's Telegram* **12475** (2019) 1.

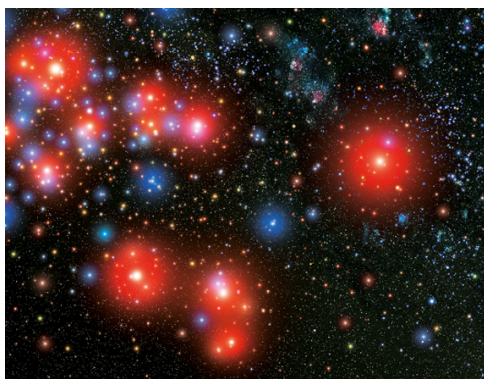
## Observation of classically 'forbidden' electromagnetic wave propagation and implications for neutrino detection.

To cite this article: S.W. Barwick *et al* JCAP07(2018)055

### Related content

- [The IceCube Neutrino Observatory: instrumentation and online systems](#)  
M.G. Aartsen, M. Ackermann, J. Adams et al.
- [Feasibility of determining diffuse ultra-high energy cosmic neutrino flavor ratio through ARA neutrino observatory](#)  
Shi-Hao Wang, Pisin Chen, Jiwoo Nam et al.
- [Status of RadioWave Neutrino Detection](#)  
Dave Besson

View the [article online](#) for updates and enhancements.



**IOP Astronomy ebooks**

Part of your publishing universe and your first choice for astronomy, astrophysics, solar physics and planetary science ebooks.

[iopscience.org/books/aas](http://iopscience.org/books/aas)

# Observation of classically ‘forbidden’ electromagnetic wave propagation and implications for neutrino detection.

**S.W. Barwick,<sup>a</sup> E.C. Berg,<sup>a</sup> D.Z. Besson,<sup>b,c</sup> G. Gaswint,<sup>a</sup> C. Glaser,<sup>a</sup> A. Hallgren,<sup>d</sup> J.C. Hanson,<sup>e</sup> S.R. Klein,<sup>f</sup> S. Kleinfelder,<sup>g</sup> L. Köpke,<sup>h</sup> I. Kravchenko,<sup>i</sup> R. Lahmann,<sup>j</sup> U. Latif,<sup>b</sup> J. Nam,<sup>k</sup> A. Nelles,<sup>l,m</sup> C. Persichilli,<sup>a</sup> P. Sandstrom,<sup>n</sup> J. Tatar<sup>a,o</sup> and E. Unger<sup>d</sup>**

<sup>a</sup>Dept. of Physics & Astronomy, University of California,  
4129 Frederick Reines Hall, Irvine, CA 92697, U.S.A.

<sup>b</sup>Dept. of Physics and Astronomy, Univ. of Kansas,  
1082 Malott Hall, Lawrence, KS 66045, U.S.A.

<sup>c</sup>National Research Nuclear University, Moscow Engineering Physics Institute,  
31 Kashirskoye Highway, Moscow 115409, Russia

<sup>d</sup>Uppsala University Department of Physics and Astronomy,  
Regementsvägen 1, SE-752 37 Uppsala, Sweden

<sup>e</sup>Whittier College Department of Physics,  
13406 E. Philadelphia St., Whittier, CA 90602, U.S.A.

<sup>f</sup>Lawrence Berkeley National Laboratory,  
1 Cyclotron Rd., Berkeley, CA 94720, U.S.A.

<sup>g</sup>Dept. of Electrical Engineering and Computer Science, University of California,  
5200 Engineering Hall, Irvine, CA 92697, U.S.A.

<sup>h</sup>Institute of Physics, University of Mainz,  
Staudinger Weg 7, D-55099 Mainz, Germany

<sup>i</sup>Dept. of Physics and Astronomy, Univ. of Nebraska-Lincoln,  
Theodore Jorgensen Hall 208, Lincoln, NE 68588, U.S.A.

<sup>j</sup>ECAP, Friedrich-Alexander Universität Erlangen-Nürnberg,  
Erwin-Rommel-Str. 1, 91058 Erlangen, Germany

<sup>k</sup>Leung Center for Cosmology and Particle Astrophysics, National Taiwan University,  
No. 1, Sec. 4, Roosevelt Road Taipei, 10617, Taiwan, R.O.C

<sup>l</sup>Institut für Physik, Humboldt-Universität zu Berlin,  
Newtonstraße 15, 12489 Berlin, Germany

<sup>m</sup>DESY,  
Platanenallee 6, 15738 Zeuthen, Germany

<sup>n</sup>Dept. of Physics and Wisconsin IceCube Particle Astrophysics Center,  
University of Wisconsin,  
Thomas C Chamberlin Hall, Madison, WI 53706, U.S.A.

<sup>o</sup>Research Cyberinfrastructure Center, University of California,  
100 Campus Dr., Irvine, CA 92697, U.S.A.

E-mail: [sbarwick@uci.edu](mailto:sbarwick@uci.edu), [gravity@ecberg.com](mailto:gravity@ecberg.com), [zedlam@ku.edu](mailto:zedlam@ku.edu),  
[ggaswint@uci.edu](mailto:ggaswint@uci.edu), [christian.glaser@uci.edu](mailto:christian.glaser@uci.edu), [allan.hallgren@physics.uu.se](mailto:allan.hallgren@physics.uu.se),  
[jhanson2@whittier.edu](mailto:jhanson2@whittier.edu), [srklein@lbl.gov](mailto:srklein@lbl.gov), [stuartk@uci.edu](mailto:stuartk@uci.edu),  
[lutz.koepke@uni-mainz.de](mailto:lutz.koepke@uni-mainz.de), [ikrav@unl.edu](mailto:ikrav@unl.edu),  
[robert.lahmann@physik.uni-erlangen.de](mailto:robert.lahmann@physik.uni-erlangen.de), [uzair.latif@ku.edu](mailto:uzair.latif@ku.edu), [namjiwoo@gmail.com](mailto:namjiwoo@gmail.com),  
[anna.nelles@desy.de](mailto:anna.nelles@desy.de), [cperish@uci.edu](mailto:cperish@uci.edu), [sandstrom@icecube.wisc.edu](mailto:sandstrom@icecube.wisc.edu),  
[jetatar@gmail.com](mailto:jetatar@gmail.com), [lisa.unger@physics.uu.se](mailto:lisa.unger@physics.uu.se)

Received April 30, 2018

Revised July 6, 2018

Accepted July 13, 2018

Published July 24, 2018

**Abstract.** Ongoing experimental efforts in Antarctica seek to detect ultra-high energy neutrinos by measurement of radio-frequency (RF) Askaryan radiation generated by the collision of a neutrino with an ice molecule. An array of RF antennas, deployed either in-ice or in-air, is used to infer the properties of the neutrino. To evaluate their experimental sensitivity, such experiments require a refractive index model for ray tracing radio-wave trajectories from a putative in-ice neutrino interaction point to the receiving antennas; this gives the degree of signal absorption or ray bending from source to receiver.

The gradient in the density profile over the upper 200 meters of Antarctic ice, coupled with Fermat’s least-time principle, implies ray “bending” and the existence of “forbidden” zones for predominantly horizontal signal propagation at shallow depths. After re-deriving the formulas describing such shadowing, we report on experimental results that, somewhat unexpectedly, demonstrate the existence of electromagnetic wave transport modes from nominally shadowed regions. The fact that this shadow-signal propagation is observed both at South Pole and the Ross Ice Shelf in Antarctica suggests that the effect may be a generic property of polar ice, with potentially important implications for experiments seeking to detect neutrinos.

**Keywords:** cosmic ray experiments, ultra high energy photons and neutrinos

**ArXiv ePrint:** [1804.10430](https://arxiv.org/abs/1804.10430)

---

## Contents

<b>1</b>	<b>Introduction</b>	<b>1</b>
<b>2</b>	<b>Formalism</b>	<b>3</b>
2.1	Fermat’s principle and ray tracing	3
2.2	Horizontal and near-surface propagation	5
2.3	Density and propagation-time measurements in Antarctica	6
<b>3</b>	<b>Observation of signal propagation from shadow zones</b>	<b>7</b>
3.1	Measurements made by the RICE experiment at South Pole	7
3.1.1	Comparison with expectation	9
3.1.2	Estimate of attenuation length from shadowed transmissions	12
3.1.3	Cross-checks and possible systematic errors	13
3.2	Observation of horizontal propagation with the ARIANNA experiment at Moore’s Bay, Ross Ice-Shelf, Antarctica	13
3.2.1	Experimental technique	14
3.2.2	Measurements between boreholes	14
3.2.3	Measurements in ARIANNA stations	16
3.2.4	Measurement from single borehole to buried LPDA	18
<b>4</b>	<b>Conclusions</b>	<b>19</b>

---

## 1 Introduction

Owing to its remote location and isolation from anthropogenic sources, excellent transparency at wavelengths ranging from optical through radio, and also the presence of extensive scientific support at several locations, Antarctica now supports multiple astronomy and astrophysics-oriented projects. Within the last five years, the IceCube experiment, sensitive to optical and near-optical Cherenkov radiation resulting from neutrino interactions in-ice, has reported on the first observation of a diffuse flux of extraterrestrial neutrinos at energies greater than 10 TeV [1], with a ‘hard’ spectrum extending to  $10^{15}$  eV. At higher energies, in-ice detection of longer-wavelength (radio) radiation is likely a more sensitive measurement strategy, owing to the Askaryan effect [2–4], combined with the measured kilometer-scale radio-wave attenuation length for cold polar ice [5, 6]. This has prompted several experimental initiatives based on experimental radio receiver arrays either elevated 35–40 km (ANITA [7]), near the Antarctic ice-air interface at Moore’s Bay, Antarctica (ARIANNA [8]), or at depths of up to 200 m at South Pole (pioneering RICE [9] and successor ARA [10]). In addition, exploratory work has been conducted within the last few years at Summit, Greenland to assess the radio-glaciological suitability of that site for a future neutrino-detection experiment [11]. Each of the possible neutrino-observation schemes (synoptic, surface detection of antennas, or antennas embedded in the ice sheet) has its own inherent advantages and trade-offs.

The variable specific gravity through the firn [12], over which the ice density varies between approximately 40–100% of the asymptotic value ( $917 \text{ kg/m}^3$ ), results in an electromagnetic wave-speed decreasing with depth. By Fermat’s principle, this results in not only curved ray trajectories, but also the expectation that, for the case where transmitter

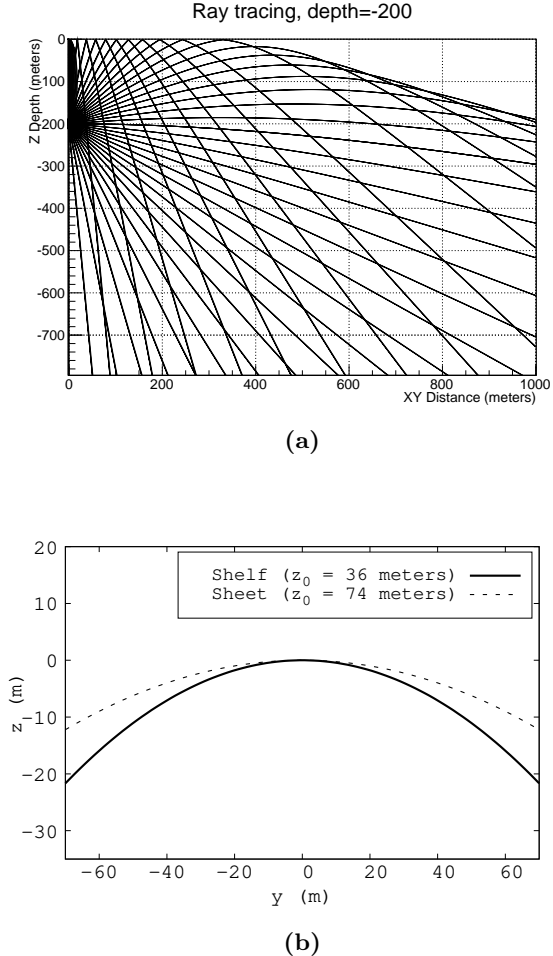


**Figure 1.** (a) Simulation of rays emitted from a transmitter at the South Pole at  $z=-200$  m, showing curved paths. The shadow zone in the upper right is expected in the case of a smoothly-varying  $n(z)$  profile in the absence of impurities. For the RICE measurements described later, the XY-distance was approximately 3000 meters, at typical depths of 100 meters (b) Examples of quadratic ray-paths in media with index of refraction profiles with the form of eq. (1.1). The dashed line corresponds to a particular solution of eq. (2.7) with  $z_0 = 74$  m. The solid line corresponds to eq. (2.7) with  $z_0 = 36$  m.

(Tx) and/or receiver (Rx) is deployed either on the surface or at near-surface depths, signals emanating from sufficiently large horizontal angles may be refracted downwards before they can be observed (“shadowing”). In the Huygens picture, these shadowed regions correspond to volumes for which the superposition of all contributing wavelets, properly weighted by distance, sum to zero net amplitude for all observation times  $t$ , as illustrated in figure 1.

We note that the standard Huygens picture is typically applicable in the case where phase information is preserved by each scatterer, assumed to be small compared to one wavelength (i.e., the Rayleigh limit), and results (assuming zero signal absorption in the medium) in the usual  $1/r$  length scaling of the electric field  $\vec{E}$ . If the scatterer is not point-like (e.g., scattering size  $\sim \lambda$ ) or, if, for any other reason, the phase shift across the scatterer is random, this leads to  $|\vec{E}| \propto 1/r^2$ .

For dielectric materials like snow and ice, the signal wave-speed is determined by the local index of refraction, which can be approximated as a linear equation of density:

$n(z) \approx 1 + b\rho(z)$ , with  $z=0$  at the surface and increasingly negative with depth. The specific dependence for ice is given by the Schytt equation:  $n(x, y, z) = 1 + 0.78\rho(x, y, z)/\rho_0$ , where  $\rho(x, y, z)$  is the local ice density and  $\rho_0$  is the density for solid ice ( $917 \text{ kg/m}^3$ ). Designating  $n_s$  as the index of refraction of snow (see section 2.3),  $n_{\text{ice}}$  that of solid ice, and  $\Delta n = n_{\text{ice}} - n_s$ , then it can be shown from classical gravity and density considerations that the index versus scale depth  $z/z_0$  ( $z_0 > 0$ ) dependence follows:

$$n(z) = n_{\text{ice}} - \Delta n e^{z/z_0}. \quad (1.1)$$

From the same classical treatment that produces eq. (1.1), it may be shown that  $z_0^{-1} = (g\chi_0\rho_s)$ , where  $g$  is the gravitational acceleration, and  $\rho_s$  and  $\chi_0$  are the density and volumetric compressibility of snow, respectively. The snow density and compressibility are inversely proportional, while measurements of natural snow compressibility vary in the literature and depend on the measurement technique [13]. Taking compressibility values from fit F of figure 3 of [14] at  $\rho_s = 300 \text{ kg m}^{-3}$  yields a  $z_0$  value of 25 m. Rather than measure  $\chi$  and  $\rho$  independently, we fit  $z_0$  as a free-parameter obtained from  $\rho(z)$  data from various locations around Antarctica (see figure 2 and table 1). We find agreement with prior measurements [5, 15], and also find that  $z_0$  varies by a factor of  $\approx 2$  between Moore's Bay and the South Pole. Snow formation conditions near the surface vary considerably across polar regions, so there is no reason to expect the compressibility of surface snow to be uniform across different glaciological regions.

Allowing  $\chi$  to vary with  $z$  in the density versus depth model yields the following boundary-value relation for  $\chi_s$ , the compressibility of surface snow,  $\chi_{\text{ice}}$  the compressibility of deep ice, and  $\chi_f$ , the compressibility of the firn:

$$(\Delta\rho)\chi_f = \rho_s\chi_s - \rho_{\text{ice}}\chi_{\text{ice}}. \quad (1.2)$$

In eq. (1.2),  $\chi_f$  is a density-weighted difference between snow and ice compressibility, which serves as a useful average for the firn, as a whole. Although the depth-dependence of the compressibility of the firn  $\chi(z)$  is outside the scope of this work, we note that if  $\chi$  depends monotonically on depth, eq. (1.1) disallows horizontal ray tracing solutions. To explain horizontal ray tracing, a perturbation in the index profile can be added to eq. (2.2) (see section 2).

## 2 Formalism

In this section, ray tracing theory is reviewed. We begin with Fermat's principle and conclude with a discussion of conditions that lead to horizontal ray propagation, anticipating the experimental results described below.

### 2.1 Fermat's principle and ray tracing

Fermat's Principle states that optical lengths of light ray trajectories are minimized. Ray paths that satisfy Fermat's Principle depend on the index of refraction  $n$ . If  $n$  depends only on  $z$ , Fermat's Principle can be expressed in variational form as:

$$\delta \int_A^B n(z)(1 + \dot{y}^2)^{1/2} dz = \delta \int_A^B L(z, \dot{y}) dz = 0. \quad (2.1)$$

Derivatives indicated with a dot are with respect to  $z$ . Because  $n(z)$  does not depend on  $x$  or  $y$ , the problem exhibits cylindrical symmetry. Without loss of generality we can choose

$x = \dot{x} = 0$ . Note that  $\dot{y} = dy/dz$  is unit-less, and  $\ddot{y}$  has units of inverse length. Minimizing the variation in the path, and substituting  $u = \dot{y}$  gives

$$\dot{u} = -\left(\frac{\dot{n}}{n}\right)(u^3 + u). \quad (2.2)$$

Inserting eq. (1.1) for  $n(z)$ , the equation of motion is

$$\dot{u} = z_0^{-1} \left( \frac{\Delta n e^{z/z_0}}{n_{\text{ice}} - \Delta n e^{z/z_0}} \right) (u^3 + u). \quad (2.3)$$

As a check, note the deep ice limit:  $|z| \gg z_0$ ,  $z < 0$ :

$$\dot{u} = 0. \quad (2.4)$$

The solution to this equation of motion is

$$z(y) = a + by. \quad (2.5)$$

Eq. (2.5) shows that rays propagate in straight lines far below the firn where  $n$  is constant, as expected.<sup>1</sup> Another straight-line solution to eq. (2.3) is the vertical ray ( $u = 0$ ), which remains straight while progressing through all regions of  $n(z)$ .

For the case of a shallow ray ( $z \rightarrow 0$ ) with  $n \approx n_{\text{ice}} - \Delta n(1 + z/z_0)$  and  $\dot{n} \approx -\Delta n/z_0$  initially propagating with a horizontal velocity component satisfying  $u^3 \gg u$ , the main equation of motion (eq. (2.3)) reduces to

$$\frac{du}{dz} = \frac{1}{z_0} \left( \frac{\Delta n}{n_{\text{ice}} - \Delta n(1 + z/z_0)} \right) u^3, \quad (2.6)$$

Keeping only first order terms in  $(z/z_0)$ , a particular solution is

$$z(y) = -\frac{1}{2z_0} \left( \frac{n_{\text{ice}} - n_s}{n_s} \right) (y - y_1)^2. \quad (2.7)$$

Equation (2.7) shows that the shortest travel time between two near-surface points is given by a quadratic path, if the initial velocity vector is mostly horizontal.

For example, take  $z_0 = 36$  m and  $n_s = 1.30$  to describe refraction at Moore's Bay, Antarctica (site of the ARIANNA experiment), and  $z_0 = 74$  m,  $n_s = 1.35$  to describe South Polar refraction (see table 1 for measured values). These two ray paths are compared in figure 1. The curvature of the quadratic in eq. (2.7) is controlled by  $z_0^{-1}$ .

The ray tracing framework yields near-surface ray paths that are downward bending quadratic curves, with *smaller*  $z_0$  values corresponding to steeper bending. The data presented in section 3 include observations of rays that not only do not propagate with quadratic downward bending, but propagate horizontally in Moore's Bay where the value of  $z_0$  is approximately a factor two smaller than that of the South Pole. If rays are not shadowed in Moore's Bay, it should be even less likely that they are shadowed in the firn of the South Pole, and data presented in section 3 also support this hypothesis.

---

<sup>1</sup>Note that a horizontal solution to eq. (2.3) would imply  $\dot{u} \rightarrow \infty$ , requiring  $\dot{n} \rightarrow 0$  in eq. (2.2). However,  $\dot{n} = 0$  cannot occur without an under-density or over-density in the firn, since index and density are proportional.

## 2.2 Horizontal and near-surface propagation

Perturbations from the smooth profile can be introduced by variable yearly melting and sintering mechanisms, and bulk re-alignment of the crystal orientation fabric. Chapter 2 of [16] summarizes these mechanisms, and such observations of layers are common [17, 18]. We observe layering in Moore’s Bay and South Pole data as  $\approx 5\%$  deviations from a smooth fit to the density profile (see figures 2 and 10). Over-densities (such as those observed near the South Polar surface) and under-densities can lead to local minima and maxima in the index of refraction profile.

Let one such local feature be described by a quadratic perturbation from an otherwise constant  $n_0$  value, with a strength  $a$  at a depth  $z_d$ :

$$n(z) = n_0 + a(z - z_d)^2 \quad (2.8)$$

$$\dot{n} = 2a(z - z_d) \quad (2.9)$$

$$q = z - z_d, \quad (2.10)$$

Let  $\omega^2 = 2 \left( \frac{a}{n_0} \right)$ . Introducing  $n(z)$  from eq. (2.8) into eq. (2.2), and neglecting terms higher than order  $q^2$ , the variables-separable differential equation may be solved near  $q = 0$ :

$$q(y) = C_0 \sin(\pm C_1 \omega y - C_2) \quad (2.11)$$

The constants  $C_i$  are determined by the boundary conditions and the shape of the perturbation, and two of them are independent. The approximation is accurate as long as  $\omega^4 q^4 \ll 1$ . Solving the problem in the same limit with  $a \rightarrow -a$  in eq. (2.8) amounts to replacing the sine function with a sinh function in eq. (2.11), making the path  $q(y)$  unbounded.

A quadratic perturbation in  $q$  can only be added in a piecewise-continuous fashion to eq. (1.1), if the boundary conditions  $n \rightarrow n_{\text{ice}}$  as  $z \rightarrow -\infty$  and  $n(0) = n_s$  are to be preserved. Admitting a Gaussian perturbation yields the physical behavior of the locally quadratic perturbation, while keeping  $n(z)$  fully continuous and differentiable:

$$n(z) = n_0 + a \exp \left( -\frac{1}{2} \left( \frac{q}{\sigma} \right)^2 \right) \quad (2.12)$$

The prior definition of  $\omega$  with the  $a$ -value from eq. (2.8) has units of inverse length. The  $a$ -value in eq. (2.12) is unit-less, but the perturbation width  $\sigma$  has units of length. Repeating the procedure leading to eq. (2.11), in the limit that  $(\omega q / \sigma)^4 \ll 1$ , the solution is

$$q(y) = C_0 \sin \left( \pm C_1 \frac{\omega y}{\sigma} - C_2 \right) \quad (2.13)$$

If horizontal ray-propagation were observed, there would be several potential conclusions. First, the  $n(z)$  profile could be described by eq. (1.1) with local density perturbations. According to eq. (2.13), the rays would oscillate about the perturbation with a spatial frequency and amplitude determined by the shape of the perturbation. A second possibility is that the perturbations could have such large  $a$ -values and such small  $\sigma$ -values that rays are simply reflected by them. Groups of such internal layers could form reflective channels, trapping rays in horizontal states through total internal reflection. Although we do not discern from the data which mechanism is present in the ice sheets and ice shelves, we note that ice layers are common in the upper firn, and that over- and under-densities do appear in residual fits of eq. (1.1) to the  $n(z)$  data (see figure 2).

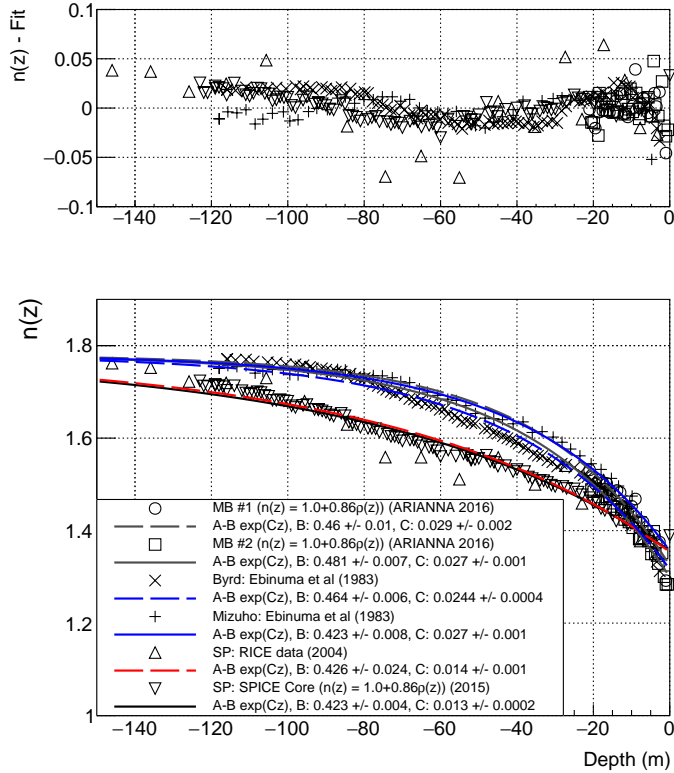


**Figure 2.** Compilation of density and index of refraction measurements. “MB” results (circles and squares) refer to density measurements made by the authors during the 2016-17 austral season at Moore’s Bay, Antarctica, and expressed here as index of refraction via the Schytt equation. The Byrd and Mizuho density data (x’s and crosses) are taken from [19] and translated to index of refraction in the same fashion. The RICE data (triangles) are direct measurements of index using RF signals from [20]. The SPICE-core data (upside-down triangles) come from the 2015 SPICE core density measurements from the South Pole, and are translated via the Schytt equation. The residual difference between the fit lines and the data are plotted in the upper panel.

### 2.3 Density and propagation-time measurements in Antarctica

Measurements of density and index of refraction have been compiled in figure 2 for a variety of Antarctic locations. Table 1 contains the coefficients  $A = n_{\text{ice}}$ ,  $B = \delta n$ , and  $C = z_0^{-1}$  determined from a fit of the form  $n(z) = A - B \exp(Cz)$ . Relative to a smooth functional dependence, variations in measured density are observed at the level of a few percent, larger than the intrinsic systematic errors (estimated at less than 1% relative), and decreasing with depth.

In Moore’s Bay, the parameter  $n_s$  (index of refraction of the snow near the surface), has been measured in two ways. First, surface snow density measurements were recorded and converted to index via the usual Schytt equation to determine  $n_s = 1.3$  [21]. Second, the absolute timing of an RF pulse transmitted at 2–4 wavelengths below the surface through the snow along a 543 meter baseline corresponded to a measurement of  $n_s = 1.29 \pm 0.02$  [15]. These results are in agreement with the fits to the density data versus depth shown in figure 2 and table 1, and in agreement with  $n_s$  values obtained from density measurements at the South Pole and two other locations.

ref./Location	$B = \Delta n$	$n_s = n_{\text{ice}} - B$	$C^{-1} = z_0$ (m)
MB#1/Moore’s Bay	$0.46 \pm 0.01$	$1.32 \pm 0.01$	$34.5 \pm 2$
MB#2/Moore’s Bay	$0.481 \pm 0.007$	$1.299 \pm 0.007$	$37 \pm 1$
Ebinuma (1983)/Byrd	$0.464 \pm 0.006$	$1.316 \pm 0.006$	$41 \pm 1$
Ebinuma (1983)/Mizuho	$0.423 \pm 0.008$	$1.357 \pm 0.008$	$37 \pm 1$
RICE (2004)/South Pole	$0.43 \pm 0.02$	$1.35 \pm 0.02$	$71 \pm 5$
SPICE (2015)/South Pole	$0.423 \pm 0.004$	$1.357 \pm 0.004$	$77 \pm 2$

**Table 1.** Fit parameters for the curves shown in figure 2. The function fit to the data is  $n(z) = A - B \exp(Cz)$ . The second-order differential equation derived in the first section requires  $A = n_{\text{ice}} = 1.78$  and  $B = \Delta n$  as the two boundary conditions.

The RICE data presented in figure 2 was collected with a 0.5-km distance between RF transmitter and receiver, and relied on relative timing between stationary RF receiver channels as a single transmitter is lowered into an ice borehole. A direct RF-based measurement of the South Pole  $n(z)$  was conducted in December 2003 using two RF antennas co-lowered into boreholes separated by 30 m horizontally; those data are presented in figure 3. The absolute timing between RF transmitter and receiver provides a direct measurement of  $n(z)$ . By contrast, the “MB” data in figure 2 is density data that has been converted to  $n(z)$  via the Schytt equation. The near-surface comparison of the 2003 RICE measurements with the density data is particularly interesting — here, the local-minimum in SPICE density measurements at  $z=-12$  m suggestively correlates with a local minimum in RF propagation time at that same depth. This is consistent with the presence of ‘inversion’ layers which, as demonstrated in section 2 of this document, owing to the least-time principle, can result in signals arriving horizontally from nominally ‘shadowed’ regions.

### 3 Observation of signal propagation from shadow zones

Experimental measurements of the radio-frequency dielectric permittivity have been made over the last 15 years in Antarctica [6] and also more recently in Greenland [11]. In those previous measurements, radio wave signals propagate vertically from a surface or near-surface transmitter, and are observed in a surface or a near-surface receiver via their reflection either from an in-ice horizontal conducting layer, e.g., or the underlying bedrock. This approach has the advantage that the transmitter and receiver can be easily moved on the surface, and flexible triggers configured. However, since the solid angle for neutrino acceptance varies with polar angle  $\theta$  as  $\sin \theta$ , the neutrino effective target volume becomes diminishingly small viewing vertically, and such measurements therefore have limited applicability to neutrino sensitivity estimates.

#### 3.1 Measurements made by the RICE experiment at South Pole

Given its importance vis-a-vis neutrino sensitivity, verification of shadowing was given high priority in the early stages of the RICE experiment [9, 20]. During the period Dec. 2003–Jan. 2004, microsecond-duration “tone” signals were transmitted horizontally over a baseline of 3.3–3.5 km, at depths of 70, 120 and 125 meters from a borehole drilled originally for the National Oceanic and Atmospheric Administration (NOAA). The 20-channel RICE antenna

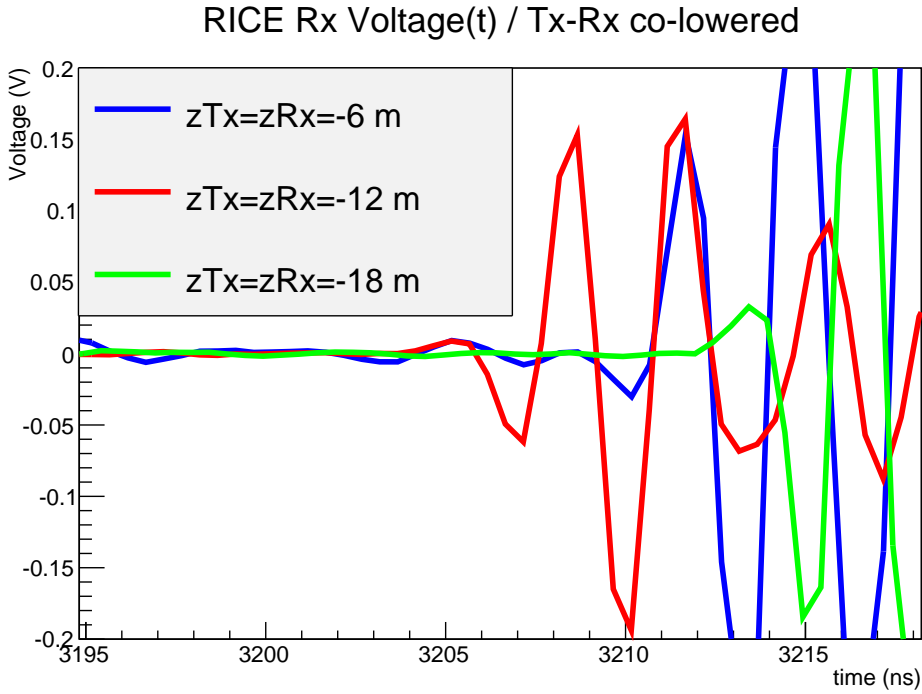


**Figure 3.** Received signals for cases where transmitter/receiver depths are 6 m (red), 12 m (blue) and 18 m (green), from dedicated, 2003 data taken with RICE experimental hardware, illustrating earlier arrival time for 12-meter depth compared to 6-meter depth, consistent with observed local fluctuation in SPICE density profile. Horizontal separation between transmitter and receiver is approximately 30 m for these data. Systematic error on relative signal arrival time is of order 0.1 ns.

array, based at South Pole and including 17 receiver antennas deployed at depths between 105 and 350 meters, was located in the nominal ‘shadow’ zone, as evident from figure 1 above.

For reference, and to simplify a calculation of attenuation length based on relative received signal strengths, data were also collected, using exactly the same transmitter set-up, from a closer location embedded within the RICE array itself, and unshadowed. With two such transmitter locations,  $L_{\text{atten}}$  can be numerically extracted using the ratio of signal amplitudes measured at the far transmitter location ( $A_{\text{far}}$ ) relative to the ‘near’ transmitter location ( $A_{\text{near}}$ ), and assuming that electric field strengths vary inversely with distance

$$A_{\text{far}}/A_{\text{near}} = (\cos \theta_{Tx \rightarrow Rx}^{\text{near}} / \cos \theta_{Tx \rightarrow Rx}^{\text{far}}) |r_{\text{near}}/r_{\text{far}}| \times e^{-(r_{\text{far}}-r_{\text{near}})/L_{\text{atten}}}, \quad (3.1)$$

with the values of  $r$  defined individually for each Tx/Rx pair; the  $\cos \theta$  term accounts for the antenna dipole beam pattern of the dipoles.

Broadcast signals were produced as follows:

1. A signal generator ( $SG$ ), producing continuous waves in the interval 211–500 MHz, is gated open once per second by a GPS pulse per second (pps) trigger, for a period of between one and 20 microseconds.
2. This signal generator output is then split into two copies: one copy is routed to an above-surface TV log-periodic-dipole-antenna (LPDA) ( $TV$ ) pointed at a similar above-surface receiver LPDA antenna co-located with the RICE receiver array and fed (arbi-

trarily) into RICE channel 11. Receipt of that above-ice signal in channel 11 provides the event trigger for the RICE array, initiating readout of the remaining channels.

3. The second copy is passed through a 100W amplifier, and then routed into a 300-meter length of 7/8" Andrews coaxial cable, at the end of which is the buried RICE Dipole (*DI*) antenna transmitter, efficient over the interval 200-500 MHz, and used to broadcast under-ice signal to the RICE Dipole (*DI*) receiver array. An additional delay unit staggers the  $SG \rightarrow TV$  vs.  $SG \rightarrow DI$  signals to ensure that they are emitted roughly simultaneously.

In principle, multiple signal paths are possible from the two transmitters to the RICE receivers, which we designate as  $TV \rightarrow TV$  (signals measured in the above-air receiver from the above-air TV transmitter, and providing the RICE event trigger),  $TV \rightarrow DI$  (signals measured in the in-ice RICE Dipole receiver channels from the above-air TV transmitter), and  $DI \rightarrow DI$  (signals measured in the in-ice RICE Dipole receiver channels from the in-ice Dipole transmitter). These multiple signal paths are indeed seen as signals in the RICE channels.

Although signals cannot be averaged during data-taking, to improve the signal-to-noise of the  $DI \rightarrow DI$  signal, the in-ice receiver traces were phase-aligned, event-by-event, using the event-by-event relative phase shifts derived from the bright  $TV \rightarrow TV$  signals, which are observed as nearly pure sinusoids. Figure 4 shows the signals observed in three RICE channels (channel 0: top row, receiver  $z = -166$  m; channel 6: middle row, receiver  $z = -170$  m; channel 15: bottom row, receiver  $z = -367$  m), for data taken at the three transmitter depths (left column:  $z = -70$  m, middle column:  $z = -120$  m, and right column:  $z = -125$  m), after phase alignment. Figure 5 shows the same traces after filtering around the carrier.

Clearly observed in these dipole receiver plots are two signals, offset in time by approximately 10 microseconds, which we interpret as the  $TV \rightarrow DI$  and  $DI \rightarrow DI$  signals, respectively.

### 3.1.1 Comparison with expectation

Since the entire RICE array is in the nominal shadow zone for this geometry, observation of the latter of these signals is immediately in conflict with naive expectations. For non-shadowed signal propagation, received signals should: i) be of time duration identical to the broadcast signal, and ii) for each RICE channel, exhibit a signal strength which is independent of the depth of the transmitter, since the difference in path-length between 70 meter transmitter depth (the experimental minimum) and 125 meter transmitter depth (the experimental maximum) is negligible, given the approximately 3 km horizontal propagation baseline. By contrast, the experimentally received signals show unexpectedly large variation in amplitude, compared to the simple  $1/r$  expectation, for relatively small vertical displacements (120 m vs. 125 m, e.g.); a model that adequately describes these variations is currently under development. We note that the large variations observed in received signal strength, for 5-meter variations in transmitter depth, cannot be explained by channel-to-channel gain uncertainties, as those uncertainties are inherent, and identical for the transmitter at any depth.

To determine the possible ray trajectories consistent with the observed timing of these signals, we compare these data with simplified models of ray propagation. Owing to uncertainties in the surface elevation map, and thus the point-of-entry into the ice for the  $TV \rightarrow DI$  path, our model for the  $TV \rightarrow DI$  ray is ‘extreme’ (and unphysical) — namely, we calculate the expected timing for a ray traveling horizontally through air, then bending ninety degrees into the ice to the in-ice receiver. Nevertheless, this model differs from the expected signal

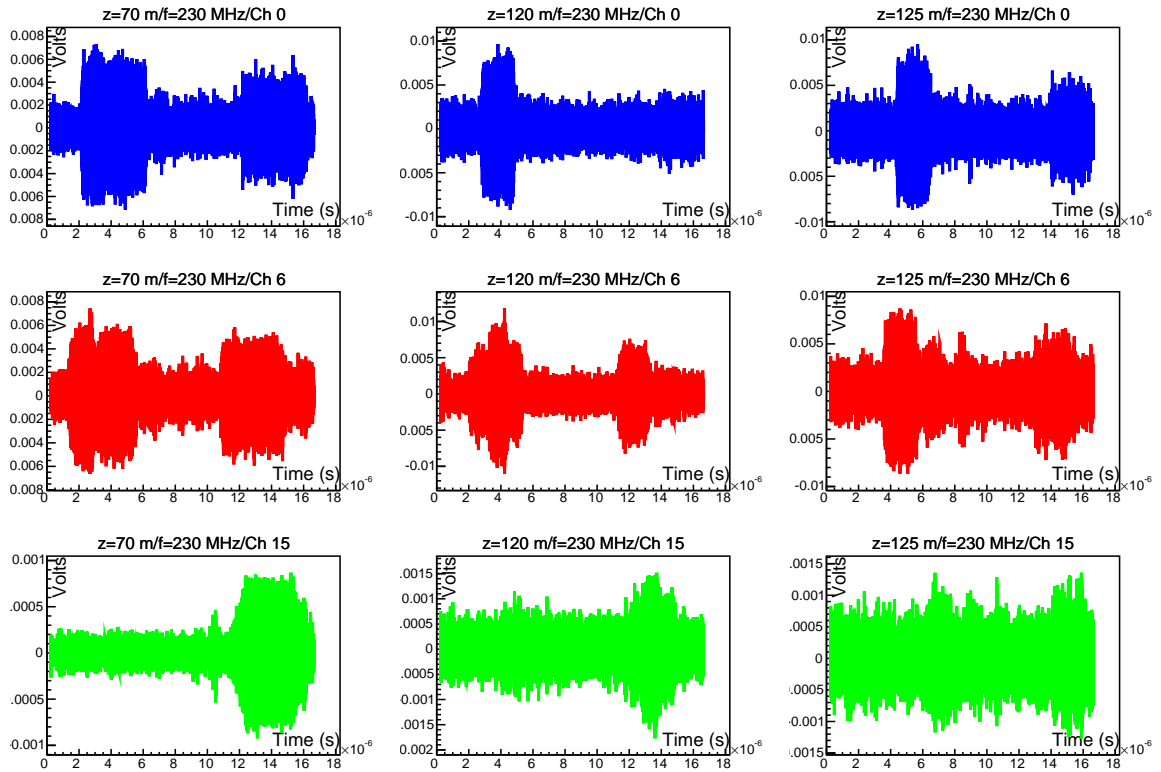


**Figure 4.** Phase-aligned sum of signals observed for three RICE channels, with transmitter at indicated depths  $-70\text{ m}$ ,  $-120\text{ m}$ , or  $-125\text{ m}$ . Receiver depths are  $-166\text{ m}$  (Ch 0),  $-170\text{ m}$  (Ch 6) and  $-367\text{ m}$  (Ch 15), respectively.

trajectory by only  $\mathcal{O}(100\text{ ns})$  in transit time, which is commensurate with the magnitude of our overall total timing uncertainties. For the  $DI \rightarrow DI$  path, we use the ARA Collaboration experimental model [22] for the index-of-refraction profile, which we integrate, assuming straight-line ray propagation from source in-ice dipole transmitter to in-ice receiver, to determine the total transit time. These predictions are overlaid with data in figure 6. In general, our very crude model matches data to within  $\sim 0.5\text{ }\mu\text{s}$ , commensurate with the sum of uncertainties due to ray trajectory, cable delays, trigger time delays, etc. Expressed fractionally, that uncertainty is  $\sim 5\%$  on the total travel time, or  $\sim 0.02\text{--}0.03$  in the refractive index.

Figure 6 (right) overlays the signal arrival for the case where the transmitter is at a depth of  $-70\text{ m}$  vs.  $-120\text{ m}$ . We observe  $\sim 0.8\text{ }\mu\text{s}$  time delay stagger in the latter relative to the former, compared with  $\sim 0.75\text{ }\mu\text{s}$  assuming least-time propagation to the RICE channel 12 receiver ( $z = -110\text{ m}$ ). This observed time delay difference is incompatible with through-air or surface signal propagation from the transmitter at the two depths ( $z = -70\text{ m}$  and  $z = -120\text{ m}$ ) to the receiver, which would imply a much shorter time stagger in their received signals of no more than  $0.2\text{ }\mu\text{s}$ . We also note an extended period of signal onset, indicating a wide range of contributing ray trajectories, consistent with the observation that many of the received  $DI \rightarrow DI$  signals are apparently temporally broadened compared to the nominal tone signal duration.

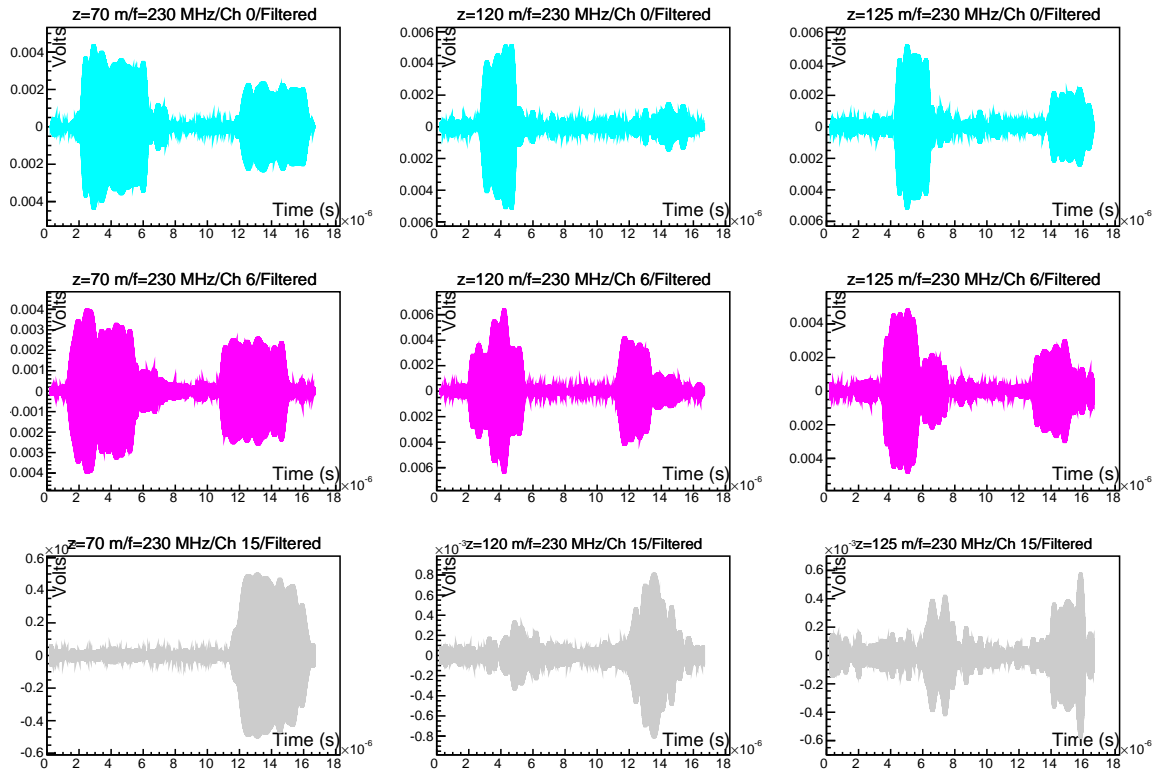


**Figure 5.** Same signals as in previous plot, after filtering  $\pm 2$  MHz around known broadcast frequency. Vertical axis: Volts; Horizontal axis: time (s).

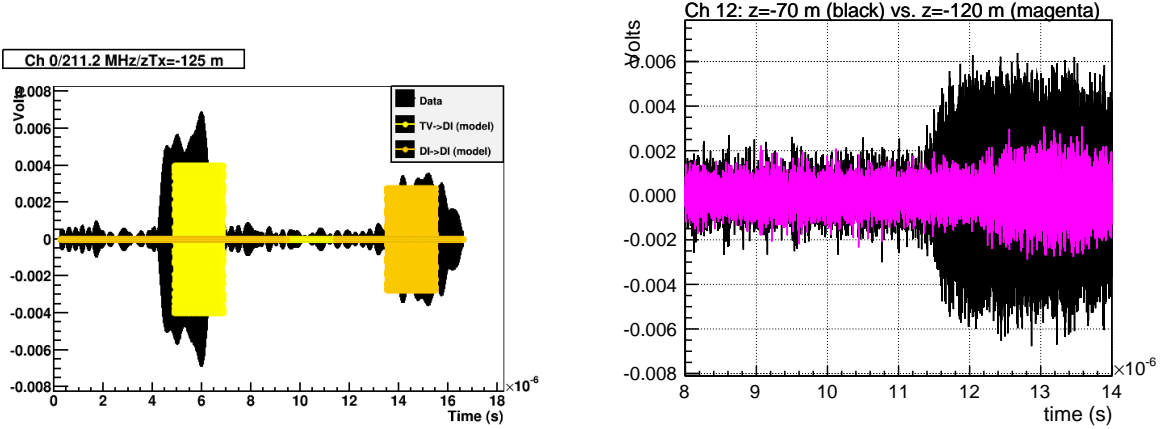


**Figure 6.** Left: overlay of raw data obtained in 2003 horizontal propagation experiments with model predictions for  $TV \rightarrow DI$  (light yellow) and also  $DI \rightarrow DI$  (dark yellow). Right: comparison of  $DI \rightarrow DI$  signal arrival times in RICE channel 12 ( $z = -110$  m) for transmitter in NOAA borehole, at depths  $z = -70$  m (black) vs.  $z = -120$  m (magenta; scaled), illustrating time delay of latter relative to former.

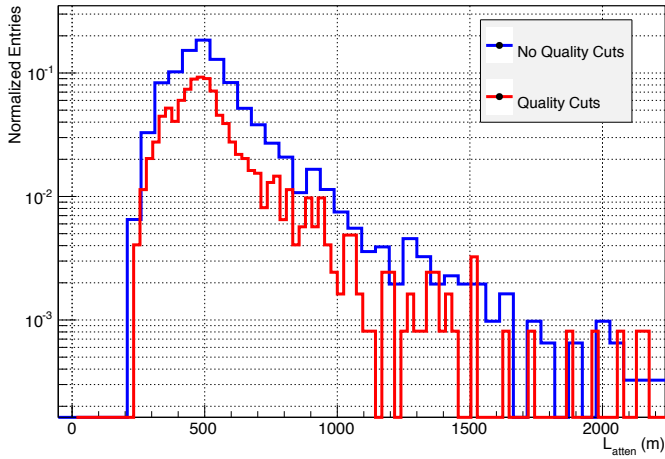


**Figure 7.** Distribution of field attenuation lengths calculated using RICE signal amplitudes measured from ‘far’ transmitter relative to ‘near’ transmitter. “Quality Cuts” refers to restricting data sample for which receiver Signal-to-Noise Ratio (SNR) exceeds 6:1 in amplitude.

### 3.1.2 Estimate of attenuation length from shadowed transmissions

Given multi-channel RICE receiver data, and using multiple data runs taken at both the near and far locations to sample a variety of depths and frequencies as well as a range of possible systematics, the attenuation length for horizontal propagation can be calculated by normalizing the signal strengths measured, channel-by-channel and run-by-run, for broadcasts over 3.3–3.5 km baselines, to signal strengths measured, channel-by-channel and run-by-run, to broadcasts when the transmitter is located within the RICE array itself (“near” transmission). Assuming the simplest  $1/r$  electric field dependence, we apply corrections for the distance difference between the near and far locations, and also for the  $\cos \theta$  dependence of the dipole beam pattern, as outlined previously. The ensemble of electric field attenuation lengths extracted in this manner is presented in figure 7. As a systematic check, we have sub-divided our samples by depth of the transmitter at the far location and also frequency of signal broadcast (table 2). Our observed scatter in calculated attenuation lengths is consistent with our estimated systematic errors. In principle, possible dispersive effects for shadow propagation can be probed by measuring the signal onset time, relative to the  $TV \rightarrow TV$  trigger, over the frequency range probed in this experiment. In practice, uncertainties in such a measurement were comparable to the determination of the signal onset time, and must therefore await more precise future measurements.

The ice is expected to have complete horizontal translational symmetry, with vertical symmetry broken by the presence of conducting layers within the ice (primarily due to deposits following volcanic eruptions) and/or fluctuations in the vertical density profile. As noted earlier, such vertical asymmetries suggest models in which signal emitted isotropically might be ‘trapped’ in a horizontal channel, thus circumventing the otherwise-expected shadowing. We have therefore searched for a possible inverse dependence of the calculated attenuation length on the vertical separation between transmitter and receiver. Our data suggest a possible slight decrease in attenuation length with the magnitude of  $z_{Tx} - z_{Rx}$ , although insufficient to be conclusive.

Numerically, our extracted attenuation length for all possible near/far combinations ( $550 \pm 10$  m, where the error shown is the error on the mean) is consistent with the result

$z_{Tx}$	$\langle SNR \rangle$	$L_{\text{atten}}$ (m)
70	$13.9 \pm 1.9$	$521 \pm 12.2$
120	$11.4 \pm 0.8$	$476 \pm 8.5$
125	$13.4 \pm 1.3$	$491.2 \pm 9.8$

frequency (MHz)	$L_{\text{atten}}$ (m)
211.2	$484.4 \pm 4.5$
230	$495.7 \pm 2.8$
490	$563.2 \pm 27.3$

**Table 2.** Observed signal-to-noise ratio and calculated average field attenuation length dependence on transmitter depth (top, and summing over all frequency data), and on frequency (bottom, and summing over all transmitter depth values); statistical errors only are shown. Estimated systematic errors are comparable in magnitude to the spread observed in the data points.

obtained when we restrict our calculation to those ‘high-quality’ combinations having high signal-to-noise only ( $542 \pm 16$  m).

We also note that similar broadcasts from the 8-km distant SPRESO hole (South Pole Remote Earth Science and Seismological Observatory), with transmitter at  $z=-300$  m, yielded no observable signal in the RICE channels. This is consistent with the large number of implied e-foldings ( $\sim 16$ ) to the RICE receiver array by a 550 m attenuation length. Unshadowed propagation from that source point should have yielded SNR values approximately  $2-3 \times$  larger than those observed from the NOAA source location.

### 3.1.3 Cross-checks and possible systematic errors

For the RICE measurements described herein, the uncertainty in the signal arrival times is estimated as approximately one time sampling bin (i.e., one nanosecond), which is insignificant compared to the  $\sim 10$  microsecond total travel times. Uncertainties in the attenuation length measurement are reflected in the width of the distribution shown in figure 7, or approximately 25 meters. Additional cross-checks were made to ensure that signal was not otherwise being lost in the signal path from generator to in-ice dipole, including checks for: a) faulty cables, connectors, antennas, or amplifiers (checked by swapping in/out other cables, connectors, antennas, or amplifiers), b) non-linearity of the power amplifier to the in-field transmitter, which was checked by direct measurement, c) sensitivity to possible coupling of the in-ice dipole antennas to the sides of the borehole, which was checked by taking multiple measurements after successively entirely raising and lowering the transmitter dipole, and d) saturation of the near-hole receiver amplifiers, which was also checked by verifying the linearity of the received near-hole signals with transmitter gain.

## 3.2 Observation of horizontal propagation with the ARIANNA experiment at Moore’s Bay, Ross Ice-Shelf, Antarctica

After earlier prototypes, deployment of the pilot-stage ARIANNA Hexagonal Array (HRA) began in 2014 and has since demonstrated successful operation under harsh Antarctic conditions [23]. ARIANNA employs high-gain log-periodic dipole antennas (*LPDAs*) with excellent broad-band response between 100 MHz and 900 MHz, primarily sensitive to signals polar-

ized parallel to the antenna tines. ARIANNA comprises multiple *stations*, each acting as an independent autonomous neutrino and cosmic ray detector and including four (or more) LP-DAs deployed just below the snow surface, admitting easy access and repair when necessary. The sensitivity to radio signals from neutrino interactions is enhanced by the high dielectric contrast at the ice-water interface at the bottom of the Ross Ice-Shelf, resulting in efficient reflection of down-going emission back towards the antennas [15, 24].

The first installed HRA stations have been used to derive limits on the neutrino flux [8] and to measure the radio emission of air showers, which are an important background for arrays with antennas close to the surface, while simultaneously providing equally important proof-of-concept and calibration [25]. ARIANNA measurement of air showers has demonstrated that the hardware response of the experiment, including antennas and amplifiers, is well-understood, as the predicted signal shape is well-matched by the detected signal shapes [25]. ARIANNA is, thus far, the only ground-based experiment to successfully self-trigger on radio emissions from air showers, with a high purity and efficiency independent of particle detectors.

The deployment of the HRA was accompanied by several ice properties measurements in subsequent years [15]. For many tests, such as studies of signals reflected off the ice-water interface on the bottom of the ice-shelf, early signals were measured in stations for which in-ice propagation was believed to be forbidden by the shadowing effect. These were initially not emphasized because they were considered as either potential in-air propagation or artifacts of the measurement set-up [26]. Additional analysis ruled out those possibilities, indicating that such signals were likely due to horizontal propagation, putative shadowing notwithstanding, prompting recent direct measurements of this phenomenon.

### 3.2.1 Experimental technique

During the 2016-17 polar season, two dedicated boreholes, separated by about 100 meters, were drilled to a depth of 20 meters in the ice, to permit the detailed study of horizontally propagating signals. (In practice, snow infall in the hole resulted in data taken at  $z = -19$  m, rather than  $z = -20$  m.) While transmitting and receiving between the two boreholes, multiple ARIANNA stations, schematically outlined in figure 8, were also regularly recording data, allowing for redundant cross-checks of propagation over multiple baselines. Signals were broadcast from the same RICE fat-dipoles used in the 2003 RICE study described previously.

### 3.2.2 Measurements between boreholes

High-amplitude (few kV), short-duration signals ( $< 20$  ns) were generated using a Pockels Cell Driver (*PCD*), which was routed directly to the transmitting antenna located in one borehole. Absolute timing was achieved by using a BNC Model 555 pulser to simultaneously trigger the PCD and send a triggering pulse to an oscilloscope for monitoring the signals received in the other borehole.

For reference, the entire set-up was lifted into the air, both on the ice-shelf and also pre-deployment in a park in California (i.e. dry ground, very little conductivity, flat area, little high vegetation); recorded signals were observed to be of similar strength at both locales.

For all tested in-ice configurations of different depths, strong pulses are observed. This is despite the fact that simple ray tracing would only allow for signals in certain combinations as shown on the left in figure 9. The figure also shows sample pulses recorded in different configurations of Tx/Rx. The signal shapes are observed to be very similar, despite the fact that, absent shadowed propagation, only the in-air configurations and the Tx/Rx depth of

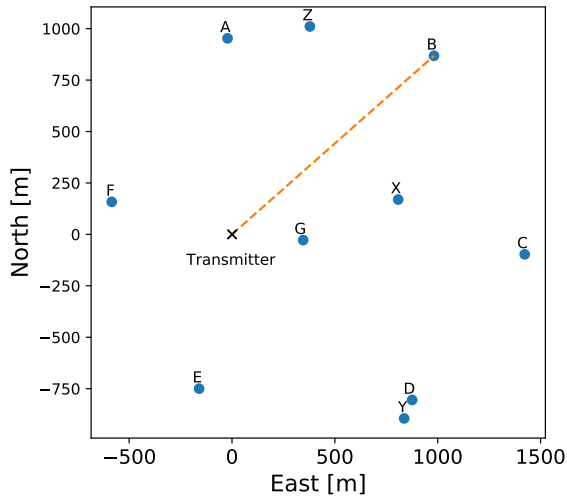


**Figure 8.** ARIANNA HRA array in the Antarctic season 2016/17. The transmitter for these studies was positioned at the origin in these coordinates. An example path of propagation to the station at position B is indicated by the dashed line.

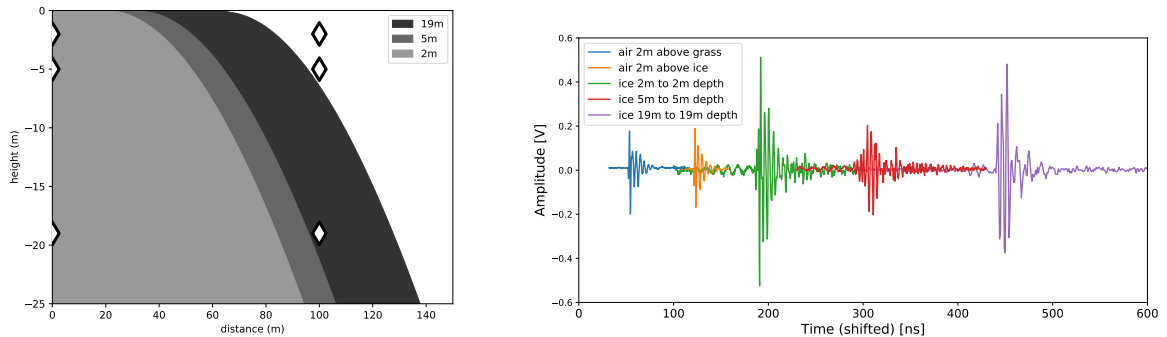


**Figure 9.** Left: illustration of shadowing at the ARIANNA site. Shaded regions indicate the horizon visible to a receiver (right) at the indicated depths of each transmitter (left). Diamonds show the location of the different transmitters and receiver positions in the first and second bore-hole, respectively. Right: pulses as recorded when transmitting from a RICE dipole to a receiving RICE dipole at varying transmitter/receiver depths at Moore's Bay. For reference measurements in air (in Moore's Bay and in California) are also depicted. Pulses have been arbitrarily shifted horizontally to better illustrate signal shapes.

19 meters should be visible. Interestingly, the amplitudes vary quite significantly, despite no changes in the set-up. This can at this point only tentatively be attributed to multi-path effects which lead to constructive and destructive interference.

We note that a) signal timing is consistent with horizontal propagation (as we quantify below), and b) no special transition was experimentally observed when the transmitter was moved across the shadow/non-shadow zone boundary.

In order to confirm that the observed pulses propagate through ice vs. air, the average index of refraction was measured for every combination of dipole depths from the signal arrival times, and then compared to the index-of-refraction calculated from ice density measurements obtained during hole-drilling. As figure 10 shows, the timing is fully compatible

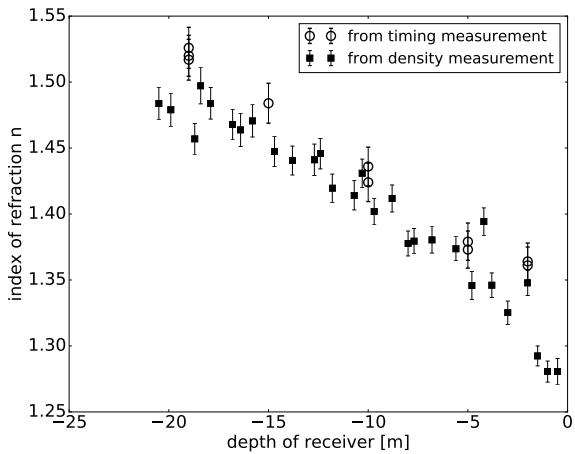


**Figure 10.** Measured index of refraction as function of depth. Filled squares indicate the index of refraction as calculated from ice density measurements of the bore holes. The open circles show the index of refraction calculated from absolute timing of the propagation of the pulses, using the leading edge of each pulse to obtain signal arrival times.

with propagation through the ice, and incompatible with through-air propagation ( $n \approx 1.0$ ), for a variety of depths. It is also incompatible with the ice-water boundary bounce hypothesis, as the measured timing cannot be reconciled with two-way propagation through the ice-shelf ( $\sim 1000$  m) and an index of refraction  $n > 1.0$ .

It should be noted that there seems to be a systematic offset between the index of refraction derived from the timing measurements and the ice density measurements (perhaps resulting from multi-path effects). As the index of refraction obtained from the air→air measurement ( $n=1.016$ ) is approximately 1.6% higher than expectation, this offset may also be a systematic effect. To exclude the possibility that signals were the result of accidental emission of the PCD itself, it was also verified that no signals were observed when the transmitting antenna in the ice was disconnected from the PCD.

The pulses received in the shadow zone (Tx 19 to Rx 2) have an average signal-to-noise ratio (SNR) of 25. Albeit being longer than the pulses received in the allowed zone (SNR = 193) the signals are still well-above the noise floor and contain significant power.

### 3.2.3 Measurements in ARIANNA stations

While pulsing in the boreholes, signals were captured in all normally operational ARIANNA stations with their nominal trigger settings. Figure 11 shows signals as recorded in a station at a distance of 953 meters from the transmitter, for which shadowing would otherwise prohibit signal observation. Since there is no absolute timing information between the transmitter and the ARIANNA station, to demonstrate that observed radio signals are propagating horizontally and are not the result of reflections from the underlying Ross Sea-Ross Ice Shelf boundary, one can consider arrival times within a station. Every HRA station is equipped with two co-polarized pairs of 6-meter separated LPDAs, with different pairs oriented perpendicularly, allowing direct polar angle-of-incidence inference based on a single antenna pair.

Figure 12 shows the contrast between expected and measured arrival directions when using the *bounce* hypothesis vs. the horizontal propagation hypothesis. For both hypotheses the time difference between pulses in antenna pairs are calculated (y-axis) and compared to

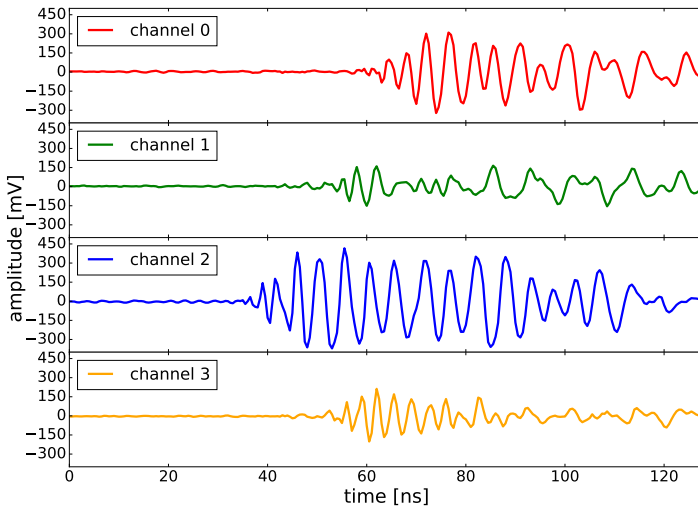


**Figure 11.** Horizontally propagating signals recorded in ARIANNA station *A*, at a horizontal distance of 953 meters from the transmitter. All pulses show a sharp leading edge with signal persisting for tens of nanoseconds, possibly extending beyond the length of the ARIANNA waveform record. The antennas of channels 0 and 2 are aligned roughly perpendicular to the arrival direction from the transmitter, while channels 1 and 3 are almost parallel. Channel 2 is closest to the transmitter and channel 0 furthest away, with a difference in distance of about 6 meters.

the measured time difference (x-axis). A good agreement is reached, when the points follow the dashed line through the origin and prediction matches measurement.

While there is significant scatter (partly due to the rather simple method chosen to identify the timing of the signal, as well as the short waveform length), the observed signals clearly favor horizontal propagation. We also observe no strong polarization dependence in those received signals.

The time structure of the pulses suggests some dispersion, as the received signal is elongated in time as compared to the emitted signal (figure 11). Some dispersion is expected from the antenna and amplifier response of the ARIANNA stations [27]. Amplifiers with a small group-delay are difficult to accommodate in low-power, broadband systems and the LPDAs are also slightly dispersive due to their broadband nature. However, even assuming the least sensitive direction for the LPDAs (a fully vertically polarized signal arriving in the null of the antenna i.e. parallel to the tines) cannot account for the dispersion of the signal observed.

Dispersive effects have the negative consequence of stretching the signal in the time domain and thereby reducing the instantaneous amplitude, but also offer the possibility that the relative arrival time of different frequency components can provide information on the distance-to-vertex for future in-ice neutrino searches, which is essential for a neutrino energy estimate.

The electric field attenuation lengths extracted from the data collected with all ARIANNA stations and the neighboring borehole are compiled in figure 13. Two calculations have been made to cross-check whether there is a significant difference when accounting for possible dispersive effects. Neglecting differences in the systematic uncertainties between the data obtained with an oscilloscope and ARIANNA station data, the best fit results in an attenuation length of  $447 \pm 146$  meters for the time-integrated absolute amplitude and

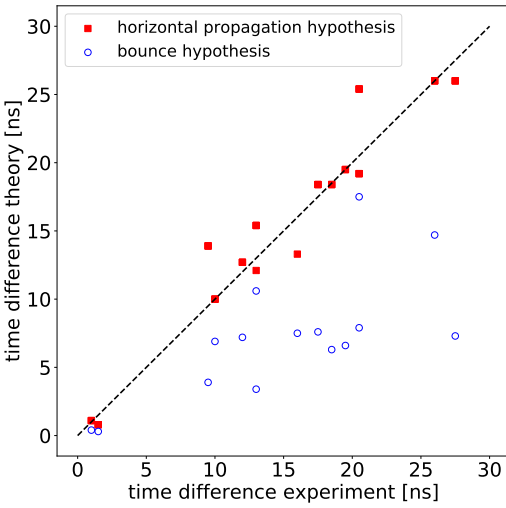


**Figure 12.** Measured (x-axis) vs. expected (y-axis) signal arrival times in ARIANNA stations for two different propagation hypotheses. The filled squares correspond to the *bounce*-hypothesis, while the open circles represent the hypothesis of horizontal propagation. The proximity to the dashed line through the origin with slope one illustrates that the arrival times match horizontal propagation through the ice better than a reflection from the underlying Ross Sea.

$651 \pm 270$  meters based on the peak observed pulse amplitude only. These values are commensurate with those obtained at South Pole for horizontal propagation. These results imply that  $1/r$  geometric signal reduction dominates over attenuation for horizontal propagation, which is an intriguing perspective for the effective volume for an ARIANNA-like detector with a station spacing of about one kilometer.

### 3.2.4 Measurement from single borehole to buried LPDA

The same set-up with the PCD was also used to recorded pulses between the transmitter in a borehole and an LPDA buried at a depth of one meter in December of 2017. The LPDA was placed at a distance of 500 meters, which corresponds to the longest signal cable available. The tines of the LPDA were rotated perpendicular to the line connecting its position and the borehole for maximum gain. Using a cabled set-up and the long record of an oscilloscope allows for absolute timing.

Three pulses were observed as shown in figure 14. Solely from timing, the three pulses can be attributed to different paths between transmitter and receiver. The first small pulse has to travel (mainly) through the air, as its arrival time corresponds to a propagation with the speed of light in air ( $n = 1.0$ ). The signal is no longer present when the Tx antenna is disconnected from the PCD, so the signal is emitted by the antenna and has to propagate up and out of the firn first and then along the surface. The second pulse is compatible with the horizontal propagation through the firn, as its start-time corresponds to a propagation through a medium having  $n = 1.36$ . At a distance of 500 meters this horizontal propagation is not an allowed solution of classical ray tracing. The third pulse is found at the time required to travel twice through the ice-shelf and is therefore the reflection of the original signal off the bottom of the ice-shelf.

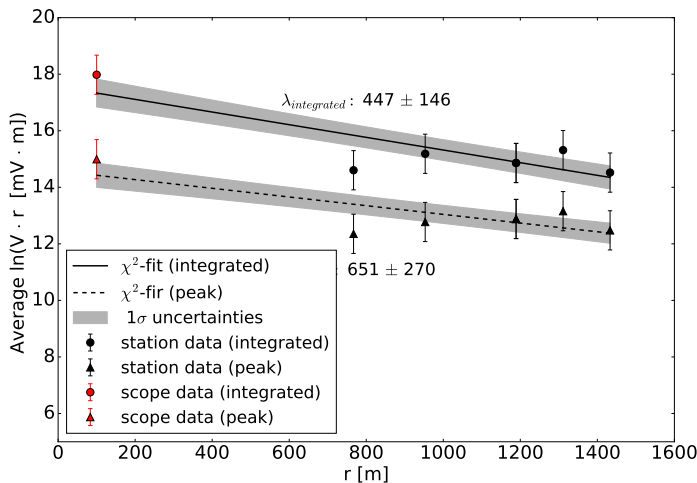


**Figure 13.** Field attenuation derived from all measured signals. Two calculations are made, one using the peak amplitudes of the signals and one using integrated absolute amplitudes (150–250 MHz), to account for possible dispersion. The reconstructed attenuation lengths from the pulse amplitude is  $651 \pm 270$  meters; for the integrated amplitude, the corresponding value is  $447 \pm 146$  meters. Note that exclusion of the left-most data point, which has been measured with an oscilloscope and not a station and therefore might be subject to different uncertainties, results in an even longer estimated attenuation length.

The figure depicts the raw data waveforms recorded in the field, with no applied gain correction. As an LPDA is rather insensitive to signals arriving perpendicular to the plane formed by the dipole elements (at least 3 dB compared to its front-lobe), the signals arriving horizontally are suppressed in this measurement, and may well contain more power than the reflected signal. An exact quantification requires knowledge of the precise arrival direction and the polarization of the incoming signal, which is impossible with the single LPDA which has been used to conduct these measurements. The reported signal strength is therefore a lower limit on the true power in the horizontally propagating signal.

Additional data, taken during the 2017-18 Antarctic field season, is currently being analyzed and should improve the understanding of signal propagation at Moore’s Bay. Additional studies, focusing of signal polarization, are foreseen for the 2018-19 season.

#### 4 Conclusions

We have presented evidence for electromagnetic signals propagating from nominally shadowed source locations. Although forbidden in the ray optics picture for the case of a smooth and monotonic variation of wave-speed with depth, reflective layers or local deviations from the smooth  $n(z)$  profile can result in local signal channeling.

The measured attenuation length of  $\sim 500$  m, from both the South Polar and the Ross Ice Shelf locales, is slightly larger than the average unshadowed attenuation length measured at Moore’s Bay [15], and approximately one-third that observed for unshadowed radio signal propagation at South Pole [28] in the upper 1.5 km of ice. This value is also compatible with what might be expected in a model where microscopic scattering occurs entirely incoherently, and phase information is lost in the scattering process.

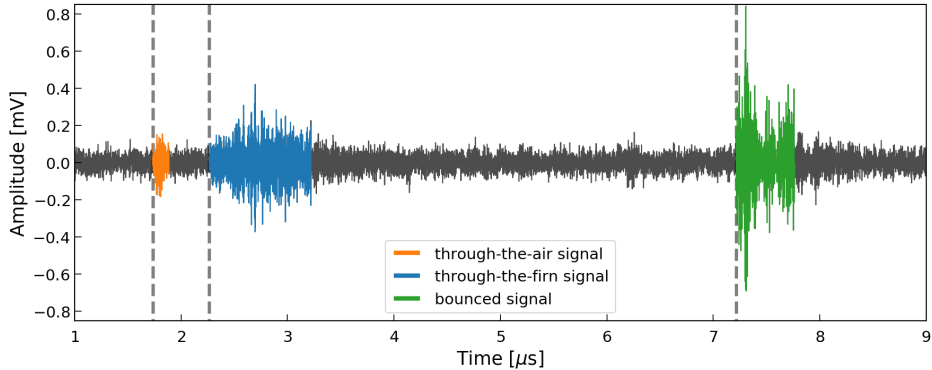


**Figure 14.** Pulses recorded with an LPDA buried at one meter depth, transmitted from a dipole at 19 meters depth at 500 meters distance. The dashed lines correspond to the calculated travel times in air ( $n = 1.0$ , + propagation up through firn), firn ( $n=1.36$ ) and the ray tracing solution for a pulse reflecting from the bottom of the ice-shelf, assuming a thickness of 578 meters.

The attenuation length for horizontal propagation presented herein is comparable to the maximum detectable range for  $\sim 10$  PeV neutrinos using the radio technique. Contrary to previous expectation, experimental observation of such neutrinos is therefore not limited by shadowing. This neutrino energy regime is particularly interesting experimentally, as it represents the maximum upper energy reach of the IceCube experiment and the detected astrophysical neutrino flux. A radio detector with such an energy threshold may measure the continuation of the IceCube flux, which is likely orders of magnitude larger than the flux caused by the interaction of cosmic rays with the cosmic microwave background at 100 PeV. As the horizontally propagating signals are well above the noise floor, this result therefore suggests that a future neutrino detector constructed at relatively shallow depths (< 30 meters) might optimize the balance between science return and the logistical overhead associated with hole drilling.

During the 2017-18 austral season, a transmitter based on the HiCal [29] piezo-electric model was lowered into the SPICE core hole [30] and broadcast to both the ARA array (deep) as well as a single ARIANNA station at the surface, allowing a more systematic map of signal transmission over a range of depths. Data analysis is currently in progress. A second generation of those studies will be conducted in 2018-19.

## Acknowledgments

We are grateful to the U.S. National Science Foundation-Office of Polar Programs, the U.S. National Science Foundation-Physics Division and the U.S. Department of Energy. We thank generous support from the German Research Foundation (DFG), grant NE 2031/1-1, NE 2031/2-1 and GL 914/1-1, the Taiwan Ministry of Science and Technology, the “Wallenbergs-tiftelsen” (Wallenberg Foundation) and the “Liljewalch stipendier” (Liljewalch scholarships).

## References

- [1] ICECUBE collaboration, M.G. Aartsen et al., *Observation and characterization of a cosmic muon neutrino flux from the northern hemisphere using six years of IceCube data*, *Astrophys. J.* **833** (2016) 3 [[arXiv:1607.08006](#)] [[INSPIRE](#)].
- [2] G.A. Askaryan, *Excess negative charge of an electron-photon shower and its coherent radio emission*, *Sov. Phys. JETP* **14** (1962) 441 [*Zh. Eksp. Teor. Fiz.* **41** (1961) 616] [[INSPIRE](#)].

- [3] G.A. Askaryan, *Excess negative charge of electron-photon shower and the coherent radiation originating from it. Radiorecording of showers under the ground and on the moon*, *J. Phys. Soc. Jpn.* **17** (1962) 257.
- [4] G.A. Askaryan, *Coherent radio emission from cosmic showers in air and in dense media*, *Sov. Phys. JETP* **21** (1965) 658.
- [5] T. Barrella, S.W. Barwick and D. Saltzberg, *Ross Ice Shelf (Antarctica) in situ radio-frequency attenuation*, *J. Glaciol.* **57** (2011) 61.
- [6] S.W. Barwick, D. Besson, P. Gorham and D. Saltzberg, *South polar in situ radio-frequency ice attenuation*, *J. Glaciol.* **51** (2005) 231.
- [7] ANITA collaboration, P.W. Gorham et al., *The Antarctic Impulsive Transient Antenna ultra-high energy neutrino detector design, performance and sensitivity for 2006–2007 balloon flight*, *Astropart. Phys.* **32** (2009) 10 [[arXiv:0812.1920](#)] [[INSPIRE](#)].
- [8] ARIANNA collaboration, S.W. Barwick et al., *A first search for cosmogenic neutrinos with the ARIANNA hexagonal radio array*, *Astropart. Phys.* **70** (2015) 12 [[arXiv:1410.7352](#)] [[INSPIRE](#)].
- [9] RICE collaboration, I. Kravchenko et al., *Performance and simulation of the RICE detector*, *Astropart. Phys.* **19** (2003) 15 [[astro-ph/0112372](#)] [[INSPIRE](#)].
- [10] ARA collaboration, P. Allison et al., *Performance of two Askaryan Radio Array stations and first results in the search for ultrahigh energy neutrinos*, *Phys. Rev. D* **93** (2016) 082003 [[arXiv:1507.08991](#)] [[INSPIRE](#)].
- [11] J. Avva, J.M. Kovac, C. Miki, D. Saltzberg and A.G. Vieregg, *An in situ measurement of the radio-frequency attenuation in ice at Summit Station, Greenland*, *J. Glaciol.* **61** (2015) 1005.
- [12] D. Pearce and J. Walker, *An empirical determination of the relative dielectric constant of the Greenland Ice Cap*, *J. Geophys. Res.* **72** (1967) 5743.
- [13] Cold Regions Research and Engineering Laboratory (U.S.), M. Mellor, *A review of basic snow mechanics*, U.S. Army Cold Regions Research and Engineering Laboratory, U.S.A., (1974).
- [14] B. Gerling, H. Löwe and A. van Herwijnen, *Measuring the elastic modulus of snow*, *Geophys. Res. Lett.* **44** (2017) 11,088.
- [15] J.C. Hanson et al., *Radar absorption, basal reflection, thickness and polarization measurements from the Ross Ice Shelf*, *J. Glaciol.* **61** (2015) 438.
- [16] V.V. Bogorodsky, C.R. Bentley and P.E. Gudmansen, *Radioglaciology*, Reidel, Dordrecht, Netherlands, (1985).
- [17] S. Gerland, H. Oerter, J. Kipfstuhl, F. Wilhelms, H. Miller and W.D. Miners, *Density log of a 181 m long ice core from Berkner Island, Antarctica*, *Ann. Glaciol.* **29** (1999) 215.
- [18] J.A. Dowdeswell and S. Evans, *Investigations of the form and flow of ice sheets and glaciers using radio-echo sounding*, *Rept. Prog. Phys.* **67** (2004) 1821.
- [19] N. Maeno and T. Ebinuma, *Pressure sintering of ice and its implication to the densification of snow at polar glaciers and ice sheets*, *J. Phys. Chem.* **87** (1983) 4103.
- [20] I. Kravchenko, D. Besson and J. Meyers, *In situ index-of-refraction measurements of the south polar firn with the RICE detector*, *J. Glaciol.* **50** (2004) 522.
- [21] L. Gerhardt et al., *A prototype station for ARIANNA: a detector for cosmic neutrinos*, *Nucl. Instrum. Meth. A* **624** (2010) 85 [[arXiv:1005.5193](#)] [[INSPIRE](#)].
- [22] U. Abdul et al., *Measurement of the real dielectric permittivity  $\epsilon_r$  of glacial ice*, [arXiv:1712.03301](#) [[INSPIRE](#)].
- [23] S.W. Barwick et al., *Design and performance of the ARIANNA HRA-3 neutrino detector systems*, *IEEE Trans. Nucl. Sci.* **62** (2015) 2202 [[arXiv:1410.7369](#)] [[INSPIRE](#)].

- [24] C.S. Neal, *The dynamics of the Ross Ice Shelf revealed by radio echo-sounding*, *J. Glaciol.* **24** (1979) 295.
- [25] S.W. Barwick et al., *Radio detection of air showers with the ARIANNA experiment on the Ross Ice Shelf*, *Astropart. Phys.* **90** (2017) 50 [[arXiv:1612.04473](#)] [[INSPIRE](#)].
- [26] J. Hanson, *The performance and initial results of the ARIANNA prototype*, Ph.D. thesis, University of California, Irvine, CA, U.S.A., July 2013.
- [27] S.W. Barwick et al., *Time domain response of the ARIANNA detector*, *Astropart. Phys.* **62** (2015) 139 [[arXiv:1406.0820](#)] [[INSPIRE](#)].
- [28] P. Allison et al., *Design and initial performance of the Askaryan Radio Array prototype EeV neutrino detector at the South Pole*, *Astropart. Phys.* **35** (2012) 457 [[arXiv:1105.2854](#)] [[INSPIRE](#)].
- [29] P.W. Gorham et al., *The HiCal 2 instrument: calibration and Antarctic surface reflectivity measurement for the ANITA experiment*, [arXiv:1710.11175](#) [[INSPIRE](#)].
- [30] K.A. Casey et al., *The 1500 m South Pole ice core: recovering a 40 ka environmental record*, *Ann. Glaciol.* **55** (2014) 137.

# Measurement of the real dielectric permittivity $\epsilon_r$ of glacial ice

Allison, P.<sup>b,c</sup>, Archambault, S.<sup>d</sup>, Auffenberg, J.<sup>e</sup>, Bard, R.<sup>f</sup>, Beatty, J.J.<sup>b,c</sup>, Beheler-Amass, M.<sup>e</sup>, Besson, D.Z.<sup>a,g</sup>, Beydler, M.<sup>e</sup>, Chen, C.C.<sup>h</sup>, Chen, C.H.<sup>h</sup>, Chen, P.<sup>h</sup>, Christenson, A.<sup>e</sup>, Clark, B.A.<sup>b,c</sup>, Connolly, A.<sup>b,c</sup>, Cremonesi, L.<sup>i</sup>, Deaconu, C.<sup>j</sup>, Duvernois, M.<sup>e</sup>, Friedman, L.<sup>f</sup>, Gaior, R.<sup>d</sup>, Hanson, J.<sup>b,c</sup>, Hanson, K.<sup>e</sup>, Haugen, J.<sup>e</sup>, Hoffman, K.D.<sup>f</sup>, Hong, E.<sup>b,c</sup>, Hsu, S.Y.<sup>h</sup>, Hu, L.<sup>h</sup>, Huang, J.J.<sup>h</sup>, Huang, M.-H. A.<sup>h</sup>, Ishihara, A.<sup>d</sup>, Karle, A.<sup>e</sup>, Kelley, J.L.<sup>e</sup>, Khandelwal, R.<sup>e</sup>, Kim, M.-C.<sup>d</sup>, Kravchenko, I.<sup>k</sup>, Kruse, J.<sup>k</sup>, Kurusu, K.<sup>d</sup>, Kuwabara, T.<sup>d</sup>, Landsman, H.<sup>l</sup>, Latif, U.A.<sup>a</sup>, Laundrie, A.<sup>e</sup>, Li, C.-J.<sup>h</sup>, Liu, T.-C.<sup>h</sup>, Lu, M.-Y.<sup>e</sup>, Mase, K.<sup>d</sup>, Meures, T.<sup>e</sup>, Nam, J.<sup>d</sup>, Nichols, R.J.<sup>i</sup>, Nir, G.<sup>l</sup>, Novikov, A.<sup>a,g</sup>, Oberla, E.<sup>j</sup>, O' Murchadha, A.<sup>e</sup>, Pan, Y.<sup>m</sup>, Pfendner, C.<sup>b,c</sup>, Ratzlaff, K.<sup>a</sup>, Relich, M.<sup>c</sup>, Roth, J.<sup>m</sup>, Sandstrom, P.<sup>e</sup>, Seckel, D.<sup>m</sup>, Shiao, Y.S.<sup>h</sup>, Shultz, A.<sup>k</sup>, Song, M.<sup>f</sup>, Touart, J.<sup>f</sup>, Varner, G.S.<sup>n</sup>, Vieregg, A.<sup>j</sup>, Wang, M.Z.<sup>h</sup>, Wang, S.H.<sup>h</sup>, Wissel, S.<sup>o</sup>, Yoshida, S.<sup>d</sup>, Young, R.<sup>a</sup>

<sup>a</sup>Dept. of Physics and Astronomy, Univ. of Kansas, Lawrence, KS, USA

<sup>b</sup>Dept. of Physics, The Ohio State University, 191 West Woodruff Avenue, Columbus, OH, USA

<sup>c</sup>Center for Cosmology and Astro-Particle Physics, The Ohio State University, 191 West Woodruff Avenue, Columbus, OH, USA

<sup>d</sup>Dept. of Physics, Chiba University, Tokyo, Japan

<sup>e</sup>Dept. of Physics and Wisconsin IceCube Particle Astrophysics Center, University of Wisconsin, Madison, WI, USA

<sup>f</sup>Dept. of Physics, Univ. of Maryland, College Park, MD, USA

<sup>g</sup>National Research Nuclear University, Moscow Engineering Physics Institute, Moscow, Russia

<sup>h</sup>Dept. of Physics, Grad. Inst. of Astrophys., & Leung Center for Cosmology and Particle Astrophysics, National Taiwan Univ., Taipei, Taiwan

<sup>i</sup>Dept. of Physics and Astronomy, Univ. College London, London, United Kingdom

<sup>j</sup>Dept. of Physics, University of Chicago, Chicago, IL, USA

<sup>k</sup>Dept. of Physics and Astronomy, Univ. of Nebraska-Lincoln, NE, USA

<sup>l</sup>Weizmann Institute of Science, Rehovot, Israel

<sup>m</sup>Dept. of Physics and Astronomy, Univ. of Delaware, Newark, DE, USA

<sup>n</sup>Dept. of Physics and Astronomy, Univ. of Hawaii, Manoa, HI, USA

<sup>o</sup>Dept. of Physics, California Polytechnic State University, San Luis Obispo, CA, USA

## Abstract

Owing to their small interaction cross-section, neutrinos are unparalleled astronomical tracers. Ultra-high energy (UHE;  $E > 10$  PeV) neutrinos probe the most distant, most explosive sources in the Universe, often obscured to optical telescopes. Radio-frequency (RF) detection of Askaryan radiation in cold polar ice is currently regarded as the best experimental measurement technique for UHE neutrinos, provided the RF properties of the ice target can be well-understood. To that end, the Askaryan Radio Array (ARA) experiment at the South Pole has used long-baseline RF propagation to extract information on the index-of-refraction ( $n = \sqrt{\epsilon_r}$ ) in South Polar ice. Owing to the increasing ice density over the upper 150–200 meters, rays are measured along two, nearly parallel paths, one of which refracts through an inflection point, with differences in both arrival time and arrival angle that can be used to constrain the neutrino properties. We also observe (first) indications for RF ice birefringence for signals propagating along predominantly horizontal trajectories, corresponding to an asymmetry of order 0.1% between the ordinary and extra-ordinary birefringent axes, numerically compatible with previous measurements of birefringent asymmetries for vertically-propagating radio-frequency signals at South Pole. Qualitatively, these effects offer the possibility of redundantly measuring the range from receiver to a neutrino interaction in Antarctic ice, if receiver antennas are deployed at shallow ( $z \sim 25$ –100 m) depths. Such range information is essential in determining both the neutrino energy, as well as the incident neutrino direction.

## 1. Introduction

The glacial ice in Antarctica offers a unique opportunity for detection of neutrinos. There are currently three Antarctic experiments which seek detection, via the Askaryan effect[1, 2, 3], of UHE neutrinos using the ice sheet as a neutrino target[4]. Hadronic and electromagnetic showers resulting from neutrino collisions with ice molecules acquire, as they evolve, a net negative charge as atomic electrons are Compton scattered into the forward-moving shower and shower positrons depleted via annihilation with atomic electrons, resulting in a coherent, detectable electromagnetic signal at radio wavelength scales, distributed on a Cherenkov cone approximately 1–2 degrees in transverse width, and with half-opening angle  $\sim 57^\circ$ . Above 10 EeV, the most promising (“cosmogenic”) neutrino source for these experiments[5, 6, 7, 8] results from photoproduction of pions due to interactions of ultra-high energy nucleons with cosmic microwave background (CMB) photons, with subsequent decays to neutrinos. Recent measurements by the IceCube experiment of PeV-scale neutrinos[4] have intensified interest in a large-scale radio array capable of measuring the continuation of that spectrum at higher energies; the observation of the first identified extra-galactic neutrino source has provided additional impetus[9].

The Askaryan Radio Array[10, 11, 12] (ARA) at the South Pole (Figure 1) has proposed multiple, independent stations in a hexagonal array with inter-station spacing of 2 km. Following the initial 2010/11 deployment of a “TestBed”

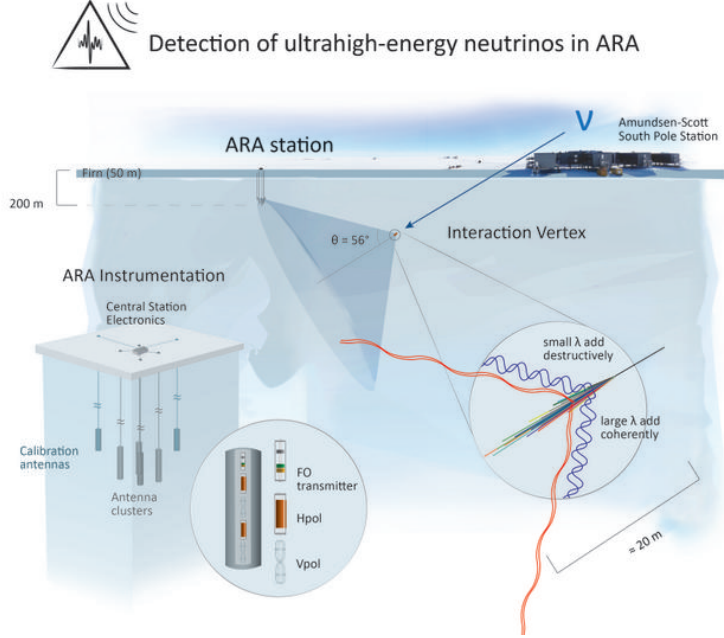


Figure 1: Schematic of ARA neutrino detection, showing the ARA receiver antennas illuminated by radio-frequency Cherenkov signal resulting from an in-ice neutrino interaction.

in the upper 30 meters of the South Polar ice sheet, three more (ARA-1, ARA-2, and ARA-3) stations were deployed in 2011/12 and 2012/13, with two more (ARA-4 and ARA-5) commissioned in 2017/18, including an advanced trigger system exploiting phased array techniques[13] on ARA-5. The analysis described below is based on the pre-2017 station configuration, as shown in Figure 2.

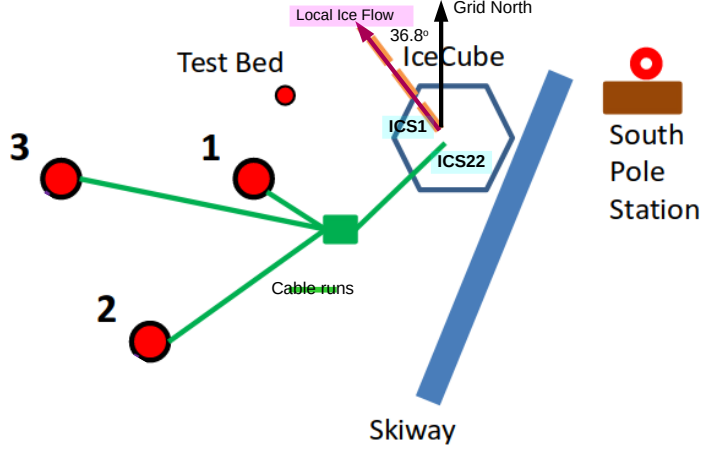


Figure 2: Station geometry for measurements described herein.

Following ARA-1, for which a drill malfunction limited deployment to approximately 40% of the desired 200 meter depth, the subsequent station receivers were deployed at depths of 175-200 m. Each station includes 16 antennas, 8 sensitive to vertically polarized (Vpol) and 8 sensitive to horizontally polarized (Hpol) radiation, with in-ice bandwidths of approximately 150-700 MHz and 250-400 MHz, respectively. Surface antennas, sensitive over the 25–800 MHz regime, deployed on the TestBed, ARA-1, ARA-2 and ARA-3, can be used to monitor low-frequency galactic noise, although they rarely give signals coincident with the in-ice antennas, given the typical time delays in signal arrival times between the surface and the deep station antennas. In-ice antennas are installed on four strings defining the corners of a cuboid approximately 20m in height and 20m along the horizontal diagonal. An H/V pair is located at each corner of the

cuboid, consisting of an Hpol antenna deployed 2m–3m above a Vpol antenna, such that H/V signal arrival times should be synchronous to within 10 ns. Signals are amplified at the antenna, passed by an in-ice RF-over-optical fiber link to the surface, and then converted back to RF voltage signals by a surface optical fiber receiver before entering the data acquisition system. Full station data collection is triggered whenever (3 of 8 Hpol) .OR. (3 of 8 Vpol) antennas exceed some voltage threshold within a time window (170 ns) inclusive to the RF travel time across the station. Thresholds are dynamically adjusted to maintain a combined event trigger rate of 5–7 Hz, comfortably below the saturation data-taking rate of 25 Hz. Following the issue of a valid trigger, signals from all 16 antennas are digitized and stored, with a readout window typically wide enough to include ~100 ns of pre-trigger and ~300 ns of post-trigger waveform data. A local calibration pulser, approximately 30 meters displaced from the centroid of the receiver array, emits signals at one pulse per second, to monitor receiver performance. For the testbed, received cal pulser signals in both HPol and VPol are presented elsewhere[10]. The response of the vertically-polarized receivers to the local, vertically-polarized cal pulser, for ARA-2 is shown in Figure 3.

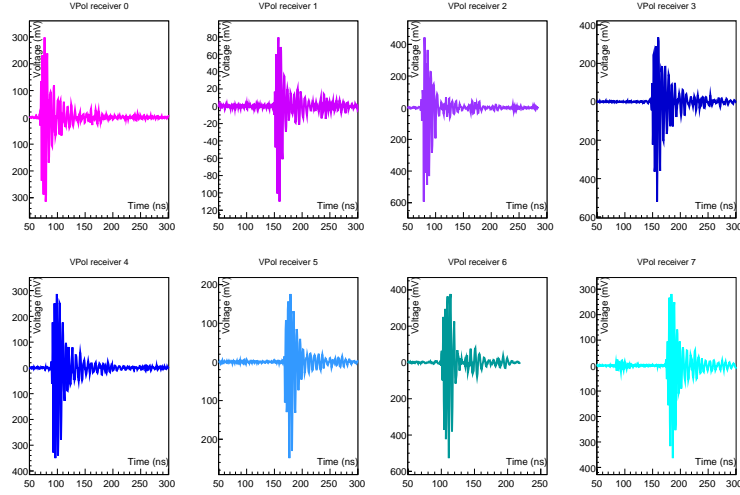


Figure 3: ARA-2 VPol response to the local, VPol calibration pulser, shown for the eight vertically-polarized (VPol) channels. HPol signals (not shown) show only noise for these events.

ARIANNA[14], located on the Ross Ice Shelf, features an isolated, radio-quiet site with log-periodic dipole antennas deployed on the surface. Downward-pointing antennas search for upcoming Askaryan signal generated by neutrino interactions in the ice; upward-pointing antennas have been used to measure down-coming Askaryan-like ‘geomagnetic’ signals generated by charged cosmic rays interacting in the Earth’s atmosphere[15]. The ANITA experiment[16] features a suite of radio-frequency horn antennas suspended from a balloon flying at an elevation of 38 km in a circumpolar orbit over the Antarctic continent, scanning for upcoming radio signals resulting from charged cosmic ray or neutrino interactions.

## 2. Geometric Optics and Ray tracing

The sensitivity of any neutrino-search experiment such as ARA depends on a) the degree of signal absorption in the target ice medium (determined by the imaginary component of the ice dielectric permittivity), and b) the volume of ice ‘visible’ to the radio receiver array (determined by the real component of the ice dielectric permittivity). The absorption length for RF signals in the frequency range of interest (100–1000 MHz) has been measured to exceed one km in the upper 1.5 km of the South Polar ice sheet, making it an ideal medium for neutrino detection[17]. However, the changing density of the ice results in a group velocity varying monotonically with depth. In such a case, Fermat’s Least-time principle implies that a) rays will follow curved paths, and b) there may be regions which are ‘shadowed’, for which the superposition of all contributing rays gives zero net amplitude. Moreover, there may be multiple signals observed from a single source, resulting from either continuous refraction through the ice itself, or reflection from the upper ice/air interface as illustrated in Figure 4.

The index-of-refraction should itself roughly scale with the local ice density. Robin suggested the parameterization  $n(z)=1+0.86\rho(z)$ [18] based on a clever interferometric technique, in which signals recorded on the surface from a transmitter lowered into a Devon Island ice bore hole were mixed with a fixed frequency; the wavelength of the ice at the depth of the transmitter was then inferred from the measured beats. Similar parameterizations can be found elsewhere ( $n(z)=0.992+0.848\rho(z)$ , e.g., as determined from a fit to McMurdo Sound ice measurements[19]), although not all obey the expectation that  $n(z)\rightarrow 1$  in the limit of  $\rho=0$ .

In a recent companion publication, also addressing the question of the index-of-refraction profile at the South Pole and elsewhere on the Antarctic continent, the general refractive index form is derived from Fermat’s Least Time

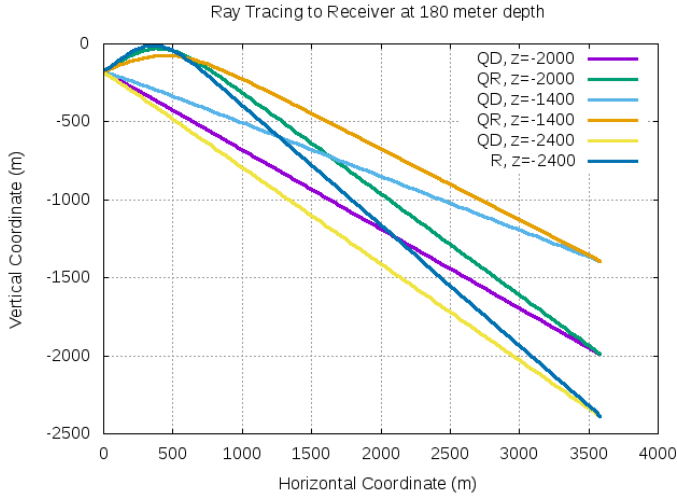


Figure 4: Simulation of ray tracing assuming ARA index-of-refraction profile with depth ( $n(z)=1.78-0.43\exp(13.2z)$ ), showing trajectories of Quasi-Direct (QD), Quasi-Refracted (QR) rays and surface-reflected (R) rays as a function of lateral distance ( $x$ , in meters) and vertical distance ( $z$ , in meters). Signals are modeled from three possible source depths (1400m, 2000m, or 2400m) 3600m laterally displaced from a receiver 180m deep. Refracted and direct rays are typically separated by approximately 40 degrees at the measurement point with corresponding launch angles at the source separated by  $\sim 5$  degrees. By comparison, (QD,QR) launch angle separations for neutrino interactions are limited to two degrees. Note shadow zones in upper right of plot.

principle[20]. Also presented in that reference are fits to the density data and the inferred best-fit parameters. We note that the density data at South Pole show considerable variations from experiment-to-experiment, as well as considerable deviations from smoothness, which could, in principle, result in sub-dominant ‘channeling’ effects. This possibility is especially interesting in the context of reports of horizontal propagation of in-ice RF signals emanating from within the ‘shadow zone’ expected in the presence of a gradient to the index of refraction[21, 22, 20, 23]. Such propagation could occur if there are density layers in the firn. A density inversion could produce a horizontal waveguide where radiation is confined by refraction, similar to an optical fiber with a graded index of refraction. Similarly, weak discontinuities in density can result in scattering surfaces for highly inclined rays, producing a “channel” for horizontal propagation.

## 2.1. Deep pulser broadcasts to the ARA array

In the middle of the expected cosmogenic neutrino energy spectrum ( $E_\nu \sim 10^{18.5}$  eV), ARA is designed to detect sources several km distant. It is therefore critical to understand the properties of the ice within the array, especially at the 1-2 km depths corresponding to the regime over which the bulk of detectable neutrinos are expected to interact. Anticipating this, during the last year (2010-11) of IceCube construction, two pulsers were deployed on IceCube string 1 at depths  $z=-1400$  m and  $z=-2450$  m (“ICS1” and “ICD1”, respectively), and one on IceCube string 22 (“ICS22”) at a depth  $z=-1400$  m, proximal to the planned ARA. The pulser at 2450 m depth was operated in conjunction with the ARA TestBed to validate the South Pole index of refraction profile with depth  $n(z)$  and also the RF attenuation dependence on depth[10], but failed within the first year of operation. The pulsers at depths of 1400 m were operated in 2014/15 as part of the calibration of ARA-2 and ARA-3, and again in 2016/17 after the ARA-2 trigger timing and readout window was adjusted, enabling capture of an extended waveform.

Given the monotonic increase of  $n(z)$  with depth over the upper 150 meters of the ice sheet, the presence of two rays from source to receiver is generic for our geometry (Fig. 4), with a quasi-direct (QD) ray typically upcoming at the station and either a reflected or a quasi-reflected ray (“QR”, cresting prior to “true” reflection at the upper surface) downgoing. The maximum in-ice height of the QR ray can be determined from Snell’s law and either the launch angle of the ray at the source, or the received angle at the station. The time delay between arrival of the QD and the QR rays is of order hundreds of ns; with the exception of the 2016/17 ARA-2 data, this time lag is generally larger than the waveform capture window.

## 2.2. Analysis of QD and QR rays

Figures 5 and 6 show deep pulser events which trigger ARA-2 and ARA-3, respectively. The QD rays travel exclusively through deep ice; the sharpness of their leading edge implies relatively little scattering and/or dispersive effects, consistent with studies of vertical echoes[24]. By contrast, the pulses identified as QR rays suggest a precursor which, we speculate, may be due to scattering in the firn layer near the top of the pulse trajectory. The somewhat irregular signal shapes from the deep pulser have been considered in a previous article[10]. In addition to evident saturation of the front-end amplifiers, resulting in compression and signal dilation, we speculate that the transmitters

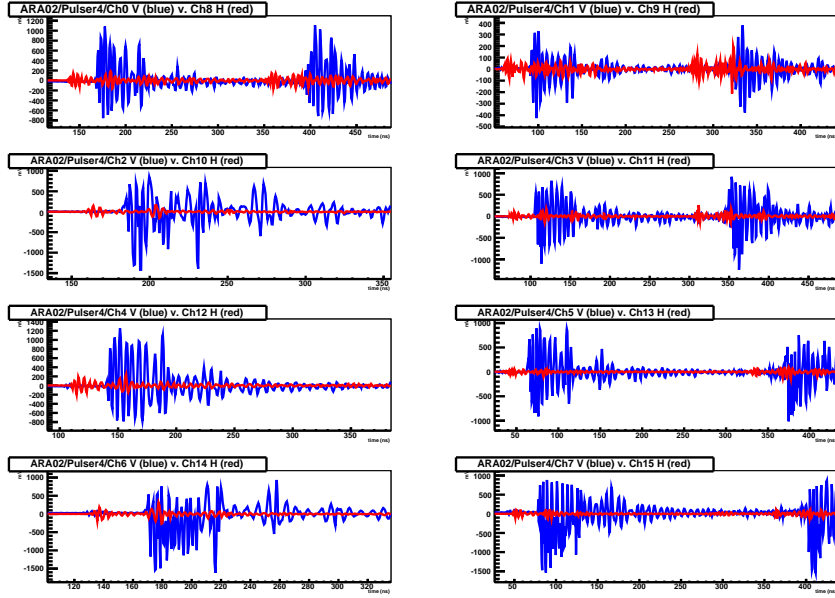


Figure 5: ICS1 waveform captures registered by ARA-2 station showing 16 channels in 8 H/V co-located pairs (blue=VPol [Channels 0–7]; red=HPol [Channels 8–15], with significantly smaller amplitude). The QD and QR signals, separated by hundreds of ns, are clearly evident in five of the eight panels. We also observe a time advance of the lower-amplitude HPol channels (red) relative to the VPol channels.

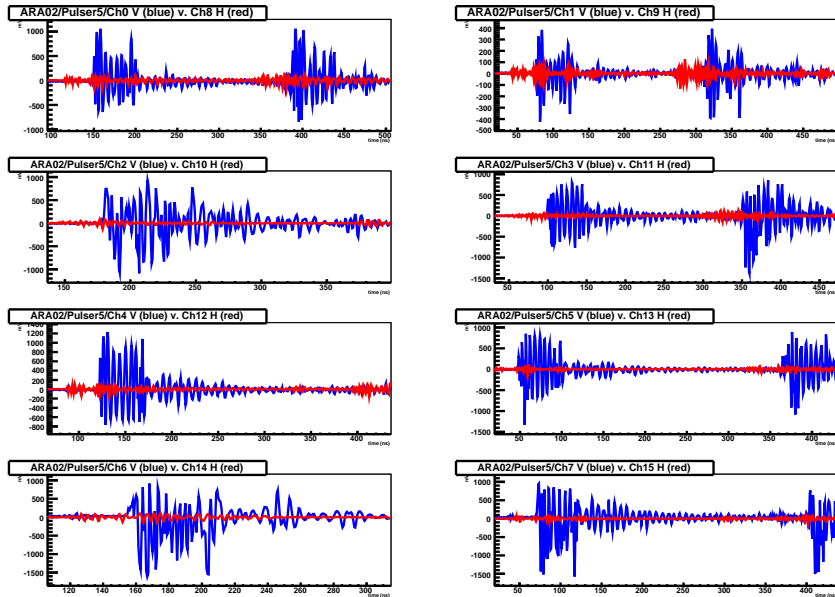


Figure 6: ICS22 waveform captures registered by ARA-2 station showing 16 channels in 8 H/V pairs (blue=VPol [Channels 0–7]; red=HPol [Channels 8–15]).

may have suffered damage after deployment<sup>1</sup>, resulting in imperfect coupling of the transmitter itself to the antenna used to broadcast the signal. Such imperfect coupling can result in loss of fidelity, as well as enhanced cross-polarization gain.

The observed received HPol signals, having magnitude  $\sim 5\text{--}10\%$  relative to VPol, from the nominally deep VPol transmitters is somewhat unexpected. In addition to possible HPol emission at the source, such an effect might arise from (at least) two sources, in isolation or in combination:

- cross-talk at the electronics level between VPol and HPol DAQ electronics traces, and/or mutual inductance between the receiver antennas (the fact that the HPol antennas are in the null of the VPol beam pattern notwithstanding), and/or cross-polarized VPol response from a dominantly HPol receiver antenna, all of which should lead to observed H/V signals which are simultaneous in time. This is, however, inconsistent with observations of local in-ice VPol calibration pulser transmitter signals, at distances of approximately 30-50 meters from the receiver array, which show no evident HPol signals comparable to those observed here.
- An ice-related effect, including:
  - Inclined conducting layers within the ice, which act as an *in situ* polarizer.
  - “circular” birefringence, for which the birefringence basis is Left Circular Polarization vs. Right Circular Polarization, and which could “rotate” a pure VPol signal at the source to a mixture of VPol and HPol, resulting in, on average, an equal admixture of VPol and HPol propagating signals. The actual relative strengths of the two components would roughly vary linearly with distance. The fact that the HPol/VPol received signal amplitudes appear to be more-or-less constant, in all channels, for all receiver stations, disfavors this hypothesis.
  - “linear” birefringence, in which the signal projects onto two (presumably perpendicular) propagation axes, referred to as the “ordinary” (“O”, with a refractive index  $n_O$  and a ‘fast’ propagation velocity  $c_0/n_O$ , with  $c_0$  the vacuum velocity of light) or “extra-ordinary” (“E”, with a ‘slow’ propagation velocity  $c_0/n_E$ ) axes. Upon arrival at the receiver, each of the O and E signals then project back onto the receiver antenna axis, resulting in an expected doublet of signals for both V or H, with amplitude dependent on the inclination angle of the underlying birefringent basis relative to “true” horizontal/vertical, and a separation time dependent on the magnitude of the  $n_O - n_E$  difference.

We consider the last of these hypotheses in more detail in Section 3.

#### 2.2.1. Comparison of observed D-R time difference against model

The observed QD/QR time delays can be used to discriminate between putative  $n(z)$  models. Several functional  $n(z)$  forms were tested against the measured timings. These included:

- Krav04:  $n(z)=1.37-(4.6z+13.72z^2)$  for  $z > -0.18$  km, as suggested by a polynomial fit to direct radio wavespeed measurements at South Pole[25].
- Model 2:  $n(z)=0.8+0.98/(1+\exp(30z))$
- ARA:  $n(z)=1.78-0.43\exp(13.2z)$ ,

with  $z$  in units of km, and increasingly negative with increasing depth. The last two exponential forms match the density dependence expected in a gravitational field. For each putative model, we calculate the sum, over all 16 ARA channels, of the squared deviation between the measured (QR,QD) arrival time difference, and the time difference predicted by a ray tracing model, assuming a given  $n(z)$  form, as shown in Table 1. We find that the profile  $n(z)=1.78-0.43\exp(13.2z)$  currently used in the ARA Monte Carlo simulation provides the best fit to both the available density data (presented in [20]), and also to the measured time differences between the QR and QD rays, observed in our experimental data. This functional form also matches the  $n_{surface}(z=0)=1.35$  and  $n_{deep}(z<-0.2)\rightarrow 1.78$  boundary conditions, consistent with density measurements at the South Pole.

Channel-by-channel, Figure 7 compares the calculated, expected time difference between the arrival of the QD and QR rays using our putative  $n(z)$  model (the default ARA model) with data. Given the inherent uncertainty in discerning hit times algorithmically, the two show acceptable agreement.

#### 2.3. QD vs. QR zenith angle direction reconstruction

The pre-saturation leading-edges of the received waveforms are adequate to infer source timing, and therefore source location reconstruction. Using the calibrated station geometry, one can calculate the zenith angle of the arriving rays and verify their consistency with the QR/QD arrival-angle hypothesis. For this reconstruction, we determine the incidence angles for the set of all QD rays, and the set of all QR rays, separately and independently. As shown in

---

<sup>1</sup>Unfortunately, the cross-polarization characteristics of the transmitter were not measured prior to deployment.

ARA station	Functional Form	$\Sigma(\delta_t^{QD-QR}(Model - Data))^2$ (ns <sup>2</sup> ) (IC22S/IC1S)
2	Krav04	652230/1378220
2	Model 2	576483/1014030
2	ARA	61752/23360
3	Krav04	1099209/487622
3	Model 2	974600/391978
3	ARA	72309/43107

Table 1: Comparison of index-of-refraction model predictions to measured QD-QR time differences. Numbers in third column represent sum, over all channels, of squares of differences between model-predicted (QD,QR) time difference relative to measurement, for IC22S and IC1S double pulses, respectively.

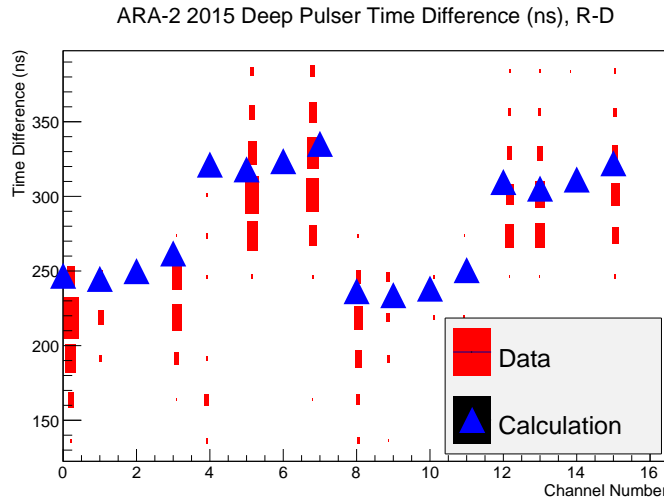


Figure 7: Measured time differences between QD and QR rays for ARA-2 2017 deep pulser data, compared with calculation.

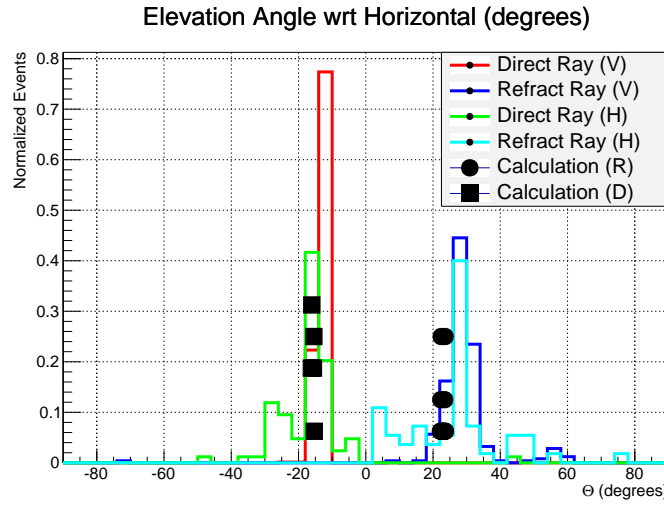


Figure 8: Calculated zenith angle of incidence, relative to horizontal, for ARA-2 2017 deep pulser data. Histograms show the measured incidence angles for the QD and QR rays for both VPol (red for QD and blue for QR) and also HPol (green for QD and cyan for QR) receiver channels. Points overlaid show expectation from model simulation, based on ARA index-of-refraction profile. We note an approximately 40 degree difference between reception angle for QD vs. QR.

Figure 8, the earlier QD set of pulses arrive from below the horizontal; the later QR set of pulses arrive from above the horizontal, consistent with expectations for the QD and QR rays, respectively.

#### 2.4. Source Reconstruction in both Azimuth and Elevation

The standard ARA interferometry-based analysis event reconstruction[10] cross-correlates the waveforms ( $\text{QD}_i$ ,  $\text{QD}_j$ ), where  $\text{QD}_i$  and  $\text{QD}_j$  are the quasi-direct signals on channels i and j. Through a fast look-up table of calculated, expected arrival times, a set of predicted  $\delta t_{ij}$  ( $r, \theta, \phi$ ) are produced for every possible source position. These are used to sample the Hilbert envelope of the  $i-j$  cross correlation function and give weights to the putative  $\delta t_{ij}$ [26]. For this particular study, a second table for QR signal arrival times is built, and the cross correlation is extended to include all the available QR signals. Thus, the full reconstruction incorporates contributions from all possible QD–QD, QD–QR, and QR–QR pairs, and assesses the consistency of a putative 1 square degree source position in the sky with the ensemble of observed QD and QR hit times. The source location map constructed for a deep pulser event is shown in Figure 9; the brightest  $1^\circ \times 1^\circ$  pixel in that map is identified as the best-fit source position. The distribution of reconstructed deep pulser directions, as defined by the maximum intensity pixel in each event, is presented in Figures 10 and 11. In general, we reconstruct the source direction with accuracy 1–2 degrees in both azimuth and elevation.

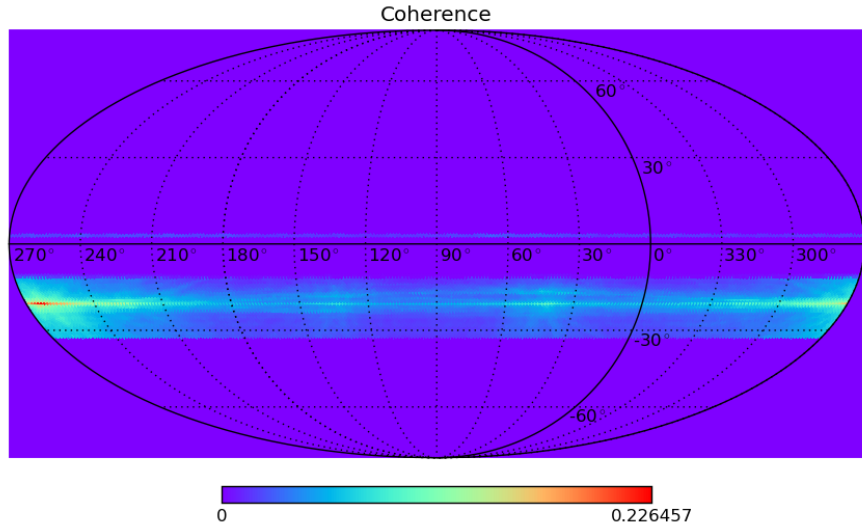


Figure 9: Reconstructed interferometric image of ARA ICS22 deep pulser, using standard azimuth (horizontal) vs. zenith (i.e., elevation [vertical]) coordinates. Highest intensity pixel is visible in lower left.

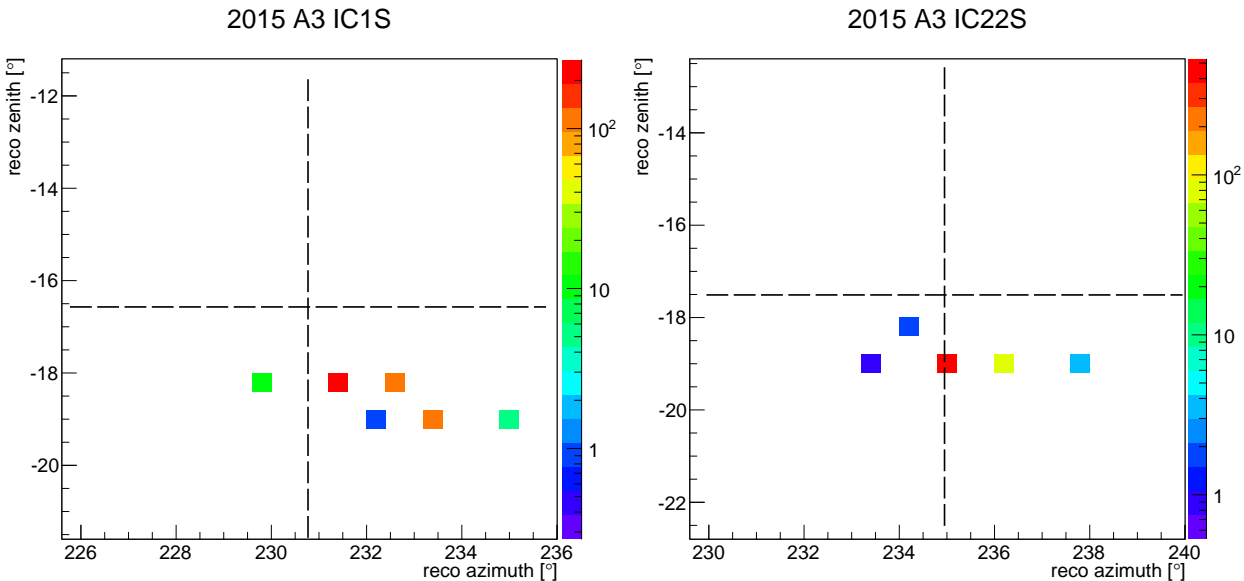


Figure 10: ARA-3 azimuthal ( $\phi$ ) vs. zenith ( $\theta$ ) reconstructed source locations during time when ICS1 (left) and ICS22 (right) was pulsing. Dashed lines indicate “true” source location. There are two and zero outliers, respectively, not shown, beyond the plot boundaries.

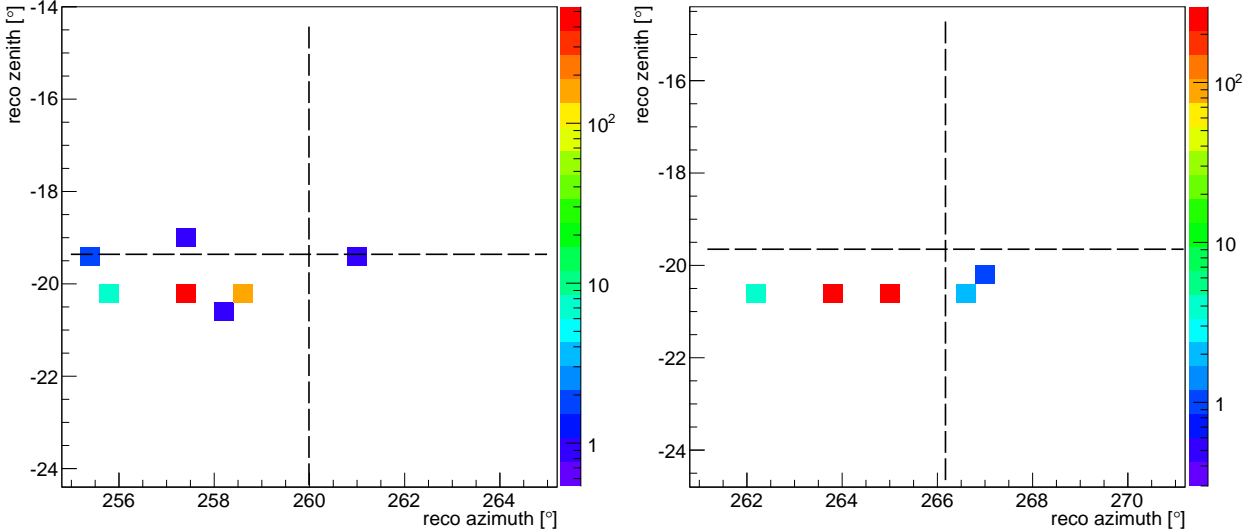


Figure 11: ARA-2 azimuthal ( $\phi$ ) vs. zenith ( $\theta$ ) reconstructed source locations during time when IC1S (left) and ICS22 (right) were pulsing. There are 11 and 9 outliers, respectively, not shown, beyond the plot boundaries.

## 2.5. Range Reconstruction

The reconstruction from QD rays permits a good direction to the vertex, but determining the distance to the vertex is more difficult, as (absent additional QR information) this requires a determination of the curvature of the radiation front, which is limited by both the modest 20 m baseline of the station and the inherent signal arrival time resolution. There is  $\sim 100$  ps resolution in the time-difference between hit times, as determined by waveform cross-correlations. If the antenna locations, the index-of-refraction profile, individual channel cable delays and antenna group delays were all exactly known, the wavefront reconstruction would be entirely determined by this 100 ps timescale. Unfortunately, there are significant uncertainties in all of these quantities, which have a combined error at least an order of magnitude larger than the 100 ps timescale.

In the case where both the QD and QR signals are observed, however, comparison of the QD with the QR signal arrival times allows improved estimation of range-to-vertex without use of wavefront curvature information. Considering the quasi-reflected ray as if it were detected by an “image” station above the ice surface, for a 200m deep receiver, the baseline for reconstruction by both rays is of order twice the depth of the station, or 400m, enabling a full 3D reconstruction.

Similar to the procedure followed for interferometric reconstruction of azimuth and elevation, we can empirically determine the source range most consistent with the observed QD-QR time difference. The results of this exercise are presented in Figure 12 for ARA-2 reconstruction of the ICS1 and ICS22 pulsers. We observe that deviations in elevation reconstruction of order one degree typically translate into range errors of tens of percent. Table 2 summarizes our results numerically, and indicates that we can use the time difference between QD and QR signals to estimate the range to within  $\sim 15\%$ .

Station/Source	Nominal/Reconstructed		
	$\theta$ (deg)	$\phi$ (deg)	r (m) (deviation)
A2/IC1S	$-19.36/-20.19 \pm 0.07$	$259.99/257.6 \pm 0.56$	$3666 \pm 543/4215 (+15\%)$
A2/IC22S	$-19.65/-20.64 \pm 0.02$	$266.17/264.4 \pm 0.64$	$3609 \pm 530/4896 (+36\%)$
A3/IC1S	$-16.57/-18.21 \pm 0.35$	$230.77/232.2 \pm 0.95$	$4269 \pm 696/4711 (+10\%)$
A3/IC22S	$-17.51/-18.9 \pm 0.05$	$234.95/235.2 \pm 0.45$	$4040 \pm 603/4298 (+6\%)$

Table 2: Summary of reconstructed deep pulser source locations compared with “known” source location. For each pair presented, the first value represents the nominal (‘true’) value; the second value (in bold) represents the value our source reconstruction algorithm returns, along with the associated statistical error.

## 3. Study of H/V relative signal timing and evidence for birefringence

The pathlengths from the ICS1 and ICS22 transmitters to the ARA receiver stations is of order 3–5 km, along a predominantly horizontal trajectory. To our knowledge, this is the longest horizontal baseline used for testing electro-

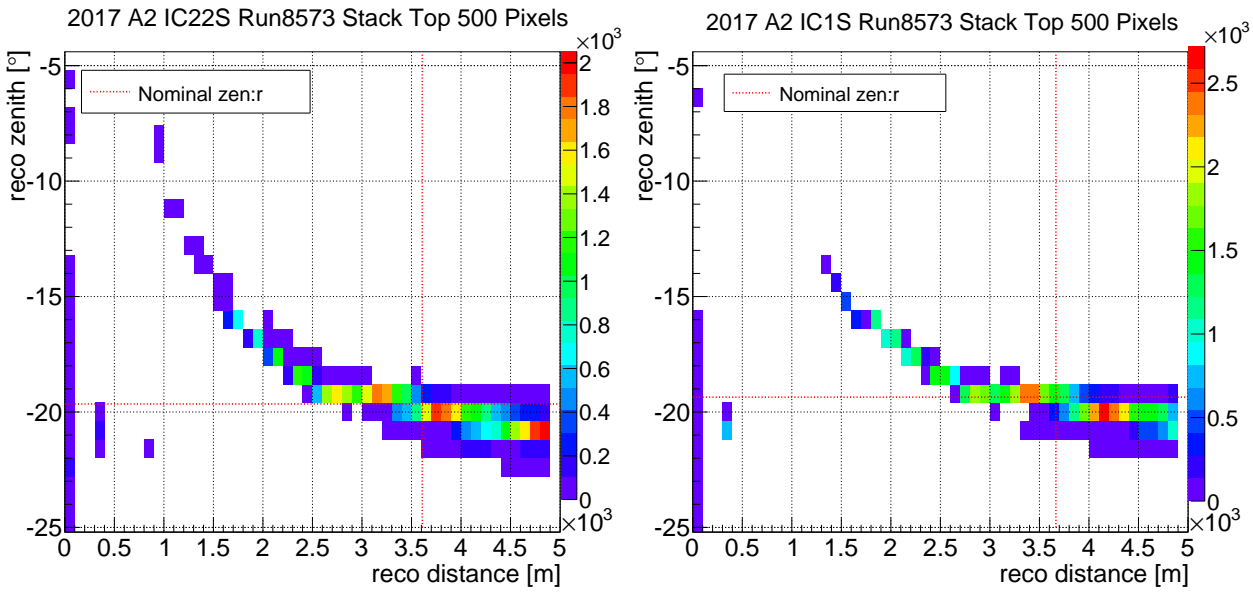


Figure 12: ARA-2 “stacked” pixels range vs. elevation( $\theta$ ) distribution. Ranking by source likelihood, we plot the (range,  $\theta$ ) of the highest 500 pixels of each event. Shown is this stacked distribution from events during time when ICS22 was pulsing. The color intensity scale indicates the frequency of a putative (range,  $\theta$ ) point.

magnetic signal propagation, of any type, in the polar regions. As such, this provides a singular opportunity to probe the wavespeed variation with polarization. As shown in Figures 5 and 6, and zoomed for two ARA-2 channels in Figure 13, the HPol signal from the deep pulsers is clearly advanced by 20–30 ns, for both ARA-2 and ARA-3, relative to the signal registered in the co-located VPol receiver. Since the elevation angles of the signal arrival are within  $\sim$ 20 degrees of horizontal (Figure 8), the expected signal arrival times should be nearly identical for this H/V channel pair.

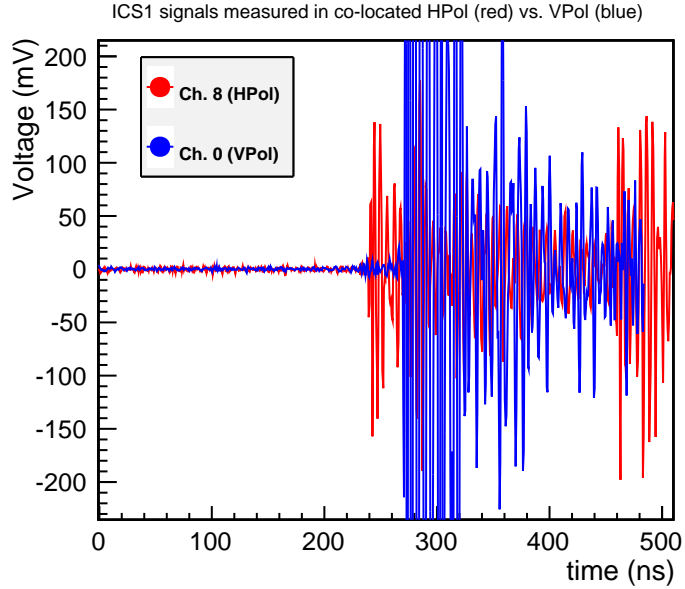


Figure 13: Zoom of channels 0 (VPol) and 8 (co-located HPol) for signals received from IC1S, illustrating time difference between HPol and VPol waveforms.

Given that ice crystals are known to exhibit linear, but not circular birefringence[27], we consider the arrival of the HPol signals prior to the arrival of the VPol signals to be most plausibly explained by linear ice birefringence, although this requires some bulk ice crystal alignment. In the absence of any ice crystal directional asymmetry, one would expect the radio-frequency wavespeed to be uniform in all directions. Isotropy of the Antarctic ice sheet is broken in two directions – vertically, due to the gradient in hydrostatic pressure with depth and resulting in a compressional stress on ice crystals, and horizontally, due to the local ice flow direction and resulting in a torsional strain, and therefore, a preferred axis laterally.

To calculate the magnitude of the birefringent asymmetry between H/V pairs in data, we must correct for the 2–3 meter shallower deployment depth of the H-pol antenna of the pair, leading to a timing correction  $\delta_t^{corr} \approx n(z)\delta z(\sin\theta_i)/c_0$ ,

with  $\delta z$  the vertical separation of the HPol vs. VPol receivers,  $\theta_i$  the ray incidence angle relative to the horizontal,  $n(z)$  the local index-of-refraction, and  $c_0$  the velocity of light in vacuum. After applying this correction, the calculated HPol advance relative to same-string VPol channels is summarized in Figure 14, for deep pulser signals observed in ARA-2 and ARA-3. In the Figure, the horizontal value corresponds to the  $i^{th}$  VPol receiver channel; the y-value gives the measured time difference, after correction, relative to the zero birefringence expectation, for the nearest HPol channel. We note that prior to the vertical-displacement correction described above, the ARA-2 and ARA-3  $\delta_t^{V-H}$  values are

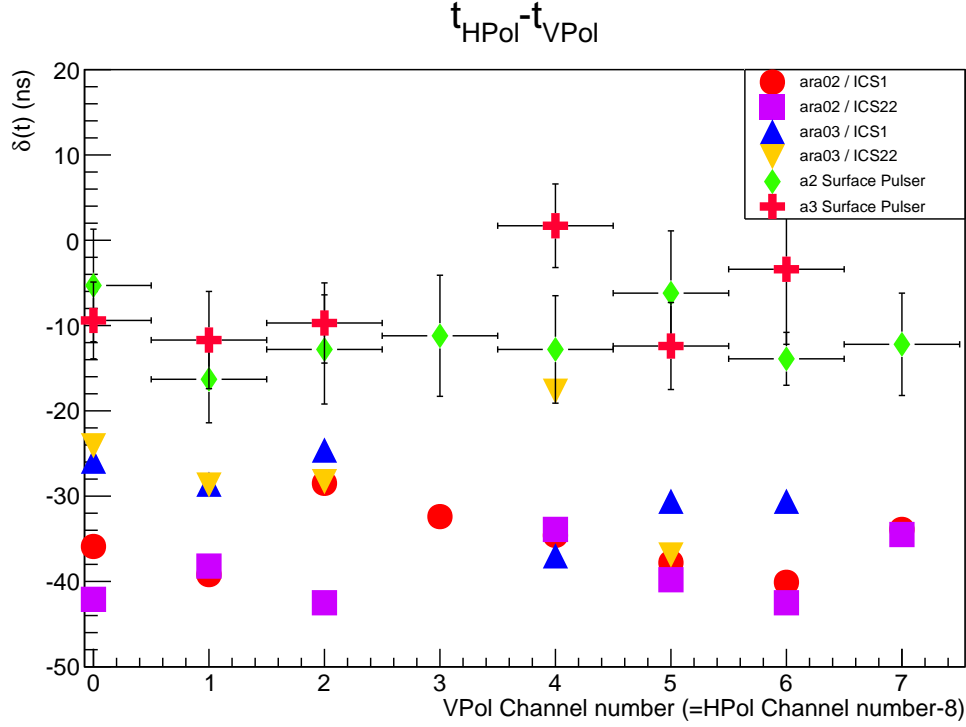


Figure 14:  $\delta_t^{V-H}$  ARA-2 and ARA-3 data. x-axis refers to channel number of vertically-polarized receiver; y-value gives the (corrected) time difference between registered signal arrival time on the co-located HPol channel for that hole/station relative to registered VPol signal arrival time for an H/V pair. For comparison, results from a surface transmitter survey, at lateral distances 100–200 meters from each station, are also shown. In the absence of birefringence and/or timing miscalibration, all data points should approximately lie on the x-axis, consistent with zero propagation-time difference. We observe that ARA-2 has typical time differences of 30–40 ns relative to a propagation time of approximately 20  $\mu$ s; for ARA-3, values are approximately 5–10 ns smaller. Systematic errors on ARA2 and ARA3 H/V time differences are indicated by surface pulser survey data, and estimated at 3–4 ns.

consistent with each other; after correction, the value of  $\delta_t^{V-H}$ (ARA-3) is typically 15–20% smaller than for ARA-2, despite the fact that the propagation distance from the deep pulsers to the ARA-3 station is approximately 15% longer. A simple explanation for this is, of course, that the H-V pair vertical separations have been mis-tabulated by  $\sim 1.5$  meters. Alternately, in the birefringent model, this result may suggest that the vector from the deep pulsers to ARA-3 is more aligned with the underlying birefringent basis than ARA-2. Geometrically, the line from IC1 to ARA-2 is very nearly directly perpendicular to the horizontal ice flow direction; the line from IC1 to ARA-3 is offset by  $\sim 30$  degrees relative to that line (Figure 2).

### 3.1. Cross-checks

Aside from birefringence, the observed time delay between the arrival of the HPol vs. VPol signals could, in principle, be due to a simple mis-calibration of the HPol vs. VPol receivers. To test this, we considered data taken during an RF survey of stations 2 and 3 for which a surface transmitter was broadcast from a dipole, with its long axis inclined at an angle of 45 degrees relative to vertical, within 200 m laterally of each station. Given the transmitter inclination angle, these data should have roughly equal amounts of HPol and VPol broadcast signal. We observe in Figure 14 an offset between H and V of approximately  $-5$  –  $-10$  ns, consistent in sign, but of somewhat smaller magnitude than we observe for broadcasts from the deep pulsers.<sup>2</sup> From inspection of the waveforms themselves, we observe a sharper rise time for the VPol signals, which we attribute to the smaller bandwidth of the HPol antennas compared to VPol antennas; however, this effect should have the result of staggering, rather than advancing the peaks of the HPol signals relative to VPol. Therefore, pending additional investigation, we interpret these data as conditional evidence for birefringence for signals propagating from the  $\sim 1450$ -m deep pulsers.

<sup>2</sup>This effect is, in principle, consistent with horizontal birefringence through the upper firn layer of the ice sheet.

The evidence for birefringence must be interpreted in the context of previous results. The RICE Collaboration observed birefringence in vertical propagation of rays which reflect off the bedrock[24]. They conclude that the time delays accumulate mostly in the deep ice, below about 1200 m, as they observe no evidence for birefringence in the upper ice. This is consistent with a crystal orientation fabric (COF) determined by shear in the ice flow[28], which is rather modest in the upper ice. The current results, however, suggest that the upper ice does exhibit birefringence for horizontal propagation. If the COF of the upper ice is dominated by gravity, then a vertical ray would not exhibit birefringence, but a horizontal ray would since the Vpol would be along the net  $c$ -axis while Hpol would be transverse to it.

#### 4. Conclusions and Discussion

As shown herein, the time difference between the registration of direct vs. refracted (or reflected) rays permits an estimate of the range-to-vertex, once the azimuth and elevation of an incident signal has been determined through interferometry. Additionally, if the time delay between signal arrival times for HPol vs. VPol receivers ( $\delta_t^{V-H}$ ) can be quantified for all geometries, then an additional constraint on the event geometry may be afforded by the measured magnitude of birefringent time difference.

At South Pole, the ARA strategy thus far has been based on receiver deployment at approximately 200 meters. In evaluating the optimal depth to site a future radio receiver array, one must consider the following:

- The launch angle difference between the QD and the QR rays increases as the receiver depth  $z_{Rx}$  also increases. The data presented here are based on reception of signals from an in-ice transmitter dipole with a very broad beam pattern, however, the Cherenkov cone from a neutrino has only a 1–2 degree transverse thickness.
- As the receiver depth  $z_{Rx}$  increases to 200 meters, the measured time difference between reception of the QD and the QR rays also increases, approaching one microsecond, and therefore requiring  $\sim 2\mu s$  of data buffering, per channel, to ensure capturing both the QD and the QR rays.

These considerations, combined with the logistical overhead associated with drilling ice-holes down to 200 meters, suggest that a shallow receiver array, deployed at a depth of 25–50 meters may retain high efficiency for observation of the QD and QR rays from a neutrino interaction, have good (of order hundreds of meters) range resolution, and sufficient timing resolution to measure  $\delta_t^{V-H}$  (giving a redundant measure of range-to-vertex) within a tight (512 ns) waveform capture time window.

The observations presented here are a small part of the radio-glaciological data needed to fully characterize RF propagation of relevance to the ARA experiment. In this regard, within the last two years, a 1700-m deep ice core, 0.5–several km from current ARA stations, was extracted from the South Pole ice[29]. With the consent of the NSF, a piezo-electric technology radio-frequency transmitter, based on the same model as that employed in the balloon-borne HiCal experiment[30], was used in January, 2018 to sample the upper 800 meters of the SPICE borehole. The beam pattern of that transmitter is somewhat more isotropic than that used in the deep pulser studies described herein, and, by design, contains significant HPol as well as VPol content. Those data are currently under analysis. In parallel, we are working to develop a first-principles model, based on measurements of the crystal orientation fabric, that absolutely predicts, for any polarization and  $k$ -vector, an observed birefringent asymmetry.

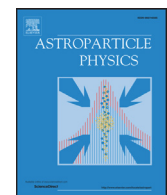
#### 5. Acknowledgments

We thank the National Science Foundation for their generous support through Grant NSF OPP-1002483 and Grant NSF OPP-1359535. We further thank the Taiwan National Science Councils Vanguard Program: NSC 102-2628-M-002-010 and the Belgian F.R.S.-FNRS Grant4.4508.01. We are grateful to the U.S. National Science Foundation-Office of Polar Programs and the U.S. National Science Foundation-Physics Division. We also thank the University of Wisconsin Alumni Research Foundation, the University of Maryland and the Ohio State University for their support. Furthermore, we are grateful to the Raytheon Polar Services Corporation and the Antarctic Support Contractor, for field support. A. Connolly thanks the National Science Foundation for their support through CAREER award 1255557, and also the Ohio Supercomputer Center. K. Hoffman likewise thanks the National Science Foundation for their support through CAREER award 0847658. A. Connolly, H. Landsman, and D. Besson thank the United States-Israel Binational Science Foundation for their support through Grant 2012077. A. Connolly, A. Karle, and J. Kelley thank the National Science Foundation for the support through BIGDATA Grant 1250720. B. A. Clark thanks the National Science Foundation for support through the Graduate Research Fellowship Program Award DGE-1343012. D. Besson and A. Novikov acknowledge support from National Research Nuclear University MEPhI (Moscow Engineering Physics Institute). R. Nichol thanks the Leverhulme Trust for their support.

## References

- [1] G. Askaryan. Excess negative charge of an electron-photon shower and its coherent radio emission. *Soviet Physics JETP*, 14:441–443, 1962.
- [2] G. A. Askaryan. Excess negative charge of electron-photon shower and the coherent radiation originating from it. radiorecording of showers under the ground and on the moon. *J. Phys. Soc. Japan*, Vol. 17, Suppl. A-III:257, 1962.
- [3] G. A. Askaryan. Coherent Radio Emission from Cosmic Showers in Air and in Dense Media. *Soviet Phys. JETP*, 21:658, 1965.
- [4] Francis Halzen. High-energy neutrino astrophysics. *Nature Physics*, 13(3):232–238, 2017.
- [5] Ralph Engel, David Seckel, and Todor Stanev. Neutrinos from propagation of ultrahigh energy protons. *Physical Review D*, 64(9):093010, 2001.
- [6] Kumiko Kotera, Denis Allard, and Angela V Olinto. Cosmogenic neutrinos: parameter space and detectability from PeV to ZeV. *Journal of Cosmology and Astroparticle Physics*, 2010(10):013, 2010.
- [7] Markus Ahlers and Francis Halzen. Minimal cosmogenic neutrinos. *Physical Review D*, 86(8):083010, 2012.
- [8] Katsuaki Asano and Peter Mszros. Ultrahigh-energy cosmic ray production by turbulence in gamma-ray burst jets and cosmogenic neutrinos. *Phys. Rev.*, D94(2):023005, 2016.
- [9] IceCube Collaboration et al. Multimessenger observations of a flaring blazar coincident with high-energy neutrino icecube-170922a. *Science*, 361(6398):eaat1378, 2018.
- [10] P. Allison and J. Auffenberg and R. Bard and J. J. Beatty and D. Z. Besson and S. Boeser and C. Chen and P. Chen and A. Connolly and J. Davies and M. DuVernois and B. Fox and P. W. Gorham and E. W. Grashorn and K. Hanson and J. Haugen and K. Helbing and B. Hill and K. D. Hoffman and M. Huang and M. H. A. Huang and A. Ishihara and A. Karle and D. Kennedy and H. Landsman and A. Laundrie and T. C. Liu and L. Macchiarulo and K. Mase and T. Meures and R. Meyhandan and C. Miki and R. Morse and M. Newcomb and R. J. Nichol and K. Ratzlaff and M. Richman and L. Ritter and B. Rotter and P. Sandstrom and D. Seckel and J. Touart and G. S. Varner and M.-Z. Wang and C. Weaver and A. Wendorff and S. Yoshida and R. Young. Design and initial performance of the Askaryan Radio Array prototype EeV neutrino detector at the South Pole. *Astroparticle Physics*, 35(7):457–477, 2012.
- [11] P. Allison, J. Auffenberg, R. Bard, J. J. Beatty, D. Z. Besson, C. Bora, C.-C. Chen, P. Chen, A. Connolly, J. P. Davies, M. A. DuVernois, B. Fox, P. W. Gorham, K. Hanson, B. Hill, K. D. Hoffman, E. Hong, L.-C. Hu, A. Ishihara, A. Karle, J. Kelley, I. Kravchenko, H. Landsman, A. Laundrie, C.-J. Li, T. Liu, M.-Y. Lu, R. Maunu, K. Mase, T. Meures, C. Miki, J. Nam, R. J. Nichol, G. Nir, A. O'Murchadha, C. G. Pfendner, K. Ratzlaff, M. Richman, B. Rotter, P. Sandstrom, D. Seckel, A. Shultz, J. Stockham, M. Stockham, M. Sullivan, J. Touart, H.-Y. Tu, G. S. Varner, S. Yoshida, and R. Young. First constraints on the ultra-high energy neutrino flux from a prototype station of the Askaryan Radio Array. *Astroparticle Physics*, 70:62–80, 2015.
- [12] P. Allison, R. Bard, J. J. Beatty, D. Z. Besson, C. Bora, C.-C. Chen, C.-H. Chen, P. Chen, A. Christenson, A. Connolly, J. Davies, M. Duvernois, B. Fox, R. Gaior, P. W. Gorham, K. Hanson, J. Haugen, B. Hill, K. D. Hoffman, E. Hong, S.-Y. Hsu, L. Hu, J.-J. Huang, M.-H. A. Huang, A. Ishihara, A. Karle, J. L. Kelley, D. Kennedy, I. Kravchenko, T. Kuwabara, H. Landsman, A. Laundrie, C.-J. Li, T. C. Liu, M.-Y. Lu, L. Macchiarulo, K. Mase, T. Meures, R. Meyhandan, C. Miki, R. Morse, J. Nam, R. J. Nichol, G. Nir, A. Novikov, A. O'Murchadha, C. Pfendner, K. Ratzlaff, M. Relich, M. Richman, L. Ritter, B. Rotter, P. Sandstrom, P. Schellin, A. Shultz, D. Seckel, Y.-S. Shiao, J. Stockham, M. Stockham, J. Touart, G. S. Varner, M.-Z. Wang, S.-H. Wang, Y. Yang, S. Yoshida, and R. Young. Performance of two Askaryan Radio Array stations and first results in the search for ultrahigh energy neutrinos. *Physical Review D*, 93(8):082003, 2016.
- [13] AG Vieregg, K Bechtol, and A Romero-Wolf. A technique for detection of PeV neutrinos using a phased radio array. *Journal of Cosmology and Astroparticle Physics*, 2016(02):005, 2016.
- [14] S. W. Barwick and E. C. Berg and D. Z. Besson and E. Cheim and T. Duffin and J. C. Hanson and S. R. Klein and S. A. Kleinfelder and T. Prakash and M. Piasecki and K. Ratzlaff and C. Reed and M. Roumi and A. Samanta and T. Stezelberger and J. Tatar and J. Walker and R. Young and L. Zou. Design and Performance of the ARIANNA Hexagonal Radio Array Systems. *IEEE Trans. Nucl. Sci.*, 62(5):2202–2215, 2015.
- [15] SW Barwick, DZ Besson, Alexander Burgman, E Chiem, Allan Hallgren, JC Hanson, SR Klein, SA Kleinfelder, A Nelles, C Persichilli, et al. Radio detection of air showers with the ARIANNA experiment on the Ross Ice Shelf. *Astroparticle Physics*, 90:50–68, 2017.

- [16] P. W. Gorham, P. Allison, S W. Barwick, and et al. The Antarctic Impulsive Transient Antenna ultra-high energy neutrino detector: Design, performance, and sensitivity for the 2006-2007 balloon flight. *Astropart. Phys.*, 32(1):10 – 41, 2009.
- [17] Barwick, S and Besson, D and Gorham, P and Saltzberg, D. South Polar in situ radio-frequency ice attenuation. *Journal of Glaciology*, 51(173):231–238, 2005.
- [18] G de Q Robin. Velocity of radio waves in ice by means of a bore-hole interferometric technique. *Journal of Glaciology*, 15(73):151–159, 1975.
- [19] Austin Kovacs, Anthony J Gow, and Rexford M Morey. A reassessment of the in-situ dielectric constant of polar firn. Technical report, COLD REGIONS RESEARCH AND ENGINEERING LAB HANOVER NH, 1993.
- [20] SW Barwick, EC Berg, DZ Besson, G Gaswint, C Glaser, A Hallgren, JC Hanson, SR Klein, S Kleinfelder, L Köpke, et al. Observation of classically forbidden electromagnetic wave propagation and implications for neutrino detection. *arXiv preprint arXiv:1804.10430*, 2018.
- [21] S.H. Wang et al. Calibration, Performance, and Cosmic Ray Detection of ARIANNA-HCR Prototype Station. In *Proceedings of the 35th ICRC, Busan, Korea*, volume 1, pages 1–8, 2017.
- [22] Jordan Hanson. *The Performance and Initial Results of the ARIANNA Prototype*. PhD thesis, University of California, Irvine, July 2013.
- [23] C Deaconu, AG Vieregg, SA Wissel, J Bowen, S Chipman, A Gupta, C Miki, RJ Nichol, and D Saltzberg. Measurements and modeling of near-surface radio propagation in glacial ice and implications for neutrino experiments. *arXiv preprint arXiv:1805.12576*, 2018.
- [24] Dave Besson, Ilya Kravchenko, Andres Ramos, and Juliet Remmers. Radio Frequency Birefringence in South Polar Ice and Implications for Neutrino Reconstruction. *Astropart. Phys.*, 34:755–768, 2011.
- [25] Ilya Kravchenko, David Besson, and Josh Meyers. In situ index-of-refraction measurements of the south polar firn with the rice detector. *Journal of Glaciology*, 50(171):522–532, 2004.
- [26] M Beheler-Amass, M Beydler, A Karle, JL Kelley, and MY Lu. Interferometric Neutrino Event Reconstruction in Inhomogeneous Media with the Askaryan Radio Array. 1:1–8, 2017.
- [27] Hargreaves, ND. The radio-frequency birefringence of polar ice. *Journal of Glaciology*, 21(85):301–313, 1978.
- [28] P Buford Price, Oleg V Nagornov, Ryan Bay, Dmitry Chirkin, Yudong He, Predrag Miocinovic, Austin Richards, Kurt Woschnagg, Bruce Koci, and Victor Zagorodnov. Temperature profile for glacial ice at the South Pole: Implications for life in a nearby subglacial lake. *Proceedings of the National Academy of Sciences*, 99(12):7844–7847, 2002.
- [29] Kimberly Ann Casey, TJ Fudge, TA Neumann, EJ Steig, MGP Cavitte, and DD Blankenship. The 1500 m South Pole ice core: recovering a 40 ka environmental record. *Annals of Glaciology*, 55(68):137–146, 2014.
- [30] PW Gorham, P Allison, O Banerjee, JJ Beatty, K Belov, DZ Besson, WR Binns, V Bugaev, P Cao, C Chen, et al. Antarctic Surface Reflectivity Measurements from the ANITA-3 and HiCal-1 Experiments. *Journal of Astronomical Instrumentation*, page 1740002, 2017.



# Complex analysis of Askaryan radiation: A fully analytic treatment including the LPM effect and Cascade Form Factor<sup>☆</sup>



Jordan C. Hanson\*, Amy L. Connolly

*Center for Cosmological and AstroParticle Physics, Department of Physics, The Ohio State University, Columbus, OH 43210, United States*

## ARTICLE INFO

### Article history:

Received 16 May 2016

Revised 8 March 2017

Accepted 28 March 2017

Available online 30 March 2017

### Keywords:

Cosmogenic neutrinos

GZK effect

Askaryan effect

## ABSTRACT

The Askaryan effect describes coherent electromagnetic radiation from high-energy cascades in dense media with a collective charge. We present an analytic model of Askaryan radiation that accounts simultaneously for the three-dimensional form factor of the cascade, and quantum mechanical cascade elongation via the Landau-Pomeranchuk-Migdal effect. These calculations, and the associated open-source code, allow the user to avoid computationally intensive Monte Carlo cascade simulations. Searches for cosmogenic neutrinos in Askaryan-based detectors benefit from computational speed, because scans of Askaryan parameter-space are required to match neutrino signals. The Askaryan field is derived from cascade equations verified with Geant4 simulations, and compared with prior numerical and semi-analytic calculations. Finally, instructive cases of the model are transformed from the Fourier domain to the time-domain. Next-generation *in situ* detectors like ARA and ARIANNA can use analytic time-domain signal models to search for correlations with event candidates.

© 2017 Published by Elsevier B.V.

## 1. Introduction

The landmark observation of PeV neutrino interactions in Antarctic ice by the IceCube collaboration [1] has highlighted the urgency for progress in ultra-high energy cosmogenic neutrino (UHE- $\nu$ ) searches, at energies  $10^{16} - 10^{20}$  eV [2–4]. Cosmogenic neutrinos represent a long awaited prize in both astrophysics and particle physics, because of the potential to explain the origin of UHE cosmic rays (UHECR), as well as the chance to study electroweak interactions at record-breaking energies.

The GZK process is a  $p\gamma$  interaction yielding UHE- $\nu$  from the UHECR flux through the cosmic microwave background (CMB) [5,6]. UHECR models lead to the conclusion that  $100 \text{ km}^3$ -volume detectors are required to measure cosmogenic UHE- $\nu$  flux [7–10]. UHE- $\nu$  also present the possibility revealing physics beyond the Standard Model, via measurements of UHE- $\nu$  deep-inelastic scattering cross-sections [11,12]. Models matching simultaneously the PeV- $\nu$  flux from IceCube, the diffuse GeV gamma-ray flux, and the UHECR flux, are now placing constraints on cosmogenic UHE- $\nu$  flux [9,13,14].

The next generation of UHE- $\nu$  detectors is based on the Askaryan effect, in which a UHE- $\nu$  interaction produces a cascade

that radiates radio-frequency (RF) pulses from within a dielectric medium [15–17]. These detectors use the special RF properties of Antarctic ice, in order to search for UHE- $\nu$  cascades efficiently [18–20]. The Radio Ice Cernekov Experiment (RICE) conducted the pioneering search [21]. The Antarctic Impulsive Transient Antenna (ANITA) is a balloon-borne detector [22,23]. The Askaryan Radio Array (ARA), and the Antarctic Ross Ice Shelf Neutrino Array (ARIANNA) are two *in situ* detectors similar to RICE, but designed on a much larger scale [24–28]. The ExaVolt Antenna (EVA) is a proposed design to improve on the ANITA detection scheme [29].

The expected Askaryan RF pulse in the detectors must be understood in detail. Zas, Halzen, and Stanev (ZHS) created a Monte Carlo (MC) simulation which yielded the Askaryan field by tracking the radiation from every cascade particle above  $\approx 1 \text{ MeV}$ , using the Fraunhofer approximation [30]. This technique is computationally intensive and is difficult to scale to UHE- $\nu$  energies. Semi-analytic models [31–33] by Alvarez-Muniz, Romero-Wolf, Vazquez, and Zas (AVZ, ARVZ) solve Maxwell's equations, treating the cascade charge excess as a source current. These models require only the MC profile (charge versus depth) of the cascade. Semi-classical methods become fully analytic when the Greisen and Gaisser–Hillas treatments provide the profile [34].

Ralston and Buniy (RB) [35] presented a complex analysis of Askaryan radiation. This approach yields theoretical insight into observable properties of the field, while matching the ZHS MC. The model includes an explanation of signal causality, and merges

\* Open-source code associated with this work: <https://github.com/918particle/AskaryanModule>

\* Corresponding author.

E-mail addresses: [hanson.369@osu.edu](mailto:hanson.369@osu.edu), [918particle@gmail.com](mailto:918particle@gmail.com) (J.C. Hanson).

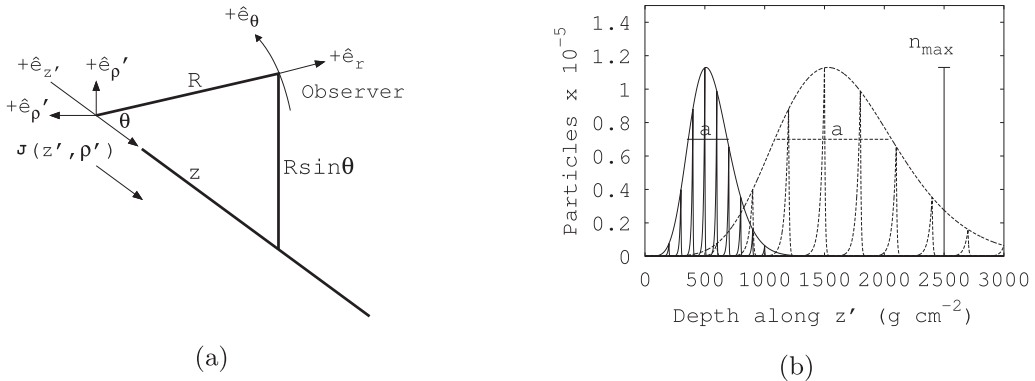


**Fig. 1.** (a) Coordinate systems. Un-primed coordinates refer to the observer, and primed coordinates refer to the reference frame of the vector current. (b) The curves represent the total charge content, with the instantaneous charge density (ICD) shown by the internal curves, versus depth after the first interaction in the medium. The solid curves were made for shower energy  $10^{14}$  eV and the dashed curves for a shower profile having been stretched by either the LPM effect, or simply by going to a higher energy. The Greisen model was used for the form of the cascade profile. The  $n_{\max}$  parameter will refer to the negative charge excess.

coherence zones (Near-Field, Fresnel, Fraunhofer) continuously. A proper handling of non-Fraunhofer zones is vital for lowering energy thresholds in the *in situ* Askaryan detectors, because the lowest-energy events are only detectable above thermal backgrounds when the neutrino vertex is in coherence zones other than the Fraunhofer zone. Lowering energy thresholds is critical for maximizing detected UHE- $\nu$ , because the flux is expected to increase with decreasing energy.

We generalize the RB model by including two effects. We derive and implement the three-dimensional Cascade Form Factor from lateral MC charge diffusion,  $\tilde{F}(\omega, \theta)$ , and we introduce smooth cascade-elongation from the Landau-Pomeranchuk-Migdal (LPM) effect. Among the consequences of these extensions to RB are the constraint of the high-frequency ( $\approx 1$  GHz) Fourier modes and the solid angle of the radiation. Parameters in  $\tilde{F}(\omega, \theta)$  are derived from Geant4 MC ( $> 1$  PeV) using a sub-cascade technique, and the electromagnetic MC cascades match the Greisen treatment, laterally and longitudinally [36]. Finally, the functional form of the Askaryan field is derived for special cases useful for Askaryan signal template-creation for UHE- $\nu$  searches with ARA/ARIANNA.

### 1.1. Advantages of a fully analytic treatment with the form factor and LPM elongation

The challenge of detecting UHE- $\nu$  with ARA/ARIANNA is one of distinguishing natural RF pulses from backgrounds. Every RF antenna observes thermal radiation associated with the temperature of the observed medium. ARA/ARIANNA background rates are a mixture of thermal radiation from ice, the sky, and the Milky Way [24,28,37]. Thermal noise is uncorrelated with digital signal templates generated by convolving theoretical Askaryan pulses with detector response. Signal templates have been used recently to detect UHECR with the ARIANNA Hexagonal Radio Array (HRA) [38]. More significantly, vibrational signal templates were used to detect gravitational wave signals in the Advanced LIGO detector [39]. In each case, a *template library* was created, in which individual templates share a physical origin, but use different functional parameters that span parameter-space.

Creating template libraries with semi-analytic and fully analytic models is far more efficient than creating them with particle MC codes. The Askaryan field is derived in semi-analytic models from cascade profiles computed via MC codes, accounting for stochastic effects in cascade profiles [31]. Fully analytic models are derived mathematically, where every model parameter has a physical origin and explanation. Template libraries may then be generated by tuning continuously parameters, accounting for regions of

parameter-space where the form factor  $\tilde{F}(\omega, \theta)$  and LPM elongation dominate. Although the resulting template library would not account for stochastic processes, it would contain the effects of the form factor and LPM elongation, which control the sensitivity and design of Antarctic detectors. Examples of parameter-space variables are: the range to the interaction  $R$ , the frequencies  $\nu$ , the length of the cascade  $a$ , the viewing angle  $\theta$ , the fraction of the cascade that is electromagnetic or hadronic, the total cascade energy  $E_C$ , and the lateral width of the cascade  $\sqrt{2\pi}\rho_0$ .

## 2. Units, definitions, and conventions

All calculations in this work have been encapsulated into an open-source C++ class, available online.<sup>1</sup> The primary function of this code is to predict the electric fields that Askaryan-based detectors would detect. In all sections, this class will be called the *associated code*, or simply *the code*.

The coordinate systems are shown in Fig. 1a. Observer coordinates are un-primed, and charge excess coordinates are primed. The cascade current  $\mathbf{J}(t')$  is described in Section 3.2, and will be called the instantaneous charge distribution (ICD) in subsequent sections. The vectors  $\rho$  and  $\rho'$  refer to the lateral distance from the cascade axis, and  $z$  and  $z'$  refer to the cascade axis. The origin for both systems is the location of the cascade maximum, with  $z' = z = 0$  and  $\rho = \rho' = 0$ . The viewing angle is  $\theta$ . Bold variables, and variables with a circumflex,  $\hat{e}_i$ , refer to vectors. The observer distance is  $R = |\mathbf{x} - \mathbf{x}'|$ ,  $\omega$  refers to the angular frequency, and  $k = (2\pi)/n\lambda$  and  $\mathbf{q} = n(\omega R, \omega\rho)/(cR)$  refer to one- and three-dimensional wavevectors in the dielectric, with a refractive index  $n$ . Although the code takes  $n = 1.78$  as a default value, it may be altered to apply to other uniform media. The Cherenkov angle is defined by the index of refraction:  $\cos\theta_C = 1/n$ . The index of refraction at RF frequencies for bulk ice in Antarctica is  $1.783 \pm 0.003$  [40].

The archetypal cascade profile is shown in Fig. 1b, in which the total number of cascade particles is shown, versus depth along the  $z'$  axis. The depth is  $Pz'$ , where  $P$  is the bulk density of ice ( $0.917 \text{ g/cm}^3$ ). The parameter  $n_{\max}$  will refer to the net number of negatively charged particles (typically  $\approx 20\%$  of the total – see Section 3.4.1 and the Appendix Section A.2 for details). The parameter  $a$  is the Gaussian width of the cascade profile near cascade maximum. The cascade is initiated by an electroweak neutrino interaction, where the neutrino energy is  $E_\nu$ , and the total energy of the cascade is  $E_C$ .

<sup>1</sup> <https://github.com/918particle/AskaryanModule>.

The units of the electromagnetic field in the Fourier domain are V/m/Hz, often converted in the literature to V/m/MHz. To make the distance-dependence explicit, both sides of field equations are multiplied by  $R$ , making the units V/Hz. In Section 4, the field normalization constant is  $E_0$ , and it contains the energy-dependence.  $E_0$  may be linearly scaled with energy, provided the parameters  $a$  and  $n_{\max}$  are derived consistently from the Greisen model. Equations in Section 4 are proportional to  $\omega E_0$ , so the units of  $E_0$  are V/Hz<sup>2</sup>.

In the original RB work, the following convention for the Fourier transform  $\tilde{G}(\omega)$  of a function  $g(t)$  was used:

$$\tilde{G}(\omega) = \int_{-\infty}^{\infty} e^{i\omega t} g(t) dt \quad (1)$$

$$g(t) = \frac{1}{2\pi} \int_{-\infty}^{\infty} e^{-i\omega t} \tilde{G}(\omega) dt \quad (2)$$

The sign convention shown in the exponent is used in RB, though the opposite sign convention is more common in mathematical physics. The definitions in Eqs. (1), (2) have been kept for consistency with Section V of [35]. The sign convention may be toggled in the code, but the output does not depend on this choice, because the appropriate transformation in time is applied. All frequencies are shown in MHz in spectral plots, for comparison to the literature. The symbol  $\sim$  above a function denotes a Fourier-domain quantity. In Sections 3.2 and 3.4, the three-dimensional Fourier transform is used to describe the form factor in three-dimensional frequency-space, with the normal sign convention:

$$\tilde{F}(\mathbf{q}) = \int d^3x' f(\mathbf{x}') e^{-i\mathbf{q}\cdot\mathbf{x}'} \quad (3)$$

### 3. Combination of the RB model, the LPM effect, and the Cascade Form Factor

In Section 3.1, the RB model [30] is presented for clarity, beginning with all assumptions made. Next, the model is enhanced by treating two new effects: the LPM effect (Section 3.3) and the Cascade Form Factor,  $\tilde{F}$  (Section 3.4).

#### 3.1. General assumptions, and the basic RB model

The conventions are taken from Section 2 to build the RB model in the code [35]. RB derive the Askaryan fields from Maxwell's equations in the Lorentz gauge for a dielectric medium, by expanding with a special scalar parameter  $\eta$ . The source current,  $\mathbf{J}(t', \mathbf{x}')$ , is described by an ICD  $f(z' - vt, \rho')$ , excess charge profile  $n(z')$ , and cascade speed  $\mathbf{v}$ :

$$\mathbf{J}(t', \mathbf{x}') = \mathbf{v}n(z')f(z' - vt, \rho') \quad (4)$$

$$\eta = \left( \frac{a}{\Delta z_{\text{coh}}} \right)^2 = \frac{k}{R}(a \sin \theta)^2 \quad (5)$$

The function  $f(z' - vt, \rho')$  is the 3D ICD. Eq. (5) is the squared ratio of  $a$ , and  $\Delta z_{\text{coh}}$ , the longitudinal range where the Askaryan radiation must be coherent. To understand  $\Delta z_{\text{coh}}$ , consider Feynman's formula [30]. Radiation from an accelerating point charge is proportional to the angular acceleration  $\ddot{\theta}$  relative to the observer. The coherence regime is defined by  $|z'| \lesssim \Delta z_{\text{coh}}$ , where  $\ddot{\theta}$  and  $R(z')$  are constant in time to first order, and  $\ddot{\theta}$  is maximized. RB show that if  $\Delta R(z') < \lambda$  in this limit,  $\Delta z_{\text{coh}} < (R/(ks \sin^2 \theta))^{1/2}$ .

The dominant Askaryan radiation occurs when  $|z'| \lesssim \Delta z_{\text{coh}}$ . In the Fresnel and Fraunhofer (far-field) regimes,  $\eta < 1$ . The calculations, however, are valid for any  $\eta$ , rather than only the in the far-field ( $\eta \rightarrow 0$ , and  $kR \gg 1$ ,  $R \gg a$ ). If  $a \ll \Delta z_{\text{coh}}$ , then the fields have spherical symmetry, and the limit  $kR \gg 1$  corresponds to the

far-field. Conversely, if  $a \gg \Delta z_{\text{coh}}$ , then  $\eta \rightarrow \infty$ , the fields have cylindrical symmetry.

The longitudinal cascade width  $a$ , and therefore  $\eta$ , is derived in the code from either the Greisen (electromagnetic) or Gaisser-Hillas (hadronic) cascade profile functions (Sections 3.4–3.4.1), and can be elongated by the LPM effect. The associated code requires the type of cascade profile (hadronic or electromagnetic) as an input, and whether the LPM effect must be applied. If the user specifies a purely hadronic cascade, no further action is taken if the LPM effect is activated [31].

#### 3.2. The RB field equations

RB insert the vector current  $\mathbf{J}(t', \mathbf{x}')$  into Maxwell's equations, and solve for the vector potential:

$$c\mathbf{A}(\mathbf{x}') = \int d^3x' \frac{e^{ik|\mathbf{x}-\mathbf{x}'|}}{|\mathbf{x}-\mathbf{x}'|} \int dt' e^{i\omega t'} \mathbf{J}(t', \mathbf{x}') \quad (6)$$

RB then define  $R(z') = \sqrt{(z-z')^2 + \rho'^2}$ , and expand around  $\rho' = 0$ :

$$|\mathbf{x}-\mathbf{x}'| \approx R(z') - \frac{\rho \cdot \rho'}{R(z')} + \frac{\rho'^2}{2R(z')} \quad (7)$$

In Eq. (7), the third term on the right-hand side is dropped, because  $\rho' \ll R(z')$ . The vector potential in Eq. (6) is then factored into the form factor  $\tilde{F}(\omega)$  and a vector potential.  $\tilde{F}(\omega)$  is the three-dimensional Fourier transform of the ICD, and the vector potential is governed by  $n(z')$ . Thus,  $\tilde{F}(\omega)$  describes the charge distribution, and the vector potential describes the charge evolution. Eqs. (8) and (9) summarize the result. In Eqs. (8) and (9),  $\tilde{\mathbf{A}}^{\text{FF}}$  is the vector potential, named the Fresnel-Fraunhofer (FF) potential in RB.

$$\tilde{\mathbf{A}}(\omega, \theta) = \tilde{\mathbf{A}}^{\text{FF}}(\omega, \theta) \int d^3x' e^{-i\mathbf{q}\cdot\mathbf{x}'} f(\mathbf{x}') \quad (8)$$

$$\tilde{\mathbf{A}}(\omega, \theta) = \tilde{F}(\omega, \theta) \tilde{\mathbf{A}}^{\text{FF}}(\omega, \theta) \quad (9)$$

Eqs. (10)–(13) express the general RB result for the electric field  $\mathbf{E} = -\partial\mathbf{A}/\partial t$ , in terms of the frequency  $\nu$ , viewing angle  $\theta$ , and  $\eta$ :

$$\frac{R\tilde{\mathbf{E}}(\nu, \theta, \eta)}{\left[ \frac{\nu}{\text{MHz}} \right]} = 2.52 \times 10^{-7} \frac{a}{[\text{m}]} \frac{n_{\max}}{[1000]} \frac{\nu}{[\text{GHz}]} \tilde{F}(\mathbf{q}) \psi \mathcal{E} \quad (10)$$

$$\psi = -ie^{ikR} \sin \theta \quad (11)$$

$$\begin{aligned} \mathcal{E} &= \mathcal{W}(\eta, \theta) \left( \frac{\cos \theta_C - \cos \theta}{\sin \theta} \right) \hat{e}_r \\ &\quad + \mathcal{W}(\eta, \theta) \left( 1 - i\eta \frac{\cos \theta_C}{\sin^2 \theta} \frac{\cos \theta - \cos \theta_C}{1 - i\eta} \right) \hat{e}_\theta \end{aligned} \quad (12)$$

$$\begin{aligned} \mathcal{W}(\eta, \theta) &= \left( 1 - i\eta \left( 1 - 3i\eta \frac{\cos \theta}{\sin^2 \theta} \frac{\cos \theta - \cos \theta_C}{1 - i\eta} \right) \right)^{-1/2} \\ &\quad \times \exp \left( -\frac{1}{2} (ka)^2 \frac{(\cos \theta - \cos \theta_C)^2}{1 - i\eta} \right) \end{aligned} \quad (13)$$

Eq. (10) is the total field, with an overall phase factor defined in Eq. (11). Eq. (12) contains the vector structure, and Eq. (13) governs the phase and angular structure.

#### 3.3. The Landau-Pomeranchuk-Migdal (LPM) effect

The Landau-Pomeranchuk-Migdal (LPM) effect is a suppression of the pair-creation and bremsstrahlung cross-sections at cascade energies above a material-dependent constant known as the LPM energy or  $E_{\text{LPM}}$  [41]:

$$E_{\text{LPM}} = \frac{(mc^2)^2 \alpha X_0}{4\pi c \hbar} = 7.7 \text{ TeV/cm} \cdot X_0 \quad (14)$$

In Eq. (14),  $m$  is the electron mass,  $\alpha$  is the fine-structure constant, and  $X_0$  is the radiation distance ( $E_{\text{LPM}} = 0.303$  PeV for ice). If  $E_C > E_{\text{LPM}}$ , the quantum mechanical *formation length* of these interactions is longer than atomic separations, leading to quantum interference and suppressing cross-sections. The result is a *longitudinal shower elongation*, from the non-interacting, higher-energy particles. The LPM effect is reviewed by S.R. Klein in Ref. [41].

The LPM changes how the RB model must be applied. Under normal circumstances, the quantity  $n_{\max}a$  approximates the area under the cascade profile for particles with energy greater than some critical energy:  $n_{\max}a \propto E_C$ . It is shown in Ref. [42] that in the LPM-regime,  $a \propto \sqrt{E_C/E_{\text{crit}}}$ . While it may appear that changing the energy scaling of  $a$  violates energy conservation through the field normalization  $n_{\max}a$ , this is not necessarily the case.

First, the amount of *radiated* energy does not have to track the *total* energy, if the cascade shape is modified. The Frank-Tamm radiation distribution for a charge moving through a track of length  $L$  states:  $d^2P/d\Omega d\omega \propto L^2$  [35]. The LPM effect would increase  $L$ , increasing the radiated energy. The increase is contingent on  $L$  remaining comparable to  $\Delta z_{\text{coh}}$ , avoiding spectral cut-off. It is shown in Section 3.6 (graphically) and Section 4 (mathematically) that enhancements due to cascade elongation are attenuated by a combination of decoherence,  $\tilde{F}$ , and narrowed Cherenkov cone-width.

Second, it should not be assumed naively that  $n_{\max}$  must be decreased in direct proportion to the increase in  $a$ , under LPM elongation. Absent the LPM effect, the inverse relationship between  $a$  and  $n_{\max}$  merely reflects that  $E_C$  is a constant, with  $\approx 10^{-7}$  of the energy in TeV passing to Askaryan radiation in V/m/MHz. Figs. 12–13 of Ref. [43] demonstrate LPM elongation, but  $n_{\max}$  is not reduced in direct proportion to  $a$ . Fig. 12 of Ref. [43] shows that  $X_{\max}$  grows and fluctuates at energies above  $E_{\text{LPM}}$ . However, Fig. 13 of Ref. [43] shows that the energy-dependence of  $n_{\max}$  stays approximately the same, and  $n_{\max}$  fluctuates mildly. Further, Fig. 3 of [31] suggests that charged-current induced cascades, with mixed hadronic and electromagnetic components, have no reduction in  $n_{\max}$  relative to neutral-current induced cascades, for which the LPM effect is not relevant [44].

Physically, all particle energies must decrease below  $E_{\text{LPM}}$  eventually. This takes place before the cascade maximum, so to first order  $n_{\max}$  is still governed by non-LPM physics, even if  $E_C > E_{\text{LPM}}$ . Conversely, ZHS and others have shown that the radiated field strength below 500 MHz is proportional to the weighted, projected track length of charged particles [30]. The LPM effect cannot enhance dramatically the weighted projected track length, because the number of LPM-elongated tracks is a small fraction of the total number. The associated code contains a flag (*strictLowFreqLimit*) which directs the model to retain this limit by inversely scaling  $n_{\max}$  in direct proportion to the increase in  $a$ . Requiring this limit is equivalent to stating that sub-showers with  $E < E_{\text{LPM}}$  occur both *before* and *after* cascade maximum, *smearing*  $n(z')$ . From the arguments and references above, this is the most conservative approach.

Finally, S.R. Klein notes in Ref. [41] that the LPM effect may influence  $\tilde{F}(\omega, \theta)$ . The lateral ICD is influenced by multiple scattering (MSC) effects that lead to a mean scattering angle  $\langle \theta_{\text{MSC}} \rangle$  for cascade particles incident on atoms [36,41]. In Ref. [41],  $\langle \theta_{\text{MSC}} \rangle$  takes the following form for a particle of energy  $E$ :

$$\langle \theta_{\text{MSC}} \rangle = \frac{E_s}{E} \sqrt{\frac{d}{X_0}} \quad (15)$$

$X_0$  is the radiation distance,  $d$  is the distance over which the scattering occurs, and  $E_s$  is the Molière scattering energy ( $E_s = mc^2/\sqrt{4\pi/\alpha} \approx 21.2$  MeV). The LPM effect increases  $d$  relative to  $X_0$ , increasing  $\langle \theta_{\text{MSC}} \rangle$ . Although  $\langle \theta_{\text{MSC}} \rangle$  is enhanced by the LPM effect, it is also inversely proportional to energy. This implies that the

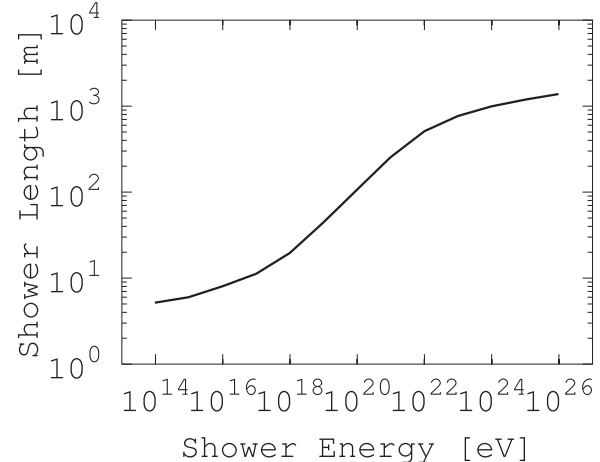


Fig. 2. The length of the neutrino-induced cascade, including the LPM effect, from ref. [42].

pile-up of particle energies at  $E_{\text{crit}} \approx E_s$  actually governs the ICD width.

Finally, a remark about “shower fluctuations” is prudent. While the LPM effect may cause the cascade maximum location to fluctuate, the *location* of cascade maximum is irrelevant, because Askaryan radiation is independent of the origin of the coordinate system. The origin in the associated code is the location of cascade maximum, *wherever it occurs*. Stochastic features of the LPM effect, such as the multi-peaked cascade profile, are not treated in this work. However, it is shown in Ref. [45] that the sub-peaks only alter the waveform in certain circumstances, such as being off-cone by  $\approx 10^\circ$  in the Fraunhofer regime. The waveforms in Ref. [45] all contain the basic bi-polar structure produced by the associated code, despite the multi-peaked cascade profile.

In summary, the main effect LPM physics has on Askaryan radiation is the angular and frequency filtering via the cascade elongation. The effect is quantified in the code by drawing an elongated shower width  $a$  from calculations by Klein and Gerhardt shown in Fig. 2 [42]. In scenarios where LPM is unimportant, such as initial hadronic-dominated processes [44] and cascades with  $E_C < E_{\text{LPM}}$ , the associated code draws the width and height of the negative charge excess profile from the usual Greisen and Gaisser–Hillas formulations [36,46].

### 3.4. The Cascade Form Factor, $\tilde{F}$

The factorization of the longitudinal charge excess evolution,  $\tilde{A}^{FF}(\omega, \theta)$ , and the instantaneous properties of the lateral charge distribution,  $\tilde{F}(\omega)$ , leads to the interpretation of  $\tilde{F}(\omega)$  as a filter. Filters are fully described by pole-zero diagrams, which display the Laplace transform of the filter transfer function. Impulsive E-fields with no DC-component automatically approach 0 as  $|\omega| \rightarrow 0$ , meaning  $\tilde{F}$  should not require any zeros. Thus,  $\tilde{F}(\omega)$  should be completely defined by poles in the complex  $\omega$ -plane.

D. Garcia-Fernandez *et. al.* (Ref. [47]) show that the integrals over individual tracks in the ZHS algorithm can be generalized to all coherence regimes, when integrated numerically. The authors of Ref. [47] then insert the form factor chosen in Ref. [48] into the RB framework to demonstrate agreement (Fig. 7 of Ref. [47]). This agreement occurs at frequencies below 120 MHz, below the bandwidths of ARA/ARIANNA. The lateral  $\rho'$ -dependence of the chosen form factor is Gaussian ( $f \propto \exp(-\rho'^2)$ ), yielding gaussian behavior in the Fourier domain ( $|\tilde{F}| \propto \exp(-\omega^2)$ ). Geant4 simulations and the Greisen model show that  $f(x')$  is not Gaussian (Section 3.4.1 and Appendix Section A.2). Additionally, the ultra-violet divergence

in Ref. [47] is attributed to the assumption that the dielectric constant  $\epsilon(\omega)$  is not absorptive, however, the effect of  $\tilde{F}(\omega)$  is apparent in that model near 1 GHz. This is because the filtering effect of  $\tilde{F}(\omega, \theta)$  occurs when the Askaryan radiation of all finite tracks in a cascade are summed.

The ZHS form factor,  $\tilde{F}_{\text{ZHS}}(\omega)$ , is constructed of poles which imply that the lateral ICD  $f \propto \exp(-\rho')$ . The key result for  $\tilde{F}(\omega)$  is given in Eq. (16), in terms of the viewing angle  $\theta$ , the angular frequency  $\omega$ , and  $(\sqrt{2\pi}\rho_0)^{-1}$ , the distance from the cascade axis ( $\rho' = 0$ ) at which the negative charge excess has decreased by  $1/e$ .

$$\tilde{F}(\omega, \theta) = \frac{1}{(1 + (\frac{(\omega/c)\sin\theta}{\sqrt{2\pi}\rho_0})^2)^{3/2}} \quad (16)$$

Intuitively, the squared ratio in the denominator of Eq. (16) compares the lateral projection of the wavevector with the physical extent of the charge excess. If the charge excess is laterally large, compared to the wavelength, then Eq. (16) begins to act as a low-pass filter. By substituting Eq. (16) into Eq. (10), the RB model is completed, properly accounting for LPM elongation and the ICD. The form factor  $\tilde{F}(\omega, \theta)$  is derived from fits to Geant4 cascades, for  $E_C = 1\text{--}100$  PeV. Once the quality of these fits is established, one may proceed with the theoretical cascade models, with no need of further numerical simulation.

### 3.4.1. The Greisen model

K. Greisen provided a comprehensive review of the longitudinal charge evolution, and lateral distribution, within electromagnetic cascades [36], by combining earlier work by Molière, Nishimura and Kamata, Landau, and others. The integrated charge at depth  $z_0$  in the medium is

$$n_{\text{tot}}(z_0) = \frac{0.31}{\sqrt{\ln(E_C/E_{\text{crit}})}} \exp\left\{z_0\left(1 - \frac{3}{2}\ln(s)\right)\right\} \quad (17)$$

In Eq. (18),  $z_0$  is in units of radiation length ( $36.08 \text{ g cm}^{-2}$ ), and the cascade energy  $E_C$  in units of GeV ( $E_{\text{crit}} = 73 \text{ MeV}$ ) [30,34]. The shower age is  $s = 3z_0/(z_0 + 2\ln(E_C/E_{\text{crit}}))$ . Eq. (17) contains the cascade maximum  $z_{\text{max}} = \ln(E_C/E_{\text{crit}})$ . Additionally,  $\langle \ln n_{\text{tot}} \rangle \approx 0.7(s - 1 - 3\ln s)$ . When  $s = 1$  at  $z_{\text{max}}$ ,  $\langle \ln n_{\text{tot}} \rangle = 0$ , implying negligible  $n_{\text{max}}$  fluctuation. Approximating  $n_{\text{tot}}(z_0)$  by a Gaussian,  $a \propto \sqrt{z_{\text{max}}}$ . For  $n_{\text{max}} = n_{\text{tot}}(z_{\text{max}})$ ,  $n_{\text{max}}a \propto E_C/E_{\text{crit}}$ . The factor  $n_{\text{max}}a$  approximates the area under the peak of Eq. (17).

The lateral ICD arises from multi-scattering effects (MSC processes in Geant4), with average scattering angle  $\langle \theta_{\text{MSC}} \rangle$  (Eq. (15)), and a Molière radius defined by  $\rho_1 = E_{\text{MSC}}/E_c$ , in radiation lengths. Large errors arise for angles  $\theta \gg \langle \theta_{\text{MSC}} \rangle$ , or ( $\rho' > \rho_1$ ), but few particles have  $\rho' > \rho_1$ . The  $\langle \theta_{\text{MSC}} \rangle$  is expressed in Eq. (18), for particles of energy  $\epsilon$  in electromagnetic cascades [41]:

$$\langle \theta_{\text{MSC}} \rangle = \frac{E_{\text{MSC}}}{\epsilon} \sqrt{z_0} = \frac{m_e c^2 \sqrt{4\pi z_0/\alpha}}{\epsilon} \approx \frac{21.2[\text{MeV}]}{\epsilon} \sqrt{z_0} \quad (18)$$

Eq. (18) implies the lateral ICD should be widest near  $n_{\text{max}}$ , where  $\epsilon$  is minimized. The widening lateral ICD causes most particles to lag behind the cascade front by  $\mathcal{O}(1\text{--}10)$  cm at  $n_{\text{max}}$  (see Eq. (13) of [41]). Nishimura and Kamata refine the approximation, providing the lateral charged particle density,  $D$ . The result is known as the NKG-function, shown in Eq. (19).

$$D = \frac{n_{\text{tot}}}{2\pi\rho_1^2} \frac{\Gamma(4.5-s)}{\Gamma(s)\Gamma(4.5-2s)} \left(\frac{\rho'}{\rho_1}\right)^{s-2} \left(1 + \frac{\rho'}{\rho_1}\right)^{s-4.5} \quad (19)$$

Agreement between this work and Eqs. (17)–(19) is shown Section A.2 in the Appendix. The ICD is assigned a three-dimensional function  $f(\mathbf{x}')$ , and in Section 3.4.2,  $\tilde{F}(\omega)$  is derived analytically from  $f(\mathbf{x}')$ . Other efforts to model the ICD and the resulting Askaryan radiation can be found in Refs. [49–51].

### 3.4.2. Analytic formula for $\tilde{F}(\omega, \theta)$

The definition of  $\tilde{F}(\omega, \theta)$  is

$$\tilde{F}(\mathbf{q}) = \int d^3x' e^{-i\mathbf{q}\cdot\mathbf{x}'} f(\mathbf{x}') \quad (20)$$

The ICD  $f(\mathbf{x}')$  is given by a general parameterization of the Greisen model:

$$f(\mathbf{x}') = \rho_0^2 \delta(z') \exp(-\sqrt{2\pi}\rho_0\rho') \quad (21)$$

The choice of Eq. (21) is motivated by Section 3.4.1 (see Appendix Section A.2 for more detail). Recall that the ICD is meant to describe the number density of the negative charge excess, not the total charged particle number density. Geant4 MC calculations and the Greisen model predict the exponential form, and the ZHS parameterization suggests it in the Fourier domain. Hu *et al* chose a double-Gaussian form [48], which is not accurate near  $\rho' = 0$ , but highlights the relationship between theoretical parameters and numerical fields. Note that the units of the  $1/e$  width  $\sqrt{2\pi}\rho_0$  and  $\delta(z')$  are inverse length, giving  $f(\mathbf{x}')$  units of number density.

Fitted results for the parameter  $\sqrt{2\pi}\rho_0$  for times between 20–30 ns ( $s \approx 1$ ) indicate that  $\sqrt{2\pi}\rho_0 \sim$  is constant with respect to cascade depth. The solution to Eq. (20) is as follows: the trivial  $z'$  integration is performed, setting  $z' = 0$  without loss of generality. Next, two convenient variables are defined, and shown in Eqs. (22) and (23).

$$\gamma = \frac{\omega}{c} \sin\theta \quad (22)$$

$$\sigma = \frac{\gamma}{\sqrt{2\pi}\rho_0} \quad (23)$$

The variable  $\gamma$  is the lateral projection of the wavevector, and  $\sigma$  is the product of  $\gamma$  and the lateral charge extent. The variable  $\sigma$  compares the laterally-projected wavelength to the lateral extent of cascade excess charge. In Section 4,  $\sigma = \omega/\omega_{\text{CF}}$ , so that  $\omega_{\text{CF}}$  is the limiting frequency. Substituting Eqs. (21)–(23) into Eq. (20),  $\tilde{F}(\omega, \theta)$  becomes

$$\tilde{F}(\omega, \theta) = \rho_0^2 \int_0^\infty d\rho' \rho' \exp\left\{-\frac{\gamma}{\sigma}\rho'\right\} \int_{-\pi}^\pi d\phi' \exp\{-i\rho'\gamma \cos(\phi')\} \quad (24)$$

From the cylindrical symmetry of  $f(\mathbf{x}')$ , the  $\phi'$  coordinate may be rotated. With  $\phi' \rightarrow \phi' - \pi/2$ , the  $\phi'$ -integral becomes a 0th-order Bessel function. A similar result in Ref. [49] contains the Bessel function in Eq. (24). In Ref. [49], however, the lateral ICD is not evaluated analytically, but through numeric integrals. After making the substitution  $u' = \gamma\rho'$ , the remaining  $\rho'$ -integral may be found in standard tables.

$$\tilde{F}(\omega, \theta) = \sigma^{-2} \int_0^\infty du' u' \exp\left\{-\frac{u'}{\sigma}\right\} J_0(u') \quad (25)$$

$$\tilde{F}(\omega, \theta) = \frac{1}{(1 + \sigma^2)^{3/2}} \quad (26)$$

The result for  $\tilde{F}(\omega, \theta)$  is shown in Eq. (26). The Askaryan spectrum is attenuated like  $\omega^{-3}$  for  $\sigma \gg 1$ , for wavelengths much smaller than the lateral ICD. For  $\sigma \lesssim 1$ ,  $\tilde{F}(\omega, \theta) \approx (1 + (3/2)\sigma^2)^{-1}$ . Given the location of complex poles for  $\sigma \ll 1$ , one might suspect problems with causality. It is important to note, upon transforming the model to the time domain, including the LPM effect and the effect of  $\tilde{F}(\omega, \theta)$ , that the fields do not violate the causality criterion stated by RB [35].

Eq. (16) in Ref. [32] contains the Askaryan vector potential versus retarded time ( $t_r$ ), matched to MC at  $\theta = \theta_C$ , with six numerical parameters, not counting the overall normalization. This

equation is restated as Eq. (27), and the  $x_i$  have unique values for  $t_r > 0$  and  $t_r < 0$ .

$$\frac{R\mathbf{A}(t_r, \theta_C)}{[V \cdot s]} = -E'_0 \sin(\theta_C) \hat{e}_\theta (\exp(-2|t_r|/x_0) + (1+x_1|t_r|)^{-x_2}) \quad (27)$$

Eq. (26) fully describes the cascade shape, is analytic, and when combined with  $\tilde{\mathbf{A}}^{FF}$ , produces fields that obey causality (see Section 3.5). Additionally,  $\tilde{F}$  only needs one MC constant:  $\sqrt{2\pi}\rho_0$ . Although the second term in Eq. (27) accounts for the asymmetric MC vector potential in an ad-hoc fashion, this asymmetry flows directly from Eq. (26) (Section 4), and special cases of the  $x_i$  are derived. Rather than requiring six raw MC numbers, the associated code relies on Eq. (26), and one MC parameter ( $\sqrt{2\pi}\rho_0$ ).

### 3.4.3. Generalization of Eq. (26)

In the Appendix Section A.2, the lateral distribution of excess charge near cascade maximum is shown to follow Eq. (21) for  $\rho' < \rho_1$ , where  $\rho_1$  is the Molière radius. To include the effect of charges beyond a single Molière radius, the following form for  $f(\mathbf{x}')$  may be taken:

$$f(\mathbf{x}') = \delta(z') \sum_i^N a_i \exp(-\sqrt{2\pi}\rho_i\rho') \quad (28)$$

The normalization requirement for the ICD provides the following constraint on the  $2N$  free parameters:

$$\sum_i^N \left( \frac{a_i}{\rho_i^2} \right) = 2\pi \quad (29)$$

Note that the units of the  $a_i$  parameters are the same as the normalization  $\rho_0^2$  in the single-exponential case. Let  $\alpha_i$  and  $\sigma_i$  take the following definitions:

$$a_i = \alpha_i \rho_i^2 \quad (30)$$

$$\sigma_i = \frac{\gamma}{\sqrt{2\pi}\rho_i} \quad (31)$$

With this definition, Eq. (26) may be generalized to arbitrary Molière radii, taking the following form:

$$\tilde{F}(\omega, \theta) = \sum_i^N \frac{\alpha_i}{(1+\sigma_i^2)^{3/2}} \quad (32)$$

It is shown in Section 4.2 that in the far-field limit, at  $\theta = \theta_C$ , the effect of extending the form factor  $\tilde{F}$  to arbitrary Molière radii is equivalent to adding a set of additional poles to the Askaryan field in the complex  $\omega$ -plane. In the time domain, the Askaryan field picks up a series of exponential terms corresponding to the added poles.

### 3.5. Results of the Model: RB+LPM+ $\tilde{F}(\omega, \theta)$

The associated code output  $\hat{e}_\theta \cdot \mathbf{E}(t)$ , including all effects is shown in Fig. 3, with  $E_C = 1000$  PeV. Fig. 3 contains contour graphs, in units of mV/m, versus the retarded time in nanoseconds, and  $\theta$  in degrees. The quadratic grey dashed line on the contours is a causal requirement from RB, showing how the arrival time (e.g. group delay) of the signal depends on  $\theta$ . Phase delays  $t_\phi$  about the quadratic are allowed:  $t_\phi = -\phi(\omega)/\omega$ . Phase delays are most prominent when  $\tilde{F} \neq 1$ ,  $\theta \neq \theta_C$ , and when the LPM effect is strong. See Appendix Section 3.6 for further detail.

The fields are shown for  $R = 200$  m (panels c and d) and 1000 m (panels a and b),  $(\sqrt{2\pi}\rho_0)^{-1} = 5$  cm (panels a and c) and 10 cm (panels b and d) in Fig. 3. The causality requirement from RB leads to off-cone regions have a higher effective velocity. A larger  $R$

value leads to wider separation in arrival times, as these off-cone modes have longer to outpace the other modes (earlier times correspond to more negative retarded times).

An enticing implication of the effective velocity variation is that the degeneracy between a low-energy event interacting close to the observer, and a high-energy event interacting correspondingly farther from the observer would be broken. Recall that  $\tilde{\mathbf{E}} \propto R^{-1}$  in the far-field. An event with  $R = 100$  m and  $E_C = 10$  PeV would have the same amplitude as an event with  $R = 1000$  m and  $E_C = 100$  PeV, neglecting secondary effects like ice absorption. The temporal signature shown by the quadratics in Fig. 3 would be different in the two cases.

From Eq. (12), the field  $\tilde{\mathbf{E}}$  has both  $\hat{e}_r$  and  $\hat{e}_\theta$  components. For the extreme Fraunhofer limit, as  $\eta \rightarrow 0$ , the ratio of the amplitudes of these components is independent of frequency:

$$\frac{\hat{e}_r \cdot \tilde{\mathbf{E}}}{\hat{e}_\theta \cdot \tilde{\mathbf{E}}} = -\left( \frac{\cos \theta - \cos \theta_C}{\sin \theta} \right) \quad (33)$$

Eq. (33) shows that the  $\hat{e}_r$ -component of  $\mathbf{E}(t)$  is positive above the Cherenkov angle, and negative below it. Since the  $\hat{e}_r \cdot \mathbf{E}(t) = 0$  at  $\theta_C$ , the maximum in the  $\hat{e}_r$ -component is always at some angle  $\theta \neq \theta_C$ . The contour graphs of Fig. 4 represent the  $\hat{e}_r$ -component of the same fields as Fig. 3. Because  $\hat{e}_r \cdot \tilde{\mathbf{E}} < \hat{e}_\theta \cdot \tilde{\mathbf{E}}$ , the Askaryan field is usually given with a pure  $\hat{e}_\theta$ -polarization. Though the  $\hat{e}_r$ -component is small compared to the  $\hat{e}_\theta$ -component, the code does not neglect it. The polarization ratio (Eq. (33)) is both complex, and frequency-dependent if  $\eta \neq 0$ .

### 3.6. Spectral, phase, and angular comparisons to previous work

It is shown in Figs. 5 and 6 where the associated code agrees with the ZHS parameterization for  $E_C < E_{LPM}$ . Eqs. (10)–(13), via the associated code, are compared in Figs. 5–6 to Eqs. 20–21 from [30], with  $\Delta\theta = 2.4^\circ(v_0/\nu)$ , and  $v_0 = 0.5$  GHz, shown for convenience in Eqs. (34) and (35). In Fig. 5, the spectra are scaled by  $R[m]/E_C[\text{TeV}]$ , where  $E_C$  is the cascade energy in TeV.

$$\frac{R|\tilde{\mathbf{E}}(\omega, \theta = \theta_C)|}{\left[ \frac{V}{\text{MHz}} \right]} = 1.1 \times 10^{-7} \frac{E_0}{[\text{TeV}]} \left( \frac{\nu}{v_0} \right) \frac{1}{1 + (\nu/v_0)^2} \hat{e}_\theta \quad (34)$$

$$\tilde{\mathbf{E}}(\omega, \theta) = \tilde{\mathbf{E}}(\omega, \theta = \theta_C) \exp \left[ -\frac{1}{2} \left( \frac{\theta - \theta_C}{\Delta\theta} \right)^2 \right] \hat{e}_\theta \quad (35)$$

The  $|\tilde{\mathbf{E}}(\omega, \theta_C)|$  derived from Eq. (16) from ARVZ [32] is also shown in Fig. 5(a) for comparison, as well as an off-cone example given in Fig. 3 of ARVZ [32]. The on-cone ARVZ case is given as a vector potential, so  $\mathbf{E}(t) = -\tilde{\mathbf{A}}(t, \theta_C)$  is applied before extracting  $|\tilde{\mathbf{E}}(\omega, \theta_C)|$ . When  $\theta = \theta_C$ , the various  $\tilde{F}(\omega)$  are the cause of the attenuation above 1 GHz. The choice of  $\tilde{F}(\omega)$  for the associated code corresponds to a lateral cascade width of  $\approx 5$  cm, and  $\tilde{F}(\omega)$  attenuates the spectrum above 1 GHz more realistically than ZHS. When  $\theta \neq \theta_C$ , the width of the Cherenkov cone is the cause of the high-frequency attenuation. The associated code is compared to ZHS at several angles, and the off-cone ARVZ lies in between the other results above 1 GHz, due to the smaller off-cone angle ( $0.3^\circ$ ). In Fig. 5(b), the angular dependence of the associated code and ZHS is compared at 0.25, 0.5 and 1.0 GHz. The cone-width is also inversely proportional to  $a$  in the RB model - an important feature that accounts for cone-width narrowing when LPM elongation is important (see Figs. 7 and 8 below). In Fig. 5 (b), the results with  $\tilde{F} \neq 1$  are systematically lower than those with  $\tilde{F} = 1$ , as expected.

The phase  $\phi(\omega)$  of  $\hat{e}_\theta \cdot \tilde{\mathbf{E}}$  versus frequency is shown in Fig. 6, for several values of  $\theta - \theta_C$ . The phase  $\phi(\omega)$  is unwrapped after taking the arctangent of the ratio of the imaginary to the real parts of the Fourier transform of the model waveforms. Shown for comparison are the phases of Eq. (16) of ARVZ [32], and ZHS (Fig. 16 of

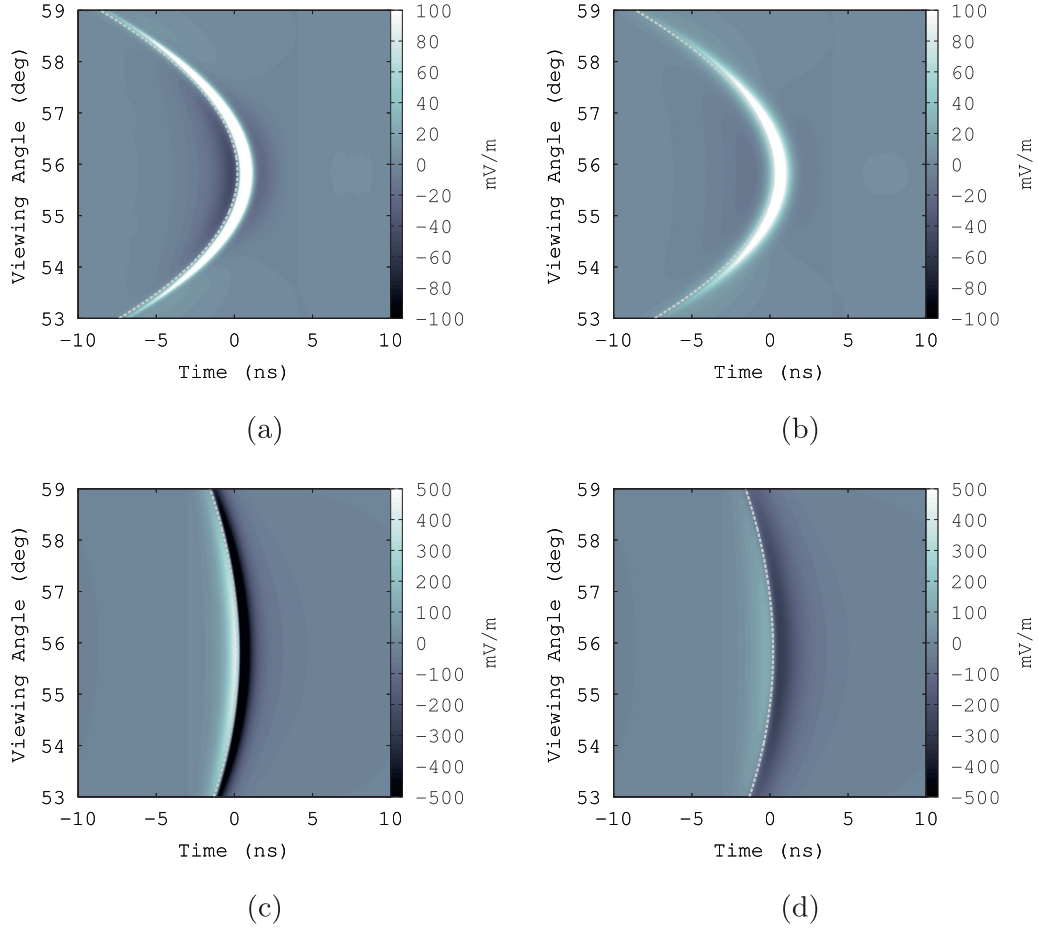


**Fig. 3.** Contours of  $\hat{e}_\theta \cdot \mathbf{E}(t)$ , for a cascade energy of 1000 PeV. (a)  $R=1000$  m, lateral ICD width of 5 cm. (b)  $R=1000$  m, lateral ICD width of 10 cm. (c)  $R=200$  m, lateral ICD width of 5 cm. (d)  $R=200$  m, lateral ICD width of 10 cm. The LPM effect has been taken into account. See text for details.

[30]), both at  $\theta = \theta_C$ . For the ARVZ case, which is a vector potential  $\mathbf{A}(t, \theta_C)$ ,  $\mathbf{E}(t) = -\dot{\mathbf{A}}(t, \theta_C)$  is applied before extracting the phase. All the models have  $\phi(\omega) \sim 90^\circ$  for  $\nu < 100$  MHz.<sup>2</sup> The  $\phi(\omega)$  functions diverge above 100 MHz, where the radiated power is reduced off-cone. The group delay ( $-d\phi/d\omega$ ) in this regime is roughly constant. Therefore, the ARVZ model and the associated code differ in phase above 100 MHz, but not group delay. Exploring all effects on  $\phi(\omega)$ , including LPM elongation and coherence, is outside the scope of this work.

The influence of LPM elongation on  $|\hat{e}_\theta \cdot \tilde{\mathbf{E}}(\omega)|$  is shown in Fig. 7, revealing two effects relative to other models. First, there is a mild enhancement below 100 MHz in panels (b) and (d). Fig. 7, panels (a) and (c) show spectra with the *strictLowFreqLimit* flag activated in the associated code (see Section 3.3). Fig. 7, panels (b) and (d) show spectra without the *strictLowFreqLimit* flag, by default. As long as  $\eta = ka^2 \sin^2 \theta / R \lesssim 1$ , so that the stretched  $a$  is still  $\lesssim \Delta z_{coh}$ , the mild low-frequency enhancement in panels (b) and (d) may be attributed to radiation from an elongated cascade.

Second, spectra in panels (a) and (b) have different values of  $\eta$  than the spectra in panels (c) and (d), leading to a counter-intuitive high-frequency dependence. Eq. (13) at fixed  $\theta$  implies a Gaussian frequency distribution:  $|\mathcal{W}(\eta, \theta)| \propto \exp(-\frac{1}{2}(\Delta \cos \theta)^2(ka)^2)/(1 + \eta^2)$ , with  $\Delta \cos \theta = \cos \theta - \cos \theta_C$ . The Gaussian width in  $\nu$  is

$$\sigma_\nu(a, \eta, \theta) = \frac{c}{2\pi a \Delta \cos \theta} (1 + \eta^2)^{1/2} \quad (36)$$

<sup>2</sup>  $\mathcal{F}_\omega(-\dot{\mathbf{A}}(t, \omega_C)) = \tilde{\mathbf{E}}(\omega, \theta_C) = -i\omega \tilde{\mathbf{A}}(\omega, \theta_C) = -e^{i\pi/2}\omega \tilde{\mathbf{A}}(\omega, \theta_C)$ , so a low-frequency phase of  $\pi/2$  (see Section A.1)

For  $a \lesssim R$ , as in panels (a) and (b), the  $\eta$ -term on the right side of Eq. (36) dominates for large  $\nu$  because  $\eta > 1$ , which leads to  $\sigma_\nu \sim \nu(a/R)$ . The spectra in panels (a) and (b) are wider than the low-energy spectra in panels (c) and (d) due to the frequency-dependent  $\sigma_\nu$ , which changes the high-frequency attenuation from Gaussian to linear attenuation at high-frequencies. Conversely, the low-energy spectra in panels (c) and (d) have  $a \ll R$ , and  $\eta \ll 1$ , implying from Eq. (36) that  $\sigma_\nu \sim 1/a$ , while the high-energy spectra encounter the former limit, because the  $a$  values are enlarged by LPM elongation. Thus, the low-energy spectra do not have the enhancement at high-frequencies, but the high-energy spectra have the enhancement. These various limits are important because the simulated range of neutrino interaction ranges detectable to ARA/ARIANNA are typically 100–1000 m [28,52].

Finally,  $|\hat{e}_\theta \cdot \tilde{\mathbf{E}}|$  versus  $\theta$  is compared with ZHS and AVZ [31] in Fig. 8. As with Fig. 7, a counter-intuitive situation arises when  $\eta > 1$ . Similar to the derivation of Eq. (36) from Eq. (13), the angular distribution at fixed frequency is Gaussian in  $\Delta \cos \theta = \cos \theta - \cos \theta_C$ :  $|\mathcal{W}(\eta, \theta)| \propto \exp(-\frac{1}{2}(\Delta \cos \theta/\sigma_{\Delta \theta})^2)$ , with Cherenkov cone-width

$$\sigma_{\Delta \theta}(a, \nu, \eta) = \frac{c}{2\pi a \nu} (1 + \eta^2)^{1/2} \quad (37)$$

LPM elongation has been applied in Fig. 8, implying that the width of the Cherenkov cone-width should be narrower than ZHS curves. In panel (a), the electromagnetic case agrees with AVZ at 100 MHz ( $E_C = 10$  EeV). The AVZ field for large  $|\theta - \theta_C|$  corresponds to radiation from sub-dominant peaks in the cascade profile not modelled by RB. The LPM effect is not applied

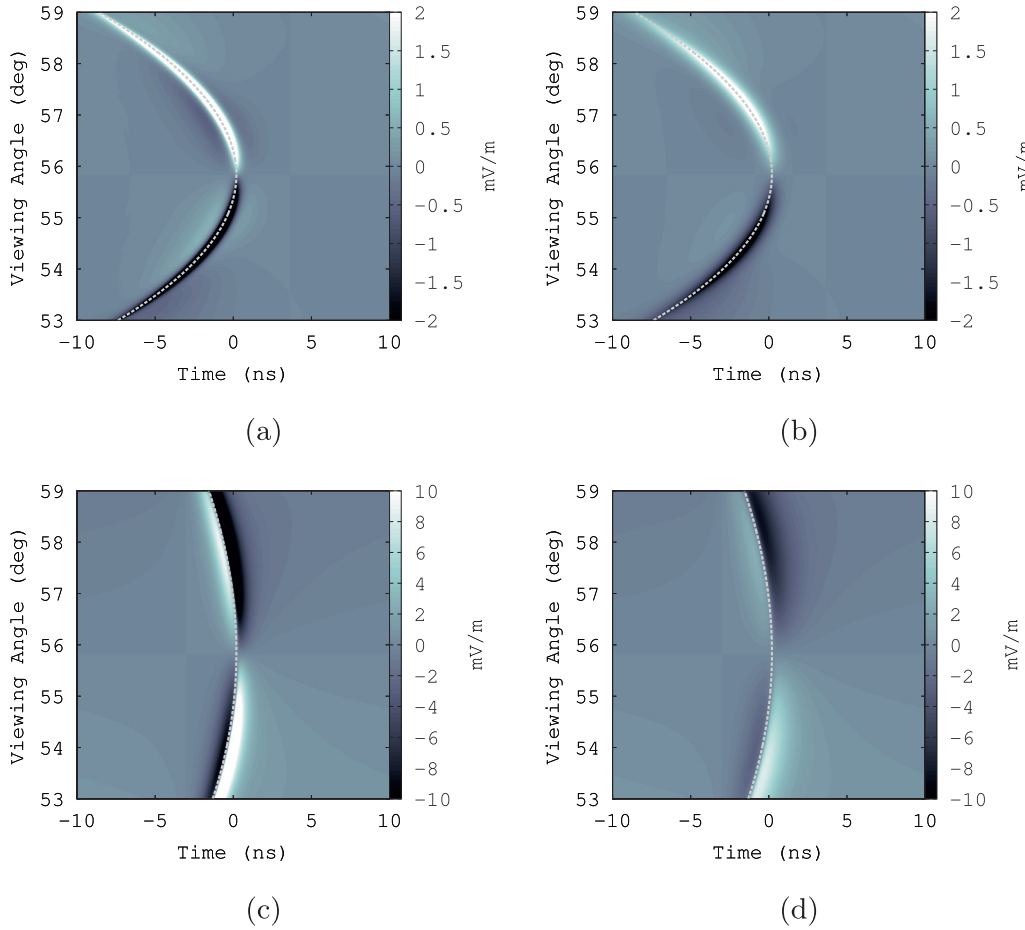


**Fig. 4.** Contours of  $\hat{e}_r \cdot \mathbf{E}(t)$ , for a cascade energy of 1000 PeV. (a)  $R=1000$  m, lateral ICD width of 5 cm. (b)  $R=1000$  m, lateral ICD width of 10 cm. (c)  $R=200$  m, lateral ICD width of 5 cm. (c)  $R=200$  m, lateral ICD width of 10 cm. In all cases, the gray dashed line represents the causality requirement. See text for details.

to the hadronic case in the associated code [44]. The hadronic case is therefore wider in panel (a), because  $\eta < 1$  and from Eq. (37),  $\sigma_{\Delta\theta} \sim 1/a\nu$ . This result follows past far-field approximations in the literature: the Cherenkov-cone is narrower for higher frequencies, and narrower for larger  $a$ . However, pure hadronic cone-widths from the code should be narrower than AVZ pure hadronic cases, because AVZ do not have the  $1/a$  dependence of Eq. (37). In panel (b) ( $E_C = 1$  EeV), the code is compared to a mixed hadronic/electromagnetic cascade from [31]. AVZ note that pure electromagnetic cascades do not result from electroweak neutrino interactions, because the charged-current case always has a hadronic component. Thus, a linear combination of the solid black and solid gray curves that sum to the black dashed curve will be observed for charged-current interactions. The lower energy in panel (b) relative to panel (a) leads to a wider cone-width because LPM elongation is proportional to  $E_C$ .

In panel (c) of Fig. 8, the same scenario as in panel (a) is depicted, but the frequency is an order of magnitude larger. In panel (d), the same scenario as in panel (b) is depicted, but the frequency is an order of magnitude larger as well. For both scenarios,  $\eta \gg 1$ , so the Cherenkov cone *loses dependence on frequency*:  $\sigma_{\Delta\theta} \sim \frac{a}{R} \sin^2 \theta$ . This result is that the electromagnetic contribution to the Cherenkov cone is actually *wider* than the hadronic contribution, because the LPM elongation increases the  $a$  of the electromagnetic component, but not the hadronic component. Note that the solid black and solid gray curves do not have to agree with the dashed curves, because they represent different frequencies. The AVZ and ZHS results are identical in all panels, and kept for reference in panels (c) and (d).

#### 4. Time-domain properties at the Cherenkov angle

The analytic RB+LPM+ $\tilde{F}(\omega, \theta)$  model is derived in the time-domain for limiting cases, and parameters from the semi-analytic treatment in Ref. [32] are derived analytically. The purpose of this section is to connect each parameter in the analytic Askaryan pulse to a physical origin in the cascade. Similar efforts have been attempted. The authors of [49] provide a formula along the lines of Eqs. (26) and (32) involving Bessel function evaluation, but rely on MC techniques to complete the model. The authors of [48] chose a mathematically tractable ICD and connected ICD parameters to simulated Askaryan radiation properties. However, the choice of ICD in [48] was for convenience, and does not necessarily agree with MC results. Here, we have attempted to both choose a 3D ICD that matches Geant4 results, and evaluate the Askaryan field analytically. See Appendix (Section A.2) for further detail.

Two cases are considered:  $\tilde{F} = 1$ , followed by  $\tilde{F}(\omega, \theta) \neq 1$ . The limiting frequency of the former,  $\omega_C$ , is governed by coherence. The latter has two limiting frequencies,  $\omega_C$  and  $\omega_{CF}$ , which leads to an asymmetry in the vector potential, and therefore, asymmetry in  $\tilde{\mathbf{E}}$ . The SI units of terms like  $R\tilde{\mathbf{E}}$  in the Fourier domain are [V/Hz], while they are just [V] for  $R\mathbf{E}$  in the time-domain. The overall scale of the field is not relevant in this section, so the unit of frequency is left as [Hz], rather than [MHz]. In each derivation, the viewing angle is  $\theta = \theta_C$ .

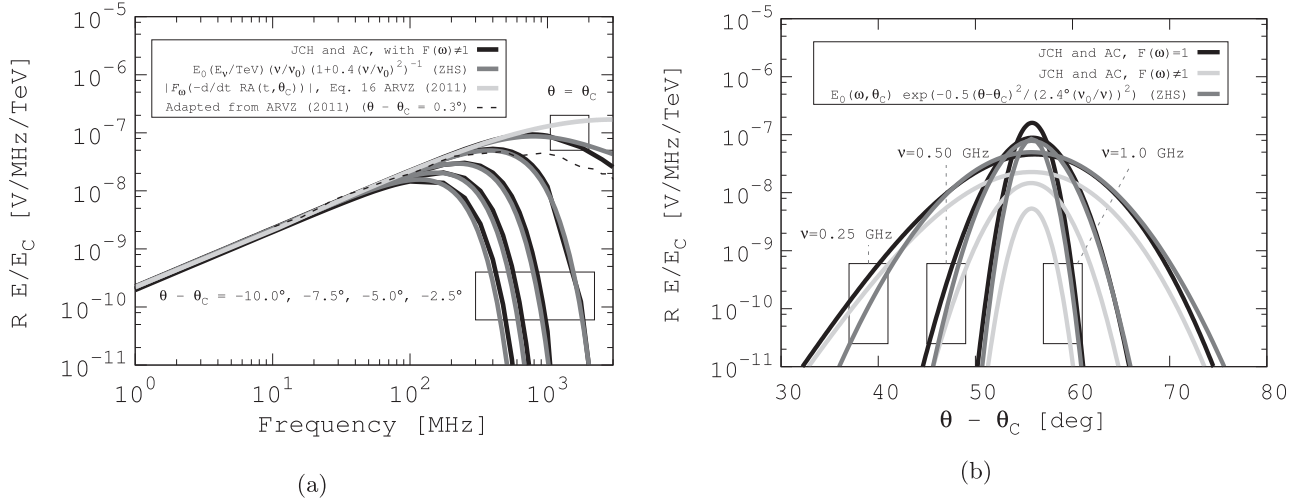


**Fig. 5.** (a) A comparison of the magnitude of the Askaryan field in different models versus  $v$  for  $E_C = 100$  TeV scaled by  $R/E_C$ . Models shown are: the associated code  $|\hat{e}_\theta \cdot \tilde{\mathbf{E}}(\omega)|$  (black), ZHS parameterization (dark gray), the  $|\hat{e}_\theta \cdot \tilde{\mathbf{E}}(\omega)|$  from Eq. (16) from ARVZ [32] (light gray), and the spectrum adapted from Fig. 3 of [32] (dashed line). For the associated code (black),  $a = 1.5$  m,  $R = 1000$  m,  $\tilde{F} \neq 1$ . The upper right box encompasses cases for which  $\theta = \theta_C$ , and the lower left box encompasses cases for which  $\theta \neq \theta_C$ . The cases are (from right to left)  $\theta_C = -2.5^\circ$ ,  $\theta_C = -5.0^\circ$ ,  $\theta_C = -7.5^\circ$ , and  $\theta_C = -10.0^\circ$ . (b) The angular dependence of the associated code  $|\hat{e}_\theta \cdot \tilde{\mathbf{E}}(\omega)|$ ,  $\tilde{F}(\omega) = 1$  (black), ZHS parameterization (dark gray), and the associated code  $|\hat{e}_\theta \cdot \tilde{\mathbf{E}}(\omega)|$ ,  $\tilde{F}(\omega) \neq 1$  (light gray).

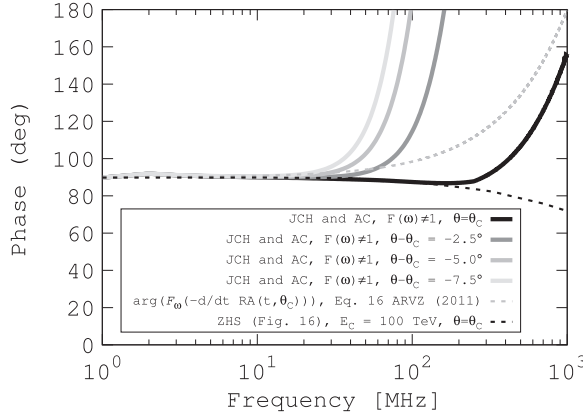


**Fig. 6.** A comparison of the phase of the Askaryan field in different models versus  $v$  for  $E_C = 100$  TeV,  $R = 1000$  m. The associated code produces the solid lines at viewing angles of  $\theta_C$  and  $\theta - \theta_C = \{-2.5^\circ, -5.0^\circ, -7.5^\circ\}$ . The gray dashed line is the phase of Eq. (16) ( $\theta = \theta_C$ ), and the black dashed line is the ZHS result.

#### 4.1. The limit $\eta < 1$ , $\tilde{F}(\omega, \theta_C) = 1$

Recall from Eq. (10) of Section 3.2 that the vector-form of the on-cone field from the RB formalism takes the form:

$$\frac{R\tilde{\mathbf{E}}(\omega, \theta_C)}{[V/\text{Hz}]} = -\frac{i\omega E_0 \sin \theta_C e^{i\omega R/c}}{(1 - i\eta)^{1/2}} \hat{e}_\theta \quad (38)$$

Let  $\hat{E}_0 = E_0 \sin \theta_C \hat{e}_\theta$ , and define  $\omega_C$  from  $\eta$ :  $\eta = \omega/\omega_C$ . Eq. (38) may be approximated to first order in the limit  $\eta < 1$ , or  $\omega < \omega_C$ , equivalent to requiring  $\lambda R \gtrsim 5a^2$ . Using the definition of  $\eta$ ,  $\nu_C = \omega_C/(2\pi)$  is

$$\nu_C = \frac{cR}{2\pi a^2 \sin^2 \theta_C} \quad (39)$$

Applying the given limit to Eq. (38), and taking the inverse Fourier transform, yields

$$RE(t_r, \theta_C) \approx \frac{i\omega_C \hat{E}_0}{\pi} \frac{d}{dt_r} \int_{-\infty}^{\infty} d\omega \frac{e^{-it_r\omega}}{\omega + 2i\omega_C} \quad (40)$$

The sign convention in the exponential in Eq. (40) is chosen to remain consistent with the RB formalism. The integral may be performed using the Cauchy integral formula, provided that

the numerator is analytic ( $\exp(-i\omega t_r)$ ) obeys the Cauchy–Riemann equations.

Contour integration of Eq. (40) requires a contour  $C$  that satisfies Jordan's lemma and includes all  $\omega \in [-\infty, \infty]$ . For the  $t_r > 0$  case, the integral converges along the contour defined by the infinite lower semi-circle because the magnitude of the numerator decreases like  $\exp(\text{Im}\{\omega\})$ . Note that this is a negatively-oriented contour. For the case  $t_r < 0$ , use the fact that  $\mathcal{F}_\omega(x(-t)) = \tilde{X}(-\omega)$ , so  $x(-t) = \mathcal{F}_\omega^{-1}(\tilde{X}(-\omega))$ , where  $\mathcal{F}_\omega(x) = \tilde{X}(\omega)$  is the Fourier transform of a function  $x(t)$ . The final solution is piecewise:

$$\frac{RE(t_r, \theta_C)}{[V]} \approx 4\hat{E}_0 \omega_C^2 \begin{cases} \exp(2\omega_C t_r) & t_r \leq 0 \\ -\exp(-2\omega_C t_r) & t_r > 0 \end{cases} \quad (41)$$

MC calculations show the transition at  $t_r = 0$  to be smooth [34]. Eq. (41) has a characteristic width of  $1/\omega_C = 1/(2\pi\nu_C)$ , implying that the pulse-width is controlled by coherence, in the absence of a form factor. Fig. 9 shows  $\nu_C$  versus the observer distance  $R$  and the shower width  $a$ .

Under the Lorentz gauge condition for Maxwell's equations, in the absence of static potentials, the negative derivative of the vector potential yields the electric field:  $-\partial\mathbf{A}/\partial t = \mathbf{E}$ . Using Eq. (41), the vector potential is

$$\frac{R\mathbf{A}(t_r, \theta_C)}{[V \cdot s]} \approx -2\hat{E}_0 \omega_C \begin{cases} \exp(2\omega_C t_r) & t_r \leq 0 \\ \exp(-2\omega_C t_r) & t_r > 0 \end{cases} \quad (42)$$

Eq. (16) of [32] is the vector potential at  $\theta = \theta_C$ :

$$\frac{R\mathbf{A}(t_r, \theta_C)}{[V \cdot s]} = -E'_0 \sin(\theta_C) \hat{e}_\theta (\exp(-2|t_r|/x_0) + (1 + x_1|t_r|)^{-x_2}) \quad (43)$$

Eq. (43) is a formula that is used in MC by ARA/ARIANNA [28,34,53], corresponding to a fit to MC similar to ZHS. By comparing Eqs. (42) and (43), a natural, theoretical explanation of the fit parameters in [32] arises, albeit from a special case:  $\tilde{F} = 1$ , and  $x_0 = 1/(\omega_C)$ , with  $x_2 \gg 1$ , or  $x_1 \sim 0$ . Thus, the result from [32] has been derived from first principles, rather than fitting to MC.

The fits in Ref. [32] have  $x_2 \approx x_1 \approx 3$ . The fact that  $x_1$  and  $x_2$  are not relevant to Eq. (42) is precisely because stipulating that  $\tilde{F}(\omega, \theta_C) = 1$  leaves the spectral limiting to  $\nu_C$  rather than  $\tilde{F}(\omega, \theta)$ . Such a scenario can be important when dealing with observations of cascades with  $R = \mathcal{O}(100)$  m, under the influence of the LPM

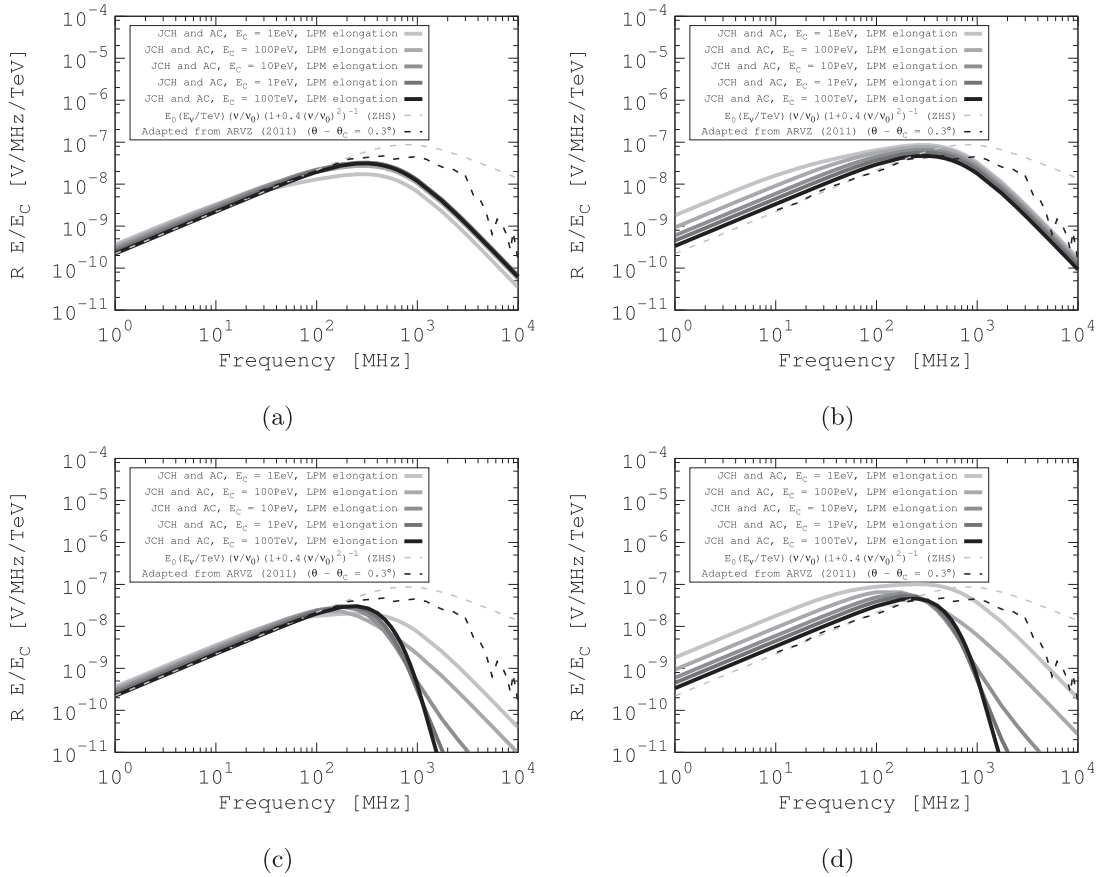


**Fig. 7.** The influence of LPM elongation on  $|\hat{e}_\theta \cdot \tilde{\mathbf{E}}(\omega)|$ , for different values of  $\eta$ . (a)  $|\hat{e}_\theta \cdot \tilde{\mathbf{E}}(\omega)|$ , for  $R = 200$  m, and  $\theta = 57^\circ$ , low-frequency restricted. (b)  $|\hat{e}_\theta \cdot \tilde{\mathbf{E}}(\omega)|$ , for  $R = 200$  m, and  $\theta = 57^\circ$ . (c)  $|\hat{e}_\theta \cdot \tilde{\mathbf{E}}(\omega)|$ , for  $R = 1000$  m, and  $\theta = 57^\circ$ , low-frequency restricted. (d)  $|\hat{e}_\theta \cdot \tilde{\mathbf{E}}(\omega)|$ , for  $R = 1000$  m, and  $\theta = 57^\circ$ . In all graphs, the black dashed line is the ZHS result with no LPM elongation, and the gray dashed line is the ARVZ result adapted from Fig. 3 of [32]. See text for detail.

effect. In this case, only a small fraction of the shower excess profile is within  $\Delta z_{\text{coh}}$ , and  $\nu_C$  cuts off the spectrum. Another example in which spectral limiting is due to  $\nu_C$ , rather than  $\tilde{F}(\omega, \theta)$ , is when the dielectric medium is denser than ice. The Askaryan spectra extends to  $\approx \mathcal{O}(10)$  GHz at  $\theta = \theta_C$  in salt, for example [54]. Higher density leads to a more compact ICD, suppressing the effect of  $\tilde{F}(\omega, \theta)$ . Fig. 9 shows a parameter space for  $\nu_C$  relevant to ARA/ARIANNA.

The result  $x_0 = 1/(\omega_C)$  also has a useful physical analogy for the shower width,  $a$ . Let the signal propagation time be  $T$ , such that (to first order)  $R = cT/n$ . Eq. (44) then relates the pulse width  $x_0$  from Eq. (43) to the shower width  $a$ :

$$x_0 = \left( \frac{a \sin \theta_C}{c} \right) \left( \frac{a \sin \theta_C}{R} \right) = T \left( \frac{a \sin \theta_C}{\sqrt{n} R} \right)^2 \quad (44)$$

Eq. (44) demonstrates that the pulse width is a fraction of the propagation time  $T$ , and proportional to  $(a/R)^2$ .

#### 4.2. The limit $\eta < 1$ , $\sigma < 1$ , $\tilde{F}(\omega, \theta_C) \neq 1$

Askaryan radiation from cascades experiences further low-pass filtering from  $\tilde{F}(\omega, \theta) \neq 1$  (Section 3.4). The parameter  $\sigma$  can be used to define a limiting frequency:  $\sigma = \omega/\omega_{\text{CF}}$ , similar to  $\eta = \omega/\omega_C$ . The electric field of Eq. (38), combined with the form factor  $\tilde{F}(\omega, \theta_C)$  of Eq. (26), is

$$\begin{aligned} \frac{\tilde{\mathbf{E}}(\omega, \theta_C)}{[\text{V}/\text{Hz}]} &= -\tilde{F}(\omega, \theta) \frac{i\omega E_0 \sin \theta_C e^{i\omega R/c}}{(1 - i\omega/\omega_C)^{1/2}} \hat{e}_\theta \\ &= -\frac{i\omega E_0 \sin \theta_C e^{i\omega R/c}}{(1 - i\omega/\omega_C)^{1/2} (1 + (\omega/\omega_{\text{CF}})^2)^{3/2}} \hat{e}_\theta \end{aligned} \quad (45)$$

In the limit  $\sigma < 1$ , and  $\eta < 1$ , Eq. (45) may be approximated as shown in Eq. (46), using  $t_r = t - R/c$ , and  $\omega_0 = \sqrt{2/3} \omega_{\text{CF}}$ .

$$\frac{R\mathbf{E}(t_r, \theta_C)}{[\text{V}]} \approx \frac{i\omega_0^2 \omega_C}{\pi} \hat{E}_0 \frac{d}{dt_r} \oint d\omega \frac{e^{-it_r \omega}}{(\omega + 2i\omega_C)(\omega + i\omega_0)(\omega - i\omega_0)} \quad (46)$$

There are two poles in the lower-half complex plane, and one in the upper-half plane. If  $t_r > 0$ , the contour integral around the lower infinite semi-circle converges because the numerator approaches zero exponentially as  $\text{Im}\{\omega\} \rightarrow -\infty$ . Conversely for  $t_r < 0$ , the contour integral converges along the upper infinite semi-circle. The final field is given by Eq. (47), to first-order in  $\epsilon$ , with  $\epsilon = \omega_0/\omega_C$ .

$$\frac{R\mathbf{E}(t_r, \theta_C)}{[\text{V}]} \approx \frac{\hat{E}_0 \omega_{\text{CF}}^2}{3} \begin{cases} (1 - \frac{1}{2}\epsilon) \exp(\omega_0 t_r) & t_r \leq 0 \\ -\exp(-\omega_0 t_r) + 2 \exp(-2\omega_C t_r) & t_r > 0 \end{cases} \quad (47)$$

Consulting Fig. 9 reveals regions of parameter space where  $\omega_C \leq 1$  GHz. Consulting Eq. (23) and (39) shows that  $\epsilon < 1$  is typical for cascades with  $a \leq \mathcal{O}(1 - 10)$  m. The relative strengths of  $\omega_C$  and  $\omega_{\text{CF}} = \sqrt{3/2}\omega_0$  are shown in Fig. 10, versus the longitudinal and lateral cascade widths. The vector potential corresponding to Eq. (47) is

$$\frac{R\mathbf{A}(t_r, \theta_C)}{[\text{V} \cdot \text{s}]} \approx -\frac{\hat{E}_0 \omega_{\text{CF}}}{\sqrt{6}} \begin{cases} (1 - \frac{1}{2}\epsilon) \exp(\omega_0 t_r) & t_r \leq 0 \\ \exp(-\omega_0 t_r) - \epsilon \exp(-2\omega_C t_r) & t_r > 0 \end{cases} \quad (48)$$

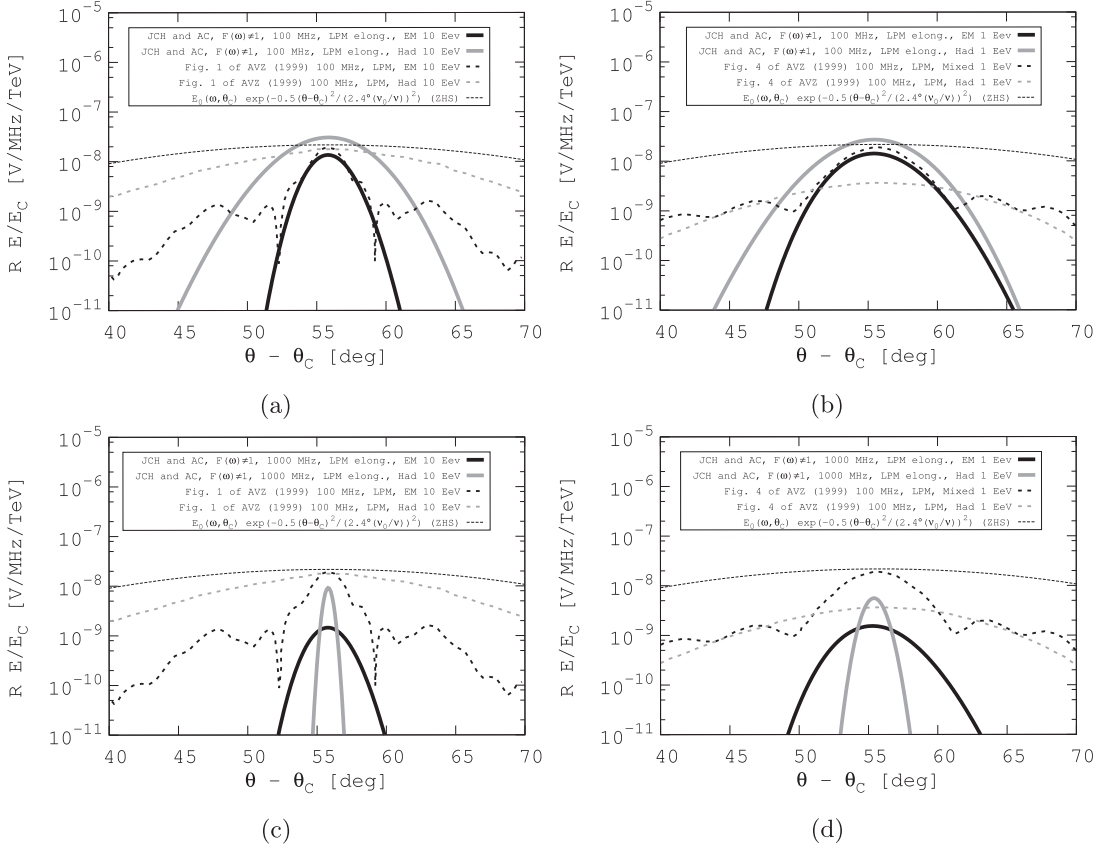


**Fig. 8.** (a)  $|\hat{e}_\theta \cdot \tilde{\mathbf{E}}(\omega)|$  versus  $\theta$ , for  $\nu = 100 \text{ MHz}$ ,  $E_C = 10 \text{ EeV}$ , and  $R = 2000 \text{ m}$ , accounting for LPM elongation, in the pure electromagnetic (solid black) and pure hadronic (solid gray) cases. Shown for comparison are the pure electromagnetic (dashed black) and pure hadronic (dashed gray) from Fig. 1 of [31]. (b)  $|\hat{e}_\theta \cdot \tilde{\mathbf{E}}(\omega)|$  versus  $\theta$ , for  $\nu = 100 \text{ MHz}$ ,  $E_C = 1 \text{ EeV}$ , and  $R = 500 \text{ m}$ , accounting for LPM elongation, in the pure electromagnetic (solid black) and pure hadronic (solid gray) cases. Shown for comparison are the mixed (dashed black) and pure hadronic (dashed gray) from Fig. 4 of [31]. (c) Same as (a), but with  $\nu = 1000 \text{ MHz}$ . (d) Same as (b), but with  $\nu = 1000 \text{ MHz}$ . Notice that for  $\nu = 1000 \text{ MHz}$ , the electromagnetic cone-width is larger than the hadronic cone-width. See text for details.

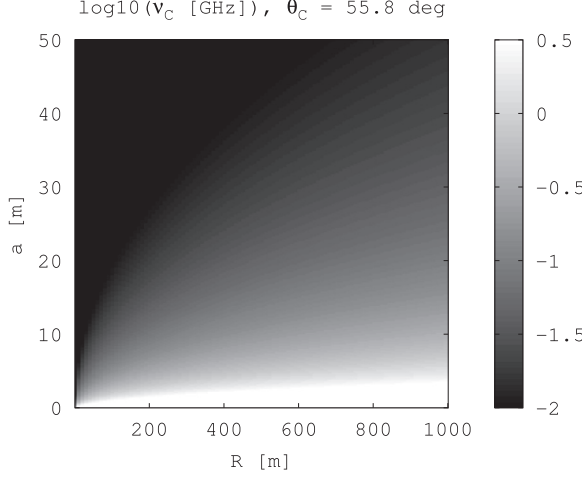


**Fig. 9.** A contour graph of  $\log_{10}v_C$ , for a parameter space relevant for ground-based radio-Askaryan detectors. Notice that  $v_C < 1 \text{ GHz}$  if  $a \gtrsim 1 \text{ m}$ .

Eqs. (47) and (48) show that the field remains bipolar but asymmetric, and asymmetric in time, from the interplay between coherence and the form factor. The pulse width is enhanced due to the presence of two different limiting frequencies,  $\omega_0 = \sqrt{2/3}\omega_{\text{CF}}$ , and  $\omega_C$ . Eq. (49) defines a parameter showing the relative importance of the two limiting frequencies:

$$\epsilon' = \omega_{\text{CF}}/\omega_C = (\sqrt{2\pi}\rho_0\rho)\left(\frac{a}{R}\right)^2 \quad (49)$$

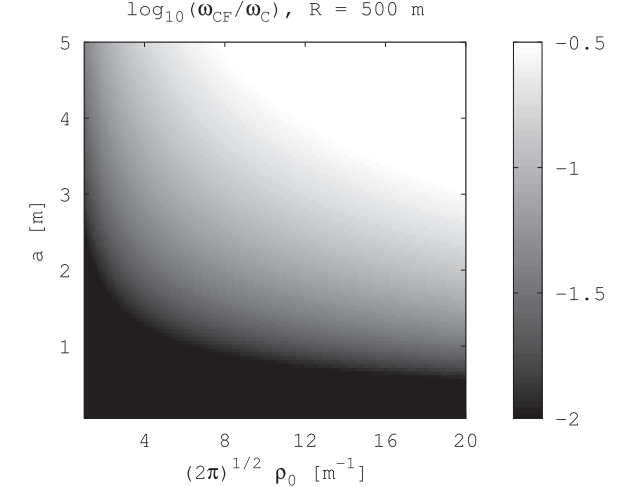


**Fig. 10.** A contour plot of  $\omega_{\text{CF}}/\omega_C = v_{\text{CF}}/v_C$ , for a parameter space relevant for ground-based radio-Askaryan detectors.

**Fig. 10** is a contour graph of  $\epsilon'$  in a parameter space relevant for ARA/ARIANNA. The first term in parentheses in Eq. (49) represents the relative importance of  $\tilde{F}(\omega, \theta)$ . The second term in parentheses is the ratio of the longitudinal cascade width to the observer distance, and it represents the quality of the Fraunhofer limit.

#### 4.3. Generalization of Eq. (45)

The purpose of Eq. (32) is to account for excess charge at lateral distances greater than one Molière radius. Consequently, Eq. (45) may be generalized to

$$\frac{R\tilde{\mathbf{E}}(\omega, \theta_C)}{[V/\text{Hz}]} = - \sum_{j=0}^N \frac{\alpha_j i\omega \hat{E}_0 e^{i\omega R/c}}{(1 - i\omega/\omega_C)^{1/2} (1 + (\omega/\omega_{CF,j})^2)^{3/2}} \quad (50)$$

Making the same approximations leading up to Eq. (46), and exchanging the order of summation and integration, yields

$$\begin{aligned} \frac{R\mathbf{E}(t_r, \theta_C)}{[V]} &\approx \sum_{j=0}^N \alpha_j \frac{i\omega_C \omega_{0,j}^2}{\pi} \hat{E}_0 \frac{d}{dt_r} \oint d\omega \\ &\quad e^{-it_r\omega} \\ &\quad \frac{(\omega + 2i\omega_C)(\omega + i\omega_{0,j})(\omega - i\omega_{0,j})}{(51)} \end{aligned}$$

Thus, accounting for wider lateral scales in the ICD (here in the far-field case) amounts to adding more poles in the complex- $\omega$  plane. The problem mirrors the addition of complex poles to digital filters to achieve a desired filter impulse response. The summation terms of Eq. (51) are equal to Eq. (47), with the substitution  $\omega_0 \rightarrow \omega_{0,j}$ :

$$\begin{aligned} \frac{R\mathbf{E}(t_r, \theta_C)}{[V]} \\ \approx \sum_{j=0}^N \alpha_j \frac{\hat{E}_0 \omega_{0,j}^2}{2} \begin{cases} (1 - \frac{1}{2} \frac{\omega_{0,j}}{\omega_C}) \exp(\omega_{0,j} t_r) & t_r \leq 0 \\ -\exp(-\omega_{0,j} t_r) + 2 \exp(-2\omega_C t_r) & t_r > 0 \end{cases} \quad (52) \end{aligned}$$

The pair of poles in Eq. (45) from the form factor  $\tilde{F}$  follow from fitting the  $\rho'$ -component of the ICD with a single exponential function. The next-most complex case is to fit the ICD  $\rho'$ -component with two exponentials ( $N = 1$  in Eq. (52), with  $\Delta_{0,j} = 2\omega_C - \omega_{0,j}$ ):

$$\begin{aligned} \frac{R\mathbf{E}(t_r, \theta_C)}{[V]} \\ \approx \begin{cases} \hat{E}_0 (\alpha_0 \omega_{0,0} \epsilon_0 \Delta_{0,0} e^{\omega_{0,0} t_r} + \alpha_1 \omega_{0,1} \epsilon_1 \Delta_{0,0} e^{\omega_{0,1} t_r}) & t_r \leq 0 \\ \hat{E}_0 e^{-2\omega_C t_r} (\alpha_0 \omega_{0,0}^2 (1 - \frac{1}{2} e^{-\Delta_{0,0} t_r}) + \alpha_1 \omega_{0,1}^2 (1 - \frac{1}{2} e^{-\Delta_{0,1} t_r})) & t_r > 0 \end{cases} \quad (53) \end{aligned}$$

#### 5. Summary

The Askaryan fields for a UHE- $\nu$  induced cascade have been presented, accounting for LPM elongation, and the 3D ICD of the cascade. The calculations are analytic, and the associated code encapsulates them into a model that is computationally efficient and in agreement with prior studies. The entire field in both  $\hat{e}_r$  and  $\hat{e}_\theta$  components is computed in the code, for any set of initial conditions chosen by users. The cascade model was verified with Geant4, and the 3D MC cascade structure formed the shape of the 3D ICD model. Evaluating the spatial Fourier transform of the 3D ICD yielded the form factor,  $\tilde{F}(\omega, \theta)$ . The effects of  $\tilde{F}(\omega, \theta)$  and LPM elongation were explored mathematically and graphically. Table 1 contains brief summary of the results and tools presented in this work.

The effect of LPM elongation was modelled as an energy-dependent increase in the longitudinal cascade width,  $a$ . LPM elongation is found to modify low-frequency emission, to suppress high-frequency emission, and to narrow the Cherenkov cone under far-field conditions.  $\tilde{F}(\omega)$  is similar to a two-pole, low-pass filter, with the limiting frequency determined by cascade Molière radius and viewing angle  $\theta$ . The  $\theta$ -dependence in the form of  $\tilde{F}(\omega, \theta)$  implies that the filtered radiation depends on the laterally-projected

**Table 1**  
A summary of new results.

Effect	Eq./Fig.	Sec.
Cascade Form Factor, $\tilde{F}(\omega, \theta)$ , single-pole	Eq. (26)	Section 3.4.2
Cascade Form Factor, $\tilde{F}(\omega, \theta)$ , multi-pole	Eq. (32)	Section 3.4.3
Contours of complete model (RB+LPM+ $\tilde{F}(\omega, \theta)$ ) $\hat{e}_\theta \cdot \tilde{\mathbf{E}}(t, \theta)$	Fig. 3	Section 3.5
Contours of complete model (RB+LPM+ $\tilde{F}(\omega, \theta)$ ) $\hat{e}_r \cdot \tilde{\mathbf{E}}(t, \theta)$	Fig. 4	Section 3.5
Complete model (RB+LPM+ $\tilde{F}(\omega, \theta)$ ) $\hat{e}_\theta \cdot \tilde{\mathbf{E}}(\omega)$ comparison	Fig. 7	Section 3.6
Complete model (RB+LPM+ $\tilde{F}(\omega, \theta)$ ) $\hat{e}_\theta \cdot \tilde{\mathbf{E}}(\theta)$ comparison	Fig. 8	Section 3.6
$E(t, \theta_C), \tilde{F}(\omega, \theta) = 1, \eta < 1$	Eq. (41)	Section 4.1
$E(t, \theta_C), \tilde{F}(\omega, \theta) \neq 1, \eta < 1$ , single-pole	Eq. (47)	Section 4.2
$\omega_{CF}/\omega_C$ Figure of Merit	Eq. (49)	Section 4.2
$E(t, \theta_C), \tilde{F}(\omega, \theta) \neq 1, \eta < 1$ , two-pole	Eq. (53)	Section 4.3

wavevector. Although these conclusions are in line with expectations, alternate scenarios were explored, yielding novel results (see Figs. 7 and 8). The field shows interesting causal structure that could serve as a discrimination technique between the distance  $R$  and the cascade energy, for *in situ* detectors such as ARA/ARIANNA (see Figs. 3 and 4).

Finally, time-domain field equations were derived by computing the inverse Fourier transform of the RB model. Future work will focus exclusively on the time domain, for viewing angles  $\theta \neq \theta_C$ , and expanded ranges of  $\eta$  and  $\omega$ . Producing theoretical, time-dependent field equations under specific limits facilitates UHE- $\nu$  signal template generation by bypassing altogether the need for Askaryan RF code, provided the limits are satisfied. Rejecting thermal noise in the *in situ* Antarctic detectors, in favour of UHE- $\nu$  signals, is an exercise in the mathematical analysis of thermal fluctuations [55]. The associated code presented in this work has been made freely available to all researchers involved in discriminating cosmogenic UHE- $\nu$  pulses from thermal backgrounds.

#### Acknowledgements

We thank the NSF for the support received under the NSF CAREER award 1255557, and for support from the NSF award for the Askaryan Radio Array (Grant 1404266). We are grateful to the Ohio Supercomputing Center [56] for their staff support, training, and resources. Contributions were also received from The Ohio State University, the Center for Cosmology and Astroparticle Physics (CCAPP), and the United States-Israel Binational Science Foundation Grant 2012077. We thank John Ralston and Roman Buny for their helpful remarks regarding the mathematical physics. Also, special thanks are in order for John Beacom and Steve Barwick for practical advice.

#### Appendix A

##### A1. Causal features and poles of Askaryan Radiation

The complex pole-structure of the various models each demonstrate how the models treat the issue of causality. The E-field of ZHS, on-cone in Eq. (34) takes the form

$$\frac{R\mathbf{E}}{[V/\text{Hz}]} = -E_0 \omega_0^2 \frac{i\omega}{(\omega + i\omega_0)(\omega - i\omega_0)} \hat{e}_\theta \quad (54)$$

Figure 16 of ZHS shows that the E-field phase is  $\sim 90^\circ$  below 1 GHz, or a phase factor of  $\exp(i\pi/2) = i$ . The overall minus sign in Eq. (54) is just a convention. Taking the inverse Fourier transform, the time-domain form of the field at the Cherenkov angle may be

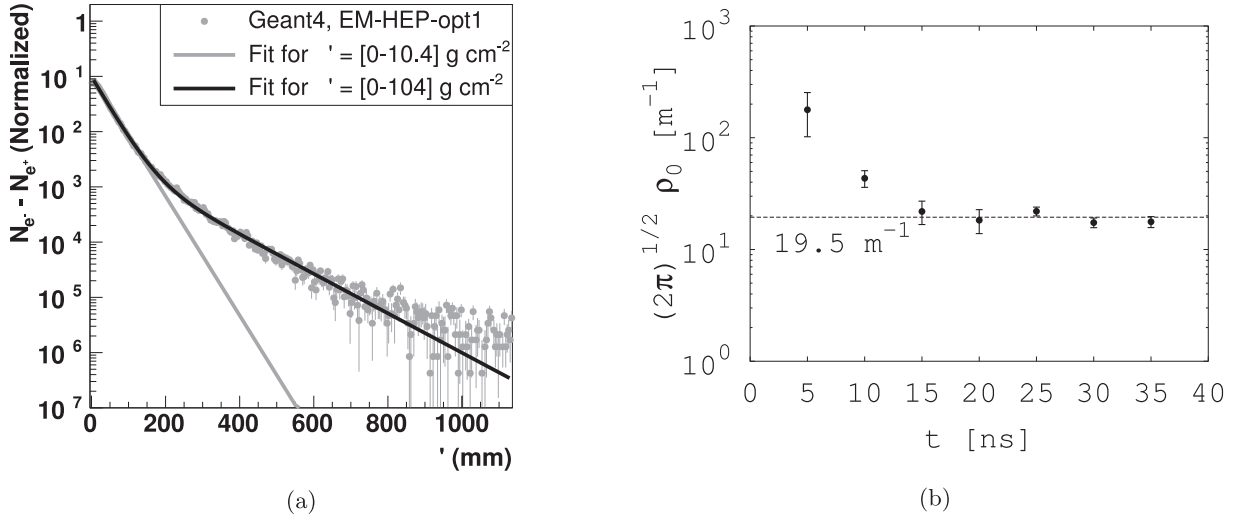


**Fig. 11.** (a)  $N_{e^-} - N_{e^+}$ , versus  $\rho'$  at 25 ns into a 100 PeV shower (gray points). A single-exponential model (gray line, Eq. (21) with slope  $\sqrt{2\pi}\rho_0$  is fit for  $\rho' < 10.4 \text{ g cm}^{-2}$ . A double-exponential model (black line, Eq. (28)) is fit for  $\rho' < 104 \text{ g cm}^{-2}$ . (b) Fit results for the parameter  $\sqrt{2\pi}\rho_0$  vs. time within the shower, using Eq. (21). The dashed line is the average of the points between 15–35 ns.

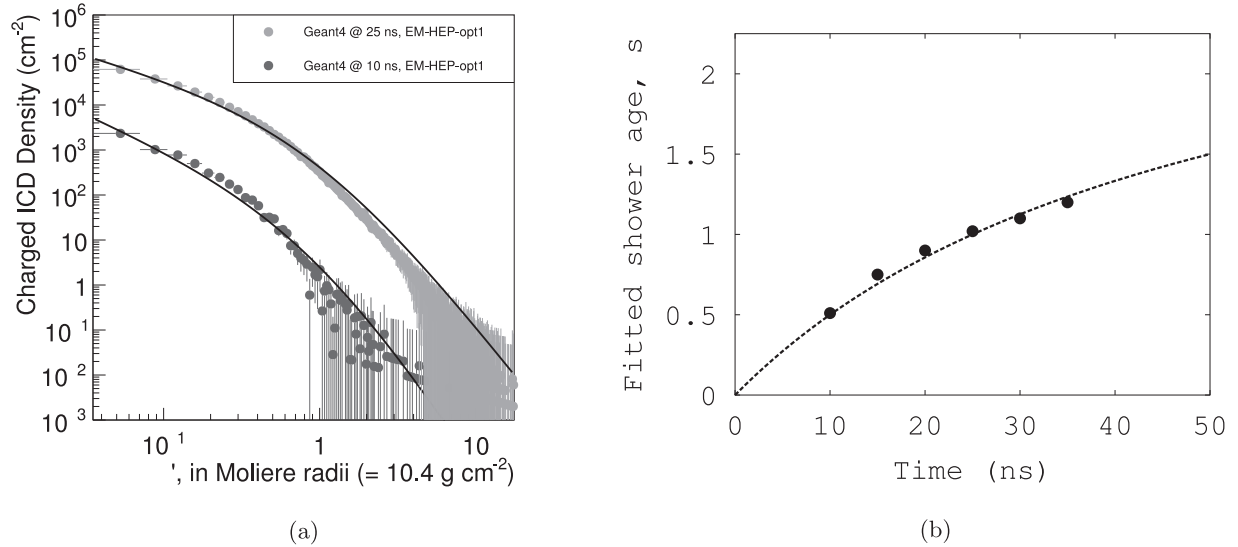


**Fig. 12.** (a) The charged ICD density, at 10 ns and 25 ns after the first interaction. The solid lines are fits of Eq. (19) to the points with the shower age,  $s$ , as free parameter. (b) The fitted shower age,  $s$ , versus time since first interaction. The dashed line is the theoretical expectation.

written

$$\frac{RE(t)}{|V|} = \omega_0^2 E_0 \frac{d}{dt} \int_{-\infty}^{\infty} \frac{e^{-i\omega t}}{(\omega + i\omega_0)(\omega - i\omega_0)} d\omega \quad (55)$$

The integral converges via Jordan's lemma if the contour is the infinite upper semi-circle for  $t < 0$ , and, for  $t > 0$ , the infinite lower semi-circle. There is an overall minus sign from the clockwise contour. The result is

$$\frac{RE(t)}{|V|} = \omega_0^2 E_0 \hat{e}_\theta \begin{cases} \exp(\omega_0 t) & t \leq 0 \\ -\exp(-\omega_0 t) & t > 0 \end{cases} \quad (56)$$

The existence poles above and below the real line is deemed a causality violation by RB. Physically, the field changes overall sign when the angular acceleration of the charge relative to the observer changes sign. Feynman's formula [30] states that the field from an accelerating charge goes like  $\mathbf{E} \propto \text{sgn}(1 - \hat{n} \cdot \vec{\beta}) \hat{u} \times \vec{\theta}$ , where  $\vec{\beta}$  is the velocity of the charge, and  $\hat{u}$  is a unit vector at the charge location in the direction of the observer.  $\mathbf{E}$  changes sign as the charge crosses the plane in which  $R$  is minimized. The quan-

tit  $\vec{\theta}$  increases rapidly, until the plane crossing, after which it decreases rapidly.

From Eq. (55)  $\tilde{F}_{ZHS}(\omega) \propto (\omega + i\omega_0)^{-1} (\omega - i\omega_0)^{-1}$ . Treating  $t > 0$  and  $t < 0$  separately, the inverse Fourier transform of  $\tilde{F}_{ZHS}(\omega)$  with respect to the coordinate  $\rho'$  yields  $f(\mathbf{x}') \propto \exp(-\rho')$ . Therefore, a logical inference is that the full, 3D ICD responsible for  $\tilde{F}(\omega, \theta)$  is distributed exponentially. Geant4 simulations show this to be correct in Section A.2.

## A2. Numerical study of the excess charge distribution

Geant4 [57,58] is used to derive numbers for  $\sqrt{2\pi}\rho_0$ , and those results are checked with Eqs. (17)–(19). Refs. [49–51] are other works that used GEANT/Pythia to calculate Askaryan radiation properties. The GEANT4 high-energy electromagnetic option-1 physics list was used, with a MC threshold of 1 MeV,  $e^\pm$  primaries, and ice of density  $0.917 \text{ g/cm}^3$  and at a temperature of 240 K. Although the LPM effect is important primarily for electro-

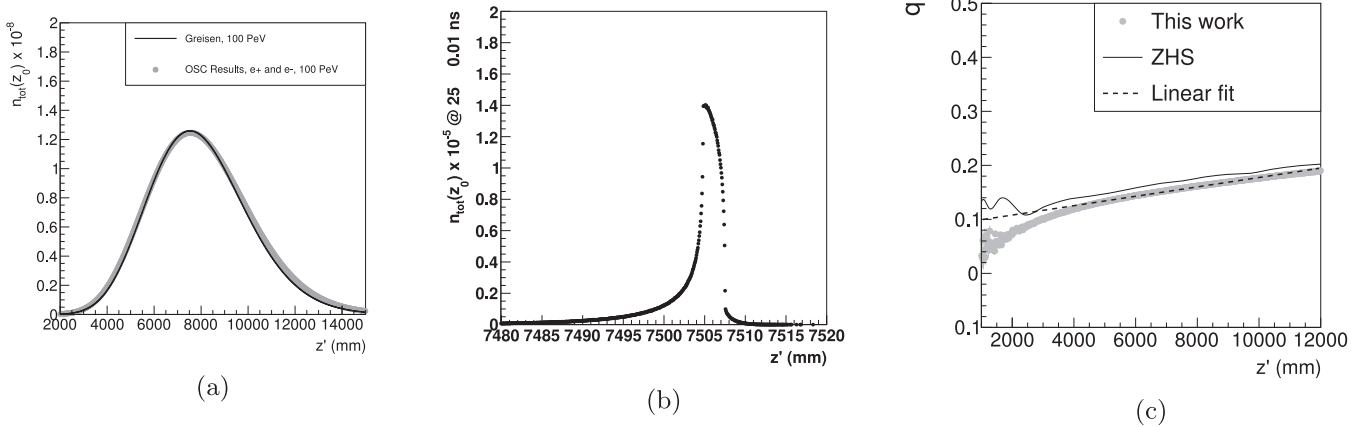


**Fig. 13.** (a)  $n_{\text{tot}}(z')$  versus  $z'$ , for a 100 PeV cascade. (b) The ICD at  $25 \pm 0.01$  ns after the first interaction. (c) The fractional negative charge excess of a 100 PeV shower, with a 5 MeV MC threshold from Geant4. The solid line is the ZHS result with a 5 MeV MC threshold, and the dashed line is a linear fit to the OSC results.

magnetic cascades,  $\tilde{F}(\omega, \theta)$  does not depend on  $a$ , so it is also valid for hadronic cascades.

CPU memory constraints forbid accounting for all tracks, so a pre-shower/sub-shower approach is taken to access more memory. A pre-shower drops all particles with energy below 0.1 PeV. The trajectory, position and type of the pre-shower particles generated by the primary are recorded and sent to separate CPUs. Each particle in the pre-shower then becomes an independent cascade, with a second MC threshold of 1 MeV.

The lateral ICD is shown in Fig. 11 (a). The results follow  $\propto \exp(-\sqrt{2\pi}\rho_0\rho')$  in the range  $\rho' = [0, \rho_1/d_{\text{ice}}]$  (0–113 mm in ice, with  $\rho_1 = 10.4 \text{ g cm}^{-3}$  and  $d_{\text{ice}} = 0.917 \text{ g cm}^{-3}$ ). The gray data corresponds to Geant4 tracks inside a 100 PeV cascade,  $25 \pm 0.01$  ns from the beginning of the first Geant4 interaction. The single exponential (single-pole) fit diverges when  $\rho' > \rho_1$ , however a double exponential (two-pole) model, comprised of a sum of exponential functions, fits the data for  $\rho' > \rho_1$ .

The results for  $\sqrt{2\pi}\rho_0$  are shown in Fig. 11 (b), averaged over 10 cascades with  $E_C = 100$  PeV. Each point contains tracks existing within 10 ps of the time on the x-axis. Early in the cascade, the particles have not yet diffused laterally, implying a higher value of  $\sqrt{2\pi}\rho_0$ . The dashed horizontal line represents the average between 15–35 ns, when lateral diffusion saturates.

The ICD per unit area, vs. Molière radius, is shown in Fig. 12 (a), plotted along with Eq. (19). Fig. 12 (b) shows the fitted shower age  $s$  as a function of time after the first interaction. Eq. (19) was fit to the MC data sets at each time bin, with  $s$  as a free parameter. The results match the definition of  $s$ , from which the gray dashed line in Fig. 12 is derived.

Fig. 13(a) matches Eq. (17) to MC data, neglecting photons, with a 1 MeV MC threshold. The Gaussian form is evident [59], justifying the RB saddle-point expansion. The ICD as a function of  $z'$  is shown in Fig. 13b. The width of  $f(x')$  versus  $z'$  is proportional to the width of the time-window (10 ps), justifying its approximation as a  $\delta$ -function in  $f(x')$ .

The parameter  $n_{\text{max}}$  in RB is the number of excess negative charges. The fractional excess charge is  $\Delta q = (N_{e^-} - N_{e^+})/(N_{e^-} + N_{e^+})$ , so  $n_{\text{max}} = N\Delta q$ . The MC shows that  $\Delta q$  is linear with depth. The y-intercept is sensitive to the MC threshold, but the slope is not. The associated code includes the linear dependence of  $\Delta q$  on depth by sampling the linear fit at  $z_{\text{max}}$ . Fig. 13(c) shows  $\Delta q$  and that of ZHS.

## References

- [1] M.G. Aartsen, et al., First observation of PeV-energy neutrinos with icecube, Phys. Rev. Lett. 111 (2013) 021103, doi:[10.1103/PhysRevLett.111.021103](https://doi.org/10.1103/PhysRevLett.111.021103).
- [2] O.E. Kalashev, V.A. Kuzmin, D.V. Semikoz, G. Sigl, Ultrahigh-energy neutrino fluxes and their constraints, Phys. Rev. D 66 (2002) 063004, doi:[10.1103/PhysRevD.66.063004](https://doi.org/10.1103/PhysRevD.66.063004).
- [3] K. Kotera, D. Allard, A. Olinto, Cosmogenic neutrinos: parameter space and detectability from PeV to ZeV, J. Cosmol. Astropart. Phys. 2010 (10) (2010) 013.
- [4] J.G. Learned, K. Manheim, High-energy neutrino astrophysics, Nucl. Part. Sci. 50 (2000) 679–749, doi:[10.1146/annurev.nucl.50.1.679](https://doi.org/10.1146/annurev.nucl.50.1.679).
- [5] K. Greisen, End to the cosmic-ray spectrum? Phys. Rev. Lett. 16 (1966) 748–750, doi:[10.1103/PhysRevLett.16.748](https://doi.org/10.1103/PhysRevLett.16.748).
- [6] G. Zatsepin, V. Kuzmin, Phys. Lett. B 8 (1969) 423.
- [7] E. Waxman, J. Bahcall, High energy neutrinos from astrophysical sources: an upper bound, Phys. Rev. D 59 (1998) 023002, doi:[10.1103/PhysRevD.59.023002](https://doi.org/10.1103/PhysRevD.59.023002).
- [8] R. Engel, D. Seckel, T. Stanev, Neutrinos from propagation of ultrahigh energy protons, Phys. Rev. D 64 (2001) 093010, doi:[10.1103/PhysRevD.64.093010](https://doi.org/10.1103/PhysRevD.64.093010).
- [9] K. Murase, M. Ahlers, B.C. Lacki, Testing the hadronuclear origin of PeV neutrinos observed with icecube, Phys. Rev. D 88 (2013) 121301, doi:[10.1103/PhysRevD.88.121301](https://doi.org/10.1103/PhysRevD.88.121301).
- [10] J.C. Joshi, W. Winter, N. Gupta, How many of the observed neutrino events can be described by cosmic ray interactions in the Milky Way? Mon. Not. R. Astron. Soc. 439 (4) (2014) 3414–3419, doi:[10.1093/mnras/stu189](https://doi.org/10.1093/mnras/stu189).
- [11] A. Connolly, R.S. Thorne, D. Waters, Calculation of high energy neutrino-nucleon cross sections and uncertainties using the Martin-Stirling-Thorne-Watt parton distribution functions and implications for future experiments, Phys. Rev. D 83 (2011) 113009, doi:[10.1103/PhysRevD.83.113009](https://doi.org/10.1103/PhysRevD.83.113009).
- [12] P.W. Gorham, A. Connolly, Implications of ultrahigh energy neutrino flux constraints for Lorentz-invariance violating cosmogenic neutrinos, Phys. Rev. D 86 (2012) 103006, doi:[10.1103/PhysRevD.86.103006](https://doi.org/10.1103/PhysRevD.86.103006).
- [13] M. Ahlers, L. Anchordoqui, M. Gonzalez Garcia, F. Halzen, S. Sarkar, GZK neutrinos after the Fermi-LAT diffuse photon flux measurement, Astropart. Phys. 34 (2) (2010) 106–115. <http://dx.doi.org/10.1016/j.astropartphys.2010.06.003>.
- [14] K. Murase, D. Guetta, M. Ahlers, Hidden cosmic-ray accelerators as an origin of TeV-PeV cosmic neutrinos, Phys. Rev. Lett. 116 (2016) 071101, doi:[10.1103/PhysRevLett.116.071101](https://doi.org/10.1103/PhysRevLett.116.071101).
- [15] G. Askaryan, Excess negative charge of electron-Photon shower and the coherent radiation originating from it. Radiorecording of showers under the ground and on the Moon, J. Phys. Soc. Jpn. 17 (Suppl A) (1962).
- [16] D. Saltzberg, et al., Observation of the Askaryan effect: coherent microwave Cherenkov emission from charge asymmetry in high-Energy particle cascades, Phys. Rev. Lett. 86 (2001) 2802–2805, doi:[10.1103/PhysRevLett.86.2802](https://doi.org/10.1103/PhysRevLett.86.2802).
- [17] P.W. Gorham, et al., Observations of the Askaryan effect in ice, Phys. Rev. Lett. 99 (2007) 171101, doi:[10.1103/PhysRevLett.99.171101](https://doi.org/10.1103/PhysRevLett.99.171101).
- [18] J.C. Hanson, Ross ice shelf thickness, radio-frequency attenuation and reflectivity: implications for the ARIANNA UHE neutrino detector, in: International Cosmic Ray Conference, 4, 2011, p. 169, doi:[10.7529/ICRC2011/V04/0340](https://doi.org/10.7529/ICRC2011/V04/0340).
- [19] J.C. Hanson, Radar absorption, basal reflection, thickness and polarization measurements from the Ross ice shelf, Antarctica, J. Glaciol. 61 (227) (2015) 438–446.
- [20] D. Besson, et al., In situ radioglaciological measurements near Taylor Dome, Antarctica and implications for Ultra-High Energy (UHE) neutrino astronomy, Astropart. Phys. 29 (2) (2008) 130–157. <http://dx.doi.org/10.1016/j.astropartphys.2007.12.004>.
- [21] I. Kravchenko, S. Hussain, D. Seckel, D. Besson, E. Fensterholz, J. Ralston, J. Taylor, K. Ratzlaff, R. Young, Updated results from the RICE experiment and future prospects for ultra-high energy neutrino detection at the South Pole, Phys. Rev. D 85 (2012) 062004, doi:[10.1103/PhysRevD.85.062004](https://doi.org/10.1103/PhysRevD.85.062004).
- [22] P.W. Gorham, et al., Observational constraints on the ultrahigh energy cosmic neutrino flux from the second flight of the ANITA experiment, Phys. Rev. D 82 (2010) 022004, doi:[10.1103/PhysRevD.82.022004](https://doi.org/10.1103/PhysRevD.82.022004).

- [23] P. Gorham, et al., The antarctic impulsive transient antenna ultra-high energy neutrino detector: design, performance, and sensitivity for the 20062007 balloon flight, *Astropart. Phys.* 32 (1) (2009) 10–41. <http://dx.doi.org/10.1016/j.astropartphys.2009.05.003>.
- [24] S. Barwick, et al., A first search for cosmogenic neutrinos with the ARIANNA hexagonal radio array, *Astropart. Phys.* 70 (2015a) 12–26. <http://dx.doi.org/10.1016/j.astropartphys.2015.04.002>.
- [25] S. Barwick, et al., Time-domain response of the ARIANNA detector, *Astropart. Phys.* 62 (2015b) 139–151. <http://dx.doi.org/10.1016/j.astropartphys.2014.09.002>.
- [26] S.W. Barwick, E.C. Berg, D.Z. Besson, T. Duffin, J.C. Hanson, S.R. Klein, S.A. Kleinfelder, K. Ratzlaff, C. Reed, M. Roumi, T. Stezelberger, J. Tatar, J. Walker, R. Young, L. Zou, Design and performance of the ARIANNA HRA-3 neutrino detector systems, *IEEE Trans. Nucl. Sci.* 62 (5) (2015c) 2202–2215, doi:10.1109/TNS.2015.2468182.
- [27] P. Allison, et al., First constraints on the ultra-high energy neutrino flux from a prototype station of the Askaryan radio array, *Astroparticle Physics* 70 (2015) 62–80. <http://dx.doi.org/10.1016/j.astropartphys.2015.04.006>.
- [28] P. Allison, et al., Design and initial performance of the Askaryan radio array prototype EeV neutrino detector at the South Pole, *Astropart. Phys.* 35 (7) (2012) 457–477. <http://dx.doi.org/10.1016/j.astropartphys.2011.11.010>.
- [29] P. Gorham, F. Baginski, P. Allison, K. Liewer, C. Miki, B. Hill, G. Varner, The ExaVolt antenna: a large-aperture, balloon-embedded antenna for ultra-high energy particle detection, *Astropart. Phys.* 35 (5) (2011) 242–256. <http://dx.doi.org/10.1016/j.astropartphys.2011.08.004>.
- [30] E. Zas, F. Halzen, T. Stanev, Electromagnetic pulses from high-energy showers: implications for neutrino detection, *Phys. Rev. D* 45 (1992) 362–376, doi:10.1103/PhysRevD.45.362.
- [31] J. Alvarez-Muniz, R.A. Vazquez, E. Zas, Characterization of neutrino signals with radiopulses in dense media through the Landau-Pomeranchuk-Migdal effect, *Phys. Rev. D* 61 (1999) 023001, doi:10.1103/PhysRevD.61.023001.
- [32] J. Alvarez-Muñiz, A. Romero-Wolf, E. Zas, Practical and accurate calculations of Askaryan radiation, *Phys. Rev. D* 84 (2011) 103003, doi:10.1103/PhysRevD.84.103003.
- [33] J. Alvarez-Muñiz, A. Romero-Wolf, E. Zas, Čerenkov radio pulses from electromagnetic showers in the time domain, *Phys. Rev. D* 81 (2010) 123009, doi:10.1103/PhysRevD.81.123009.
- [34] E. Hong, *Searching for Ultra-high Energy Neutrinos with Data from a Prototype Station of the Askaryan Radio Array, The Ohio State University, 2014 Ph.D. thesis*.
- [35] R.V. Buniy, J.P. Ralston, Radio detection of high energy particles: coherence versus multiple scales, *Phys. Rev. D* 65 (2001) 016003, doi:10.1103/PhysRevD.65.016003.
- [36] K. Greisen, Progress in cosmic ray physics. J. G. Wilson, ed. Amsterdam: North-Holland Pub.; New York: Interscience, 1952. 557 pp., *Science* 115 (2990) (1952) 426–427, doi:10.1126/science.115.2990.426-a.
- [37] P. Allison, Performance of two Askaryan radio array stations and first results in the search for ultrahigh energy neutrinos, *Phys. Rev. D* 93 (2016) 082003, doi:10.1103/PhysRevD.93.082003.
- [38] S.W. Barwick, Radio detection of air showers with the ARIANNA experiment on the Ross ice shelf, *Astropart. Phys.* 90 (2017) 50–68. <http://dx.doi.org/10.1016/j.astropartphys.2017.02.003>.
- [39] B.P. Abbott, et al., Observation of gravitational waves from a binary black hole merger, *Phys. Rev. Lett.* 116 (2016) 061102, doi:10.1103/PhysRevLett.116.061102.
- [40] V.V. Bogorodsky, C.R. Bentley, P.E. Gudmandsen, *Radioglaciology*, D. Reidel Publishing Co., 1985.
- [41] S. Klein, Suppression of Bremsstrahlung and pair production due to environmental factors, *Rev. Mod. Phys.* 71 (1999) 1501–1538, doi:10.1103/RevModPhys.71.1501.
- [42] L. Gerhardt, S. Klein, Electron and photon interactions in the regime of strong Landau-Pomeranchuk-Migdal suppression, *Phys. Rev. D* 82 (7) (2010), doi:10.1103/physrevd.82.074017.
- [43] A. Cillis, H. Fanchiotti, G.C. Canal, S. Sciutto, Influence of the LPM effect and dielectric suppression on particle air showers, *Phys. Rev. D* 59 (11) (1999) 113012, doi:10.1103/PhysRevD.59.113012.
- [44] J. Alvarez-Muiz, E. Zas, The LPM effect for EeV hadronic showers in ice: implications for radio detection of neutrinos, *Phys. Lett. B* 434 (34) (1998) 396–406. [http://dx.doi.org/10.1016/S0370-2693\(98\)00905-8](http://dx.doi.org/10.1016/S0370-2693(98)00905-8).
- [45] C.-Y. Hu, C.-C. Chen, P. Chen, Near-field effects of Cherenkov radiation induced by ultra-high energy cosmic neutrinos, *Astropart. Phys.* 35 (7) (2012) 421–434, doi:10.1016/j.astropartphys.2011.11.008.
- [46] T. Gaisser, A. Hillas, Reliability of the method of constant intensity cuts for reconstructing the average development of vertical showers, in: *Proceedings of the 15th International Cosmic Ray Conference*, 8, 1977.
- [47] G. Daniel, A. Jaime, W.R. Carvalho, R. Andrés, E. Zas, Calculations of electric fields for radio detection of ultra-high energy particles, *Phys. Rev. D* 87 (023003) (2012), doi:10.1103/physrevd.87.023003.
- [48] Chia Yu-Hu, Chih-Ching Chen, Pisin Chen, Near-field effects of Cherenkov radiation induced by ultra high energy cosmic neutrinos, *Astropart. Phys.* 35 (2012) 421–434, doi:10.1016/j.astropartphys.2011.11.008.
- [49] S. Razzaque, Coherent radio pulses from GEANT generated electromagnetic showers in ice, *Phys. Rev. D* 65 (103002) (2002), doi:10.1103/PhysRevD.65.103002.
- [50] J. Alvarez-Muniz, Comparative study of electromagnetic shower track lengths in water and implications for Čerenkov radio emission, *Phys. Rev. D* 68 (043001) (2003), doi:10.1103/PhysRevD.68.043001.
- [51] D. McKay, S. Hussain, Comparative study of radio pulses from simulated hadron-, electron-, and neutrino-initiated showers in ice in the GeV-PeV range, *Phys. Rev. D* 70 (103003) (2004), doi:10.1103/PhysRevD.70.103003.
- [52] K. Dookayka, *Characterizing the Search for Ultra-High Energy Neutrinos with the ARIANNA Detector*, The University of California, Irvine, 2011 Ph.D. thesis.
- [53] J.C. Hanson, *The Performance and Initial Results of the ARIANNA Prototype*, The University of California, Irvine, 2013 Ph.D. thesis.
- [54] P. Miočinović, et al., Time-domain measurement of broadband coherent Čerenkov radiation, *Phys. Rev. D* 74 (2006) 043002, doi:10.1103/PhysRevD.74.043002.
- [55] S.O. Rice, Mathematical analysis of random noise, *Bell Syst. Tech. J.* 23 (3) (1944) 282–332, doi:10.1002/j.1538-7305.1944.tb00874.x.
- [56] OSC, Ohio supercomputer center, 1987, (<http://osc.edu/ark:/19495/f5s1ph73>).
- [57] S. Agostinelli, et al., Geant4 a simulation toolkit, *Nucl. Instrum. Methods Phys. Res. Sect. A* 506 (3) (2003) 250–303. [http://dx.doi.org/10.1016/S0168-9002\(03\)01368-8](http://dx.doi.org/10.1016/S0168-9002(03)01368-8).
- [58] J. Allison, et al., *Geant4 developments and applications*, *IEEE Trans. Nucl. Sci.* 53 (1) (2006) 270–278.
- [59] B. Rossi, *High-Energy Particles*, NJ, 1952.

# Radio detection of air showers with the ARIANNA experiment on the Ross Ice Shelf

S. W. Barwick<sup>a</sup>, D. Z. Besson<sup>b,c</sup>, A. Burgman<sup>d</sup>, E. Chiem<sup>e</sup>, A. Hallgren<sup>d</sup>, J. C. Hanson<sup>f</sup>, S. R. Klein<sup>g,h</sup>, S. A. Kleinfelder<sup>e</sup>, A. Nelles<sup>a,\*</sup>, C. Persichilli<sup>a</sup>, S. Phillips<sup>a</sup>, T. Prakash<sup>e</sup>, C. Reed<sup>a</sup>, S. R. Shively<sup>a</sup>, J. Tatar<sup>a,i</sup>, E. Unger<sup>d</sup>, J. Walker<sup>a</sup>, G. Yodh<sup>a</sup>

<sup>a</sup>*Dept. of Physics and Astronomy, University of California, Irvine, USA*

<sup>b</sup>*Dept. of Physics and Astronomy, University of Kansas, USA*

<sup>c</sup>*National Research Nuclear University MEPhI (Moscow Engineering Physics Institute) 115409, Moscow, Russia*

<sup>d</sup>*Dept. of Physics and Astronomy, Uppsala University, Sweden*

<sup>e</sup>*Dept. of Electrical Engineering and Computer Science, University of California, Irvine, USA*

<sup>f</sup>*Center for Cosmology and Astro-Particle Physics (CCAPP), Dept. of Physics, Ohio State University, USA*

<sup>g</sup>*Lawrence Berkeley National Laboratory, USA*

<sup>h</sup>*Dept. of Physics, University of California, Berkeley, USA*

<sup>i</sup>*Office of Information Technology, Research Computing, University of California, Irvine, USA*

---

## Abstract

The ARIANNA hexagonal radio array (HRA) is an experiment in its pilot phase designed to detect cosmogenic neutrinos of energies above  $10^{16}$  eV. The most neutrino-like background stems from the radio emission of air showers. This article reports on dedicated efforts of simulating and detecting the signals of cosmic rays. A description of the fully radio self-triggered data-set, the properties of the detected air shower signals in the frequency range of 100-500 MHz and the consequences for neutrino detection are given. 38 air shower signals are identified by their distinct waveform characteristics, are in good agreement with simulations and their signals provide evidence that neutrino-induced radio signals will be distinguishable with high efficiency in ARIANNA. The cosmic ray flux at a mean energy of  $6.5_{-1.0}^{+1.2} \times 10^{17}$  eV is measured to be  $1.1_{-0.7}^{+1.0} \times 10^{-16}$  eV $^{-1}$ km $^{-2}$ sr $^{-1}$ yr $^{-1}$  and one five-fold coincident event is used to illustrate the capabilities of the ARIANNA detector to reconstruct arrival direction and energy of air showers.

*Keywords:* Cosmic rays, Neutrinos, Radio emission

98.70.Sa, 95.85.Ry, 95.55.Vj, 95.55.Jz

---

## 1. Introduction

The ARIANNA experiment (Antarctic Ross Ice shelf ANtenna Neutrino Array) is a surface array of radio antennas designed to detect cosmogenic neutrinos [1]. Currently in its pilot phase the hexagonal radio array (HRA) [2], the experiment has been taking data since 2014.

ARIANNA is aimed at detecting the radio emission of neutrino induced showers in ice. The radio emission is caused by the changing charge imbalance that is created in the shower front as it accumulates electrons from the medium and shower positrons are annihilated [3]. While test-beam experiments have shown that radio emission is indeed created in a shower [4], the first measurement of the radio emission due to a neutrino is still being awaited.

Considerable progress has been made in the last years in radio detection of air showers (see [5] for a review). Radio emissions of air showers are now routinely measured at various experiments, such as AERA [6], LOFAR [7] and Tunka-Rex [8] in coincidence with particle arrays or optical methods such as Fluorescence or Cherenkov detectors. Detections have also been reported from the balloon-based experiment ANITA [9].

---

\*Corresponding author: anelles@uci.edu

The radio emission of air showers is created analogously to the emission of showers in dense media (such as ice), with differences due to differing density and index of refraction of the two media. In the atmosphere the shower develops over several kilometers, and its development is affected by its propagation through the geomagnetic field. The magnetic field leads to a charge separation of electrons and positrons, which creates a changing transverse current that is responsible for the dominant *geomagnetic emission* in air showers [10, 11]. The charge imbalance, or *Askaryan effect* [3], is only of secondary importance in air, and accounts for about 5-20% of the total emission depending on zenith angle and observer distance to the shower axis [12, 13]. In ice, the increased density enhances the charge excess effect and causes showers to develop over a shorter length-scale, which diminishes the geomagnetic effect. Both contributions can be identified by their polarization signature. The polarization of the geomagnetic emission is determined for all observer positions through the Lorentz-force and so set by the shower axis and the geomagnetic field. Since the charge excess is symmetric around the shower axis, the polarization of the electric-field vector induced by the Askaryan effect always points toward the shower axis for all observer positions. The signal power radiated from each effect scales with the number of particles in the shower, which itself scales with the energy of the primary particle. Experimental results support the theoretical findings that the pulse amplitude scales linearly with the energy of the shower [6].

The frequencies at which the radio emission of a shower is observable are determined by the length-scale (in space and time) of the shower front, because it is a coherence effect. The size of the shower front determines the minimum wavelength over which the radiation is coherent. The shower front in air is larger than the one in ice, so air showers generally show the strongest power at frequencies below 100 MHz, while the power emitted from neutrino showers peaks above 100 MHz [14]. Whether coherence is obtained at a given observer location is also subject to the index of refraction of the medium. At the Cherenkov angle the emitted radiation of all frequencies will arrive at the same time, increasing the signal amplitude. In air, the typical Cherenkov angle is about  $1^\circ$ . For a vertical air shower observed at sea-level,  $1^\circ$  corresponds to a distance of less than 100 m from the shower axis. At this radius, the signals undergo Cherenkov-like compression and a ring of strong emission is visible [15]. Longer wavelengths remain coherent further off the Cherenkov cone than shorter wavelengths, so most of the air shower detectors operating at 30-80 MHz observe a non-uniformly illuminated ellipse in the order of hundred meters in radius, showing a clear increase in size with zenith angle [16]. In cold ice, the index of refraction is about 1.7, corresponding to a Cherenkov angle of about  $53^\circ$ . For all frequencies the emission from neutrino showers in ice will therefore be on a ring distant from the shower axis, with its width determined by the observing frequency band [17, 18].

The radio emissions of both types of showers will only be detectable once their emitted power exceeds the ambient background, determined by the thermal noise of antenna systems as well as man-made and astronomical radio emission. The pulse power at a fixed distance from the shower scales quadratically with the energy of the primary particle [6]. The exact threshold energy of detectability is also determined by the observation frequency band, as well as the gain of the antenna system. In addition, real trigger effects such as spacing of the antenna array, the threshold of an external particle array or the efficiency of the self-trigger have to be considered.

Short, bipolar, nanosecond-scale pulses are predicted for showers from both neutrinos and cosmic rays, where the frequency content of the pulse is determined by the dimensions of the shower and the observer location. Consequently, air showers, as they are more abundant than neutrinos interactions at energies of  $10^{16}$  eV, are a significant confusion background for neutrino observations. They will therefore have to be identified and removed for any neutrino analysis. However, measuring air showers with neutrino telescopes will provide a unique calibration source and a training set for methods and algorithms designed to identify neutrino signals. Both aspects of air shower detection will be covered in this article.

## 2. The ARIANNA experiment

The design concept of ARIANNA is to deploy high-gain, directional, and wide bandwidth (100 MHz - 1 GHz) antennas just under the surface of the Ross ice shelf, facing downward into the ice. This will allow for the detection of the radio emission created by particle showers induced by neutrinos of energy above  $10^{16}$  eV [1]. At these energies, the Earth is no longer transparent to neutrinos, with the exception of  $\nu_\tau$ -regeneration.

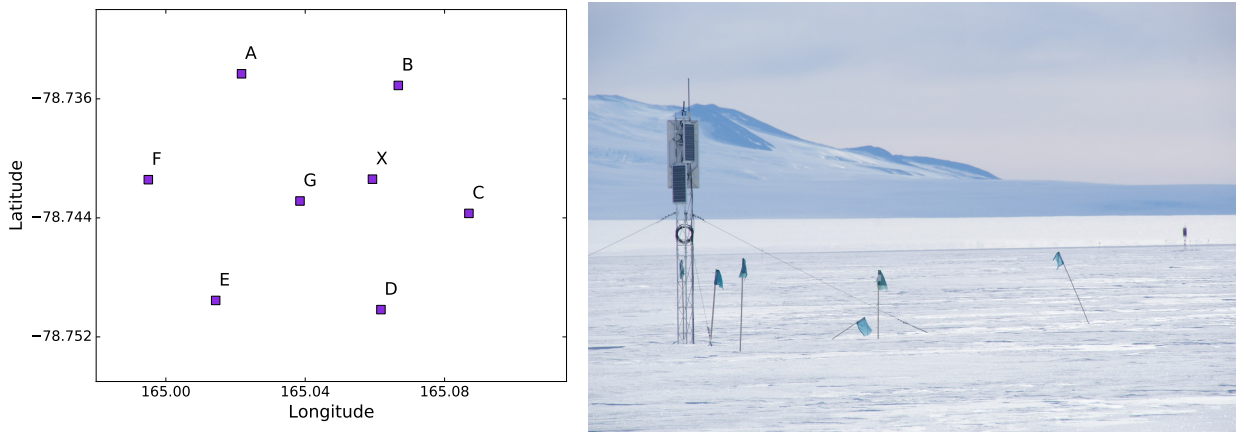


Figure 1: The layout of the ARIANNA HRA. The left panel shows the locations of the seven stations, while the photo on the right shows station X with station B in the background. The image has been taken in the 2015/16 polar season.

So ARIANNA will mostly detect neutrinos arriving from near, or above, the horizon. Additional sensitivity to downward going neutrinos is gained by using the reflective properties of the water-ice interface at the bottom of the ice shelf. The ARIANNA-site is located in an area of very smooth ice, where the reflectivity at the bottom interface is high [19].

ARIANNA targets the neutrino flux that is proposed to be caused by cosmic rays above an energy of  $10^{19}$  eV and their interactions with the cosmic microwave background [20, 21, 22]. The best current limits on these fluxes have been found by IceCube [23] and the Pierre Auger Observatory [24]. This article will show that, in addition to improving on the sensitivity of current neutrino limits by more than an order of magnitude at  $10^{18}$  eV, ARIANNA will also be sensitive to cosmic rays themselves.

### 2.1. Experimental set-up of the HRA

The ARIANNA baseline design comprises 1296 autonomous stations on a grid of  $36 \times 36 \text{ km}^2$ . Each station will be equipped with at least four downward and two upward facing antennas (Create CLP5130-2N). The antennas are log-periodic dipole antennas (LPDA) and are sensitive from 100 to 1000 MHz in air, and down to 80 MHz when immersed in firn [25]. The directionality of the LPDAs allows the downward facing antennas to be sensitive to the neutrino signal, while the upward facing antennas provide a unique tag for cosmic ray induced showers, which will be used to calibrate the array as discussed later in this article.

A pilot program of the ARIANNA observatory, the Hexagonal Radio Array (HRA), consists of seven stations (A-G) with four downward facing antennas each. The HRA was completed in 2014, and was augmented in 2015 by the addition of one station, marked as X in Figure 1, targeted at the detection of air showers, with two upward and two downward facing antennas. The upward facing antennas are tilted by  $45^\circ$  and point North and West, respectively. The layout of the array is shown in Figure 1, together with a photo from the site taken in 2015.

ARIANNA stations are designed for an extremely low power consumption of 4 W per station. This allows each station to operate continuously from sunrise in mid-September until sunset at the end of April [26], powered by solar panels and cold-resistant batteries (LiFePO<sub>4</sub>). Direct communications with the stations is enabled through either long-range wifi via a relay station on a nearby mountain, or short burst data (SBD) messages using the Iridium network. Both modes allow for real-time data transfer and remote configuration of the stations in-situ, if needed [2].

### 2.2. Data acquisition

The data-acquisition (DAQ) boards for the HRA contain SST-chips which were custom designed for the HRA. The SST samples data on four channels at 2 Gsamples/s (HRA) or 1 Gsamples/s (station X) into

ring-buffers of 256 samples, with a dynamic range of 12 bits RMS and at a bandwidth of 1.5 GHz [27]. Each channel is connected to one LPDA after amplification. The boards also house an embedded CPU, which can perform simple online analysis and can be remotely programmed. Data is stored on the local 32 GB solid-state disk and is transmitted in real-time to the server in the United States as soon as the stations enter a communication window. The trigger is formed with minimal buffering. The current trigger requires the waveform voltage to exceed a high and a low threshold within 5 ns on one channel, and again on another channel within 32 ns for a two of four majority logic requirement. The relative timing of the chips is extremely stable with a trigger-jitter in the order of picoseconds. The absolute timing is based on the Iridium network and accurate to microseconds. As the HRA stations are independent, there is no high-precision time-synchronization between them.

The DAQ system is designed to be easily reconfigured during its normal operation. A configuration file is added to a queue on the communication server, which is transmitted and applied to the station when it communicates with the server at the next regular interval. The configuration file contains parameters to control, among other things, trigger thresholds and logic, application of the level one (L1) trigger, frequency of forced triggers to collect background data, if/how to transmit data, and the time between communication windows. HRA stations pause data-taking while they are communicating, which is usually true for a couple minutes every half-hour.

The trigger thresholds are tuned to obtain a target trigger rate. Given the extreme quietness of the ARIANNA site, the stations generally run a two out of four majority logic coincidence at  $4\sigma$  of the thermal noise level, and still obtain trigger rates of less than  $10^{-3}$  Hz. There are very few narrow-band transmitters detectable at the ARIANNA site. The only relevant signals are a radio communication frequency (VHF band) at 140 MHz, air-traffic control at 220 MHz and a search and rescue channel at 400 MHz. Once communication is on-going on these channels, the transmitted power increases and the signal triggers the ARIANNA DAQ. This is typically the case only a few minutes per day. Since these signals are sinusoidal, they maximize the trigger rate when they are active. To suppress these narrow-band transmitters a L1 trigger has been designed that vetoes events on station level. Whenever the power in one frequency bin is higher than a set-able fraction (typically 0.3) of the remaining spectrum, the event will be vetoed. This L1 veto has an efficiency to retain more than 99.99% of simulated neutrino signals. The stations are also equipped with a pre-scale that records a fraction of the otherwise vetoed signals.

### 3. Simulation framework

Identifying cosmic rays – and ultimately neutrinos – in ARIANNA relies solely on methods developed with Monte Carlo simulations, as the radio emission is measured without coincidence with another method such as a particle detector. Several studies have shown that the radio signal of air showers is well understood. Especially in the frequency range of 30-80 MHz, which is used by dedicated radio air shower experiments, details are well studied. The dependence on energy or the absolute scale of the signal [28, 6], the height of the shower maximum [29, 30, 31], and the signal distribution on ground [16, 32] are reproduced with deviations of less than 10% by air shower codes such as CoREAS [33] and ZHAireS [34]. In combination with a full detector-simulation, these codes are used to precisely predict the characteristics of the signals of air showers in ARIANNA.

A thorough understanding of the detector response is prerequisite for a signal prediction. For radio detectors, the most important component remains the antenna [35]. The measured ARIANNA antenna characteristics have been discussed in previous work [36]. A simulation of the antenna response has the advantage of being able to study systematic effects and to have a uniform parameter space for arrival directions and frequencies. In this chapter, all steps of the simulation chain and its uncertainties will be discussed.

#### 3.1. Antenna modelling

The software WIPL-D [37], which has been used earlier by the LOFAR Collaboration [7], has been chosen to model the frequency and phase dependence of the ARIANNA antennas. A detailed model of the

antenna has been constructed in WIPL-D, including all plastic parts and connector wires. The program can simulate antennas immersed in any dielectric medium, as well as close to a boundary to study reflection and refraction effects. For the purpose of this analysis the antenna was placed in an infinite firn medium,  $n = 1.3$ ,  $\epsilon = 1.7$ , which is an approximation for the depth of a couple of meters below the snow surface [25]. The software returns the response of the antenna to an incoming electric field of a certain polarization as a function of frequency. The response is a complex number, so it contains the gain and phase response.

The antenna response is mostly influenced by the detailed antenna dimensions. Immersing the antenna in firn shifts its sensitivity to lower frequencies, which is explained by the change in the propagation speed from air to firn. While the antenna response in firn will be used throughout the cosmic ray analysis, the antenna simulation itself was checked with data taken in air [36], and augmented by measurements of gain and group delay with different antennas from the same manufacturer to help assess systematic variations of the LPDA response. More details can be found in Appendix A.

Systematic offsets in gain and group delay have been found between simulations and data of order 10%, while the spread between data and simulation is on average 30%. For a single frequency, the systematic difference as a function of incident angle has been found to be as low as 3% and as high as 35%.

It has been determined that the detailed features of the frequency dependent response are very sensitive to the precise antenna tine length, where high frequencies are subject to larger changes. Small changes, such as bending or shortening by a few millimeters, induce changes as function of frequency, while the overall gain remains similar. For small deformations, the changes in the angular response are small and therefore negligible. It should, however, be noted that small changes affect the back-lobe sensitivity more than the front-lobe, which makes the accurate reconstruction of signal measurements with the back-lobe more challenging. Significant differences have been found between two measurement set-ups. It is likely that these are due to systematics of the measurement set-ups, such as size of the Anechoic chamber, other local interference, or other external influences, as the same measurement of two antennas in the same set-up does not reveal such large differences.

Small changes in the frequency-dependent structure of the gain or group delay of the antenna are likely to affect the pulse form. It will be discussed later in this analysis, in how far such uncertainties are problematic. However, the overall sensitivity is mostly determined by the average again, which has been found to agree to 10% between simulations and measurements.

### 3.2. Simulating air shower signals in the HRA

Predicting the radio emission of air showers with an accuracy that can match modern experiments is best done using a full air shower simulation like CORSIKA [38] or Aires [39] with their radio extensions CoREAS [33] or ZHAireS [34]. These codes take into account not only the different emission mechanisms on a particle by particle basis, but also allow one to change atmospheric and local magnetic field settings. However, they are highly CPU intensive. While parameterizations have been shown to be useful to reconstruct events [16, 40, 6], so far, they are based on total power and provide insufficient information about the precise characteristics of the electric field, which are needed for a full detailed simulation of the signal. Therefore, we chose to simulate *generic* CoREAS showers on a star-shaped pattern of antennas [30], so that showers can be reused during the analysis as they are independent of the actual detector configuration.

A set of 1300 air showers has been simulated with CoREAS (CORSIKA 7.5000, QGSJet-II-04, FLUKA 2011.2c) for the conditions at the ARIANNA site (magnetic field of 62.3 nT, inclination angle of  $-80.4^\circ$ , 30 m above sea level). As the simulations will be used to both explore the parameter space of air shower detections and for flux calculations, it has been chosen to use only proton primaries as they cover the widest range of heights of shower maximum. The simulation parameters were randomly chosen from the energy interval of  $10^{16} - 10^{20}$  eV and the arrival direction of  $\theta = [0^\circ, 90^\circ]$  and  $\phi = [0^\circ, 360^\circ]$ , while ensuring that all bins of  $\Delta \log(E) = 0.25$  and five bins in zenith angle of equal steradian were populated.

Every simulation prescribes 160 electric field vectors at different positions on the ground surrounding the shower axis. The CoREAS simulation stops at the observer position in air and delivers a time-dependent electric field in three components. The time-sampling was chosen at 0.1 ns which over-samples the fastest HRA sampling by a factor of 10 to provide sufficient frequency resolution.

For every one of the simulated electric field vectors a prediction of the signal as it would be measured in ARIANNA can be obtained. In order to be able to account for the Fresnel reflection that takes place when entering the firn and to be able to fold the electric field with the antenna response, the electric field is converted to on-sky coordinates  $\vec{e}_r$ ,  $\vec{e}_\phi$  and  $\vec{e}_\theta$  that correspond to the propagation direction and s-polarized and p-polarized radiation, respectively. Since the electric field in the propagation direction is zero, the  $\vec{e}_r$  component is commonly ignored for the calculation of the antenna response.

Using Snell's law with  $\theta_i$ , the incident angle,  $\theta_t$  the refracted angle, and the indices of refraction  $n_{\text{air}}$  and  $n_{\text{ice}}$  leads to the following standard transmitted power fractions  $T_s$  and  $T_p$ :

$$T_s = 1 - \left| \frac{n_{\text{air}} \cos(\theta_i) - n_{\text{firn}} \cos(\theta_t)}{n_{\text{air}} \cos(\theta_i) + n_{\text{firn}} \cos(\theta_t)} \right|^2, \quad T_p = 1 - \left| \frac{n_{\text{air}} \cos(\theta_t) - n_{\text{firn}} \cos(\theta_i)}{n_{\text{air}} \cos(\theta_t) + n_{\text{firn}} \cos(\theta_i)} \right|^2. \quad (1)$$

In the field calculation the square root of the values is applied. This refraction is predicted to not only weaken the signal, but also to have an effect on the overall direction of the electric field vector and thereby the polarization.

After refracting the electric field it is folded with the modeled antenna response, which converts the electric field into a voltage  $\mathcal{E}$  in the respective antenna for an arrival direction  $(\theta, \phi)$ . This operation is performed in the on-sky coordinate system  $(\vec{e}_\phi, \vec{e}_\theta)$  and in the frequency domain, where the convolution is then a multiplication of the complex electric field  $\vec{E}(f, \theta, \phi)$  with the complex antenna effective height  $\vec{h}_{\text{eff}}(f, \theta, \phi)$ :

$$\mathcal{E} = (h_\phi, h_\theta) \cdot \begin{pmatrix} E_\phi \\ E_\theta \end{pmatrix} \quad (2)$$

The simulation software WIPL-D provides the antenna effective height in terms of complex voltages  $\vec{I}(f, \theta, \phi)$  that are the reaction of the simulated antenna to a generator current of  $V_0 = 1$  Volt:

$$\mathcal{E} = \frac{2 \lambda Z(f)}{i Z_0 V_0} \cdot \vec{I}(f, \theta, \phi) \cdot \vec{E}(f, \theta, \phi), \quad (3)$$

where  $\lambda$  is the wavelength and  $Z_0$  the vacuum impedance. An example of the antenna impedance  $Z(f)$  and the complex voltages  $\vec{I}(f, \theta, \phi)$  resulting from the WIPL-D simulations are shown in Figure A.17.

In processing the simulations, the voltage  $\mathcal{E}$  is corrected for the frequency dependent amplifier gain (see [2]) and cable losses, as well as additional filtering, which then delivers the voltage that is measured by the digitizer. The conversion ADC units to Volts is applied to the data, so that simulations and data can be compared in physical units.

An example of an electric field simulation is shown in Figure 2. The signal is generated for an air shower from a specific arrival direction and distance to the shower axis. No noise from thermal fluctuations is present. By down-sampling to the instrumental sampling rate and truncating the signals *search templates* are obtained that can be used to compare to measured data. The simulation set provides more than 200,000 templates. If, in addition, real noise as recorded by forced triggers is added, mock-data is obtained that mimics recorded events. After measured noise is added to the simulations, a software trigger is applied that mimics the hardware trigger in an HRA station. Only events that pass the trigger are used for later analyses.

### 3.3. Absolute scale of signal strength

As elaborated above, the radio emission amplitude is directly proportional to the energy of the shower. For any cosmic ray study, consequently, the absolute calibration of the detector is essential to determine the threshold energy for air shower detection. The simulation codes used to predict the emission from air showers have been reported to be accurate up to the limit of current experimental uncertainties [6]. Therefore, very minimal uncertainties on the absolute scale are expected from the predicted emission of air showers. It is more difficult to obtain a calibration of the detector to such a precise scale. A detailed measurement of every single component, as well as the monitoring of temperature dependency of the components and

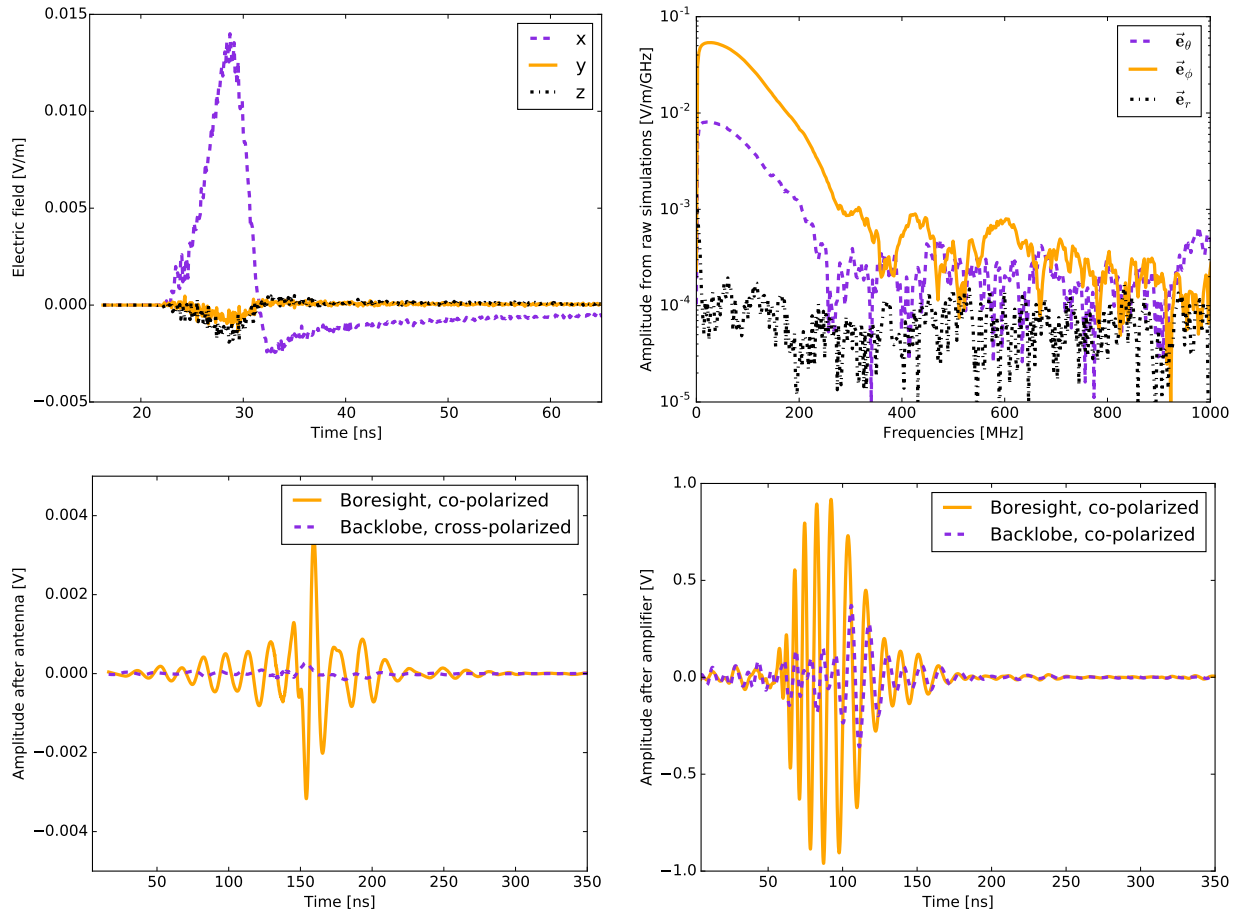


Figure 2: Illustration of the simulation chain using an air shower of an energy of  $5 \times 10^{18}$  eV. Top left: Raw electric field amplitude in air as function of time from CoREAS simulations. Top right: Frequency spectrum of the raw data, rotated to on-sky-coordinates. There is no signal in the propagation direction  $\vec{e}_r$ . Bottom left: Simulated pulse after applying the antenna model. Bottom right: Simulated pulse after amplification and filtering as it would be measured in the HRA stations. The position of the pulse is shifted due to an absolute phase offset in antenna model and measured amplifier response.

other environmental effects is needed to obtain a precision at the 10% level. The ARIANNA HRA was not designed as a precision instrument and therefore many of the following uncertainties are reducible for a future detector.

**Antenna gain:** It is not practical to measure the antenna response directly in the ice to the precision needed for this analysis. This analysis therefore relies on the simulated antenna response. As discussed in Section 3.1, it has been shown for measurements in air and at room temperature that the modeled and measured gain and group delay agree over all frequencies with a standard deviation of 30% with a systematic offset of 10%. While a fraction of these uncertainties can be explained by the measurement uncertainties, the in-ice environment adds additional uncertainties such as the index of refraction and boundary effects. Therefore, a systematic uncertainty of  $\pm 15\%$  is added for the antenna model.

**Antenna alignment:** Station X has antennas tilted towards the horizon. While it is relatively easy to ensure a perfectly vertical antenna alignment, a tilted angle is more complicated to deploy. An uncertainty of  $10^\circ$  in zenith angle is assumed, while the azimuthal alignment is accurate to  $5^\circ$ . These relatively large uncertainties also cover the fact that antennas might shift while the snow is settling, even though excavating one antenna has provided no evidence for significant movement. As these alignment uncertainties translate only indirectly into an absolute scale uncertainty, they are included as an uncertainty in the arrival direction of the air showers.

**Amplifier gain:** The amplifiers are custom made and show systematic gain variations of up to  $\pm 20\%$ . Especially with respect to the low frequencies, where high gain is achieved, the amplifiers are not uniform. In a future set-up, either the amplifiers will have to be more similar so that one calibration measurement suffices, or records of every individual component will have to be kept to reduce this uncertainty.

In addition, the gain of the amplifiers decreases with temperature. Reference measurements have been taken at room temperature. For the recorded temperatures in ice, this accounts to an uncertainty of up to  $+15\%$  of the amplitude scale. Once a model for the temperature dependence of the amplification has been developed, corrections can be applied.

**Losses in cables and connector:** All HRA stations are equipped with industrially manufactured cables and connectors. The losses have been found to increase with frequency and are about 0.5 dB at room temperature, with additional group delay. The variations between cables are small and add an uncertainty of  $\pm 2\%$ .

**ADC calibration:** The conversion from ADC counts to mV has been performed for all boards in the lab. They show a spread of 3% in the slope of the linear conversion between ADC count and voltage and a  $\pm 15\%$  uncertainty on the absolute scale. Unfortunately, the individual calibration of station X has been faulty, and therefore unusable. It was therefore decided to use an average calibration and use the spread on the measurements as the corresponding uncertainty.

**Ice parameters:** The properties of the ice at the ARIANNA-site are reasonably well-studied. The index of refraction of the firn determines the Fresnel angles and antenna properties and has been measured to be  $n = 1.29 \pm 0.02$  at the surface [19]. The index of refraction increases as a function of depth, however, the antennas remain close to the surface so that no additional correction is needed. The resulting consequences of the absolute scale are small. The same holds true for the assumption of a flat surface. The ARIANNA site shows negligible surface roughness, at least in the length scales relevant for the observing band. In addition, inhomogeneities of the firn could induce additional scattering and weaken the signal. This will have to be investigated with additional measurements. For this analysis, we add uncertainties of  $-10\%$  in signal amplitude to account for these effects.

The uncertainties are included in every relevant step of the simulation framework directly when the uncertain components are used. For all analysis a best and a worst case scenario is calculated and final parameters are given quoting the resulting scale uncertainty.

## 4. Overview of data

In this article we concentrate on data taken between December 6<sup>th</sup> 2015 and the end of data-taking at the end of April 2016. In this period the HRA was in a uniform configuration and station X was operational.

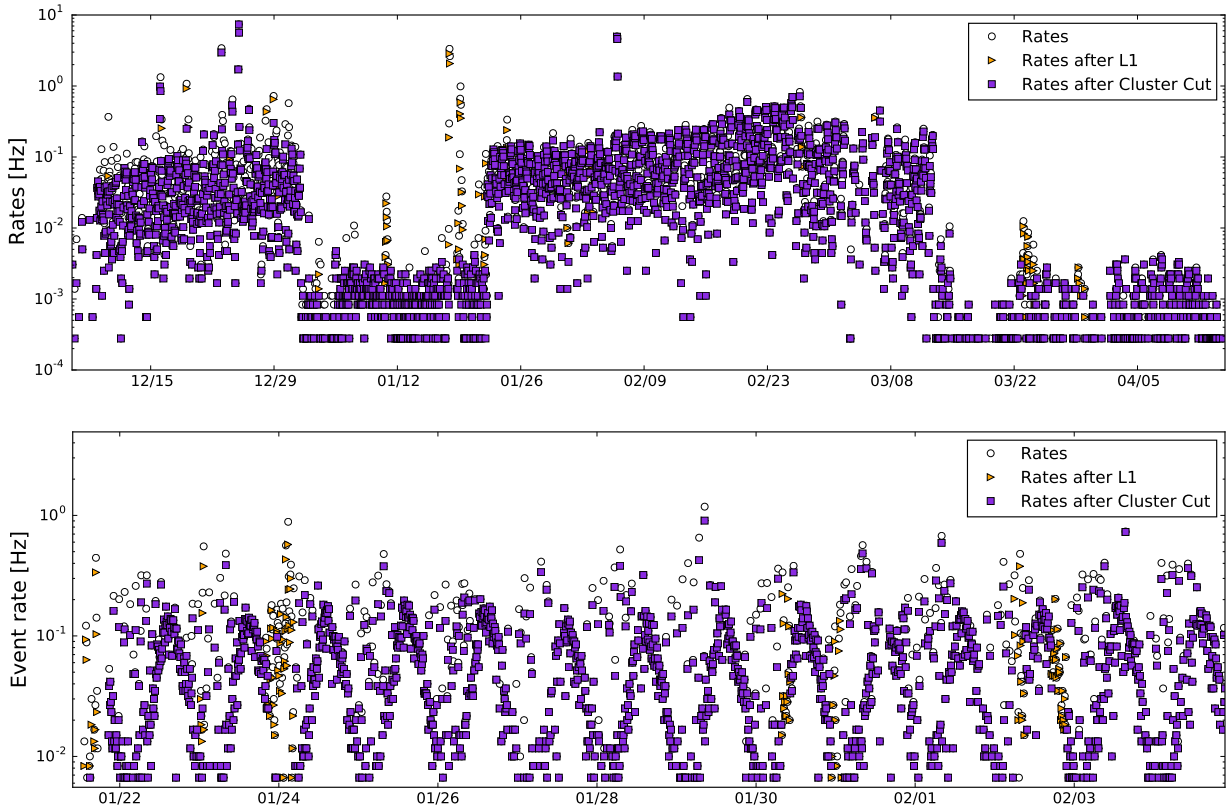


Figure 3: Top panel: Event rates as function of time from data recorded with the cosmic ray station X in the Antarctic season of 2015/16. The open circles show the recorded event rate. The triangles depict the rate after the level one trigger (on station or offline) and the filled squares indicate the cleaned event rate after L1 and cluster cut (see Section 5.1). Five periods of different trigger settings are visible as described in Table 1. Discrete event rate levels of less than  $10^{-3}$  Hz are caused by small numbers of events per time-bin. Bottom panel: Zoom on period in January, illustrating the sidereal variation.

All data is available for analysis with the exception of a fraction from station C, where data still has to be retrieved in the next polar season. The live-time fractions range between 70% and 95%. Station X has been designed with two upward and two downward facing antennas, which gives its data unique characteristics for the detection of cosmic rays. Its data will be discussed in more detail.

#### 4.1. Data taken with station X

Figure 3 and Table 1 give an overview of the data recorded with station X in the polar season of 2015/16. Several periods of distinct event rates can be identified, which correspond to different trigger conditions. During the first period, the station was triggering on a coincidence of the two upward facing antennas with no level one trigger (see Section 2.2). The latter was also true for the second period of data-taking in which the station triggered on a coincidence of the two downward facing antennas. While the thresholds were similar in both cases, the rates were significantly lower in the second period. This indicates that the directional LPDAs observed more down-coming noise. The trigger rates oscillate between  $10^{-2}$  Hz and  $10^{-1}$  Hz, with a periodicity of slightly less than 24 hours, as shown in the bottom panel of Figure 3. As will be discussed in Chapter 4.2, this periodicity is caused by Galactic emission, which dominates the signal in the upward facing antennas. On January 22<sup>nd</sup> the station was reconfigured to trigger on the upward facing antennas, and the L1 trigger to eliminate narrowband contributions was implemented. Later in the season, the thresholds were adapted to account for the increase in amplification caused by the drop in temperature.

Period	Settings
December 6 <sup>th</sup> – January 4 <sup>th</sup>	Trigger 2/2 upward channels, no L1, threshold: 70 mV
January 4 <sup>th</sup> – January 22 <sup>nd</sup>	Trigger 2/2 downward channels, no L1, threshold: 70 mV
January 22 <sup>nd</sup> – February 26 <sup>th</sup>	Trigger 2/2 upward channels, L1 on, threshold: 70 mV
February 26 <sup>th</sup> – March 2 <sup>nd</sup>	Trigger 2/2 upward channels, L1 on, threshold: 72 mV
March 2 <sup>nd</sup> – March 12 <sup>th</sup>	Trigger 2/2 upward channels, L1 on, threshold: 74 mV
March 12 <sup>th</sup> – March 14 <sup>th</sup>	Trigger 2/2 upward channels, L1 on, thresholds: 82 mV
March 12 <sup>th</sup> – April 23 <sup>rd</sup>	Trigger 2/2 upward channels, L1 on, thresholds: 84 mV

Table 1: Periods of data taking in the polar season 2015/16 with the cosmic ray station X. The trigger settings are described including the majority logic, the L1 setting and the threshold. Periods with different settings of less than one day (such as to tune thresholds) are not included. Excluding periods for data-transfer and accounting for dead-time, the total live-time for the cosmic ray station amounts to 85 days in this data-set.

In March, the thresholds were raised to allow all data to be transmitted through limited-bandwidth Iridium communication.

#### 4.2. Measuring the Galactic emission

The measurement of diffuse Galactic radio emission provides an important tool to assess the system sensitivity and quality. The brightness of the emission can be approximated by a steeply falling power-law as a function of frequency. In a well-designed system the Galactic emission should be larger than the thermal emission generated by the amplifiers and the antenna itself at frequencies below 100-150 MHz.

In station X, the periodic variation of the trigger rates (see Figure 3) is caused by a continuous variation of the detected noise power. The variation is periodic as function of local sidereal time (LST), which indicates that it is caused by an astronomical phenomenon. The power variation is strongest in the band of 80-120 MHz and the rise in power towards smaller frequencies is compatible with the expectation from the Galaxy. The lower bound on this frequency band is determined by the cutoff in frequency caused by filters and amplifiers, while the upper bound is given by the frequency where the Galactic emission is no longer detectable above the system noise [41]. The Galactic emission is used to test whether the simulation chain is an accurate representation of the data and to check the absolute scale of the predictions [42].

All background data (forced triggers) from station X have been used for this analysis. The measured waveforms of 256 ns are Fourier transformed into frequency space, squared to obtain the power and integrated between 82-121 MHz. The frequency bins are determined by the resolution of the Fourier transform (FFT), while the boundaries are chosen to maximize the observed power-variation as function of LST derived from the Galaxy. At higher frequencies the signal-to-noise ratio decreases, so only bins with a measurable power variation as function of LST are included. Finally, the average power in bins of one sidereal hour is calculated for all four channels of station X.

A model of the brightness temperature of the Galactic environment, here LFmap [41], is used to predict the power that is present in a specific frequency range,  $P_{\text{Galactic}}$ . As an example, the Galactic emission  $T_{\text{brightness}}$  at 101 MHz is shown on the left in Figure 4. The uncertainties of LFmap are quoted to better than 10% in absolute scale and to about 2% in angular variation [41].

The instantaneous Rayleigh-Jeans power spectral density  $S_\lambda$  is related to a brightness temperature  $T(\theta, \phi, \lambda)$  by:

$$S_\lambda = \frac{2ck_B}{\lambda^4} T(\phi, \theta, \lambda) \quad (4)$$

The received power  $P_r$  is then:

$$P_{r,\lambda} = S_\lambda \cdot A_{\text{eff}} \quad (5)$$

with  $A_{\text{eff}}$  the effective area of the antenna. Using the relation<sup>1</sup> between  $A_{\text{eff}}$  and the power gain  $G$

$$A_{\text{eff}}(\phi, \theta, \lambda) = \frac{G(\phi, \theta, \lambda) \cdot \lambda^2}{4\pi}, \quad (6)$$

and taking into account a factor  $\frac{1}{2}$ , because the linearly polarized antenna is only sensitive to one half of the unpolarized emission, gives:

$$P_{r,\lambda} = \frac{ck_B}{4\pi\lambda^2} T(\phi, \theta, \lambda) G(\phi, \theta, \lambda) \quad (7)$$

Integrating over the bandwidth of the LPDA that contains a detectable fraction of the Galactic power ( $\lambda = 2.50\text{-}3.75 \text{ m}$ ,  $f = 82\text{-}121 \text{ MHz}$ ) and solid angle (all angles above the horizon at a given time), gives:

$$P_{\text{Galactic}} = \frac{ck_B}{4\pi} \int_{\lambda} \int_{\Omega} \frac{1}{\lambda^2} T(\phi, \theta, \lambda) G(\phi, \theta, \lambda) d\Omega d\lambda. \quad (8)$$

The model of the Galactic emission is given in a binned map for the whole sky, which turns the integration over all angles into a sum over all steradian bins. The brightness temperature falls monotonically over the frequency band. For simplification, the emission is assumed to be constant over the frequency band and the emission at the central frequency  $f_b = 101 \text{ MHz}$  is used. The error induced by this assumption is small with respect to the absolute scale uncertainties discussed in Section 3.3.

$$P_{\text{Galactic}} = \frac{k_B}{4\pi} \cdot (121 - 83) \text{MHz} \cdot \sum_i^{\Omega} T(\phi_i, \theta_i, f_b) G(\phi_i, \theta_i, f_b) \cdot \delta\omega_i. \quad (9)$$

To obtain the voltage  $V$  measured by the HRA data-acquisition, the following equation holds:

$$V = \sqrt{P_{\text{Galactic}} \cdot Z_{\text{ant}} \cdot G_{\text{sys}}}, \quad (10)$$

with  $Z_{\text{ant}}$  the antenna impedance and  $G_{\text{sys}}$  the gain of the system at the central frequency of 101 MHz. The latter consists of half the gain of the amplifier (for an impedance matched system [43]) and losses in cables and connectors. For direct comparison to the data, the finite data length of 256 ns has to be normalized.

The model of the Galactic emission is given in right ascension and declination, so at every time of the day the emission pattern will be shifted with respect to the local coordinates  $(\theta, \phi)$ . As the signal is periodic in LST, the predicted signal power for every hour in LST for all channels is calculated. The combination of the antenna sensitivity pattern and the Galactic emission is different for all antenna orientations, as illustrated on the left of Figure 4, which leads to a different shape of the LST dependence for each antenna orientation.

To compare model results to data, the predicted Galactic power  $P_{i,\text{Galactic}}$  per channel  $i$  is co-added with thermal noise  $P_{\text{thermal}}$  from amplifiers and antenna. Even at Galactic minimum the Galactic emission detected in an antenna is still considerable, however not sufficient to explain all power observed in the system. Unfortunately, the precise fraction of thermal noise is difficult to estimate as it would require a measurement at cold temperatures, isolated from any emission from the Galactic sky. Instead,  $P_{\text{thermal}}$  was chosen as the best theoretical estimate for the noise of an amplifier at cold temperatures and is also constant in time. As this is an underestimate of the noise contribution and there are differences between channels, we allow for a free parameter  $\alpha_i$  when fitting the total power variation  $P_{i,\text{total}}$  to the data per channel with

$$P_{i,\text{total}}(t) = P_{i,\text{Galactic}}(t) + \alpha_i \cdot P_{\text{thermal}}. \quad (11)$$

The obtained values are  $\alpha_i = [1.18, 1.24, 1.23, 1.30]$  and the observed spread is consistent with the uncertainties discussed in Section 3.3.

---

<sup>1</sup>Note that  $A_{\text{eff}}$  is the absolute part of the effective antenna height  $\vec{h}_{\text{eff}}$ . Using this relation, the results from WIPL-D have been checked for consistency, see Appendix A.

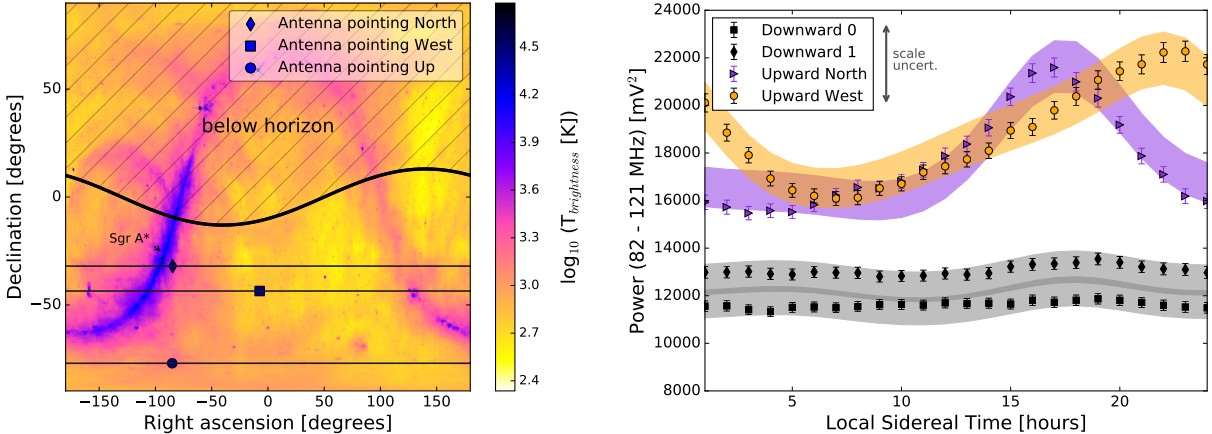


Figure 4: Left: Brightness temperature of the diffuse Galactic emission as a function of right ascension and declination at an observing frequency of 101 MHz, as given by LFmap. The broad line and hashed area indicate the horizon at the ARIANNA site at a given time. The markers indicate the pointing of the three different HRA antennas at that time. The thin lines indicate how the pointing changes throughout the day. Right: Recorded power in 256 ns as function of local sidereal time. The markers indicate the measured average power in each antenna of station X from data taken over a period of four months. The bands of the corresponding color depict the prediction derived from LFmap and the detector simulation, including systematic effects. The uncertainty on the absolute scale is illustrated by the grey arrow. This uncertainty may shift the complete model up and down within the arrow which corresponds to  $1\sigma$ .

The best fitting prediction of LFmap (bands) and the measured power (markers) are compared in Figure 4. The shape of the prediction is determined by the response of the antenna and the distribution of the Galactic emission. The thermal noise contribution is a constant offset and does not affect the shape of the oscillation in time. The bands include the uncertainties induced by the uncertainty on the antenna orientation, the uncertainty of the antenna model itself and the angular variation of LFmap. They account to between 5% and 10% of the prediction. The additional uncertainties discussed in Section 3.3 as well as the uncertainty on the absolute scaling of LFmap lead to an absolute scale uncertainty that is indicated with the vertical arrow in Figure 4. The scale uncertainty allows to shift the complete model up and down within the arrow which corresponds to  $1\sigma$ .

Agreement is found between the shape of the predicted variation and the measured power variation. For both upward-facing antennas the maxima, minima and phase have been accurately predicted and all data points are compatible with the prediction within  $1\sigma$ . Given the fitted thermal noise, the contribution of the Galactic power to the total noise budget  $P_{i,\text{Galactic}}/P_{i,\text{total}}$  accounts to between 40% and 50% in this frequency range for the upward facing antennas and between 10% and 15% for the downward facing antennas. This is in line with what is expected from a well-designed antenna system [43]. The two downward channels are, in principle, identical. The observed difference between the two is an additional indication of the scale uncertainty. The agreement of data and prediction indicates that the antenna response is adequately modeled and that the absolute scale is in agreement with the predicted emission strength.

## 5. Identification of air shower signals

Several ground-based radio air shower experiments have attempted to detect air showers solely based on their radio emission (e.g. [44, 45, 46]). The challenge usually is to select air shower signals from a background of highly abundant anthropogenic noise pulses. While it is possible to record all pulses and separate signal from background by a search for coincidences with other particle detectors, most experiments deal with the high data-rates by using sophisticated algorithms and trigger criteria at the cost of a loss in efficiency. There are several observables, such as polarization, that can be used to confirm the cosmic origin without relying on a coincidence with a particle detector [47]. However, all dedicated surface air shower experiments

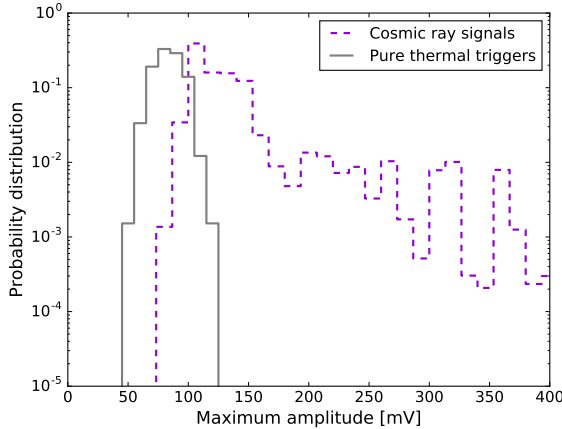


Figure 5: Probability distributions of simulated cosmic ray amplitudes as detected in station X of the HRA in comparison to the expected distribution of pure thermal noise. Isotropic arrival directions and a flux of  $E^{-3.3}$  are assumed. It should be noted that both distributions shift slightly, when the trigger thresholds are adapted. The depicted distributions were created for an average threshold of 75 mV.

ultimately rely on a particle array to uniquely flag air showers for their analyses.

In this section it will be shown that the ARIANNA site is a remarkable location and that the HRA stations do not require external confirmation to detect the radio emission of air showers. The background rates are so low that the experiment can be run at full efficiency at a low energy threshold. Also, the site has virtually no anthropogenic impulsive background that can be mistaken for signal.

The identification of air shower signals initially proceeds by selecting events from station X with upward facing antennas (see Chapter 2.1). The data from the other stations in the HRA will be used to support and augment the results. In particular, we determine the energy and arrival direction for an interesting event that was detected in five stations in the array.

First, we describe a very basic search for cosmic ray candidates that relies purely on two assumptions: Air shower signals have higher amplitudes than the thermal background (see Figure 5) and air showers are unlikely to be clustered in time. This first search is neither optimized for efficiency (finding all cosmic rays) nor for purity (finding exclusively cosmic rays), but more directly illustrates the analysis methods and the quality of the HRA data, compared to the more sophisticated analysis methods described in Section 5.2.

### 5.1. Initial candidate selection

To obtain a homogenous data-set the L1 trigger was implemented in software and applied again as a filter offline to all the data in which the L1 trigger had not been applied on station-level. As is visible in Figure 3, the stabilizing effect of the L1 trigger is obvious in December, while the small differences in January can be explained by data that had failed the L1 criterion at the station level, but was still kept as an event due to the pre-scale trigger. Those events are tagged specifically by the DAQ.

Figure 3 also shows that there are periods with higher trigger rates that are not significantly affected by the L1 criterion. As reported earlier, these are correlated to periods of high winds [1] or increased solar activity [26]. A cluster cut was implemented to remove these events from the data-set. The data is divided into sequential periods of time:  $T_c$ . Whenever two events above a certain threshold  $A_c$  occur within a short time period  $T_c$ , all events are removed within this period. The cut is implemented in two ways: to remove long periods of very high signals, such as storms:  $A_c = 300$  mV and  $T_c = 3600$  seconds, and to remove short periods of smaller signals from e.g. local transmitters:  $A_c = 150$  mV and  $T_c = 60$  seconds. The effect of the cluster cut is illustrated in Figure 6, where periods of increased signal amplitude are vetoed.

The accumulated dead-time due to the two cluster cuts is 6211 and 693 minutes, respectively, with the first being dominated by three multi-day storms. They represent a conservative estimate of the induced

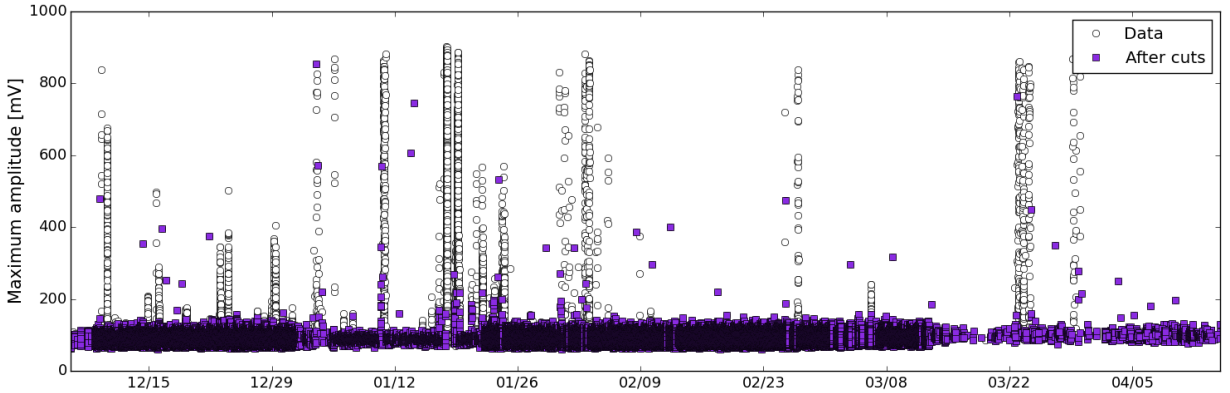


Figure 6: Maximum amplitude in any waveform recorded per event as function of time. Shown are all events in the data set (open circles) and the events remaining after L1 cut and cluster cut (filled squares).

dead-time corresponding to a loss in live-time of 6.6% of the total season. So, applying this cut removes about 7% of all cosmic rays or neutrinos randomly distributed in time, as expected from non-explosive sources.

After the L1 and cluster cut, more than 99% of the events can be found just above the trigger threshold and originate from random thermal fluctuations. Only 92 events remain above 150 mV, which is roughly twice the trigger threshold. Some of these events are likely to have survived the cluster cut, as a non-physically motivated cluster cut can hardly be fully efficient. However, these events are consistent with a random distribution in time and warrant further study.

### 5.2. Correlation analysis based on simulations

As reported earlier, the ARIANNA collaboration follows the strategy of using simulated waveforms as search templates to identify signals from neutrino interactions [1]. As discussed above, air shower signals show similar distinct characteristics, so it was chosen to apply a simulation-based correlation analysis to identify air shower signals. If the initial cut indeed selected mostly air shower signals and the correlation method has merit, then a correlation analysis will reveal the same distinct subset. Also, refining the correlation analysis with measured air shower signals, allows us to study its capabilities on real data and draw conclusions for the analysis efficiency for neutrinos of ARIANNA.

Using the simulations and templates described in Section 3.2, it is first evaluated, how similar all cosmic ray templates are with respect to each other and then how the data correlates to the templates. For this study, the variable  $\chi$  is used to describe the best correlation with one reference template out of four station channels. The variable  $\bar{\chi}$  indicates the average of all best correlations  $\chi$  over all available reference templates.

For every simulated event (four channels including noise) the values for  $\chi$  are calculated for all other 200,000 noise-free templates. As discussed in Section 3.2 the templates cover the whole expected parameter space of different distances to the shower axis, arrival directions, energies and heights of shower maximum. The resulting distribution of correlation values  $\chi$  per simulated event typically is Gaussian centered around  $\bar{\chi} = 0.8$ . The values for  $\bar{\chi}$  of these distributions range from 0.6 to 0.9 and are mostly a function of signal amplitude. Signals with high amplitudes correlate better with the templates than those where signal and noise are of similar amplitude, as the correlation is then dominated by noise. The theoretical distribution of  $\bar{\chi}$  is used to devise a cut for the data to identify air shower signals, as shown in Figure 7.

It should be noted that all distributions have a longer tail towards low correlation values ( $< 0.6$ ) and about 2% of the templates show an overall poor correlation with all other templates. These templates are due to an artifact of the CoREAS simulations. At frequencies above the coherence cut-off, the simulations are dominated by numerical noise, which scales with the energy of the shower [48], allowing cases where

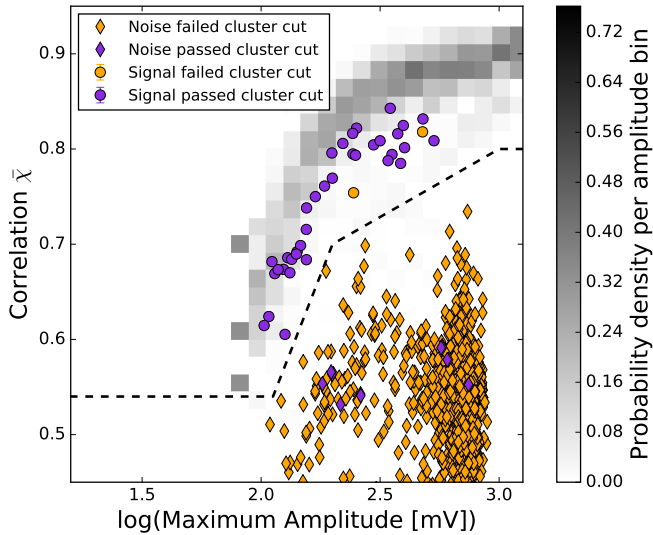


Figure 7: Average correlation  $\bar{\chi}$  as function of the maximum signal amplitude over all four channels per event. The background density map shows the probability distributions for simulated air showers given an amplitude. The markers show the average correlation value  $\bar{\chi}$  of measured events. The line indicates a cut separating the cosmic ray signals from the background. All diamonds are background events, while the signals are indicated by circles. All events corresponding to light markers are vetoed by the cluster cut.

numerical noise passes the HRA trigger condition. A perfect filter for these events is challenging without biasing against small amplitude pulses, so a contamination of about 2% is expected.

Figure 7 shows the average correlation  $\bar{\chi}$  of measured events with the search templates as a function of the maximum amplitude detected per event. In the background the same distribution is shown as obtained from correlating mock-data from simulations with the templates. The measured events surviving the cluster cut follow the distribution obtained from air shower simulations. At larger amplitudes the correlation obtained is, however, slightly smaller than predicted. This indicates that the simulations are not a perfect description of the detector. The measured pulses tend to be longer than predicted, which could indicate additional effects of the ice such as scattering, which are not modeled yet. Still, the differences in correlation are small. One can also observe that the simulations have no limit on the amplitude like the data, which is assuming a perfect linear amplification in dynamic range of the amplifiers of the HRA.

It can be seen that the cluster cut vetoes two events that belong to the cosmic ray population and does not exclude eight events that belong to the noise population, illustrating the difficulty of optimizing a cluster cut. Retaining 36 out of 38 signals is compatible with a live-time loss of 7%. We therefore choose to cut on correlation as indicated in Figure 7 as final event selection criteria, together with the narrow-band line removal L1 at station level. The cluster cut is not applied. The cut on the correlation (dashed line) contains 98.2% of the simulated templates, which is about equal to the fraction of simulated pulses that are not affected by the CoREAS artifact. This value is taken as conservative analysis efficiency of retrieving cosmic ray signals that have triggered station X.

The final event selection selects 38 cosmic ray events in station X of the HRA in the 2015/16 season. An overview of the cuts is given in Table 2. Three example events are shown in Figure 8. All events show the fall-off in frequency characteristic of air shower signals, the typical rise and fall of a pulse, and most are strongly polarized in one of the two orthogonal antenna polarizations.

Next to ensuring that the identified signals indeed show the expected shape, several cross-checks have been conducted to ensure that these events are valid air showers. For example, there is an overlap of 25 events between those 92 events that survived the cluster cut and the amplitude cut of 150 mV and the 38 selected events. Given the unknown noise contribution in the 92 events, it can only be concluded that

Description	Number of events	Fraction	Note
All data	653,447	100%	
After L1	578,745	88%	On station level: 75%
<hr/>			
Option 1:			
After cluster cut	538,198	82%	Live-time loss: 6.6%
Events above 150 mV	92	0.01%	Unclear contamination with noise
<hr/>			
Option 2:			
Cut on correlation	38	0.005%	> 98% analysis efficiency, 100% live-time

Table 2: Overview of the different cuts to obtain the event selections as discussed in sections 5.1 and 5.2. Two different options are given, of which the latter is used as final cut criterion.

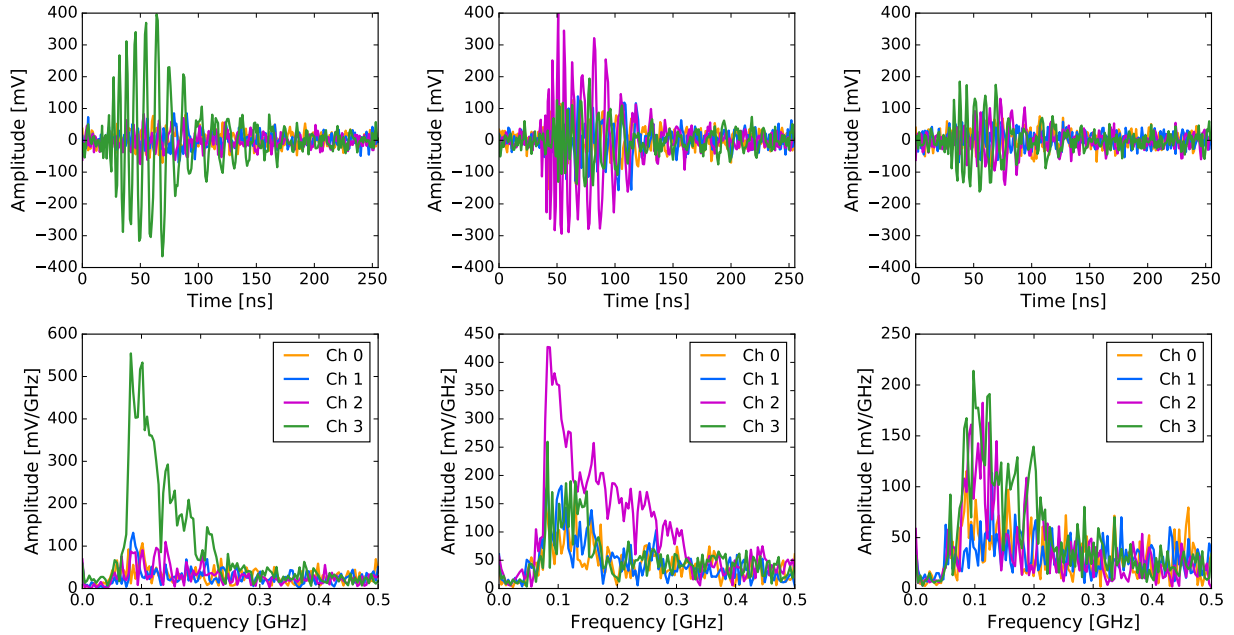


Figure 8: Three examples of events selected during the cosmic ray search. The top row shows the recorded waveforms, the bottom row the corresponding frequency spectra. Channels 0 and 1 are the downward facing antennas, antenna 2 points upward north and antenna 3 upward west.

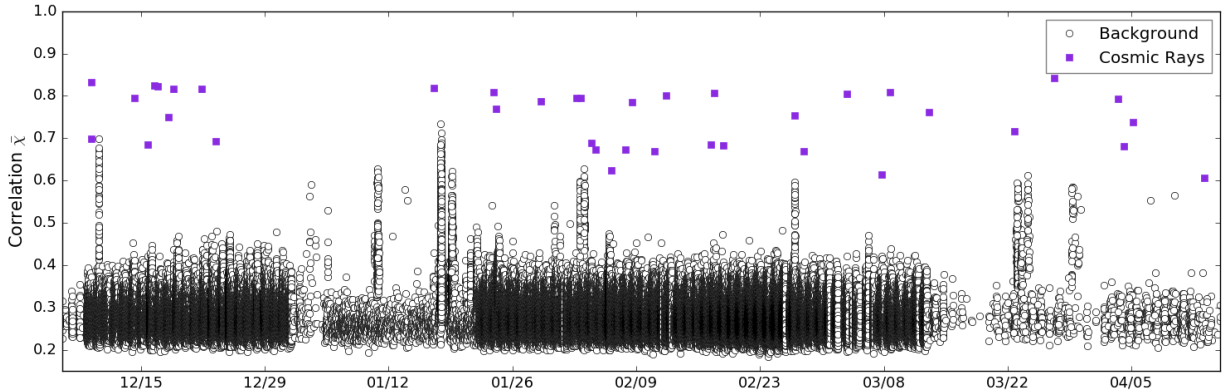


Figure 9: Average correlation values  $\bar{\chi}$  for all data of station X as function of arrival time. Shown are all events in the data set (open circles) and the data events after using the selection as shown in Figure 7 based on amplitude and correlation (filled squares).

selecting 25 out of 38 by an amplitude cut is within what has been expected from simulations. In addition, it has been confirmed that the selected events are compatible with stemming from a Poisson distribution in time. There is no evidence for a periodicity in the event times and the distribution of the inter-arrival times is well-described ( $\chi^2/\text{ndf} = 0.8$ ,  $p = 0.6$ ) by an exponential function. The distribution of arrival times is shown in Figure 9. Furthermore, all events show larger amplitudes in the upward facing antennas than in the downward facing antennas, which is consistent with directional antennas and signals arriving from above. The ratio between the amplitudes in the two upward facing antennas is compatible with a uniform distribution. As air shower signals are at the ARIANNA-site to first order polarized horizontally and orthogonal to the arrival direction, a uniform distribution of amplitude ratios is compatible with random arrival directions. A final cross-check to confirm the cosmic origin of these signals is the search for coincidences with other stations.

### 5.3. Coincidences with station X

Simulations indicate that about 40% of cosmic ray events measured in station X will trigger also another station in the HRA, even though those stations have antennas that face downwards. However, the L1, which is extremely efficient for neutrino and air shower signals arriving in the antenna front-lobe, is less efficient for back-lobe events. In the back-lobe, the antennas act like a dipole antenna and therefore the signal is likely to be strongest in one frequency bin that corresponds to the longest antenna tine and will trigger the L1 veto. Consequently, the efficiency for back-lobe cosmic ray signals is about 50%. When also correcting for the live-time of the stations, we expect  $7 \pm 3$  out of 38 air showers to have been measured in coincidence with at least one other station.

The HRA stations have coordinated absolute times to one second accuracy. While every station uses the time set by the Iridium network, which allows for a time-coordination of 0.01 s, the stations currently only record the second of each event and the time-difference between events in microseconds [2]. In an initial search, multi-station coincidences were identified using a  $\pm 1$  second window around the time of the air shower pulse in station X. We find coinciding events for five air showers. On visual inspection, all five waveforms show a pulsed signal, which is in agreement with the predicted  $7 \pm 3$  coinciding events. A search with a broader search window has revealed no additional pulses, only random coincidences of thermal triggers. Of the five coincidences, four events are a two-fold coincidence involving only one other station, while one is a coincidence of five stations. The expected number of five-fold coincidences was 0.1.

The pulses detected through the back-lobe have different characteristics than those detected in the front-lobe due to the rather different antenna response as discussed in Section 3.2, especially with respect to high frequencies. The expectations are consistent with the observed waveforms (Figure 10), providing evidence for the downward direction of the coincidence events, and the cosmic-ray hypothesis.

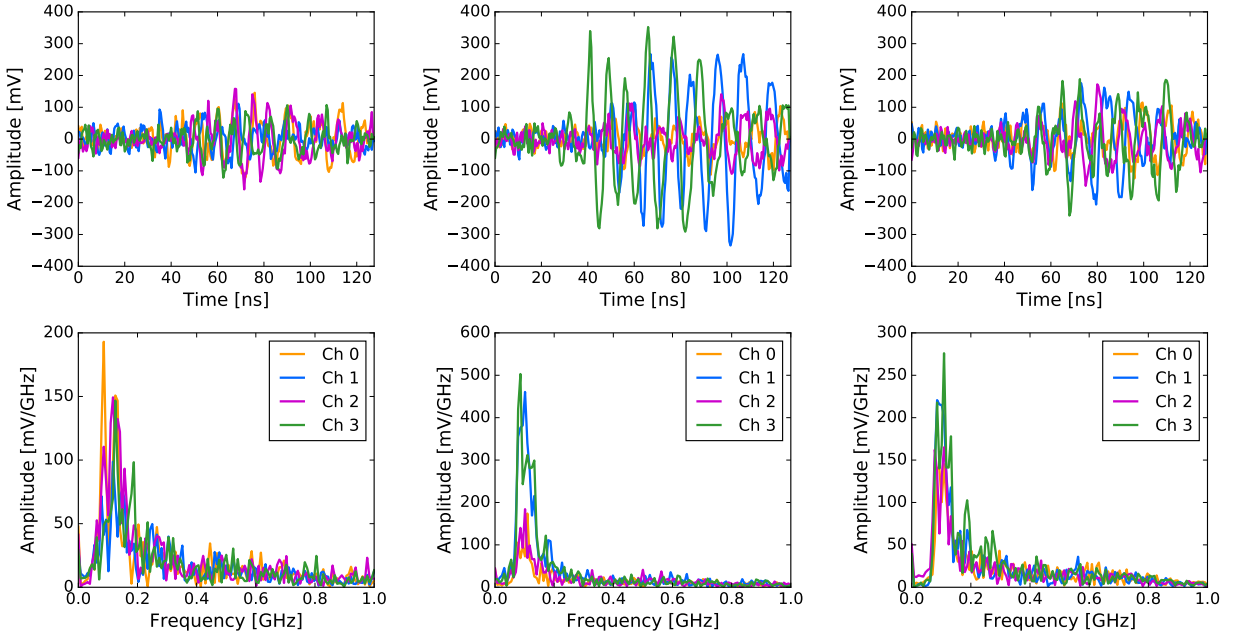


Figure 10: Three examples of signals detected in downward-facing antennas in coincidence with air shower signals in station X. Shown are the waveforms as function of time (top row) and the corresponding amplitude spectra (bottom row). It should be noted that both time and frequency resolution are different in the standard HRA stations compared to station X.

#### 5.4. Coincidences between standard stations

The coincident waveforms in standard HRA stations are not as unique as the ones in station X. Since the back-lobe suppresses high frequencies and all pulsed background signals arrive from above, there is insufficient discrimination power between cosmic rays signals and noise to reliably identify cosmic ray events in these stations. Also, due to the faster sampling, the recorded waveforms in the regular HRA stations are a factor of two shorter than the ones of station X, which means that the full pulse of an air shower is not always recorded, again hampering the identification of cosmic ray events.

If we repeat the correlation study from Section 5.2 for simulated events including noise with clean templates for regular HRA stations, the signal space is no longer fully disjunct from the tails and statistical fluctuation of the background noise. As opposed to the front-lobe templates, the back-lobe templates show a broad distribution of correlation with each other, so they cannot be used to uniquely identify air shower signals without additional information such as the arrival direction. That said, the templates show a correlation better than pure thermal noise, so they can still be used to tag likely air shower signals.

Interestingly, all identified coincident signals with station X show correlations between 0.5 and 0.9 with each other, with high correlations between events measured in the same stations. This provides evidence that the back-lobe might be more affected by physical differences between antennas than the arrival direction and therefore might not be uniform between antennas. Evidence can also be found in Figure 10, where parallel channels (0 and 2, 1 and 3) are not identical. It was therefore chosen to apply both the L1 and the cluster cut to all data of the standard stations before a back-lobe template is used for a correlation study. All events that show a correlation of better than 0.5 are selected and a coincidence between two or more stations in a time-window of one second is required. This identifies three two-fold, and two three-fold coincidences. For four out of these five coincidence events, station X was in a communications window during which the trigger was disabled. The non-detection of one of the events in station X is compatible with the prediction of a size-limited signal footprint.

If considering all ten identified coincidences, the central station G, is a part of a coincidence event in six cases, which can be explained by its closeness to station X and its central location. All but one station have

been found in at least one coincidence. All these characteristics provide confidence that air shower signals have been detected in multiple stations.

Simulations predict that there should be fewer events in the regular HRA stations as opposed to station X due to the suppressed gain. Since ARIANNA is focussed on neutrino detection, the suppression of cosmic ray signals in the back-lobe signal is desirable. However, upward facing antennas are needed to uniquely tag cosmic rays. The baseline design of ARIANNA includes upward facing antennas at all locations to allow for cosmic ray identification with high efficiency and allow for a full reduction of the relatively small possibility to confuse back-lobe cosmic ray signals with neutrino signals.

### 5.5. Event properties derived from five-fold event

To illustrate the capabilities of ARIANNA, the five-fold multi-station event discussed in the previous section will be investigated in more detail. The following section describes different methods to obtain the energy and arrival direction for this particular event.

#### 5.5.1. Reconstruction of arrival direction

It is possible to reconstruct the direction of an arriving pulse accurately from two pairs of antennas in a single station using cross-correlation, given that the positions of the antennas are well known, and the timing of the system is stable [1]. The antenna positions within a station of the HRA have been measured to an accuracy of about 10 cm with respect to each other, the timing stability of the electronics boards is better than 100 ps and the cable lengths have been measured to sub-nanosecond timing [2]. With a baseline of 6 m, this should allow for an angular reconstruction for signals arriving in the forward-direction to the theoretical limit of 0.2°. This number assumes fully efficient fitting algorithms, a limited influence of noise and that signals modulo noise are the same in parallel channels. For back-lobe signals, it is therefore unclear whether the same accuracy can be reached.

Station X, the only station that measures signals in the forward direction of the antenna, has a non-optimal geometry for direction reconstruction. The two upward facing antennas are rotated by 90 degrees to each other and tilted by 45 degrees to vertical. This design was chosen to maximize the detection efficiency for cosmic rays, confirm that the signal is strongly polarized and study the up-to-down ratio in signal amplitude. Consequently, any signal from an air shower will arrive in different sectors of antenna sensitivity and simulations indicate that the signals will look very different due to the variation in gain and group-delay. This complicates using cross-correlations of parallel channels to obtain an arrival direction. An iterative loop of direction fitting and unfolding the antenna response can provide a more complete angular reconstruction, after weighting the two strong signals and two weak signals. For now, the angular analysis excludes station X. The reconstructed arrival directions are shown in Figure 11. The clustering is encouraging, however, the space angle between the directions is 15°, which serves as estimator for all events detected by a standard station in the back-lobe. Including Fresnel refraction, the average arrival direction of the detected air shower was found to be  $\theta = 75.0^\circ, \phi = 47.3^\circ$ .

#### 5.5.2. Reconstruction of the energy using the slope of the frequency spectrum

Typically, the received power on ground is used to reconstruct the energy of an air shower (e.g. [40]). The arrival direction is determined from timing and the signals are transformed into the shower plane, where a multi-parameter fit is executed, containing a dependence on the distance to the shower axis, the energy and the distance to the shower maximum. This procedure has been optimized for radio measurements in the frequency range of 30-80 MHz, with at least 3 independent measurements of the full electric-field of the shower. The energy resolution is at least comparable to particle arrays (25-50%) [47, 40]. If the methods are adapted to the frequency range of ARIANNA, they should deliver similar results for all air showers measured in at least three stations, which will be less than 20% of the detected air showers.

Radio measurements have also shown to be sensitive to the height of shower maximum with accuracies between 15 g/cm<sup>2</sup> for dense (distance between antennas  $\sim 10$  m) and 40 g/cm<sup>2</sup> for sparse arrays (distance between antennas  $\sim 200$  m) [29, 31, 47]. A similar sensitivity is likely for ARIANNA, however, we will focus on the energy reconstruction in this analysis.

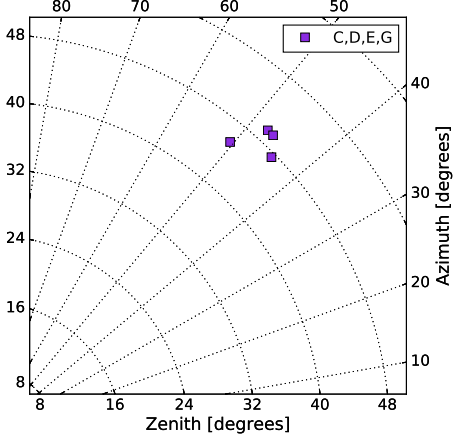


Figure 11: The reconstructed signal arrival directions corresponding to the five-fold coincidence event. The event has been detected in the standard stations C, D, E, and G, as well as station X.

The above mentioned reconstruction methods are based on the total power. They do not use the detailed signal shape of the waveforms (their frequency and phase content). It has been suggested (e.g. [49, 50, 51]) that one can extract shower parameters from just a single measurement of the electric field of the shower. The general form of a signal spectrum has been shown in Figure 2. Air shower signals usually show the strongest power at frequencies  $< 100$  MHz, with a characteristically falling spectrum towards higher frequencies. The slope of this falling spectrum, as well as the frequency at which the power is strongest, depend on the distance to the Cherenkov cone, where the slope is the flattest as coherence is obtained for all frequencies. The position of the Cherenkov cone with respect to the shower axis depends on the geometric shower development, mostly the distance to the height of the shower maximum. Given the changing frequency content, the absolute power contained in a pulse is also a function of the distance to the shower axis. However, at the same distance from the Cherenkov cone, the amplitude of the pulse scales on average linear with energy [40], so all determining air shower parameters are encoded in the signal shape. In recent air shower experiments, the bandwidth of 30-80 MHz limits the power of the spectral slope in comparison to other methods. For a wider frequency band, such as in ARIANNA, this is no longer necessarily true. As the ANITA collaboration has shown [9] an estimate of the shower energy with statistical uncertainties of as low as 25% can be determined from a pulse measurement with a wide frequency-band.

The spectral slope as an energy estimator is tested with the five-fold coincidence event. An exponential function  $\ln(A) = I + \gamma \cdot f$  is fit to the amplitude spectrum  $A$  of the pulse in the interval  $f = [100 \text{ MHz}, 300 \text{ MHz}]$ , which is where the combination of the expected pulse power and the ARIANNA sensitivity maximizes the signal-to-noise-ratio. The slope  $\gamma$  and the y-axis intercept  $I$  are fitted to the data of station X, which is shown on the left in Figure 12. The slope measurements with the downward-facing antennas in both station X and in the standard-stations carry very large uncertainties compared to the upward facing antennas and will not be included for the energy reconstruction. In addition to the measured data,  $I$  and  $\gamma$  are fitted for a dedicated set of simulated showers having the same arrival direction as the measured one (average of stations C, D, E, and G,  $\theta = 75.0^\circ, \phi = 47.3^\circ$ ). 30 showers with this arrival direction have been simulated, covering different values of  $X_{\max}$  and several discrete steps of energy. The resulting  $I$  and  $\gamma$  from a subset of simulations are shown together with the measured values from the cosmic ray event on the right in Figure 12.

The slope  $\gamma$  for one shower varies strongly with the distance to shower axis (e.g. smallest absolute value at the Cherenkov angle, largest at the shower axis). Secondary effects are the interplay of the antenna response and the polarization of the signal, as well as the height of the shower maximum. Together, these three effects explain the distribution of combination of  $I$  and  $\gamma$  for the same energy. The energy determines the intercept that is found at the Cherenkov angle. An increase in energy, while keeping all other parameters fixed,

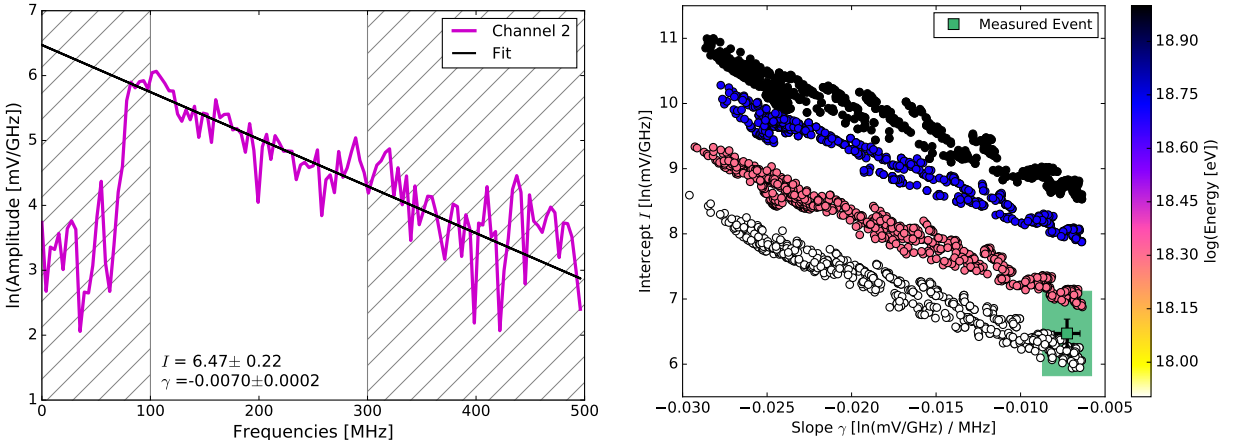


Figure 12: Left: Measured frequency spectrum of the five-fold cosmic ray event in station X. The strongest channel is highlighted together with the fit to the data between 100 MHz and 300 MHz. Right: The two fitted spectral parameters, slope  $\gamma$  and intercept  $I$ , as functions of each other. The colors of the circles indicate the energy of the simulated showers. Their signals have been processed to include the hardware effects. Shown are four discrete energies ( $8 \times 10^{17}$ ,  $2 \times 10^{18}$ ,  $5 \times 10^{18}$ , and  $10^{19}$  eV). The square marker indicates the measured value of the spectral slope in the channel with the strongest amplitude in station X. Systematic uncertainties are denoted with the box. Note that the relation between  $I$  and  $\gamma$  is different for different arrival directions and for different antenna configurations.

corresponds to a vertical shift upward in the diagram. Additional information can be found in Appendix B.

In the absence of noise and for this particular arrival direction, the slope derived from a single LPDA yields an energy resolution of about 50%. This is due to the statistical uncertainties of the fit and the intrinsic limitation due to the degeneracy between distance to the shower axis, height of the shower maximum and energy. Adding polarization information will improve the method. In addition, the contribution of noise has to be accounted for. Adding thermal noise to the simulations tends to flatten the reconstructed slope by about 30%, and therefore also the uncertainty on the intercept increases correspondingly. This dominates the systematic uncertainty together with the uncertainties discussed in Section 3.3. Including noise effects, we estimate the energy of the five-fold coincident event to be between  $8 \times 10^{17}$  eV and  $3 \times 10^{18}$  eV from the slope of a single antenna.

We cross-check this result with an adapted method similar to [30]. We use all 30 showers that have been simulated with the reconstructed arrival direction. For each of these showers, we generate an amplitude map of the shower footprint and shift the core position of the shower within the array until the best agreement between measured and simulated amplitudes is found for every station position. There are only very few combinations of shower core, energy and  $X_{\max}$  that provide a good fit; one of them is shown in Figure 13. The energy of the best fitting event falls into the interval determined by the frequency slope method.

To assess the full utility of the slope method and its energy resolution power, an HRA station will be upgraded. With four upward facing antennas, this station will allow us to better determine the uncertainties on the slope measurement and the arrival direction. In addition, a reconstruction of the polarization and the unfolding of the antenna response is foreseen, which will allow us to test hardware independent parameterizations. For the complete ARIANNA with 1296 stations, roughly 20% of the detected events will be coincidences of three or more stations, so a combination of several slope measurements will yield additional improvements.

### 5.6. Cosmic ray flux calculation

The HRA has detected 38 air showers in station X between December 2015 and May 2016. As mentioned, the energy of the individual events cannot be obtained from the data from station X alone due to the reduced

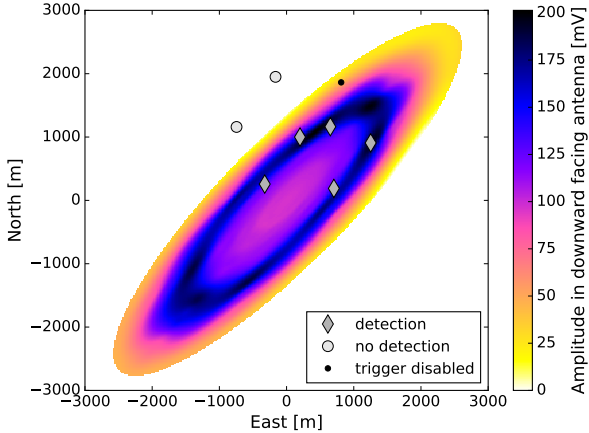


Figure 13: One of the best fitting simulations for the five-fold coincidence event. The markers indicate the HRA station positions. The background map shows a simulated event of  $75^\circ$  zenith angle, an energy  $3 \times 10^{18}$ eV and an  $X_{\text{max}}$  of  $812 \text{ g/cm}^2$ . The signal strengths are given for the downward-facing antennas. The pattern in the upward-facing antennas is slightly different and about a factor of 5 stronger for this particular arrival direction.

capabilities to reconstruct the incoming direction. However, the most probable energy of an ensemble of events was obtained from simulations, which allows us to derive a flux measurement.

Using the simulation chain described in Section 3.2, the efficiency of Station X to detect air showers is established. As will be elaborated, this leads both to a most probable energy  $\langle E \rangle$  and the time-integrated aperture or exposure  $\mathcal{E}$  for station X in the season of 2015/16. The flux  $J$  is then calculated as

$$J(E) = \frac{N_{\text{CR}}}{\langle E \rangle \cdot \mathcal{E} \cdot \eta}, \quad (12)$$

where  $\eta = 0.98$  is the efficiency of having identified all cosmic rays in the measured sample (see Section 5.2).

In the analysis procedure, all showers are binned in energy and zenith angle, as the detection efficiency depends strongly on both and only secondarily on the azimuth angle since the magnetic field points almost vertically upwards at the ARIANNA site. For every simulated shower, 10,000 core positions are randomly thrown on a circular area  $A$  with a radius of 20 km around station X. This area is larger than the longest major axis of the longest detectable footprint obtained in a simulation and was chosen to avoid saturation effects in the efficiency due to geometrically large showers.

For every one of the 10,000 realizations of the same shower, the relevant signal in the antenna is extracted from the simulation and a trigger decision is made. The fraction of showers that fulfill the trigger condition for the 10,000 shower realizations gives the efficiency  $\varepsilon$  of Station X to detect this shower. The binned efficiency  $\varepsilon$  for the ensemble of all simulations is shown on the left of Figure 14. The efficiency increases with zenith angle and energy, with the threshold energy increasing with inclination. For events above  $80^\circ$  the Fresnel reflection starts to limit the efficiency as very little emission enters the ice.

Multiplying the efficiency  $\varepsilon$  by the live-time of station X, the area  $A$  over which the cores were simulated and the relevant steradian space angle, results in the time-integrated aperture, the exposure  $\mathcal{E}$ . This quantity is shown in bins of zenith angle on the right side of Figure 14. The bands in the figure provide a measure of the uncertainty and stem from two calculations of the exposure; the most optimistic and most pessimistic case with one sigma uncertainties for all relevant parameters. Binning the simulations adds an uncertainty, which is, however, small in comparison to the calibration uncertainties.

As discussed already in Section 3.2, only proton primaries were simulated. For the radio emission of air showers, the energy reconstruction is not affected by the type of primary particle, so this choice has no direct effect on the energy resolution [16]. However, the choice of primary could affect the exposure calculation. Protons cover a wider range of values for the height of the shower maximum, than for example

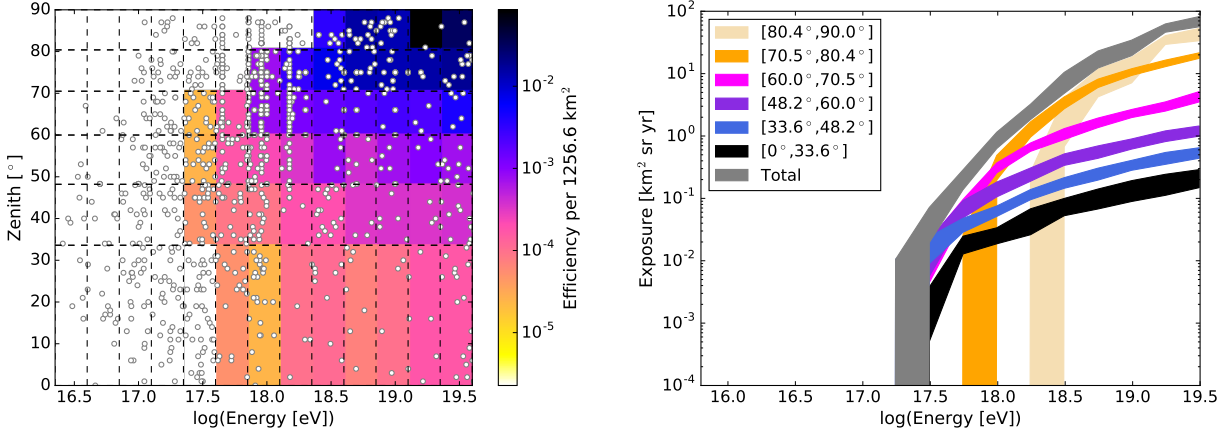


Figure 14: Left: Detection efficiency  $\varepsilon$  as a function of energy and zenith angle. The background colors show the binned efficiency, the markers show the number of simulated showers per bin. Left: Exposure  $\mathcal{E}$  of station X in the 2015/16 season as a function of energy for different zenith angle bins.

iron primaries. The exposure increases with zenith angle, owing to the increase in footprint size and the lack of attenuation of the radio emission in the atmosphere. If one had used only iron primaries, the propagation distance would have been larger on average, the efficiency better and therefore the exposure also larger. This effect can be simulated excluding showers with large values of  $X_{\max}$ . The change introduced by this is smaller than the other uncertainties that factor into the current analysis. For future analyses, a more realistic composition will have to be studied.

With a given spectral index of the flux of cosmic rays and the efficiency  $\varepsilon$ , the most probable energy can be obtained. From published measurements such as [52, 53], the spectral index below  $10^{18} \text{ eV}$  is known to be  $-3.3 \pm 0.04$ . Since the most probable energy will be close to the threshold, which is also below  $10^{18} \text{ eV}$ , a change in the spectral index above the ankle is less relevant for this calculation, but was considered for the uncertainty calculation. By multiplying the efficiency  $\varepsilon$  binned in zenith angle by an arbitrary absolute flux with a defined spectral index and normalizing the sum of the distribution to one, we obtain the result shown on the left of Figure 15. The energy distribution can be approximated by a Gaussian as most showers will be measured very close to the threshold energy. The best fit is centered around  $\log(E) = 17.80$  (corresponding to  $6.5 \times 10^{17} \text{ eV}$ ) with  $\sigma = 0.45$ . The broad shoulder towards higher energies is driven by horizontal showers for which the efficiency and energy threshold are higher. The mean of the Gaussian is the most probable energy  $\langle E \rangle$  and  $\sigma$  determines the energy bin, where most of the air showers are expected. The statistical uncertainty on  $\langle E \rangle$  is given by  $\sigma/\sqrt{N}$ , where  $N$  are the 38 detected cosmic rays.

Using equation 12 with the most probable energy  $\langle E \rangle$  leads to a flux measurement for the HRA as shown in Figure 15. The flux at  $\langle E \rangle = 6.5^{+1.2}_{-1.0} \times 10^{17} \text{ eV}$  has been measured to  $J = 1.1^{+1.0}_{-0.7} \times 10^{-16} \text{ eV}^{-1} \text{ km}^{-2} \text{ sr}^{-1} \text{ yr}^{-1}$ , which is in agreement with values from the literature. The statistical uncertainties include all propagated uncertainties in the efficiency calculation, as well as the uncertainty of the spectral index of the flux. The band in Figure 15 illustrates the systematic uncertainty on the absolute energy.

## 6. Consequences for neutrino detection and the ARIANNA array

From the studies of the air shower signals in the HRA a number of conclusions can be drawn for both neutrino and cosmic-ray detection with ARIANNA. Overall, no external background that mimics the predicted neutrino or cosmic ray signals has been found. This is both a statement of quality for the ARIANNA site on the Ross ice shelf and an indication that the current stations have reached the design goal of having a very low intrinsic noise level.

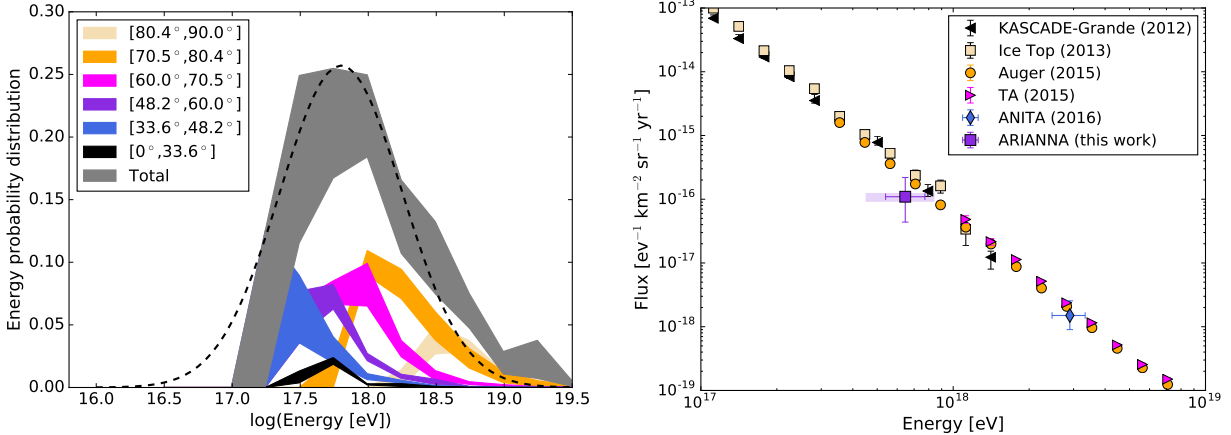


Figure 15: Left: Probability of a detected air shower of a certain arrival direction to be of a certain energy. Curves including uncertainties are shown for different zenith angle bins. A Gaussian fit to the total distribution is also shown. Right: Flux of cosmic rays as function of energy. The data from the HRA as derived in this work is shown together with published flux data from KASCADE-Grande [54], the Pierre Auger Observatory [53], Telescope Array [55], IceTop [52] and ANITA [9]. The errorbars indicate the uncertainty on the mean energy as well as the exposure. The uncertainty on the scale of the energy is indicated by the shaded area.

The full detector simulation of radio emission of air showers has produced signal waveform templates that show a high correlation with the measured waveforms. Average correlations of 0.8 are common and indicate that a good understanding of the detector has been reached. While there is room for improvement, as the data does not perfectly match the predictions, the quality of the predictions is at a stage where 98% analysis efficiency for cosmic rays is reached. As the neutrino capability of ARIANNA is based on the same type of template matching, we expect high analysis efficiencies for the neutrino search.

Since the radio signals of neutrinos and cosmic rays are similar, the more abundant cosmic rays will be a confusion background for neutrinos. Equipping every station with upward facing antennas will eliminate the confusion of direct signals with the help of the directivity of the antennas. In all cosmic ray simulations, no signal has been found that is stronger in the downward facing antennas than in the upward-facing antennas, which predicts a false positive rate of  $\ll 1\%$  for cosmic rays in the neutrino analysis.

It has been suggested that the transition radiation of air showers hitting the ice could produce a confusion signal [56]. It is still unclear whether this phenomenon will still be a strong background for a detector at sea-level, where few showers still contain a significant amount of particles, and if realistic ice conditions are taken into account. Strictly following the calculations in [56], we have extrapolated that there is an, albeit small, chance for the HRA to detect the transition radiation within a couple of months of run time. So far, no evidence was found that the measured rate of air showers is significantly higher than predicted from direct signals. This means either that there is no evidence yet for strong signals of transition radiation or that the signals no longer resemble the original air shower signals due to surface scattering or other propagation effects. Nonetheless, it is too early to exclude the phenomenon and more statistics need to be gathered.

ARIANNA with 1296 stations will detect a significant number of cosmic rays. The exact numbers will depend on features such as the antenna orientation (straight up, down, tilted), station configuration (how many antennas, trigger on the coincidence of two or four channels) and trigger configuration (trigger on up- or downward antennas). As shown in Figure 16 in an array triggering on two upward facing antennas about 300,000 air showers will be registered per half-year of live-time. These cosmic rays will have a threshold energy of  $8 \times 10^{16}$  eV and event detections of up to  $10^{20}$  eV are likely. If triggering only on the coincidence of two downward facing antennas, the threshold will rise to  $8 \times 10^{17}$  eV, which reduces the number of total triggers to about 14,500 per half year of live-time, but does not affect the exposure at the highest energies.

For efficient rejection of cosmic rays from the neutrino data-set, at least two upward facing antennas

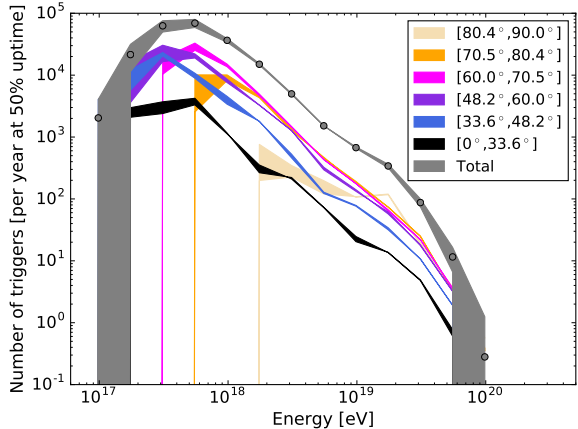


Figure 16: Expected air shower measurements with ARIANNA with 1269 station with four upward facing antennas each, deployed over a hexagonal-grid of 1 km baseline. Shown are the number of events per quarter decade of energy and per year, assuming a 50% uptime. The calculations are based on the published flux of the Pierre Auger Observatory [53]. The bands depict the uncertainty on the numbers derived from simulations. No systematic uncertainty on the flux is included.

per station are needed, covering two perpendicular polarizations. Adding two more antennas, will convert ARIANNA into a fully functional cosmic ray detector, while retaining full efficiency for neutrino detection. Such a detector can provide arrival directions for all measured cosmic rays ( $\Delta\theta = 1^\circ$ ), as well as an energy estimate. The precise energy resolution will depend on methods still to be developed. For horizontal air showers, which are likely to trigger more than one station, an energy-resolution of 20% should be achievable, extrapolating from other radio detectors that employ multiple station detections [6]. At 1296 km<sup>2</sup> ARIANNA will be the largest stand-alone radio cosmic ray detector, being about half the size of the Pierre Auger Observatory and slightly larger than the current surface array of Telescope Array. It is anticipated that such a detector would be in a good position to measure both the energy spectrum, as well as a possible anisotropy of cosmic rays between  $8 \times 10^{17}$  eV and  $10^{20}$  eV.

Irrespective of potential independent cosmic ray science, the cosmic ray signals will act both as a calibration signal and as training set for neutrino reconstruction algorithms. Extended flux measurements of cosmic rays will lead to an energy calibration of the detector, as well as algorithms for the energy reconstruction of neutrinos. The polarization of the neutrino signal is needed to solve for the ambiguity between signal arrival direction and direction of the neutrino. Since the polarization structure of air showers is well understood, the data will determine the accuracy of the polarization measurements and thereby the angular resolution for neutrinos more precisely.

## 7. Conclusions

The first measurements of cosmic ray induced air showers with the HRA of ARIANNA have been presented. Between December 2015 and April 2016, 38 air showers have been detected in one station optimized for cosmic ray detection. The air shower signals are identified with an efficiency of better than 98%, with a trigger efficiency solely determined by live-time and signal amplitude and thereby the energy of the air showers. All air showers have been detected with a radio-self trigger without additional particle detectors.

The cosmic ray flux measured with the HRA of ARIANNA at  $\langle E \rangle = 6.5_{-1.0}^{+1.2} \times 10^{17}$  eV has been measured to be  $J = 1.1_{-0.7}^{+1.0} \times 10^{-16}$  eV<sup>-1</sup>km<sup>-2</sup>sr<sup>-1</sup>yr<sup>-1</sup> and is in agreement with measurements by other experiments. With increasing statistics a more detailed measurement of the cosmic ray flux and the slope of the energy spectrum will be possible. The future ARIANNA array will not only be sensitive to neutrinos above  $10^{16}$  eV, but also to cosmic rays above  $8 \times 10^{16}$  eV with detections likely up to  $10^{20}$  eV at an area of 1296 km<sup>2</sup>.

There is currently no evidence for backgrounds that mimic cosmic ray or neutrino radio signals. Impulsive radio signals recorded during periods of high winds increase the trigger rates, but are cleanly removed during data-analysis. The trigger-rate of the stations is dominated by thermal noise fluctuations and a simple threshold trigger is sufficient to detect cosmic ray and neutrino signals.

Measurements in the upcoming season will help to quantify both the energy and angular resolution of the ARIANNA stations, by measuring cosmic rays in a dedicated station with four upward facing antennas. This data will be used to further train reconstruction algorithms for energy and polarization.

## 8. Acknowledgements

The authors wish to thank the staff of the Antarctic Support Contractors and the entire crew at McMurdo Station for their continued support.

This work was supported in part by U.S. National Science Foundation under grants PLR-08339133, PHY-0970175, and PLR-1126672, as well as PLR-1413661, PHY-1607719, and PHY-1607199. We acknowledge support from the U.S. Department of Energy under contract number DE-AC-76SF00098, from the German Research Foundation (DFG), grant NE 2031/1-1, a Uppsala University Vice-Chancellor's travel grant from the Knut and Alice Wallenberg foundation, and a Liljewalchs travel scholarship.

## Appendix A. Antenna simulations and measurements

The ARIANNA LPDAs were simulated in detail using the software WIPL-D (WIPL-D Pro v13). The simulations were performed in an infinite firn medium using 1157 unknowns at  $\epsilon = 1.78$ ,  $\mu = 1$  and  $\sigma(S/m) = 10^{-6}$ . Examples of the output of the simulation of the complex antenna response are shown in Figure A.17.

The simulated antenna characteristics were compared to dedicated measurements both at the University of Kansas (KU) and Uppsala University in Sweden. Examples of these measurements and the corresponding simulations can be found in Figures A.18 and A.19. As discussed in Section 3.1, the simulation and measurements show differences between 10% and 50% in linear gain, where a large fraction of this uncertainty stems from small details in the antenna simulations (differences in length of mm) and systematic differences between the two measurement set-ups. Measurements of two antennas of the same type reveal significantly smaller differences than between two measurements at different locations. The width of the uncertainty bands given in the Figure has been established based on the measurements of two antennas at the same site.

## Appendix B. The spectral slope and its dependencies

As was discussed in Section 5.5.2, the slope of the frequency spectrum of a detected air shower pulse can be used to reconstruct the energy of the shower. The presented analysis is detector-dependent, as the quantities used are not related to the frequency spectrum of the incoming electric field, but to the one measured in an HRA station, therefore containing also the frequency response of antenna and amplifier. A forthcoming publication will discuss a more general approach of using the frequency spectrum in a system with a large band-width. For this work, however, some additional insight in the dependencies might be interesting to the reader.

Figure B.20 shows the comparison of two air shower simulations with the same energy and arrival direction, but different heights of shower maximum. The Figure shows in detail how the frequency spectrum changes as function of distance to the shower axis. Near the shower axis the slope of the spectrum is steepest, while it is close to flat at the Cherenkov angle. It never reaches the theoretically expected fully flat spectrum in an HRA station, due to the response of the system and the distances between the sampling points, which not necessarily provide a position directly at the Cherenkov angle. It should be noted that the shape of the depicted distribution (*"the slope of slopes"*) is strongly zenith angle dependent and when including the antenna response also azimuth dependent.

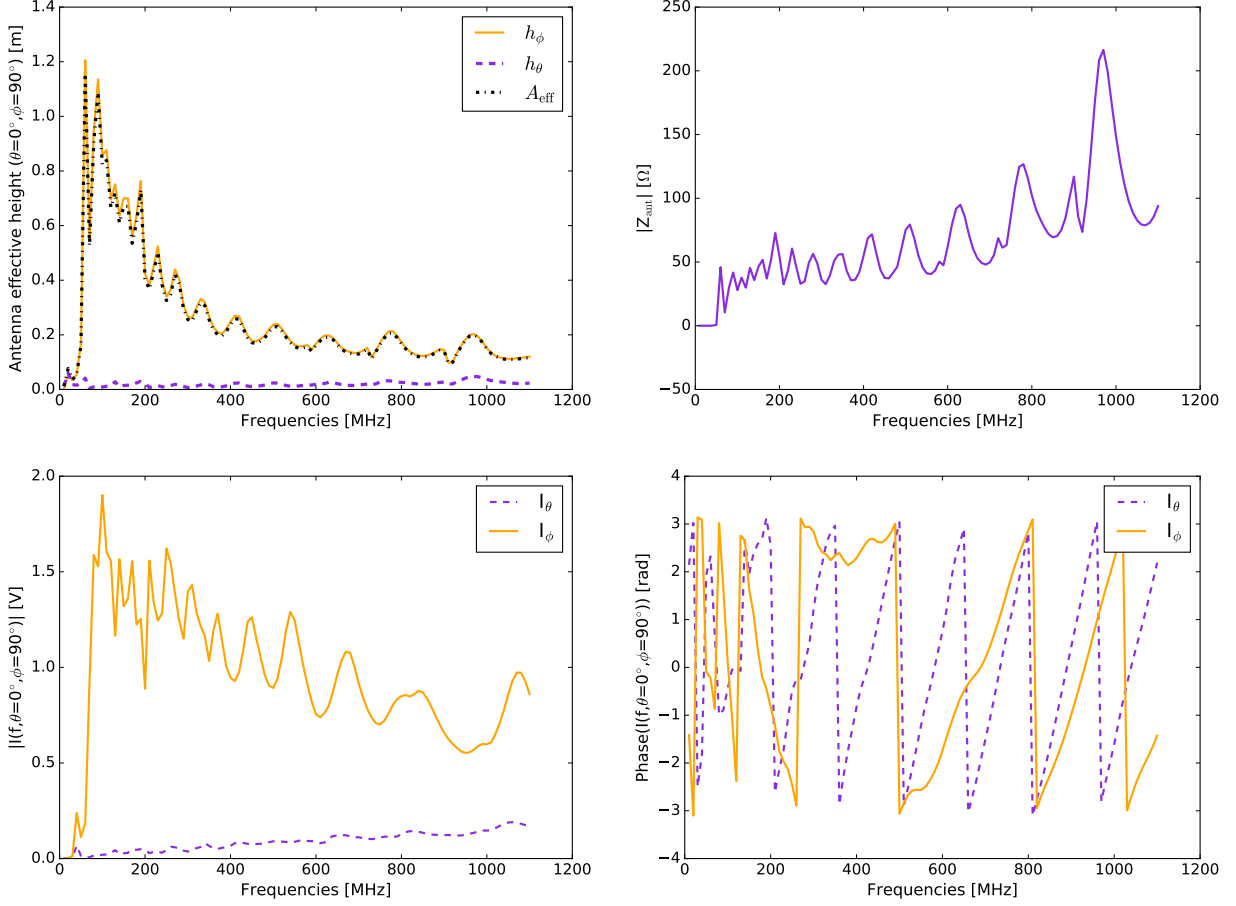


Figure A.17: Antenna characteristics as simulated with WIPL-D. The top left figure shows the antenna effective height as function of frequency. The antenna effective height is calculated using directly the complex currents and the gain of the simulations (see discussion in Section 4.2). The top right figure shows the absolute value of the antenna impedance as function of frequency. In the two bottom figures examples of the complex antenna voltages for an electric field arriving at the antenna front-lobe are shown. Shown are both the absolute component (left) and the complex argument (right).

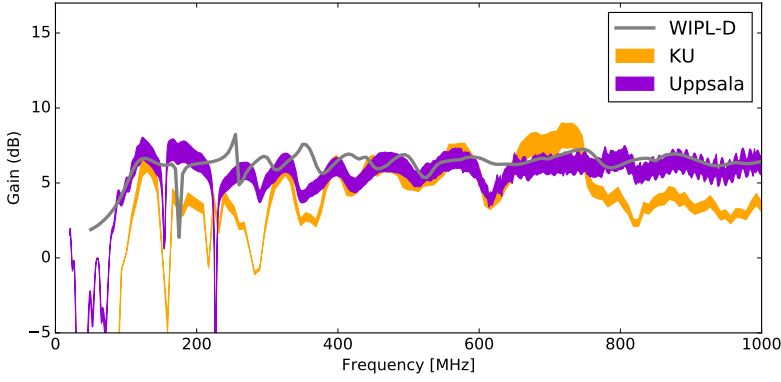


Figure A.18: Absolute gain of the ARIANNA LPDAs as a function of frequency. Shown are both measurements with uncertainties (colored bands), as well as the WIPL-D simulation (line).

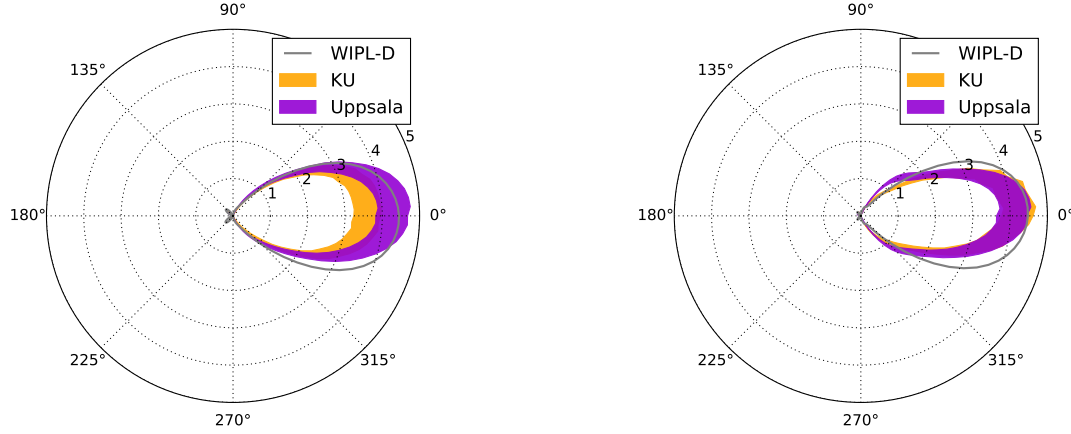


Figure A.19: Gain as function of direction in the plane of the antenna tines at 330 MHz (left) and 400 MHz (right). The highest gain is found along the axis in the direction of the smallest tines (here at  $0^\circ$ , front-lobe). Shown are both measurements (colored bands) and the simulated response of WIPL-D.

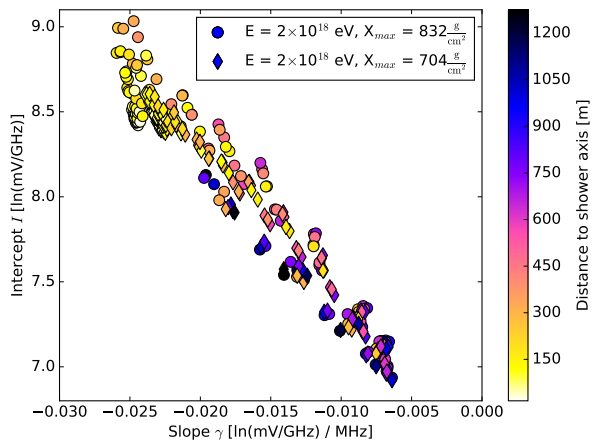


Figure B.20: A subset of the simulated air showers shown in Figure 12 are depicted. Here, two showers of the same energy are contrasted. The colors describe the distance to the shower axis and the markers distinguish between the two showers of different values of the height of the shower maximum.

The height of the shower maximum causes only a secondary effect in this way of presenting the data. The inherent spread is mostly driven by different observer angles around the shower axis. In a future analysis, the full electric-field will be reconstructed, which will avoid projection effects of the signal polarization into the antenna sensitivities, which introduces additional spread. Such a reconstruction of the full electric-field is foreseen for ARIANNA.

## References

- [1] S. W. Barwick, E. C. Berg, D. Z. Besson, et al., A first search for cosmogenic neutrinos with the ARIANNA Hexagonal Radio Array, *Astroparticle Physics* 70 (2015) 12–26. arXiv:1410.7352, doi:10.1016/j.astropartphys.2015.04.002.
- [2] S. W. Barwick, E. C. Berg, D. Z. Besson, et al., Design and Performance of the ARIANNA HRA-3 Neutrino Detector Systems, *IEEE Transactions on Nuclear Science* 62. arXiv:1410.7369, doi:10.1109/TNS.2015.2468182.
- [3] G. A. Askar'yan, Coherent Radio Emission from Cosmic Showers in Air and in Dense Media, *Soviet Journal of Experimental and Theoretical Physics* 21 (1965) 658.
- [4] P. W. Gorham, S. W. Barwick, J. J. Beatty, et al., Observations of the Askaryan Effect in Ice, *Physical Review Letters* 99 (17) (2007) 171101. arXiv:hep-ex/0611008, doi:10.1103/PhysRevLett.99.171101.
- [5] T. Huege, Radio detection of cosmic ray air showers in the digital era, *Physics Reports* 620 (2016) 1–52. arXiv:1601.07426, doi:10.1016/j.physrep.2016.02.001.
- [6] A. Aab, P. Abreu, M. Aglietta, et al., Measurement of the Radiation Energy in the Radio Signal of Extensive Air Showers as a Universal Estimator of Cosmic-Ray Energy, *Physical Review Letters* 116 (24) (2016) 241101. arXiv:1605.02564, doi:10.1103/PhysRevLett.116.241101.
- [7] P. Schellart, A. Nelles, S. Buitink, et al., Detecting cosmic rays with the LOFAR radio telescope, *Astronomy and Astrophysics* 560 (2013) A98. arXiv:1311.1399, doi:10.1051/0004-6361/201322683.
- [8] P. A. Bezyazeekov, N. M. Budnev, O. A. Gress, et al., Measurement of cosmic-ray air showers with the Tunka Radio Extension (Tunka-Rex), *Nuclear Instruments and Methods in Physics Research A* 802 (2015) 89–96. arXiv:1509.08624, doi:10.1016/j.nima.2015.08.061.
- [9] H. Schoorlemmer, K. Belov, A. Romero-Wolf, et al., Energy and flux measurements of ultra-high energy cosmic rays observed during the first ANITA flight, *Astroparticle Physics* 77 (2016) 32–43. arXiv:1506.05396, doi:10.1016/j.astropartphys.2016.01.001.
- [10] F. D. Kahn, I. Lerche, Radiation from Cosmic Ray Air Showers, *Proceedings of the Royal Society of London Series A* 289 (1966) 206–213. doi:10.1098/rspa.1966.0007.
- [11] O. Scholten, K. Werner, F. Rusydi, A macroscopic description of coherent geo-magnetic radiation from cosmic-ray air showers, *Astroparticle Physics* 29 (2008) 94–103. arXiv:0709.2872, doi:10.1016/j.astropartphys.2007.11.012.
- [12] A. Aab, P. Abreu, M. Aglietta, et al., Probing the radio emission from air showers with polarization measurements, *Physical Review D* 89 (5) (2014) 052002. arXiv:1402.3677, doi:10.1103/PhysRevD.89.052002.
- [13] P. Schellart, S. Buitink, A. Corstanje, et al., Polarized radio emission from extensive air showers measured with LOFAR, *JCAP* 10 (2014) 014. arXiv:1406.1355, doi:10.1088/1475-7516/2014/10/014.
- [14] F. Halzen, E. Zas, T. Stanev, Radiodetection of cosmic neutrinos. A numerical, real time analysis, *Physics Letters B* 257 (1991) 432–436. doi:10.1016/0370-2693(91)91920-Q.
- [15] A. Nelles, P. Schellart, S. Buitink, et al., Measuring a Cherenkov ring in the radio emission from air showers at 110–190 MHz with LOFAR, *Astroparticle Physics* 65 (2015) 11–21. arXiv:1411.6865, doi:10.1016/j.astropartphys.2014.11.006.
- [16] A. Nelles, S. Buitink, H. Falcke, et al., A parameterization for the radio emission of air showers as predicted by CoREAS simulations and applied to LOFAR measurements, *Astroparticle Physics* 60 (2015) 13–24. arXiv:1402.2872, doi:10.1016/j.astropartphys.2014.05.001.
- [17] J. Alvarez-Muñiz, R. A. Vázquez, E. Zas, Calculation methods for radio pulses from high energy showers, *Physical Review D* 62 (6) (2000) 063001. arXiv:astro-ph/0003315, doi:10.1103/PhysRevD.62.063001.
- [18] J. C. Hanson, A. L. Connolly, Complex Analysis of Askaryan Radiation: A Fully Analytic Treatment including the LPM effect and Cascade Form Factor arXiv:1605.04975.
- [19] J. C. Hanson, S. W. Barwick, E. C. Berg, et al., Radar absorption, basal reflection, thickness and polarization measurements from the Ross Ice Shelf, Antarctica, *Journal of Glaciology* 61 (2015) 438–446. doi:10.3189/2015JoG14J214.
- [20] F. W. Stecker, Ultrahigh Energy Photons, Electrons, and Neutrinos, the Microwave Background, and the Universal Cosmic-Ray Hypothesis, *Astrophys. Space Sci.* 20 (1973) 47–57. doi:10.1007/BF00645585.
- [21] V. S. Beresinsky, G. T. Zatsepin, Cosmic rays at ultra high energies (neutrino?), *Physics Letters B* 28 (1969) 423–424. doi:10.1016/0370-2693(69)90341-4.
- [22] V. S. Beresinsky, A. I. Smirnov, Cosmic neutrinos of ultra-high energies and detection possibility, *Astrophys. Space Sci.* 32 (1975) 461–482. doi:10.1007/BF00643157.
- [23] M. G. Aartsen, K. Abraham, M. Ackermann, et al., Constraints on Ultrahigh-Energy Cosmic-Ray Sources from a Search for Neutrinos above 10 PeV with IceCube, *Physical Review Letters* 117 (24) (2016) 241101. arXiv:1607.05886, doi:10.1103/PhysRevLett.117.241101.
- [24] A. Aab, P. Abreu, M. Aglietta, et al., Improved limit to the diffuse flux of ultrahigh energy neutrinos from the Pierre Auger Observatory, *Physical Review D* 91 (9) (2015) 092008. arXiv:1504.05397, doi:10.1103/PhysRevD.91.092008.
- [25] L. Gerhardt, S. Klein, T. Stezelberger, et al., A prototype station for ARIANNA: A detector for cosmic neutrinos, *Nuclear Instruments and Methods in Physics Research A* 624 (2010) 85–91. arXiv:1005.5193, doi:10.1016/j.nima.2010.09.032.

- [26] A. Nelles, C. Persichilli, ARIANNA Collaboration, Livetime and sensitivity of the ARIANNA Hexagonal Radio Array, *Proceedings of Science ICRC2015* (2015) 1087. arXiv:1509.00115.
- [27] S. A. Kleinfelder, E. Chiem, P. T., The SST Multi-G-Sample/s Switched Capacitor Array Waveform Recorder with Flexible Trigger and Picosecond-Level Timing Accuracy, submitted to IEEE arXiv:1508.02460.
- [28] W. D. Apel, J. C. Arteaga-Velázquez, L. Bähren, et al., Improved absolute calibration of LOPES measurements and its impact on the comparison with REAS 3.11 and CoREAS simulations, *Astroparticle Physics* 75 (2016) 72–74. arXiv:1507.07389, doi:10.1016/j.astropartphys.2015.09.002.
- [29] W. D. Apel, J. C. Arteaga-Velázquez, L. Bähren, et al., Reconstruction of the energy and depth of maximum of cosmic-ray air showers from LOPES radio measurements, *Physical Review D* 90 (6) (2014) 062001. arXiv:1408.2346, doi:10.1103/PhysRevD.90.062001.
- [30] S. Buitink, A. Corstanje, J. E. Enriquez, et al., Method for high precision reconstruction of air shower  $X_{max}$  using two-dimensional radio intensity profiles, *Phys. Rev. D* 90 (8) (2014) 082003. arXiv:1408.7001, doi:10.1103/PhysRevD.90.082003.
- [31] P. A. Bezyazeekov, N. M. Budnev, O. A. Gress, et al., Radio measurements of the energy and the depth of the shower maximum of cosmic-ray air showers by Tunka-Rex, *Journal of Cosmology and Astroparticle Physics* 1 (2016) 052. arXiv:1509.05652, doi:10.1088/1475-7516/2016/01/052.
- [32] D. Kostunin, P. A. Bezyazeekov, R. Hiller, et al., Reconstruction of air-shower parameters for large-scale radio detectors using the lateral distribution, *Astroparticle Physics* 74 (2016) 79–86. arXiv:1504.05083, doi:10.1016/j.astropartphys.2015.10.004.
- [33] T. Huege, M. Ludwig, C. W. James, Simulating radio emission from air showers with CoREAS, in: R. Lahmann, T. Eberl, K. Graf, et al. (Eds.), *American Institute of Physics Conference Series*, Vol. 1535 of *American Institute of Physics Conference Series*, 2013, pp. 128–132. arXiv:1301.2132, doi:10.1063/1.4807534.
- [34] J. Alvarez-Muñiz, W. R. Carvalho, M. Tueros, E. Zas, Coherent Cherenkov radio pulses from hadronic showers up to EeV energies, *Astroparticle Physics* 35 (2012) 287–299. arXiv:1005.0552, doi:10.1016/j.astropartphys.2011.10.002.
- [35] P. Abreu, M. Aglietta, M. Ahlers, et al., Antennas for the detection of radio emission pulses from cosmic-ray induced air showers at the Pierre Auger Observatory, *Journal of Instrumentation* 7 (2012) P10011. arXiv:1209.3840, doi:10.1088/1748-0221/7/10/P10011.
- [36] S. W. Barwick, E. C. Berg, D. Z. Besson, et al., Time-domain response of the ARIANNA detector, *Astroparticle Physics* 62 (2015) 139–151. arXiv:1406.0820, doi:10.1016/j.astropartphys.2014.09.002.
- [37] B. Kolundzija, WIPL-D: From university software to company product, in: *Proceedings of the 5th European Conference on Antennas and Propagation (EUCAP)*, 2011, pp. 2844–2846.
- [38] D. Heck, J. Knapp, J. N. Capdevielle, G. Schatz, T. Thouw, CORSIKA: a Monte Carlo code to simulate extensive air showers., 1998.
- [39] S. J. Sciutto, AIRES: A system for air shower simulations (Version 2.2.0)arXiv:astro-ph/9911331.
- [40] A. Nelles, S. Buitink, A. Corstanje, et al., The radio emission pattern of air showers as measured with LOFAR – a tool for the reconstruction of the energy and the shower maximum, *JCAP* 5 (2015) 018. arXiv:1411.7868, doi:10.1088/1475-7516/2015/05/018.
- [41] E. Polisensky, LFmap: A Low Frequency Sky Map Generating Program., Long Wavelength Array (LWA) Memo Series 111.  
URL <http://www.astro.umd.edu/~milp/LFmap/>
- [42] A. Nelles, J. R. Hörandel, T. Karlskens, et al., Calibrating the absolute amplitude scale for air showers measured at LOFAR, *Journal of Instrumentation* 10 (2015) P11005. arXiv:1507.08932, doi:10.1088/1748-0221/10/11/P11005.
- [43] J. D. Kraus, R. J. Marhefka, *Antennas for all applications*, 2002.
- [44] P. Abreu, S. Acounis, M. Aglietta, et al., Results of a self-triggered prototype system for radio-detection of extensive air showers at the Pierre Auger Observatory, *Journal of Instrumentation* 7 (2012) P11023. arXiv:1211.0572, doi:10.1088/1748-0221/7/11/P11023.
- [45] T. Asch, W. D. Apel, J. C. Arteaga, et al., Trigger Strategy for Radio Detection in Atmospheric Air Showers with LOPESTAR, *30th International Cosmic Ray Conference* 5 (2008) 1081–1084.
- [46] J. L. Kelley, Data acquisition, triggering, and filtering at the Auger Engineering Radio Array, *Nuclear Instruments and Methods in Physics Research A* 725 (2013) 133–136. arXiv:1205.2104, doi:10.1016/j.nima.2012.11.153.
- [47] A. Aab, P. Abreu, M. Aglietta, et al., Energy estimation of cosmic rays with the Engineering Radio Array of the Pierre Auger Observatory, *Physical Review D* 93 (12) (2016) 122005. doi:10.1103/PhysRevD.93.122005.
- [48] T. Huege, Theory and simulations of air shower radio emission, in: R. Lahmann, T. Eberl, K. Graf, et al. (Eds.), *American Institute of Physics Conference Series*, Vol. 1535 of *American Institute of Physics Conference Series*, 2013, pp. 121–127. arXiv:1301.2135, doi:10.1063/1.4807533.
- [49] K. Belov, Anita Collaboration, Towards determining the energy of the UHECRs observed by the ANITA detector, in: R. Lahmann, T. Eberl, K. Graf, et al. (Eds.), *American Institute of Physics Conference Series*, Vol. 1535 of *American Institute of Physics Conference Series*, 2013, pp. 209–213. doi:10.1063/1.4807550.
- [50] S. Grebe, Finger on the pulse of cosmic rays, Ph.D. thesis, Radboud University Nijmegen (2013).
- [51] S. Jansen, Radio for the masses, Ph.D. thesis, Radboud University Nijmegen (2016).
- [52] M. G. Aartsen, R. Abbasi, Y. Abdou, et al., Measurement of the cosmic ray energy spectrum with IceTop-73, *Physical Review D* 88 (4) (2013) 042004. doi:10.1103/PhysRevD.88.042004.
- [53] The Pierre Auger Collaboration, A. Aab, P. Abreu, et al., The Pierre Auger Observatory: Contributions to the 34th International Cosmic Ray Conference (ICRC 2015), ArXiv e-printsarXiv:1509.03732.
- [54] W. D. Apel, J. C. Arteaga-Velázquez, K. Bekk, et al., The spectrum of high-energy cosmic rays measured with KASCADE-Grande, *Astroparticle Physics* 36 (2012) 183–194. doi:10.1016/j.astropartphys.2012.05.023.

- [55] T. Abu-Zayyad, R. Aida, M. Allen, et al., Energy spectrum of ultra-high energy cosmic rays observed with the Telescope Array using a hybrid technique, *Astroparticle Physics* 61 (2015) 93–101. doi:10.1016/j.astropartphys.2014.05.002.
- [56] K. D. de Vries, S. Buitink, N. van Eijndhoven, et al., The cosmic-ray air-shower signal in Askaryan radio detectors, *Astroparticle Physics* 74 (2016) 96–104. arXiv:1503.02808, doi:10.1016/j.astropartphys.2015.10.003.

# First Upper Limits on the Radar Cross Section of Cosmic-Ray Induced Extensive Air Showers

R.U. Abbasi<sup>a</sup>, M. Abe<sup>b</sup>, M. Abou Bakr Othman<sup>c</sup>, T. Abu-Zayyad<sup>a</sup>, M. Allen<sup>a</sup>, R. Anderson<sup>a</sup>, R. Azuma<sup>d</sup>, E. Barcikowski<sup>a</sup>, J.W. Belz<sup>a,\*</sup>, D.R. Bergman<sup>a</sup>, D. Besson<sup>e,f</sup>, S.A. Blake<sup>a</sup>, M. Byrne<sup>a</sup>, R. Cady<sup>a</sup>, M.J. Chae<sup>g</sup>, B.G. Cheon<sup>h</sup>, J. Chiba<sup>i</sup>, M. Chikawa<sup>j</sup>, W.R. Cho<sup>k</sup>, B. Farhang-Boroujeny<sup>c</sup>, T. Fujii<sup>l</sup>, M. Fukushima<sup>l,m</sup>, W.H. Gillman<sup>n</sup>, T. Goto<sup>o</sup>, W. Hanlon<sup>a</sup>, J.C. Hanson<sup>e</sup>, Y. Hayashi<sup>o</sup>, N. Hayashida<sup>p</sup>, K. Hibino<sup>p</sup>, K. Honda<sup>q</sup>, D. Ikeda<sup>l</sup>, N. Inoue<sup>b</sup>, T. Ishii<sup>q</sup>, R. Ishimori<sup>d</sup>, H. Ito<sup>r</sup>, D. Ivanov<sup>a</sup>, C. Jayanthmurthy<sup>c</sup>, C.C.H. Jui<sup>a</sup>, K. Kadota<sup>s</sup>, F. Kakimoto<sup>d</sup>, O. Kalashev<sup>t</sup>, K. Kasahara<sup>u</sup>, H. Kawai<sup>v</sup>, S. Kawakami<sup>o</sup>, S. Kawana<sup>b</sup>, K. Kawata<sup>l</sup>, E. Kido<sup>l</sup>, H.B. Kim<sup>h</sup>, J.H. Kim<sup>a</sup>, J.H. Kim<sup>w</sup>, S. Kitamura<sup>d</sup>, Y. Kitamura<sup>d</sup>, S. Kunwar<sup>e</sup>, V. Kuzmin<sup>t</sup>, Y.J. Kwon<sup>k</sup>, J. Lan<sup>a</sup>, S.I. Lim<sup>g</sup>, J.P. Lundquist<sup>a</sup>, K. Machida<sup>q</sup>, K. Martens<sup>m</sup>, T. Matsuda<sup>x</sup>, T. Matsuyama<sup>o</sup>, J.N. Matthews<sup>a</sup>, M. Minamino<sup>o</sup>, K. Mukai<sup>q</sup>, I. Myers<sup>a</sup>, K. Nagasawa<sup>b</sup>, S. Nagataki<sup>r</sup>, T. Nakamura<sup>y</sup>, T. Nonaka<sup>l</sup>, A. Nozato<sup>j</sup>, S. Ogio<sup>o</sup>, J. Ogura<sup>d</sup>, M. Ohnishi<sup>l</sup>, H. Ohoka<sup>l</sup>, K. Oki<sup>l</sup>, T. Okuda<sup>z</sup>, M. Ono<sup>aa</sup>, A. Oshima<sup>ab</sup>, S. Ozawa<sup>u</sup>, I.H. Park<sup>ac</sup>, S. Prohira<sup>e</sup>, M.S. Pshirkov<sup>ad,t</sup>, A. Rezazadeh-Reyham<sup>c</sup>, D.C. Rodriguez<sup>a</sup>, G. Rubtsov<sup>l</sup>, D. Ryu<sup>w</sup>, H. Sagawa<sup>l</sup>, N. Sakurai<sup>o</sup>, A.L. Sampson<sup>a</sup>, L.M. Scott<sup>ae</sup>, D. Schurig<sup>c</sup>, P.D. Shah<sup>a</sup>, F. Shibata<sup>q</sup>, T. Shibata<sup>l</sup>, H. Shimodaira<sup>l</sup>, B.K. Shin<sup>h</sup>, J.D. Smith<sup>a</sup>, P. Sokolsky<sup>a</sup>, R.W. Springer<sup>a</sup>, B.T. Stokes<sup>a</sup>, S.R. Stratton<sup>a,ae</sup>, T.A. Stroman<sup>a</sup>, T. Suzawa<sup>b</sup>, H. Takai<sup>af</sup>, M. Takamura<sup>l</sup>, M. Takeda<sup>l</sup>, R. Takeishi<sup>l</sup>, A. Taketa<sup>ag</sup>, M. Takita<sup>l</sup>, Y. Tameda<sup>p</sup>, H. Tanaka<sup>o</sup>, K. Tanaka<sup>ah</sup>, M. Tanaka<sup>x</sup>, S.B. Thomas<sup>a</sup>, G.B. Thomson<sup>a</sup>, P. Tinyakov<sup>t,ai</sup>, I. Tkachev<sup>t</sup>, H. Tokuno<sup>d</sup>, T. Tomida<sup>aj</sup>, S. Troitsky<sup>t</sup>, Y. Tsunesada<sup>o</sup>, K. Tsutsumi<sup>d</sup>, Y. Uchihori<sup>ak</sup>, S. Udo<sup>p</sup>, F. Urban<sup>ai</sup>, G. Vasiloff<sup>a</sup>, S. Venkatesh<sup>c</sup>, T. Wong<sup>a</sup>, R. Yamane<sup>o</sup>, H. Yamaoka<sup>x</sup>, K. Yamazaki<sup>o</sup>, J. Yang<sup>g</sup>, K. Yashiro<sup>i</sup>, Y. Yoneda<sup>o</sup>, S. Yoshida<sup>v</sup>, H. Yoshii<sup>al</sup>, R. Zollinger<sup>a</sup>, Z. Zundel<sup>a</sup>

<sup>a</sup>High Energy Astrophysics Institute and Department of Physics and Astronomy, University of Utah, Salt Lake City, Utah, USA

<sup>b</sup>The Graduate School of Science and Engineering, Saitama University, Saitama, Saitama, Japan

<sup>c</sup>Department of Electrical and Computer Engineering, University of Utah, Salt Lake City, Utah, USA

<sup>d</sup>Graduate School of Science and Engineering, Tokyo Institute of Technology, Meguro, Tokyo, Japan

<sup>e</sup>University of Kansas, Lawrence, Kansas, USA

<sup>f</sup>Moscow Engineering and Physics Institute, Moscow, Russia

<sup>g</sup>Department of Physics and Institute for the Early Universe, Ewha Womans University, Seodaemun-gu, Seoul, Korea

<sup>h</sup>Department of Physics and The Research Institute of Natural Science, Hanyang University, Seongdong-gu, Seoul, Korea

<sup>i</sup>Department of Physics, Tokyo University of Science, Noda, Chiba, Japan

<sup>j</sup>Department of Physics, Kinki University, Higashi Osaka, Osaka, Japan

<sup>k</sup>Department of Physics, Yonsei University, Seodaemun-gu, Seoul, Korea

<sup>l</sup>Institute for Cosmic Ray Research, University of Tokyo, Kashiwa, Chiba, Japan

<sup>m</sup>Kavli Institute for the Physics and Mathematics of the Universe (WPI), Todai Institutes for Advanced Study, the University of Tokyo, Kashiwa, Chiba, Japan

<sup>n</sup>Gillman & Associates, Salt Lake City, Utah, USA

<sup>o</sup>Graduate School of Science, Osaka City University, Osaka, Osaka, Japan

<sup>p</sup>Faculty of Engineering, Kanagawa University, Yokohama, Kanagawa, Japan

<sup>q</sup>Interdisciplinary Graduate School of Medicine and Engineering, University of Yamanashi, Kofu, Yamanashi, Japan

<sup>r</sup>Astrophysical Big Bang Laboratory, RIKEN, Wako, Saitama, Japan

<sup>s</sup>Department of Physics, Tokyo City University, Setagaya-ku, Tokyo, Japan

<sup>t</sup>National Nuclear Research University, Moscow Engineering Physics Institute, Moscow, Russia

<sup>u</sup>Advanced Research Institute for Science and Engineering, Waseda University, Shinjuku-ku, Tokyo, Japan

<sup>v</sup>Department of Physics, Chiba University, Chiba, Chiba, Japan

<sup>w</sup>Department of Physics, School of Natural Sciences, Ulsan National Institute of Science and Technology, UNIST-gil, Ulsan, Korea

<sup>x</sup>Institute of Particle and Nuclear Studies, KEK, Tsukuba, Ibaraki, Japan

<sup>y</sup>Faculty of Science, Kochi University, Kochi, Kochi, Japan

<sup>z</sup>Department of Physical Sciences, Ritsumeikan University, Kusatsu, Shiga, Japa

<sup>aa</sup>Department of Physics, Kyushu University, Fukuoka, Fukuoka, Japan

<sup>ab</sup>Engineering Science Laboratory, Chubu University, Kasugai, Aichi, Japan

<sup>ac</sup>Department of Physics, Sungkyunkwan University, Jang-an-gu, Suwon, Korea

<sup>ad</sup>Sternberg Astronomical Institute Moscow M.V.Lomonosov State University, Moscow, Russia

<sup>ae</sup>Department of Physics and Astronomy, Rutgers University - The State University of New Jersey, Piscataway, New Jersey, USA

\*Corresponding Author. Tel.: +01 801 585-9620. Addr.: 115 S 1400 E #201 JFB

Email address: belz@physics.utah.edu (J.W. Belz)

<sup>a</sup>*Brookhaven National Laboratory, Upton, New York, USA*

<sup>ag</sup>*Earthquake Research Institute, University of Tokyo, Bunkyo-ku, Tokyo, Japan*

<sup>ab</sup>*Graduate School of Information Sciences, Hiroshima City University, Hiroshima, Hiroshima, Japan*

<sup>ai</sup>*Service de Physique Théorique, Université Libre de Bruxelles, Brussels, Belgium*

<sup>aj</sup>*Department of Computer Science and Engineering, Shinshu University, Nagano, Nagano, Japan*

<sup>ak</sup>*National Institute of Radiological Science, Chiba, Chiba, Japan*

<sup>al</sup>*Department of Physics, Ehime University, Matsuyama, Ehime, Japan*

---

## Abstract

TARA (Telescope Array Radar) is a cosmic ray radar detection experiment colocated with Telescope Array, the conventional surface scintillation detector (SD) and fluorescence telescope detector (FD) near Delta, Utah, U.S.A. The TARA detector combines a 40 kW, 54.1 MHz VHF transmitter and high-gain transmitting antenna which broadcasts the radar carrier over the SD array and within the FD field of view, towards a 250 MS/s DAQ receiver. TARA has been collecting data since 2013 with the primary goal of observing the radar signatures of extensive air showers (EAS). Simulations indicate that echoes are expected to be short in duration ( $\sim 10 \mu\text{s}$ ) and exhibit rapidly changing frequency, with rates on the order  $1 \text{ MHz}/\mu\text{s}$ . The EAS radar cross-section (RCS) is currently unknown although it is the subject of over 70 years of speculation. A novel signal search technique is described in which the expected radar echo of a particular air shower is used as a matched filter template and compared to waveforms obtained by triggering the radar DAQ using the Telescope Array fluorescence detector. No evidence for the scattering of radio frequency radiation by EAS is obtained to date. We report the first quantitative RCS upper limits using EAS that triggered the Telescope Array Fluorescence Detector.

**Keywords:** cosmic ray, radar, digital signal processing, radar cross-section

---

## 1. Introduction

Ultra-high energy cosmic ray (UHECR, primary energy  $E_0 > 10^{18} \text{ eV}$ ) research is limited primarily by low flux. There are currently two dominant detection techniques, surface detectors (SD) comprised of plastic scintillator or water Cherenkov detectors, and fluorescence telescope detectors (FD). Conventional detection methods have been successful in mapping out the UHECR spectrum, observing the GZK cutoff [1, 2, 3] and locating a potential “hotspot” in CR arrival directions [4]. However, large SD arrays are expensive to build and maintain, and FD telescopes have limited statistics due to their low duty cycle ( $\sim 10\%$ ).

Recently proposed alternative detection methods include those using the geo-magnetic synchrotron [5] and Askaryan [6] effects, both of which require a large instrumentation area. Radar detection has the potential to be a remote detection technique with 100% duty cycle. The idea was initially suggested in 1941 [7] when reflections from extensive air showers (EAS) were proposed as a possible explanation for anomalous atmospheric radar echoes.

Telescope Array Radar (TARA) seeks to observe radar echoes in coincidence with the Telescope Array (TA) and determine the viability of the radar technique

for UHECR detection. TARA is the most advanced CR radar detection experiment to date, improving upon other experiments with several key attributes:

- The transmitter is under the direct control of experimenters, and in a radio-quiet area isolated from other radio frequency (RF) sources. The power and radiation pattern are known at all times.
- Forward power up to 40 kW and gain exceeding 20 dB maximize energy density in the radar field.
- Continuous wave (CW) transmission gives 100% duty cycle, as opposed to pulsed radar.
- TARA utilizes a high sample rate DAQ (250 MS/s).
- TARA is colocated with a large state-of-the-art conventional CR observatory, allowing the radar data stream to be sampled at the arrival times of known cosmic ray events.

Each of these attributes of the TARA detector has been discussed in detail in the literature [8]. A map showing the TA SD array and the location of the TARA transmitter and receiver is shown in Figure 1.

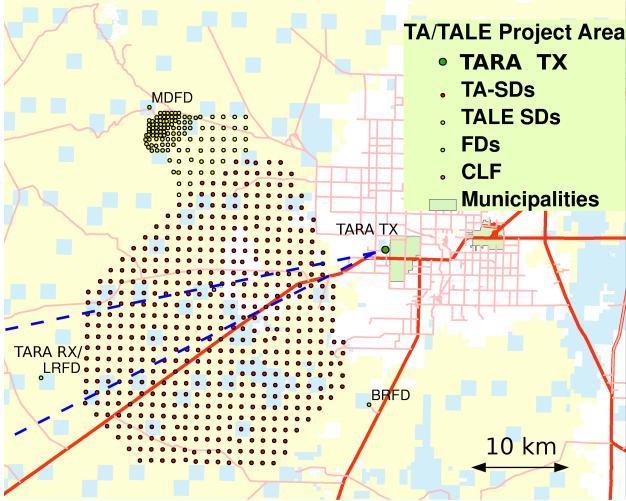


Figure 1: Map of Telescope Array (TA) detector facilities, both SD and FD, and TARA transmitter and receiver sites. The radar carrier is broadcast from the transmitter site toward the TA Long Ridge Fluorescence Detector (FD). Dashed blue lines indicate the beamwidth at the points 3 dB below the peak gain. This map is taken from Reference [8].

Section 2 of this paper includes a description of air shower plasmas and possible radio scattering mechanisms. Theoretical and experimental parameters that influence radio scattering are presented and discussed. We justify use of the *thin wire model* in a radar echo simulation that predicts echo waveforms, which we will subsequently (Section 6) use in placing limits on the air shower radar cross section (RCS). Sections 3 and 4 describe TARA data and offline processing techniques. In Section 5, we describe the signal search using simulated waveforms as matched filter (MF) templates in order to maximize sensitivity. Section 6 describes the procedure for calculating a scale factor to the RCS model described in Section 2, the results of which are used in placing the first quantitative upper limit on the EAS radar cross-section (RCS). In Section 7 we summarize these results and discuss the viability of radar detection of cosmic rays in light of the TARA findings.

## 2. EAS Radio Scattering

We begin with an overview of the issues relevant to RF scattering by EAS, focusing on those which inform the design of the TARA detector and its data analysis.

### 2.1. Air Shower Plasmas

The bi-static radar equation

$$P_R = P_T \frac{G_T}{4\pi R_T^2} \sigma \frac{G_R}{4\pi R_R^2} \frac{\lambda^2}{4\pi}, \quad (1)$$

is a simple geometrical formula used to calculate received power when the transmitter (TX) and receiver (RX) are at different locations.  $P_R$  is received power,  $P_T$  is transmitter power,  $G_R$  and  $G_T$  are the receiver and transmitter station antenna gains, respectively,  $\lambda$  is the radar wavelength,  $R_T$  is distance between transmitter and target,  $R_R$  is distance between target and receiver, and  $\sigma$  is the RCS. Most of the parameters in the bi-static radar equation are known *a priori* or can be measured. In the case of EAS, the RCS is currently unknown and, as will be shown, is difficult to calculate directly.

Scattering occurs from interaction of the radar wave with free electrons liberated from air molecules by passing shower particles. Therefore, the RCS is proportional to the density and area of the plasma body. This merits a discussion of the calculation of ionization density created by EAS.

Standard EAS parameters include primary particle energy  $E_0$  (eV), depth  $X_{\max}$  ( $\text{g}/\text{cm}^2$ ) in the atmosphere where the number of shower particles reaches a maximum  $N_{\max}$ , and the depth of first interaction  $X_0$  ( $\text{g}/\text{cm}^2$ ). The critical energy  $E_c$  (eV) is the energy below which the dominant energy loss mechanism is collisional rather than bremsstrahlung. In air,  $E_c$  is 81 MeV [9]. When the average particle energy decreases below  $E_c$ , particle production ceases and the EAS starts to decrease in size.

Gaisser and Hillas [10] have parameterized the average shower longitudinal profile — the number of charged shower products  $N(X)$  — as a function of depth  $X$  in the atmosphere. Nishimura, Kamata, and Greisen (NKG) [11] have created a function describing the number area density as a function of radius, at a specific shower age  $s$  [12], as a function of  $N(X)$ . Together, Gaisser-Hillas and NKG describe charged particle density as the shower evolves. Electrons and positrons are the dominant component of charged shower particles [12], outnumbering other species such as muons, to the extent that  $N(X)$  can be approximated as the total number of electrons and positrons produced by the shower. This assumption is maintained in this paper.

Together with the Gaisser-Hillas and NKG functions, atmospheric energy deposition models permit the calculation of ionization yield. Nerling et al. [13] have parameterized  $\alpha_{\text{eff}}(X)$ , where  $\alpha_{\text{eff}}(X) N(X) = \frac{dE}{dX}(X)$ . Combined with the mean ionization energy in the atmosphere,  $I = 33.8$  eV [14], the energy deposit  $\frac{dE}{dX}(X)$  from Nerling can be used to estimate the EAS plasma properties. Atmospheric ionization occurs at a greater rate in regions where the shower particle density is high. Therefore, it is expected that the total plasma density follows the shower lateral distribution described by

NKG.

Figure 2 shows the ionization density predicted by the NKG distribution for an  $E_0 = 10^{19}$  eV air shower at  $X_{\max}$ , compared with an unthinned simulated shower produced with the CORSIKA [15] package using the QGSJETII-03 [16] high-energy interaction model. The ionization electron density is calculated for the CORSIKA shower as follows:

$$N_{ions} = \frac{E_e \times (1 - \frac{1}{e}) \times \rho_{air}}{X_{rad} \times E_{ion}} \quad (2)$$

where  $E_e$  is the electron or positron energy from CORSIKA,  $\rho_{air}$  is the density of air at 1500 m M.S.L.,  $X_{rad}$  is the electron radiation length in air, and  $E_{ion}$  is the mean ionization energy of air. Agreement between the NKG and CORSIKA predictions is good near the critical region close to the shower core, where electron density is highest.

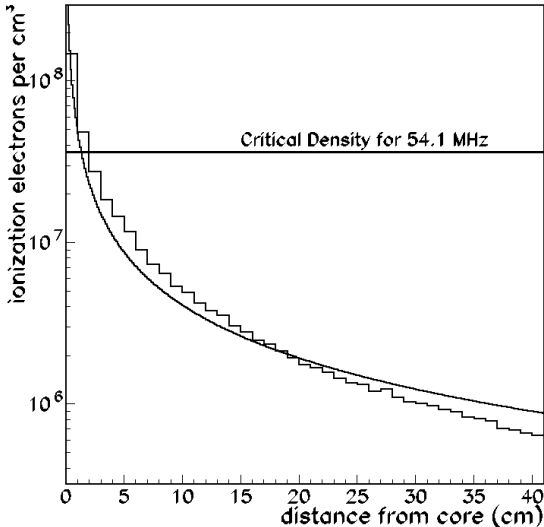


Figure 2: The comparison of the ionized plasma densities calculated with CORSIKA (histogram) and with Gaisser-Hillas and NKG functions (curve) as a function of radius near  $X_{\max}$  for a  $10^{19}$  eV vertical shower.

## 2.2. Plasma Scattering

In the presence of an incident time-varying electric field, a low density plasma will oscillate according to the equation of motion:

$$e\mathbf{E} = m \frac{\partial^2 \mathbf{r}}{\partial t^2}, \quad (3)$$

where  $\mathbf{r}$  is the electron displacement vector. Both  $\mathbf{E}$  and  $\mathbf{r}$  have the harmonic component  $\exp(-i\omega_r t)$ , with  $\omega_r$  the

radar carrier frequency. This equation can be used [17] to obtain the index of refraction as a function of the plasma frequency:

$$n^2 = 1 - \frac{Ne^2}{\omega_r^2 \epsilon_0 m} = 1 - \frac{\omega_e^2}{\omega_r^2} \quad (4)$$

where  $N$  is the number density of electrons. In this low density plasma, collisions between free electrons and molecules, as well as geomagnetic effects are neglected. The plasma frequency is

$$\omega_e \equiv \sqrt{\frac{Ne^2}{\epsilon_0 m}} \quad (5)$$

The index of refraction can be either real or imaginary. If  $\omega_e > \omega_r$  (overdense),  $n$  is imaginary and the waves cannot penetrate the medium. Specular reflection is the typical scattering regime for overdense plasma bodies. In the case  $\omega_e < \omega_r$  (underdense), waves penetrate the medium. Scattering in the underdense regime is primarily via Thomson scattering [18] which, depending on the size of the scattering body relative to the wavelength, can interfere either constructively or deconstructively at the receiver.

Figure 3 shows the plasma frequency as a function of radius, calculated from Gaisser-Hillas and NKG in a manner similar to the values obtained in Figure 2. Given the TARA 54.1 MHz radar carrier, the shower only appears overdense at small radii,  $\sim 1$  cm.

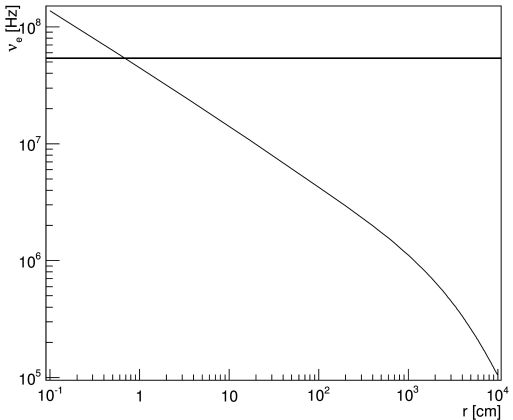


Figure 3: Plasma frequency as a function of radius at  $X_{\max}$  for a  $10^{19}$  eV shower calculated using Gaisser-Hillas and NKG parameterizations. Gaisser-Hillas parameters are averages of values obtained by CORSIKA simulations. The horizontal black line corresponds to the TARA radar carrier frequency at 54.1 MHz.

### 2.3. Collisional Damping

Collisions between free electrons and atmospheric molecules will tend to damp reradiation as the electrons' motion becomes incoherent. Scattered power can be expected to decrease as the effective collision frequency  $\nu$  increases, particularly when  $\nu$  becomes large compared to the sounding frequency. We can modify Equation 3 to include the effects of collisional damping by adding a term assuming that all of an electron's excess momentum gained from the radar carrier is lost upon collision with a molecule.

$$e\mathbf{E} = m \frac{\partial^2 \mathbf{r}}{\partial t^2} - mv \frac{\partial \mathbf{r}}{\partial t}. \quad (6)$$

The index of refraction is then given by

$$n^2 = 1 - \frac{\omega_e^2}{\omega_r^2(1 - i\nu/\omega_r)}. \quad (7)$$

With collisional effects included,  $n$  is thus complex. Specifically,  $n \equiv \mu - i\chi$ , with  $\chi$  the absorption coefficient and  $\mu$  the real part of the index of refraction. When collisions are included, there are no longer two distinct regimes; rather incident waves are both partially reflected and partially absorbed.

Figure 4 gives values of  $\nu$  for atmospheric plasmas as calculated by several authors, as well as a simple estimate obtained by dividing the mean thermalized electron velocity by the mean free path.

Not including the simple estimate, all values were calculated as functions of the momentum transfer cross-section and electron velocity [19]:

$$\nu(v) = v \left( N_{N_2} Q_m^{N_2}(v) + N_{O_2} Q_m^{O_2}(v) \right). \quad (8)$$

$Q_m(v)$  is the momentum transfer cross-section as a function of velocity  $v$  and  $N$  is the number density.

By definition, the average shower particle energy at  $X_{\max}$  in air is  $E_c = 81$  MeV. Electron temperatures up to 1000 K ( $\langle E \rangle = \frac{3}{2}k_B T$ ) were used in Equation 8 to calculate the resultant values, which corresponds to  $\sim 0.1$  eV. Ionization electron energies increase with that of incident particles [25] (shower electrons), therefore the electron velocities used to calculate the values in Figure 4 are likely too low.

Above 1 keV,  $Q_m^{N_2}$  decreases nearly two orders of magnitude for each decade increase in electron energy [25]. Data for electron energies in the range of interest ( $\sim 10$  MeV) do not exist in the literature. If the trend of decreasing momentum transfer cross-section continues, then effective collision frequency values in Figure 4 are overestimates, caused by assuming a near-thermal secondary electron energy distribution.  $N_{O_2}$

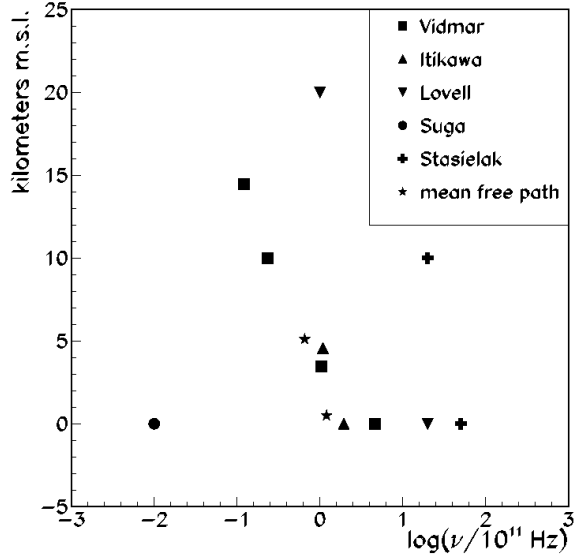


Figure 4: Survey of estimates of electron-neutral collision frequency as a function of altitude, mean sea level. Data points are from Vidmar [20], Itikawa [21], Lovell [22], Suga [23], and Stasielak *et al.* [24]. A simple estimate is also shown, the result of dividing mean electron speed by the mean free path.

is small compared to  $N_{N_2}$  and the momentum transfer cross-section of oxygen molecules appears to flatten as it approaches 1 keV [26]. Therefore, it is unlikely the oxygen term in Equation 8 will compete with the nitrogen term.

Without the benefit of high-energy electron data, one can estimate the effect of collisional damping assuming that the collision rate in air is  $\sim 10^{11}$  Hz. Comparing Equations 4 and 7, an effective mass can be defined as  $m_{\text{eff}} = m \left( 1 - i \frac{\nu}{\omega_r} \right)$ . Scattering power is proportional to  $(\partial^2 \mathbf{r} / \partial t^2)^2 \propto 1/m^2$ . The damping factor is

$$\left| \frac{m_{\text{eff}}}{m} \right|^2 \simeq \left( \frac{\nu}{\omega_r} \right)^2. \quad (9)$$

Given  $\omega_r = 10^8$  Hz and a possibly overestimated collision frequency  $\nu = 10^{11}$  Hz, the damping factor is  $10^6$ . The damping phenomenon is potentially catastrophic to the radar detection scheme, a fact that has been neglected in recent radar detection literature [27].

Figure 5 shows  $\mu$  and  $\chi$  as a function of radar carrier frequency near 54.1 MHz at three different plasma frequencies  $\omega_e = (10^{-3}, 10^{-2}, 10^{-1})\nu$ , with  $\nu = 10^{11}$  Hz. The refractive part of the index of refraction,  $\mu$ , does not deviate appreciably from unity at 54.1 MHz and plasma frequency  $\omega_e$  equal to  $10^{-3}\nu$ . Absorption in the medium

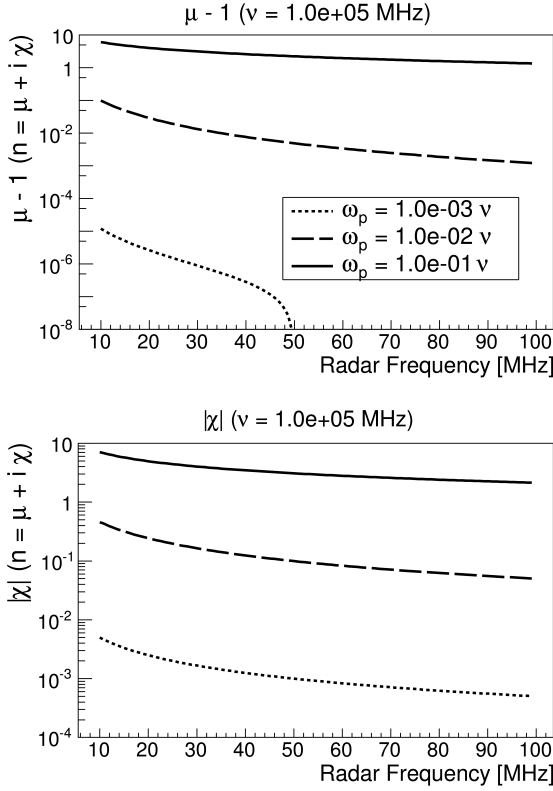


Figure 5: Real and imaginary parts of the index of refraction ( $n = \mu - i\chi$ ) with  $10^{11}$  Hz collision frequency each with  $\omega_e = (10^{-3}, 10^{-2}, 10^{-1})\nu$ .  $\mu - 1$  is plotted to emphasize the difference between the  $10^{-2}\nu$  and  $10^{-3}\nu$  curves which are very close to unity. The TARA radar frequency is 54.1 MHz.

is of order  $10^{-3}$ . Thus we might expect that scattering power is very small even when the plasma frequency meets and exceeds the radar frequency ( $\omega_e \approx 10^{-3}\nu$ ).

#### 2.4. Forward-scattering Enhancement

The relative size of the radar wavelength  $\lambda$  to the characteristic lateral size of the target  $a$  determines if there is a peak in the scattered radiation pattern. Figure 6 shows a comparison of metallic cylinder forward-scattering radiation patterns as a function of the angle from the forward direction for several different cylinder radii  $a$  expressed as fractions of the radar wavelength. The diffraction peak vanishes when  $a/\lambda < 0.1$ .

If the majority of scattered power comes from near the shower core in the region that would be considered overdense in the collisionless regime, the scattering region with radius  $a \sim 1$  cm can be represented as a thin conductive wire with no forward enhancement. In the case in which we consider a cylinder with radius equal

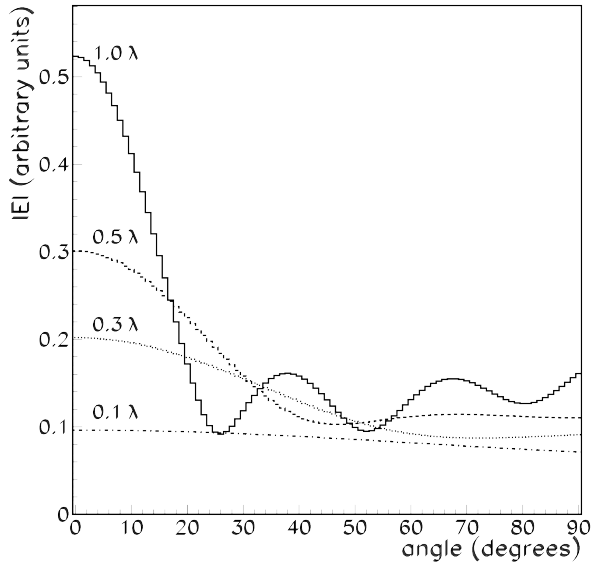


Figure 6: Relative scattered electric field [28] magnitude for several different cylinder radii, expressed as fractions of the incident wavelength, as a function of angular deviation from the forward scattering direction.

to  $\lambda$ , the scattering is expected to have appreciable forward enhancement.

#### 2.5. Simulation

Energetic shower particles travel in a disk coaxial with the EAS direction of propagation. Less energetic products are quickly thermalized on a time scale of the order of the free electron lifetime. From the perspective of a radar system, an EAS is a (narrow) disk moving through the atmosphere at the speed of light, leaving a quickly fading plasma trail. The simulation of radar echoes is made possible using the bi-static radar equation, TARA detector geometry and known EAS dynamics to calculate the received signal based on a scattering model, as detailed below.

The superposition principle implies that multiple scattering path lengths from different segments of the shower track (see Figure 7) result in summation of scattered rays of the same frequency but with different phase. Unlike other radar applications, the target is moving at essentially the same speed as the interrogating wave, so phase evolves rapidly. EAS radar echoes exhibit rapidly changing frequency [29]. Such signals are often referred to as “chirps”.

During a given time step  $\delta t$  (2 ns for the present TARA analysis, roughly one tenth of the period of the

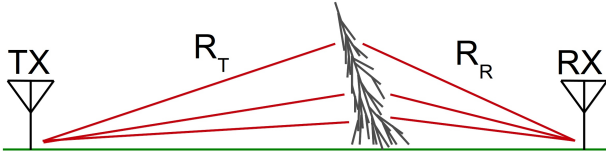


Figure 7: Contributions from paths of varying lengths,  $\text{TX} \rightarrow \text{target} \rightarrow \text{RX}$ , summed at the receiver result in a chirp signal (bi-static configuration).

sounding radiation) at time  $t_i$ , the bi-static radar equation is applied to each longitudinal shower segment (each with length  $c\delta t$ ) from which light could have reached the receiver. A segment  $j$  is included if the shower progress  $\mathcal{P}_i$ , the distance the shower has travelled since first interaction, is greater than the distance from segment  $j$  to the receiver  $R_{R,j}$  minus the progress of the shower at segment  $j$ ,  $\mathcal{P}_j$ . The plasma state of segment  $j$ , and thus RCS properties, are that of the segment at retarded time  $t'_{i,j} = (\mathcal{P}_i - R_{R,j} - \mathcal{P}_j)/c$ . The time  $(\mathcal{P}_i - R_{R,j})/c$  is defined by scattered light from segment  $j$  leaving the segment. It does not include shower age which must be tracked carefully to include the effect of plasma dissipation.

Each segment has magnitude and phase determined by the segment's total path length, radar wavelength, RCS at the current point in the shower, shower geometry relative to the TX and RX and geometrical antenna factors. The integrated contribution of all segments  $j$  is the received signal at time  $t_i$

$$V_{R,i} = \sum_j \sqrt{P_j(t'_i) Z}. \quad (10)$$

$P_j(t'_i)$  is the received power from the bi-static radar equation (Equation 1) calculated at the retarded time, and  $Z$  is the impedance of the receiving antenna. The sum should properly account for phase factors in  $P_j$ . In practice, antenna impedance  $Z$  is a function of frequency. Here, a fixed value is assumed. Error introduced from this assumption is discussed in Section 6.3.

Signal components scattered early in shower evolution when the RCS is small and path length is large will have low amplitude, while segments near  $X_{\max}$  (typically 3-5 km from ground level at the location of the detector) have larger RCS due to high plasma density near  $X_{\max}$  and have shorter path lengths so the expected received signal is greater at later times in the shower development.

Several physical models are included in the simulation to increase accuracy. Gaisser-Hillas parameters are coded as functions of primary energy  $E_0$  using COR-

SIKA Monte Carlo data [30]. The NKG function combined with Nerling's parameterization [13] of  $\alpha$  describe the ionization lateral distribution. Atmospheric density as a function of altitude is obtained from the 1976 Standard Atmosphere [31]. Electron lifetime as a function of altitude comes from Vidmar [20]. Transmitter and receiver radiation patterns have been simulated [32] and confirmed observationally (see [8]).

The electron lifetime may be underestimated due to the assumption of near-thermal electrons. This is the analog to overestimation of effective collision frequency in the Section 2.2. Electron lifetime for near-thermal electrons (500 K) is  $\tau \approx 10$  ns [20, 33]. Electrons with greater energy require additional collisions with neutral molecules before attachment/recombination can occur. Without strong evidence in favor of decreasing momentum-transfer cross section, near-thermal electron lifetime is used in the simulation. Underestimated electron lifetime results in lower predictions for received power.

### 2.5.1. The Thin Wire Model

In order to examine the radar target presented by particular air showers, we adopt a simplified “thin wire model” in terms of which we can quantify the RCS.

As described in Section 2.4, the bulk of coherent scattered power will occur in a cylindrical region with radius less than  $\lambda$ , possibly much less due to the steep shower density profile. Only the narrow overdense region (collisionless model) is used in the simulation. It may be regarded as a short-lived, thin conductive wire. The overdense region radius is determined from the lateral distribution, which is used in the thin-wire approximation to give the segment cross-section. Forward scattering enhancement (Section 2.4) is not expected from a scattering region with radius much less than  $\lambda$ . Neglecting the possibility of such enhancement conservatively underestimates received power, thus preventing underestimation of the RCS upper limit discussed below in Section 6.

The RCS of a perfectly conducting thin wire  $\sigma_{\text{TW}}$  several wavelengths long but only a fraction of a wavelength in diameter is given by [34],

$$\sigma_{\text{TW}} = \frac{\pi L^2 \sin^2 \theta \left[ \frac{\sin \eta}{\eta} \right]^2}{\left( \frac{\pi}{2} \right)^2 + \left( \ln \frac{\lambda}{\gamma \pi a \sin \theta} \right)^2} \cos^4 \phi, \quad \eta = \frac{2\pi L}{\lambda} \cos \theta. \quad (11)$$

$L$  is the wire length,  $\theta$  is the angle between the wire and the direction of incidence,  $\phi$  is the angle between the incident wave polarization and the wire axis,  $a$  is the

radius,  $\lambda$  is the wavelength and  $\gamma$  is 1.78,  $e$  raised to the power of Euler's constant 0.577.

In the simulation, the thin-wire radius  $a$  is dependent on the shower lateral distribution, and the state of the plasma at retarded time  $t'$ . Segment  $j$  at time step  $i$  is described by NKG with  $N = N_{0,j} \exp(-t'_{i,j}/\tau)$ , where  $N_{0,j}$  is the initial number of ionization electrons in segment  $j$  and  $\tau$  is electron lifetime. The thin-wire radius  $a$  is the largest radius for a given shower segment within which the free electron density exceeds the density that corresponds to a plasma frequency of 54.1 MHz.

We note the following features of the thin-wire model [34] and Equation 11:

- The dependence on polarization enters as  $\cos^4 \phi$ , peaked for polarization parallel to the wire axis and zero for polarization perpendicular to wire axis. To maximize received signal, E-field polarization should be parallel to the air shower trajectory.
- The radius  $a$  of the wire contributes logarithmically to the radar cross section. Since the radius of the overdense region is linearly dependent on  $E_0$ , the RCS will be only logarithmically dependent on primary energy and not proportional to primary energy as might be expected in a simpler model.
- Unlike scattering in the  $a \approx \lambda$  regime, scattered radiation will not be enhanced in the forward direction (Figure 6). Rather, short-thin-wire radiation is treated as dipole emission.
- A change of  $\sim 30^\circ$  in aspect  $\theta$  will cause significant oscillations in  $\sigma_{TW}$  because of amplification in the  $(\sin \eta/\eta)^2$  term.

Known shortcomings of the model include:

- High electron density air shower core ionization will likely be an imperfect conductor, due again to the high rate of collisions with neutral molecules. Significant damping of RCS is expected due to this effect.
- Even absent collisional effects, plasmas have an associated “skin depth” given by  $\delta = c/\omega_p$ . If the radius of the wire  $a \ll \delta$ , only a small part of the incident radiation may be absorbed and re-radiated by the wire.
- Contributions from parts of the shower with radii greater than  $a$  are neglected.

### 2.5.2. Frequency Shift: The “Chirp”

Some of the characteristics of the chirp can be understood using geometrical arguments. Let  $R$  be the total path length  $R_T + R_R$  and  $\dot{R} = dR/dt$  the instantaneous rate of change of path length.  $\dot{R}$  is proportional to chirp rate. If  $\dot{R} > 0$  the received frequency is less than the radar frequency and if  $\dot{R} < 0$  the received frequency is greater than the radar frequency. Time-dependent frequency is analogous to Doppler shifted light or sound waves, though not identical because the wavelength of scattered radar carrier is fixed at the receiver—only combined phase changes.

CR air showers which start far away and move toward the Earth’s surface produce “down chirps” (decreasing frequency) starting above the carrier frequency as long as the core location is between TX and RX. There are geometries in which  $\dot{R}$  approaches zero, then becomes positive as the shower crosses the line connecting TX and RX. In this case, the chirp frequency will first descend to, then fall below the radar frequency. Neutrino air showers originating close to the Earth’s surface or low in the atmosphere could produce down chirps that start below the radar frequency and descend to lower frequencies.

The chirp signature contains information about air shower geometry. With the exception of lateral symmetry about a plane perpendicular to the ground and containing the TX and RX points, and a rotational symmetry about a line connecting the transmitter and receiver, radar echoes are unique.

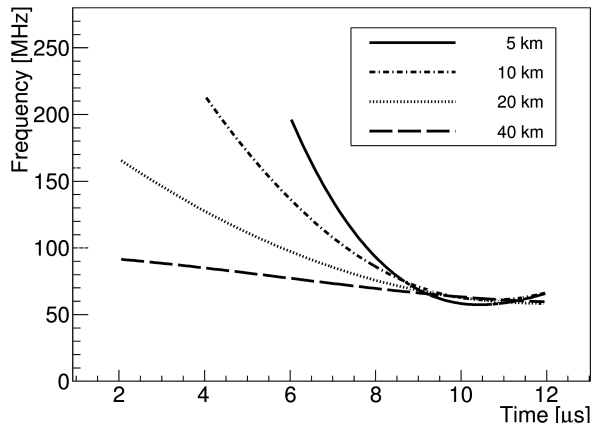


Figure 8: Simulated chirp spectra fits to highest amplitude frequency component for four different geometries. Each simulation represents a vertical, 10 EeV CR shower located midway between transmitter and receiver. TX → RX separation distances are shown on the legend. Both the time offsets and absolute frequency ranges have been justified for direct chirp rate comparison.

Figure 8 shows frequency vs. time for four chirps with different TX/RX separation distances. These chirps are simulated radar echoes from small zenith angle, 10 EeV air showers located midway between the transmitter and the receiver. The curves represent the highest amplitude frequency component in each time bin. In the following sections, duration is defined as the total time during which received power is within 10 dB of maximum. Bandwidth is the frequency difference between the two maximum–10 dB power points, on either side of the frequency at maximum power. The plot indicates that echoes with small TX/RX separation distances are short in duration and have large chirp rates.

A simple simulation that only tracks the phase of a point source with speed  $c$  will correctly yield the chirp signature of a given geometry. This fact is important because the assumption of a scattering model does not affect the frequency vs. time graph. Three radar echoes have been simulated with the same geometry and different electron lifetimes. Spectrograms of the simulated waveforms are shown in Figure 9. The first two have constant cross-sections; each segment has the same value of  $\sigma$  in the bi-static radar equation. The third uses the thin-wire approximation described above for the RCS, the parameters of which are informed by air shower evolution models and evolving electron lifetime [20].

Simulation 1 (top) has a very short, fixed, free electron lifetime, similar to a very small metallic sphere moving with speed  $c$ . There is only one scattering path length per time step. Simulation 2 (middle) has a lifetime longer than the travel time of the shower from first interaction to ground level, similar to a thin metallic cylinder that grows toward the ground at speed  $c$ . Simulation 3 is the output of the full simulation including lookup tables for the TARA TX and RX antennas in three dimensions, shower evolution models (Gaisser-Hillas, NKG, Nerling, Standard Atmosphere, etc., as above), and the thin-wire approximation for the RCS. The frequency vs. time graphs for the three simulations are superimposed in Figure 10, where only the maximum frequency in a given time bin is plotted. This comparison shows that frequency vs. time is independent of the radar target.

Figure 11 shows the spectrogram of a typical shower generated with the full TARA detector simulation. Properties relevant to detection are chirp slope ( $\sim 2 \text{ MHz}/\mu\text{s}$ ), frequency at maximum power  $F_{\max}$  (near 60 MHz), and chirp duration ( $\sim 10 \mu\text{s}$ ).

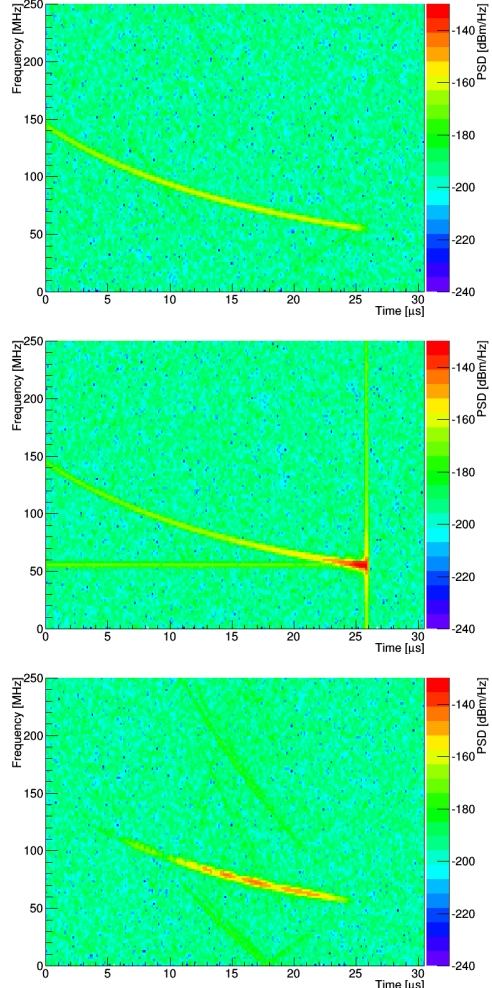


Figure 9: Spectrograms showing simulated radar echoes for a shower midway between transmitter and receiver and inclined 30° out of the TX/RX plane. Top: Electron lifetime is fixed at 1 ns and antenna gain is held constant. This configuration simulates a small scattering object travelling at the speed of light toward the ground. Middle: Electron lifetime is fixed at 100,000 ns and antenna gain is held constant. This configuration simulates a scattering rod beginning high in the atmosphere and growing toward the ground at the speed of light. Bottom: Electron lifetime is determined from empirical models and RCS comes from the thin-wire approximation and shower evolution models. Antenna gain is determined from lookup tables generated by NEC [32]. This configuration simulates a cosmic ray radar echo.

### 3. Radar Receiver and DAQ

The TARA DAQ (described in detail in [8]) records custom binary files that each contain a metadata header and 1,000 triggers. DAQ settings are contained in the metadata header and each trigger includes its own header and four waveforms, each 130.976  $\mu\text{s}$  in duration, or 32,744 samples at 250 MS/s, composed of

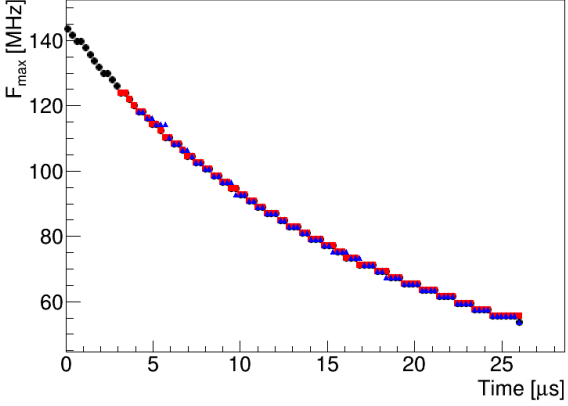


Figure 10: Plot showing  $F_{\max}$  vs. time for the three simulated echo waveforms shown in Figure 9. Black points represent  $F_{\max}$  for the short lifetime waveform. Red and blue points represent  $F_{\max}$  for the long lifetime and full simulation waveforms, respectively.

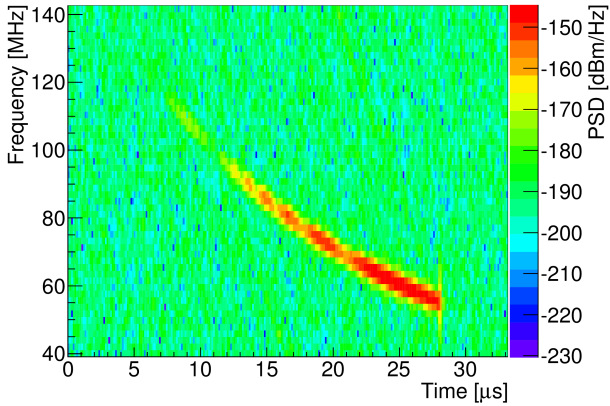


Figure 11: Radar echo spectrogram from a hypothetical  $10^{19}$  eV shower located midway between transmitter and receiver inclined  $30^\circ$  out of the plane connecting the two.

16 bit signed integer samples. Each waveform corresponds to one of four DAQ input channels, which are fed by two dual-polarized log periodic dipole antennas (LPDA). While collecting data used in the present analysis, the TARA transmitter was operated with horizontal polarization and hence we are primarily concerned with the horizontal receiver channels in which the sensitivity will be greatest.

Signals first pass through a series of RF filters and an amplifier on the front end of the RF DAQ system. Sequentially, the components are: lightning arrestor, which grounds the center conductor during periods of excessive voltage; RF limiter, which limits power to +11 dBm (decibels relative to mW); 30 dB amplifier;

40 MHz high pass (HP) filter, which attenuates frequency components below 40 MHz; FM band stop, which attenuates frequency components in the range 88–108 MHz; and a 90 MHz low pass (LP) filter, which attenuates frequencies above 90 MHz.

A single binary output file contains both FD triggers and “snapshot” triggers. Snapshot triggers are taken automatically once per minute, and are used to estimate the noise background. The receiver is located on the campus of the Long Ridge fluorescence detector, located southwest of the TA surface detector. During FD data acquisition, trigger pulses are sent to the radio receiver DAQ. The hardware level trigger from the FD to the TARA DAQ forces one event and a time stamp to be recorded. The FD triggers used were low-level triggers, a subset of which corresponded to actual CR events. Star light intensity fluctuations, passing airplanes and self-calibration triggers are included in low-level hardware triggers. The rate of these triggers during standard FD acquisition is 3–5 Hz, about three orders-of-magnitude higher than that expected for high energy CR events.

Snapshot triggers occur once per minute and are not correlated to any external trigger. These triggers offer an unbiased representation of the RF background, assuming there is no additional trigger noise from the FD electronics or TARA DAQ. A quantitative comparison of snapshot and FD triggers is shown in Figure 12. Recall that the majority of FD triggers are the result of low level FD trigger noise, and therefore should not have special waveform features. The black histogram is the distribution of VRMS values for all matched FD-trigger events. The red histogram is the distribution of snapshots selected for analysis (selection process described below) from the FD observation period. Good agreement between snapshot and FD-trigger RMS distributions indicates that there is not additional FD noise that can obscure signal.

FD triggers and snapshots are used in the present analysis. FD triggers comprise a promising dataset because a subset of these triggers are radar data obtained during actual CR events in the field of view of the detector. It only operates when the moon is below the horizon on clear, dry nights. The average duty cycle is approximately 10%.

#### 4. Offline Processing

TARA events from FD triggers are time-matched with reconstructed Long Ridge FD events [35] to remove noise triggers, after which the following reconstruction parameters are available: GPS time stamp, pri-

Table 1: Long Ridge FD-reconstructed event quality cuts. (NPE = number of photo-electrons; SDP = shower detector plane; see Figure 13. Pseudo-distance is the speed of light divided by the angular speed of the track.)

Cut Name	Criteria	Description
good tube fraction	$\geq 3.5\%$	data quality, noise reduction
good tubes	$\geq 6$	data quality, noise reduction
NPE/degree	$\geq 25$	data quality, sufficient signal
pseudo-distance	$\geq 1.5 \text{ km}$	geometry, shower resolution
SDP angle	$< 80^\circ$	geometry
$R_p$	$\geq 1 \text{ km}$	geometry
$\Psi$	$0^\circ \leq \Psi < 150^\circ$	geometry
$\delta\Psi$	$< 36^\circ$	fit reconstruction, $\Psi$ error
tangent fit	$\chi^2/\text{DOF} < 10$	fit reconstruction
zenith angle	$< 70^\circ$	geometry
$t_0$	$< 25.6 \mu\text{s}$	event occurs in trigger window
$R_p$ and $t_0$	$(R_p > 5 \text{ km}) \text{ or } (t_0 > 3 \mu\text{s})$	geometry
first tube depth	$150 < X_1 < 1200 \text{ g/cm}^2$	geometry, first tube illuminated from reasonable depth
observed slant depth	$> 150 \text{ g/cm}^2$	geometry, minimum track length
$X_{\max}$	$400 < X_{\max} < 1200 \text{ g/cm}^2$	fit reconstruction

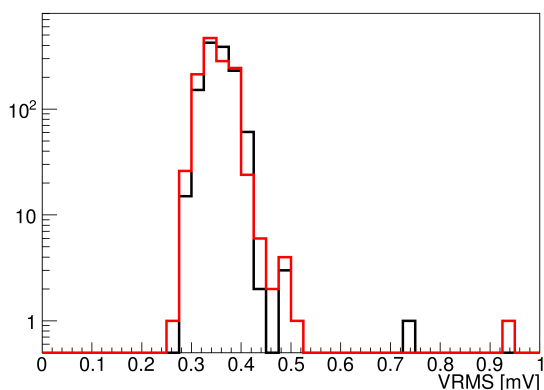


Figure 12: Voltage RMS distribution of all matched FD-triggered events in black overlaid with that of snapshots in red, recorded during several FD observation periods from August, 2013 to April, 2014. Waveforms are notch- and HP-filtered before the RMS is calculated. A fixed number of matched events occur during each FD observation period. The number of snapshot RMS values included in the histogram, per run, is equal to the number of included FD trigger values.

mary energy, core location, zenith/azimuth angle and  $X_{\max}$ . The reconstructed FD events from Long Ridge are selected by quality cuts designed to remove those which are reconstructed with large uncertainty. Table 1 gives the list of cuts and their descriptions. Figure 13 shows a diagram of the FD geometry.

Triggers are matched with an absolute time difference less than 200  $\mu\text{s}$ . Figure 14 shows a histogram of

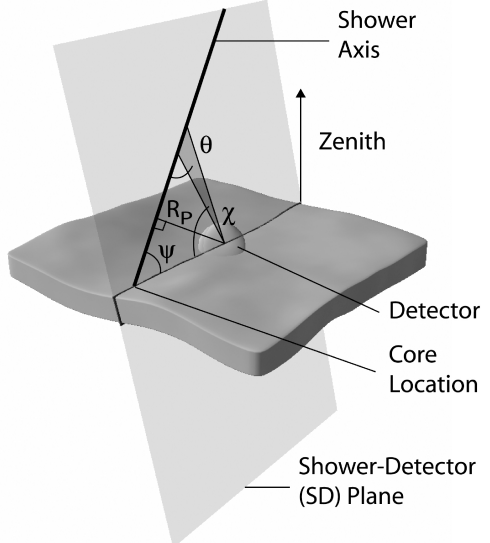


Figure 13: Fluorescence detector geometry [36].

the time difference between TARA FD triggers and reconstructed TA FD events collected over the course of several FD observation periods between August, 2013 and April, 2014. Matched FD-triggered events recorded during this date range are the focus of this analysis. Ignoring the delay in trigger formation, absolute timing uncertainty is 20 ns [37].

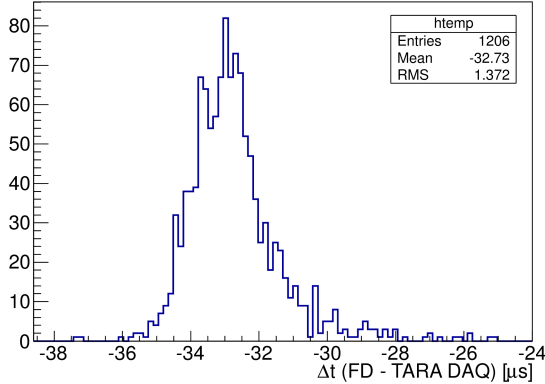


Figure 14: Time difference between FD reconstructed events and the TARA FD-triggered events recorded during FD observation periods between August, 2013 and April, 2014. The  $33\ \mu\text{s}$  delay is caused by FD DAQ trigger formation, cable delay and TARA DAQ delay in signaling an event to the GPSY [37] GPS event logger.

#### 4.1. Trigger Time Range

Spurious noise (discussed in Section 4.2) can interfere with the signal search and possibly mimic a positive detection. Therefore, a fixed time range of waveform samples is included in the analysis to reduce the probability that noise is present in the analyzed portion of the waveform. Any waveform samples or features outside this time range are not considered in any steps of the analysis. Only signals occurring between  $48\ \mu\text{s}$  before and  $5\ \mu\text{s}$  after the expected arrival time were considered.

#### 4.2. Filtering

The radar carrier frequency component at  $54.1\ \text{MHz}$  dominates all other frequencies and obscures low-power features in the time domain. Waveforms are therefore digitally notch- and high pass-filtered (see [38] for a discussion of each). The carrier is removed with an adaptive two-tap, recursive least squares (RLS) filter [39]. The high pass (HP) filter passes all frequencies above some cut-off frequency. It is designed using the Parks-McClelland [40] algorithm with input zero amplitude filter response at  $31.25\ \text{MHz}$  and  $43.75\ \text{MHz}$ . Here it is referred to simply as the  $30\ \text{MHz}$  HP filter. Figure 15 shows the first  $10\ \mu\text{s}$  of the  $132\ \mu\text{s}$  snapshot event display after applying a  $54.1\ \text{MHz}$  notch and a  $30\ \text{MHz}$  HP filter. Near the beginning of the time and frequency domain plots the high amplitude  $54.1\ \text{MHz}$  frequency component can be seen. It diminishes as the notch filter adapts its phase and amplitude to cancel the carrier.

Radio noise is minimal at the location of the receiver. There are no static noise sources, but intermittent carriers and spurious impulsive noise must be considered in

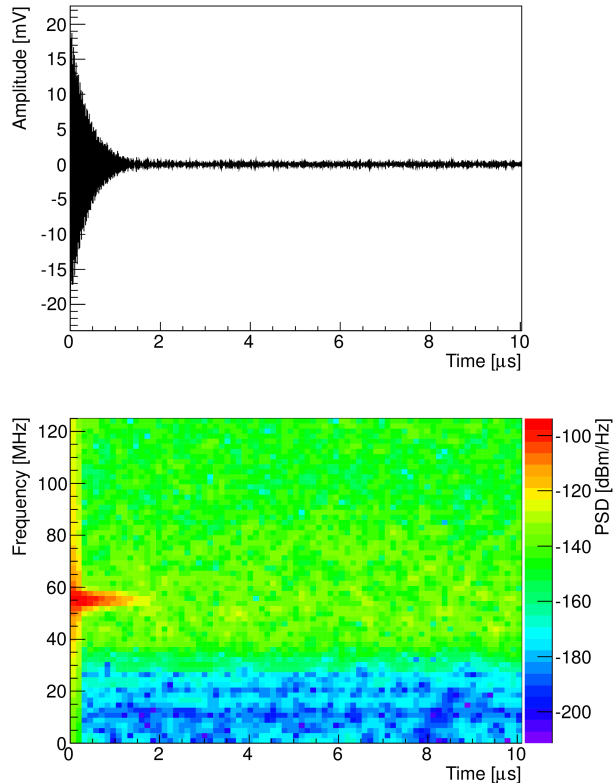


Figure 15: Event display for a snapshot chosen at random from the August, 2013 FD run with both  $54.1\ \text{MHz}$  notch and  $30\ \text{MHz}$  high pass digital filters applied. Only the first  $10\ \mu\text{s}$  of the  $132\ \mu\text{s}$  waveform is shown to emphasize filter characteristics. The high pass filter is fixed and attenuates frequencies below approximately  $30\ \text{MHz}$  from the beginning of the waveform. Carrier amplitude decreases as the adaptive notch filter finds the correct amplitude and phase.

the background estimation. Broadband transients (Figure 16) are the most common noise source and pose the worst threat of interfering in analysis because of the similarity to radar echoes, being broadband with short duration. Detection sensitivity is ultimately limited by the DAQ noise floor which has been shown to be consistent with galactic radio noise [8].

## 5. Signal Search

Section 2 describes the thin-wire approximation to the RCS. It is emphasized that this model is a reasonable representation of the scattering geometry of the true RCS and that it overestimates the received power because collisional damping and skin depth are not included. Any observed signals are expected to have absolute power significantly below the simulation prediction and the same frequency versus time characteristic.

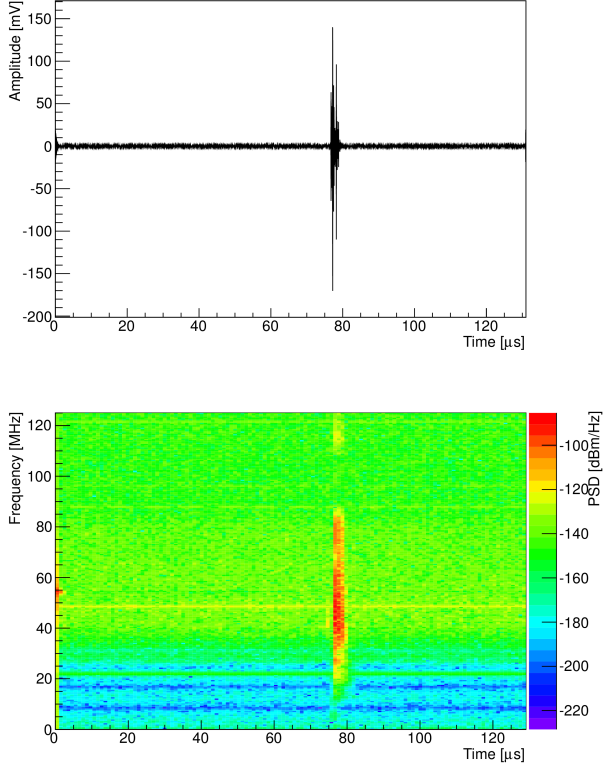


Figure 16: Event display of high amplitude, transient broadband noise. This type of noise has high MF response.

If signal power were not overestimated, receiver data would be replete with radar echo coincidences with TA reconstructed events. The following analysis shows that this is not the case. Data are searched with a matched filter (MF) tuned to a specific event via echo simulation. Section 5.1 introduces the concept of matched filtering. Section 5.2 gives a description of how the RF front end is simulated such that simulated echoes have the same frequency characteristics as the physical RF front end. In Section 5.3, the MF threshold is described and the following two sections detail the signal search.

### 5.1. Matched Filter

Matched Filtering (MF) is a digital signal processing (DSP) technique for detecting the presence of a known signal or “template” in a test waveform. The MF template is the ideal (no noise) digitized signal. The MF response is the convolution between the test waveform and the time-reversed template.

Figure 17 shows three examples of a test waveform and MF output. In each case a simulated radar echo

is superimposed on a random, filtered snapshot waveform. A template identical to the superimposed wave is used to calculate the absolute value of MF response as a function of the time after the convolution calculation begins (right plots). Peak MF response occurs at 60  $\mu$ s where the template and the superimposed wave coincide in time and phase. The amplitude signal-to-noise ratios (ASNR)

$$\text{ASNR} = \frac{V_{\max, c}^2}{\sigma_{\text{noise}}^2}. \quad (12)$$

(where  $V_{\max, c}$  is the maximum chirp amplitude and  $\sigma_{\text{noise}}$  is the standard deviation of the background noise) of the three examples are 10, 0 and -10 dB. In this analysis, noise comprises all frequencies that remain after notch and HP filtering. (The more common SNR is defined as

$$\text{SNR} = \frac{P_c}{\sigma_{\text{noise}}^2}, \quad (13)$$

where  $P_c$  is the chirp signal power, the square of the chirp waveform RMS.)

The simulated radar echoes are decimated down to the DAQ rate of 250 MS/s. Templates are then scaled such that the maximum voltage sample is 1.0 mV. The MF response is calculated in the trigger range of interest by computing the inner product of the template and predicted waveform. The result is a series of MF responses as a function of time in the window when the MF is applied, similar to the MF responses in Figure 17. Only the maximum value (peak response) from the series of MF outputs is saved for further analysis.

### 5.2. Front End Simulation

Simulation of the receiver front end electronics in TARA is necessary to understand the response of the system to theoretical chirp signals and, ultimately, to estimate the cross-section upper limit of UHECR air showers. The receiver antenna response is included in the simulation when radiation pattern lookup tables are queried for the gain specific to a shower segment, the location of which has specific geometry in the antenna coordinate system. Other front end components are characterized through the frequency response  $H$  (see Figure 18), measured as the transmission coefficient  $S_{21}$  *in situ* with a two-port vector network analyzer (VNA). Components in the RF frontend including RF limiter, amplifiers and filters, are detached from the antenna and transmission line to the DAQ. The input and output of the RF chain is then connected to the VNA, where  $S_{21}$  is measured at discrete frequency points in the 0 – 125 MHz DAQ band.

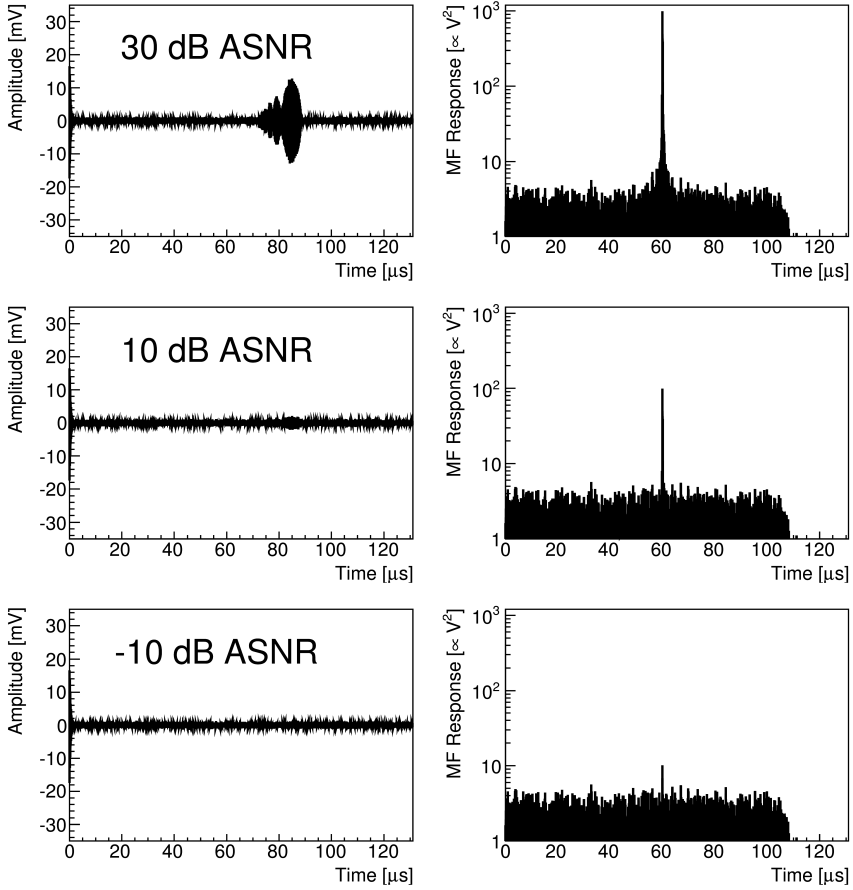


Figure 17: Three examples of test waveform composed of a notch and HP filtered snapshot background superimposed with a simulated canonical radar echo (left plots) and their Matched Filter (MF) responses (right plots). The MF response is calculated using same superimposed simulated echo waveform as a template. Peak response occurs at  $60 \mu\text{s}$  at the location of the below-noise beginning of the superimposed waveform, where the template and superimposed echo are aligned and the dot product between the two is maximized. The top, middle and bottom plots show results from superimposing the simulated echo at 30, 10 and  $-10 \text{ dB}$  amplitude signal-to-noise ratio (ASNR).

Data from the  $S_{21}$  measurement are used to construct a filter which can be applied in the time domain to simulated echoes. Echoes filtered in this manner exhibit a frequency response as if the waveform had passed through the actual RF frontend. The procedure for creating the time domain filter from desired frequency response  $H$  is introduced in digital signal processing (DSP) texts [38]. In practice, filter coefficients are obtained by calculating the inverse Fourier transform of  $H$ .

Figure 19 shows two spectrograms featuring Gaussian and post-filtered Gaussian noise. The frequency response  $H$  of the RF frontend for the acquisition channel used in the present analysis is plotted in Figure 18, where it has been reflected about zero. Features of the frequency response are clearly seen in the bottom plot in Figure 19. All simulated echoes are filtered in this

manner before being used in analysis.

### 5.3. MF Threshold

Snapshots of the TARA data stream are selected from the FD run according to the following criteria: the transmitter must be on at the time the snapshot was acquired, the snapshot must occur in a five-minute bin in which the average FD trigger rate is at least 1 Hz, and no dead channels or DAQ interruptions can be present in the waveform. The same quality cuts are applied to matched FD triggers.

Parameters from matched TA events are used to simulate radar echoes. Each matched TARA FD-trigger has a unique, simulated echo which is used to create a MF template. The radar echo simulation produces theoretical received signals according to transmitter power, detector and shower geometry, antenna gain

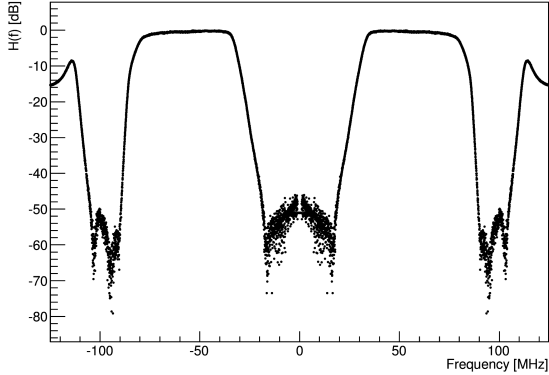


Figure 18: Frequency response  $H$ , which has been reflected about 0 MHz, or DC. These data are the transmission coefficient  $S_{21}$  which is measured at filter bank 3 and used to emulate a digital filter.

and shower parameters. Matched triggers have associated CR energy, geometry,  $X_{\max}$  and core locations determined from the reconstructed FD event to which they are matched. These data are used in the radar echo simulation.

Templates are created by filtering simulated echoes to emulate the RF front end response (see Section 5.2), decimating to 250 MS/s, and then truncating by removing samples at the beginning and end of the waveform that are below 5% of the peak. Low amplitude parts of the template do not greatly affect MF response and processing time is reduced by removing low amplitude tails.

Candidate events are selected by first estimating the noise response of each MF independently. A peak MF response distribution is created for each matched FD-triggered event by applying the simulated echo template as a MF to a set of 400 selected snapshots. The RMS of this distribution is calculated, and the threshold for positive detection is set at  $3 \times \text{RMS}$ . Because TARA is a discovery experiment, this fairly loose criteria was chosen so as to identify candidate events in the widest practical range. An example distribution and threshold is shown in Figure 20.

This MF detection scheme, in which the MF peak response distribution mean and RMS determine the threshold, has high efficiency at signal levels more than 10 dB ASNR below the galactic noise floor. Figure 21 shows detection efficiency as a function of ASNR for a typical event geometry.

#### 5.4. Search: Reconstructed Events

Of 1,206 events processed in the data set (including FD runs from August, 2013 to April, 2014), 17 events

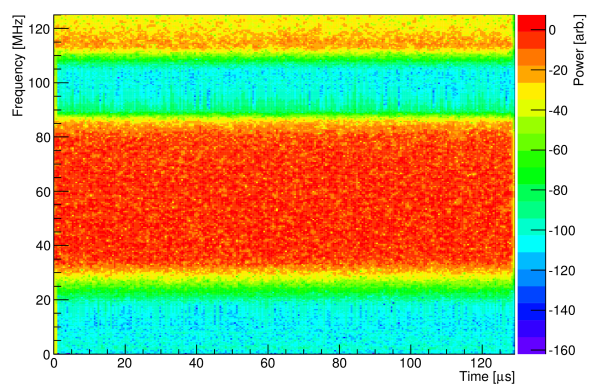
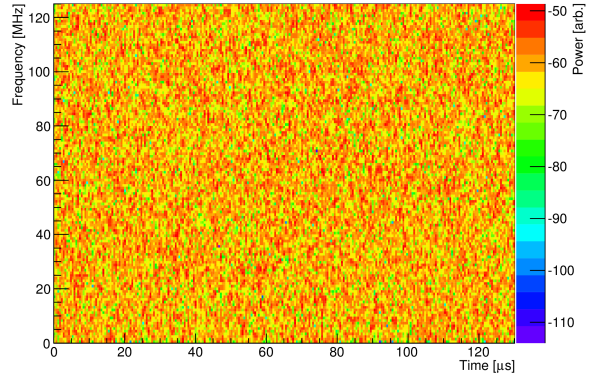


Figure 19: Spectrograms showing simulated Gaussian noise (top) and the same noise filtered with an FIR filter designed from the frequency response shown in Figure 18. Amplitude features can be directly compared between the spectrogram and the desired response.

are found to have MF response greater than 3 RMS. The statistical significance of this value is calculated using the expected value of snapshot false positives.

Recall that distributions of the snapshot peak MF response are used to calculate the detection threshold. In the majority of these distributions, which are created for each event, several snapshot MF responses exceed the threshold. Figure 20 shows the MF response distribution for an event from August, 2013. The threshold is  $\bar{x} + 3\text{RMS} = 51.8$ . Seven snapshots out of 400 exceed the threshold.

Figure 22 shows the number of snapshots exceeding threshold for all 1,206 events included in the analysis. On average, 1.34% of snapshots exceed the 3 RMS threshold, leading to a false-positive estimate of 16.2 events for our current sample. This is completely consistent with our observation of 17 positive detections. We thus interpret our positive detections as false positives, caused by common background noise.

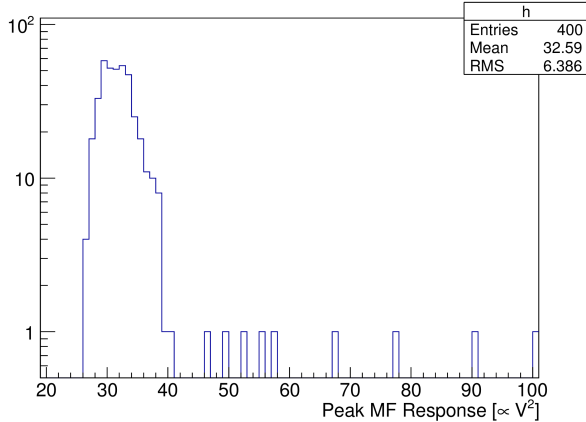


Figure 20: Peak MF response distribution for an August, 2013 FD-triggered matched event using 400 snapshots with a simulated radar echo MF template. The 3 RMS threshold for this particular event is 51.8.

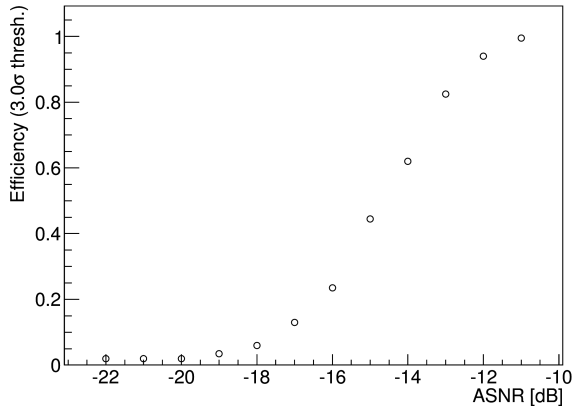


Figure 21: Matched filter detection efficiency as a function of ASNR using a simulated radar echo, for a 10 EeV shower midway between transmitter and receiver. Selected snapshots from the August, 2013 FD run are used both to determine the 3 RMS response threshold and as backgrounds on which scaled echo waveforms are superimposed.

Nevertheless, the 17 background events were scrutinized in more detail to insure that we were not ignoring potential signal. All were determined to be short-duration broadband transients. The background events satisfied the matched-filter threshold condition due to their large amplitude, rather than because their frequency structure was a particularly good match for the expected chirp. (See Figure 16.) These events display obvious differences between their spectral structure and the chirp expectation (Figure 11). Further, as is clear in Figure 20 that the background events are not a part or tail of the galactic distribution. We conclude

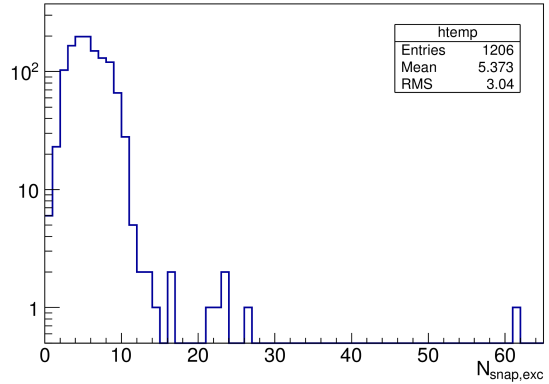


Figure 22: Distribution of  $N_{\text{snap},\text{exc}}$ , the number of snapshots with peak MF responses that exceed threshold. One entry per matched FD-triggered event.

that these background events are likely anthropogenic in origin, perhaps arising from electronic noise sources within the fluorescence detector and its power system.

### 5.5. Search: Nearby Events

The previous analysis only considered events which can be fully reconstructed by the FD. This restricts the number of events by requiring a minimum  $R_p$  of 1 km (see Table 1). Events that occur close to the FD pass through the telescope field of view quickly relative to the DAQ trigger sampling rate such that shower evolution and profile are not clearly observed: the events are not reconstructible. The bistatic radar equation (Equation 1) predicts maximum received power when the target is close to either the transmitter or receiver. There are no FD-triggered events that occur near the transmitter station because it is beyond the detection range of the FD, but many events occur close to the FD where the TARA receiver is located.

A search was conducted for evidence of CR radar echoes in FD triggers that fail the  $R_p$  cut. After time-matching TARA FD triggers with events that fail the  $R_p$  cut in the same manner as above, 2124 events remain. Simulated radar echoes of nearby Monte Carlo events are used to create a set of matched filters which will be used in the search. A large set of FD-triggering Monte Carlo events was narrowed down to a total of 673 events by requiring that  $E_0 > 3 \times 10^{17}$  eV and  $R_p < 1$  km.

Radar echoes from the nearby and unreconstructible Monte Carlo events are simulated and analyzed for chirp slope and duration within the passband. Due to the proximity of the shower and receiver, many of the simulated events are undetectable due to large frequency

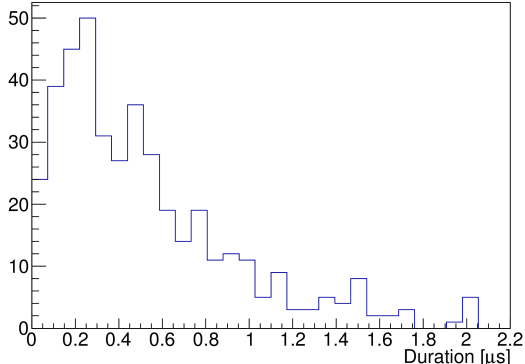


Figure 23: Distribution of radar echo durations within the TARA [40, 80] MHz passband. Duration is defined as the period during which the peak power occurs, with endpoints 10 dB below the peak.

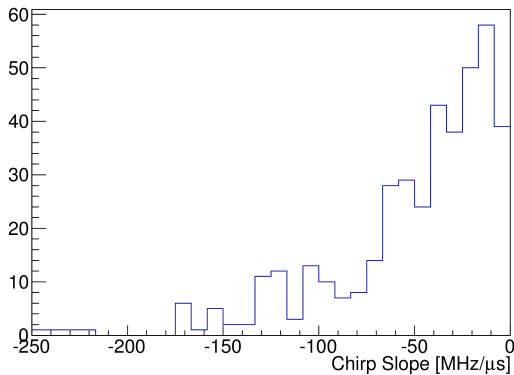


Figure 24: Distribution of radar echo chirp slopes within the TARA [40, 80] MHz passband. The slope is calculated from a simple straight line fit to the power spectrogram.

shifts that place echoes above the 80 MHz passband ceiling. Duration and slope distributions of the simulated events are shown in Figures 23 and 24. Entries with zero duration or slope are events with echoes outside the passband.

A set of 21 linear chirp, constant amplitude matched filters (MF) were created to broadly represent the Monte Carlo distributions: MFs are 400 ns in duration, span 140 MHz of chirp rate in seven discrete steps (10, 20, 30, 40, 50, 100, and 150 MHz/μs), and represent three different frequency bands, starting at 80, 70, and 60 MHz. A 3RMS threshold is determined for each of the 21 MF templates. No signal candidates were found in the relaxed  $R_p$  signal search.

## 6. RCS Calculation

### 6.1. $\Gamma_{90}$ Calculation

The search described in the previous section indicates that there is no echo signal present in the dataset described in this paper. Now, we use this information to place quantitative limits on the RCS.

While a general set of guidelines exist in the literature for setting 90% CL limits in event-based analyses [9], several considerations make placing limits in this case unique. First, we do not expect there to be a unique value for the extensive air shower radar cross section. Each individual showers cross section will depend on its primary energy, shower maximum, zenith angle, and on the atmosphere in which the shower develops. Further, the TARA detector has a wide range of sensitivities to cross sections depending on the shower geometry relative to the transmitter beam and receiver antenna geometry. Therefore, we place limits on the radar cross section on an *event-by-event* basis in a manner which is consistent with the accepted meaning for confidence levels: If the radar cross section of a particular air shower exceeds the 90% CL limit, then 90% of the time TARA would have reported a positive detection.

We make use of the thin-wire model described in Section 2, and assume that the cross section is proportional to the thin wire cross section  $\sigma_{\text{TW}}$ :

$$\sigma_{\text{EAS}} = \Gamma \sigma_{\text{TW}}, \quad (14)$$

(where  $\Gamma$  is a dimensionless scale factor) and place 90% c.l. upper limits on the RCS within the thin-wire model. The basic strategy is to vary the scale factor  $\Gamma$  until 90% of the simulated waveforms exceed the MF threshold determined by the algorithm described in Section 5.3. This value of  $\Gamma$  is then designated  $\Gamma_{90}$  for a particular event.

### 6.2. $\Gamma_{90}$ Results

Figure 25 shows a histogram of all  $\Gamma_{90}$  values for events with a MF response of less than 3 RMS (“negative detection”).

Figure 26 is a plot showing the locations at which the air shower core strikes the ground, including only events with  $\Gamma_{90} < 0.1$ . Red, dashed lines indicate the transmitter antenna  $-3$  dB beamwidth. Event core locations are clustered near – but not under – the main lobe. Very few of the selected events will have small zenith angles due to the horizontal polarization of the transmitted signal. Small scale factor events must be those that pass through the main lobe, therefore there will be few

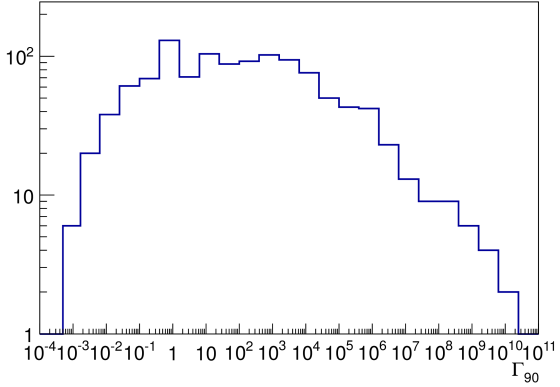


Figure 25:  $\Gamma_{90}$  distribution of all negative detection events. Large  $\Gamma_{90}$  occurs when matched-event geometry specifies an EAS that occurs outside the antenna main lobe.

events along the center of the beam.  $\Gamma_{90} > 0.1$  events comprise the majority of events and are those to which TARA is least sensitive.

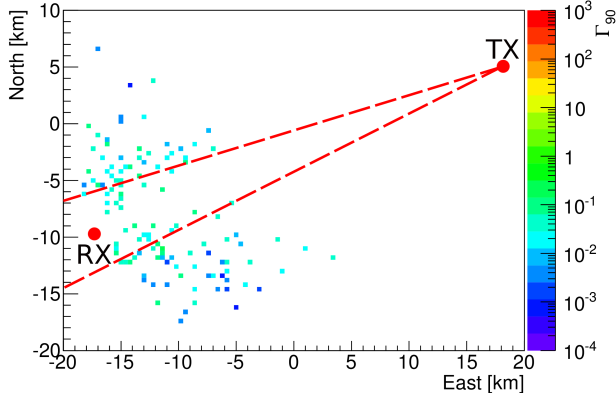


Figure 26:  $\Gamma_{90}$  (color scale) for negative detection events with  $\Gamma_{90} < 0.1$  shown at reconstructed core locations in Telescope Array CLF coordinates. Red dashed lines mark the primary beam -3 dB beamwidth.

The effect of the transmitter antenna main lobe on the scale factor can be seen in Figure 27, which restricts the set of events to those with azimuth greater than  $90^\circ$  and less than  $180^\circ$ . (The azimuth origin is due east. All events in the plot point back to the source toward the second quadrant (upper left). Events above the beam have very high scale factors because those events do not interact with the main lobe. The lowest scale factor events are those that produce high echo voltages due to optimal geometry and interaction with the main lobe. Reversing the general pointing direction of events, by limiting azimuth to greater than  $270^\circ$  and less than  $360^\circ$ ,

produces a similar plot, but with the high  $\Gamma_{90}$  events below the main lobe and low  $\Gamma_{90}$  above the main lobe.

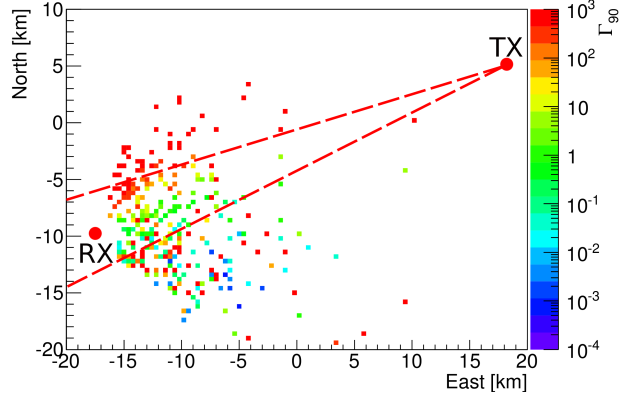


Figure 27:  $\Gamma_{90}$  (color scale) negative detection events restricted to those with  $90^\circ < \text{azimuth} < 180^\circ$  shown at reconstructed core locations in Telescope Array CLF coordinates. Red dashed lines mark the primary beam -3 dB beamwidth.

Figure 28 is similar to the plot in Figure 26, but includes green arrows that point at the core location of the five lowest  $\Gamma_{90}$  events and point in the direction the shower travels toward the ground. Arrow length is proportional to zenith angle. One observes that the five events with the lowest  $\Gamma_{90}$  are highly inclined to match transmitter and receiver polarization and have azimuth values which allow them to interact with the main lobe.

We note that none of the events for which TARA had particularly high sensitivity (including the five events in Table 2) had matched filter responses exceeding the 3 RMS threshold. Thus they do not enter into the particular limits reported in this paper.

### 6.3. Systematic Uncertainties

In the previous section, we describe the calculation of 90% c.l. upper limits on the radar cross section for particular Telescope Array events. Systematic uncertainties in the terms in the bistatic radar equation (Equation 1) make necessary relatively small adjustments to the upper limits reported.

The total transmitter power is logged, and is known at any particular time to better than 1%. Transmitter forward gain is modelled as a function of angle by Numerical Electromagnetics Code [32] (NEC), which has been confirmed by direct measurements as an accurate representation of the relative gain to within 10% [8].

The receiver gain is also modeled using NEC, at 54.1 MHz. An uncertainty arises from variations in the

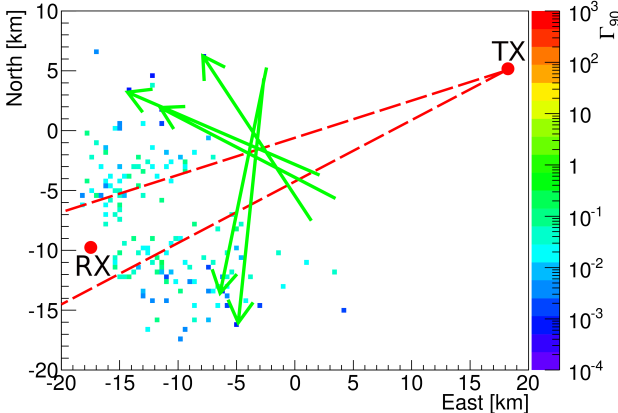


Figure 28:  $\Gamma_{90}$  (color scale) for negative detection events with  $\Gamma_{90} < 0.1$ , similar to Figure 26. Additionally, green arrows point in the direction the shower propagates through the atmosphere at the core location of the five lowest  $\Gamma_{90}$  events. Arrow length is proportional to zenith angle.

receiver gain as a function of frequency, which is not included in the waveform simulations. This effect is estimated to be 3% or less for events in geometries to which TARA is most sensitive.

Monocular FD reconstruction uncertainties of approximately 17% in the energy of air showers and approximately  $70 \text{ g/cm}^2$  in the depth of shower maximum enter in to the expectation for the target cross-section. Within the thin wire model the effect due to uncertainty in energy is weak, owing to the log-squared dependence of cross section on wire diameter (and therefore energy, Equation 11). Shifting the location of shower maximum  $X_{max}$  by  $100 \text{ g/cm}^2$  is also found to be a small effect, shifting  $\Gamma_{90}$  by less than 1%.

Uncertainties in the transmitter-to-target ( $R_T$ ) and target-to-receiver ( $R_R$ ) distances come from uncertainty in the air shower geometries arising from monocular fluorescence reconstruction. The largest effect derives from the uncertainty in the shower-detector plane angle  $\Psi$ , shown in Figure 13. The uncertainty in  $\Psi$  is typically  $8^\circ$ . Fluctuations of either sign in  $\Psi$  are found to have the effect of increasing  $\Gamma_{90}$  by as much as 60%. This is by far the dominant contribution to systematic uncertainty in the cross-section upper limit. We account for this systematic by increasing the lower limits by the amounts shown in Table 2.

#### 6.4. Discussion; RCS Upper Limits

Estimates of the detectable RCS for the TARA detector have been made previously [8], and shown to be of order  $50 \text{ cm}^2$ , without the post-processing technique

used in the present paper. For comparison, we may consider the best result in Table 2:

$$\sigma \leq 0.00077 \sigma_{TW} \quad (90\% \text{ c.l.}) \quad (15)$$

Figure 29 shows the total integrated thin-wire RCS as a function of time during shower evolution and propagation toward the ground for this specific event. The RCS is integrated over every longitudinal segment of the shower with plasma age less than  $5\tau$  at each 2 ns time step and phase factors attributed to differing path length are included in each term in the sum. The peak RCS is  $5.5 \text{ m}^2$ .

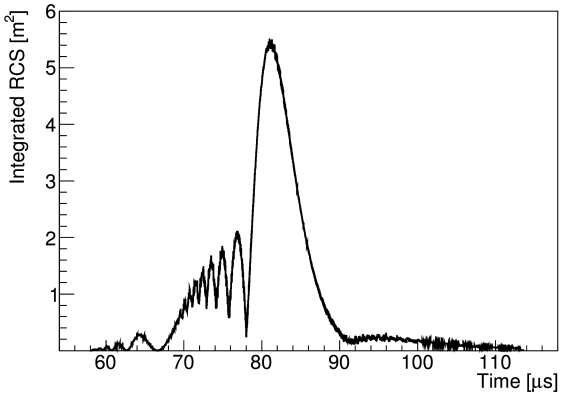


Figure 29: Integrated EAS RCS using the thin-wire approximation to RCS for a radar echo simulated with reconstructed shower parameters. Phase factors are included in the sum of the total RCS to properly account for each longitudinal shower segment.

After including detector sensitivity, nonobservation of signal and the effect of systematic uncertainty the effective RCS upper limit may be expressed as a product of the peak RCS with  $\Gamma_{90}$ , equal to approximately  $42 \text{ cm}^2$  at 90% c.l. This is in good agreement with the earlier estimate. The implications of such a small upper limit will be discussed in the conclusion.

Figure 30 shows simulated received power versus time for the event with  $\Gamma_{90} = 0.00077$ . The top (black) curve is the unmodified simulated power for this shower, within the thin-wire scattering model. The middle (blue) curve is the thin-wire simulated power for this shower modified by the  $\Gamma_{90} = 0.00077$  scale factor. The bottom (green) curve is the thin-wire simulated power modified by the  $10^{-6}$  collisional damping factor calculated in Section 2.2. The red line is the integrated TARA passband noise power, which is calculated from data which have been amplified by 30 dB in the RF frontend. This plot confirms earlier predictions: damping is large, and this analysis technique can detect signal below the noise floor.

Table 2: Summary of five lowest  $\Gamma_{90}$  events. The values presented for  $\Gamma_{90}$  include an increase — by as much as 60% — due to systematic uncertainties associated with uncertainties in the shower-detector plane angle. Core location pairs (x,y) are in units of kilometers relative to TA's central laser facility (CLF). In this coordinate system the transmitter is located at (17.9, 4.7) and the receiver site is located at (-18.4, -9.9).

Date	Energy [EeV]	Core Loc. [km]	Zen. [deg.]	Azi. [deg.]	$X_{\max}$ g/cm <sup>2</sup>	$\Gamma_{90} \times 10^4$
20130809	1.22	(-11.5,1.9)	65.7	301.6	772	13.4
20130816	1.43	(-7.9,6.2)	68.6	280.5	755	10.8
20130926	1.38	(-14.3,3.2)	54.9	299.5	837	12.5
20131105	1.83	(-4.8,-16.0)	59.6	121.4	805	13.1
20131202	11.04	(-6.4,-13.6)	62.7	114.6	859	7.7

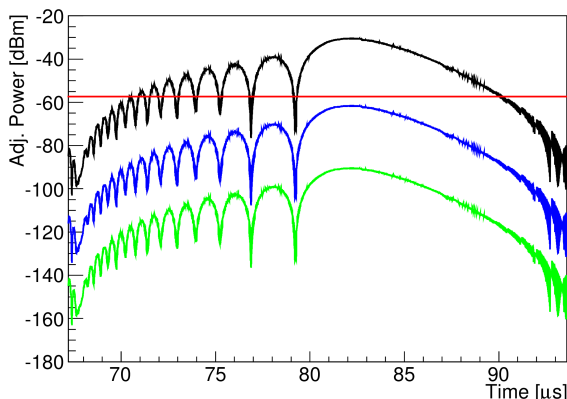


Figure 30: Received power vs. time for the event with  $\Gamma_{90} = 0.00077$  (black) after adjusting for uncertainty in reconstruction parameters. The same received power curve is shown multiplied by  $\Gamma_{90}$  (blue) or the damping factor  $10^{-6}$  (green) calculated in Section 2.2 to account for collisional damping. The red line is integrated background noise power in the TARA passband.

## 7. Conclusion

The TARA detector is the first facility designed specifically to search for the radar signature of UHECR. It combines a dedicated 40 kW, 54.1 MHz transmitter, high-gain (23 dB) phased antenna array, dual-polarized log periodic receiver antennas and a 250 MS/s receiver, colocated with the conventional Telescope Array cosmic ray observatory in radio-quiet western Utah, U.S.A.

In this paper, we have reported the null result of a search for radar echoes in a set of radio waveforms which were collected by triggering on the Telescope Array Long Ridge fluorescence detector. None of the cosmic-ray coincident waveforms contained signals comparable to the high rate “chirps” expected for EAS radar echoes. A small subset of waveforms contained broadband transients, at a level consistent with the expectation from random snapshots of the radar receiver

stream. These were likely due to anthropogenic sources not related to EAS.

Based on these observations, we have for the first time set upper limits on the radar cross sections of individual EAS. These limits are set based on the assumption that the radar cross section of EAS is dominated by a relatively narrow (few cm) core, corresponding to the overdense regime in a plasma in the absence of collisional damping effects. Skin-depth considerations are also ignored. Such an airshower may be treated as a thin wire relative to our 5.5 meter sounding wavelength, and we designate its theoretical cross section as  $\sigma_{TW}$ . For the most geometrically ideal EAS we studied in the present analysis, we place an upper limit of  $7.7 \times 10^{-4} \sigma_{TW}$ , at 90% c.l.

Although model dependent, this limit is consistent with heavy attenuation of RF scatter by the collisional damping mechanism. The evidence suggests that the prospects are poor for detection of cosmic ray air showers via the radar technique, in this regime of sounding frequencies and ionization densities.

## 8. Acknowledgments

TARA is supported by NSF PHY-0969865, PHY-1126353 (MRI), PHY-1148091, and the W.M. Keck Foundation. The Telescope Array experiment is supported by the Japan Society for the Promotion of Science through Grants-in-Aids for Scientific Research on Specially Promoted Research (21000002) “Extreme Phenomena in the Universe Explored by Highest Energy Cosmic Rays” and for Scientific Research (19104006), and the Inter-University Research Program of the Institute for Cosmic Ray Research; by the U.S. National Science Foundation awards PHY-0307098, PHY-0601915, PHY-0649681, PHY-0703893, PHY-0758342, PHY-0848320, PHY-1069280, PHY-1069286, PHY-1404495 and PHY-1404502; by the National Research Foundation of Ko-

rea (2007-0093860, R32-10130, 2012R1A1A2008381, 2013004883); by the Russian Academy of Sciences, RFBR grants 11-02-01528a and 13-02-01311a (INR), IISN project No. 4.4509.10 and Belgian Science Policy under IUAP VII/37 (ULB). The foundations of Dr. Ezekiel R. and Edna Wattis Dumke, Willard L. Eccles and the George S. and Dolores Dore Eccles all helped with generous donations. The State of Utah supported the project through its Economic Development Board, and the University of Utah through the Office of the Vice President for Research. The experimental site became available through the cooperation of the Utah School and Institutional Trust Lands Administration (SITLA), U.S. Bureau of Land Management, and the U.S. Air Force. We also wish to thank the people and the officials of Millard County, Utah for their steadfast and warm support. We gratefully acknowledge the contributions from the technical staffs of our home institutions. An allocation of computer time from the Center for High Performance Computing at the University of Utah is gratefully acknowledged.

## References

- [1] R. Abbasi, et al., First Observation of the Greisen-Zatsepin-Kuzmin Suppression, *Phys. Rev. Lett.* 100 (2008) 101101.
- [2] T. Abu-zayyad, et al., The Cosmic-Ray Energy Spectrum Observed with the Surface Detector of the Telescope Array Experiment, *Astrophys. J. Lett.* 768 (1) (2013) L1.
- [3] J. Abraham, et al., Observation of the Suppression of the Flux of Cosmic Rays above  $4 \times 10^{19}$  eV, *Phys. Rev. Lett.* 101 (2008) 061101.
- [4] R. Abbasi, et al., Indications of Intermediate-Scale Anisotropy of Cosmic Rays with Energy Greater than 57 EeV in the Northern Sky Measured with the Surface Detector of the Telescope Array Experiment, *Astrophys. J. Lett.* 790 (2014) L21.
- [5] H. Falcke, et al., Detection and Imaging of Atmospheric Radio Flashes from Cosmic Ray Air Shower, *Nature* 435 (2005) 313–316.
- [6] G. Askaryan, Excess Negative Charge of an Electron-Photon Shower And Its Coherent Radio Emission, *Sov. J. Exp. Theor. Phys.* 14 (2) (1962) 441–443.
- [7] P. Blackett, et al., Radio Echoes and Cosmic Ray Showers, *Proc. Roy. Soc. A* 177 (969) (1941) 183–186.
- [8] R. Abbasi, et al., Telescope Array Radar (TARA) observatory for Ultra-High Energy Cosmic Rays, *Nucl. Instrum. Meth. A* 767 (2014) 322–338.
- [9] K. Olive, et al., Review of Particle Physics, *Chin. Phys. C* 38 (2014) 090001.
- [10] T. Gaisser, A. Hillas, Reliability of the Method of Constant Intensity Cuts for Reconstructing the Average Development of Vertical Showers, in: Proceedings of the 15th ICRC, Vol. 8, 1977, p. 353.
- [11] K. Greisen, Cosmic Ray Showers, *Ann. Rev. Nucl. Sci.* 10 (1960) 63–108.
- [12] P. Sokolsky, Introduction to Ultrahigh Energy Cosmic Ray Physics, Westview Press, Boulder, Colorado, 2004.
- [13] F. Nerling and others, Universality of Electron Distributions in High-energy Air Showers — Description of Cherenkov Light Production, *Astropart. Phys.* 24 (2006) 421–437.
- [14] B. Rossi, High Energy Particles, Prentice-Hall, Inc., Englewood Cliffs, NJ, 1952.
- [15] D. Heck, et al., CORSIKA: A Monte Carlo Code to Simulate Extensive Air Showers, *Wissenschaftliche Berichte FZKA* 6019.
- [16] S. Ostapchenko, QGSJET-II: Towards Reliable Description of Very High Energy Hadronic Interactions, *Nucl. Phys. B-Proc. Suppl.* 151 (2006) 143–146.
- [17] K. Davies, Ionospheric Radio Waves, Blaisdell Publishing Company, Waltham, Massachusetts, 1969.
- [18] J. Jackson, Classical Electrodynamics, Third Edition, John Wiley & Sons, Inc., 1999.
- [19] I. Shkarofsky, Collision Frequency Associated with High Temperature Air and Scattering Cross-sections of the Constituents, *Planet. Space Sci.* 6 (1961) 24–46.
- [20] R. Vidmar, On the Use of Atmospheric Pressure Plasmas as Electromagnetic Reflectors and Absorbers, *IEEE T. Plasma Sci.* 18 (4) (1990) 733–741.
- [21] Y. Itikawa, Effective Collision Frequency of Electrons in Atmospheric Gases, *Planet. Space Sci.* 19 (1971) 993.
- [22] Sir Bernard Lovell, F.R.S., Reminiscences and Discoveries, The Blackett-Eckersley-Lovell Correspondence of World War II and the Origin of Jodrell Bank, *Notes Rec. R. Soc. Lond.* 47 (1) (1993) 119–131.
- [23] K. Suga, Methods for Observing Extremely Large Extensive Air Showers, in: Proc. Fifth Interamerican Sem. on Cosmic Rays, Vol. XLIX, 1962.
- [24] J. Stasielak, et al., Feasibility of Radar Detection of Extensive Air Showers, ArXiv e-printsarXiv:1411.7295.
- [25] Y. Itikawa, et al., Cross Section for Collisions of Electrons and Photons with Nitrogen Molecules, *J. Phys. Chem. Ref. Data* 15 (1986) 985–1010.
- [26] Y. Itikawa, et al., Cross Section for Collisions of Electrons and Photons with Oxygen Molecules, *J. Phys. Chem. Ref. Data* 18 (1989) 23–42.
- [27] P. Gorham, On the Possibility of Radar Echo Detection of Ultra-high Energy Cosmic Ray- and Neutrino-induced Extensive Air Showers, *Astropart. Phys.* 15 (2001) 177–202.
- [28] R. King, T. Wu, The Scattering and Diffraction of Waves, Harvard University Press, Cambridge, Massachusetts, 1959.
- [29] D. Underwood, Large Doppler Shift in RADAR Detection of Ultra-high Energy Eosmic Rays, in: Radar Conference, RADAR '08, IEEE, 2008, pp. 1–5.
- [30] A. Zech, A Measurement of the Ultra-High Energy Cosmic Ray Flux with the HIRES FADC Detector, Ph.D. thesis, Rutgers University (2004).
- [31] NASA, U.S. Standard Atmosphere, Tech. rep., U.S. Government Printing Office (1976).
- [32] G. Burke, et al., NEC - Numerical Electromagnetics Code for Antennas and Scattering, in: Antennas and Propagation Society International Symposium, Vol. 17, 1979.
- [33] A. Dogariu, et al., Versatile Radar Measurement of the Electron Loss Rate in Air, *Appl. Phys. Lett.* 103 (2013) 224102.
- [34] J. Crispin, A. Maffett, Radar Cross-Section Estimation of Simple Shapes, *P. IEEE* 53 (8) (1965) 833–848.
- [35] R. Abbasi, et al., Monocular Measurement of the Spectrum of UHE Cosmic Rays by the FADC Detector of the HiRes Experiment, *Astropart. Phys.* 23 (2005) 157–174.
- [36] B. Stokes, A Search for Anisotropy in the Arrival Directions of Ultra High Energy Cosmic Rays Observed by the High Resolution Fly's Eye Detector, Ph.D. thesis, University of Utah (2006).
- [37] J. Smith, et al., GPSY2: A Programmable Hardware Module for Precise Absolute Time Event Generation and Measurement, in:

- Proceedings of the 30th ICRC, Vol. 5, 2008, pp. 997–1000.
- [38] J. Proakis, D. Manolakis, Digital Signal Processing, Third Edition, Prentice Hall, Upper Saddle River, NJ, 1995.
  - [39] M.H. Hayes, Statistical Digital Signal Processing and Modeling, Wiley, 1996, 9.4: Recursive Least Squares.
  - [40] Digital Signal Processing Committee of the IEEE Acoustics, Speech, and Signal Processing Society, eds., Programs for Digital Signal Processing, IEEE Press, New York, 1979, algorithm 5.1.

# Performance of the ARIANNA Hexagonal Radio Array

---

**Corey Reed\* for the ARIANNA Collaboration**

*Department of Physics and Astronomy, University of California, Irvine*

*Irvine, CA 92697-4575, USA*

*E-mail:* [cjreed@uci.edu](mailto:cjreed@uci.edu)

Installation of the ARIANNA Hexagonal Radio Array (HRA) on the Ross Ice Shelf of Antarctica has been completed. This detector serves as a pilot program to the ARIANNA neutrino telescope, which aims to measure the diffuse flux of very high energy neutrinos by observing the radio pulse generated by neutrino-induced charged particle showers in the ice. All HRA stations ran reliably and took data during the entire 2014-2015 austral summer season. A new radio signal direction reconstruction procedure is described, and is observed to have a resolution better than a degree. The reconstruction is used in a preliminary search for potential neutrino candidate events in the data from one of the newly installed detector stations. Three cuts are used to separate radio backgrounds from neutrino signals. The cuts are found to filter out all data recorded by the station during the season while preserving 85.4% of simulated neutrino events that trigger the station. This efficiency is similar to that found in analyses of previous HRA data taking seasons.

*The 34th International Cosmic Ray Conference,  
30 July- 6 August, 2015  
The Hague, The Netherlands*

---

\*Speaker.

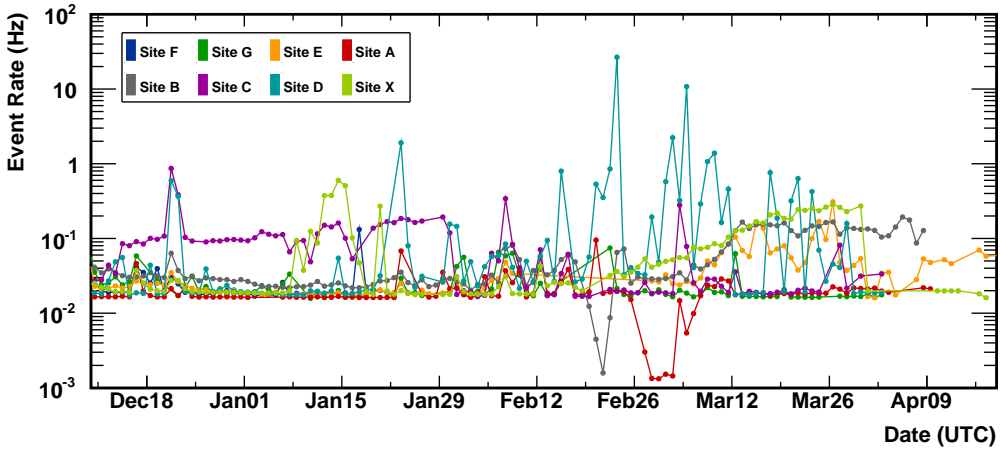


**Figure 1:** Daily average trigger rates of each HRA station during the 2014-2015 data taking season. See text for details.

## 1. The ARIANNA Hexagonal Radio Array

The ARIANNA Collaboration plans to construct a neutrino telescope capable of measuring the diffuse flux of high energy neutrinos in the  $10^8 - 10^{10}$  GeV range [1]. The ARIANNA Hexagonal Radio Array (HRA) serves as a pilot program to the full ARIANNA telescope. During the 2014-2015 austral summer, the HRA installation was completed at the ARIANNA detector site on the Ross Ice Shelf of Antarctica [2]. It consists of eight independent detector stations, each of which has four Log-Periodic Dipole Antenna (LPDA), an autonomous data acquisition (DAQ) system (with local data storage and remote data transfer capabilities) as well as local solar power. The stations measure radio pulses in the 50 MHz – 1 GHz frequency range, making them sensitive to the radio emission produced by charged particle showers generated by neutrino interactions in the ice, known as the Askaryan effect [3, 4, 5]. Details on the station hardware may be found in Refs. [2, 6].

All eight stations were installed by early December, 2014 and ran until the sun began to set around early April, 2015. The layout of the detector stations can be found in Refs. [1, 2]. Figure 1 shows the trigger rate of each station during the 2014-2015 austral summer data taking season.

Similar to previous seasons, trigger rates were generally low and minimal threshold tuning was required. While each station is similar, small variations can lead to noticeable differences in the trigger rates. The majority of Site F data has not yet been transferred off station and does not appear in the figure. During late February and early March, the trigger requirements at Sites A and B were temporarily increased to lower the rates. This was done to test the reliability of sending radio waveform data off Antarctica using satellite communications [2] limited to 340 bytes per message. The strong solar burst on December 20, 2014 is visible in a correlated rise of trigger rates on all stations [2] (it is also visible in Fig. 6, discussed in Sect. 3.3). The higher rates of Site C early in the season are simply due to low triggering thresholds (which were later corrected). The high rate spikes of Site D later in the season are caused by radio bursts emitted when the station’s battery switches on (station powered by battery) and off (station powered directly by solar panels).

This will be corrected during the 2015-2016 deployment season by installing a new battery inside the radio-tight DAQ box. Other rate increases are correlated with storms (i.e. February 8) and the dramatic temperature drop that occurs during the beginning of March. As the temperature falls from about  $0^{\circ}$  C to  $-20^{\circ}$  C, the gain of the amplifiers increases, leading to a rise in trigger rates unless thresholds are adjusted to compensate.

## 2. Radio Signal Direction Determination

The direction from which radio signals arrive at a detector station is reconstructed using the cross-correlation of the time dependent radio signals observed by parallel LPDAs. Each HRA station has four LPDAs, arranged symmetrically around the station DAQ box. Antennas situated across from each other (not adjacent) are oriented with parallel tines and separated by 6 m. Thus there are two such parallel LPDA pairs, so that a signal perfectly co-polarized with one antenna pair will be perfectly cross-polarized with the other antenna pair. Cross-correlations are used to determine the likelihood that the measured data is consistent with the expected time delays between parallel channels for a radio signal (with a planar wave-front) arriving from a particular direction.

The most likely radio arrival direction is determined by comparing two separate fit procedures. The first procedure uses a genetic minimization algorithm to choose the most likely arrival direction. The second procedure simply scans the entire angular phase space in  $1^{\circ} \times 1^{\circ}$  bins. In both procedures, the arrival direction estimate is further refined using the Migrad minimization algorithm. The two resulting fits are compared and the one with the best likelihood is chosen.

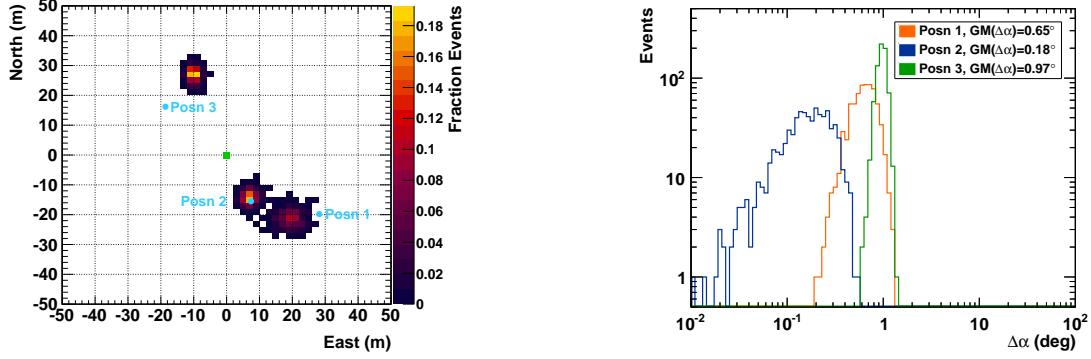
Special calibration data has been collected in order to quantify the radio pulse arrival direction resolution. A Pockels Cell Driver (PCD) is used to generate a very short (about 3 ns) uni-polar pulse that is transmitted from an LPDA. The transmitting antenna is oriented with its boresight vertically downward and placed at various positions on the ice around a station. The calibration pulse travels downward through the firn and ice, reflects off the sea water below the ice shelf and then travels up through the ice and firn where it is measured by the station. The reflection has been observed to preserve polarization [7]. The station is triggered externally in order to veto radio noise produced by the PCD pulser.

Figure 2 shows the reconstructed transmitter location, relative to the station located at the origin, for events in three sets of calibration data. The true transmitter positions are shown by the blue markers. At each location, the transmitting LPDA is oriented such that its tines are at a  $45^{\circ}$  angle to the tines of all four receiving LPDAs.

The angular deviation between the reconstructed signal direction and the true direction is shown in Fig. 3. This represents the *radio pulse* direction resolution, not a neutrino direction resolution. The neutrino direction resolution is expected to be on the order of a few degrees, mainly due to the finite resolution with which the polarization of the radio signal can be determined [1].

## 3. Search for Neutrinos in Site B Data

The station at Site B has a configuration that, among currently deployed HRA stations, contains the most pieces of hardware planned for use in a full ARIANNA station. This includes a new signal digitizing chip, amplifiers with a flatter response over the frequency bandwidth and a



**Figure 2:** The reconstructed calibration pulse transmitter location. The true transmitter locations are shown by the blue markers. The station sits at the origin, marked by the green square. The transmitter LPDA is always oriented such that the plane of its tines are offset by 45 degrees from those of each receiving LPDA.

**Figure 3:** The angular deviation of the reconstructed radio pulse arrival direction from the expected direction for events shown in Fig. 2. The resolution is quantified by the geometric mean of each distribution, shown in the legend. Note that this does not represent a neutrino direction resolution.

reliable battery. A preliminary search for neutrino signals in the data taken by this station has been conducted (although no such signals are expected given the small aperture and short exposure time of this single station).

Data taken by Site B from December 10, 2014 (UTC) until the end of the season, around April 9, 2015 (UTC), is used in the analysis described in this proceeding. Data collected by the station but not yet transferred off Antarctica, most of which was taken during the last weeks of March, is not yet included in the analysis. Also excluded from the analysis is calibration data and data collected while the station’s communication peripherals were powered on. This latter data is not particularly noisy and may be included in future analyses, but has been excluded here for simplicity. The analyzed data set comprises 93.1 days of livetime, corresponding to about a 90% uptime [2] during the data taking periods used in the analysis. The 10% downtime is due to the frequency with which the station transmits its data off Antarctica. This is tuneable remotely and may be reduced in the future, but was deemed an acceptable cost given the benefits of receiving station data in near real time.

A set of neutrino simulation events have been generated according to the procedure described in Ref. [1]. The same trigger is applied in the generation of the neutrino signal simulation as has been applied in the Site B data set. Namely, that two of the four receiving LPDAs show a bipolar pulse having both the high and low crests extending beyond the high and low thresholds, each set at four times the thermal noise RMS.

### 3.1 Rejecting Single Frequency Resonance Events

Some events collected by the station contain a large amount of their power at a single frequency. Such waveforms stand in stark contrast to the waveform expected for a neutrino, which contains significant power across the 50 MHz to 1 GHz frequency band due to the very short time duration of the Askaryan pulse. These “sinusoidal” events in the data are likely caused by detector

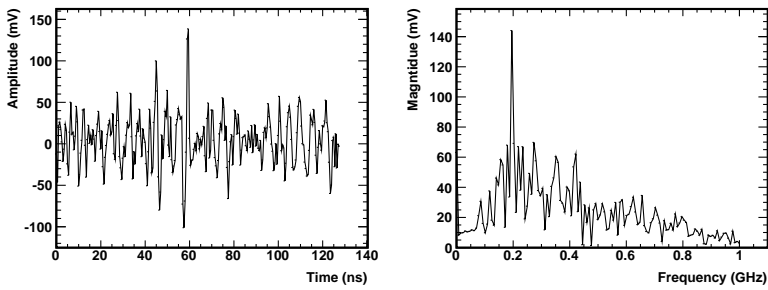


**Figure 4:** Example of a waveform displaying a strong resonance near 200 MHz that is filtered out by the  $\eta$  cut. This waveform is from the north LPDA. The event was recorded at Site B on March 13, 2015 at 16:46:19 UTC. Left: the waveform in the time domain. Right: the waveform in the frequency domain.

electronics, such as radio noise emitted by the external charge controller of the battery switching on and off. An example of such an event is shown in Fig. 4.

Potential neutrino candidate events are required to have a significant amount of power at several different frequencies. This is done by first calculating the discrete Fourier transform of the voltage versus time measured by an LPDA (after amplification). The frequency bin containing the largest amount of power is then identified;  $p_{max}$  represents the amount of power in this bin. The number of frequency bins that contain more than  $p_{max}/4$  on the LPDA is called  $\eta_{LPDA}$ . The smallest  $\eta_{LPDA}$  value in the event is defined as  $\eta$  for the event.

Potential neutrino candidates are required to have  $\eta > 3$  frequency bins. After applying this cut, 74.3% of the Site B data remains, while 99.3% of simulated neutrino events that trigger the station survive.

### 3.2 Finding External Pulses

The vast majority of triggers recorded by the station are caused by continuous thermal radio emission. These events are distinguished from neutrino pulses as they show little to no correlation between parallel LPDA measurements.

The angular reconstruction procedure described in Sect. 2 is used to identify events that may have been produced by an external radio pulse. The angular direction fit likelihood,  $-\log(L)$  is required to be reasonably good for potential neutrino candidate events. The cut on the likelihood is fairly loose,  $-\log(L) < 1.7$ , for low amplitude events and becomes stronger,  $-\log(L) < 0.5$ , for high amplitude events.

The fit likelihood cut is shown as a function of the peak to peak amplitude in Fig. 5 for neutrino simulations (left), Site B triggered data (middle) and pure thermal noise data recorded at Site B using software forced triggers (right). The peak to peak amplitude of an event is quantified by calculating the peak to peak value of the waveforms on all LPDA channels of an event, and keeping the smallest peak to peak value. Events outside (below) the blue shaded region are kept as potential neutrino candidates.

This cut removes nearly all of the purely thermal events recorded by Site B. Only 2.7% of the Site B data events have both  $\eta > 3$  and  $-\log(L) < f(p)$ , where  $f(p)$  is a function of the minimum peak to peak amplitude of the event. The function  $f(p)$  is shown by the lower edge of

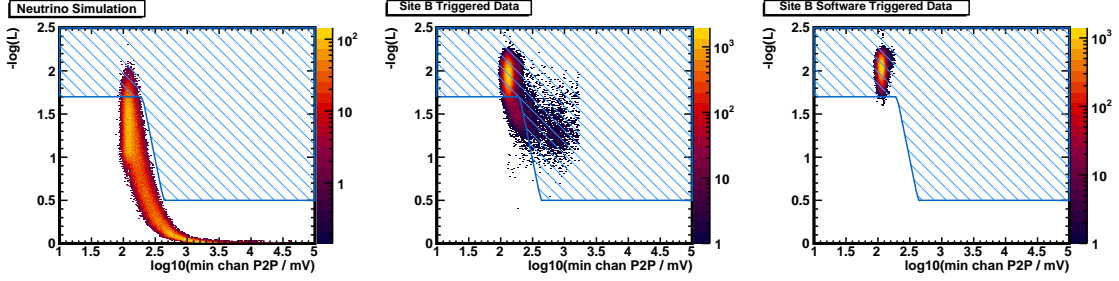


**Figure 5:** The fit likelihood versus the log of the peak to peak signal size on the LPDA channel with the smallest peak to peak signal in three different data sets. Left: the neutrino simulation. Middle: Site B triggered data. Right: Site B software triggered data (pure thermal noise). Events in the blue shaded region do not pass the fit likelihood cut. Only events passing the  $\eta > 3$  cut are shown for each data set.

the blue region in Fig. 5. Of the simulated neutrino events that trigger the station, 96.0% survive the application of both cuts.

### 3.3 Finding Neutrino-Like Signals

After the application of the  $\eta$  and  $-\log(L)$  cuts, many of the events remaining in the Site B data set are non-thermal radio pulses. Much of this data was recorded during periods of high winds as weather systems pass over the ARIANNA site on the Ross Ice Shelf. During the 2014-2015 data taking season, the largest storm occurred during February. From February 6-8, winds above 40 knots were recorded at New Zealand’s Scott Base, about 100 km from the ARIANNA site and over Minna Bluff. Wind data is not currently available for the ARIANNA site itself. A second important source of the non-thermal Site B data is the battery electronics, which emit radio frequency noise when switching on and off. This occurs toward the end of the season, as the station alternates drawing power from the battery and solar panels while periods of strong sunlight become shorter and less frequent.

Simulations of the time dependent waveforms produced by neutrino signals are used to distinguish background radio pulses from potential neutrino observations. The time dependent neutrino simulations are described in Refs. [1, 8]. The simulations include the measured responses of the ARIANNA LPDA as well as the amplifiers used at Site B, which play a large role in determining the expected waveform recorded upon observation of a neutrino-induced Askaryan pulse.

For a given event, the reconstructed signal direction is used to determine the arrival direction of the signal in the local frame of the LPDA. The neutrino waveform expected for a signal probing this part of the antenna response (and passing through the amplifiers of Site B) is then looked up from a table of such neutrino waveform templates. The template lookup table is binned in  $10^\circ \times 10^\circ$  wide bins in the local frame of the antenna. Thus, the reconstruction presented in Sect. 2 is much more accurate than necessary for the analysis presented in this proceeding.

The cross-correlation between the chosen neutrino waveform template and the actual recorded waveform is then calculated. The maximal value of this correlation (at any time offset) is defined as  $\xi_{LPDA}$ . Because the absolute polarization of the potential neutrino signal is not determined in the

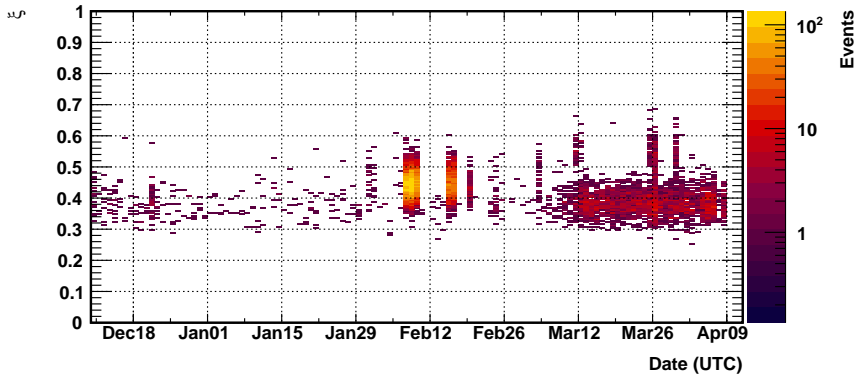


**Figure 6:** The daily  $\xi$  distribution of events recorded by Site B that pass both the  $\eta < 3$  and  $-\log(L) < f(p)$  cuts. The solar burst is visible in mid December. The large storm in early February is also visible. The increased number of events with poor  $\xi$  values toward the end of the season is a result of the higher trigger rates, due to a combination of colder temperatures and radio noise emitted by the battery turning on and off.

data, it is not known whether the neutrino template or its inverse should compare more favorably to the recorded waveform. Therefore, both are tried and the larger value is assigned to  $\xi_{LPDA}$ .

A new cut variable,  $\xi$ , is then defined as the largest  $\xi_{LPDA}$  observed on any LPDA channel. Figure 6 shows the distribution of the  $\xi$  variable in 24-hour wide bins over the course of the season for events recorded at Site B that pass both the  $\eta < 3$  and  $-\log(L) < f(p)$  cuts.

Potential neutrino candidate events are required to have  $\xi > 0.7$ . None of the Site B data survives the application of all three cuts, while 85.4% of the simulated neutrino events that trigger the station survive the  $\eta > 3$ ,  $-\log(L) < f(p)$  and  $\xi > 0.7$  cuts. This signal efficiency is comparable to that seen in the analyses of previous HRA season data sets.

The preliminary analysis of the data collected at Site B between December 10, 2014 and April 9, 2015 has produced a set of simple selection criteria that are able to separate potential neutrino candidate events from radio backgrounds in the data. Data taken from the other HRA stations is currently under analysis. A search for neutrino signals in the combined 2014-2015 season HRA data is expected to improve upon the diffuse neutrino flux limit presented in Ref. [1], assuming no neutrino candidates are found in the data.

#### 4. Conclusions

The complete HRA detector has been installed at the ARIANNA site on the Ross Ice Shelf of Antarctica. All eight stations ran reliably and took data from the time the installation crew departed the site in early December until the sunlight faded in late March to early April. The installation performed during the 2014-2015 austral summer made use of upgraded detector hardware, some of which is described in Ref. [2].

A radio signal direction reconstruction package has been developed and applied to both calibration pulse data as well as to triggered data recorded by the stations. The angular resolution of the reconstruction is found to be on the order of or better than a degree in both simulations and calibration data.

The reconstruction has been used in a preliminary search for neutrino signals in the 93.1 days of data recorded by the station situated at Site B. Three cuts are employed by the potential neutrino candidate search to find events that (a) have power at multiple frequencies, (b) fit well to an incoming plane wave and (c) have waveforms resembling those expected for a neutrino.

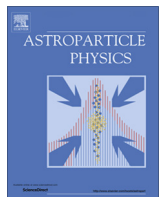
The vast majority of data removed by these cuts are due to simple thermal radio noise. Similar to previous seasons, the majority of non-thermal backgrounds are recorded during periods of high winds at the ARIANNA site. This season, some noise has been observed originating from the station battery while it is switched on and off by its charge controller. In future seasons, batteries will be deployed inside the radio-tight DAQ boxes to eliminate this radio noise source.

No events recorded by the station at Site B pass the application of all cuts, while 85.4% of simulated neutrino events that trigger the station survive the cuts. This signal efficiency is comparable to that obtained in analyses of previous HRA data taking seasons [1]. A similar analysis of the data collected by all HRA stations is currently underway, after which a limit on the diffuse neutrino flux will be placed (assuming no neutrino candidates are found in the data).

The authors thank the staff of Antarctic Support Contractors, Lockheed, and the entire crew at McMurdo Station for excellent logistical support. This work was supported by funding from the Office of Polar Programs and Physics Division of the US National Science Foundations, grant awards ANT-08339133, NSF-0970175, and NSF-1126672. A. Nelles is supported by a research fellowship of the German Research Foundation (DFG), grant NE 2031/1-1.

## References

- [1] **ARIANNA** Collaboration, S. Barwick et al., *A First Search for Cosmogenic Neutrinos with the ARIANNA Hexagonal Radio Array*, *Astropart.Phys.* **70** (2015) 12–26, [[arXiv:1410.7352](https://arxiv.org/abs/1410.7352)].
- [2] A. Nelles and C. Persichelli for the ARIANNA Collaboration, *Measuring Neutrinos with the ARIANNA Hexagonal Radio Array*, *These Proceedings* (2015).
- [3] G. A. Askaryan *JETP* **14** (1962) 441.
- [4] G. A. Askaryan *JETP* **21** (1965) 658.
- [5] **ANITA** Collaboration, P. Gorham et al., *Observations of the Askaryan effect in ice*, *Phys.Rev.Lett.* **99** (2007) 171101, [[hep-ex/0611008](https://arxiv.org/abs/hep-ex/0611008)].
- [6] **ARIANNA** Collaboration, S. W. Barwick et al., *Design and Performance of the ARIANNA HRA-3 Neutrino Detector Systems*, *IEEE Trans.Nucl.Sci.*, (in press) (2014) [[arXiv:1410.7369](https://arxiv.org/abs/1410.7369)].
- [7] **ARIANNA** Collaboration, S. W. Barwick et al., *Radio-frequency Attenuation Length, Basal Reflectivity, Depth, and Polarization Measurements from Moore’s Bay in the Ross Ice-Shelf*, *J.Glaciol.* **61** (2015), no. 227 [[arXiv:1410.7134](https://arxiv.org/abs/1410.7134)].
- [8] **ARIANNA** Collaboration, S. Barwick et al., *Time Domain Response of the ARIANNA Detector*, *Astropart.Phys.* **62** (2014) 139–151, [[arXiv:1406.0820](https://arxiv.org/abs/1406.0820)].



# A first search for cosmogenic neutrinos with the ARIANNA Hexagonal Radio Array



S.W. Barwick<sup>a</sup>, E.C. Berg<sup>a</sup>, D.Z. Besson<sup>c,g</sup>, G. Binder<sup>e,f</sup>, W.R. Binns<sup>m</sup>, D.J. Boersma<sup>j</sup>, R.G. Bose<sup>m</sup>, D.L. Braun<sup>m</sup>, J.H. Buckley<sup>m</sup>, V. Bugaev<sup>m</sup>, S. Buitink<sup>k</sup>, K. Dookayka<sup>a</sup>, P.F. Dowkontt<sup>m</sup>, T. Duffin<sup>a</sup>, S. Euler<sup>j</sup>, L. Gerhardt<sup>e</sup>, L. Gustafsson<sup>j</sup>, A. Hallgren<sup>j</sup>, J.C. Hanson<sup>c,a</sup>, M.H. Israel<sup>m</sup>, J. Kiryluk<sup>i</sup>, S.R. Klein<sup>e,f</sup>, S. Kleinfelder<sup>b</sup>, H. Niederhausen<sup>i</sup>, M.A. Olevitch<sup>m</sup>, C. Persichelli<sup>a</sup>, K. Ratzlaff<sup>d</sup>, B.F. Rauch<sup>m</sup>, C. Reed<sup>a,\*</sup>, M. Roumi<sup>b</sup>, A. Samanta<sup>b</sup>, G.E. Simburger<sup>m</sup>, T. Stezelberger<sup>e</sup>, J. Tatar<sup>a,h,\*</sup>, U.I. Uggerhoj<sup>l</sup>, J. Walker<sup>a</sup>, G. Yodh<sup>a</sup>, R. Young<sup>d</sup>, ARIANNA Collaboration

<sup>a</sup> Dept. of Physics and Astronomy, University of California, Irvine, USA

<sup>b</sup> Dept. of Electrical Engineering and Computer Science, University of California, Irvine, USA

<sup>c</sup> Dept. of Physics and Astronomy, University of Kansas, USA

<sup>d</sup> Instrumentation Design Lab, University of Kansas, USA

<sup>e</sup> Lawrence Berkeley National Laboratory, USA

<sup>f</sup> Dept. of Physics, University of California, Berkeley, USA

<sup>g</sup> Moscow Engineering and Physics Institute, Russia

<sup>h</sup> Center for Experimental Nuclear Physics and Astrophysics, University of Washington, USA

<sup>i</sup> Dept. of Physics and Astronomy, Stony Brook University, USA

<sup>j</sup> Dept. of Physics and Astronomy, University of Uppsala, Sweden

<sup>k</sup> IMAPP, Radboud University of Nijmegen, The Netherlands

<sup>l</sup> Dept. of Physics and Astronomy, Aarhus University, Denmark

<sup>m</sup> Dept. of Physics and McDonnell Center for the Space Sciences, Washington University, St. Louis, USA

## ARTICLE INFO

### Article history:

Received 4 November 2014

Received in revised form 20 March 2015

Accepted 6 April 2015

Available online 13 April 2015

### Keywords:

Radio

Antarctica

Neutrino

Cosmogenic

GZK

High energy

## ABSTRACT

The ARIANNA experiment seeks to observe the diffuse flux of neutrinos in the  $10^8$ – $10^{10}$  GeV energy range using a grid of radio detectors at the surface of the Ross Ice Shelf of Antarctica. The detector measures the coherent Cherenkov radiation produced at radio frequencies, from about 100 MHz–1 GHz, by charged particle showers generated by neutrino interactions in the ice. The ARIANNA Hexagonal Radio Array (HRA) is being constructed as a prototype for the full array. During the 2013–14 austral summer, three HRA stations collected radio data which was wirelessly transmitted off site in nearly real-time. The performance of these stations is described and a simple analysis to search for neutrino signals is presented. The analysis employs a set of three cuts that reject background triggers while preserving 90% of simulated cosmogenic neutrino triggers. No neutrino candidates are found in the data and a model-independent 90% confidence level Neyman upper limit is placed on the all flavor  $\nu + \bar{\nu}$  flux in a sliding decade-wide energy bin. The limit reaches a minimum of  $1.9 \times 10^{-23}$  GeV $^{-1}$  cm $^{-2}$  s $^{-1}$  sr $^{-1}$  in the  $10^{8.5}$ – $10^{9.5}$  GeV energy bin. Simulations of the performance of the full detector are also described. The sensitivity of the full ARIANNA experiment is presented and compared with current neutrino flux models.

© 2015 Elsevier B.V. All rights reserved.

## 1. Introduction

While the flux of cosmic rays has been measured to energies greater than  $10^{10}$  GeV [1], the sources of such high energy particles

remain a mystery. No known galactic source could accelerate particles to such energies, and no particular sources of the very highest energy particles, with large rigidities, have been found [2–5]. Potential sources of such ultra-high energy (UHE) cosmic rays are limited to our local supercluster (within about 50 Mpc) due to their interaction with the cosmic microwave background (CMB) [6,7]. The mesons produced by this process promptly decay to leptons, leading to a flux of UHE neutrinos [8–10].

\* Corresponding authors at: Dept. of Physics and Astronomy, University of California, Irvine, USA (C. Reed, J. Tatar).

E-mail addresses: [cjreed@uci.edu](mailto:cjreed@uci.edu) (C. Reed), [jtatar@uci.edu](mailto:jtatar@uci.edu) (J. Tatar).

Cosmogenic neutrinos may reveal cosmic accelerators beyond our local supercluster, as the mean free path of neutrinos through the CMB is larger than the visible universe. Such neutrinos would be produced within about 50 Mpc of the cosmic ray sources and would travel to Earth without deflection by magnetic fields, potentially pointing back to the accelerating objects.

Several large projects (AMANDA [11], IceCube [12,13], ANITA [14–16] and RICE [17,18]) exploit the fact that ice is transparent to Cherenkov radiation (at both optical and radio wavelengths) in order to search for cosmogenic neutrinos. These experiments complement cosmogenic neutrino searches by air shower detectors such as the Pierre Auger Observatory [19,20] and HiRes [21,22]. Below energies of  $10^{10}$  GeV, IceCube currently provides the best constraints on the UHE neutrino flux and in the  $10^4$ – $10^6$  GeV range, IceCube has observed an extra-terrestrial diffuse neutrino flux [23].

A new generation of neutrino experiments is emerging with the efforts of ARA [24,25], GNO [26] and the Antarctic Ross Ice Shelf Antenna Neutrino Array (ARIANNA, described in this paper). These experiments seek to extend the neutrino flux measurements to ultra-high energies by constructing radio Cherenkov detectors that are orders of magnitude larger in effective sensitive volume than current experiments using well-understood and inexpensive technology. Preparation is underway for the next generation of balloon-borne experiments as well [27], with efforts like that of EVA [28]. A large number of models predict cosmogenic neutrino fluxes that are measurable by such experiments with improved sensitivity to neutrinos above  $10^8$  GeV, particularly in the  $10^8$ – $10^{10}$  GeV range. See Section 2.2 for examples of such models.

The ARIANNA and ARA experiments are proposing the construction of arrays of radio detectors in Antarctica that will reach effective volumes  $\mathcal{O}(100)$  km<sup>3</sup>. A third radio experiment, GNO, is exploring the construction of a radio neutrino telescope in Greenland. These experiments will measure the radio-frequency (RF) pulse emitted by the charged particle shower resulting from a UHE neutrino interaction in ice via the Askaryan effect [29,30]. The Askaryan radio pulse has been measured in a variety of dielectric materials using particle accelerators to induce charged particle showers [31,32].

The ARIANNA collaboration plans to construct a  $36 \times 36$  km<sup>2</sup> array of 1296 independent, autonomous radio detector stations just below the surface of the Ross Ice Shelf. The ice to water interface below the Ross Ice Shelf serves as a mirror for radio waves, allowing the stations to observe neutrinos arriving from the sky above the detector as well as from the horizon. The detector will measure radio frequencies between about 100 MHz–1 GHz. This bandwidth is sensitive to the linear increase in power of the Askaryan pulse with frequency up to  $\sim 1$  GHz for signals measured on the Cherenkov cone [33].

The ARIANNA site is roughly 100 km from the McMurdo Antarctic Station, which provides logistical support during construction. Despite the relative closeness of McMurdo, the ARIANNA site is free of anthropogenic RF noise due to its being buffered by Minna Bluff to the north and the Transantarctic Mountains to the west.

Properties of the ice at the ARIANNA site have been measured by transmitting polarized radio pulses into the ice and observing the reflected pulses at multiple locations. These measurements indicate that the ice to water interface is a near perfect mirror. The attenuation length, measured to be between 400 and 500 m for radio frequencies, is found to be comparable to the average thickness of the Ross Ice Shelf. The ice shelf thickness has been measured to be  $576 \pm 8$  m [34] including a firn layer within the upper 60–70 m [35] (approximately). The firn layer is characterized by a monotonic increase in mass density as a function of

depth. A more complete discussion of the ice properties at the ARIANNA site is presented in Ref. [34].

The construction of the ARIANNA Hexagonal Radio Array (HRA) is approved for completion during the 2014–2015 austral summer. This array of seven ARIANNA stations serves as a research and development project for the full ARIANNA array [36]. Each HRA station consists of four log-periodic dipole antennas (LPDAs), a high-speed data acquisition (DAQ) system, wireless communication peripherals and local renewable power generation.

The expected performance of the full ARIANNA telescope is presented in Section 2. The performance of the HRA stations is discussed in Section 3. A first search for neutrino signals in the HRA data is described in Section 4.

## 2. The ARIANNA telescope

The ARIANNA experiment plans to measure the cosmogenic neutrino flux using a large surface array of radio receivers. ARIANNA will build upon previous UHE neutrino searches by greatly increasing the size of the detector. This will improve the sensitivity to neutrinos of  $10^8$ – $10^{10}$  GeV by a factor of 13 or more, depending on model, relative to the current best limits (see Section 2.2.2). In order to maximize the effective volume of the telescope, each ARIANNA station of the  $36 \times 36$  array will be separated from neighboring stations by 1 km, so that a typical neutrino pulse will be observed by a single station. The stations will measure the amplitude and direction of the incoming radio pulse using multiple antennas, allowing the energy and source direction of the primary neutrino to be determined.

The ice to water interface at the bottom of the Ross Ice Shelf provides a near perfect mirror for radio waves [34]. This allows the surface detectors to measure reflected radio pulses produced by down-going neutrino-induced showers, in addition to directly measuring the Askaryan radiation of horizontal showers. As the Earth is opaque to UHE neutrinos, this (greater than)  $2\pi$  sr solid angle acceptance contributes heavily to the high sensitivity of the ARIANNA telescope. The sensitivity of the experiment also benefits from a low energy threshold (below  $10^8$  GeV) and from the large number of detector stations made possible by the ease of installation at the ice surface.

The flagship measurement of the ARIANNA telescope will be the observation of the flux of cosmogenic neutrinos in the  $10^8$ – $10^{10}$  GeV range. The predicted flux of these neutrinos depends on the chemical composition of UHE cosmic rays, the cosmic ray injection spectrum and the cosmic ray source evolution [37]. A measurement of the neutrino flux will provide additional input to help constrain these parameters and thus improve the understanding of both neutrino and cosmic ray sources.

The observation of a significant number of neutrinos by ARIANNA would allow further measurements to be performed. The shape of the neutrino energy spectrum can help distinguish a flux due to strong source evolution from one due to a soft injection spectrum [38,39]. A search for point-like sources of UHE neutrinos will be a primary goal and has the potential to reveal particle accelerators at distances beyond our local supercluster. Further, the neutrino-nucleon cross section can be measured at center of mass energies around 10 TeV through the angular dependence of the flux [40,41]. In addition, the flavor composition of the neutrino flux may be explored [42]. Once the flux of neutrinos is known, such observations may be improved by redeploying the surface detectors in order to maximize angular and energy resolution.

Even the lack of a measurable neutrino flux would have profound consequences. Such a scenario would imply that either the sources of the highest energy cosmic rays are local, or that the sources have astrophysically interesting properties, such as an

iron-dominated composition with a hard energy injection spectrum and an acceleration energy cutoff below the photo-fragmentation threshold [43].

The expected performance of the full ARIANNA experiment, described in Section 2.2, is determined through the simulation of stations with eight downward facing LPDAs, as shown in Fig. 1. Studies of cosmic ray air showers suggest that ARIANNA may trigger on radio pulses from such events. To that end, the addition of two antennas that are directed upward at a 45° angle has been studied, as presented in Section 2.3.

## 2.1. Simulation methods

The performance of the ARIANNA telescope, detailed in Section 2.2, has been characterized by simulating the production and detection of radio signals in the frequency domain. An additional simulation package, presented in Section 2.1.2, has been developed to study the response of the detector in the time domain. The analysis of HRA data, discussed in Section 4, combines both simulation tools in order to estimate expected neutrino signals.

### 2.1.1. Frequency domain

A set of simulation tools has been developed and used to calculate the sensitivity and model the performance of the ARIANNA telescope. A summary of the simulation is provided below, and further details may be found in Ref. [44]. These tools simulate the production of the Askaryan radio pulse resulting from neutrino interactions and propagate it through the ice and firn to the detector.

Neutrino interactions are simulated by forcing neutrinos to interact within a fiducial volume and weighting the resulting events by the probability with which they would occur. This probability accounts for neutrinos lost to absorption within the atmosphere and the Earth's crust, as well as tau neutrinos recovered due to  $\nu_\tau$  regeneration effects [45]. The neutrino-nucleon cross section follows the parametrization presented in Ref. [46], e.g.  $1.45 \times 10^{-32} \text{ cm}^2$  at  $E_\nu = 10^9 \text{ GeV}$ . As ARIANNA stations are designed to be independent, simulations are focused predominately on calculating the response of a single ARIANNA station. For this purpose, the interaction volume is chosen to be a rectangular prism having a height 575 m, roughly equal to the ice thickness (see Section 1). The horizontal cross section of the prism ranges from 3 to 10 km<sup>2</sup>, depending on the neutrino energy. Consistent ice depth measurements at multiple locations, separated by 1 km, have been performed at the ARIANNA site [34]. These measurements have motivated the use of a simple uniform ice thickness model in the simulations. The neutrino interaction vertices

are uniformly distributed within the fiducial volume and the neutrino arrival directions are isotropically distributed.

The neutrino energy is selected randomly according to a specified flux. For the results presented in this article, the ESS cosmogenic flux [38] described in Section 2.2.2 has been used. Neutrinos of each flavor have been simulated with equal arrival rates, consistent with the 1:1:1 flavor ratio expected of neutrinos generated by pion decay at distant sources [47]. Roughly two-thirds of the neutrinos undergo a charged-current interaction, while the remainder interact via the neutral current. The fraction of the neutrino energy carried over to the resulting hadronic shower, the inelasticity  $y$ , is randomly chosen following the distributions presented in Ref. [48]. This leads to an average inelasticity of 20% for cosmogenic neutrinos in the energy range of interest to ARIANNA.

The maximum strength of the electric field is parametrized [33] on the Cherenkov cone 1 m from the neutrino interaction vertex. This field strength is proportional to the fraction of neutrino energy deposited into the hadronic shower. The strength of the electric field at angles off the Cherenkov cone,  $\delta\theta_c$ , is parametrized by a Gaussian whose width is calculated according to Ref. [49] for hadronic and Ref. [50] for electromagnetic showers.

For charged current  $\nu_e$  interactions, the field strength is increased by radiation from the prompt electromagnetic shower. For such interactions at energies above  $\sim 10^9 \text{ GeV}$ , however, the longitudinal shower profile increases faster than  $\log E_{\nu_e}$ , rising as fast as  $\sqrt{E_{\nu_e}}$  [51]. These elongated showers lead to a sharper reduction of the electric field strength at angles off the Cherenkov cone. This Landau-Pomeranchuk-Migdal (LPM) effect is simulated by reducing the Gaussian width of the Cherenkov cone spread by an amount proportional to  $E_{\nu_e}^{-1/3}$ .

The electric field is then propagated from the neutrino interaction vertex to the detector. The ice is modeled by a 75 m firn layer atop a 500 m ice shelf. The bulk ice is taken to have a refractive index  $n = 1.78$  [52]. The index of refraction in the firn layer is calculated as a function of depth using the Schytt model [53] combined with previous ice core measurements taken from the Ross Ice Shelf [54], varying from  $n = 1.30$  at the surface to  $n = 1.78$  in the ice.

Radio signals propagating through the ice are attenuated by a factor that depends only on column depth. The frequency dependence of the attenuation length is averaged over the bandwidth of the LPDA, taken to be around 100 MHz–1 GHz [55]. The variation of attenuation length with depth arises from the changing temperature of ice with depth, ranging from roughly  $-30^\circ\text{C}$  at the surface of the ice to  $-2^\circ\text{C}$  at bottom of the ice shelf. This depth variation results in an average attenuation length of  $400 \pm 18 \text{ m}$ . Further power may be lost for radio pulses reflecting off the ice-seawater boundary. The simulations halve the power of the pulse ( $-3 \text{ dB}$ ) upon reflection, although in situ measurements show the reflectivity,  $R$ , of the boundary to be between  $\sqrt{R} = 0.82 \pm 0.07$  [34].

### 2.1.2. Time domain

The time domain response of the detector has been studied by constructing a collection of “waveform templates” that quantify the voltage measured by an antenna over time for an Askaryan radio pulse. Each waveform template is calculated for a radio frequency (RF) pulse arriving at a particular angle with respect to the antenna, as well as for a particular observation angle  $\delta\theta_c$  relative to the Cherenkov cone.

The electric field produced by the Askaryan effect in ice is calculated as a function of time [56,57] for an electromagnetic particle shower of a specified energy. The charge excess is modeled as a pancake with a charge profile that varies as the shower propagates. The effect of the lateral structure of the particle shower on the

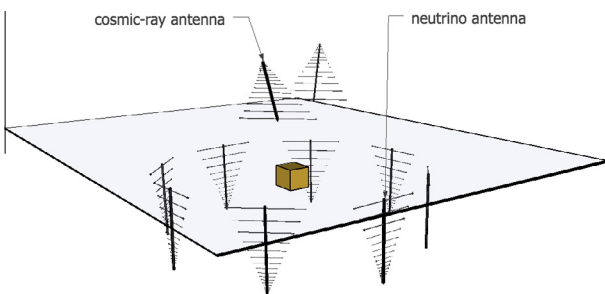


**Fig. 1.** An illustration of the antenna arrangement in a single ARIANNA station. For simulations of cosmic ray showers, all ten antennas are included in the simulation. For simulations of the detector response to neutrino signals, only the eight downward facing antennas are simulated. The stations built for the HRA detector use a smaller subset of only four downward facing antennas, arranged in a square.

electric field is parametrized as a function of time using a form factor obtained from shower simulations [33].

The measured responses of the ARIANNA amplifier and LPDA are convolved with the electric field in order to produce the voltage observed by an antenna as a function of time. The propagation of the electric field through the ice reduces the strength of the field, but has a negligible effect on the relative frequency content compared to the impact of the hardware response. The antenna response is quantified in bins of two angles, both relative to bore-sight: one in the plane of the tines (the E-plane) and one normal to the plane of the tines (the H-plane).

Full details of the procedure used to calculate the time-dependent waveform templates may be found in Ref. [55].

## 2.2. Expected performance

The properties of neutrino interactions that produce a radio pulse at a station with sufficient power to trigger the detector have been studied. Studies of the angular and energy resolution of ARIANNA are performed using a simulation of an eight downward LPDA station configuration. Simulated stations are triggered when the observed radio signal is larger than four times the noise on at least three out of the eight downward facing antennas. This threshold level has been achieved in situ with stations running a two out of four antenna channel trigger (see Section 3.2).

### 2.2.1. ARIANNA aperture

Neutrinos that trigger an ARIANNA station arrive predominately from the sky above the station, creating a radio pulse that reflects off the ice and water interface at the bottom of the ice shelf. Fig. 2 shows the relative sensitivity of an ARIANNA station to neutrinos, averaged over flavor, as a function of local zenith angle. In addition to down-going neutrinos, ARIANNA is also sensitive to neutrinos arriving from the horizon. Such events may be triggered either through a reflected pulse or by a direct observation of the Cherenkov wavefront, depending on geometry.

The portion of the sky that ARIANNA observes with this angular sensitivity is shown in Galactic coordinates in Fig. 3. The line in the figure represents the view of an ARIANNA-like detector located at the South Pole. Note that the local zenith acceptance of an ARA-like detector falls off rapidly for neutrinos originating more than 45° above the detector [24]. Thus, an ARA-like detector would have reduced visibility of the sky around the southern polar region.

The effective volume of the full ARIANNA telescope in which neutrino interactions will be triggered has been studied as a

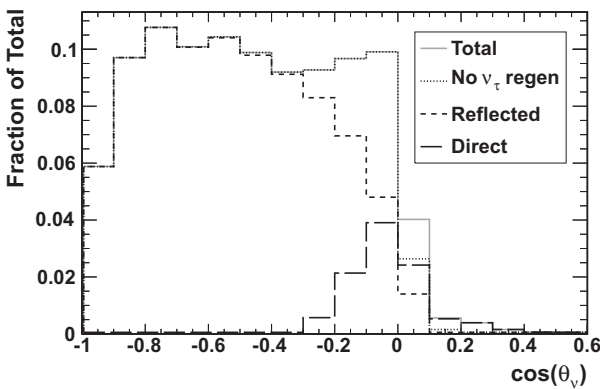


**Fig. 2.** The number of neutrino triggers observed in each bin relative to the total number of cosmogenic [38] neutrino triggers as a function of the local zenith neutrino arrival angle. The station triggers on neutrinos arriving from the horizon through either direct or reflected radio pulses. The majority of triggers are due to reflected pulses from locally down-going neutrinos. Figure adapted from Ref. [44].

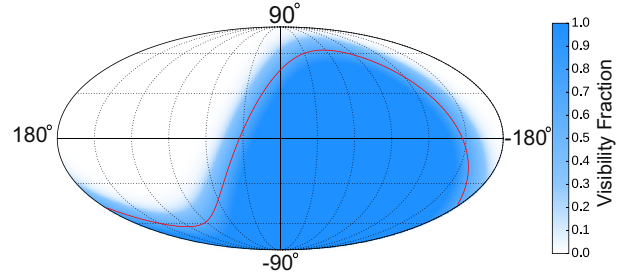


**Fig. 3.** The angular coverage in Galactic coordinates. The color scale represents the fraction of livetime that a patch of the sky is visible. The solid line shows the sky visible to an ARIANNA-like detector at the South Pole.

function of energy, presented in Fig. 4, and is compared to that of the ARA-37 experiment [24]. The effective volume shown in Fig. 4 is integrated over the viewing angle of ARIANNA, allowing the expected number of neutrino triggers due to a neutrino flux,  $\Phi$ , to be calculated as

$$dN(E) = \Phi(E) \frac{\varepsilon V_{\text{eff}}(E) \Omega}{L_{\text{int}}(E)} t_{\text{live}} dE \quad (1)$$

where  $dN$  is the number of neutrinos in an energy bin,  $E$  is the average neutrino energy in the bin,  $dE$  is the width of the bin,  $\varepsilon$  is the efficiency with which neutrino triggers are preserved by an analysis,  $V_{\text{eff}}$  is the effective volume at the trigger level,  $\Omega$  is the viewing angle in steradians,  $L_{\text{int}}$  is the water-equivalent interaction length of neutrinos in the ice ( $\approx 10^3$  km at  $10^9$  GeV) and  $t_{\text{live}}$  is the livetime of the experiment.

This effective volume leads to an energy distribution of cosmogenic neutrino triggers that has 90% of detected neutrinos between  $10^{8.4}$  and  $10^{10.4}$  GeV, as shown in Fig. 5. On an absolute scale, the all flavor  $\nu + \bar{\nu}$  sensitivity of ARIANNA to trigger on neutrinos is presented in Fig. 6. This sensitivity has been calculated for 1296 ARIANNA stations running for three calendar years, with a livetime equal to 58% of each calendar year, and a signal efficiency of 83% (see Section 4.4). The fractional livetime corresponds to stations powered by batteries and/or solar panels and is based on the observed behavior of previously and currently deployed prototype stations. The sensitivity is calculated as the average Neyman upper limit with an expected Poissonian background of 0.3 events (see Section 4.4); i.e.  $dN = 2.47$  neutrinos in the sliding decade-wide energy bin.

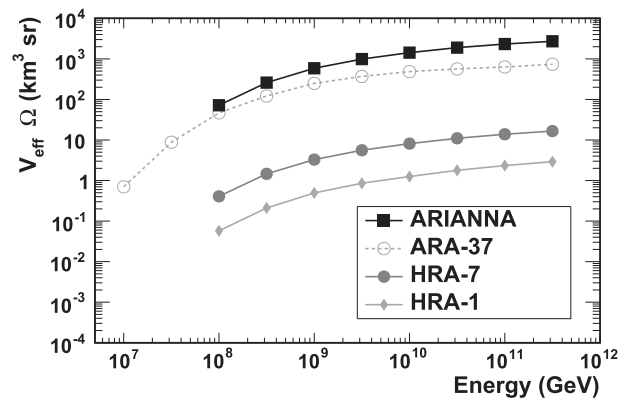


**Fig. 4.** The effective volume times total viewing angle, at the trigger level with  $4\sigma$  thresholds, of a 1296 station ARIANNA telescope as a function of energy. The effective volumes are averaged over neutrino flavors as well as over neutrinos and anti-neutrinos. Also shown are the  $V_{\text{eff}} \Omega$  for a single HRA station, a seven station HRA, and the ARA-37 detector [24].

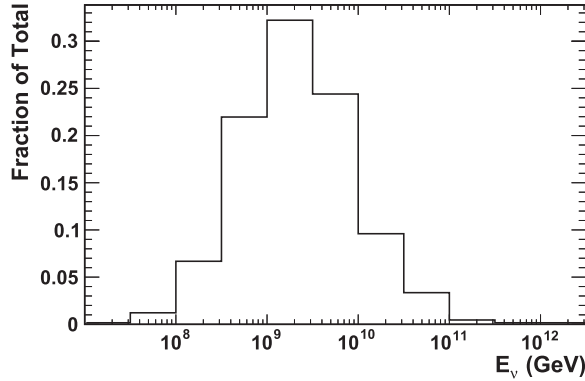


**Fig. 5.** The number of neutrino triggers observed in each bin relative to the total number of cosmogenic [38] neutrino triggers as a function of the true simulated neutrino energy. Figure adapted from Ref. [44].

The systematic uncertainty band on the sensitivity shown in Fig. 6 accounts for uncertainties on the models used to describe various physics processes in the simulations. The neutrino-nucleon cross section is calculated from parton distribution functions extrapolated to the as yet unmeasured low- $x$  values appropriate for  $E_\nu \geq 10^7$  GeV, an estimation that may over or underestimate rates. The simulation of the LPM effect does not fragment the charge excess into separate clumps, which would give rise to competing effects: a reduction of the overall RF signal strength and an increase of the relative amplitude at angles away from the Cherenkov cone.

Other models employed by the simulations are understood to either increase or decrease expected rates. No RF contribution of the  $\mu$  lepton arising from charged current  $\nu_\mu$  interactions is simulated, which underestimates trigger rates [42]. However, the  $\nu_\tau$  trigger rates are likely overestimated since the  $\tau$  lepton resulting from a  $\nu_\tau$  interaction is not propagated. Instead, the shower with the greater energy, either from the  $\nu_\tau$  interaction or the  $\tau$  decay (if it produces a shower), is simulated at the neutrino interaction location. Thus,  $\tau$  lepton decays that produce very high energy showers outside the fiducial volume are allowed to trigger a station.

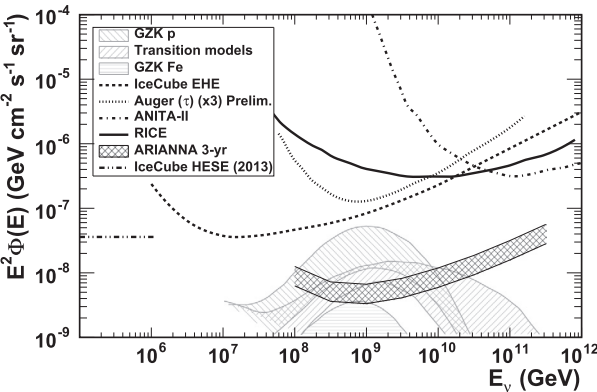


**Fig. 6.** The all flavor  $\nu + \bar{\nu}$  differential sensitivity of a 1296 station ARIANNA telescope running for 58% of three years with a signal efficiency of 83% (see Section 4.4). The sensitivity is calculated in a sliding decade-wide neutrino energy bin. See text for a discussion of the width of the sensitivity band. Limits on the flux of neutrinos are shown for several experiments [58–61], with ANITA [15,16] providing the most stringent limits at the highest energies and IceCube [12] at lower energies. The cosmogenic neutrino flux predicted by several models is shown for different assumptions of the cosmic ray composition [37].

Uncertainties on the ice properties used in the simulations also contribute to the sensitivity band. Simulated pulses lose half their power upon reflection, however measurements at the site suggest a significantly larger reflection coefficient. Similarly, ice property measurements at the site suggest the RF signal loss due to refraction and attenuation in the firn layer is likely overestimated.

### 2.2.2. Expected neutrino rates

The number of neutrino triggers that ARIANNA can expect to record after 3 calendar years of running is presented in Table 1 for a variety of neutrino flux models. Unless otherwise stated, neutrino fluxes are generated through photopion production by a flux of cosmic rays. The evolution of cosmic ray sources follows the evolution of potential source populations, such as the star formation history. This is typically approximated by an increasing emissivity per co-moving volume proportional to  $(1+z)^m$  out to a first break point at  $z = z_{max}$ , where  $z$  is the redshift of the source.

The ESS model [38] shown in Table 1 assumes cosmic sources evolve with  $m = 4$  and  $z_{max} = 1.9$  in a flat universe. The WB model [62] follows the luminosity density evolution of quasi-stellar objects (QSOs) with  $m = 3$  for  $z_{max} = 1.9$ . The Yuksel et al. [63] model parameterizes a very strong source evolution according to the gamma ray-burst (GRB) rate, with  $m = 4.8$  up to  $z_{max} = 1$ . Three of the Kotera et al. [64] models vary the source evolution of a flux of protons, with  $m = 3.4$  up to  $z_{max} = 1$  for a star formation rate (SFR1) evolution. The GRB2 model from Kotera et al. closely follows the SFR1 evolution, but continues to gradually increase beyond  $z > 4$ . The Kotera et al. FRII model employs a very steep evolution out to  $z_{max} = 4$ . The Yoshida and Teshima [65] also assumes a strong evolution,  $m = 4$ , out to  $z_{max} = 4$ . The Ahlers et al. [66] models take  $m = 4.6$  until  $z_{max} = 2$  and constrain the energy spectra of particles injected to the cosmic ray accelerating source using gamma ray measurements taken by the Fermi-LAT. The cross-over energy between galactic and extragalactic cosmic

**Table 1**

The expected number of triggers due to neutrinos of all flavors with  $E_\nu > 10^8$  GeV in 1296 ARIANNA stations after running for 3 calendar years given different models of the cosmogenic neutrino flux. A flavor ratio of 1:1:1 at Earth is assumed. A realistic livetime of 58% per year and a signal efficiency of 83% (see Section 4.4) has been used for the ARIANNA rates. See text for an explanation of the model types. For reference, if 0.3 background events are expected in the data set (see Section 4.4), 6.4 neutrino events would push the number of observed events beyond a  $5\sigma$  background fluctuation in 50% of experiments (prior to any trial factor penalties). Published neutrino rates for IceCube with 333.5 days of IC40, 285.8 days of IC79 and 330.1 days of IC86 data [12] are shown where available. The numbers in parentheses show the IceCube rates increased by 39% to facilitate direct comparison with the ARIANNA 3 year rates.

Neutrino model	Model type	$N_\nu$ triggers	
		$(E_\nu > 10^8 \text{ GeV})$	ARIANNA
ESS [38]	$m = 4, \Omega_M = 1$	55	
WB [62]	$E_\nu^{-2}$ QSO source evolution	65	
Yuksel et al. [63]	$E_\nu^{-2}$ GRB source evolution	100	
Kotera et al. [64]	Protons, SFR1 evolution	7.3	0.46 (0.64)
Kotera et al. [64]	Protons, GRB2 evolution	9.0	0.48 (0.67)
Kotera et al. [64]	Protons, FRII evolution	48	2.9 (4.0)
Yoshida et al. [65]	$m = 4, z_{max} = 4$	34	2.0 (2.8)
Ahlers et al. [66]	$E_{min} = 10^{10} \text{ GeV}$ (best fit)	26	1.5 (2.1)
Ahlers et al. [66]	$E_{min} = 10^{10} \text{ GeV}$ (maximal)	58	3.1 (4.3)
Kotera et al. [64]	Mixed composition	7.4	
Kotera et al. [64]	Pure iron	2.5	
Ave et al. [67]	Pure iron, $m = 4, z_{max} = 1.9$	18	
Olinto et al. [43]	Pure iron, $E_{max}/Z = 10^{11} \text{ GeV}$	0.097	
Aartsen et al. [23]	$E_\nu^{-2.3}$ IceCube best fit	2.8	
Fang et al. [68]	Young pulsar sources	43	

rays is parameterized by a lower energy break in the injection spectra of  $E_{min} = 10^{10}$  GeV.

The possibility of a chemical composition of the cosmic ray flux that is not purely proton is also explored. The Kotera et al. mixed composition model assumes that the chemical composition of particles injected to the cosmic ray source matches the composition of the low energy galactic cosmic ray flux. The Kotera et al. pure iron model tests the case of a purely iron nucleus composition. In both cases, the sources evolve according to the SFR1 parameterization. The Ave et al. [67] model also uses a purely iron composition, but includes a stronger source evolution of  $m = 4$  out to  $z_{max} = 1.9$ . The Olinto et al. [43] tests a purely iron composition combined with a uniform source evolution and a cutoff in the source acceleration at  $E_{max}/Z = 10^{11}$  GeV.

The Aartsen et al. [23] flux represents the best fit to the neutrino flux measurement obtained by the IceCube collaboration after the observation of 37 neutrino candidate events with energies up to 2 PeV. A measurement of this flux by ARIANNA would extend the currently measured spectrum to higher neutrino energies by at least two orders of magnitude.

ARIANNA can also search for alternative sources of UHE neutrinos such as young pulsars that accelerate particles through surrounding supernova remnant material, as modeled by Fang et al. [68]. In this model, sources evolve according to the star formation rate.

ARIANNA can expect to see about 13 times as many neutrinos above  $10^8$  GeV as IceCube, depending on the flux model, and a comparable number of neutrinos to ARA [24] for similar model parameters. This increase in sensitivity relative to current limits will create the opportunity to study nearly all mixed composition models (currently favored by Auger data) that include a power law injection spectrum, and to probe alternate scenarios of cosmic ray acceleration such as young pulsar sources.

### 2.2.3. Angular resolution

The angular resolution of an ARIANNA station has been estimated through the use of a simple reconstruction procedure on simulated neutrino events. The arrival direction of the radio pulse is found by fitting the time difference between pulses in different antennas, on a single ARIANNA station, to a planar wavefront. Thanks to the better than 100 ps timing of ARIANNA stations [69], the angular error on the direction of the RF signal at the station is better than  $1^\circ$  [70].

To determine the direction of the neutrino, however, it is necessary to estimate both the signal propagation direction as well as the signal polarization direction. For example, a signal arriving vertically upward and on the Cherenkov cone would be produced by a neutrino with a zenith angle equal to the Cherenkov angle. Any azimuth angle would produce the same upward propagating signal. The polarization angle serves to break this degeneracy, as the polarization is perpendicular to the signal propagation direction and points away from the shower axis.

An ARIANNA station with eight downward-facing LPDAs has been simulated in order to quantify the neutrino angular resolution. The polarization of the incoming radio pulse is determined by the relative amplitude of the pulses recorded by non-parallel antennas. The voltage recorded by an antenna is proportional to the component of the electric field vector in the direction parallel with the tines of the LPDA. The constant of proportionality depends on the incoming direction of the radio signal and on the in-ice antenna response.

The polarization is reconstructed by first finding the antenna with the largest recorded pulse. The voltage recorded by each of the two adjacent antennas is then used to obtain the magnitude of the electric field component that is parallel to the tines of that

antenna. The ratio of these electric field components gives the tangent of the azimuth angle of the polarization vector (the component in the plane of the ice surface). The reconstruction is improved by averaging the signal of each antenna with its parallel counterpart antenna prior to calculating the ratio. This improves the signal to noise of the measurement of each electric field component and gives a more accurate estimate of the azimuth angle of the polarization vector.

The zenith angle of the polarization vector is then constrained by the requirement that the polarization and signal propagation vectors be orthogonal. This yields two degenerate polarization vectors, each having the same azimuth angle and each being perpendicular to the signal propagation. Given that only the signal propagation vector is needed to measure the energy of the neutrino, this degeneracy does not affect a measurement of the diffuse neutrino flux. For point source searches, however, it will result in two possible neutrino source directions. The correct degenerate direction will always roughly point back to the source, while the incorrect degenerate direction will vary depending on the station orientation (and time). Thus, only a single point of excess signal would be expected for a given neutrino source.

The angular resolution expected for this method is shown in Figs. 7 and 8. The resolution is calculated using the more accurate (compared to the true direction) of the two degenerate candidates, since this is the relevant quantity for a neutrino point source search. The local zenith and azimuth angular resolutions are  $\sigma_\theta = 2.9^\circ$  and  $\sigma_\phi = 2.5^\circ$ , respectively.

These values are conservative, in that they have been obtained by a reconstruction that assumes that each antenna is observing the electric field exactly at the Cherenkov cone, i.e.  $\delta\theta_c = 0$ . In fact, on average  $\delta\theta_c$  is found to be about  $2.2^\circ$ , and some triggers are produced by antennas observing signals up to  $15^\circ$  off-cone. The assumption that all signals are on the Cherenkov cone is a major source of inaccuracy in the reconstruction of the neutrino direction. Determining the  $\delta\theta_c$  to within  $1.5^\circ$  improves the neutrino direction angular resolution by over 50% in zenith and over 20% in azimuth.

### 2.2.4. Energy resolution

The energy of an individual neutrino event is reconstructed by determining the strength of the electric field at the station and propagating it back through the ice to the shower location. The shower energy is proportional to the amplitude of the electric field at the shower. The constant of proportionality is calculated using measured antenna response properties. The energy of the original neutrino is then estimated using the average fraction of neutrino energy transferred to a shower that results in a trigger. The trigger

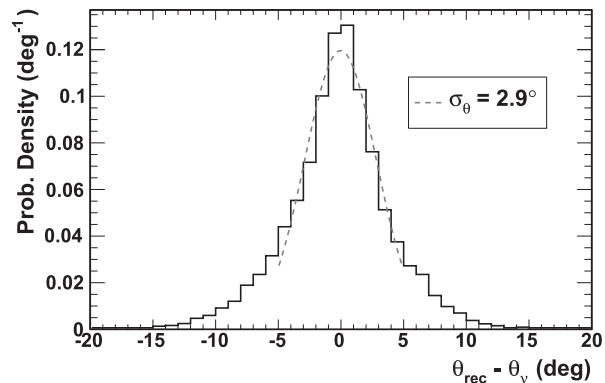


**Fig. 7.** The angular difference between the reconstructed and true neutrino direction in the local zenith direction. A resolution of  $\sigma_\theta = 2.9^\circ$  is found for an eight-antenna ARIANNA station. Figure adapted from Ref. [44].

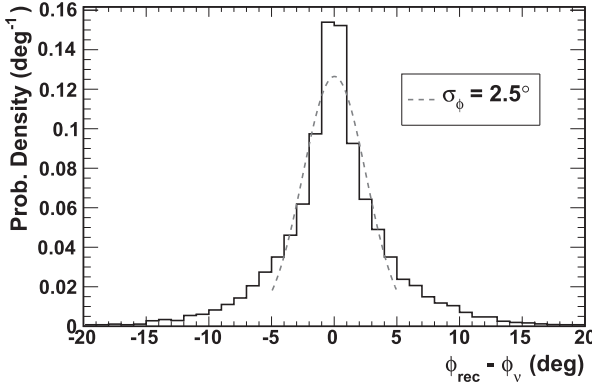


**Fig. 8.** The angular difference between the reconstructed and true neutrino direction in the local azimuth direction. A resolution of  $\sigma_\phi = 2.5^\circ$  is found for an eight-antenna ARIANNA station. Figure adapted from Ref. [44].

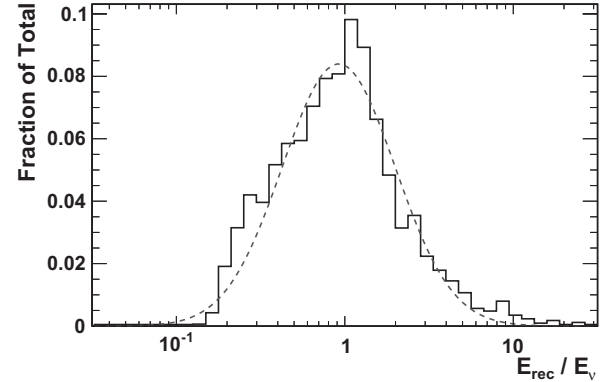


**Fig. 9.** The energy resolution of an eight-antenna ARIANNA station to a cosmogenic flux [38] is  $\sigma(\log(E_{\text{rec}}/E_{\nu})) = 0.34$ , so that  $\sigma(E_{\text{rec}}/E_{\nu}) = 2.2$  for cosmogenic neutrinos, summed over neutrino flavor. Figure adapted from Ref. [44].

requirement selects a subset of neutrino interactions for which a large fraction of the energy, about 0.8, is transferred to the shower. An average path length of radio pulses is used in lieu of a shower vertex reconstruction. The average path length is determined from simulations as a function of the zenith angle of the radio signal propagation, which itself is readily determined using timing (see Section 2.2.3).

There are two dominant sources of error on the neutrino energy estimate. The first arises due to the Gaussian dependence of the electric field amplitude on  $\delta\theta_c$ . Uncertainties on  $\delta\theta_c$  form the largest source of error on the energy estimate. The unknown amount of energy transferred from the neutrino to the charged particle shower is the second significant source of error on the energy estimate. The distribution and average value of these two parameters depend on neutrino flavor, which is assumed to be unknown in the current analysis. As more sophistication is applied to event reconstruction, it should be possible to identify the flavor and thereby improve the energy resolution. Errors due to the inexact pulse propagation length, electric field losses due to reflection at the ice and water boundary and inaccuracies in the antenna response are each on the order of 20%–25%, and are negligible by comparison.

In the analysis presented here, there is no attempt to determine the angular deviation from the Cherenkov cone,  $\delta\theta_c$ . Inserting the average value obtained from simulation studies, the energy resolution is found to be  $\sigma(E_{\text{rec}}/E_{\nu}) \approx 5$ , under the assumption that  $E_{\text{sh}}/E_{\nu} = 0.8$  for triggered events, where  $E_{\text{sh}}$  ( $E_{\nu}$ ) is the energy of the shower (neutrino). However, because the frequency and phase content of the Askaryan pulse depends on  $\delta\theta_c$ , it can be exploited in future analyses to reduce this uncertainty. Such a potential measurement of  $\delta\theta_c$  has been modeled in Ref. [44] in order to investigate the reduction in energy resolution. The result of this study is shown in Fig. 9, which indicates that the average neutrino energy resolution is reduced to  $\sigma(E_{\text{rec}}/E_{\nu}) = 2.2$ , an improvement by a factor greater than 2.

### 2.3. Cosmic ray detection

Ultra-high energy cosmic rays are a plausible source of (reducible) background for ARIANNA. Charged particle showers in the atmosphere above the telescope, produced by UHE cosmic rays, can emit a detectable radio pulse. Much of this background is reduced naturally by the 15 dB decrease in sensitivity of the LPDA back lobe relative to boresight. The addition of two upward facing antennas eliminates the remaining cosmic ray background. These antennas allow RF pulses originating from the atmosphere

to be efficiently distinguished from neutrino pulses originating in the ice.

Dedicated cosmic ray simulations have been performed to study the rate at which an ARIANNA station triggers on air showers and the efficiency with which such events are separated from neutrino events. The simulation of the cosmic ray air showers are performed using the CoREAS software [71–73]. Proton interactions between  $10^{8.4}$  and  $10^{10.5}$  GeV are simulated by Corsika [74] using the QGSJetII-04 [75] hadronic model and weighted by the high energy cosmic ray flux measured by the Auger experiment [76].

Cosmic rays are studied over a local zenith angle range from  $0^\circ$ – $75^\circ$  under the assumption of an isotropic flux. The azimuth direction and interaction vertex position relative to the station are varied for each combination of energy and zenith direction.

The radio pulse from the charged particle shower is generated and propagated to the surface of the ice by CoREAS. The electric field at the station in the frequency domain is convolved with the measured ARIANNA antenna response, the result of which is then convolved with the measured amplifier response to obtain the voltage expected on each readout channel of the DAQ. A trigger is generated if the signal in three or more of the eight downward facing antenna channels is above four times the noise ( $4\sigma$ ). This is the same trigger criteria used in Section 2.2 to study neutrino signals. Finally, finite bandwidth noise consistent with that observed by HRA stations is added to the signal. The trigger is applied prior to the addition of noise in order to avoid over-counting due to events that will be rejected by any analysis.

The rate of cosmic ray triggers in the full ARIANNA telescope is shown in Fig. 10 as a function of cosmic ray energy. The rates are shown as the expected number of triggers per calendar year in each (tenth of a decade) energy bin. A detailed measurement of the backward lobe response of the LPDA has not yet been performed, so a conservative estimate of the cosmic ray rates has been obtained by overestimating the gain of the antennas for signals arriving from above the detector.

To study the reduction of this potential background, a ten LPDA station has been simulated for the cosmic ray studies. This station has eight downward facing antennas (see Section 2.2). In addition, two upward facing LPDAs have been added to the station geometry to help discriminate between RF pulses arriving from above or below the station. These two antennas are oriented upward at a  $45^\circ$  angle relative to the surface of the ice and do not participate in the trigger. This geometry is shown in Fig. 1.

The difference between the pulse amplitudes measured by the upward and downward facing antennas provides an efficient mechanism for distinguishing cosmic ray air showers from

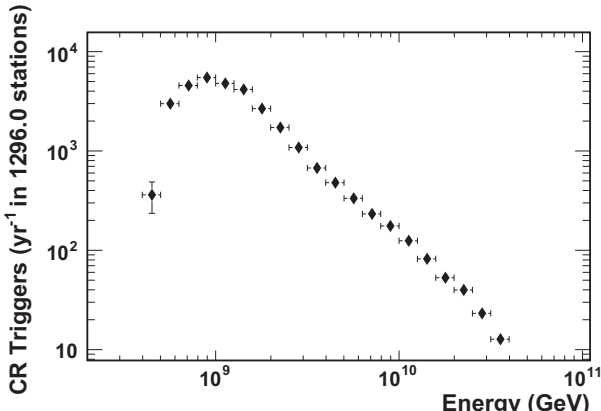


**Fig. 10.** The number of triggered cosmic ray events in 1296 ARIANNA stations per calendar year, with a livetime of 58% per year, versus the cosmic ray energy, in tenth of a decade energy bins.

neutrino signals. On each antenna, the amplitude is taken as the average of the two largest crests of the time dependent waveform in order to reduce fluctuations due to noise. Fig. 11 shows the average upward facing antenna amplitude minus the average downward facing antenna amplitude for both cosmic ray and neutrino events. Keeping only events with an amplitude difference  $< -1.2\sigma$  leads to a background rate of 0.1 cosmic rays in the full 1296 station ARIANNA telescope after 3 calendar years of running with 58% livetime per year. This cut preserves 99.7% of the cosmogenic neutrino events that trigger the station.

### 3. The Hexagonal Radio Array

The ARIANNA Hexagonal Radio Array (HRA) is being constructed on the Ross Ice Shelf and consists of seven prototype stations arranged as shown in Fig. 12. This small array, begun in 2009 [77], serves as a prototype for the development and study of ARIANNA hardware, data acquisition (DAQ) and radio data analysis. Three stations have been installed at the ARIANNA site, Stations A, C and G, to form the HRA-3 detector. The fourth station, Station D, is of a preliminary design installed during the 2011–2012 austral summer [78]. This station did not take radio event data during the 2013–14 season as its DAQ electronics were

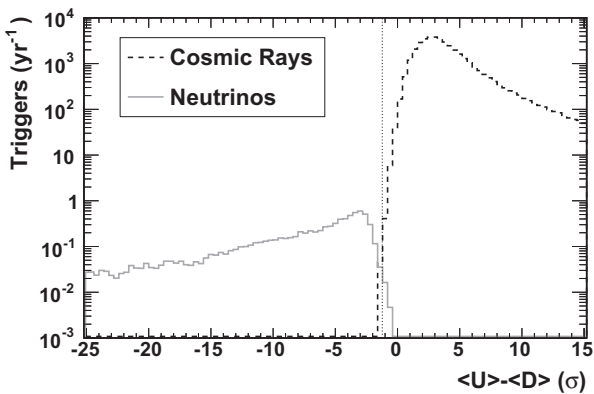


**Fig. 11.** The number of triggered neutrino and cosmic ray events in 1296 ARIANNA stations per calendar year versus the difference in the average amplitude of upward facing antennas and the average amplitude of downward facing antennas. Requiring the difference to be  $< -1.2\sigma$  yields a background rate of 0.1 cosmic rays in 3 calendar years of data from the full array while preserving 99.7% of the triggered neutrino events. The neutrino rate is arbitrarily scaled to  $10 v$  per year for illustration purposes.

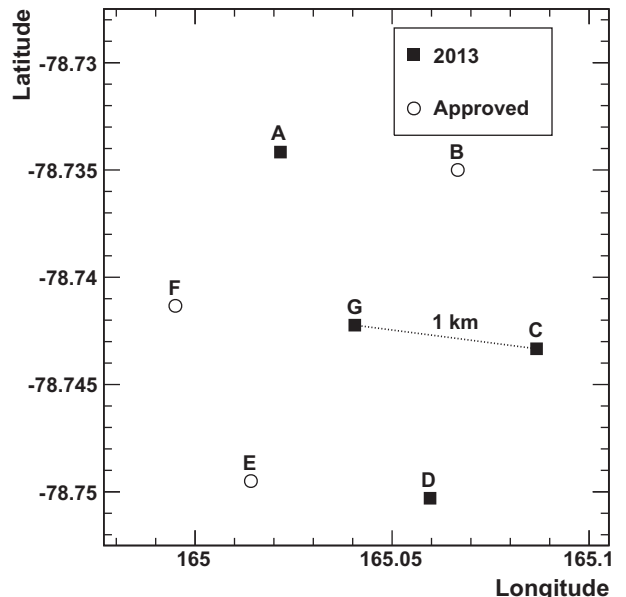


**Fig. 12.** The locations of the seven Hexagonal Radio Array stations. The HRA-3 station locations are shown by the closed squares marked “A”, “C” and “G”, an earlier prototype station location is marked “D”, while the approved sites of the remaining four stations by open circles. Figure from Ref. [69].

removed from the station for calibration. A search has been performed for cosmogenic neutrino signals using data taken by the HRA-3 during the 2013–14 deployment season.

#### 3.1. The HRA-3 stations

Three stations have been used to collect radio data during the 2013 deployment season. Each station consists of four downward facing LPDAs connected to a local DAQ. The radio antennas are positioned symmetrically around the DAQ box which lies at the center. Each antenna is 3 m from the DAQ and is oriented such that the normal vector of the plane containing the antenna tines points toward the DAQ. The data acquisition is able to transmit data from Antarctica in near real-time while drawing an average of only about 7 W.

Radio signals measured by the LPDAs are amplified and digitized at the data acquisition box. Signals are carried to custom amplifiers through heavily shielded coaxial cables. The output of each amplifier is then sampled at 1.92 GHz using a custom Advanced Transient Waveform Digitizer (ATWD) chip [79]. The chip records waveform data in 128 samples and voltages are digitized using 12 bit analog to digital converters.

Two complementary communication systems are used to transfer data taken by a station to off-site locations. These systems are powered off during data taking in order to minimize radio noise and to conserve power. A long range wireless Ethernet link is facilitated by an AFAR modem [80] that connects to the Internet via a relay positioned on Mt. Discovery and a receiver at McMurdo Station. Each station is also equipped with an Iridium Short Burst Data (SBD) modem [81] that allows 320 byte binary messages to be sent via satellite when an AFAR connection cannot be established.

Station configuration parameters, such as trigger thresholds, are specified remotely by shift crews and transmitted to the stations using the communication peripherals. Each station periodically connects to computers in California in order to transmit diagnostic data. During the connection, radio event data may be transferred and new configuration parameters may be specified. This

facilitates near real-time data analysis and station monitoring throughout the data taking season.

During the 2013 deployment season, events were recorded by an HRA-3 station when the time-dependent waveforms on two of four antenna channels matched a pattern trigger. The coincidence is required to occur within 64 ns. The pattern requires the crossing of both positive and negative  $4\sigma$  thresholds and is efficient for bipolar pulses of frequencies within the LPDA and amplifier bandwidths. The bipolar pulse requirement reduces triggers on random electronics noise while preserving those due to neutrino-induced Askaryan pulses, as the finite bandwidth of the LPDA and amplifier will always yield a bipolar pulse (due to ringing).

To facilitate studies of the thermal environment noise, the collection of data at random times is facilitated by software forced triggers. The stations typically record such an “unbiased” event once every 67 s.

A detailed description of the HRA-3 power, communications and data acquisition hardware and performance may be found in Ref. [69].

### 3.2. Operation of the HRA-3

The HRA-3 stations installed in the 2013 deployment season took data until the lack of solar power caused the batteries to deplete in April, 2014. The communication systems functioned as expected during the entire data taking season. Connections over the wireless internet link began to fail in early April due to the loss of reliable power at the relay on Mt. Discovery. Satellite connections over the Iridium network continued to function until the loss of station power in mid-April.

The bipolar trigger requirement on two of four antenna channels, described in Section 3.1, allowed the stations to run at low trigger rates while also keeping thresholds low. As shown in Fig. 13, the trigger rate of Station A was typically below 0.1 Hz and an average rate of  $10^{-3}$  Hz has been achieved with  $4\sigma$  thresholds.

Several features in the triggering rates can be found in Fig. 13 during the periods marked by the letters. Small diurnal trigger rate fluctuations seen in periods A and B are attributed to daily temperature variations of the amplifiers. The gradual increasing of the trigger rate during period B is caused by an overall cooling of the amplifier electronics. This cooling raised the gain of some amplifiers more than others, leading to different effective thresholds on different channels and allowing small diurnal temperature fluctuations to affect trigger rates during period B. Once the station is fully buried in snow and thresholds are balanced, the trigger rates are found to be stable. Such periods are observed after each

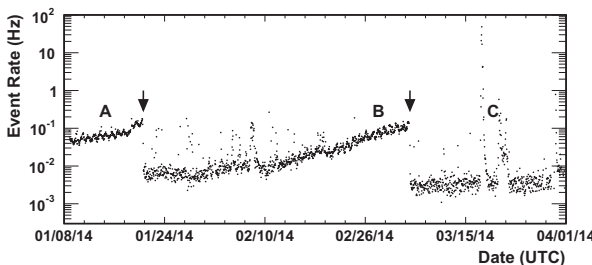


**Fig. 13.** The rate of thermal triggers over time for Station A. The letters indicate periods in which different features are seen in the rates. During periods A and B, both the small diurnal variations in rate as well as the overall gradual increase in rate is due to variations in the temperature of the amplifiers. The arrows indicate the two adjustments made to the trigger thresholds. During period C, a large storm passed through the ARIANNA site, resulting in large fluctuations of the trigger rate. Figure from Ref. [69].

threshold tuning, marked by the arrows. Other HRA-3 stations exhibited a similar dependence of trigger rates on temperature.

The typical observed thermal trigger rates match the rates expected for the threshold values. The trigger thresholds were only adjusted twice during the 2013–14 data taking season, denoted by the arrows in Fig. 13. The threshold adjustments primarily served to re-balance the single-channel trigger rates. This allows each channel to participate equally in the trigger requirement that at least two out of four antenna channels have significant bipolar signals.

An increase in the trigger rate during storms at the ARIANNA site has been observed. One such period, marked as period C, is visible in Fig. 13. The precise cause of these triggers continues to be investigated. During periods of high wind speeds, above roughly 20 knots, a correlated rise in rates among all stations is seen. However, not all high wind periods result in elevated trigger rates. The events recorded during these periods are readily distinguishable from expected neutrino signals, as discussed in Section 4.

## 4. Search for neutrino signals in HRA-3 data

### 4.1. The data set

Data taken by the HRA-3 between January 3 and April 9, 2014 has been analyzed to search for neutrino-induced Askaryan signals. The former date corresponds to the departure of the deployment crew from the Ross Ice Shelf. The latter date is chosen to include all data successfully transferred off of Antarctica. The entire data set taken by the HRA-3 and transferred off site is included in the analysis, resulting in a combined livetime for the three stations of 170 days.

The bulk of the livetime deficit is not attributable to operational deadtime. Towards the end of March, the wireless Internet connection to the stations became less reliable, and a significant portion of the data set taken during this period remained on the stations. With the resumption of operations in the austral summer, the remaining data will be transferred off site and added to the data set for analysis. In addition, the continuous taking of radio data by Station G was halted during a period of severe weather at the site just prior to midnight, February 12, 2014 (UTC). An unnecessary diode train (not present on other stations) between the solar panel and battery of the station failed, breaking the electrical connection between the two. To conserve battery power, a short period each day was used to collect radio data. The station was otherwise kept in a low power configuration during which the battery power supply was monitored. The station continued to operate for 3 months without external charging. Removal of the diode train during the following summer season allowed the station's batteries to charge.

The deadtime of each station during its normal data-taking operation was typically 6% or less. During such periods, each station takes radio data continuously, pausing only for periodic off site communications and for brief calibration data collection, as described in Section 3.1. The off site communications typically last for 1 min and occur every half hour, accounting for a 4%–5% deadtime, depending on the connection stability. A deadtime of 1% results from the collection calibration data, performed for 10 min every 12 h. These two interruptions of radio data taking constitute the entirety of the station deadtime during normal operation. Deadtime due to triggering and data acquisition is negligible as trigger rates are far below the maximum acquisition rate. The intentional disabling of radio data collection, such as the low-power operation of Station G after its batteries were no longer able to be charged, has not been included in the calculation of the fractional deadtime observed during data taking.

#### 4.2. Neutrino candidate selection

The search for neutrino signals in the data set has been performed using a simple analysis for which the reconstruction of the radio signal direction is unnecessary [82]. Neutrino candidate events are required to meet three criteria. First, the event should pass a filter designed to reject purely random thermal triggers. Second, the event should not show evidence of electronics noise characterized by sinusoidal waveforms. Third, to separate neutrino candidates from non-thermal background events such as those associated with strong winds, the waveform observed by at least one LPDA is required to correspond reasonably well to the waveform expected for a neutrino.

The impact of the cuts on neutrino signals has been estimated using simulations. Neutrino events are generated according to a cosmogenic flux energy distribution and radio signals are propagated to the detector station in the frequency domain, as described in Section 2.1.1. These simulated neutrino events are required to pass the same trigger requirement used in the HRA-3 data: at least 2 of 4 antennas must have bipolar signals beyond  $4\sigma$ . The time-dependent waveform measured by an antenna is then determined by first choosing the appropriate neutrino waveform template (see Section 2.1.2) based on the relative orientation of the LPDA and the incoming radio signal direction. Each template is then scaled such that its amplitude corresponds to that calculated by the frequency-domain simulation. Finally, finite bandwidth noise is added to each waveform.

Purely random triggers are identified in the data by noting that continuous white noise has an autocorrelation function with a perfect correlation at zero time offset, and no correlation at other time offsets. This property is used to distinguish purely random thermal triggers from non-thermal events. Fig. 14 contrasts the autocorrelation of a waveform from a software forced trigger (purely thermal noise) with that of a waveform expected for a typical neutrino signal.

Non-thermal events are taken to be those for which the minimum value of the autocorrelation function,  $\alpha$ , falls below  $-0.45$  on any antenna. All other events are attributed to pure thermal noise. This requirement correctly identifies as purely thermal 99% of software forced triggers in the HRA-3 data set. Of the regularly triggered events (radio signals, thermal noise, etc.), 69% are identified as purely thermal. This filter is planned to be implemented locally on the stations as a real-time “level zero trigger.” Such a level zero trigger will reduce event rates sufficiently to allow the near real-time transfer of radio event data from the full 1296 station ARIANNA detector using only low bandwidth Iridium SBD communications.

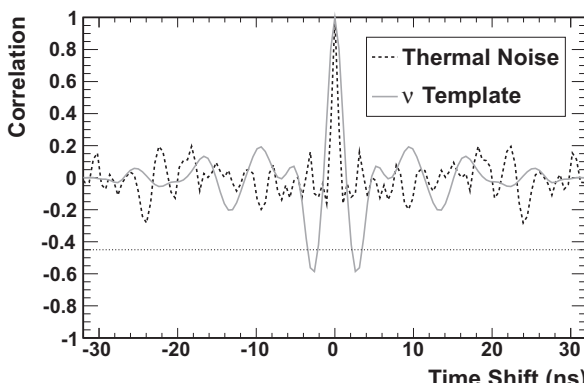


**Fig. 14.** A comparison of the autocorrelation function for a purely thermal noise waveform (from a software forced trigger) and a neutrino template waveform. The dotted horizontal line shows the cut value ( $\alpha < -0.45$ ) used in the analysis.

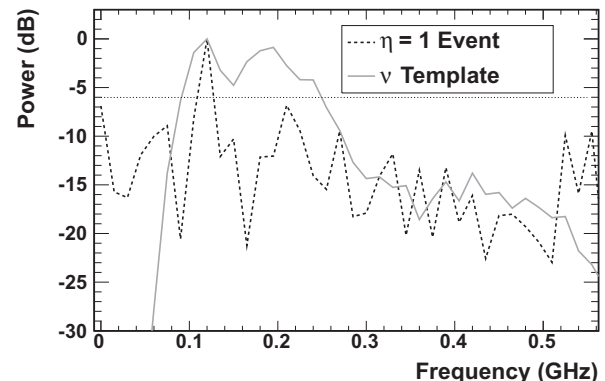


**Fig. 15.** A comparison of the frequency spectrum of a non-thermal event that has a very low number of high magnitude frequency bins, in this case a single sharp peak at 120 MHz, and a neutrino template waveform with no noise. Each spectrum is normalized to have its peak power at 0 dB. The dotted horizontal line shows the cut value used in the analysis (-6 dB).

As expected, the autocorrelation cut rejects very few of the neutrino signal events, with 99.5% of the neutrino events having  $\alpha < -0.45$ .

Some non-thermal events are present in the data that resemble detector electronic noise rather than external radio noise. Such events are not associated with external conditions like high winds. Instead, they are characterized by strong sinusoidal waveforms and timing between antennas that is inconsistent with a physical external signal. While the latter property facilitates a powerful rejection based on signal direction reconstruction, the sinusoidal structure of the waveform is already sufficient to identify the events. These events are identified by a strong, narrow peak in the frequency spectrum of the waveform recorded by at least one antenna.

Fig. 15 shows the frequency spectrum, measured in 10.6 MHz bins, of such a sinusoidal-like waveform compared to that expected for a typical neutrino signal. The frequency spectrum of a neutrino candidate waveform is required to have more than 3 frequency bins at or above half of the magnitude of the frequency bin containing the maximum magnitude. This variable is referred to as  $\eta$ . It is equivalent to the number of frequency bins containing more than one quarter of the maximum power.

The  $\eta$  distribution of the thermal noise data has been compared to the distributions in both software forced triggers as well as simulated finite bandwidth noise, as shown in Fig. 16. This comparison shows that the cut variable behaves as expected.

Events with a strong frequency peak, so that  $\eta \leq 3$ , are rejected as being due to detector noise. This cut removes 85% of the remaining non-thermal triggered events across all three stations. The  $\eta > 3$  requirement also preserves the vast majority of neutrino signals, with 97% of the neutrino events passing the cut. The distributions of  $\eta$  in the neutrino signal simulations and in the data for events with  $\alpha < -0.45$  are shown in Fig. 17.

The third and final neutrino candidate selection criteria requires that the waveform recorded in at least one antenna resemble that expected for a neutrino signal. This is done by calculating the maximum correlation value (for any time shift) between the waveform reported by an antenna with a reference neutrino signal template (see Section 2.1.2). The relative amplitude between the waveform recorded in the data and the neutrino template does not affect the Pearson correlation value [83].

As the signal direction is not reconstructed, the relative geometry of the signal direction and antenna orientation is not used to determine the proper neutrino waveform template to be used as a reference. Instead, the neutrino template corresponding to a

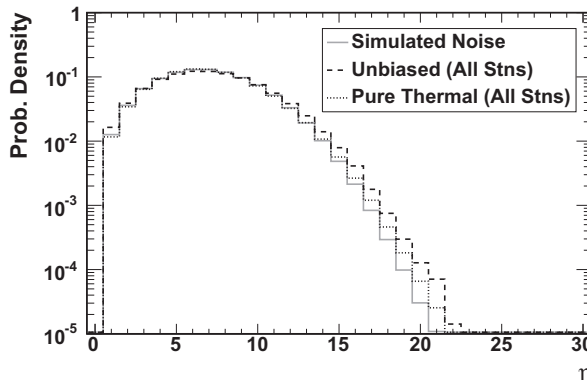


**Fig. 16.** Comparison of the  $\eta$  distribution of pure thermal data, software forced (unbiased) triggered data and simulated finite bandwidth noise data.

signal arriving with local E-plane and H-plane angles (see Section 2.1.2) of  $30^\circ$  is taken as a reference for every antenna in every event. This reference was chosen as it represents the average relative geometry observed in the simulations.

The calculation of the correlation between a waveform and the reference neutrino template is complicated by the unknown relative polarity between the recorded signal and the reference template. For example, an LPDA with its tines oriented from East to West and its cable connector facing South may record a bipolar pulse with a *positive* initial crest for some incoming signal. On the other hand, rotating the LPDA by  $180^\circ$  so that its cable connector faces North, with its tines oriented from West to East, would result in a bipolar pulse with a *negative* initial crest being recorded for the same signal. To account for this effect, the correlation is calculated for all possible unique combinations of relative polarity between each antenna and the reference template. The best correlation found between the reference and any antenna, across all possible polarity orientations, is referred to as  $\chi$ .

A comparison of the  $\chi$  distribution of thermal noise data, software forced triggers and simulated finite bandwidth noise is shown in Fig. 18. This comparison shows that the  $\chi$  variable behaves as expected.

Neutrino candidate events are required to have a  $\chi > 0.81$ . This seemingly large correlation value arises from the choice of cutting on the best correlation. As shown in Fig. 19, which compares the  $\chi$  distributions of neutrino signal simulations and events in the data having both  $\alpha < -0.45$  and  $\eta > 3$ , the cut value is not large compared to the correlation value expected for neutrino signals.

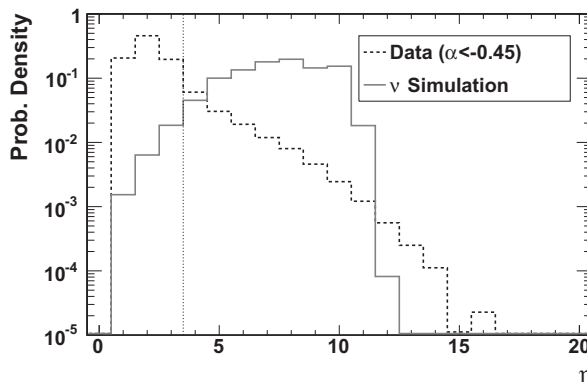


**Fig. 17.** The  $\eta$  distribution of events in the data (of all stations) and the neutrino signal simulations. The cut,  $\eta > 3$ , is shown by the dotted vertical line. Only events with  $\alpha < -0.45$  are shown for each population.

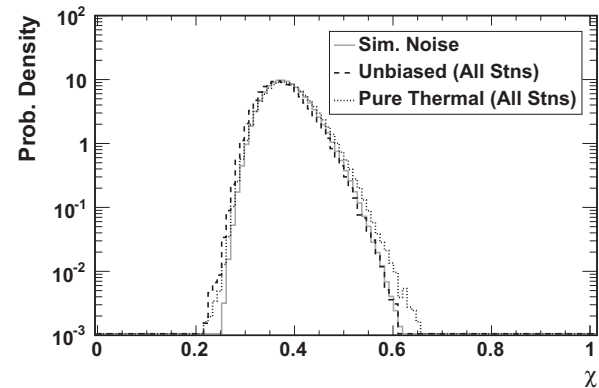


**Fig. 18.** Comparison of the  $\chi$  distribution of pure thermal data, software forced (unbiased) triggered data and simulated finite bandwidth noise data.

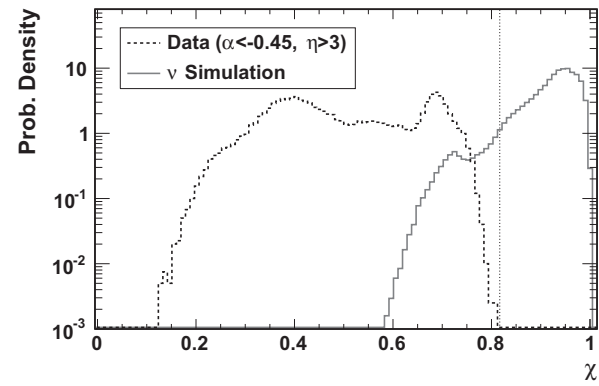


**Fig. 19.** The distribution of  $\chi$  in the data (of all stations) and the neutrino signal simulations. The cut,  $\chi > 0.81$ , is shown by the dotted vertical line. Only events with both  $\alpha < -0.45$  and  $\eta > 3$  are shown for each population. The peak in the data around  $\chi \approx 0.68$  is due to events associated with high wind periods (see Fig. 20).

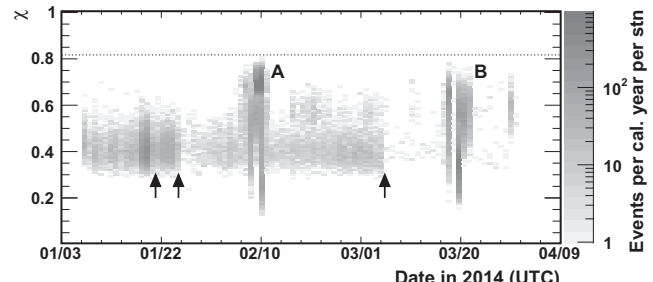


**Fig. 20.** The  $\chi$  value of events with  $\alpha < -0.45$  and  $\eta > 3$  on all three stations is shown as a function of time. A sharp reduction in pure thermal events is seen after threshold tunings, indicated by the arrows (each station was tuned only twice, but not all on the same days). An excess of non-thermal background events is seen during the high wind periods indicated by "A" and "B." The dotted line indicates the neutrino candidate cut ( $\chi > 0.81$ ) applied in the analysis.

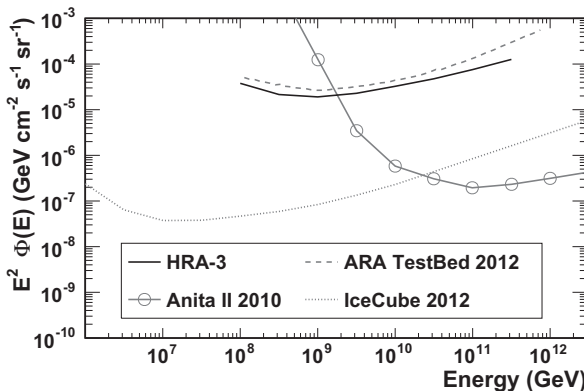
None of the remaining events in the data set survive the  $\chi > 0.81$  requirement. The requirement that  $\chi > 0.81$  preserves 93% of the remaining signal events.

Fig. 20 shows the  $\chi$  value as a function of time for events with  $\alpha < -0.45$  and  $\eta > 3$ . The band of events with  $\chi \approx 0.4$  is formed by purely thermal events that survive the rather loose autocorrelation cut. Threshold tuning, indicated by the arrows, results in a sharp reduction of these events. Although each station had its threshold tuned only twice, different stations were tuned at different times. An increase in non-thermal background events is clearly seen

**Table 2**

A summary of the number of neutrino candidates remaining with the successive application of each cut. The fractions in parentheses are with respect to the totals. See text for a brief discussion of the excess background in the data from Station G.

	Station A	Station G	Station C	All data	Cosmogenic ν's (%)
Triggers	203,562	248,772	512,931	965,265	100
$\alpha < -0.45$	51,327 (25%)	102,599 (41%)	142,243 (28%)	296,169 (31%)	99.5
$\eta > 3$	3159 (2%)	26,868 (11%)	13461 (3%)	43,488 (4.5%)	97
$\chi > 0.81$	0 (0%)	0 (0%)	0 (0%)	0 (0%)	90



**Fig. 21.** The 90% confidence level Neyman upper limit on the all flavor  $\nu + \bar{\nu}$  flux, calculated in a sliding decade-wide energy bin, arising from the lack of neutrino candidate events in the HRA-3 data set collected during the 2013–14 season. The limit is compared to that of the ARA TestBed [25] as well as to the current best limits set by Anita II [15,16] at high energies and IceCube [12] at lower energies.

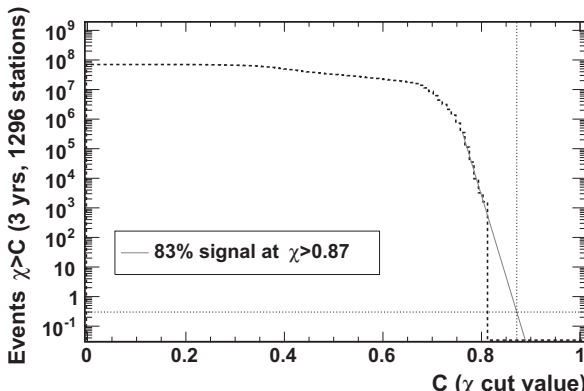


**Fig. 22.** The cumulative background distribution from the current HRA-3 analysis, scaled up to a livetime equivalent to 1296 stations running for 58% of 3 years. The solid gray line shows an exponential fit to the tail used to extrapolate the cut necessary to allow 0.3 background events in the full detector data set. This cut preserves 83% of the cosmogenic neutrino triggers.

during high wind periods, indicated by the labels “A” and “B.” While background rates increased on all stations during these storms, Station G recorded many more background events than the other two stations during the storm indicated by label A. It was during this storm that the batteries of Station G stopped receiving charge. This period accounts for both the larger number of background events taken by Station G as well as the peak in the data around  $\chi \approx 0.68$ , visible in Fig. 19.

The application of all cuts preserves 90% of the cosmogenic neutrino triggers while removing all events recorded by the HRA-3 during the 2013–14 data taking season. A summary of the number of neutrino candidates that remain after the successive application of each selection criterion is presented in Table 2.

The analysis of the 2013–14 HRA-3 data has employed a similar procedure to that used on the HRA-3 data from the 2012–13 season [82] and on prototype HRA-1 data [84]. These analyses also found high signal efficiency values using background rejection procedures that produced no neutrino candidate events.

#### 4.3. Flux limit

An upper limit on the total diffuse neutrino flux can be determined due to the absence of any observed events. With no observed events and no background events, the Neyman formalism is used to place an upper limit of 2.3 neutrino events at the 90% confidence level in each energy bin. Fig. 21 shows this limit translated to a limit on the all flavor neutrino flux as a function of neutrino energy. No neutrino flux model has been assumed in the calculation of the limit. Instead, Eq. (1) is used to determine the flux that would produce 2.3 neutrinos in a sliding decade-wide energy bin by taking  $E$  to be the energy at the center of the bin,  $dN \leq 2.3$  to be the limit on the number of neutrinos in the energy bin and  $dE = E \ln 10 d \log E = E \ln 10$  to be the width of the decade-wide energy bin. That is,

$$E^2 \Phi(E) \leq \frac{2.3}{\ln 10} \frac{E}{eV_{\text{eff}} \Omega t_{\text{live}}} L(E) \quad (2)$$

where  $V_{\text{eff}} \Omega$  is the single station effective volume, averaged over neutrino flavor, shown in Fig. 4. Also shown in Fig. 21 is the recent limit placed by the ARA TestBed detector with 224 days of livetime [25], as well as the current best limits from Anita II [16,15] at high energies and IceCube [12] at lower energies. Decade-wide energy bins have been chosen to facilitate comparison with the differential limits from ARA and IceCube.

#### 4.4. The full ARIANNA detector

A search for neutrino signals in the data from the full ARIANNA detector will make use of all information recorded by the detector in each event. Full likelihood fits will be used to reconstruct the radio signal direction, the incoming neutrino direction and the neutrino energy. This will facilitate the use of further, and almost certainly more powerful, selection criteria with which to separate neutrino signals from radio backgrounds.

However, it is worthwhile to investigate how the simple analysis presented in this article would perform for data taken by the full detector. For this purpose, the full detector is taken to operate for 58% of the year, from mid-September to early April, and to consist of 1296 stations.

The deadtime of the full detector will be reduced relative to that of the HRA-3 stations. With the autocorrelation filter implemented as a local level zero trigger (see Section 4.2) average event rates of  $10^{-4}$  Hz are easily achievable, even with  $4\sigma$  thresholds. Each station can then immediately send every event off site via the Iridium SBD satellite connection, allowing near real-time data transfer. With such a setup, each station would transfer fewer than 9 events per day, leading to a deadtime of 2% due to data transfer

and communications. The calibration data will likely be collected somewhat less often, leading to a deadtime of < 1%.

Fig. 22 shows the cumulative number of background events expected to pass a  $\chi > C$  cut as a function of the cut value,  $C$ . The cumulative distribution is obtained by scaling that of the HRA-3 analysis (see Fig. 19) up to the livetime expected for a 1296 station detector running for 58% of 3 years. An exponential function is fit to the tail of the cumulative distribution in order to determine the correlation cut necessary to admit only 0.3 background events in the full detector data set. The extrapolated correlation cut value of  $\chi > 0.87$  preserves 83% of the cosmogenic neutrino triggers. This result assumes, by necessity, that no new type of background event will be observed that changes the shape of the tail of the correlation cut distribution.

The signal efficiency for an analysis with the full ARIANNA detector should further improve, given the expectation that a reconstruction of the neutrino angle and energy will strengthen the signal and background separation. Also note that the extrapolation of the HRA-3 data includes background events caused by cosmic rays. The prior rejection of cosmic rays using upward facing antennas, as described in Section 2.3, may reduce the background further, allowing for a less strict  $\chi$  cut and a correspondingly improved signal efficiency.

## 5. Conclusions

The ARIANNA experiment proposes the use of the Askaryan effect to search for a diffuse flux of neutrinos in the  $10^8$ – $10^{10}$  GeV energy range. The experiment will exploit the long attenuation length of ice at radio frequencies by populating the surface of the Ross Ice Shelf of Antarctica with a grid of radio detectors to reach an effective volume on the order of  $100 \text{ km}^3$ . The ice to water interface at the bottom of the ice shelf acts as a mirror to radio pulses, making ARIANNA sensitive to neutrinos arriving from above the detector as well as from the horizon.

The response of such a detector to the electric fields generated by the Askaryan effect has been simulated in both the frequency and time domains. The angular resolution of the neutrino direction is found to be about  $2.9^\circ$  in the local zenith angle and  $2.5^\circ$  in the local azimuth angle. Determination of the angle between the Cherenkov cone peak and the observation angle of the detector to within  $1.5^\circ$  improves the angular resolution on the neutrino direction by 50% in zenith and 20% in azimuth. The resolution on the energy of the neutrino is found to be about a factor of 5 with no knowledge of the Cherenkov observation angle, and a factor of 2.2 if the angle is known to about  $1.4^\circ$  on average.

To facilitate the construction of the full ARIANNA detector, a prototype of seven radio detector stations, the HRA, is currently under construction at the Ross Ice Shelf. During the 2013–14 austral summer, three such stations collected radio data. This data set has been analyzed in a search for high energy neutrino signals. No neutrino-like signals were found in the data. The majority of data collected consists of purely random thermal triggers. Two other principal sources of backgrounds were observed, one showing oscillatory waveforms indicative of detector electronics effects and another associated with periods of high winds at the site.

The rejection of these backgrounds by a simple analysis that does not rely on reconstructing the radio signal direction is found to preserve 90% of cosmogenic neutrino triggers. A model-independent differential upper limit has been placed at the 90% confidence level on the all flavor  $\nu + \bar{\nu}$  flux in a sliding decade-wide energy bin. The limit reaches a minimum of  $1.9 \times 10^{-23} \text{ GeV}^{-1} \text{ cm}^{-2} \text{ s}^{-1} \text{ sr}^{-1}$  in the  $10^{8.5}$ – $10^{9.5}$  GeV energy bin.

The analysis presented in this article has been extrapolated to the full 1296 station ARIANNA experiment being run during the

austral summer for 3 years. Background rejection levels are found that allow only 0.1 background events per year in the entire detector while preserving 83% of cosmogenic neutrino triggers. The actual performance of the full experiment may be further improved by the reconstruction of the neutrino direction and energy.

The ARIANNA experiment has the potential to extend the measurement of the diffuse neutrino flux to higher neutrino energies by two orders of magnitude in energy. The current UHE neutrino flux measurement by the IceCube collaboration [61] would produce about 2.8 neutrinos in 3 calendar years of ARIANNA data, even if there is no additional source of high energy neutrinos, as shown in Table 1. A measurement of the neutrino flux at such energies would likely generate comparable levels of interest in the growing field of ultra-high energy neutrino astronomy. Measurements of the diffuse flux could be improved by expanding the array, while dedicated point searches with improved angular resolution could be performed by increasing the density of the array.

## Acknowledgements

The authors wish to thank the staff of Antarctic Support Contractors, Lockheed, and the entire crew at McMurdo Station for excellent logistical support. The authors also thank Prof. De Flaviis for the use of the Far Field Anechoic Chamber at U.C. Irvine and would like to acknowledge and thank the CReSIS project and the Anechoic Chamber facility management for the use of the world class anechoic chamber at the University of Kansas.

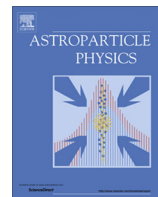
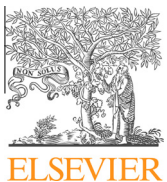
This work was supported by generous funding from the US National Science Foundation (both the Physics Division and the Office of Polar Programs) including via Grant Awards ANT-08339133, NSF-0970175, and NSF-1126672.

## References

- [1] A. Letessier-Selvon, T. Stanev, Ultrahigh energy cosmic rays, Rev. Mod. Phys. 83 (2011) 907–942, <http://dx.doi.org/10.1103/RevModPhys.83.907> (arxiv: 1103.0031).
- [2] P. Abreu et al., Constraints on the origin of cosmic rays above  $10^{18}$  eV from large scale anisotropy searches in data of the Pierre Auger Observatory, Astrophys. J. 762 (2012) L13, <http://dx.doi.org/10.1088/2041-8205/762/1/L13> (arXiv: 1212.3083).
- [3] T.J. Weiler, Extreme energy cosmic rays: puzzles, models, and maybe neutrinos, AIP Conf. Proc. 579 (2001) 58–77, <http://dx.doi.org/10.1063/1.1398161> (arXiv: hep-ph/0103023).
- [4] G. Sigl, The Enigma of the highest energy particles of nature, Annals Phys. 303 (2003) 117–141, [http://dx.doi.org/10.1016/S0003-4916\(02\)00021-0](http://dx.doi.org/10.1016/S0003-4916(02)00021-0) (arXiv: astro-ph/0210049).
- [5] G. Sigl, Particle and astrophysics aspects of ultrahigh-energy cosmic rays, Lect. Notes Phys. 556 (2000) 259–300 (arXiv: astro-ph/0008364).
- [6] K. Greisen, End to the cosmic ray spectrum?, Phys. Rev. Lett. 16 (1966) 748–750, <http://dx.doi.org/10.1103/PhysRevLett.16.748>.
- [7] G. Zatsepin, V. Kuzmin, Upper limit of the spectrum of cosmic rays, JETP Lett. 4 (1966) 78–80.
- [8] F. Stecker, Ultrahigh energy photons, electrons and neutrinos, the microwave background, and the universal cosmic ray hypothesis, Astrophys. Space Sci. 20 (1973) 47–57, <http://dx.doi.org/10.1007/BF00645585>.
- [9] V. Berezinsky, G. Zatsepin, Cosmic rays at ultrahigh-energies (neutrino?), Phys. Lett. B28 (1969) 423–424, [http://dx.doi.org/10.1016/0370-2693\(69\)90341-4](http://dx.doi.org/10.1016/0370-2693(69)90341-4).
- [10] V. Berezinsky, A.Y. Smirnov, Cosmic neutrinos of ultra-high energies and detection possibility, Astrophys. Space Sci. 32 (1975) 461–482, <http://dx.doi.org/10.1007/BF00643157>.
- [11] J. Ahrens et al., Search for extraterrestrial point sources of neutrinos with AMANDA-II, Phys. Rev. Lett. 92 (2004) 071102, <http://dx.doi.org/10.1103/PhysRevLett.92.071102> (arXiv: astro-ph/0309585).
- [12] M. Aartsen et al., Probing the origin of cosmic-rays with extremely high energy neutrinos using the IceCube Observatory, Phys. Rev. D88 (2013) 112008 (arXiv: 1310.5477).
- [13] F. Halzen, S.R. Klein, IceCube: an instrument for neutrino astronomy, Rev. Sci. Instrum. 81 (2010) 081101, <http://dx.doi.org/10.1063/1.3480478> (arXiv: 1007.1247).
- [14] P. Gorham et al., New limits on the ultra-high energy cosmic neutrino flux from the ANITA experiment, Phys. Rev. Lett. 103 (2009) 051103, <http://dx.doi.org/10.1103/PhysRevLett.103.051103> (arXiv: 0812.2715).

- [15] P. Gorham et al., Observational constraints on the ultrahigh energy cosmic neutrino flux from the second flight of the anita experiment, *Phys. Rev. D* 82 (2010) 022004, <http://dx.doi.org/10.1103/PhysRevD.82.022004>.
- [16] P. Gorham et al., Erratum: observational constraints on the ultra-high energy cosmic neutrino flux from the second flight of the ANITA experiment, *Phys. Rev. D* 85 (2012) 049901 (arXiv: 1011.5004, doi: 10.1103/PhysRevD.82.022004, 10.1103/PhysRevD.85.049901).
- [17] I. Kravchenko et al., Limits on the ultra-high energy electron neutrino flux from the RICE experiment, *Astropart. Phys.* 20 (2003) 195–213, [http://dx.doi.org/10.1016/S0927-6505\(03\)00181-6](http://dx.doi.org/10.1016/S0927-6505(03)00181-6) (arXiv: astro-ph/0206371).
- [18] I. Kravchenko et al., Rice limits on the diffuse ultrahigh energy neutrino flux, *Phys. Rev. D* 73 (2006) 082002, <http://dx.doi.org/10.1103/PhysRevD.73.082002> (arXiv: astro-ph/0601148).
- [19] J. Abraham et al., Upper limit on the diffuse flux of UHE tau neutrinos from the Pierre Auger Observatory, *Phys. Rev. Lett.* 100 (2008) 211101, <http://dx.doi.org/10.1103/PhysRevLett.100.211101> (arXiv: 0712.1909).
- [20] J. Abraham et al., Limit on the diffuse flux of ultra-high energy tau neutrinos with the surface detector of the Pierre Auger Observatory, *Phys. Rev. D* 79 (2009) 102001, <http://dx.doi.org/10.1103/PhysRevD.79.102001> (arXiv: 0903.3385).
- [21] R.U. Abbasi et al., An upper limit on the electron-neutrino flux from the HiRes detector, *Astrophys. J.* 684 (2008) 790–793, <http://dx.doi.org/10.1086/590335> (arXiv: 0803.0554).
- [22] K. Martens, Hires estimates and limits for neutrino fluxes at the highest energies, 2007, arXiv: 0707.4417.
- [23] M. Aartsen et al., Observation of high-energy astrophysical neutrinos in three years of IceCube data, *Phys. Rev. Lett.* 113 (2014) 101101, <http://dx.doi.org/10.1103/PhysRevLett.113.101101> (arXiv: 1405.5303).
- [24] P. Allison et al., Design and initial performance of the Askaryan radio array prototype EeV neutrino detector at the South Pole, *Astropart. Phys.* 35 (2012) 457–477, <http://dx.doi.org/10.1016/j.astropartphys.2011.11.010> (arXiv: 1105.2854).
- [25] P. Allison, et al., First constraints on the ultra-high energy neutrino flux from a prototype station of the Askaryan radio array, Submitted to *Astropart. Phys.* arXiv: 1404.5285.
- [26] A.G. Vieregg, D. Saltzberg, Greenland Neutrino Observatory(GNO): Radio Detector of Ultra-high Energy Neutrinos at Apex Station in Greenland, 2014. <<http://kicp.uchicago.edu/aviergegg/gnoWhitepaper.pdf>>.
- [27] P.W. Gorham, Particle astrophysics in NASA's long duration balloon program, *Nucl. Phys. Proc. Suppl.* 243–244 (2013) 231–238, <http://dx.doi.org/10.1016/j.nuclphysbps.2013.09.012>.
- [28] P. Gorham, F. Baginski, P. Allison, K. Liewer, C. Miki, et al., Balloon-embedded antenna for ultra-high energy particle detection, *Astropart. Phys.* 35 (2011) 242–256, <http://dx.doi.org/10.1016/j.astropartphys.2011.08.004> (arXiv: 1102.3883).
- [29] G.A. Askaryan, *JETP* 14 (1962) 441.
- [30] G.A. Askaryan, *JETP* 21 (1965) 658.
- [31] D. Saltzberg, P. Gorham, D. Walz, et al., Observation of the Askaryan effect: coherent microwave Cherenkov emission from charge asymmetry in high-energy particle cascades, *Phys. Rev. Lett.* 86 (2001) 2802–2805, <http://dx.doi.org/10.1103/PhysRevLett.86.2802> (arXiv: hep-ex/0011001).
- [32] P. Gorham et al., Observations of the Askaryan effect in ice, *Phys. Rev. Lett.* 99 (2007) 171101, <http://dx.doi.org/10.1103/PhysRevLett.99.171101> (arXiv: hep-ex/0611008).
- [33] J. Alvarez-Muniz, R. Vazquez, E. Zas, Calculation methods for radio pulses from high-energy showers, *Phys. Rev. D* 62 (2000) 063001, <http://dx.doi.org/10.1103/PhysRevD.62.063001> (arXiv: astro-ph/0003315).
- [34] S.W. Barwick, et al., Radio-frequency attenuation length, basal reflectivity, depth, and polarization measurements from Moores bay in the Ross ice-shelf, Accepted for publication in *J. Glaciol.* (2015).
- [35] J.A. Dowdeswell, S. Evans, Investigations of the form and flow of ice sheets and glaciers using radio-echo sounding, *Rep. Progr. Phys.* 67 (10) (2004) 1821. <<http://stacks.iop.org/0034-4885/67/i=10/a=R03>>.
- [36] S.W. Barwick for the ARIANNA Collaboration, Performance of the ARIANNA Prototype Array, in: *Proc. 33rd Intern. Cosmic Ray Conf.*, 2013.
- [37] K.-H. Kampert, M. Unger, Measurements of the cosmic ray composition with air shower experiments, *Astropart. Phys.* 35 (2012) 660–678, <http://dx.doi.org/10.1016/j.astropartphys.2012.02.004> (arXiv: 1201.0018).
- [38] R. Engel, D. Seckel, T. Stanev, Neutrinos from propagation of ultrahigh-energy protons, *Phys. Rev. D* 64 (2001) 093010, <http://dx.doi.org/10.1103/PhysRevD.64.093010> (arXiv: astro-ph/0101216).
- [39] D. Seckel, T. Stanev, Neutrinos: the key to UHE cosmic rays, *Phys. Rev. Lett.* 95 (2005) 141101, <http://dx.doi.org/10.1103/PhysRevLett.95.141101> (arXiv: astro-ph/0502244).
- [40] A. Connolly, R.S. Thorne, D. Waters, Calculation of high energy neutrino-nucleon cross sections and uncertainties using the MSTW parton distribution functions and implications for future experiments, *Phys. Rev. D* 83 (2011) 113009, <http://dx.doi.org/10.1103/PhysRevD.83.113009> (arXiv: 1102.0691).
- [41] S.R. Klein, A. Connolly, Neutrino absorption in the earth, neutrino cross-sections, and new physics, arXiv: 1304.4891.
- [42] S.-H. Wang, P. Chen, M. Huang, J. Nam, Feasibility of determining diffuse ultrahigh energy cosmic neutrino flavor ratio through ARA neutrino observatory, *JCAP* 1311 (2013) 062, <http://dx.doi.org/10.1088/1475-7516/2013/11/062> (arXiv: 1302.1586).
- [43] A.V. Olinto, K. Kotera, D. Allard, Ultrahigh energy cosmic rays and neutrinos, *Nucl. Phys. Proc. Suppl.* 217 (2011) 231–236, <http://dx.doi.org/10.1016/j.nuclphysbps.2011.04.109> (arXiv: 1102.5133).
- [44] K. Dookayka, Characterizing the search for ultra-high energy neutrinos with the ARIANNA detector (Ph.D. thesis), University of California, Irvine, 2011.
- [45] F. Halzen, D. Saltzberg, Tau-neutrino appearance with a 1000 megaparsec baseline, *Phys. Rev. Lett.* 81 (1998) 4305–4308, <http://dx.doi.org/10.1103/PhysRevLett.81.4305> (arXiv: hep-ph/9804354).
- [46] R. Gandhi, C. Quigg, M.H. Reno, I. Sarcevic, Neutrino interactions at ultrahigh-energies, *Phys. Rev. D* 58 (1998) 093009, <http://dx.doi.org/10.1103/PhysRevD.58.093009> (arXiv: hep-ph/9807264).
- [47] T.K. Gaisser, F. Halzen, T. Stanev, Particle astrophysics with high-energy neutrinos, *Phys. Rep.* 258 (1995) 173–236, [http://dx.doi.org/10.1016/0370-1573\(95\)00003-Y](http://dx.doi.org/10.1016/0370-1573(95)00003-Y) (arXiv: hep-ph/9410384).
- [48] R. Gandhi, C. Quigg, M.H. Reno, I. Sarcevic, Ultrahigh-energy neutrino interactions, *Astropart. Phys.* 5 (1996) 81–110, [http://dx.doi.org/10.1016/0927-6505\(96\)00008-4](http://dx.doi.org/10.1016/0927-6505(96)00008-4) (arXiv: hep-ph/9512364).
- [49] J. Alvarez-Muniz, E. Zas, The LPM effect for EeV hadronic showers in ice: implications for radio detection of neutrinos, *Phys. Lett. B* 434 (1998) 396–406, [http://dx.doi.org/10.1016/S0370-2693\(98\)00905-8](http://dx.doi.org/10.1016/S0370-2693(98)00905-8) (arXiv: astro-ph/9806098).
- [50] J. Alvarez-Muniz, E. Zas, Cherenkov radio pulses from EeV neutrino interactions: the LPM effect, *Phys. Lett. B* 411 (1997) 218–224, [http://dx.doi.org/10.1016/S0370-2693\(97\)01009-5](http://dx.doi.org/10.1016/S0370-2693(97)01009-5) (arXiv: astro-ph/9706064).
- [51] L. Gerhardt, S.R. Klein, Electron and photon interactions in the regime of strong LPM suppression, *Phys. Rev. D* 82 (2010) 074017, <http://dx.doi.org/10.1103/PhysRevD.82.074017> (arXiv: 1007.0039).
- [52] C.B.V. Bogorodsky, P.E. Gudmandsen, *Radioglaciology*, Reidel Publishing Co., The Netherlands, 1985.
- [53] V. Schytt, Scientific results, *Norsk Polarinstitutt (Norwegian-British-Swedish Antarctic Expedition)* (1958) 113–151.
- [54] T. Barrella, S.W. Barwick, D. Saltzberg, Ross Ice Shelf in situ radio-frequency ice attenuation, *J. Glaciol.* 57 (2011) 61–66, [http://dx.doi.org/002214311795306691](http://dx.doi.org/10.3189/002214311795306691) (arXiv: 1011.0477).
- [55] S. Barwick, E. Berg, D. Besson, T. Duffin, J. Hanson, et al., Time domain response of the ARIANNA detector, *Astropart. Phys.* 62 (2014) 139–151, <http://dx.doi.org/10.1016/j.astropartphys.2014.09.002> (arXiv: 1406.0820).
- [56] J. Alvarez-Muniz, A. Romero-Wolf, E. Zas, Cherenkov radio pulses from electromagnetic showers in the time-domain, *Phys. Rev. D* 81 (2010) 123009, <http://dx.doi.org/10.1103/PhysRevD.81.123009> (arXiv: 1002.3873).
- [57] J. Alvarez-Muniz, A. Romero-Wolf, E. Zas, Practical and accurate calculations of Askaryan radiation, *Phys. Rev. D* 84 (2011) 103003, <http://dx.doi.org/10.1103/PhysRevD.84.103003> (arXiv: 1106.6283).
- [58] P. Abreu et al., Search for point-like sources of ultra-high energy neutrinos at the Pierre Auger observatory and improved limit on the diffuse flux of tau neutrinos, *Astrophys. J.* 755 (2012) L4, <http://dx.doi.org/10.1088/2041-8205/755/1/L4> (arXiv: 1210.3143).
- [59] R. Abbasi et al., Constraints on the extremely-high energy cosmic neutrino flux with the IceCube 2008–2009 data, *Phys. Rev. D* 83 (2011) 092003 (arXiv: 1103.4250, doi: 10.1103/PhysRevD.84.079902, 10.1103/PhysRevD.83.092003).
- [60] I. Kravchenko, S. Hussain, D. Seckel, D. Besson, E. Fenholz, et al., Updated results from the RICE experiment and future prospects for ultra-high energy neutrino detection at the South Pole, *Phys. Rev. D* 85 (2012) 062004, <http://dx.doi.org/10.1103/PhysRevD.85.062004> (arXiv: 1106.1164).
- [61] M. Aartsen et al., Evidence for high-energy extraterrestrial neutrinos at the IceCube detector, *Science* 342 (2013) 1242856, <http://dx.doi.org/10.1126/science.1242856> (arXiv: 1311.5238).
- [62] E. Waxman, J.N. Bahcall, High-energy neutrinos from astrophysical sources: an upper bound, *Phys. Rev. D* 59 (1999) 023002, <http://dx.doi.org/10.1103/PhysRevD.59.023002> (arXiv: hep-ph/9807282).
- [63] H. Yuksel, M.D. Kistler, Enhanced cosmological GRB rates and implications for cosmogenic neutrinos, *Phys. Rev. D* 75 (2007) 083004, <http://dx.doi.org/10.1103/PhysRevD.75.083004> (arXiv: astro-ph/0610481).
- [64] K. Kotera, D. Allard, A.V. Olinto, Cosmogenic neutrinos: parameter space and detectability from PeV to ZeV, *JCAP* 1010 (2010) 013, <http://dx.doi.org/10.1088/1475-7516/2010/10/013> (arXiv: 1009.1382).
- [65] S. Yoshida, M. Teshima, Energy spectrum of ultrahigh-energy cosmic rays with extragalactic origin, *Prog. Theor. Phys.* 89 (1993) 833–845, <http://dx.doi.org/10.1143/PTP.89.833>.
- [66] M. Ahlers, L. Anchordoqui, M. Gonzalez-Garcia, F. Halzen, S. Sarkar, GZK neutrinos after the fermi-LAT diffuse photon flux measurement, *Astropart. Phys.* 34 (2010) 106–115, <http://dx.doi.org/10.1016/j.astropartphys.2010.06.003> (arXiv: 1005.2620).
- [67] M. Ave, N. Busca, A.V. Olinto, A.A. Watson, T. Yamamoto, Cosmogenic neutrinos from ultra-high energy nuclei, *Astropart. Phys.* 23 (2005) 19–29, <http://dx.doi.org/10.1016/j.astropartphys.2004.11.001> (arXiv: astro-ph/0409316).
- [68] K. Fang, K. Kotera, K. Murase, A.V. Olinto, A decisive test for the young pulsar origin of ultrahigh energy cosmic rays with IceCube, arXiv: 1311.2044.
- [69] S.W. Barwick, et al., Design and Performance of the ARIANNA Hexagonal Radio Array Systems, Submitted to *IEEE Trans. Nucl. Sci.* (2015).
- [70] C. Reed, for the ARIANNA Collaboration, Performance of the ARIANNA Neutrino Telescope Stations, in: *Proc. 33rd Intern. Cosmic Ray Conf.*, 2013.
- [71] T. Huege, M. Ludwig, C.W. James, Simulating radio emission from air showers with CoREAS, arXiv: 1301.2132.
- [72] T. Huege, The Renaissance of Radio Detection of Cosmic Rays, in: *Proc. 33rd Intern. Cosmic Ray Conf.*, 2013, highlight Contribution, arXiv: 1310.6927.

- [73] T. Huege, C.W. James, Full Monte Carlo simulations of radio emission from extensive air showers with CoREAS. arXiv: 1307.7566.
- [74] D. Heck, G. Schatz, T. Thouw, J. Knapp, J. Capdevielle, CORSIKA: A Monte Carlo code to simulate extensive air showers.
- [75] S. Ostapchenko, Non-linear screening effects in high energy hadronic interactions, Phys. Rev. D74 (2006) 014026, <http://dx.doi.org/10.1103/PhysRevD.74.014026> (arXiv: hep-ph/0505259).
- [76] P. Abreu, et al., The Pierre Auger observatory I: The cosmic ray energy spectrum and related measurements. arXiv: 1107.4809.
- [77] Gerhardt, Lisa, et al., Nucl. Instrum. Meth. A624 (2010) 85–91, <http://dx.doi.org/10.1016/j.nima.2010.09.032>, and others, (arXiv: 1005.5193).
- [78] S. Kleinfelder, Design and performance of the autonomous data acquisition system for the Arianna high energy neutrino detector, IEEE Trans. Nucl. Sci. 60 (2) (2013) 612–618, <http://dx.doi.org/10.1109/TNS.2013.2252365> (for the ARIANNA Collaboration).
- [79] S. Kleinfelder, S. Chiang, W. Huang, Multi-GHz synchronous waveform acquisition with real-time pattern-matching trigger generation, IEEE Trans. Nucl. Sci. 60 (5) (2013) 3785–3792, <http://dx.doi.org/10.1109/TNS.2013.2279660>.
- [80] Model AR-24027E, AFAR Communications Inc., Santa Barbara, CA (2008).
- [81] Model 9602-N, NAL Research Corp., Manassas, VA (2010).
- [82] J.E. Tatar, Performance of sub-array of ARIANNA detector stations during first year of operation (Ph.D. thesis), University of California, Irvine, 2013.
- [83] G. Upton, I. Cook, *A Dictionary of Statistics*, second ed., Oxford University Press, 2008.
- [84] J.C. Hanson, The performance and initial results of the ARIANNA prototype (Ph.D. thesis), University of California, Irvine, 2013.



## Time-domain response of the ARIANNA detector

S.W. Barwick<sup>a</sup>, E.C. Berg<sup>a</sup>, D.Z. Besson<sup>b,f</sup>, T. Duffin<sup>a</sup>, J.C. Hanson<sup>a,b,\*</sup>, S.R. Klein<sup>d</sup>, S.A. Kleinfelder<sup>c</sup>, M. Piasecki<sup>e</sup>, K. Ratzlaff<sup>e</sup>, C. Reed<sup>a</sup>, M. Roumi<sup>c</sup>, T. Stezelberger<sup>d</sup>, J. Tatar<sup>a,g</sup>, J. Walker<sup>a</sup>, R. Young<sup>e</sup>, L. Zou<sup>c</sup>

<sup>a</sup>Dept. of Physics and Astronomy, University of California, Irvine, United States

<sup>b</sup>Dept. of Physics and Astronomy, University of Kansas, United States

<sup>c</sup>Dept. of Electrical Engineering and Computer Science, University of California, Irvine, United States

<sup>d</sup>Lawrence Berkeley National Laboratory, United States

<sup>e</sup>Instrumentation Design Lab, University of Kansas, United States

<sup>f</sup>Moscow Physics and Engineering Institute, United States

<sup>g</sup>Dept. of Physics, University of Washington, United States

### ARTICLE INFO

#### Article history:

Received 5 June 2014

Received in revised form 26 August 2014

Accepted 9 September 2014

Available online xxxx

#### Keywords:

GZK neutrinos

Askaryan effect

Radio detector

### ABSTRACT

The Antarctic Ross Ice Shelf Antenna Neutrino Array (ARIANNA) is a high-energy neutrino detector designed to record the Askaryan electric field signature of cosmogenic neutrino interactions in ice. To understand the inherent radio-frequency (RF) neutrino signature, the time-domain response of the ARIANNA RF receiver must be measured. ARIANNA uses Create CLP5130-2N log-periodic dipole arrays (LPDAs). The associated *effective height* operator converts incident electric fields to voltage waveforms at the LDPA terminals. The effective height versus time and incident angle was measured, along with the associated response of the ARIANNA RF amplifier. The results are verified by correlating to field measurements in air and ice, using oscilloscopes. Finally, theoretical models for the Askaryan electric field are combined with the detector response to predict the neutrino signature.

© 2014 Published by Elsevier B.V.

## 1. Introduction and theory

The origin of ultra-high energy cosmic rays (UHECRs) is an enduring mystery in astrophysics. Because cosmic-rays with energies above  $4 \times 10^{19}$  eV interact with the cosmic microwave background radiation, they have a limited range, so terrestrial cosmic-ray detectors can only probe UHECR sources within  $\approx 75$  Mpc. In these interactions, cosmic-ray protons are excited to a  $\Delta^+$  resonance; when the  $\Delta^+$  decays, it produces neutrinos with energies in the range of  $10^{17}$ – $10^{20}$  eV [1–3]. These neutrinos can be used to probe UHECR sources at cosmic distances.

ARIANNA is designed to detect these neutrinos [4], by observing the coherent radio Cerenkov emission produced when UHE neutrinos interact in Antarctic ice. ARIANNA is located in Moore's Bay on the Ross Ice Shelf, about 100 miles south of McMurdo station. There, the ice is about 570 m thick [5,6], with the Ross Sea beneath it. ARIANNA is placed in Moore's Bay because aerial radar surveys show that the ice-water interface there is smooth and undisturbed, enabling clean reflections of downward-going radio waves off of the interface [7].

High energy particle cascades in ice contain an excess of negatively charged particles (mostly electrons), and radiates coherently at wavelengths that are large compared with the transverse size of the cascade [8]. For a cascade containing  $10^{11}$  particles, the RF radiation is greatly enhanced. When observed along the Cerenkov cone, the radio signal grows linearly with frequency, up to a cutoff given by the size of the negative charge excess – about 1 GHz in ice. Away from the cone, the cutoff frequency is lower; one can use the observed spectrum to determine how far the detector is from the Cerenkov cone.

A number of experiments have used the Askaryan effect to search for cosmogenic neutrinos. One of the first was RICE, which placed antennas in holes drilled at the South Pole [9]. It pioneered the concept of using Antarctic ice to search for neutrinos via radio waves. The ANITA experiment flies an array of horn antennas in the skies above Antarctica, to search for neutrino interactions in the ice [10], having completed two missions thus far. A number of experiments have also used radio-telescopes to search for ultra-high energy ( $> 10^{20}$  eV) neutrino interaction in the Moon [11]. Detectors under construction, like ARIANNA (Moore's Bay) and ARA (South Pole), seek to observe the GZK neutrino flux via surface-array detectors.

\* Corresponding author at: University of Kansas, United States.

E-mail address: j529h838@ku.edu (J.C. Hanson).

ARIANNA detects the radio waves using antennas that are buried shallowly in the ice. The current prototype stations each have four log-periodic dipole antennas (LPDAs) that are buried in a square pattern, facing downward. The antennas on opposite sides of the square are separated by 6 m. The direction to the neutrino interaction can be found by cross-correlating signals in these opposite antennas. The signal polarization is measured by comparing the signals from adjacent antennas. Between this polarization measurement and the determination of the frequency spectrum, the neutrino arrival direction can be determined, given enough channels above background [12] (doubling the channel number from 4 to 8 improves the solution). The amplitude of the waveforms, corrected for distance and ice absorption, provide knowledge of the interaction energy. The shape of the initial electric field, derived from the observed waveforms, would point to variables like the angle with respect to Cerenkov angle and the hadronic/electromagnetic nature of the event.

Monte Carlo simulations have been used to predict the signals that would be produced by neutrino interactions in the ice [13,14]. Both charged current (CC) and neutral current (NC) interactions are of interest. In NC interactions, neutrinos scatter from a target nucleus, depositing an average of 20% of their energy in the ice, in the form of a hadronic cascade. Charged-current interactions are similar, except that the neutrino produces a lepton which carries the remaining energy. Charged-current  $\nu_e$  interactions produce an electron, creating an additional electromagnetic cascade (this discussion does not distinguish particle from anti-particle). Tau leptons from CC interactions also produce Askaryan pulses, albeit at a significant separation ( $\approx 1$  km) from the point of the neutrino interaction.

## 2. Antenna effective height

The antenna response to time-varying Askaryan electric field may be parameterized in terms of an effective height operator. This height may be determined by measuring the antenna response to a broad-band signal. To measure the LPDA effective height, two identical LPDAs were placed inside an anechoic chamber, facing each other. One LPDA transmitted an impulse, and the other received it, a distance  $r$  away. The received signal voltage is shown in Eq. (1) and derived below.

$$V_L(t) = \frac{2^2}{2\pi rc} \left( \frac{Z_L Z_0}{(Z_L + Z_{in})^2} \right) \vec{h}_{rx} \circ \vec{h}_{rx} \circ \dot{V}_{src}(t) \quad (1)$$

In Eq. (1), the circles denote the convolution operator,  $Z_0$  is the impedance of free space ( $\approx 120\pi$ ),  $Z_{in}$  is the antenna impedance ( $\approx 50\Omega$ ),  $c$  is the speed of light ( $\approx 0.3$  m/ns),  $V_L$  is the received voltage at the antenna port,  $V_{src}$  is the original voltage impulse transmitted through the first antenna, and  $\vec{h}_{rx}$  is the vector-like effective height. Measurements in this work were co-polarized, so the vector symbols will be dropped from now on. For similar measurements of LPDA effective height characterization, see [15,16]. Convolution is linear, commutative, and overall time-invariant.

Eq. (1) is now derived. A receiver with input line impedance  $Z_L$  is connected to an antenna of impedance  $Z_{in}$ . The voltage seen by the receiver is reduced by a factor

$$\frac{V_L}{V_{O.C.}} = \frac{Z_L}{Z_L + Z_{in}} \quad (2)$$

The open-circuit voltage of the antenna-receiver system is  $V_{O.C.}$ . The effective height is proportional to this factor [17,18]. The authors of [18] also include a factor of 2 such that the voltage delivered to the receiver is

$$V_L(t) = 2 \left( \frac{Z_L}{Z_L + Z_{in}} \right) h_{rx}(t) \circ E(t) \quad (3)$$

The factor of two out front in Eq. (5) is consistent with [18], in which the effective height operator was used to predict (correctly) the Askaryan amplitude of an electromagnetic cascade in the lab. The factor of two corrects  $V_L$  from the observed data on the  $50\Omega$ -scope to the voltage actually produced by the antenna. For the transmitter, the ratio of the voltage delivered to the antenna to the open-circuit voltage is [17]

$$\frac{V_A}{V_{O.C.}} = \left( \frac{Z_{in}}{Z_{in} + Z_L} \right) \left( \frac{Z_0}{Z_{in}} \right) \quad (4)$$

The additional factor  $Z_0/Z_{in}$  is included to account for the antenna coupling the radiated electric field to the impedance of free space. The electric field radiated by the transmitter is therefore

$$E(t) = \frac{1}{2\pi rc} \left( \frac{Z_{in}}{Z_{in} + Z_L} \right) \left( \frac{Z_0}{Z_{in}} \right) h_{tx} \circ V_{src}(t) \quad (5)$$

Before combining Eqs. (3) and (5), the relationship between  $h_{rx}$  and  $h_{tx}$  must be mentioned, and it is shown in Eq. (6). The authors of [17,16] differ on the factor of 2 in Eq. (6), but only due to slightly different definitions of antenna quantities. One motivation of the time-derivative in Eq. (6) is that antennas do not radiate DC voltages; in the Fourier domain, time-derivation becomes multiplication of the original function by the frequency, so that  $h_{rx}(\omega) \rightarrow 0$  for  $\omega \rightarrow 0$ .

$$h_{tx} = 2\partial_t h_{rx} \quad (6)$$

Integration by parts, and the *stability condition* of the linear time-invariant system ( $h_{rx}(t) \rightarrow 0$  for  $t \rightarrow \pm\infty$ ) allows the transfer of the time-derivative to the input signal. Therefore, Eq. (5) can be rewritten:

$$E(t) = \frac{1}{\pi rc} \left( \frac{Z_{in}}{Z_{in} + Z_L} \right) \left( \frac{Z_0}{Z_{in}} \right) h_{rx} \circ \dot{V}_{src}(t) \quad (7)$$

Combining (3) and (7) produces

$$V_L(t) = \frac{2^2}{2\pi rc} \left( \frac{Z_L Z_0}{(Z_L + Z_{in})^2} \right) h_{rx} \circ h_{rx} \circ \dot{V}_{src}(t) \quad (8)$$

The LPDAs in the anechoic chamber are co-polarized and impedance matched to the  $50\Omega$  input impedance of the oscilloscope and amplifier ( $Z_L \approx Z_{in}$ ), so (8) simplifies to

$$V_L(t) = \frac{1}{2\pi rc} \left( \frac{Z_0}{Z_L} \right) h_{rx} \circ h_{rx} \circ \dot{V}_{src}(t) \quad (9)$$

Eq. (9) provides the basis for measuring the effective height. Using the effective height, and similar *transfer functions* for the other components in the ARIANNA data acquisition, neutrino signals may be predicted for a given model of Askaryan radiation. The impedance matching criterion is discussed further in the appendix.

## 3. Experimental technique

**Fig. 1** contains a diagram of the LPDA, a Create CLP5130-2N, and defines the terms E- and H-plane, with respect to the antenna design. The geometry of the LPDA provides the advantage of frequency-independent broadband response, similar to a radio horn. The advantage over a horn (as is revealed by the data) is the uniformity of the response over a wide range of angles. The beam width, VSWR, radiated power, and gain are all favorable over the 105–1300 MHz range. Monte Carlo simulations [12] show that such an antenna maximizes broadband neutrino signal over backgrounds.

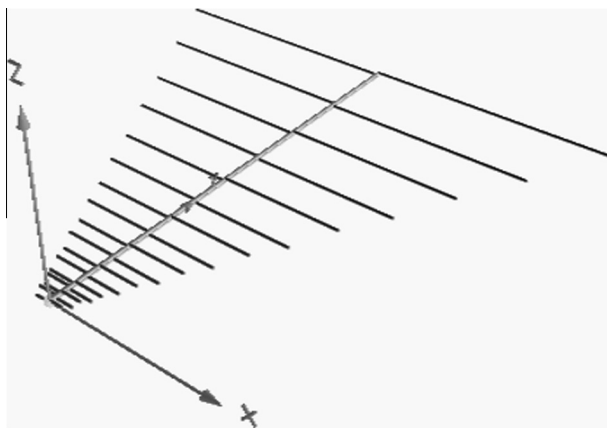


**Fig. 1.** A diagram of the LPDA, demonstrating the logarithmic spacing and dipole length. The  $x$ - $y$  plane contains the dipole elements (*tines*), and is denoted the E-plane. The H-plane, in this case, is the  $y$ - $z$  plane. The  $-y$  direction is the forward direction of the LPDA. The longest ( $\lambda/2$ ) dipole is 1.45 m, and the length ratio of adjacent dipoles is 0.83. The 1.385 m-long spine holds the dipoles in place, and the feed point is at the shortest dipole (at the origin).

Two LPDAs were arranged a distance  $r = 5.72$  m apart, facing towards each other (boresight configuration), inside of an anechoic chamber. A 400 ps wide impulse from an Avtech pulser was sent through coaxial cable to the transmitter, and the received signal was recorded on a Tektronix TDS5104 oscilloscope with a nominal bandwidth of 1 GHz. The spectrum of this raw impulse signal, as measured with the oscilloscope, matches the spectrum taken with a 2.5 GHz bandwidth spectrum analyzer up to a frequency of 1.25 GHz. Above this frequency, the oscilloscope begins to attenuate the data. Results above this benchmark frequency should not be trusted. Fig. 2 shows the experimental setup. The receiving LPDA was attached to a post via a rotating flange, and the post is fixed to a rotating turntable. The flange and turntable apparatus enabled independent rotation of the receiver in both  $\theta$  and  $\phi$ .

The total system transfer function besides that of the antennas was shown to be a small correction, by comparing the raw pulse with the pulse propagated through all cables in the system (Fig. 3). The 400 ps width of the pulse sent to the transmitter was sufficiently narrow to guarantee that the highest frequencies

of the LPDA were probed. To ensure that the entire bandwidth was accessible to the instrumentation, the voltage standing wave ratio (VSWR) was measured by a network analyzer built into the chamber systems (Fig. 3). The VSWR is a standard RF probe of antenna efficiency; a VSWR of 1.0 indicates all transmitted energy is being radiated with high efficiency.

In the anechoic chamber, the antenna was properly grounded and isolated from interfering electronic equipment, and the VSWR is near 1.0 for the experimental bandwidth. The VSWR of these antennas was measured previously during the installation of the first ARIANNA prototype station [19]. Those measurements recorded a VSWR of  $\approx 1.5$  from 100 MHz to above 1 GHz, when the antenna was  $\approx 1.5$  m above the snow surface. When the antenna was buried in densely packed snow, the VSWR was 1.5 down to 80 MHz. The index of refraction of the surface snow in Moore's Bay is  $n = 1.29 \pm 0.02$  [5], and this result has been measured with several techniques [19,20]. The LPDA responds to the longest wavelength that physically can exist on the longest  $\lambda/2$  dipoles. In a dielectric medium, the wavelength corresponding to a given frequency decreases by one factor of the index, meaning that 80 MHz can fit onto the 1.45 m LPDA dipoles (the longest pair). This effect is confirmed in NEC4 simulations [21], where the accompanying shift in antenna impedance is not enough to reduce the efficiency. This point will be discussed further in Section 5.2.

The programmable turntable was used to rotate the receiving antenna in both the E- and H-planes. The E-plane is the plane containing the LPDA tines (associated with the spherical coordinate  $\phi$ ), and the H-plane (associated with the spherical coordinate  $\theta$ ) is orthogonal to the E-plane, and contains the LPDA central spine (Fig. 1). For the pulsed measurements, waveforms were measured in 10 degree increments in the E and H-planes, beginning with  $0^\circ$  in each. The configuration at  $0^\circ$  in both planes is the boresight configuration, with the LPDA receiver facing the transmitter head-on. The E-plane was fully probed by the pulsed data, and 67% of the H-plane was probed. The missing third of the H-plane arose from limitations in the rotating flange, which was not able to tilt beyond  $\pm 63^\circ$  in the H-plane.

The response is not expected to vary significantly versus  $\theta$  until the incident wave is outside the H-plane front lobe (Fig. 4). The network analyzer was used to map the radiation pattern, shown in Fig. 4. A simple model of log-periodic antennas [22] is shown as well. The model is tuned to have the same geometric parameters as the CLP5130-2N, and the same bandwidth and number of dipole elements. The agreement is good for the forward lobes in the E and H-planes, and the back lobe in the H-plane. The E-plane result agrees in overall scale, but fluctuates around the average model prediction. For the experimental bandwidth, a front-to-back ratio of  $\approx -15$  dB is observed across the bandwidth, in accordance with the manufacturer specifications. The front-to-back ratio is the ratio of received power at  $180^\circ$  to  $0^\circ$  in the E-plane, for identical transmission signals. Note that, in Fig. 4, the H-plane angle of  $0^\circ$  indicates the forward direction. In subsequent figures, the H-plane is associated with the polar angle,  $\theta$ , in which case the forward direction is  $\theta = 90^\circ$ , where the antenna rests in the  $x$ - $y$  plane.

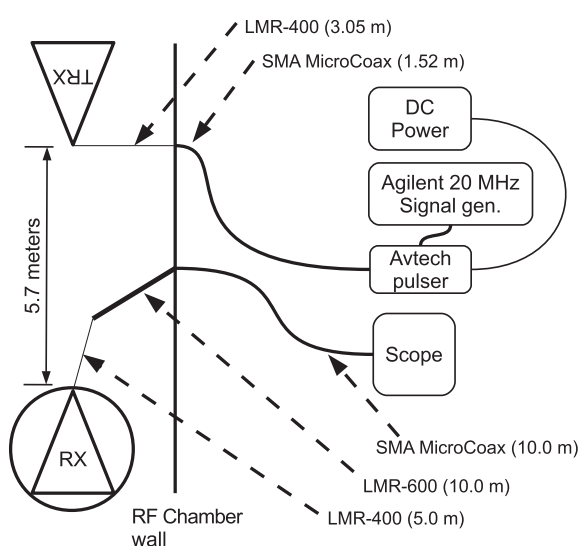


**Fig. 2.** The experimental setup of the bore-sight configuration. The Avtech was a model AVP-AV-1S type pulser, capable of 0.4 ns pulse widths.

## 4. Results and analysis

### 4.1. Data

The data from the boresight configuration is shown in Fig. 5. The scope recorded a downward-chirping signal approximately 40 ns wide, probing all frequencies accessible to the LPDA, according to the VSWR measurements (Fig. 3). A reflection is observed 67.5 ns after the initial pulse, and can be verified with auto-correlation

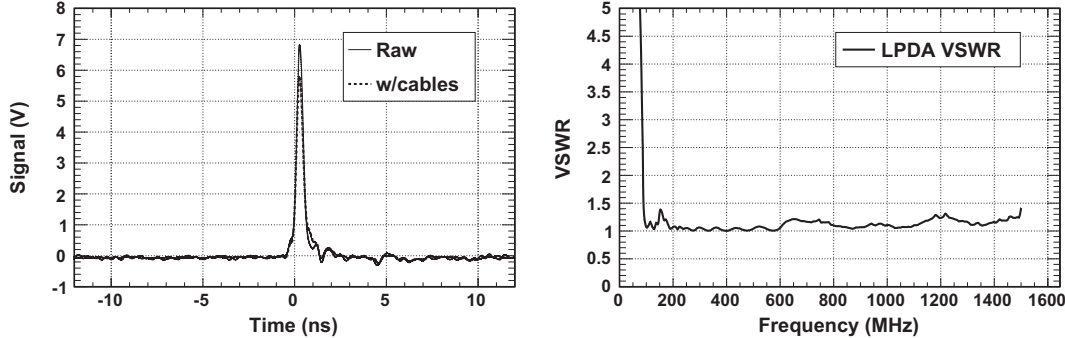


**Fig. 3.** (Left) The raw pulse sent to the transmitting antenna, as measured on the 1 GHz scope (Fig. 2), along with the raw pulse after having propagated through all coaxial cables in the system. (Right) The VSWR of the receiving antenna, measured by a network analyzer just outside the anechoic chamber.

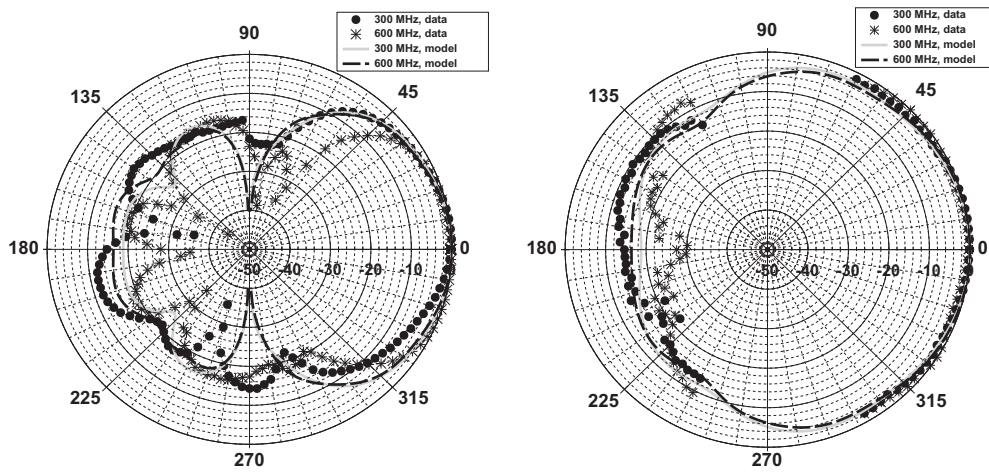


**Fig. 4.** The radiation pattern of the CLP-5130-2N LDPA (normalized to 0 dB maximum). The angles are relative to boresight in the counter-clockwise sense. (Left) the E-plane radiation pattern at 300 and 600 MHz, compared to a log-periodic simulation of the E-plane. (Right) the H-plane radiation pattern at 300 and 600 MHz, compared to the same simulation for H-plane. Note that 0° in the H-plane indicates the forward direction in this graph.

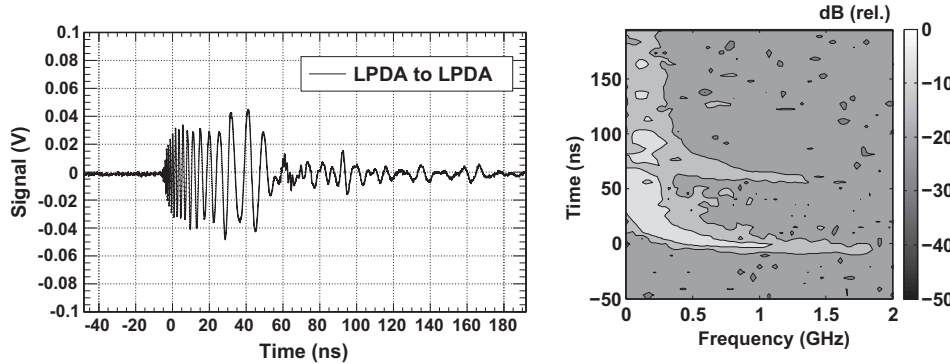


**Fig. 5.** (Left): The boresight time-domain results, shifted such that the trigger location is at 0 ns. (Right): a spectrogram of the boresight data, with the oscilloscope DC offset removed. The power is in units of dB, relative to maximum power.

of the data. The analysis was performed only on the first 67.5 ns of data, before the reflection. Similar pulse data was taken at all available turntable angles, and the input pulse was not changed. The chirping form of the impulse data has a simple explanation: the placement of the feed point on the LDPA causes the radiated phase, and group delay, to have predictable dependencies on frequency:

$$\phi(\omega) = \frac{\pi}{\ln \tau} \ln \left( \frac{\omega}{\omega_1} \right) \quad (10)$$

$$\tau_g(\omega) \equiv -\frac{d\phi}{d\omega} = -(2\pi \ln \tau)^{-1} \quad (11)$$

The overall minus sign in the group delay  $\tau_g(\omega)$  simply indicates a physical delay, rather than an earlier signal. In Eq. (10),  $\omega_1$  is the angular frequency of the shortest radiating dipole, and  $\tau$  is the ratio of the length of adjacent dipole elements. The location of the LPDA feed-point delays radiation of components with lower frequencies. Fortunately, this effect can be undone with a knowledge of the components' frequencies, and the LPDA  $\tau$ -parameter

( $\tau = 0.83$  for the CLP-5130-2N) [23,24]. Because of the simple form of Eq. (10), an operator which commutes with the detector response can be constructed that removes the phase dispersion.

Examples of data from off-boresight configurations are shown in Figs. 6 and 7. These data demonstrate that it is not sufficient, for a broadband antenna, to model the time-response as the bore-sight function times the relative gain versus angle of the antenna. The radiation pattern depends on frequency, and the phasing must be studied at all angles to accurately predict signals. For example, a high-frequency incident plane wave interacting with the antenna at oblique angles changes the order in which antenna elements produce a voltage. Thus, the relative phasing between elements must depend on the orientation of the system.

#### 4.2. Analysis

Eq. (9) represents the model used to explain the time-domain data. Eq. (9) can be re-written:  $xV_L(t) - h \circ h \circ \dot{V}_{src}(t) = 0$ , with  $x = (Z_L/Z_0)2\pi rc$ . An algorithm was developed to derive the waveform representation of  $h$  that solves this equation. Fig. 8 demonstrates how, after many iterations, a solution for  $h$  was found that satisfies the equation with  $x$  defined as above. Because of the shape of the LPDA, the expectation for the solution is a rapidly oscillating chirp that decreases in frequency as time increases.

During each iteration, the algorithm adds a small amount of white noise to the effective height samples  $[s_1 : s_n]$ , and nothing to subsequent samples  $[s_{n+1} : s_N]$ , where there are  $N$  samples total. The result is kept only if the solution to  $xV_L(t) - h \circ h \circ \dot{V}_{src}(t) = 0$  improves. Improvement is defined as a decrease in the mean squared-difference between model and data, denoted the score,  $S$ :

$$S = N^{-1} \sum_{i=1}^N (s_{i,data} - s_{i,model})^2 \quad (12)$$

If the score decreases, there is a 1%-percent chance that  $n \rightarrow n + 1$  (a randomly drawn number between 0 and 1 must be less than 0.01). Thus, the algorithm focuses early action on the high-frequency content of the response, leaving the simpler low-frequency oscillations for the end of the calculation. The calculation terminates when the score has decreased by a factor of  $\approx 100$ , which is typical of convergence (subsequent iterations produce only marginal improvement).

The algorithm was applied to all the angles measured with the anechoic chamber turntable. The main lobe results converge and provide the effective height versus time. The LPDA null zones are not studied in detail, as the neutrino signals are heavily attenuated there. Several instances of the results are shown below in Fig. 9. The beam-width of the LPDA is 60° in the E-plane, meaning

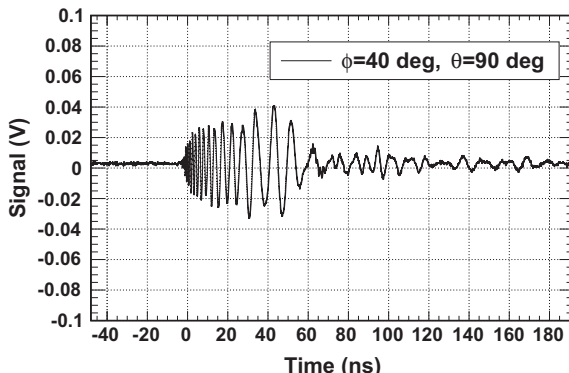


Fig. 6. The pulse data from the anechoic chamber at an angle of  $\phi = 40^\circ$  ( $\phi$ : angle in E-plane), and  $\theta = 90^\circ$  ( $\theta$ : angle in H-plane, with 90° corresponding to boresight).

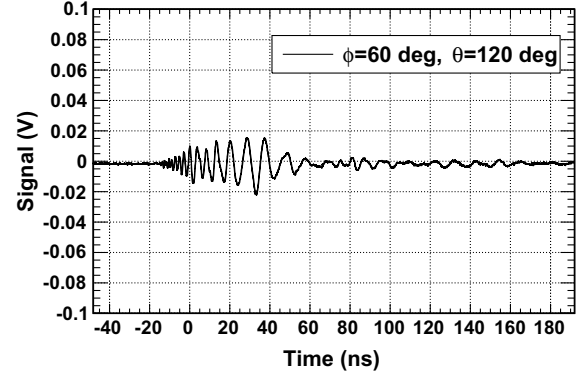


Fig. 7. Similar to Fig. 6, except at  $\phi = 60^\circ$ ,  $\theta = 120^\circ$ .

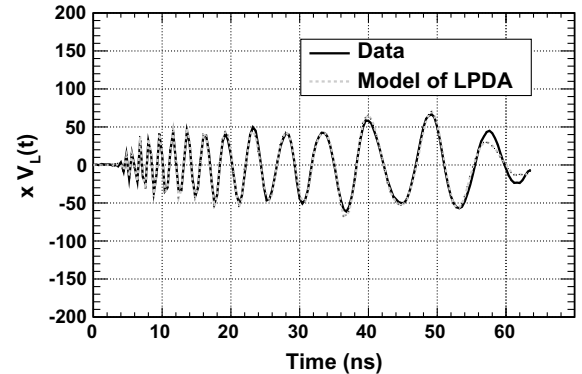


Fig. 8. The algorithm finds a solution for the effective height,  $h(t)$ , vs. time. The solution found by the algorithm (model of LPDA), solves the equation  $xV_L(t) - h \circ h \circ \dot{V}_{src}(t) = 0$ , in order to match the anechoic chamber data (data). The algorithm terminates after the mean squared-difference between model and data (the score) has improved by a factor of  $\approx 100$ .

radiated power is reduced by 3 dB at  $\pm 30^\circ$  from boresight. As the observation in the E-plane (Fig. 9, top) begins to take place outside the beam width, the amplitude shifts more rapidly, and is concentrated at lower (100–200 MHz) frequencies. The H-plane dependence (Fig. 9, bottom) is gradual, because the beam width is wider and more consistent in frequency.

#### 5. Confirmations of measurements

Although the solutions for the LPDA response converge such that they match laboratory data, it is necessary to show that response solutions explain multiple independent measurements. Section 5.1 demonstrates that anechoic chamber measurements with the ARIANNA low-noise amplifier can be explained with the impulse response of the amplifier, combined with the that of the LPDA. Section 5.2 involves independent measurements of the temperature-averaged RF attenuation length of the ice beneath the deployed ARIANNA stations in Moore's Bay.

In this section, pulses reflected from the ocean/ice interface are modeled using the ice properties and antenna properties. Time series data from the 2006–7 and 2013–14 Antarctic seasons are used. The 2013 oscilloscope data was observed to agree with the ARIANNA data acquisition system, a result that has been demonstrated before [25]. The measurements of the ice properties were made in the interim (2010–10 and 2011–12), and are calibrated to be independent of the antenna model. Section 5.3 uses data taken in 2010 in Aldrich Park at UC Irvine, with different antenna orientations.

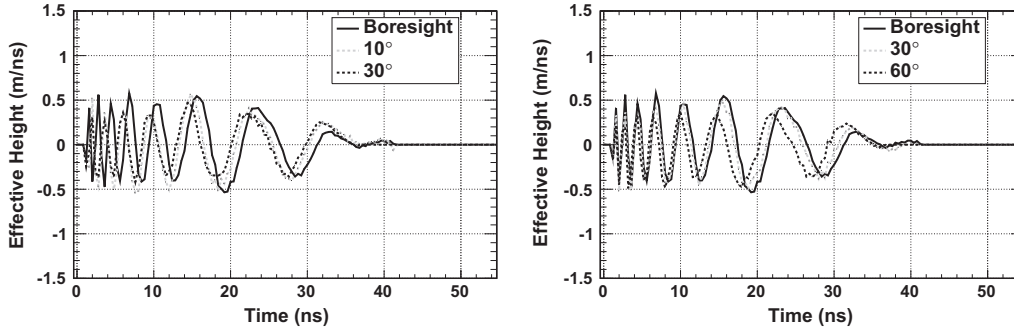


**Fig. 9.** The results for the effective height. (Left): selection of E-plane results, with  $\phi$  varying,  $\theta = 90^\circ$ . (Right): the same for the H-plane, with  $\theta$  varying,  $\phi = 0^\circ$ . In all cases the radiated wave polarization is parallel to the transmitter E-plane, which was kept fixed.

### 5.1. ARIANNA custom amplifier

The ARIANNA amplifier was designed to match the antenna signals to the ARIANNA waveform digitizers, while maintaining a high signal to noise ratio (a small noise figure). The specific design used here was developed in 2012, powered by 3.3 V DC, with a [50–1000] MHz bandwidth. The gain decreases with frequency (Fig. 10), so the impulse response function is not a  $\delta$ -function. To measure the impulse response, a 0.5-ns wide pulse was attenuated and fed directly into the amplifier. The output waveform was recorded, and from that waveform the impulse response was computed such that convolution of the response and the impulse produced the output waveform. The gain versus frequency, and impulse response are plotted in Fig. 10.

The amplifier was inserted into the anechoic chamber system, between the 1 GHz oscilloscope and the LPDA receiver, with a total of 36 dB of attenuation added in the system. The resulting data in Fig. 11 has been corrected for attenuators. The data matches the model, in amplitude and shape. The (Pearson) correlation coefficient,  $\rho$ , is used to quantify agreement between signals  $x$  and  $y$ :

$$\rho = \frac{\text{Cov}(x, y)}{\sqrt{\text{Var}(x)\text{Var}(y)}} \quad (13)$$

For the result in Fig. 11,  $\rho = 0.89$ . The equation for the modeled waveform is identical to that of the anechoic chamber system (Eq. (9)), with the amplifier impulse response (denoted  $A$ ) added. (The constant numerical factors in front of Eq. (14) commute with the convolution operators). If either the amplifier transfer function, or the LPDA response function are not included, then the correlation coefficient drops to insignificant levels. The model amplitudes for early times, corresponding to higher frequency content, are slightly smaller than the data. This has little effect on  $\rho$ , however, because  $\rho$  values are driven by the most powerful amplitudes.

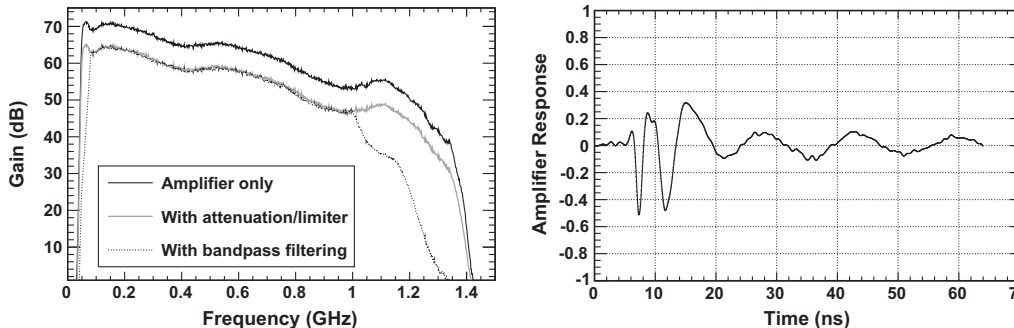


**Fig. 10.** (Left): The gain vs. frequency of the ARIANNA amplifier. (Right): The impulse response of the ARIANNA amplifier. The y-axis has been normalized such that the auto-correlation of this response is 1.0.

**Fig. 11.** Anechoic chamber amplified data, with model. The recorded data is shown as a solid line, and the dashed line is the model from Eq. (14). Agreement between the model and data is considered good because  $\rho = 0.89$ .

$$V_L(t) = \frac{1}{2\pi c} \left( \frac{Z_0}{Z_L} \right) A \circ h_{rx} \circ h_{tx} \circ \dot{V}_{src}(t) \quad (14)$$

### 5.2. Ice shelf data

The RF attenuation length of the ice shelf in Moore's Bay has been measured several times (c.f. [5,20]), and will be updated in a forthcoming publication. In each radio echo measurement, a calibration pulse is recorded by the receiver and transmitter system. The antennas are then pointed down, and the recording oscilloscope is triggered on a delay such that it records the reflection from the ice/ocean interface beneath. By comparing the calibration pulse to the reflected pulse, the attenuation length is measured. The shelf depth is extracted from the oscilloscope time delay that captures

the reflection. The shelf-depth obtained this way is  $576 \pm 8$  m. The attenuation length  $\lambda(v)$  causes the electric field mode  $E(v)$  at frequency  $v$  to be absorbed in the ice as  $\propto \exp(-r/\lambda(v))$ . The introduction of the reflection coefficient for electric fields accounts for the ocean/ice interface. Table 1 summarizes linear fits to the attenuation length vs. frequency data over several seasons in Moore's Bay, assuming 100% reflection at the ocean surface.

The linear fits to the data from all seasons are consistent, as demonstrated in Table 1. The attenuation lengths are conservative, because some of the returned power loss could be attributed to a non-ideal reflection coefficient. Prior measurements indicate that the interface in Moore's Bay is smooth compared to the shelf ice near the coast, [7,26]. Newer measurements of the reflection coefficient  $\sqrt{R}$  indicate that  $\sqrt{R} \approx 1$  [5,6], with almost negligible surface roughness. A more detailed discussion of the ice properties of Moore's Bay can be found in [5], and in forthcoming publications. Following convention,  $R$  is the reflection coefficient for signal power, and  $\sqrt{R}$  for electric field amplitudes. To model the reflections from the ocean, Eq. (14) is applied, with an additional step to account for the frequency-dependent attenuation length, and a reflection coefficient (Eqs. (15)–(17)). The 180-degree phase-shift caused by reflection between ice and salt water requires an overall minus sign.

$$E(t) = \left(\frac{1}{2\pi c}\right) \left(\frac{Z_0}{Z_L}\right) h_{rx} \circ \dot{V}_{src}(t) \quad (15)$$

$$\tilde{E}(v) = F_v(E(t)) e^{-i\lambda(v)/r} \quad (16)$$

$$V_L(t) = -\sqrt{R} h_{rx} \circ F_v^{-1}(\tilde{E}(v)) \quad (17)$$

Eq. (15) is just Eq. (7) for the matched-impedance case, and the input pulse  $V_{src}$  was typically a 2.5 kV, 1 ns wide pulse from a Pockel Cell driver. In the 2006 measurement, the receiver and transmitter antennas were Seavey radio horns, and the measured effective height, at boresight, is shown in [10]. In the 2013 measurement, the receiving antenna was the ARIANNA LPDA. Because the attenuation length depends on frequency, the data is transformed to the Fourier domain, multiplied by the frequency-dependent attenuation factor, and transformed back to the time domain (Eqs. (16) and (17)). The operators  $F_v$  and  $F_v^{-1}$  represent the Fourier transform and inverse Fourier transform, respectively. Eq. (17) is just Eq. (3), in the matched-impedance case. No correction is made to  $h_{rx}(t)$  for the effect of the surface snow, which has an index of  $1.29 \pm 0.02$  (see below).

Fig. 12, left, presents the comparison of the 2006 data, and Fig. 12, right, the more recent data. A prototype of the ARIANNA analogue transient waveform digitizer (ATWD) was brought to Moore's Bay in 2010, and recorded similar results [25]. The linear fit  $\lambda(v) = -(140 \pm 20) \text{ m/GHz} + (470 \pm 20) \text{ m}$  was used for the attenuation length, and  $\sqrt{R} = 1.0$ , from Table 1 (These numbers are consistent with prior measurements, and will be updated in a forthcoming publication). Notice that, in either comparison, the negative sign in front of Eq. (15) is necessary to obtain the correct phase, indicating that the reflection at the ocean/ice interface is taking place between two materials with differing indices of refraction ( $n_2 > n_1$ ).

**Table 1**

Attenuation length fit parameters, assuming 100% reflection at the shelf-bottom. The year and transmitter/receiver models (TX/RX) are shown in the first and second columns, respectively. The constant and slope of the linear fits are in the third and forth columns, respectively, and the  $\chi^2/\text{dof}$  is shown in the fifth column. The form of the linear fit is  $\lambda(v) = L_0 + \alpha v$ . The 2006 data was published with 25 MHz bins, and has a larger  $\chi^2/\text{dof}$ . With 150 MHz bin-width, the  $\chi^2/\text{dof}$  is reduced to 0.4. The final row indicates a fit to the average of all data collected.

Year	TX/RX	$L_0$ (m)	$\alpha$ (m/GHz)	$\chi^2/\text{dof}$
2006	S/S	$450 \pm 10$	$-120 \pm 10$	2.4
2011	L/L, S/L	$475 \pm 30$	$-150 \pm 60$	0.42
Ave.	L/L, S/L, S/S	$470 \pm 20$	$-140 \pm 20$	0.3

The correlation coefficients are larger than the naive expectation for signal correlation with noise:  $\rho \approx 0$ . Further studies of the thermal noise environment at the temperatures of Moore's Bay with the ARIANNA system indicate that the correlation between signal and realistic noise is  $\approx 0.2$  for un-altered bandwidth, and  $\approx 0.3$  for bandwidth-limited noise in the presence of band-pass filtering [27]. A good discussion of this subject can be found in [28]. Fig. 13 demonstrates that if the pulse from Fig. 12 is sent through the air, with the same equipment, the comparison still indicates agreement. That is, the quality of the model does not depend on the frequency dependent attenuation profile of the ice.

It is important to note that the snow plays no role in the agreement between model and data in Fig. 12. Several factors that could be corrected, due to the snow, are the medium conductivity, antenna impedance and the group delay. The antenna simulation package NEC4 [21] was used to reproduce in-air properties of the LPDA (such as impedance, VSWR, and radiation pattern), by solving for the antenna current using a method-of-moments approach. The simulation package allows the antenna to be embedded in a dielectric medium, with tunable index,  $n$ , and conductivity. The conductivity of Antarctic surface snow is small ( $\approx 10 \mu\text{S}/\text{m}$ ) [29]. Varying the conductivity by an order of magnitude technically changes the antenna impedance, but not enough to effect  $h_{rx}(t)$ .

The simulated NEC antenna impedance is affected mainly by  $n$ : the real and imaginary parts of  $Z_{in}$  are shifted down by a factor of  $n$ , and to lower frequencies:  $v \rightarrow v/n$ . However, the LPDA is designed for broadband, frequency-independent use, and the shift in lower cutoff frequency from 105 to 80 MHz has little effect on the structure of  $h_{rx}(t)$  (derived from simulated parameters). The reduction by a factor  $n$  in  $Z_{in}$  could have caused a  $\approx 15\%$  reduction in the amplitude of  $h_{rx}(t)$  (which goes as  $|\sqrt{Z_{in}}|$ ). However, the average  $|Z_{in}|$  is  $80\Omega$  in the NEC4 model (agreeing with network analyzer measurements in air), whereas Eq. (9) assumes  $50\Omega$ . The measured  $h_{rx}(t) \circ h_{rx}(t)$  must therefore be a factor of  $(Z_L + Z'_{in})^2 / (Z_L + Z_{in})^2$  larger, to compensate. With  $Z_L = 50\Omega$ ,  $Z'_{in} = 80\Omega$ , and  $Z_{in} = 50\Omega$ , this factor is  $1.3^2$ , which is equal to the measured  $n^2$ . When the antennas are placed in snow (and each  $h_{rx}(t)$  drops by  $\sqrt{n}$ ),  $Z_0 \rightarrow Z_0/n$ . Thus, these effects in Eq. (9) cancel when the LPDA is placed in the snow. Ultimately, the empirical data matches the model, and it is safe to assume the role of the snow is negligible.

The NEC model was also used to check that the position of the LPDA does not strongly affect the results. The depth of the LDPA does not affect the impedance as long as  $n$  is constant near the surface. Near the air/snow interface, this is most likely a first-order approximation. However, measurements of the VSWR in [19] reveal that the LPDA bandwidth extends down to 80 MHz, verifying the NEC model prediction near the surface. Because the front-to-back (F/B) ratio of the LPDA is  $-15$  dB, surface effects likely do not matter as long as the antenna is facing downward. Density measurements of the surface firn vs. depth [5,20] indicate that treating the index as a constant for the first few meters is reasonable. Finally, because the group delay is the derivative of the S21 phase, it is a relative quantity should not be affected as long as the index is constant. As a final check, the simulated impedance, gain, and the theoretical group delay equation were folded into the standard formula for  $h_{eff}(v)$  [30] and inverse Fourier-transformed to obtain  $h_{rx}(t)$ . The snow and air versions of  $h_{rx}(t)$  had a correlation coefficient of 0.98 in this case.

### 5.3. Further comparisons in air

The time-domain model derived from anechoic chamber data must be checked for a variety of situations, including locations with no ice or snow, and different band-pass filtering. In 2010, data was taken in Aldrich Park to investigate the LPDA waveform shape for a variety of angles. Filters rejecting CW noise were applied.

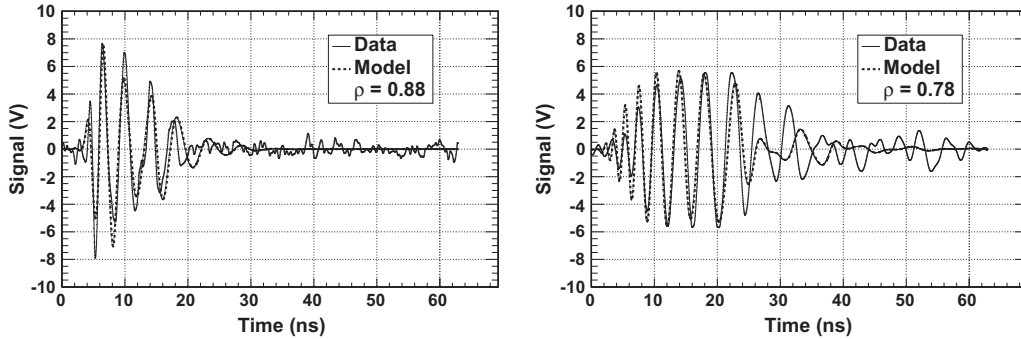


**Fig. 12.** (Left): 2006 Moore's Bay comparison. (Right): 2013 Moore's Bay comparison. The recorded data are shown as solid lines, and the model from Eq. (15) is shown as a dashed line. The value of  $\rho$  is 0.88 for the 2006 data and 0.78 for the 2013 data, indicating agreement. The waveforms have been corrected for attenuators used to keep amplitudes in the linear range of amplifiers and oscilloscopes.

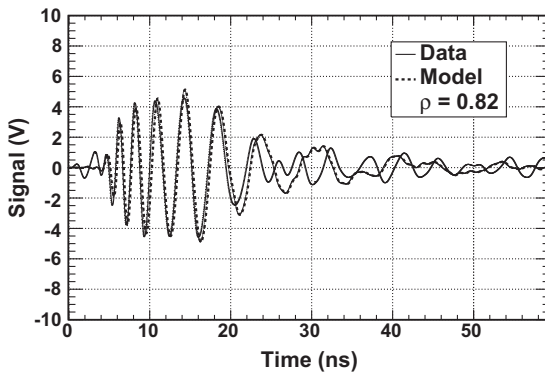


**Fig. 13.** In-air Seavey to LPDA calibration through 23 m of air. The recorded data is shown as a solid line, and the model from Eq. (15) is shown as a dashed line ( $r = 23$  m,  $\lambda = \infty$ ). The value of  $\rho = 0.82$ . The waveforms have been corrected for attenuators used to keep amplitudes in the linear range of amplifiers and oscilloscopes.

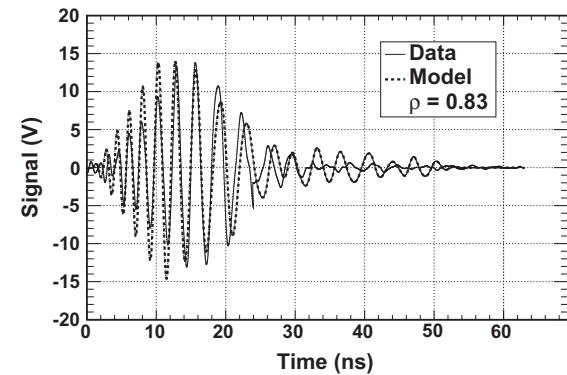


**Fig. 14.** A model of a pulse obtained in Aldrich Park in 2010, using two LPDA antennas, a PCD, and filters, with a separation of 5 m. The correlation coefficient is  $\rho = 0.79$ .

**Table 2**

Correlation coefficients,  $\rho$ , determined from the different measurements described in the text.

Exp. Setting	Fig.	$\rho$
Chamber+amplifier	11	0.89
Ice sounding (Moore's Bay 2006)	12	0.88
Ice sounding (Moore's Bay 2013)	12	0.78
In-air over ice (Moore's Bay 2012)	13	0.82
In-air (Aldrich Park 2010)	14	0.83

time from the signal, and the noise level produced the same signal to noise ratio as the data when added to the model.

## 6. Askaryan pulses in ARIANNA data

Given an understanding of how the Askaryan electric field would be transformed in the data acquisition, the next logical step is to predict properties of the signal based on a theoretical understanding of the neutrino interaction. Various authors have studied the problem theoretically [13,14,31], and several experimental confirmations have been achieved [32,33]. The experimental observations recreate the ultra-high energy electroweak interaction by building a cascade energy equivalent to the expectation for a cosmogenic neutrino. The total energy is equal to the sum of the separate energies of the charged particles in a beam built from photons or electrons.

The negative charge excess that develops over several meters in the dielectric material leads to RF radiation, and the shape of the pulse reflects the details of the longitudinal development of charge,

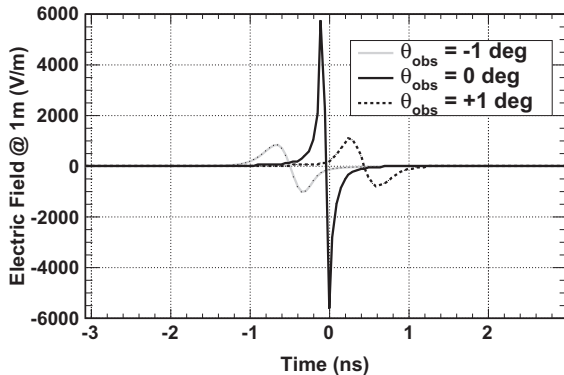


**Fig. 15.** The electric field pulse created by a 100 TeV event, scaled to an energy of 10 EeV,  $\theta_{\text{obs}} = -1^\circ, 0^\circ$  and  $1^\circ$ .

and perspective from which the pulse is observed, since the highest frequencies are confined to the Cerenkov angle. In Section 6.1, signal predictions are shown with respect to the observation angle relative to the Cerenkov angle. In Section 6.2, the result of varying the angle at which the Askaryan pulse interacts with the ARIANNA antenna is presented.

#### 6.1. Prediction vs. observation angle

A description of how Askaryan electric fields are generated from the negative charge excess profile versus cascade depth can be found in [13,14], and early Monte Carlo studies in [34]. Several key observations arise from these calculations. First, the electric field amplitude (and vector potential) scales with the total energy, due to coherence effects. Second, the shape of the electric field corresponds to a temporal derivative with respect to the retarded time of the excess negative charge profile. Because the charge excess is moving in the lab frame, the pulse shape traces the derivative of the excess charge with respect to cascade depth. The LPM effect [35] stretches the charge excess profile above  $10^{16}$  eV, and therefore stretches the pulse, while reducing the amplitude. Secondary peaks in the charge distribution and therefore the electric field are also caused by the LPM effect. Because the pattern of energy deposition varies from event to event in the strong-LPM regime, there can be considerable event-to-event variation in the radio frequency spectrum.

Fig. 15 displays Askaryan pulses derived from the ZHS Monte Carlo [34], with subsequent modifications for non-cylindrical form factors of the charge distribution [14]. The electric fields are scaled to correspond to a total energy of 10 EeV, but were created from charge excess profiles from 100 TeV events (the scaling is linear).

Because the LPM effect becomes relevant above  $10^{16}$  eV [12], the pulses are unaffected by it, and are smooth and unstretched. The center of graph corresponds to a retarded time of zero. The pulse asymmetry (difference in maximum and minimum values) for non-zero observation angles (color scale) is caused primarily by the non-symmetric charge distribution. For negative observation angles, the retarded time dictates that the end of the charge excess profile is observed first, and the electric field is anti-symmetric for reflections across the y-axis where the retarded time is zero.

The time-domain response of both the ARIANNA LPDA and the low-noise amplifier produce results that match data. Theoretical Askaryan pulses can be combined with them to produce experimental predictions for the neutrino signal, or *templates*. For electric fields not subject to the LPM effect, the accuracy of the templates is limited only by model and experimental uncertainties. Electric fields subject to the LPM effect have also been studied, to establish how the templates change. However, this study is not meant to be comprehensive. Assuming a matched coaxial cable, and including amplifier effects, Eq. (3) reduces to  $V_L(t) = A(t) \circ h_{rx}(t) \circ E_v(t)$ , where  $A(t)$  again represents the transfer function of the amplifier. Fig. 16 shows the signal templates  $V_L(t)$ , while varying the observation angle. Technically, ice absorption is also taken into account over a 1000 m path length, however, it is shown below that this has a negligible effect on waveform structure.

While the signal amplitudes are predicted by the analysis, the waveforms have been scaled such that the maximum voltage is 1.0, so that shapes can be compared (Fig. 16). The only change in the templates with respect to observation angle, besides overall amplitude, is the frequency content early in the wave. Higher frequency modes are expressed early in the wave as the observation angle decreases to zero, however these modes are lost off-cone. The structure of the LPDA response causes the high frequency modes to be recorded earlier, because the smaller dipole elements are located nearer to the antenna feed point. (The next section shows templates for non-boresight angles).

The LPM versions of the templates demonstrate a stronger dependence on the observation angle than the non-LPM versions. There are three main effects. First, the on-cone ( $0^\circ$ ) versions are identical, because the electric fields are identical. That is, an extreme narrowing of the Cerenkov cone width is irrelevant, if the observation is taking place at precisely the Cerenkov angle. Second, for off-cone observations, the high frequency modes near the beginning of the waves are suppressed, because those modes are suppressed in the original electric field. Finally, the lower frequency modes (near the end of the waves) appear to be enhanced relative to the  $0^\circ$  case. This is an artifact of the normalization, which sets the maximum voltage (whenever it occurs) to 1.0. In the un-normalized templates, oscillations between 20 and 30 ns from the  $0^\circ$  case are the largest in the set. It is important to

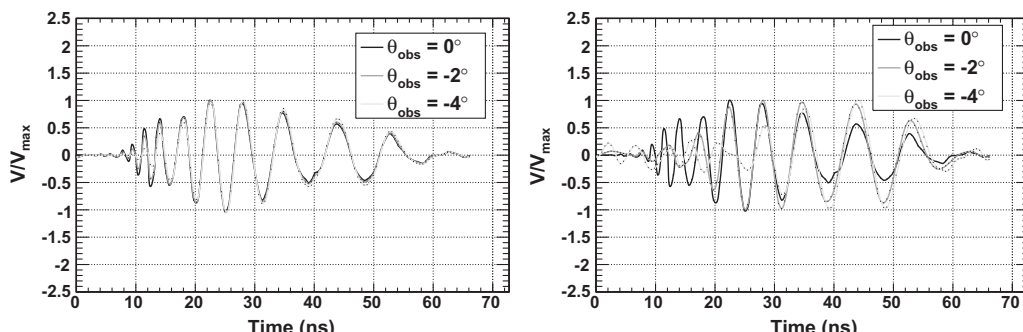


**Fig. 16.** Signal templates for a 10 EeV neutrino, via the Askaryan effect. The LPDA observes the cascade at boresight, and the results for observation angles of  $0^\circ$ ,  $-2^\circ$  and  $-4^\circ$  are shown. (Left): Signals generated by NC neutrino interactions, appropriate for CC interactions in the absence of significant LPM suppression. (Right): the same events, with the LPM effect included, appropriate for electron-type CC interactions.

mention here that the LPM-templates shown in Fig. 16 are not meant to be comprehensive, and demonstrate the need for further analysis.

Correlating templates with each other produces an interesting result: if the E-plane angle (next section) is restricted to two beam-widths or less ( $\approx 60^\circ$ ), the correlations between templates obey  $\rho \geq 0.8$ . This result includes varying the E- and H-plane angles, and the observation angle. Because 0.8 is much larger than auto-correlation coefficients produced by noise in ARIANNA analyses, typically  $\rho \lesssim 0.3$ , it is acceptable to use the time-dependent pulse generated from an electromagnetic cascade at energies below the influence of the LPM, and scale it to higher energies to predict the waveforms from the dominant hadronic cascades. LPM-dominated events (CC events with energies greater than 1 EeV) make up 20%–30% of the total event rate [12] in ARIANNA, and do not obey  $\rho \geq 0.8$ , for correlations between all templates from the LPDA forward lobe. To understand the final fraction of events which do undergo the LPM effect, future development of this work will extend template production to include LPM physics.

## 6.2. Prediction vs. antenna angle

Although the effect of the observation angle is interesting theoretically, the majority of detectable signals in the ARIANNA system will be electric fields with small observation angles, above the detector threshold. The effect of the LPDA on the signal must be clear, since this effect (and of the amplifier) must be deconvolved to reveal the electric field. Fig. 17 demonstrates the effect of the LPDA responses from Fig. 9, and the amplifier, on an on-cone Askaryan pulse at 10 EeV. In each case, the signal is assumed to be co-polarized. The cross-polarization fraction [5,6], which

measures how much power leaks into the cross-polarized direction due to ice propagation, is  $\leq 5\%$  for the data in ice soundings taken in Moore's Bay. Fig. 17 retains the properties of Fig. 9. The LPDA response approaches uniformity within the main lobe of the E- and H-planes, especially at lower frequencies.

Although ice absorption over the total path length affects the overall amplitude in a triggered event, it has been checked that the effect on the waveform shape is small (Fig. 18). The slope of the measured attenuation length vs. frequency is not steep enough to produce a difference comparable to the shelf depth over a few hundred MHz. The differences in high and low frequency attenuation do not have enough time to warp the waveform shape. With an average (measured) shelf depth of  $576 \pm 8$  m, the attenuation effect works out to approximately a  $-16$  dB/km overall scale factor, which is nearly independent of frequency.

## 6.3. Confirmation of ARIANNA Monte Carlo amplitudes

The ARIANNA Monte Carlo simulation, ShelfMC, predicts the overall exposure and sensitivity to neutrino flux, given a variety of parameters [12]. Natural factors, such as the chemical composition of cosmic rays and the distribution of cosmic ray sources with respect to redshift [36], must be determined independently or taken as free parameters. However, once the neutrino flux interacts in the ice, it produces a cascade. The cascade electric field strength versus frequency (in ice) has been measured experimentally [32] for cascades of equivalent total energy to GZK events. The ShelfMC simulation has been adapted from that of prior experiments [9,10]. These Monte Carlo simulations multiply the electric field strength (parameterized as in [37]) with an effective height equation in the following way:

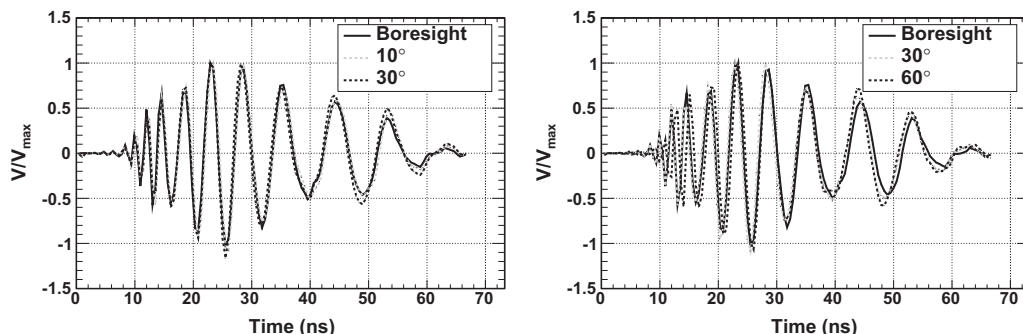


**Fig. 17.** Signal templates for a 10 EeV neutrino, via the Askaryan effect. The LPDA observes the cascade at varying angle with respect to boresight, and the observation angle is kept constant at  $0^\circ$ . (Left): Varying antenna angle in the E-plane only. (Right): Varying the antenna angle in the H-plane only.

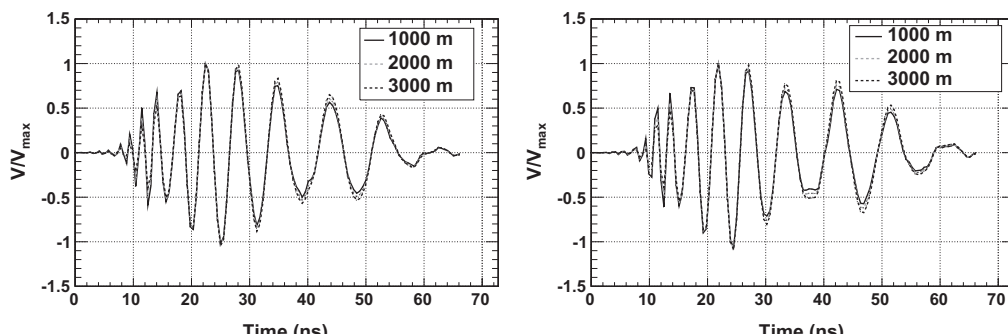


**Fig. 18.** These signal templates includes the usual suite of electronics effects (LPDA, filters, and amplifier), and the effect of the ice. The measured attenuation length vs. frequency is  $\lambda(v) = (470 \pm 20) - (140 \pm 20)v[\text{GHz}]$  (meters). The path length is varied and shown in the legend, and the shape changes accordingly. The waveforms are normalized such that the maximum voltage is 1.0. (Left): LPDA boresight. (Right):  $60^\circ$  in the H-plane.

$$E_v^{1m} \left[ \frac{V}{\text{m MHz}} \right] = \left( \frac{f}{f_0} \right) \frac{E[\text{TeV}] \times 2.53 \times 10^{-7}}{1 + (f/f_0)^{1.44}} \left( \frac{\sin \theta_{obs}}{\sin \theta_c} \right) \quad (18)$$

$$E_v(\theta_{obs}, r, f) = E_v^{1m}(f) \exp \left( -\ln 2 \left( \frac{\theta_{obs} - \theta_c}{\Delta \theta(f)} \right)^2 \right) \frac{e^{-r/\lambda}}{r} \quad (19)$$

$$V_{ant} = \frac{\sqrt{R} \Delta f}{2\sqrt{2}} \sum_i h_{eff}(f_i) (f_{had} + f_{em}) E_v(\theta_{obs}, r, f_i) G(\theta_E, \theta_H) \quad (20)$$

In Eq. (18), the basic electric field strength is shown, and  $f_0 = 1150$  MHz. In Eq. (19),  $\theta_{obs} - \theta_c$  measures how far the observation is from the Cerenkov cone,  $\Delta \theta$  is the width of the Cerenkov cone, and  $\theta_c = 56^\circ$  is the Cerenkov angle in ice. The cone width  $\Delta \theta$  depends on frequency, and whether the event is electromagnetic or hadronic in nature. Eq. (21) below gives the electromagnetic dependence, which depends on the LPM effect. In Eq. (19),  $r$  and  $\lambda$  are the distance from the neutrino vertex and ice attenuation length, respectively. In Eq. (20),  $f_{em}$  and  $f_{had}$  are the fractions of energy in the electromagnetic and hadronic component of the neutrino cascade, and the function  $G$  averages (in-quadrature) Gaussian models of the forward lobe of the LPDA radiation pattern in the E- and H-planes. If the event reflects from the ocean, then  $R$  is the reflection coefficient for power. Finally,  $h_{eff}$  is the scalar expression for antenna effective height at a given wavelength [30].

$$\Delta \theta(E_v, f) = 2.7 \cdot \frac{f_0}{f} \left( \frac{E_{LPM}}{0.14 E_v + E_{LPM}} \right) \quad (21)$$

The convolution theorem states that multiplication of two functions in the Fourier domain is identical to convolving those functions in the time domain. Eq. (20) multiplies the scalar effective height formula for a single frequency ( $h_{eff}$ ) with the electric field. Thus, Eq. (20) is like the proper convolution of the electric field and antenna response ( $h_{rx}(t)$ ) with the complex phase factor neglected. For pure ice,  $E_{LPM} \approx 0.3$  PeV [35], depending on the ice density, and the cascade begins to elongate near 2 PeV. The nominal ice density of 0.92 g/cc is assumed here. The frequency  $f_0$  is the same as above. Antenna beam widths of  $60^\circ$  and  $120^\circ$  are used as the Gaussian widths in  $G$  in Eq. (20), for the E- and H-planes respectively, and  $\theta_E$  and  $\theta_H$  are the incoming angles in the respective antenna planes. This description of the antenna main lobe is an approximation best suited for directions within one beam-width of the forward direction.

The full calculation of the antenna voltage yields a number meant to be compared to rms voltage fluctuations from thermal noise. The fractional deviation of ShelfMC from the maximum voltage in this work's model is shown in Fig. 19, with  $\theta_E$  and  $\theta_H$  varied through all the angles measured in the anechoic chamber, subject to  $\theta_E < 60^\circ$ . The convolution method from this work is denoted TD for time-domain. The Askaryan pulse comes from [14], using  $E_v = 3 \times 10^{18}$  eV,  $\theta_{obs} - \theta_c = 0.3^\circ$ ,  $f_{em} = 1$ . No distance, reflection, or attenuation effects were applied to either the TD or ShelfMC numbers, since these effects equally shift both distributions. Thus, a comparison can be made between the ShelfMC expression for the maximum voltage, and the maximum voltage of the signal templates.

Fig. 19 demonstrates that the fractional difference between ShelfMC and TD is typically 10%. The  $\chi^2/dof$  indicates a good fit. The excess near  $-0.4$  comes from an overestimation by ShelfMC, where the Gaussian functions  $G$  describing the radiation pattern over-predict the LPDA relative gain (Eq. (20)). In reality, the Gaussian approximation is valid only for angles well within one or two beam widths in the E-plane (about  $60^\circ$ , centered on forward direction), because the real radiation pattern (Fig. 4) decreases more quickly. Fig. 19 indicates that the errors in the signal to noise  $V_{ant}/V_{thermal}$  from ShelfMC are modest (for constant  $V_{thermal}$ ) when the more realistic TD model is employed. The TD model incorporates

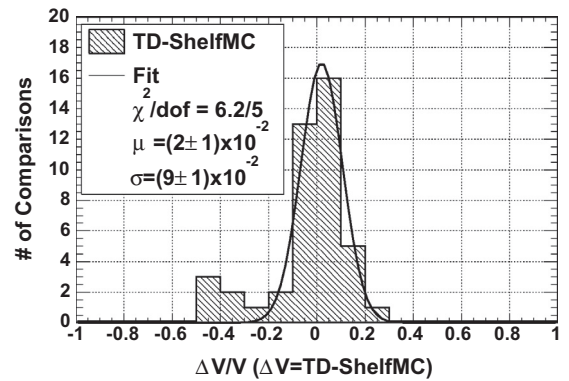


**Fig. 19.** The fractional voltage difference between ShelfMC (which relies on the formalism of Eqs. (18)–(20)) and the TD model of this work. The Askaryan signal is convolved with the each LPDA  $h_{rx}(t)$  measured in the anechoic chamber, for each  $\theta_E, \theta_H$  from the chamber turn-table positioning system. A restriction of  $\theta_E < 60^\circ$  has been applied (approximately two beam widths), for a total of 43 comparisons.

antenna phase effects, and even predicts the waveform shape (the templates). The thermal fluctuations are characterized by the system temperature, which remains constant because the antenna aperture and bandwidth are constant in either case.

## 7. Summary and conclusions

The RF response of the ARIANNA DAQ has been measured, with the purpose of predicting and quantifying the signatures from high energy neutrino interactions in Antarctic ice. This includes an iterative procedure to compute the effective height of the log-periodic dipole arrays (LPDA) serving as receiving antennas for the system, and the amplifier transfer function of the amplifier feeding the antenna signal to the digitizer. The LPDA response was determined in air, but prior work [19] and evidence presented in this paper demonstrates that the response remains valid for LPDA embedded in low density firn less than a few meters from the surface. This work has defined a procedure to compute the time-dependent signal Askaryan signal from the RF response, and this calculation is used to produce signal templates in several examples. The measured response is confirmed by data from multiple field contexts. The level of agreement between predicted and observed time domain waveforms produced correlation coefficients larger than 0.79. The predicted time-dependent wave packet is approximately 40 ns wide, changing shape according to the observation angle with respect to the Cerenkov cone, and the arrival direction with respect to the antenna. The change in shape due to the arrival direction is smooth and continuous in the forward lobe of the LPDA.

The example neutrino templates were computed from theoretical calculations of the time dependent signals generated from electromagnetic cascades [13,14,37] and convolved with the RF response function of the detector. The correlation coefficient between templates obeys  $\rho \geq 0.8$ , for variation of the E- and H-plane angles, and the observation angle. This result indicates that imprecise knowledge of the viewing angle has little impact on the overall form of the waveform, because the duration of electromagnetic pulse is short compared to the time scales of the system response. For similar reasons, there is little variation in the time-dependent waveform from hadronic or electromagnetic cascades, except in the case where the LPM effect is strong. Thus, it is acceptable to use the time-dependent pulse generated from an electromagnetic cascade at energies below the influence of the LPM, and scale it to higher energies to predict the waveforms from the dominant hadronic cascades. Though LPM-dominated events are sub-dominant in ARIANNA, [12], future development

of this work will extend the template production to include a broader range of LPM associated physics. Finally, it was also shown that the additional frequency dependence introduced by ice attenuation has negligible impact on the time dependent shape of the waveform for interaction distances relevant to ARIANNA.

The ARIANNA digitizers operate via a positive and negative voltage threshold trigger that separates random thermal noise from signal-like templates like those presented in this work. Rates are kept low, while maintaining low voltage thresholds, by requiring that a signal rise above a positive threshold and drop below a negative threshold. Such a system is triggered by a generic bi-polar waveform. While there are risks to searching for a specific signal shape in data, the potential benefits include highly efficient thermal-noise trigger rejection. It has been shown in this work that the signal templates are bi-polar, and contain high-frequency (1 GHz) content in spite of ice absorption and antenna effects. Further, an understanding of the energy-scaling of the signal is required for energy measurement. The template analysis provides this benefit, confirmed at the 10%-level by Monte Carlo simulation (for events near the Cerenkov angle).

Finally, correlations between all computed templates (for varying Cerenkov observation angles, and incoming angles in the LDPA main lobe) remain above 0.85, implying that the templates are consistent enough to use in ARIANNA data analysis routines [27], without *a priori* knowledge of the observation or incoming angles. By comparing the average  $\rho$ -value between data channels and templates, random thermal triggers are rejected for entire seasons of data with relatively few complex calculations. Future directions along the lines published here include studying cross-polarized measurements to constrain Askaryan field polarization, and the production of templates corresponding to high-energy cosmic rays. The latter effort involves use of the CoREAS code [38,39].

## Acknowledgements

We wish to thank the staff of Antarctic Support Contractors, Raytheon Polar Services and Lockheed Martin, and the entire crew at McMurdo Station for excellent logistical support. We would like to acknowledge and thank the CReSIS project and the Anechoic Chamber facility management for the use of the world class anechoic chamber at the University of Kansas. This work was supported by generous funding from the Office of Polar Programs and Physics Division of the US National Science Foundation, grant awards ANT-08339133, NSF-0970175, and NSF-1126672.

## Appendix A. Further equations

This section reviews the definition of the antenna effective height used in Section 2, and the assumption that  $Z_{in} \approx Z_L$ . Eq. (9), which produces the result for the signal recorded in the anechoic chamber (used to solve for the antenna effective height), has been simplified assuming  $Z_{in} \approx Z_L$ . The signal  $V_L(t)$  recorded in a line impedance-matched configuration on an oscilloscope, in response to an incident electric field  $E(t)$ , is given by Eq. (3):

$$V_L(t) = 2 \left( \frac{Z_L}{Z_L + Z_{in}} \right) h_{rx}(t) \circ E(t) \quad (\text{A.1})$$

The operator ( $\circ$ ) refers to convolution. The left-hand side of this equation is strictly real. Taking the imaginary part of both sides:

$$\text{Im}V_L(t) = 2\text{Im} \left( \frac{Z_L}{Z_L + Z_{in}} \right) h_{rx} \circ E(t) \quad (\text{A.2})$$

$$0 = \text{Im} \left( \frac{Z_L}{Z_L + Z_{in}} \right) \quad (\text{A.3})$$

$$0 = \text{Im}\{Z_L Z_{in}^*\} \quad (\text{A.4})$$

$$\text{Im}Z_L \text{Re}Z_{in} = \text{Im}Z_{in} \text{Re}Z_L \quad (\text{A.5})$$

From the last statement, it follows that the phases of  $Z_L$  and  $Z_{in}$  must be equal. If the real parts are equal, then the imaginary parts are equal as well, and  $Z_{in} = Z_L$ . For most RF equipment, the real part is just  $50\Omega$ , and this is true for the cables in this work. As discussed in Section 5.2, however, the real part of the LDPA impedance is  $80\Omega$  on average. When placed in snow with an index of refraction  $n = 1.3$ , however,  $|Z_{in}|$  drops to  $\approx 50\Omega$ , and the assumptions hold.

For an impulsive electric field, described by  $E(t) = E_0 \delta(t - t_0)$ , the voltage read out by the antenna is

$$V_L(t) = 2 \left( \frac{Z_L}{Z_L + Z_{in}} \right) h_{rx}(t) \circ E(t) = h_{rx} \circ E_0 \delta(t - t_0) \quad (\text{A.6})$$

$$V_L(t) = E_0 h_{rx}(t) \circ \delta(t - t_0) = E_0 h(t - t_0) \quad (\text{A.7})$$

The antenna cannot reproduce the impulsive signal, and instead reads out a copy of the response function  $h_{rx}$  at a time  $t - t_0$ , with the units of volts versus time, proportional to the electric field amplitude.

## References

- [1] K. Greisen, Phys. Rev. D 16 (1966) 748–750, <http://dx.doi.org/10.1103/PhysRevLett.16.748>.
- [2] G.T. Zatsepin, V.A. Kuz'min, JETP Lett. 4 (1966) 78–80.
- [3] V.S. Berezinsky, G.T. Zatsepin, Phys. Lett. B 28 (1969) 423.
- [4] S.W. Barwick, J. Phys. Conf. Ser. 60 (2007) 276–283, <http://dx.doi.org/10.1088/1742-6596/60/1/060>.
- [5] J.C. Hanson, The performance and initial results of the ARIANNA prototype (Ph.D. thesis), University of California at Irvine, 2013.
- [6] J.C. Hanson et al. (The ARIANNA Collaboration), Proceedings of the 32nd International Cosmic Ray Conference, Beijing, China. doi:<http://dx.doi.org/10.7529/ICRC2011/V04/0340>.
- [7] C.S. Neal, J. Glaciol. 24 (1979) 295–307.
- [8] G. Askaryan, Sov. Phys. JETP 14 (1962) 441–443.
- [9] I. Kravchenko et al. (The RICE Collaboration), Phys. Rev. D 85. doi:<http://dx.doi.org/10.1103/PhysRevD.85.062004>.
- [10] P.W. Gorham et al., The ANITA Collaboration, J. Astropart. Phys. 32 (2009) 10–41, <http://dx.doi.org/10.1016/j.astropartphys.2009.05.003>.
- [11] S. Klein, Nucl. Phys. Proc. Supl. 229–232 (2012) 284–288, <http://dx.doi.org/10.1016/j.nuclphysbps.2012.09.045>.
- [12] K. Dookayka, Characterizing the search for ultra-high energy neutrinos with the ARIANNA detector (Ph.D. thesis), University of California at Irvine, 2011.
- [13] J. Alvarez-Muniz, A. Romero-Wolf, E. Zas, Phys. Rev. D 81 (2010) 123009.
- [14] J. Alvarez-Muniz, A. Romero-Wolf, E. Zas, Phys. Rev. D 84 (2011) 103003, <http://dx.doi.org/10.1103/PhysRevD.84.103003>.
- [15] W. Sorgel, W. Wiesbeck, EURASIP J. Appl. Signal Process. 2005 (2005) 296–305, <http://dx.doi.org/10.1155/ASP.2005.296>.
- [16] A. Shilivski, E. Heyman, R. Kastner, IEEE Trans. Antennas Propag. 45 (1997) 1140–1149, <http://dx.doi.org/10.1109/8.596907>.
- [17] C. Baum, IEEE Trans. Electromagn. Compat. 44 (2002) 18–24, <http://dx.doi.org/10.1109/15.990707>.
- [18] P. Miocinovic et al., Phys. Rev. D 74 (2006) 043002, <http://dx.doi.org/10.1103/PhysRevD.74.043002>.
- [19] J.C. Hanson, L. Gerhardt, S. Klein, T. Stezelberger, S.W. Barwick, K. Dookayka, R. Nichol, Nucl. Instrum. Methods A 624 (2010) 85–91, <http://dx.doi.org/10.1016/j.nima.2010.09.032>.
- [20] T. Barrella, D. Saltzberg, S.W. Barwick, J. Glaciol. 57 (2011) 61–66, <http://dx.doi.org/10.3189/002214311795306691>.
- [21] Gerald Burke, Andrew Poggio, <[http://en.wikipedia.org/wiki/Numerical\\_Electromagnetics\\_Code](http://en.wikipedia.org/wiki/Numerical_Electromagnetics_Code)>.
- [22] C. Balanis, *Antenna Theory: Analysis and Design*, 3rd ed., John Wiley and Sons, 2005.
- [23] J. McClean, R. Sutton, Antennas and Propagation Society Intl. Symposium 3, 2003, pp. 571–574. doi:<http://dx.doi.org/10.1109/ICUWB.2009.5288811>.
- [24] J. McClean, H. Foltz, R. Sutton, Conference on Ultra-Wide Band Systems and Technologies, 2004, pp. 317–321. doi:<http://dx.doi.org/10.1109/UWBST.2004.1320987>.
- [25] S.A. Kleinfelder et al., The ARIANNA Collaboration, IEEE Trans. Nucl. Sci. 60 (2013) 612–618, <http://dx.doi.org/10.1109/TNS.2013.2252365>.
- [26] C.S. Neal, Ann. Glaciol. 3 (1982) 216–221.
- [27] J. Tatar, Performance of sub-array of arianna detector stations during first year of operation (Ph.D. thesis), University of California at Irvine, 2013.
- [28] S.O. Rice, Bell Syst. Tech. J. 23 (1944) 282–332, <http://dx.doi.org/10.1002/j.1538-7305.1944.tb00874.x>.

- [29] V.V. Bogorodsky, C.R. Bentley, P.E. Gudmandsen, *Radioglaciology*, D. Reidel Publishing, 1985.
- [30] J. Kraus, R. Marhefka, *Antennas*, 3rd ed., McGraw-Hill, 2003.
- [31] D. Seckel, Int. J. Mod. Phys. A 21-1 (2006) 70–74, <http://dx.doi.org/10.1142/S0217751X06033398>.
- [32] P.W. Gorham et al., The ANITA Collaboration, Phys. Rev. Lett. 99 (2007) 171101, <http://dx.doi.org/10.1103/PhysRevLett.99.171101>.
- [33] D. Saltzberg et al., Phys. Rev. Lett. 86 (2001) 2802, <http://dx.doi.org/10.1103/PhysRevLett.86.2802>.
- [34] E. Zas, F. Halzen, T. Stanev, Phys. Rev. D 45 (1992) 362–376.
- [35] L. Gerhardt, S. Klein, Phys. Rev. D 82 (2010) 074017, <http://dx.doi.org/10.1103/PhysRevD.82.074017>.
- [36] K. Kotera, D. Allard, A.V. Olinto, JCAP 10 (2010), <http://dx.doi.org/10.1088/1475-7516/2010/10/013>.
- [37] J. Alvarez-Muniz et al., Phys. Rev. D 62 (2000) 063001, <http://dx.doi.org/10.1103/PhysRevD.62.063001>.
- [38] D. Heck, J. Knapp, J.N. Capdevielle, G. Schatz, T. Thouw, Report FZKA 6019, 1998, Forschungszentrum Karlsruhe.
- [39] T. Huege, M. Ludwig, C.W. James. arXiv:1301.2132.

# Radar absorption, basal reflection, thickness and polarization measurements from the Ross Ice Shelf, Antarctica

Jordan C. HANSON,<sup>1,2</sup> Steven W. BARWICK,<sup>1</sup> Eric C. BERG,<sup>1</sup> Dave Z. BESSON,<sup>2,3</sup> Thorin J. DUFFIN,<sup>1</sup> Spencer R. KLEIN,<sup>4</sup> Stuart A. KLEINFELDER,<sup>5</sup> Corey REED,<sup>1</sup> Mahshid ROUMI,<sup>1</sup> Thorsten STEZELBERGER,<sup>4</sup> Joulien TATAR,<sup>1</sup> James A. WALKER,<sup>1</sup> Liang ZOU<sup>1</sup>

<sup>1</sup>Department of Physics and Astronomy, University of California, Irvine, Irvine, CA, USA

<sup>2</sup>Department of Physics and Astronomy, University of Kansas, Lawrence, KS, USA

<sup>3</sup>Moscow Physics and Engineering Institute, Moscow, Russia

<sup>4</sup>Lawrence Berkeley National Laboratory, Berkeley, CA, USA

<sup>5</sup>Department of Electrical Engineering and Computer Science, University of California, Irvine, CA, USA

Correspondence: Jordan C. Hanson <918particle@gmail.com>

**ABSTRACT.** Radio-glaciological parameters from the Moore's Bay region of the Ross Ice Shelf, Antarctica, have been measured. The thickness of the ice shelf in Moore's Bay was measured from reflection times of radio-frequency pulses propagating vertically through the shelf and reflecting from the ocean, and is found to be  $576 \pm 8$  m. Introducing a baseline of  $543 \pm 7$  m between radio transmitter and receiver allowed the computation of the basal reflection coefficient,  $R$ , separately from englacial loss. The depth-averaged attenuation length of the ice column,  $\langle L \rangle$  is shown to depend linearly on frequency. The best fit (95% confidence level) is  $\langle L(\nu) \rangle = (460 \pm 20) - (180 \pm 40)\nu$  m ( $20$  dB km $^{-1}$ ), for the frequencies  $\nu = [0.100\text{--}0.850]$  GHz, assuming no reflection loss. The mean electric-field reflection coefficient is  $\sqrt{R} = 0.82 \pm 0.07$  (1.7 dB reflection loss) across [0.100–0.850] GHz, and is used to correct the attenuation length. Finally, the reflected power rotated into the orthogonal antenna polarization is <5% below 0.400 GHz, compatible with air propagation. The results imply that Moore's Bay serves as an appropriate medium for the ARIANNA high-energy neutrino detector.

**KEYWORDS:** ice/ocean interactions

## INTRODUCTION

The vast Antarctic ice sheet has become important to high-energy neutrino physics in recent years (Barwick, 2007; ANITA Collaboration, 2010; Klein, 2012; Kravchenko and others, 2012; IceCube Collaboration, 2013), motivated by the convenient properties of glacial ice, including optical and radio-frequency (RF) dielectric properties. High-energy cascades induced by neutrinos emit Cherenkov photons; photons with 350–500 nm wavelengths can propagate 10–100 m in Antarctic ice before being detected by photomultiplier tubes (AMANDA Collaboration, 2006). Similarly, at energies 0.1 EeV, neutrinos begin to produce measurable Askaryan pulses (Askaryan, 1962), a form of coherent Cherenkov radiation in the RF regime. Moore's Bay, part of the Ross Ice Shelf, presents an attractive target volume for studying these particle interactions, because the radiation experiences minimal attenuation in the cold ice, and can be reflected back towards the surface by the ocean. Knowledge of the dielectric properties of the ice shelf is required to build such an experiment.

By transmitting a ~1 ns pulse through a transmitting antenna downwards through the ice shelf, and recording the reflections from the oceanic interface, bulk ice attenuation and the reflection coefficient of the interface can be inferred. Using reflected radio pulses to study ice sheets and shelves is known as radio-echo sounding, and has been used to study glaciers and ice shelves in various locations on the Ross Ice Shelf (RIS) and the high plateau (Neal, 1979, 1982;

Besson and others, 2008; Allison and others, 2012; Fretwell and others, 2013).

Basal reflection in Moore's Bay has been studied previously. Neal (1979, 1982) reported on the RIS, using a 60 ns wide, 60 MHz pulse, recording the returned power vs location. Flights 1 km above the RIS were performed, including several points over Moore's Bay. Basal reflection coefficients were derived in 10 dB increments, assuming no losses from dust or other impurities, for contours across the shelf. Moore's Bay produces reflection coefficients near the Fresnel limit (~0.82 dB, or ~0.91 for the electric field), and two explanations were offered. First, Moore's Bay is far from brine percolation zones that are traced from the grounding line to the shelf front, which are correlated with ice velocity. Second, the melt rate near the grounding line for basal ice prevents the formation of an abrupt basal layer of saline ice, and instead replaces glacial ice with saline ice over time. The freeze-on of saline ice at the shelf bottom does occur; however, these regions are far from the location of the Antarctic Ross Ice-Shelf ANtenna Neutrino Array (ARIANNA), and the average accumulation rate of bottom saline ice is only  $0.3 \pm 0.1$  m a $^{-1}$  in the east RIS (Rignot and others, 2013).

Neal (1982) showed that two parameters besides peak power can be extracted from the data. First, the width of the peak power distribution for a specific location pertains to vertical roughness at the oceanic interface. Second, the spatial correlation of power measurements reveals horizontal correlation lengths for roughness. These measurements must

be compared to theoretical distributions of the same parameters, from the theory of rough-surface scattering (Dookayka, 2011). The most general statistical surface, with the fewest parameters, was chosen: a Gaussian surface roughness described by normal fluctuations about a mean depth, and a specified horizontal correlation length. Neal reports vertical root-mean-square (rms) of 3 cm at the ocean/ice boundary, spread over correlation lengths of 27.5 m, 30 km east of Ross Island. The results make no use of absolute power measurements, and thus are independent of assumptions of RF absorption.

To measure the reflection coefficient separately from englacial loss, the transmitting and receiving antennas may be separated by a baseline comparable to the shelf depth. The signal path is longer with the baseline, providing different absorption but the same reflection loss (Hanson, 2011, 2013). By comparing total loss in the set-up with and without a baseline, absorption and reflection loss can be measured separately. A map of the site studied in this work is shown in Figure 1.

## RF attenuation length

The amplitude of an electric field decreases by  $1/e$  after propagating one attenuation length. For an electromagnetic plane wave travelling through a dielectric medium with a complex index of refraction  $n = n' - in''$ , the electric field is

$$\mathbf{E} = \mathbf{E}_0 \exp(-i(nkx - \omega t)) = \mathbf{E}'_0 \exp\{-n''kx\} \quad (1)$$

The electric field attenuation length is then  $(n''k)^{-1} = L$  ( $\omega$  is the angular frequency). When measured over a volume of material with varying dielectric absorption, the attenuation length is averaged over the effect of depth on the dielectric constant  $\epsilon = \epsilon' - i\epsilon''$ , and in turn the loss tangent,  $\tan \delta = \epsilon''/\epsilon'$ . If  $\tan \delta \ll 1$ , it can be shown that

$$\langle L \rangle^{-1} = (\pi\nu/c)\sqrt{\epsilon'} \tan \delta (\text{m}^{-1}) \quad (2)$$

$$N_L (\text{dB km}^{-1}) = 8686.0 \langle L[m] \rangle^{-1} \quad (3)$$

Equation (3) is the conversion from attenuation length to absorption loss,  $N_L$ . The Debye model shows that  $\nu \tan \delta$  is approximately constant, provided the frequency is far from any molecular resonances (this is true for 0.1–1 GHz). Additionally,  $\epsilon'$  (in ice) is constant for the bandwidth 0.1–2 GHz. Thus, frequency dependence in  $\langle L \rangle$  is attributed to other effects, such as acids and sea-salt impurities (Bogorodsky and others, 1985; Matsuoka and others, 2012).

## Reflection coefficient

Under the Debye model, with a single relaxation time, the ice conductivity is  $\sigma = 2\pi\epsilon_0\epsilon'\nu\tan \delta \approx 10 \mu\text{S m}^{-1}$  at 100 MHz (Dowdeswell and Evans, 2004). By comparison, sea water has a conductivity of a few  $\text{S m}^{-1}$ , with a skin depth of 30 mm, at 60 MHz (Dowdeswell and Evans, 2004; Somaraju and others, 2006). The reflection coefficient for the electric fields ( $\sqrt{R}$ , where  $R$  refers to power) is given by  $(n_1 - n_2)/(n_1 + n_2)$ , given the complex  $n_1 = \sqrt{\epsilon_1}$  and  $n_2 = \sqrt{\epsilon_2}$  for the dielectric and conductive media, respectively.

$$\begin{aligned} \lim_{\tan \delta_2 \gg 1, \tan \delta_1 \rightarrow 0} |\sqrt{R}| &= \frac{1 - n_2/n_1}{1 + n_2/n_1} \\ &= \frac{1 - \sqrt{\alpha}e^{-i\delta_2/2}}{1 + \sqrt{\alpha}e^{-i\delta_2/2}} = \left( \frac{1 + \alpha - \sqrt{2\alpha}}{1 + \alpha + \sqrt{2\alpha}} \right)^{1/2} \end{aligned} \quad (4)$$

Equation (4) demonstrates that  $|\sqrt{R}| \rightarrow 1$ , where  $n_1$  refers to

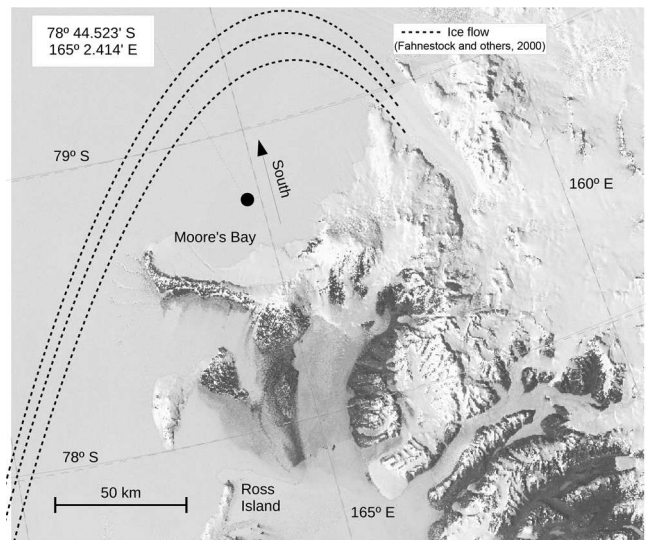


**Fig. 1.** The site studied in this work is marked with the black circle. Moore's Bay is the area south of Ross Island, enclosed by Minna Bluff. The satellite data are available by the US Geological Survey (USGS, 2012). The main ice flowlines are illustrated with dashed lines. Fahnestock (2000) provides further analysis and discussion.

the ice and  $n_2$  refers to the ocean, given the limits  $\tan \delta_2 \gg 1$ , and  $\tan \delta_1 \approx 0$ , and  $\alpha = \epsilon_2''/\epsilon_1'$ . In Eqn (4), the fact that  $\delta_2 \rightarrow \pi/2$  has been used. Equation (4) is completely general as long as the limit is satisfied. The right-hand side has a global minimum at  $\alpha = 1$ , or  $\epsilon_2'' = \epsilon_1'$ , corresponding to a minimum electric field reflection coefficient of  $\sqrt{R}_{\min} \approx 0.41$ . Realistic values for both ice and sea water indicate  $\alpha$  ranges from 20 to 30, depending on the salinity and temperature of the sea water (Dowdeswell and Evans, 2004; Somaraju and others, 2006). Neal (1979) suggested that the reflection coefficient in Moore's Bay is approximately  $-0.82 \text{ dB}$ , or  $\sqrt{R} = 0.91$ , based on the properties of the sea water beneath the RIS. These upper and lower bounds form an allowed range of  $\sqrt{R} = 0.41\text{--}0.91$ .

In addition to vertical radio echoes, measurements were taken with a baseline distance between transmitter and receiver, introducing a new overall path length. In this work, these measurements are named angled bounce studies. For the angled bounce studies reported here, Eqn (5) shows that the reflected power limits to the expression for normal incidence (for s-polarized waves). Also, the initial transmission angle from normal is reduced, because the upper firn layer bends the transmitted pulse downward (to  $\theta \gtrsim 30^\circ$ ), given the initial antenna orientation of  $45^\circ$ . Ignoring the cosine dependence in Eqn (5) amounts to a 1–5% correction, depending on  $n_2$ :

$$\sqrt{R} \approx \frac{n_1(1 - \theta^2/2) - n_2(1 - \frac{1}{2}(\epsilon\theta)^2)}{n_1(1 - \theta^2/2) + n_2(1 - \frac{1}{2}(\epsilon\theta)^2)} \approx \frac{n_1 - n_2}{n_1 + n_2} \quad (5)$$

## Ice thickness calculation

The upper 60–70 m of the ice shelf is firn with density  $\approx 0.4 \text{ g cm}^{-3}$  near the surface (Gerhardt and others, 2010). This result is in agreement with the value  $0.36 \text{ g cm}^{-3}$  from Dowdeswell and Evans (2004). Looyenga's equation,  $n_{\text{ice}}$  and the firn surface density predict the firn index to be  $n_{\text{firn}} \approx 1.3$ . This value was confirmed with pulse propagation timing at the surface, over a distance of  $543 \pm 7 \text{ m}$  (see

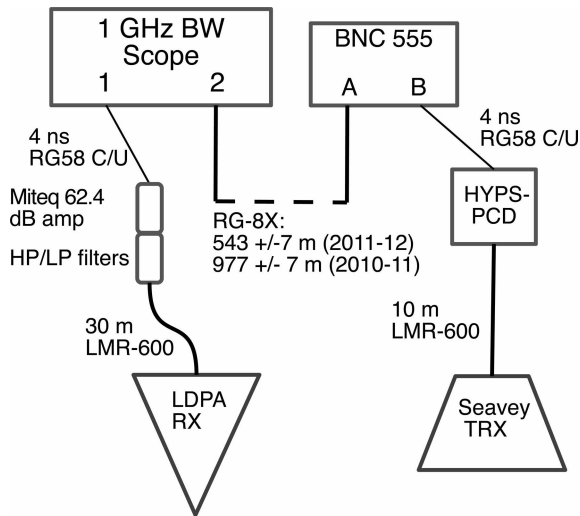


**Fig. 2.** The general set-up of the radio-sounding experiments. Measured and physical time delays are shown in Table 2.

below for detail). From the pulse arrival time, the implied wave speed indicated an index of  $n_{\text{surf}} = 1.29 \pm 0.02$  (Hanson, 2013).

The density and thus the index of refraction has an exponential depth dependence, according to the Schytt model:

$$n(z) = 1.78 = n(z \geq 67\text{m}) \quad (6)$$

$$n(z) = n_0 + p \exp(-z/q) \quad (z < 67\text{m}) \quad (7)$$

In Eqn (7),  $n_0 = 1.86$ ,  $p = -0.55$  and  $q = 35.4\text{ m}$ , with the upper layer density  $\rho \approx 0.4\text{ g cm}^{-3}$ , and  $z > 0$  for increasing depth. A different model with a constant firn correction (to sounding propagation times) and no exponential density profile yields shelf depths consistent within errors (Gerhardt and others, 2010). Equations (6) and (7) are based on measurements taken at Williams Field near McMurdo station (Schytt, 1958; Barrella and others, 2011). Given the measured physical delay between pulse and reflection,  $\Delta t$ , the shelf depth can be obtained from integrating over the total path length  $d$  (Eqns (8) and (9)). Error propagation yields Eqn (10), where  $D_f = 67 \pm 10\text{ m}$  is the firn depth (Dowdeswell

**Table 1.** The various experimental configurations used, by year, for the data in this work. S stands for Seavey horn, and L stands for LDPA (log-periodic dipole array)

Year	Vertical/Angled	Ant. (TX/RX)	$G_1 G_2$
2010	Vertical	L/L	1.0
2011	Vertical	S/L	1.0
2011	Angled	S/L	0.5
2011	Vertical	L/L	1.0

and Evans, 2004). A density profile for the RIS in figure 2 of the latter reference is consistent with this model.

$$\frac{c\Delta t}{2} = \int_0^{d_{\text{ice}}} n(z) dz \quad (8)$$

$$d_{\text{ice}} = \frac{c\Delta t}{2n} - \frac{D_f(n_0 - n)}{n} + \frac{qp}{n} (e^{-D_f/q} - 1) \quad (9)$$

$$\sigma_{d, \text{ice}} = \sqrt{\left(\frac{\sigma_t c}{2n}\right)^2 + \left(\frac{\sigma_n c \Delta t}{2n^2}\right)^2 + k \sigma_{D_f}^2} \quad (10)$$

$$\approx \frac{c}{2n} \sqrt{\left(\frac{\sigma_n}{n}\right)^2 \Delta t^2 + \sigma_t^2}$$

The fractional difference between  $n_0$  and  $n$  is small, and  $\exp(-D_f/q)$  is small, so  $k$  turns out to be of order  $10^{-2}$ . The term in Eqn (10) involving  $k$  is a factor of 10 below the others so it may be dropped. For similar reasons, cross-terms involving firn properties and  $\sigma_n$  have been neglected.

## EXPERIMENTAL TECHNIQUE

The experimental set-up is shown in Figure 2, with additional detail in Table 1. Figure 3 shows the vertical and angled bounces. To create broadband RF pulses, a 1 ns wide, 1–2.5 kV pulse was delivered from the HYPS Pockels Cell Driver (PCD) to a transmitting antenna, and the reflection is received by a second antenna. The PCD and the 1 GHz bandwidth oscilloscope (Tektronix TDS540A in 2010, Agilent HP54832D thereafter) were triggered with a tunable delay generator (Berkeley Nucleonics 555 2-port). From the programmed delay, reflection time and relevant cable delays, the shelf depths were derived for each season. The RG-8X cable between port A of the BNC 555 and the oscilloscope enabled the introduction of a long baseline between the antennas.

Voltage standing wave ratio (VSWR) measurements were performed to study antenna transmission in snow. In all cases, the VSWR of the transmitting and receiving antennas demonstrates good transmission and reception when buried in the surface snow (Gerhardt and others, 2010; Barrella and others, 2011). Noise above and below the receiver bandwidth was filtered with MiniCircuits NHP and NLP filters, and amplified by a 62.4 dB Miteq AM-1660 low-noise amplifier (typical noise figure of 1.5 dB). Signals were attenuated by 3–20 dB where appropriate, to remain in the linear regime of the amplifier.

For the 2006 season (Barrella and others, 2011), the transmitter and receiver were Seavey radio horns used in the ANITA (ANTarctic Impulsive Transient Antenna) experiment (ANITA Collaboration, 2009), with a bandwidth of [200–1300] MHz. In the data from the 2010 season, the receiver and transmitter were log-periodic dipole arrays (LPDAs;

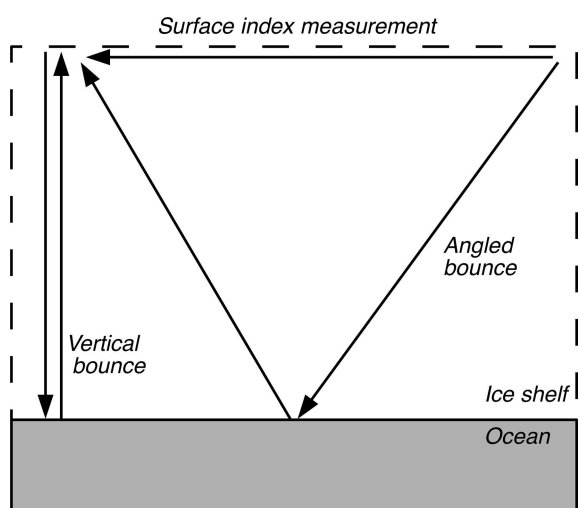


**Fig. 3.** The vertical and angled bounce tests. The surface propagation set-up was used to derive the surface index of refraction,  $n_{\text{surf}}$ .

Create Corp. CLP5130-2N) with a bandwidth of [100–1300] MHz. The Seavey is a dual polarization quad-ridge horn antenna that has higher gain above 200 MHz than the LPDA. The LPDA antennas have a wider bandwidth, but stretch the signal in time with respect to the horn (Barwick and others, 2015). In the 2011 season, the data were recorded with a Seavey transmitter and an LPDA receiver. The 2010 data have been published (Hanson, 2011, 2013). In this work, the thickness results from 2010 are compared to three new measurements, and a new reflection coefficient and attenuation length analysis are presented.

In the surface test, we measured the pulse propagation time over the  $543 \pm 7$  m baseline, and extracted the surface index of refraction from the speed. The result was  $n_{\text{surf}} = 1.29 \pm 0.02$ , and is needed for the boundary conditions in the shelf-thickness model. In the *vertical bounce* measurements, where the transmitter and receiver are co-located, the separation in 2006 was typically 9 m. In 2010 and 2011 the separation was 19 and 23 m, respectively. This ensures that the receiver is in the far field of the transmitter during calibration. Comparing vertical bounce soundings to calibration measurements allows derivation of  $\langle L \rangle$  assuming a value for  $\sqrt{R}$ .

The *angled-bounce* measurements are also compared to calibration measurements and vertical bounce cases to measure both  $\langle L \rangle$  and  $\sqrt{R}$ . Angled signals were captured without having to account for complex ray tracing near the surface. During angled bounce tests, the transmitter and receiver were angled  $45^\circ$  downward from horizontal. For the angled bounce measurements, the 2010 baseline was  $977 \pm 7$  m, and the 2011 baseline was  $543 \pm 7$  m. The angled bounce measurements in 2010 and 2011 had signal path lengths of  $1517 \pm 8$  m and  $1272 \pm 7$  m, respectively. The incident angle with respect to normal refracts closer to  $30^\circ$  when the pulse reaches the ocean, because the firn index  $n_{\text{firn}} = 1.3$  is smaller than the bulk ice index  $n_{\text{ice}} = 1.78$ .

The Friis equation relates the power received,  $P_r$ , to the transmitted power  $P_t$  in a lossless medium at a given wavelength. For two identical antennas in air, it may be written

$$P_r = \frac{P_t(G_a c)^2}{(4\pi\nu d)^2} = \frac{P_0}{d^2} \quad (11)$$

Here  $G_a$  is the intrinsic gain of the antennas and  $\nu$  is the frequency.  $P_r$  and  $P_t$  are the received and transmitted power, respectively. To account for absorption losses and possible losses upon reflection, the Friis equation is modified to

$$P_r = \frac{P_0 R G_1 G_2}{d^2} \exp\left(-\frac{2d}{\langle L \rangle}\right) \quad (12)$$

By convention, the factor of 2 in the exponential means  $\langle L \rangle$  refers to electric field, and the reflection coefficient for the power is  $R$ . The factor  $G_1 G_2$  accounts for the relative power radiation pattern of the transmitter and receiver (Table 1).  $G_1$  and  $G_2$  are 1 for the vertical bounce measurements, in which the signal is transmitted and received in the forward direction of the antennas. As the angle at which the signal interacts with the antenna increases,  $G_1 G_2$  decreases from 1 according to the antenna radiation patterns. The radiation patterns have been both simulated and measured (ANITA Collaboration, 2009; Barwick and others, 2015). Manipulating Eqn (12) gives Eqn (13), the left-hand side of which may be plotted vs path length  $d$  to obtain a line with a slope  $-1/\langle L \rangle$ , and a constant y-intercept. The reflection coefficient is treated as a free parameter in the fit. The error in the

**Table 2.** A summary of total and physical time delays for the various seasons, and calculated shelf thicknesses. The physical time delay  $\Delta t_{\text{phys}}$  is the measured delay  $\Delta t_{\text{meas}}$ , with equipment delays subtracted. The total precision is quoted in the earlier measurements (Gerhardt and others, 2010; Barrella and others, 2011). The width of the reflected pulse,  $\sigma_{\text{pulse}}$ , is caused by the response of the antennas

Year	$\Delta t_{\text{meas}}$	$\Delta t_{\text{phys}}$	$\sigma_{\text{stat}}$	$\sigma_{\text{sys}}$	$\sigma_{\text{pulse}}$	$\sigma_{\text{tot}}$	$d_{\text{ice}}$
	ns	ns					m
2006	–	6783	–	–	–	10	$577.5 \pm 10$
2009	–	6745	–	–	–	15	$572 \pm 6$
2010	7060	6772	5.0	8.0	10	14	$576 \pm 6$
2011	6964	6816	4.0	5.0	10	12	$580 \pm 6$

left-hand side of Eqn (13) is given by Eqn (14).

$$f(d) = \ln \sqrt{\frac{d^2 P_r}{R G_1 G_2}} = -d/\langle L \rangle + \text{const} \quad (13)$$

$$\sigma_f = \sqrt{\left(\frac{\sigma_d}{d}\right)^2 + \left(\frac{\sigma_{P_r}}{2P_r}\right)^2} \quad (14)$$

## ICE-THICKNESS RESULTS

The measured propagation times, both total and corrected for cable delays, are shown in Table 2, along with statistical and systematic uncertainties. Using Eqns (8–10), the times are converted to thickness. Systematic errors arise from cables, the response time of the pulser, and delay generator precision (see Fig. 2). For the long cables, a conservative 5% error in the propagation time is assumed, because the endpoints of the baselines were measured with GPS, with waypoint precision of 5 m. The distance between the 2006 site and the site for the remaining three thickness measurements was  $\sim 1$  km, and the GPS location of the latter site is accurate to within a horizontal uncertainty of 5 m.

The reflected pulse from the 2009 set-up was only several mV above noise backgrounds, so the entire pulse width was included as systematic error (Gerhardt and others, 2010). For the 2011 data, the location and uncertainty in peak voltage oscillations in the reflections were used instead, because the signal was well above backgrounds. The low-frequency ringing in the reflected data originates from group delay in the LPDA, which is 10 ns at 0.2 GHz (the lowest frequency emitted by the transmitter). When folded into the timing uncertainties, smaller but comparable errors to 2006 are obtained for the thickness. Timing uncertainties are lowest in 2006 because both transmitter and receiver were Seavey horns, which have lower group delay than the LPDA.

In general, statistical errors come from Eqn (10), with  $n = 1.78 \pm 0.02$ , and total timing error from Table 2. The magnitude of  $\sigma_n$  comes from measurements made at the surface ( $n_{\text{surf}} = 1.29 \pm 0.02$ ) (Hanson, 2013). Fluctuations in  $n$  are largest at the surface, making this a conservative estimate for the bulk ice, and it is similar to previous work (Gerhardt and others, 2010; Barrella and others, 2011). The total error from 2006 is higher because a larger error on the dielectric constant was used. The mean thickness over all seasons is  $d_{\text{ice}} = 576 \pm 8$  m (statistical and systematic added in quadrature). Errors in Table 2 other than from the index of refraction are treated as systematic. A linear fit to the four

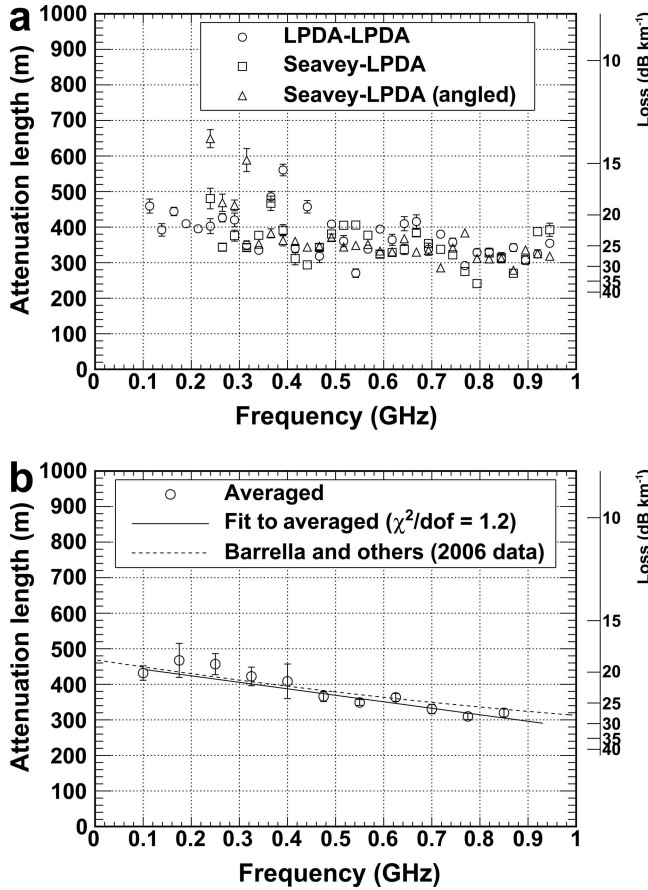


**Fig. 4.** (a) The depth-averaged attenuation length vs frequency, with standard deviations from error propagation in Eqn (18). The attenuation length is converted to englacial loss ( $\text{dB km}^{-1}$ ), at right. (b) The data from (a) averaged into 75 MHz bins, with standard deviations. The linear fit has  $\chi^2/\text{dof} = 1.2$ , a slope of  $-180 \pm 40 \text{ m GHz}^{-1}$  and an offset of  $460 \pm 20 \text{ m}$ . The dashed line is a fit to prior data taken 1 km from our site (Barrella and others, 2011).

data points together yields a slope consistent with zero (within errors). The measurement from 2006 took place 1 km from the location of subsequent seasons, and does not deviate strongly from the mean.

## AVERAGE ATTENUATION LENGTH, $\langle L \rangle$ , VS FREQUENCY

The technique of measuring  $\sqrt{R}$  and  $\langle L \rangle$  simultaneously is more challenging than assuming a constant  $\sqrt{R}$  and comparing the raw power spectra of only vertical bounce data and calibration data. Assuming a uniform reflection coefficient with respect to frequency assumes that the reflecting surface is dominated by specular, rather than diffuse, reflection. As long as the first few Fresnel zones  $D_m$  of the transmitted pulse are not significantly larger than the horizontal correlation length  $L_C$  of roughness features along the shelf base, then the effect of the vertical roughness scales on the reflection coefficient is avoided (Peters and others, 2005). Prior data collected at two locations on the Ross Ice Shelf, near Moore's Bay, indicate horizontal correlation lengths  $L_C = 12.5 \text{ m}$  and  $L_C = 27.5 \text{ m}$  at the two sites (Neal, 1982). The glaciological Fresnel zone equation, for an observation point a distance  $h$  above the snow surface, with a shelf thickness of  $z$ , shelf index of refraction  $n$ , Fresnel

zone number  $m$ , and an in-air wavelength  $\lambda$  is

$$D_m \approx \sqrt{2m\lambda\left(h + \frac{z}{n}\right)} \quad (15)$$

The approximation arises from the small angle approximation, and is sound because the Fresnel zones are small compared to  $z$ . The measurements take place at the surface, so  $h = 0$ . Using  $n = 1.78$ ,  $\lambda = 3 \text{ m}$  and the measured shelf thickness, Eqn (15), gives  $D_1 = 10\text{--}40 \text{ m}$ , for the bandwidth. Vertical rms fluctuations at the ocean/ice surface were reported to be 3 cm and 10 cm for two sites, spread out over a typical length scale of  $L_C$ . Vertical height fluctuations of 10 cm and 3 cm spread out over 12.5 m and 27.5 m, respectively, mean that specular reflection is a good approximation for this bandwidth (Neal, 1982). The attenuation lengths derived assuming constant  $\sqrt{R}$  are revised in the next section, to account for reflection loss ( $\sqrt{R} < 1.0$ ).

Consider the calibration pulse,  $V_C$ , the vertical bounce pulse,  $V_{\text{ice}}$ , and the depth-averaged attenuation length vs frequency,  $\langle L(\nu) \rangle$ , all at a frequency  $\nu$ :

$$V_C(\nu) = V_0/d_C \quad (16)$$

$$V_{\text{ice}}(\nu) = \frac{V_0}{d_{\text{ice}}} \exp\left(-\frac{d_{\text{ice}}}{\langle L(\nu) \rangle}\right) \quad (17)$$

$$\langle L(\nu) \rangle = \frac{d_{\text{ice}}}{\ln((V_C(\nu)d_C)/(V_{\text{ice}}(\nu)d_{\text{ice}}))} \quad (18)$$

Because the surface of the firn is snow, with a density of  $0.4 \text{ g cm}^{-3}$  and an index of refraction  $n = 1.3$ , the reflection coefficient (for power) between air and snow is  $\sim 0.02$ , so potential interference from surface reflections is not expected to modify Eqn (16). The antennas were placed at the maximum height allowed by the cables and other equipment (1.5 m), and this calibration was compared to the case with the antennas buried in snow slots. Because of the low snow density, dielectric absorption is negligible over the calibration distances (23 m). The antenna calibrations produced similar waveforms with the antennas lowered in snow. The waveform amplitude increases when LPDAs are in the snow, due to the shift in the lower cut-off frequency by the index of refraction. This effect is confirmed in Numerical Electromagnetic Code (NEC) antenna simulations, and VSWR data (Barwick and others, 2015).

The 2011 data are shown in Figure 4a. In Eqns (16–18), the voltages are defined  $V \propto \sqrt{P(\nu)}$ , where  $P$  is the measured power at the frequency  $\nu$ . The antenna impedance is the same for the calibration and bounce studies, making it irrelevant in the ratio in Eqn (18) (Barwick and others, 2015). The 2011 power spectra begin at the low-frequency cut-offs of the transmitter type (200 MHz for the Seavey, and 100 MHz for the LPDA). The englacial loss ( $\text{dB km}^{-1}$ ) is also shown (Eqn (3)).

The 2011 data extend to 0.850 GHz, where the signal-to-noise ratio is close to 1.0, and the error bars are the standard deviation from error propagation in Eqn (18). About 10 m of the error is due to uncertainty in the shelf thickness, and 10 m is due to uncertainty in the power spectrum. Data above 0.850 GHz appear to be rising due to noise floor contributions. Also, systematic fluctuations in the vertical bounce power spectra lead to systematic fluctuations in  $\langle L(\nu) \rangle$ . Systematic errors arise from differences in system frequency response after changing the transmitter location and type, and reflections within the system. The angled bounce data at 0.240 and 0.315 GHz, in particular, are

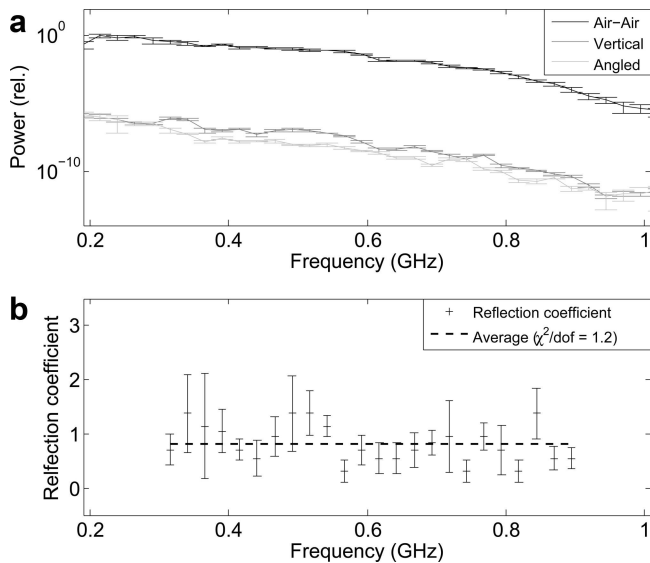


**Fig. 5.** The electric-field reflection coefficient,  $\sqrt{R}$ , vs frequency. The three power spectra correspond to three measurements: a surface power calibration (black), vertical bounce (dark grey) and angled bounce (light grey) cases. The three measurements at each frequency determine a reflection coefficient through a linear fit to Eqn (13), with errors from Eqn (14) attributed to  $\sqrt{R}$ .

systematically high. The Seavey transmitter was placed in a snow cavity rather than fully buried for the angled test, which can lead to cavity resonance effects.

The frequency resolution is maximized in Figure 4a, with no window function. A higher resolution extends the upper frequency limit by avoiding folding noise into the highest-frequency bins. The correction for potential angular dependence of the reflection coefficient only applies to the angled bounce data ( $\sim 4$  m). In Figure 4a, the data are averaged into 0.075 GHz bins, with a linear fit. The best-fit slope is  $-180 \pm 40 \text{ m GHz}^{-1}$ , and the best-fit offset is  $460 \pm 20 \text{ m}$  (95% confidence level,  $\chi^2/\text{dof} = 1.2$ ). Data above 0.850 GHz are neglected in the average and fit shown in Figure 4; however, the  $\chi^2/\text{dof}$  only increases to 1.8 if it is included. As in Figure 4a, the averaged attenuation length is converted to  $\text{dB km}^{-1}$  on the right-hand y-axis using Eqn (3).

Despite the systematic fluctuations, the fit to the data in Figure 4 is in close agreement with the quadratic fit to the data from 2006 (Barrella and others, 2011). In the publication of the 2006 data, the reflection loss was assumed to be 0 dB. If a lower value is assumed (see below), the attenuation length increases, because the returned voltage per unit frequency in Eqn (18) must remain constant. The level of systematic variation in  $\sqrt{R}$  shown below will also generate  $\sim 5\%$  systematic uncertainty in  $\langle L \rangle$ , but only to increase it. The 2006 and 2011 data agree, even though the measurements were made 1 km apart. The area of Moore's Bay near Minna Bluff is far from any zones of high glacial velocity that could cause depth or basal reflection variations, and crevasses have not been observed in the area, so the ice is expected to be relatively uniform.

## BASAL REFLECTION COEFFICIENT

The 2006 season  $\langle L \rangle$  results were derived from vertical bounce measurements assuming  $\sqrt{R} = 1.0$ . Using the path lengths derived from shelf thickness, and the measured

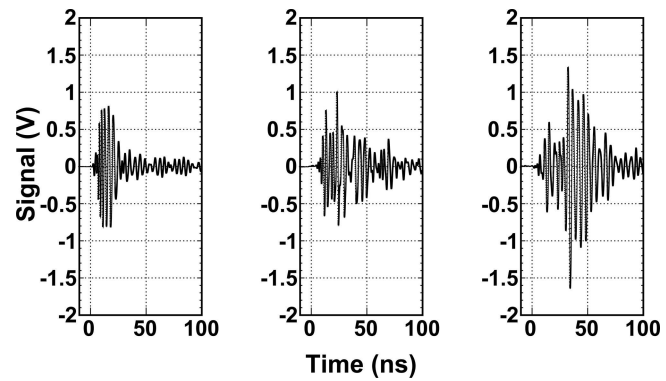


**Fig. 6.** Typical waveforms from 2011, averaged over 100 triggers. (a) The calibration pulse. (b) The vertical bounce reflection. (c) The angled bounce reflection. The vertical and angled bounce data have been amplified by the 60 dB Miteq amplifier. The data have been scaled to account for in-line attenuators (the data were kept within the amplifier linear range).

power spectra of the calibration, vertical bounce and angled bounce reflections,  $\sqrt{R}$  can be derived separately from the attenuation length. The errors in  $\sqrt{R}$  arise from propagating errors in path length (from thickness, and geometry) and returned power through Eqn (13).

The three tests (calibration, vertical and angled bounce) serve as three measurements of  $f(d)$  for different values of the path length  $d$ , given the free parameter  $\sqrt{R}$ . The measurements are compared to the linear model  $f_{\text{model}} = -d/\langle L \rangle + f_0$ , which is scanned through  $(\sqrt{R}, \langle L \rangle)$  parameter space. The y-intercept is irrelevant to the physics, coming from the linear fit upon each iteration. (The overall power at a given frequency is relative to the calibration pulse power.) Each iteration produces a  $\chi^2$  value, and  $(\sqrt{R}, \langle L \rangle)$  were scanned until a global minimum was reached at each frequency.

The averaged power spectra of the time-dependent waveforms are shown in Figure 5a. The spectra are constructed from averaging the modulus-squared of the fast Fourier transform of the time-dependent signals, and plotted relative to the maximum calibration power. The error bars are the error in the mean for each bin. Examples of waveforms from which these power spectra are derived are shown separately in Figure 6. For all recorded waveforms, a sampling rate of 5 GHz was used on the 1 GHz bandwidth oscilloscope. The spectra in Figure 5 have a frequency resolution of 0.025 GHz.

The 2010 data for  $\sqrt{R}$  vs  $\langle L \rangle$  have been analysed by Hanson (2011, 2013). The basic results were  $480 \text{ m} \leq \langle L \rangle \leq 510 \text{ m}$  ( $17\text{--}18 \text{ dB km}^{-1}$ ), and  $0.72 \leq \sqrt{R} \leq 0.88$  ( $1.1\text{--}2.8 \text{ dB loss}$ ), for the average attenuation length and reflection coefficient (68% confidence level). The set-up (Fig. 2) demonstrated good transmission through surface snow for frequencies below 0.180 GHz that season, and the LDPA lower limit in the snow is 0.080 MHz. The index of refraction of snow extends the LPDA response to 0.080 GHz from a lower limit of 0.105 GHz (Barwick and others, 2015). A shorter angled bounce baseline ( $543 \pm 7 \text{ m}$ ) was chosen for the 2011 season, relative to the prior year, to boost signal at higher frequencies; however, the snow absorption effect was not observed in 2011.

Figure 5b shows the  $\sqrt{R}$  results from the 2011 season. The baseline sets the path length difference between the

**Table 3.** Summary of dielectric parameters. The first column is the frequency,  $\nu$ , followed by the attenuation lengths, which are uncorrected ( $\langle L_0 \rangle$ ) and corrected ( $\langle L \rangle$ ) for  $\sqrt{R} = 0.82 \pm 0.07$ . The fourth column is  $\langle L \rangle$  expressed in dB km $^{-1}$ . The imaginary part of the dielectric constant,  $\epsilon''$ , is shown in the fifth column. The final column shows  $\nu \tan \delta$  (GHz). The typical error on the quantity  $\nu \tan \delta$  is  $0.2 \times 10^{-4}$

$\nu$ GHz	$\langle L_0 \rangle$ m	$\langle L \rangle$ m	$\langle L \rangle$ dB km $^{-1}$	$\epsilon'' \times 10^3$	$\nu \tan \delta \times 10^4$ GHz
0.100	432	449	19.3	3.8	1.2
0.175	467	487	17.8	2.0	1.1
0.250	457	476	18.2	1.4	1.1
0.325	422	438	19.8	1.2	1.2
0.400	408	423	20.5	1.0	1.3
0.475	366	378	23.0	0.95	1.4
0.550	349	360	24.1	0.86	1.5
0.625	363	375	23.2	0.72	1.4
0.700	331	341	25.5	0.71	1.6
0.775	310	319	27.2	0.69	1.7
0.850	320	329	26.4	0.61	1.6
Ave.	$380 \pm 16$	$400 \pm 18$	$22 \pm 1$	$1.3 \pm 0.3$	$1.37 \pm 0.06$

angled and vertical cases, introducing a trade-off. A shorter baseline causes the attenuation length to become large compared to the difference in path length between the angled and vertical bounce tests ( $\sim 130$  m in 2011). At low frequencies, the difference in power loss between vertical and angled cases becomes smaller than the errors in the power spectra ( $\sim 3$  dB at 0.300 GHz). Alternatively, the baseline for the angled bounce can be increased, which increases the path length difference between angled and vertical bounces. While this increases the low-frequency precision, the high-frequency precision suffers due to increased absorption in the angled bounce data. The vertical and angled signal power are equal within statistical errors up to 0.300 GHz in Figure 5a, but differences in the vertical and angled power are measurable up to 0.850 GHz.

Figure 5b shows  $\sqrt{R}$ , with statistical errors from the fit, at each frequency. The errors are conservative, in that all the deviation from a perfect linear model (Eqn (14)) is attributed to error in  $\sqrt{R}$ . The mean is  $\sqrt{R} = 0.82 \pm 0.07$  ( $-1.7$  dB), and a flat model at this mean has a chi-squared result of  $\chi^2/\text{dof} = 1.2$ . Despite fluctuations in the data, no data point deviates above the physical region by much more than one standard deviation. At each point in the bandwidth where the gap between the reflected and calibration spectra randomly decreases, the parameter  $\sqrt{R}$  must fluctuate upwards to produce a linear fit to  $f(d)$ . These data have larger error bars, because the deviation in  $f(d)$  from a linear model is larger for those bins. An unweighted flat-line fit to the data is shown; this fit produces the same results, within statistical uncertainties, as a weighted fit (that de-emphasizes the points with large errors). If the bins with  $\sqrt{R} > 1$  are ignored in the fit, then the mean decreases by 20% ( $\sqrt{R} = 0.6$ ).

Ignoring the data above 1.0, however, would raise the attenuation length results, because the total power loss must be conserved (Table 3). As the attenuation length has the stronger impact on the design of the future ARIANNA detector, relative to the reflection coefficient, it is important to be conservative with regard to the attenuation length in

Table 3 (Dookayka, 2011). The origin of the roughness in the reflected spectra is likely noise interference, since the signal-to-noise ratio is lower than in the calibration study.

Finally, knowledge of the basal reflection coefficient allows the correction of the attenuation length numbers in Figure 4 to more realistic values. If  $\langle L_0 \rangle$  is the measured attenuation length, assuming  $\sqrt{R} = 1.0$ , then the actual attenuation length  $\langle L \rangle$  can be expressed as

$$\frac{\langle L \rangle}{\langle L_0 \rangle} = \left( 1 + \frac{\langle L_0 \rangle}{2d_{\text{ice}}} \ln R \right)^{-1} \quad (19)$$

Using the  $\langle L_0 \rangle$  values from Figure 4, Table 3 shows the  $\langle L \rangle$  results for the mean value of  $\sqrt{R} = 0.82 \pm 0.07$ , vs frequency. Table 3 also shows the imaginary part of the dielectric constant, derived from  $n''$ , via  $\langle L \rangle^{-1} = n''k$ , where  $k$  is the free-space wavenumber. Assuming  $\tan \delta \ll 1$ , the expression  $\epsilon'' = 2n''\sqrt{\epsilon'}$ , with  $\sqrt{\epsilon'} = 1.78$ , relates the two quantities.

The  $\epsilon''$  results are in agreement with an earlier low-frequency projection for typical ice-shelf temperatures (Matsuoka and others, 1996). The Debye model predicts  $\epsilon'' \propto \nu^{-1}$  for frequencies below 2 GHz, and the  $\epsilon''$  data follow this trend. The quantity  $\nu \tan \delta$  is expected to be small and constant for a simple dielectric material, and Table 3 also displays this quantity in the final column, which agrees with an estimate from analysis of the 2006 data (Barrella and others, 2011). Although  $\nu \tan \delta$  varies with frequency, this variation is such that no measurement is more than one standard deviation ( $0.2 \times 10^{-4}$ ) from the mean ( $1.37 \pm 0.06$ ).

## POLARIZATION MEASUREMENTS

The  $\sqrt{R}$  result shows that little power is lost from the basal reflection. In this section, we assess potential losses by scattering or rotation of the linearly polarized signal. For any non-ideal linearly polarized antenna system, a small amount of power can leak into the cross-polarized channel. Significant transfer of power into the cross-polarized direction would indicate polarization rotation in the ice, and bias the attenuation length results. Birefringence and surface roughness effects at the water–ice interface at the bottom of the ice shelf are expected to generate power in the cross-polarized direction.

To quantify the polarization rotation, the cross-polarization fraction,  $F_{\text{ice}}$ , was measured in the vertical bounce configuration, and compared to  $F_{\text{air}}$ .  $F$  is defined in Eqn (20), where  $P_{\perp}$  and  $P_{\parallel}$  refer to the measured power in the cross-polarized and co-polarized direction with respect to the linear polarization of the transmitter at a given frequency:

$$F = \frac{P_{\perp}}{P_{\perp} + P_{\parallel}} \quad (20)$$

The leakage between co-polarized and cross-polarized channels is expected to be low across the bandwidth, but difficult to observe at high frequencies. Cross-polarized signals are weaker than co-polarized, and the vertical bounce data in the cross-polarized state are subject to noise interference above 0.4 GHz. The intrinsic transfer into the cross-polarized direction of a specified antenna pair was estimated by facing the transmitter toward the receiver in air.  $F_{\text{air}}$  is computed from the power observed between co-polarized and cross-polarized orientation of the receiver. The results of this study are shown in the third column of

Table 4. It was verified that the snow surface 1.5 m below the antennas scatters back a negligible amount of power.

$F_{\text{ice}}$  was obtained from the vertical bounce set-up, with a Seavey transmitter and LPDA receiver. The Seavey antenna transmits very little power below 0.175 GHz, and the cross-polarized signal is weaker than the co-polarized signal, limiting  $F_{\text{ice}}$  results to frequencies below 0.4 GHz. These measurements are shown in column 4 of Table 4. These data can be compared to measurements taken in 2010, in which  $F_{\text{ice}}$  and  $F_{\text{air}}$  were shown to agree at 0.1 GHz with a LPDA transmitter and LPDA receiver at the same location as the 2011 measurements (Hanson, 2011). A comparison of  $F_{\text{air}}$  with  $F_{\text{ice}}$  reveals no excess power in the cross-polarization direction, with the possible exception of data at 0.400 GHz, which show a  $2\sigma$  deviation from intrinsic antenna effects. These data do not confirm the  $F_{\text{ice}}$  analysis of the 2006 data, which showed  $F_{\text{ice}} = 0.7$  at 0.4 GHz.

## DISCUSSION

The data are in agreement with independent analyses and models. A study from Greenland found the total transfer function of the Greenland ice sheet, and models the different contributions from basal reflection and attenuation (Paden and others, 2005). A reflection coefficient (for power) of  $-37$  dB is reported for the North Greenland Ice Core 2 (NGRIP2) location, and ice absorption of  $\sim 56$  dB. Given the depth of 3.1 km, a loss rate of  $\sim 9.0$  dB km $^{-1}$  is obtained. (The Greenland study was limited to 0.11–0.5 GHz.) The upper half of the Greenland ice sheet is colder than Moore's Bay, lowering the attenuation rate through temperature dependence of  $\epsilon''$ . The reflection coefficient from that study ( $-37$  dB) is much smaller than that of Moore's Bay. However, other authors have estimated it to be higher (Bamber and others, 2001; Avva and others, 2014), with an absorption rate of 9.2 dB km $^{-1}$ , conservatively assuming no reflection loss (attributing all loss to absorption). The Greenland site also exhibits a frequency dependence that produces a change of 8.5 dB km $^{-1}$  over the bandwidth (0.11–0.5 GHz). The slope of the loss rate vs frequency is therefore  $8.5/(0.55 - 0.11) \approx 22$  dB km $^{-1}$  GHz $^{-1}$ . The corresponding value for the ARIANNA site is 9.3 dB km $^{-1}$  GHz $^{-1}$ , from Table 3.

Another study presents models for ice absorption across the entire Antarctic continent, given an array of inputs, such as temperature and chemistry data (Matsuoka and others, 2012). That expansive study presents results for shelf and sheet depth across the continent, and the portion depicting the Ross Ice Shelf, near the ARIANNA site, is in agreement with our thickness measurements. The RIS depth is peaked at 500 m in that model, and we find  $576 \pm 8$  m. The inputs to this model indicate that the Ronne Ice Shelf has smaller absorption rates (dB km $^{-1}$ ) than the Ross Ice Shelf, which leads to a double-peaked distribution of loss rates, with one peak near 12.5 dB km $^{-1}$ , and the other near 22.5 dB km $^{-1}$ . The ARIANNA site average absorption rate is within one standard deviation of the mean for the entire distribution ( $15.1 \pm 6.2$  dB km $^{-1}$ ), and is in agreement with the second peak in the distribution of loss rates, corresponding to the Ross Ice Shelf.

Finally, a study of the Ross Ice Shelf at 2 MHz reveals large-scale thickness uniformity in the shelf, up to 40 km from the grounding line of the glaciers flowing into the shelf

**Table 4.** A comparison of cross-polarization fraction measurements vs frequency

Frequency GHz	$F_{\text{air}}$	$F_{\text{ice}}$
0.175	$0.06 \pm 0.02$	$0.08 \pm 0.05$
0.200	$0.04 \pm 0.01$	$0.01 \pm 0.01$
0.225	$0.04 \pm 0.02$	$0.02 \pm 0.01$
0.250	$0.02 \pm 0.01$	$0.01 \pm 0.01$
0.275	$0.02 \pm 0.01$	$0.02 \pm 0.01$
0.300	$0.02 \pm 0.01$	$0.07 \pm 0.04$
0.325	$0.01 \pm 0.005$	$0.03 \pm 0.01$
0.350	$0.04 \pm 0.01$	$0.08 \pm 0.03$
0.375	$0.02 \pm 0.01$	$0.11 \pm 0.07$
0.400	$0.03 \pm 0.01$	$0.22 \pm 0.09$

(MacGregor, 2011). The measurements are obtained from basal echoes with travelling transmitters and receivers at the surface. In some cases, multiple echoes are observed, corresponding to multiple round trips made by the signal, from surface to base. This technique provides excellent constraints on the thickness and absorption rate. Specifically, this study shows that our depth measurement is typical for large expanses of ice, a key requirement for large-scale ground arrays in neutrino detectors.

## CONCLUSION

During the 2011/12 Antarctic season, radio-echo sounding measurements were performed in Moore's Bay with high-voltage broadband RF pulses in the 0.1–0.850 GHz bandwidth, to understand the dielectric properties of the ice shelf. The shelf thickness determined from the total propagation time was  $576 \pm 8$  m. The echo soundings revealed depth-averaged attenuation lengths well fit by the linear function  $\langle L(\nu) \rangle = (460 \pm 20) - (180 \pm 40) \times \nu \text{ m}$  (19.3–26.4 dB km $^{-1}$ ), where  $\nu$  is the frequency (GHz). The  $\chi^2/\text{dof}$  of this linear fit to the combination of multiple datasets was 1.2, with 9 degrees of freedom. The fit is consistent with prior measurements (Barrella and others, 2011), and the functional dependence is compatible with theoretical expectations (Matsuoka and others, 1996; Somaraju and others, 2006).

Vertical echo soundings were compared to echo soundings with a  $543 \pm 7$  m baseline between transmitter and receiver, which allowed independent measurement of the basal reflection coefficient, found to be  $\sqrt{R} = 0.82 \pm 0.07$  ( $-1.7$  dB). The slope of  $\sqrt{R}$  vs frequency is consistent with a flat-mirror approximation. The average value of  $\sqrt{R}$  is consistent with earlier studies performed at lower frequencies (Neal, 1979). The short duration of the observed pulses (90% of the power contained within 100 ns) precludes significant multi-path effects. The Fresnel zones of the pulses at the shelf base are not significantly larger than measured horizontal correlation lengths. After correcting attenuation lengths for the effect of  $\sqrt{R}$  on returned power, dielectric quantities like  $\epsilon''$  and  $\nu \tan \delta$  were derived. The results for  $\epsilon''$  and  $\nu \tan \delta$  agree with theoretical expectations (Matsuoka and others, 1996). Finally, the fraction of scattered power by the ice into the cross-polarized direction,  $F_{\text{ice}}$ , is  $< 10\%$  (0.100–0.400 GHz), compatible with the fraction of power

due to intrinsic limitations of the transmitting and receiving antennas. Both the large value of  $\sqrt{R}$  and the small value of  $F_{\text{ice}}$  suggest that the bottom surface of the Ross Ice Shelf at Moore's Bay is smooth. The measurements of  $F_{\text{ice}}$  do not demonstrate any significant features below 0.400 GHz, where cross-polarized power is noise-limited. This result, combined with the measured field attenuation length at frequencies between 0.100 and 0.850 GHz, suggests that the Moore's Bay region of the Ross Ice Shelf will be an excellent medium for the ARIANNA high-energy neutrino project.

## ACKNOWLEDGEMENTS

We thank the staff of Antarctic Support Contractors, Lockheed, Raytheon Polar Services, and the entire crew at McMurdo station for excellent logistical support. This work was supported by generous funding from the Office of Polar Programs and Physics Division of the US National Science Foundation, grant awards ANT-08339133, NSF-0970175 and NSF-1126672. In 2010, additional funding was provided through the US Department of Energy under contract DE-AC-76SF-00098. Finally, we thank David Saltzberg for comments and suggestions throughout the expeditions and analysis.

## REFERENCES

- Allison P and 47 others (2012) Design and initial performance of the Askaryan Radio Array prototype EeV neutrino detector at the South Pole. *Astropart. Phys.*, **35**, 457–477
- AMANDA Collaboration (2006) Optical properties of deep glacial ice at the South Pole. *J. Geophys. Res.*, **111**(D13), D13203 (doi: 10.1029/2005JD006687)
- ANITA Collaboration (2009) The Antarctic Impulsive Transient Antenna ultra-high energy neutrino detector: design, performance, and sensitivity for 2006–2007 balloon flight. *Astropart. Phys.*, **32**(1), 10–41
- ANITA Collaboration (2010) Observational constraints on the ultrahigh energy cosmic neutrino flux from the second flight of the ANITA experiment. *Phys. Rev. D*, **82**(2), 022004 (doi: 10.1103/PhysRevD.82.022004)
- Askaryan GA (1962) Excess charge of an electron-photon shower and its coherent radio emission. *Sov. Phys. JETP*, **14**(2), 441–442
- Avva J, Kovac JM, Miki C, Saltzberg D and Vieregg AG (2014) An in situ measurement of the radio-frequency attenuation in ice at Summit Station, Greenland. arXiv:1409.5413
- Bamber JL, Layberry RL and Gogineni SP (2001) A new thickness and bed data set for the Greenland ice sheet: 1. Measurement, data reduction, and errors. *J. Geophys. Res.*, **106**(D24), 33 773–33 780
- Barrella T, Barwick S and Saltzberg D (2011) Ross Ice Shelf (Antarctica) in situ radio-frequency attenuation. *J. Glaciol.*, **57**(201), 61–66
- Barwick SW (2007) ARIANNA: a new concept for UHE neutrino detection. *J. Phys. Conf. Ser.*, **60**, 276–283 (doi: 10.1088/1742-6596/60/1/060)
- Barwick SW and 14 others (2015) The time-domain response of the ARIANNA detector. *Astropart. Phys.*, **62**, 139–151 (doi: 10.1016/j.astropartphys.2014.09.002)
- Besson D and 42 others (2008) In-situ radioglaciological measurements near Taylor Dome, Antarctica and implications for UHE neutrino astronomy. *Astropart. Phys.*, **29**(2), 130–157
- Bogorodsky VV, Bentley CR and Gudmandsen PE (1985) *Radio-glaciology*. Reidel Publishing Co., Dordrecht
- Dookayka K (2011) Characterizing the search for ultra-high energy neutrinos with the ARIANNA Detector. (PhD thesis, University of California, Irvine)
- Dowdeswell JA and Evans S (2004) Investigations of the form and flow of ice sheets and glaciers using radio-echo sounding. *Rep. Progr. Phys.*, **67**(10), 1821–1861
- Fahnestock MA, Scambos TA, Bindschadler RA and Kvaran G (2000) A millennium of variable ice flow recorded by the Ross Ice Shelf, Antarctica. *J. Glaciol.*, **46**(155), 652–664
- Fretwell P and 55 others (2013) Bedmap2: improved ice bed, surface and thickness datasets for Antarctica. *Cryosphere*, **7**(1), 375–393 (doi: 10.5194/tc-7-375-2013)
- Gerhardt L and 6 others (2010) A prototype station for ARIANNA: a detector for cosmic neutrinos. *Nucl. Instrum. Meth. Phys. Res. A*, **624**(1), 85–91
- Hanson JC (2011) Ross Ice Shelf thickness, radio-frequency attenuation and reflectivity: implications for the ARIANNA UHE neutrino detector. *Proceedings of the 32nd International Cosmic Ray Conference, 11–18 August, Beijing, China*. Institute of High Energy Physics, Beijing
- Hanson JC (2013) The performance and initial results of the ARIANNA prototype. (PhD thesis, University of California, Irvine)
- IceCube Collaboration (2013) Evidence for high-energy extra-terrestrial neutrinos at the IceCube detector. *Science*, **342**(6161), 1242856 (doi: 10.1126/science.1242856)
- Klein, SR (2012) Radiodetection of neutrinos. *Nucl. Phys. Proc. Suppl.*, **229–232**, 284–288
- Kravchenko I and 8 others (2012) Updated results from the RICE experiment and future prospects for ultra-high energy neutrino detection at the south pole. *Phys. Rev. Lett. D*, **85**, 062004
- MacGregor J, Anandakrishnan S, Catania GA and Winebrenner DP (2011) The grounding zone of the Ross Ice Shelf, West Antarctica, from ice-penetrating radar. *J. Glaciol.*, **57**(205), 917–928
- Matsuoka K, Fujita S and Mae S (1996) Effect of temperature on dielectric properties of ice in the range 5–39 GHz. *J. Appl. Phys.*, **80**(10), 5884–5890
- Matsuoka K, MacGregor JA and Pattyn F (2012) Predicting radar attenuation within the Antarctic ice sheet. *Earth Planet. Sci. Lett.*, **359–360**, 173–183 (doi: 10.1016/j.epsl.2012.10.018)
- Neal CS (1979) The dynamics of the Ross Ice Shelf revealed by radio echo-sounding. *J. Glaciol.*, **24**(90), 295–307
- Neal CS (1982) Radio echo determination of basal roughness characteristics on the Ross Ice Shelf. *Ann. Glaciol.*, **3**, 216–221
- Paden J, Allen CT, Gogineni S, Jezek KC, Dahl-Jensen D and Larsen LB (2005) Wideband measurements of ice sheet attenuation and basal scattering. *Geosci. Remote Sens. Soc. Newslett.*, **2**(2) (doi: 10.1109/LGRS.2004.842474)
- Peters M, Blankenship DD and Morse DL (2005) Analysis techniques for coherent airborne radar sounding: application to West Antarctic ice streams. *J. Geophys. Res.*, **110**(B6), B06303 (doi: 10.1029/2004JB003222)
- Rignot E, Jacobs S, Mouginot J and Scheuchl B (2013) Ice-shelf melting around Antarctica. *Science*, **341**(6143), 266–270 (doi: 10.1126/science.1235798)
- Schytt V (1958) The inner structure of the ice shelf at Maudheim as shown by core drilling. In *Norwegian–British–Swedish Antarctic Expedition, 1949–52, scientific results*. Norsk Polarinstitutt, Oslo, 113–151
- Somaraju R and others (2006) Frequency, temperature and salinity variation of the permittivity of seawater. *IEEE Trans. Antennas Propag.*, **54**(11), 3441–3448
- United States Geological Survey (USGS) (2012) *Landsat Image Mosaic of Antarctica (LIMA)*. lima.usgs.gov/

# Design and Performance of the ARIANNA HRA-3 Neutrino Detector Systems

S. W. Barwick, E. C. Berg, D. Z. Besson, T. Duffin, J. C. Hanson, S. R. Klein,  
*S. A. Kleinfelder, Senior Member, IEEE*, K. Ratzlaff, C. Reed, M. Roumi,  
 T. Stezelberger, J. Tatar, J. Walker, R. Young, and L. Zou

**Abstract**—We report on the development, installation, and operation of the first three of seven stations deployed at the ARIANNA site’s pilot Hexagonal Radio Array (HRA) in Antarctica. The primary goal of the ARIANNA project is to observe ultrahigh energy ( $> 100$  PeV) cosmogenic neutrino signatures using a large array of autonomous stations, each 1 km apart on the surface of the Ross Ice Shelf. Sensing radio emissions of 100 MHz to 1 GHz, each station in the array contains RF antennas, amplifiers, 1.92 G-sample/s, 850 MHz bandwidth signal acquisition circuitry, pattern-matching trigger capabilities, an embedded CPU, 32 GB of solid-state data storage, and long-distance wireless and satellite communications. Power is provided by the sun and buffered in LiFePO<sub>4</sub> storage batteries, and each station consumes an average of 7 W of power. Operation on solar power has resulted in  $\geq 58\%$  per calendar-year live-time. The station’s pattern-trigger capabilities reduce the trigger rates to a few milli-Hertz with 4-sigma voltage thresholds while retaining good stability and high efficiency for neutrino signals. The timing resolution of the station has been found to be 0.049 ns, RMS, and the angular precision of event reconstructions of signals bounced off of the sea–ice interface of the Ross Ice Shelf ranged from 0.14 to 0.17°.

**Index Terms**—Analog integrated circuits, Antarctica, antenna arrays, astrophysics, embedded software, ice shelf, mesh networks, programmable logic arrays, switched capacitor circuits.

## I. INTRODUCTION

THE Antarctic Ross Ice-shelf ANtenna Neutrino Array (ARIANNA) project is a surface array of radio receivers planned to span  $\sim 1000$  km<sup>2</sup> of the Ross Ice Shelf in Antarctica, viewing  $\sim 0.5$  Teratons of ice [1]–[4]. The project will detect

Manuscript received March 03, 2015; revised June 30, 2015; accepted July 28, 2015. Date of publication September 29, 2015; date of current version October 09, 2015. This work was supported by funding from the Office of Polar Programs and the Physics Division of the U.S. National Science Foundation, including via grant awards ANT-08339133, NSF-0970175, and NSF-1126672. (Corresponding author: S. A. Kleinfelder.)

S. W. Barwick, E. C. Berg, T. Duffin, C. Reed, and J. Walker are with the Department of Physics and Astronomy, University of California, Irvine, Irvine, CA 92697 USA.

S. A. Kleinfelder, M. Roumi, and L. Zou are with the Department of Electrical Engineering and Computer Science, University of California, Irvine, Irvine, CA 92697 USA (e-mail: stuartk@uci.edu).

D. Z. Besson and J. C. Hanson is with the Department of Physics and Astronomy, University of Kansas, Lawrence, KS 66045 USA, and the Moscow Engineering Physics Institute, Moscow, Russia.

S. R. Klein, T. Stezelberger, and J. Tatar are with the Lawrence Berkeley National Laboratory, Berkeley, CA 94720 USA.

K. Ratzlaff and R. Young are with the Instrumentation Design Laboratory, University of Kansas, Lawrence, KS 66045 USA.

Color versions of one or more of the figures in this paper are available online at <http://ieeexplore.ieee.org>.

Digital Object Identifier 10.1109/TNS.2015.2468182

radio waves originating from high energy neutrino interactions with atoms in the ice via the Askaryan Effect [5]. Neutrino interactions produce a shower of secondary particles, plus, for  $\nu_\mu$  charged current interactions, an energetic muon. The secondary particles produce an electromagnetic or hadronic shower which extends over a length of many meters increasing logarithmically with energy, with a transverse dimension of about 10 cm. For wavelengths much larger than this transverse dimension, electromagnetic radiation is coherent, and thus depends on the net charge in the shower. Compton scattering of atomic electrons, and annihilation of shower positrons on atomic electrons both contribute to a net negative charge in the shower, leading to an intense Cherenkov radiation pulse, with a peak electric field that scales linearly with the shower energy. The frequency range of the radiation depends on the angle of observation of the shower. In ice, near the Cherenkov angle of about 56 degrees, the coherent radiation extends up to a maximum frequency of about 1 GHz; away from the Cherenkov angle, the cutoff is lower. ARIANNA is designed to improve the sensitivity to neutrinos with energies in excess of  $10^{17}$  eV by at least an order of magnitude relative to existing limits [6], [7]. Its goals include a confirmation and measurement of the Greisen–Zatsepin–Kuzmin neutrino flux [8], [9], which results from cosmic rays interacting with the diffuse cosmic microwave background, and to measure the neutrino-nucleon cross-section.

ARIANNA takes advantage of unique geophysical features of the Ross Ice Shelf [10], [11]. At ARIANNA’s location on the ice shelf, approximately 78.7°S, 165°E, the water–ice interface of the ice shelf acts as a nearly perfect mirror for radio pulses generated by extremely high-energy neutrinos traveling downward and interacting in the interface [12]. The ice’s long attenuation length allows for the detection of direct and reflected radio pulses at the surface, far from the interaction point. This and the ice shelf’s relative proximity to McMurdo Station ( $\sim 100$  km away) significantly simplifies the deployment of a large array. Moreover, by its uninhabited location, the site has been found to be essentially free of anthropogenic noise.

ARIANNA stations are easy to deploy, maintain, and upgrade. Each station (see Fig. 1) contains RF antennas, amplifiers, triggering, digitization, computing, power management, data storage, long-distance wireless networking and satellite communications, solar power and battery backup, plus experimental wind power. Four stations have been installed, including an early prototype deployed in 2011 [4] and three pilot stations from the pilot seven-station Hexagonal Radio Array (HRA),

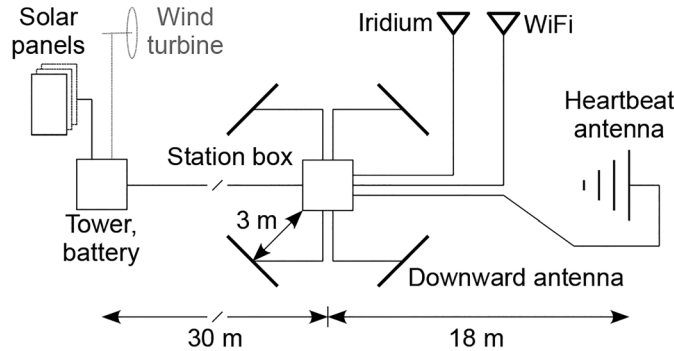


Fig. 1. Schematic station overview showing basic elements and distances (not to scale) of an ARIANNA Hexagonal Radio Array station.

which were deployed in December of 2012 and are the subject of this paper.

ARIANNA is a surface array, with most components buried less than 1 m beneath the snow surface. This design has many practical advantages when compared with deep-ice experiments [13]–[17], the most obvious of which is that no drilling is necessary to deploy the stations, saving an enormous amount of fuel, environmental impact, expense, effort and time. Surface deployment imposes far fewer geometric constraints on receiver antennas and electronic systems than deep-ice designs. In particular, the receiving antennas, which are unconstrained by the need to fit within boreholes, can provide much better measurement of the Cherenkov polarization and, therefore, the event geometry. Cabling between antennas and electronics, etc., are also minimized and at the surface. Deployed equipment is fully retrievable, and servicing or upgrades are possible while keeping most of the installed infrastructure intact.

Sections II–VI of this paper focuses on the design of the major subsystems of the stations deployed in 2012 as part of a pilot phase of the ARIANNA project, known as the HRA. Section VII describes the system software for station monitoring and remote control. It also outlines the data collection, transmission and archiving procedures. Section VIII provides a discussion of the operational performance of the power systems, monitoring systems, trigger rates and environmental influences, and evaluation of the data quality.

## II. ARIANNA HEXAGONAL RADIO ARRAY

In 2010, the National Science Foundation approved the HRA pilot program of the ARIANNA project, consisting of seven stations dispersed on the ice in a hexagonal grid with 1 km between neighboring stations. The HRA's focus is to develop the technologies needed for a network of autonomous stations that achieve the performance necessary for the physics aims of the full-scale ARIANNA project. Stations must provide their own power, and must allow unattended remote monitoring, data retrieval and control. Operation at temperatures to  $-30^{\circ}\text{C}$  or lower, and survival during harsh Antarctic conditions is a necessity. The electronics must be highly-sensitive over a 100–1000 MHz frequency range and perform without creating any radio frequency noise in this spectrum. Stations must be cost-effective and quick to deploy.

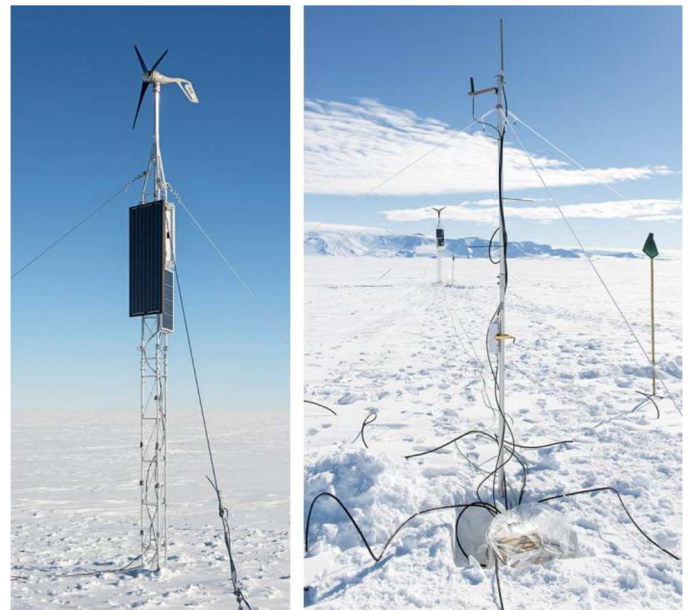


Fig. 2. HRA system on the Ross Ice Shelf during deployment in 2012, showing a power tower (left), a communication's mast (right) with a station box inside clear plastic at the foot of the mast, and a flag marking the location of one of four buried downward-pointing instrumentation antennas.

An early prototype station including a new 1.92 G-samples/s waveform acquisition and advanced real-time triggering system (“ATWD”) was deployed in December of 2011 [4]. In December of 2012, ARIANNA deployed the first three HRA stations, and converted the 2011 station to a weather monitoring post and WiFi repeater. The second-generation ARIANNA design replaced the prototype’s hand-assembled electronics with a unified, mass-produced printed-circuit electronics system, replaced separate hand-constructed solar panel and wind turbine support structures with an integrated commercial tower system, and made many other refinements resulting in a much lower power ( $< 7\text{ W}$  average), much lower cost, lighter weight, lower noise, better calibrated and much faster and easier to deploy system.

The National Science Foundation (NSF) approved deployment of the HRA’s remaining four stations during the 2014–2015 Austral summer. These stations include simplifications of the power tower, including the integration of the communications antennas, improved amplifiers, and a simpler, lower-cost, lower-power, single board data acquisition system incorporating a new multichannel signal acquisition chip, including deeper waveform storage and simplified trigger formation.

Each ARIANNA HRA station deployed thus far is divided into two major components: a power tower and an instrumentation and communications box with associated antennas. A power tower is shown in Fig. 2 (left), and a communication mast is shown (Fig. 2, right) with an omnidirectional antenna for mesh-connected wireless communications with McMurdo Station via a repeater on Mt. Discovery, plus an antenna for Iridium satellite short-burst messaging.

A station and amplification box assembly (see Sections III and IV) lies at the foot of the communications mast

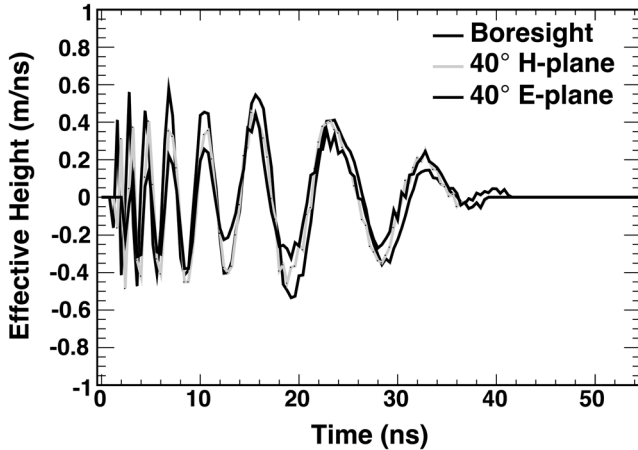


Fig. 3. Example antenna effective height versus off-axis angle for the E- and H-planes at 0° (“boresight”) and 40° off-axis.



Fig. 4. The 2012 ARIANNA station’s amplifier box (inputs to the left, outputs and power to the right). It contains four amplifiers, each with four AC-coupled 1.5 GHz GaAs amplifier stages with interstage bandwidth shaping.

(Fig. 2, right), wrapped in plastic to prevent ice build-up on its connectors, etc. Four signal acquisition antennas surround the communications mast, with the position of one marked by the green flag on the right-hand side of the photo.

### III. ANTENNAS AND AMPLIFICATION

Each station includes four log-periodic dipole antennas (Creative Design Co. model CLP5130-2N), positioned as two orthogonal pairs of parallel antennas 6 m apart, pointing straight down into the ice. These antennas have 17 elements and are about 1.4 m long, with the span of its largest tines being 1.45 m. The frequency response ranges from 105–1300 MHz with a VSWR of 2.0:1 or less across the band (in air; in snow, their lower frequency limit is expected to be 70–80 MHz, e.g. in [1]). The forward gain was measured to be 7–8 dBi, with a front-to-back ratio of 15 dB. An example plot of the antenna’s measured effective height (ratio of the induced voltage to the incident field) in the E-plane and H-plane at a common 40° off-axis angle is shown in Fig. 3 [18]. The antennas are connected via ~5 m low-loss LMR-400 cable (N-type connectors on both ends) to an RF-tight box containing four radio-frequency amplifiers (Fig. 4). Band-pass filtering leaves a frequency range of 100–1000 MHz intact.

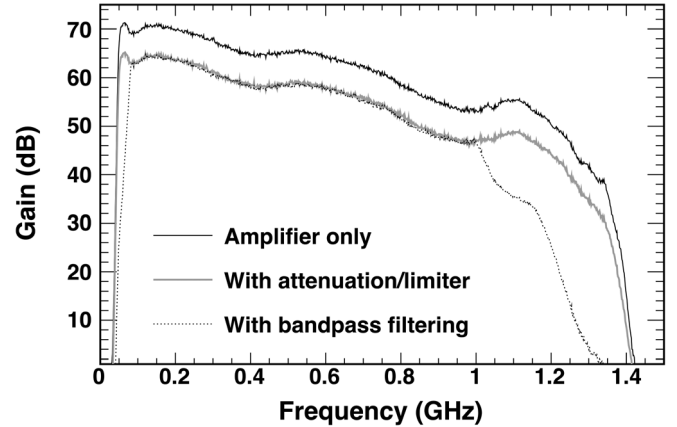


Fig. 5. ARIANNA amplifier gain versus frequency plot. From top to bottom, the curves show the amplifier alone, the amplifier plus output attenuation and limiting, and the former with input band-pass filtering.

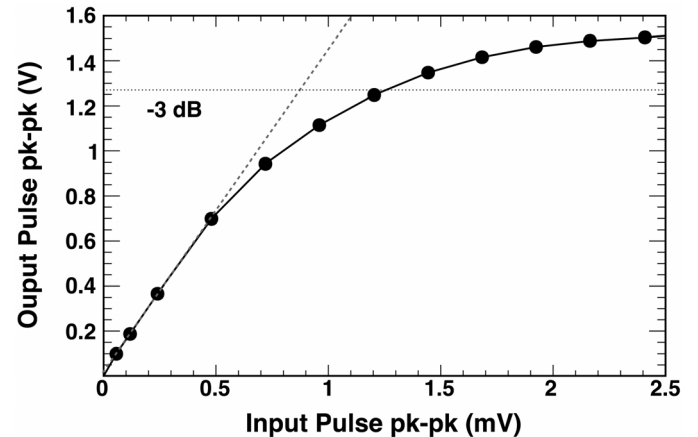


Fig. 6. Amplification system response to an impulsive input signal of varying magnitude, including input band-pass filtering and output limiting and attenuation. Note that the vertical scale is three orders of magnitude greater than the horizontal scale (V versus mV).

Each amplifier consists of four AC-coupled 1.5 GHz GaAs gain stages (Avago MGA-68563) with interstage filtering, yielding about 50–70 dB of gain over the frequency range of interest (Fig. 5). Power is conditioned in the main data acquisition enclosure and is supplied via coaxial cable to the amplifier box. Each amplifier consumes about 250 mW of power at 3.3 V. Amplifiers are housed in individual brass enclosures that help prevent cross-talk between stages and between amplifiers. The amplifier’s output range must be matched to the signal sampling and digitization electronics, and hence attenuation and limiting components were added to the amplifier’s outputs. The limiting components cause compression of large signals, as shown in Fig. 6, as the departure from linear response for input signals greater than about 0.5 mV.

#### A. Heartbeat Generation

In order to monitor the health and stability of the ARIANNA stations, each station includes an auxiliary antenna that can transmit a radio-frequency “heartbeat” signal when triggered by the system software. The heartbeat pulse is produced by an FPGA on the system’s motherboard, and its width is set in



Fig. 7. Example of an HRA station’s amplifier box (top portion) and main system box (bottom) containing all data acquisition, control and communications electronics. For scale, the width of the front of the box as shown is 9 in, the depth is 12 in, and the total height is 11.5 in.

firmware to be about 1.5 ns full-width at half-maximum. The resulting signal is sent via LMR 600 cable to the same model log-periodic dipole array antenna as the receiving antennas. The heartbeat antenna is laid  $\sim$ 18 m away from the center of the station with its E-plane parallel to the ground (i.e., flat on the surface), pointing back at the center of the station’s antenna array, and aimed approximately along the diagonal between the four instrumentation antennas (i.e., as in Fig. 1).

Heartbeat events are directed to occur on a programmable basis, typically at 1 Hz or less for 5 min every 6 h. The stations trigger-on and record the heartbeat events via their downward-facing receiving antennas, and transmit the digitized waveforms back to the University of California Irvine (UCI) along with other normal events. Heartbeat signals are attenuated such that only the local station can pick them up, and indeed there is no evidence to the contrary. The heartbeat signal verifies correct station operation and detects any short or long-term changes in antenna and amplifier response due to temperature or due to any accumulation of snow. As the understanding of this behavior matures, the use of the heartbeat will diminish or cease, and future systems may delete the function entirely.

#### IV. DATA ACQUISITION SYSTEM

A new HRA data acquisition system has been prepared and deployed. The main advances of this system are reduced power consumption, greatly improved manufacturability, lower cost, lower noise, improved physical integrity, lighter weight, and more compact dimensions. The overall power consumption has been reduced from  $\sim$ 30 W to  $< 7$  W during typical data taking or communications, with as little as 0.6 W possible in a minimum-power maintenance mode.



Fig. 8. ARIANNA Hexagonal Array data acquisition electronics. It includes four 1.96 GHz data acquisition channels, a 96 MHz 32-bit CPU, communications channels for wireless and satellite short-burst message system, a 32 GB memory card holder for data storage, power conditioning and control for all components, trigger I/O, “heartbeat” pulse generator, etc.

This power reduction maximizes the control, communication and acquisition time during days of waxing and waning sun and/or heavy overcast.

The amplifier and system boxes, as seen in Fig. 7, can be bolted together or kept separate. The amplifier box has four antenna inputs, four amplified outputs, and a 3.3 V power input. The main system box has four amplified signal inputs, 3.3 V power output for the amplifier box, a main power input, a “heartbeat” pulse output, an external trigger input useful during tests, and output ports for Iridium and WiFi communications. The completed station boxes are roughly one cubic foot in size and set up very rapidly in the field.

Fig. 8 shows the 2012 station electronics, consisting of four daughter-cards (one per-channel) and a motherboard (RF amplifiers and the two communications modules not shown). A block diagram of the system is shown in Fig. 9. Each daughter-card contains a 1.92 G-samples/s synchronous switched capacitor array analog sampling and digitization chip (the “ATWD”), a bias-tee module that adapts the dc offset of the incoming signal level to maximize the dynamic range of the ATWD, mode switches, power conditioning, digital-to-analog converters (DACs) for threshold range settings, and a field-programmable gate array (FPGA) that aids in operating the ATWD and allows cards to function as standalone single-channel devices if desired. Although the ATWD chips themselves include 128 ten-bit analog-to-digital converters (ADCs) for fast parallel data conversion, a higher-resolution 12-bit ADC is included on each daughter-card for signal digitization.

The system’s motherboard contains all computing, communications interface hardware, data storage and power management circuitry necessary to run the station. It includes power regulation for the antenna amplifiers, a power I/O terminal block, solid-state relays for peripheral power control, voltage and power monitoring circuitry, daughter-card power regulation and control, a holder for a 1.5 Ah lithium battery backup for the real-time clock, a 96 MHz 32-bit ARM Cortex M3 micro-controller, an external trigger input, an FPGA programming port, an Ethernet port used for WiFi communications, an RS-232 port used for Iridium satellite messaging, a 32 GB SDHC flash memory card slot, four daughter-card slots, an FPGA for fast system functions, and the “heartbeat” pulse output.

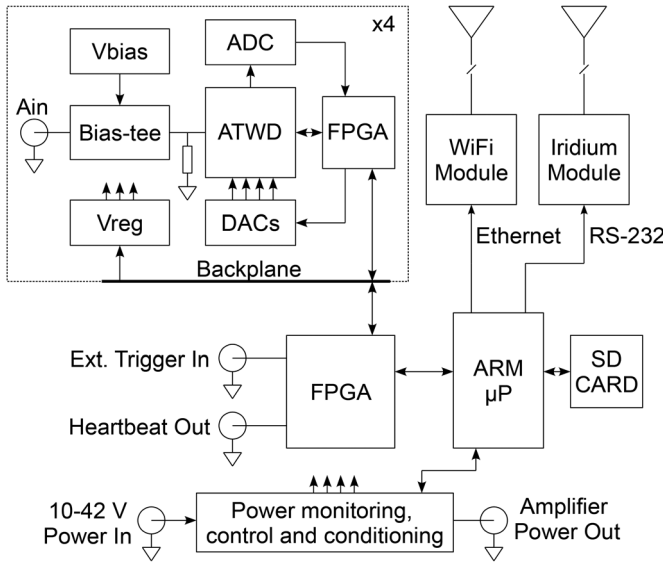


Fig. 9. Simplified block diagram of the ARIANNA system hardware.

## V. WAVEFORM ACQUISITION, TRIGGERING, AND DIGITIZATION

Triggering and waveform capture is performed by a custom CMOS integrated circuit (Advanced Transient Waveform Digitizer (ATWD) [19]–[22]) running at 1.92 G-samples/s and with  $\sim 11.5$  bits of dynamic range [23], [24]. A block diagram of the chip's internals is shown in Fig. 10. The chip incorporates real-time pattern-matching trigger functionality that allows, for example, the detection of a bipolar waveform of a certain magnitude and frequency range. A prompt trigger is produced within about 15 ns of the targeted waveform's arrival.

### A. Sample Rate and Analog Bandwidth

The ATWD uses a synchronous sample clocking scheme that leads to high sample-to-sample timing uniformity. For convenience, it is driven by a low-speed external clock, which is boosted by a factor of 32 by an on-chip phase-locked loop system and then doubled via interleaving (using both clock phases) by an additional factor of two. The ARIANNA system operates with a 30 MHz reference clock and hence achieves 1.92 G-samples/s operation. By observing a test clock output from the ATWD chips, the timing uniformity of this system has been measured to be  $\sim 1$  ppm, RMS.

The analog bandwidth of the ATWD sampling and digitization system is an important figure of merit. With a 1.92 GHz nominal sample rate, the Nyquist-limited bandwidth would be 960 MHz, and ARIANNA's amplifiers are low-pass limited to approximately match this frequency. Fig. 11 shows a plot of the frequency response of the data acquisition system as seen in Fig. 8. The frequency response of the entire system (excluding RF amplification) is seen to be flat to under  $\pm 1$  dB to about 700 MHz, and its  $-3$  dB frequency is about 860 MHz.

### B. Trigger Thresholds and Calibration

The ATWD chips perform dual (high and low) threshold triggering in real-time using a unique pattern-searching capability that is applied to the sampled signals rather than the input signal

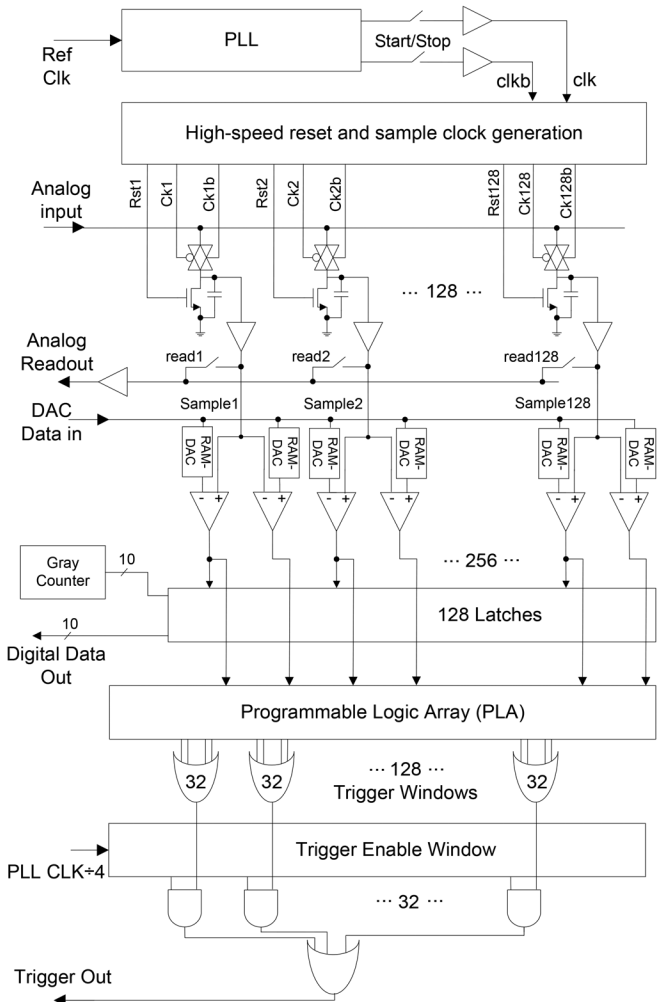


Fig. 10. Block diagram of the 2 G-samples/s synchronous ATWD integrated circuit, showing sampling, comparison, and programmable trigger logic.

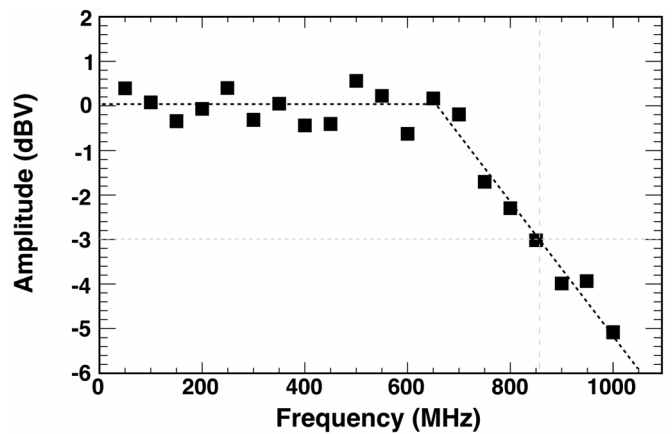


Fig. 11. Data acquisition system bandwidth (excluding amplification), with the slope representing a fit to the higher-frequency data. The bandwidth is flat to under  $\pm 1$  dB out to  $\sim 700$  MHz, and the  $-3$  dB bandwidth is  $\sim 850$  MHz.

directly. This postsample comparison obviates the need to split the input signal to a separate trigger circuit. It also allows the comparators to be lower in power and slower, yet still, in effect,

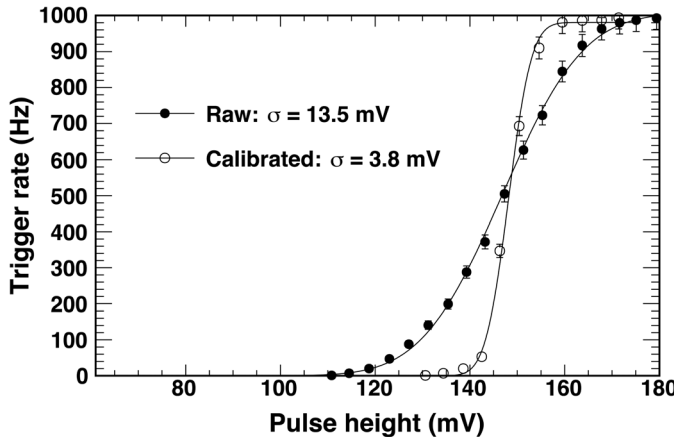


Fig. 12. Example trigger calibration for a single threshold showing trigger rate as a function of pulse height. The curve after calibration shows the variation in thresholds dropping by a factor of 3.6 to a sigma of 3.8 mV.

reach the full bandwidth of the ATWD’s sampling system (i.e.,  $\sim 860$  MHz).

The basic high and low thresholds are set analogically via external DACs. However, as is the nature of all such electronic circuits, each comparator has a certain random input offset, and hence the ATWD chips include internal digital-to-analog conversion on a per-comparator basis to null these offsets for higher uniformity in triggering performance. To first order, the offsets are a form of “fixed pattern noise” and hence calibrations generally need to be done only once.

Fig. 12 shows an example distribution of the offsets from one set of 128 comparator trigger thresholds (all “high” thresholds of a chip) before and after calibration. The “pulse height” axis represents the magnitude of a unipolar pulse at the channel’s ac-coupled analog input that is narrow enough for its peak to be fully contained in one sample. These pulses, produced at 1 kHz, arrive asynchronously with respect to the ATWD’s 1.92 GHz sample clock, and hence can arrive at any comparator’s sample and hold. With ideal (zero) offsets, the transfer function between pulse height and trigger rate would be a step function from 0 Hz to 1 kHz at a single pulse height. However, in a realistic circuit, differing comparator input offsets lead to curves as seen in the figure. Nulling of these input offsets in this example is found to reduce variation in trigger thresholds from a sigma of 13.5 mV to a sigma of 3.6 mV. The latter number includes the noise of the signal generator itself, and yet is still less than a fifth of the sigma of the amplified thermal output noise from the amplifiers ( $\sim 22$  mV). Since such fixed pattern noise sources are independent and add only in quadrature to thermal noise, variations in trigger thresholds after calibration (in this case) results in only a  $\sim 2\%$  net increase over thermal noise in the trigger. The trigger offset nulling DAC values are stored on each daughter-card’s FPGA’s nonvolatile memory, and are loaded into the ATWDs upon a command to cycle the data acquisition power.

#### C. Trigger Rate Control

The ATWD has pattern-matching trigger capabilities that aid in trigger rate control [25]. Up to 72 patterns can be loaded into each chip. Each pattern may be a combination of input

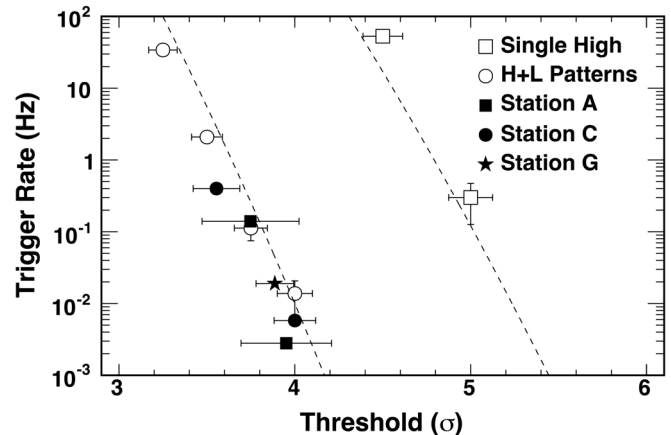


Fig. 13. Laboratory and *in situ* measurements of trigger thresholds versus trigger rates. The “Single High” laboratory measurements represent trigger rates for any crossing above a high threshold. The “H+L Patterns” represent laboratory measurements for an H and L trigger combination coincident within 4 ns. The “Station A, C, and G” data points were from measurements made from three different stations, using the same “H+L Patterns” trigger criteria.

signal conditions, namely  $H$ —the signal must be above a high threshold;  $L$ —the signal must be below a separate low threshold;  $N$ —neither above nor below (i.e., between the two threshold levels); or  $X$ —don’t care (does not veto triggers regardless of the signal level). Each pattern consists of eight such conditions, representing eight consecutive samples. A trigger pattern of  $HXXXXXXX$ , for example, looks for a bipolar signal in which a pair of high and low comparator values are about 2 ns apart (at 1.92 G-samples/s, each sample is 0.52 ns apart).

ARIANNA further employs a second-level trigger that can require a coincidence between a combination of individual channel’s triggers, with a programmable level of majority imposed (i.e., 1 or any 2, 3, or all 4 channels coincident within a certain time period). The combination of bipolar trigger patterns, programmable trigger thresholds, and second-level trigger majority logic can flexibly control trigger rates over many orders of magnitude.

Fig. 13 shows laboratory tests of the trigger rate versus threshold while comparing two different patterns, plus *in situ* measurements from the prototype HRA data. The threshold is expressed in terms of the amplifier noise sigma (predominantly amplified thermal noise). The lines represent theoretical estimates of the expected rates. The “Single High” points denote trigger rates when a pattern of  $HXXXXXXX$  is used. This pattern will trigger on any over-threshold sample and is one of the least restrictive patterns that can be used. The “H+L” patterns trigger on any signal that passes both the high and low thresholds centered over a span of time ranging from 1.56–3.65 ns (based on a 1.92 GHz clock). This set of patterns is more restrictive than the single threshold case yet is efficient for neutrino signatures. The resulting trigger rate drops by over five orders of magnitude for the same threshold values.

The *in situ* measurements are from field data collected after two calibrations made during remote operation in early 2014. These calibrations and measurements were made with the same

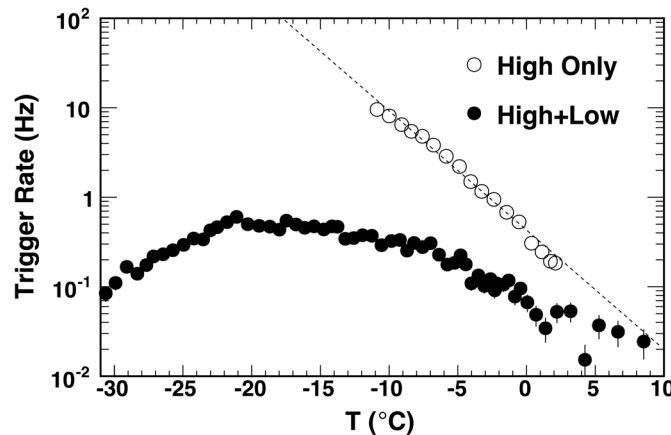


Fig. 14. Thermal trigger rates versus temperature for a single high threshold trigger (open circles), and for a trigger that requires passing a high and a low threshold within 4 ns (filled circles).

five-pattern trigger criteria used in the “H+L” laboratory measurements. Note that all of the data shown in Fig. 13 are also using a “majority-2” criterion, namely that at least two channels must pass the individual channel’s trigger criterion within a set period of time (in this case, ~64 ns).

Fig. 14 shows trigger rates in a laboratory test of temperature stability. Two sets of data are shown, one with a High threshold only, and one with an equivalent High and Low coincidence required (over the space of 4 ns). For a single threshold (i.e., High only), a change such as a baseline drift of just a few mV will cause a significant change in trigger rates, and indeed the figure shows about two orders of magnitude change over approximately 15°C, with at least another two orders of magnitude projected down to  $-30^{\circ}\text{C}$  (measurements were rate-limited to  $\sim 10\text{ Hz}$ , higher than expected *in situ* rates). By contrast, using an equivalent High and Low coincidence results in only one order of magnitude change in trigger rates over the entire expected temperature range once buried in the snow of 0 to  $-30^{\circ}\text{C}$ .

A simple automatic threshold monitoring and adjustment system will eventually be put in place in ARIANNA’s system software. However, ARIANNA’s experience is that remotely performed threshold changes need only be made a few times a year to remain within the system’s range of operation and memory capacity. ARIANNA’s end goal may be to maintain rates such that all data can be retrieved by Iridium, e.g., rates in the milli-Hz regime, in order to reduce or eliminate any dependence on the high-speed WiFi link, and indeed  $\sim 2\text{ MHz}$  rates have been demonstrated in practice.

## VI. POWER SYSTEMS

Given the ARIANNA site’s isolation, and the 1 km distance between stations, each station is fully autonomous, including power provision. For the 2012 deployment, the power system for each station consisted of three solar panels, LiFePO<sub>4</sub> storage batteries, and experimental use of a wind-turbine.

### A. Power Tower and Solar Panels

The HRA stations deployed in 2012 used standard commercially-available radio tower components that were taller and quicker to assemble than the prior custom-made solution,

and which integrated both solar and wind power. Each tower was 16 feet in height excluding the wind-turbine extension, and were tied-down by three steel cables connected to wooden anchors buried in the snow. Constructed almost completely of aluminum, the tower assemblies including solar and wind power systems were light enough to be raised manually by one individual.

Solar panels perform well in the Antarctic environment due to the high reflectivity of the snow. For the 2012 deployment, the ARIANNA power towers employed three solar panels mounted in a fixed, vertical, triangular configuration (see Fig. 2, above). A primary 100 W panel was oriented north, and provided more than sufficient power to run the station and maintain a peak battery charging state for nearly as long as the sun remains up. Two secondary 30 W panels were mounted on the other two faces of the triangular tower for supplementary power when the sun is behind the main panel. During the summer, the panels provide enough power that the stations run continuously and exclusively on solar power nearly 100% of the time, even during periods of extensive cloud cover. The panels, being nearly black in color and mounted vertically, have been observed to remain completely free of snow and ice during summer months. Antarctica is exceedingly dry, and indeed no significant snow or ice accumulation has been observed on any above-ice hardware, though drifting snow can accumulate at the surface.

### B. Batteries at Cold Temperatures

The pilot ARIANNA stations included batteries to store power for use during overcast days and weeks while the sun is rising and setting. LiFePO<sub>4</sub> batteries were selected based on this technology’s high physical and chemical stability and safety, and after ARIANNA’s experimental tests of performance at cold temperatures. Each of the 3 HRA stations deployed thus far incorporated 2 LiFePO<sub>4</sub> batteries of 112 Ah nominal capacity when rated at room temperature (224 Ah total). These were configured in an automobile starting-battery form-factor (Braille Battery Co. model OSGC-12112iB). The batteries include integrated charge controllers which disconnect the batteries when fully charged (e.g., during summer when solar power is plentiful) and when the batteries are nearly depleted, to prevent damage from over-charging and over-discharging.

ARIANNA conducted laboratory tests at  $-30^{\circ}\text{C}$  (previously measured to be the lowest expected winter temperature when buried in the snow) and demonstrated that the selected batteries retained about 70% of their nominal storage capacity when charged and discharged at these temperatures. At  $-30^{\circ}\text{C}$ , they were capable of accepting a charging current of at least 7 A (ARIANNA’s expected maximum), and easily provided the expected maximum discharge current consumed by the station electronics of 1 A. Fig. 15 displays an example charging and discharging profile of a single 112 Ah (nominal) battery at  $-30^{\circ}\text{C}$ . Starting from empty and at  $-30^{\circ}\text{C}$ , it required  $\sim 89$  Ah of charge to reach a full state, at which point the charge controller disconnected the battery. From this state, discharged at 1 A, the battery delivered  $\sim 79$  Ah of charge until it disconnected. Minor discontinuities in terminal voltages were seen at some points during transitions between a normal and cautionary state indicated by an LED on the battery housing that is driven

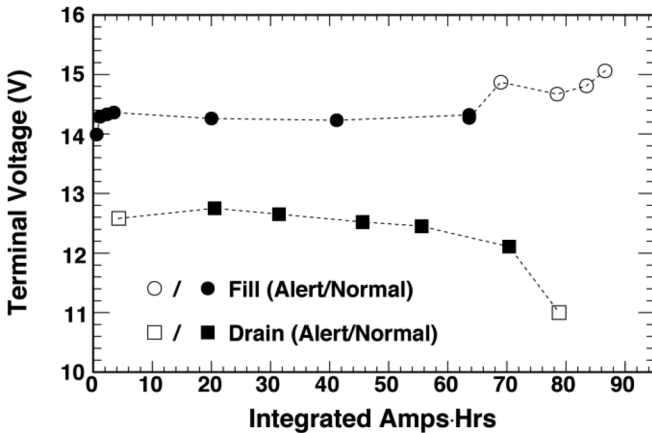


Fig. 15. Terminal voltage of a single battery charging at 7 A and discharging at 1 A, both at  $-30^{\circ}\text{C}$ . The “alert” versus “normal” measurements denote when an LED on the battery housing indicated a nearly full or nearly empty status.

by the battery’s internal charge controller, presumably due to internal switching or rebalancing of cells. Using ARIANNA’s expected “worst case” usage profile, these results indicate a useful storage capacity of  $\sim 70\%$  of one battery’s nominal rating at  $-30^{\circ}\text{C}$ , and an efficiency of  $\sim 89\%$ . The net power available from two batteries stored, charged and discharged at  $-30^{\circ}\text{C}$  is thus at least 158 Ah, or enough to run the station by itself at full power for at least one week, and for up to one month in a low-duty-cycle power-savings mode.

The batteries for the ARIANNA stations as deployed were contained in insulated enclosures, and all connections between the power tower, the battery box, and the station box were via bayonet connectors and hence were very fast and easy to complete while wearing gloves in the field.

### C. Wind Power

Even at  $< 7$  W average power consumption, it has not been considered practical to power the stations by battery alone during the winter. Therefore, ARIANNA has experimented with a number of wind turbines. For the 2012 Austral summer deployment, each of the four stations (the three HRA stations plus the earlier prototype) were equipped with 150 W maximum wind turbines (Southwest Windpower—now Primus Wind Power—model Air 40). As a precaution, the turbines were disassembled and their bearings re-packed with aircraft-grade grease rated to  $-70^{\circ}\text{C}$ . The Air-40 model uses glass-reinforced nylon blades which, in all stations, survived a year of operation without any issues. Unfortunately, the body of one turbine split open near its mounting collar (apparently a single casting of aluminum or aluminum alloy), leaving it unbalanced and unable to transmit power. A second turbine failed when a bearing burned and seized. Evidence points to both of these failures occurring during a single powerful storm. The third and fourth wind turbines remained intact and fully functional.

During the 2013 servicing mission, the wind turbines were removed from the three 2012 HRA stations, which have henceforth operated on solar power and batteries only. The 2011 prototype station maintained its turbine for continued experimental use, and was reconfigured as an environmental

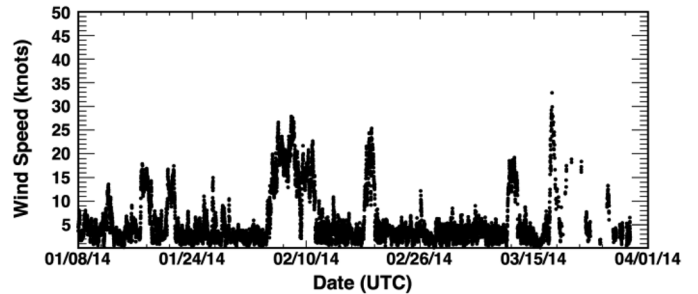


Fig. 16. Wind speed versus time from the 2011 prototype station’s anemometer.

monitoring station including air speed and temperature measurements. Fig. 16 shows this station’s anemometer data. Wind speeds at the ARIANNA site have been found to be sufficient for significant up-time during winter months, motivating continued interest in experimenting with wind power generation.

## VII. MONITORING, CONTROL AND DATA COLLECTION

The HRA stations are designed to operate autonomously, with remote monitoring, control and data collection made possible by two redundant communications modalities—long distance wireless via a repeater located on Mt. Discovery and satellite short-burst messaging. Communications with each of the ARIANNA stations are handled by a custom software suite built in C++ and Python, via computing facilities at UCI. The Python code works with the Twisted framework to handle TCP communications (“WiFi”) and email communications (Iridium Short Burst Data messaging) to and from the stations. Multiple stations can and do communicate concurrently.

### A. Communications Overview

The long-range wireless system allows fast and efficient retrieval of all station data, as well as control over each station, including the timing and duration of data acquisition and communications windows, control over which major subsystems are powered, and even the capability of loading new software for the stations’ microcontrollers. The wireless modules used are AFAR Communications AR-24027E-SA units, operating at 2.4 GHz. For robustness, the station’s wireless communications are mesh-connected, in that every station can act as an intermediate for each other. Communications thus takes place through the “best” path, either directly from a station to McMurdo via repeater on Mt. Discovery, or via a different station that has a stronger signal. It has been found that the 2.4 GHz communications frequency, which is well above the station’s sensitive range, does not interfere with the station’s data acquisition. Therefore, these modules can remain on, acting as bridges for other stations, during normal operation.

As an alternative, each HRA station is equipped with an Iridium satellite short-burst data (SBD) messaging system. This provides functionality similar to that of a mobile-phone’s text messaging system, with messages received by the station consisting of 270 bytes and sent messages containing 340 bytes. Although messages are short, they are densely encoded, and every function available by WiFi is available by SBD. The Iridium modules used are by NAL Research Co., model

9602-N. These operate at  $\sim 1.6$  GHz, which could interfere with local station signal acquisition (though it is far too weak to be detected by neighboring stations). Thus, they are powered on only during communication, when data acquisition is off. Finally, the Iridium receiver is used to synchronize each station's real-time clock to a highly-precise time received from satellites.

### B. System Software and Operation

Each HRA station's system software runs on an NXP LPC1768 embedded microcontroller using a 96 MHz ARM Cortex-M3 core with 32 kB of on-chip RAM and 512 kB of on-chip flash memory. Acquired data are stored on a 32 GB Compact Flash memory card, which is spacious enough to hold a year's worth of data or more even at the highest expected rates.

The system software is programmed in C/C++ without the benefits or overhead of a real-time operating system. The software divides system operation into two major modes or "windows," namely communications and data taking. Generally, these alternate; when communicating, data taking is suppressed and powered-down, and during data taking, communications systems are powered down.

Configuration commands sent to a station during a communications window include parameters such as trigger threshold levels, file and event compression parameters, and communications parameters such as timeout values for communications windows in case two-way communications are not established, the time between communications windows (equivalent to the duration of the data-taking windows), and what data to transmit during communications windows.

During data taking windows the system can collect "thermally" triggered events, periodic forced triggers in which the system takes an event unbiased by the trigger circuitry, and "heartbeat" events, in which the station generates an RF pulse itself and collects the resulting event. Data files collected during these windows include unique event numbers, time-stamp information, voltage readings, losslessly compressed ADC values, bits confirming the type of trigger that resulted in the event (e.g., thermal, forced, etc.), and a 32-bit CRC value to aid in confirming data integrity.

The systems include several features intended to enhance robustness, with particular attention to preventing a system from finding itself in some erroneous state whereby it may lose its ability to communicate, etc. These include a hardware-level "watchdog" timer that will reboot the system if the station becomes locked out of normal operation. The system will also completely reboot if it fails to achieve confirmed communications for five communications windows in a row. Furthermore, received control parameters are not allowed to fall outside of reasonable ranges to prevent user errors from accidentally disabling the stations. For example, it is not possible to set both WiFi and Iridium off during communications windows. Finally, it is possible to remotely upload a new software revision to the station, which, if it passes a CRC check, etc., will take control.

Since there are likely to be periods during which power conservation becomes important, it is possible to individually control which of the major peripherals (amplifiers, data acquisition,

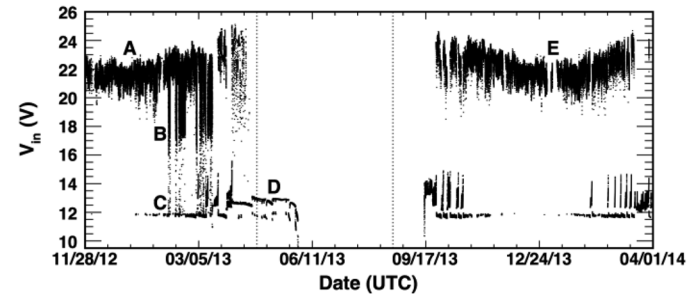


Fig. 17. Example station's power supply voltage versus time. Periods of operation primarily on solar power ("A"), wind power ("B"), battery backup ("C") and solely on battery power ("D") are indicated. Period "E" shows interrupted power during station servicing, and also demonstrates a relationship between seasonal changes and solar power efficiency ("E" was midsummer). The vertical lines indicate the last and first days of sun.

WiFi, and Iridium SBD) are on or off during the communications and data-taking windows. For example, the lower-power SBD system can be used exclusively when conserving power becomes important. Finally, the systems can be placed in a strict power-savings mode, in which all data taking is powered down, and communications windows can be less frequent, etc. This mode can be entered automatically by a station when the battery voltage drops below a specified value. Hysteresis is implemented with a second value that prevents the station from dropping into and out of this mode too quickly. A very low-power mode gives operators the ability to maintain control when solar or battery power is low.

## VIII. SYSTEM PERFORMANCE

The performance of the first three HRA systems have been extensively studied [26], [27]. This section describes the performance of the power systems, trigger rate performance and stability, noise performance, radio-pulse reflection studies, correlations to neutrino templates, station timing resolution, and event reconstruction resolution.

### A. Power Systems Performance

As an example of the power system's performance, Fig. 17 shows voltage readings for an example station ("Site A") during about 14 months of operation, from the time it was turned on in late November 2012 until late December, 2013, when it was disconnected for servicing, and subsequently through March 31, 2014. As evidenced by voltages in the 17–24 V range (regions "A" and "E" in Fig. 17), the solar panels provided nearly all power during the Austral summer. Interestingly, the output voltage of the solar panels climbed during colder months, presumably due to lower levels of recombination and dark current in the solar cells. Battery power is seen supplementing the station's operation in voltage ranges of  $\sim 12$  to  $\sim 14$  V (e.g., region "C"). Wind power was observed via voltages between  $\sim 14$  and  $\sim 17$  V (region "B") to be frequently and strongly supplementing solar power from early February until mid-March of 2012, when the wind turbine evidently failed during a storm. Beyond this point, solar panels continued to provide significant power, and the batteries were observed to be fully charged during peak daytime hours until mid-April, even when the sun reached only about 2 degrees

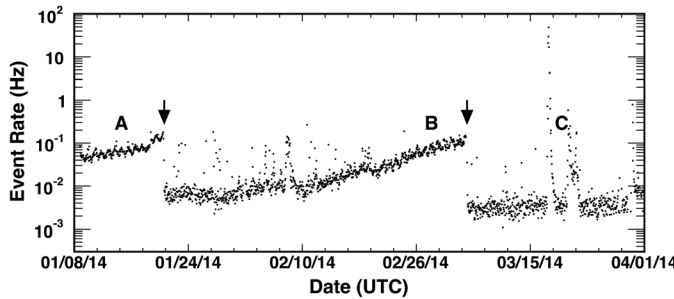


Fig. 18. Total event rates (triggered events only) versus time for Site A from January 8 through March 31, 2014. During periods A and B, slight diurnal rates changes are visible, as is a gradual increase in rates related to a drop in temperature. Two adjustments in rates were made, indicated by the two downward arrows, on or about 1/23 and 3/06. During period C, a powerful storm swept through the area, and an increase in rates was noted.

maximum height and only about one week before the last sunset on April 24, 2013. After the last sunset (first vertical line in Fig. 17), the station was alternately directed between normal and lower-powered modes in order to prolong testing of the station, e.g. of temperature effects, etc. During this time (region “D”), the station subsisted on battery power only. The station experienced a normal shut-down during while in full data-taking and communications modes on May 30, 2013, 36 days after the last sunset.

The first autonomous communication of the next spring occurred on September 12, 2013, about 3 weeks after the first sunrise (August 19, 2013, indicated by the second vertical line in Fig. 17). This was a day on which the sun had reached a maximum height of 8 degrees. On September 16, 2013, the station began uninterrupted operation until it was serviced in late December 2013. The station thus maintained 256 days of operation out of 365, or 70% of the year including the use of power savings modes. When run at full power continuously, at least 58% live-time over the course of a full year has been achieved.

#### B. Trigger Rates Versus Temperature and Wind

Fig. 18 shows an example station’s (“Site A”) thermal-triggered event rate from January 2, 2014 and March 13, 2014. The amplifier’s gain has been noted to rise slightly as the temperature drops, leading to increased thermal trigger rates. Once the stations are covered in snow, diurnal temperature changes have been found to be less significant than seasonal changes. Since re-commissioning in January of 2014, the station’s thresholds have been remotely adjusted twice, as noted by the two downward arrows in Fig. 19. All stations behaved similarly and required only the same two adjustments.

A partial correlation between storms and/or wind velocity and event rates has been observed. In Fig. 18, the period “C,” for example, shows an increase in rates during a storm. The cause and nature of the excess events is being studied, but a few comments can be made: Elevated event rates have been found to be correlated between stations. Generally, only wind speeds above  $\sim 20$  knots have resulted in elevated event rates, but not all such periods of higher wind speeds have resulted in higher rates. Most of these temporary increases have had negligible impact on event collection efficiency, i.e., less than seasonal temperature variations. No additional noise has been found in forced

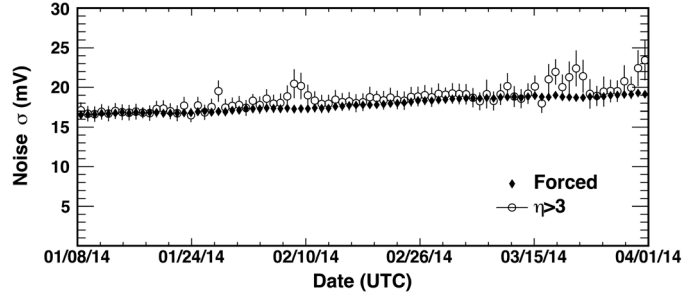


Fig. 19. Noise sigma for channel 2 at Site A between January 8, 2014 and March 31, 2014, binned into one-day periods. The “Forced” data points are unbiased by the system’s trigger and reflect highly-Gaussian thermal noise (average of 17.6 mV). The  $\eta > 3$  data reflects all data collected due to the station’s trigger system except for brief periods or events that include minor amplifier oscillations. Aside from a bias that the trigger imposes, these data are also largely Gaussian, although episodes of greater noise are seen that are correlated with periods of storms including high winds.

(unbiased) events during storms, and so there is no evidence that increased trigger rates are due to any gradual, consistent change in the level of noise. Rather, these noise events appeared to be sparse and random. Only one few-hour-long instance (to the left of “C” in Fig. 18) resulted in excess event rates that significantly impacted dead-time. Analysis of the excess triggered events has concluded that they do not resemble expected neutrino events, and that these excess events can be removed from the data with high efficiency, as discussed in the next section.

#### C. Thermal Noise Measurements

Fig. 19 shows an example plot of recorded noise sigma in mV versus time for a representative data set from 2014 (“Station A,” channel 2), binned into one-day intervals. The “Forced” time series consists of all data from “unbiased” events taken at periodic intervals without the involvement of the station’s trigger system. These data are highly Gaussian and essentially displays the channel’s thermal noise (average  $\sigma = 17.6$  mV for all forced triggers). A slight rise in noise versus calendar time is due to the slowly cooling temperatures, which has been found to increase the amplifier’s gain and hence the level of recorded noise.

The “ $\eta > 3$ ” time series contains all events acquired via the system’s trigger, but excludes those events associated with brief periods in which the station’s amplifiers have displayed a sympathetic oscillation between channels (this issue has since been rectified by a revised amplifier design). The parameter “ $\eta$ ,” detailed in [28], is a count of the number of frequencies containing a large fraction of a waveform’s power. A small value of  $\eta$  signifies a single, strong peak at a particular frequency.

The amplitudes measured by each sample in the triggered data are also substantially normally distributed, although amplitudes at the trigger threshold values occur with a higher probability as expected. It is noted that fluctuations in triggered-event noise levels rise modestly above the unbiased event noise levels over the same storm or high-wind periods as seen in Fig. 16 and concomitant with the event rate increases seen in Fig. 18.

#### D. 2014 Data-Set Correlation Distributions

Data taken between January 8, 2014 and March 31, 2014 have been studied in an exploratory search for neutrino-like

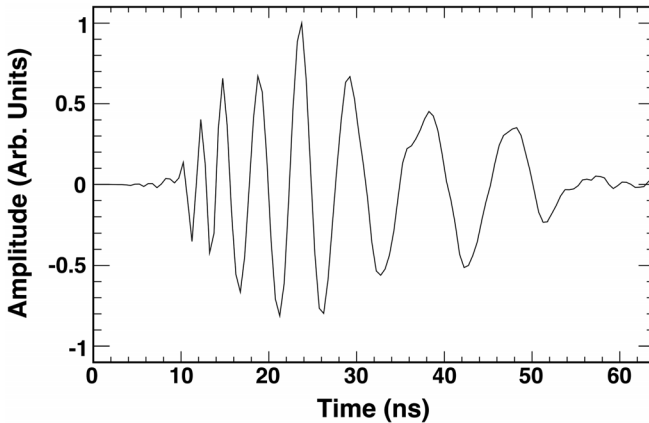


Fig. 20. Example neutrino signal template (40 degrees off-axis in the E-plane) including ice propagation, antenna, amplifier response, but excluding thermal noise, and sampled at 1.92 GHz (Y-axis units are arbitrary).

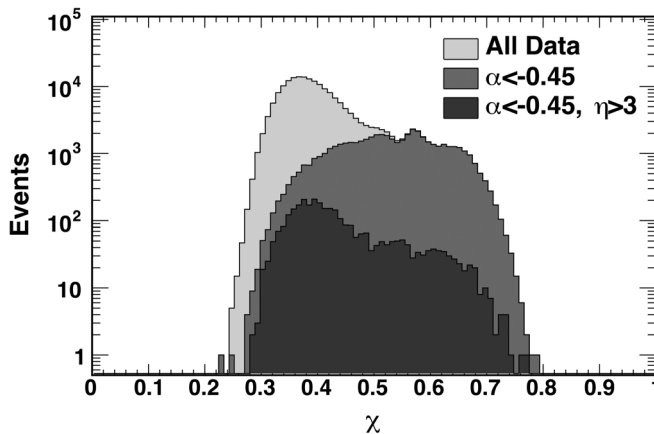


Fig. 21. Distribution of  $\chi$  in the 2014 data set for Station A, channel 2, for all data, after the  $\alpha < -0.45$  cut, and after both the  $\alpha$  cut and the " $\eta > 3$ " cut.

signals [28]. An expected neutrino signal has been generated from the time dependent electric field at the neutrino interaction vertex, propagated through a model of the ice and convolved with measured antenna and amplifier response functions. The neutrino signals are determined as a function of two space angles defining the orientation of the incident electric field relative to the antenna, as well as the angle between the antenna and the Cherenkov cone. The resulting time dependent neutrino waveform “templates” (e.g., Fig. 20) can then be compared to recorded data by computing its maximum correlation value with each antenna waveform.

Prior to reconstruction of the event direction and polarization, waveforms from all four channels, including both the recorded waveform and its inverse (it is not *a priori* obvious which face of the antenna is presented to the incoming radio wave, hence whether the initial pulse would be positive or negative), for a total of eight waveforms per station, are compared to a single reference template corresponding to  $30^\circ$  in the E- and H-planes. The best correlation between any of these eight signals and the reference template is designated as  $\chi$ . Fig. 21 shows values of  $\chi$  in the representative “Site A” data set for all events (“All Data”) in its light-gray area, including a total of 203 562 events.

The majority of triggered events are purely random in nature (i.e., thermal noise). These are identified by an autocorrelation function whose results are noted to have a perfect correlation at zero time offset. Nonthermal-noise events are taken to be those for which the minimum autocorrelation function  $\alpha$  is below  $-0.45$  on any antenna. These remaining nonthermal events are shown in medium-gray in Fig. 21 (“ $\alpha < -0.45$ ”).

The “ $\eta > 3$ ” cut mentioned in the previous subsection is then made in addition to the “ $\alpha < -0.45$ ” cut. This, again, is intended to remove a small subset of events that contain sympathetic amplifier oscillations between channels. To pass this cut, it is required that the frequency spectrum of a neutrino candidate have more than three frequency bins ( $\eta > 3$ ) at or above 50% of the magnitude of the maximum bin—that is, that the candidate contains more than essentially the single-frequency oscillation that is seen in misbehaving amplifiers. Long term, this cut may be unnecessary given demonstrated improvements in amplifier stability. The combination of the  $\alpha$  and  $\eta$  cuts is seen in dark gray in Fig. 21. Neutrino candidates are required to pass both the autocorrelation and oscillation cuts, while also correlating well with the expected neutrino signal. The application of the  $\alpha < -0.45, \eta > 3$  and  $\chi > 0.81$  cuts, described in detail in [28], yields no neutrino candidate events from the data and is found to preserve 90% of simulated neutrino signals.

#### E. Radio Frequency Reflection Comparisons

Radio-frequency reflection studies on a representative HRA station (“Site G”) have been performed. These involved delivering a fast electrical pulse, generated by a Pockels Cell driver (Grant Applied Physics model HYPS) to a quad-ridged polarization horn antenna (Seavey Engineering Inc., now Antenna Research Associates; antenna custom-designed for the ANITA project and described in [29]). The antenna was placed face-down to the ice at various locations both near to and far from the station, as well as oriented in several polarizations relative to the receiving antennas. The transmitted RF pulse therefore passed down through the ice (~550 m thick), bounced off of the water–ice interface, and back up to the station. The station electronics includes an external trigger input that allows the capture of waveforms at precise times, and this was used to trigger the station’s data acquisition at the time of arrival of the reflected pulse.

A comparison of reflected waveforms was made between those collected by an ARIANNA station’s electronics and equivalent waveforms using same ARIANNA channel’s antenna and amplifier but captured by an oscilloscope (Agilent model DSO 7104B; 1 GHz bandwidth, 5 G-samples/s acquisition). As examples, two plots are shown from the same location (“Site G”), with the horn antenna located for a straight down-and-up reflection. It is important to note that the overlapping waveforms shown in these figures are from different transmitted pulses, since it was not possible to record the same reflections at the oscilloscope and station simultaneously while using the same antennas and amplifiers.

The first comparison plot, Fig. 22, shows the station’s channel 2’s response to the reflected pulse (antenna oriented with parallel polarization to the transmitted pulse) superimposed on an

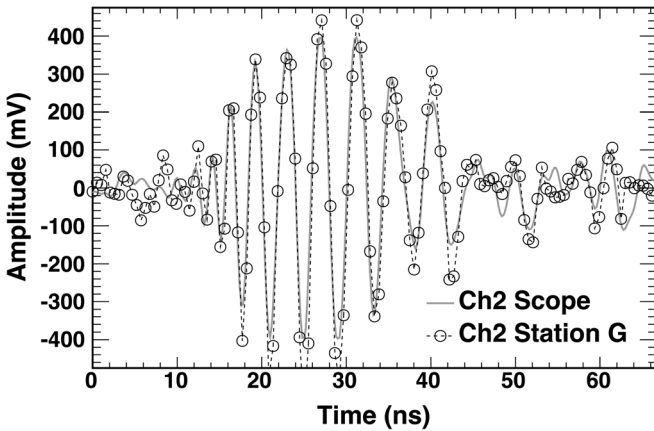


Fig. 22. Overlapping comparison of a representative antenna and amplifier response to separate but equivalent RF pulses reflected off of the bottom of the Ross Ice Shelf, as received by the Station G electronics and by a 1 GHz bandwidth oscilloscope. The polarization of the transmitted pulse was parallel to that of the receiving antenna.

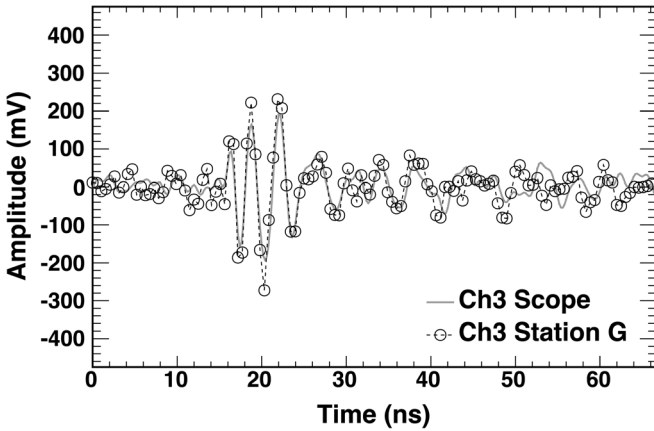


Fig. 23. Overlapping comparison of an antenna and amplifier response to separate but equivalent RF pulses reflected off of the bottom of the Ross Ice Shelf, as in Fig. 22. The polarization of the pulse was orthogonal to the receiving antenna and hence is attenuated.

equivalent pulse's response as recorded by the oscilloscope. Adjustments of the station's response to the vertical scale were made solely according to the station's calibration for gain.

Fig. 23 compares a pulse received at the station's channel 1, whose antenna is orthogonal to that of channel 2 and thus orthogonal to the polarization of the transmitted pulse. Channel 1's response is attenuated compared to channel 2's, consistent with the difference in orientation. The polarization is evidently substantially maintained even after the reflection and transmission through a total of  $\sim 1100$  m of ice.

It can be seen that the waveforms shown in Figs. 22 and 23 are well-matched within the limits of noise ( $\sim 22$  mV RMS for the amplified thermal noise).

#### F. Station Timing Resolution

"Site G" reflection studies, performed over a period of 24 h for a variety of surface locations, have been used to determine the station's timing resolution. For a given surface location, a reference event was arbitrarily selected to generate four  $\Delta t_i$  values, where  $\Delta t_i$  represents the time difference in the

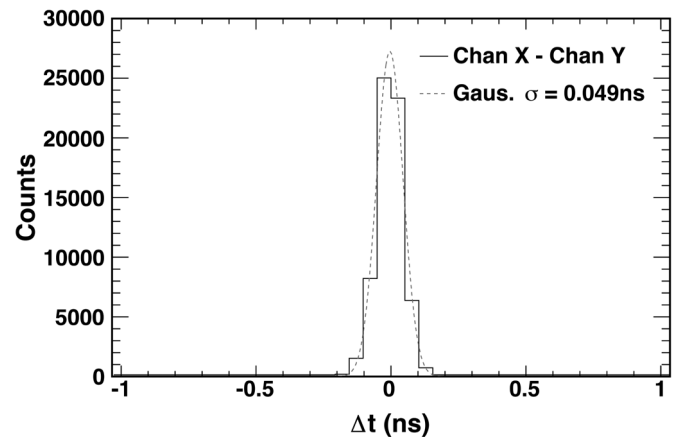


Fig. 24. Measured net timing resolution of the station at Site G, found via reflection studies initiated from a number of locations on the ice. The sigma of a fitted Gaussian is 0.049 ns.

pulse arrival time between channel  $i$  in the reference and current event. The time difference is taken to be that which maximizes the Pearson correlation between the waveforms on the  $i$ th channel in the reference and current event. This time difference may be nonzero due to jitter in the electronics used to generate the transmission pulse. However, all channels should have the same  $\Delta t_i$  value, since jitter in the pulse transmission time should affect all channels equally. The difference in  $\Delta t_i$  values between channels gives a measure of the readout timing resolution. Fig. 24 shows the time difference  $\Delta t = \Delta t_i - \Delta t_j$  for all six combinations of unique channel pairs  $i$  and  $j$ , integrated over all events taken at all transmission locations. A net timing resolution of 0.049 ns, obtained from a Gaussian fit to the peak, fully satisfies the experimental requirements of ARIANNA.

#### G. Angular Resolution and Event Reconstruction

Analysis of event reconstruction was performed using data taken in 2012 [30]. In brief, maximum cross-correlations were found between waveforms from all combinations of different channels. This leads to computed time differences between the channels and hence the angle at which a plane-wave is presumed to have struck the different antennas. The reconstructed angle at the station is then corrected for propagation through the firn layer (a layer of compacted snow from prior seasons) with a simple model of ice density as function of depth to produce a predicted signal-source location on the surface of the ice. The median value for the precision of the angular measurements for several different locations ranged between 0.14 to 0.17 degrees, consistent with the measured timing resolution of the data acquisition system, i.e., Fig. 24.

#### IX. ON-GOING AND FUTURE EFFORT

The HRA systems have demonstrated that the ARIANNA site is substantially free of anthropogenic noise, achieving  $\sim 2$  MHz trigger rates at 4-sigma thresholds. Current research is aimed at reducing both thresholds and rates even further by improved triggering configurations, e.g. by requiring higher levels of channel trigger coincidences and with enhanced data processing. In this way, the use of Iridium satellite communications

alone may suffice. Recent efforts have demonstrated that this is achievable using existing remotely-programmable configuration changes. The “WiFi” repeater on Mt. Discovery is a genuine and valued convenience, but it requires maintenance and is a point of potential failure. An Iridium-only solution, by contrast, would make each station completely independent.

Many of the challenges to this project have centered on its remoteness, necessitating autonomous operation, and on the harshness of the environment, including cold temperatures and powerful storms. It has been found that fixed mechanical and electronic systems, whether buried or exposed, including solar panels and satellite communications, have functioned well and reliably. Remote monitoring, control and near-real-time full data transmission by long-distance wireless and satellite, and even the remote updating of the station’s system software, have also been reliable.

On the other hand, wind power, at least when using low-cost turbines that have not been ruggedized for Antarctic conditions, has not proven to be mechanically reliable enough given the powerful storms that can occur. Since good up-time has been achieved with solar only, wind turbines have been deleted from the project for the sake of cost and deployment time and effort. This has the side effect of drastically reducing the battery capacity required per station, as quite large batteries are needed to outlast lulls in wind power. Instead, a taller integrated tower containing solar panels and all communications, co-located with the station electronics, will be employed. Without the clearance required for wind-turbines, and using 20-ft towers instead of 16 ft, solar panels and antennas can be mounted higher, extending ARIANNA’s operational lifetime in the face of drifting snow.

Similarly, batteries are a perennial concern in Antarctica due to their reduced performance and increased vulnerability at very cold temperatures. Given the transition to a solar power-only mode, it is expected that considerably smaller batteries, sufficient to sustain the stations during days of waxing and waning sun or cloud cover, etc., will be used. These will be enclosed inside the station box seen in Fig. 7, containing any possible electronic noise from their charge controllers and keeping them considerably warmer during operation, hence improving their performance. The deletion of wind turbines and the concomitant reduction in required battery capacity alone saves about 30% of a station’s cost. The sum of the above also substantially reduces per-station deployment time, and it eliminates the great majority of a station’s risk profile.

Finally, improved amplifiers and a new, very low power (~1.7 W) single-board electronics system, including a new four-channel, 256-sample-per-channel Switched Capacitor Array waveform recording chip, the “SST” [31], have been developed. These were designed for complete drop-in physical and electrical compatibility with the systems described in this paper. The new amplifiers have flatter frequency response and incorporate the filtering and limiting components seen in Fig. 4, reducing costs. The new single-board system electronics similarly reduces that system’s expense by approximately a factor of 5, while reducing its power by a factor of 3 and lowering its calibration overhead. The SST chip has equal or higher performance in essentially every respect, including performance and

features that significantly improves upon analog bandwidth, trigger sensitivity and ease of calibration.

In early to mid-December of 2014, four new HRA systems using most of the above improvements, including the new amplifiers and the new SST-based data acquisition systems, were successfully deployed. Measurement and evaluation of their design and performance is currently on-going and will be the subject of future publications.

## ACKNOWLEDGMENT

The authors wish to thank the staff of Antarctic Support Contractors, Lockheed, and the entire crew at McMurdo Station for excellent logistical support. The authors also thank W. Huang and S.-H W. Chiang for their efforts in the design of the ATWD circuit as discussed in Section V and in [23] and [24]. Lastly, the authors also thank Prof. De Flaviis for the use of the Far Field Anechoic Chamber at the University of California, Irvine.

## REFERENCES

- [1] L. Gerhardt *et al.*, “A prototype station for ARIANNA: A detector for cosmic neutrinos,” *Nucl. Inst. Meth. A*, vol. 624, no. 1, pp. 85–91, May 2010.
- [2] S. W. Barwick for the ARIANNA Collaboration, “ARIANNA—A new concept for high energy neutrino detection,” in *Proc. 32nd Int. Cosmic Ray Conf.*, Beijing, China, pp. 238–239, 2011.
- [3] S. Klein for the ARIANNA Collaboration, “A radio detector array for cosmic neutrinos on the Ross Ice Shelf,” *IEEE Trans. Nucl. Sci.* vol. 60, no. 2, pp. 637–643, Apr. 2013.
- [4] S. A. Kleinfelder for the ARIANNA Collaboration, “Design and performance of the autonomous data acquisition system for the ARIANNA high energy neutrino experiment,” *IEEE Trans. Nucl. Sci.* vol. 60, no. 2, pp. 612–618, Apr. 2013.
- [5] G. A. Askaryan, “Excess negative charge of an electron-photon shower and its coherent radio emission,” *J. Exp. Theor. Phys.*, vol. 14, pp. 441–443, Feb. 1962.
- [6] K. Dookayka, “Characterizing the search for ultra-high energy neutrinos with the ARIANNA detector,” Ph.D. dissertation, Univ. California, Irvine, CA, USA, 2011.
- [7] K. Dookayka for the ARIANNA Collaboration, “Characterizing the search for UHE neutrinos with the ARIANNA detector,” in *Proc. 32nd Int. Cosmic Ray Conf.*, Beijing, China, 2011.
- [8] K. Greisen, “End to the cosmic-ray spectrum?,” *Phys. Rev. Lett.*, vol. 16, no. 17, pp. 748–750, Apr. 1966.
- [9] G. T. Zatsepin and V. A. Kuzmin, “Upper limit of the spectrum of cosmic rays,” *J. Experimental and Theo. Phys. Lett.*, vol. 4, pp. 78–80, 1966.
- [10] C. S. Neal, “The dynamics of the Ross ice shelf revealed by radio echosounding,” *J. Glaciol.*, vol. 24, pp. 295–307, 1979.
- [11] S. W. Barwick for the ARIANNA Collaboration, “Performance of the ARIANNA prototype array,” in *Proc. Int. Cosmic Ray Conf.*, Rio De Janeiro, Brazil, Jul. 2013.
- [12] J. C. Hanson for the ARIANNA Collaboration, “Ross ice shelf thickness, radio-frequency attenuation and reflectivity: Implications for the ARIANNA UHE neutrino detector,” in *Proc. Int. Cosmic Ray Conf.*, Beijing, China, 2011.
- [13] T. Barrella, S. Barwick, and D. Saltzberg, “Ross ice shelf in situ radio-frequency ice attenuation,” *J. Glaciol.*, vol. 57, no. 201, pp. 61–66, Feb. 2011.
- [14] E. Andres *et al.*, “The AMANDA neutrino telescope: Principle of operation and first results,” *Astropart. Phys.*, vol. 13, no. 1, pp. 1–20, Mar. 2000.
- [15] I. Kravchenko *et al.*, “Limits on the ultra-high energy electron neutrino flux from the RICE experiment,” *Astropart. Phys.*, vol. 20, no. 2, pp. 195–213, Nov. 2003.
- [16] J. Ahrens *et al.*, “Sensitivity of the icecube detector to astrophysical sources of high energy muon neutrinos,” *Astropart. Phys.*, vol. 20, no. 5, pp. 507–532, Feb. 2004.
- [17] P. Allison *et al.*, “Design and initial performance of the askaryan radio array prototype eev neutrino detector at the south pole,” *Astropart. Phys.*, vol. 35, no. 7, pp. 457–477, Feb. 2012.

- [18] S. W. Barwick *et al.*, “Time-domain response of the ARIANNA detector,” *Astropart. Phys.*, vol. 62, pp. 139–151, Sep. 2014.
- [19] S. A. Kleinfelder, “A multi-gigahertz analog transient waveform recorder integrated circuit,” Thesis, Univ. California, Berkeley, 1992.
- [20] S. A. Kleinfelder, “Advanced transient waveform digitizers,” in *Proc. SPIE Particle Astrophysics Instrumentation*, Aug. 2002, vol. 4858, pp. 316–326.
- [21] S. A. Kleinfelder, “A multi-GHz, multi-channel transient waveform digitization integrated circuit,” in *Proc. IEEE Nuclear Science Symp.*, Orlando, FL, USA, Oct. 2002.
- [22] S. A. Kleinfelder, “GHz waveform sampling and digitization circuit design and implementation,” *IEEE Trans. Nucl. Sci.*, vol. 50, no. 4, pp. 955–962, Aug. 2003.
- [23] W. Huang, S. W. Chiang, and S. Kleinfelder, “Waveform digitization with programmable windowed real-time trigger capability,” in *Proc. IEEE Nuclear Science Symp.*, Orlando, FL, USA, Oct. 2009.
- [24] S. A. Kleinfelder, S. W. Chiang, and W. Huang, “Multi-GHz waveform sampling and digitization with real-time pattern-matching trigger generation,” *IEEE Trans. Nucl. Sci.*, vol. 60, no. 5, pp. 3785–3792, Oct. 2013.
- [25] M. Roumi, “Advanced pattern-matching trigger system for the ARIANNA high-energy neutrino detector,” Ph.D. dissertation, Univ. California Irvine, Irvine, CA, USA, 2014.
- [26] J. Tatar, “Performance of sub-array of ARIANNA detector stations during first year of operation,” Ph.D. dissertation, Univ. California Irvine, Irvine, CA, USA, 2013.
- [27] J. C. Hanson, “The performance and initial results of the arianna prototype,” Ph.D. dissertation, Univ. California Irvine, Irvine, CA, USA, 2013.
- [28] S. W. Barwick *et al.*, “A first search for cosmogenic neutrinos with the ARIANNA hexagonal radio array,” *Astropart. Phys.*, vol. 70, pp. 12–26, Oct. 2015.
- [29] P. Gorham *et al.*, “The Antarctic impulsive transient antenna ultra-high energy neutrino detector (ANITA): Design, performance, and sensitivity for 2006–2007 balloon flight,” *Astroparticle Phys.*, vol. 32, pp. 10–41, 2009.
- [30] C. Reed for the ARIANNA Collaboration, “Performance of the ARIANNA neutrino telescope station,” in *Proc. Int. Cosmic Ray Conf.*, Rio De Janeiro, Brazil, Jul. 2013.
- [31] S. A. Kleinfelder, E. Chiem, and T. Prakash, “The SST fully-synchronous multi-GHz analog waveform recorder with Nyquist-rate bandwidth and flexible trigger capabilities,” in *IEEE Nuclear Science Symp. Conf. Rec.*, Seattle, WA, Nov. 2014.

# Telescope Array Radar (TARA) Observatory for Ultra-High Energy Cosmic Rays

R. Abbasi<sup>a</sup>, M. Abou Bakr Othman<sup>a</sup>, C. Allen<sup>b</sup>, L. Beard<sup>c</sup>, J. Belz<sup>a</sup>, D. Besson<sup>b,g</sup>, M. Byrne<sup>a</sup>, B. Farhang-Boroujeny<sup>a</sup>, A. Gardner<sup>a</sup>, W.H. Gillman<sup>d</sup>, W. Hanlon<sup>a</sup>, J. Hanson<sup>b</sup>, C. Jayanthmurthy<sup>a</sup>, S. Kunwar<sup>b</sup>, S.L. Larson<sup>e</sup>, I. Myers<sup>a,\*</sup>, S. Prohira<sup>b</sup>, K. Ratzlaff<sup>b</sup>, P. Sokolsky<sup>a</sup>, H. Takai<sup>f</sup>, G.B. Thomson<sup>a</sup>, D. Von Maluski<sup>a</sup>

<sup>a</sup>University of Utah, Salt Lake City, UT 84112 U.S.A.

<sup>b</sup>University of Kansas, Lawrence, KS 66045 U.S.A.

<sup>c</sup>Purdue University, West Lafayette, IN 47907 U.S.A.

<sup>d</sup>Gillman & Associates, Salt Lake City, UT 84106 U.S.A.

<sup>e</sup>Utah State University, Logan, Utah 84322 U.S.A.

<sup>f</sup>Brookhaven National Laboratory, Upton, NY 11973 U.S.A.

<sup>g</sup>Moscow Engineering and Physics Institute, 31 Kashirskaya Shosse, Moscow 115409 Russia

## Abstract

Construction was completed during summer 2013 on the Telescope Array RAdar (TARA) bi-static radar observatory for Ultra-High-Energy Cosmic Rays (UHECR). TARA is co-located with the Telescope Array, the largest “conventional” cosmic ray detector in the Northern Hemisphere, in radio-quiet Western Utah. TARA employs an 8 MW Effective Radiated Power (ERP) VHF transmitter and smart receiver system based on a 250 MS/s data acquisition system in an effort to detect the scatter of sounding radiation by UHECR-induced atmospheric ionization. TARA seeks to demonstrate bi-static radar as a useful new remote sensing technique for UHECRs. In this report, we describe the design and performance of the TARA transmitter and receiver systems.

**Keywords:** cosmic ray, FPGA, radar, digital signal processing, chirp

## 1. Introduction

Cosmic rays with energies per nucleon in excess of  $\approx 10^{14}$  eV [1] create cascades of particles with electromagnetic and hadronic components in the atmosphere, known as Extensive Air Showers (EAS). Conventional cosmic ray experiments detect events through coincident shower front particles in an array of surface detectors [2, 3] or through fluorescence photons that radiate from the shower core [4, 5, 6] which permit fluorescence telescopes to study shower longitudinal development. Another technique takes advantage of two naturally-emitted radio signals: the Askaryan effect [7] and geomagnetic radiation from interactions with the Earth’s magnetic field [8].

With ground arrays, air shower particles are observed directly. The land required to instrument ground arrays is large, *cf.* Telescope Array’s 700 km<sup>2</sup> surface detector covers roughly the same land area as New York City. The costs of the equipment required to instrument such

a large area are substantial, and the available land can only be found in fairly remote areas.

A partial solution to the difficulties and expense involved in ground arrays is found in the fluorescence technique. Here, the atmosphere itself is part of the detection system, and air shower properties may be determined at distances as remote as 40 km. Unfortunately fluorescence observatories are typically limited to a ten percent duty cycle by the sun, moon and weather.

The possibility of radar observation of cosmic rays dates to the 1940’s, when Blackett and Lovell [9] proposed cosmic rays as an explanation of anomalies observed in atmospheric radar data. At that time, a radar facility was built at Jodrell Bank to detect cosmic rays, but no results were ever reported. Recent experimental efforts utilizing atmospheric radar systems were conducted at Jicamarca [10] and at the MU-Radar [11]. Both observed a few signals of short duration indicating a relativistic target. However in neither case were the measurements made synchronously with a conventional cosmic ray detector.

A new approach, first attempted by the MARIACHI [12, 13] project, is to utilize *bi-static* or two-

\*Corresponding Author. Tel.: +01 801 5879986. Addr.: 115 S 1400 E #201 JFB

Email address: isaac@cosmic.utah.edu (I. Myers)

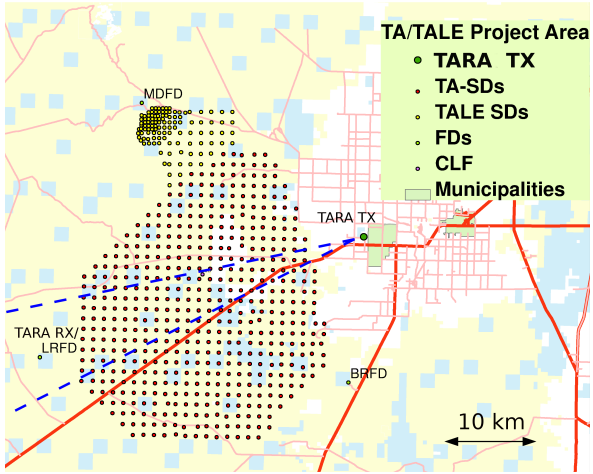


Figure 1: Map of TARA Observatory sites (transmitter and receiver) along with the Telescope Array (TA) detector facilities. The transmitter broadcasts as station WF2XZZ near Hinckley, Utah, towards a receiver site located at the TA Long Ridge Fluorescence Detector (FD). The sounding radiation illuminates the air over the central portion of the TA Surface Detector array, shown with dashed blue lines that indicate the beamwidth 3 dB below the peak gain.

station radar in conjunction with a conventional set of cosmic ray detectors. Air shower particles move very close to the speed of light, so the Doppler shift is large compared with airplanes or meteors. The bi-static configuration in which the sounding (interrogating) wave Poynting vector is generally perpendicular to shower velocity (as shown in Figure 3) minimizes the large Doppler shift in frequency expected of the reflected signal (see [14, 15], and Section 2 below.) This scenario is unlike that explored in [15] in which the two vectors are roughly anti-parallel. In the latter case, the relativistic frequency shift is maximized. Also, depending on the size of the radar cross section relative to the square of the sounding wavelength, scattering in the forward direction might be enhanced relative to back scatter [16], thus providing an advantage in detecting the faintest echoes in comparison to mono-static radar (ranging radar).

Co-location with a conventional detector allows for definitive coincidence studies to be performed. If coincidences are detected, the conventional detector's information on the shower geometry will allow direct comparison of echo signals with the predictions of air shower Radio Frequency (RF) scattering models.

The Telescope Array Radar (TARA) project is the next logical step in the development of the bi-static radar technique. Whereas MARIACHI made parasitic use of commercial television carriers as a source of sounding radiation (now impossible due to the transition

to digital broadcasts), TARA employs a single transmitter in a vacant VHF band which is under the experimentalists' control. The TARA receiver consists of broadband log-periodic antennas, which are read out using a 250 MS/s digitizer. TARA is co-located with the Telescope Array, a state-of-the-art “conventional” cosmic ray detector, which happens to be located in a low-noise environment. The layout of the TA and TARA detection facilities are shown in Figure 1.

This work begins with a brief description of the nature of air shower echoes expected for the TARA configuration. Next, we describe the transmitter and receiver system in some detail, including tests of system performance. Finally we describe upgrades to the system which are currently in progress.

## 2. Extensive Air Showers, Radar Echoes

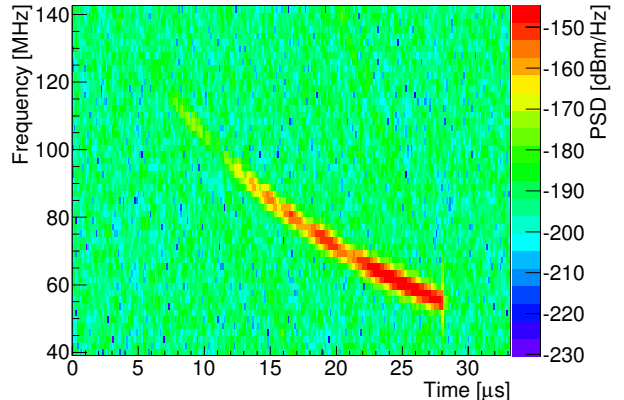


Figure 2: Spectrogram of a chirp signal produced by the radar echo simulation for an EAS located midway between the transmitter and receiver with a zenith angle of 30° out of the transmitter-receiver plane. A weighted fit to the power of this signal gives a  $-2.3 \text{ MHz}/\mu\text{s}$  chirp rate. Color scale is Power Spectral Density (PSD) given as dBm/Hz.

As the EAS core ionizes the atmosphere, liberated charges form a plasma with plasma frequency  $\nu_p = (2\pi)^{-1} \sqrt{n_e e^2 / m_e \epsilon_0}$ , where  $n_e$  is the electron number density,  $e$  is the charge of the electron, and  $m_e$  is the electron mass. A shower is denoted *under-dense* or *over-dense* (See Figure 3 in [17]) relative to the sounding frequency  $\nu$  depending on whether  $n_e$  corresponds to  $\nu_p > \nu$  or  $\nu_p < \nu$ . The radar cross-section of the under-dense region is expected to be greatly attenuated due to collisional damping [18, 19, 20]. Therefore, we expect the dominant contribution to EAS radar cross-section  $\sigma_{EAS}$  to be the over-dense region, which is modeled as

a thin-wire conductor [21]. Figure 2 displays a “typical” EAS echo from simulation, where standard shower models of particle production and energy transport have been assumed [22].

The mechanism of radar echo detection of EAS differs from other radio applications because the target is small (i.e., small RCS) and moving near the speed of light. However, letting  $R_T$  and  $R_R$  represent the transmitter/shower and receiver/shower distances, respectively, the bi-static geometry (Figure 3) minimizes the phase shift because the total path length  $L = R_R + R_T$  evolves slowly with time. The time-dependence of the path length causes the phase of the echo to evolve, while the transmission maintains a constant frequency. The result is an echo that has a time-dependent frequency – a *chirp* signal [14] (Figure 2).

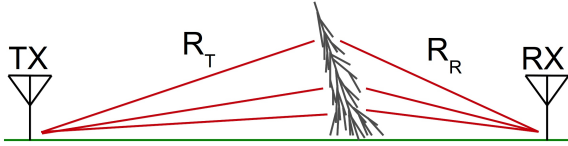


Figure 3: Bi-static geometry of a radar sounding wave interrogating an EAS to scale in the TARA geometry.  $R_T$  and  $R_R$  are the distances from transmitter (TX) to shower and shower to receiver (RX), respectively. The TX/RX antenna symbols represent location only. Actual antenna sizes are smaller than a pixel if represented to scale.

Chirp signals are ubiquitous in nature, although CR radar echos have very unique signatures. A simulation [23] has been designed that requires as inputs the CR energy, geometry and transmitter and receiver details, and which evolves an EAS according to standard particle production and energy transport models [22] while tracking the phase and amplitude of the radar echo. Shower parameters are functions of the primary particle energy [24]. The simulation indicates (see, for example, a “typical” TARA geometry simulation spectrogram in Figure 2) that CR radar echoes are short in duration (comparable to the shower life-time,  $\approx 10 \mu\text{s}$ ), have chirp rates of a few times  $1 \text{ MHz}/\mu\text{s}$  and span a bandwidth on order of the sounding frequency (see Figures 4 and 5).

The energy and geometry of a distribution of 10000 cosmic rays detected at the TA surface detector array have been simulated. Figures 4 and 5 show distributions of the chirp rate and duration for these events. Data obtained from the simulation have been used to guide the design of the DAQ, transmitter system, and the receiver antennas. A 54.1 MHz radar sounding frequency (the TARA licensed frequency) implies the need to resolve

a bandwidth of roughly 100 MHz and therefore implement a DAQ with at least 200 MS/s ADC. An FPGA based design is necessary to implement real-time digital filters that will trigger the DAQ on signals that resemble chirp radar echos.

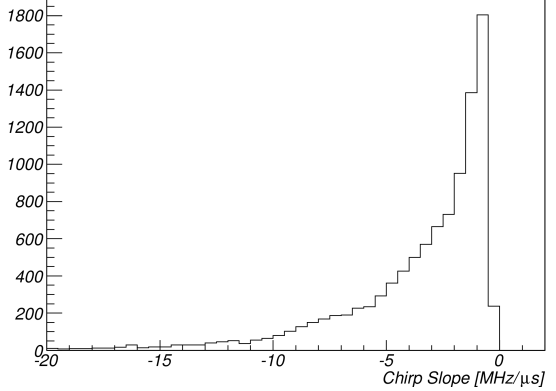


Figure 4: Simulated chirp rate distribution from a set of 10000 TA cosmic ray events. The rate is calculated from a weighted fit (by power) to the spectrogram of the simulated signal.

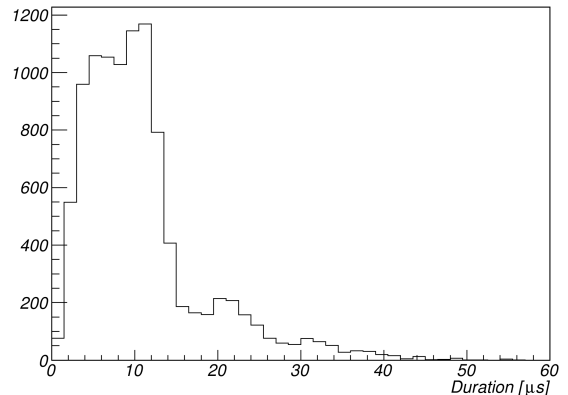


Figure 5: Chirp duration distribution from 10000 simulated radar echoes from TA cosmic ray events. Duration is defined as  $d = t_1 - t_0$ , where  $t_0$  is the time where the maximum power is received and  $t_1$  is the *later* time when the received power drops by 20 dB below the maximum, which approximates the end of the shower.

Air showers are uniquely defined by their radar echo signatures with the exception of a lateral symmetry with respect to a plane connecting the transmitter and receiver and also a rotational symmetry about a line connecting the transmitter and receiver. Stereo detection is necessary (at minimum) to break this symmetry. Section 8 discusses the remote station prototype that will supplement our primary receiver for stereo detection.

The actual radar cross section  $\sigma_{EAS}$  is currently unknown. The bi-static radar equation gives the received power  $P_R$  as a function of transmitter power  $P_T$ . Given the transmitter wavelength  $\lambda$  and receiver and transmitter antenna gains  $G_R$  and  $G_T$ , the bi-static radar equation is written as

$$\frac{P_R}{P_T} = \left( \frac{G_T}{4\pi R_T^2} \right) \sigma_{EAS} \left( \frac{G_R}{4\pi R_R^2} \right) \frac{\lambda^2}{4\pi}. \quad (1)$$

Detection possibility depends on the signal-to-noise ratio (SNR), defined as

$$SNR = \frac{P_c}{\sigma_v^2}, \quad (2)$$

where  $P_c$  is the chirp signal power and  $\sigma_v$  is the standard deviation of the background noise. A second definition is necessary for signals with time-varying amplitude like those predicted by the EAS radar echo simulation. For such signals we use the amplitude signal-to-noise ratio (ASN)

$$ASN = \frac{v_{max,c}^2}{\sigma_v^2}. \quad (3)$$

$v_{max,c}$  is the maximum chirp amplitude. The TARA DAQ can trigger on realistic chirp signals as low as 7 dB below the noise (-7 dB ASN, see Section 7.4.2). A simple calculation will show that, if the thin wire approximation  $\sigma_{tw}$  is assumed to correctly model the actual radar cross section (RCS)  $\sigma_{EAS}$ , TARA expects radar echoes with positive SNR (in dB).

TARA detector parameters are given in Table 1. Consider a 60 MHz Doppler shifted tone, scattered from an EAS located midway between the transmitter and receiver, which have a 39.5 km separation distance. Received power can be calculated from Equation 1 if  $\sigma_{EAS} \approx \sigma_{tw}$  is known. Some basic assumptions allow a quick calculation of  $\sigma_{tw}$ : Shower  $X_{max}$  occurs roughly 2 km from the ground; the antennas' polarization vector and shower axis are in the same plane; the length  $L$  of the scattering region of the shower is the speed of light multiplied by the electron attachment/recombination lifetime  $\tau = 10$  ns [18], which implies  $L = 3$  m; the over-dense region radius near  $X_{max}$  is the thin wire radius [17]  $a = 0.01$  m. With these assumptions the thin-wire cross section [21] is  $\sigma_{tw} \sim 1$  m<sup>2</sup> and the received power is -79 dBm.

Section 5, Figure 20 shows a plot of receiver system background noise superimposed with galactic noise. Receiver sample rate and Fourier transform window size used in the calculation were 250 MS/s and 32768,

Parameter	Value
UHECR energy	$10^{19}$ eV
$P_T$	40 kW
$G_T$	22.6 dBi (Section 4.3)
$G_R$	12.6 dBi (Section 5)
$R_T = R_R$	19.75 km

Table 1: The list of the parameters assumed for calculating received power from a 60 MHz Doppler shifted radar echo scattered from an EAS.

respectively. The power spectral density (PSD) of a -79 dBm tone detected by this system is  $-79 + 10 \log_{10}(32768/250 \cdot 10^6) = -117$  dBm/Hz. The reader should note that antenna patterns are both assumed to be at their maximum, which rarely occurs in practice. Further, polarization angle differences ( $\phi$ ) between the shower axis and antennas can yield another reduction in power  $\propto \cos^4(\phi)$ .

The receiver background noise plot demonstrates that, in the TARA frequency band of interest, backgrounds are dominated by galactic noise. At 60 MHz, the background noise PSD is -160 dBm/Hz, much lower than that of a narrow-band Doppler shifted radar echo at -117 dBm/Hz scattered from an ideal thin wire. Under reasonable assumptions for signal parameters, combined with our measured irreducible backgrounds and system response, the thin wire approximation for the radar cross-section  $\sigma_{EAS}$  implies high values of signal-to-noise.

### 3. Transmitter

#### 3.1. Hardware

TARA operates a high power, Continuous Wave (CW), low frequency radar transmitter built from repurposed analog TV transmitter equipment with FCC call sign WF2XZZ, an experimental license. The transmitter site (39° 20' 19.82400" N, 112° 42' 3.24000" W) is just outside Hinckley, UT city limits where human exposure to RF fields is of little concern. A high gain Yagi array (Section 4) focuses the radar wave toward the receiver station (Section 5) located 40 km away. Figure 1 shows the transmitter location near Hinckley and relative to the TA SD array [2]. The geometry was chosen to maximize the possibility of coincident SD and radar echo events.

Figure 6 shows a schematic of the transmitter hardware configuration. A Tektronix arbitrary function generator (AFG 3101; Tektronix, Inc.) provides the primary sine wave, which is amplified over nine orders of

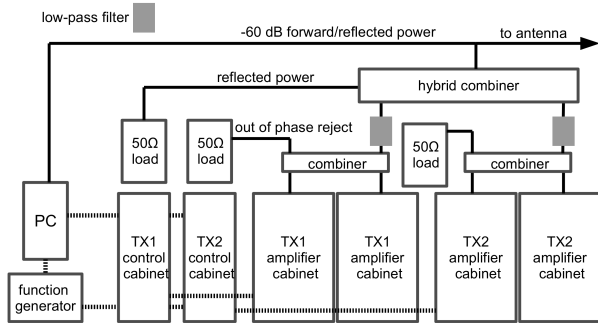


Figure 6: Schematic of the transmitter hardware configuration. A computer connected to RF sensor equipment, an arbitrary function generator and transmitter control electronics orchestrates the two distinct transmitters and provides remote control and logging. RF power from each transmitter's two amplifier cabinets is combined with out of phase power rejected into a  $50\ \Omega$  load. A hybrid combiner sums the combined output of each transmitter and sends that power to the antenna. Power reflected back into the hybrid combiner is directed to a third  $50\ \Omega$  load.

magnitude before reaching the antenna. 54.1 MHz was chosen as the sounding frequency because of the lack of interference in the vacated analog channel two TV band and the 100 kHz buffer between it and the amateur radio band which ends at 54.0 MHz.

Two 20 kW analog channel 2 TV transmitters have a combined 40 kW power output. The primary signal from the function generator is split to feed both transmitters (Harris Platinum HT20LS, p/n 994-9236-001; Harris Broadcast) with the same level of gain. Each transmitter includes a control cabinet and two cabinets of power amplifier modules. RF power from each cabinet is combined in a passive RF combiner (620-2620-002; Myat, Inc.) that routes any out-of-phase signal to a  $50\ \Omega$  load. The combined output of each transmitter is sent to a  $90^\circ$  hybrid combiner (RCHC-332-6LVF; Jampro, Inc.) that sums the total output of each transmitter. Between the final combined input and each transmitters' combined output there is an inline analog channel 2 low pass filter (visual low-pass filter, 3 1/8"; Myat, Inc.) to minimize harmonics. RF power leaves the building through 53 m of semi-flexible 3 1/8" circular air-dielectric wave guide (HJ8-50B; Andrew, Inc.).

Modifications were made to the transmitters to bypass interlocks that detect the presence of aural and visual inputs and video sync pulses necessary for standard TV transmission. Control cabinet electronics were calibrated to measure the correct forward and reflected power of the 54.1 MHz tone instead of the RF envelope during the sync pulse. Currently, total power output is limited to 25 kW because of limitations that arise from amplifying a single tone versus the full 6 MHz TV band.

Air conditioning and ventilation are critical to high power transmitter performance. Currently, transmitter efficiency is slightly better than 30%, which implies that nearly 75 kW of heat must be removed from the building. The environment at the site is very dry and dusty, so all of the air brought into the building is filtered and positive gauge pressure is maintained. A single 25 ton AC unit filters and pumps cool air into the building. An economizer will shut down the compressor if the outside air temperature drops below  $15.6^\circ\text{ C}$  ( $60^\circ\text{ F}$ ). However, if the room is not cooling quickly with low outside ambient temperature, the compressor will be turned back on. Hot air near the ceiling is vented as necessary to maintain a slight positive pressure.

Future improvements to the transmitter will include biasing the power amplifiers for class B operation, in which amplification is applied to only half the 54.1 MHz cycle. Resonance in the transmitter and antenna allow the second half of the wave to complete the cycle. Efficiency will nearly double compared with the current configuration.

### 3.2. Remote Monitoring and Control

Remote monitoring and control of the transmitter is important for two reasons. First, Federal Communications Commission (FCC) regulations require that non-staffed transmitter facilities be remotely controlled and several key parameters monitored. Second, forward power and other parameters must be logged for receiver data analysis.

A computer interfaces with digital I/O and analog input devices that, in turn, are connected to the transmitters' built in digital I/O and analog output interface. RF power sensors (PWR-4GHS; Mini-Circuits) measure the final forward and reflected power via strongly attenuating sample ports on the wave guide near the building exit port. The sum of the two control cabinets' forward and reflected power measurements can be compared with the separate RF final forward and reflected power measurements.

The host computer monitors transmitter digital status, analog outputs and RF power sensors and controls the function generator. Logs are updated every five minutes with forward and reflected power for each transmitter, *final* (re: antenna) forward and reflected power, room temperature and various transmitter status and error states. Warning and error thresholds can trigger emails to the operators and initiate automatic shutdown. The program also provides a simple interface that allows the operator to remotely turn the transmitter on and off, increase or decrease forward power, and add a text log entry.

### 3.3. Performance

TV transmitters are designed for 100% duty cycle operation. Similarly, the TARA transmitter is intended for continuous operation to maximize the probability of detection of UHECRs. With fixed gain and input signal, power is strongly correlated with transmitter room ambient temperature. Large temperature fluctuations in April 2013 resulted in a  $\sim 3$  kW spread in output power (Figure 7).

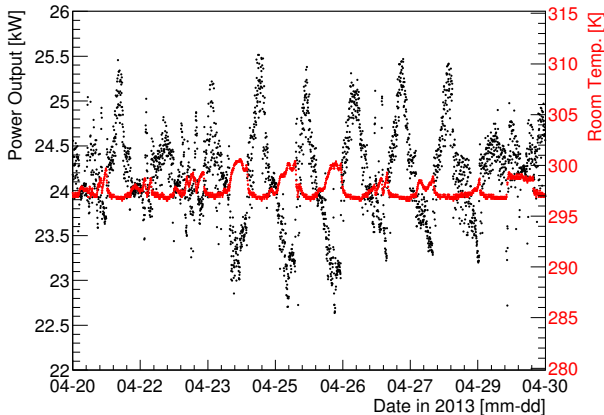


Figure 7: Transmitter forward power (black) and room temperature (red) during April 2013. Poor air conditioning calibration resulted in daily temperature fluctuations which caused large output power modulation.

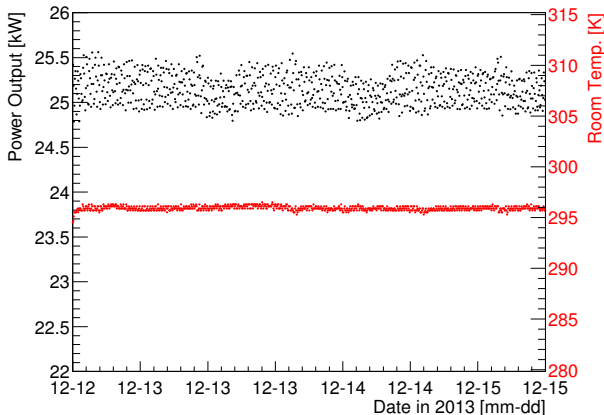


Figure 8: Transmitter forward power (black) and room temperature (red) during December 2013. A well-calibrated air conditioning system keeps room temperature stable and increased automatic gain control minimizes forward power fluctuations.

Transmitter forward power is more stable if room temperature is kept lower than 300 K ( $80^{\circ}$  F). Figure 8

shows forward power fluctuations in August 2013 are much smaller than April. Built-in automatic gain control was increased during this period as well. The average power in December is higher than the average power in April because a slightly higher power input signal was used in later months. Reflected power is typically  $\sim 100$  W, which is very low for such a high power system. This can be attributed to very good impedance matching with the extremely narrow-band Yagi antenna array.

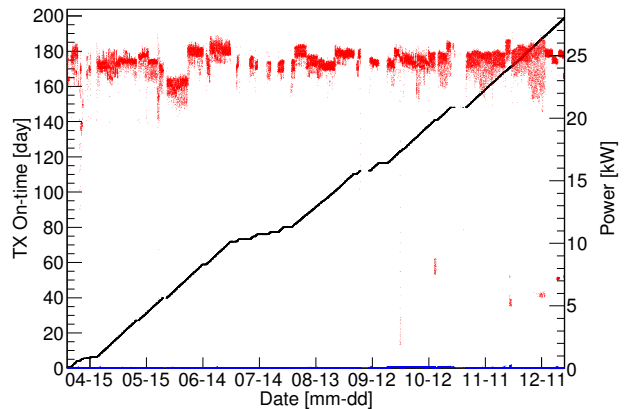


Figure 9: Transmitter on-time in days (black, left vertical axis) and forward and reflected power in units of kW (red and blue, right vertical axis) during 2013. Total duty cycle during this period is 83%.

Figure 9 shows the total forward and reflected power in red and blue, respectively, referenced to the right vertical axis and the integrated on-time in black, referenced to the left vertical axis, since its commissioning in late March, 2013. The transmitter has been turned off several times for maintenance and testing and during periods when our receiver equipment was removed from the field for upgrades. Although forward power is not continuous and fluctuations were large in the past, we consider 200 days of operation in the first year to bode well for future data collection.

Harmonics have been measured to confirm compliance with FCC regulations and to avoid interfering with other stations. With total forward output at 25 kW, the fundamental and several harmonic frequencies were measured from a low power RF sample port. The first five harmonics are about 60 dB below the fundamental (see Table 2). Harmonics will be further attenuated by about 30 dB by the intrinsic bandpass of the antenna.

Frequency (MHz)	Power (dBm)
54.1	8.5
108.2	-66.0
162.3	-68.3
216.4	-84.4
270.5	-89*
324.6	-77*
378.7	-94*
432.8	-87*
486.9	-98*
541.0	-91*

Table 2: Power of fundamental frequency and first ten harmonics for the 54.1 MHz radar sounding wave. These measurements were taken from a highly attenuated final forward power RF sample port. Total transmitted power was approximately 25 kW. FM and TV stations are required by the FCC to limit the first ten harmonics to at least 60 dB below their approved total transmitted power. Experimental station WF2XZZ is exempt from this requirement although it readily meets it. (\*fluctuating value,  $\pm 5$  dB)

## 4. Transmitting Antenna

### 4.1. Physical Design

As the bi-static radar equation (Equation 1) shows, the received power is the product of the scattering cross section, transmitted power, transmitter antenna gain, receiver antenna gain and receiver aperture. Because the physics of the radar scattering cross section is not well understood, an antenna with high gain and directivity was chosen to maximize received power.

The TARA transmitting antenna is composed of 8 narrow band Yagi antennas designed and manufactured by M2 Antenna Systems, Inc. Each Yagi is constructed of aluminum and capable of handling 10 kW of continuous RF power. The specifications for each Yagi are a frequency range of 53.9 - 54.3 MHz, 12 dBi free space gain, front to back ratio of 18 dB, and beamwidths (defined as the angle in the plane under consideration over which the radiated power is within three dB of the maximum) of  $27^\circ$  and  $23^\circ$  in the vertical and horizontal planes respectively.

Each Yagi antenna is composed of five elements: a reflector, driven element, and three directors, and are mounted on a 21.6 ft long, 2" diameter boom. A balanced t-match is fed from a 4:1 coaxial balun which transforms the unbalanced  $50\ \Omega$  input to the balanced  $200\ \Omega$  used to drive the antenna. A  $50\ \Omega$  7/8" coaxial waveguide connects the balun to the four port power dividers. Table 3 describes the lengths and positions of the antenna elements on the boom. All elements

are constructed of aluminum tubing of 3/4" outer diameter. Each element, except for the driven element is constructed of two equal sections that are joined at the boom via 7/8" outer diameter sleeve elements. The weight is 35 lbs when completely assembled.

Element	Length (in)	Position (in)
Reflector	107.625	-44.375
Driven Element	100.500	0.000
Director 1	99.500	51.125
Director 2	97.250	131.625
Director 3	97.000	193.625

Table 3: Length and relative boom position of antenna elements of the TARA Yagi antennas. All elements have a diameter of 0.75".

Transmitter output power is delivered to the antenna array via approximately 100 feet of CommScope HJ8-50B 3 1/8" Heliax air dielectric coaxial wave guide. The Heliax then connects to a two port power divider located at the base of the antenna array. Each output port of the power divider feeds equal length 1 5/8" coaxial cables, which in turn feed a four port power divider. Each four port power divider then delivers power to the individual Yagi antennas via equal length 7/8" coaxial cables. All components in the transmission line chain are impedance matched to  $50\ \Omega$ .

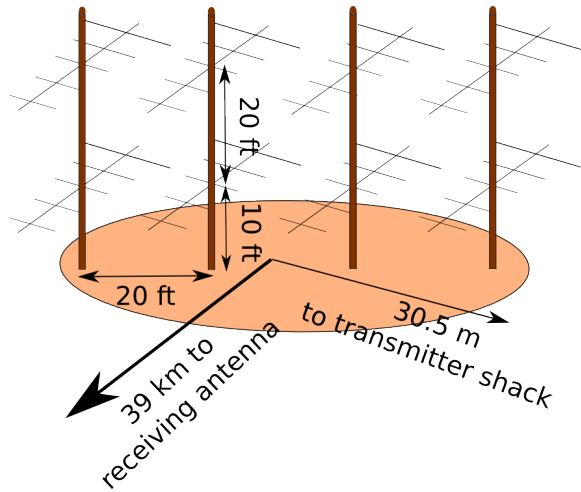


Figure 10: Configuration of the eight Yagi antennas and mounting poles which comprise the TARA transmitting antenna array.

The antennas are mounted on four wooden telephone poles, two stacked vertically on each pole. The bottom and top antennas on each pole are located 10 ft and 30 ft above the ground respectively. Currently, the antennas are mounted in a configuration that provides a horizontally polarized signal. Wooden poles were used to allow

a change of polarization. The poles, separated by 20 ft, are aligned in a plane perpendicular to the line pointing toward the receiver site located at the Long Ridge fluorescence detector 39 km to the southwest. Figure 10 shows the antenna array configuration.

#### 4.2. Theoretical Performance

The eight Yagi antennas are operated as a phased array to take advantage of pattern multiplication to improve gain and directivity relative to the individual antennas. The design philosophy of the antenna array is to deliver a large amount of power in the forward direction in a very narrow beam to maximize the power density over the TA surface detector. High power density is equivalent to a large  $P_T G_T$  factor in the bi-static radar equation, which is needed to increase the chance of detection of a cosmic ray air shower via radar echo given the uncertainty in the radar scattering cross section  $\sigma_{EAS}$ . Before construction, modeling of the array was performed using version two of NEC [25], an antenna modeling and optimization software package.

Figure 11 shows the radiation pattern of the full eight Yagi array when configured as shown in Figure 10. Forward gain is 22.6 dBi, horizontal beam width is 12°, vertical beam width is 10°, the front-to-back (F/B) ratio is 11.8 dB and the elevation angle of the main lobe is 9°.

Simulations were performed to find the best spacing between the mounting poles, vertical separation of antennas and height above ground to shape and direct the main lobe in a preferred direction. Antenna pole spacing influences the main lobe beam width. A narrower beam width can be obtained at the expense of transferring power to the side lobes which do not direct RF energy over the TA surface detector. Elevation angle is manipulated by antenna height above ground. Changing this parameter does little else to the main lobe. Elevation angle and beam width were selected to increase the probability that air shower  $X_{\max}$  would fall in the path of the main lobe where the charged particle density is the greatest. The 9° main lobe elevation angle is chosen such that the sounding wave illuminates the mean  $X_{\max}$  midway between transmitter and receiver for a distribution of showers (varying zenith angle) of order  $10^{19}$  EeV [26].

#### 4.3. Measured Performance

The ability of an antenna to transmit energy is best characterized by the reflection coefficient  $S_{11}$  (also called return loss when expressed in dB). It is a measure of the ratio of the voltage reflected from a transmission line relative to input. Large reflection coefficient implies

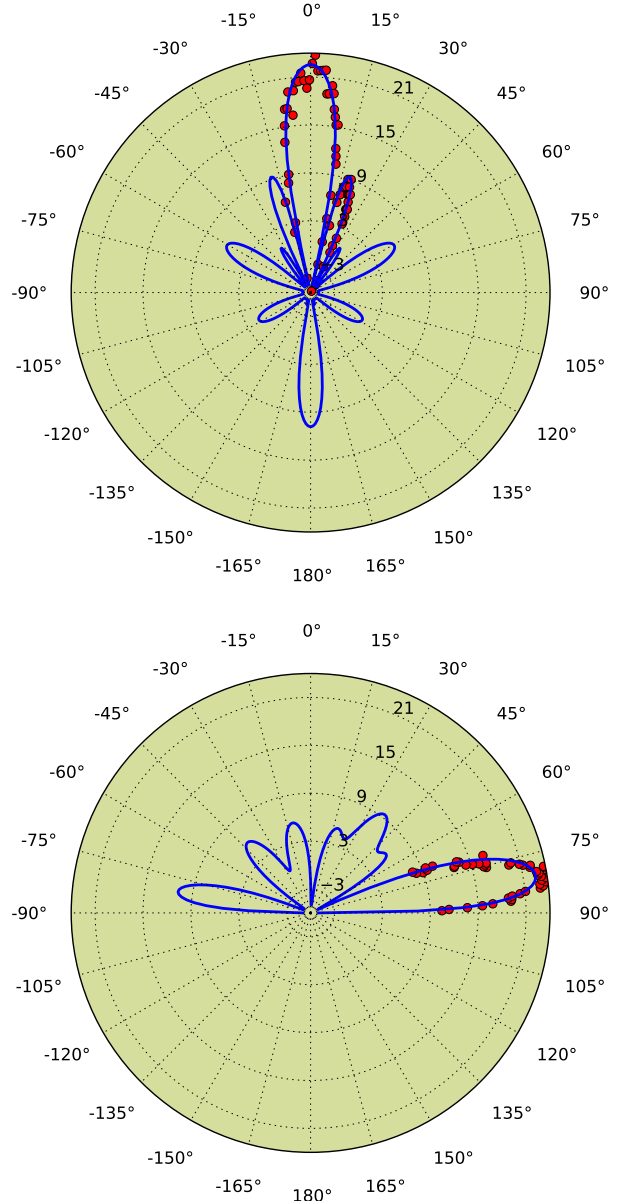


Figure 11: Simulated horizontal (top) and vertical (bottom) radiation patterns of the eight Yagi TARA antenna array shown in blue. Red points are measured data that have been uniformly scaled to best fit the model. Forward gain is 22.6 dBi, beam width is 12° horizontal, 10° vertical, and the F/B ratio is 11.8 dB.

significant energy is reflected back into the transmitter building which can interfere with other electronics, elevate ambient temperature and even damage the transmitter. Figure 12 shows the reflection coefficient for the Yagi array. It shows a return loss of -37.25 dB at the sounding frequency, which is excellent.  $S_{11}$  of -20 dB

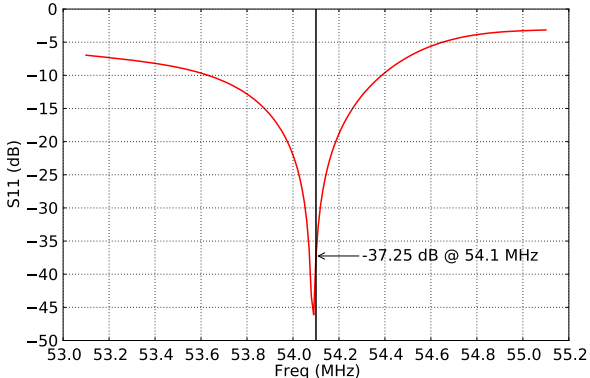


Figure 12: Reflection coefficient ( $S_{11}$ ) for the eight Yagi array.

or less is considered good.

To verify that the transmitting antenna is operating as designed, an RF power meter or similar device can be used to measure the power as a function of position relative to the antenna. This measurement is challenging because it must be performed in the far field of the antenna (typically  $r \gg \lambda$ ). To fully probe the radiation pattern of the TARA transmitting antenna, power measurements must be made high above the ground since the main lobe is inclined 9° relative to horizontal.

Vertical radiation pattern measurements were taken by using antenna transmitting/receiving symmetry. A tethered weather balloon was floated with a custom battery powered 54.1 MHz signal generator that fed a dipole antenna. Over a range of discrete heights, received power was recorded at the output (normally the input) of the Yagi array.

The horizontal (azimuthal) radiation pattern was measured using a spectrum analyzer on the ground to determine the pointing direction and shape of the main lobe. Measurements of transmitted RF power were taken at distances between 650 and 1000 m radially from the center of the array. Power was measured along a road that does not run perpendicular to the pointing direction of the transmitter so a  $1/r^2$  correction was made. Figure 11 shows the measured points for the horizontal and vertical patterns overlayed on the models. These measurements are all relative, not absolute, so a uniform scale factor was determined by minimizing  $\chi^2$  between the model and data. The measured pattern agrees very well with the model in pointing direction and shape.

## 5. Receiver Antenna

The TARA receiver antenna site is located at the Telescope Array Long Ridge Fluorescence Detector



Figure 13: Dual polarized TARA Log Periodic Dipole Antenna (LPDA).

Element	Length (in)	Position (in)
1	21.875	3.625
2	26.625	18.0625
3	32.5	35.625
4	39.625	57.0
5	48.3125	83.125
6	58.3125	115.0

Table 4: Length and relative boom position of antenna elements of the TARA Log Periodic Dipole Antennas. All elements have a diameter of 0.25".

(39° 12' 27.75420" N, 113° 7' 15.56760" W). Receiver antennas are dual-polarized log periodic dipole antennas (LPDA) designed to match the expected  $< 100$  MHz signal frequency characteristics. Due to noise below 30 MHz and the FM band above 88 MHz, the effective band is reduced to 40 to 80 MHz. Each antenna channel is comprised of a series of six  $\lambda/2$  dipoles. The ratio of successive dipole lengths is equal to the horizontal spacing between two dipoles (the defining characteristic of LPDA units), with the longest elements farthest from the feed-point to mitigate large group delay across the passband. Table 4 gives the lengths and positions of the antenna elements on the boom from the front edge to the back. All elements are constructed of aluminum tubing of 1/4" outer diameter. Figure 13 shows a schematic of the receiver LPDA.

The impedance of the antenna against a 50 Ω transmission line was measured in an anechoic chamber at the University of Kansas. The standing wave ratio (SWR), the magnitude of the complex reflection coefficient ( $S_{11}$ ), is shown as a function of frequency in Fig-

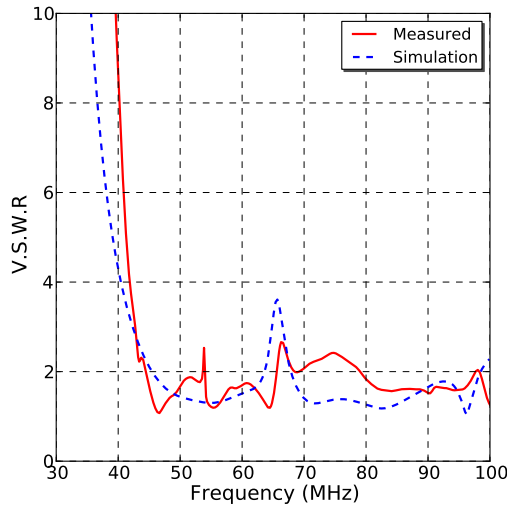


Figure 14: SWR of a horizontally polarized TARA LPDA as measured in an anechoic chamber.

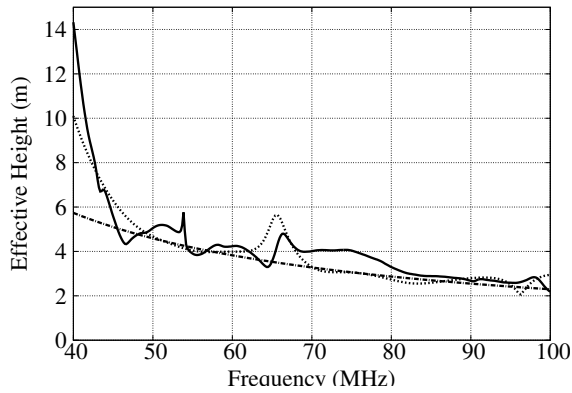


Figure 15: Effective height in meters vs. frequency in MHz of the TARA receiver LPDA. The  $S_{11}$  parameter and gain of the receiver antenna are inserted into Equation 4 and plotted vs. frequency using the anechoic chamber data (solid line), simulated data from NEC (fine dashed), and simulated data with the 54.1 MHz values of  $S_{11}$  and gain held constant (dot-dashed line).

ure 14. An SWR of 3.0 implies greater than 75% signal power is transmitted from the antenna to the receiver at a given frequency.

The complex  $S_{11}$  measurement also quantifies the *effective height* of the LPDA. The effective height translates the incident electric field strength in V/m to a voltage at the antenna terminals. It is given as  $\mathbf{E}_{inc} \cdot \mathbf{h}_{eff} = |E_{inc}| |h_{eff}| \cos(\theta) = V$ , where  $\theta$  is the polarization angle and the antenna is assumed to be horizontally polarized. The boresight effective height can be expressed [27] as

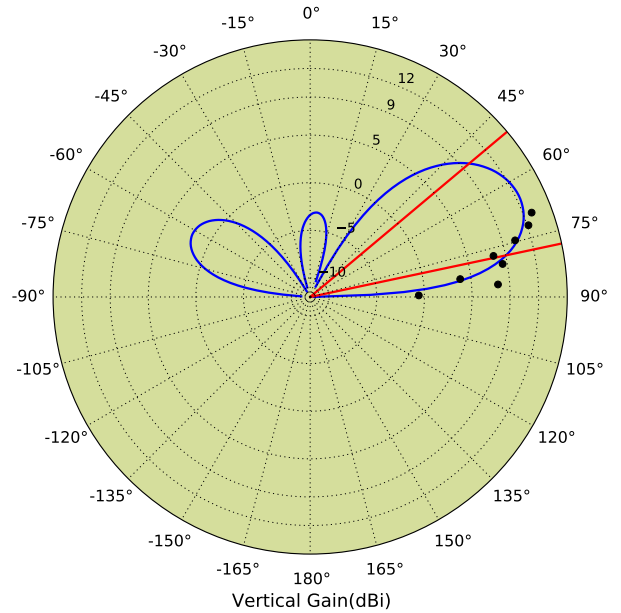
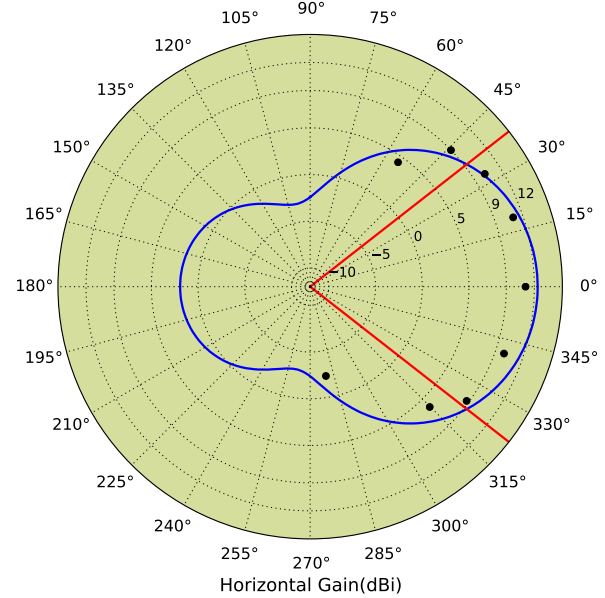


Figure 16: Simulated horizontal (top) and vertical (bottom) radiation pattern of a horizontally polarized TARA LPDA at the transmitter sounding frequency of 54.1 MHz. Beamwidths ( $-3$  dB below peak gain) are shown with red lines. Peak gain is 12.6 dBi.

$$h(v) = 2 * \sqrt{\frac{Gc^2|Z_{in}|}{4\pi v^2 Z_0}}. \quad (4)$$

In the effective height expression,  $G$  is the measured gain of 12.6 dBi (see Figure 16),  $c$  is the speed of light,

$Z_{in}$  is the complex antenna impedance,  $\nu$  is the frequency, and  $Z_0 = 120\pi$  is the impedance of free space. In terms of the measured complex reflection coefficient  $S_{11}$ , the impedance is given by  $|Z_{in}| = \left| \frac{1+S_{11}}{1-S_{11}} \right| 50 \Omega$ . The frequency-dependent magnitude of the effective height is plotted in Figure 15.

Receiver antenna gain is a factor in the bi-static radar equation that affects detection threshold. NEC was used in simulating the radiation pattern of the antenna to confirm directionality (see Figure 16). Simulated forward gain is 12.6 dBi and the vertical beamwidth is 23° at the carrier frequency, 54.1 MHz. Figure 17 displays measured beamwidth in the band of interest.

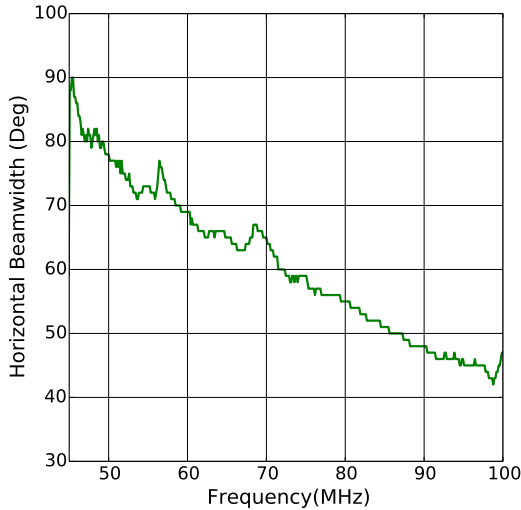


Figure 17: Beamwidth of a single channel LPDA as measured in an anechoic chamber at the University of Kansas.

## 6. Receiver Front-end

There are three dual-polarization antennas at the receiver site, two of which are currently connected to the DAQ (Section 7). RF signal from the antennas pass through a bank of filters and amplifiers. The components include an RF limiter (VLM-33-S+; Mini-Circuits), broad band amplifier, low pass filter (NLP - 100+; Mini-Circuits), high pass filter and an FM band stop filter (NSBP-108+; Mini-Circuits). Both polarizations from one antenna are filtered (37 MHz cutoff frequency high pass filter, SHP-50+; Mini-Circuits) and amplified (40 dB, ZKL-1R5+; Mini-Circuits) at the antenna, where a bias tee (ZFBT-4R2G+; Mini-Circuits) is used to bring DC power from the control room.

The second antenna's channels are filtered (25 MHz high pass filter, NHP-25+; Mini-Circuits) and amplified (30 dB, ZKL-2R5+; Mini-Circuits) inside the control room. The lightning arrester (LSS0001; Inscape Data) minimizes damage to sensitive amplifiers by electric potentials that accrue during thunderstorms. The RF limiter prevents damage by transient high amplitude pulses (see Section 7.2).

Signal conditioning in the amplifier/filter banks is characterized by the transmission coefficient (Figure 18)  $S_{21}$ . It is a measure of the ratio of the voltage at the end of a transmission line relative to the input. Impedance mismatch relative to a  $50 \Omega$  transmission line, insertion loss for the various devices and gain from the amplifiers are combined in  $S_{21}$  data. Of note in Figure 18 is the flat, high-gain (30 dB), broadband ( $\approx 40$  MHz) passband necessary for Doppler-shifted radar echoes.

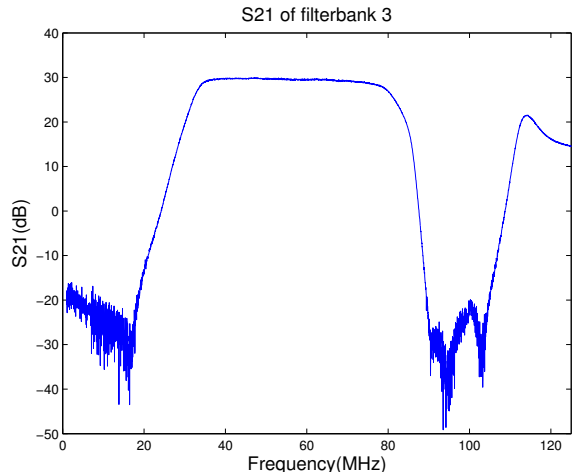


Figure 18:  $S_{21}$  (transmission coefficient) of the filter and amplifier bank connected to the triggering channel of the DAQ.

In any RF receiver system, sensitivity is limited by the combination of external noise entering through the antenna and internal noise from various sources like low noise amplifiers and other resistive losses from filters, cables and couplers. Noise entering the antenna is generated by the sky, earth and antenna resistive loss. Diffuse radio noise from the galactic plane is non-polarized and is the dominant noise source in the TARA frequency band. Figure 19 shows diurnal variation in the snapshot (forced trigger,  $1 \text{ min}^{-1}$ ) spectrum that remains consistent in data taken six months apart. Each plot shows the Power Spectral Density (PSD, units of  $\text{dBm}/\text{Hz}$ ) averaged over eight days versus Local Mean Sidereal Time (LMST). Horizontal and vertical error bars are bin width and std. dev. of the mean, respectively. The effect

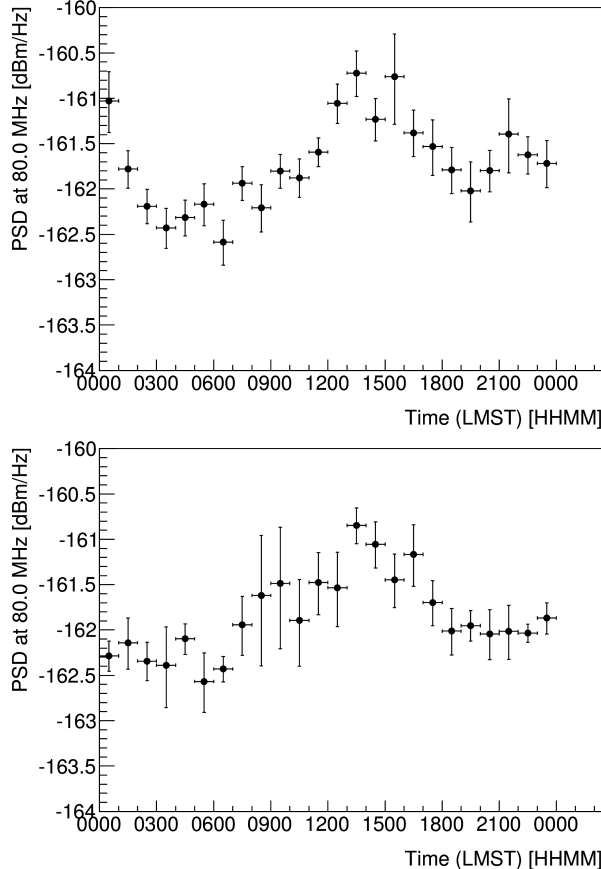


Figure 19: Snapshot (forced trigger) Power Spectral Density (PSD) at 80.0 MHz averaged over eight days versus Local Mean Sidereal Time (LMST). Top: Data taken in December, 2013. Bottom: Data taken in May, 2014. There is strong correlation in peak PSD and sidereal time which indicates the signal is galactic in origin. Horizontal error bars show bin width. Vertical error bars are std. dev. in the mean.

of amplifiers and cable losses have been removed such that absolute received power is shown. Data taken in December, 2013 are shown in the top plot, with those recorded in May, 2014 shown in the bottom plot. We observe that the peak occurs at the same time and power in each plot. Our conclusion is diurnal fluctuations are caused by changing perspective on the galactic center.

By accounting for amplifier and instrumental gains and losses, the observed noise background can be compared with the irreducible galactic noise background [29] across the passband. Our average measured system noise is calibrated by removing the effects of individual components in the receiver RF chain from average snapshot spectra to determine the absolute received power. Without any other scaling, our corrected received power compares nicely with the galactic noise standard [28] (Figure 20). Important components for

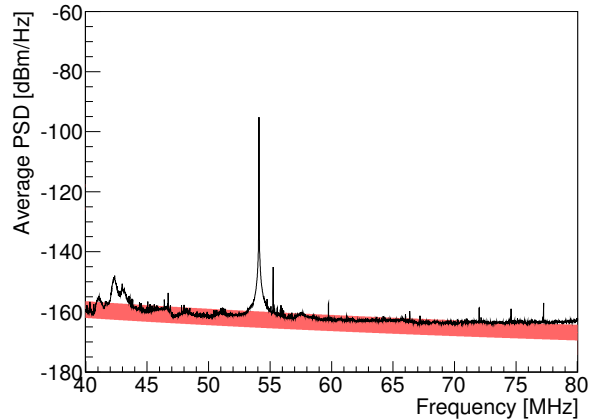


Figure 20: Average receiver system noise floor (black) Power Spectral Density (PSD) in dBm/Hz superimposed with a fit to measured galactic background noise and its associated error [28]. System attenuation, filters and amplifiers were accounted for to determine absolute received power. No other calibration or scaling was applied to the receiver data.

which adjustments were made include filters and amplifiers via the measured transmission coefficient  $S_{21}$  and LMR-400 transmission line with attenuation data. Anthropogenic noise sources are transient and stationary noise is absent within our measurement band due to the receiver site's remote location. In this frequency region, galactic noise dominates thermal and other noise sources.

## 7. Receiver DAQ

### 7.1. DAQ Structure

The National Instruments FlexRIO system provides an integrated hardware and software solution for a custom software defined radio DAQ. It is composed of three basic parts: adapter module, FPGA module and host controller (as shown in the lower box of Figure 21). A description of each of these subsystems follows.

The NI-5761 RF adapter module is a high-performance digitizer that defines the physical inputs and outputs of the DAQ system. It digitizes four analog input channels at a rate of 250 MS/s with 14-bit resolution. Eight TTL I/O lines are available for additional control, some of which are used in custom DAQ triggering schemes.

The NI-7965R FPGA module is based on the PXI express platform which uses a Xilinx Virtex-5 FPGA with 128MB on board DRAM. FPGA design provides accurate timing and intelligent triggering. The PXI-express platform has a high-speed data link to the host controller, which is connected to the development machine,

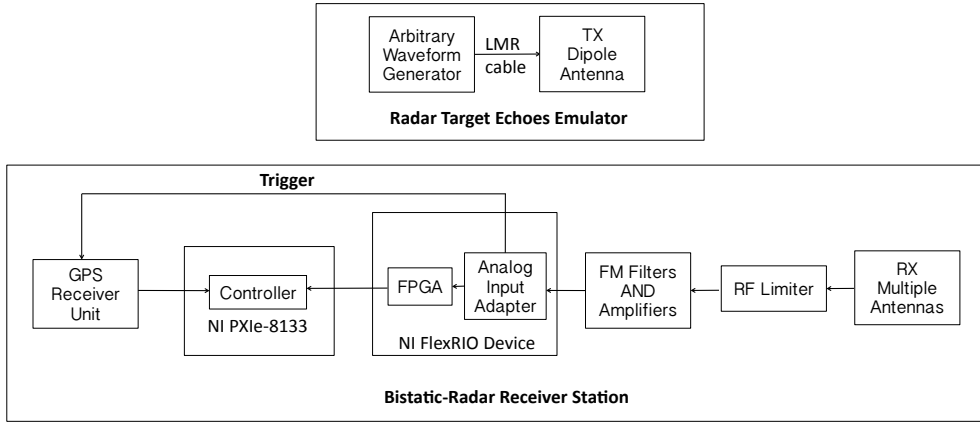


Figure 21: Elements of the radar receiver station.

a Windows based computer, which uses the LabVIEW environment to design and compile FPGA code. A host controller application, also designed in LabVIEW, runs on the development machine.

### 7.2. Design Challenges

Based on the high velocity of the radar target, echoes are expected to be characterized by a rapid phase modulation-induced frequency shift, covering tens of MHz in  $10\ \mu\text{s}$ . As the magnitude of the Doppler blue shift decreases as the shower develops in the atmosphere, these signals sweep (approximately) linearly from high to low frequency and are categorized as linear-downward chirp signals. Echo parameters are dependent on the physical parameters of the air showers. Thus, unlike existing chirp applications, we are interested in the detection of chirp echoes of variable amplitude, center frequency and frequency rates within a relatively wide band. In addition, the detection threshold must be minimized in order to increase the probability of detecting radar echoes with SNR less than one.

Furthermore, UHECR events are rare and random in time. TA receives only several  $> 10^{19}\ \text{eV}$  events per week, so background noise and spurious RF activity dominate.

Figure 22 shows a spectrogram of data acquired in the field using the complete receiver and test system (Figure 21), where FM radio and noise below  $\sim 30\ \text{MHz}$  are filtered out. The time-frequency representation shows that the background noise of our radar environment is rich with multiple undesirable components including stationary tones outside the 40-80 MHz effective band located at 28.5 MHz and, inside the band, the carrier at 54.1 MHz as well as broadband transients. Sudden amplitude modulation of stationary sources and powerful,

short-duration broadband noise can cause false-alarms. A robust signal processing technique is needed to confront these challenges [30].

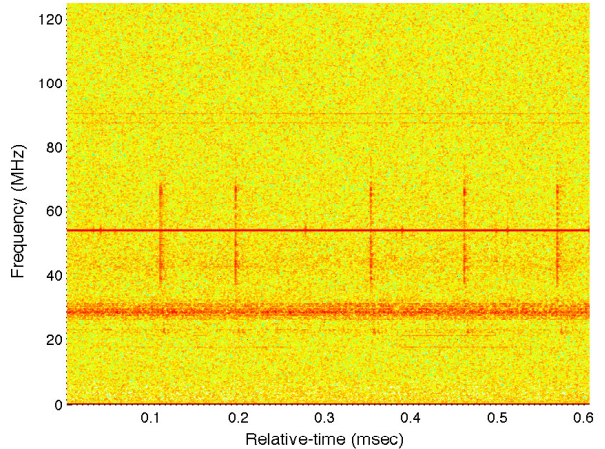


Figure 22: Spectrogram of background noise at the receiver site. Frequency and time are on the vertical and horizontal axes, respectively, with color representing the power in a particular frequency component. The carrier signal is represented by the horizontal line at 54.1 MHz. Broadband transients are the vertical lines and stationary noise sources are the horizontal band near 30 MHz.

### 7.3. DAQ Implementation

The DAQ is designed to detect chirp echoes and confront the problem of a variable noise environment. Two antennas feed the DAQ's four input channels. Each antenna is a dual-polarized LPDA (Section 5) with one output channel each for horizontal and vertical polarization. Data are collected simultaneously from each of the four analog channels with one horizontal channel

considered the triggering channel, then sampled using a 250 MS/s ADC (Texas Instruments; ADS62P49). Analog to digital conversion is followed by fast digital memory storage on the FPGA chip, which stores the incoming samples from each channel sequentially, in a  $131\ \mu s$  (32744 sample) continuous circular buffer such that data in each buffer are continually overwritten. Three distinct trigger modes are implemented: “snapshot”, “Fluorescence Detector (FD) external”, and “matched-filter bank”.

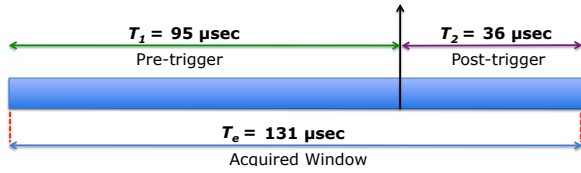


Figure 23: Position of the triggering pulse within the data window that is written to disk.

When a trigger occurs, the circular buffer information is sent to the host controller to be permanently stored on the computer’s disk. A  $320\ \mu s$  dead-time is required to transfer data from a buffer to FPGA memory, during which the DAQ cannot accept triggers. Sustained maximum trigger rate is 50 Hz due to FPGA-to-host data transfer limitations. As depicted in Figure 23, *pre/post* trigger acquisition is set to  $95\ \mu s$  and  $36\ \mu s$ , respectively, to allow for delay and jitter in the FD trigger timing ( $33\ \mu s$  delay,  $1\ \mu s$  jitter) and sufficient post-trigger data to see an entire echo wave form. A GPS time stamp is retrieved from a programmable hardware module [31] and recorded for each trigger with an absolute error of  $\pm 20\ ns$ .

The snapshot trigger is an unbiased trigger scheme initiated once every minute that writes out an event to disk. These events will (likely) contain background noise only. Unbiased triggers are crucial for background noise estimation and analysis.

During active FD data acquisition periods, the Long Ridge FD (the location of the TARA receiver site) emits a NIM (Nuclear Instrumentation Module) pulse for each low level trigger with a typical rate of  $\sim 3\text{--}5\ Hz$  or much higher during FD calibration periods. The low level trigger is an OR of individual FD telescope mirror triggers. Dead time due to high FD-trigger rates are as high as several milliseconds during calibration periods. This does not reduce data acquisition time significantly because these periods occur only for several minutes and less than half a dozen times per FD data acquisition period. Further, FD operation only amounts

to 10% duty cycle on average. The FlexRIO is forced to trigger by each pulse received from the FD. Each FD run will result in many thousands of triggers which can be narrowed to several events that coincide with real events found in reconstructed TA data.

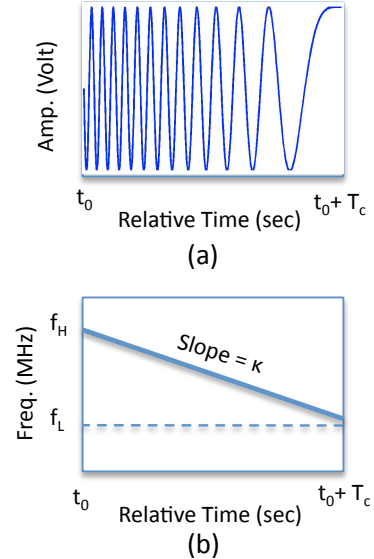


Figure 24: Linear down-chirp signal. (a) Signal in time-domain. (b) Signal in time-frequency domain.

The matched filter (MF) bank is a solution for the problem of detecting radar chirp echoes in a challenging noise background using signal processing techniques. The signal of interest is assumed to be a down-chirp signal that has duration  $T_c$  seconds with a constant amplitude, start (high) frequency  $f_H$ , center frequency  $f_C$ , end (low) frequency  $f_L$  and chirp rate  $\kappa\ Hz/sec$ . An example of the signal of interest is shown in Figure 24. Assuming that it is centered around time  $t = 0$ , such a chirp signal is written as

$$s(t) = \text{rect}\left(\frac{t}{T_c}\right) \cos(2\pi f_C t - \pi \kappa t^2). \quad (5)$$

where  $\text{rect}(x)$  is the rectangle function and  $t$  is the time in seconds.

We limit our interest to detecting the presence of  $s(t)$  within a certain bandwidth, without prior knowledge of the chirp rate  $\kappa$ . Based on simulation of the physical target, reflected echoes are expected to have a peak amplitude within or near the range [60-65] MHz. Thus, we consider  $f_H$  to be 65 MHz and  $f_L$  to be 60 MHz.

Since the chirp rate varies, we use a bank of filters matched to a number of quantized chirp rates,  $\kappa_1, \kappa_2,$

$\dots, \kappa_M$ . A functional block diagram of the detection process is illustrated in Figure 25.

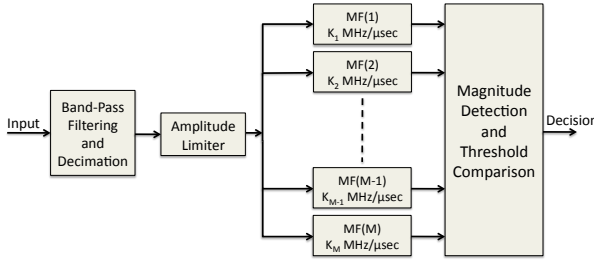


Figure 25: Block diagram of the matched-filter-type detector.

Let  $\mathbf{y}_m$  denote the output samples of the  $m$ th matched filter and  $\gamma_m$  the threshold at the filter output. As depicted in Figure 25, a trigger decision is made at the output of the matched-filter bank by comparing magnitudes of the elements of  $\mathbf{y}_1, \mathbf{y}_2, \dots, \mathbf{y}_M$ , each, against the corresponding threshold levels  $\gamma_1, \gamma_2, \dots, \gamma_M$ , respectively.

Threshold levels are defined as  $n_\gamma$  units of the signal level (equivalently, noise standard deviation) at the output of each filter, denoted by  $\sigma_m$  for the  $m$ th matched filter. Every time a trigger condition (the presence of a chirp) is met, an event is declared. Since the background noise level varies with time,  $\sigma_m$  is measured every five seconds to maintain a constant data acquisition rate.

The most probable chirp-rate interval for a distribution of simulated radar echoes is  $\mathcal{K} = [-3, -1] \text{ MHz}/\mu\text{s}$ . We choose  $M = 5$  and the chirp rates (in  $\text{MHz}/\mu\text{s}$ ) as

$$\begin{aligned} \kappa_1 &= -1.1161, \kappa_2 = -1.3904, \kappa_3 = -1.7321, \\ \kappa_4 &= -2.1577, \kappa_5 = -2.6879. \end{aligned}$$

### 7.3.1. Amplitude Limiter

Radio background at the remote receiver site is clear of stationary interference signals in the frequency band of interest, 40–80 MHz. Therefore, the broadband transients mentioned in Section 7.2 are the primary source of false alarms. Consequently, the threshold of the MF detector must be raised in order to maintain the desired false alarm rate. The result is high data rate in return for low trigger thresholds. A digital amplitude limiter applied immediately before the input to the MF detector helps to minimize false alarms while keeping the detection threshold as low as possible and without significantly degrading detection efficiency.

The amplitude limiter clips the amplitude of the received signal to a fraction  $k$  of its RMS value before

clipping. Its mathematical expression is

$$\begin{cases} y = x, & |x| < k\sigma_s \\ y = k\sigma_s, & x > k\sigma_s \\ y = -k\sigma_s, & x < -k\sigma_s. \end{cases} \quad (6)$$

where  $x$  is the raw input,  $y$  is the amplitude limited output, and  $\sigma_s$  is the RMS value of the signal before clipping. The result is a reduced relative power ratio of the spurious impulses to the non-perturbed background. Clipping also lowers the waveform RMS in proportion to the clipping level.

### 7.3.2. Band-Pass Filtering

We observe considerable CW noise within the 40–80 MHz band, including the carrier signal. The carrier and other persistent tones can have large amplitudes and lead to high matched filter RMS output which can, as shown in the next section, prevent detection of low SNR chirp signals. Such tones, including the carrier, can be easily filtered out. Before the amplitude limiter, a narrow band-pass filter eliminates all frequencies outside a 60–65 MHz band with -80 dB stop band attenuation. Data stored in the ring buffer are not filtered this way.

## 7.4. Performance Evaluation

Detection performance of the MF detector has been evaluated under two test signal conditions: noise only or signal plus noise. For each test, the Boolean result of the threshold comparison with the MF outputs is recorded. The probability of signal plus noise exceeding MF thresholds is the efficiency and the average rate of erroneous detection decisions caused by filtered noise is false alarm rate.

The ability to detect a received chirp signal in background noise depends on the ratio of the signal power to the background noise power. Radar carrier power dominates the background so two quantities are used to describe the background noise. First, we define the ratio of the test chirp signal power to the radar carrier power as the signal-to-carrier ratio (SCR). Second, we use either the SNR (Equation 2) or ASNR (Equation 3), depending on the type of test chirp signal input to the matched-filter bank, after filtering out the powerful carrier signal.

Consider the following observations about performance analysis. First, it is clear that system performance depends on the chosen threshold level  $n_\gamma$  (user defined, a multiple of  $\sigma_m$  as defined previously) for each SNR value. False alarm rate is expected to decrease as the threshold level increases, at the expense

of detection efficiency of low SNR chirp signals. Conversely, detection efficiency increases as the threshold decreases. Second, the false alarm rate is expected to decrease as the amplitude limiter level decreases because high amplitude transients are effectively removed. To this date, radar echoes from CR air showers have not been detected, so it's unlikely that the EAS cross section is large enough to produce such large amplitude impulses. Therefore such signals are dismissed *a priori*. Our strategy is to choose the threshold and amplitude limiter level that gives high detection efficiency for a given SNR and low false alarm rate.

Two tests are conducted to determine the ideal amplitude limiter level and the efficiency as a function of MF threshold. The goal of the first test is to measure the average false alarm rate of the non-Gaussian noise environment and evaluate the improvement that could be achieved by adding the amplitude limiter. Results are shown in Figure 26 for three different amplitude limiter levels, which clearly show that the limiter level has a significant effect on the false alarm rate. Efficiency curves for different amplitude limiter levels (described in the next paragraphs) show that the amplitude limiter does not *decrease* detection performance of chirp signals, although they are also clipped.

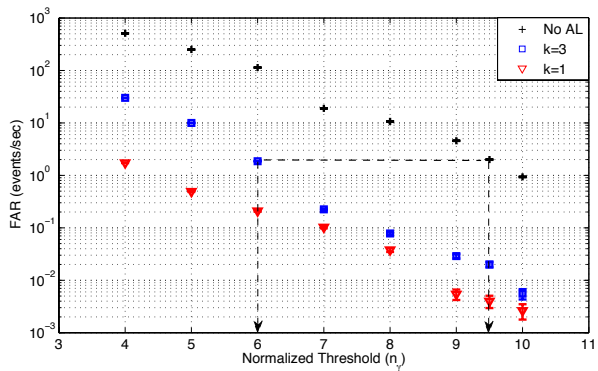


Figure 26: False-Alarm Rate versus relative threshold ( $n_y$  units of the standard deviation at each filter output) for different amplitude limiter levels.

Consider the following interpretation of Figure 26. In order to achieve a 2 Hz false alarm rate,  $n_y$  has a value of six for  $k = 3$  and 9.5 for  $k = 10$  (black dashed line). Thus, detection thresholds can be decreased which enhances positive detection of low SNR signals.

The second test applies a theoretical chirp signal with various chirp rates and SNR values that correspond to a reasonable false alarm rate. Based on data storage and post-processing computational requirements, we have decided that a false alarm rate of  $\sim 1$  Hz is reasonable.

Artificially generated chirp signals are transmitted *in situ* to the receiving antennas by an arbitrary waveform generator (AFG 3101; Tektronix, Inc.) and a dipole antenna. Both linear chirp signals and a simulated radar echo (see Section 2) are used in measuring detection performance.

#### 7.4.1. Linear chirp signal

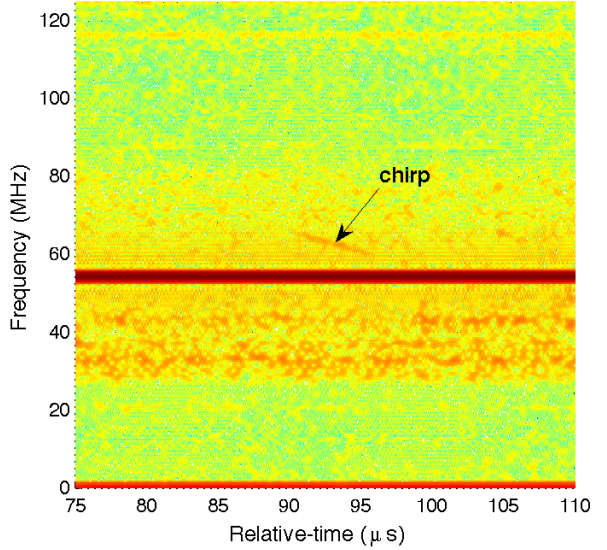


Figure 27: Time-frequency (spectrogram) representation of a linear,  $-1 \text{ MHz}/\mu\text{s}$ ,  $-10 \text{ dB}$  SNR received chirp signal as recorded by the DAQ system.

A periodic, linear chirp with  $-1 \text{ MHz}/\mu\text{s}$  rate is embedded in a real receiver site background wave form. Figure 27 shows the spectrogram of a chirp embedded with  $-10 \text{ dB}$  SNR and  $-40 \text{ dB}$  SCR value.

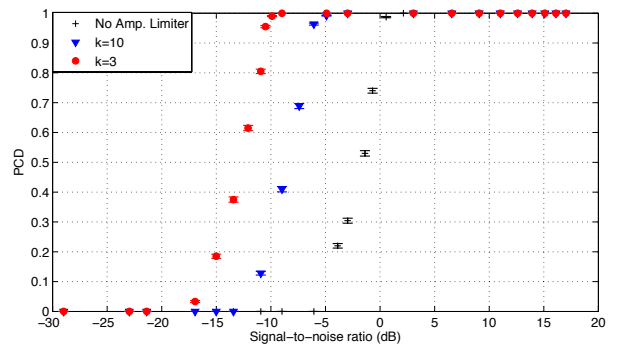


Figure 28: Probability of detection for the matched-filter-type detector with  $n_y = 6$ .

Figure 28 shows detection performance for a 2 Hz false alarm rate. Efficiency is shown for cases where the

amplitude limiter is removed and at two different levels that result in the same false alarm rate, each with different threshold levels. The minimum SNR for which complete detection is achieved is 5 dB when no amplitude limiter is applied, 0 dB for  $k = 10$  (*soft clipping*), -6 dB for  $k = 3$  (*hard clipping*). These results imply that by using the amplitude limiter, high detection performance can be achieved with low complexity. To maximize detection ability, the amplitude limiter is currently fixed at  $k = 3$ .

#### 7.4.2. Simulated Air Shower

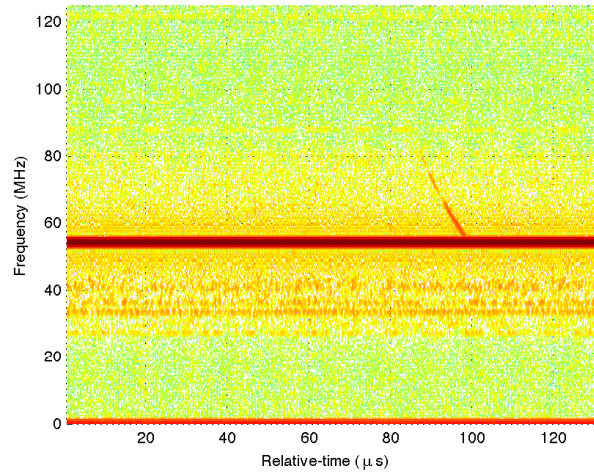


Figure 29: Spectrogram of simulated air shower radar echo with 5 dB ASNR. The radar echo is from a simulated shower inclined 30° out of the  $TX \rightarrow RX$  plane and located midway between the transmitter and receiver.

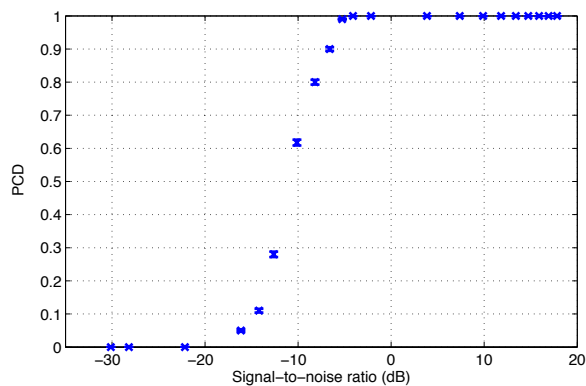


Figure 30: Probability of correct detection for the matched-filter detector using  $n_y = 6$  for a simulated air-shower echo that is scaled and emulated with a function generator.

In a more realistic test, a simulated radar echo from a 10 EeV air shower inclined 30° out of the  $TX \rightarrow RX$

plane and located midway between the transmitter and receiver is scaled and transmitted to the receiving antennas using a function generator. Figure 29 shows a spectrogram of the received waveform with 5 dB ASNR and -25 dB SCR. The echo is broadband (about 25 MHz) and short in duration (10  $\mu$ s). Detection efficiency of the emulated chirp is shown in Figure 30. The minimum ASNR for which complete detection is achieved is -7 dB.

## 8. Remote Receiver Station

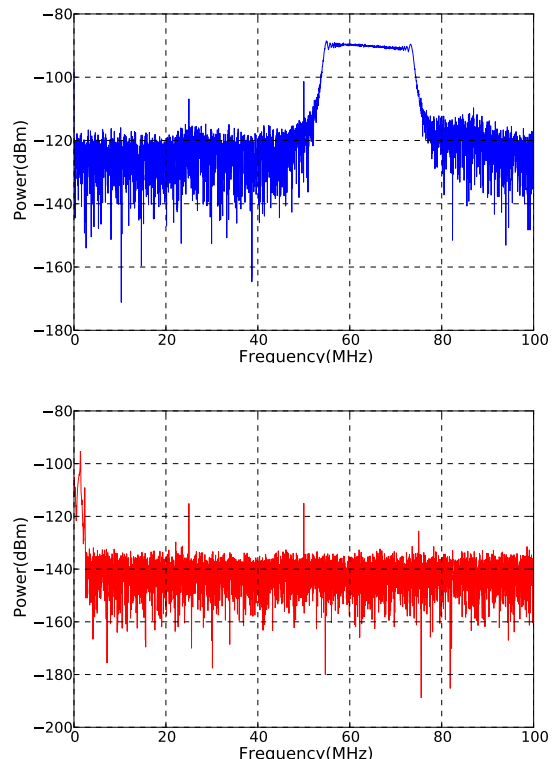


Figure 31: Top: the power spectrum of a -10 MHz/ $\mu$ s chirp created by a signal generator, prior to mixing. Bottom: the power spectrum of a 1 MHz monotone signal after signal mixing and passing through a low pass filter. The chirp is evident as the left-most peak in this distribution.

In addition to signal detection using matched filtering in the FlexRIO, an alternative technique has been developed that accomplishes chirp detection using a primarily analog signal chain. Remote stations, by definition, are generally subject to less radio interference, and add stereoscopic measurement capabilities which theoretically allow unique determination of CR geometry and core location. In contrast to the FlexRIO system, a mostly analog data acquisition system has lower power

consumption at a cost which is also comparatively inexpensive. Triggering logic for our remote receiver station and some specific details of hardware components are discussed in the next couple subsections.

### 8.1. Remote Triggering

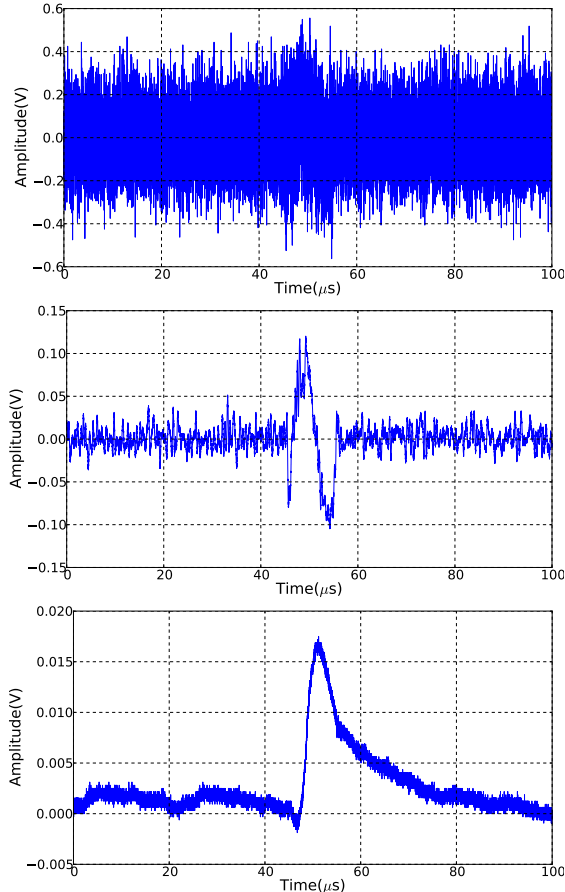


Figure 32: Top: A 0 dB SNR and  $1 \text{ MHz}/\mu\text{s}$  chirp embedded in noise prior to mixing. Second from top: The monotone signal after input chirp is mixed with delayed copy of itself and passed through a low-pass filter. Bottom: Monotone passed through the Agilent 8471D power detector.

The alternative approach is based on an analog frequency mixer. The input signal is mixed with a delayed copy of itself, i.e.,  $s(t) \otimes s(t - \tau)$ . For an incident chirp signal, the non-linear components in the mixer result in a product term that yields a monotone at a beat frequency  $f_{\text{beat}} = \kappa\tau$ ; dependent only on the delay time  $\tau$  and the chirp rate  $\kappa$ . The delay is created with 100 ft of LMR-600 cable, which produces negligible losses and removes the need for power consuming active components. With appropriate filtering, the

problem of chirp detection is ultimately reduced to that of detecting a down-converted monotone. This is illustrated in Figure 31. Portrayed here with an oscilloscope is a  $-10 \text{ MHz}/\mu\text{s}$  chirp which has been converted to a  $1 \text{ MHz}$  monotone by mixing with a delayed copy of itself.

After mixing, the signal is passed through an envelope detector (8471D; Agilent, Inc.). The entire time domain signal chain is illustrated in Figure 32. In this oscilloscope based example, a chirp with 0 dB SNR at a rate of  $-1 \text{ MHz}/\mu\text{s}$  is first band-pass filtered (41-100 MHz) and then amplified by 20 dB. The signal is then mixed and low-pass filtered (DC-1.9 MHz) and passed through the Agilent power detector.

The expected value of chirp rates from EAS echos is typically between  $-1$  to  $-10 \text{ MHz}/\mu\text{s}$  (see Section 2). Consequently, with 100 ns delay, the down-converted signal has a frequency between 100 kHz and 1 MHz. To trigger on such signals, the mixed signal is split into multiple copies. Each copy is then passed through custom band-pass filters and an envelope detector. Different frequency bands are then compared by majority logic in an FPGA, requiring no more than one band to form a trigger in order to suppress impulsive noise. Each of the frequency banded outputs corresponds to a separate range of chirp rates. The block diagram in Figure 33 outlines this triggering procedure.

### 8.2. Remote Station Electronics

The layout of the full remote station, currently in the field outside of Delta, UT, including the Chirp Acquisition Module (CAM), power systems, acquisition electronics, and communications blocks is shown in Figure 34.

The Chirp Acquisition Module has a modular design enabling quick debugging of the constituent components. This unit is comprised of a custom triggering board encompassing four band pass filters and envelope detectors, and a four channel ADC (AD80066; Analog Devices) with 16 bit resolution sampling at 4 MS/s per channel to sample the signal out of the envelope detectors. A high speed ADC (AD9634 evaluation board; Analog Devices) sampling at 200 MS/s directly samples the raw data from the Antenna and an FPGA (Spartan - 6 LX16; Xilinx) performs the majority comparison logic to trigger and capture triggered data before transferring to a single board computer. A Raspberry Pi (Rev. 2) single board computer stores triggered data in an SD card along with GPS time stamps (M12M; i-Lotus).

Another major component is the System Health Monitor [32] (SHM), which both monitors performance and

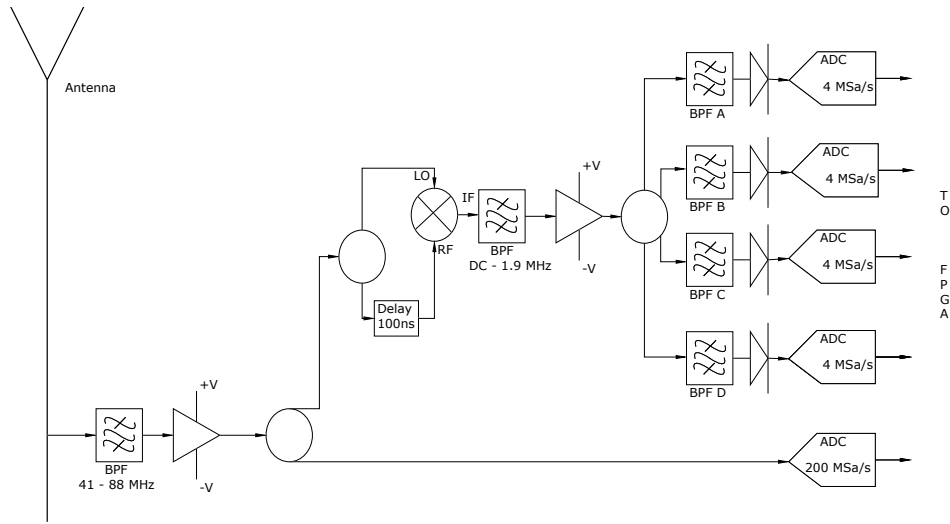


Figure 33: Block diagram of the event triggering to be employed in the remote station.

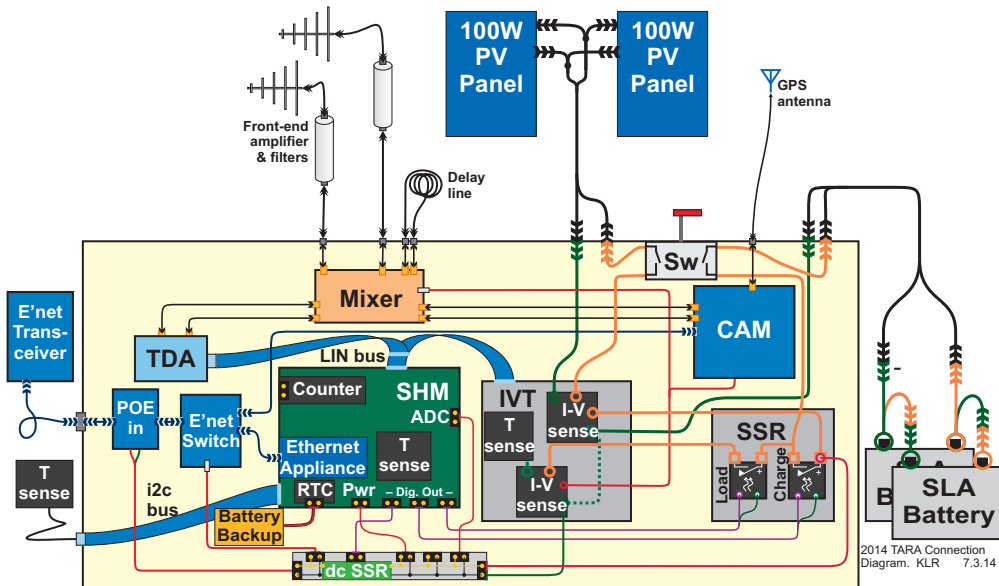


Figure 34: Schematic block diagram of the remote detector electronics. Chirp acquisition module (CAM), power systems, acquisition electronics, and communications blocks are all shown in this figure.

controls, via Solid State Relays (SSRs), the system solar (two 100 Watt photo-voltaic panels) and battery (sealed lead acid) power. The SHM also records antenna data digitized by the TDA receiver on local SD flash memory. The TDA (Transient Detector Apparatus) receiver has two channels with front-end amplifiers, followed by filters and a logarithmic amplifier. Finally, the SHM and

CAM are connected to a 5 GHz Ethernet transceiver via a switch for remote system control and data access.

### 8.3. Remote Station Prototype Studies

To understand the required power budget (Table 5) from the perspective of solar resources in Western Utah, a prototype with system requirements nearly identical

Component	Power Consumption(W)
Single Board Computer	5.0
Low Speed 4 Ch. ADC	0.5
High Speed 1 Ch. ADC	0.4
FPGA	3.0
RMS Counter	2.0
System Health Monitor	1.0
60 dB Amplifier (x2)	4.0
25 dB Amplifier (x2)	0.4
GPS	0.2
GPS and GPS Antenna	0.4
Communication Antenna	3.0
<b>Total</b>	<b>19.9</b>

Table 5: Estimated power budget for the remote station.

to those of the current, full scale remote detector station was deployed at the Telescope Array Fluorescence Detector site at Long Ridge, Utah in the spring of 2013.

The deployed hardware included a system health monitor (SHM) to monitor performance and power provision, four data acquisition channels, a 12 W dummy-load and Ethernet communications. The first prototype remote site was deployed several hundred meters from the LR site. Four detector channels include horizontal and vertical polarizations of the standard TARA receiver LPDA, a spiral (frequency-independent) antenna, and  $50\ \Omega$  terminator for comparison to system noise. Antennas feed four bulkhead connectors through LMR-400 coaxial cable, where the signals are amplified and fed into TDA detectors.

TDA detectors record a hit when voltage rises above a tunable threshold (set to 100 mV). Independent of the presence of “hits”, the trigger rate is reported in software over regular 10 s intervals. The software controlling the detectors and power management of the station is located in micro-controllers on the System Health Monitor (SHM).

The SHM also supports remote communications, however the prototype station was connected to the FD facilities through 200 m of CAT6 Ethernet cable, with power-over-Ethernet (PoE) offering ample capability to include system monitoring. Several environmental variables in addition to antenna TDA voltage rates are recorded: solar panel current, voltage, battery voltage, the status of the SSRs (the dummy load), temperature measurements, and support for an anemometer. The prototype remote station recorded solar panel power throughout the summer of 2013, quantifying the amount of solar energy available over time. Figure 35 displays the results. Each day, the station consumed ap-

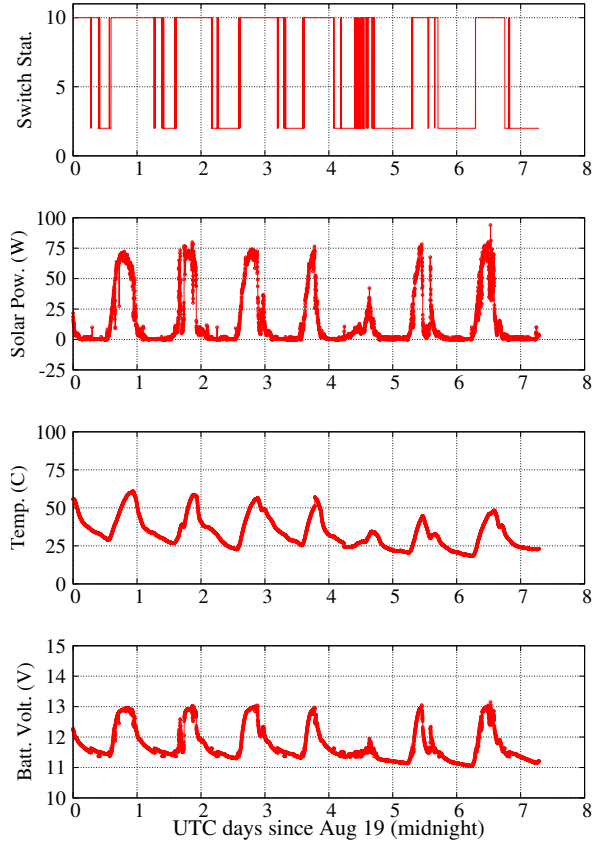


Figure 35: Remote station solar power data for August.

proximately 13 W, or  $\approx 26$  Ahr. Data were transmitted via Ethernet and stored locally.

The data show a clear diurnal variation. With the 100 W rated solar panel oriented toward the sun at 12 p.m. on June 1st, approximately 75 W peak power delivery was observed. Solar power curves (second from top in Figure 35) have a 3.6 hr full-width half-maximum, meaning the station collected 21.5 Ahr per day. After 40 days the station began to switch off the dummy load at night via the SSRs as the battery became depleted. The y-axis of the upper graph is a binary number representing the switch status; 10 (1010 in binary) indicates that both the solar power and dummy load are connected and 2 (0010 in binary) indicates that the dummy load switch has been disconnected by the SHM.

Two improvements to the remote station have been implemented as a result of these prototype data. First, solar photo-voltaic power has been doubled (relative to the prototype) to 200 W using two panels. The power

requirement is 20 W for the current remote station (see Table 5). After accounting for other prototype inefficiencies, two 100 W panels result in a positive power budget. Second, fine-tuning of SSR shutdown and start-up voltages has been implemented in the new remote station to protect the batteries.

The first autonomous remote station was deployed in June 2014, approximately 5 km NNE of the Long Ridge receiver station. This station and its performance will be described in greater detail in a forthcoming submission to this journal.

## 9. Conclusion

The TARA detector is designed to search for unique cosmic ray radar echoes with very small radar cross sections (RCS). Specifically, the following key characteristics strongly reduce the minimum detectable RCS: high transmitter power (40 kW, Section 3), high-gain transmitter antenna (22.6 dBi, 182 linear, Figure 11, Section 4.2), low noise Radio Frequency (RF) environment consistent with galactic backgrounds (Figure 20, Section 5), innovative triggering scheme that permits detection of signals 7 dB below the noise (Section 7.4.2), and broadband receiver antenna (12.6 dBi gain, 18.2 linear, Figure 16, Section 5).

Figure 36 shows a calculation of the minimum detectable TARA RCS for a cosmic ray Extensive Air Shower (EAS) located in several positions along a line perpendicular to the transmitter/receiver plane, midway between the transmitter and receiver. The bi-static radar equation (Equation 1, Section 2) permits this simple calculation that assumes a constant power radar echo self-triggered in the DAQ 5 MHz band (Section 7.3.2) with chirp rate in [-3,-1] MHz/ $\mu$ s (Section 7.3). Maximum transmitter/receiver gains are used for each point, given the azimuthal position of the shower core location. Further, the signal is assumed to have constant wavelength and is Doppler-shifted into the DAQ [60,65] MHz band, for which the -7 dB noise floor correction is appropriate, and scattered near the ground (to simplify distance calculation).

The TARA project represents the most ambitious effort to date to detect the radar signature of cosmic ray induced atmospheric ionization. These signals will be characterized by their low power, large Doppler shift (several tens of MHz), and short duration ( $\sim 10 \mu$ s). TARA combines a high-power transmitter with a state-of-the-art high sampling rate receiver in a low-noise environment in order to maximize the likelihood of cosmic ray echo detection. Importantly, TARA is co-located with the Telescope Array astroparticle observa-

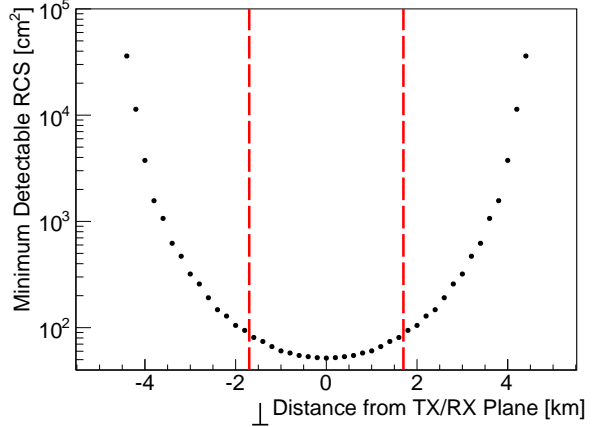


Figure 36: Minimum detectable radar cross section (RCS) as a function of distance perpendicular to the plane connecting the transmitter and receiver. The transmitter antenna main lobe points along this plane. For simplicity, the minimum RCS is calculated from the bi-static radar equation (Equation 1, Section 2) for a cosmic ray air shower midway between transmitter and receiver with maximum transmitter and receiver gains. The 5 MHz FlexRIO passband trigger scheme (Section 7.3.2) was assumed to detect a constant amplitude radar echo with chirp rate in [-3,-1] MHz/ $\mu$ s (Section 7.3) and signal-to-noise (SNR) ratio 7 dB (Section 7.4.2) below background noise (Figure 20, Section 5), the empirical detection performance for the 5 MHz DAQ passband. Further assumptions are ground-level detection and constant wavelength  $\lambda$ . Vertical dashed red lines show the -3 dB beamwidth of the transmitter antenna.

tory, which will allow for definitive confirmation that any echoes observed are the result of cosmic ray interactions in the atmosphere.

## 10. Acknowledgments

This work is supported by the U.S. National Science Foundation grants NSF/PHY-0969865 and NSF/MRI-1126353, by the Vice President for Research of the University of Utah, and by the W.M. Keck Foundation. L. B. acknowledges the support of NSF/REU-1263394. We would also like to acknowledge the generous donation of analog television transmitter equipment by Salt Lake City KUTV Channel 2 and ABC Channel 4, and the cooperation of Telescope Array collaboration.

We would like to specifically thank D. Barr and G. McDonough from Telescope Array for their services.

## References

- [1] P. Auger, et al., Extensive Cosmic-Ray Showers, Rev. Mod. Phys. 11 (1939) 288–291.
- [2] T. Abu-Zayyad, et al., The Surface Detector Array of the Telescope Array Experiment, Nucl. Instrum. Meth. A 689 (2012) 87 – 97.

- [3] I. Allekotte, et al., The Surface Detector System of the Pierre Auger Observatory, *Nucl. Instrum. Meth. A* 586 (2008) 409–420.
- [4] H. Tokuno, et al., New Air Fluorescence Detectors Employed in the Telescope Array Experiment, *Nucl. Instrum. Meth. A* 676 (2013) 54–65.
- [5] J. Abraham, et al., The Fluorescence Detector of the Pierre Auger Observatory, *Nucl. Instrum. Meth. A* 620 (2010) 227–251.
- [6] N.M. Budnev, et. al, The Tunka Experiment: Towards a 1-km-square EAS Cherenkov Light Array in the Tunka Valley, *Int. J. Mod. Phys. A* 20 (2005).
- [7] G. Askaryan, Excess Negative Charge of an Electron-Photon Shower And Its Coherent Radio Emission, *Sov. J. Exp. Theor. Phys.* 14 (1962).
- [8] F.D. Kahn and I. Lerche, Radiation from Cosmic Ray Air Showers, *P. Roy. Soc. Lond. A* 289 (1966).
- [9] P.M.S. Blackett, et al., Radio Echoes and Cosmic Ray Showers, *Proc. Roy. Soc. A* 177 (1941) 183–186.
- [10] D. Wahl, et al., The Search for Vertical Extended Air Shower Signals at the Jicamarca Radio Observatory, in: Proceedings of the 30th ICRC, volume 5, 2008, pp. 957–960.
- [11] T. Terasawa, et al., Search for Radio Echoes from EAS with the MU Radar, Shigaraki, Japan, in: Proceedings of the 31st ICRC, 2009.
- [12] M.F. Bugallo, et. al, MARIACHI: A Multidisciplinary Effort to Bring Science and Engineering to the Classroom, in: IEEE Internation Conference on Acoust., Speech, Signal Process., 2008, pp. 2661–2664.
- [13] M.F. Bugallo, et. al, Hands-on Engineering and Science: Discovering Cosmic Rays Using Radar-based Techniques and Mobile Technology, in: IEEE Internation Conference on Acoust., Speech, Signal Process., 2009, pp. 2321–2324.
- [14] D.G. Underwood, Large Doppler Shift in RADAR Detection of Ultra-high Energy Eosmic Rays, in: Radar Conference, RADAR '08. IEEE, 2008, pp. 1–5.
- [15] M.I. Bakunov, et al., Relativistic Effects in Radar Detection of Ionization Fronts Produced by Ultra-high Energy Cosmic Rays, *Astropart. Phys.* 33 (2010) 335–340.
- [16] N.J. Willis, Bistatic Radar, Scitech Publishing, Raleigh, NC, 1995.
- [17] P. Gorham, On the Possibility of Radar Echo Detection of Ultra-high Energy Cosmic Ray - and Neutrino - induced Extensive Air Showers, *Astropart. Phys.* 15 (2001).
- [18] R.J. Vidmar, On the Use of Atmospheric Pressure Plasmas as Electromagnetic Reflectors and Absorbers, *IEEE T. Plasma Sci.* 18 (2002).
- [19] Y. Itakawa, Effective Collision Frequency of Electrons In Atmospheric Gases, *Planet. Space Sci.* 19 (1971) 993.
- [20] Y. Itakawa, Effective Collision Frequency of Electrons In Gases, *Phys. Fluids* 16 (1973) 831.
- [21] J.W. Crispin and A.L. Maffett, Radar Cross-Section Estimation of Simple Shapes, *P. IEEE* 53 (1965) 833–848.
- [22] T.K. Gaisser and A.M. Hillas, in: Proceedings of the 15th ICRC, volume 8, 1977, p. 353.
- [23] H. Takai, et al., Forward Scattering Radar for Ultra High Energy Cosmic Rays, in: Proceedings of the 32nd International Cosmic Ray Conference, 2011.
- [24] A. Zech, A Measurement of the Ultra-High Energy Cosmic Ray Flux with the HIRES FADC Detector, Ph.D. thesis, Rutgers University, 2004.
- [25] G. Burke, et al., NEC - Numerical Electromagnetics Code for Antennas and Scattering, in: Antennas and Propagation Society International Symposium, volume 17, 1979.
- [26] R.U. Abbasi, et al., Indications of Proton-Dominated Cosmic-Ray Composition Above 1.6 EeV, *Phys. Rev. Lett.* 104 (2010).
- [27] J. Kraus, R. Marhefka, *Antennas For All Applications*, 3 ed., McGraw-Hill, New York, NY, 2003.
- [28] H.V. Cane, Spectra of the Non-thermal Radio Radiation from the Galactic Polar Regions, *Mon. Not. R. Astron. Soc.* 189 (1979).
- [29] G.A. Dulk, et al., Calibration of Low-frequency Radio Telescopes Using the Galactic Background Radiation, *Astron. Astrophys.* 365 (2001) 294–300.
- [30] M. Othman, et al., On Radar Detection of Chirp Signals with Nondeterministic Parameters in Challenging Noise Background, in: Radar Conference (RADAR), 2013 IEEE, 2013, pp. 1–6.
- [31] J.D. Smith, et al., GPSY2: A Programmable Hardware Module for Precise Absolute Time Event Generation and Measurement, in: Proceedings of the 30th ICRC, volume 5, 2008, pp. 997–1000.
- [32] D.Z. Besson, et al., Design, Modeling and Testing of the Askaryan Radio Array South Pole Autonomous Renewable Power Stations, *Nucl. Instrum. Meth. A* 763 (2014).

# Design and Performance of the ARIANNA Hexagonal Radio Array Systems

S. W. Barwick<sup>1</sup>, E. C. Berg<sup>1</sup>, D. Z. Besson<sup>2,3</sup>, E. Cheim<sup>4</sup>, T. Duffin<sup>1</sup>, J. C. Hanson<sup>1,2</sup>, S. R. Klein<sup>5</sup>, S. A. Kleinfelder<sup>4\*</sup>, T. Prakash<sup>4</sup>, M. Piasecki<sup>2</sup>, K. Ratzlaff<sup>6</sup>, C. Reed<sup>1</sup>, M. Roumi<sup>4</sup>, A. Samanta<sup>4</sup>, T. Stezelberger<sup>5</sup>, J. Tatar<sup>1,7</sup>, J. Walker<sup>1</sup>, R. Young<sup>6</sup>, and L. Zou<sup>4</sup>

<sup>1</sup>Dept. of Physics and Astronomy, University of California, Irvine, <sup>2</sup>Dept. of Physics and Astronomy, University of Kansas, <sup>3</sup>Moscow Physics and Engineering Institute, <sup>4</sup>Dept. of Electrical Engineering and Computer Science, University of California, Irvine, <sup>5</sup>Lawrence Berkeley National Laboratory, <sup>6</sup>Instrumentation Design Lab, University of Kansas, <sup>7</sup>Center for Experimental Nuclear Physics and Astrophysics, University of Washington

**Abstract**— We report on the development, installation and operation of the first three of seven stations deployed at the ARIANNA site’s pilot Hexagonal Radio Array in Antarctica. The primary goal of the ARIANNA project is to observe ultra-high energy ( $>100$  PeV) cosmogenic neutrino signatures using a large array of autonomous stations each dispersed 1 km apart on the surface of the Ross Ice Shelf. Sensing radio emissions of 100 MHz to 1 GHz, each station in the array contains RF antennas, amplifiers, 1.92 G-sample/s, 850 MHz bandwidth signal acquisition circuitry, pattern-matching trigger capabilities, an embedded CPU, 32 GB of solid-state data storage, and long-distance wireless and satellite communications. Power is provided by the sun and LiFePO<sub>4</sub> storage batteries, and the stations consume an average of 7W of power. Operation on solar power has resulted in  $\geq 58\%$  per calendar-year live-time. The station’s pattern-trigger capabilities reduce the trigger rates to a few milli-Hertz with 4-sigma thresholds while retaining good stability and high efficiency for neutrino signals. The timing resolution of the station has been found to be 0.049 ps, RMS, and the angular precision of event reconstructions of signals bounced off of the sea-ice interface of the Ross Ice Shelf ranged from 0.14 to 0.17°. A new fully-synchronous 2+ G-sample/s, 1.5 GHz bandwidth 4-channel signal acquisition chip with deeper memory and flexible  $>600$  MHz,  $<1$  mV RMS sensitivity triggering has been designed and incorporated into a single-board data acquisition and control system that uses an average of only 1.7W of power. Along with updated amplifiers, these new systems are expected to be deployed during the 2014-2015 Austral summer to complete the Hexagonal Radio Array.

## I. INTRODUCTION

THE ARIANNA project (Antarctic Ross Ice-shelf ANtenna Neutrino Array) is a surface array of radio receivers planned to span  $\sim 1,000$  km<sup>2</sup> of the Ross Ice Shelf in Antarctica, viewing  $\sim 0.5$  Teratons of ice [1-4]. The project will detect radio waves originating from high energy neutrino interactions with atoms in the ice via the Askaryan Effect [5].

\* Corresponding author: Stuart A. Kleinfelder, University of California, 4416 Engineering Hall, Irvine CA, 92697, U.S.A. Voice: 949-824-9430, Email: stuartk@uci.edu.

Neutrino interactions produce a shower of secondary particles, plus, for  $\nu_\mu$  charged current interactions, an energetic muon. The secondary particles produce an electromagnetic or hadronic shower which extends over a length of many meters increasing with energy, with a transverse dimension of a few centimeters. For wavelengths much larger than this transverse dimension, electromagnetic radiation is coherent, so depends on the net charge in the shower. Compton scattering of atomic electrons, and annihilation of shower positrons on atomic electrons both contribute to lead to a net negative charge in the shower, leading to an intense Cherenkov radiation pulse, with a peak electric field that scales linearly with the shower energy. The frequency range of the radiation depends on the angle of observation of the shower. In ice, near the Cherenkov angle of about 56 degrees, the coherent radiation extends up to a maximum frequency of about 1 GHz; away from the Cherenkov angle, the cutoff is lower in frequency. ARIANNA is designed to improve the sensitivity to neutrinos with energies in excess of  $10^{17}$  eV by at least an order of magnitude relative to existing limits [6, 7]. ARIANNA’s goals includes a confirmation and measurement of the Greisen-Zatsepin-Kuzmin neutrino flux [8, 9], which results from cosmic rays interacting with the diffuse cosmic microwave background, and to measure the neutrino-nucleon cross-section.

ARIANNA takes advantage of unique geophysical features of the Ross Ice Shelf [10, 11]. The water-ice interface of the ice shelf acts as a nearly-perfect mirror for radio pulses generated by extremely high-energy neutrinos traveling downward and interacting in the ice [12]. The ice’s long attenuation length allows for the detection of direct and reflected radio pulses at the surface. This and the ice shelf’s relative proximity to McMurdo Station ( $\sim 100$  km away) significantly simplifies the deployment of a large array. A ridge known as Minna Bluff separates the ARIANNA site from McMurdo Station, and by this and its uninhabited location, the site has been found to be essentially free of anthropogenic noise. Being a surface array, ARIANNA stations are easy to deploy, maintain and upgrade.

Each ARIANNA station contains RF antennas, amplifiers, triggering, digitization, computing, power management, data storage, long-distance wireless networking and satellite communications, solar power and battery backup, plus experimental wind power. Four stations have been installed, including an early prototype deployed in 2011 [4] and the three HRA stations deployed in December of 2012, which are the subject of this paper. A block diagram of an HRA station configuration is shown in Fig. 1.

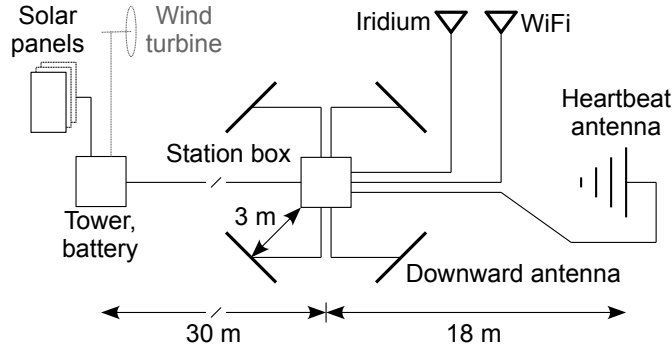


Fig. 1: Schematic station overview showing basic elements and distances (not to scale) of an ARIANNA Hexagonal Radio Array station.

ARIANNA is a surface array, with most components buried less than a meter beneath the snow surface. This design has many practical advantages when compared with deep-ice experiments [13-17], the most obvious of which is that no drilling is necessary to deploy the stations, saving an enormous amount of fuel, environmental impact, expense, effort and time. Surface deployment imposes fewer geometric constraints on receiver antennas and electronic systems than deep-ice designs. Cabling between antennas and electronics, etc., are minimal and at the surface. Deployed equipment is fully retrievable, and servicing or upgrades are eminently possible while keeping most of the installed infrastructure intact.

Sections II-VI of this paper focuses on the design of the major subsystems of the stations deployed in 2012 as part of a pilot phase of the ARIANNA project, known as the Hexagonal Radio Array. Section VII describes the system software for station monitoring and remote control. It also outlines the data collection, transmission and archiving procedures. Section VIII provides a discussion on the operational performance of the power systems, monitoring systems, trigger rates and environmental influences, and evaluation of the data quality. Section IX concludes with a discussion of improved data acquisition electronics intended for the completion of the HRA during the 2014-2015 Austral summer.

## II. THE ARIANNA HEXAGONAL RADIO

In 2010, the National Science Foundation approved a pilot program of the ARIANNA project, called the Hexagonal Radio Array (HRA), consisting of 7 stations dispersed on the ice in a hexagonal grid with 1 km between neighboring stations. The HRA's focus is to develop the technologies needed for a network of autonomous stations that achieve the

performance necessary for the physics aims of the full-scale ARIANNA project. Stations must provide their own power, and must allow unattended remote monitoring, data retrieval and control. Operation at temperatures down to -30C or lower, and survival during harsh Antarctic conditions is a necessity. The electronics must be highly-sensitive over a 100-1,000 MHz frequency range and perform without themselves creating any radio frequency noise in this spectrum. Stations must be cost-effective and quick to deploy. Adapting to these requirements, and growing experience with instrument deployment in Antarctica's harsh conditions, has resulted in a rapid evolution of increasingly more robust, higher-performance, lower-powered and lower cost HRA hardware.

### A. HRA Timeline and Configuration

An early prototype station including a new 1.92 G-samples/s waveform acquisition and advanced real-time triggering system ("ATWD") was deployed in December of 2011 at Site D in Fig. 2 [4]. In December of 2012, ARIANNA deployed the first three HRA stations at sites A, C and G in Fig. 2, and converted the old Site D station to a weather monitoring post and WiFi repeater. This second-generation ARIANNA design replaced the prototype's hand-assembled electronics with a unified, mass-produced printed-circuit electronics system, replaced separate hand-constructed solar panel and wind turbine support structures with an integrated commercial tower system, and made many other refinements resulting in a much lower power (7 W average), much lower cost, lighter weight, lower noise, better calibrated and much faster and easier to deploy system. The station's reconstructed angular precision was found to be 0.17 degrees (see Section VIII-G)

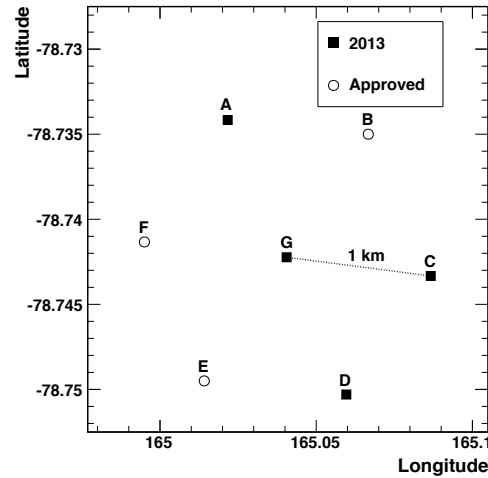


Fig. 2: Position and designation of the existing and approved HRA sites.

A curtailment of Antarctic operations during the 2013-2014 Austral summer permitted only a brief service mission. During this, the surface-array benefits of ARIANNA allowed a number of HRA system changes to be made, leading to performance that reached the levels needed for ARIANNA's physics goals. On-site radio reflection studies confirmed that the ARIANNA stations can achieve timing resolution of ~49 ps (see Section VIII-F).

The NSF has approved deployment of the HRA's remaining four stations during the 2014-2015 Austral summer. Plans include simplifications of the power tower, including the integration of the communications antennas. Improved amplifiers with flatter frequency response, improved stability and with integrated band-pass filtering and limiting have been fabricated. A simpler, lower-cost, lower-power, single board data acquisition system incorporating a new multi-channel signal acquisition chip, including deeper waveform storage and simplified trigger formation, will also be deployed.

### B. HRA System Overview

Each ARIANNA HRA station deployed thus far is divided into two major components: a power tower and an instrumentation and communications box with associated antennas. A power tower is seen in Fig. 3 (left), and a communication mast is seen (right) with an omni-directional antenna for mesh-connected wireless communications with McMurdo Station via a repeater on Mt. Discovery, plus an antenna for Iridium satellite short-burst messaging.

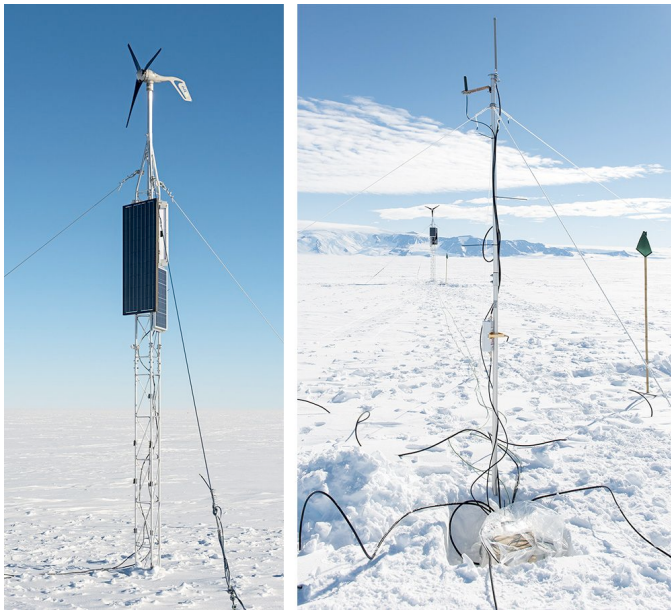


Fig. 3: An HRA system on the Ross Ice Shelf during deployment in 2012, showing a power tower (left), a communication's mast (right) with the tower in the background, a station box inside clear plastic at the foot of the mast (later buried), and a flag marking the location of one of four buried downward-pointing instrumentation antennas.

Section VII describes the power-tower, which includes 160W of solar panels, experimental inclusion of a 150W wind turbine, and an insulated battery box buried at the foot of the tower. For the 2012 deployment, the power and electronics assemblies were separated by about 30m due to concerns over potential RF noise emanating from the wind turbine. Hence, a separate communications mast was deployed along with the instrumentation box. The wind turbines were removed from the HRA systems during the 2013-2014 service mission due to reliability issues and to remove them from consideration as a source of anthropogenic noise. For the completion of the Hexagonal Array, no wind turbines will be deployed, and

unified power, instrumentation and communications systems is planned (see Section IX).

A station and amplification box assembly (see Sections III and IV) is seen at the foot of the communications mast (Fig. 3, right), wrapped in plastic to prevent ice built-up on its connectors, etc., and was later buried. Four signal acquisition antennas are disbursed surrounding the communications mast, with the position of one seen marked by the green flag on the right-hand side of the photo.

## III. ANTENNAS AND AMPLIFICATION

### A. Antennas.

Each station includes four log-periodic dipole antennas (Creative Design Co. model CLP5130-2N), positioned as two orthogonal pairs of parallel antennas 6 meters apart, pointing straight down into the ice. These 50 Ohm antennas have 17 elements and are about 1.4m long, with the span of its largest tines being 1.45m. The frequency response is quoted by the manufacturer as ranging from 105-1,300 MHz with a VSWR of 2.0:1 or less across the band (in air; in snow, their lower frequency limit is expected to be 70-80 MHz, e.g. in [1]). The forward gain is quoted as 11-13 dBi, with a front-to-back ratio of 15 dB. An example plot of the antenna's measured effective height (ratio of the induced voltage to the incident field) in the E-plane and H-plane in a common 40° off-axis angle is shown in Fig. 4 [18]. The antennas are connected via 5 meter LMR-400 cable (N-type connectors on both ends) to an RF-tight box containing four radio-frequency amplifiers (Fig. 5). Band-pass filtering leaves a frequency range of 100-1,000 MHz intact.

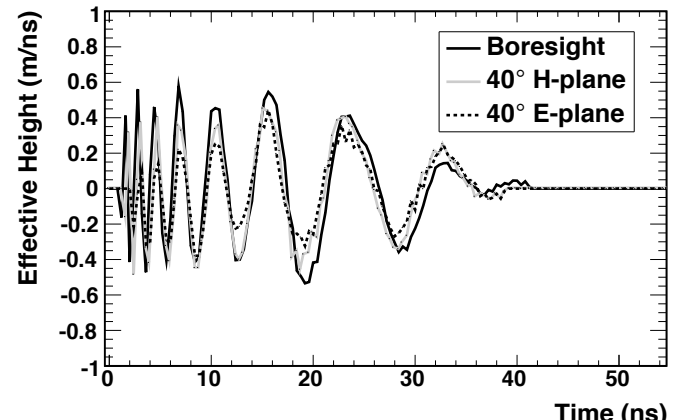


Fig. 4: Example antenna effective height vs. off-axis angle for the E and H-planes at 0° ("boresight") and 40° off-axis.

### B. Amplification.

Each amplifier consists of four AC-coupled 1.5 GHz GaAs gain stages (Avago MGA-68563) with inter-stage filtering, yielding about 50-70 dB of gain over the frequency range of interest (Fig. 6). Power is conditioned in the main data acquisition enclosure and is supplied via coaxial cable to the amplifier box. Each amplifier consumes about 250 mW of power at 3.3V. Amplifiers are housed in individual brass enclosures that help prevent cross-talk between stages and between amplifiers. The amplifier's output range must be

matched to the signal sampling and digitization electronics, and hence attenuation and limiting components were added to the amplifier's outputs. The limiting components cause compression of large signals, e.g., those above about half of the full 1.5V output range, as seen in Fig. 7.



Fig. 5. The 2012 ARIANNA station's amplifier box (inputs to the left, outputs and power to the right). It contains four amplifiers, each with four AC-coupled 1.5 GHz GaAs amplifier stages with inter-stage bandwidth shaping. The box includes two RF filters per channel to constrain the frequency range to that of interest (~100-1,000 MHz), and output limiting and attenuation to optimize matching with the station's electronics.

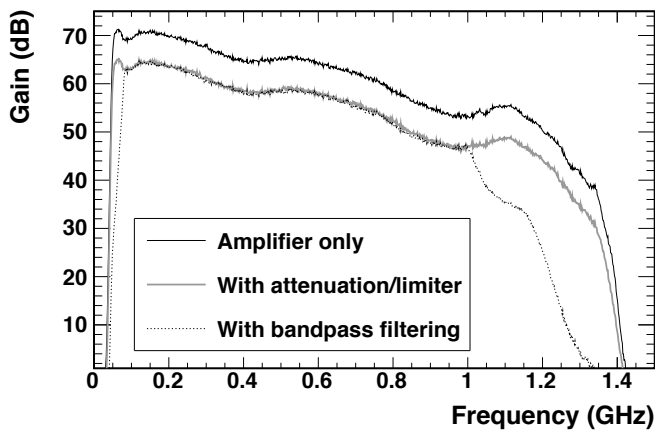


Fig. 6: ARIANNA amplifier gain vs. frequency plot. From top to bottom, the curves show the amplifier alone, the amplifier plus output attenuation and limiting, and the former with input band-pass filtering.

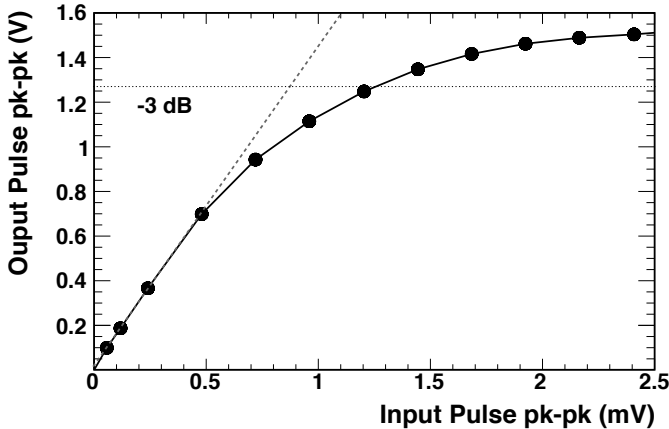


Fig. 7: Amplification system response to an impulsive input signal of varying magnitude, including input band-pass filtering and output limiting and attenuation. Note that the vertical scale is three orders of magnitude greater than the horizontal scale (V vs. mV).

### C. Heartbeat generation.

In order to monitor the health and stability of the ARIANNA stations, each station includes an auxiliary antenna that can transmit a radio-frequency signal to the other, instrumented, antennas. This “heartbeat” signal is typically triggered by the system software with some periodicity such as 1 Hz or less. The heartbeat pulse is produced by an FPGA on the system's motherboard, and its width is set in firmware to be about 1.5 ns full-width at half-maximum. The resulting signal is sent via LMR 600 cable to the same model log-periodic dipole array antenna as the receiving antennas. The heartbeat antenna is laid ~18 meters away from the center of the station with its E-plane parallel to the ground (i.e., flat on the surface), pointing back at the center of the station's antenna array, and aimed approximately along the diagonal between the four instrumentation antennas (i.e., each instrumentation antenna, pointing down, presents its face at a ~45 degree angle to the heartbeat antenna, as seen in Fig. 1). Monitoring the heartbeat pulse is a simple way to verify the functionality of virtually the entire signal acquisition, processing and transmission chain, and is also of potential use to watch for changes due to temperature, etc.

## IV. DATA ACQUISITION SYSTEM

A new HRA data acquisition system has been prepared and deployed. The main advances of this system are reduced power consumption, greatly improved manufacturability, lower cost, lower noise, improved physical integrity, lighter weight and more compact dimensions. The over-all power consumption has been reduced from ~30 W to ~7W during typical data taking, with as little as 0.6W possible in a minimum-power maintenance mode. This power reduction maximizes the control, communication and acquisition time on solar power and batteries during days of waxing and waning sun and/or heavy overcast.

The amplifier and system boxes, as seen in Fig. 8, can be bolted together or kept separate. The amplifier box has four antenna inputs, four amplified outputs, and a 3.3V power input. The main system box has four amplified signal inputs, 3.3V power output for the amplifier box, a main power input, a “heartbeat” pulse output, an external trigger input that is useful during tests, and output ports for Iridium and WiFi communications. The completed station boxes are roughly one cubic foot in size and set up very rapidly in the field.

Figure 9 shows the 2012 station electronics, consisting of four daughter-cards (one per-channel) and a motherboard, comprising the entire station except for the RF amplifiers and the two communications modules. A block diagram of the system is shown in Fig. 10.

Each daughter-card contains a 1.92 G-samples/s synchronous switched capacitor array analog sampling and digitization chip (the “ATWD”), a bias-tee module that adapts the DC offset of the incoming signal level to maximize the dynamic range of the ATWD, mode switches, power conditioning, DACs for threshold range settings, and a field-programmable gate array (FPGA) that aids in operating the

ATWD and allows cards to operate as stand-alone devices if desired. Although the ATWD chips themselves include 128 10-bit analog to digital converters for fast parallel data conversion, a higher-resolution 12-bit ADC is included on each daughter-card for signal digitization.



Fig. 8. An example of an HRA station’s amplifier box (top portion) and main system box (bottom) containing all data acquisition, control and communications electronics. For scale, the width of the front of the box as shown is 9 inches, the depth is 12 inches, and the total height is 11.5 inches.



Fig. 9. The ARIANNA Hexagonal Array data acquisition electronics. It includes four 1.96 GHz data acquisition channels, a 100 MHz 32-bit CPU, communications channels for wireless and satellite short-burst message system, a 32 GB flash memory card holder for event data storage, power conditioning and control for all primary components, trigger I/O, “heartbeat” pulse generator, etc.

The system’s motherboard contains all computing, communications interface hardware, data storage and power management circuitry necessary to run the station. It includes two-stage power regulation for the antenna amplifiers, a power I/O terminal block, solid state relays for peripheral power control, voltage and power monitoring circuitry, daughter-card power regulation and control, power regulation for the

embedded CPU, a holder for a 1.5 Ah lithium battery backup for the real-time clock, a 100 MHz 32-bit ARM Cortex M3 micro-controller, an external trigger input, an FPGA programming port, an Ethernet port used for WiFi communications, an RS-232 port used for Iridium satellite messaging, a 32 G-Byte SDHC flash memory card slot, four daughter-card slots, an FPGA for fast system functions, and an output for the production of a fast “heartbeat” pulse.

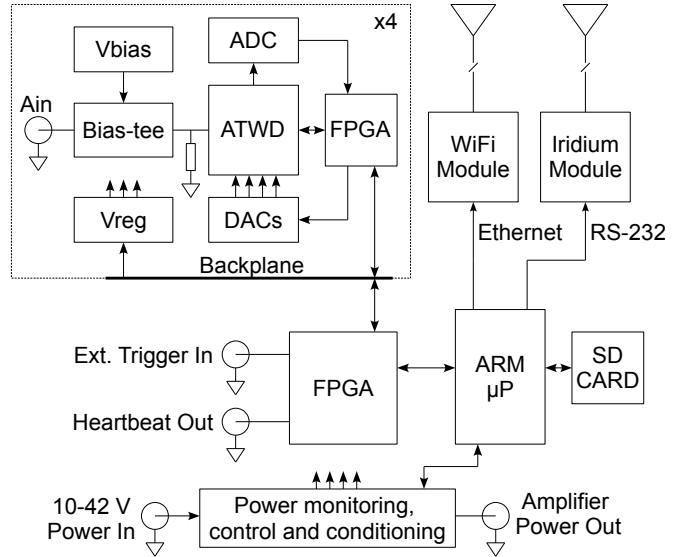


Fig. 10: Simplified block diagram of the ARIANNA system hardware.

## V. WAVEFORM ACQUISITION, TRIGGERING AND DIGITIZATION

Triggering and waveform capture is performed by a custom CMOS IC (“Advanced Transient Waveform Digitizer” or ATWD [19-22]) running at 1.92 G-samples/s and with ~11.5 bits of dynamic range [23, 24]. A block diagram of the chip’s internals is shown in Fig. 11. The chip incorporates real-time pattern-matching trigger functionality that allows, for example, the detection of a bipolar waveform of a certain magnitude and frequency range. A prompt trigger is produced within about 15 ns of the targeted waveform’s arrival.

### A. Sample rate and analog bandwidth.

The ATWD uses a synchronous sample clocking scheme that leads to high sample-to-sample timing uniformity. For convenience, it is driven by a low-speed external clock, which is boosted by a factor of 32 by an on-chip phase-locked loop system and then doubled via interleaving (using both clock phases) by an additional factor of two. The ARIANNA systems thus operates with a 30 MHz reference clock and achieves a net 1.92 GHz sample rate. By observing a test clock output from the ATWD chips with a histogramming period/frequency counter, the timing uniformity of this system has been measured to be ~1 ppm, RMS.

The analog bandwidth of the ATWD sampling and digitization system is an important figure of merit. With a 1.92 GHz nominal sample rate, the Nyquist-limited bandwidth would be 960 MHz, and ARIANNA’s amplifiers are low-pass limited to approximately this frequency as well. Figure 12

shows a plot of the frequency response of the data acquisition system as seen in Fig. 9 (excluding amplification). This plot was obtained by applying sine waves of a fixed amplitude of 500 mV but varying frequency (50 to 1,000 MHz in steps of 50 MHz). At each frequency, 1,000 waveforms were collected by the system and histogrammed. Two peaks are expected to appear in these histograms, corresponding to the high and low peaks of the sine waves as captured and digitized. The span of the peaks can thus be compared to the input sine wave, and as expected the magnitude of the output starts to drop as the bandwidth limitations of the system are reached. The frequency response of the entire system (excluding RF amplification) is seen to be relatively flat out to about 650 MHz, and its -3 dB frequency is about 860 MHz, near to the system's Nyquist limit of 960 MHz (1.92 GHz/2).

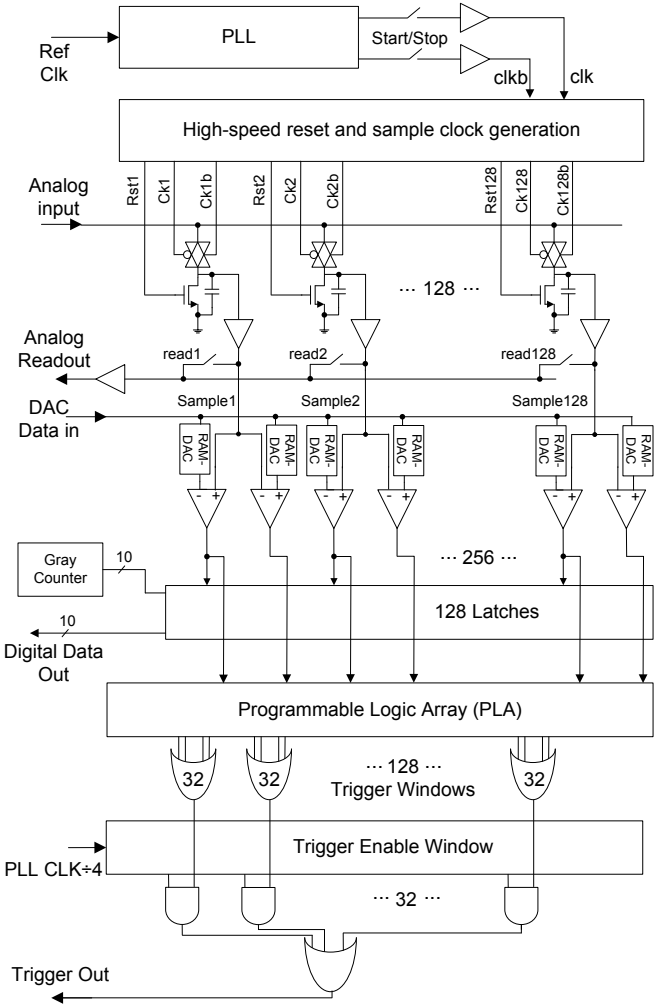


Fig. 11. A block diagram of the 2 GHz synchronous ATWD integrated circuit, showing sampling, comparison, and programmable trigger logic.

#### A. Trigger thresholds and calibration.

The ATWD chips perform dual (high and low) threshold triggering in real-time using a unique pattern-searching capability that observes the sampled signals rather than the input signal directly. This post-sample comparison does away with the need to split the input signal to a separate trigger

circuit. It also allows the comparators to be lower in power and slower, yet still, in effect, reach the full bandwidth of the ATWD's sampling system (i.e., ~860 MHz).

The basic high and low thresholds are set analogically via external DACs. However, as is the nature of all such electronic circuits, each comparator has a certain random input offset, and hence the ATWD chips include internal digital to analog conversion on a per-comparator basis to null these offsets for higher uniformity in triggering performance. To first order, the offsets are a form of “fixed pattern noise” and hence calibrations generally need to be done only once.

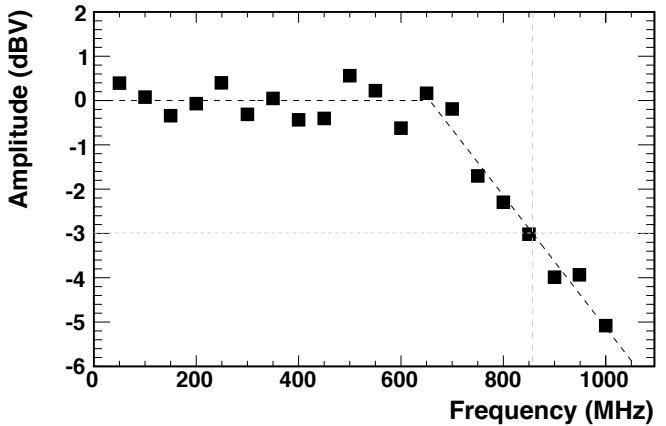


Fig. 12: Data acquisition system bandwidth measurements from digitized data, with the slope representing a fit to the higher-frequency data. The bandwidth is flat to ~650 MHz, and the -3dB bandwidth is ~850 MHz.

Figure 13 shows an example distribution of the offsets from one set of 128 comparator trigger thresholds (all “high” thresholds of a chip) before and after calibration. The “pulse height” axis represents the magnitude of a unipolar pulse at the channel's AC-coupled analog input that is narrow enough for its peak to be fully contained in one sample (the specific height is somewhat arbitrary, it's the trigger's response to varying heights as the pulse crosses a desired threshold that is of interest). These pulses, produced at 1 kHz, arrive asynchronously with respect to the ATWD's 1.92 GHz sample clock, and hence can arrive at any comparator's sample and hold. With ideal (zero) offsets, the transfer function between pulse height and trigger rate would be a step function from 0 Hz to 1 kHz at a single pulse height. However, in a realistic circuit, differing comparator input offsets lead to curves as seen in the figure. Nulling of these input offsets in this example is found to reduce variation in trigger thresholds from a sigma of 13.5 mV to a sigma of 3.6 mV. The latter number includes the noise of the signal generator itself, and yet is still less than a fifth of the sigma of the amplified thermal output noise from the amplifiers (~22 mV). Since such fixed pattern noise sources are independent and add only in quadrature to thermal noise, variations in trigger thresholds after calibration (in this case) results in only a ~2% net increase in noise in the trigger. The trigger offset nulling DAC values are stored on each daughter-card's FPGA's non-volatile memory, and are loaded into the ATWDs upon a command to cycle the data acquisition power.

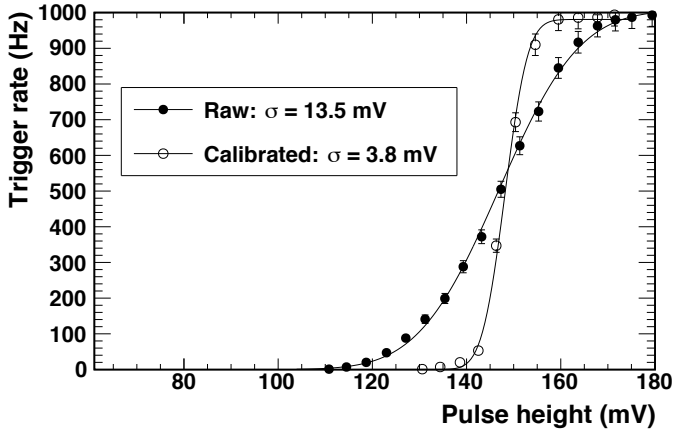


Fig. 13: Example trigger calibration for a single threshold showing trigger rate as a function of pulse height. The curve after calibration shows the variation in thresholds dropping by a factor of 3.6 to a sigma of 3.8 mV.

### B. Trigger rate control.

The ATWD has pattern-matching trigger capabilities that aids in trigger rate control [25]. Up to 72 patterns can be loaded into each chip. Each pattern may be a combination of input signal conditions, namely  $H$  – the signal must be above a high threshold,  $L$  – the signal must be below a separate low threshold,  $N$  – neither above nor below (i.e., between the two threshold levels), or  $X$  – don't care (does not veto triggers regardless of the signal level). Each pattern consists of 8 such conditions, representing 8 consecutive samples. A trigger pattern of  $HXXXLXXX$ , for example, looks for a bipolar signal in which a pair of high and low comparator values are about 2 ns apart (at 1.92 GHz, each sample is 0.52 ns apart).

ARIANNA further employs a second-level trigger that can require a coincidence between a combination of individual channel's triggers, with a programmable level of majority imposed (i.e., 1 or any 2, 3 or all 4 channels coincident within a certain time period). The combination of bipolar trigger patterns, programmable trigger thresholds, and second-level trigger majority logic can flexibly control trigger rates over many orders of magnitude. Furthermore, an advantage of a bipolar trigger over a simple unipolar threshold is that the former tends to stabilize trigger rates even when drifts, e.g., of the signal baseline, are occurring.

Figure 14 shows laboratory tests of the trigger rate vs. threshold while comparing two different patterns, plus *in-situ* measurements from the prototype HRA data. The threshold is expressed in terms of the amplifier noise sigma. The lines represent theoretical estimates of the expected rates. The “Single High Only” points denote trigger rates when a pattern of  $HXXXXXXX$  is used. This pattern will trigger on any over-threshold sample and is one of the most liberal patterns that can be used. The “H+L” patterns trigger on any signal that passes both the high and a low thresholds over a span of time ranging (technically) from 1.56-3.65 ns, i.e., the same range depicted in Fig. 13. This set of patterns is considerably more restrictive than the single threshold case yet more realistic for neutrino signatures. The resulting trigger rate drops by over 5 orders of magnitude for the same threshold values.

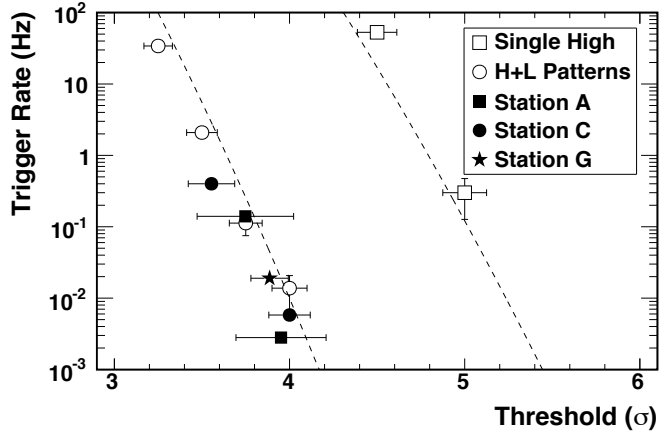


Fig. 14: Laboratory and *in-situ* measurements of trigger thresholds vs. trigger rates. The “Single High” laboratory measurements represent trigger rates for any crossing above a high threshold. The “H+L Patterns” represent laboratory measurements for a H and L trigger combination coincident within 4 ns. The “Station A, C and G” data points were from measurements made from three different stations, remotely collected during 2014 using the same “H+L Patterns” trigger criteria.

The *in-situ* measurements are from field data collected after two calibrations made during remote operation in early 2014. These calibrations and measurements were made with the same 5-pattern trigger criteria used in the “H+L” laboratory measurements. Note that all of the data shown in Fig. 17 are also using a “majority-2” criteria, namely that at least 2 channels must pass the individual channel's trigger criteria within a set period of time (in this case, ~64 ns).

The stability of the trigger under changing environmental conditions is also important. The ability to trigger on coincidences of High and Low thresholds has demonstrated significant gains in trigger stability across a wide range of temperatures. For example, a baseline drift due to a temperature change (e.g., due to the temperature coefficient of a voltage regulator) may cause the High threshold to increase in trigger frequency, while the Low threshold would decrease, counteracting each other and substantially moderating any net change in trigger rates.

Figure 15 shows trigger rates in a laboratory test of temperature stability. Two sets of data are shown, one with a High threshold only, and one with an equivalent High and Low coincidence required (over the space of 4 ns). For a single threshold (i.e., High only), a change such as a baseline drift of just a few mV will cause a significant change in trigger rates, and indeed the figure shows about two orders of magnitude change over approximately 15 degrees C, with at least another two orders of magnitude projected down to -30C (measurements were rate-limited to ~10 Hz, higher than expected *in-situ* rates). By contrast, using an equivalent High and Low coincidence results in about one order of magnitude change in trigger rates over the entire expected temperature range once buried in the snow of 0 to -30 C.

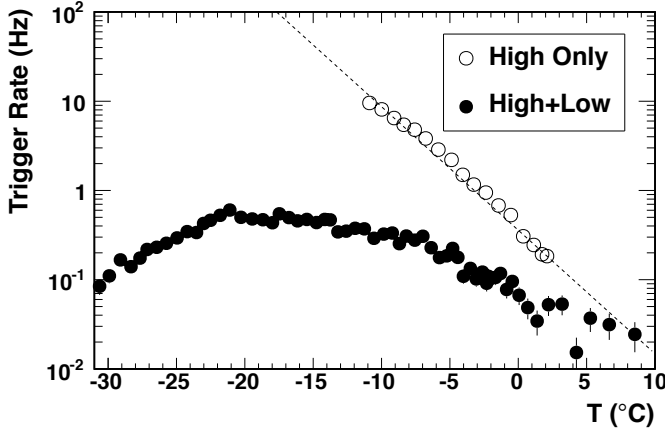


Fig. 15: Thermal trigger rates vs. temperature for a single high threshold trigger (open circles), and for a trigger that requires passing a high and a low threshold within 4 ns (filled circles).

A simple automatic threshold monitoring and adjustment system will eventually be put in place in ARIANNA’s system software. However, ARIANNA’s experience is that remotely-performed threshold changes need only be made a few times a year to remain within the system’s range of operation and memory capacity. ARIANNA’s end goal may be to maintain rates such that all data can be retrieved by Iridium, e.g., rates in the mHz regime, in order to reduce or eliminate any dependence on the high-speed WiFi link, and indeed  $\sim 2$  mHz rates have been demonstrated in practice.

## VI. POWER SYSTEMS

Given the ARIANNA site’s isolation, and the 1 km distance between stations, each station is fully autonomous, including by producing their own power. For the 2012 deployment, the power system for each station consisted of three solar panels, experimental use of a wind-turbine, and lithium-iron-phosphate storage batteries.

### A. Power tower and solar panels.

Each station deployed in 2012 and prior years have been equipped with solar panels, an experimental wind turbine, and a battery for power buffering. The HRA stations deployed in 2012 used standard commercially-available radio tower components that were taller and quicker to assemble than the prior custom-made solution, and which integrated both solar and wind power. Each tower was 16 feet in height excluding the wind-turbine extension, and were tied-down by three steel cables connected to wooden anchors buried in the snow. Constructed almost completely of aluminum, the tower assemblies including solar and wind power systems were light enough to be raised manually by one individual.

Solar panels perform well in the Antarctic environment due to the high reflectivity of the snow. For the 2012 deployment, the ARIANNA power towers employed three solar panels in a triangular configuration. A primary 100W panel was oriented north, and provided more than sufficient power to run the station and maintain a peak battery charging state for nearly as long as the sun remains up. Two secondary 30W panels were mounted on the other two faces of the triangular tower for

supplementary power when the sun is behind the main panel. During the summer, the solar panels provide enough power that the stations run continuously and exclusively on solar power nearly 100% of the time, even during periods of extensive cloud cover.

### B. Batteries at cold temperatures.

ARIANNA stations include batteries to store power for use during overcast days and weeks while the sun is rising and setting. LiFePO<sub>4</sub> batteries were selected based on this technology’s high physical and chemical stability and safety, and after ARIANNA’s experimental evidence of performance at cold temperatures. Each of the 3 HRA stations deployed thus far incorporated 2 LiFePO<sub>4</sub> batteries of 112 Ah nominal capacity when rated at room temperature (224 Ah total). These were configured in an automobile starting-battery form-factor (Braille Battery Co. model OSGC-12112iB). The batteries include integrated charge controllers which disconnect the batteries when fully charged (e.g., during summer when solar power is plentiful) and when the batteries are nearly depleted, to prevent damage from over-charging and over-discharging. Disconnects upon reaching full charge occurred transparently and did not cause any disruption of the station electronics. Disconnects when fully discharged, e.g. after the final setting of the sun for the year, caused the station to power down in an orderly fashion. Autonomous power-up has also been orderly.

ARIANNA conducted laboratory tests at -30°C (previously measured to be the lowest expected winter temperature when buried in the snow) and demonstrated that the selected batteries retained about 70% of their nominal storage capacity when charged and discharged at these temperatures. At -30°C, they were capable of accepting a charging current of at least 7A (ARIANNA’s expected maximum), and easily provided the expected maximum discharge current consumed by the station electronics of 1A. Figure 16 displays an example charging and discharging profile of a single 112 Ah (nominal) battery at -30°C. Starting from empty and at -30°C, it required ~89 Ah of charge to reach a full state, at which point the charge controller disconnected the battery. From this state, discharged at 1 A, the battery delivered ~79 Ah of charge until it disconnected. Minor discontinuities in terminal voltages were seen at some points during transitions between a normal and cautionary state indicated by an LED on the battery housing that is driven by the battery’s internal charge controller, presumably due to internal switching or rebalancing of cells.

Using ARIANNA’s expected “worst case” usage profile, these results indicate a useful storage capacity of ~70% of one battery’s nominal rating at -30°C, and an efficiency of ~89%. With two batteries in parallel (as in the stations deployed in 2012), being charged and discharged at half of these rates per battery, slightly better performance may be expected. The net power available from two batteries stored, charged and discharged at -30°C is thus at least 158 Ah, or enough to run the station by itself at full power for at least one week, and in low-power modes (e.g., with reduced data acquisition and communications duty cycles) for up to one month.

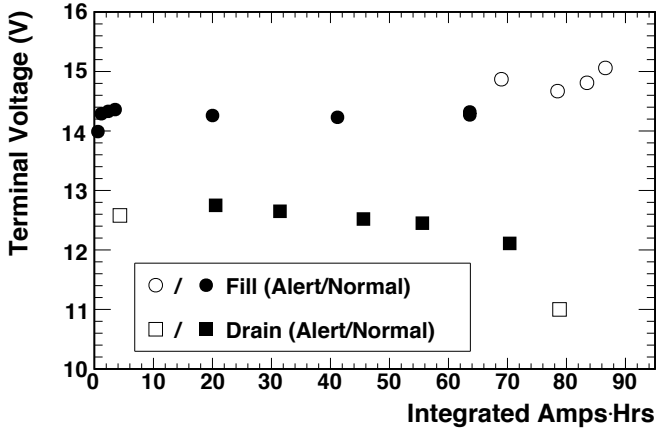


Fig. 16: Terminal voltage of a single battery charging at 7A and discharging at 1A, both at -30C. The “alert” vs. “normal” measurements denote when an LED on the battery housing indicated a nearly full or nearly empty status.

The batteries for the ARIANNA stations as deployed were contained in insulated enclosures so that any self-heating from charging and discharging them (i.e., from inefficiency losses) may warm the batteries, and to help stabilize any diurnal temperature changes. All connections between the power tower, the battery box and the station box were via bayonet connectors and hence were very fast and easy to complete while wearing gloves in the field.

#### C. Wind power.

Even at ~7W average power consumption, it has not been considered practical to power the stations by battery alone during the winter. Therefore, ARIANNA has experimented with a number of wind turbines. For the 2012 Austral summer deployment, each of the four stations (the three HRA stations plus the earlier prototype) were equipped with 150 watt maximum wind turbines (Primus Wind Power Air 40). As a precaution, the turbines were disassembled and their bearings re-packed with aircraft-grade grease rated to -70C. The Air-40 model uses glass-reinforced nylon blades which, in all stations, survived a year of operation without any issues. Unfortunately, the vertical rotation collar failed on one turbine, leaving it unbalanced and unable to transmit power. A second turbine failed when an internal mechanical part seized. Evidence points to both of these failures occurring during a single powerful storm. The third and fourth wind turbines remained functional.

During the 2013 servicing mission, the wind turbines were removed from all three HRA stations, which have hence-forth operated on solar power and batteries only. The Site D prototype station maintained its turbine for continued experimental use, and was reconfigured as an environmental monitoring station including air speed and temperature measurements. Figure 17 shows this station’s data, supplemented with wind speed measurements made at Scott Base later in the season. Wind speeds at the ARIANNA site have been found to be sufficient for significant up-time during winter months, motivating continued interest in experimenting with wind power generation.

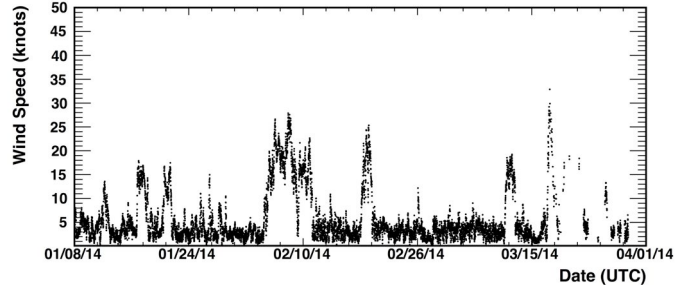


Fig. 17: Wind speed plot from Station 2’s anemometer, supplemented at later dates with data from measurements made at Scott Base.

## VII. MONITORING, CONTROL AND DATA COLLECTION

The HRA stations are designed to operate autonomously, with remote monitoring, control and data collection possible by two redundant communications modalities – long distance wireless via a repeater located on Mt. Discovery and satellite short-burst messaging. Communications with each of the ARIANNA stations are handled by a custom software suite built in C++ and Python, via computing facilities at U.C. Irvine (UCI). The Python code works with the Twisted framework to handle TCP communications (“WiFi”) and email communications (Iridium Short Burst Data messaging) to and from the stations. Multiple stations can and do communicate concurrently.

### A. Communications Overview

The long-range wireless system allows fast and efficient retrieval of all station data, as well as control over each station, including the timing and duration of data acquisition and communications windows, control over which major subsystems are powered, and even the capability of loading new software for the stations’ microcontrollers. For robustness, the station’s wireless communications are mesh-connected, in that every station can act as a repeater for each other, and each can separately reach Mt. Discovery. Communications thus takes place through the “best” path, either directly from a station to McMurdo, or possibly first hopping through a different station that has a stronger signal. In particular, the early-prototype Site D station is currently set up as an always-on repeater.

As an alternative to the high-speed long-range wireless communications, each HRA station is equipped with an Iridium satellite short-burst data (SBD) messaging system. This provides functionality similar to that of a mobile-phone’s text messaging system, with messages received by the station consisting of 270 bytes and sent messages containing 340 bytes. The SBD messaging system has been found to be very reliable; more so than the previous use of Iridium modem technology, which was prone to dropping connections. Although messages are short, they are densely encoded, and each transmits or receives a significant amount of control and monitoring data. Virtually every function available by WiFi is available by SBD. However, due to limited bandwidth, it is primarily used for control and monitoring, and to retrieve samples of data events. In this, it is important, as the ARIANNA stations have demonstrated longer calendar-time operational duration than the Mt. Discovery repeater, and so

Iridium is the only method of communicating with the stations during portions of the year. Finally, the Iridium receiver is used to synchronize each station's real-time clock to a highly-precise time received from satellites.

### B. System Software and Operation

Each HRA station's system software runs on an NXP LPC1768 embedded microcontroller using a 96 MHz ARM Cortex-M3 core with 32 kB of on-chip RAM and 512 kB of on-chip flash memory. Acquired data is stored on a 32 GB Compact Flash memory card, which is capacious enough to hold a year's worth of data or more even at the highest expected rates.

The system software is programmed in C/C++ without the benefits or overhead of a real-time operating system. The software breaks system operation into two major modes or "windows," namely communications and data taking. Generally, these alternate; when communicating, data taking is suppressed and powered-down, and during data taking, communications systems are powered down. Although it is possible to run the hardware associated with these modes simultaneously, these windows are kept separate because powering-up communications breaks RF-silence and may cause the collection of corrupted data. A communications window always precedes a data taking window to provide an opportunity to set parameters such as thresholds, window durations, etc.

At the start of a communications window, the system is normally set to attempt to use WiFi (the faster of the two) to send a status message and then waits for a response. If there is none (e.g., because the Mt. Discovery repeater is down), it defaults to SBD communications and tries again. If there is still no response, it will revert back to WiFi and make a programmable number of repeated tries. With no response in a certain number of tries, the system maintains its previously-programmed procedures, performs a data taking window, and tries to communicate again later. If communications are established, a control message is sent stating that there are no new commands (proceed as before), or else new commands and configurations can be sent to the station.

Because both WiFi and SBD communications are supported, effort has gone into creating a consistent, compact protocol that works well with both. Communications are in units termed "frames." Each frame has a 5-byte header that specifies the frame type and the size of its payload. A station can send data as an individual event (especially useful for sending a sample event via SBD) or entire data files.

Configuration commands sent to a station during a communications window include parameters such as trigger threshold levels, file and event compression parameters, and communications parameters such as timeout values for communications windows in case two-way communications are not established, the time between communications windows (equivalent to the duration of the data-taking windows), and what data to transmit during communications windows.

During data taking windows the system can perform data taking functions such as collecting "thermally" triggered events, periodic forced triggers in which the system takes an event unbiased by the trigger circuitry, and "heartbeat" events, in which the station generates an RF pulse itself and collects the resulting event. Data files collected during these windows include unique event numbers, time-stamp information, voltage readings, losslessly-compressed ADC values, bits confirming the type of trigger that resulted in the event (e.g., thermal, forced, etc.), and a 32-bit CRC value to aid in confirming data integrity.

The systems includes several features intended to enhance robustness, with particular attention to preventing a system from finding itself in some erroneous state whereby it may lose its ability to communicate, etc. These include a hardware-level "watchdog" timer that will completely reboot the system unless the watchdog is reset at least every 20 minutes (i.e., if the station becomes locked out of normal operation). The system will also completely reboot if it fails to achieve confirmed communications for 5 communications windows in a row. Furthermore, received control parameters are not allowed to fall outside of reasonable ranges to prevent user errors from accidentally disabling the stations. For example, the communications window duration is not allowed to be set to be less than 10 minutes. Finally, it is possible to remotely upload a new software revision to the station, which, if it passes a CRC check, etc., will take over. Thus far, there has not been cause to use this feature.

Since there are likely to be periods during which power conservation becomes important, it is possible individually control which of the major peripherals (amplifiers, data acquisition, WiFi, and Iridium SBD) are on or off during the communications and data-taking windows. For example, WiFi consumes substantially more power than Iridium SBD, and although it is much faster, the lower-power SBD system can be used exclusively when power savings becomes important. Finally, the systems can be placed in a strict power-savings mode, in which all data taking is powered down, and communications windows can be less frequent, etc. This mode can be entered automatically by a station when the battery voltage drops below a specified value. Hysteresis is implemented with a second value that prevents the station from dropping into and out of this mode too quickly. A very low-power mode gives operators the ability to maintain control when battery power is low.

## VIII. SYSTEM PERFORMANCE

The performance of the first three HRA systems have been extensively studied [26, 27]. This section describes the performance of the power systems, trigger rate performance and stability, noise performance, radio-pulse reflection studies, correlations to neutrino templates, station timing resolution, and event reconstruction resolution.

### A. Power systems performance.

As an example of the power system's performance, Fig. 18 shows voltage readings for an example station (Site A) during

about 14 months of operation, from the time it was turned on in late November 2012 until late December, 2013, when it was disconnected for servicing, and subsequently through March 31, 2014. As evidenced by voltages in the 17-24V range (regions “A” and “E” in Fig. 23), the solar panels provided nearly all power during the Austral summer. In an interesting observation, the output voltage of the solar panels climbed during colder months, presumably due to lower levels of recombination and dark current in the solar cells, perhaps combined with the more direct angle of attack of the sun upon the panels. Battery power is seen supplementing the station’s operation in voltage ranges of ~12 to ~14V (e.g., region “C”). Wind power was observed via voltages between ~14 and ~17V (region “B”) to be frequently and strongly supplementing solar power from early February until mid-March of 2012, at which point the wind turbine evidently failed during a storm. Beyond this point, solar panels continued to provide significant power, and the batteries were observed to be fully charged during days out until mid-April, even at a time when the sun reached only about 2 degrees maximum height and only about one week before the last sunset on April 24, 2013. After the last sunset (first vertical line in Fig. 18), the station was alternately directed between normal and lower-powered modes in order to prolong testing of the station, e.g. of temperature effects, etc. During this time (region “D”), the station subsisted on battery power only.

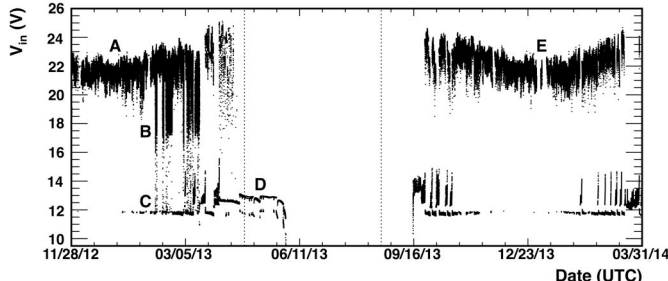


Fig. 18: Example station’s power supply voltage vs. time. Periods of operation primarily on solar power (“A”), wind power (“B”), battery backup (“C”) and solely on battery power (“D”) are indicated. Period “E” shows interrupted power during station servicing, and also demonstrates a relationship between seasonal changes and solar power efficiency (“E” was mid-summer). The vertical lines indicate the last and first days of sun. The last day of operation was May 30, 2013 PST. The station made first contact again on September 12, 2013 PST and realized 100% up-time within four days later. Operation with 100% up-time was achieved during ~70% of a year.

In late May 2013, the battery’s measured voltage began to decline precipitously, indicating that its reserve of power was close to exhaustion. Therefore, on May 28, 2013, the station was placed back in a full-power continuous data-taking and communications mode in order to test whether it would shut down in an orderly fashion and reboot autonomously from that state upon the return of the sun. The station thus shut down May 30, 2013, 36 days after the last sunset.

The first autonomous communication of the next spring occurred on September 12, 2013, about 3 weeks after the first sunrise (August 19, 2013, indicated by the second vertical line in Fig. 18). This was a day on which the sun had reached a maximum height of 8 degrees. On September 16, 2013, the

station began uninterrupted operation until it was serviced in late December 2013. The station thus maintained 256 days of operation out of 365, or 70% of the year while including the use of power savings modes. When run at full power continuously, at least 58% of a year has been achieved.

#### B. Trigger rates vs. temperature and wind.

Figure 19 shows an example station’s (Site A) thermal-triggered event rate from January 2, 2014 and March 13, 2014. The amplifier’s gain has been noted to rise slightly as temperature drops, leading to increased thermal trigger rates. Once the stations are covered in snow, diurnal temperature changes have been found to be less significant than seasonal changes. Since re-commissioning in January of 2014, the station’s thresholds have been remotely adjusted twice, as noted by the two downward arrows in Fig. 20. All stations behaved similarly and required only the same two adjustments.

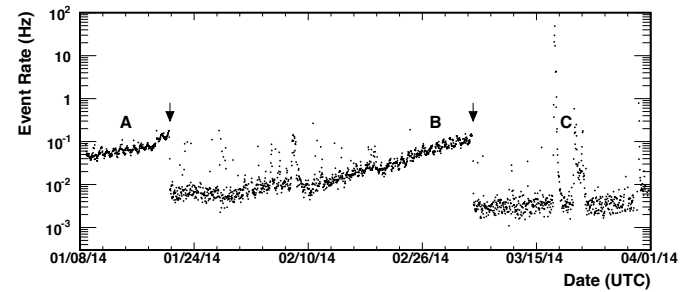


Fig. 19: Total event rates (triggered events only) vs. time for Site A from January 8 through March 31, 2014. During periods A and B, slight diurnal rates changes are visible, as is a gradual increase in rates related to a drop in temperature. Two adjustments in rates were made, indicated by the two downward arrows, on or about 1/23 and 3/06. During period C, a powerful storm swept through the area, and an increase in rates was noted.

A partial correlation between storms and/or wind velocity and event rates has been observed. In Fig. 20, the period “C,” for example, shows an increase in rates during a storm. The cause and nature of the excess events is being studied, but a few comments can be made: Elevated event rates have been found to be correlated between stations. Generally, only wind speeds above ~20 knots have resulted in elevated event rates, but not all such periods of higher wind speeds have resulted in higher rates. Most of these temporary increases have had negligible impact on event collection efficiency, i.e., less than seasonal temperature variations. No additional noise has been found in forced (unbiased) events during storms, and so there is no evidence that increased trigger rates are due to any gradual, consistent change in the level of noise. Rather, these noise events appeared to be sparse and random. Only one few-hour-long instance (to the left of “C” in Fig. 19) resulted in excess event rates that significantly impacted dead-time, increasing it by ~1% over that limited time period. Analysis of the excess triggered events has concluded that they do not resemble expected neutrino events, and that these excess events can be removed from the data with high efficiency, as discussed in the next section.

### C. Thermal noise measurements.

Fig. 20 shows an example plot of recorded noise sigma in mV vs. time for the 2014 Station A, channel 2 data set, binned into 1-day intervals. The “Forced” time series consists of all data from “unbiased” events taken at periodic intervals without the involvement of the station’s trigger system. This data is highly Gaussian and essentially displays the channel’s thermal noise (average  $\sigma=17.6$  mV for all forced triggers). A slight rise in noise vs calendar time is due to the slowly cooling temperatures, which has been found to increase the amplifier’s gain and hence the level of recorded noise.

The “ $\eta>3$ ” time-series, by contrast, contains all “thermally” triggered measurements (those acquired due to the system’s trigger), but excluding events that have been identified with brief periods in which the station’s amplifiers have displayed a sympathetic oscillation between channels (this problem has been rectified by a revised amplifier design as discussed in Section IX). The amplitudes measured by each sample in the triggered data are also substantially normally distributed, although amplitudes in at the trigger threshold values occur with a higher probability as expected. It is noted that fluctuations in triggered-event noise levels rise modestly above the unbiased event noise levels over the same storm or high-wind periods as seen in Fig. 17 and concomitant with the event rate increases seen in Fig. 19.

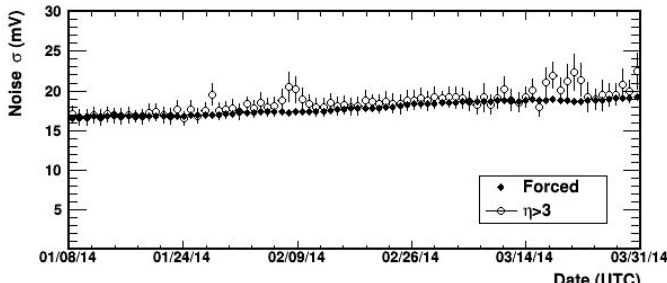


Fig. 20: Noise sigma for channel 2 at Site A between January 8, 2014 and March 31, 2014, binned into 1-day periods. The “Forced” data points are unbiased by the system’s trigger and reflect highly-Gaussian thermal noise (average of 17.6 mV). The  $\eta>3$  data reflects data collected due to the station’s trigger system. Aside from a bias that the trigger imposes, this data is also substantially Gaussian, although episodes of greater noise are seen that are correlated with periods of storms including high winds.

### D. 2014 data-set correlation distributions.

Data taken between January 8, 2014 and March 31, 2014 has been studied in an exploratory search for neutrino-like signals [28]. An expected neutrino signal has been generated from the time dependent electric field at the neutrino interaction vertex, propagated through a model of the ice and convolved with measured antenna and amplifier response functions. The neutrino signals are determined as a function of two space angles defining the orientation of the incident electric field relative to the antenna, as well as the angle between the antenna and the Cherenkov cone. The resulting time dependent neutrino waveform “templates” (e.g., Fig. 21) can then be compared to recorded data by computing its maximum correlation value with each antenna waveform.

Prior to reconstruction of the event direction and

polarization, waveforms from all four channels, including both the recorded waveform and its inverse (it is not *a priori* obvious which face of the antenna is presented to the incoming radio wave, hence whether the initial pulse would be positive or negative), for a total of 8 waveforms per station, are compared to a single reference template corresponding to 30° in the E and H-planes. The best correlation between any of these 8 signals and the reference template is designated as  $\chi$ . Figure 23 shows values of  $\chi$  in the Station A data set for all events (“All Data”) in its light-gray area, including a total of 203,562 events. In this analysis, which is described in much greater detail in [28], it is required that a neutrino candidate have a  $\chi>0.81$ .

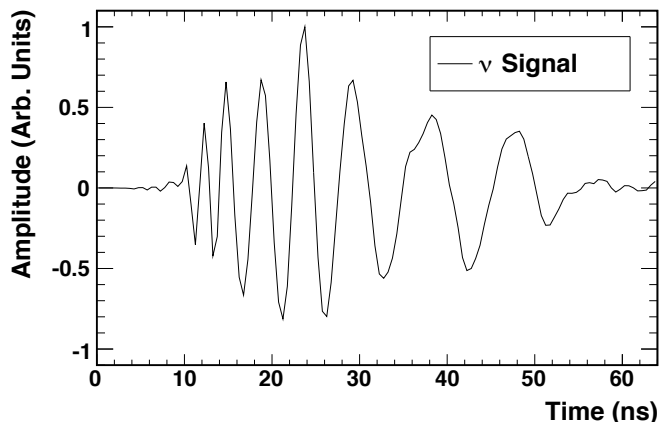


Fig. 21: Example neutrino signal template (40 degrees off-axis in the E-plane) including ice propagation, antenna, amplifier response, but excluding thermal noise, and sampled at 1.92 GHz (Y-axis units are arbitrary).

The majority of triggered events are purely random in nature (i.e., thermal noise). These are identified by an autocorrelation function whose results are noted to have a perfect correlation at zero time offset. Non-thermal-noise events are taken to be those for which the minimum autocorrelation function  $\alpha$  is below -0.45 on any antenna. These remaining non-thermal events are shown in medium-gray in Fig. 22 (“ $\alpha<-0.45$ ”), and comprise 25% of the “All Data” set. This cut preserves 99.5% of neutrino candidates.

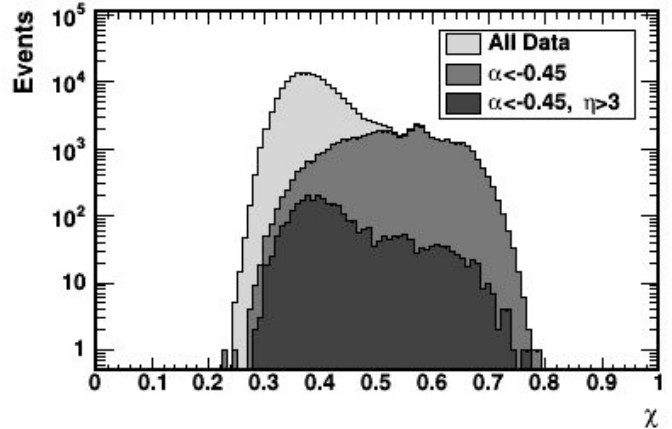


Fig. 22: Distribution of  $\chi$  in the 2014 data set for Station A, channel 2, for all data, after the  $\alpha<-0.45$  cut, and after both the  $\alpha$  cut and the “ $\eta>3$ ” cut.

The “ $\eta > 3$ ” cut mentioned in the previous sub-section is then made in addition to the “ $\alpha < -0.45$ ” cut. This, again, is intended to remove a small subset of events that contain sympathetic amplifier oscillations between channels. To pass this cut, it is required that the frequency spectrum of a neutrino candidate have more than 3 frequency bins ( $\eta > 3$ ) at or above 50% of the magnitude of the maximum bin – that is, that the candidate contains more than essentially the single-frequency oscillation that is seen in misbehaving amplifiers. This cut removes 85% of the events remaining after the  $\alpha < -0.45$  cut and preserves 97% of neutrino candidates. Long term, this cut may be unnecessary given amplifier stability improvements discussed in Section IX. The combination of the  $\alpha$  and  $\eta$  cuts is seen in dark gray in Fig. 22, resulting in 3,159 remaining events (~1.5% of the full data set) and preserving 90% of expected cosmogenic neutrino events.

#### E. Radio frequency reflection studies.

Radio-frequency reflection studies on one of the Site G HRA station have been performed. These involved delivering a fast electrical pulse, generated by a Pockels Cell driver (Grant Applied Physics model HYPS) to a quad-ridged polarization horn antenna (Seavey Engineering Inc., now Antenna Research Associates; antenna custom-designed for the ANITA project and described in [29]). The antenna was placed face-down to the ice at various locations both near to and far from the station, as well as oriented in several polarizations relative to the receiving antennas. The transmitted RF pulse therefore passed down through the ice (~550 m thick at Site G), bounced off of the water-ice interface, and back up to the station. The station electronics includes an external trigger input that allows the capture of waveforms at precise times. Inserting a controlled delay between the generation of the RF pulse and the station trigger was thus used to trigger the station’s data acquisition at the time of arrival of the reflected pulse.

During the 2013-2014 service mission, a comparison of reflected waveforms was made between those collected by an ARIANNA station’s electronics and equivalent waveforms using same ARIANNA channel’s antenna and amplifier but captured by an oscilloscope (Agilent model DSO 7104B; 1 GHz bandwidth, 5 G-samples/s acquisition). As examples, two plots are shown from the same location (Station G), with the horn antenna located for a straight down-and-up reflection. The first comparison plot, Fig. 23, shows the station’s channel 2’s response to the reflected pulse (antenna oriented with parallel polarization to the transmitted pulse) superimposed on an equivalent pulse’s response as recorded by the oscilloscope. Adjustments of the station’s response to the vertical scale were made solely according to the station’s calibration for gain. No adjustments to the oscilloscope’s response was made.

Figure 24 compares a pulse received at the station’s channel 1, whose antenna is orthogonal to that of channel 2 and thus orthogonal to the polarization of the transmitted pulse. Channel 1’s response is attenuated compared to channel 2’s, consistent with the difference in orientation. The polarization is evidently substantially maintained even after the reflection

and transmission through a total of ~1100 meters of ice.

It can be seen that the waveforms within Fig.’s 23 and 24 are well-matched within the limits of noise (~22 mV RMS for the amplified thermal noise). It’s also important to note that the overlapping waveforms shown in these figures are from different transmitted pulses, since it was not possible to record the same reflections at the oscilloscope and station simultaneously while using the same antennas and amplifiers. The evident degree to which the separate waveforms overlap therefore also supports the expectation that radio pulses traveling along identical trajectories through the ice and reflecting from the same patch on the ice-water interface are consistent from event to event, limited only by thermal effects.

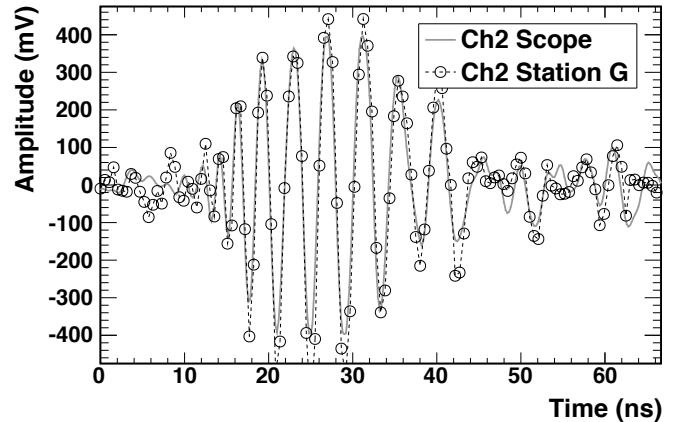


Fig. 23: An overlapping comparison of a representative antenna and amplifier response to separate but equivalent RF pulses reflected off of the bottom of the Ross Ice Shelf, as received by the Station G electronics and by a 1 GHz bandwidth oscilloscope. The polarization of the transmitted pulse was parallel to that of the receiving antenna.

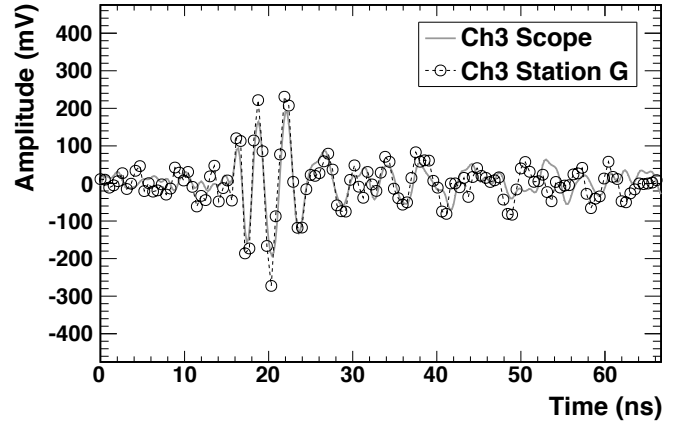


Fig. 24: An overlapping comparison of an antenna and amplifier response to separate but equivalent RF pulses reflected off of the bottom of the Ross Ice Shelf, as in Fig. 24. The polarization of the pulse was orthogonal to the receiving antenna and hence is attenuated.

#### F. Station timing resolution.

Site G reflection studies, performed over a period of 24 hours for a variety of surface locations, have been used to determine the station’s timing resolution. For a given surface location, a reference event was arbitrarily selected to generate four  $\Delta t_i$  values, where  $\Delta t_i$  represents the time difference in the pulse arrival time between channel  $i$  in the reference and

current event. The time difference is taken to be that which maximizes the Pearson correlation between the waveforms on the  $i^{\text{th}}$  channel in the reference and current event. This time difference may be non-zero due to jitter in the electronics used to generate the transmission pulse. However, all channels should have the same  $\Delta t_i$  value, since jitter in the pulse transmission time should affect all channels equally. The difference in  $\Delta t_i$  values between channels gives a measure of the readout timing resolution. Figure 25 shows the time difference  $\Delta t = \Delta t_i - \Delta t_j$  for all six combinations of unique channel pairs  $i$  and  $j$ , integrated over all events taken at all transmission locations. A net timing resolution of 0.049ns, obtained from a Gaussian fit to the peak, fully satisfies the experimental requirements of ARIANNA.

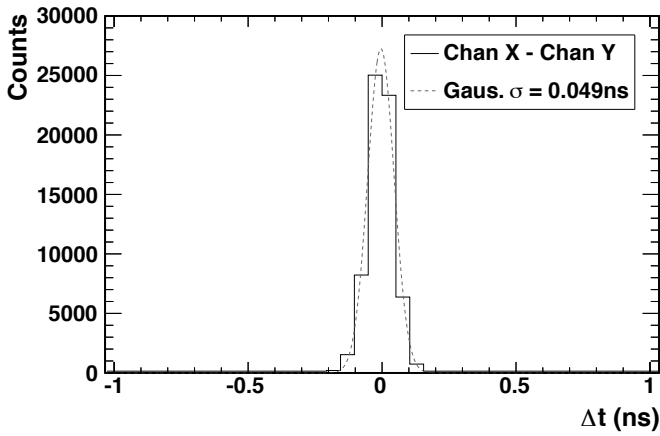


Fig. 25: Measured net timing resolution of the station at Site G, found via reflection studies initiated from a number of locations on the ice. The sigma of a fitted Gaussian is 0.049 ns.

#### G. Angular resolution and event reconstruction.

Analysis of event reconstruction was performed using data taken in 2012 [30]. In brief, maximum cross-correlations were found between waveforms from all combinations of different channels. This leads to computed time differences between the channels and hence the angle at which a plane-wave is presumed to have struck the different antennas. The reconstructed angle at the station is then corrected for propagation through the firn layer (a layer of compacted snow from prior seasons) with a simple model of ice density as function of depth to produce a predicted signal-source location on the surface of the ice. The median value for the precision of the angular measurements for several different locations ranged between 0.14 to 0.17 degrees.

## IX. NEXT-GENERATION SYSTEM

A substantial redesign of the system electronics has been made, targeting deployment during the 2014-2015 Austral summer campaign. This has included the design of a new fast sampling chip, the development of a new single-board system to replace the motherboard/daughter-card system, and an updated amplifier design. The resulting hardware has improved electrical and physical robustness, better features and performance, uses substantially less power, is less costly, and is easier to calibrate. It maintains full “drop-in”

compatibility with the installed HRA systems, yet facilitates easy scaling to 8-channel ARIANNA stations.

#### A. Updated amplification.

An updated amplifier has been designed (Fig. 26), targeting deployment in 2014. It features enhanced stability, flatter frequency response and more symmetrical gain. To reduce system cost, it also eliminates the need for the external band-pass and limiting components seen in Fig. 5, with at most only a single attenuator needed to match the system board’s input range.

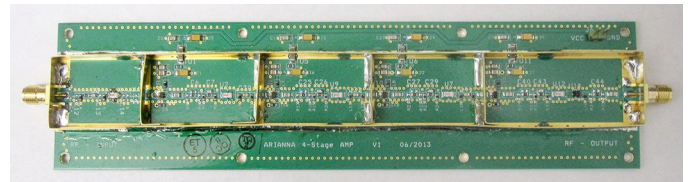


Fig. 26: Improved ARIANNA amplifier with cover shield removed.

#### B. The SST, a new 2+ G-samples/s acquisition I.C.

A new signal acquisition integrated circuit has been designed and fabricated [31]. Containing 4 channels of 256 samples per channel, the “SST” Synchronous Sampling plus Triggering I.C. incorporates substantially the same trigger functionality as the ATWD system as described in Section VI, but in a greatly simplified, easier to use and lower-power form. The sampling is completely synchronous, using no PLL or any delay-based timing, and is simply driven by an external LVDS clock for extremely-high timing uniformity and stability. Because of its fully-synchronous design, the SST operates with clock rates spanning over 6 orders of magnitude, from <2 kHz to >2 GHz. Its leakage rate is so low (<200 mV/s) that operation down to <2 kHz is fully practical. Optimized design and packaging yielded a nearly-flat analog bandwidth to ~1.2 GHz using a standard 50-Ohm signal source and a -3 dB bandwidth of ~1.5 GHz. The use of an inexpensive 0.25 μm CMOS process allows a large input voltage range of 1.9V on a 2.5V supply. Table I summarizes some of the SST’s main performance figures.

The SST includes a per-channel dual-threshold windowed coincidence trigger that operates with <1 mV RMS resolution and >600 MHz equivalent input bandwidth (e.g., it is sensitive to small-signal pulses down to 500 ps FWHM or better, with 0% to 100% triggers spanning less than 4mV in pulse height differences). An AND or an OR can be formed between comparators per channel over a window of ~3.5 ns or greater to form a bipolar trigger. For example, if set to 5ns, a bipolar signal of greater than 100 MHz, as is ARIANNA’s specification, can be required in order to pass this first-level trigger. Output pins are available for each individual trigger comparator for easy calibration and rate monitoring or else, during typical operation, the AND of each channel’s two comparators can be output in differential form. In AND mode, the SST stretches each trigger output to allow the simple formation of a second-level trigger that finds temporal coincidences between channels. The trigger outputs can be

CMOS or will adapt to lower voltage levels (e.g., differential PECL) to help prevent noise coupling from the trigger outputs back to the analog inputs.

Table I: SST Figures of Merit

Parameter	Value
Technology:	0.25 $\mu$ m CMOS
Supply voltage:	2.5V
Number of channels:	4
Samples per channel:	256
Package size:	8mm by 8mm
Number of package pins:	56
Input clock (ARIANNA):	1 GHz LVDS
Sample rate (ARIANNA):	2 GHz
Minimum sample rate:	< 2 kHz
Maximum sample rate:	> 2.5 GHz
Maximum power per channel:	40 mW at 2 GHz
Analog input range:	0-1.9V
Analog bandwidth:	> 1.5 GHz, -3dB
Dynamic range:	~ 11.5 bits, RMS
Fixed pattern (pedestal) noise:	< 7 mV, RMS
Trigger comparators per channel:	2 (high and low)
Trigger sensitivity:	< 1 mV, RMS
Trigger bandwidth:	> 600 MHz
Trigger functions per channel:	AND/OR, windowed
Trigger output modalities:	Differential/single-ended
Trigger output voltage:	0.8, 1.2 or 2.5V CMOS

The SST requires no programming, and only 3 active signals are required to operate it: Reset, Run/Stop, and Read-clock. The power consumption of the chip depends on the clock rate, the duty cycle of acquisition vs. digitization, and the bias on the comparators. When operating at the HRA's normal 2 G-samples/s acquisition speed, the worst-case power consumption is about 160 mW, or 40 mW per channel, with a more typical consumption of ~25 mW per channel.

### C. Next-generation system board.

A next-generation single-board data acquisition system board has been created, targeting use for the completion of the HRA in 2014. The new system, seen in Fig. 27, is designed for full physical and electrical drop-in compatibility with the HRA systems described in Section IV above. It includes one on-board 4-channel SST chip in place of four daughter-cards.

Power management has been improved, achieving higher input voltage tolerance (42V) along with the incorporation of on-board static discharge protection. The former was seen to be a potential necessity if wind power is reconsidered, while the latter was precautionary. A lower-power default turn-on state was also implemented, and attention was made to lowering parasitic power loss by the DC-DC converters and linear regulators that are on-board. The new system, and the SST in particular, has resulted in dramatic power reduction, from ~5.8W for the HRA system seen in Fig. 9 to ~1.7W for that in Fig. 27. Given the lower power consumption, the sensitivity and accuracy of the system board's voltage and

current measurements was also enhanced. Finally, the board includes digital ambient temperature monitoring that is calibrated down to -55C.

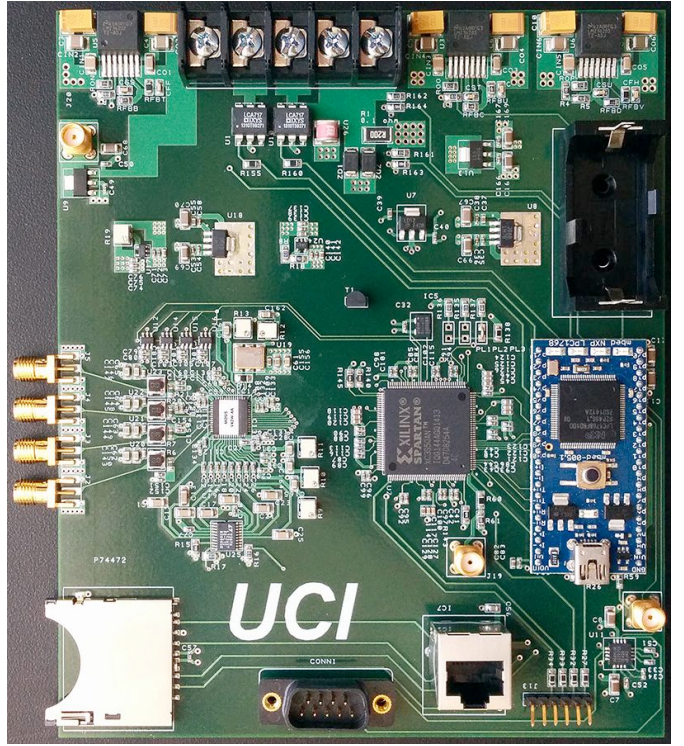


Fig. 27: The next-generation ARIANNA single-board data acquisition system. It includes one four-channel SST chip (left of center), improved power management and protection, on-board temperature monitoring, and has significantly-lower cost and calibration requirements. Average power consumption has been reduced from ~5.8W to ~1.7W.

The system firmware has also been significantly changed. In this version, all triggering and waveform digitization is managed independently by the board's FPGA. The FPGA forms second-level triggering (i.e., merging multiple channel's triggers), autonomously stops the SST, and digitizes its data, storing it in the FPGA's own block memory. Once digitization is completed, it delivers a flag to the system's microcontroller, indicating that an event has been taken and is available. This relieves the system's microcontroller from close, time-critical interaction, and permits higher levels of parallelism in a multi-SST system.

While the new system board was designed for electrical and physical compatibility with the first three HRA systems, it anticipates the creation of a compact, single-board, 8-channel version for full-scale ARIANNA stations. This would have the same or lower power consumption as the currently-deployed 4-channel systems, while offering a wider input range, longer record length, simpler trigger rate monitoring and calibration, easier fabrication and lower cost.

### D. Power systems changes for 2014.

For the 2014-2015 Austral summer completion of the Hexagonal Radio Array, the next four stations are currently planned for operation on solar power only. Therefore, the

pyramidal upper tower segment and clearance necessary to accommodate a wind turbine as seen in Fig. 3 is not needed, and the upper tower will instead consist of a normal “straight” segment. This allows the solar panels to be mounted higher on the tower, allowing longer operation despite any snow accumulation. Furthermore, the deletion of wind power requires less battery capacity, since the primary purpose of larger batteries had been to buffer power between periods of higher wind when there is no sun available; a more stringent requirement than buffering cloudy periods. Hence, for 2014, only one battery of 112 Ah capacity (nominal) will be used per newly-installed station.

Since with solar power only there are no known or expected sources of anthropogenic RF noise remaining on the towers, the 2014 station’s electronics will be placed at the foot of the power tower, with its signal antennas distributed about the tower, and the tower itself will be used to host the communications antennas. The resulting deletion of a separate communications mast further simplifies the system and reduces cost, deployment time and potential points of failure. Station electronics and batteries are planned to be co-located so that power used by the stations will help maintain an efficient battery temperature.

Experience and modeling have shown that the three-panel configuration used thus far (one north-facing 100W panel and two 30W panels) can be simplified to a single north-facing 100W panel without materially compromising useful powered life-time. The deletion of the wind turbine and the two auxiliary solar panels means that the tower’s complexity and mass is reduced, and the power towers are thus simpler, quicker to set-up, lighter, and can be made taller if desired. It is expected that two 10-foot segments will be targeted for ARIANNA’s full-scale deployment, gaining a further 4 feet of height with no added complexity.

Finally, instead of steel guying cable as used in the 2012 towers, Aramid cable will be used. This cable, marketed as a replacement for steel in these applications, including at low temperatures and under UV exposure, is much lighter and is essentially transparent to electromagnetic radiation. Hence, it can be used for guying near the RF antennas without influencing their performance.

## SUMMARY AND CONCLUSIONS

The Hexagonal Radio Array is a pilot program for the ARIANNA project, intended to develop and demonstrate the technologies that the full project will rely on. Three HRA stations have been deployed, and each has gained over a year of operational exposure. The HRA systems have demonstrated low-power ( $\sim 7\text{W}$ ) and high-performance, including achieving 0.049 ns RMS timing resolution,  $\sim 2\text{ mHz}$  trigger rates at 4-sigma thresholds, 58-70% per-year operation on solar power and battery backup (depending on power and operation modes), angular reconstruction precision of 0.14 to 0.17 degrees, and with continuous remote monitoring, control and frequent full data transmission and control by long-distance wireless and satellite.

A simplification of several aspects of the HRA’s systems hardware is being prepared with an aim of further reducing station power consumption, complexity, cost, calibration requirements and installation time per station. These include simplified power tower design and co-location of power, instrumentation and communications. An updated amplifier design with better stability, flatter frequency response, fewer external band-pass and limiting components has been fabricated. A new four-channel version of the ATWD waveform acquisition chip, the “SST,” has also been designed, achieving twice the sample depth, 16 times lower power, wider input range, nearly twice the analog bandwidth, and much simpler operation. These simplifications and improvements are expected to be incorporated in the last four HRA stations due to be deployed in the 2014-2015 Austral summer. They allow ARIANNA’s full-scale data acquisition system to be created as a single board for reduced system cost, mechanical overhead and power consumption.

In conclusion, the technical goals that the pilot Hexagonal Radio Array sought to have been substantially accomplished. The ARIANNA site has been proven to be virtually free from anthropogenic noise, autonomous operation with near-real-time full data retrieval has been demonstrated, and all critical system performance figures have been met. The 2014 hardware simplifications will allow full-scale ARIANNA systems to economically reach their goals, including the use of additional downward-facing antennas plus upward-facing antennas to co-locate the discrimination of cosmic rays and neutrino signatures.

## ACKNOWLEDGMENTS

We wish to thank the staff of Antarctic Support Contractors, Lockheed, and the entire crew at McMurdo Station for excellent logistical support. We thank Wei Huang and Shiu-hua Wood Chiang for their efforts in the design of the ATWD circuit, e.g. as depicted in Fig. 11. We also thank Prof. De Flaviis for the use of the Far Field Anechoic Chamber at U.C. Irvine.

This work was supported by generous funding from the Office of Polar Programs and the Physics Division of the US National Science Foundation, including via grant awards ANT-08339133, NSF-0970175, and NSF-1126672, and NSF-1126672, and by the Dept. of Physics and Astronomy, Uppsala University.

## REFERENCES

- [1] L. Gerhardt, et al., “A Prototype Station for ARIANNA: A Detector for Cosmic Neutrinos,” Nucl. Inst. Meth. A624, 2010, 85.
- [2] S. W. Barwick, et al., “ARIANNA – A New Concept for High Energy Neutrino Detection,” 32nd Intern. Cosmic Ray Conf., Beijing, 2011, pp 238-239.
- [3] S. Klein, et al., “A radio detector array for cosmic neutrinos on the Ross Ice Shelf,” IEEE Transactions on Nuclear Science, Vol. 60, No. 2, pp. 637-643, April 2013.
- [4] S. A. Kleinfelder, et al., “Design and performance of the autonomous data acquisition system for the ARIANNA high energy neutrino experiment,” IEEE Transactions on Nuclear Science, Vol. 60, Issue 2, pp 612-618, April 2013.
- [5] G. A. Askaryan, JETP 14, 441 (1962); 21, 658 (1965).

- [6] K. Dookayka, "Characterizing the Search for Ultra-High Energy Neutrinos with the ARIANNA Detector," Dissertation, University of California, Irvine, 2011.
- [7] K. Dookayka, et al., "Characterizing the Search for UHE Neutrinos with the ARIANNA Detector," 32nd Intern. Cosmic Ray Conf., Beijing, 2011, 124.
- [8] K. Greisen, "End to the Cosmic-Ray Spectrum?," Physical Review Letters 16 (17): 748–750, 1966.
- [9] G. T. Zatsepin, V. A. Kuz'min, "Upper Limit of the Spectrum of Cosmic Rays". Journal of Experimental and Theoretical Physics Letters 4: 78–80, 1966.
- [10] C. S. Neal, "The dynamics of the Ross Ice Shelf revealed by radio echosounding," Journal of Glaciology, 24, 295–307, 1979.
- [11] S. Barwick, et al., "Performance of the ARIANNA Prototype Array," Proc. Int. Cosmic Ray Conf., Rio De Janeiro, July 2013.
- [12] J. C. Hanson, et al., "Ross Ice Shelf Thickness, Radio-frequency Attenuation and Reflectivity: Implications for the ARIANNA UHE Neutrino Detector." Proc. Int. Cosmic Ray Conf., Beijing, China, 2011.
- [13] T. Barrella, S. Barwick, D. Saltzberg, "Ross Ice Shelf in situ radio-frequency ice attenuation," J. Glaciology, Vol 57, No. 201, pp. 61-66, Feb. 2011.
- [14] E. Andres, et al., "The AMANDA neutrino telescope: principle of operation and first results," Astroparticle Physics 13.1 (2000): 1-20.
- [15] I. Kravchenko, et al. "Limits on the ultra-high energy electron neutrino flux from the RICE experiment," Astroparticle Physics 20.2 (2003): 195-213.
- [16] J. Ahrens, et al., "Sensitivity of the IceCube detector to astrophysical sources of high energy muon neutrinos," Astroparticle Physics 20.5 (2004): 507-532.
- [17] P. Allison, et al., "Design and Initial Performance of the 1351 Askaryan Radio Array Prototype EeV Neutrino Detector at the South Pole," Astropart. Phys. 35 (2012) 457–477.
- [18] J. C. Hanson, et al., "Time-domain response of the ARIANNA detector," submitted to Astroparticle Physics.
- [19] S. A. Kleinfelder, "A Multi-Gigahertz Analog Transient Waveform Recorder Integrated Circuit," 1992, Thesis, University of California, Berkeley.
- [20] S. A. Kleinfelder, "Advanced transient waveform digitizers," Proceedings of the SPIE Particle Astrophysics Instrumentation, Vol. 4858, pp. 316-326, August, 2002.
- [21] S. A. Kleinfelder, "A multi-GHz, multi-channel transient waveform digitization integrated circuit," Proceedings of the 2002 IEEE Nuclear Science Symposium, Orlando, FL, October 2002.
- [22] S. A. Kleinfelder, "GHz waveform sampling and digitization circuit design and implementation," IEEE Transactions on Nuclear Science, Vol. 50, No. 4, pages 955-962, August 2003.
- [23] W. Huang, S.W. Chiang, S. Kleinfelder, "Waveform Digitization with Programmable Windowed Real-Time Trigger Capability," Proceedings of the 2009 IEEE Nuclear Science Symposium, Orlando, FL, October 2009.
- [24] S. A. Kleinfelder, et al., "Multi-GHz waveform sampling and digitization with real-time pattern-matching trigger generation," IEEE Transactions on Nuclear Science, Vol. 60, No. 5, pp. 3785-3792, October 2013.
- [25] M. Roumi, "Advanced Pattern-Matching Trigger System for the ARIANNA High-Energy Neutrino Detector," Dissertation, U.C. Irvine, 2014.
- [26] J. Tatar, "Performance of Sub-Array of ARIANNA Detector Stations during First Year of Operation," Dissertation, U.C. Irvine, 2013.
- [27] J. C. Hanson, "The Performance and Initial Results of the ARIANNA Prototype," Dissertation, U.C. Irvine, 2013.
- [28] S.W. Barwick, et al., "A First Search for Cosmogenic Neutrinos with the ARIANNA Hexagonal Radio Array, submitted to Astroparticle Physics, 2014.
- [29] P. W. Gorham et al., "The Antarctic Impulsive Transient Antenna Ultra-high Energy Neutrino Detector (ANITA): Design, performance, and sensitivity for 2006-2007 balloon flight," Astroparticle Physics, 32:10–41, 2009.
- [30] C. Reed, et al., "Performance of the ARIANNA Neutrino Telescope Station," Proc. Int. Cosmic Ray Conf., Rio De Janeiro, July 2013.
- [31] S. A. Kleinfelder, E. Chiem, T. Prakash, "The SST Fully-Synchronous Multi-GHz Analog Waveform Recorder with Nyquist-Rate Bandwidth and Flexible Trigger Capabilities," Conference Record of the 2003 IEEE Nuclear Science Symposium, 2014, in press.



## Ross Ice Shelf Thickness, Radio-frequency Attenuation and Reflectivity: Implications for the ARIANNA UHE Neutrino Detector

JORDAN C. HANSON<sup>1</sup>, FOR THE ARIANNA COLLABORATION

<sup>1</sup>*Department of Physics and Astronomy, University of California at Irvine, Irvine, CA 92697*

*jchanson@uci.edu*

DOI: 10.7529/ICRC2011/V04/0340

**Abstract:** The ARIANNA high energy neutrino detector is planned to be deployed on the surface of the Ross Ice Shelf to search for astrophysical neutrinos. Collisions with nuclei in the ice generate showers of particles that emit short pulses of radiation, created by the Askaryan mechanism, in the frequency range of 100 MHz to 1 GHz. The ARIANNA site is located about 65 miles from McMurdo Station, the main hub of US Antarctic operations, and is protected from ambient RF interference by a geologic formation known as Minna Bluff. In this work, we report preliminary results for the frequency interval 90-180 MHz from site studies of the field attenuation length (averaged over depth), and reflection and polarization properties of the saltwater-ice boundary.

**Keywords:** ARIANNA, Antarctica, GZK, neutrino astronomy, Ross Ice Shelf, attenuation length

### 1 Introduction

The Antarctic Ross Ice Shelf Antenna Neutrino Array (ARIANNA) is designed to detect ultra-high energy (UHE) cosmogenic neutrinos, via the Askaryan effect [1, 2, 3, 4, 5]. When a neutrino interacts in bulk matter with an index of refraction, the resulting hadronic and electromagnetic cascades can produce coherent GHz radiofrequency (RF) pulses. High energy scattering processes and positron annihilation cause a negative charge excess to build up in the cascades, creating an effective radiating dipole moment. This radiation is coherent, since the coherent radiated power from Cherenkov radiation scales quadratically with the charge of the emitter [6], and the wavelengths are set by the lateral size of the shower initiated by the original neutrino interaction. Simulation studies show that the signal pulses from high energy neutrinos usually arrive at ARIANNA surface receivers by first reflecting from the ice-water interface at the bottom of the Ross Ice Shelf (RIS), and then propagating through the bulk ice [7]. Relatively few neutrino signals propagate directly from the interaction vertex to the surface receivers. Therefore, the sensitivity and capabilities of ARIANNA depends on the ice properties such as the attenuation length and reflection efficiency. In this work, we report on several key properties of the ARIANNA site.

The ARIANNA detector consists of an array of autonomous stations deployed on the surface of the RIS, viewing 513 km<sup>3</sup> of glacial ice centered at (77° 44' 523" S, 165° 02' 414" E) in western Antarctica. Prior studies of the electromagnetic properties of the ARIANNA site have

measured the electric field attenuation length by using vertically reflected pulses and assumed a value for the reflection coefficient from the ice-water boundary at the bottom [11]. In this work, we examine reflected pulses over several baselines to determine both the field attenuation length and reflection coefficient. We also show that the reflected pulse preserves its polarization orientation. Measurements of the reflection coefficient have been made independently [8, 9], revealing strongly reflected RF pulses in regions free of sub-glacial flow lines and sea-ice freezing zones. ARIANNA is in Moore's Bay, which is far from glacial irregularities [8] and in good RF isolation. For a similar study of attenuation lengths performed in ice located in a different region of Antarctica, see Besson (2008) [10].

We quantify absorptive losses experienced by an electromagnetic wave by adding an imaginary component to the dielectric constant, parameterized by

$$\alpha = -8.686(\pi\nu/c)(\sqrt{\epsilon'}\tan \delta) \quad (\text{dB/m}) \quad (1)$$

Here, the vacuum speed of light is  $c$ ,  $\nu$  is the frequency in Hz,  $\epsilon'$  is the real part of the dielectric and the loss tangent  $\tan \delta$  is the imaginary part of the dielectric over the real part  $\epsilon''/\epsilon'$ . The electric field attenuation length is then defined as [11]

$$L_\alpha = 1/\ln \sqrt{10^{\alpha/10}} \quad (2)$$

which is the distance the electromagnetic wave travels before decreasing in amplitude by a factor  $e^{-1}$ .

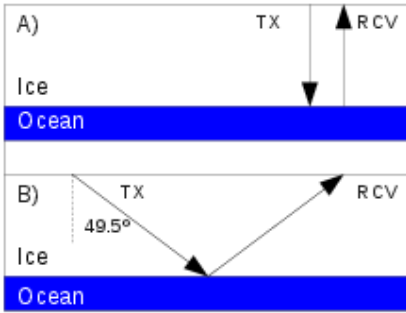


Figure 1: A) A schematic of the direct bounce experimental geometry. B) The angled bounce experimental geometry.

## 2 Experimental Methods

To create broad band RF pulses for propagation through the ice shelf, a short duration (1 ns wide), kilovolt pulse is delivered from the HYPS Pockel Cell Driver to a log-periodic dipole array (LPDA) transmitter (105 MHz-1300 MHz), supplied by Creative Design Corp (CLP5130-2). These antennas are directional, with a gain of 6-7 dBi. An identical LPDA serves as a receiver. Along with a precise measurement of the ice-shelf depth at the ARIANNA site, we have the S11 and voltage standing wave ratio (VSWR) parameters for the antennas as they couple to the dielectric properties of the snow around them [5]. The lowest frequency measurable by the LPDA in snow decreases to approximately 80 MHz because the wave speed slows down in the snow, while the antenna response remains constant. The VSWR is close to one for all relevant frequencies in this work. The signal from the receiver is filtered with both a NHP-50+ highpass filter and a NLP-1200+ lowpass filter, and amplified by a 1 GHz Miteq AM-1660 low-noise amp before being recorded on a Tektronix oscilloscope with 1 GHz bandwidth. We also attenuate by 20 dB where appropriate to obtain manageable signal amplitudes.

Figure 1 shows two distinct reflection geometries employed in these studies for the antennas, both of which are buried in the low density firn snow and pointed down. The direct bounce configuration (1a) is indicated by the vertical path between the transmitter and receiver antennas, which are separated by 18.7 m. The radio pulse travels 576 m to the water-ice interface and reflected back to the surface for a total path length of 1152 m. The angled bounce configuration (1b) is similar to the direct bounce, where the two antennas oriented vertically downward, but the separation between the two antennas is increased to 977 m, which increases the total path length to 1510 m (see Table 1). The unattenuated signal amplitude is determined by rotating the LPDA antennas to point toward each other through the surface snow while separated by 18.7 m. The path length for this test is the shortest of the three configurations. In practice, R, G, and the exponential factor are set to 1 in eqn. (4).

Since the signal in this test is relatively strong, the amplifier is removed for this measurement.

The analysis presented here focuses on the frequency range between 90 MHz and 180 MHz, where the measured power was well above thermal noise for the three configurations. It assumes that losses due to RF scattering in the ice medium are negligible for the frequencies of interest, and that the field reflection coefficient does not depend significantly on incidence angle of the two reflection configurations. We verified with a noise source that cable losses are negligible at these frequencies.

The Friis equation relates the power received ( $P_r$ ) to the transmitted power ( $P_t$ ) in a lossless medium at a given wavelength. For two identical antennas, separated by a distance  $d$ , it becomes

$$P_r = \frac{G_a^2 \lambda^2}{(4\pi)^2 d^2} = \frac{P_0}{d^2} \quad (3)$$

where  $G_a$  is the intrinsic gain of the antenna and  $\lambda$  is the electromagnetic wavelength. The factor  $P_0$  can be treated as a constant at each frequency for all configurations since the variation in LPDA intrinsic gain is small for the frequency interval of this study.  $P_0$  was determined from the short distance configuration with the antennas rotated to point toward each other. To account for absorption losses and possible losses upon reflection, the Friis equation is modified to

$$P_r = \frac{P_0 R G^2}{d^2} \exp\left(-2 \frac{d}{\langle L_\alpha \rangle}\right) \quad (4)$$

The factor  $R$  is the reflection coefficient, defined for power. The factor of 2 is required in the exponential if  $\langle L_\alpha \rangle$  is the electric field attenuation length, rather than a quantity associated with the power. The brackets around  $\langle L_\alpha \rangle$  indicate that the attenuation length is averaged over the full depth of the ice, and thereby integrated over the temperature dependence of the path<sup>1</sup>. Following convention, the reflection coefficient for the electric field is then  $R^{1/2}$ . The factor  $G^2$  accounts for the difference in relative antenna gain for each antenna.  $G$  is 1 for the direct bounce, where the returned signal is aligned along the receiver boresight. The orientation of the antennas remained vertical for the angled bounce configuration, so the signal pulses were emitted and received at an angle of 49.5°. At this angle in the H-plane of the antennas,  $G = 0.80$ .

1. This temperature dependence arises from the modest temperature dependence of the imaginary part of the dielectric constant of bulk ice, which is roughly one part in a thousand.

Year/site	Delay (ns)	Depth (m)
2006 [11]	$6783 \pm 10$	$577.5 \pm 10$
2009 [12]	$6745 \pm 15$	$572 \pm 6$
2010 [this work]	$6772 \pm 15$	$576 \pm 10$

Table 1: The result from this work was produced using the same  $n(z)$  model as the result in the first row. The larger final uncertainties come from using slightly larger uncertainties on the index of refraction of bulk ice.

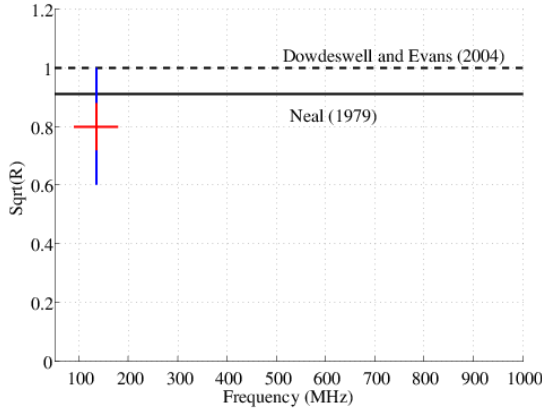


Figure 2: Expected field reflection coefficient  $R^{1/2}$  vs. frequency, for an ideal flat surface. The longest vertical error bar indicates 95% confidence. The horizontal error bar indicates the range of frequencies used in this analysis.

### 3 Data and Analysis

#### 3.1 Depth of the Ice Shelf

The thickness of the ice at the ARIANNA site can be determined by the round-trip travel time and knowledge of the index of refraction,  $n(z)$ , as a function of depth. For depths greater than 65–75 m, the ice is uniform with  $n = 1.78$ . At shallower depths, the mass density of the firn is characterized with an exponential dependence [11]. Along with the linear dependence between index of refraction and mass density, we have a complete description of  $n(z)$  in the firn ice. Table 1 summarizes the calculations of ice thickness at the ARIANNA site. The 2009 and 2010 measurements were performed at the same geographical location on the ice shelf, whereas the 2006 measurement was performed at a location about 1 km from the 2009 and 2010 tests. The round trip travel times agree to within two standard deviations. The uncertainties in the depth measurements include statistical errors in the round trip travel time and index of refraction in the uniform ice, and systematic errors due to the functional variation of  $n(z)$ . The larger errors associated with the 2006 and 2010 depths are due to slightly larger uncertainties for the index of refraction in the bulk ice.

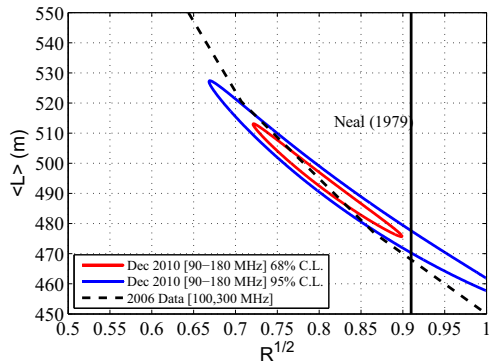


Figure 3: Contour plot of the depth averaged attenuation length  $\langle L_\alpha \rangle$  (m) vs.  $R^{1/2}$  showing 1 and 2- $\sigma$  errors. Dashed curve was obtained from [11], as explained in the text. Vertical line indicates theoretical expectation of  $R^{1/2} = 0.91$  from [9].

#### 3.2 Attenuation Length, Reflectivity and Signal Polarization

After correcting for the geometrical effects of path length for the three different configurations and relative antenna gain, the field reflection coefficient  $R^{1/2}$  and  $\langle L_\alpha \rangle$  are treated as free parameters in eqn. (4). The statistical errors in  $P_r$  were obtained from the rms fluctuation over the entire frequency band. The 1 and 2- $\sigma$  contours in figure 3 were obtained from a reduced chi-squared fit. The contours match the dashed curve, which was derived by varying the reflection coefficient  $R^{1/2}$  assumed in [11] for the quoted attenuation lengths at 100 and 300 MHz. The attenuation length is determined to be  $495 \pm 15$  m at 68 % C.L., in agreement with previous values from 2006 [11], and the field reflection coefficient  $R^{1/2} = 0.80 \pm 0.08$  at 68% C.L., in agreement with a theoretical expectation ( $R^{1/2} = 0.91$ ) for an ideal ice-saltwater interface [9].

Our measurements indicate that the field reflection coefficient at the ARIANNA site is compatible with an ideal flat surface, although values as small as 0.7 are also permitted. The reflection coefficient is not expected to vary significantly with frequency for specular reflection, as shown in figure 2. If the permittivity of sea-water is assumed to be very large for 100–1000 MHz, then the field reflection coefficient is 1 with no frequency dependence (the upper horizontal line in figure 2) [12]. In addition, multi-path effects are safely ignored in this analysis because the maximum duration of our signal pulses (100 ns) is small compared to the total propagation time.

The radio pulse from the neutrino interaction is perfectly linearly polarized, with the orientation perpendicular to the direction of the propagation of the pulse. It lies in the plane defined by the neutrino direction vector and propagation vector. Therefore, the polarization information helps to determine the direction of the neutrino, and reflected signals must retain a known correlation with the initial polarization.

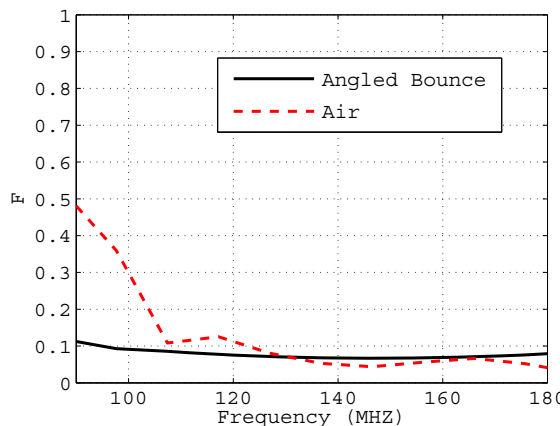


Figure 4: Polarization fraction,  $F$ , is shown as a function of frequency for transmission through air (dashed line) and for the angled bounce configuration at the ARIANNA site (solid line).

We investigate this by comparing the co-polarized power,  $P_{\parallel}$ , to the cross-polarized power,  $P_{\perp}$  for the angled bounce configuration. The fraction of cross-polarized power to total power is

$$F = \frac{P_{\perp}}{P_{\parallel} + P_{\perp}} \quad (5)$$

Figure 4 compares  $F$  for the angled bounce configuration (solid curve) to a study performed in air (dashed curve). Due to imperfections in the LPDA antennas, some power will leak into the cross-polarized configuration, representing a lower limit to  $F$ . This is estimated by air measurements with the LPDA antennas oriented to point toward each other, and separated by 10 m to avoid near-field effects. The sudden rise to a value of 0.5 (the value of  $F$  for unpolarized noise) at frequencies below 105 MHz is due to the antenna response. In air, the VSWR of the LPDA increases dramatically below 105 MHz, whereas the VSWR for LPDAs buried in snow remains low down to 80 MHz [5]. The good agreement between the angled bounce configuration and the air studies suggests that little power is transferred from the co-polarized direction to the cross polarized direction after reflection from the water-ice boundary.

#### 4 Conclusion

Preliminary studies of the site properties in the frequency band 90-180 MHz confirm large field attenuation lengths ( $495 \pm 15$  m), and show that the reflection coefficient is compatible with theoretical expectations for a smooth saltwater-ice interface ( $R^{1/2} = 0.80 \pm 0.08$ ), and signal polarization is preserved. Further work is required over multiple baselines to distinguish the smooth water-ice hypothesis from potential small losses due to surface roughness

at the ARIANNA site. We note that Neal [9] reported very small levels of surface roughness at sites in the RIS characterized by large reflection coefficients at 60 MHz. Such small effects will have little, if any, impact on signal attenuation and time profiles if similar values for vertical rms fluctuations from flatness and horizontal correlation lengths are found at higher frequencies.

#### 5 Acknowledgements

This work was supported by the U.S. NSF Office of Polar Programs and the U.S. NSF Physics Division, award numbers 0839133 and 0970175, and by the Dept. of Energy under contract DE-AC-76SF-00098. We also thank the dedicated staff of Raytheon Polar Services for their logistical support of the ARIANNA program.

#### References

- [1] Askaryan,G., Soviet Physics JETP, 1962, **14**: 441-442
- [2] Barwick,S. (ARIANNA Collab.), J. Phys.: Conf. Ser., 2007, **60**: 276-283
- [3] Hoffman, K. *et al.* (ARA Collab.) J. Phys.: Conf. Ser., 2007, **81**(1): 012022
- [4] Gorham, P. *et al.* (ANITA Collab.), Phys. Rev. D, 2010 **82**: 022004
- [5] Gerhardt, L. *et al.* Nucl. Inst. and Meth., 2010 **624**(1): 85-91
- [6] Gorham, P. *et al.* (ANITA Collab.), Phys. Rev. 2007, **99**: 171101
- [7] ARIANNA Collaboration, paper 0144, these proceedings.
- [8] Neal, C.S., J. Glaciology, 1979, **24**(90): 295-307
- [9] Neal, C.S., Annals of Glac., 1982, **3**: 216-221
- [10] Besson, D. *et al.* Astropar. Phys., 2008, **2**: 130-157
- [11] Barrella, T. *et al.* J. Glaciology, 2011 **57**(201): 61-66
- [12] Dowdeswell, J.A. and Evans, S. Rep. Prog. Phys. **67**: 1821

# A prototype station for ARIANNA: a detector for cosmic neutrinos

Lisa Gerhardt, Spencer Klein, and Thorsten Stezelberger

Nuclear Science Division, Lawrence Berkeley National Laboratory, Berkeley CA, 94720  
USA

Steve Barwick, Kamlesh Dookayka, and Jordan Hanson

Department of Physics, University of California, Irvine, CA 92697, USA

Ryan Nichol

Department of Physics and Astronomy, University College London, United Kingdom

## Abstract

The Antarctic Ross Iceshelf Antenna Neutrino Array (ARIANNA) is a proposed detector for ultra-high energy astrophysical neutrinos. It will detect coherent radio Cherenkov emission from the particle showers produced by neutrinos with energies above about  $10^{17}$  eV. ARIANNA will be built on the Ross Ice Shelf just off the coast of Antarctica, where it will eventually cover about  $900 \text{ km}^2$  in surface area. There, the ice-water interface below the shelf reflects radio waves, giving ARIANNA sensitivity to downward going neutrinos and improving its sensitivity to horizontally incident neutrinos. ARIANNA detector stations will each contain 4-8 antennas which search for brief pulses of 50 MHz to 1 GHz radio emission from neutrino interactions.

We describe a prototype station for ARIANNA which was deployed in Moore's Bay on the Ross Ice Shelf in December 2009, discuss the design and deployment, and present some initial figures on performance. The ice shelf thickness was measured to be  $572 \pm 6$  m at the deployment site.

## Introduction

Ultra-high energy (UHE) astrophysical neutrinos are a compelling target in high-energy particle astrophysics. Cosmic-ray protons with energies above about  $4 \times 10^{19}$  eV can interact with ambient cosmic microwave background photons, forming a  $\Delta^+$  resonance. The  $\Delta^+$  decay starts a chain whose final products include neutrinos; these are known as GZK neutrinos [1].

Observation of a significant (100 event) sample of GZK neutrinos would provide a wealth of physics information on the origin and composition of UHE cosmic rays, and would also probe some important questions in particle and nuclear physics [2]. For example, a measurement of the neutrino-nucleon cross-section would provide information about low-x parton distributions in nuclei.

Despite much effort, GZK neutrinos remain as-yet unobserved; only now are current experiments beginning to set limits on their flux. These experiments look for optical,

acoustic [3] or radio emission from neutrino showers. The current best limits come from the AMANDA optical Cherenkov detector at the South Pole [4], and from the ANITA balloon experiment [5]. ANITA circled Antarctica twice, in 2006-7 and 2008, at an altitude of 35,000 km, looking for radio waves emitted by neutrino interactions in the Antarctic ice; ANITA currently has the most restrictive limits at energies above about  $10^{19}$  eV [5]. Other groups have looked for evidence of neutrino interactions in Greenland [6] or in the horizontal air showers in the atmosphere [7]. Other experiments have also looked for radio emission from neutrino interactions in the moon [8]. In these ‘standoff’ experiments, where the neutrino interaction target is separated from the detectors, the threshold is typically above  $10^{19}$  or  $10^{20}$  eV, enough only for the upper tail of GZK neutrinos.

Other experiments, such as ARIANNA [9], RICE [10] and the proposed ARA [11] experiments, at the South Pole, avoid this problem by co-locating their receivers in the detection volume, so they have lower threshold energies, of order  $10^{17}$  eV. ARIANNA benefits from the strong radio reflectivity of the ice-water interface below the ice shelf; this interface reflects radio waves from downward-going neutrinos, greatly increasing ARIANNA’s angular coverage [9]. Since UHE neutrinos are absorbed by the earth, this leads to a large increase in effective area.

### Radio emission from neutrino showers

Particle showers from neutrino interactions in Antarctic ice produce short duration ( $\sim 1$  ns) radio pulses via a process known as the Askaryan effect [12]. The pulse occurs because electromagnetic and hadronic showers produced in neutrino interactions (or by any other high-energy interaction) contain more electrons than positrons. The excess electrons are created late in the shower, when the average shower particle energy is near the critical energy, 79 MeV in ice; this is when the shower multiplicity is at its highest. Then, photons Compton scatter from atomic electrons, while shower positrons can annihilate on atomic electrons. These factors lead to a net negative charge; the magnitude of the excess is about 25 % of the total number of charged particles in the shower [13].

As these particles move faster than the speed of light in the medium, they emit Cherenkov radiation. At wavelengths that are large compared to the lateral spread of the shower, the Cherenkov amplitudes add coherently, and the Cherenkov radiation scales as the square of the charge excess, i.e. as the square of the neutrino energy. In ice, this coherence holds for radio waves with frequencies up to a few GHz. Near the maximum frequency, the radiation is narrowly concentrated near the Cherenkov angle; as the frequency decreases, the spread around the Cherenkov angle becomes wider. Accelerator studies have shown that calculations of the Askaryan effect are accurate [13].

## **ARIANNA – the concept**

GZK neutrinos travel great distances through the universe and arrive at the earth isotropically. Since the GZK neutrinos are energetic enough to be absorbed while travelling through the earth, most of the neutrinos that can be observed near the surface are either travelling near horizontally or in a downward direction.

ARIANNA observes the radio pulses generated by UHE neutrino interactions with oxygen and hydrogen nuclei in the ice of the Ross Ice Shelf. These interactions produce a shower of particles which in turn produce a radio pulse with a forward directed conical emission pattern; radiation is centered on the Cherenkov angle, about 41 degrees in ice. If the neutrino is travelling downward, the cone of radio waves will travel down to the saltwater-ice boundary (located 570 m beneath the snow surface), which acts like a mirror and reflects the pulse back to the top surface of the ice shelf. This reflection greatly increases the angular acceptance of ARIANNA and drives its design. ARIANNA consists of an array of autonomous stations that are deployed on the surface. Each station consists of 4-8 directional antennas. To maximize the sensitivity to reflected events, the antennas are oriented to point downward.

ARIANNA will be sited in Moores Bay on the Ross Ice Shelf ( $78^{\circ} 44' 523''$  S,  $165^{\circ} 02' 414''$ ), which is about 110 km south of McMurdo station, the main US base in Antarctica. The stations will be installed over a 30 km x 30 km region. A high ridge, Minna Bluff, separates Moores Bay from McMurdo, so it blocks the vast majority of anthropogenic radio noise. Except for a few aircraft overflights a day during the Austral summer, we expect very small levels of impulsive radio noise at the ARIANNA site.

## **The Prototype Detector**

To test out the ARIANNA concept, and also to learn more about the site and the technology, we built a prototype detector which was deployed at the ARIANNA site for 1 year. The main goals were to study:

- Radio signal attenuation in the ice and reflection at the ice-seawater interface
- Radio backgrounds, especially anthropogenic noise
- Wind speed, with an eye to using a wind generator to power the station
- Temperature profiles over the year
- Performance of the prototype hardware in the Polar environment

## **Detector Overview**

Figure 1 shows a block diagram of the prototype detector. Four log-periodic dipole antennas are buried in the Ross Ice Shelf in Moore's bay. Each antenna feeds a low-noise amplifier, which itself feeds a switched capacitor array (SCA) analog-to-digital

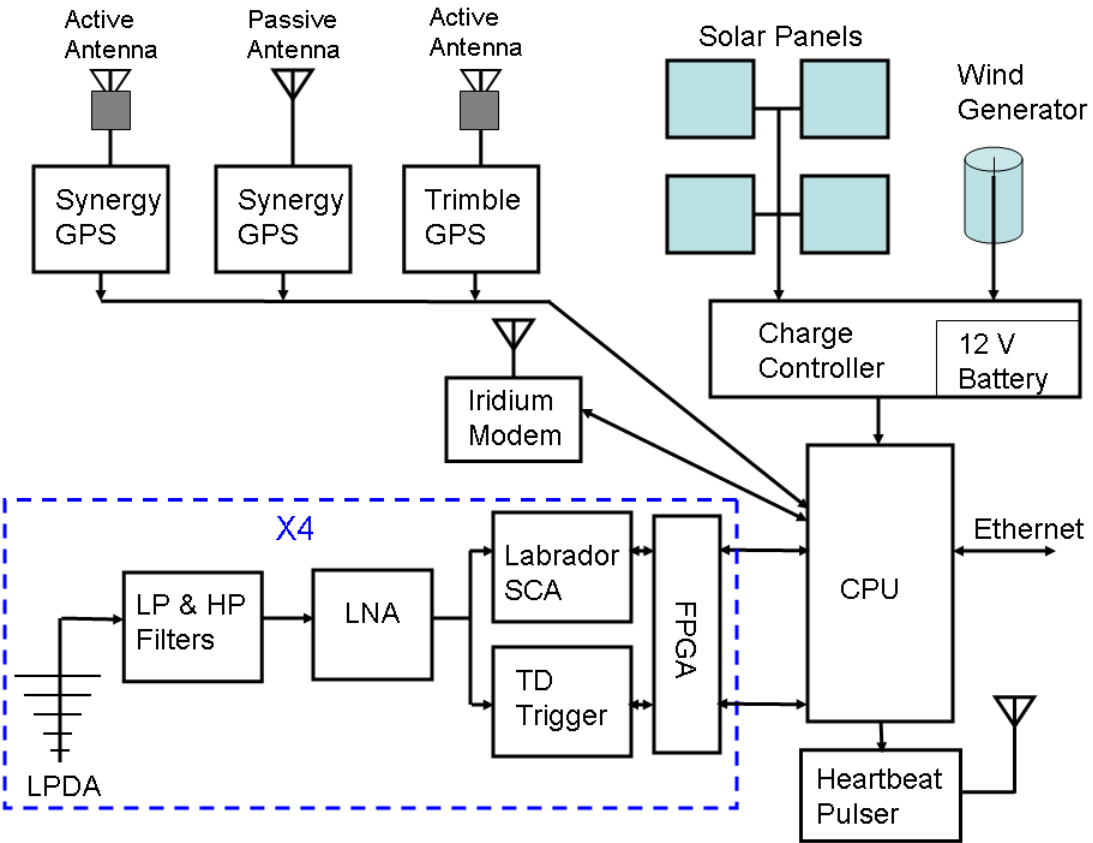


**Figure 1.** Block diagram of the ARIANNA prototype electronics. Each log periodic dipole antenna (LPDA) feeds low-pass (LP) and high-pass (HP) filters (in series), a low noise amplifier (LNA) which go to a tunnel diode (TD) trigger and the Labrador switched capacitor array (SCA) digitizer. The trigger and SCA are controlled by a field programmable gate array (FPGA). The 3 GPS receivers were for comparison purposes. The ‘heartbeat’ pulser transmits test pulses.

converter (ADC) and programmable trigger circuit. The SCAs are digitized and read out whenever the trigger fires. The standard trigger requires signals in at least two of the four antennas.

The system is controlled by a PC104plus linux-based computer with an 8 GByte flash disk. GPS receivers are used for accurate time-keeping. The station has 3 GPS receivers, so we can compare two different models; for one model we are comparing two versions, with active and passive antennas.

The station communicates via an Iridium satellite modem. During the summer, it also had a wired Ethernet connection which was connected to a wireless Bridge station. This station communicated with a repeater which was installed on Mt. Discovery, about 40 km away, which in turn connected to McMurdo Station. When fully operational, the station

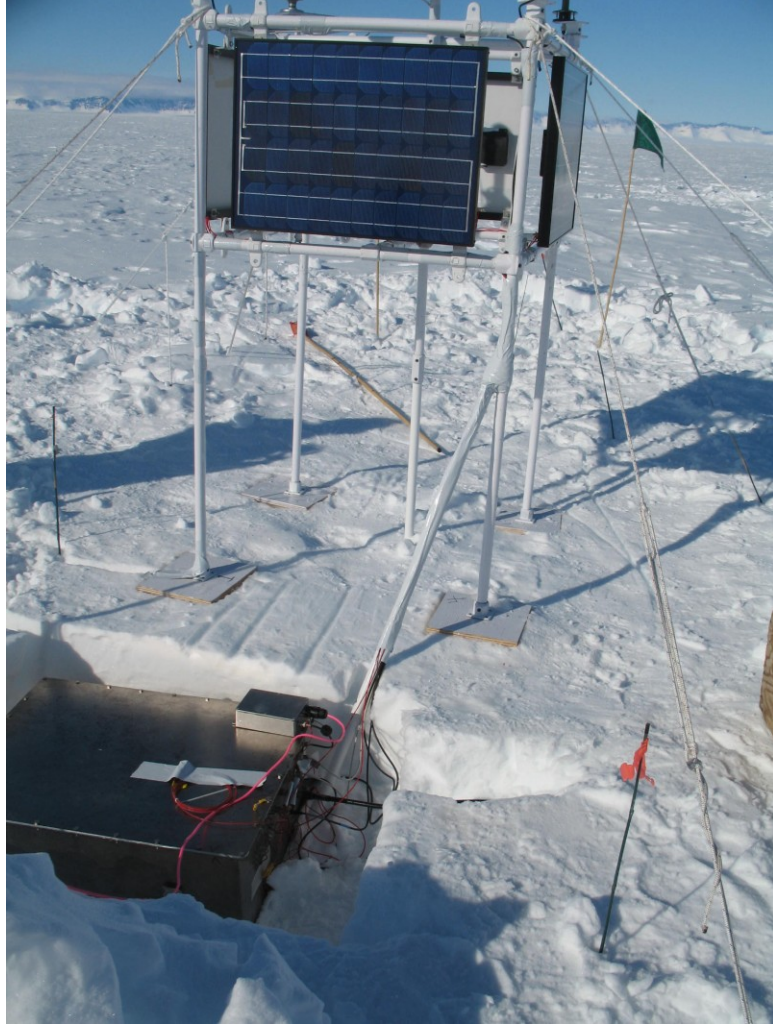


**Figure 2.** A photo of the ARIANNA station during installation, showing the tower structure and solar panels. The main electronics box is visible in the foreground, before being covered in snow. The small box with the pink cable is an Ethernet converter module. The plywood supports were later buried in snow. For scale, the four tower support legs form a square with sides about 96 cm long.

consumes about 25 Watts. During the summer, power is provided by four 30-Watt solar panels. In the winter, a Forgen 1000LT wind generator will provide some power. The power controller includes a gel battery to buffer the generators through periods of darkness (during the spring/fall) and/or low winds. The computer can turn off various pieces of the station (including data collection) to reduce the power consumption.

Most of the electronics are in a steel box which is buried with its top flush with the snow level. The power controller and battery are in a separate box, which was buried about a foot away. The antennas, four solar panels, a wind generator and an anemometer are mounted on a square tower structure shown in Fig. 2. The tower is constructed of aluminum pipe held together with cast aluminum fittings, supported (on the ground) by plywood ‘feet’. The plywood and pipes were painted white to minimize solar heating. The towers are stabilized by 8 guy lines (each  $\frac{1}{4}$  inch nylon rope) each tied to ‘deadman’

anchors – roughly 40 cm long pieces of bamboo which were buried about 40 cm under the ice. The plywood ‘feet’ were covered in snow for additional support.

The prototype was deployed in Moore’s Bay, from Dec.11-Dec. 21, 2009, where it will collect data for approximately one year. During the installation of the station, we also collected data on various performance metrics.

## Ice

The ice shelf is a key part of our detector. The prototype was deployed at GPS coordinates  $78^{\circ} 44' 523''$  S,  $165^{\circ} 02' 414''$  East, about 110 kilometers south of McMurdo station). This is about 1 km from the original site coordinates. There, the ice is about 572 m thick (the details of our measurement are discussed below). The shelf is solid ice at depths greater than about 75 m, but above this it is firn, a gradual transition from packed snow (at the surface) to ice. A plot of the measured density vs. depth for the Ross Ice Shelf is given in Fig. 2 of Ref. [14]; the transition to solid ice occurs at a shallower depth than in central Antarctica.

The surface is flat and relatively featureless. However, from first-hand observations, it is clear that the surface density of the snow varies. We made 4 measurements of snow density; one at the surface, two at a depth of 30-cm, and another about 46 cm deep. For each, we used a saw and a shovel to cut a roughly 10 cm by 10 cm by 15 cm cube of snow and weigh it. These measured snow density at the surface was  $0.32 \text{ g/cm}^3$ , while the other measures were about  $0.4 \text{ g/cm}^3$ . These values are consistent with the roughly  $0.36 \text{ g/cm}^3$  in Ref. [14].

We also probed the deeper ice by bouncing signals off the ice-water interface; these measurements are discussed below.

## Antennas

The ARIANNA prototype uses four Creative Design Corp. CLP5130-2 [15], 17-element log-periodic dipole antennas, much like VHF/UHF TV antennas. Ideally, the antennas would be oriented pointing down, forming a square, so that two antennas are sensitive to each polarization. Because of the need to avoid the ‘deadman’ anchors for the guy wires, the antenna pairs (North and South, East and West) were deployed parallel to each other, but not in a square; this departure from the ideal is only relevant in considering relative arrival times for perpendicular antennas (i.e. East and North). The antennas are connected to the prototype box by 6 meters of LMR-600 cable.

The antennas are designed for frequencies (in air) of 105 to 1300 MHz. They are specified to have an 7-8 dBi forward gain in free space, and half power angles of  $60\text{-}70^{\circ}$  in the E plane, and  $110\text{-}130^{\circ}$  in the H plane; this provides a good ‘field of view’ for neutrino hunting. They have 50 ohm impedance and a quoted VSWR of 2:1 or better across our frequency range of interest.

The antennas, which have a 1.4 m boom length, were buried by digging pits about 1.8 m deep, 1.8 m long and 30 cm wide. The antennas were buried pointing down, with their topmost element between 15 cm and 25 cm below the surface. At this depth, the snow-air interface can still affect the received radiation.

Snow has an index of refraction different from air, so the antenna environment will affect both the antenna frequency response and impedance. For radio waves, the index of refraction depends linearly on snow density, and is almost independent of frequency [16]; a density of 0.4 g/cm<sup>3</sup> corresponds to a dielectric constant of 1.8 (index of refraction,  $n$ , about 1.34). This may alter the impedance of the antenna spine, reducing the impedance matching with the preamplifier.

We studied this by comparing the voltage standing wave ratio (VSWR) with the antenna in air (about 1 ½ m above the snow surface), lying flat on the snow, buried in an air-filled pit, and buried in snow. It should be noted that the snow in the refilled hole might not have been the same average density as the undisturbed snow, and, despite efforts to pulverize the snow before filling the hole, that the snow density was not perfectly uniform. Also, the antennas burials were shallow enough that there may be effects from the snow-air interface.

The VSWR was measured with an Agilent “FieldFox” N9912A network analyzer. Figure 2 shows the VSWR for one antenna at the different stages of deployment. There are clear changes in the VSWR, with the positions of various small resonances changing with the conditions. However, in the region from 200 to 1200 MHz, the VSWR is always less than 2.5. At higher frequencies, the VSWR rises, except for the study with the buried antenna; it may be that the increased dielectric constant shifted this increase to higher frequencies.

At low frequencies, the VSWR for the first three conditions increases dramatically below 100 MHz; for the buried antenna, the increase is at a lower frequency, 80 MHz. This is not surprising; for a given frequency, the wavelength in ice is reduced by a factor  $1/n$ , so one might expect the response of a fixed-size antenna to be shifted to somewhat lower frequencies.

Also, the snow moderates the increase in VSWR seen at low frequencies. The antennas in the air filled holes exhibits significant variation with frequencies; this may be due to some sort of a resonant effect from the width of the hole. Small antenna-to-antenna differences were seen in the VSWR, likely due to slight mechanical differences in assembly.

### Low Noise Amplifiers

The Low Noise Amplifiers (LNAs) amplify the received antennas signals before they are fed into the trigger and the digitizer. One LNA is used per antenna. In the prototype, an 800MHz low pass filter and a 50MHz high pass filter at the input of the LNA block out of band frequencies. This is to remove local generated signals, for example from the

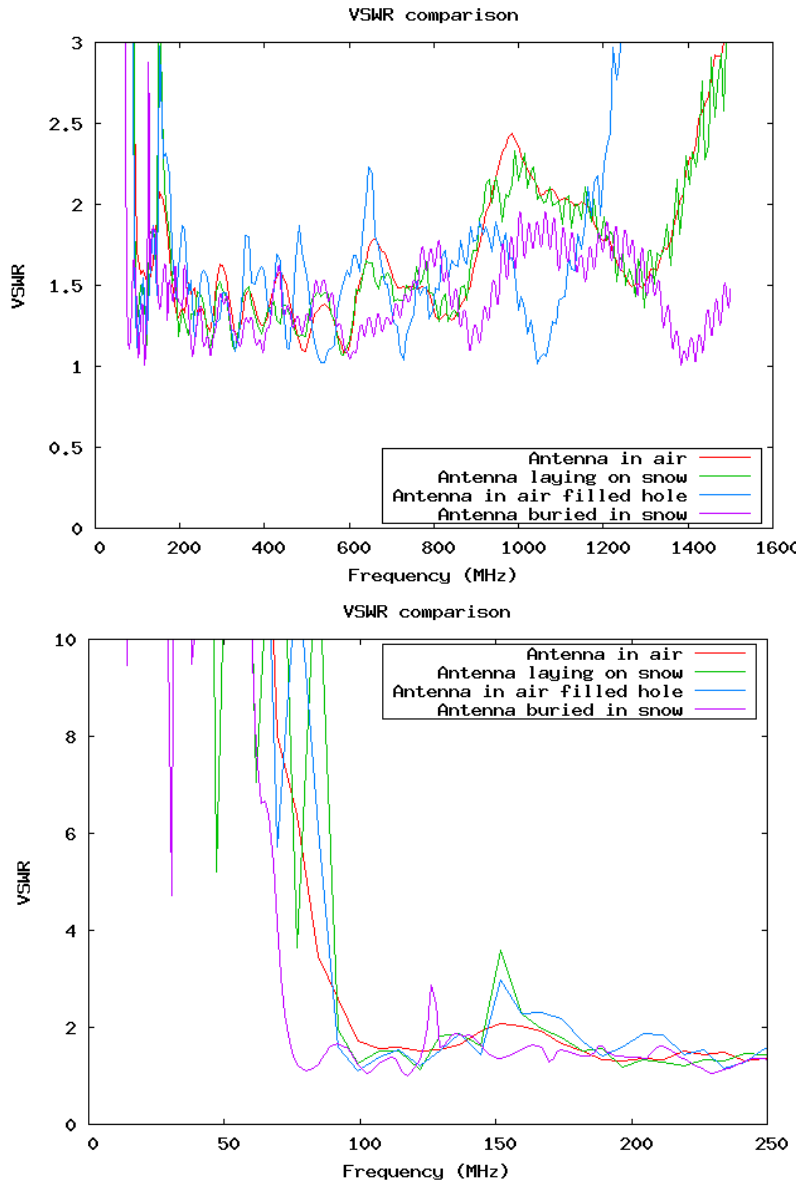


**Figure 3.** Voltage Standing Wave Ratios (VSWR) for one of the log periodic dipole antennas under different conditions, (top) from 50 to 1500 MHz and (bottom) up to 250 MHz. Although the visible peaks and valleys move around depending on the antenna's environment, the VSWR remains below 2.5 in the range of 200 MHz to 1200 MHz, and is generally below 2. It is likely that some of the larger peaks seen in the air filled holes are due to resonances. The VSWR increases dramatically below 100 MHz for the first three cases, and above 80 MHz for the antenna buried in snow.

802.11 WiFi link and the Iridium modem and external signals like short wave radio stations. In addition the 50MHz high pass reduces low frequency reflections, which could form standing waves in the antenna cable.

Each LNA has 4 stages, each consisting of an Avago MGA-68563 GaAs MMIC amplifier. They are broadband, with a gain of 58 dB from 50MHz to 1GHz, and a quoted noise figure of 1.1 dB. The chips are run off of +5V and the power consumption is 250 mW/channel.

To prevent coupling and feedback, each amplifier is individually shielded. In addition, the 4 LNAs are mounted in a shielded box with filtered power feed throughs to prevent possible coupling from other system components like the CPU.

### Data Acquisition and Trigger Circuitry

The data acquisition system is a modified version of the system used on the ANITA balloon flight [5]. Data is recorded with a LABRADOR [17] ASIC which is a switched capacitor array (SCA) waveform sampler. Each channel of the trigger uses a tunnel-diode detector and FPGA discriminator [18]. The whole setup is controlled by a Xilinx Spartan 3 field-programmable gate array (FPGA).

The LABRADOR SCA is a single chip with 8 channels (plus a 9<sup>th</sup> reference timing channel), each containing 260 (256+4) capacitors. The chip has an analog bandwidth of approximately 1 GHz, and, in ARIANNA, samples at 2.5 Giga-samples/second (GSPS). Each antenna is connected to one channel. A 5<sup>th</sup> channel is connected to a 40 MHz clock; this is used to calibrate the sampling rate. The other four channels are unused. The chip has 2340 Wilkinson ADCs, so can digitize all of the stored samples in parallel, to 12 bits, in under 50  $\mu$ s.

The trigger circuit divides the input signal into two frequency bands: 130 to 460 MHz and 650 to 990 MHz. The low-band frequencies are defined by a Mini-Circuits LFCN-320 low-pass filter and a discrete LC circuit, while the high-band is defined by a Mini-Circuits HFCN-650 high-pass filter and a LFCN-800 low-pass filter. The filters have a fairly gradual roll-off; the low-band had a -3dB roll off of 460 MHz, so the intermediate ‘gap’ was not so important. The two bands were used to allow for improved background rejection of low or high frequency noise. Each band feeds a tunnel diode based trigger which acts as a square-law detector. After amplification the tunnel diode feeds an FPGA-based discriminator with a programmable threshold [19].

The circuit threshold is electrically adjustable. Each of the 8 trigger bits (two frequency bands for four channels), are connected to the FPGA, which forms a logical trigger. For most of the prototype running, we used a trigger that ORed the outputs of the two frequency bands from a single antenna, and required at least two of the antennas to trigger.

The prototype station detected significant noise at 300 MHz and 600 MHz, most likely the subharmonics of the 2.4 GHz wireless carrier used to communicate with McMurdo station. So, the thresholds for the lower frequency tunnel diodes were set quite high; most of the triggers were formed using the higher frequency bands.

When the system triggers, the FPGA initiates a LABRADOR digitization cycle and reads out the chip. Data is stored uncompressed, and can be transmitted North over the wireless or Iridium modem.

## **Control, Communication, and Housekeeping**

The entire system is controlled by a PC104plus based computer [20]. The processor is a 133MHz AMD ELAN, running Slackware 12.2 Linux. The disk is an 8 GByte solid state disk divided into a system and a data partition. The interface to the data acquisition and trigger circuitry is done via USB2.0. In addition to the USB interface the CPU uses several serial ports to talk to peripherals and a Analog/Digital I/O card. The serial ports are assigned to a serial console for debugging work, to an Iridium data modem, and to three GPS receivers.

Only 1 GPS receiver is required, but several different devices were deployed for testing. The first GPS receiver, a Trimble Resolution T, was used before and was known to work. The other two GPS receivers are “M12M Timing Oncore™”, which are specified with higher accuracy and lower power consumption. One has an active antenna and the other uses a passive antenna.

The Analog/Digital I/O card is a Diamond – MM-AT-104. It monitors the battery and power supply voltages, measure current draw, and monitors 3 temperature sensors and an anemometer that measures the wind speed. The digital outputs control solid-state power switches which can shut down parts of the station to reduce power consumption. The switches control the RF amplifier, SCA and readout, GPS units, Iridium modem, Trimble GPS, anemometer, heartbeat pulser, and the Ethernet media converters.

Until early February, the system communicated primarily via a wired Ethernet connection to a wireless relay station (erected by the McMurdo Station IT Communications Department) about 15 meters away; the electronics for this relay were removed in early February, before the Austral winter began.

To minimize the possibility of radio interference on the Ethernet connection, a pair of media converters was used. The twisted pair signals from the computer were converted to coaxial cable Ethernet inside the box. Outside the box, a separate unit converted the coaxial signals back to twisted pair Ethernet.

After the wireless link was removed, the station communicated via an Iridium satellite modem. It is configured to ‘call home’ once every 15 minutes during the summer and 3h during the winter, giving housekeeping data and a few sample waveforms. During this period, most of the data is stored on the flash drive for retrieval next Astral summer.

## **Power System**

Power is a problem for any Antarctic experiment, especially one that will work through the sunless winter. When fully operational, the deployed ARIANNA prototype draws about 25 Watts; much of this goes to the computer (~7W), the data acquisition and trigger circuitry (~5.5W) and the Ethernet media converters (8W); in the next version of the station, the power consumption will be significantly reduced.

The system has two power sources: four 30-Watt solar panels and a Forgen 1000LT wind driven generator. The power generated is buffered by a 100 Ah gel sealed lead-acid battery to bridge windless periods during the Antarctic night. The battery is about 30% efficient at Antarctic temperatures (buried, the battery temperature is expected to be around -28<sup>0</sup>C).

The four solar panels provide ample energy to power the system during the summer, and even during ‘shoulder periods’ when the sun sets for part of the day. This will be the primary data collection period for the prototype.

The wind generator produces about 10 Watts in a 15 m/s (~30 knots) wind. This may provide enough power to provide partial operation during the winter with the data acquisition system turned off, so the system is largely recording housekeeping data. A major goal of this mode is to gather environmental data to determine if there is enough wind to generate useful power during the winter.

In case wind power is inadequate, we installed two autonomous temperature loggers, one inside the buried electronics box and one on the frame near the GPS antennas. These loggers record the temperature every 30 minutes for a year, function down to -78<sup>0</sup>C, and do not require an external power supply.

### **Calibrations and the “Heartbeat” system**

To verify system performance and overall functionality during the winter, the prototype includes a “Heartbeat” pulser, an Avtech: AVP-AV-1S-P-UCIA, connected through about 10 meters of cable to another CLP5130-2 LPDA antennas, also buried pointing downward, at about a 45 degree angle to the other antennas. The pulser produces a single pulse with a width of about 1.5 ns FWHM and amplitude 6 volts (into 50 ohms).

It is programmed to pulse at the beginning of each run, and should provide a quick ‘liveness’ test and also a continuing calibration signal.

### **Ice Soundings**

During the field season, we studied the properties of the ice sheet by transmitting signals from one buried antenna to another, bouncing them off of the ice/water interface. The Avtech “Heartbeat” pulser was used as a transmitter.

For this, we instrumented the receiving antenna with a Miteq AM-1660-11326 low-noise amplifier; this module has a 58 db gain from 1 kHz to 1 GHz, with a roughly 1.4 dB noise figure. A 1 GHz low pass filter and a 150 MHz high-pass filter were installed before the Miteq LNA; the low pass filter was needed to remove 2.4 GHz RF from a



**Figure 4.** Oscilloscope trace of the signal reflected from the ice-water interface. Signal averaging (65536 averages) was used. The main reflected pulse train is about 15 ns long.

wireless network connection installed in camp, while the 150 MHz filter removed low-frequency oscillations due to reflections in the antenna cable from the antenna and the amplifier.

The data was recorded by an Agilent DSO7054A oscilloscope with an adjustable delay. The oscilloscope was triggered with the same signal that triggered the Avtech pulser. Data was taken with both parallel antennas orientations (e.g. North to South) and perpendicular (e.g. North to East). Figure 4 shows an example of a reflected trace, using signal averaging; the pulse-to-pulse jitter was small. The reflected pulse is about 20 ns long. This is consistent with what is expected from a smooth ice-water interface. For comparison, Fig. 5 shows a similar signal, taken when two antennas were placed facing each other (nose-to-nose) with a 2.7 m spacing, in air. Here, no low-pass filter was used. The signal is somewhat longer for the air-to-air transmission, likely because there was less attenuation of low-frequency components. However, the two signals are quite compatible, indicating that the ice-water interface provides smooth reflection

For both the parallel and perpendicular orientations, a return signal was observed at time  $t = 6.745 \mu\text{s}$  after the original downgoing pulse; the pulse amplitude at the oscilloscope input was about 6 mV peak-to-peak for the parallel orientation, and about 1/3 that for the perpendicular orientation. This is consistent with the expectations due to the antenna radiation patterns. Signal averaging was required to accurately measure these signals. We attribute a  $\pm 15 \text{ ns}$  uncertainty to the round-trip travel time, to account for uncertainties in the cable lengths, geometry, and arrival times (due to the pulse width).

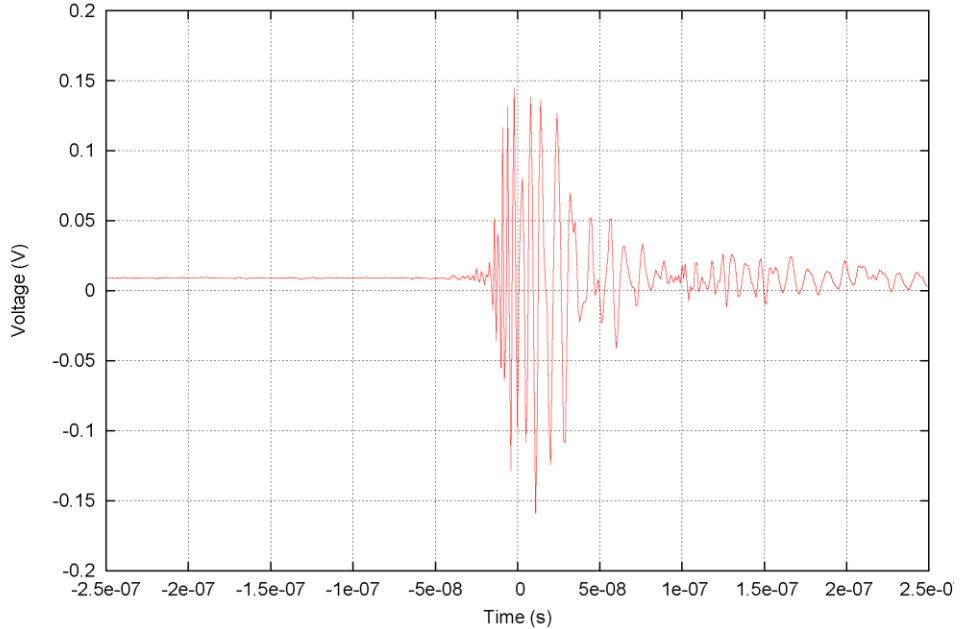


**Figure 5.** The transmitted signal from an Avtech pulser sent between two CLP5130-2 LPDA antennas sitting head-to-head, in air, separated by 2.7 m.

The relationship between the round-trip travel time and the ice thickness depends on the index of refraction in the ice, which itself depends on the density, and, to a much lesser extent, on the possible presence of impurities [14, 21]. The ice in Moore's bay is glacial ice, so should be free of impurities; we do not see any evidence of infiltrating brine layers in the radio reflections.

Our calculation follows Ref. [14]. The index of refraction,  $n$ , is the square root of the dielectric constant  $\epsilon$ . The index of refraction of pure, solid ice has a very slight temperature dependence,  $\epsilon = (3.18 \pm 0.01) + (8 \times 10^{-4} T)$ , where  $T$  is in Centigrade. The ice temperature varies with depth, from near  $0^{\circ}\text{C}$  at the ice-water interface, to about  $-20^{\circ}\text{C}$  just below the surface [22]. We assume a mean temperature (averaged over the radio path) of  $-10 \pm 5^{\circ}\text{C}$ , giving an average index of refraction of  $n=1.78$  for solid ice. The upper 75 m of ice is firn, which has a lower density, where the radio signal will travel faster;  $(n-1)$  scales linearly with the density. Dowdeswell and Evans [22] treat this region by including a correction in the calculated ice thickness:

$$D = \frac{1}{2} \left( \frac{ct}{n} + z_f \right)$$

where  $c$  is the speed of light. For the Ross Ice Shelf, the correction  $z_f$  is  $+7 \pm 2$  m. From this, we find a thickness of 572 m, with uncertainties due to the travel time (5 m), temperature (1 m), index of refraction (1 m) and firn correction (2 m), giving a total uncertainty of  $\pm 6$  m.

## Conclusions

ARIANNA is designed to detect cosmic GZK neutrinos; it will eventually comprise an array with an active volume of at least  $100 \text{ km}^3$  with a threshold of around  $10^{17} \text{ eV}$ .

We have built a prototype detector which reads out four log-periodic dipole antennas, using switched capacitor array digitizers. The prototype was deployed in Moore's Bay, Antarctica, in December 2009, where it will collect data for one year, providing valuable information about conditions during the Antarctic winter and backgrounds for a neutrino search. We also bounced radio signals off the ice-water interface, and measured an ice thickness of  $572 \pm 6 \text{ m}$ .

Work on the next prototype is beginning now. This will be an integrated design, with simpler electronics interfaces and greatly reduced power consumption. It will likely incorporate 8 antennas per station, quite possibly including one upward-facing antenna for background rejection. This design will be used in a 7 station array to be deployed within 2-3 years.

## Acknowledgements

We thank Martha Story for invaluable help with camp management and David Saltzberg for useful conversations. Gary Varner and Larry Ruckman developed much of the data acquisition system. We thank the National Science Foundation, Office of Polar Programs for major logistical support. This work was funded in part by the National Science Foundation under grant number 0653266, by the Department of Energy under contract number DE-AC-76SF-00098 and by the Royal Society.

## References

- [1] K. Greisen, Phys. Rev. Lett. **16** (1966) 748; G. T. Zatsepin and V. A. Kuz'min, JETP Lett. **4** (1966) 78.
- [2] F. Halzen and S. Klein, Phys. Today **61N5** (2008) 29.
- [3] J. Vandebroucke, Giorgio Gratta, N. Lehtinen, Ap. J. **621** (2005) 301.
- [4] M. Ackermann *et al.*, Ap. J. **675** (2008) 1014.
- [5] P. W. Gorham *et al.*, arXiv:1003.2961.
- [6] N. G. Lehtinen *et al.*, Phys. Rev. **D69** (2004) 013008.
- [7] J. Abraham *et al.*, Phys. Rev. **D79** (2009) 102001.
- [8] O. Scholten *et al.*, Phys. Rev. Lett. **103** (2009) 191301; P. W. Gorham *et al.*, Phys. Rev. Lett. **93** (2004) 041101; C. W. James *et al.*, Phys. Rev. **D81** (2010) 042003.
- [9] S. Barwick, Nucl. Instrum & Meth. **A602** (2009) 279. \
- [10] I. Kravchenko *et al.*, Phys. Rev. D**73** (2006) 082002; D. P. Horgan, Nucl. Instrum & Meth. **A604** (2009) S76.
- [11] P. Allison, *et al.*, Nucl. Instr. and Meth. A **604** (2009) S64.
- [12] G. A. Askarian, JETP **14** (1962) 441.

- [13] P. W. Gorham *et al.*, Phys. Rev. **D72**, 023002 (2005).
- [14] J. A. Dowdeswell and S. Evans, Rep. Prog. Phys. **67** (2004) 1821.
- [15] <http://www.scannermaster.com/v/vspfiles/files/pdf/CLP-5130-1N-manual.pdf>
- [16] D. Besson *et al.*, Astropart. Phys. **29** (2008) 130; D. Seckel *et al.*, “Radiofrequency properties of Antarctic ice and calibration of the RICE detector,” in Proc. of the 2001 Intl. Cosmic Ray Conf.
- [17] G. S. Varner *et al.*, Nucl. Instrum. & Meth. **A583** (2007) 447.
- [18] G. S. Varner *et al.*, in *Proc. Intl. Symp. on Detector Development for Particle, Astroparticle and Synchrotron Radiation Experiments (SNIC 2006)*, Menlo Park, CA, 3-6 Apr 2006.
- [19] G. S. Varner, JINST **1** (2006) P07001.
- [20] The computer is a Parvus-CPU-1421.
- [21] A. Kovacs, A. J. Gow and R. M. Morey, Cold Regions Science & Technology **23**, (1995) 245.
- [22] D. MacAyeal, O. Sergienko T. Scambos, and A. Muto. 2008. *Ross Ice Shelf firn temperature, Antarctica*. Boulder, Colorado USA: National Snow and Ice Data Center. Digital Media.

## Detection and Imaging of $\text{He}_2$ Molecules in Superfluid Helium

W. G. Rellergert, S. B. Cahn, A. Garvan, J. C. Hanson, W. H. Lippincott, J. A. Nikkel, and D. N. McKinsey\*

*Department of Physics, Yale University, New Haven, Connecticut 06520, USA*

(Received 10 September 2007; revised manuscript received 15 November 2007; published 15 January 2008)

We present data that show a cycling transition can be used to detect and image metastable  $\text{He}_2$  triplet molecules in superfluid helium. We demonstrate that limitations on the cycling efficiency due to the vibrational structure of the molecule can be mitigated by the use of repumping lasers. Images of the molecules obtained using the method are also shown. This technique gives rise to a new kind of ionizing radiation detector. The use of  $\text{He}_2$  triplet molecules as tracer particles in the superfluid promises to be a powerful tool for visualization of both quantum and classical turbulence in liquid helium.

DOI: 10.1103/PhysRevLett.100.025301

PACS numbers: 67.25.D-, 29.40.Gx, 67.25.dk

Ionizing radiation events in liquid helium produce unstable  $\text{He}_2$  molecules in both singlet and triplet states [1–4]. The singlet state molecules radiatively decay in a few nanoseconds [5], but the triplet state molecules are metastable because a radiative transition to the ground state of two free atoms requires a strongly forbidden spin flip. The radiative lifetime of the triplet molecules has been calculated to be 18 s in vacuum [6] and measured to be 13 s in liquid helium [7]. Here we present data supporting our previous proposal [8] to detect and image the triplet molecules by driving them through multiple fluorescence-emitting transitions during their lifetime.

The lowest-lying electronic states and two relevant vibrational levels of the triplet molecules are shown in Fig. 1, as well as one cycling transition used to detect them. Two infrared photons can excite a triplet molecule from the ground  $a^3\Sigma_u^+$  state to the  $d^3\Sigma_u^+$  state. Calculations of the branching ratios indicate that about 10% of the excited molecules will decay to the  $c^3\Sigma_g^+$  state, while the remaining 90% will decay to the  $b^3\Pi_g$  state, emitting detectable red photons at 640 nm. Molecules in both the  $c^3\Sigma_g^+$  and  $b^3\Pi_g$  states then decay back to the  $a^3\Sigma_u^+$  state, and the process can be repeated. Since the  $d^3\Sigma_u^+ \rightarrow b^3\Pi_g$  transition emits a photon that is well separated in wavelength from the excitation photons, scattered laser light can be blocked by appropriate filters. As the entire cycle occurs in roughly 50 ns, it could in principle be repeated enough times to allow for single molecule detection.

The molecular structure complicates matters because molecules in an excited electronic state may decay to excited rotational or vibrational levels of the electronic ground state. If those levels have long relaxation times, and are out of resonance with the excitation lasers, the rate at which a molecule can be cycled is greatly reduced. For  $\text{He}_2$  molecules in the liquid, the absorption spectral lines are  $120 \text{ cm}^{-1}$  wide [4,9], which is considerably larger than the spacing of the rotational levels ( $7 \text{ cm}^{-1}$ ) [10]. The vibrational levels, on the other hand, are separated by about  $1500 \text{ cm}^{-1}$  [10], and the vibrational relaxation time is over 100 ms [9]. Therefore, molecules falling to excited vibrational levels of the  $a^3\Sigma_u^+$  state are trapped in off-resonant

levels and are lost for subsequent cycles. They can be recovered, however, with the use of repumping lasers. As an example, a molecule that decays to the first vibrational level of the  $a^3\Sigma_u^+$  state,  $a(1)$ , can be driven into the zeroth vibrational level of the  $c^3\Sigma_g^+$  state,  $c(0)$ , with light at 1073 nm (Fig. 1). Our calculations of the Franck-Condon factors imply that a molecule in  $c(0)$  will decay back to  $a(0)$  around 95% of the time. As there are only two excited vibrational levels below  $b(0)$ , two repumping lasers are likely all that are needed to ensure that molecules are recovered for high cycling rates in this scheme.

A typical 1 MeV electronic recoil event in liquid helium creates about 32 000  $\text{He}_2$  molecules. About 60% of those molecules are created in the singlet state and 40% are

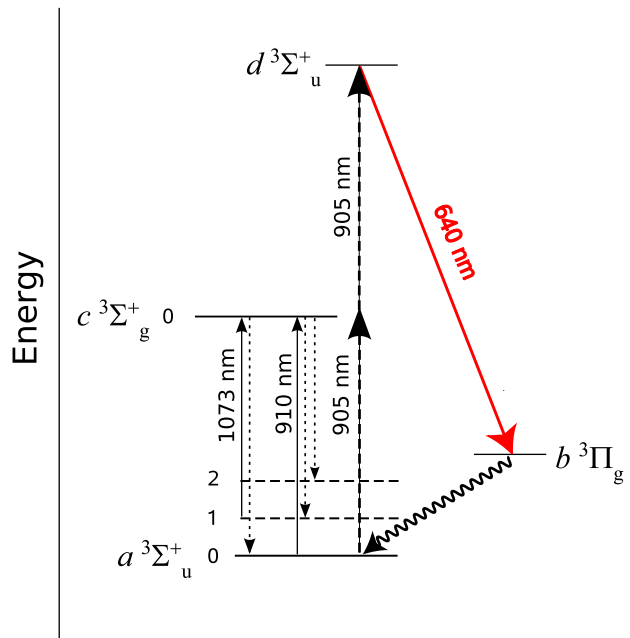


FIG. 1 (color online). Shown schematically are the lowest energy levels of the  $\text{He}_2$  triplet molecule in liquid helium. A cycling transition used to detect and image the molecules is indicated, as well as transitions that control the populations of the  $a^3\Sigma_u^+$  vibrational levels.

created in the triplet state [11]. For our laser-induced fluorescence studies, we used a  $1 \mu\text{Ci}$   $^{113}\text{Sn}$  beta source immersed in the superfluid ( $1.9 \pm 0.1$  K) to create the molecules. The 364 keV betas emitted by the  $^{113}\text{Sn}$  nuclei deposit most of their energy within 1 cm [11] of the source and create about  $2.5 \times 10^8$  triplet molecules in steady state. Laser beams illuminate this region, and the resulting fluorescence is recorded with either a photomultiplier tube or a camera as shown in Fig. 2.

Figure 3(a) shows excitation spectra we obtain by scanning a tunable  $Q$ -switched pulsed laser [12] in combination with a continuous-wave diode laser. The wavelength of the pulsed laser is scanned from 760 to 1200 nm in steps of 1 nm. The pulse energy is 5 mJ and the repetition rate is 2 Hz. The pulsed laser beam is overlapped with the diode laser beam and both are expanded to a spot size of  $1 \text{ cm}^2$ . The solid red curve shows the fluorescence signal as the pulsed laser is scanned with a  $60 \text{ mW/cm}^2$  diode laser at 1073 nm. The filters used to block the scattered excitation light allow for the detection of fluorescence in the wavelength range from 515 to 750 nm. Peaks in the fluorescence signal are observed when the pulsed laser wavelength is at either 800 or 905 nm. The wavelength dependence of the fluorescence is measured with a monochromator equipped with short-pass filters that transmit wavelengths less than 875 nm. For both 800 and 905 nm excitation, all observed fluorescence is contained in one peak centered at 640 nm, which is consistent with  $d^3\Sigma_u^+ \rightarrow b^3\Pi_g$  emission [Fig. 3(b)]. It should be noted that the wavelength resolution is limited by the slit size of the monochromator. A fit of the average fluorescence signal detected by the photo-

multiplier tube yields  $48 \pm 2$  ns for the  $d^3\Sigma_u^+$  state lifetime [Fig. 3(c)].

The fluorescence resulting from laser pulses near 800 nm was previously observed by Benderskii *et al.* [13,14]. By calculating potential energy curves for molecules in liquid helium, they determined that the  $d^3\Sigma_u^+$  state is shifted up in energy when the molecule is in the liquid. The shift is attributed to the change in size of the bubble formed by the molecule. The two-photon absorption line at 800 nm is therefore thought to drive  $a(0) \rightarrow c(1) \rightarrow d(2)$ . As the difference in energy between two 905 nm photons and two 800 nm photons is  $3000 \text{ cm}^{-1}$ , which is roughly twice the expected spacing for the vibrational levels of the  $d^3\Sigma_u^+$  state [10], it is likely that the peak at 905 nm is driving  $a(0) \rightarrow c(0) \rightarrow d(0)$ . As our attempts to produce more fluorescence by using two pulsed lasers at different wavelengths were unsuccessful, a single pulse at 905 nm appears to be the most efficient way to excite the molecules to  $d(0)$ . Being able to excite the molecules with only one pulsed laser, instead of two as originally proposed [8], is a major simplification. With single wavelength excitation, 2D position information can be obtained by either rastering the laser beam or taking an image with a camera. A second scan (or image) in an orthogonal direction can then yield 3D information.

The dashed blue curve in Fig. 3(a) shows the resulting fluorescence when a  $90 \text{ mW/cm}^2$  diode laser at 910 nm is substituted for the diode laser at 1073 nm. Shown schematically in Fig. 1, this laser depletes  $a(0)$  by driving

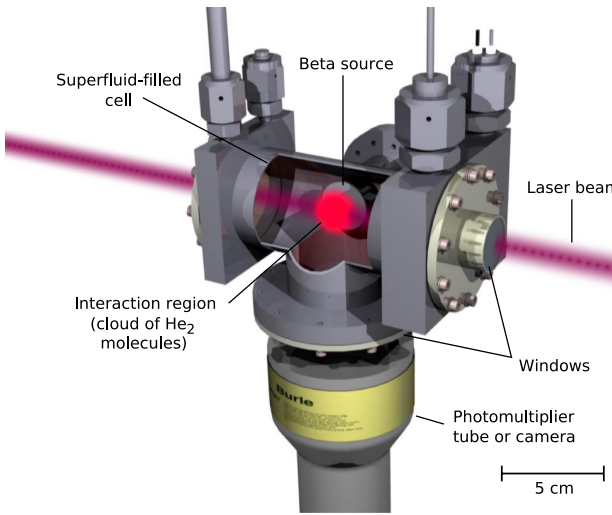


FIG. 2 (color online). Experimental setup. Lasers enter and exit the superfluid-filled cell through 25 mm diameter windows and a light detector views the interaction region through a 25 mm diameter window on the bottom of the cell. The cutaway section in the middle shows the radioactive beta source and the interaction region. The source is deposited on a 25 mm diameter metal disk and is mounted on a flange on the side of the cell. It can also be mounted from the top of the cell.

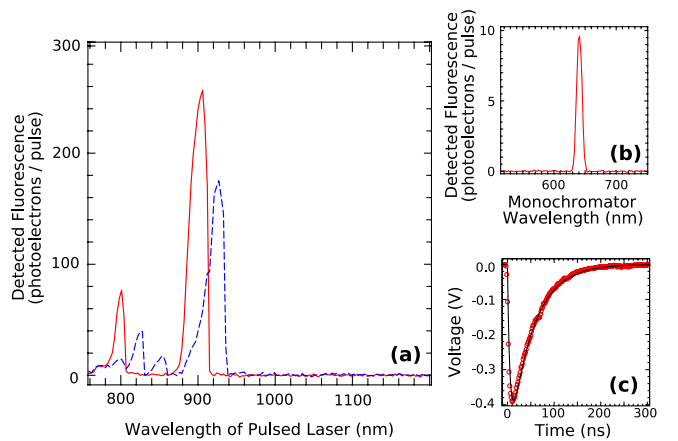


FIG. 3 (color online). Laser-induced fluorescence data. (a) Two excitation spectra obtained by scanning a pulsed laser from 760 to 1200 nm in combination with a diode laser are shown. The solid red line shows the fluorescence signal intensity when a diode laser at 1073 nm is used. The dashed blue line shows the signal when a diode laser at 910 nm is substituted for the 1073 nm diode laser. (b) The wavelength dependence of the fluorescence resulting from laser pulses at 905 nm is measured using a monochromator. All observed fluorescence is centered at 640 nm. (c) The red circles show the average trace from a photomultiplier tube when the pulsed laser is fixed at 905 nm. The black line shows a fit which gives a  $48 \pm 2$  ns lifetime for the  $d^3\Sigma_u^+$  fluorescence.

molecules into  $a(1)$  and  $a(2)$ , which are long lived. The peaks at 800 and 905 nm are significantly reduced showing that the population of  $a(0)$  is indeed lowered, and new peaks in fluorescence are observed at 825, 850, and 925 nm. The suspected excitation scheme for these peaks is  $a(1) \rightarrow c(2) \rightarrow d(3)$  for 825 nm,  $a(2) \rightarrow c(3) \rightarrow d(4)$  for 850 nm, and  $a(1) \rightarrow c(1) \rightarrow d(1)$  for 925 nm.

The ability to repump molecules that fall to  $a(1)$  is demonstrated in Fig. 4, which shows the dependence of the fluorescence signal on the pulse number in a sequence of 64 consecutive pulses of 905 nm laser light ( $2.5 \text{ mJ/cm}^2$ ). Before the pulse sequence, the laser pulses are blocked with a shutter for 6.4 s to allow the molecules to come to equilibrium. The shutter then opens, and the molecules are excited with a laser pulse every 100 ms for 6.4 s. The shutter then closes, and the process is repeated. Figure 4 shows the average of ten such consecutive pulse sequences both with and without the use of a repumping diode laser. Without a repumping laser, the signal drops to 25% of the initial value by the tenth pulse indicating that molecules are being lost by some mechanism when cycled. With the addition of a diode laser at 1073 nm, however, the signal remains above 85% of the initial value. These data demonstrate that the molecules are indeed being cycled multiple times, that the primary loss mechanism is deexcitations to  $a(1)$ , and that the molecules in  $a(1)$  can be driven back to  $a(0)$  by a repumping laser.

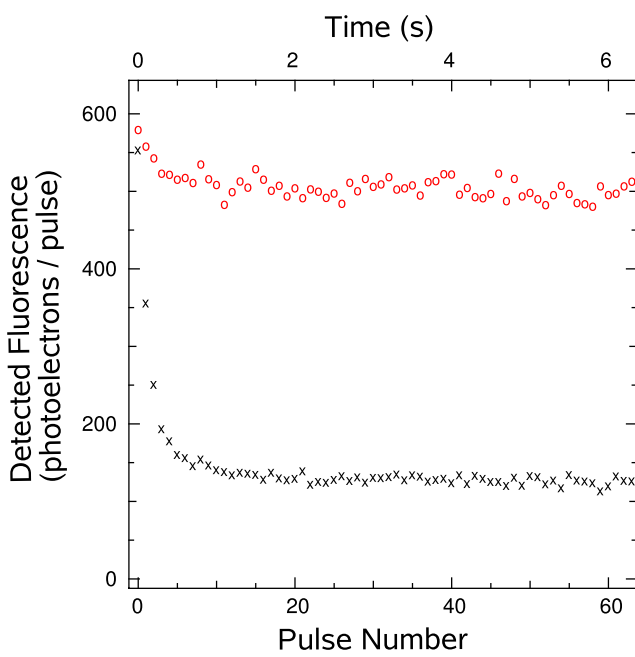


FIG. 4 (color online). These data show the dependence of the fluorescence signal on the pulse number in a sequence of 64 consecutive pulses of 905 nm laser light. Without a repumping laser (black  $\times$ 's), the signal drops to 25% of the initial value by the tenth pulse. With the addition of a diode laser at 1073 nm (red circles), however, the signal remains above 85% of the initial value.

The size of the signal in Fig. 4 can be used to obtain a lower bound on the percentage of molecules that are emitting a 640 nm photon. Taking into account the laser beam size and its position, we estimate that it overlaps at most 30% of the molecules produced by the beta source. The solid angle subtended by the photomultiplier tube (0.75%), its quantum efficiency (5%), and the transmission of the various windows and optical filters (30%) indicate that about 1 out of every  $10^4$  emitted photons are detected. Therefore, detection of more than 500 photoelectrons suggests that for each pulse at least 5% of the molecules in the laser beam are emitting a 640 nm photon.

Images of the molecules are obtained with amplified CCD cameras. A false-color image of the cloud of molecules created by the beta source is shown in Fig. 5(a). The fluorescence is produced by pulsing one laser at 905 nm and a second laser at 925 nm, exciting molecules in both  $a(0)$  and  $a(1)$ . The repetition rate of each laser is 10 Hz, and the pulse energies are 5 mJ. The total exposure time is 5 min. The spatial extent of the cloud agrees with the expected beta particle track length of 1 cm taking into account the 5 mm distance from the laser beam to the source. An image taken with a collimator on the beta source is shown in Fig. 5(b). A single pulsed laser at 905 nm and a 60 mW/cm<sup>2</sup> continuous-wave repumping laser at 1073 nm are used to produce the fluorescence. The repetition rate and pulse energy are again 10 Hz and 5 mJ, respectively, but the exposure time is 2.5 min. As expected, the shape of the cloud is determined by the limited angular spread of the beta particle trajectories.

The technique outlined above gives rise to a new detector technology using liquid helium. In addition to the qualities and applications of such a detector that have already been proposed [8], the method may be useful for a Compton gamma ray imager. If a gamma ray scatters in liquid helium and is subsequently absorbed in a second detector, the locations of those events and total energy deposited can be used to kinematically determine the energy and trajectory of the incoming gamma ray.

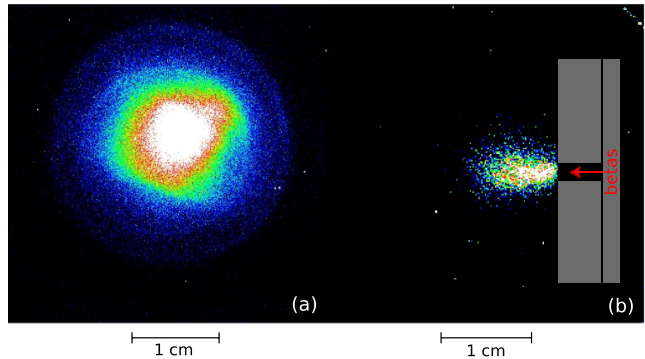


FIG. 5 (color online). Images of the molecules obtained using amplified CCD cameras. In (a) the beta source is facing the camera. In (b) the image is formed by collimating the beta source and imaging it from the side. A sketch of the source and collimator has been added to show its location.

Helium has three characteristics that are desirable for such a detector. First, the low atomic number of helium makes it more likely that a gamma ray will scatter in the liquid rather than be absorbed. Second, the uncertainty in the initial momentum of the electron from which a gamma ray scatters is smaller than it would be for materials with higher atomic numbers, leading to a lower uncertainty in the determination of the initial energy and direction of a scattered gamma ray. Finally, the track of molecules produced by the recoiling Compton electron may be imaged to further reduce the uncertainty in the initial gamma ray direction.

Laser-induced fluorescence of the molecules also provides a new tool for visualization of quantum and classical turbulence in liquid helium [15–17]. Particle image velocimetry has been used to visualize liquid helium flows [18,19], but it appears that the required micron-sized particles are too large to act as passive tracers. A possible reason is their interaction with vortices in the liquid. The He<sub>2</sub> triplet molecules are much smaller (7 Å radius [14]) and should be unaffected by vortices at temperatures above 1 K [20]. Also, the small size of the molecules might allow for resolution of the Kolmogorov length scale. Additionally, at sufficiently low temperatures the molecules will become trapped on vortices [20] as has been observed for ions [21,22] and micron-sized solid hydrogen particles [23]. Stereoscopic imaging of the laser-induced fluorescence of the molecules could then be used to obtain 3D images of vortex lines and their dynamics in the superfluid.

Seeding the flow with the triplet molecules can be done in a relatively easy and unintrusive manner with a radioactive source or an intense, focused laser pulse. By adding a heater in the liquid helium, and monitoring the distribution of the triplet molecules as a function of heater power, one can obtain their diffusion coefficient in the same way that neutron absorption tomography allowed for the determination of the diffusion coefficient of <sup>3</sup>He [24]. That information also allows one to obtain velocity fields in liquid helium [25].

In addition, the vibrational levels of the triplet molecule can be used to image and tag a group of molecules in a specific region of the liquid and image their location some time later. For example, after pumping all molecules into *a*(0), a laser pulse at 800 or 905 nm will result in  $d^3\Sigma_u^+ \rightarrow b^3\Pi_g$  fluorescence and also create a population in *a*(1) which would otherwise not be present. A well collimated laser pulse at one of those wavelengths can therefore be used to image a line of molecules, and, a short while later, a second, expanded laser pulse at 925 nm would show how that line has deformed by imaging those molecules that fell to *a*(1) after the first excitation. This method is similar to that of a study that used oxygen molecules to measure turbulence in air, and allows one to measure transverse velocity increments which can be used to determine the

single-point probability density of velocity fluctuations [26].

In conclusion, we have detected and imaged He<sub>2</sub> triplet molecules in liquid helium using laser-induced fluorescence. We have demonstrated good control over the vibrational structure of the molecules with the use of continuous-wave diode lasers which allow the molecules to be cycled multiple times over the course of their 13 s lifetime. The cycling rate has so far been limited only by the 10 Hz repetition rate of our lasers.

This work was supported by the Defense Threat Reduction Agency under Grant No. DTRA01-03-D-0009-0011.

\*daniel.mckinsey@yale.edu

- [1] H. Fleishman, H. Einbinder, and C. S. Wu, Rev. Sci. Instrum. **30**, 1130 (1959).
- [2] C. M. Surko and F. Reif, Phys. Rev. **175**, 229 (1968).
- [3] W. S. Dennis *et al.*, Phys. Rev. Lett. **23**, 1083 (1969).
- [4] J. C. Hill, O. Heybey, and G. K. Walters, Phys. Rev. Lett. **26**, 1213 (1971).
- [5] P. C. Hill, Phys. Rev. A **40**, 5006 (1989).
- [6] C. F. Chabalowski *et al.*, J. Chem. Phys. **90**, 2504 (1989).
- [7] D. N. McKinsey *et al.*, Phys. Rev. A **59**, 200 (1999).
- [8] D. N. McKinsey *et al.*, Phys. Rev. Lett. **95**, 111101 (2005).
- [9] V. B. Eltsov, A. Y. Parshin, and I. A. Todoshchenko, Sov. Phys. JETP **81**, 909 (1995).
- [10] G. Herzberg, *Molecular Spectra And Molecular Structure Vol. I—Spectra Of Diatomic Molecules* (Krieger, Malabar, FL, 1950).
- [11] J. S. Adams, Ph.D. thesis, Brown University, 2001.
- [12] EKSPLA Model NT342/1.
- [13] A. V. Benderskii *et al.*, J. Chem. Phys. **110**, 1542 (1999).
- [14] A. V. Benderskii *et al.*, J. Chem. Phys. **117**, 1201 (2002).
- [15] J. J. Niemela and K. R. Sreenivasan, J. Low Temp. Phys. **143**, 163 (2006).
- [16] W. F. Vinen, J. Low Temp. Phys. **145**, 7 (2006).
- [17] D. Charalambous *et al.*, J. Low Temp. Phys. **145**, 107 (2006).
- [18] T. Zhang and S. W. Van Sciver, J. Low Temp. Phys. **138**, 865 (2005).
- [19] C. M. White, A. N. Karpetis, and K. R. Sreenivasan, J. Fluid Mech. **452**, 189 (2002).
- [20] W. F. Vinen, in *Low Temperature Physics*, AIP Conf. Proc. No. 850 (AIP, New York, 2006), p. 169.
- [21] E. J. Yarmchuk, M. J. V. Gordon, and R. E. Packard, Phys. Rev. Lett. **43**, 214 (1979).
- [22] W. Guo and H. Maris, J. Low Temp. Phys. **148**, 199 (2007).
- [23] G. P. Bewley, D. P. Lathrop, and K. R. Sreenivasan, Nature (London) **441**, 588 (2006).
- [24] S. K. Lamoreaux *et al.*, Europhys. Lett. **58**, 718 (2002).
- [25] M. E. Hayden *et al.*, Phys. Rev. Lett. **93**, 105302 (2004).
- [26] A. Noulez *et al.*, J. Fluid Mech. **339**, 287 (1997).

## **Research Application: Exploration of Antarctic Ice Sheets with Drones**

A gap exists in Askaryan-based UHE-v science. We have made detailed measurements of the RF attenuation length in ice, a critical parameter in our detector designs. However, we cannot currently repeat this measurement throughout detector ice volumes, which would cover kilometers of ice in every direction away from the center of IceCube-Gen2 at the South Pole. Though measurements from aircraft have been collected elsewhere, there is very little aircraft data near the South Pole.

### **The Open Polar Server Data Gaps, and Drones**

The Open Polar Server (OPS) is a service provided by CReSIS at the University of Kansas (KU). Researchers may download data from Greenland and Antarctica. The data are recorded from aircraft over the ice, and the RF attenuation length can be extracted from radar echoes. There are three disadvantages to flight data. First, there may not be a flight near the detector. Second, flights only give a snapshot of the ice at the time. Third, the bandwidth of CReSIS radar does not always overlap with the proposed IceCube-Gen2 bandwidth. There is a trade-off between spatial and temporal data in radio sounding. A plane flight covers hundreds of kilometers, once. Conversely, an embedded station records data over time, but only at one location.

A dedicated drone could constrain the attenuation length in both regimes. In my machine shop and RF design lab, a student and I constructed a 3D printed drone, with 1 kg payload, powered by LiPo batteries. Before the pandemic hit, we had plans to equip it with solar charging and cold-temperature components. A similar effort is underway at CReSIS at KU: Prof. Emily Arnold of the KU Dept. of Aerospace Engineering has begun an NSF CAREER grant to utilize RC military drones to study the Jakobshavn glacier in Greenland. Thus, there is a potential for collaboration between CReSIS and IceCube-Gen2 and PUEO to solve a common problem: the rechargeable ice attenuation length measurement system. Our drone design can be 3D printed and assembled from commercial parts for < \$1k.

### **Connection to Whittier Scholars Program, Office of Naval Research, and Climate Science**

This research ties together several aspects of our other research programs at Whittier College, connecting climate science, neutrino physics research, and RF engineering. We seek to mount RF transmitting antennas to the drone, along with a transceiver payload. We need a lightweight, broadband RF antenna suited to the task. Thus, our ONR research into 3D printing RF antennas designed with the MIT Electromagnetic Equation Propagation (MEEP) package connects to the drone research. We are currently working on 3D printed RF antennas designed with MEEP that will serve IceCube Gen2 and the Navy in a variety of ways. By constructing a drone capable of landing and recharging in a polar environment, we would unlock a new regime of climate-related measurements by improving the time and spatial resolution of glaciological measurements.

Two undergraduate researchers have helped with this research. The first was a physics and business double major, who helped design and 3D-print the drone, which has autonomous flight capability. The second is a Whittier Scholars Program major who graduated after completing several expeditions to Iceland, Alaska, and Montana to study glaciers. The hope was that he could have performed test flights in Antarctica with the drone, however that expedition was impeded by the pandemic. This student helped further design and test the drone. Finally, we wrote a Whittier Scholars Program thesis exploring the evolution of glaciers within a climate science context, and the connection between glaciers and culture. The work was informed by data collected from our student's expeditions, my past glaciological research, and work connected to the drone (Fig. 1). *A copy of the Whittier Scholars Program Thesis has been included in this dossier.*



**Figure 1.** Our custom designed, 3D printed quad-rotor drone with autonomous flight capability. The communications antenna is visible atop the hull. The four engines are mounted on carbon fiber arms, within 3D printed housing components. The guidance, power, and communications electronics are all contained within the hull.

## Research Application: Workforce Development for Naval Surface Warfare Systems (NSWC), Corona Division

In the Summers of 2020, 2021, and 2022, I have received Summer Faculty Research Fellowship grants from the Office of Naval Research (ONR). One of my tasks given by ONR was to develop online interactive engineering courses for new personnel. New personnel often join Navy operations, either as civilians or soldiers, with a need for customized training in fields like radar or digital signal processing (DSP).

As a STEM educator at a liberal arts institution, I have a unique set of skills that is highly valued by the Navy. I continue to create interactive engineering courses designed for a diverse audience that has a varying level of expertise in the RF engineering field. Course audiences have been new sailors or field engineers tasked with radar or RF equipment maintenance on aircraft carriers and other warships, and acquisition personnel tasked with purchasing and overseeing new surveillance, GPS, and weapons systems. These diverse personnel need to understand relevant engineering topics quickly, at the right level of detail, and at their own pace.

Luckily, my research often involves synthesizing concepts from RF, radar, DSP, and mathematical physics. I have been able to leverage my knowledge and research experiences in these areas to deliver two summer online courses for the Navy. The first was a general introduction to RF Field Engineering. The second, currently in progress, is an Introduction to GPS M-Code signals for On-boarding of Navy Personnel. Examples of content from each course are included in this dossier.

# RF Field Engineer Course: A Practical Introduction

---

Jordan Hanson

June 8, 2021

Whittier College Department of Physics and Astronomy

# Course Introduction

1. Professor Jordan Hanson
2. Email: [jhanson2@whittier.edu](mailto:jhanson2@whittier.edu), [918particle@gmail.com](mailto:918particle@gmail.com)
3. Mobile: 562-351-0047
4. Zoom Credentials: (ID) 796 092 0745 (Passcode) 667725
5. **Reading: Stimson's Introduction to Airborne Radar, 3rd Edition.** (Hughes Radar Handbook)
6. Box Folder: <https://app.box.com/s/qalsptcztyeq8hjvu3pmf4mlodmopop7>

## Summary

---

## Reading: Stimson3 ch. 1-6

- **Week 1:** Units and estimation. **Key skills:** mental math, wave concepts
  - Electromagnetic units, estimation, and decibels
  - Waves and the wave equation
  - Reflections, refraction, and diffraction
  - Phase, amplitude, frequency, polarization
- **Week 2:** Basic Training in Mathematics. **Key skills:** estimate pulse bandwidth, pulse trains and uncertainty principle
  - **Complex numbers:** applications to phasors and radio waves, complex impedance of filters and antennas
  - **Fourier series and transforms,** filters and attenuation, properties of waveforms, power spectra, and spectrograms, cross-correlation and convolution
  - **Statistics and probability:** applications to noise, signal-to-noise ratio

## Reading: Stimson3 ch. 7-11

- Week 3: RF Antenna Properties. **Key skills:** characterize an antenna, diagnose a problem with an antenna system
  - Radiation pattern, directivity, and gain
  - Complex impedance and reflection coefficient, S11, S21
  - Bandwidth, narrow and wide
  - Antenna temperature
  - Angular resolution
  - Attenuation: applications to remote sensing
- Week 4: **Electronically Scanned Antenna Systems**
  - **Basics:** spacing, wavelength, and scan angle
  - **Design classes:** AESA and PESA
  - **Wideband considerations:** Scan losses, time-delays
  - **Bonus:** FDTD demonstrations of ESAs
- Week 5: Review of Weeks 1-4, pulsed radar concepts

## Reading: Stimson3 ch. 12-13, part IV (18-22), 23

- Week 6: Range Equations. Key skills: diagnose issues with distance target detection, estimate radar cross section (RCS)
  - Radar cross-section
  - Noise and noise figure, signal-to-noise ratio (SNR)
  - Thermal noise floor and detection probability
  - Ranging techniques: pulse compression, frequency modulation
- Week 7: Overview of Pulse Doppler Radar (Cumulative Example)
  - Connections with Telemetry
  - See Stimson3 part IV
  - Connections to digital signal processing: sampling and digitization
- Week 8: Clutter and Attenuation
  - Clutter: sources and spectra
  - Attenuation: absorption and scattering, components

# Course Summary

- Week 9: Link Budgets (Cumulative Example)
  - Assembling the pieces
  - Example calculations
- Week 10: Course Review
  - Review Weeks 1-9
  - Skill Review
    1. Estimation and approximations
    2. Conceptual challenge questions
    3. Worked examples

## Estimation, Approximation, Units

---

# Estimation, Approximation, Units

RF radiation travels at a constant speed.

$$\frac{c}{n} = \nu\lambda \quad (1)$$

$$\Delta x = \left(\frac{c}{n}\right) \Delta t \quad (2)$$

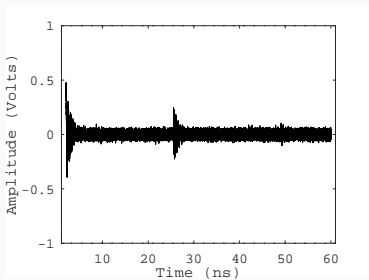
$$T = \frac{1}{\nu} \quad (3)$$

- $c$ : speed of light in vacuum, 0.299792458 m/ns,  $\approx 0.3$  m GHz
- $\nu$ : frequency of the radiation, Hz.
- $\lambda$ : wavelength of the radiation, meters.
- $\Delta x$ : displacement
- $\Delta t$ : time duration

# Estimation, Approximation, Units

A signal enters a cable that is 3 meters long and reflects at the end back towards the source. How many nanoseconds after the signal enters the cable will the signal return to the end?

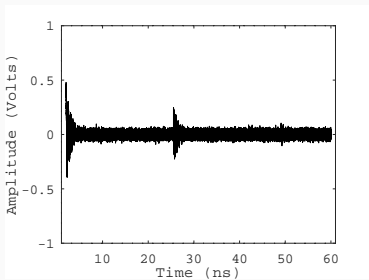
- How does it work conceptually? Distance equals speed multiplied by time duration.
- How do you correct for the speed in the cable?
- How could we apply this to radar? Remember, this is a *reflection*.



# Estimation, Approximation, Units

A signal enters a cable that is 3 meters long and reflects at the end back towards the source. How many nanoseconds after the signal enters the cable will the signal return to the end?

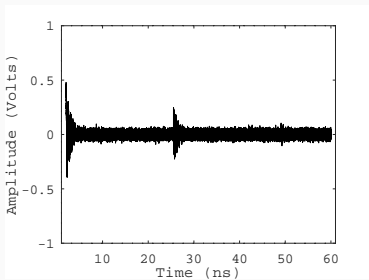
- $20 \text{ ns} \times 0.3 \text{ (m/ns)} \approx 6 \text{ m}$ .  
Why 6 meters?
- How do you correct for the speed in the cable?
- How could we apply this to radar? Remember, this is a reflection.



# Estimation, Approximation, Units

A signal enters a cable that is 3 meters long and reflects at the end back towards the source. How many nanoseconds after the signal enters the cable will the signal return to the end?

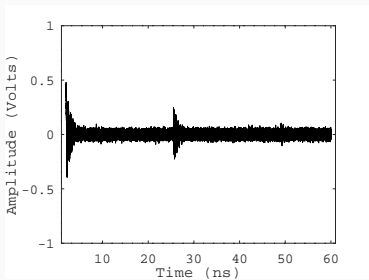
- $20 \text{ ns} \times 0.3 \text{ (m/ns)} \approx 6 \text{ m}$ .  
Why 6 meters?
- Typical speed in RF cable:  
85% speed of light. What  
is  $\Delta t$  for 6 meters at  
reduced speed?
- How could we apply this to  
radar? Remember, this is a  
*reflection*.



# Estimation, Approximation, Units

A signal enters a cable that is 3 meters long and reflects at the end back towards the source. How many nanoseconds after the signal enters the cable will the signal return to the end?

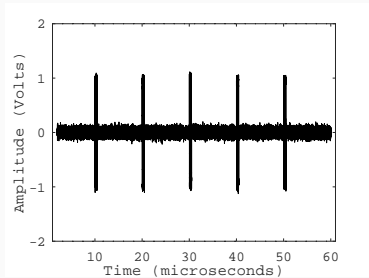
- $20 \text{ ns} \times 0.3 \text{ (m/ns)} \approx 6 \text{ m}$ .  
Why 6 meters?
- Typical speed in RF cable:  
85% speed of light. What  
is  $\Delta t$  for 6 meters at  
reduced speed?
- If a radar echo returns 30  
microseconds later, how  
far away is the reflector?



# Estimation, Approximation, Units

What does this mean? A radar system creates a 20 MHz sine wave modulated by a 5 percent duty-cycle. The pulse repetition frequency is 0.1 MHz.

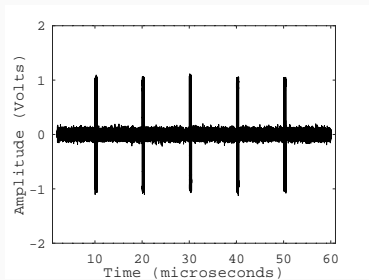
- What's the period of a 20 MHz sine wave? Which part of the waveform at left represents this oscillation?
- If a signal is repeated regularly, it has a PRF, or pulse repetition frequency. Work out the PRF of the waveform at left.
- What does duty cycle mean?



# Estimation, Approximation, Units

What does this mean? A radar system creates a 20 MHz sine wave modulated by a 5 percent duty-cycle. The pulse repetition frequency is 0.1 MHz.

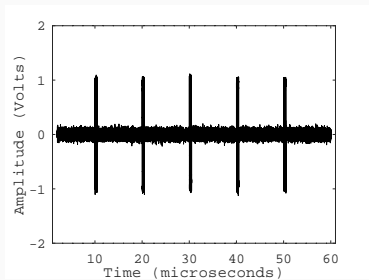
- $1/20.0 \text{ MHz}^{-1} = 0.05 \mu\text{s} = 50 \text{ ns}$ . These oscillations are within the pulses.
- If a signal is repeated regularly, it has a PRF, or pulse repetition frequency. Work out the PRF of the waveform at left.
- What does duty cycle mean?



# Estimation, Approximation, Units

What does this mean? A radar system creates a 20 MHz sine wave modulated by a 5 percent duty-cycle. The pulse repetition frequency is 0.1 MHz.

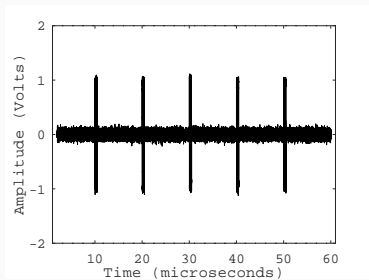
- $1/20.0 \text{ MHz}^{-1} = 0.05 \mu\text{s} = 50 \text{ ns}$ . These oscillations are within the pulses.
- It appears the pulses are separated by  $\approx 10 \mu\text{s}$ . Invert to find  $1/10 \text{ MHz}$ .
- What does duty cycle mean?



# Estimation, Approximation, Units

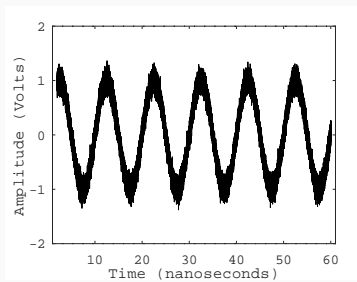
What does this mean? A radar system creates a 20 MHz sine wave modulated by a 5 percent duty-cycle. The pulse repetition frequency is 0.1 MHz.

- $1/20.0 \text{ MHz}^{-1} = 0.05 \mu\text{s} = 50 \text{ ns}$ . These oscillations are within the pulses.
- It appears the pulses are separated by  $\approx 10 \mu\text{s}$ . Invert to find  $1/10 \text{ MHz}$ .
- 100 percent corresponds a constant 20 MHz sine tone. Fifty percent is half-on, half-off ...  $D = PW/T \times 100$ .



# Estimation, Approximation, Units

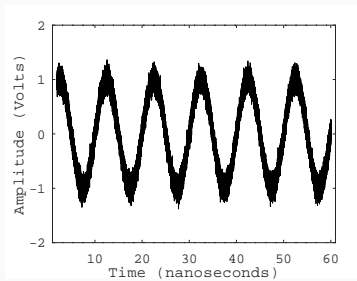
What is the wavelength of the received radio wave in the figure? Recall  $c \approx 0.3 \text{ m/ns}$ .



- What is the period? Pay attention to the units on the axes.
- What is the frequency? (How do you convert period to frequency?)
- What is the wavelength?
- What size antenna would receive this signal?

# Estimation, Approximation, Units

What is the wavelength of the received radio wave in the figure? Recall  $c \approx 0.3 \text{ m/ns}$ .

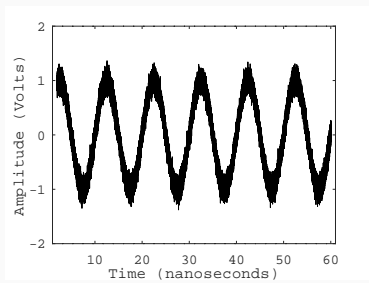


- The period appears to be about 10.0 ns.
- What is the frequency? (How do you convert period to frequency?)
- What is the wavelength?
- What size antenna would receive this signal?

# Estimation, Approximation, Units

What is the wavelength of the received radio wave in the figure? Recall  $c \approx 0.3 \text{ m/ns}$ .

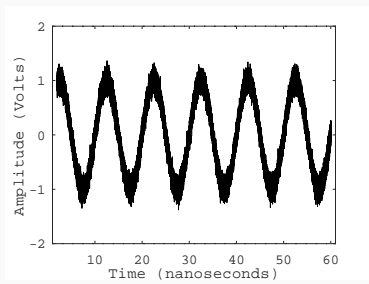
- The period appears to be about 10.0 ns.
- Invert the period:  
 $1/10 \text{ ns}^{-1} = 100 \text{ MHz}$ .
- What is the wavelength?
- What size antenna would receive this signal?



# Estimation, Approximation, Units

What is the wavelength of the received radio wave in the figure? Recall  $c \approx 0.3 \text{ m/ns}$ .

- The period appears to be about 10.0 ns.
- Invert the period:  
 $1/10 \text{ ns}^{-1} = 100 \text{ MHz}$ .
- What is the wavelength of a 100 MHz signal?



$$0.3 \text{ m GHz} = 100 \text{ MHz}(\lambda) \quad (4)$$

$$\frac{0.3 \text{ m GHz}}{100 \text{ MHz}} = \lambda \quad (5)$$

$$\lambda = 3 \text{ m} \quad (6)$$

- What size antenna?

# Estimation, Approximation, Units

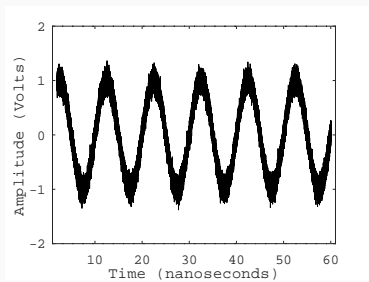
What is the wavelength of the received radio wave in the figure? Recall  $c \approx 0.3 \text{ m/ns}$ .

- The period appears to be about 10.0 ns.
- Invert the period:  
 $1/10 \text{ ns}^{-1} = 100 \text{ MHz}$ .
- What is the wavelength of a 100 MHz signal?

$$0.3 \text{ m GHz} = 100 \text{ MHz}(\lambda) \quad (7)$$

$$\frac{0.3 \text{ m GHz}}{100 \text{ MHz}} = \lambda \quad (8)$$

$$\lambda = 3 \text{ m} \quad (9)$$



- About 1.5 meter dipole.

# Decibels

---

# Decibels

RF parameters have a large dynamic range, and it becomes necessary to use logarithmic definitions.

$$P_{\text{dB}} = 10 \log_{10} \left( \frac{P_2}{P_1} \right) \quad (10)$$

$$\frac{P_2}{P_1} = 10^{P_{\text{dB}}/10} \quad (11)$$

- $P_{\text{dB}}$ : power ratio in decibels.
- $P_1$ : input power, transmitted power.
- $P_2$ : output power, received power.

## Historical motivations for the decibel:

- $V(x) = V_i \exp(-x/\lambda)$ ,  $\lambda$  is attenuation factor, such that if  $x = \lambda$  for telephone cable,  $P_{\text{dB}} \approx -1$ .

# Decibels

RF parameters have a large dynamic range, and it becomes necessary to use logarithmic definitions.

$$P_{\text{dB}} = 10 \log_{10} \left( \frac{P_2}{P_1} \right) \quad (12)$$

$$\frac{P_2}{P_1} = 10^{P_{\text{dB}}/10} \quad (13)$$

- $P_{\text{dB}}$ : power ratio in decibels.
- $P_1$ : input power, transmitted power.
- $P_2$ : output power, received power.

## Historical motivations for the decibel:

- Let  $P_1$  and  $P_2$  be the initial and final acoustic power.  
 $P_{\text{dB}} \approx -1$  represents smallest change we can hear.

# Estimation, Approximation, Units

If our transmit power is 1 W, and our return (echo) is only 2.5 mW, what is that in decibels?

$$P_{\text{dB}} = 10 \log_{10} \left( \frac{P_2}{P_1} \right) \quad (14)$$

$$\frac{P_2}{P_1} = 10^{P_{\text{dB}}/10} \quad (15)$$

1. Which is  $P_2$  and which is  $P_1$ ?  
What's the ratio?
2. Perform logarithm on power  
of 10 and decimal separately.
3. Memorize the basics.

# Estimation, Approximation, Units

If our transmit power is 1 W, and our return (echo) is only 2.5 mW, what is that in decibels?

$$P_{\text{dB}} = 10 \log_{10} \left( \frac{P_2}{P_1} \right) \quad (16)$$

$$\frac{P_2}{P_1} = 10^{P_{\text{dB}}/10} \quad (17)$$

1. Transmit power ( $P_1$ ) is 1 W, and receive power ( $P_2$ ) is 2.5 mW, so  $P_2/P_1 = 2.5 \text{ mW W}^{-1} = 2.5 \times 10^{-3}$
2. Perform logarithm on power of 10 and decimal separately.
3. Memorize the basics.

# Estimation, Approximation, Units

If our transmit power is 1 W, and our return (echo) is only 2.5 mW, what is that in decibels?

$$P_{\text{dB}} = 10 \log_{10} \left( \frac{P_2}{P_1} \right) \quad (18)$$

$$\frac{P_2}{P_1} = 10^{P_{\text{dB}}/10} \quad (19)$$

1. Transmit power ( $P_1$ ) is 1 W, and receive power ( $P_2$ ) is 2.5 mW, so  $P_2/P_1 = 2.5 \text{ mW W}^{-1} = 2.5 \times 10^{-3}$
2. Take the  $\log_{10}$  of the number and multiply by 10:  
 $10 \log_{10}(2.5) + 10 \log_{10}(10^{-3}) = -30 + 10 \log_{10}(2.5).$
3. Memorize the basics.

# Estimation, Approximation, Units

If our transmit power is 1 W, and our return (echo) is only 2.5 mW, what is that in decibels?

$P_{\text{dB}}$	$P_2/P_1$
0	1
1	1.26
2	1.6
3	2
4	2.5
5	3.2
6	4
7	5
8	6.3
9	8

1. Transmit power ( $P_1$ ) is 1 W, and receive power ( $P_2$ ) is 2.5 mW, so  $P_2/P_1 = 2.5 \text{ mW W}^{-1} = 2.5 \times 10^{-3}$
2. Take the  $\log_{10}$  of the number and multiply by 10:  
$$10 \log_{10}(2.5) + 10 \log_{10}(10^{-3}) = -30 + 10 \log_{10}(2.5).$$
3. So we know it's about  $-30$  dB. What is  $10 \log_{10}(2.5)$ ? About  $+4$ , so  $-30 + 4 = -26$  dB.

## Graphical Analysis and Radar Echoes

---

# Graphical Analysis

As an example, let's consider a radar echo, on a graph of signal frequency versus time.

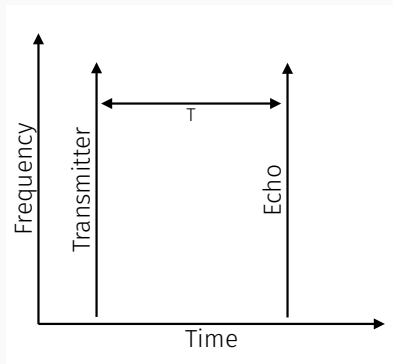


Figure 1

1. What does it mean to have a signal *at all frequencies* at a single time, for the transmitter?
2. What determines the echo time,  $T$ ?
3. How will the graph change if the radar target moves closer to the transmitter?

# Graphical Analysis

As an example, let's consider a radar echo, on a graph of signal frequency versus time.

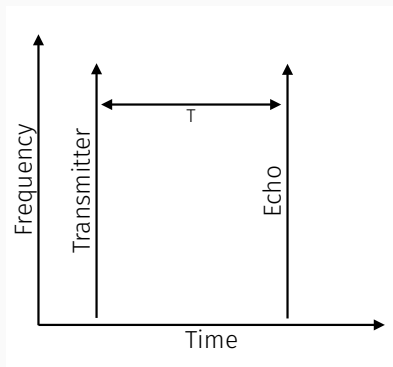


Figure 2

1. A pulse is a short time-duration signal. Pulses can be conceptualized as many signals of different frequencies added together with the right phases.
2. What determines the echo time,  $T$ ?
3. How will the graph change if the radar target moves closer to the transmitter?

# Graphical Analysis

As an example, let's consider a radar echo, on a graph of signal frequency versus time.

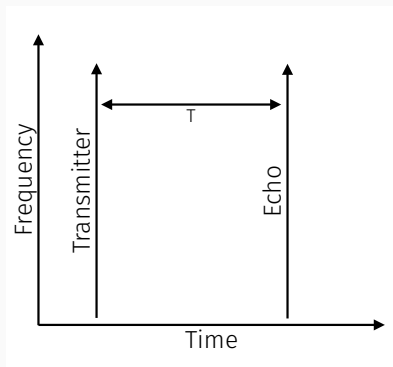


Figure 3

1. A pulse is a short time-duration signal. Pulses can be conceptualized as many signals of different frequencies added together with the right phases.
2.  $T = R/c$ , the range divided by the speed of light.
3. How will the graph change if the radar target moves closer to the transmitter?

# Graphical Analysis

As an example, let's consider a radar echo, on a graph of signal frequency versus time.

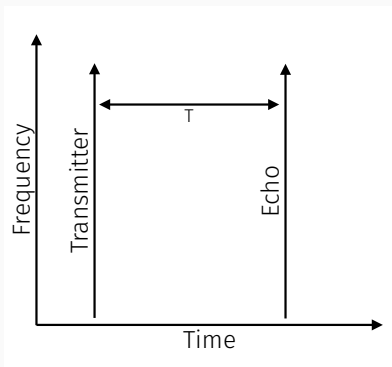


Figure 4

1. A pulse is a short time-duration signal. Pulses can be conceptualized as many signals of different frequencies added together with the right phases.
2.  $T = R/c$ , the range divided by the speed of light.
3.  $T = R/c$ , so if  $R$  decreases,  $T$  will decrease and thus the echo line will move left.

# Graphical Analysis

Now a little more complex, we consider FM ranging. Imagine the transmitter chirps, and the echo returns.

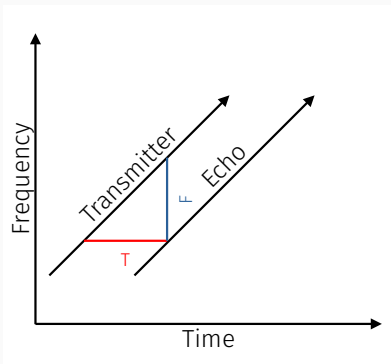


Figure 5

1. What does it mean to chirp? What is the chirp rate, and what are the units of chirp rate?
2. How are  $T$  and  $F$ , the time difference and frequency difference of the transmitter and echo, connected to range?
3. How can we derive the range without explicitly measuring  $T$ ?

# Graphical Analysis

Now a little more complex, we consider FM ranging. Imagine the transmitter chirps, and the echo returns.

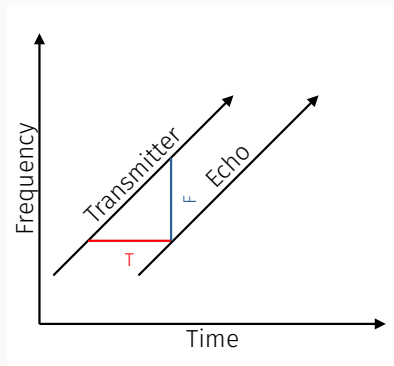


Figure 6

1. A chirp is a signal for which the frequency changes with time. The linear chirp rate is the slope of the transmitter signal, with units of  $1\text{Hzs}^{-1}$ .
2. How are  $T$  and  $F$ , the time difference and frequency difference of the transmitter and echo, connected to range?
3. How can we derive the range without explicitly measuring  $T$ ?

# Graphical Analysis

Now a little more complex, we consider FM ranging. Imagine the transmitter chirps, and the echo returns.

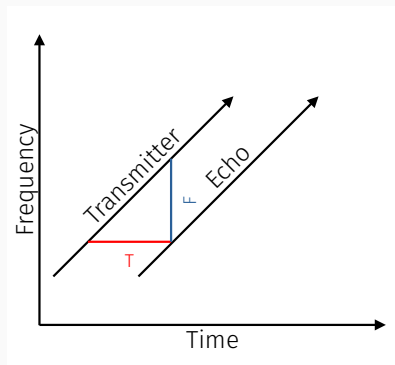


Figure 7

1. A chirp is a signal for which the frequency changes with time. The linear chirp rate is the slope of the transmitter signal, with units of  $\text{Hz s}^{-1}$ .
2.  $R = (c/2)T$ . Show that  $F = kT$ .
3. How can we derive the range without explicitly measuring  $T$ ?

# Graphical Analysis

Now a little more complex, we consider FM ranging. Imagine the transmitter chirps, and the echo returns.

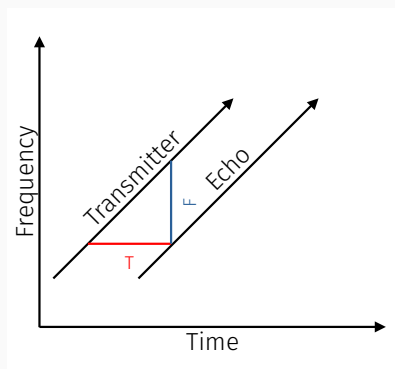
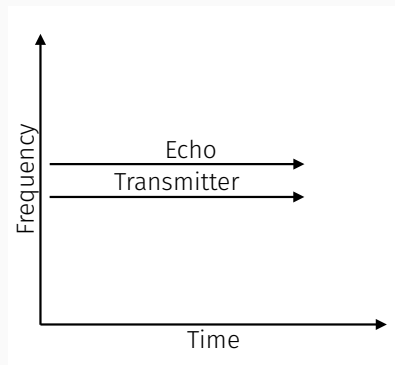


Figure 8

1. A chirp is a signal for which the frequency changes with time. The linear chirp rate is the slope of the transmitter signal, with units of  $\text{Hz s}^{-1}$ .
2.  $R = (c/2)T$ . Show that  $F = kT$ .
3. This means:  $R = (c/2)(F/k)$ , so the range can be found without measuring  $T$ . Build a chirping system that measures  $F$ .

# Graphical Analysis

Finally, the doppler shift of RF waves is a small effect introduced by relative target-source motion that changes the frequency.



1. What is significance the ratio of frequencies?
2. What is the relationship between transmitter and echo frequencies?
3. What is a practical limitation of this technique?

Figure 9

# Graphical Analysis

Finally, the doppler shift of RF waves is a small effect introduced by relative target-source motion that changes the frequency.

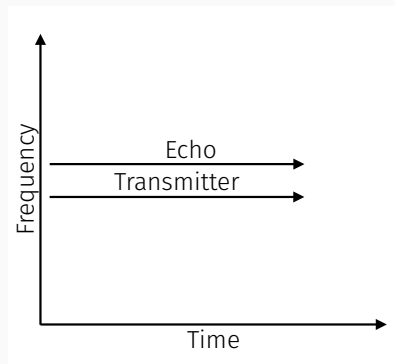


Figure 10

1. If  $f_e > f_t$ , the target is approaching the transmitter.  
If  $f_e < f_t$ , the target is moving away from the transmitter.
2. What is the relationship between transmitter and echo frequencies?
3. What is a practical limitation of this technique?

# Graphical Analysis

Finally, the doppler shift of RF waves is a small effect introduced by relative target-source motion that changes the frequency.

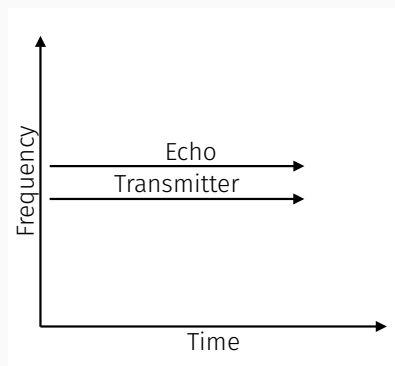


Figure 11

1. If  $f_e > f_t$ , the target is approaching the transmitter.  
If  $f_e < f_t$ , the target is moving away from the transmitter.
2.  $\Delta f \approx 2(\Delta v/c)f_t$ , with  $\Delta v$  equal to the relative velocity.
3. What is a practical limitation of this technique?

# Graphical Analysis

Finally, the doppler shift of RF waves is a small effect introduced by relative target-source motion that changes the frequency.

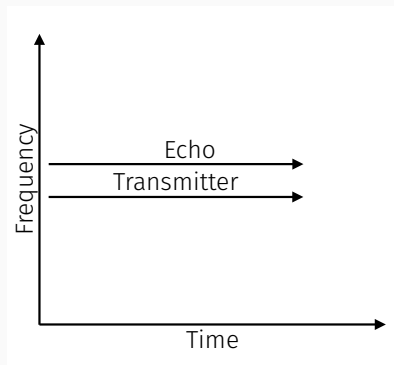


Figure 12

1. If  $f_e > f_t$ , the target is approaching the transmitter.  
If  $f_e < f_t$ , the target is moving away from the transmitter.
2.  $\Delta f \approx 2(\Delta v/c)f_t$ , with  $\Delta v$  equal to the relative velocity, and  $\Delta f = f_e - f_t$ .
3. For Earth-bound, anthropogenic targets,  $\Delta v/c \ll 1$ , so frequency shifts are very small.

## Graphical Analysis

Finally, the doppler shift of RF waves is a small effect introduced by relative target-source motion that changes the frequency.

$$\Delta f = 2(\Delta v/c)f_t \quad (20)$$

1. If the relative velocity, or range rate, of the target is  $400 \text{ km h}^{-1}$ , and  $f_t = 400 \text{ MHz}$ , what is  $f_e$ ?
2. How would we observe this shift? (Think about a *beat frequency*).

## Conclusion

---

# Summary

Introductory concepts:

- Units, estimation, approximation
  - Decibels
  - Graphical analysis, range, and doppler shift
1. Professor Jordan Hanson
  2. Email: [jhanson2@whittier.edu](mailto:jhanson2@whittier.edu), [918particle@gmail.com](mailto:918particle@gmail.com)
  3. Mobile: 562-351-0047
  4. Zoom Credentials: (ID) 796 092 0745 (Passcode) 667725
  5. **Reading: Stimson's Introduction to Airborne Radar, 3rd Edition.** (Hughes Radar Handbook)
  6. Box Folder: <https://app.box.com/s/qalsptcztyeq8hjvu3pmf4mlodmopop7>



# Introduction to GPS M-Code Signals for Onboarding of Navy Personnel

---

Jordan Hanson

Assistant Professor of Physics and Computer Science

Department of Physics and Astronomy, Whittier College

Summer Research Fellow with the Office of Naval Research

June 24, 2022

# Outline

---

# Outline

---

## Introduction to GPS M-Code Signals - Six Easy Pieces

1. Radio transmission equation and signal strengths
2. Signals: amplitude versus time
3. More on binary signals
4. Power spectral densities
5. Mixing signals, carrier frequencies
6. Auto-correlation functions

**Synthesis:** Putting the pieces together

## Radio transmissions and signal strengths

---

# Radio transmissions and signal strengths

1. Problem statement
2. Derivation of Friis transmission equation
3. Practical examples (interactive)
4. Application to GPS signals

# Radio transmissions and signal strengths

## Problem Statement

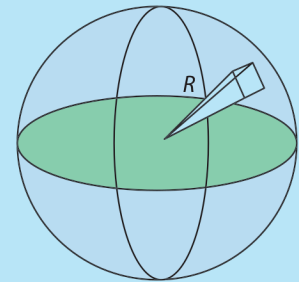
Given how far away a radio transmitter is, and the transmitter and receiver antenna characteristics, how do we predict the received signal strength?

Variables we need to understand:

---

- Distance between radio TX and RX:  $R$
- Gain of radio TX and RX,  $G_t$  and  $G_r$
- Wavelength of radio signal:  $\lambda$
- Transmitted and received power:  $P_t$  and  $P_r$

# Radio transmissions and signal strengths



$$G = \frac{4\pi R^2}{R^2 \lambda^2 / ab}$$

$$= \frac{4\pi A_e}{\lambda^2}$$

where  $A_e = a \times b$  is the effective area of the antenna

**Figure 1:** Adapted from Chapter 8 of *Introduction to Airborne Radar*, by Stimson, Griffiths, Baker, and Adamy. SciTech Publishing (2014).

# Radio transmissions and signal strengths

*How to translate the idea in the diagram into a formula for the gain:*

$$s = r\theta \quad (1)$$

$$\theta_1 \approx \lambda/a \quad (2)$$

$$\theta_2 \approx \lambda/b \quad (3)$$

$$s_1 \approx R\lambda/a \quad (4)$$

$$s_2 \approx R\lambda/b \quad (5)$$

$$G = (4\pi R^2)/(s_1 s_2) = (4\pi R^2 ab)/(R^2 \lambda^2) \quad (6)$$

$$A = ab \quad (7)$$

$$G = (4\pi A)/(\lambda^2) \quad (8)$$

# Radio transmissions and signal strengths

## Antenna Gain

The **gain** of a radio antenna with aperture efficiency  $\epsilon$ , effective area  $A$ , radiating at a wavelength  $\lambda$  is

$$G = \frac{4\pi A}{\lambda^2} \epsilon \quad (9)$$

Note that the wavelength  $\lambda$  and frequency  $f$  are related by the *speed of light*:  $f = c/\lambda$ .

For radio waves in the atmosphere and space,  $c \approx 0.3 \text{ m/ns}$ , or  $0.3 \text{ km}/\mu\text{s}$ .

# Radio transmissions and signal strengths

Gain is typically quoted in a unit called a **dBi**: a decibel relative to isotropic sources. The decibel is a type of logarithmic unit widely used in RF fields.

$$G_{dBi} = 10 \log_{10}(G) \quad (10)$$

**Interactive Question:** Suppose we have a radio transmitter equipped with an antenna that operates at a wavelength of 10 cm, and an effective area of 40 cm by 40 cm. What is the gain in dBi, if the efficiency at this wavelength is 70%?

- A: 10 dBi
- B: 13 dBi
- C: 21.5 dBi
- D: 23 dBi

# Radio transmissions and signal strengths

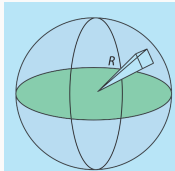
Now we can use the concept of *gain* to understand received power by a receiving antenna (RX) from a transmitting antenna (TX).

Variables we need to understand:

---

- Distance between radio TX and RX:  $R$
- *Gain* of radio TX and RX,  $G_t$  and  $G_r$
- *Wavelength* of radio signal:  $\lambda$
- Transmitted and received power:  $P_t$  and  $P_r$
- **Power density:**  $P_t/(4\pi R^2)$

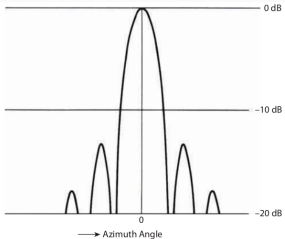
# Radio transmissions and signal strengths



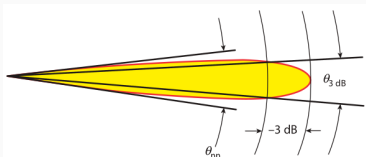
$$G = \frac{4\pi R^2}{R^2 \lambda^2 / ab}$$
$$= \frac{4\pi A_e}{\lambda^2}$$

where  $A_e = a \times b$  is the effective area of the antenna

(a) The concept of *gain*.



(b) The concept of *radiation pattern (dB) vs. angle*.



(c) The concept of *radiation pattern*, visualized in 2D.



**Figure 8-1.** This three-dimensional plot shows the strength of the radiation from a pencil beam antenna.

(d) The concept of *radiation pattern*, visualized in 2D.

# Radio transmissions and signal strengths

Now we can use the concept of *gain* to understand received power by a receiving antenna (RX) from a transmitting antenna (TX).

Suppose we have a TX transmitting  $P_t$ , received by RX with  $P_r$ . The transmitted power density will be  $p = P_t/(4\pi R^2)$ , augmented by  $G_t$  (Eq. 11). When  $p$  arrives at the RX, it will be collected over the  $A$  of the RX (Eq. 12). Changing variables from  $A$  to  $G_r$  (Eq. 13), we arrive at the Friis transmission formula (Eq. 14):

$$p = P_t/(4\pi R^2)G_t \quad (11)$$

$$P_r = P_t/(4\pi R^2)G_t A \quad (12)$$

$$A = \frac{G_r \lambda^2}{4\pi} \quad (13)$$

$$\frac{P_r}{P_t} = \frac{G_t G_r \lambda^2}{(4\pi R)^2} \quad (14)$$

# Radio transmissions and signal strengths

## Radio transmission signal strength

According to the Friis transmission formula, the ratio of received to transmitted radio power is

$$\frac{P_r}{P_t} = \frac{G_t G_r \lambda^2}{(4\pi R)^2} \quad (15)$$

Each gain factor includes non-ideal behavior due to aperture efficiencies.

**Interactive questions:** (1) What is the RX power in dB? (2) What gain is necessary to achieve specified RX power?

## Radio transmissions and signal strengths

**Interactive question (1).** For the system in the prior interactive question, imagine that the TX and RX are similar antennas separated by  $R = 900$  m. We have  $\lambda = 0.1$  m,  $G_t = 13$  dBi, and  $G_r = 13$  dBi. What is  $P_r/P_t$  in dB? This is known as *path loss*.

- A: -25 dB
- B: -75 dB
- C: -125 dB
- D: -175 dB

## Radio transmissions and signal strengths

**Interactive question (2).** For the system in the prior interactive question, imagine that the design needs to change such that the overall path loss is now -60 dB. We cannot change  $R$  or  $\lambda$ , so all we can do is boost the gain. What should the new gain be, in dB, for the antennas?

- A: 5 dB
- B: 10 dB
- C: 20 dB
- D: 60 dB

# Radio transmissions and signal strengths

**Application to GPS signals:** large path losses. In Fig. 3, three reference TX send signals to one RX. Knowing the signal strength of each signal constrains (via a system of equations) the location of the RX. The trouble is the distances represented by L1, L2, and L3.

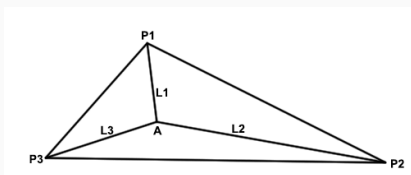


Figure 3: Trilateration with several GPS satellite TX and one RX.

A typical distance from a GPS RX to a satellite is 20,000 km.

# Radio transmissions and signal strengths

**Interactive question (3).** What is the path loss of a TX/RX system (according to the Friis transmission equation) if  $R = 20,000$  km? Assume  $\lambda = 1$  m and  $G = 10$  dB.

- A: -148 dB
- B: -158 dB
- C: -168 dB
- D: -204 dB

Satellite signals introduce path losses that must be counteracted if the signal is to be used for navigation.

## Signals: amplitude versus time

---

# Signals: amplitude versus time

1. Basic anatomy of a signal - part 1: units of time and amplitude
2. Example 1 with GNU Octave: plotting signals
3. Special topic: sinusoids and complex signals
4. Square pulses and binary sequences
5. Special topic: counting in binary
6. Sampling theorem
7. Example 2 with GNU Octave: aliasing, part 1

## Signals: amplitude versus time

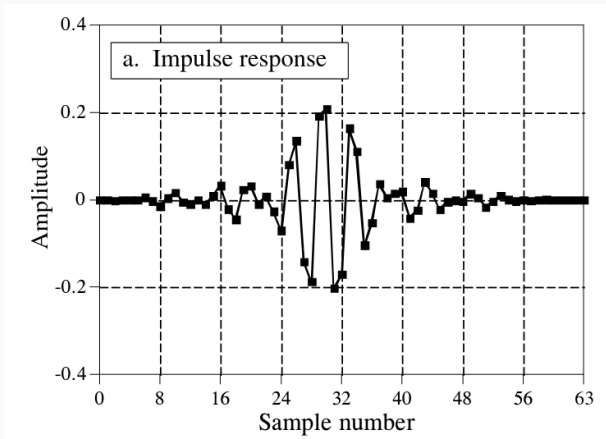


**Figure 4:** An example of a sampled, digitized signal representing the basic signal produced by an RF circuit when that circuit receives a pulse.

# Signals: amplitude versus time

## Time-domain signal properties:

1. Units of the y-axis: (A) amplitude from radio receivers as a voltage. For example,  $\mu\text{V}$ . (B) digitized samples, as in  $[0 : 2048]$ , with the numbers corresponding to specific voltages.
2. Units of the x-axis: (A) specific times. For example,  $\mu\text{s}$ . (B) sampled times, such as  $[0 : 63]$ , with samples related by  $\Delta t$ .

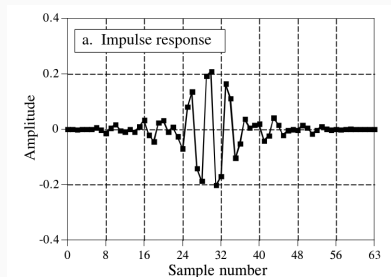


Figure 5: Amplitude versus sample number.

## Signals: amplitude versus time

GNU Octave code example: "amplitude\_time.m"

```
t_samples = 0:255;
sampling_frequency = 200.0; %Hz
delta_t = 1/sampling_frequency; %seconds
t = t_samples*delta_t;
frequency = 2.0; %Hz
signal = cos(2.0*pi*frequency.*t);
plot(t,signal,'linewidth',3,'color','black');
axis([0 max(t) -2 2]);
xlabel('Time (s)');
ylabel('Amplitude (V)');
set(gca(),'fontname','Calibri','fontsize',20);
grid on;
print('-dpdf','amp_time_2.pdf');
```

## Signals: amplitude versus time

GNU Octave code example: “amplitude\_time.m”

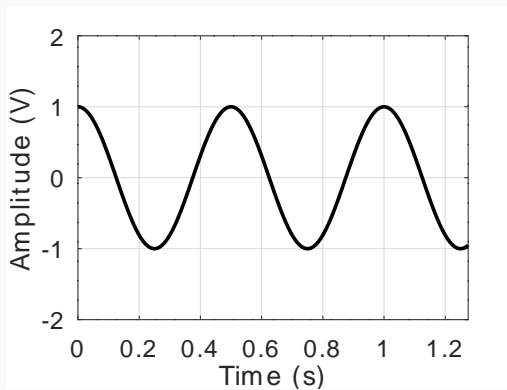


Figure 6: The figure created by the GNU Octave example.

## Signals: amplitude versus time

**GNU Octave exercise:** Make the following changes, separately, to understand the impact on the signal:

```
t_samples = 0:511;
signal = 2*cos(2.0*pi*frequency.*t);
frequency = 4.0; %Hz
```

Other important quantities:

- *Power*: square each amplitude sample, and sum each value.
- *Average value*: sum the amplitude samples and divide by  $N$ .

# Signals: amplitude versus time

```
P = sum(signal.^2); %Power  
average_value = mean(signal); %Average
```

Other important quantities:

- *Power*: square each amplitude sample, and sum each value.  
What happens to the power when you calculate it with  $f = 2 \text{ Hz}$  or  $f = 4 \text{ Hz}$ ?
- *Average value*: sum the amplitude samples and divide by  $N$ .  
What should be the average of a sinusoid, when the signal includes a whole number of periods?

# Signals: amplitude versus time

## Complex Signals: A tool for understanding signals

Let  $j = \sqrt{-1}$ ,  $f$  be the frequency of a sinusoidal signal, and  $t$  be the time. Euler's theorem states that

$$\exp(2\pi jft) = \cos(2\pi ft) + j \sin(2\pi ft) \quad (16)$$

The *real* part of the signal is  $\cos(2\pi ft)$ , and the *imaginary* part is  $\sin(2\pi ft)$ .

Also note, exponentials and complex numbers have some useful properties:

- $\exp(x) \exp(y) = \exp(x + y)$
- $(x + jy) + (a + jb) = (x + a) + j(y + b)$

# Signals: amplitude versus time

Treating real signals as complex

$$A \cos(2\pi ft) = \Re\{A \exp(2\pi jft)\} \quad (17)$$

By “taking the real part,” we recover the cosine. “Taking the imaginary part” of a complex exponential gives the sine portion:

$$A \sin(2\pi ft) = \Im\{A \exp(2\pi jft)\} \quad (18)$$

Treating signals as exponentials allows us to multiply them easily, to understand product signal behavior.

**Interactive Question (4).** What happens when you multiply two signals with frequencies  $f_1$  and  $f_2$ ? (Start complex, then take the real part at the end).

## Signals: amplitude versus time

**Interactive Question (5).** What happens when you multiply two signals with the same frequency  $f$ , but with different phases?

$$s_1(t) = a \cos(2\pi ft + \phi_1) \quad (19)$$

$$s_2(t) = a \cos(2\pi ft + \phi_2) \quad (20)$$

$$T(t) = s_1(t)s_2(t) \quad (21)$$

(Treat them as complex, then take the real part at the end).

## Signals: amplitude versus time

**Final GNU Octave exercise:** Make the following change to the amplitude versus time code to understand the impact on the signal:

```
t_samples = 0:255;  
sampling_frequency = 10.0; %Hz  
delta_t = 1/sampling_frequency; %seconds  
t = t_samples*delta_t;  
frequency = 2.0; %Hz
```

How does this distort the signal?

- Frequency greater than sampling frequency divided by 2
- Frequency less than sampling frequency divided by 2

## More on binary signals

---

## More on binary signals

1. **Binary numbers**: digital signals from analog signals
2. Practical examples (interactive)
3. Chips and spreading symbols, chip rate, and data rate
4. Example 3 with GNU Octave: plotting a pseudo-random code sequence
5. Binary offset carriers

# More on binary signals

First of all, what is an *analog* circuit?

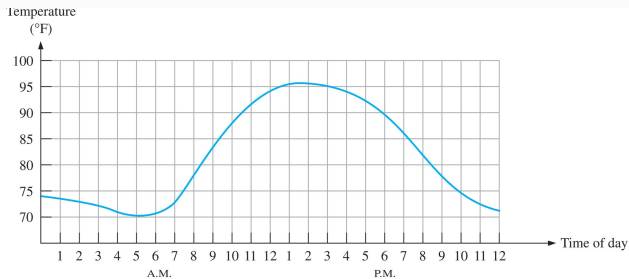


Figure 7: An example of an analog signal from a temperature sensor, converted from voltage.

## More on binary signals

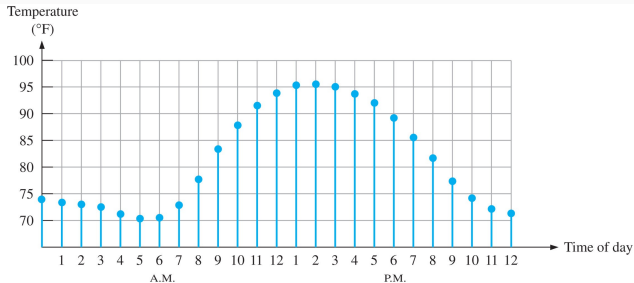
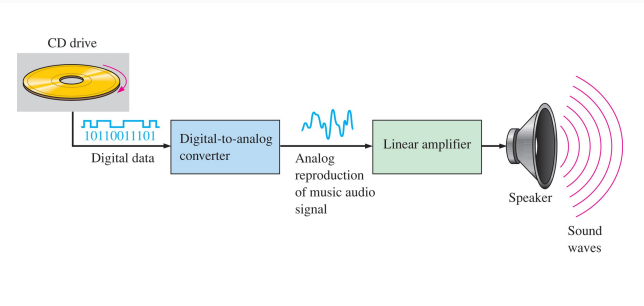


Figure 8: An example of that same signal, digitized and sampled.

Digital data forms the basis of computation:

- Noise issues, lossless transmission
- Constructed from *digits* ... 1 and 0

# More on binary signals



**Figure 9:** An example of a digital signal converted from binary to analog voltage signal.

# More on binary signals

How do we build up digital data from analog signals?

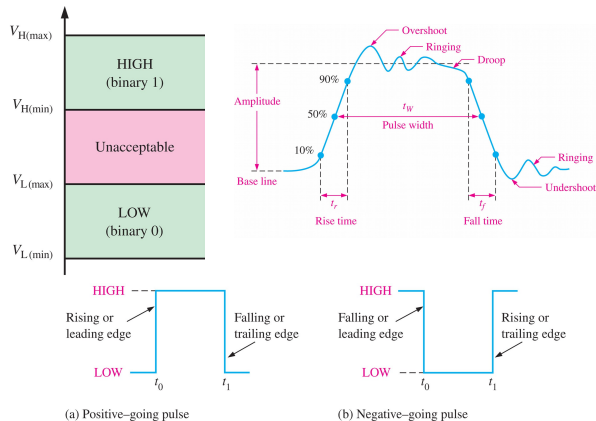


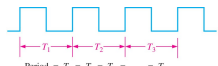
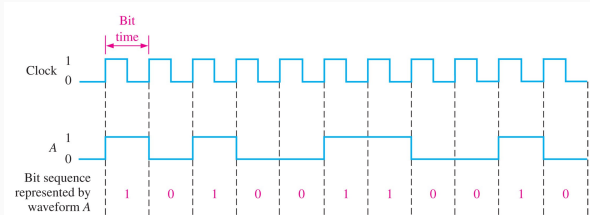
Figure 10: Logical “1” and “0.”

# More on binary signals

Terminology for digital signals:

1. **Frequency**,  $f$  and **period**,  $T$ : Signals per second, time between signals ( $f = 1/T$ ).
2. **Pulse width**,  $t_W$ : time duration a pulse is HIGH.
3. **Duty cycle**:  $t_W/T \times 100\%$

# More on binary signals



Period =  $T_1 = T_2 = T_3 = \dots = T_n$

$$\text{Frequency} = \frac{1}{T}$$

(a) Periodic (square wave)



(b) Nonperiodic

**Figure 11:** A clock signal is an example of a digital bitstream: alternating 1 and 0. It has a period and a frequency. Data can be *periodic* or *non-periodic*. (Professor: do some examples here).

## More on binary signals

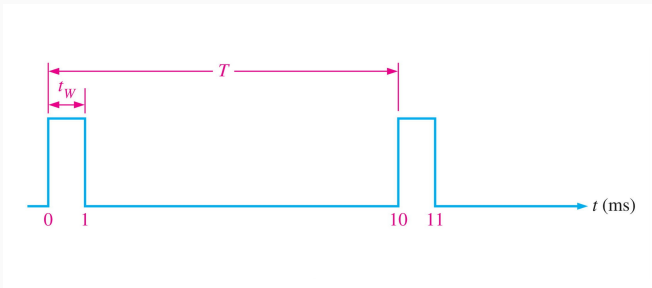


**Figure 12:** A periodic pulse demonstrating the concept of duty cycle.  
(Professor: do an example here and vary duty cycle).

What is the duty cycle in Fig. 12? What is the frequency?

## More on binary signals

A script to produce a binary signal (install the “signal” package):

```
pkg load signal
t_samples = 0:255;
sampling_frequency = 200.0; %Hz
delta_t = 1/sampling_frequency; %seconds
t = t_samples*delta_t;
frequency = 2.0; %Hz
signal = square(2.0*pi*frequency.*t);
plot(t,signal,'linewidth',3,'color','black');
axis([0 max(t) -2 2]);
xlabel('Time (s)');
ylabel('Amplitude (V)');
set(gca(),'fontname','Calibri','fontsize',20);
grid on;
print('-dpdf','amp_time_3.pdf');
```

## More on binary signals

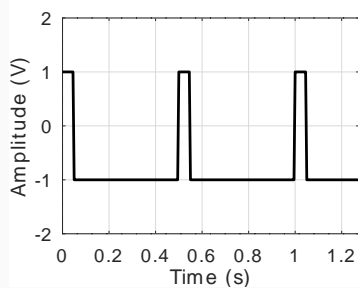


**Figure 13:** A periodic pulse demonstrating the concept of duty cycle.  
(Professor: do an example here and vary duty cycle). What is the frequency, period, and duty cycle of the signal?

## More on binary signals

Make the following change to the code:

```
...
frequency = 2.0; %Hz
signal = square(2.0*pi*frequency.*t,10);
plot(t,signal,'linewidth',3,'color','black');
...
print('-dpdf','amp_time_4.pdf');
```

**Interactive Question (6).** If a binary signal repeats with period  $1\ \mu s$ , but has a pulse width of  $0.2\ \mu s$ , what is the duty cycle?

- A: 10 percent
- B: 20 percent
- C: 200 percent
- D: 2 percent

# More on binary signals

**Interactive Question (7).** Draw in your notes a binary signal representing the following bit sequence: 11001101. **Bonus:** How could we make our code represent this signal?

```
t_samples = 0:255;
sampling_frequency = 200.0; %Hz
delta_t = 1/sampling_frequency; %seconds
t = t_samples*delta_t;
period = length(t_samples)/8;
seq = [1 1 0 0 1 1 0 1];
signal = []
for i=seq
    signal = [signal ones(1,period)*i];
endfor
plot(t,signal,'linewidth',3,'color','black');
axis([0 max(t) -2 2]);
xlabel('Time (s)');
ylabel('Amplitude (V)');
set(gca(),'fontname','Calibri','fontsize',20);
grid on;
print('-dpdf','amp_time_4.pdf');
```

# More on binary signals

Encoding our signals. What if we don't want someone to intercept our data and use it? Consider the following signal:

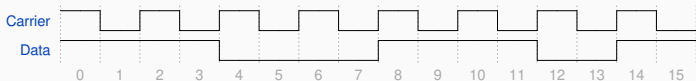


Figure 14: (Top) A binary carrier signal, and (Bottom) a binary sequence representing some data: 11001101, at the same rate as the clock signal.

**Notice:** The pulse width of the “Carrier” signal in Fig. 14 is one half the minimum pulse width of the “Data” signal. For one period of the carrier, we have one data bit. The fastest *data rate* is equal to the carrier frequency.

# More on binary signals

Encoding our signals. What if we don't want someone to intercept our data and use it? Consider the following signal:

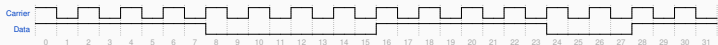
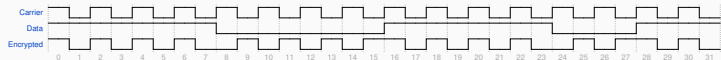


Figure 15: (Top) A binary carrier signal, and (Bottom) a binary sequence representing the same data as Fig. 14, 11001101, at one half the rate as in Fig. 14.

**Notice:** The pulse width of the “Carrier” signal in Fig. 14 is one fourth the minimum pulse width of the “Data” signal. For two periods of the carrier, we have one data bit. The fastest *data rate* is equal half of the carrier frequency.

## More on binary signals

Now multiply the carrier and the data signals. The result is a *pseudo-random code*:



**Figure 16:** (Top) A binary carrier signal, (Middle) The data stream. (Bottom) the product of the carrier and the data stream.

**Notice:** The encrypted data stream now appears as random data at the carrier frequency. If the data stream is already encrypted through binary techniques, the signal at the bottom of Fig. 16 would be very difficult to intercept and use.

## More on binary signals

**The spreading symbol:** By taking the data bit and multiplying it by 1010, the data is said to be *spread* by a *spreading symbol* 1010.

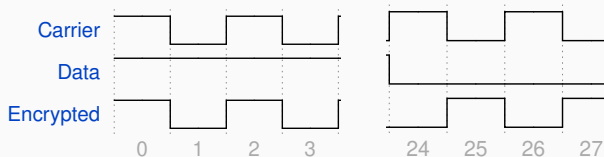


Figure 17: (Left) The first data bit. (Right) The second to last data bit.

**Interactive Question (8).** Suppose we have a binary carrier with a period of  $0.1 \mu\text{s}$ , and a data stream of 1011 0010 to transmit. (a) Write out the encrypted data sequence by multiplying the carrier with the data stream. Assume the data rate is half the frequency of the carrier. (b) How long (in time) is the encrypted data?

# More on binary signals

## Some vocabulary:

1. **Chip**: the unit of the data in the encrypted result.
2. **Symbol**: the pieces of data made from multiple chips.
3. **Chip rate**: the rate of the encrypted signal.
4. **Symbol rate**: the rate of the data stream.
5. **Spreading factor**: the ratio of the chip rate to the data rate.

## Power spectral densities

---

# Power spectral densities

1. Basic anatomy of a signal - part 2: units of frequency and power
2. The Fourier transform and FFT algorithm
3. Example 4 with GNU Octave: aliasing, part 2
4. Units: dB, dBw and dBm, and dB/Hz
5. Practical examples (interactive)

## Mixing signals, carrier frequencies

---

# Mixing signals, carrier frequencies

1. Mathematics of mixing signals:
  - Trigonometric identities
  - Complex signals
2. Block diagram of mixing
3. Example 5 with GNU Octave: moving a signal to a carrier frequency

## Auto-correlation functions

---

# Auto-correlation functions

1. Mixing a signal with itself: auto-correlation function (ACF)
2. Example 6 with GNU Octave: auto-correlation of a square pulse
3. Applications to GPS signal timing

# Artemis Program: The Internet of Things (IoT) and Wearable Technology

Dr. Jordan Hanson - Whittier College Dept. of Physics and Astronomy

January 22, 2020

## Abstract

Electronics engineering has become an activity available to the benchtop tinkerer thanks to low-cost microprocessors, vibrant maker communities and simple, widely-distributed computer-code packages. In this version of the Artemis program, we will attempt to design an electronic safety bracelet system that sends location data of a lost loved one. The project involves Arduino circuit boards and code development, as well as integration of WiFi and GPS hardware and data.

**Regular meeting times:** Mondays, 4:30 - 5:45 pm in Science and Learning Center, Room 228. Optional meetings on Wednesdays, same time and place, as needed.

**Instructor contact information:** [jhanson2@whittier.edu](mailto:jhanson2@whittier.edu), tel. 562.351.0047

**Attendance/Absence:** Participants are encouraged to attend as many meetings as possible. If a participant misses more than one meeting that will preclude participation in SCCUR and URSCA conferences.

### Program expectations:

- Attend as many meetings as possible
- Bring laboratory notebook and take notes during meetings
- Perform a weekly study activity outside meeting times
- Construct a piece of wearable circuitry (for example, a bracelet) that signals the location of the wearer if the wearer is lost
- Gain experience with the Arduino development platform
- Prepare a scientific poster to present at URSCA and SCCUR. URSCA stands for Undergraduate Research, Scholarship, and Creative Activity, which is conference and poster session held annually at Whittier College. SCCUR stands for Southern California Conferences for Undergraduate Research, and is held annually at a college or university in Southern California.

### Schedule:

1. Meeting 1: February 5th, 2020. **Introduction to Arduino development, 1**
  - (a) Powering up devices, using the software development environment, LEDs and printing to screen
  - (b) *Weekly assignment: download Arduino SDE and practice toggling an LED, code practice*
2. Meeting 2: February 10th, 2020. **Introduction to Arduino development, 2**
  - (a) Code control flow and the event loop
  - (b) Adding conditional features to code, involving switch and if/else statements
  - (c) *Weekly assignment: Activate LED with a button or switch*
3. Meeting 3: February 17th, 2020. **Pinouts, schematics, and other nerdy things**
  - (a) Learn how to read a pinout schematic
  - (b) Learn how to search for parts and diagram prototype
  - (c) *Weekly assignment: search for schematic of GPS module for our Arduino boards*
4. Meeting 4: February 24th, 2020. **Breadboards, power supplies, and connectors**
  - (a) Practice hooking things together, prototyping and troubleshooting
  - (b) Common laboratory equipment: voltmeters, probes and power supplies
  - (c) *Weekly assignment: measure car battery voltage*

5. Meeting 5: March 2nd, 2020. **Arduino and GPS**

- (a) Major milestone no. 1: print GPS coordinates to screen, from Arduino over USB.
- (b) What is GPS, and what are latitude and longitude? What distances do they represent?
- (c) *No pre-defined assignment: troubleshoot issues that arise.*

6. Meeting 6: March 9th, 2020. **Arduino and WiFi**

- (a) Connect WiFi shield to Arduino and demonstrate signal RX/TX (receiving and transmitting)
- (b) *No pre-defined assignment: troubleshoot issues that arise.*
- (c) **March 13th: URSCA abstracts are due.**

7. **March 16th - 20th: Whittier College Spring Break**

8. Meeting 7: March 23rd, 2020. **Arduino + WiFi + GPS, 1**

- (a) Systems integration of main board, GPS receiver, and WiFi shield
- (b) First attempt to share GPS data over WiFi via SMS text message
- (c) Begin with breadboard setup, investigate form factor solution
- (d) *Weekly assignment: search for code/example to send SMS message or email over WiFi from Arduino*

9. Meeting 8: March 30th, 2020. **Arduino + WiFi + GPS, 2**

- (a) Continuation of activities from previous week
- (b) *Code/example to send SMS message or email over WiFi from Arduino*

10. Meeting 9: April 6th, 2020. **Arduino + WiFi + GPS, 3**

- (a) Integration into wearable technology
- (b) Battery power and power consumption calculations
- (c) *Weekly assignment: determine the power consumption of a household appliance or piece of technology in your home*

11. Meeting 10: April 13th, 2020. **Final production, 1**

- (a) Arduino + WiFi + GPS + battery power.
- (b) Troubleshooting and testing.
- (c) Guidelines for creating a polished figure for presentations
- (d) *Weekly assignment: test WiFi on network other than that of Whittier College*
- (e) **Poster presentation due: April 15th, 2020 (send to Samantha Ruiz)**

12. Meeting 11: April 20th, 2020. **Final production, 2**

- (a) Arduino + WiFi + GPS + battery power + wearable fitting.
- (b) Troubleshooting and testing.
- (c) *Weekly assignment: test different modes of carrying and wearing, battery life*
- (d) April 23rd, 2020: optional URSCA practice with Samantha Ruiz

13. **April 25th (Saturday), 2020: URSCA.**

14. Meeting 12: April 27th, 2020. **Final wrap-up, program summary**

- (a) Review of accomplishments
- (b) Logistics for SCCUR

15. Meeting 13: May 4th, 2020

- (a) Additional optional meeting, in case we need more time (we will).
- (b) May the 4th be with you!

## **Application for Diversity, Equity & Inclusion Innovative Initiatives Grants**

Jordan C. Hanson, PhD

Department of Physics and Astronomy

Whittier College

**Abstract:** Whittier College serves a diverse set of undergraduates with a variety of preparation levels for introductory STEM courses. These courses serve large cohorts of students and are required for many majors and professional schools. Our goal is to develop a mobile application infused with machine-learning and educational data-mining (EDM) that will boost equity and inclusiveness in foundational physics courses. Based on published examples developed at other institutions, we will create a customized tool that will strengthen our students' skills and abilities. Diverse undergraduate experts in digital storytelling and design will drive and shape the digital presentation of content. Our application will include the voices, narrative themes, and imagery of the diverse students actually attending foundational physics courses. The result will be an open educational resource (OER) designed to foster equity and inclusion for Whittier College Physics students.

**Physics education at Whittier College represents a precious opportunity:** to engage and inspire students of color and women to a wide variety of scientific, mathematical, and engineering principles. A pervasive myth at Whittier College is that “STEM tends to be white and male-dominated.”<sup>1</sup> *This is not true.* According to our institutional research, 25% of all white male Whittier College students select major in STEM disciplines, but represent just 10% of STEM majors at Whittier College (data selected for the period of 2019-2022). White men accounted for just 18% of all majors in disciplines tied to engineering, 10% of all KNS majors, and just 6.3% of all biology majors. Introductory physics students are mostly biology and biochemistry majors who plan to attend medical school, KNS majors who plan to attend physical therapy school, and engineering students.<sup>2</sup> Bolstering student success in these courses is intrinsically anti-racist, because this large group of students is on the pathway to join and diversify fields in medicine, biotechnology, and engineering.

Another myth is that “systems designed by white men” cannot “address the needs of students of color and women who are marginalized in STEM.”<sup>3</sup> *Again, not true.* Consider a proof by contradiction: introductory STEM courses at Whittier College are “systems” often created by white men, so by this logic no students of color or female students should succeed in such courses. But many do, as evidenced by course evaluation data and in our learning outcomes. If they did not, a large fraction of introductory physics students would fail. Introductory physics instructors regularly attend American Associated of Physics Teachers (AAPT) conferences on teaching techniques for undergraduates. Currently, we are attending Cottrell Scholars Network webinars on *Inclusivity in Introductory STEM Courses*. In the first of this 3-part series, the speaker presented social science research that reveals how affirming the dignity of students builds a sense of belonging as a scientist. One major motivation for this proposal is to

---

1 Though this quote is taken from the initial response to this grant proposal, the sentiment being shared has been shared informally in a variety of faculty forums.

2 Note that in the data period (2019-2021), there were  $N = 530$  students who took introductory physics courses. Student demographic data at the course-level was not available. Disciplines tied to engineering include physics, math, computer science, and the 3-2 program.

3 As your friend and colleague, I was astonished to read such a strong remark in the initial response to this proposal. We must always trust the goodness of colleagues’ motivations.

affirm the dignity of students of color and young women by providing them with a tool designed for them by myself *and by their peers*. There are two underlying problems, according to research, for those that struggle in introductory physics courses. (1) They perceive themselves to be less effective at science despite having the same grades as others, and (2) when they do struggle with physics concepts, they must be helped in a way that affirms their dignity. We propose to develop a tool that helps them automatically by showing them that (a) they are not alone in their anxiety about physics courses, and (b) peers have built tools designed to strengthen their skills. According to the social science research, differences in self-efficacy vanish when one addresses (a), and addressing (b) through dignity-affirming peer-built tools should strengthen the students.

Currently, in introductory physics courses, students engage with self-designed laboratory experiments, group projects, and active-learning strategies that include peer-learning. These elements are used because Physics Education Research (PER) has shown them to be more effective than traditional physics teaching techniques [1]. One major reason we propose this new application in DEI innovation is the engagement of students of color and young women *before* they begin foundational STEM courses. Physics instructors already collect data on student performance during the introductory courses, which informs us on how well students' conceptual understanding shifts between the beginning to the end of the semester [2]. Similar to our post-doctoral experience with bridge programs for first-year students [3], we seek to *prime* the students via digital content.

This strategy serves multiple purposes. The first is to affirm the students' dignity and foster belonging. Students of color and young women often wonder why the instructor "is not like them." By infusing the digital content with the voices and identities of their peers, and avatars created by their peers, the incoming students' dignity and identities will be affirmed in advance to foster a sense of shared belonging in the course. Our current strategy for fostering belonging in *Calculus-Based Physics I* (PHYS150) places the instructor's cohort of first-year advisees in the same sections of PHYS150 and INTD100 (College Writing Seminar). The digital strategy proposed here is extensible to all introductory physics courses. The second purpose for such a digital instructional tool is to sharpen and refresh the students' skills before the course begins. This strategy allows the instructor to tailor precious course time for the needs of the diverse population of students. Online physics homework systems already give some insight, but the data is collected *during* the course and contains no demographic data [4]. Gains in equity could be larger if we could tailor the course to people of color and young women *before it began*.

**We propose to enhance student belonging and learning by creating an application that combines digital storytelling with machine learning.** Physics instructors already work with staff from Wardman Library to help infuse our courses with training in digital storytelling ([www.diglibarts.whittier.edu](http://www.diglibarts.whittier.edu)), so our students learn to present the results of self-designed scientific experiments to their peers using tools like WeVideo (<https://www.wevideo.com>). Within the Math and Physics departments, we have experience using machine-learning techniques [5, 6]. Further, the literature on educational data mining (EDM) contains a plethora of examples used to understand undergraduate STEM learning patterns [7]. An example of such an application using this two-pronged strategy for language learning is DuoLingo (<https://www.duolingo.com>), in

which digital storytelling is used to welcome and strengthen the learner in stages. Learners of all backgrounds are affirmed through the visual storytelling aspect of the application, and their skills are strengthened incrementally such that the user feels empowered, rather than deficient. These ideas are at the core of this proposal. Finally, the EDM literature also recognizes that the earlier struggling students are identified and aided by the instructor, the better their outcomes [9]. Several examples of such digital tools have been created specifically for STEM courses [10,11]. Our hypothesis is that the digital storytelling aspect will raise student engagement by relating the content to their own experiences. One final point about the tool we propose: this tool is not based around any “deficit model” of student achievement. Rather, as we argue above and below, this strategy focuses on building strengths and building belonging within introductory STEM courses. To this end, more data from the *Inclusivity in Introductory STEM Courses* is relevant.

In the second of the 3-part series, *Inclusivity in Introductory STEM Courses* through the Cottrell Scholars Network, the speaker discusses self-efficacy and long-term success in STEM fields for women and people of color. If our proposed tool could show the students (anonymously) that they are not the only one who gets wrong answers initially, self-efficacy gaps tend to vanish [8]. Thus, it is important to note that any such data collection the tool might perform will be anonymous. Thus, the tool we propose actually has nothing to do with so-called “deficit models,” but is more aptly described as an **antidote** to deficit models. Students will be shown that they are *not alone*, rather than be shown that they are the only one who struggles. Digital tools have already helped our students connect and grow, despite the quarantines induced by COVID-19.

The COVID-19 pandemic forced our department to shift to digital educational platforms. Normally, our introductory STEM curricula is centered on both laboratory and lecture courses. In 100-level physics courses, we have merged lecture and lab at the introductory level, using concepts from workshop physics models and peer-instruction (PI) [1]. Peer-instruction models have the students play an active role in teaching each other, and the content is transmitted through the instructor *and peers*, leading to better learning outcomes. Components of our courses remain online and asynchronous going forward. One example is the Pivot Interactives lab platform, in which students can complete lab activities remotely in a way that fits into their schedule [13]. Thus, there is precedent for the further use of digital tools to boost student success in STEM.

One final idea for the proposed digital tool is derived from a novel entitled *The Diamond Age*, by Neal Stephenson. In the book, a digital tool called *The Primer* falls into the hands of a young orphan named Nell. Nell engages with the tool, which teaches her mathematics, design principles, physics, and leadership skill. The key to her development is that *The Primer adapts* to her educational needs in real time, and provides a narrative for her growth in terms of creating a land for her fellow orphans. The MathBot project [10] already has achieved a conversational model similar to that of *The Primer*. To these already-successful models, we would add the narrative through digital storytelling of *The Primer* by incorporating digital-storytelling and graphic design from Whittier College. As the story progresses, students would be prompted to solve progressively more challenging problems in order to build strength. Duolingo combines digital storytelling and machine-learning in this way. Thus, the project would have a liberal arts component, and a software design component. In the coming sections, we describe the software design and digital storytelling of the proposed tool. We also

provide an assessment plan with more detail regarding important objectives and milestones.

**Two essential actions would be performed by the software as the student progresses.**

First, exercise and demographic data such as response rate and time, correct percentage, and student race and gender, would be recorded anonymously for further analysis. Machine-learning algorithms (see below) would be run on trial data to help instructors understand student learning patterns. Insights derived could be taken into account in our courses. If we find, for example, that students of color regularly struggle with vector addition and momentum conservation (most likely due to non-exposure to these topics in high-school or at Whittier) then providing more in-class practice in those topics should *boost* equity, rather than exacerbate it. The second action performed by the code would be to establish the pace and intensity of the course. If we find that historically marginalized students demonstrate strength in certain topics, relatively less in-class practice should be spent on those topics. The net gain for marginalized students is that they are exposed to *more content* than they would experienced without the data-driven model. Thus, the software facilitates an adaptable course that maximizes the learning of people who have traditionally been marginalized.

**Whenever one encounters digital storytelling or narrative anywhere in this proposal, do not forget that it will not be and should not be a physics instructor creating these stories and themes.**

Rather, we plan to recruit Whittier Scholars Program students, digital design students, and staff members from Wardman Library to drive creation in this area. There are three reasons it makes sense to do the project this way. First, the Digital Liberal Arts area already has the experience to help students tell their own stories. As stated above, we regularly invite staff members such as Sonia Chaidez from Digital Liberal Arts to train students in introductory physics courses how to create a digital story about their science projects (usually with WeVideo). Having gained experience with tools like WeVideo, we now have access to a plethora of institutional wisdom in digital storytelling. Second, undergraduates from diverse backgrounds will be recruited to create the digital storytelling piece, so the narrative themes should be recognizable and dignity-affirming to the user, unlike a sterile traditional textbook. Third, the format will move the data collection and analysis anonymously to the back end, so that the students are anonymously helping their instructors learn about them.

**Current physics students at Whittier College already generate data that goes unused, and our students of color and female students are not yet benefiting from its analysis.**

There are many examples in EDM literature that demonstrate how clustering and classification algorithms are used in STEM education. One example of clustering algorithms was [14], in which researchers identified patterns in self-regulated learning (SRL) in a large asynchronous online statistics course. Another example was [15], in which student problem-solving clusters emerged from data generated in a physics MOOC (massive open online course). On occasion, EDM researchers develop educational protocols and tools based on the results. Probably the most applicable example to our introductory physics courses is the MathBot [10].

In introductory physics courses, we have been using the Force and Motion Concept Evaluation (FMCE) in introductory physics courses [2]. We use the FMCE data primarily to evaluate our progress as instructors. However, we do not *continue* to record data that *re-informs* our picture of our students, nor do we systematically tailor content to the

students as they evolve. In addition, we would like to make our proposed tool cognizant of student demographic data. To strive to be as equitable as possible in our 100-level physics courses, we should at least be using the data that students of color and young women generate. No matter the background of the student, the adaptability the machine-learning tools in EDM literature should be deployed to form an equitable foundation of skills for Whittier Poets.

**Equity and inclusion are core values of Whittier College.** The idea that each student could be given free access to a digital tool that helps train them in advance of and during introductory physics courses fosters equity and inclusion at our institution. It is our hope that we will affirm the dignity of our physics students and customize their course content by creating this tool. Seventy percent of our student body identify as people of color, which is not true of Whittier faculty. By allowing students to drive the creation of the digital-storytelling, we will infuse it with narrative themes and imagery that align with the identities of the very people we instruct.

**The ideas behind this project are in alignment with our Racial Justice and Equity Action Plan.** For example, part of the plan calls for increased data collection and analysis with a focus on equity, inclusion, and retention of Black students. We should strive to collect educational data so that their educational experience may be improved. Another portion of the plan calls for an associate dean to “lead efforts in evaluating, modifying, and implementing policy and practices and augmenting faculty development.” Bringing this tool to the instructional landscape will demonstrate exactly how faculty can evolve their teaching practices to better serve our students.

### Project Timeline and Project Assessment

- *Team recruitment and planning stages*
  - Because we propose designing an app for Android OS, it would be helpful to recruit a computer science student involved in the Whittier Scholars Program. Prof. Hanson of the Dept. of Physics and Astronomy advises at least one such student per year, so this should not be difficult. Other programming expertise can come from projects created via PHYS396: Physics Research for Credit.
  - We need to recruit motivated Whittier Scholars Program (WSP) and digital design students interested in creating digital artwork and storytelling themes for the application. We had anticipated being able to reward these students financially. Those in charge of the POET internship program have indicated this is a strong proposal for such a POET intern, however, funding would have to arrive in the next academic year because the application window is closed. This should not hinder progress, however, because the nature of this project is such that we must create a skeleton of software first before infusing it with digital narratives.
  - We estimate a timeline of 1 month for software design recruitment
- *Character creation, story development, and STEM content generation*
  - We assume that the digital storytelling side of this project will undergo refinement such that there is a workable story and set of digital designs that can be implemented as the visual content of the application. The portfolio should be broad, to account for students moving through it via multiple pathways. We estimate two semesters to complete this, starting in Fall 2022.
  - On the coding and analysis side, we must have the minimum ability to collect data from a device running the application in a central location, and separately run machine-learning algorithms on it. We estimate two semesters in parallel with the digital storytelling side for this work.

- Optimally, we should determine how to execute machine-learning algorithms tools within the application. Ideally, we'd like to have this integrated at the end of the second semester.
- *Initial machine-learning studies*
  - In the second and third semesters of this work, we will run machine-learning studies on the data generated by volunteer users.
  - We will investigate the usage of cited EDM algorithms, but we will make time for more detailed and broad studies of how this data is processed. The analysis of this data could form the backbone of a Whittier Scholars Program major design.
  - In the final stages, we must demonstrate that the application can change based on the user, in the same sense as DuoLingo.
  - We estimate this work taking place during the third semester of the project.
- *Expanded testing on larger sets of student volunteers*
  - This would mark a useful stopping point for this work.
  - If we succeed up to this phase, the moment would be ripe to apply for an external grant focused on scaling up the processes to incorporate more introductory STEM courses.

## **Financial Compensation**

Given that external sources such as POET internships will be sought for student compensation, there is no financial component to that part of the project. However, Prof. Hanson will be writing software for this project, so we do request the maximum of \$500.00 from the proposal call.

## **Bibliography**

- [1] E. Mazur, Peer Instruction: A User's Manual. Pearson Education, 2013.
- [2] Ramlo, Susan. "Validity and reliability of the force and motion conceptual evaluation," American Journal of Physics vol 76. (2008) p. 882
- [3] The Ohio State University Young Scholars Program (YSP). For more information, visit <https://odi.osu.edu/young-scholars-program>
- [4] One example for STEM: "The OpenStax Tutor System," <https://tutor.openstax.org/>?
- [5] J.C. Hanson et al. "Time-Domain Response of the ARIANNA Detector." Astroparticle Physics Journal vol. 62 (2015) pp. 139-151
- [6] K. Bui, F. Park, S. Zhang, Y. Qi, J. Xin, "l<sub>0</sub> Regularized Structured Sparsity Convolutional Neural Networks," Pre-print manuscript on arXiv.org: arXiv:1912.07868 (2019)
- [7] Dongjo Shin and Jaekwoun Shim. "A Systematic Review on Data Mining for Mathematics and Science Education," International Journal of Science and Mathematics Education (2020) pp. 1-21
- [8] Binning, K. R. et al. "Changing Social Contexts to Foster Equity in College Science Courses: An Ecological-Belonging Intervention." Psychological Science, vol. 31, n. 9, pp.
- [9] Cameron Cooper and Paul Pearson. "A Genetically Optimized Predictive System for Success in General Chemistry Using a Diagnostic Algebra Test," Journal of Science Education and Technology vol. 21 no. 1 (2011)
- [10] J. Grossman, Z. Lin, H. Sheng, J. Wei, J. Williams, and S. Goel. "MathBot: Transforming Online Resources for Learning Math into Conversational Interactions," Copyright, 2019 Association for the Advancement of Artificial Intelligence ([www.aaai.org](http://www.aaai.org))
- [11] H.S. Lee et al. "Automated text scoring and real - time adjustable feedback: Supporting revision of scientific arguments involving uncertainty," Science Education Journal vol. 103 no. 3 (2019)
- [12] "PhysPort: Supporting Physics Teaching with Research Based Resources." <https://www.physport.org/> methods/method.cfm?G=Peer\_Instruction. A teaching material repository for PI module questions.
- [13] "Pivot Interactives." [www.pivotinteractives.com](http://www.pivotinteractives.com). Copyright Pivot Interactives 2020 SBC. Example of online physics laboratory instruction modules.
- [14] D. Kim, M. Yoon, I. H. Jo, and R. M. Branch. "Learning analytics to support self-regulated learning in asynchronous online courses: A case study at a women's university in South Korea," Computers & Education vol. 127 (2018)
- [15] Y. Lee. "Using Self-Organizing Map and Clustering to Investigate Problem-Solving Patterns in the Massive Open Online Course: An Exploratory Study," Journal of Educational Computing Research vol. 57 no. 2 (2018)

## CHANGING GLACIERS: SO MUCH MORE THAN SEA LEVEL RISE

How changing glaciers will influence every aspect of life on earth, case study: Iceland, and  
photo essay.

Nicolas Bakken-French

March 8, 2021

Project Sponsor: Jordan Hanson

Undergraduate in Environmental Science and Policy

Minor in Glaciology

*Abstract: Glaciology is an evolving science during a time in which our increased understanding of glaciers will become critical to understanding and adapting to our future of life on earth. Current glaciological research can predict the impacts of glacial change on a warming planet with steadily increasing precision in a variety of contexts. This study catalogues a diverse range of glacial impacts on human activity through a variety of geographic case studies. First, glacial influence on ocean currents and sea level rise is analyzed through our understanding of the Greenland and Antarctic ice sheets. Second, glacial influence on fresh water availability, agriculture, fisheries, tourism, and biodiversity is analyzed through our understanding of the Himalaya region, Wyoming state, Washington state, New Zealand, and California state. Third, glacial ice cores from Antarctica reveal information on past climate, and geological analysis of Yosemite National Park offers further insight. Fourth, the influence of glacial change on cultures and spiritual practice is analyzed. Because Iceland presents a unique combination of glacial influences, the geological and cultural impacts of glaciers there are analyzed. Finally, this study is further contextualized by a photo essay of Iceland's Glaciers by the author.*

## Table of Contents

<b>Introduction.....</b>	3
<b>Defining Glaciers .....</b>	4
<b>Glaciers Influence on Global Climate.....</b>	6
IPCC & Sea Level Rise .....	7
Albedo .....	7
Ocean Currents.....	8
Polar Glacial Dynamics.....	9
Operation Icebridge.....	11
<b>Glacial Influences Downstream.....</b>	13
Fresh Water Source: Himalaya, the Water Tower of Asia.....	15
Impacts on agriculture: Wyoming.....	17
Impacts on fisheries: Washington Salmon.....	18
Glacier Tourism: New Zealand.....	21
Biodiversity & Endemic Species: Trinity Alps, CA.....	23
<b>What Glaciers Can Tell Us About the Past.....</b>	24
Ice Cores.....	24
Previously Glaciated Landscapes: Yosemite, CA.....	25
<b>Glacial Impacts on Culture and Identity.....</b>	26
Indigenous Perspectives.....	27
<b>Iceland.....</b>	29
Geological Impacts.....	29
Natural and Anthropogenic, Post Little Ice-Age Recessions.....	30
Proglacial Lake Formation & Glacial Behavior.....	33
Future of the Southeast Iceland Landscape.....	34
Cultural Impacts.....	36
Iceland's Booming Tourism.....	37
<b>Photo Essay: Vatna &gt; Jökull.....</b>	38
<b>Conclusion.....</b>	48
<b>Acknowledgments.....</b>	48
<b>References.....</b>	49

*I found that we can have the very best data, statistics, and models chronicling glacier change, but if that information is not grounded within the human stories of place, then that information is largely powerless. If people do not see themselves in the story, then they are not part of the story.*

- Dr. M. Jackson

## **Introduction**

My academic focus and personal passion over the past two years have been focused on exploring the changing natural world. My interest was sparked by my travels in Norway, exploring the country's dynamic landscape. During one visit, I realized a profound truth: how quickly climate change is impacting our earth. I had returned to a glacier that I had climbed as a teenager, not so many years before, and saw that in those few short years the glacier had nearly vanished into the mountain. As if a fire had started in my heart, this realization consumed me and I became obsessed. Since then, I have made ice the focus of my studies, travels, and life's ambition. These studies and experiences have taken me all over the world, and it has become clear there is a mandate for a lifelong pursuit of the knowledge of how glaciers directly impact human societies.

Glaciers have changed my life. They have given me purpose and companionship and, standing in their majesty, I have found bliss and spiritual resolve. Glaciers are dramatically beautiful: the continuous movement of ice on rock, cutting crevasses and procuring sediment, chiseling mountain faces and carving wide valleys, fertilizing the land and rivers below, giving life to all those downstream. Glaciers are truly the greatest artists of the natural world. On a time scale, their movement and change is slow enough to miss with the naked eye, but fast enough to observe profound changes when revisiting. And changing they are, faster every day. Glaciers are the thermometers of a warming planet, but they are also so much more.

Physical science observes changing ice through measurements of mass-balance and glacial dynamics. Geomorphology observes changing ice through constantly evolving glacial foregrounds. In environmental science, glacier change is observed through influences on downstream ecosystems. Politics and economics observe glacial change through the fiscal value of ecosystem services a glacier can provide. Art explores the dramatic and subtle ways changing

glaciers intersects with humanity and nature. Glaciers are also viewed through the eyes of communities whose cultures and spirituality are shaped by glacial change. Glaciology is the study of glaciers and, thus, the combination of all of these observations and more.

## **Defining Glaciers**

Glaciers are found on every continent on the planet except Australia, which itself bears the scars of recent glaciations evident on Mount Kosciuszko. Glaciers are found in the Maoke Mountains in Indonesia, Mt. Kenya in Kenya, and Nevado Cayembe in Ecuador, all sitting on or just near the equator. Glaciers rest on the Andes, in the form of tiny glacierettes to large ice caps, along the entire western portion of South America, in Venezuela, Columbia, Ecuador, Peru, Bolivia, Chile, and Argentina. A glacier covers the caldera on Volcán Iztaccíhuatl, just south of Mexico City, Mexico. In the U.S., glaciers can be found in the Colorado Rockies and the California Sierra Nevada. There are small glaciers in the Pyrenees in Spain. Four thousand glaciers cover the European Alps in France, Italy, Switzerland, Austria, and Slovenia. Glacial meltwater from the Himalaya provides a critical water source for 1.9 billion people, over a quarter of the global population, throughout Afghanistan, Pakistan, India, Nepal, China, Bhutan, Bangladesh, and Myanmar. Ice covers nearly the entire Antarctic Circle: 79% of Greenland, 10% of Iceland, and 5% of the state of Alaska. Glaciers cover 10% of the earth's surface. There are about 198,000 glaciers in the world, from glacierettes that barely cover 0.1 square kilometres to the Antarctic Ice Sheet that cover 14 million square kilometers. All of these glaciers are melting away, some faster than others, but all more rapidly than ever in Earth's known history.

At its core, glacial formation is simple. Glaciers form when winter snowfall exceeds summer melt, creating positive mass-balance. Snow compresses over many years and pressure forms ice. Mass balance in glaciology refers to the accumulation or loss of mass in a glacier. A glacier with negative mass balance is losing ice while a glacier with positive mass balance is gaining ice. To be considered a glacier, however, the ice must be moving. Glaciers create outward and downward pressure that force the ice away from its accumulation zone with gravity. Like a river, the ice then flows away from the source towards its ablation zone or melt zone where the ice

melts away during summer. Glaciers have an accumulation zone, where ice is formed, and an ablation zone where ice melts. For a glacier to be in equilibrium, the accumulation zone must be slightly greater than the ablation zone, though this is rarely the case. Throughout natural history, glaciers either advance or recede following global climatic changes, but local atmospheric and geological influences can also influence glacier change.

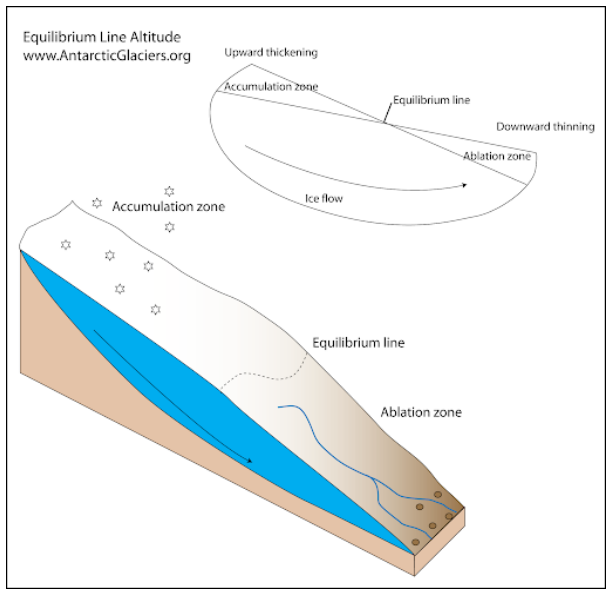


**Figure 1:** Glacial dynamics: The equilibrium line separates the upper accumulation zone, where the glacier increases mass, and the lower ablation zone, where it loses mass. A positive mass balance indicates the glacier's accumulation zone is greater than the ablation zone; a negative mass balance indicates a negative mass balance. In late summer, the accumulation zone on glaciers is covered in snow and the ablation zone is exposed ice. (AntarcticGlaciers.org)

There are many types of glaciers, and what differs between glaciers are mainly temperature and geography. First, there are two main types of glaciers when classified using temperature: *polar glaciers* and *temperate glaciers*. Polar glaciers are glaciers where the temperature within the majority of the ice is below 0 degrees celsius. These occur mainly in the globe's coldest climates at the poles. For instance, the majority of the glaciers in Antarctica and northern Greenland are polar glaciers. Glaciers in which the ice is mainly above 0 degrees celsius are called temperate. The Vatnajökull icecap in Iceland and the Juneau icefield in Alaska are temperate glaciers, in which meltwater is constantly moving through and under the ice. Glaciers that are neither polar nor temperate are referred to as polythermal glaciers or subpolar glaciers, in which there is as much ice below 0 degrees celsius as there is above 0 degrees celsius (Glasser, 2011). The surface ice and basal ice in these glaciers are temperate during the melt season while the core remains well below 0 degrees celsius. Many of the glaciers in Nunavut, Canada, and Svalbard, Norway, are polythermal glaciers.

Glaciers come in many shapes and sizes. In non-polar regions, the most common types of glaciers are valley glaciers and cirque glaciers. These are glaciers that form and flow from mountains. Valley glaciers often begin on the sides of mountains and flow down from the mountain in a single and concentrated direction through valleys. Cirque glaciers are often smaller glaciers that remain in high mountain basins and do not flow down into the valleys below. These glaciers hug the sides of the mountain face. These glaciers are common in the Cascade Range in the U.S. states of Washington and Oregon. If a valley glacier flows through a valley and terminates into the ocean, it is called a tidewater glacier. Tidewater glaciers are common in coastal Alaska, flowing from mountain ranges such as the Chugach Mountains and Kenai Fjords National Park.

Glaciers that cover entire landmasses and flow out in all directions are referred to as ice caps or icefields. The largest are referred to as ice sheets of which there are two in the world: the Antarctic ice sheet and the Greenland ice sheet. Ice caps can have valley glaciers flowing from them, such as the case as the Jostedalsbreen icecap in Norway which has tens of named valley glaciers flowing from the ice cap.

## **Glaciers Influence on Global Climate**

Earth's cryosphere is about as critical as a life-supporting system as the atmosphere. When glaciers melt, it will mean so much more than rapid sea level rise. Glaciers stabilize global climate, support ecosystems, provide freshwater and nutrients, hold landmasses in place and even keep volcanoes from producing devastating eruptions. Glaciers and ice sheets play a large role in the wind and ocean currents of the Earth. Ice directly affects the thermohaline circulation of the oceans by cooling water temperatures and trapping freshwater at the poles, therefore increasing salinity. Cold air temperatures influenced by the cooling of ice at the poles creates high air density and high-pressure systems at the poles which cause divergence: the movement of cold air away from poles and towards the tropics. Decreasing ice mass at the poles could, therefore, dramatically change these global systems, completely altering the globe's climate.

### *IPCC & Sea Level Rise*

The most recent assessment report by the United Nations' Intergovernmental Panel on Climate Change (IPCC) in 2014 highlighted the dire state of the cryosphere. The report stated that current glacial extents are not in balance with current atmospheric temperature, meaning that, globally, glaciers will continue to shrink. As long as warming continues, that imbalance will grow (IPCC, 2014). The IPCC adopted the representative concentration pathway (RCP) atmospheric carbon concentration model to predict global atmospheric temperature trajectory. RCP2.5, referring to the concentration of greenhouse gases that will contribute to global warming at 2.5 watts per square meter, is the best case minimal warming scenario, RCP8.5 is the most extreme. This model is used to predict glacial change and subsequent sea level rise as ice mass decreases and will be referenced throughout this study. The latest IPCC report concerning the cryosphere and sea level rise estimates that under RCP2.5, global sea level will rise by 0.95 feet by the end of the century; under RCP8.5, sea level will rise by over 3.5 feet (IPCC, 2019). Nearly every coastal community in the globe will be impacted by this sea level rise as an estimated 200 million people currently live below where sea level is projected to be in 2100 (Kulp & Straus 2019). The consequences of such sea level rise are difficult to fathom and predict. As well, glacial melt is not the only contributor. Thermal expansion is also a factor in sea level rise, in which the water molecules expand under increasing temperature. The severity of consequences of sea level rise will depend on how we respond and adapt, but the ramifications could result in mass migrations and massive economic losses.

### *Albedo*

Much is unknown about precisely how the melting of the planet's cryosphere will affect global systems, but we do know that melting ice will trigger global positive feedback loops that will further decrease ice mass and coverage and alter global climate. Possibly the best studied feedback loop is the ice-albedo positive feedback loop. Surface albedo refers to the reflectivity of a surface. Ice has a high albedo and reflects much of the sun's rays and, therefore, solar energy back into space, cooling and stabilizing the climate. But decreasing global ice coverage means that less solar energy will be reflected back into space as more solar energy (heat) is absorbed by less reflective surfaces. This will trigger further melt, decreasing ice coverage, and

increasing global temperatures. Another factor decreasing ice albedo is the buildup of sediment, especially on ice caps and sheets as they melt. Sediment is much darker in color and attracts solar energy, further heating and melting the ice, exposing more sediment, another feedback loop.

What is not yet included in models predicting glacial melt, due to its rather recently discovered relevance, is bioalbedo. Bioalbedo refers to decreases in ice surface albedo due to the growth of microorganisms on the ice surface. Eukaryotic algae on Greenland's ice sheet, for example, can appear during spring algal blooms and can change the snow color to green or red in massive blotches, which can potentially have significant impacts on albedo (Benning et al. 2014). Bioalbedo is another of many factors influencing glacial dynamics and global climate that we are just beginning to comprehend.

### *Ocean Currents*

While it is understood that melting ice will likely trigger intense feed-back loops that will further accelerate the rate of melt, less is known about how it could affect global ocean currents. The ocean's currents are driven by wind and differences in density caused by variations in water temperature and salinity. Glaciers and sea ice at the poles directly impact the salinity and temperature of the water. As currents move water towards the poles, the water becomes colder and increases in salinity, therefore, more dense. The increase in salinity is attributed to the freezing of sea ice, which freezes as fresh water, excluding salt and, in turn, making unfrozen sea water saltier. This increase in density triggers the water to sink and form deep water ocean currents where water travels back to the mid-Atlantic and upwells, producing what is called thermohaline circulation (O'Hare, 2011). This is precisely how the gulf stream works in the North Atlantic: wind-driven currents push warm water from the Gulf of Mexico to the Arctic, where it cools and becomes dense, and that water then sinks and moves back south. But melting ice will increase the amount of freshwater input into the Arctic and less sea ice and glacial coverage will lead to a warmer Arctic Ocean. One hypothesis is that the decrease in salinity, increase in temperature and the following decrease in density, could reverse the Gulf Stream. If the water is not dense enough to sink, then deep water currents from the Arctic to mid-Atlantic could fail, instead upwelling from deep ocean currents from the Antarctic could occur in the

Arctic, taking over in place of the Gulf Stream, water which would then travel south through the ocean surface effectively reversing the ocean current (O'Hare, 2011). Although it is also possible that the westerly winds that drive the warm surface water north from the Gulf of Mexico could intensify, pushing more warmer water north and counteracting any effects from decreased water density in the Arctic.

A study completed in 2020, conducted by NASA, discovered that the Beaufort Gyre in the Arctic Ocean is intensifying due to melting sea ice. The Beaufort Gyre is driven clockwise around the Arctic Ocean by westerly winds, collecting freshwater from glacial melt, sea ice melt, precipitation and river runoff that it then gradually releases into the North Atlantic when winds change direction every 5-7 years. But the westerly winds have not changed course in two decades, which has allowed the freshwater to collect in the gyre. As well, due to melting sea ice, more surface water has been exposed, allowing the westerly winds to intensify the current. Once the winds finally change course, it could release this freshwater in astronomical amounts, certainly affecting the density of sea water in the North Atlantic and therefore altering the Gulf Stream (Armitage et al. 2020).

A dead Gulf Stream may mitigate warming effects of climate change in the North Atlantic and Europe by decreasing water temperature as warm water stops flowing north. Alternatively, a Gulf Stream that remains intact will work to intensify climatic changes. But it is more likely that the effects of melting sea ice and glaciers in the Arctic will alter the Gulf Stream in ways that are difficult to predict. Whether weakening or intensifying the Gulf Stream, melting ice will certainly cause profound changes to ocean currents that will affect global climate and nutrient cycling.

### *Polar Glacial dynamics*

Understanding glacial dynamics, especially in glaciers in Greenland and Antarctica, is critical in understanding how rapidly and to what effect changing glaciers will influence global climate systems. In Antarctica, ice shelves act like giant barriers that hold back glaciers on land from rapidly advancing and calving into the ocean. In 2002, the Larsen B ice shelf off Graham Land in the Antarctic Peninsula collapsed. The Larsen B ice shelf completely broke away and began

drifting towards the Atlantic ocean and, in a sense, opened the floodgates to the glaciers from which it broke away. Glaciers on that part of the Graham Land, whose movement had been slowed by the ice shelf that lay in their path, suddenly surged into the ocean, creating thousands of icebergs that had previously been held on land. These icebergs melted, contributing to sea level rise.

The Larsen B ice shelf broke apart due to surface meltwater percolating through a deep crevasse in the ice (Scambos, 2004). Another factor that is contributing to ice shelf collapse and glacier surge in Antarctica is warming oceans. Warming ocean temperatures melt underneath these glaciers, pushing back what is called the “grounding line,” where glaciers disconnect from land and are then held in water by buoyancy. This causes further glacial acceleration, breaking up the ice shelf as the glacier forces its way into the water. As ice shelves calve, they melt faster. With less ice shelves to hold glaciers back, glaciers continue to accelerate faster, a feedback loop that continually speeds up the melting process (Rignot et al. 2011). Antarctica is surrounded by these ice shelves which are thinning and calving, losing more and more mass every year. Knowing the thickness of these ice shelves, and the snow accumulation on the ice sheet, can help us understand how vulnerable they are to calving or completely breaking away.

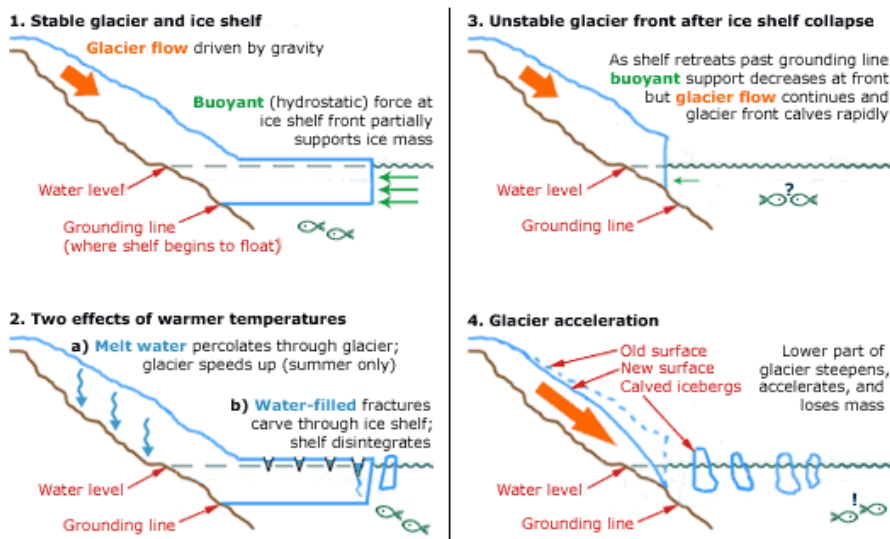


**Figure 2:** Illustrated glacial dynamics leading to ice shelf collapse and glacier acceleration (NASA)

Predicting major calving events, ice shelf collapse, and glacier advance are difficult endeavours. Our understanding of how these processes work is not fully developed. It is understood that the Greenland ice sheet is heading for total collapse due to a number of feedback loops, reduced albedo, percolation of water through and underneath the ice, and warming oceans. The ice sheet is melting and the glaciers are rapidly advancing into the ocean. Jakobshavn glacier is the major drainage stream of ice for the West Greenland ice sheet, this glacier has experienced record calving and acceleration. While the cause of calving and acceleration events is understood, predicting the timing of them remains out of reach of current models. In fact, according to some researchers, cutting edge glacial dynamics models may never catch up with the rapid retreat of the Jakobshavn glacier and the rest of the Greenland ice sheet (Gertner, 2019).

### *Operation IceBridge*

While glacial dynamics are difficult to understand, Operation IceBridge is helping us understand the volume, extent, and changes of mass to our polar ice. Operation Icebridge, run by NASA, is the largest aerial survey of ice ever conducted. Operation Icebridge began in 2009, and began collecting data where NASA's Ice, Cloud and Land Elevation Satellite (ICESat) left off. The satellite largely left the polar regions unobserved and was de-orbited in 2010. NASA's Operation Icebridge uses planes to collect data on the ice sheets instead of satellites and there are benefits and drawbacks to this approach. The drawback to using planes is that they are limited to seasonal missions, normally several weeks at a time, due to harsh polar winter conditions. As well, planes are limited to smaller areas of observation, whereas satellites can make observations all year long and observe vast areas. The major benefits of planes are that they can carry many more instruments on board, as can focus on specific areas. The instruments that NASA carries on its planes are the most important and groundbreaking instruments in radio-glaciology to date. These are radar instruments that measure snow accumulation, ice sheet depth, and the topography or sea surface below the ice. The Multichannel Coherent Radar Depth Sounder (MCoRDS) measures the ice sheet and bedrock topography while the Center for Remote Sensing of Ice Sheets (CReSIS) Snow Radar measures snow accumulation on top of the ice sheet.

MCoRDS has been one of the most important developments in radio-glaciology, allowing NASA to map the bedrock beneath the Antarctic and Greenland ice sheets and measure the thickness of an ice sheet with precision and detail. This radar is deployed in twin engine, long range, research planes and operated by scientists with the Center for Remote Sensing of Ice Sheets (CReSIS) during the entire flight line over the ice. Like echo-location, radar is helpful in the study of glaciers because the timing and strength of reflected signals may be used to map the shape and thickness of the ice below. MCoRDS uses the radio frequency receivers operating in the bandwidth [140-230] MHz. Each receiver has a tunable bandwidth to maximize the signal to noise ratio (SNR) of radio waves reflected from the ice.

CReSIS researchers deployed in Operation IceBridge planes fly over specific flight paths to map a section of the ice sheet or shelf that the scientists want to study. The machine fires radio waves as the plane flies, a radio wave is shot every few meters or so as the plane moves forward. The machine counts the amount of time, in microseconds, it takes for radio waves to bounce back off the ice sheet and bedrock and back to the plane. Then, the researcher, knowing how fast radio waves travel through air and ice, can calculate the distance it took for the radio waves to bounce back. The radio waves bounce off the ice surface as well as the bedrock. The final product of these flights is a map of the bedrock underneath the ice and the volume of the ice above the bedrock as determined by measuring the thickness. With these maps, scientists can better understand the flow of the ice across the bedrock. In Figure 3, a canyon is observed in the bedrock, highlighted in blue. Ice moves faster through this canyon because it is the path of least resistance, much like water in a river. As the ice moves through this canyon, it digs the canyon deeper, shaving off rock as it moves and pushing the bedrock down due to the immense pressure from the weight of the ice above. For instance, researchers have discovered that the center of the bedrock under the Greenland ice sheet is below sea level, forced down by the weight of the thousands of meters of ice above.

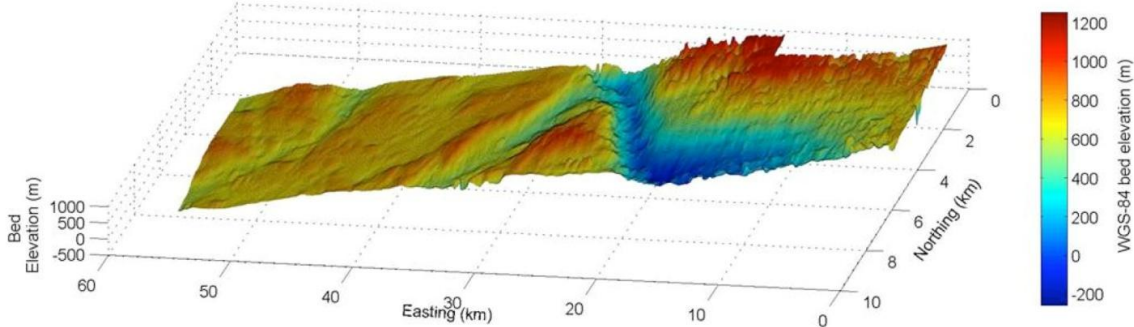


**Figure 3:** Bedrock topography produced by MCoRDS (NASA).

### Glacial Influences Downstream

Shifting focus away from the glaciers of Antarctica and Greenland, which present global climatic impacts, we observe the impacts that alpine glaciers have on downstream (more local) economies, ecosystems, and cultures. We use “downstream influences” to indicate the effects alpine glaciers have on their immediate surrounding areas. The planet's ice, most notably alpine glaciers and icefields between the poles, provide one of our most critical ecosystem services: fresh water. Glaciers provide freshwater that supports the many different uses of humans: most importantly, domestic use and agriculture. Besides being our largest reservoir for freshwater, meltwater from glaciers is a critical part of downstream ecosystems. Glaciers influence downstream ecosystems in many important ways. For instance, they provide sustained flow and regulate temperature especially during late summer months when snowmelt is no longer contributing. This temperature and flow regulation sustains productive fisheries around the globe, namely salmon fisheries. They deposit glacial till, unorganized sediment resembling clay, which provides habitat and soil. Glacial meltwater provides nutrients downstream and can help dilute pollutants in watersheds. Glaciers can also produce outburst floods, or jökulhaups, that can fatally flood populated areas, temporarily damage ecosystems or completely alter landscapes.

Meltwater and its impacts on the immediate landscape is one aspect of the importance of alpine

glaciers to their surrounding areas. Glaciers provide recreational and tourism opportunities that can be the backbone of local economies. And possibly the most overlooked, is that glaciers can form a sense of identity and be of critical cultural importance for communities that live near and far from ice. Categorizing the many impacts of glaciers to their respective downstream landscapes, ecosystems, and cultures, is difficult because, like all climatic changes, glacial change reverberates through all these systems and can have many indirect impacts. The more direct and more immediate impacts are easier to categorize. Glaciers have their largest direct impact on local economies, fisheries, agriculture, fresh water supply, and cultural identity.

Before introducing such impacts, it is important to define the difference in glacial-dominated watersheds and snow-dominated watersheds. Snow-dominated and glacial-dominated hydrological systems differ in their reservoir and timing of water discharge. Snow-dominated systems are limited by seasonal variability. Their reservoir for water will largely melt off in spring and summer once seasonal snowfall halts and atmospheric temperatures rise. As long as there is a glacier and energy to melt the glacier, there will be glacial melt. This is why summer to late summer waterscape in glaciated watersheds is primarily influenced by glacial meltwater, because by such time the influence of melting snowpack has decreased. The timing of such glacial meltwater discharge, while mainly occurring in summer, can be hard to predict, due to variability in summer temperatures, weather events, glacial dynamics, and even volcanic eruptions. In glaciated systems that rely on sustained year-round water, glacial meltwater provides sustained flow during late summer months. In many glacially dominated watersheds, glacier mass reduction due to climate change will eventually reduce or nearly eliminate late summer flows because of reduced or eliminated contribution to watersheds by glacial meltwater. In many systems, there will be an initial increase in glacial meltwater contributed streamflow over a few years as glacial melt rapidly increases and the bulk of glacial mass is reduced. But over the decades this summer flow will be reduced. This has far-reaching consequences downstream.

*Fresh Water Source: Himalaya, the water tower of Asia.*

If you live downstream of the Himalayas, the Alaska Range, the Coast Mountains of British Columbia, or Patagonia, the water you drink comes from glacial-dominated systems. Possibly nowhere else is this fact more consequential than the Himalayas. The Greater Himalayan range stretches from the Karakoram ranges of Pakistan in the west to Hkakabo Razi in Myanmar to the east. This range passes through the most populous countries on earth: China, India, and Pakistan, as well as Afghanistan, Nepal and Bhutan. The Himalaya and surrounding central Asian ranges are often referred to as the world third pole, because they contain the third largest deposit of ice and snow in the world, after Antarctica and Greenland. An estimated 1.9 billion people rely on freshwater that is sourced in glaciated catchments. Glacial meltwater is an important source of water, especially during dry months, but its importance varies across the region. For instance, in the Ganges River Basin, most freshwater is sourced from the monsoons, and only 3% of flow is sustained by glacial meltwater. On the other hand, the Indus River Basin can attribute 32% of its flow to glacial melt (Immerzeel et al. 2010). That being said, many studies have not accounted for seasonal variability in assessing contribution sources, and studies use a variety of different methods to assess glacial meltwater contribution. One study suggests that the Ganges River can attribute up to 58% of streamflow annually to glacial melt (Racoviteanu et al. 2013) and another study suggests that the Indus can attribute 80% (Zhang et al. 2013). The population of the Ganges River Basin is more than half a billion people. The population of the Indus River Basin is nearly 270 million people, mainly in Pakistan, all of which depend on that meltwater as a source of water for drinking and agriculture. The Indus River is over-allocated and considered one of the most depleted river basins in the world (Sharma et al. 2010). In addition, Pakistan withdraws 50% of its water for agriculture use from groundwater, which is severely overused and is being withdrawn faster than the groundwater can recharge itself (Watto et al. 2016). The region is likely to experience a growth in water use and a decline in water availability. Although glacial meltwater contributions may initially increase, which will be the case with glaciated systems as glaciers experience rapid melt, overtime as glaciers recede their contribution will significantly decrease. Hundreds of millions of people under severe water stress in a single location is a recipe for intense conflict and mass migration.

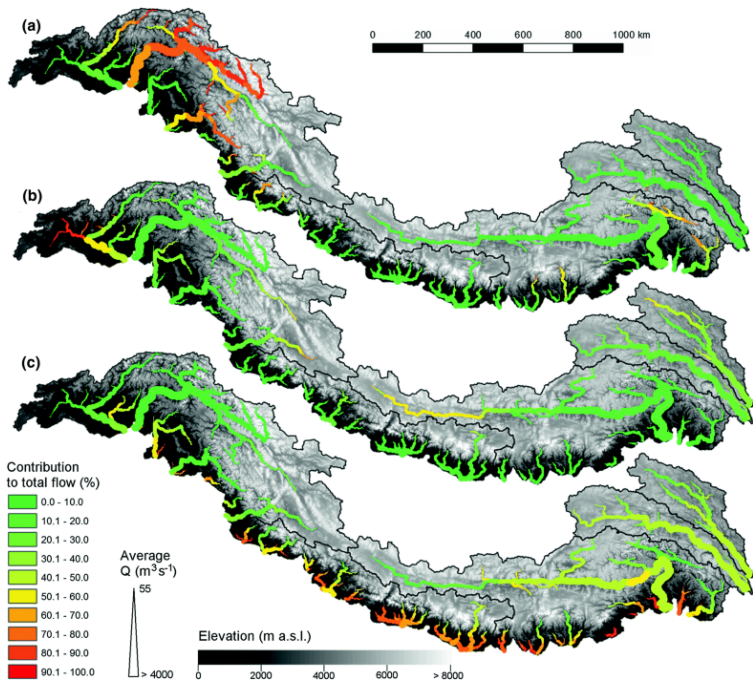


**Figure 4:** The Himalaya region. The Western basin is the Indus, followed by the Ganges and Brahmaputra to the East. Line thickness refers to the average total discharge, while color indicates the percentage of discharge that is contributed by each source. “Contribution to total flow by (a) glacial melt, (b) snowmelt, and (c) rainfall-runoff for major streams during the reference period of 1998–2007. Line thickness indicates the average discharge during the reference period” (Lutz, 2014)

While river basins, such as the Ganges and Brahmaputra, could attribute less of their annual flow to contributions from glacial melt than the Indus, seasonal variability is an important factor that requires further research in the Himalaya. For instance, in the Khumbu Valley, Nepal, a heavily glaciated catchment in the Ganges Basin, 80% of precipitation falls during the monsoon season in the months of June to September (Wood et al. 2020). The flow of the Ganges and its tributaries in non-monsoon months is much more likely to be sustained by glacial melt. For communities living in the high Himalaya catchment areas of those basins, such as the Khumbu Valley, glacial meltwater is critical in non-monsoon months. A study conducted in 2016-2020, found that 60% to 65% of the domestic water use in the region is sourced from glacial meltwater. In some communities, that number reaches 90% (Wood et al. 2020). Himalayan glaciers could lose two-thirds of their mass (calculated under the RCP8.5 climate model) by 2100 (Kraaijenbrink et al. 2017). In non-monsoon months, the 1.9 billion people that live in the shadow of the Himalaya, in glacial fed basins, could lose a majority of their freshwater access. Melting glaciers do not just pose water availability risks, but also geological hazards. Recently, a flood in the Indian Himalayas caused 50 fatalities, with another 150 still missing. The flood was caused when a massive overhanging glacier collapsed, causing a rock fall which sent tons of rock

and ice debris flying into the valley below colliding with glacial sediment. This resulted in a large landslide that flowed into the Rishiganga River, causing the river to flood with a wave of rock and ice slush (Washington Post, 2020). Receding glaciers in the Himalaya are also uncovering a large number of pro-glacial lakes, which form at the tongue of glaciers. The increase in the number and volume of these lakes is increasing glacial lake outburst flood risks (Bajracharya et al. 2020) which can produce disasters like the deadly February 2021 flood in India.

In the Himalaya region, political conflict between the largest countries -- China, India, and Pakistan -- make coordinated research efforts difficult, if not impossible. This issue is compounded by the fact that the region's geology and geography is incredibly diverse and glaciology is a new science in the region. Much is not known about the Himalayan glaciers and their exact downstream impacts and how those impacts will vary under climate change. But the impacts are clearly significant and the consequences of change monumental, so further research is critical.

#### *Impacts on agriculture: Wyoming*

In the Indus River basin, glacial meltwater sustains a massive year-round agricultural economy. The size of the agricultural product produced, which can be attributed to glacial meltwater in the Indus River Basin, is hard to quantify. To better understand the impacts that glacial meltwater have on agriculture, we review a study conducted on the cattle industry and Wind River Range glaciers in the U.S. state of Wyoming. While a much smaller study area than the Indus Basin, Wyoming glaciers represent an intricate case study that is representative of our reliance on the many smaller glacial systems around the world. Wyoming contains the largest concentration of glaciers in the American Rocky Mountains, the vast majority of which occur in the Wind River Range in western Wyoming. Until recently, the glaciers in the area were largely unstudied. Among U.S. states, Wyoming ranks 8th in barley production and 20th in hay production, which is impressive given its small growing season of about two months or less. These crops feed Wyoming's cattle, which is an \$800 million dollar business (Cheesbrough et al. 2009). The growing season coincides with maximum glacial melt, in late Summer to early Fall. Glacial meltwater from the Wind River Range supplies a steady and reliable source of water during

these months. Fremont County, encompassing the Wind River Range to the east of their crest and the foothills and plains that follow, accounts for the majority of Wyoming's irrigation water use (Boughton et al. 2006). Seventy-seven percent of the glaciers of the Wind River Range are on the eastern slopes, where the streams and rivers of Fremont County are sourced (Vandeberg et al. 2016). The Wind River flows through Fremont County and supplies the vast majority of surface water to the region. Three of its major tributaries are sourced in glaciated catchments in the Wind River Range. During the late summer months and the Wyoming growing season, one of these tributaries, Torrey Creek, could attribute an estimated 82.7% of its flow to glacial meltwater, which in turn attributed to 10.32% of Wind River flow (measured upstream from next tributary) (Vandeberg et al. 2016). The second major tributary, Dineywood Creek, could attribute an estimated 53% to 59% of its flow in 2007, which was a dry year, to glacial meltwater (Cable et al. 2011). The third, Bull Lake Creek, could attribute 55.6% of its flow to glacial meltwater (VanLooy et al. 2019).

Glaciers in the Wind River Range decreased in mass by 25% from 1985-2005 (Cheesbrough et al. 2009). Given temperature and precipitation data since 2005, the glaciers in this range are likely experiencing their peak melt rate and will soon begin to decline. These contributions to the Wind River represent a significant enough portion of late summer surface water contribution to significantly impact agricultural production in the region, especially compounded by reduction in overall snowpack and precipitation. Changes in glaciers in the Wind River Range will also have impacts on the surrounding ecosystems, including the impact of reduced streamflow to the state's trout populations.

#### *Impacts on fisheries: Washington Salmon*

Another critical resource, and a keystone species of the American West, that depends on late summer flows from glacial melt are fish. I use “resource” not in its strictly economically centered definition, but to represent something whose value can be appreciated beyond financial value, with cultural and emotional value as well. The America West is known for its abundance of trout and salmon, which form the cornerstone of many indigenous cultures and countless fisheries, and serve as the backbone of the recreational sector. But this resource has been critically abused for over a century. Through population growth in the Western United States and

the consequent increased demand for water during the 20th century, the federal Bureau of Reclamation was founded in order for water in the West to be “reclaimed” for beneficial economic use. Thousands of dams were built, damming nearly every single river in the West and creating tens of thousands of reservoirs. This was done without a single thought to the long-term economic viability of such development and with no concern for the ecosystems that would be impacted. As a result, countless ecosystems were destroyed or crippled. For salmon, this meant that they were obstructed from completing a critical part of their life cycle: spawning up river. The Columbia River that runs between the U.S. states of Washington and Oregon was once home to the world's largest and most diverse salmon runs, but is estimated that of the 10 to 16 million salmon that once spawned in this river, less than 2% remain today (New York Times, 2019). Dams and habitat loss pose a major threat to salmon. Dam removal projects are showing signs of hope in the return of salmon, such as the return of fish following dam removal in the Elwha River, Washington (Brenkman et al. 2019).

Salmon in the Pacific Northwest are facing another threat: decline in summer streamflow and subsequent water temperature increase. The state of Washington is expecting dramatic decreases in snowpack as the global temperature increases over the next few decades. The warm season (April to September), when streamflow is primarily influenced by snowpack melt and glacial melt, is expected to experience a 34% to 43 % decline by 2080 (Elsner et al. 2010). While the total annual streamflow is expected to increase on average 4% to 6% across the state by the 2080s, due to increased late fall and winter precipitation, the majority of the increase in precipitation in these months will fall as rain and, therefore, not contribute to the snowpack (Elsner et al. 2010). A study in the Nooksack River watershed in Washington highlights the importance of glaciers to summer/fall streamflow. The Nooksack River is fed by glaciers on Koma Kulshan (Mt. Baker), a heavily glaciated stratovolcano in the North Cascades. The Nooksack River watershed is separated into three basins: the north fork basin and middle fork basin are both glaciated, while the south fork is unglaciated. The glaciated basins and the unglaciated basin discharge does not significantly differ in winter/spring, but during late summer there is a significant difference in daily discharge, with the glaciated sub-basins receiving significantly higher daily discharge than the unglaciated sub-basin (Bach, 2002). High elevation snowsheds and glaciers in the north and middle fork basins contribute significantly to this late

summer discharge. It is estimated that these contributions equal 30% of summer discharge in the entire Nooksack River basin (Bach, 2002).

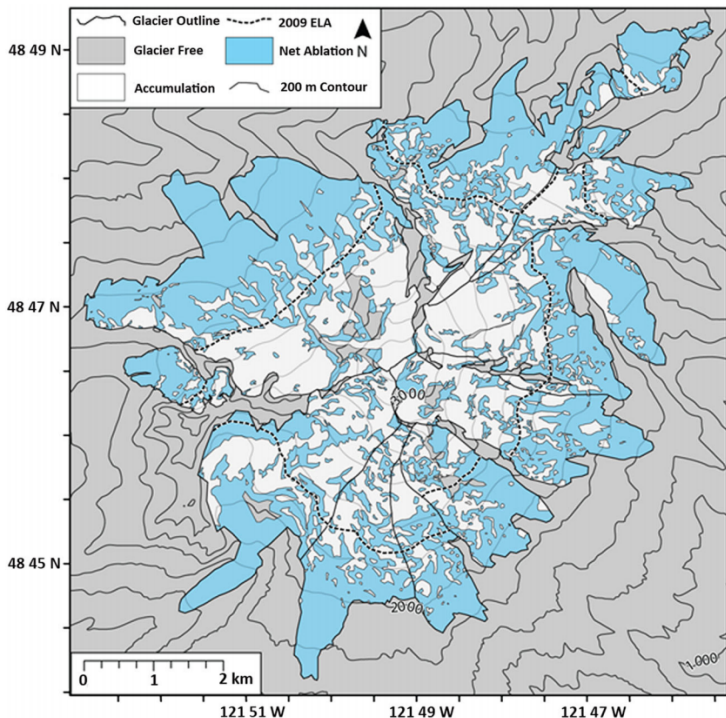


**Figure 5:** Accumulation area ratio (the ratio between a glacier's accumulation area, and total area.) observations are frequently below 30% on Mt. Baker.

Increase of ablation zone and decrease of accumulation zone is the clearest sign of a receding glacier.

(Pelto & Brown, 2012)

Glaciers on Mt. Baker had a negative mass balance entering the 21st century. From 1990-2010, glaciers on Mt. Baker lost 12% to 20% of their mass (Pelto & Brown, 2012). Under the RCP4.5 climate model, glacial extent in the North Fork Basin is estimated to decrease by 66% by 2099; under RCP8.5, it is estimated to decrease by 88% (Murphy, 2016). It is expected that glacial contribution to streamflow will increase mid-century then rapidly decrease as glacial mass is lost. As glacial mass is lost and snowpack decreases, late summer streamflows could be reduced by 40% in the Nooksack River by 2075 (Dickerson & Mitchell, 2013).

The Nooksack River watershed supports nine species of salmonids including populations of Chinook and Coho salmon. Chinook and Coho are already critically endangered in the watershed due mainly to habitat degradation. Already, current stream temperatures of the South Fork Nooksack frequently exceed 20°C, and sometimes exceed 24°C, well in excess of the temperature ranges considered optimal for Chinook incubation (11–15°C) and juvenile rearing (14.2°C –16.8°C) (Beechie et al. 2012). Low summer flows will cause a lack of deep pools and

side channels for habitat, and even further warming of stream temperatures due to increased air temperatures. High temperatures stress spawning fish and increase susceptibility to disease, which can cause pre-spawn mortality or otherwise reduce reproductive success. Continued increases in stream temperatures and reduced meltwater from glaciers due to climate change will further stress all nine species of Nooksack River salmonids during all of their life stages, including migration, spawning, rearing, and out-migration (Grah & Beaulieu, 2013).

### *Glacier Tourism: New Zealand*

Glaciers provide more than a valuable source of freshwater. They also provide outdoor recreational opportunities, which in 2019 accounted for nearly \$460 billion, or 2.1%, of the U.S. gross domestic product. Glaciers are direct and indirect contributors to revenue generated from tourism. For instance, Alaska's national parks generated \$2 billion in 2018 (Koontz & Thomas 2019). Two of the most visited national parks, Denali National Park and Glacier Bay National Park, are heavily glaciated areas. These glaciers drive visitation and, in turn, generate revenue, as people wish to observe these glaciers. This is an indirect impact on tourism, as there are many other reasons people visit Alaska's national parks. However, there are many places where glaciers are the main reason for visitation and the direct source of revenue. Glaciers are dramatic and fascinating parts of our landscape and there are few places where glaciers are easily accessible. Visitors to Alaska's national parks get can within viewing distance of glaciers, but often not much closer, due to difficulty of access. Places where glaciers occur in accessible areas, or where infrastructure to reach glaciers has been built, often experience a growth or dependence on glacial tourism. Glacial tourism takes many forms, but often revolves around physically accessing the glacier. Popular forms of access include hikes to and on the glacier, ice cave tours, ice climbing, or access by boat/kayak to a glacier terminating into a proglacial lake. Glaciers are undeniably beautiful and stand in stark contrast to their surrounding landscapes, coupled with the sense of adventure that climbing/hiking on glaciers inspires, they create attractive destinations for tourists.

A study observed the impact of glacial retreat on glacial tourism in New Zealand (Purdie, 2013). New Zealand's southern alps are home to more than 3,000 glaciers (Chinn, 1999), three of which flow into low-lying valleys which make these glaciers easier to access. These glaciers, the

Franz-Joseph, the Fox, and the Tasman glaciers, have been supporting glacier related tourism since the late 19th century, which has only experienced significant growth particularly due to the influx of international tourists (Purdie, 2013). This growth in glacial tourism has generated \$81 million in annual revenue in New Zealand and attracted 700,000 visitors to the glaciated region of New Zealand southern islands west coast (Purdie, 2013). However, these glaciers are receding. The Tasman glacier terminus has receded rapidly, leaving behind a proglacial lake into which the glacier now terminates. This lake did not exist in the late 20th century. The glacial retreat in recent decades has exposed a lake almost 7 square kilometers (Dykes & Brook, 2010). This event has created new opportunities for glacial tourism, including boat rides to the glacier's calving face, now terminating into the lake. The public knowledge of New Zealand's receding glaciers has also driven a phenomena coined "late-chance tourism" where people are attracted to landscapes that are disappearing or changing rapidly (Lemelin, 2010). This phenomena is not exclusive to New Zealand's glaciers, nor is it to glaciers. For instance, bleaching events in the Great Barrier Reef are driving an increase in tourism. Last Chance Tourism is driving an increase in methods used to access glaciers, as tour providers respond to the increase in demand. In New Zealand, helicopters are being used to bring tourists onto the Franz Joseph and Fox glaciers. As these glaciers recede, they are exposing steep and unstable slopes on valley walls normally held in place by ice (debutressing) and they have left behind large lateral moraines (Ballantyne, 2002). Both of these hazards increase the risk of rock fall and increase the risk of injury for anyone en route on foot to the glacial terminus. Methods used to increase safe access to glaciers, to accommodate the increase in "last chance tourism" visitation, can cause unintended environmental consequences. Consider the building and maintaining of roads and carbon emissions from an increased use of motorized vehicles, such as boats and helicopters, while these consequences have not been quantified, they are likely having an impact. The glacial tourism industry will adapt to glacial change and tourist operations will likely increase in size and revenue, at least while the glaciers remain. New Zealand is estimated to lose more than 80% of its glacial mass by the end of the century, according to IPCC reports (Marzeion, 2020) and glacial tourism cannot exist without glaciers.

### *Biodiversity & Endemic Species: Trinity Alps, CA*

Glaciers are fascinating components of our environments and can harbor species endemic to specific glaciers. In the Trinity Alps in Northern California, the first major paper was published in 2020 concerning the remnants of two once active glaciers in these mountains. Unique climatic and topographic properties in the Trinity Alps once supported California's lowest elevation glaciers, the only glaciers in the state below treeline. But following California's devastating 2012-2016 drought, one of these glaciers melted away and the other broke apart, its ice now stagnant. The ice was found to harbour populations of a beetle (*Nebria praedicta*) that is endemic to the Trinity Alps, and thrives, fascinatingly, in ice and snow (Garwood et al. 2020). The beetles' survival is very much tied to that of the Grizzly glacier, whose stagnant ice points to a grim future. This ice is part of an incredible and diverse interconnected ecological system. The ice sources a stream in the high alpine ecosystem that forms a creek that flows down to the Trinity River, which is full of Chinook Salmon. These salmon swim past Redwood forests, containing the tallest and most carbon dioxide absorbent trees on earth. The Chinook Salmon's decaying body provides essential nutrients for the Redwood tree. In turn, the Redwoods provide habitat for the Chinook to spawn. A bit of that water, in which the salmon swim and the Redwood roots soak, came from the ice in the mountains above. That bit of water is a drop in a lake compared to the other surface water sources in the Trinity watershed, but it is still there. There have not been studies that have quantified the contribution of stream flow that can be attributed by the Grizzly glacier and it is likely not significant, but it is fascinating and tragic to think about how a dying glacier is providing a bit of life to the world's tallest tree. The glacier's immediate impact on its surrounding environment is much more significant. What cascading impacts could extinction of the ice-loving beetle have on surrounding ecosystems? What happens when such an incredible part of an environment vanishes, no matter how small its contribution to that environment may seem? There are countless species in countless ecosystems whose dependence on glaciers is similar to that of the beetle in the Trinity Alps, all are at risk.

## What Glaciers can Tell us about the Past

### *Ice Cores*

Glaciers do not just act as the thermometer of a changing world, they are also record keepers of past climates. Snow accumulation on glaciers traps bubbles of gas, that snow is then compacted and the air bubbles become trapped in ice. This process occurs annually on the glacier accumulation zone and the bubbles preserve within them a record of atmospheric composition from that year. Researchers are able to discern the annual layers in the ice due to annual variations in snowfall and snow accumulation on the ice. As the ice gets deeper and more compressed, layers can be harder to discern. Another way ice can be dated, especially in deeper ice, is through layers of ash that accumulate on the ice surface. Layers of ash often indicate major volcanic eruptions. Antarctica and Greenland are areas with the longest and best kept records of climate in ice, the oldest ice in Antarctica is estimated to be 800,000 years old (Augustin et al. 2004).

Ice cores present us with incredible amounts of accurate information that help us reconstruct past climates. Thicker layers indicate higher rates of snow accumulation and precipitation for the year being analyzed. Bubble free layers indicate melt years with higher summer temperatures, these layers form through to the percolation of meltwater through the snow then freezing. Although possibly the most valuable information is from the gaseous composition of the trapped air bubbles. By analyzing the carbon dioxide and overall greenhouse gas content of these air bubbles, researchers can discern the overall atmospheric greenhouse composition for the year they are analyzing, this has allowed us to reconstruct atmospheric carbon content dating back 800,000 years. This has allowed us to observe the massive impact anthropogenic emissions have had on current atmospheric carbon content.

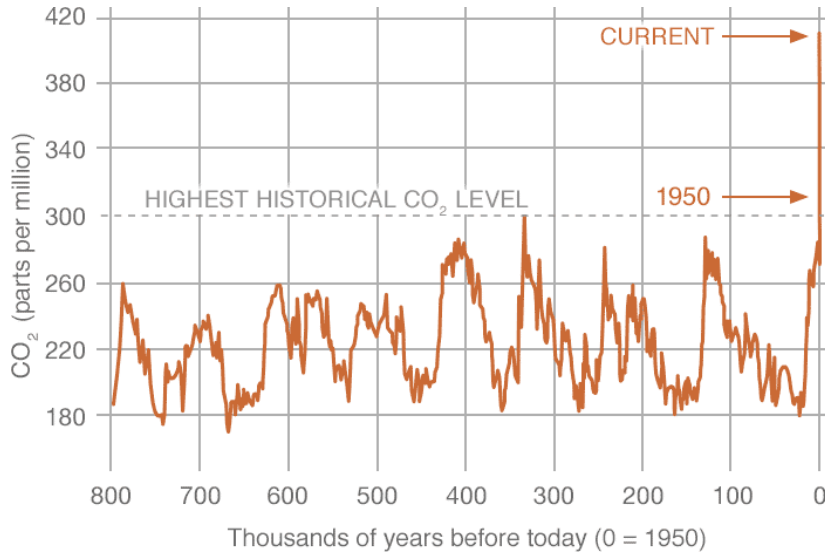


**Figure 6:** Atmospheric carbon dioxide content in parts per million over the last 800,000 years from data derived from ice cores. Historically carbon dioxide content never reached over 300 ppm, today it reaches over 400 ppm. (NASA)

### *Previously glaciated landscapes: Yosemite, CA*

John Muir was one of the first people to understand the historic extent of glaciation in the Yosemite region of the Sierra Nevada range, California. A pioneer of his time, Muir spent five summers in the 1870's studying the remaining glaciers of Yosemite and observing the geological features of the mountains that indicated previous glacial extent (Muir, 1875). Wide U-shaped valleys of polished granite, sharp mountain ridges (arêtes), steep granite walls (El Capitan), large granite domes (Half Dome), hanging valleys (Little Yosemite Valley), and wide bowl-shaped cirques just below the mountain peaks, many such as Mt. Lyell, still glaciated. Muir discovered Lyell glacier when it was a mile wide and a little less than a mile long. He stuck wooden stakes into the ice and upon revisiting these stakes, he discovered this glacier was moving at about an inch a day. At the time, no one knew glaciers were present in the Sierra Nevada, much less that the valley was shaped by them. Muir published a revolutionary paper with his findings titled "Living Glaciers of California." In the paper Muir noted: "How much longer this little glacier will live will, of course, depend upon climate and the changes slowly effected." Lyell glacier is now stagnant and technically no longer considered a glacier, due to climatic changes (Stock et al.

2016). The Lyell glacier was one of the last remaining glaciers that formed during the Little Ice Age, that once carved the great granite formations of Yosemite national park.

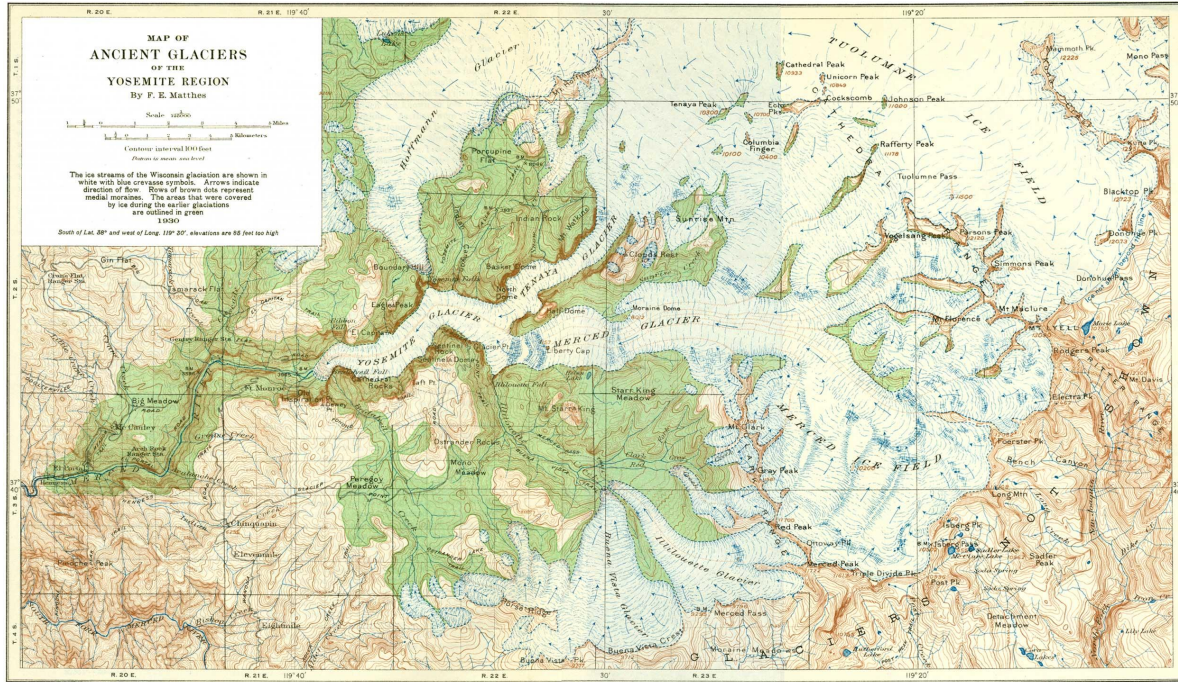


**Figure 7:** Topographic map of Yosemite national park during one of the last major glaciations highlighting previous glacial extent (USGS, 1930).

Yosemite is an excellent exhibit on how previous glaciations shape and completely transformed the landscape often in spectacular and dramatic ways. Mountainous regions all over the world have been shaped by glaciations from Mt. Kilimanjaro, Tanzania, to the Bolivian Andes. As the architects of the mountains, such as Lyell glacier, recede, more of these landscapes will be uncovered.

### Glacial Impacts on Culture and Identity

Dr. M Jackson, an Oregon state-based glaciologist and leader in research concerning the cultural and spiritual perceptions of glaciers and glacial change, writes that glaciers are more than just

single stories of melting ice. Glaciers represent so much more than global thermometers or climatological records: glaciers represent spiritual and cultural cornerstones of human life. But these stories are not often included in glaciological research. Jackson argues that this is due to a purely theoretical and eurocentric dominated field of glacial research and that incorporating a more open framework for researching glacial change could help integrate and understand the many stories of glacial change. Glaciology is a science founded in Europe, so it is understandable that it is dominated by eurocentrism. A more open framework investigates the epistemological questions relating to our gathering of glacial knowledge by investigating who has historically dominated the production of glacial knowledge, gendered structures in science, domination of eurocentric systems of science and alternative representations of glaciers (Carey et al. 2016). This framework presents us with a path to explore the perceptions of glaciers outside a single story of glacial change and explore glacial perceptions outside a purely theoretical view. For instance incorporating more qualitative knowledge in our understanding of ice could be of value to the field, for instance incorporating indigenous understanding of ice. This being said, quantitative evidence of glacial change is not to be undervalued by including these observations, rather put into context with broader stories of glacial change.

### *Indigenous Perspectives*

Often missing from glacial science and glacier stories are indigenous peoples perspectives, it has been a science dominated by a eurocentric view (Carey et al. 2016). Many of the glaciologists and researchers I have mentioned thus far have studied ice through such a lens. But human interaction with ice goes beyond the study of changes in mass and its physical impacts, ice, especially through the stories of indigenous peoples, is interacted with through profoundly spiritual and emotional lenses. For instance in the Andes mountains of Peru, the Quechua peoples believe that a receding glacier on Mt. Ausangate near where they live, is a sign of the departure of their gods from the landscape and the introduction of a new Epoch (Allison, 2015). Tens of thousands of Quechua would take part in a pilgrimage to the glacier each year to honor the appearance of Christ on the mountain, part of the ceremony would be to take a chunk of the glacier back to share with family and livestock. In order to try and preserve the glacier, the practice of taking ice from the glacier has been banned (Allison, 2015). For peoples living on the Tibetan Plateau, Mount Yulong Snow, a glaciated peak in the region, is considered their spiritual

home (Shijin & Dahe, 2015). The residents of this region have a deep understanding of climatic changes, over 97% of the population according to surveys conducted, understood they may need to leave their ancestral home once the glacier recedes due to climatic changes, which will impact the regions habitability (Shijin & Dahe, 2015). In Nepal, glacial recession is understood as a rebuke from the gods as humans move away from a moral life by polluting the planet (Allison, 2015). For many of these cultures, glaciers are understood as an *axis mundi*, a center of the world. Their recession represents the consequences of human immorality in regards to the treatment of the planet, a shift away from balance with the earth and spirituality.

Indigenous communities in North America have long perceived the connection between humans and glaciers. Indigenous communities in the Yukon interior and Alaska coast living amount the St. Elias mountains have long viewed glaciers as sentient beings. Glaciers can see, listen, smell and make moral judgments, they can take on bodily forms and transform. Surge glaciers, glaciers that rapidly advance without warning, are common in this region, and are believed to be the response of glaciers to human activities. The Lowell glacier is known as the Na'ludi by the Southern Tutchone peoples of Yukon. The Na'ludi means "fish stop" because it surged and blocked the salmon migration in the Alsek River (Cruikshank, 2012). It is believed to have done this in response to a colonial trader comparing the bald head of an indigenous shaman to the head of a glacier. It was listening, it made a moral judgment, and so transformed and surged.

The concept of glacier sentience is one that is recognized across cultures. Glaciers' constant and unpredictable movement, the otherworldly sounds they create and echo across the landscape, the glacial sourced creek ebbing and flowing like a heartbeat, and the collapse of seracs and calving of glaciers terminates to create powerful perceptions of sentience. Glaciers respond quickly to the world around them and with dramatic effect, such as we are seeing with global climate change. M Jackson writes in her book, *The Secret Lives of Glaciers*, "Perhaps thinking about a glacier's aliveness is to think about living, about what living means, about how we respond to the livingness of the world around us. In many ways, thinking about glaciers is also thinking about us." Glaciers have shaped human societies in profound ways, our existence very much intertwined, what we can take away from cultural and spiritual perceptions of glaciers is that this will always be so. Glaciers are much more than thermometers or record keepers, they are living representations of humans. There is no quantitative evidence to point to glacier sentience, but

qualitative evidence, indigenous perspectives, show us the power of ice to influence cultures. Including this perception in our research of glaciers could deepen our understanding and our sense of dependence on glaciers.

## Iceland

In the Fall of 2020 I travelled to Iceland on an undergraduate study program centered on climate changes impacts on the Arctic. I stayed in Hali, Hornafjörður, just a few kilometers from Breiðamerkurjökull. The following are my findings and observations as I researched the impact of glaciers to the geomorphology of the landscape and the lives of Icelanders.

Iceland presents us with a unique area in which the many impacts of glaciers experienced in different parts around the world are experienced all in one heavily glaciated area. Ten percent of Iceland's landmass is covered in glacial ice, 8% of which is covered by Vatnajökull, the largest icecap in the country and in Europe. Ever since Iceland was settled in the 9th century, people's lives have been heavily impacted by the country's constantly changing ice. This is especially true in Southeast Iceland, where people settled the thin stretch of coastline between the sea and Vatnajökull. People there have learned to adapt to the ever-changing ice and the hazards it poses to life on the island, such as sudden glacial outburst floods (jökulhlaup) and surging glaciers that plow over homesteads and farms. There are few places on earth where people have developed such a close connection to ice, sometimes living and farming within a few hundred meters of a glacier terminus, or unexpectedly closer. This has formed incredibly unique perspectives on glacial change during a time when Iceland's glaciers are receding faster than anytime in recorded history. These impacts are leaving profound scars on landscape and changing livelihoods -- as they always have, but current changes threaten to be permanent and highly consequential.

## Geological Impacts

Since the mid 20th century, the post Little Ice Age retreat of Vatnajökull outlet glaciers has been increasingly influenced by anthropogenic forcing over natural forcing. Increasing temperatures since the industrial revolution have correlated with the increasingly rapid recession and loss of mass balance of Vatnajökull outlet glaciers, especially glaciers in southeast Vatnajökull in the Hornafjörður region. Rapidly changing glacial behavior has caused major changes to the proglacial landscape in the Hornafjörður. The glaciers leave behind their scars in the forms of moraines, eskers, and ever-moving glacial river networks spread across vast sandurs. Most recently, however, the receding outlet glaciers of Vatnajökull have revealed ever-expanding lakes, proglacial lakes, into which the receding glaciers now terminate (Schomacker, 2010). Of all of the proglacial lakes in Iceland, none are more vast or faster growing than the one formed by the Breiðamerkurjökull outlet glacier, which is simply called jokulsarlon or glacier lagoon (Evans, 2014).

Proglacial lake behavior is directly intertwined with glacial behavior and, therefore, directly linked to climatic changes (Carrivick, 2013). The formation of proglacial lakes can be attributed to the previous advance and subsequent retreat of glaciers. Advancing ice creates terminal moraines and the overdeepening of bedrock underneath the glacier. As the glacier retreats, it leaves behind the moraine and a depression in the surface between the glacial terminus and the terminal moraine created when it was at its furthest extent. Glacial meltwater becomes dammed by the moraine, as well as by the glacial terminus and pools in the depression, creating the proglacial lake (Carrivick, 2013). As for the outlet glaciers of Vatnajökull, the terminal moraine was created by the furthest extent occurred during the Little Ice Age. The most significant change and the defining factor [between natural recession] since the Little Ice Age is the change from land-terminating to water-terminating glaciers (Evans, 2014).

#### *Natural and Anthropogenic, Post Little Ice-Age Recession*

Glaciers in Iceland advanced during the Little Ice Age (LIA), a period of global cooling from 1300-1870 (Mckinsey, 2005). At the beginning of this period, Iceland's glaciers were smaller in size than they are today. A dip in temperatures of -0.6 degrees celsius, on average, in the northern hemisphere during this period triggered a massive glacial advancing event (Rafferty,

2011). The extent to which these glaciers advanced is well preserved in the geological record by the large terminal moraines near the outlet glaciers in southeast Iceland. During the LIA, the glaciers pushed up these terminal moraines as they advanced. Once the outlet glaciers began to retreat, they left behind clearly defined and orderly mounds of rock and debris that precisely marked their farthest extent (Evans, 2016). Glacial retreat after the LIA maximum was initially caused by what most scientists accept as a period of natural warming post LIA, at the start of the 20th century. But as we progressed into the early-mid 20th century, anthropogenic forcing became the primary influencing factor of the glacial retreat of Vatnajökull. The glacial recession now is driven by warming atmospheric temperatures caused by climate change, or the anthropogenic emissions of greenhouse gasses positively influencing the atmospheric greenhouse effect. Defining the periods of natural retreat and anthropogenic retreat in southeast Iceland since the LIA maximum is important in assessing the extent to which anthropogenic forcing is accelerating glacial retreat. Equally important, when assessing the differences between these periods, is predicting geomorphological changes to the pro-glacial landscape, such as the formation of proglacial lakes.

Focusing on the main outlet glaciers of the Vatnajökull icecap in the Hornafjörður region of southeast Iceland, it is possible to assess the varying position of the glaciers as they have retreated since the LIA. This assessment can be done by observing the geological features of the proglacial landscape (Evans, 2014). For instance, the most notable feature in a proglacial landscape is what is referred to as a moraine. In a proglacial landscape, the most common is a ground moraine, which is not as notably defined as its cousins, since it consists of unorganized deposits of rock formed as a glacier moves over a landscape. It is formed by sediment deposited underneath the glacier, by small streams or by the glacier hitting various landforms. Once the glacier retreats, the ground moraine is revealed. The most notable and easily spottable moraines in a proglacial landscape are terminal moraines and lateral moraines. Lateral moraines form at the sides of a glacier. As the glacier scrapes off rock from the sides of valleys, the debris is deposited along the valley sides when the glacier retreats (Evans, 2016). Terminal moraines form at the terminus of a glacier during a period of advancement. They are formed as the glacier picks up and moves debris while advancing and when depositing the debris at its terminus. From there the glacier retreats, leaving the terminal moraine. Terminal moraines provide the most accurate

information on past glacial positions. Other proglacial landscape formations also provide hints about glacial activity, such as eskers, or piles of rock and sediment [that is, or was, ice-cored] (Chandler, 2020). Fig. 8 demonstrates how these formations are spread across a proglacial landscape.

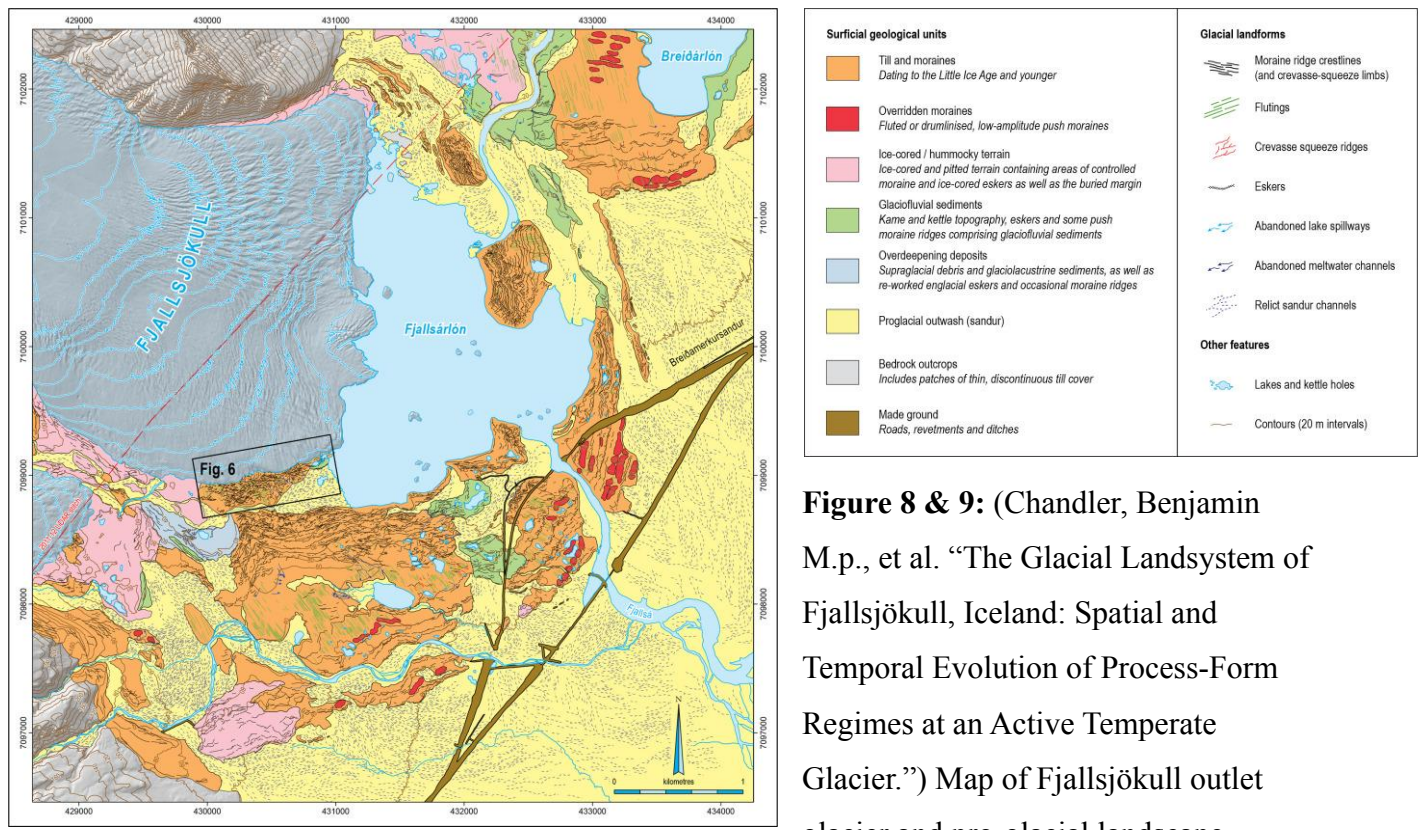


**Figure 8 & 9:** (Chandler, Benjamin M.p., et al. "The Glacial Landsystem of Fjallsjökull, Iceland: Spatial and Temporal Evolution of Process-Form Regimes at an Active Temperate Glacier.") Map of Fjallsjökull outlet glacier and pro-glacial landscape.

Highlighted are the geological features that can help determine the previous position of the glacier terminus.

Determining the difference between anthropogenic recession and natural recession can be accomplished by analyzing temperature trends through the 20th century and comparing them to previous glacial positions at Vatnajökull. Since the end of the Little Ice Age, there has been an overall recession trend and, since the turn of the 21st century, this recession has accelerated. A trend emerges when comparing atmospheric CO<sub>2</sub> concentration, global temperature, southeast Vatnajökull glacier terminus (Hoffellsjökull) and local climate. At the turn of the 21st century, as CO<sub>2</sub> and average global temperature increased (due to anthropogenic emission), Hoffellsjökull's

average summer temperature also rose, while the volume of Hoffellsjökull decreased. In Fig. 11, the data shows that decreases in the Hoffellsjökull glacier volume correspond to periods when local average temperatures increased, while Fig.10 shows similar periods of warming and cooling across the globe.

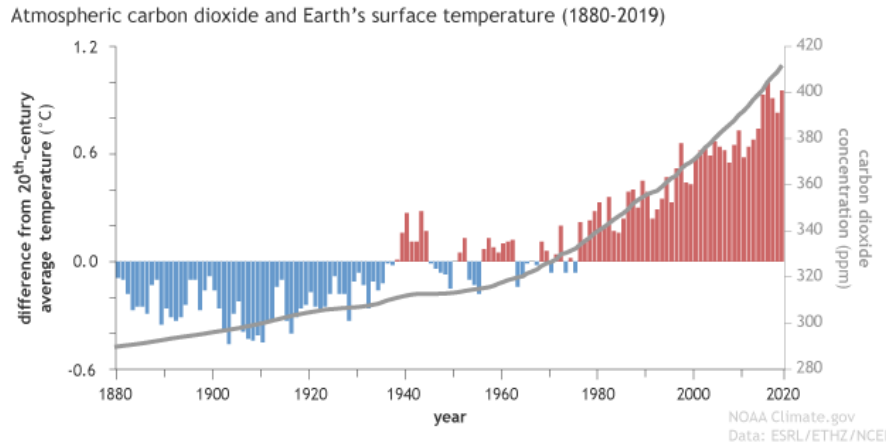


**Figure 10:** (NOAA Climate) Average global annual temperature compared to global atmospheric CO<sub>2</sub>.

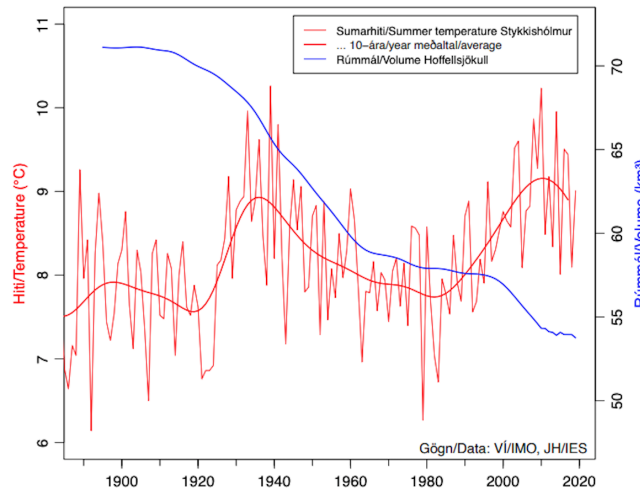


**Figure 11:** (Icelandic Meteorological Office: Melting Glaciers end of 2019 newsletter)  
Volume of Hoffellsjökull glacier (Vatnajökull outlet glacier) in kilometers squared combined with local annual summer temperature from 1900-2020.

### Proglacial Lake Formation & Glacial Behavior

Proglacial lakes in southeast Iceland form because of a process called overdeepening. Overdeepenings are subglacial basins that mark the area of maximum erosion in the bedrock due to valley glacier movement during a certain and extended period of glaciation. They occur at the equilibrium line of the glacier, between the accumulation and ablation zone, because this is the area of the glacier that reaches maximum velocity. The most erosion of bedrock occurs at this

location because of the fast-moving ice (Evans, 2014). Bedrock that is picked up as debris at the area of overdeepening is carried and transferred to the terminus of the glacier, forming a terminal moraine which helps dam and deepen the depression. As the glacier exits this period of glaciation and retreats, the depression in the landscape is revealed. This depression fills with sediment and glacial meltwater, forming a proglacial lake. Many of the outlet glaciers in southeast Vatnajökull formed these depressions through overdeepening during their maximum extent in the LIA (Evans, 2014). Since the turn of the 21st century, these glaciers are revealing -- and terminating into -- their proglacial lakes.

Lake terminating glacier behavior differs from land terminating glaciers. Glacier ice terminating into water experiences accelerated movement and accelerated ice mass loss through many mechanisms. Mainly, liquid water maintains heat better than ice, therefore, lake contact with ice will enhance melting (thermo erosion). Also, the formation of basal crevasses due to thermo erosion and accelerated movement increases the likelihood of calving. Lake terminating glaciers are buoyant and proglacial lake level fluctuates, further stressing the glacier, increasing movement and crevasse development (Carrivick, 2013).

### *Future of the Southeast Iceland Landscape*

The future of southeast Iceland will inevitably include much less ice. Even if anthropogenic greenhouse gas emissions are immediately and drastically cut, feedback loops will continue to increase temperature to melt a majority of the ice mass of Vatnajökull and certainly the outlet glaciers of southeast Vatnajökull (Björnsson et al. 2008). This glacial recession will reveal the proglacial lakes that are now partially, or nearly, covered by ice, such as those surrounding Oraefajökull in Fig 12.

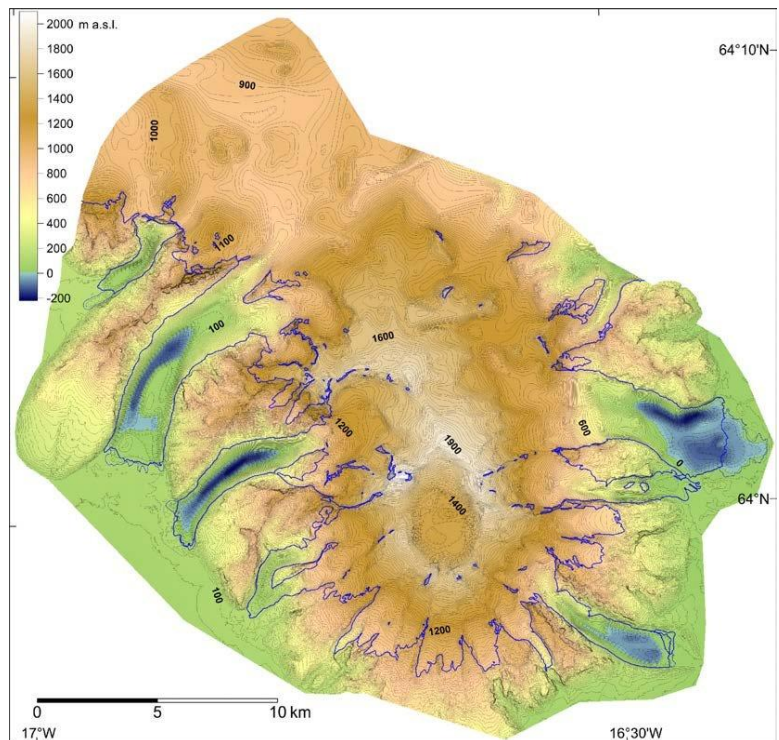


**Figure 12:** (Magnússon, Eyjólfur, and Finnur Pálsson. “Removing the Ice Cap of Oraefajökull Central Volcano, SE-Iceland: Mapping and Interpretation of Bedrock Topography, Ice Volumes, Subglacial Troughs and Implications for Hazards Assessments.” *Jökull*, vol. 62, 2012.)

A topographic map of the bedrock of Oraefajökull, the blue shaded areas indicate depressions in the bedrock, areas of overdeepening, dug by outlet glaciers. The blue lines indicate current ice extent.

Iceland is a highly volcanically active island, with the most significant recent eruption occurring in 2010. The eruption of Eyjafjallajökull, a glaciated volcano in southern Iceland, occurred in April 2010, and resulted in the near complete grounding of flights in Europe as the ash cloud covered most of the continent for one week following the initial eruption. In Iceland, the eruption triggered massive glacial outburst floods (*jökulhlaup*) that flooded rivers and glacial outwash plains (sandur). *Jökulhlaups* often occur in Iceland due to the rapid melting of ice over a volcano due to an eruption, or the burst of an ice dammed proglacial lake. Throughout Iceland's history, early settlers and current residents alike have had to adapt to these relatively frequently occurring floods, which have destroyed infrastructure, homes, and farmland. Most of Iceland's major volcanoes are covered by glacial ice. For instance, the highly active volcanoes of Grímsvötn and Bárðarbunga both lie under Vatnajökull. Melting glaciers in Iceland, and the subsequent loss of ice mass resting on top of the island's volcanoes, could increase volcanic activity. During Iceland's last cooling period, between 5,500-4,500 years ago, there was significantly less deposits of volcanic ash, suggesting that an increase in ice mass correlates with a decrease in volcanic activity (Swindles et al. 2017). This is because Iceland's glaciers act as a bottle cap on the country's volcanoes, suppressing volcanic activity. Therefore, the removal of this cap could, the melting of the ice, could reduce volcanic suppression and increase activity, possibly leading to more frequent high severity eruptions such as the 2010 eruption of Eyjafjallajökull.

Another way in which Iceland's decreasing ice mass is impacting the country is through isostatic rebound. Isostatic rebound occurs when the weight of ice is removed from a part of the earth's crust and causes the land to rise. During glaciation, the downward pull of the weight of the ice causes the crust underneath to sink into the lithosphere (isostatic depression). When the weight is removed during periods of deglaciation, the crust rebounds and rises. In Iceland isostatic

rebound is occurring at an incredible rate and accelerating every year as ice from the island's major ice caps melt away. Currently uplift rates in central Iceland and the surrounding area exceed 30mm/yr and are projected to exceed 40mm/yr in the next few years (Compton et al. 2015). A port in the town of Höfn, southeast iceland, is rising much faster than current sea level rise, and many of the fishing boats are now unable to enter the port at low tides, disrupting the local fishing economy upon which it relies.

## Cultural Impacts

Icelanders live with changing glaciers and are raised hearing stories of glaciers that either rapidly advanced or retreated. This has created an interesting perception of glacier change among Icelanders. Many, of course, recognize the dramatic impact climate change is having on their ice. In 2019, about 100 people held a funeral for Okjökull, a glacier that had recently melted away, placing a bronze plaque where the glacier once stood. The plaque read, "In the next 200 years, all our glaciers are expected to follow the same path. This monument is to acknowledge that we know what is happening and what needs to be done. Only you know if we did it." But many do not share the same perception of glacier change. Interestingly, different perceptions of glacier change are observed in the coastal communities of the Hornafjörður region, where residents live just a few kilometers from Vatnajökull. In 2016, glaciologist Dr. M Jackson was living in the Hornafjörður region exploring Icelanders perceptions of glacial change, which she recorded in her book *The Secret Lives of Glaciers*. Many who live here grow up with stories of their ancestors and relatives farms and homesteads being washed away by jokulhaups or plowed by advancing glaciers. Many of the elders live with fresh memories of such incidences. Glaciers present a constant struggle to the region, a constant battle with the elements, and many are relieved by the receding glaciers no longer threatening their livelihoods. Others are so used to glacier change and stories of glaciers receding and advancing that they believe climate induced changes to Iceland's glaciers are just part of the cycle, saying that glaciers have always been changing. Breiðamerkurjökull means "broad forest glacier" in Icelandic. At the time of settlement Iceland's glaciers were smaller than they are today. A forest of native birch once stood where the glacier is today, a period of global cooling caused the glacier to advance over this

forest. Today that glacier is receding again, leaving a large sandur where birch sprouts are beginning to grow once again.

## Iceland's Booming Tourism

In Iceland, perceptions of glacier change are also being shaped by the growth of glacier tourism in the region. Tourism in Iceland has skyrocketed during the recent decade to become one of its highest grossing economic sectors, leading Iceland's economy to be highly dependent on tourism. Of all of Iceland's attractions, Vatnajökull National Park has attracted the most visitors, especially Jökulsárlón, the ever expanding proglacial lake that fills with icebergs calving from the outlet glacier Breiðamerkurjökull. This has created many new economic opportunities for Icelanders and currently employs thousands. As glaciers in Iceland recede, tour providing operations are becoming increasingly aware and constantly adapting to the impacts of climate change. And as the knowledge of rapid glacier recession in Iceland grows, tourism to Iceland's glaciers increase as people wish to experience the ice before it leaves (Welling et al. 2020). Creating a sort of ironic situation as the emissions from transport to Iceland and the glaciers contributes to the greenhouse effect melting the ice. Some tour operations, such as Glacier Adventure, run by Haukur Ingi Einarsson in Hali, are increasingly focusing on educationally centered tours hoping to increase awareness of climatic changes and glacial recession and are conscious of their carbon footprint as well as their impact on the landscape. But many of the larger tour operations primarily focus on getting as many clients to the ice as possible creating large crowds, a heavily trodden landscape, and much waste for an area that cannot sustainably handle the influx of people. Although the pandemic has created a pause in tourism, while economically devastating, it has given the national park time to consider sustainable paths forward for the region.

## PHOTO ESSAY: VATNA > JÖKULL

*Perhaps thinking about a glacier's aliveness is to think about living, about what living means, about how we respond to the livingness of the world around us. In many ways, thinking about glaciers is also thinking about us.*

- Dr. M Jackson

In Fall 2020, I travelled to Iceland on an undergraduate study program centered on climate changes impacts on the Arctic and stayed in Hali, Hornafjörður, just a few kilometers from Breiðamerkurjökull. I was quickly exposed to islands changing glaciers and to the lives of those who centered around glaciers. Through experiencing and learning about Icelanders interaction with glaciers and perceptions of glacial change, I developed a sense of how powerful these bodies of ice were. Coupled with moments walking along the ice, the crunch of my crampons interrupted by the deep and full echos of moving ice, pulsating glacial streams, and the loud thud of ice calving off the glacier terminus and into the water, I began to understand why some Icelanders perceive glaciers as alive. The intense beauty of the ice that would stop me in my tracks, as I paused to breathe with the glacier, to feel and listen to its heartbeat, and try and comprehend what was before me. This glacier demands my respect, our fates tied together, and through that connection, it was hard not to feel its aliveness myself. With the photographs I captured, with my 35mm Canon AE-1, I hope to capture that feeling....



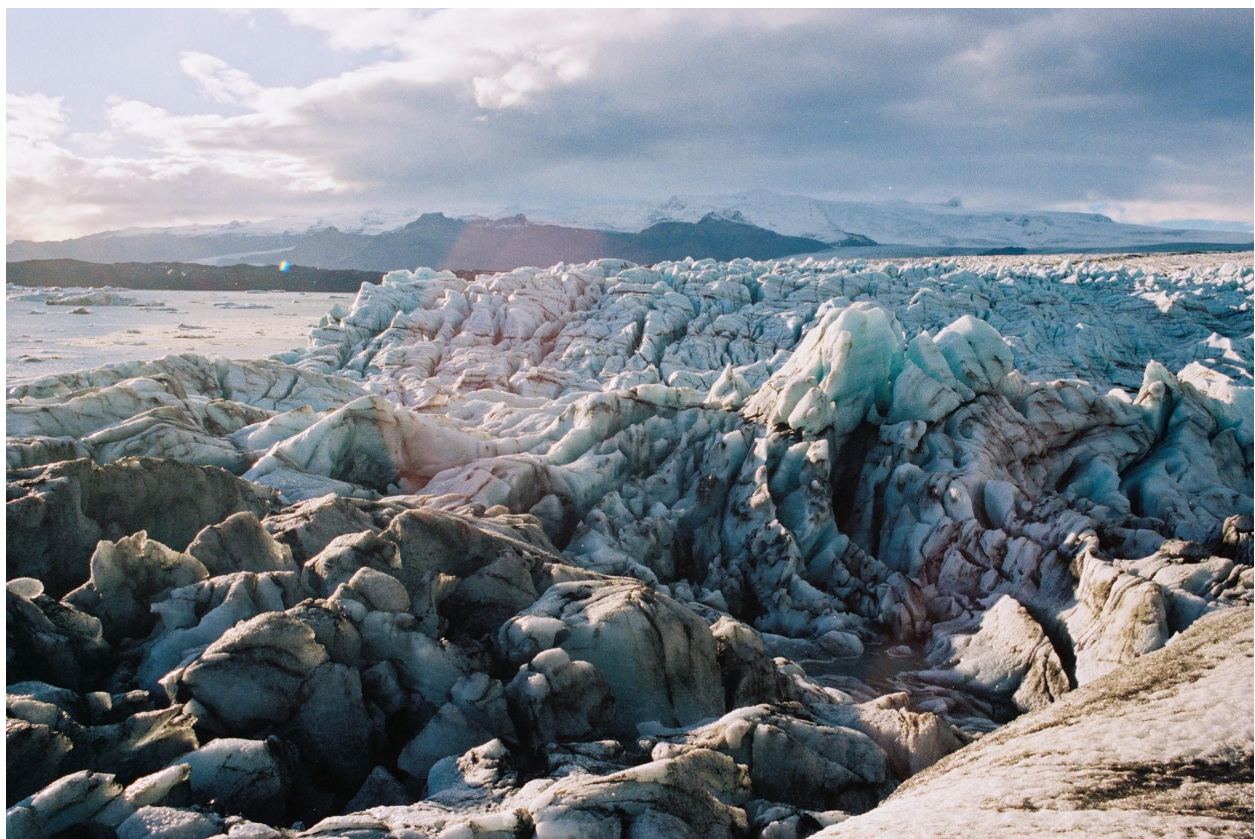


















## Conclusion

The case studies that have been presented are only a few of the many examples of the impacts of glacial change, every place on earth will be impacted by glacial change either directly through downstream changes or indirectly through global changes. There are countless stories to tell about how people interact and connect with ice. Our understanding of glaciers must dramatically improve if we are to best prepare ourselves for the inevitable changes that will occur. Our understanding must be rooted in stories that help connect people with ice and our dependence on it as much as it must be rooted in our physical understanding of ice. It is through our increased connection with, as well as understanding of, glaciers that we may come to better adapt to the changes that will occur and try to prevent the total loss of our planet's diverse and magical ice.

## Acknowledgments

There are so many people I wish to thank in my process of developing my understanding of glaciers and glacial change, and the incredible places it has taken me and the soul filling experiences it has exposed me too. My mothers for their never-ending support of my passions. Jordan Hanson, my mentor, who has guided me through this work and whose own work in Antarctica has inspired mine. Cheryl Swift, for expanding my capabilities in field work and showing me the joy of working in the field. Haukur Igni Einersson, owner and operator of Glacier Adventure, for inviting me to Hali, Iceland to experience the glaciers of his homeland and generously providing a helping hand whenever it was needed. My thanks, as well, to Mike Reid, lead guide at Glacier Adventure, for showing me how to properly travel and climb across glaciers and have a whole lot of fun doing it. My thanks to Þorvarður Árnason, for showing me the beauty of working at “the border of art and science,” whose photographs of the glaciers of Iceland are and will continue to be an inspiration. To Whittier College, NOLS, and SIT: Study Abroad for providing me with the opportunities to discover my passion for glaciers. My family and friends, whose adventurous spirits and full hearts make life exciting and meaningful.

## References

- Allison, Elizabeth A. “The Spiritual Significance of Glaciers in an Age of Climate Change.” *Wiley Interdisciplinary Reviews: Climate Change*, vol. 6, no. 5, 2015, pp. 493–508., doi:10.1002/wcc.354.
- Armitage, Thomas W., et al. “Enhanced Eddy Activity in the Beaufort Gyre in Response to Sea Ice Loss.” *Nature Communications*, vol. 11, no. 1, 2020, doi:10.1038/s41467-020-14449-z.
- Augustin et al. 2004 “Eight Glacial Cycles from an Antarctic Ice Core.” *Nature*, vol. 429, no. 6992, 2004, pp. 623–628., doi:10.1038/nature02599.
- Bach, Andrew. “Snowshed Contributions to the Nooksack River Watershed, North Cascades Range, Washington.” *Geographical Review*, vol. 92, no. 2, 2002, p. 192., doi:10.2307/4140970.
- Bajracharya, Samjwal Ratna, et al. “Inventory of Glacial Lakes and Identification of Potentially Dangerous Glacial Lakes in the Koshi, Gandaki, and Karnali River Basins of Nepal, the Tibet Autonomous Region of China, and India.” *International Centre for Integrated Mountain Development*, 2020.
- Ballantyne, Colin K. “Paraglacial Geomorphology.” *Quaternary Science Reviews*, vol. 21, no. 18-19, 2002, pp. 1935–2017., doi:10.1016/s0277-3791(02)00005-7.
- Beechie, T., et al. “RESTORING SALMON HABITAT FOR A CHANGING CLIMATE.” *River Research and Applications*, vol. 29, no. 8, 2012, pp. 939–960., doi:10.1002/rra.2590.
- Benning, Liane G., et al. “Biological Impact on Greenland’s Albedo.” *Nature Geoscience*, vol. 7, 2014, p. 691., doi:<https://doi.org/10.1038/ngeo2260>.
- Boughton, Gregory K., et al. “Estimated Water Use in Wyoming during 2000.” *Fact Sheet*, 2006, doi:10.3133/fs20063099.
- Brenkman, Samuel J., et al. “Rapid Recolonization and Life History Responses of Bull Trout Following Dam Removal in Washington’s Elwha River.” *North American Journal of Fisheries Management*, vol. 39, no. 3, 2019, pp. 560–573., doi:10.1002/nafm.10291.

- Cable, Jessica, et al. "Contribution of Glacier Meltwater to Streamflow in the Wind River Range, Wyoming, Inferred via a Bayesian Mixing Model Applied to Isotopic Measurements." *Hydrological Processes*, vol. 25, no. 14, 2011, pp. 2228–2236., doi:10.1002/hyp.7982.
- Carey, Mark, et al. "Glaciers, Gender, and Science." *Progress in Human Geography*, vol. 40, no. 6, 2016, pp. 770–793., doi:10.1177/0309132515623368.
- Carrivick, Jonathan L., and Fiona S. Tweed. "Proglacial Lakes: Character, Behaviour and Geological Importance." *Quaternary Science Reviews*, vol. 78, 2013, pp. 34–52., doi:10.1016/j.quascirev.2013.07.028.
- Chandler, Benjamin M.p., et al. "The Glacial Landsystem of Fjallsjökull, Iceland: Spatial and Temporal Evolution of Process-Form Regimes at an Active Temperate Glacier." *Geomorphology*, vol. 361, 2020, p. 107192., doi:10.1016/j.geomorph.2020.107192.
- Cheesbrough, Kyle, et al. "Estimated Wind River Range (Wyoming, USA) Glacier Melt Water Contributions to Agriculture." *Remote Sensing*, vol. 1, no. 4, 2009, pp. 818–828., doi:10.3390/rs1040818.
- Chinn, T.J. "New Zealand Glacier Response to Climate Change of the Past 2 Decades." *Global and Planetary Change*, vol. 22, no. 1-4, 1999, pp. 155–168., doi:10.1016/s0921-8181(99)00033-8.
- Compton, Kathleen, et al. "Climate-Driven Vertical Acceleration of Icelandic Crust Measured by Continuous GPS Geodesy." *Geophysical Research Letters*, vol. 42, no. 3, 2015, pp. 743–750., doi:10.1002/2014gl062446.
- Cruikshank, Julie. "Are Glaciers 'Good to Think With'? Recognising Indigenous Environmental Knowledge1." *Anthropological Forum*, vol. 22, no. 3, 2012, pp. 239–250., doi:10.1080/00664677.2012.707972.
- Dell, Rebecca, et al. "Response of Glacier Flow and Structure to Proglacial Lake Development and Climate at Fjallsjökull, South-East Iceland." *Journal of Glaciology*, vol. 65, no. 250, 2019, pp. 321–336., doi:10.1017/jog.2019.18.

- Dickerson-Lange, Susan E., and Robert Mitchell. "Modeling the Effects of Climate Change Projections on Streamflow in the Nooksack River Basin, Northwest Washington." *Hydrological Processes*, vol. 28, no. 20, 2013, pp. 5236–5250., doi:10.1002/hyp.10012.
- Dykes, Robert C., and Martin S. Brook. "Terminus Recession, Proglacial Lake Expansion and 21st Century Calving Retreat of Tasman Glacier, New Zealand." *New Zealand Geographer*, vol. 66, no. 3, 2010, pp. 203–217., doi:10.1111/j.1745-7939.2010.01177.x.
- Elsner, Marketa M., et al. "Implications of 21st Century Climate Change for the Hydrology of Washington State." *Climatic Change*, vol. 102, no. 1-2, 2010, pp. 225–260., doi:10.1007/s10584-010-9855-0.
- Evans, David J A, and Chris Orton. "Heinabergsjökull and Skalafellsjökull, Iceland: Active Temperate Piedmont Lobe and Outwash Head Glacial Landsystem." *Journal of Maps*, vol. 11, no. 3, 2014, pp. 415–431., doi:10.1080/17445647.2014.919617.
- Garwood, Justin M., et al. "20th Century Retreat and Recent Drought Accelerated Extinction of Mountain Glaciers and Perennial Snowfields in the Trinity Alps, California." *Northwest Science*, vol. 94, no. 1, 2020, p. 44., doi:10.3955/046.094.0104.
- Gertner, Jon. *Ice at the End of the World: an Epic Journey into Greenland's Buried Past and Our Perilous Future*. Random House, 2019.
- Glasser, Neil F. "Polythermal Glaciers." *Encyclopedia of Earth Sciences Series*, 2011, pp. 865–867., doi:10.1007/978-90-481-2642-2\_417.
- Grah, Oliver, and Jezra Beaulieu. "The Effect of Climate Change on Glacier Ablation and Baseflow Support in the Nooksack River Basin and Implications on Pacific Salmonid Species Protection and Recovery." *Climate Change and Indigenous Peoples in the United States*, 2013, pp. 149–162., doi:10.1007/978-3-319-05266-3\_12.
- G. Aðalgeirsdóttir, S. Guðmundsson, Helgi Björnsson, F. Palsson, T. Johannesson, et al.. Modelling the 20th and 21st century evolution of Hoffellsjökull glacier, SE-Vatnajökull, Iceland. *The Cryosphere*, Copernicus 2011, 5 (4), pp.961-975. ff10.5194/tc-5-961-2011ff. Ffhal-00640154f

- Hannesdóttir, Hrafnhildur, et al. “Variations of Southeast Vatnajökull Ice Cap (Iceland) 1650–1900 and Reconstruction of the Glacier Surface Geometry at the Little Ice Age Maximum.” *Geografiska Annaler: Series A, Physical Geography*, vol. 97, no. 2, 2015, pp. 237–264., doi:10.1111/geoa.12064.
- Hooke, Roger LeB. *Principles of Glacier Mechanics*. Cambridge University Press, 2020.
- Immerzeel, W. W., et al. “Climate Change Will Affect the Asian Water Towers.” *Science*, vol. 328, no. 5984, 2010, pp. 1382–1385., doi:10.1126/science.1183188.
- Jackson, M. *The Secret Lives of Glaciers*. Green Writers Press, 2019.
- Koontz, Lynne, and Catherine Cullinane Thomas. “Estimating Visitor Use and Economic Contributions of National Park Visitor Spending.” *Valuing U.S. National Parks and Programs*, 2019, pp. 45–57., doi:10.4324/9781351055789-3.
- Kraaijenbrink, P. D., et al. “Impact of a Global Temperature Rise of 1.5 Degrees Celsius on Asia’s Glaciers.” *Nature*, vol. 549, no. 7671, 2017, pp. 257–260., doi:10.1038/nature23878.
- Kulp, Scott A., and Benjamin H. Strauss. “New Elevation Data Triple Estimates of Global Vulnerability to Sea-Level Rise and Coastal Flooding.” *Nature Communications*, vol. 10, no. 1, 2019, doi:10.1038/s41467-019-12808-z.
- Lemelin, Harvey, et al. “Last-Chance Tourism: the Boom, Doom, and Gloom of Visiting Vanishing Destinations.” *Current Issues in Tourism*, vol. 13, no. 5, 2010, pp. 477–493., doi:10.1080/13683500903406367.
- Lutz, A. F., et al. “Consistent Increase in High Asia’s Runoff Due to Increasing Glacier Melt and Precipitation.” *Nature Climate Change*, vol. 4, no. 7, 2014, pp. 587–592., doi:10.1038/nclimate2237.
- Marzeion, Ben, et al. “Partitioning the Uncertainty of Ensemble Projections of Global Glacier Mass Change.” 2020, doi:10.5194/egusphere-egu2020-5579.
- Masiha, Niha, and Chris Mooney. “Deadly Floods in India Point to a Looming Climate Emergency in the Himalayas.” *Washington Post*, Feb. 2021.

- Mckinsey, Krista M., et al. "A Revised Chronology of Key Vatnajökull (Iceland) Outlet Glaciers during the Little Ice Age." *Annals of Glaciology*, vol. 42, 2005, pp. 171–179., doi:10.3189/172756405781812817.
- Meier, M. F., et al. "Glaciers Dominate Eustatic Sea-Level Rise in the 21st Century." *Science*, vol. 317, no. 5841, 2007, pp. 1064–1067., doi:10.1126/science.1143906.
- Milner, Alexander M., et al. "Glacier Shrinkage Driving Global Changes in Downstream Systems." *Proceedings of the National Academy of Sciences*, vol. 114, no. 37, 2017, pp. 9770–9778., doi:10.1073/pnas.1619807114.
- Muir, John. "Living Glaciers of California." *Harpers New Monthly Magazine*, 1875.
- Murphy, Ryan D., "Modeling the Effects of Forecasted Climate Change and Glacier Recession on Late Summer Streamflow in the Upper Nooksack River Basin" (2016). *WWU Graduate School Collection*. 461. <https://cedar.wwu.edu/wwuet/461>
- O'Hare, Greg. "Updating Our Understanding of Climate Change in the North Atlantic: the Role of Global Warming and the Gulf Stream." *Geography*, vol. 96, no. 1, 2011, pp. 5–15., doi:10.1080/00167487.2011.12094303.
- Pelto, Mauri, and Courtenay Brown. "Mass Balance Loss of Mount Baker, Washington Glaciers 1990-2010." *Hydrological Processes*, vol. 26, no. 17, 2012, pp. 2601–2607., doi:10.1002/hyp.9453.
- Purdie, Heather. "Glacier Retreat and Tourism: Insights from New Zealand." *Mountain Research and Development*, vol. 33, no. 4, 2013, pp. 463–472., doi:10.1659/mrd-journal-d-12-00073.1.
- Racoviteanu, Adina E., et al. "Evaluation of an Ice Ablation Model to Estimate the Contribution of Melting Glacier Ice to Annual Discharge in the Nepal Himalaya." *Water Resources Research*, vol. 49, no. 9, 2013, pp. 5117–5133., doi:10.1002/wrcr.20370.
- Rafferty, John P., "Little Ice Age" *Encyclopaedia Britannica*, 2011
- Rignot, E., et al. "Acceleration of the Contribution of the Greenland and Antarctic Ice Sheets to Sea Level Rise." *Geophysical Research Letters*, vol. 38, no. 5, 2011, doi:10.1029/2011gl046583.

- Robbins, Jim. "How Long Before These Salmon Are Gone? 'Maybe 20 Years.'" *New York Times*, Sept. 2019, www.nytimes.com/2019/09/16/science/chinook-salmon-columbia.html.
- Scambos, T. A. "Glacier Acceleration and Thinning after Ice Shelf Collapse in the Larsen B Embayment, Antarctica." *Geophysical Research Letters*, vol. 31, no. 18, 2004, doi:10.1029/2004gl020670.
- Schomacker, Anders. "Expansion of Ice-Marginal Lakes at the Vatnajökull Ice Cap, Iceland, from 1999 to 2009." *Geomorphology*, vol. 119, no. 3-4, 2010, pp. 232–236., doi:10.1016/j.geomorph.2010.03.022.
- Scott, Christopher A., et al. "Water in the Hindu Kush Himalaya." *The Hindu Kush Himalaya Assessment*, 2019, pp. 257–299., doi:10.1007/978-3-319-92288-1\_8.
- Sharma, Bharat, et al. "The Indus and the Ganges: River Basins under Extreme Pressure." *Water International*, vol. 35, no. 5, 2010, pp. 493–521., doi:10.1080/02508060.2010.512996.
- Shi, Lei, et al. "Multichannel Coherent Radar Depth Sounder for NASA Operation Ice Bridge." *2010 IEEE International Geoscience and Remote Sensing Symposium*, 2010, doi:10.1109/igarss.2010.5649518.
- Shijin, Wang, and Qin Dahe. "Mountain Inhabitants' Perspectives on Climate Change, and Its Impacts and Adaptation Based on Temporal and Spatial Characteristics Analysis: a Case Study of Mt. Yulong Snow, Southeastern Tibetan Plateau." *Environmental Hazards*, vol. 14, no. 2, 2015, pp. 122–136., doi:10.1080/17477891.2014.1003776.
- Stock, G., et al. "Retreat and Stagnation of Little Ice Age Glaciers in Yosemite National Park." *American Geophysical Union*, 2016.
- Swindles, Graeme T., et al. "Climatic Control on Icelandic Volcanic Activity during the Mid-Holocene." *Geology*, vol. 46, no. 1, 2017, pp. 47–50., doi:10.1130/g39633.1.
- Vandeberg, G. S., and J. A. VanLooy. "Continental Glacier Meltwater Contributions to Late Summer Stream Flow and Water Quality in the Northern Wind River Range, Wyoming, USA." *Environmental Earth Sciences*, vol. 75, no. 5, 2016, doi:10.1007/s12665-016-5295-0.

VanLooy, Jeffrey A., and Gregory S. Vandeberg. "Late Summer Glacial Meltwater Contributions to Bull Lake Creek Stream Flow and Water Quality, Wind River Range, Wyoming, USA." *Physical Geography*, vol. 40, no. 5, 2019, pp. 461–480., doi:10.1080/02723646.2019.1565215.

Watto, Muhammad Arif, and Amin William Mugera. "Groundwater Depletion in the Indus Plains of Pakistan: Imperatives, Repercussions and Management Issues." *International Journal of River Basin Management*, vol. 14, no. 4, 2016, pp. 447–458., doi:10.1080/15715124.2016.1204154.

Welling, Johannes, et al. "Implications of Climate Change on Nature-Based Tourism Demand: A Segmentation Analysis of Glacier Site Visitors in Southeast Iceland." *Sustainability*, vol. 12, no. 13, 2020, p. 5338., doi:10.3390/su12135338.

Wood, Leah R., et al. "Melting Himalayan Glaciers Threaten Domestic Water Resources in the Mount Everest Region, Nepal." *Frontiers in Earth Science*, vol. 8, 2020, doi:10.3389/feart.2020.00128.

Zhang, Leilei, et al. "Discharge Regime and Simulation for the Upstream of Major Rivers over Tibetan Plateau." *Journal of Geophysical Research: Atmospheres*, vol. 118, no. 15, 2013, pp. 8500–8518., doi:10.1002/jgrd.50665.